



HAL
open science

ACCREDITATION TO SUPERVISE RESEARCH
Deformation mechanisms, fluid circulation and fluid rock
interaction processes within geological domains affected
by deformation gradients. Insights on reservoir
analogues understanding by means of a multidisciplinary
approach

Ghislain Trullenque

► **To cite this version:**

Ghislain Trullenque. ACCREDITATION TO SUPERVISE RESEARCH Deformation mechanisms, fluid circulation and fluid rock interaction processes within geological domains affected by deformation gradients. Insights on reservoir analogues understanding by means of a multidisciplinary approach. Earth Sciences. UPJV, 2023. tel-04166899

HAL Id: tel-04166899

<https://hal.science/tel-04166899>

Submitted on 20 Jul 2023

HAL is a multi-disciplinary open access archive for the deposit and dissemination of scientific research documents, whether they are published or not. The documents may come from teaching and research institutions in France or abroad, or from public or private research centers.

L'archive ouverte pluridisciplinaire **HAL**, est destinée au dépôt et à la diffusion de documents scientifiques de niveau recherche, publiés ou non, émanant des établissements d'enseignement et de recherche français ou étrangers, des laboratoires publics ou privés.

ACCREDITATION TO SUPERVISE RESEARCH

Deformation mechanisms, fluid circulation and fluid rock interaction processes within geological domains affected by deformation gradients. Insights on reservoir analogues understanding by means of a multidisciplinary approach

Dr. Trullenque Ghislain

Thesis presented on June 9th 2023 at École Doctorale
Sciences technologie et santé

Université de Picardie Jules Vernes, ED 585

Committee:

Mr. Sass Ingo (Professor, GFZ Potsdam, Germany) – Reviewer and president of the committee

Mr. Bruhn David (Professor, TU Delft, The Netherlands) – Reviewer

Mr. Moscariello Andrea (Professor, Geneva University, Switzerland) – Reviewer

Mrs. Schill Eva (Professor, TU Darmstadt, Germany) – Examiner

Mrs. Falcone Gioia (Professor, Glasgow University, United Kingdom) – Examiner

Mr. Liotta Domenico (Doctor HDR, Bari University, Italy) – Examiner

Mr. Potel Sébastien (Doctor HDR, UniLaSalle, France) - Mentor

Préambule

Je ne vais pas débiter ce mémoire comme cela se fait habituellement, à savoir par une belle citation que j'aurais entendue quelque part sans retenir le nom de son auteur ou prise au hasard dans un livre que je n'aurais pas lu. Je ne vais pas dédier ce manuscrit à une ou plusieurs personnes. J'ai certes mis tous mes efforts, toute ma patience ainsi que toute mon application à la rédaction des pages qui vont suivre, mais comme tout travail de recherche, celui-ci se veut incomplet, perfectible et soumis à la critique. Les proches à qui je pense en ce moment méritent bien mieux. Je ne vais pas non plus remercier mes amis car mieux vaut être reconnaissant au hasard qui lui seul m'a permis de les rencontrer.

Que dire alors ? Je vous propose quelque chose d'essentiel.

Je viens d'évoquer le hasard. Ce dernier fait parfois bien les choses surtout lorsqu'il vous donne la chance de ne point écouter les paroles de certains Professeurs, je devrais plutôt dire « certains enseignants » des Classes Préparatoires aux Grandes Ecoles. Dans le contexte d'une habilitation, faire référence à des personnes pour qui la recherche est une discipline étrange, et par-dessus tout étrangère, peut paraître hors propos. Cela est toutefois loin d'être le cas à mes yeux. Pour une raison connue d'eux seuls, bon nombre de mes « enseignants » ont décidé de tout mettre en œuvre afin de sortir du système éducatif la jeune personne que j'étais alors, plus tout à fait un enfant mais loin encore d'être un adulte. Mesdames et Messieurs, je me demande encore aujourd'hui comment vous êtes arrivés en quelques jours à juger de mes capacités. Comment osez-vous réserver vos leçons et votre aide à un étudiant plutôt qu'à un autre ? De quel droit vous permettez-vous de me tourner le dos quand je ne comprends pas l'énoncé d'un exercice alors que vous-même n'auriez pas su le résoudre sans vos fiches explicatives ? Mesdames et Messieurs, je suis aujourd'hui plus qu'à même de juger votre travail. Il m'est utile au quotidien au poste d'enseignant chercheur que j'occupe depuis dix ans maintenant, ironie du sort, dans une Grande Ecole d'ingénieurs. Il est le plus bel exemple de médiocrité que j'ai connu et je vous renvoie à l'apprentissage des principes fondamentaux de l'enseignement. Ces derniers vous ont clairement échappé et je me demande comment dans de telles conditions vous pouvez prétendre former, je vous cite, la « future élite de la Nation ».

Je tiens maintenant à m'adresser à tous mes jeunes étudiants pleins de bonne volonté. Je le sais et je l'assume, je suis souvent dur avec vous mais vous m'avez tôt ou tard toujours remercié de vous avoir donné l'envie d'apprendre. N'acceptez jamais les attitudes que je viens de décrire, ne laissez pas de telles

personnes vous lancer au visage que vous n'êtes pas faits pour continuer dans la voie que vous avez choisie. Soyez sourds à ces misérables discours. La vocation et l'envie sont les clés du succès que je partage avec vous aujourd'hui. Si mes travaux sont d'une quelconque utilité, je souhaite qu'ils le soient d'abord pour vous et peut être en prendrez-vous un jour le relai.

Pour terminer, Mesdames et Messieurs mes « enseignants » des Classes Préparatoires aux Grandes Ecoles, j'imagine que vous n'allez pas apprécier la lecture de ces lignes. Soyez certains que je vous aime encore moins.

Content

1	Curriculum vitae	10
1.1	Professional experience.....	10
1.2	Higher education.....	10
1.3	Language, computer practice and received training	11
1.3.1	Languages	11
1.3.2	Computer practice.....	11
1.3.3	Received training	11
1.4	Memberships.....	12
1.5	Qualifications.....	12
1.6	PhD Thesis supervision.....	12
1.7	Hierarchical responsibilities.....	12
1.8	Scientific sessions organization	13
1.9	Scientific reviewer	13
1.10	Projects funding	13
1.10.1	EUTOPIA PhD program 2021	13
1.10.2	ERASMUS+ Strategic partnership	13
1.10.3	H2020-LCE-2016-2017 / H2020-LCE-2017-RES-IA program	13
1.10.4	Metchnikov program, researcher mobility (2017 call).....	14
1.10.5	Office Franco-Allemand pour la Jeunesse (OFAJ) grant.....	14
1.11	Scientific publication record	14
1.11.1	A ranking publication.....	14
1.11.2	Book chapters.....	15
1.11.3	Extended abstracts.....	16
1.11.4	Oral communications	17
1.11.5	Posters	18
1.12	Analytical facilities responsible	19
1.12.1	UniLaSalle	19
1.12.2	Albert Ludwig University (Freiburg im Breisgau, Germany, 2011-2013)	19
1.12.3	Oxford Instruments Nano analysis GmbH (Wiesbaden, Germany, 2008 -2011)	19
1.12.4	Johannes Gutenberg University (Mainz, Germany, 2005-2007)	19

1.12.5	University of Basel (Switzerland, 2001-2004).....	19
2	Career summary and motivation	20
3	Research activities in the framework of academic training	21
3.1	Diplôme d’Etudes Approfondies (DEA).....	21
3.2	PhD thesis	39
4	Research activities in the framework of professional experience	84
4.1	Training mobility	84
4.2	Research assistant at Johannes Gutenberg University	86
4.3	Application specialist at Oxford Instruments Nanoanalysis GmbH	91
4.4	Assistant Professor at Albert Ludwig University.....	117
4.5	Structural geologist at UniLaSalle	142
4.5.1	The choice of a candidature at UniLaSalle	142
4.5.2	The choice of geothermal plus carbon capture and storage	143
4.5.3	Research activities.....	146
5	Summary of supervision and teaching activities.....	390
5.1	Supervision	390
5.1.1	Mentoring of Early Stage Researchers.....	390
5.1.2	PhD supervision	390
5.1.3	Master thesis, UniLaSalle (France).....	391
5.1.4	5 th year Engineering graduation thesis, UniLaSalle (France)	391
5.1.5	4 th year Engineering project, UniLaSalle (France).....	392
5.1.6	3 rd year engineering project, UniLaSalle (France)	392
5.1.7	3 rd year apprentice project, UniLaSalle (France)	392
5.1.8	Technician application project, UniLaSalle (France)	393
5.1.9	Bachelor thesis, University of Freiburg im Breisgau (Germany)	393
5.2	Teaching activities	393
5.2.1	UniLaSalle (France) (2013- 2022).....	393
5.2.2	University of Freiburg im Breisgau (Germany) (2011-2013).....	403
5.2.3	University of Mainz (Germany) (2005-2007).....	404
5.2.4	University of Basel (Switzerland) (2001-2004).....	404
6	Perspectives.....	405
6.1	Research perspectives	405

6.1.1	Microfabric analysis of inherited magmatic foliations and their role in the guidance of fractures upon loading.....	405
6.1.2	Microfabric analysis of strained reaction-induced alteration products. Mechanical and petrophysical properties evolution of fault zones	425
6.1.3	Coupled stress, strain and flow simulations.....	428
6.2	Teaching perspectives.....	429
6.3	Future projects	430
6.3.1	The MININGHEAT project.....	430
6.3.2	The GEMINI project.....	431
7	Conclusions.....	432
8	Résumé.....	433
9	Abstract.....	434
10	References.....	435
11	Appendices.....	452

List of illustrations

Figure 1:	Overview of the four MEET demonstration sites within Variscan reservoirs (after Trullenque et al. 2018).	148
Figure 2:	Overview of the European Cenozoic Rift System (ECRIS). Graphic illustration by Christian Röhr (https://www.oberrheingraben.de/index.htm).	149
Figure 3:	Variscan tectonic framework of ECRIS (redrawn after Ziegler and Dèzes, 2005).	150
Figure 4:	Geodynamic evolution along the AA' transect in figure 3 (redrawn after Ziegler and Dèzes, 2005).	151
Figure 5:	Structural sketch map of Variscan structures in western Europe (redrawn after Edel and Weber, 1995).	152
Figure 6:	Structural scheme of Variscan domain in French Massif Central (redrawn after Thiery et al., 2009).	153
Figure 7:	a) structural scheme of the west European Variscan domain, b) structural map of the Upper Rhine Graben area with extrapolated geophysical data (redrawn after Edel et al., 2007).....	154
Figure 8:	First vertical derivation of the magnetic anomaly (redrawn after Edel et al., 2007).	155
Figure 9:	a) large scale structural map of western USA (Norton, 2011), b) Simplified structural scheme of the Death Valley area and localization of the NH (redrawn from Burchfiel and Stewart, 1966), c) pull-apart schematic representation of the Death valley area and localization of the NH range (redrawn from Burchfiel and Stewart, 1966).	157

Figure 10: NH satellite image with inserts showing dextral transcurrent deformation at the front of the range (figure taken from Klee et al., 2021a).....	364
Figure 11: a) fracture traces found within the NH and subdivision of the range in three domains, b) orientation distributions, c) geological interpretation showing that NW-SE fractures are overprinted by the E-W fracture set (figures taken from Chabani et al., 2021b).	365
Figure 12: Cross-section at the frontal part of the Noble Hills range (simplified after Niles, 2016).....	366
Figure 13: Geological map of the Upper Rhine Graben area (Voges et al., 2004).	369
Figure 14: Simplified geological map around the Schauinsland massif (after Werner et al., 2004).	370
Figure 15: Geological reconstruction of the Freiamt – Sexau mining district (figure translated from Werner and Franzke, 2001).....	371
Figure 16: Geological reconstruction of the Schauinsland mining district (figure translated from Werner et al., 2004).	372
Figure 17: Structural map and stress-field reconstruction within the Schauinsland mining district. Dextral offset of the CRZSR by ore vein Gang III is depicted (figure translated from Werner et al., 2004).....	373
Figure 18: Schematic representation from the CRZSR a) at outcrop scale, b) hand specimen (figure translated from Werner et al., 2004).	374
Figure 19: High resolution mapping of ore vein Gang VI (figure translated from Werner et al., 2004).	375
Figure 20: Detailed structural mapping showing dextral offset of the CRZSR, related to emplacement of ore vein Gang III. (figure translated from Werner et al., 2004). See position in figure 17.....	376
Figure 21: a) ore vein deviation when approaching the contact with an inherited high strain zone (figure redrawn after Klee, 2021), b) zoom on the termination of ore vein Gang VI (Werner et al., 2004), note the similar apparent drag and vein thinning.....	377
Figure 22: Conceptual model showing the observed interactions between late ore veins and a) inherited CRZ, b) high strain zones (inspired from Klee, 2021).....	378
Figure 23: a) location and geological framework of the Luconia province, b) zoom on the EX platform (after Jamaludin et al., 2021).	387
Figure 24: a) SW-NE seismic line from SW and central Luconia (Cullen, 2014), b) and c) high resolution seismic record and interpretation of platform EX (Jamaludin et al., 2021).	388
Figure 25: a) thin section overview, b) and c) fracture mapping and orientation from an experimentally deformed sample presented in Trullenque et al., 2017).	406
Figure 26: a) outline of the main diagonal clinopyroxene GSPO, b) fracture pattern (after Trullenque et al., 2017).	407
Figure 27: a) localization of the Odenwald massif within the URG, b) simplified geological map from the Odenwald massif (Trullenque et al., 2017), c) AMS distribution (data from Greiling and Verma, 2001).	408
Figure 28: a) clay fabric elements evolution during increasing strain (redrawn after Haines et al., 2013), b) representative (001) pole figure from experimentally deformed samples in compression and shear (Haines et al., 2009). Shear plane terminology according to Chester et al. (1985).	426

Figure 29: a) interpretation of an experimentally produced clay shear zone (Haines et al., 2013), b) note the striking similarity with field sampled taken along the CRZSR (modified after Werner et al., 2004). 427

List of acronyms

AMS: Anisotropy of Magnetic Susceptibility

BFM: Black Forest Massif

CCS: Carbon Capture and Storage

CPO: Crystallographic Preferred Orientation

DFN: Discrete Fracture Network

NH: Noble Hills

CRSS: Critical Resolved Shear Stress

CRZ: Clay Rich Zone

CRZSR: Clay Rich Zone Schumacher Ruschel

DV: Death Valley

EBSD: Electron Back Scattered Diffraction

EDS: Energy Dispersive Spectrometry

ESR: Early Stage Researcher

EGS: Enhanced Geothermal System

EMJD: Erasmus Mundus Joint Degree

GFZ: Garlock Fault Zone

GG: Gabe Gottes

GSPO: Grain Shape Preferred Orientation

ISP: Intensive Study Program

NFCR: Naturally Fractured Carbonate Reservoirs

RH: Rittershoffen

RS: Riedel Shear

RT: Roselend Thrust

SDVFZ: Southern Death Valley Fault Zone

SEM: Scanning electron Microscope

SHF: Sillon Houiller Fault

SSF: Soultz sous Forêts

TEM: Transmission Electron Microscopy

THM: Thermo Hydro Mechanical

THMC: Thermo Hydro Mechanical Chemical

URG: Upper Rhine Graben

URGSZ: Upper Rhine Graben Shear Zone

VM: Vosges Massif

WDS: Wavelength Dispersive Spectrometry

FRAPPE: Fonds Régional d'Aide aux Porteurs de Projets Européens

GEMINI project: GeothErMal EngINeerIng

Geo3EN project: Geothermal Engineering European Education Network

MEET project: Multidisciplinary and multi-context demonstration of EGS exploration and Exploitation Techniques and potentials

1 Curriculum vitae

Dr. Trullenque Ghislain

Structural geologist

email: ghislain.trullenque@unilasalle.fr

Institut Polytechnique UniLaSalle

French, 1 child

19 rue Pierre Waguet

Born on April, 30th 1976 in Perpignan

60026 Beauvais, France

(Pyrénées Orientales, Occitanie, France)

1.1 Professional experience

Since 2013: Structural geologist.

Institut Polytechnique UniLaSalle, Beauvais, France.

2011-2013: Assistant Professor.

Albert Ludwig University, Freiburg im Breisgau, Germany.

2008-2011: Application specialist.

Oxford Instruments Nanoanalysis GmbH, Wiesbaden, Germany.

2006-2008: Research assistant.

Johannes Gutenberg University, Mainz, Germany.

2005-2006: Training mobility.

International research plus training program at rock mineral physics laboratory, University of Minnesota Twin Cities campus, Minneapolis (USA) and high pressure and temperature laboratory, University of Utrecht (The Netherlands).

1.2 Higher education

2000-2005: PhD thesis. (Magna cum Laude grade).

Institute of geology and paleontology, UniBasel, Basel, Switzerland.

Subject: Tectonic and microfabric studies along the Penninic Front and within the Dauphinois domain between Pelvoux and Argentera massifs (western Alps, France).

Thesis director: Professor S.M. Schmid.

1999-2000: Diplôme d'Etudes Approfondies.

Laboratory of Geophysics, Tectonics and Sedimentology, Sciences et techniques du Languedoc University (Montpellier II), Montpellier, France.

Subject: Consequences of continental subduction on forearc basin and accretionary wedge deformation in SE Taiwan: insights from analogue modelling.

Supervisor: Prof. J. Malavieille.

- 1998-1999: Geophysics and Geochemistry Master degree
Paul Sabatier University, Toulouse, France.
Master Thesis: Host rock alteration facies analysis and polyphase silica saturated brines circulations: insights from ore deposits within the Bourneix district (Limousin, France).
Supervisor: Dr. F. Tollon.
- 1997-1998: Earth Sciences Bachelor degree.
Paul Sabatier University, Toulouse, France.
- 1995-1997: Diplôme d'Etudes Universitaires Générales.
Via Domitia University, Perpignan, France.
- 1995: Classe préparatoire aux grandes écoles.
Joffre Highschool, Montpellier, France.
- 1994: Baccalauréat C.

1.3 Language, computer practice and received training

1.3.1 Languages

English, German and Spanish: read, written and spoken.

Catalan: read and spoken.

Russian: beginner.

1.3.2 Computer practice

Operating systems: Mac OS, Windows, UNIX.

Reservoir modeling software: MOVE.

Geographic Information Systems software: QGIS, ARCGIS, MOVE.

Crystallographic Preferred Orientation analysis software: AZTEK, INCA CRYSTAL, FLAMENCO, TANGO, MAMBO, SALSA, MTEX, BEARTEX.

Energy Dispersive Spectrometry and Wavelength Dispersive Spectrometry: INCA.

Office and design software: Microsoft, Adobe suite, OpenOffice, INKSCAPE, GIMP.

1.3.3 Received training

Hoisting equipment operator.

First aid at work.

1.4 Memberships

Member of the géologues du Sud-Ouest association.

Member of the Géosciences 66 association.

Administration council member of Association Française des Professionnels de la Géothermie. 19 rue Claude Bernard, Paris, France.

1.5 Qualifications

2007: Maître de conférences qualification. Section 35: Earth and other planets structure and evolution.

2007: Maître de conférences qualification. Section 36: Solid earth, external envelopes geodynamics, paleo-biosphere.

1.6 PhD Thesis supervision

Mr. Avakian Benjamin

PhD Thesis started on November 1st, 2021. Thesis duration: 48 months.

Subject: Fluid circulation within shear zones affecting granitic bodies. Geothermal energy production applications.

Science and engineering Doctoral school ED SI n° 417, CY University (France).

Mrs. Poh Yee Ong

PhD Thesis started on July 1st, 2021. Thesis duration: 36 months.

Subject: CO₂ storage potential in fractured carbonate reservoir via thermo-hydro-mechanical-chemical (THMC) simulations.

Institute of Hydrocarbon Recovery (IHR) / Southeast Asia Carbonate Clastic Research Laboratory (SEACaRL), Universiti Teknologi Petronas (Malaysia).

Dr. Klee Johanne

PhD defense on November 26th, 2021. Thesis duration 37 months.

Subject: Influence of fluid-rock interaction processes and strain on strike-slip zones properties: an analogue-based multidisciplinary approach. Fractured granitic geothermal reservoirs applications.

EDSTS 585 Doctoral school – Sciences, technology and health, Picardie Jules Vernes University (France).

1.7 Hierarchical responsibilities

Research engineer, fixed term position (September 2021 – January 2022).

Communication assistant, fixed term position (March 2019 - October 2020).

1.8 Scientific sessions organization

Excursion guide book chapter. Joint Cordilleran – Rocky Mountain section, FT 14 Unraveling the Multi-Phase History of Southern Death Valley Geology. Geological Society of America, 15-17 Mars 2022. Las Vegas, Nevada, USA.

Chairman: World Geothermal Congress Reykjavik 2021, session 21B Geology 12. Reykjavik, Iceland.

Chairman: Akademie für Elektronenmikroskopie und Analytik gemeinnützige GmbH 2009, Münster, Allemagne.

1.9 Scientific reviewer

Geosciences.

Journal of Structural Geology.

IFREMER scientific projects evaluator.

Co-editor Geosciences journal special issue: “Enhanced Geothermal Systems and other Deep Geothermal Applications throughout Europe: The MEET Project”.

1.10 Projects funding

1.10.1 EUTOPIA PhD program 2021

PhD thesis Erasmus+ grant, EUTOPIA European Universities pilot project.

ID: EUTOPIA-PhD-2021-000000111

Subject: Fluid circulation within shear zones affecting granitic bodies. Geothermal energy production applications.

PhD thesis co-supervisor.

1.10.2 ERASMUS+ Strategic partnership

Call 2019 Round 1 KA2 – Cooperation for innovation and the exchange of good practices. KA203 – Strategic Partnerships for higher education.

Geo3En project (Geothermal Energy European Education Network).

FRAPPE (Fonds Régionaux d’Aide aux Porteurs de Projets Européens) Hauts de France grant.

Project coordinator.

1.10.3 H2020-LCE-2016-2017 / H2020-LCE-2017-RES-IA program

EGS in different geological conditions.

MEET project (Multidisciplinary and multi-context demonstration of EGS exploration and Exploitation Techniques and potentials).

FRAPPE (Fonds Régionaux d’Aide aux Porteurs de Projets Européens) Hauts de France grant.

Project scientific coordinator.

PhD thesis co-supervisor.

1.10.4 Metchnikov program, researcher mobility (2017 call)

Exchange mobility grant obtained from French embassy in Russia. Visit of Dr. Alfimova (Precambrian research center, St. Petersburg University, Russia) to Institut Polytechnique UniLaSalle, Beauvais campus, France.

Research theme: Insights gained by a combination of Electron Back Scattered Diffraction analysis and RAMAN spectroscopy in the understanding of weathering processes of Zircon crystals.

1.10.5 Office Franco-Allemand pour la Jeunesse (OFAJ) grant

Grant n° 2014-11-1 (2014) Workshop Grand Est: géologie du Bassin de Paris et du Bassin de la Saar.

Grant dedicated to field excursion funding for 18 German students from Freiburg im Breisgau University and 17 French students from Institut Polytechnique LaSalle Beauvais.

Project coordinator.

1.11 Scientific publication record

1.11.1 A ranking publication

Fracture spacing variability and the distribution of fracture patterns in granitic geothermal reservoir: a case study in the Noble Hills range (Death Valley, CA, USA). Chabani A., **Trullenque G.**, Klee J., Ledésert B.A. *Geosciences* 11 (12), 520, 2021. <https://doi.org/10.3390/geosciences11120520>

Fluid-rock interactions in a paleo-geothermal reservoir (Noble Hills granite, California, USA). Part 2: the influence of fracturing on granite alteration processes and fluid circulation at low to moderate regional strain. Klee J., Chabani A., Ledésert B.A., Potel S., Hébert R., **Trullenque G.** *Geosciences* 11 (11), 433, 2021. <https://doi.org/10.3390/geosciences11110433>

Fluid-rock interactions in a paleo-geothermal reservoir (Noble Hills granite, California, USA). Part 1: granite pervasive alteration processes away from fracture zones. Klee J., Potel S., Ledésert B.A., Hébert R., Chabani A., Barrier P., **Trullenque G.** *Geosciences* 11 (8), 325, 2021. <https://doi.org/10.3390/geosciences11080325>

Multiscale characterization of fracture patterns: a case study of the Noble Hills range (Death Valley, CA, USA), application to geothermal reservoirs. Chabani A., **Trullenque G.**, Ledésert B.A., Klee J. *Geosciences* 11 (7), 280, 2021. <https://doi.org/10.3390/geosciences11070280>

Scaling in a geothermal heat exchanger at Soultz-sous-forêts (upper Rhine graben, France): a XRD and SEM-EDS characterization of sulfide precipitates. Ledésert B.A., Hébert R., Mouchot J., Bosia C., Ravier G., Seibel O., Dalmais E., Ledésert M., **Trullenque G.**, Sengelen X., Genter A. *Geosciences* 11 (7), 271, 2021. <https://doi.org/10.3390/geosciences11070271>

Evidence for 40–41 km of dextral slip on the southern Death Valley fault: implications for the eastern California shear zone and extensional tectonics. Pavlis T.L., **Trullenque G.** *Geology* 49 (7), 767-772, 2020. <https://doi.org/10.1130/G48528.1>

Multiple-criteria decision-making for assessing the enhanced geothermal systems. Raos S., Ilak P., Rajšl I., Bilić T., **Trullenque G.** *Energies* 12 (9), 1597, 2019. <https://doi.org/10.3390/en12091597>

Substitution-induced internal strain and high disorder in weakly radiation damaged hydrothermal zircon from mt. Malosa, Malawi. Kempe U., **Trullenque G.**, Thomas R., Sergeev S., Presnyakov S. *European journal of mineralogy* 30 (4), 659-679, 2018. <https://doi.org/10.1127/ejm/2018/0030-2739>

High pressure phase transitions of alpha quartz under non-hydrostatic dynamic conditions: a reconnaissance study at PETRA III. Carl E.V., Mansfeld U., Liermann H.P., Danilewsky A., Langenhorst F., Ehm L., **Trullenque G.**, Kenkmann T. *Meteoritics and planetary science* 52, 2017. <https://doi.org/10.1111/maps.12840>

Properties of a pair of fracture networks produced by triaxial deformation experiments: insights on fluid flow using discrete fracture network models. **Trullenque G.**, Parashar R., Delcourt C., Collet L., Villard P., Potel S. *Hydrogeology journal* 25 (3), 813-827, 2017. <https://doi.org/10.1007/s10040-016-1468-x>

Reliability of very low-grade metamorphic methods to decipher basin evolution: case study from the Markstein basin (southern Vosges, NE France). Potel S., Maison T., Maillet M., Sarr A.C, Doublier M.P., **Trullenque G.**, Ferreira Mählmann R. *Applied clay minerals* (134) 2016. <https://doi.org/10.1016/j.clay.2016.10.003>

Deformation and melting of steel projectiles in hypervelocity cratering experiments. Kenkmann T., **Trullenque G.**, Deutsch A., Hecht L., Ebert M., Salge T., Schäfer F., Thoma K. *Meteoritics & planetary science* 48, no.1, pp.150-164, 2013. <https://doi.org/10.1111/maps.12018>

Very low-grade metamorphism in the para-autochthonous sedimentary cover of the Pelvoux massif (western Alps, France). Potel S., **Trullenque G.** *Swiss journal of geosciences*, 105, 235-247, 2012. <https://doi.org/10.1007/s00015-012-0102-8>

Electron back-scattering diffraction (EBSD) measurements of antigorite lattice-preferred orientations (LPO). Van de Moortele B., Bezacier L., **Trullenque G.**, Reynard B. *Journal of microscopy*, volume 239, issue 3, pages 245-248, 2010. <https://doi.org/10.1111/j.1365-2818.2010.03398.x>

Consequences of continental subduction on forearc basin and accretionary wedge deformation in SE Taiwan: insights from analogue modelling. Malavieille J., **Trullenque G.** *Tectonophysics*, volume 466, issues 3-4, p.377-394, 2009. <https://doi.org/10.1016/j.tecto.2007.11.016>

Effects of irradiation damage on the back-scattering of electrons, silicon-implanted silicon. Nasdala L., Kronz A., Grambole D., **Trullenque G.** *American mineralogist*, volume 92, p.1768-1771, 2007. <https://doi.org/10.2138/am.2007.2648>

Microfabrics of calcite ultramylonites as records of coaxial and non-coaxial deformation kinematics: examples from the rocher de l'Yret shear zone (western Alps). **Trullenque G.**, Kunze K., Heilbronner R., Stünitz H., Schmid S.M. *Tectonophysics*, volume 424, issues 1-2, p.69-97, 2006. <https://doi.org/10.1016/j.tecto.2006.06.004>

1.11.2 Book chapters

Editorial of Special Issue “Enhanced Geothermal Systems and Other Deep Geothermal Applications throughout Europe: The MEET Project”. Ledésert B.A., Hébert R., **Trullenque G.**, Genter A., Dalmais E., Hérisson J. *Geosciences* 12 (9), 341, 2022. <https://doi.org/10.3390/geosciences12090341>

Unraveling the multi-phase history of southern Death Valley geology. Fleming Z., Pavlis T.L, **Trullenque G.** In *Field Excursions from Las Vegas, Nevada: Guides to the 2022 GSA Cordilleran and Rocky Mountain Joint Section Meeting*, Vol. 63, p. 67, 2022. [https://doi.org/10.1130/2022.0063\(04\)](https://doi.org/10.1130/2022.0063(04))

1.11.3 Extended abstracts

Newson, J.A., **Trullenque, G.**, Bossenec, C., Sass, I., Šadek, S., Gautason, B., Greene, R.M. Graduate Geothermal training in the European Economic Area. Proceedings 44th New Zealand Geothermal Workshop 2022, Auckland, New Zealand.

Muhl, L., Avakian, B., **Trullenque, G.**, Ledésert, B.A. Influence of pre-structuration of a reservoir on permeability evolution in fracture zones. Insights from mechanical testing on an alteration profile. European Geothermal congress 2022, Berlin, Germany.

Avakian, B., Muhl, L., **Trullenque, G.**, Ledésert, B.A., Hebert, R., Claeys, P. The influence of the pre-structuration of a basement reservoir on the permeability of fracture zones. European Geothermal congress 2022, Berlin, Germany.

Dalmais, E., Genter, A., **Trullenque, G.**, Léoutre, E., Leiss, B., Mintsá, A.C., Olafsson, D., Rajšl, I. MEET project: toward large scale deployment of deep geothermal energy in europe. World Geothermal Congress 2020, Reykjavik, Iceland.

Chabani, A., **Trullenque, G.**, Parashar, R., Pomart, A. Attali, R., Sass, I. Modelling of fractured granitic geothermal reservoirs: use of deterministic and stochastic methods in discrete fracture networks and a coupled processes modeling framework. World Geothermal Congress 2020, Reykjavik, Iceland.

Klee, J., **Trullenque, G.**, Ledésert, B., Potel, S., Hébert, R., Genter, A. Petrographic and petrophysic analysis of fractured granites used as an analog of the Soultz-sous-forêts geothermal reservoir: Noble Hills, CA, USA. World Geothermal Congress 2020, Reykjavik, Iceland.

Dalmais, E., Genter, A., **Trullenque, G.**, Léoutre, E., Leiss, B., Wagner, B., Mintsá, A.C., Bär, K., Rajšl, I. Meet project: toward the spreading of EGS across europe. European geothermal congress (EGC) 2019 proceedings.

Raos, S., Ilak, P., Rajšl, I., Bilić, T., **Trullenque, G.** Assessment of enhanced geothermal projects and their optimal long-term usage plans by using the DMS-TOUGE decision-making support tool. European geothermal congress (EGC) 2019 proceedings.

Mintsá, A.C., Leveque, G., Seibel, O., **Trullenque, G.**, Léoutre, E., Marot, M., Ragnarsdóttir, K.R. Meet project: evaluation of electricity production at low temperature in various geothermal contexts, 5th international seminar on orc power systems (ORC 2019).

Leiss, B., Wagner, B., **Trullenque, G.**, Genter, A., Bär, K., Milsch, H., Rybacki, E., Vanbrabant, H., Friedel, C.H. Variscan metasedimentary rocks as target horizon for developing "enhanced geothermal systems" in europe. European geothermal congress (EGC) 2019 proceedings.

Ilak, P., Raos, S., Rajšl, I., Bilić, T., **Trullenque, G.**, Šadek, S., Marušić, A. Economic and environmental assessment of enhanced geothermal systems integration into energy systems: decision-making support tool for optimal usage of geothermal energy. Medpower, 11th Mediterranean conference on power generation, transmission, distribution and energy conversion, 2018.

Leiss, B., Wagner, B., **Trullenque, G.**, Genter, A., Bär, K., Milsch, H., Rybacki, E., Vanbrabant, Y., Friedel, C.H. Characterisation of variscan metasedimentary geothermal reservoirs: implications regarding the development of new "enhanced geothermal systems". Geothermiekongress, Essen, 27.-29. November 2018.

Trullenque, G., Genter, A., Leiss, B., Wagner, B., Bouchet, R., Léoutre, E., Malnar, B., Bär, K., Rajšl, I. Upscaling of EGS in different geological conditions: a European perspective. Proceedings, 43rd workshop on geothermal reservoir engineering Stanford university, Stanford, California, sgp-tr-213, 2018.

Carl, E.R., Danilewsky, A., Liermann, H.P., Mansfeld, U., Langenhorst, F., Ehm, L., **Trullenque, G.**, Kenkmann, T. The behavior of SiO₂ under dynamic compression and decompression in a diamond anvil cell. Bridging the gap III: impact cratering in nature, experiments and modelling, university of Freiburg, Germany, September 21-26, 2015.

Cornillon, S., **Trullenque, G.**, Potel, S., Combaud A., Henk, A., Laux, D. Intérêt de deux Approches géomatiques (SIG et LIDAR terrestre) pour la détermination de champs de contraintes. Cas du pluton granitique de Malsburg (Forêt Noire, Allemagne). SAGEO, Grenoble, France, 2014.

Heinz, C., **Trullenque, G.**, Henk, A. Fracture patterns and geomechanics of fold and thrust structures – input data for a fracture prediction workflow from the southern Pyrenees (Spain). Geofrankfurt, Frankfurt, volume 85, 2014.

Kenkmann, T., Ebert, M., **Trullenque, G.**, Deutsch, A., Hecht, L., Salge, T., Schäfer, F.K., Thoma, K. Deformation and melting of iron-rich projectiles in hypervelocity MEMIN cratering experiments. Meteoritics and planetary science supplement, september 2013.

Kenkmann, T., Poelchau, M.H., **Trullenque, G.**, Hoerth, T., Schäfer, F., Thoma, K., Deutsch, A. Shatter cones formed in a MEMIN impact cratering experiment. 75th annual meteoritical society meeting, 2012.

De Bresser, J.H.P., **Trullenque, G.**, Drury, M.R. Evidence for r <a> slip in calcite. Geophysical Research Abstracts, Vol. 10, EGU 2008 – A – 07521, 2008.

Poelchau, M.H., **Trullenque, G.**, Kenkmann, T. Feather features in quartz: structural and textural insights from first TEM and EBSD measurements. 74th annual meteoritical society meeting, 2011.

Malavieille, J., **Trullenque, G.** Evolution of sedimentary basins at the back side of orogenic wedges developed during subduction of a continental margin under a volcanic arc: insights from the Taiwan orogen and analogue models. Thrust belts and foreland basins, international meeting, rueil-malmaison, December 2005.

Trullenque, G. Tectonic and microfabric studies along the Penninic Front and within the Dauphinois domain between Pelvoux and Argentera massifs (western Alps, France). PhD thesis, Basel, 275p., 2005.

1.11.4 Oral communications

Malnar, B., Genter, A., **Trullenque, G.**, Ragnarsdóttir, K. Productivity increase of EGS plants by means of colder fluid re-injection and ORC use. AAPG GTW workshop “geothermal cross over technologies”, Utrecht, April 17-18, 2018.

Potel, S., Maison, T., Maillet, M., Sarr, A.C., Doublier, M.P., **Trullenque, G.**, Ferreiro Mählmann, F. Reliability of very low-grade metamorphic methods to decipher basin Evolution: case study from the Markstein basin (southern Vosges, NE France). 25ème Réunion des sciences de la terre, Caen, France, 24-28 Octobre 2016.

Trullenque, G., Collet L., Villard, P., Combaud A. Etude des variations de la géométrie d'une zone de fracture expérimentale en fonction de la contrainte différentielle appliquée. 24ème réunion des sciences de la terre, Pau, France. 27-31 octobre 2014.

Cornillon, S., Combaud, A., **Trullenque, G.**, Bain, O., Henk, A., Chalumeau, L., Devos, A., Lejeune, O., Potel, S. Comparaison du contrôle géomorphostructural de réseaux Hydrographiques par traitement automatique sous ARCGIS. Cas des massifs des Vosges et de la Forêt Noire. Conférence francophone ESRI – SIG, Versailles, France, 2014.

Trullenque, G., Kenkmann, T., Stein E. Deformation mechanisms active during catastrophic rock failure: preliminary results. TSK 14, Kiel, Germany, 26/03-01/04 2012.

Trullenque, G., Stünitz, H., Kunze, K., Heilbronner, R., Schmid, S.M. Tectonic and microfabric studies along the penninic front and within the dauphinois domain between Pelvoux and Argentera massifs (western alps, France). 2nd Swiss geoscience meeting, Lausanne, 2004.

Trullenque, G., Ceriani, S., Fügenschuh, B., Schmid, S.M. Polyphase tectonic activity along the penninic front: implications for the evolution of the western Alps. 1st Swiss geoscience meeting, Basel, 2003.

1.11.5 Posters

Klee, J., **Trullenque, G.**, Chabani, A., Potel, S., Ledésert, B., Hébert, R. Characterization of geothermal exploitation window in terms of fracture evolution: results from analogue studies of the southern Death Valley fault zone (CA, USA) and the upper Rhine graben (Germany and France). 12th european geothermal phd days, 2021.

Klee, J., **Trullenque, G.**, Ledesert, B., Potel, S., Hebert, R. Hydrothermal fluid circulation and alteration processes in an analogue of a fractured granitic reservoir (Noble hills range, CA, USA). 11th european geothermal phd days, 2020.

Raos, S., Ilak P., Rajšl, I., Bilić, T., **Trullenque, G.** Assessment of enhanced geothermal projects and their optimal long-term usage plans by using the DMS-TOUGE decision-making support tool. European geothermal congress (EGC) 2019.

Alfimova, N., Klimova, E., Matrenichev, V., Zinger, T., **Trullenque, G.**, 2017. Lithium in low-temperature fluid affected zircons. Paleoproterozoic weathering horizon (Karelia, Baltic shield). 19th EGU General Assembly, EGU2017, Vienna, Austria, 23-28 April 2017.

Kühn, R., **Trullenque, G.**, Douezy, M., Leiss, B. Folding mechanisms and fold kinematics within marble lenses from the axial zone of the eastern Pyrenees deduced from textural and microstructural characterization. TSK16, Bonn, Germany, March 2-6, 2016.

Trullenque, G., Parashar, R., Delcourt, C., Collet, L., Villard, P., Potel, S. Simulation des propriétés hydrauliques d'un réseau de fracture expérimental. Apports de la modélisation numérique par éléments finis. 25eme réunion des sciences de la terre, Caen, France, 24-28 Octobre 2016.

Cornillon, S., **Trullenque, G.**, Combaud A., Potel, S., Henk, A., Laux, D., 2014. Interest of Two geometical approaches (GIS and terrestrial LIDAR) in the stress-field determination: Marlsburg plutonic unit case (Black Forest, Germany). SAGEO, Grenoble, France, 2014.

Maeder, X., **Trullenque G.**, Drury M., De Bresser, H. Texture development and hybrid deformation mechanisms in fine grained calcite aggregates deformed in direct shear: constraints from electron backscatter diffraction analysis. 9th Swiss geoscience meeting, Zurich, 11-13 November 2011.

Potel, S., **Trullenque, G.** Very low-grade metamorphism in the dauphinois domain, SE of Pelvoux massif (Alps, France): relationships between deformation and metamorphic Indicators. 20ième Réunion des Sciences de la Terre, Strasbourg, 2004.

Trullenque, G., Schmid, S.M., Heilbronner, R., Stünitz, H., Kunze, K. Progressive shear in naturally deformed calcitic rocks: microfabric evolution and a new type of oblique c-axis orientation. 1st Swiss geoscience meeting, Basel, 2003.

Trullenque, G., Ceriani, S., Fuegenshuh, B., Schmidt, S.M. Polyphase activity along the penninic front between Pelvoux and Argentera massifs (Western Alps, France), EUG-UGS, Nice, France, 2003.

Trullenque, G., Kunze, K., Heilbronner, R., Stünitz, H. and Schmidt, S.M. Microfabric analysis of calcite ultramylonites as a record of coaxial and non-coaxial strain. TSK IX, Erlangen, Germany, 2002.

Trullenque G., Malavieille, J. Effets d'une subduction de prisme avant arc sur la géométrie d'un prisme d'accrétion au large de l'île de Taiwan. Une approche par modélisation analogique. 18^e réunion des sciences de la terre, Paris, 2020.

1.12 Analytical facilities responsible

1.12.1 UniLaSalle

EBSD EDS facility responsible. Tool configuration, trade, maintenance and development.

1.12.2 Albert Ludwig University (Freiburg im Breisgau, Germany, 2011-2013)

Tectonophysics laboratory responsible (Geological institute)

Scanning Electron Microscopy responsible (Crystallography institute)

1.12.3 Oxford Instruments Nano analysis GmbH (Wiesbaden, Germany, 2008 -2011)

EDS, WDS, EBSD Application specialist

Demonstration laboratory responsible (maintenance, product demonstration and customer service)

1.12.4 Johannes Gutenberg University (Mainz, Germany, 2005-2007)

Scanning Electron Microscopy responsible (Gemology institute)

EBSD EDS facility responsible, sample preparation and analysis

1.12.5 University of Basel (Switzerland, 2001-2004)

X-ray textural goniometry laboratory responsible

2 Career summary and motivation

I am here presenting my candidature in order to obtain an accreditation to supervise research in the future. I am going to give a summary of education, present my experience and perspectives in terms of teaching and research dedicated to earth sciences.

I was interested in geology back to my teenage years, and it appeared as an evidence to me that my education will be dedicated to the vast pool of disciplines related to this science.

My higher education started by one year of so called “classe préparatoire aux grandes écoles”. This one-year training was not dedicated to earth sciences, nor to integrate an engineering school. My aim was to gain solid basis in mathematics, physics and chemistry in direct continuity to my higher education. This fundamental sciences knowledge has been useful during my whole studies at University until my PhD. Willing to acquire some intensive fieldwork practice and get a first international experience, I applied to a PhD position at the University of Basel (Switzerland). The subject was dealing with a combined tectonic and microfabric study along the Penninic front in the Western alpine arc.

My PhD thesis was a great experience. I then decided to pursue my researcher career at international level and diversify my competences. I wished to gain experience in laboratory practice and tools development as I consider that technical and engineering skills are mandatory to a scientific career. I spent several years to train in both scanning electron microscopy and experimental deformation techniques while keeping a publication record. During that period, I was involved in many teaching activities as in my opinion research must also benefit to student education.

My competences cover field work, microstructure and microtexture characterization plus petrophysics. This multidisciplinary profile has been recognized suitable in terms of student training by UniLaSalle, where I am working as a structural geologist. I developed there a line of research dedicated to renewable energies development. This sector requires my whole expertise both in terms of academic knowledge and engineering. I am dealing with business-driven applications having an important societal impact while treating research-driven geological processes analysis. I am coordinator of several demonstration and education projects and I wish to further compete for similar grants in the future.

During the past ten years at UniLaSalle, I think I demonstrated my ability to lead research projects. It is time for me to demand my accreditation to supervise future research in order to obtain some form of recognition within the scientific community. I am willing to continue in supervising PhD theses and also apply to Professorship positions at University as a logical career development.

At last, I warmly acknowledge Dr. HDR Potel, GEOS College, B2R research team at UniLaSalle who accepted to assist me during the process of accreditation demand.

3 Research activities in the framework of academic training

3.1 Diplôme d'Etudes Approfondies (DEA)

I achieved my DEA (5th year University degree) within the laboratory of geophysics, tectonics and sedimentology at “Sciences et Techniques” Montpellier University (France) under supervision of Professor Malavieille. The subject was based on a sandbox analogue modeling approach and participated to the understanding of forearc oceanic lithosphere subduction on accretionary prism geometry.

The chosen geodynamic context was found at Taiwan island, at the junction between Eurasian and Philippine plates at the northern termination of the Manilla accretionary wedge. The oblique convergence between these two plates induces an important geodynamic setting evolution from the South to the North of the island, namely from an intra oceanic subduction between oceanic lithosphere of China sea and oceanic lithosphere of Philippine plate in offshore domain to a collision between Chinese continental passive margin and Philippine plate oceanic lithosphere onshore.

This change in subducted crust's nature is accompanied by a complex deformation of the forearc domain above the inter plate contact zone. Sediments of the forearc domain suffer increasing amounts of shortening which in turn form a new ridge back thrust on the non-active volcanic arc. Erosion of this newly formed tectonic prism triggers sediment deposition at the back of the Manilla accretionary wedge.

The chosen working hypothesis was based on one hand on experimental work at lithospheric scale by Chemenda et al. (1997, 1995) and studies dealing on mechanical effects of continental subduction on upper plate forearc volcanic domain (Boutelier et al., 2003; Chemenda et al., 2001) on the other hand. These authors have shown that continental margin subduction below volcanic arc may trigger forearc lithospheric domain rupture. This forearc domain entering the subduction zone induces tectonic slicing permitting to accommodate shortening together with a shift of velocity discontinuity above the volcanic arc itself. The effects of such a geodynamic setting on upper levels crustal units' deformation were unknown.

My first activities were dedicated to the conception of a double velocity discontinuity sandbox deformation apparatus. I have chosen to use a mylar film in order to represent the China sea oceanic crust. The friction coefficient on top of the mylar film could be varied either by gluing sand grains or at the opposite by depositing a fine layer of calibrated glass beads with a grain size in the range of 100 micrometers. The mylar film was pulled below a fixed and rigid backstop as an analogue to the Luzon volcanic arc. A PVC plate, assimilated to the forearc domain, was inserted at the interface between the mylar film and the rigid backstop. The analogue material was an eolian sand whose frictional properties verify the Coulomb model. The sand thickness was dimensioned in order to simulate mechanical properties of accretionary wedge sediments (Dahlen, 1984; Dahlen et al., 1984).

During the various series of tests, a first accretionary prism developed at the tip of the stationary PVC plate. A secondary prism appeared at the tip of the rigid backstop upon mobility allowance of the PVC plate.

My results permitted to understand many structures observed in the field. The tightening in space of the forearc domain and associated sediment deposits is responsible of the formation of both a new oceanic ridge back thrust on volcanic arc and orogenic basin contemporaneous to collision. Erosion products from this orogenic continental prism are trapped within a piggy-back type basin. Towards the North, on the Taiwan island itself, prism development continues by arc and forearc units' accretion.

These results have been published in the Tectonophysics journal (Malavieille and Trullenque, 2009).



Consequences of continental subduction on forearc basin and accretionary wedge deformation in SE Taiwan: Insights from analogue modeling

Jacques Malavieille^{*}, Ghislain Trullenque¹

Laboratoire Dynamique de la Lithosphère, UMR 5573, University Montpellier 2, place E. Bataillon, 34095 Montpellier Cedex 5, France

Available online 22 November 2007

Abstract

In southeastern Taiwan a slice of forearc basement belonging to the Philippine Sea Plate upper-plate is suspected to subduct under the Luzon arc as a consequence of the transition from oceanic to incipient continental subduction. Effects on the morphology, deformation, geometry of structures and tectonic evolution of the orogenic wedge in the collision area are numerous. This study examines the impact of forearc lithosphere subduction on forearc basin and accretionary wedge deformation. A morpho-structural analysis of the geological features observed onland and offshore allows describing in detail the complex deformation suffered by the area. A combined approach by analogue modeling is applied to better understand the phenomenon. Comparison between nature and experimental results shows that subduction of a forearc basement slice induces intense shortening and concomitant deformation in the forearc domain. Such process involves deformation of the forearc basin previously developed in a setting of oceanic subduction. Sediments of the forearc basin are involved in the growth of a new thrust ridge backthrust against the basement slope of the volcanic arc edifice. Sediments coming from the growing orogenic wedge are trapped in the trough developed between its backpart and the topographic high of the new rising ridge. A syn-collisional orogenic basin develops which structural evolution characterizes the progressive shortening of the forearc domain. Most of the deformation and tectonic events recorded offshore or onland in the complex area south of Taiwan can be explained using results of our specific modeling which well describe the tectonic processes associated with continental subduction under a volcanic arc.

© 2007 Elsevier B.V. All rights reserved.

Keywords: Taiwan; Continental subduction; Forearc deformation; Syn-collisional orogenic basin; Analogue modeling

1. Introduction

In convergent settings, the transition between oceanic and continental subduction induces major changes in the mechanical boundary conditions at plates boundary. Simple geological comparison from south to north of Taiwan shows that a large piece of the oceanic accretionary system is missing in the domain involving continental subduction, where remnants of the volcanic arc edifice (coastal range) are directly juxtaposed with metamorphic continental rocks of the central range. Such setting is difficult to reconcile with classical arc-continent collision models. Recent works, some based on physical and numerical modeling at lithospheric scale (Chemenda et al., 1997; Tang and Chemenda, 2000; Chemenda et al., 2001; Boutelier and Chemenda, 2003),

others based on geological and geophysical observations onland and offshore Taiwan (e.g., Malavieille et al., 1999, 2002; McIntosh et al., 2005), have demonstrated that an important tectonic process occurs which is characterized by subduction of a forearc lithosphere slice under the oceanic lithosphere constituting the upper-plate. At the beginning of the process, the subduction of the continental margin strongly increases the stress and strain in the upper-plate (Shemenda, 1994; Lallemand, 1999; Tang and Chemenda, 2000), sometimes involving failure and then subduction of a lithosphere sliver from the forearc domain. The effects of these deep processes on morphology, internal structure and tectonic evolution of the accretionary wedge-forearc basin system are numerous but scarcely studied until now. Using sandbox models, we have studied the impact of this geodynamic process on deformation at the scale of the accretionary wedge. We model a setting in which a continental margin is subducting under an oceanic lithosphere bearing a mature volcanic arc, inducing subduction of forearc lithosphere. The results of the modeling are compared with geological observations from southeast Taiwan and a new interpretation is proposed for the

^{*} Corresponding author.

E-mail address: malavie@gm.univ-montp2.fr (J. Malavieille).

¹ Presently at: Faculty of Earth Sciences, Utrecht University, P.O. Box 80.021, 3508 TA Utrecht, The Netherlands.

morphostructural evolution of the presently active transition from oceanic to continental subduction occurring in this area.

2. General setting of Taiwan

Arc-Continent collision is classically considered to be exemplified by the subduction of the continental margin of China under the Luzon island arc (e.g. Sibuet, J.-C., and Hsu, S.-K., 1997).

Two plates are involved in the complex tectonic setting that surrounds the Taiwan orogen, the Philippine Sea Plate (PSP), and the Eurasian plate (Fig. 1). Northeast of the Taiwan area, the PSP is being subducted beneath the Ryukyu arc, which belongs to the Chinese continental margin. South of the Taiwan Island, the oceanic lithosphere of the South China Sea subducts beneath the PSP, inducing the volcanism of the Luzon arc. The relative motion between the PSP and the Eurasian plate has resulted in

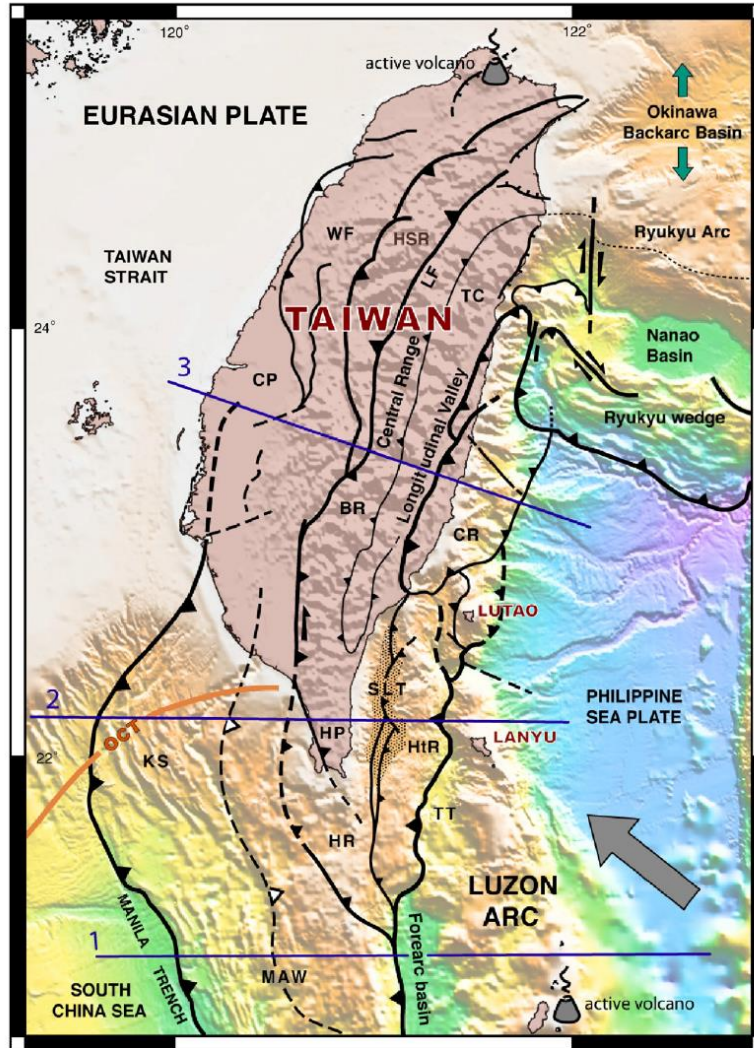


Fig. 1. Morphostructural map of the Taiwan area showing the main tectonic units which characterizes the transition from oceanic to continental subduction. Sections of Fig. 11 are localized (blue lines). CP, Coastal Plain; WF, Western Foothills; HSR, Hsueshan Range; LF, Lishan Fault; TC, Tananao Complex; BR, Backbone Range; CR, Coastal Range; SLT, "Southern Longitudinal Trough" orogenic basin; HP, Hengchun Peninsula; HR, Hengchun Ridge; HtR, Huatung Ridge; KS, Kaoping Slope; TT, Taitung Trough; MAW, Manila Accretionary Wedge; FB, Forearc Basin; OCT, inferred Ocean Continent Transition.

the progressive subduction of the Chinese continental margin and the development of the Taiwan mountain belt.

Global kinematics indicate that the PSP is currently moving northwestward ($N306^{\circ}\pm 1^{\circ}$ azimuth), with respect to the Eurasian plate (Seno, 1977; Seno et al., 1993) at a rate ranging between 80–83 mm/yr (GPS data, Yu et al., 1997; Lallemand and Liu, 1998) or 90 mm/yr (REVEL model, Sella et al., 2002). Because the Asian continental margin trends diagonally with the Luzon arc, the arc-continent collision is oblique and the point of continental subduction rapidly migrates southward (Suppe, 1984). The oceanic lithosphere of the South China Sea was subsequently subducted beneath the PSP along the Manila Trench in the early Miocene, as suggested by the Neogene age of associated volcanism along the Luzon Arc (Ho, 1986; Richard et al., 1986). The Manila accretionary wedge has developed between the two plates (Fig. 1) and is still growing today south of $21^{\circ}20' N$ (Lewis and Hayes, 1983; Hayes and Lewis, 1984; Lewis and Hayes, 1984, 1989). North of $21^{\circ}20' N$, the wedge becomes incorporated in the domain of continental margin subduction, involving progressively lower to middle Miocene slope and trench sediments (Reed et al., 1992). The southern tip of Taiwan Island represents the uplifted internal domain of the oceanic accretionary wedge currently undergoing the effects of the collision (Lundberg and Dorsey, 1990; Reed et al., 1992; Huang et al., 1997). The backpart domain of the wedge extends offshore southward of the Hengchun Peninsula in the form of the Hengchun Ridge as far as $20^{\circ}30' N$ (Fig. 1). A realistic scenario for the tectonic evolution of the submarine accretionary wedge has been proposed by Huang et al. (1997). In their model, the NW–SE oriented Kaoping Slope west of the subduction wedge of the Hengchun Ridge represents the part of the prism associated with the incipient subduction of the Chinese continental margin (e.g. Huang et al., 1997; Liu et al., 1997). The transition between oceanic and continental crust (OCT, see Fig. 1)

in the Eurasian plate is marked approximately by the 2500 m isobath (Letouzey et al., 1988). Although being oriented approximately $N 70^{\circ} E$ to the southwest of Taiwan, the present trend of this boundary is not regular suggesting that the southward propagation of collision is not a stable and continuous process as often supposed.

The geologic setting of the Taiwan orogenic wedge itself can be summarized as follows. The sedimentary cover of the Chinese continental margin (see Taiwan Strait in Fig. 1) was accreted in the northwestern part of the island, and it is still accreting in the southwestern part, against a backstop formed by the pre-Tertiary rocks of the Central Range (e.g. Lu and Malavieille, 1994). Shallow marine sequences of the passive continental margin and foreland sequences constitute the deformed units of the Coastal Plain, Western foothills and Hsüehshan Range (Ho, 1982, 1988). During convergence, they were progressively accreted to the mountain belt along a series of east-dipping thrusts. The Central Range includes the Eocene and Miocene (but not Oligocene) metamorphic Backbone Range. The Lishan Fault, west of the subduction wedge, is a high-angle west dipping fault (Lee et al., 1997), which separates the western Backbone Range from the Eocene–Oligocene units of the Hsüehshan Range, both of them forming the Slate belt (Ho, 1986; Angelier et al., 1990; Teng et al., 1991; Clark et al., 1993; Tillman and Byme, 1995). The Western Foothills correspond to a fold-and-thrust belt affecting Oligo–Miocene strata overlain by a 4-km-thick sequence of Pliocene–Quaternary molasse (Lu and Hsü, 1992). This foreland thrust belt seems inactive north of $24^{\circ} N$, but it is still growing south of this latitude as shown by seismicity and GPS measurements (Yu et al., 1997). The Central Range is bounded to the east by the Longitudinal Valley, which separates the Central Range from the Coastal Range (i.e., northernmost segment of the Luzon volcanic arc). Deformation of the PSP lithosphere within

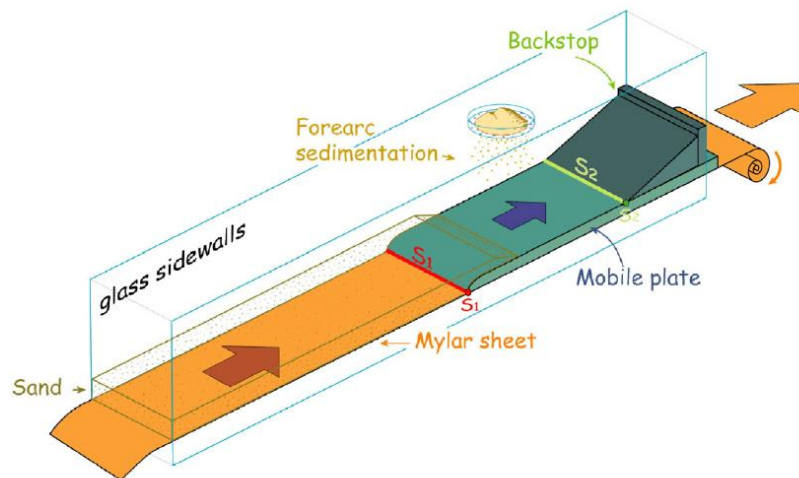


Fig. 2. Sketch of the “sandbox” deformation apparatus. S1, Velocity discontinuity associated to the displacement of the Mylar sheet; S2, Velocity discontinuity associated to the retreat of the mobile plate.

the Coastal Range is suggested by the 50-km-thick seismogenic zone beneath the arc domain (Wu et al., 1997). A large part of the Coastal Range is still well coupled to the PSP, as attested to by the GPS velocities of 63 ± 9 mm/yr in the direction of $N314^\circ \pm 8^\circ$, except north of $23^\circ 40'$ N where rates dramatically drop to 8–43 mm/yr along the azimuths $N292^\circ$ – 352° (Yu et al., 1997). About 80–90 mm/yr of plate convergence is taken up in the offshore area north of 24° N, whereas south of 24° N, the convergence is distributed across the island, with about 30–40 mm/yr accommodated in the western foothills (Simoës, 2005), 30 mm/yr in the Longitudinal Valley area (Angelier et al., 1997), and onland and offshore across the other thrusts of the Coastal Range units shown in Fig. 1 (Yu et al., 1997; Deffontaines et al., 2001; Malavieille et al., 2002; Shyu et al., 2005).

The Luzon island arc and the associated Manila Trench are generally considered as early Miocene in age (Juang and Bellon 1984). The northernmost present-day activity of the arc is observed at the latitudes of the Batan Islands. Younger ages, as recent as 30 ka, were also found using K–Ar dating on Lutao and Hsiaolanyu (a small island located south of Lanyu) islands. The activity of the northern segment thus probably ceased during

the Quaternary at the latitude of the islands of Lutao and Lanyu (Yang et al., 1996). A progressive increase in continental contamination of andesitic magmas correlates with progressively younger ages in Coastal Range volcanic rocks. This progression reflects the systematic increase through time of continentally derived sediment entering the Manila Trench (Dorsey, 1992), and the transition from oceanic to continental subduction inducing subduction of a slice of forearc lithosphere (e.g. Malavieille et al., 2002), shortly before the cessation of island-arc magmatism. North–south changes in the geology and morphology of the Taiwan orogenic wedge reflect the increasing imprint of the Chinese margin “continental subduction”.

3. Analogue modeling

At a crustal scale, the structure and dynamics of accretionary wedges has been widely studied using analogue modeling techniques, allowing a better knowledge of the various processes controlling their growth. Some of them focused on deformation, structure geometry and kinematics (Malavieille, 1984; Mulugeta, 1988; Calassou et al., 1993; Lu and Malavieille, 1994; Merle and

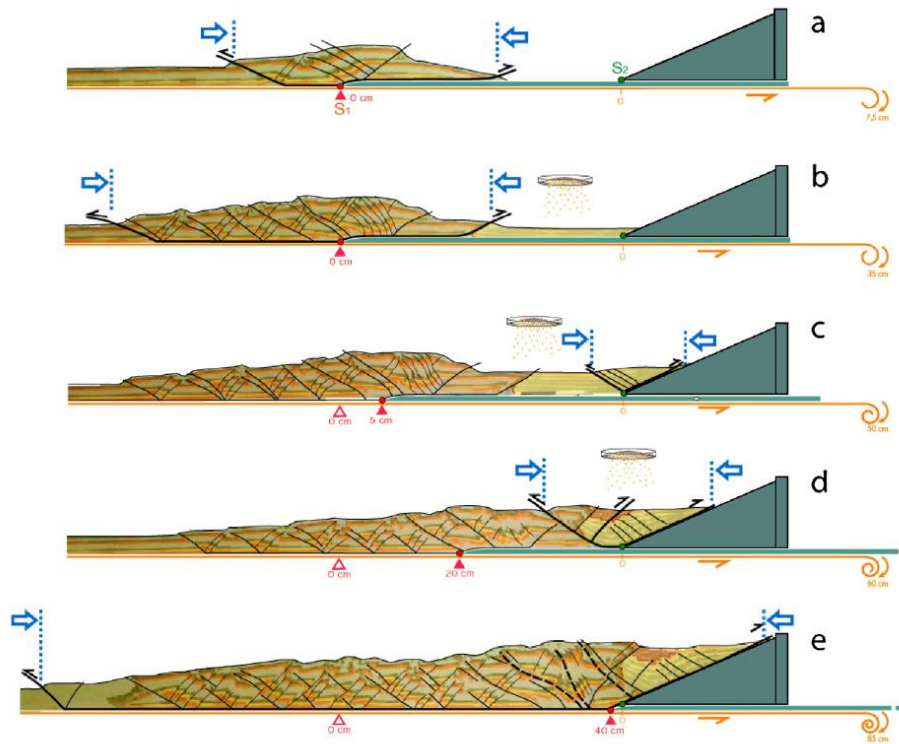


Fig. 3. Five evolutionary steps of experiment 3. Friction was low at the base of the sand cake, both on the mylar sheet and on the “forearc” plastic plate. The empty arrows outline the domain affected by active shortening at each stage.

Abidi, 1995; Gutscher et al., 1996; Mugnier et al., 1997; Gutscher et al., 1998a,b; Dominguez et al., 1998a,b, 2000; Gutscher et al., 2001; Casas et al., 2001; Cobbold et al., 2001; Kukowski et al., 2002; Martínez et al., 2002; Marques and Cobbold, 2002; Smit et al., 2003), others analyzed the impact of surface processes such as syntectonic sedimentation (Malavieille et al., 1993; Larroque et al., 1995; Storti and Mc Clay, 1995; Leturmy et al., 2000; Barrier et al., 2002; Del Castello et al., 2004) or syntectonic erosion on the dynamics of the orogenic wedge (Persson and Sokoutis, 2002; Persson et al., 2004; Konstantinovskaia and Malavieille, 2005; Hoth et al., 2006). At lithospheric scale, subduction processes have been studied using scaled models designed to be analogues for lithosphere deformation (Chemenda et al., 1995, 1997). In this frame, specific experiments devoted to study the effects of continental subduction on upper-plate island arcs, have shown that the subduction of slices of fore-arc lithosphere can occur under specific mechanical boundary conditions (e.g. Chemenda et al., 2001; Boutelier and Chemenda, 2003). They show that subduction of a continental margin beneath a volcanic arc, may induce failure of the arc lithosphere at the vicinity of the volcanic arc, subsequent shortening involving

slicing and subduction of part of the fore-arc domain. In such a geodynamic setting, processes and deformations occurring in the upper levels of the crust (i.e., at the scale of the accretionary wedge or the forearc basin) are poorly known. Our study concerns the modeling of the accretionary wedge–forearc basin deformation and evolution, in relation with the subduction of a slice of upper-plate lithosphere in front of a volcanic arc. The aim was to better understand the evolution of the complex deformation that occurs southeast of Taiwan due to the progressive implication of the Chinese continental margin in the subduction. The geological features suspected to be correlated with such a tectonic process are analyzed in the light of our modeling results.

Experimental apparatus and procedure: Each experiment was performed under normal gravity using an apparatus (Fig. 2) which simulates the basic geometry and general kinematics of a subduction zone. The classical sandbox device, close to the one used by Malavieille (1984) and Lallemand et al. (1992), is constituted by a horizontal basement bounded by two sidewall glasses. A 10 cm wide mylar sheet (analogue of the oceanic plate), lying on the horizontal plate, is pulled beneath a rigid backstop allowing more than 1.5 m of convergence for each

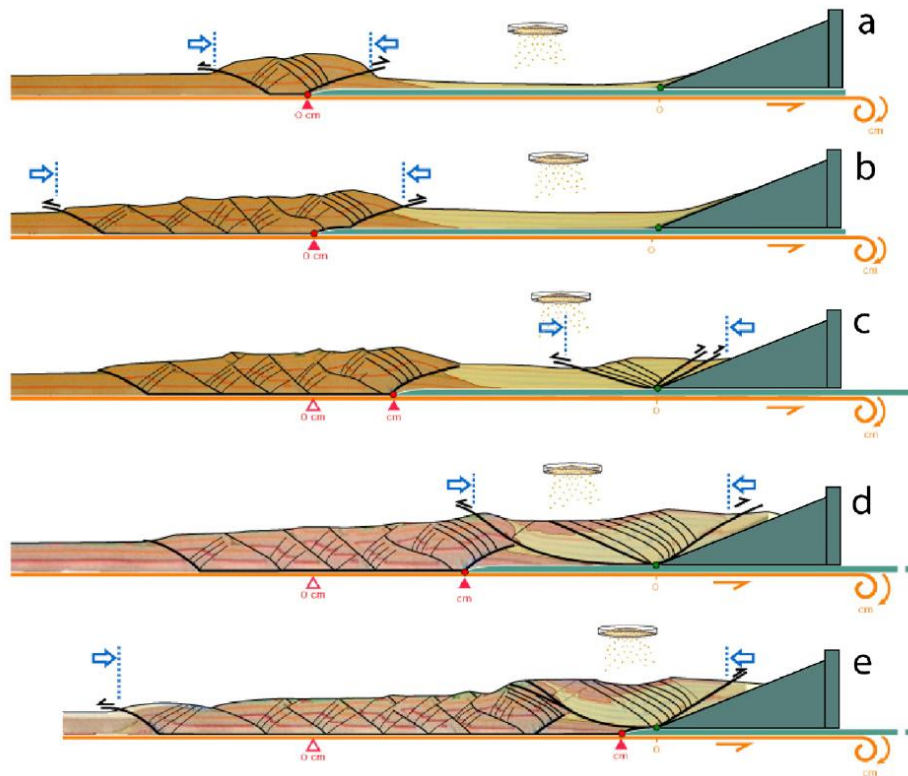


Fig. 4. Experiment 7. Friction was low on the mylar sheet at the base of the sand cake, and high on top of the “forearc” plastic plate.

experiment. Different roughness of the plastic sheet are used to test the effect of different frictions at the base of the sand cake. The rigid backstop (fixed) presents a shape with a low dipping slope (15°) that represents the volcanic edifice of the island arc against which the sediments are deformed. To model the specific kinematic boundary conditions imposed by the subduction of a forearc basement slice in front of the volcanic arc, we add a thin mobile plate (PVC plastic) on the mylar sheet in front of the rigid backstop. The buttress that bounds the sandbox remains fixed during the experiment, whereas the plastic plate can slide beneath it, involving progressive shortening of the forearc domain during convergence. The friction can be adapted on the backstop surface and on the top surface of the mobile plate.

On the mylar sheet, 3 cm of successive coloured sand layers simulate the oceanic sediments (Fig. 2). They allow building of the initial accretionary wedge (Manila accretionary wedge) that developed before the beginning of continental subduction. The same material is used to progressively fill the trough (forearc

basin) that develops between the rear of the model sand wedge (accretionary prism) and the rigid backstop (front of the volcanic arc). The back motion of the PVC plate (analogue of the forearc basement) is controlled during the experiment run.

The aeolian sand used in this study is rounded with a grain size of less than 300 micrometers and a density of 1690 kg/m^3 . The internal coefficient of friction is 0.57 and the cohesion $C_0 = 20 \text{ Pa}$. The model materials have frictional properties satisfying the Coulomb theory (Dahlen et al., 1984; Dahlen, 1984) and thus, it is a fair analogue of the rocks of the upper crust (Krantz, 1991). Sandbox scaling has been widely discussed (see for example; Lallemand et al., 1992, 1994; Kukowski et al., 1994; Gutscher et al., 1996, 1998b; Kukowski et al., 2002; Lohrman et al., 2003) and 1 cm in our experiment is roughly equivalent to 1 km in nature. The same dry sand is used to simulate the sediments of the accretionary wedge and the sediments filling the basin (analogue of the forearc basin) located between the back of the thrust wedge and the rigid backstop. Two cameras and one video recorder recorded each

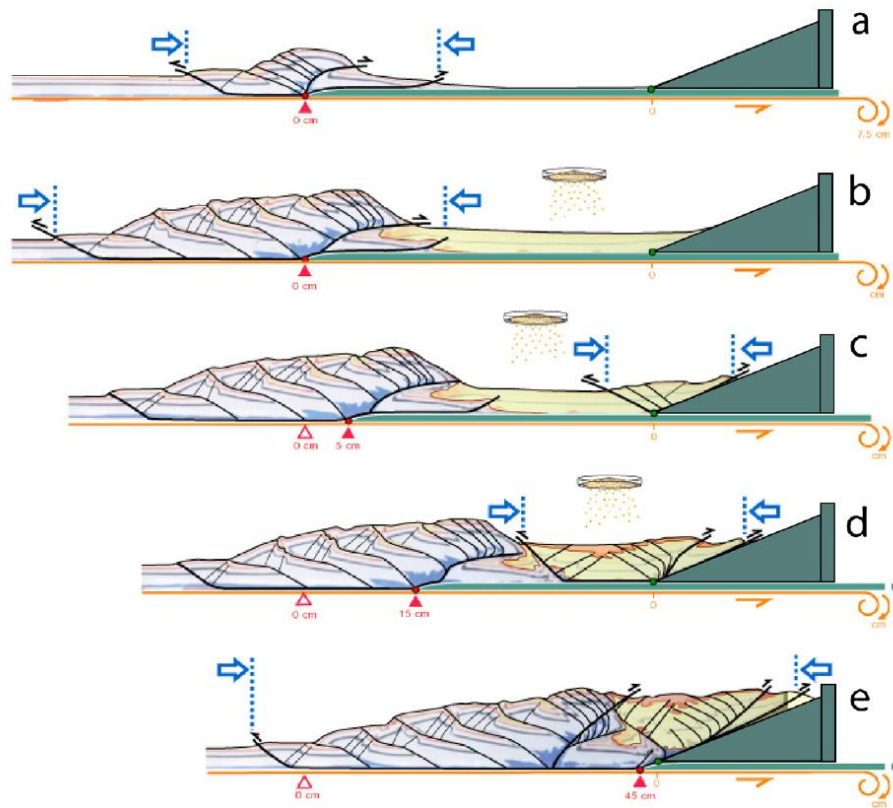


Fig. 5. Experiment 5. Friction was high on the mylar sheet at the base of the sand cake, and low on top the “forearc” plastic plate.

stage of deformation. Structural interpretations are based on planar views recorded at the same time as the morphological perspective views presented.

Each experiment has been performed following three stages.

1) During the first stage, the PVC plate (forearc basement) remains fixed to the rigid backstop. Motion of the mylar sheet allows the growth of a typical doubly vergent sand wedge which geometry is controlled by the velocity break (S_1) located at the tip of the PVC plate. The internal deformation of the wedge is characterized by dominant frontward-vergent thrusts with regular narrow spacing and frontward sequences of thrust development on one side and, localized backthrusting on the backside. Backthrusting controls basin development during shortening and syntectonic sedimentation (see a detailed study of this process in Malavieille et al., 1993; Larroque et al., 1995).

2) During the second stage, a mechanical coupling is realized between the mylar sheet and the PVC plate. Then, a second velocity discontinuity (S_2) works at the tip of the rigid backstop inducing shortening in the “forearc” domain. Such a coupling can be total (this is the case in four of the five experiments presented) or partitioned (this has been tested on experiment 4). In the first situation, the retreat of the PVC plate occurs at the same velocity as the motion of the mylar sheet making the S_1 velocity break inactive whereas S_2 concentrates the deformation. The experiment 4 was designed to test a more complex tectonic situation in which the rate of subduction of the forearc slice is supposed to be slower than the main subduction. It has been run to check the effect of a differential velocity between S_1 and S_2 , the two velocity discontinuities working together during shortening. The equivalent of a syn-orogenic basin is initiated since the beginning of this stage. In the experiments syn-deformation deposit of sand layers with

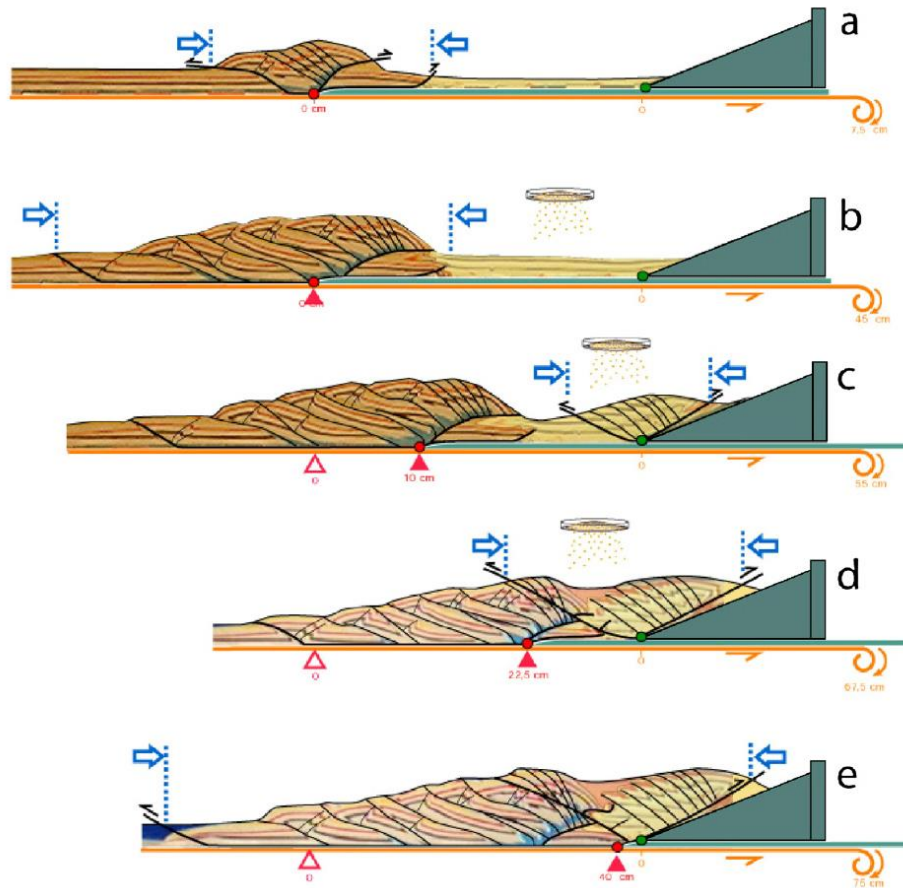


Fig. 6. Experiment 6. Friction was high on the mylar sheet at the base of the sand cake, and high on top the “forearc” plastic plate.

different colours allows to visualize the shape and deformation state of the new “piggy-back” orogenic basin.

- 3) Third stage: after complete removal of the PVC plate shortening goes on some tens of centimeters until the end of the experiment.

In the next part, we describe and compare the results obtained on several laboratory experiments varying two main parameters, the friction at the base of the sediments and the relative shortening ratio between the rigid backstop, the moving PVC plate and basal plastic sheet. The low and high basal friction in the different parts of the models are obtained respectively by polishing (low friction) the rigid backstop, the PVC plate and the basal plastic sheet and by sticking sand grains on their surfaces (high friction). These major changes in boundary conditions induce the specific deformation and evolution suffered by the prism and the associated basins developed on its backpart.

4. Results of experiments

A series of five significant experiments have been analyzed allowing to determine the main effects of the different tested parameters. One of them (experiment 3) is described in detail (Fig. 3), whereas, as the differences in the others concern minor points of models evolution, only their original characters are summarized.

In experiment 3, basal friction on the plastic sheet was low and friction on top of the PVC plate and rigid backstop was low too. Kinematics of deformation is analyzed using photographs taken each 2.5 cm of shortening. During shortening, the step-by-step input of sand (sediments) in the back part of the developing thrust wedge allows filling of a syntectonic basin (in a forearc setting). The sand input is generally chosen to partly fill the topographic low that develops between the domain of backthrusting in the wedge (domain of major topographic high

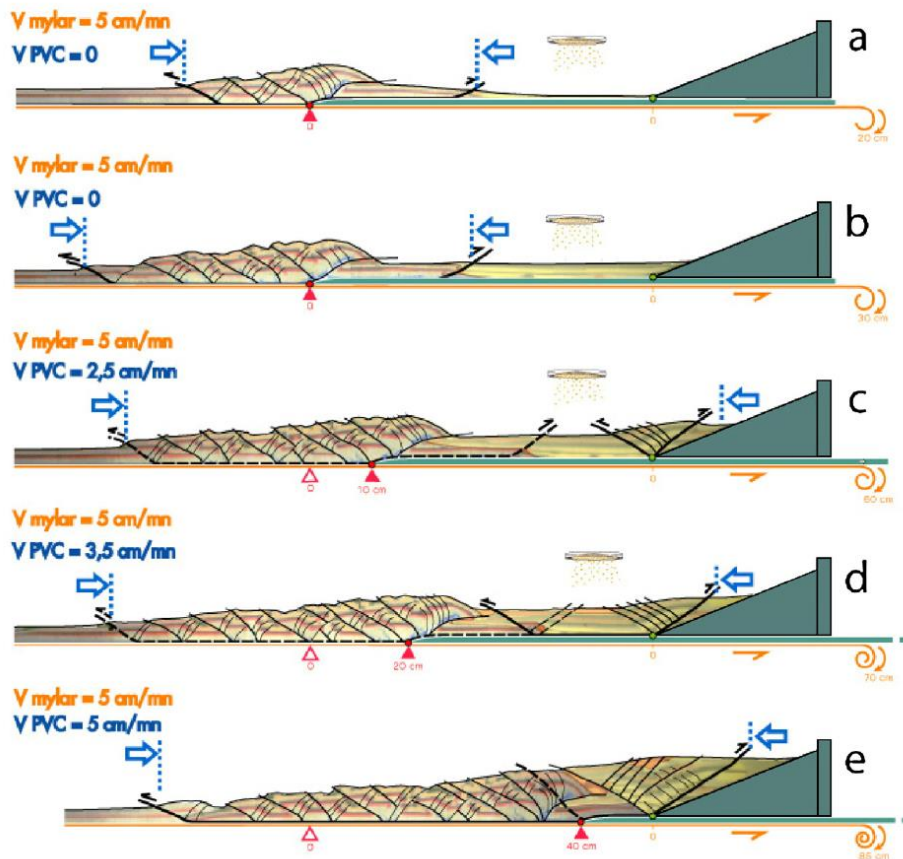


Fig. 7. Experiment 4. Friction was low on the mylar sheet at the base of the sand cake, and low on top the “forearc” plastic plate. The PVC plate is removed, the velocity of the mylar sheet (V_{mylar} on the Fig. 7), is higher than the velocity of the PVC plate (V_{PVC}). The reference is given relative to the fixed backstop ($V_{\text{backstop}}=0$).

in actual oceanic wedges) and the rigid backstop (equivalent of the inner slope of the volcanic edifice). This choice is based on observation of the present area extent of the forearc basin developed south of Taiwan, where the accretionary wedge is simple. The wedge domains affected by faulting and deformation are shown on figures by the blue arrows.

During the first stage of modeling (about 40 cm shortening, Fig. 3a and b), the PVC plate remains coupled with the rigid backstop. A typical low-friction wedge develops which double vergence is controlled by the velocity discontinuity located at the tip of the PVC plate (S_1 on all the figures). The wedge grows rapidly by frontal accretion of small thrust units bounded by a set of antithetic thrusts. The dip of the slope is low. The zone of backthrusting developed at the rear of the wedge allows the growth of the basin which deposits remain undeformed except at the vicinity of the major backthrust.

When the size of the model wedge and associated basin are assumed to be reasonably comparable to its natural equivalent (the oceanic accretionary wedge presently observed south of Taiwan, far from the collision zone, i.e. south of 21° N), we initiate the retreat of the PVC plate (by coupling the plate with the plastic sheet underneath) simulating forearc subduction. This induces major changes in the wedge dynamics characterizing the second tectonic stage. The frontal growth of the wedge stops and the deformation concentrates now at the back part of the system, in

front of the rigid backstop. A major backthrust allows backthrusting of the basin sequences onto the backstop. A series of low dip thrusts initiate from the new velocity discontinuity (S_2 on the figures), they cut and deform the layers of the basin developing a topographic ridge against the backstop (Fig. 3, stage c). When the new ridge reaches a critical slope, it growth forward and most of the basin sequences are thrust on the rear part of the accretionary wedge.

As shortening increases, deformation allows a new syntectonic basin to be developed in the synformal structure bounded by the forearc ridge and the back of the accretionary wedge (Fig. 3, stage d). This new "orogenic basin" is strongly deformed due to syn-shortening sedimentation. During the last steps of the PVC plate retreat and after its complete removal, the main décollement located at the base of the thrust wedge is reactivated allowing wedge growth by frontal accretion of new tectonic units. Then, thrust partitioning resumes, S_2 controls wedge growth and the whole model behaves again as a classical accretionary wedge (Fig. 3, stage d).

The differences induced by parameter changes in each of the other experiments are listed below.

In the experiment 7, the friction on top of the PVC plate and rigid backstop is high. The general evolution of the sandwedge (Fig. 4, stages a, b, c) is quite similar to experiment 3, but the new ridge developed against the buttress during retreat of the

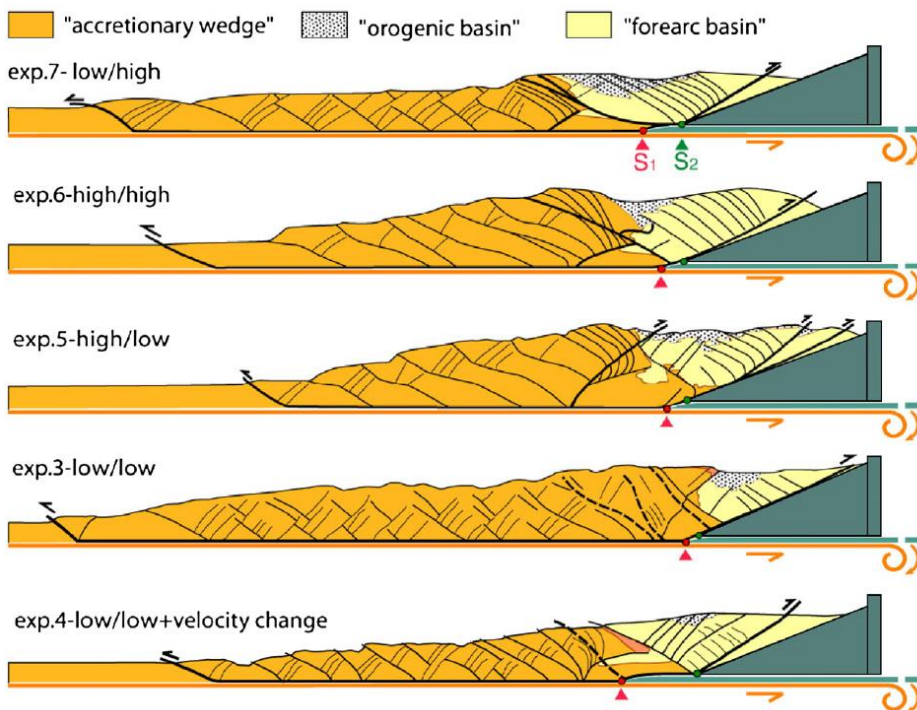


Fig. 8. All experiments drawn at last deformation stage, showing the geometry and structure of the main tectonic units.

PVC plate overthrusts the back part of the accretionary wedge, giving an open syncline geometry to the deformed basin in the last stages of shortening (Fig. 4, stages d, e). The orogenic basin is mainly affected by forward thrusting.

In the experiment 5, the friction is high on the mylar sheet whereas it is low on top of the PVC plate and backstop. The model shows the characters of typical high friction wedge with a high dipping slope and forward growth by stacking of long thrust units (Fig. 5, stages a, b). Here again, as in exp. 7, retreat of the PVC plate induces ridge growth and overthrusting of the syntectonic sequences of the basin on the rear part of the accretionary wedge (Fig. 5, stages c, d). After complete removal of PVC plate, as deformation resumes, the whole thrust wedge grows again and a new out of sequence backthrust develops at the boundary between the deformed basin and the rear of the wedge (Fig. 5, stage e). Backthrusting is more developed in this experiment and affects the orogenic basin too.

In the experiment 6, the basal friction is high everywhere. Result is very close to model 5 (Fig. 6, stages a, b). Retreat of the PVC plate induces growing of a doubly vergent ridge above S_2

(Fig. 6, stages c, d). During last stages of shortening, the last formed out of sequence forethrust cuts the back of the accretionary wedge, whereas thrusting resumes at the front (Fig. 6, stage e). The orogenic basin is relatively little affected by faulting as it is passively displaced on top of the sequences of the previous basin.

In the experiment 4, since the PVC plate is removed, the velocity of the mylar sheet (V_{mylar} on the Fig. 7), is higher than the velocity of the PVC plate (V_{PVC}). The reference is given relative to the fixed backstop ($V_{\text{backstop}}=0$). It was designed to test a more complex tectonic situation in which the rate of subduction of the forearc slice is supposed to be slower than the main subduction. The basal friction was low everywhere in the model as for experiment 3. The evolution of the sandwedge is similar as exp. 3. As both velocity breaks S_1 and S_2 act together, deformation of the thrust wedge goes on while the domain of the basin is deformed (Fig. 7, c, d, e). Backthrusting develops at the rear of the thrust wedge, whereas a new thrust ridge growth in the basin against the backstop. Both thrust systems work concomitantly until the end of PVC plate retreat. At the end of shortening, the deformed basin

Table 1
Table summarizing the main characters of the five experiments described in the text

Experiment number	Exp.7	Exp.6	Exp.5	Exp.3	Exp.4
Friction on top of the moving sheet	Low	High	High	Low	Low
Friction on top of the mobile PVC plate	High	High	Low	Low	Low
Friction on top of the fixed backstop	High	High	Low	Low	Low
Motion of velocity breaks S_1 and S_2 relative to fixed upper-plate (tip of fixed backstop)	Step1: $V_{\text{lower-plate}}=C_{\text{ste}}$ and $V_{\text{moving plate}}=0$ Step 2: $V_{\text{lower-plate}}>V_{\text{moving plate}}>0$	Step 1: $V_{\text{lower-plate}}=C_{\text{ste}}$ and $V_{\text{moving plate}}=0$ Step 2: $V_{\text{lower-plate}}>V_{\text{moving plate}}>0$	Step1: $V_{\text{lower-plate}}=C_{\text{ste}}$ and $V_{\text{moving plate}}=0$ Step 2: $V_{\text{lower-plate}}>V_{\text{moving plate}}>0$	Step1: $V_{\text{lower-plate}}=C_{\text{ste}}$ and $V_{\text{moving plate}}=0$ Step 2: $V_{\text{lower-plate}}>V_{\text{moving plate}}>0$	Step1: $V_{\text{lower-plate}}=C_{\text{ste}}$ and $V_{\text{moving plate}}=0$ Step2: $V_{\text{lower-plate}}=0$ and $V_{\text{moving plate}}=C_{\text{ste}}$. S_1 & S_2 acting together
Structure of the accretionary wedge	Basal décollement and frontal accretion of small thrust units bounded by a set of antithetic thrusts. Minor backthrusting in the retro-wedge	Forward growth by stacking of long thrust units. Major backthrusting in the retro-wedge controls basin formation.	Forward growth by stacking of long thrust units. Major backthrusting in the retro-wedge controls basin formation.	Basal décollement and frontal accretion of small thrust units bounded by a set of antithetic thrusts. Major backthrusting in the retro-wedge	Basal décollement and frontal accretion of small thrust units bounded by a set of antithetic thrusts. Major backthrusting in the retro-wedge
Dip of the slope	Low	High	High	Low	Low
Main stages of deformation in the forearc basin	1 — arc-vergent main thrust+minor forethrusts 2 — major overthrusting of the basins on the rear part of the wedge	1 — deformation against the backstop. Arc-vergent main thrust+minor forethrusts 2 — major backthrusting of the basin on the backstop. Antithetic forethrust cuts the rear part of the wedge	1 — deformation against the backstop. Arc-vergent main thrust+minor forethrusts 2 — basal décollement in the forearc controls shortening in a complex synformal basin	1 — arc-vergent main thrust+minor forethrusts 2 — major shortening of the basins between the rear part of the wedge and the backstop	1 — arc-vergent main thrust+minor forethrusts 2 — major shortening of the basins between the rear part of the wedge and the backstop
Structure of the orogenic basin	Large synformal structure controlled by antithetic thrusts (pop down)	Narrow asymmetric basin resting unconformably on the rear slope of the wedge. Backstop side is deformed by small forethrusts.	Wide and shallow basin with a complex synformal structure controlled by antithetic thrusts (pop down)	Small synformal structure controlled by antithetic thrusts (pop down)	Small “pop down” structure on top of deformed forearc basin

overthrusts the rear part of the accretionary wedge. It results in a synformal basin structure bounded by two antithetic thrusts and carrying in its center a small “orogenic basin” (Fig. 7, stage e). The orogenic basin is mainly deformed by backthrusting.

The Fig. 8 and Table 1 summarize the main characters of deformation for the five experiments.

5. Insights of modeling results on the structural evolution of southern Taiwan

The complex geology and tectonic features of the area south of Taiwan are presented using original structural maps (Figs. 1

and 9) and geologic cross sections (Fig. 10). The maps and sections have been designed combining published and unpublished terrestrial and marine data. They include personal field observations in the southern part of the Taiwan belt, new analysis of seismic lines obtained on the area during the 1996 RV L’Atalante, ACT cruise (Lallemand and Liu, 1997) or older lines of the 1990 Moana Cruise (given by the courtesy of C-S Liu) as well as insights of modeling results on the structural evolution of southern Taiwan.

The transition from oceanic to continental subduction along the Manila Trench occurs near 22° N, but the impact on deformation of this major change in the nature of the two plates

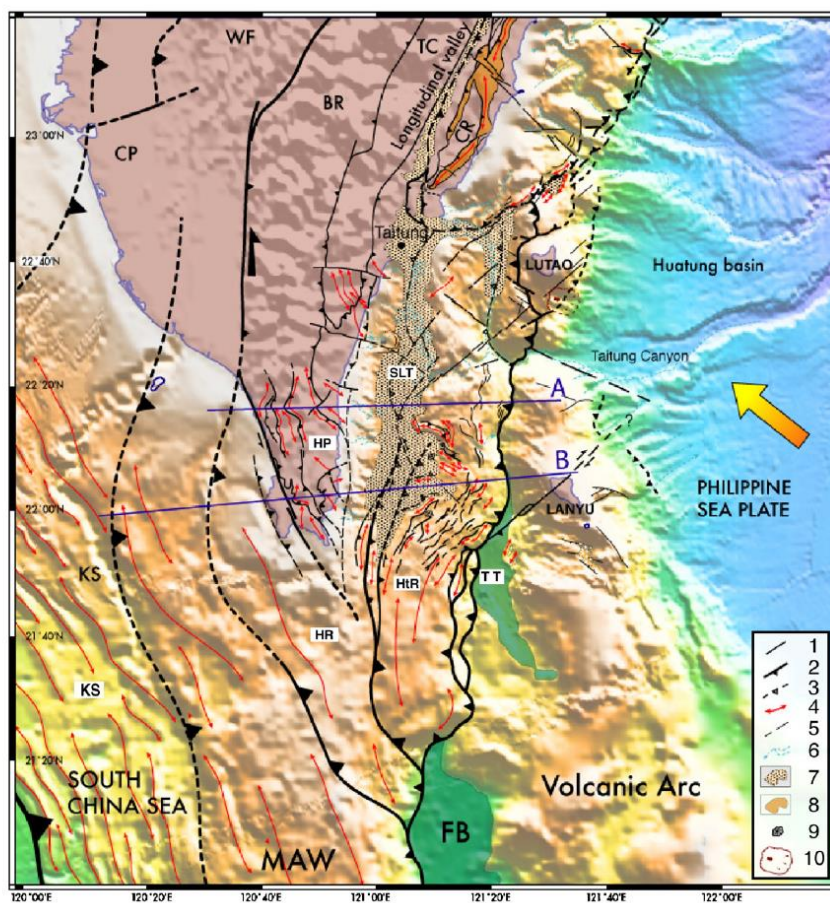


Fig. 9. Detailed morphostructural sketch map of southern Taiwan area. Onland and offshore structures and tectonic units are correlated. Symbols and patterns: 1 — fault, 2 — thrust (teeth on upper plate), 3 — inactive thrust (teeth on upper plate), 4 — fold axis, 5 — minor fault, 6 — drainage, 7 — recent collisional basin, 8 — volcanic rocks of the Coastal Range, 9 — mud volcano, 10 — mass wasting. A and B lines show location of detailed geological cross sections of Fig. 10. Same abbreviations as in Fig. 1.

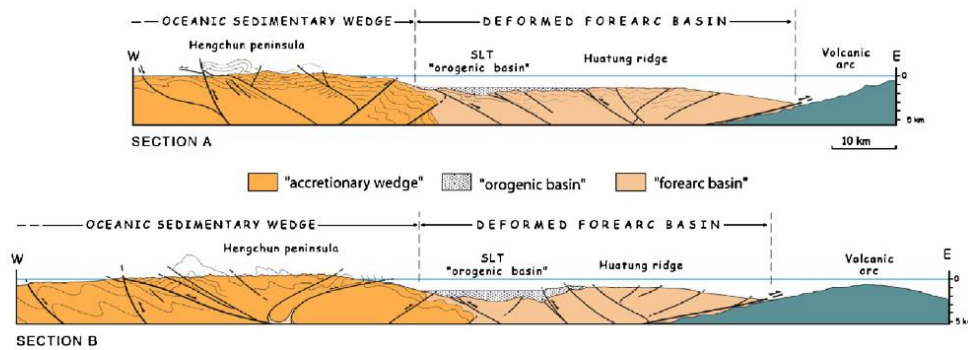


Fig. 10. Detailed geologic cross-sections in the domain of incipient continental subduction.

is observed as far south as 21° N. Three main morphostructural domains characterize this transition:

1) Domain of oceanic subduction.

South of 21° N (Fig. 11, section 1), the offshore domain is characterized by the subduction of the South China Sea oceanic lithosphere under the PSP. The typical Manila oceanic accretionary wedge develops by accretion of the sediments deposited in the Manila trench against the Luzon arc basement. A wide forearc basin develops at the rear of the thrust wedge, mainly filled by arc sediments. This simple setting is the present-day analogue of processes acting in the past more to the north, before the beginning of the continental margin subduction. In our experiments, the first stages of accretionary wedge growth simulate the processes acting during oceanic subduction. During model shortening the wedge grows by frontal accretion of small thrust units. The step by step input of sand (sediments) in the back part of the developing wedge allows filling of a syntectonic basin (in a forearc setting), which development is controlled by tectonic wedging and backthrusting (Figs. 3–6, stages a, b). A recent similar interpretation is proposed by Chi et al. (2003), based on the detailed analysis of seismic lines (Taicrust experiment) and gravity data.

2) Domain of incipient continental subduction.

The general map of Fig. 1 shows the main structural elements and morphological units that characterize the deformation in this domain where a forearc basement sliver is proposed to be subducting beneath the PSP upper-plate. It reflects the complex tectonic history suffered by the area. Six morphotectonic structures constitute the domain of incipient continental subduction: (1) The Kaoping Slope (KS), (2) the Hengchun Peninsula (HP) and its submarine equivalent the Hengchun Ridge (HR), (3) the Southern Longitudinal Trough (SLT) south of the on-land Longitudinal Valley (LV), (2) the elongated Huatung Ridge (HR) forming the eastward dam of the Southern Longitudinal Trough, (3) the Taitung Trough (TT), marked by a sinuous V-shaped

valley, and (4) the Luzon volcanic arc including the islands of Lanyu and Lutaou.

Offshore south of 22° N, the size, morphology and structure of the accretionary wedge change significantly owing to the first effects of the continental margin subduction (Fig. 9). The forearc basin is shortened in between the rear of the wedge and the volcanic edifice of the arc. Three morphotectonic units appear: — a lower-slope wedge with a very low dipping slope, — the HR is an uplifted domain of the wedge bounded by a slope break and characterized by a steeply dipping upper-slope, — the HrR smaller ridge, composed by deformed strata of forearc sedimentary deposits, separated from the rear of the wedge by the TT narrow north–south-oriented trough.

Different mechanical interpretations have been proposed for these tectonic features. Reed et al. (1992) suggested significant shortening of the central domain of the wedge, with out-of-sequence thrusting at the boundary between upper and lower slopes and major backthrusting in the forearc domain. Underplating of thrust units in the core of the thrust wedge represents a possible cause for changes in the dip of the slope, the domain of low dip slope representing the zone of frontal accretion, the high dip upper slope marking the area of underplating at depth (see also experimental studies of Gutscher et al., 1998a, or Kukowski et al., 2002). The smaller HrR has been interpreted as deformed sediments of the forearc basin (e.g. Malavieille et al., 2002). In all the experiments (Figs. 3–7), the development of a topographic ridge against the low dip backstop marks the evolution of the sand wedge during the progressive retreat of the PVC plate. This confirms that in southern Taiwan, the subduction of a forearc sliver in front of the arc edifice could be a good explanation for the growth of the Huatung Ridge east of the accretionary prism.

North of 22° N, the HP represents the emerged continuation of the submarine HR (Fig. 9). At this latitude, a large part of the slope sediments from the continental margin is involved in the accretionary wedge. Onland, the deformation structures of southern Taiwan characterize the main tectonic events that occurred during the growth of the orogenic wedge. Thick series of Miocene deposits in this area suffered low-grade metamorphism

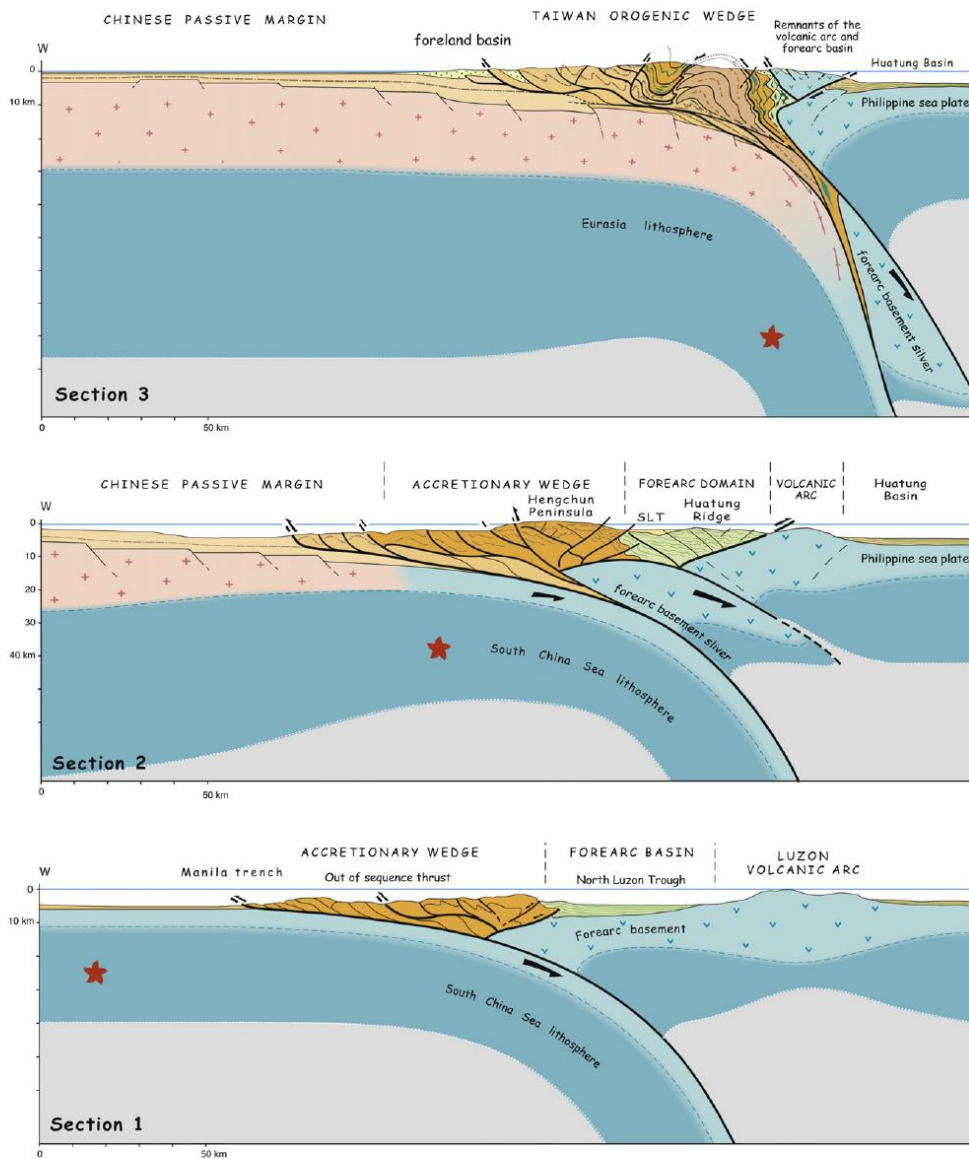


Fig. 11. General interpretative sections showing the tectonic evolution of the orogenic wedge. Section 1, oceanic subduction and growth of a sedimentary wedge south of Taiwan; Section 2, incipient subduction of the continental margin and subduction of a slice of forearc basement inducing intense shortening of the forearc sedimentary units; Section 3, mature continental subduction and growth of the Taiwan orogenic wedge.

and ductile–brittle deformation during the Late Cenozoic orogeny. Most of the recent field investigations and structural analysis realized in this area (Chang et al., 2000, 2001; Lu et al., 2001; Chang et al., 2003) distinguish three main stages in the deformation history that can be summarized as follows: (1) a first

stage involving an early west-vergent deformation and volume loss resulting in thrusting, regional tilting of strata, slumping and subsequent folding (early slumping being sometimes considered as a first synsedimentary deformation phase, but as this deformation occurs during the growth of the accretionary

wedge, such structures were probably syntectonic of the first phase); (2) a second stage being dominated by general shear, which resulted in widespread east-vergent back-folding and back-thrusting associated with isoclinal folding; and (3) a third stage mainly involving transpression in association with E–W contractional thrusting and folding, as well as a new penetrative cleavage. Many of the well-characterized structures in the study area disappeared progressively towards the north as deformation becomes more complex and as exhumation exposes more and more deep rocks of the Central Range. The evolution of structures in sandbox models suggests a possible scenario to account for the complex tectonic history of this area. Early structures of the first phase (slumping, west vergent thrusting and folding) develops during the forward growth of the marine accretionary wedge, before incoming of slope margin sediments. As sedimentary input dramatically increases with the approach of the continental slope, it will change the behaviour of the coulomb wedge. Such a phenomenon has similar consequences on wedge deformation and structures as incoming of asperities (ridges, seamounts, plateaus, area of rough basement with strong basal coupling...) in a critical wedge (see for example modeling of this process in Lallemand et al., 1994; Dominguez et al., 1998a,b, 2000). Thus, change in the critical taper and subsequent thickening of the wedge occur inducing fault reactivations, out of sequence backthrusting and associated backfolding. The structures observed onland attributed to a second tectonic stage could reflect such event. As major consequence, strain and stress increase induced in the thrust wedge could be responsible for the

strong deformation that affects the forearc domain, involving subduction of a slice of forearc basement (Fig. 11, section 2). As subduction is oblique transpressive strain partitioning lately concentrates in this active area producing the E–W contractional thrusting and folding that is attributed onland to a third tectonic event (see orientation of fold axis in Fig. 9).

Malavieille et al. (2002) have shown that major shortening occurs today offshore in the forearc domain, between the Luzon Arc (islands of Lutaio and Lanyu) and the Hengchun Peninsula of Taiwan. South of Taitung, the difference between GPS data obtained on the arc islands (Lutaio and Lanyu) and on east coast of the HP confirms that about 40 mm/yr (half of the total convergence) (Yu et al., 1997) is accommodated offshore. It is mainly absorbed by west-dipping thrusting beneath the HtR and in addition by folding and thrusting within the ridge (Fig. 10). The map (Fig. 9) and digital elevation model oblique view (Fig. 12) show that two main morphostructural units, the HtR and the SLT constitute the present forearc domain. Sections a and b of Fig. 10 show the geometry, deformation structures and tectonic setting of these units. The SLT is a proximal orogenic basin developed in a forearc position (e.g., Lundberg and Dorsey, 1988; Lundberg et al., 1997; Fuh et al., 1997). Elongated in a north–south direction between 21°50'N and 22°40'N, it is bounded to the west by the 10°-east-dipping structural slope of the HP and to the east, by an antiformal narrow ridge which extends westward from the HR overthrusting onto the Luzon arc near 22°05'N. The basin is filled by Holocene orogenic sediments coming from the Central

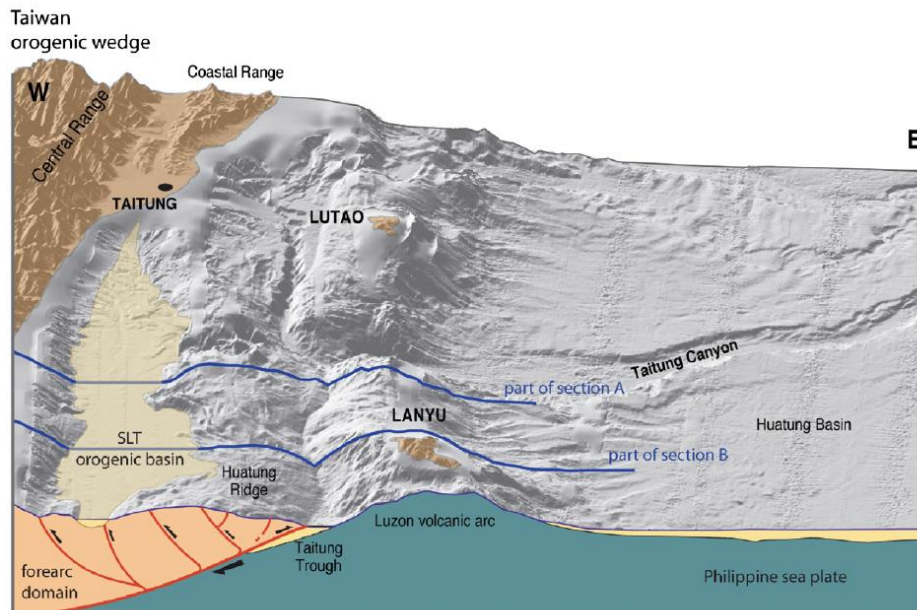


Fig. 12. Oblique view (Digital Elevation Model) of the offshore domain SE of Taiwan Island suffering intense forearc shortening. Yellow color outline the “Southern Longitudinal Trough” orogenic basin.

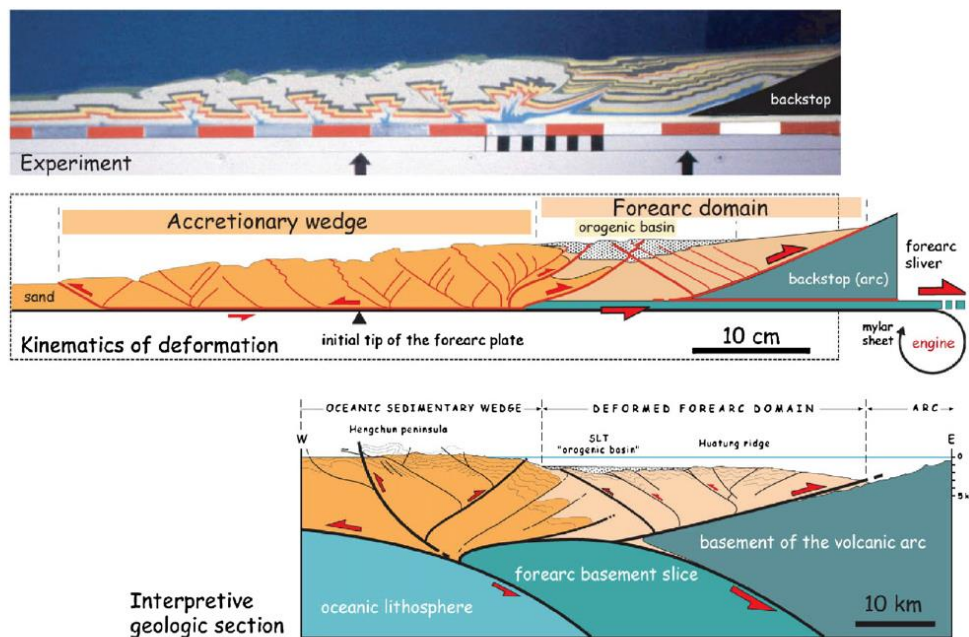


Fig. 13. Geological section of Fig. 10B interpreted at depth using the comparison with structures of a sandbox experiment. Subduction of a forearc basement slice well accounts for deformation, structures and basin geometry observed SE of Taiwan.

Range (Huang et al., 1992). Filling by growth strata record the relative uplift of the HR, forming a dam for sediments (Lundberg et al., 1992, 1997). Complex deformation and progressive tilting of lower series have been imaged from east–west and north–south seismic lines (Lundberg et al., 1997; Malavieille et al., 2002). The upper series of the basin are relatively flat, onlapping the HR to the south, whereas at depth, the lower strata overlying an irregular basement are gently deformed. These sequences lie unconformably on top of older, folded and faulted sequences of the former forearc basin. The Fig. 13 compares an evolved stage of a sand model to the geological section (section a, Fig. 10) drawn using all available data. The interpretation proposed for the processes responsible at depth for the observed structures is directly inspired by the experiments. It summarizes the main characters of deformation (geometry and kinematics) and shows possible mechanisms able to produce the complex deformation suffered by the area during subduction of a forearc basement slice.

2) Domain of mature continental subduction and orogenic wedge growth.

From 22°40'N to about 24°N, the collision is completed and the forearc domain is drastically reduced. This northern domain represents the area where the continental margin of China is largely involved in the subduction (Cheng et al., 2002). The wedge grows again by frontal accretion to the west (e.g., Simoes, 2005; Simoes et al., 2007), underplating in the central part of the belt (Beyssac et al., 2006), accretion of parts of the

arc-forearc domain, backthrusting and tectonic wedging in the eastern side of the orogenic belt to the east (Malavieille et al., 2002). The Coastal Range volcanic rocks and associated residual basins are detached from the Philippine sea plate, overthrusting the central Range to the west and backthrusting onto the Huatung Basin to the east. From Taitung to 23°40'N, 30 mm/yr of shortening are taken up today along the east-dipping thrusts of the Longitudinal Valley (e.g. Angelier et al., 1997), and about 20 mm/yr through west-dipping thrusts located offshore close to the base of the slope (Yu et al., 1997; Malavieille et al., 2002). The section 3 of Fig. 11 illustrates the deformation of the main tectonic units constituting the mature Taiwan belt, showing an evolved stage of processes acting today more to the south. In this area, the slice of forearc basement is completely subducted under the PSP lithosphere. Such situation is equivalent to the mature stages of the experiments when the retreat of the intermediate PVC plate is completed. The wide orogenic wedge constituted by all the various accreted units and growing foreland basin is presently indented by the basement of the volcanic arc. The tectonic history of this domain is described in Malavieille et al. (2002).

6. Conclusion

Most of the deformation and tectonic events recorded offshore or onland in the complex area south of Taiwan can be better explained using results of our specific modeling which

well describe the tectonic processes and basin development associated with continental subduction under a volcanic arc.

To the south, incipient subduction of the continental margin induces increasing stress and strain in the upper plate. Subsequent subduction of a forearc basement slice produces intense shortening and concomitant deformation in the forearc domain. Such process involves deformation of the forearc basin previously developed in a setting of oceanic subduction. Volcaniclastic sediments of the forearc are involved in the growth of a new thrust ridge backthrust against the basement slope of the volcanic arc edifice. A syn-collisional orogenic basin develops which structural evolution characterizes the progressive shortening of the forearc domain. Thus, detrital sediments coming from the growing continental orogenic wedge are trapped in the piggy-back trough developed between its backpart and the topographic high of the new rising ridge.

North of the latitude of Taitung, the forearc basement of the Luzon volcanic arc no longer exists. The wedge grows again by frontal accretion to the west, underplating in the central part of the belt, accretion of parts of the arc–forearc domain, backthrusting and tectonic wedging in the eastern side of the orogenic belt to the east. Reconstruction of these processes may be useful for the understanding of the early stages of mountain building in fossil orogens.

Acknowledgments

We thank “Institut National des Sciences de l’Univers”, the French Institute in Taipei (Ministry of Foreign Affairs), and the National Science Council (Taiwan) for funding and supporting this work. We thank S. Dominguez and E. Konstantinovskaia for stimulating discussion about experiments and C-Y. Lu and K-J Chang for their geological help and kindness during our field trips in Taiwan. Many thanks to A. Delplanque for helping draft most of the figures in this paper. Critical reviews and comments by Wei-Hau Wang and an anonymous reviewer are highly appreciated. Figs. 1, 9 and 12, were produced using GMT software (Wessel and Smith, 1995).

References

- Angelier, J., Bergerat, F., Chu, H.-T., Lee, T.-Q., 1990. Tectonic analysis and the evolution of a curved collision belt: the Hsuehsan Range, northern Taiwan. *Tectonophysics* 183, 77–96.
- Angelier, J., Chu, H.-T., Lee, J.C., 1997. Shear concentration in a collision zone: kinematics of the Chihshang Fault as revealed by outcrop-scale quantification of active faulting, Longitudinal Valley, eastern Taiwan. *Tectonophysics* 274, 117–143.
- Barrier, L., Nalpas, T., Gapais, D., Proust, J.N., Casas, A., Bourquin, S., 2002. Influence of syntectonic sedimentation on thrust geometry. Field examples from the Iberian Chain (Spain) and analogue modelling. *Sedimentary Geology* 146, 91–104.
- Beyssac, O., Simoes, M., Avouac, J.P., Farley, K.A., Chen, Y.G., Chan, Y.C., Goffe, B., 2006. Late Cenozoic metamorphic evolution and exhumation of Taiwan. *Tectonics* 26, TC6001. doi:10.1029/2006TC002064.
- Boutelier, D., Chemenda, A., 2003. Subduction versus accretion of intra-oceanic volcanic arcs: insights from thermo-mechanical analogue experiments. *Earth and Planetary Sciences Letters* 212, 31–45.
- Calassou, S., Larroque, C., Malavieille, J., 1993. Transfer zones of deformation in thrust wedges: an experimental study. *Tectonophysics* 221, 325–344.
- Casas, A.M., Gapais, D., Nalpas, T., Besnard, K., Roman-Berdiel, T., 2001. Analogue models of transpressive systems. *Journal of Structural Geology* 23, 733–743.
- Chang, C.-P., Angelier, J., Huang, C.-Y., 2000. Origin and evolution of a melange: the active plate boundary and suture zone of the Longitudinal Valley, Taiwan. *Tectonophysics* 325, 43–62.
- Chang, C.P., Angelier, J., Huang, C.Y., Liu, C.-S., 2001. Structural evolution and significance of a melange in a collision belt: the Lichi Melange and the Taiwan arc–continent collision. *Geological Magazine* 138, 633–651.
- Chang, C.-P., Angelier, J., Lee, T.-Q., Huang, C.-Y., 2003. From continental margin extension to collision orogen: structural development and tectonic rotation of the Hengchun peninsula, southern Taiwan. *Tectonophysics* 361, 61–82.
- Chemenda, A.I., Mattauer, M., Malavieille, J., Bokun, A., 1995. A mechanism for syn-collisional deep rock exhumation and associated normal faulting: Results from physical modeling. *Earth and Planetary Sciences Letters* 132, 225–232.
- Chemenda, A.I., Yang, R.K., Hsieh, C.-H., Groholsky, A.L., 1997. Evolutionary model for the Taiwan collision based on physical modelling. *Tectonophysics* 274, 253–274.
- Chemenda, A.I., Yang, R.K., Konstantinovskaia, E.A., Ivanov, G.M., 2001. New results from physical modeling of arc-continent collision in Taiwan: evolutionary model. *Tectonophysics* 333 (1–2), 159–178.
- Cheng, W.-B., Wang, C., Shyu, C.-T., Shin, T.-C., 2002. Crustal structure of the convergent plate-boundary zone, eastern Taiwan, assessed by seismic tomography. *Geological Society of America* 358, 161–175 special paper.
- Chi, W.-C., Reed, D.L., Moore, G., Nguyen, T., Liu, C.-S., Lundberg, N., 2003. Tectonic wedging along the rear of the offshore Taiwan accretionary prism. *Tectonophysics* 374, 199–217.
- Clark, M.B., Fisher, D.M., Lu, C.-Y., Chen, C.H., 1993. Kinematic analysis of the Hsuehsan Range, Taiwan: a large-scale pop-up structure. *Tectonics* 12, 205–217.
- Cobbold, P.R., Durand, S., Mourgues, R., 2001. Sandbox modelling of thrust wedges with fluid-assisted detachments. *Tectonophysics* 334, 245–258.
- Dahlen, F.A., 1984. Noncohesive critical Coulomb wedges: an exact solution. *Journal of Geophysical Research* 89, 10,125–10,133.
- Dahlen, F.A., Suppe, J., Davis, D., 1984. Mechanics of fold-and-thrust belts and accretionary wedges: cohesive Coulomb theory. *Journal of Geophysical Research* 89, 10,087–10,101.
- Deffontaines, B., Liu, C.-S., Angelier, J., Lee, C.-T., Sibuet, J.-C., Tsai, Y.-B., Lallemand, S., Lu, C.-Y., Lee, C.-S., Hsu, S.-K., Chu, H.-T., Lee, J.-C., Pathier, E., Chen, R.-F., Cheng, C.-T., Liao, C.-W., Lin, C.-C., Hsu, H.-H., 2001. Preliminary Neotectonic Map of Onshore–offshore Taiwan. *Terrestrial, Atmospheric and Oceanic Sciences, Supplementary Issue*, 269–286, May 2001.
- Del Castello, M., Pini, G.A., McClay, K.R., 2004. Effect of unbalanced topography and overloading on Coulomb wedge kinematics: Insights from sandbox modelling. *Journal of Geophysical Research* 109 no. B05405.
- Dominguez, S., Lallemand, S.E., Malavieille, J., Von Huene, R., 1998a. Upper plate deformation associated with seamount subduction. *Tectonophysics* 293, 207–224.
- Dominguez, S., Lallemand, S., Malavieille, J., Schnurle, P., 1998b. Oblique subduction of the Gagua Ridge beneath the Ryukyu accretionary wedge system: Insights from marine observations and sandbox experiments. *Marine Geophysical Research* 20, 383–402.
- Dominguez, S., Malavieille, J., Lallemand, S.E., 2000. Deformation of margins in response to seamount subduction: insights from sandbox experiments. *Tectonics* 19, 182–196 N° 1.
- Dorsey, R.J., 1992. Collapse of the Luzon volcanic arc during onset of arc-continent collision: evidence from a Miocene–Pliocene unconformity; Eastern Taiwan. *Tectonics* 11, 177–191.
- Fuh, S.C., Liu, C.S., Lundberg, N., Reed, D., 1997. Strike–slip faults offshore southern Taiwan: Implications for the oblique arc–continent collision processes. *Tectonophysics* 274, 25–39.
- Gutscher, M.-A., Kukowski, N., Malavieille, J., Lallemand, S.E., 1996. Cyclical behavior of thrust wedges: insights from high basal friction sandbox experiments. *Geology* 24, 135–138.

- Gutscher, M.A., Kukowski, N., Malavieille, J., Lallemand, S., 1998a. Material transfer in Accretionary Wedges from Analysis of a systematic series of Analog Experiments. *Journal of Structural Geology* 20 (4), 407–416.
- Gutscher, M.A., Kukowski, N., Malavieille, J., Lallemand, S., 1998b. Episodic Imbricate thrusting and underthrusting: analog experiments and mechanical analysis applied to the alaskan accretionary wedge. *Journal of Geophysical Research* 103, 10161–10176.
- Gutscher, M.A., Klaeschen, D., Flueh, E., Malavieille, J., 2001. Non-Coulomb “wrong-way” thrusting, and natural hazard in Cascadia. *Geology* 29, 379–382.
- Hayes, D.E., Lewis, S.D., 1984. A geophysical Study of the Manila Trench, Luzon, Philippines 1. Crustal Structure, Gravity, and regional tectonic evolution. *Journal of Geophysical Research* 89, 9171–9195.
- Ho, C.-S., 1982. Tectonic evolution of Taiwan. Explanatory Text of the Tectonic Map of Taiwan. Ministry of Economic Affairs, Taiwan, R.O.C., pp. 1–126.
- Ho, C.-S., 1986. A synthesis of the geologic evolution of Taiwan. *Tectonophysics* 125, 1–16.
- Ho, C.-S., 1988. An introduction to the geology of Taiwan (second Edition). Explanatory text of the geologic map of Taiwan. Ministry of Economic Affairs, Taiwan, R.O.C., p. 192.
- Hoth, S., Adam, J., Kukowski, N., Oncken, O., 2006. Influence of erosion on the kinematics of divergent orogens: Results from scaled sandbox simulations. *Special Paper: Tectonics, Climate, and Landscape Evolution*, vol. 398, pp. 201–225.
- Huang, C.-Y., Shyu, C.-T., Lin, S.B., Lee, T.-Q., Sheu, D.D., 1992. Marine geology in the arc-continent collision zone off southeastern Taiwan: implications for Late Neogene evolution of the Coastal Range. *Marine Geology* 107, 183–212.
- Huang, C.-Y., Wu, W.-Y., Chang, C.P., Tsao, S., Yuan, P.B., Lin, C.W., Kuan-Yuan, X., 1997. Tectonic evolution of accretionary prism in the arc-continent collision terrane of Taiwan. *Tectonophysics* 281, 31–51.
- Juang, W.S., Bellon, H., 1984. The Potassium–Argon dating of andesites from Taiwan. *Proceedings of the Geological Society of China* 27, 86–100.
- Konstantinovskaia, E., Malavieille, J., 2005. Erosion and exhumation in accretionary orogens: experimental and geological approaches. *Geochemistry, Geophysics, Geosystems* 6 (2), 25. doi:10.1029/2004GC000794 26 February 2005, Q02006, ISSN: 1525–2027.
- Krantz, R.W., 1991. Measurement of friction coefficients and cohesion for faulting and fault reactivation in laboratory models using sand and sand mixtures. *Tectonophysics* 188, 203–207.
- Kukowski, N., Von Huene, R., Malavieille, J., Lallemand, S., 1994. Sediment accretion against a buttress beneath the Peruvian continental margin as simulated by sandbox modelling. *Geologische Rundschau* 83, 822–831.
- Kukowski, N., Lallemand, S.E., Malavieille, J., Gutscher, M.A., Reston, T.J., 2002. Mechanical decoupling and basal duplex formation observed in sandbox experiments with application to the Mediterranean Ridge accretionary complex. *Marine Geology* 186, 29–42.
- Lallemand, S.E., 1999. La subduction océanique. Gordon and Breach Science Publishers, Amsterdam, p. 192.
- Lallemand, S., Liu, C.-S., 1998. Geodynamic implications of present-day kinematics in the southern Ryukyus. *Journal of the Geological Society of China* 41, 551–564.
- Lallemand, S.E., Malavieille, J., Calassou, S., 1992. Effects of oceanic Ridge subduction on accretionary wedges: Experimental modeling and marine observation. *Tectonics* 11, 1301–1313.
- Lallemand, S.E., Schnürle, P., Malavieille, J., 1994. Coulomb theory applied to accretionary and non-accretionary wedges: Possible causes for tectonic erosion and/or frontal accretion. *Journal of Geophysical Research* 99, 12,033–12,055.
- Lallemand, S.E., Liu, C.-S., ACT scientific crew, 1997. Swath bathymetry mapping reveals details of the active arc-continent collision offshore Taiwan. *EOS, Transactions, AGU* 78, 173–175.
- Larroque, C., Calassou, S., Malavieille, J., Chanier, F., 1995. Experimental modeling of forearc basin development during accretionary wedge growth. *Basin Research* 7, 255–268.
- Lee, J.-C., Angelier, J., Chu, H.-T., 1997. Polyphase history and kinematics of a complex major fault zone in the northern Taiwan mountain belt: the Lishan Fault. *Tectonophysics* 274, 97–115.
- Letouzey, J., Sage, L., Müller, C., 1988. Geological and structural map of eastern Asia: Introductory notes. *American Association of Petroleum Geologists* 52.
- Leturmy, P., Mugnier, J.L., Vinour, P., Baby, P., Colletta, B., Chabron, E., 2000. Piggyback basin development above a thin-skinned thrust belt with two detachment levels as a function of interactions between tectonic and superficial mass transfer; the case of the Subandean Zone (Bolivia). *Tectonophysics* 320, 45–67 no. 1.
- Lewis, S.D., Hayes, D.E., 1983. The tectonics of northward propagating subduction along eastern Luzon, Philippine Islands. In: Hayes, D.E. (Ed.), *The tectonic and geologic evolution of the southeast Asian Seas and Islands*, part 2. *Geophysical Monograph*, vol. 27. American Geophysical Union, Washington, pp. 57–78.
- Lewis, S.D., Hayes, D.E., 1984. A geophysical Study of the Manila Trench, Luzon, Philippines. 2. Fore Arc Basin Structural and Stratigraphic Evolution. *Journal of Geophysical Research* 89, 9196–9214.
- Lewis, S.D., Hayes, D.E., 1989. Plate convergence and deformation, North Luzon Ridge, Philippines. *Tectonophysics* 168, 221–237.
- Liu, C.-S., Huang, L.L., Teng, L.S., 1997. Structural features off southwestern Taiwan. *Marine Geology* 137, 305–319.
- Lohrman, J., Kukowski, N., Adam, J., Oncken, O., 2003. The impact of analogue material properties on the geometry, kinematics and dynamics of convergent sand wedges. *Journal of Structural Geology* 25, 1691–1711.
- Lu, C.-Y., Hsü, K.-J., 1992. Tectonic evolution of the Taiwan mountain belt. *Petroleum Geology of Taiwan* 27, 21–46.
- Lu, C.-Y., Malavieille, J., 1994. Oblique convergence, indentation and rotation tectonic in Taiwan Mountain belt: Insights from experimental modelling. *Earth and Planetary Sciences Letter* 121, 477–494.
- Lu, C.-Y., Chang, K.J., Malavieille, J., Chan, Y.-C., Chang, C.-P., Lee, J.-C., 2001. Structural evolution of the southeastern Central Range, Taiwan. *Western Pacific Earth Sciences* 1, 213–226 N° 2.
- Lundberg, N., Dorsey, R.J., 1988. Synorogenic sedimentation and subsidence in a Plio-Pleistocene collisional basin, eastern Taiwan. In: Klein-spehn, K.L., Paola, C. (Eds.), *New perspectives in basin analysis*. Springer-Verlag, New-York, pp. 265–280.
- Lundberg, N., Dorsey, R.J., 1990. Rapid Quaternary emergence, uplift and denudation of the Coastal Range, eastern Taiwan. *Geology* 18, 638–641.
- Lundberg, N., Reed, D.L., Lieskes Jr., J.H., 1992. Structural controls on orogenic sedimentation, submarine Taiwan collision. *EOS Transactions, American Geophysical Union*, 73, p. 539.
- Lundberg, N., Reed, D.L., Liu, C.-S., Lieskes Jr., J.H., 1997. Forearc-basin closure and arc accretion in the submarine sutre zone south of Taiwan. *Tectonophysics* 274, 5–24.
- Malavieille, J., 1984. Modélisation expérimentale des chevauchements imbriqués: application aux chaînes de montagnes. *Bulletin de la Société Géologique de France* 26, 129–138.
- Malavieille, J., Calassou, S., Larroque, C., 1993. Modélisation expérimentale des relations tectonique sédimentation entre bassin avant-arc et prisme d'accrétion. *Comptes Rendus de l'Académie des Sciences, Paris* 316, 1131–1137.
- Malavieille, J., Lallemand, S., Dominguez, S., Deschamps, A., Lu, C.-Y., Liu, C.-S., Schnürle, P., 1999. Arc-continent collision in Taiwan. *Marine Observations and Geodynamic Model: abstract, Thrust Tectonics Meeting*, 26–29 April 1999. Royal Holloway Univ. of London, England.
- Malavieille, J., Lallemand, S.E., Dominguez, S., Deschamps, A., Lu, C.-Y., Liu, C.-S., Schnürle, P., ACT Scientific Crew, 2002. Arc-continent collision in Taiwan: new marine observations and tectonic evolution. In: Byrne, T.B., Liu, C.-S. (Eds.), *Geology and Geophysics of an Arc-Continent collision*, Taiwan, 358, pp. 187–211. Republic of China: Boulder, Colorado, Geological Society of America Special Paper.
- Marques, F.O., Cobbold, P.R., 2002. Topography as a major factor in the development of arcuate thrust belts; insights from sandbox experiments. *Tectonophysics* 348, 247–268 no. 4.
- Martinez, A., Malavieille, J., Lallemand, S., et Collot, J.Y., 2002. Partition de la déformation dans un prisme d'accrétion sédimentaire en convergence oblique: approche expérimentale. *Bulletin de la Société Géologique de France* t.173, 17–24.
- McIntosh, K., Nakamura, Y., Wang, T.-K., Shih, R.-C., Chen, A., Liu, C.-S., 2005. Crustal-scale seismic profiles across Taiwan and the western Philippine Sea. *Tectonophysics* 401, 23–54.

- Merle, O., Abidi, N., 1995. Approche expérimentale du fonctionnement des rampes émergentes. *Bulletin de la Société Géologique de France* 166, 439–450 no. 5.
- Mugnier, J.L., Baby, P., Colletta, B., Vinour, P., Bale, P., Leturmy, P., 1997. Thrust geometry controlled by erosion and sedimentation; a view from analogue models. *Geology (Boulder)* 25, 427–430 no. 5.
- Mulugeta, G., 1988. Modelling of the geometry of the Coulomb thrust wedges. *Journal of Structural Geology* 10, 847–859.
- Persson, S., Sokoutis, D., 2002. Analogue models of orogenic wedges controlled by erosion. *Tectonophysics* 356, 323–336.
- Persson, K.S., Garcia-Castellanos, D., Sokoutis, D., 2004. River transport effects on compressional belts: First results from an integrated analogue-numerical model. *Journal of Geophysical Research* 109, B01409. doi:10.1029/2002JB002274.
- Reed, D.L., Lundberg, N., Liu, C.H., Kuo, B.Y., 1992. Structural relations along the margins of the offshore Taiwan accretionary wedge: implications for accretion and crustal kinematics. *Acta Geologica Taiwanica* 30, 105–122.
- Richard, M., Bellon, H., Maury, R., Barrier, E., Juang, W.-S., 1986. Miocene to recent calc-alkalic volcanism in eastern Taiwan: K–Ar ages and petrography. *Tectonophysics* 125, 87–102.
- Sella, G.F., Dixon, T.H., Mao, A., 2002. REVEL: a model for recent plate velocities from space geodesy. *Journal of Geophysical Research* 107, 2081.
- Seno, T., 1977. The instantaneous rotation vector of the Philippine Sea plate relative to the Eurasian Plate. *Tectonophysics* 42, 209–225.
- Seno, T., Stein, S., Grip, A.E., 1993. A model for the motion of the Philippine Sea plate consistent with NUVEL-1 and geologic data. *Journal of Geophysical Research* 98, 17941–17948.
- Shemenda, A., 1994. Subduction: insights from physical modelling. Kluwer Academic Publishers, Dordrecht, p. 215.
- Shyu, J.B.H., Sieh, K., Chen, Y.-G., 2005. Neotectonic architecture of Taiwan and its implications for future large earthquakes. *Journal of Geophysical Research* 110. doi:10.1029/2004JB003251.
- Sibuet, J.-C., Hsu, S.-K., 1997. Geodynamics of the Taiwan arc–arc collision. *Tectonophysics* 274, 221–251.
- Simoès, M., 2005. Déformation crustale et évolution thermique d’une chaîne de collision: l’exemple de Taiwan. Thesis, Institut de Physique du Globe de Paris, Paris, pp. 248.
- Simoès, M., Avouac, J.P., Beyssac, O., Goffe, B., Farley, K.A., Chen, Y.-G., 2007. Mountain building in Taiwan: A thermokinematic model. *Journal of Geophysical Research* 112, B11405. doi:10.1029/2006JB004824.
- Smit, J.H.W., Brun, J.P., Sokoutis, D., 2003. Deformation of brittle–ductile thrust wedges in experiments and nature. *Journal of Geophysical Research* 108 (B10), 2480. doi:10.1029/2002JB002190.
- Storti, F., Mc Clay, K., 1995. Influence of syntectonic sedimentation on thrust wedges in analogue models. *Geology* 23, 999–1002.
- Suppe, J., 1984. Kinematics of arc-continent collision, flipping of subduction, and back-arc spreading near Taiwan. *Memoir of the Geological Society of China* 6, 21–33.
- Tang, J.-C., Chemenda, A.I., 2000. Numerical modeling of Arc-Continent Collision: Application to Taiwan. *Tectonophysics* 325, 23–42.
- Teng, L.S., Wang, Y., Tang, C.H., Huang, C.Y., Huang, T.C., Yu, M.S., Ke, A., 1991. Tectonic aspects of the Paleogene depositional basin of northern Taiwan. *Proceedings of the Geological Society of China* 34, 313–336.
- Tillman, K.S., Byrne, T.B., 1995. Kinematic analysis of the Taiwan Slate Belt. *Tectonics* 14, 322–341.
- Wessel, P., Smith, W.H.F., 1995. New Version of the Generic Mapping Tools Released EOS (Transactions, American Geophysical Union) AGU 76, 329.
- Wu, F., Rau, R.-J., Salzberg, D., 1997. Taiwan orogeny: thin-skinned or lithospheric collision? *Tectonophysics* 274, 191–220.
- Yang, T.F., Lee, T., Chen, C.-H., Cheng, S.-N., Knittel, U., Punongbayan, R.S., Rastdas, A.R., 1996. A double island arc between Taiwan and Luzon: consequence of ridge subduction. *Tectonophysics* 258, 85–101.
- Yu, S.-B., Chen, H.-Y., Kuo, L.-C., 1997. Velocity field of GPS stations in the Taiwan area. *Tectonophysics* 274, 41–59.

3.2 PhD thesis

I presented in the previous section my experience in the treatment of large-scale geodynamic processes. Being missing some fieldwork experience and willing to investigate ductile driven deformation mechanisms within fault zones I decided to seek for a PhD thesis dedicated to a regional geology thematic. I paid the utmost attention that the subject included a substantial amount of field practice in terms of cartography and sampling.

The subject proposed by the research group of Prof. S.M. Schmid, director of the Institute of geology and paleontology at the University of Basel (Switzerland) hold my attention. The thesis was aiming to a better understanding of the formation of the western external alpine arc between Pelvoux and Argentera massifs. The enrolment was planned for a duration of four years and included ten months of investigations in the field within a scientifically renowned team. I could include in the PhD theme some microfabric investigations on highly deformed rocks and a low-grade metamorphic study. I had appreciated these two disciplines during my Master thesis.

I wish here to thank Professor Schmid who considered my candidature. I am going to summarize my main results while insisting on the adopted multidisciplinary approach which is in my opinion essential to any research work.

The western alpine arc has an average radius of around 150 kilometers and is limited by SW-NE subalpines chains to the north and by NW-SE subalpine chains to the south. My field area lied within the southern portion of the arc between Pelvoux and Argentera massifs. In spite of more than a century of geological studies within the Alps, no general agreement for a reconstruction in time and space could be found in the literature. One of the main difficulties is found in the apparent 90 degrees divergence of thrusting directions between the north and the south of the Pelvoux massif and several evolution models have been proposed in

the literature (Butler et al., 1986; Platt et al., 1989; Ricou, 1984; Ricou and Siddans, 1986; Vialon et al., 1989). Ceriani et al. (2001) proposed that Adriatic block indentation was accommodated by a major out of sequence thrust, the Roselend thrust (RT), which partly reactivates the Penninic front at the rear of external crystalline massifs. According to their model, activity along the RT is accommodated by dextral movements along the Insubric line north of the alpine arc and sinistral movements within a major shear zone at the rear of the Argentera massif.

My studies have evidenced a record of polyphase deformation within the area between Pelvoux and Argentera massifs.

The first D1 deformation phase is related to Pyrenean orogeny tectonic episode. D1 is found in terms of relicts within Mesozoic Dauphinois sedimentary series and in external crystalline massifs. The deformation is visible within inverted hemi grabens type structures.

Alpine D2 deformation is found in the form of consistent NW-directed transport directions along thrusts carrying external Briançonnais units on top of pre-structured Dauphinois units. These thrusts induce spectacular mylonitisation phenomena and folding of the Dauphinois sedimentary units. This alpine phase, in a strict sense, is related to activity along the RT and is ubiquitous in the field both north and south of the Pelvoux massif.

I could therefore confirm Ceriani et al. (2001) hypothesis and described a major sinistral shear zone at the rear of the Argentera massif.

My investigations carried within para-autochthonous dauphinois series and Embrunais Ubaye nappe stack basal decollements have demonstrated that SW directed transport direction described in literature does exist and is related to a later D3 phase postdating RT activity.

The most recent D4 phase is related to the Durance fault network activity (Delacou, 2004; Sue et al., 2000, 1999) still active at present-day.

I proposed a model which confirmed hypotheses by Ceriani et al. (2001) inferring that the Adriatic bloc was transported towards the NW along the Roselend thrust. According to my model, the Embrunais Ubaye helmenthoïd flysch nappes were emplaced during this Oligo Miocene episode.

Besides this geological model gained from deciphering geological structures overprint in time and space, I could demonstrate that metamorphic conditions prevailing in the study area fall within the range between upper diagenesis and low anchizone instead of epizonal conditions as given in the literature (Potel and Trullenque, 2012).

Using literature data by Carminati et al. (2004, 1998a, 1998b) I proposed that the D3 phase is related to far-field stresses within the French SE basin transmitted during Mediterranean basin opening and Apennine formation.

The second theme of my PhD concentrated on a complete microfabric of a Priabonian marbles sample series having suffered variable amounts of deformation during the previously mentioned D2 phase.

This work was motivated by 1) the spectacular nature of outcrops encountered in the field, 2) my will to deepen my theoretical knowledge in microfabric analysis acquired during my Master degree and 3) the ambiguity related to interpretation of crystallographic preferred orientations (CPO) found in calcitic rocks where *c* axis distributions can be oriented normal or inclined either in or against the sense of shear (Schmid et al., 1987).

My results were based on a combination of studies using thin sections and X-ray textural goniometry analyses. I have shown that dislocation creep and dynamic recrystallization in the absence of twinning can lead to two distinct microfabric types. Samples presenting both orthorhombic symmetry in terms of crystallographic preferred orientation and grain axes are deformed in a co-axial strain regime. Preferential crystal glide along $\langle 10\text{-}10 \rangle$ and $\langle 02\text{-}21 \rangle$ directions along *f* and *r* planes with a minor contribution of basal

glide in the $\langle a \rangle$ direction induce a symmetric c axis distribution on each side of the pole to foliation. The second family of samples showing monoclinic symmetry has been deformed under a non-coaxial strain regime. Duplex glide in the $\langle a \rangle$ direction along the basal plane is responsible of a single c axis distribution at 15 degrees to foliation normal, in the sense of shear.

I used my model of microfabric evolution on samples collected along the Roselend thrust in order to test its applicability in terms of structural geology. I could again independently confirm the presence of broad sinistral shear zone at the rear of the Argentera massif as hypothesized by Ceriani et al. (2001). I could also outline an evolution in terms of strain regime along the Roselend thrust, non-coaxial strain becoming more intense when approaching the Pelvoux massif rigid bloc.

As a summary to this theme dedicated to microfabric analysis, I could argue that CPO in calcitic rocks can be used to determine shear senses, but care must be taken regarding twinning development as twins develop a c axis orientation against the sense of shear.

The results of my PhD thesis have been published in the form of two A ranking articles published in international scientific journals (Potel and Trullenque, 2012; Trullenque et al., 2006).

Besides research, I was responsible during my PhD of X-ray textural goniometry measurements on demand from colleagues. I developed a procedure in order to achieve a complete orientation distribution function analysis and the different routines are available in the appendices of my thesis (Trullenque, 2005).

I was also involved in teaching activities which included laboratory practice and field work supervision.



Microfabrics of calcite ultramylonites as records of coaxial and non-coaxial deformation kinematics: Examples from the Rocher de l'Yret shear zone (Western Alps)

Ghislain Trullenque^{a,*}, Karsten Kunze^b, Renee Heilbronner^a,
Holger Stünitz^a, Stefan M. Schmid^a

^a Department of Geosciences, Basel University, Bernoullistr. 30-32, CH-4056 Basel, Switzerland

^b Geological Institute, ETH Zürich, CH-8092 Zürich, Switzerland

Received 24 September 2004; received in revised form 30 May 2006; accepted 21 June 2006

Available online 10 August 2006

Abstract

Microfabrics were analysed in calcite mylonites from the rim of the Pelvoux massif (Western Alps, France). WNW-directed emplacement of the internal Penninic units onto the Dauphinois domain produced intense deformation of an Eocene-age nummulitic limestone under lower anchizone metamorphic conditions (slightly below 300 °C). Two types of microfabrics developed primarily by dislocation creep accompanied by dynamic recrystallisation in the absence of twinning. Coaxial kinematics are inferred for samples exhibiting grain shape fabrics and textures with orthorhombic symmetry. Their texture (crystallographic preferred orientation, CPO) is characterised by two *c*-axis maxima, symmetrically oriented at 15° from the normal to the macroscopic foliation. Non-coaxial deformation is evident in samples with monoclinic shape fabrics and textures characterised by a single oblique *c*-axis maximum tilted with the sense of shear by about 15°. From the analysis of suitably oriented slip systems for the main texture components under given kinematics it is inferred that the orthorhombic textures, which developed in coaxial kinematics, favour activity of <10–11> and <02–21> slip along the *f* and *r* planes, respectively, with minor contributions of basal-*a* slip. In contrast, the monoclinic textures, which developed during simple shear, are most suited for duplex *a* slip along the basal plane. The transition between the dominating slip systems for the orthorhombic and monoclinic microfabrics is interpreted to be due to the effects of dynamic recrystallisation upon texture development. Since oblique *c*-axis maxima documented in the literature are most often rotated not with but against the shear sense, calcite textures alone should not be used as unequivocal shear sense indicators, but need to be complemented by microstructural criteria such as shape preferred orientations, grain size estimates and amount of twinning.

© 2006 Elsevier B.V. All rights reserved.

Keywords: Calcite; Microstructure; Crystallographic preferred orientation; Shape preferred orientation; Shear kinematics; Coaxial and non-coaxial deformation; Texture goniometry; CIP

1. Introduction

Microfabrics, i.e. microstructures and textures, are important records of deformation conditions and kinematics in deformed rocks. The term texture refers to

* Corresponding author. Tel.: +41 61 267 3607; fax: +41 61 267 3613.

E-mail address: ghislain.trullenque@unibas.ch (G. Trullenque).

crystallographic preferred orientations (CPO) as used in materials sciences (Bunge, 1982). Calcite microfabrics are particularly used to characterise deformation under low-grade metamorphic conditions, where other minerals do not deform by intracrystalline creep but show cataclastic deformation without dynamic recrystallisation. Different texture types were distinguished for “high” or “low” temperature deformation of calcite (Wenk et al., 1987; Leiss and Ullemeyer, 1999; Leiss and Weiss, 2000; Leiss and Molli, 2003).

There has been considerable debate about the interpretation of symmetry vs. asymmetry of calcite textures and their kinematic significance as indicators for pure shear or simple shear deformation (Kern and Wenk, 1983; Wenk et al., 1987; De Bresser, 1989; Ratschbacher et al., 1991; Erskine et al., 1993; Burlini et al., 1998; Leiss et al., 1999; Bestmann et al., 2000; Kurz et al., 2000). Calcite textures in naturally and experimentally deformed rocks often exhibit *c*-axis maxima rotated against the sense of shear (Schmid et al., 1981, 1987; Lafrance et al., 1994; Casey et al., 1998). However, there are also textures reported with *c*-axis maxima either oriented exactly normal to the shear direction (Pieri et al., 2001a,b; Barnhoom et al., 2004; Oesterling et al., submitted for publication), or slightly rotated with the sense of shear (Lafrance et al., 1994; Bestmann et al., 2000). Because of such ambiguities, Lafrance et al. (1994) questioned the applicability of calcite textures altogether as shear sense criteria. Further confusion arises from inconsistency in defining the sample reference frame, i.e. whether the foliation or the shear zone boundary are taken as the reference plane, all of which are approximately parallel only after large finite shear strain. Textures with *c*-axis maxima normal to the foliation or symmetrically inclined in two conjugate orientations with respect to foliation and lineation have been interpreted as indicating pure shear deformation (Kern and Wenk, 1983; Wenk et al., 1987). This interpretation is ambiguous, as there are also textures reported with *c*-axis patterns of orthorhombic or even axial symmetry from shear zones that show convincing evidence for non-coaxial deformation (e.g. Bestmann et al., 2000). However, the inverse conclusion is certainly applicable, namely that pure shear deformation (of an initially isotropic aggregate) must lead to fabrics with at least orthorhombic symmetry. Analogously, simple shear must result in fabrics that possess at least monoclinic symmetry, but they may have higher (e.g. orthorhombic) symmetry. Torsion experiments (Pieri et al., 2001a,b; Barnhoom et al., 2004) demonstrated that one and the same simple shear kinematics and identical deformation conditions result in calcite textures with monoclinic symmetry at low strain, which evolve into textures with

either orthorhombic or monoclinic symmetry at large strain.

Apart from texture, a wide variety of microstructural features are potential kinematic indicators in deformed rocks (e.g. Passchier and Trouw, 1996). In monophase aggregates, it is particularly the grain shape fabric, here referred to as shape preferred orientation (SPO). An orthorhombic SPO is generally indicative of dominantly coaxial deformation whereas a monoclinic SPO is indicative of dominantly non-coaxial deformation (for calcite see: Schmid et al., 1987; Lafrance et al., 1994; Bestmann et al., 2000; Pieri et al., 2001a,b). Torsion experiments (Barnhoom et al., 2004) have demonstrated that a monoclinic SPO is established after low strain ($\gamma \sim 1$) and remains stable under shear deformation up to large strain.

A number of recent contributions (Herwegh and Kunze, 2002; Herwegh and Berger, 2003) have demonstrated that the presence of very small amounts of nanometer- and micron-scale second phase particles was of crucial importance regarding the microfabric evolution of calcite mylonites. Herwegh and Kunze (2002) concluded that differences in CPO and SPO geometry (symmetric vs. oblique) in calcite mylonites sampled within the Helvetic Alps are related to different amounts of second phase particles, as they influence the balance between intragranular deformation and dynamic recrystallisation.

This paper describes microstructures and textures analysed in samples of naturally deformed limestone mylonites collected along two profiles across the Rocher de l'Yret shear zone at the rim of the Pelvoux massif (Western Alps). Microfabrics and field evidence clearly indicate distinguishable cases for simple and pure shear dominated deformation for the two sample series, respectively, which should have occurred simultaneously under the same temperature and comparable strain rates. It is concluded that the systematic differences observed in microstructure and texture are due to different deformation paths. Hence the two series of samples may serve as prototypes of distinct types of textures that are indicative of the kinematics of deformation.

2. Geological framework of the study area

2.1. Regional setting

The Rocher de l'Yret Shear Zone (RYSZ), situated at the eastern rim of the Pelvoux massif (Western Alps, France; Fig. 1), separates the Dauphinois domain from the Penninic units and forms part of the Pennine/Penninic Front (Merle and Brun, 1984; Mosar et al., 1996; Bagnoud et al., 1998) also referred to as Pennine/Penninic Frontal

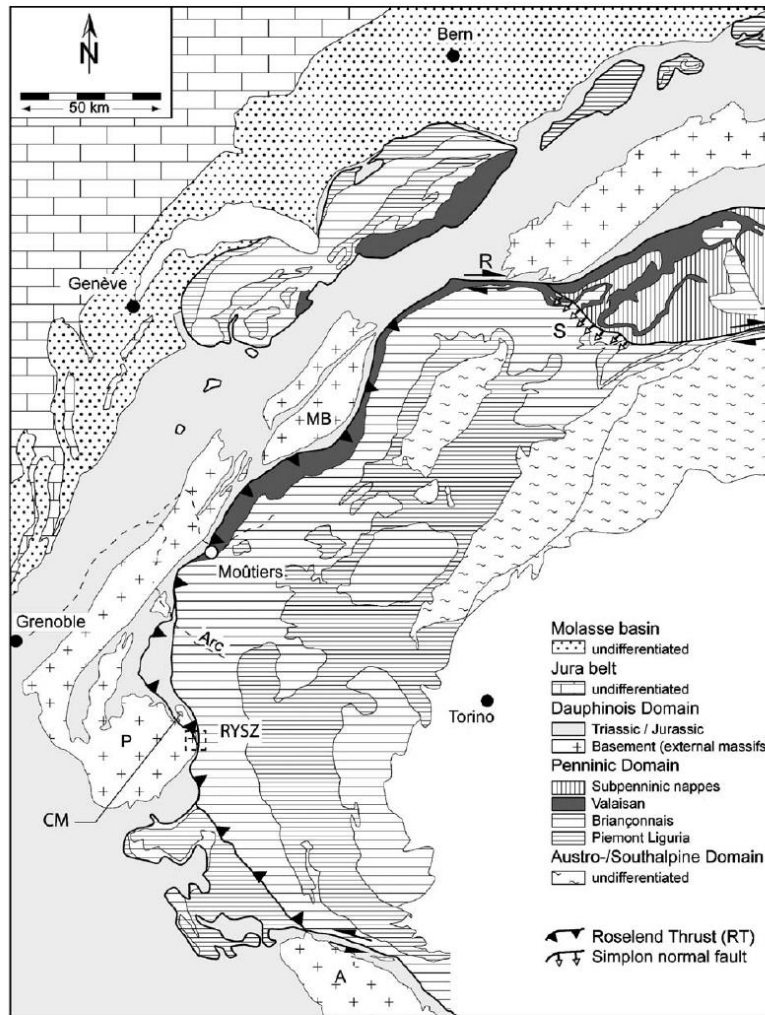


Fig. 1. Simplified geological overview of the arc of the Western Alps (A: Argentera massif, CM: Combeynot massif, MB: Mont Blanc massif, P: Pelvoux massif, R: Rhone-Simplon line, S: Simplon normal fault, T: Tonale line, RYSZ: Rocher de l'Yret shear zone; after Froitzheim et al., 1996; Ceriani et al., 2001).

thrust (Spencer, 1992; Seward and Mancktelow, 1994; Bürgisser and Ford, 1998). According to Ceriani et al. (2001), this thrust formerly represented a suture zone between Dauphinois and Briançonnais/Subbriançonnais, active during Eocene times and related to the subduction of the Valaisan Ocean. The Valaisan oceanic domain was closed in sinistral transpression, associated with a top to the north sense of movement. During a second deformation stage (Oligo–Miocene), WNW-directed thrusting along the entire Western Alps on a major out-of-sequence thrust, the Roselend thrust, completely reworked the

Penninic front. In particular, calcite mylonites were formed in Eocene sediments (nummulitic limestone) on top of a regional unconformity, which cuts across the Jurassic sediments into the basement and is defined by the deposition of a detrital calcitic conglomerate.

2.2. Temperature conditions during deformation

The degree of Alpine metamorphic overprint of the eastern rim of the Pelvoux massif, as estimated by Arahamian (1974, 1988) by means of illite crystallinity

(IC) measurements, occurred under epizonal conditions ($IC < 2.8$ for the RYSZ). Furthermore, temperatures can indirectly be derived from a contoured zircon fission track isochron map of the Western Alps compiled by Fuegenschuh and Schmid (2003). The whole eastern rim of the Pelvoux massif is characterised by zircon fission track ages older than 60 My, indicating that the corresponding rocks had not been exposed to temperatures above the upper limit of the zircon partial annealing zone, i.e. 320 °C (Tagami et al., 1998), for 60 My. Zircon fission track data from the Briançonnais and Dauphinois domains, immediately south of the RYSZ (Seward et al., 1999), yielded ages older than 100 My, which clearly excludes metamorphic temperatures above 320 °C during the Tertiary. Hence, temperatures must have been around 300 °C or even slightly below around the whole eastern rim of the Pelvoux massif. Preliminary results based on new IC data and fluid inclusion analyses indicate low anchizonal metamorphic conditions (Potel, pers. comm.),

putting the epizonal conditions proposed by Aprahamian (1974, 1988) again under question.

2.3. Structural setting

At the eastern rim of the Pelvoux massif, the Roselend thrust (RT) enters the Mesozoic cover of the external massifs. It thrusts the Combeynot massif (CM) together with its Eocene sedimentary cover over the Pelvoux massif towards the West (Fig. 1). Near the outcrop investigated in this study, the Combeynot massif joins the RYSZ, which is a km-wide shear zone that represents the RT in this area.

The RYSZ is an imbricate structure consisting of two large slices of the Pelvoux massif, the lower “Grangettes” slice, and the upper “Montagnolle” slice (Gignoux and Moret, 1938; Gidon, 1954; Gidon, 1979; Beach, 1981; Ford, 1996). Butler (1992) has described WNW-directed shearing of nummulitic limestones in a basement/cover imbricate structure forming the Rocher de l’Yret summit

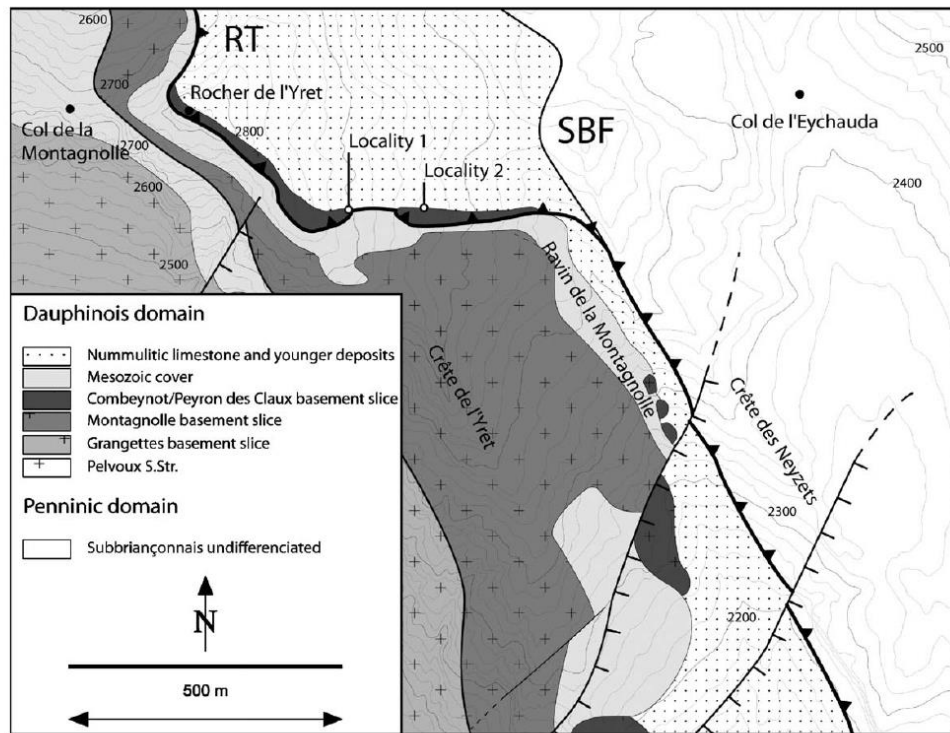


Fig. 2. Detailed geological map of the sampling area around the Rocher de l’Yret shear zone (RYSZ) after field mapping (Trullenque, 2005); sampling localities 1 and 2 are marked.

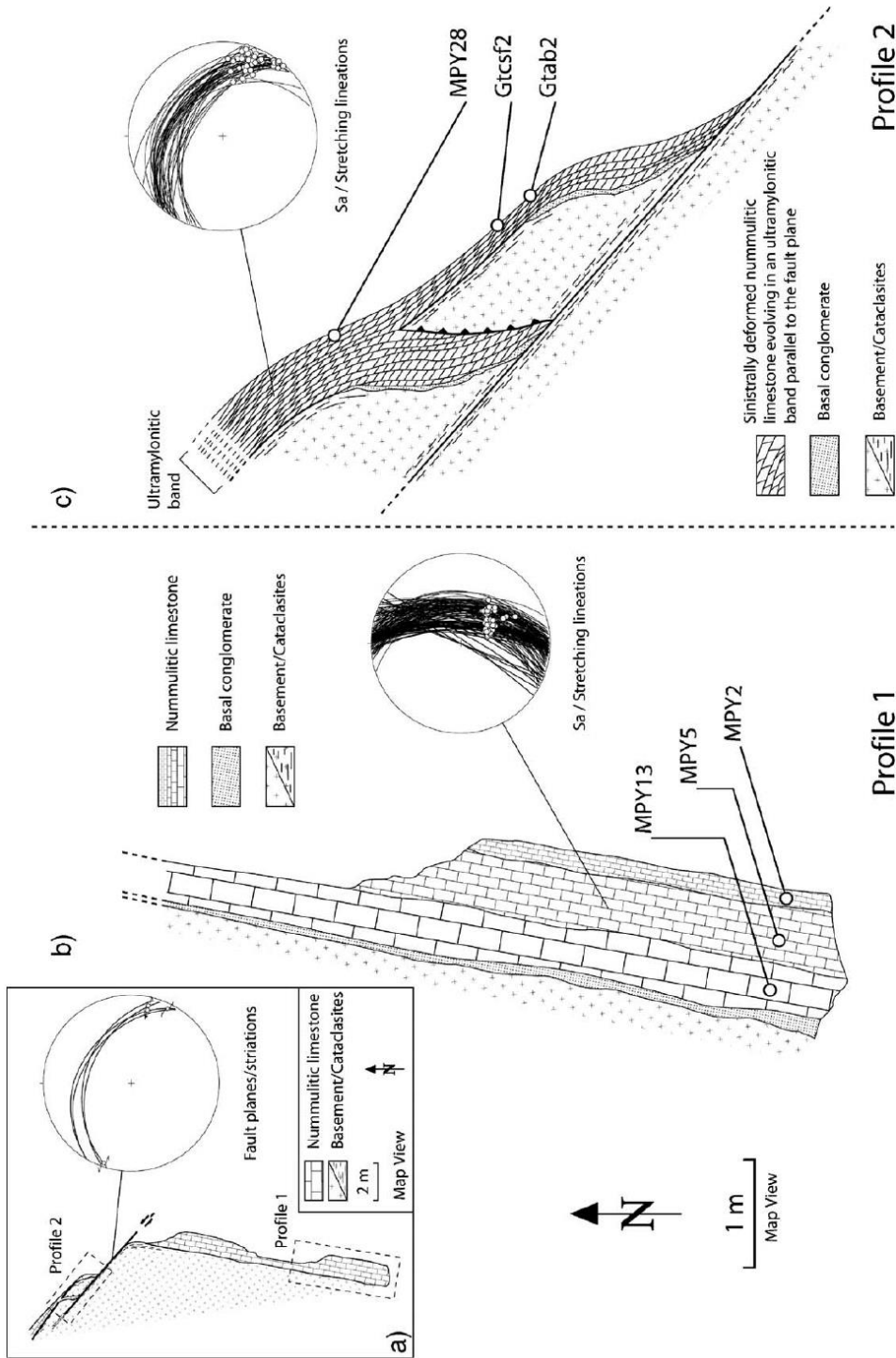


Fig. 3. a) Structural scheme of the investigated outcrop at sampling locality 1. Fault plane orientations with striations of the main strike-slip zone are reported. b) Map of profile 1 with location of samples MPY13, MPY5, MPY2; macroscopic foliations Sa with stretching lineations of nummulitic limestone. c) Map of profile 2 with location of samples Gtab2, Gtcsf2 and MPY28; macroscopic foliations Sa with stretching lineations of nummulitic limestone.

(Fig. 2). According to own regional studies (Trullenque, 2005), this summit consists of a third and very thin basement slice, together with its Eocene-age stratigraphic cover, which represents the calcite mylonites investigated by this study. Thrusting along the RT additionally led to local strike-slip faults affecting these basement-cover boudins.

Most of the samples for this study were taken from an outcrop (locality 1 in Fig. 2) situated within the top-most parts of the RYSZ. It exposes a layer of mylonitised nummulitic limestone that was originally in stratigraphic contact with an isolated basement boudin. At its northern edge, this basement-cover boudin is cut by a sinistral strike-slip zone (Fig. 3a). Lineations and associated shear sense criteria indicate top-WNW shearing over the entire area of the outcrop. Deformation inside the crystalline basement was accommodated by cataclastic faulting and/or flow (Fig. 4a, b), which is consistent with the very low-grade metamorphic conditions, while the nummulitic limestone underwent crystal–plastic deformation.

The main limestone layer is accessible over a horizontal distance of about 20 m striking NNE–SSW. Its mylonitic to ultramylonitic foliation is parallel to internal bedding and to the original stratigraphic contact with the basement boudin. The layer reaches a maximum thickness of 110 cm at the southern termination of the outcrop. Abundant nummulites, several millimetres in size, are preserved in the bottom 30 cm of the sheared limestone layer. In the vicinity to the basal conglomerate it also contains a significant portion of detrital quartz. This quartz–calcite-mixture develops a strong stretching lineation. Progressive development of a mylonitic foliation parallel to the bedding plane can be observed at increasing distance from the basement and towards the ESE. Decreasing amounts of recognizable nummulite shells correlate with increasing degree of dynamic recrystallisation in calcite,

which is also interpreted as a strong gradient in finite strain normal to foliation. In this part of the outcrop sampling was carried out along a traverse normal to the foliation (profile 1, Fig. 3b).

The strike-slip zone exposed in the northern part of the outcrop (Fig. 3a, c) is associated with the formation of a basement/cover imbricate structure. Along the strain gradient normal to the strike-slip fault, which cataclastically dissects the basement units, the limestone is intensively sheared in a sinistral sense and the upper levels of the layer are progressively bent around the basement slice.

Again, progressive disappearance of macroscopically recognizable nummulite shelves normal to the strike of the limestone indicates that this unit is affected by intensive dynamic recrystallisation. The limestone evolves into an ultramylonitic band showing numerous isoclinal folds, together with a WNW oriented stretching lineation defined by quartz grains.

All samples have been taken at the upper part of the limestone and ultramylonitic band in an orientation subparallel to the one of the strike-slip fault dissecting the basement unit (profile 2, Fig. 3c).

The transition in orientation of both foliations and stretching lineations is rather gradual between the locations of profile 1 (steeply plunging stretching lineation) and profile 2 (mostly horizontal or shallowly plunging stretching lineation) and suggests that deformation of the limestone layer was coeval in profiles 1 and 2.

A paleostress analysis was performed for a set of 124 co-genetic fault planes dissecting basement boudins and their Eocene cover. This analysis was carried out using Tectonic VB software [1] including inversion methods (Angelier and Mechler, 1977). The results (Fig. 5) show average orientations of σ_1 at N264/10 and of σ_3 at N154/60, which are considered to be representative for the

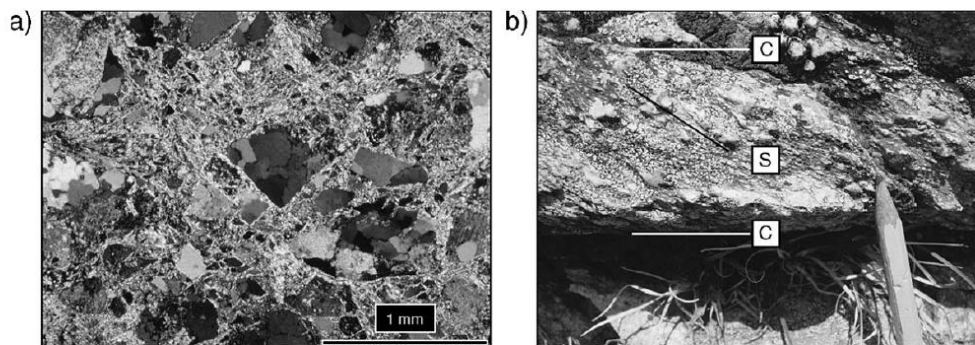


Fig. 4. a) Photomicrograph of the granitic basement cataclastic rock. Large angular patches are dominantly composed of quartz grains and quartz aggregates. b) Close view of the granitic basement cataclasite along the main strike-slip fault plane.

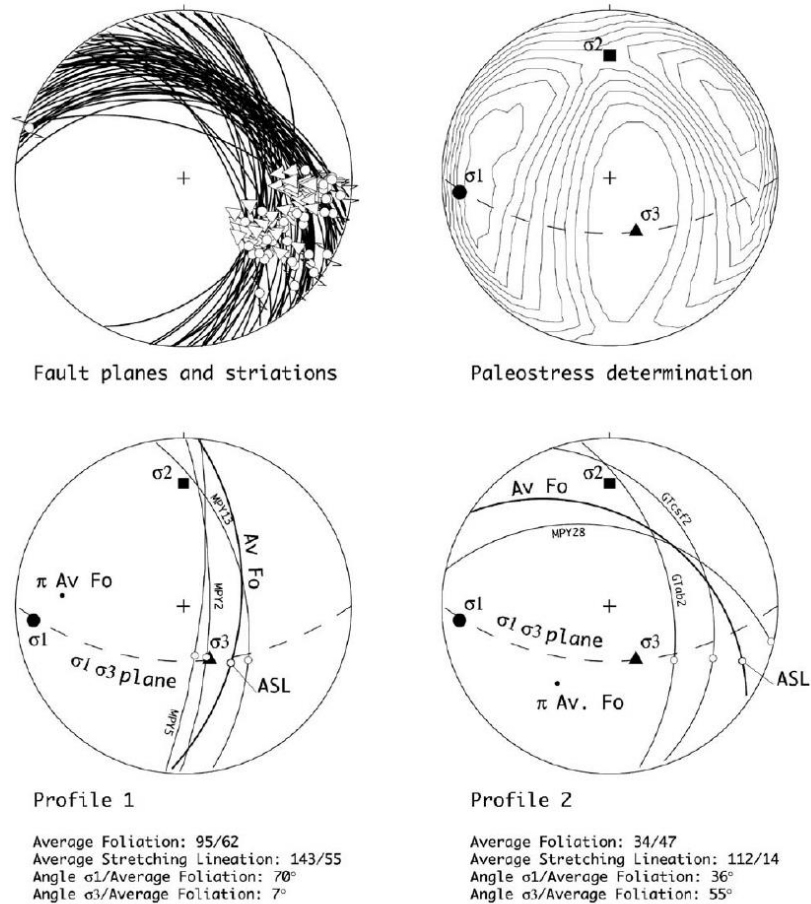


Fig. 5. Paleostress analysis in the basement adjacent to limestone mylonites; P, B and T axes derived from 124 individual fault planes; average orientation of the principal stress axes σ_1 (N264/10), σ_2 (N0/27), σ_3 (N154/60) are superposed over projections of macroscopic foliations (labeled great circles) and stretching lineations (open balls) from profiles 1 and 2 (on average and for the studied samples). Contours of σ_1 , σ_2 and σ_3 are given in multiples of a uniform distribution with a contour interval of 0.3.

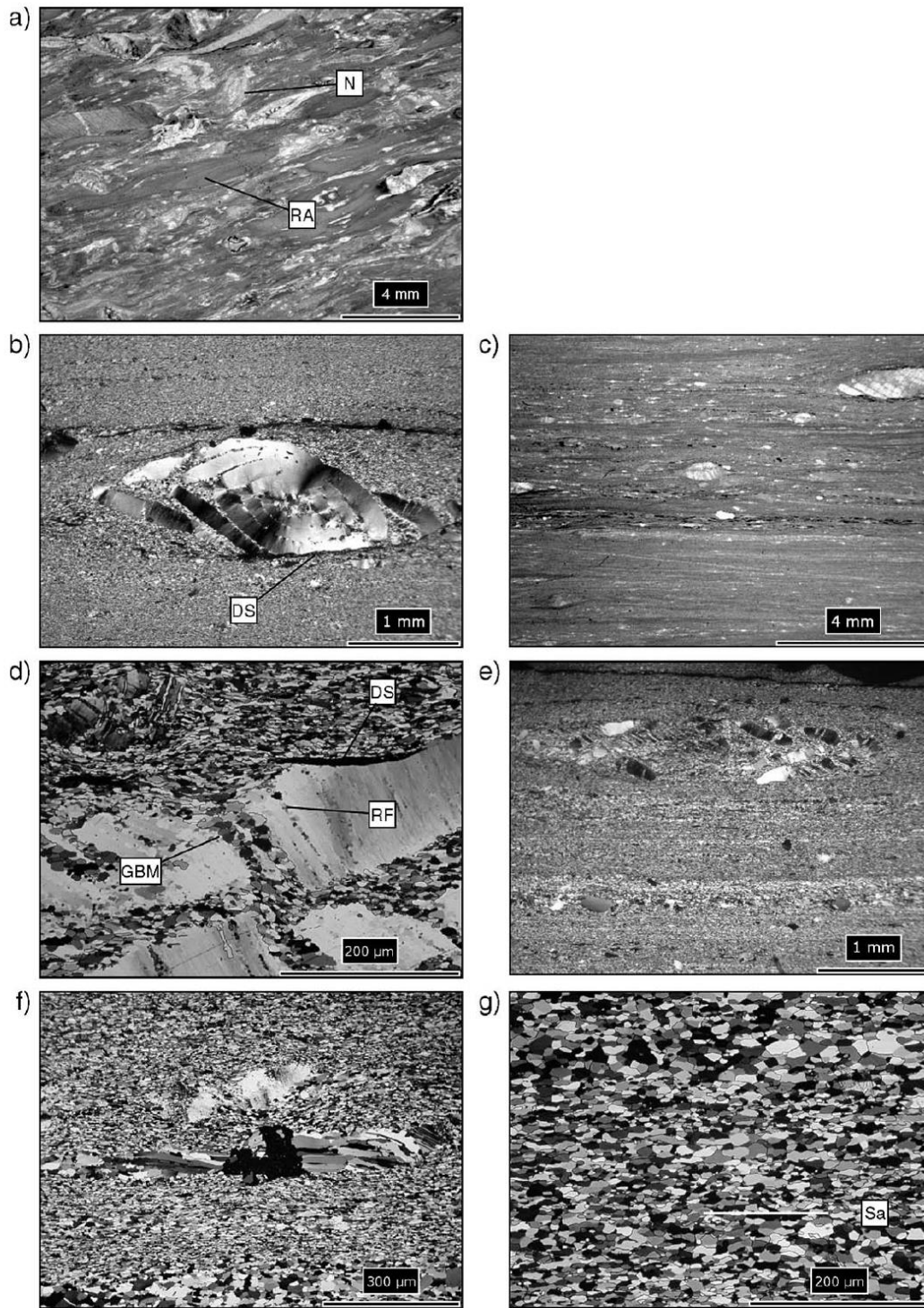
orientation of the bulk stress tensor at a larger scale in the whole RYSZ. Throughout the outcrop, foliation planes roughly intersect in the intermediate stress axis σ_2 , while stretching lineations are about perpendicular to it within the σ_1 – σ_3 plane (Fig. 5). For profile 1, the average stretching lineation falls close to σ_3 while the average foliation is oriented subnormal to σ_1 . This kinematic framework is compatible with coaxial deformation.

For the ultramylonitic band of profile 2, σ_1 and σ_3 fall at intermediate (roughly 45°) angles to the average foliation and to the average stretching lineation of the mylonitic layer (Fig. 5). This kinematic framework is indicative of non-coaxial deformation. If deformation

were restricted to plane strain, for which we do not have ultimately decisive indications, then profiles 1 and 2 could be related to pure shear respectively simple shear dominated kinematics.

3. Methods of investigation

Samples were cut normal to the macroscopic foliation (Sa) and parallel to the stretching lineation (XZ sections). Approximately 2 μm thick ultrathin sections showing first order grey in calcite in crossed polarised light were prepared for microstructural analysis and for mapping of c -axis orientations by computer integrated polarisation



(CIP) microscopy (Panozzo Heilbronner and Pauli, 1993, 1994). Vectorisation of grain boundaries was performed on digital micrographs using a combination of NIH Image [2] and own software. On average, about 3500 particles were evaluated per sample to determine their SPO and grain size distributions. The preferred orientation of the grain long axes was determined using the PAROR method, while the preferred orientation of grain boundary surfaces was analysed using the program SURFOR (Panozzo, 1983, 1984). The determination of particle grain sizes was performed using the program STRIPSTAR [3].

Pole figures were measured with a SIEMENS D5000 X-ray texture goniometer in reflexion and transmission modes for three crystallographic planes (r {10–14}, a {11–20} and h {20–22}) for each sample. Lattice planes and directions are designated here by Miller–Bravais hexagonal indices referring to the structural hexagonal unit cell with axial ratio $c/a=3.419$ as classified by Wyckoff (1920). Empirical corrections for defocusing in reflection mode and for scattering volume in transmission mode were applied before merging into complete pole figures. The orientation distribution function (ODF) was calculated using both MENTEX (Schaeben et al., 1990) and BEARTEX-WIMV (Wenk et al., 1998) software, and selected ODF sections are displayed by intensity contour plots. The quality of the ODF calculations was consistently satisfactory as verified by confidence parameters (difference pole figures, RP values, convergence rate) provided by the respective software packages. The applied convention for Euler angles (ψ_1, Φ, ψ_2) relates to the one ($\varphi_1, \Phi, \varphi_2$) defined by Casey (1981, his Fig. 3) and Bunge (1982) by $\psi_1 = \varphi_1$ and $\psi_2 = \varphi_2 + 90^\circ$, as the crystal coordinate axis X_c is placed here parallel to $+a$ instead of m . Pole figures were recalculated from the ODF for the three measured reflections and additionally for the basal (0001) and the f {01–12} planes, for the inferred slip directions $sd1$ <10–11> and $sd2$ <02–21>, and so are inverse pole figures for particular specimen directions. All pole figures and inverse pole figures were treated with inversion symmetry except for the recalculated $+a$ <–1–120> and $-a$ <11–20> (non-reduced) pole figures. All figures are displayed using equal area projections of the upper hemisphere.

The measured orientation distributions were compared to idealised textures, which are modelled to be composed of a few components around fixed ideal crystal orientations using Gaussian standard distributions of constant and isotropic angular spread (half width of 40° ; software package BEARTEX, Wenk et al., 1998). These model textures could be regarded as first approximation for a complete component fit according to the methods developed by Helming et al. (1994). Pole figures, inverse pole figures and ODF sections of these model textures were displayed analogously to those of the corresponding samples.

4. Microstructure and texture of nummulitic limestone mylonites

Microstructures and textures in limestone mylonites were quantitatively described for about 130 collected and analysed specimens along the Roselend thrust (Trullenque, 2005). In this huge data set, textural and microstructural characteristics are largely repetitive and cluster around two similar but distinct types, which are represented here by samples from profiles 1 and 2 of locality 1. Some other cases are exemplified here by one sample (Sala4) from locality 2. The protolith prior to shear zone formation is characterised by one weakly deformed sample (245a), which contains the sedimentary components still preserved.

Texture strength and degree of fabric anisotropy generally increase with distance from the basement, which will be interpreted also as gradients in finite strain and amount of recrystallisation. The three samples selected for each of the two profiles characterise these gradients.

4.1. Protolith

4.1.1. Sample 245a (Fig. 6a)

The sample was collected south of the investigated shear zone and preserves an association of nummulites, echinoderma fragments and red algae. Two types of components were observed in the thin section. The first type consists of nummulite and echinoderm fragments

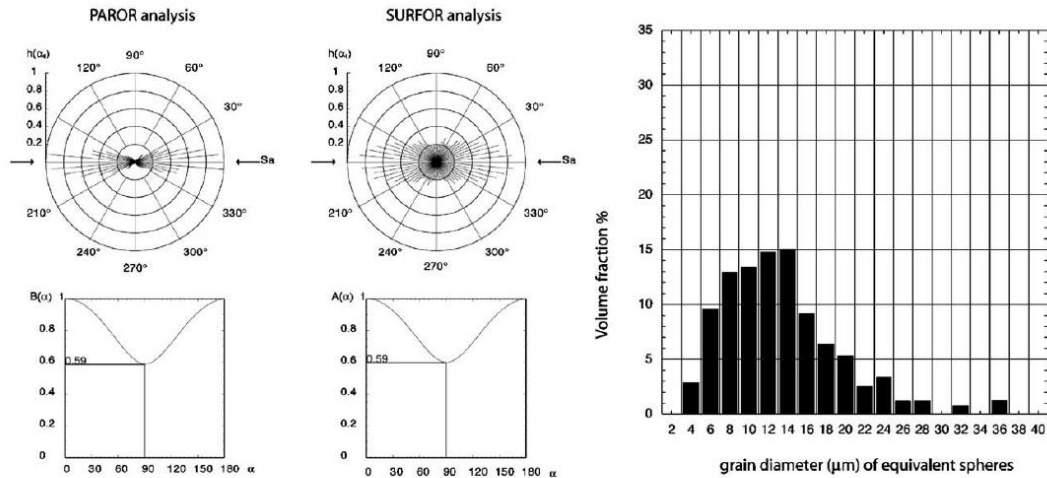
Fig. 6. Photomicrographs of different limestone samples indicating mostly coaxial deformation (profile 1). Photomicrographs were taken from standard thin sections (30 μm thick) in transmitted light without polarisers (a, c), and from ultrathin sections (2 μm thick) in cross-polarised transmitted light (b, d, e, f, g). All sections are oriented normal to foliation and parallel to lineation (horizontal). a) Nummulitic limestone protolith (sample 245a), weakly deformed prior to shear zone formation. Note the association of nummulites (N) and red algae (RA). b, c) Sample MPY13 shows a strong horizontal Sa foliation and dissolution surfaces (DS) subparallel to Sa. The original radial c -axis distribution around the nummulite shell is still preserved. d, e) Sample MPY5 shows a horizontally elongated nummulite shell. Microstructural features indicate grain boundary migration (GBM), rotation recrystallisation and pressure solution processes that have been active simultaneously. Recrystallisation festoons (RF) normal to the nummulite rim. f, g) Sample MPY2 is an entirely recrystallised limestone with a grain shape preferred orientation horizontal (parallel to Sa) and symmetric calcite pressure fringes developed at the rim of detrital quartz grains.

whose size varies between 0.4 and 3.2 mm. Nummulite species *N. garnieri* and *N. fabianii* were identified. The shell of these organisms is made up of several rims of fibrous calcite showing a typical radial *c*-axis pattern. The echinoderm fragments are rounded calcite single crystals and constitute 20% of the rock. The second type

of components consists of red algae mats. They appear as elongated patches with an average aspect ratio higher than 10:1. Their internal structure shows micritic calcite grains with very lobate boundaries and grain size ranging between 2 and 4 μm . These algae mats form between 50 and 60% of the rock. The rest of the rock

Sample MPY2

a) XZ section



b) YZ section

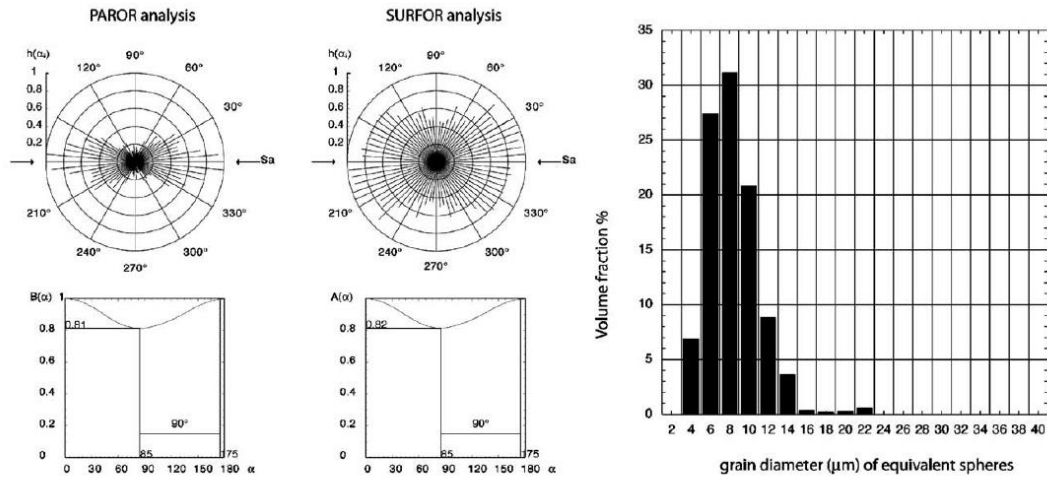


Fig. 7. Microstructural analysis of mylonite sample MPY2 indicating coaxial deformation: The average grain shape ellipsoid is triaxial and parallel to the structural reference frame. Rose diagrams for orientation distributions of particle long axes (PAROR) and of grain boundaries (SURFOR). Histograms of volume-weighted grain size distributions. a) XZ section, i.e. perpendicular to foliation and parallel to stretching lineation. b) YZ section, i.e. perpendicular to both foliation and stretching lineation.

consists of calcitic matrix material, as well as of detrital mica, quartz, or mud pellets (Fig. 6a).

Most of the clearly visible shape fabric anisotropy is attributed to primary sedimentary processes including compaction and not to tectonic deformation during thrusting. Thus sample 245a is considered a typical protolith for the mylonites described below. It shows a texture that is very close to uniform, with faint preferred orientations of *a*-axes perpendicular to and *c*-axes within the bedding plane (Fig. 8, top). A very similar texture was observed in micritic Solnhofen limestone and attributed to passive alignment of calcite grains with their *c*-axes slightly preferred into the bedding plane (Wenk et al., 1973; Casey et al., 1998).

4.2. Profile 1

Below we describe progressive deformation in three samples collected along profile 1 across the southern part of locality 1 (Fig. 3b).

4.2.1. Sample MPY13 (Fig. 6b,c)

This sample shows a protomylonitic fabric, and dynamic recrystallisation affected all the biogenic components. The recrystallisation microstructures are heterogeneous, because the extent of their development is sensitive to the initial structure of the components.

Nummulites and echinoderm fragments typically show a “core and mantle” structure. New grains were

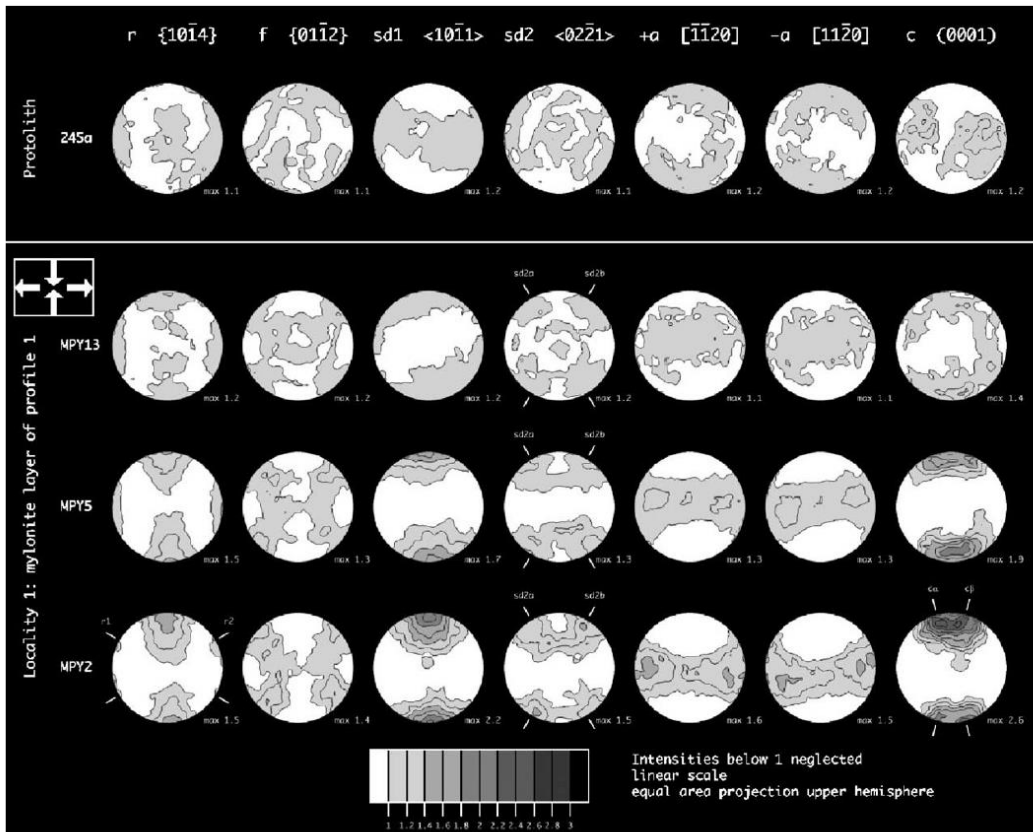


Fig. 8. Texture evolution from the protolith (sample 245a) to mylonites across the limestone layer (profile 1). The protolith shows nearly uniform distributions, which are axial symmetric with faint maxima of *a*-axes perpendicular and of *c*-axes parallel to the bedding plane (*S*₀). The three samples from profile 1 show similar textures of increasing strength with increasing degree of mylonitisation (sorted from top to bottom). Bulk textures obtained by X-ray texture goniometry, all pole figures calculated from the ODF. Pole figure contours are given in multiples of a uniform distribution with a contour interval of 0.2. Intensities below 1 are neglected. The projection is perpendicular to the macroscopic foliation and the stretching lineation is horizontal in the projection plane, equal area projection of upper hemisphere.

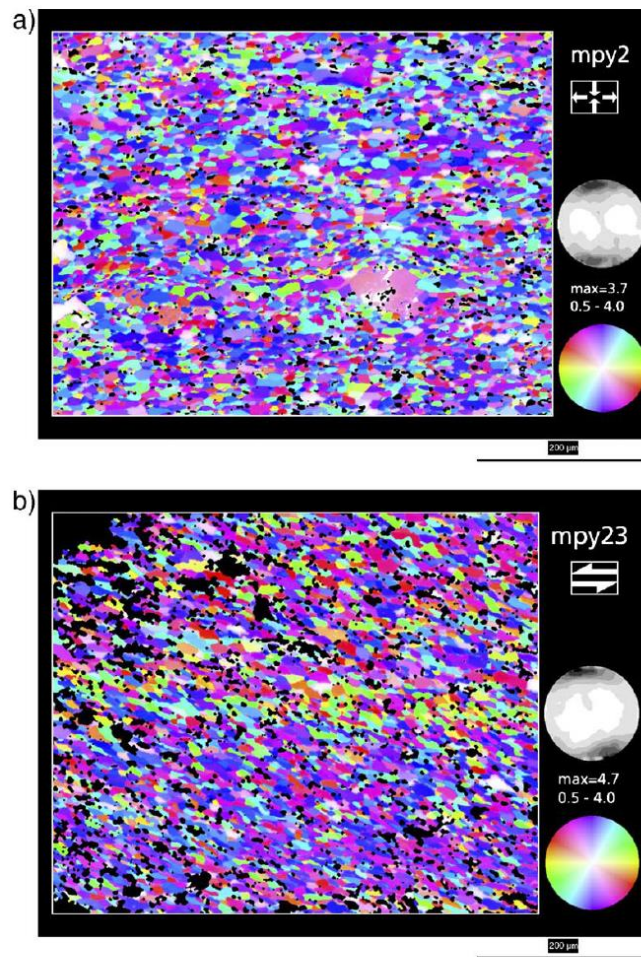


Fig. 9. Computer Integrated Polarisation (CIP) images and derived c -axis distributions. Colour look-up table stereogram at lower right. Contours of the c -axis pole figure given in multiples of uniform distribution with intervals of 0.5. Specimen orientation as above perpendicular to macroscopic foliation Sa, stretching lineation is horizontal. Holes in the thin-section together with areas of non-constant thickness have been masked using black colour and were not taken into account in the c -axis pole figure calculation. a) sample MPY2; b) sample MPY28, sinistral sense of shear.

produced by progressive subgrain rotation in echinoderm porphyroclasts. The internal structure in some nummulites is well preserved and still shows the radial c -axis pattern. Echinoderms are more competent than the surrounding fine-grained matrix and were fragmented by fracturing as well as deformed by twinning. Some 10% of the area contains nummulites and echinoderms that are still preserved.

The outer surfaces of nummulites are commonly oriented parallel to foliation. Dark outlines marked by relatively insoluble fine grained minerals (hematite,

chlorite, micas) are interpreted as remnants of dissolved material indicating that pressure solution has also contributed to the deformation of these calcite rocks. Some external rims of the nummulites are fragmented during progressive deformation. Where fragmentation occurs, the internal parts of the nummulite shells show a greater degree of dynamic recrystallisation.

4.2.2. Sample MPY5 (Fig. 6d,e)

The microstructure of this sample is characterised by further reduced volume fraction of initial

components due to progressive deformation accompanied by dynamic recrystallisation. Pressure solution was also active, evident by locally dissolved nummulite and echinoderm fragments. Deformation affected the entire nummulite shells. The calcite fibres of the nummulite shells show lobate boundaries with bulges into neighbouring crystals, indicating grain boundary migration. Usually, bulges evolve into festoons of new grains along the fragments. Some of the fibres and

their radial *c*-axis patterns are partially preserved. Nummulite shell aggregates are elongated parallel to lineation. The boundaries of primary twins in echinoderms are lobate indicating twin boundary migration. In some places, such twins are bent or overprinted by a second set of deformation twins. The percentage of nummulite and echinoderm fragments has been estimated at no more than 6%, the red algae mats constitute 20% of the rock.

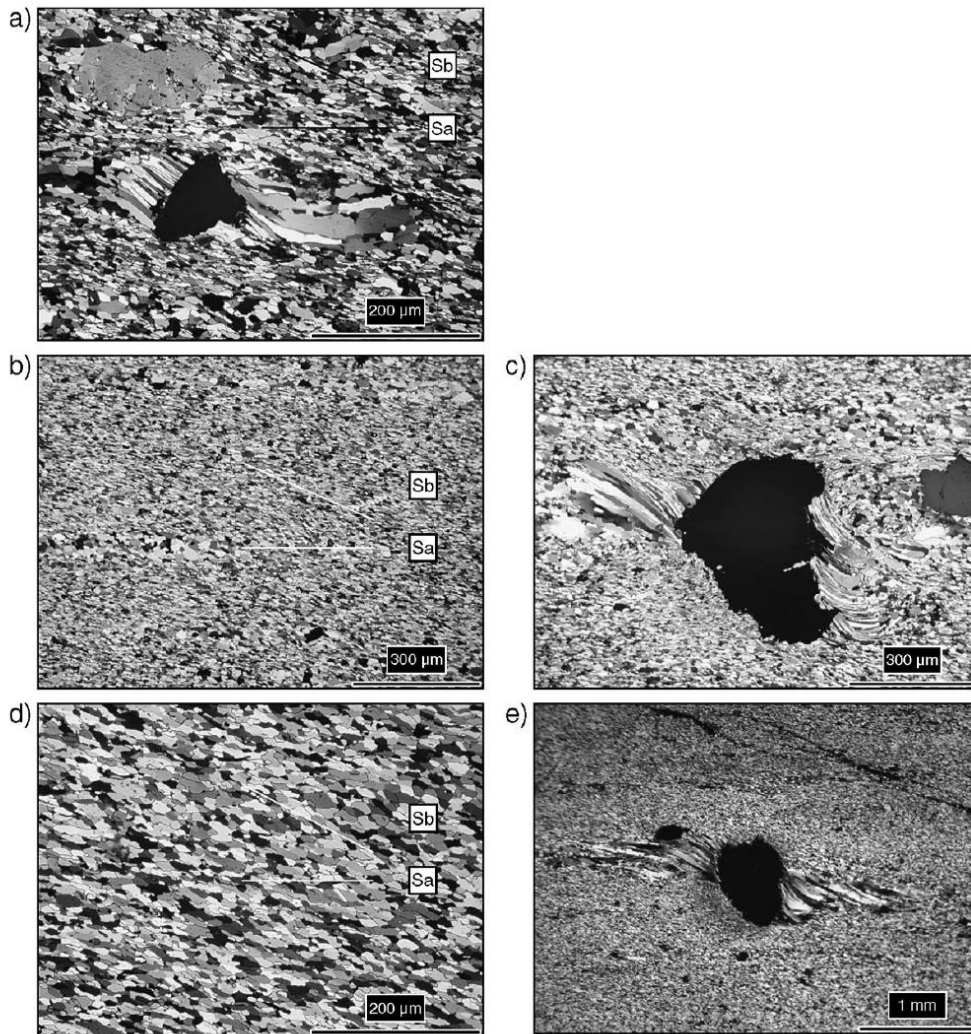


Fig. 10. Photomicrographs of samples indicating non-coaxial deformation, taken from ultrathin sections in cross-polarised light. a) Sample Gtab2; b, c) sample Gtes2; d, e) sample MPY28. Asymmetric calcite pressure fringes developed at the rim of detrital quartz grains (a, c and e). Oblique grain shape preferred orientation (Sb) consistent with sinistral sense of shearing in the rock (a, b and d).

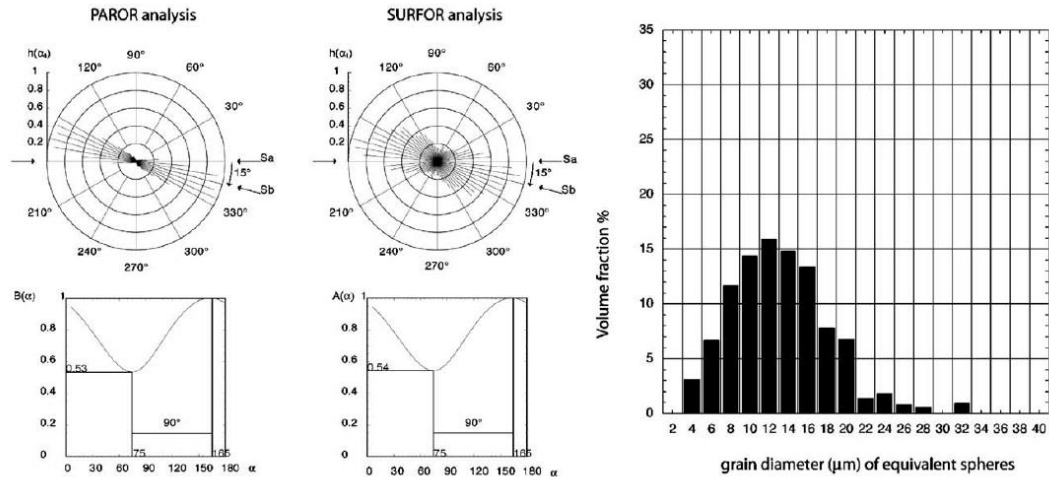
4.2.3. Sample MPY2 (Fig. 6f,g)

The main microstructural difference with respect to sample MPY5 is the lack of any relict nummulite shells.

The grains of the dynamically recrystallised matrix are completely free of deformation twins and show slightly lobate boundaries. They occupy more than 90% of the

Sample MPY28

a) XZ section



b) YZ section

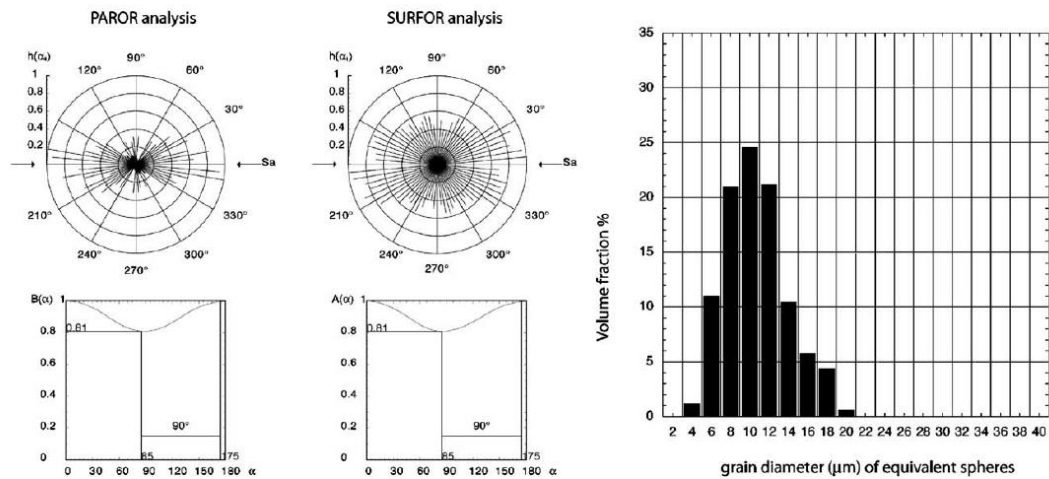


Fig. 11. Microstructural analysis of mylonite sample MPY28 indicating non-coaxial deformation: The average grain shape ellipsoid is triaxial and oblique to the structural reference frame. Same representation as Fig. 7. The grain size distributions show no major differences compared to sample MPY2. a) XZ section, i.e. perpendicular to foliation and parallel to lineation. Average grain long axis inclined by 15° to Sa, compatible with sinistral shearing. b) YZ section, i.e. perpendicular to both foliation and lineation. Note the slight flattening of the grain shape.

rock. Most pressure shadows filled with calcite fibres around detrital quartz grains are symmetrically developed with respect to the foliation.

4.2.4. SPO analysis (Fig. 7)

The SPO of the recrystallised matrix is similar in all three samples; therefore it is shown here only for sample MPY2. *X–Z* sections of the matrix grains show a strong SPO parallel to the foliation with an average aspect ratio of 0.59 and a grain size mode of 12 μm . *Y–Z* sections show SPO with the average long axis also parallel to foliation, an average aspect ratio of 0.81 and a grain size mode of 8 μm . In combination, the average grain shape ellipsoid is aligned parallel to the structural reference system *XYZ* and plots near the diagonal in a Flinn-type diagram with $K \sim 1.1$ indicating a slightly prolate grain shape. The microstructure of the dynamically recrystallised matrix displays an orthorhombic symmetry with respect to foliation and lineation (Fig. 7).

tallised matrix displays an orthorhombic symmetry with respect to foliation and lineation (Fig. 7).

4.2.5. Texture analysis (Fig. 8)

X-ray texture analysis reveals a similar texture type for all three samples of profile 1, but with strength increasing with increasing distance from the basement. The weak texture of sample MPY13 is significantly different from that of the protolith sample 245a. The pole figures display weak maxima of *c*-axes normal to foliation and *a*-axes distributed along girdles parallel to the foliation (Fig. 8).

In closer detail, pole figure maxima are elongated with some preference of rotations around the foliation normal, indicated by girdles and small circles in some pole figures. The *c*-axis pole figure of the most recrystallised sample (MPY2) shows two distinct maxima ($c\alpha$ and $c\beta$) at the

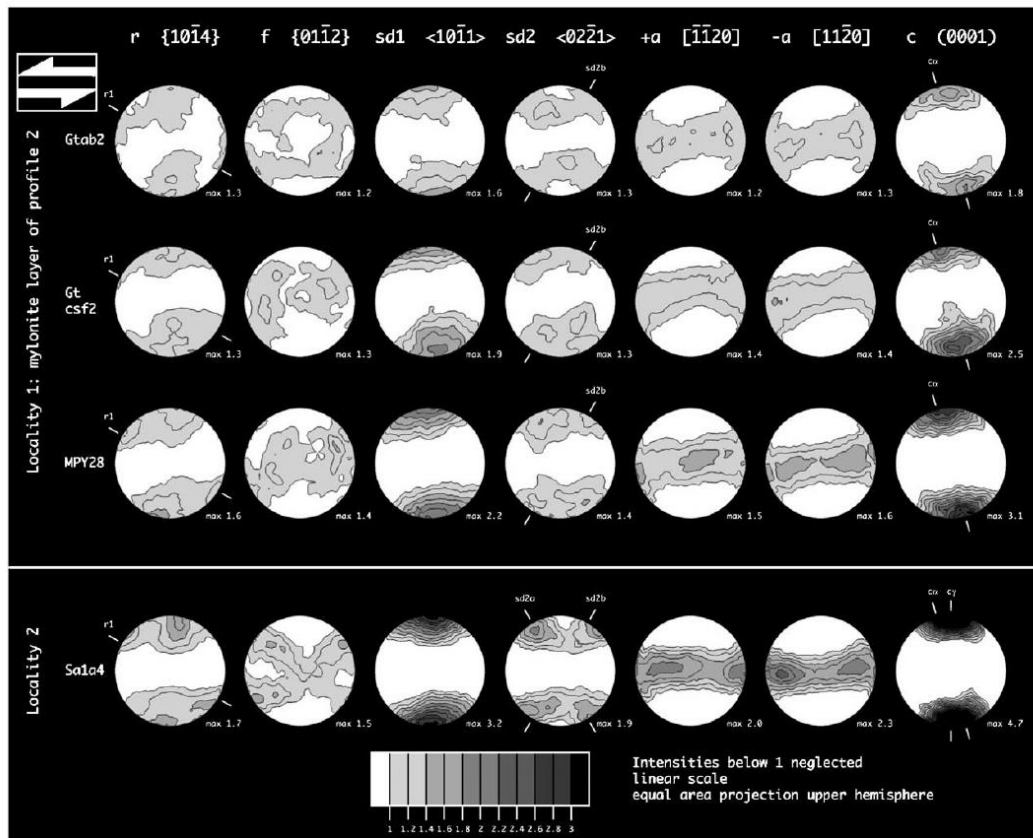


Fig. 12. Texture evolution in the ultramylonitic band (profile 2). Foliation and stretching lineation are horizontal, sinistral sense of shear. Same representation as in Fig. 8. Sample Sa1a4 originates from locality 2 (Fig. 2) and represents intermediate strain kinematics.

periphery of the pole figure, symmetrically oriented at 15° from Z. The CIP *c*-axis pole figure of the dynamically recrystallised matrix shows a similarly shaped but stronger maximum normal to the foliation (Fig. 9a). All textures are characterised by orthorhombic sample symmetry, and the non-reduced $+a$ and $-a$ pole figures are approximately identical. The overall patterns are slightly asymmetric relative to the structural reference system by some minor rotations around the lineation, which may be attributed to misalignments with respect to the foliation plane during specimen collection and preparation.

4.3. Profile 2

Below we describe progressive deformation along profile 2 across the sinistral shear zone in the northern part of the outcrop at locality 1 (Fig. 3c). These rocks were deformed under the same P–T conditions as the ones from profile 1. The specific samples were selected to match pair wise those from profile 1 in terms of the extent of dynamic recrystallisation and of texture strength.

4.3.1. Sample Gtab2 (Fig. 10a)

The dynamically recrystallised matrix possesses an inhomogeneous grain size distribution, where diffuse patches of very fine grain size result from red algae remnants. While the grain size distributions are comparable between this sample and sample MPY13 from profile 1, the SPO of their dynamically recrystallised grains is different. The asymmetric SPO is oblique to the macroscopic foliation and consistent with sinistral shearing of the rock which is further confirmed by asymmetric calcite pressure shadows developed at the rim of detrital quartz grains (Fig. 10).

4.3.2. Sample Gtcsf2 (Fig. 10b,c)

In this sample the volume fraction of recrystallised grains, and presumably also strain intensity, is similar to that of sample MPY5 from profile 1. The matrix of this sample shows a clearly oblique SPO compatible with sinistral shearing, further confirmed by asymmetric calcite pressure shadows developed at the rim of detrital quartz grains.

4.3.3. Sample MPY28 (Fig. 10d,e)

The microstructure is dominated by S–C-structures. The secondary foliation Sb is at 30° to the primary foliation Sa, and calcite fibres at the rim of detrital quartz grains show a clear asymmetry consistent with sinistral shearing of the rock. There are no deformation twins in the recrystallised matrix.

4.3.4. SPO analysis (Fig. 11)

The SPO of the recrystallised matrix is similar in all three samples; therefore it is shown here only for sample MPY28. In the *X*–*Z* section grains have an average aspect ratio of 0.53 with preferential elongation at 15° to the foliation. This SPO angle is only half the angle of Sb to Sa, which was intuitively estimated from the micrographs of Fig. 10. This indicates some bias towards grain boundaries instead of grain long axes in the visual determination of Sb. The grain size distribution has a mode of $12\ \mu\text{m}$. The measurements in the *Y*–*Z* section indicate flattening of the grains normal to the foliation with average aspect ratio of 0.81. In combination, the average grain shape ellipsoid plots near the diagonal in a Flinn-type diagram with $K \sim 1.2$ indicating a slightly prolate grain shape. Its longest and shortest axes lie in the *X*–*Z* plane and make an angle of 15° to the structural reference frame given by mylonitic foliation and lineation (Fig. 11).

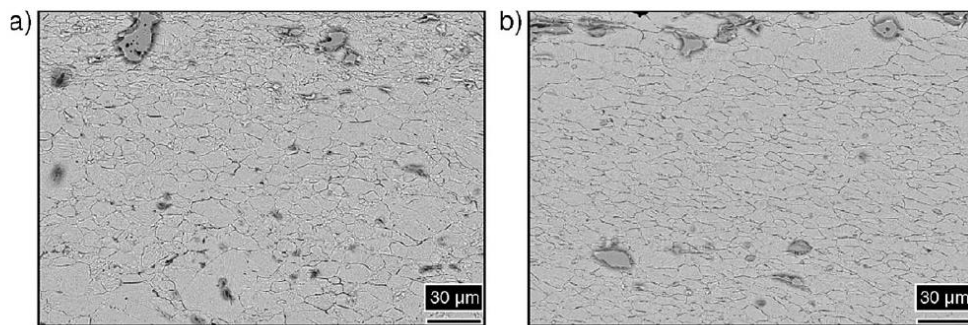


Fig. 13. SEM images (BSE mode, 20 kV acceleration voltage) of typical shape fabrics of sample MPY2 (a) and MPY28 (b). Samples were etched according to the technique described by Herwegh (2000). Light grey: Calcite; darker equant grains: Quartz; darker elongate grains: White micas. Second phase particles do not control the shape of calcite grains.

4.3.5. Texture analysis (Fig. 12)

As in the sample series of profile 1 (Fig. 8), the three samples possess textures of similar type, but with increasing strength again with increasing distance to the basement. The weakest texture of sample Gtab2 has similarly low maxima as sample MPY13, though they are strong enough to distinguish it from MPY13 as well as from the protolith sample 245a. In difference to profile 1, the textures of profile 2 are asymmetric with reference to foliation and lineation, i.e. *c*-axis maxima are at 15° from the foliation normal towards the lineation, and girdles of *a*-axes are similarly inclined to the foliation by counter clockwise rotation of 15° about the structural *Y*-axis. Corresponding asymmetries

are particularly visible in the *r* and the *sd2* pole figures. In reasonable approximation, all pole figures contain a two-fold rotational symmetry about the structural *Y*-axis (Fig. 12).

The pole figures of the most recrystallised sample MPY28 show considerably stronger maxima compared to the other two samples of profile 2. The poles to the *r* planes show one maximum close to *Z* and another one at position labelled “r1”. The pole figure for the *sd2* slip direction shows two maxima symmetrically oriented with respect to the foliation but with different intensities. Along the girdle distributions of the *a*-axes, the +*a* direction has the maximum in the projection centre, while the -*a* direction shows two maxima oppositely

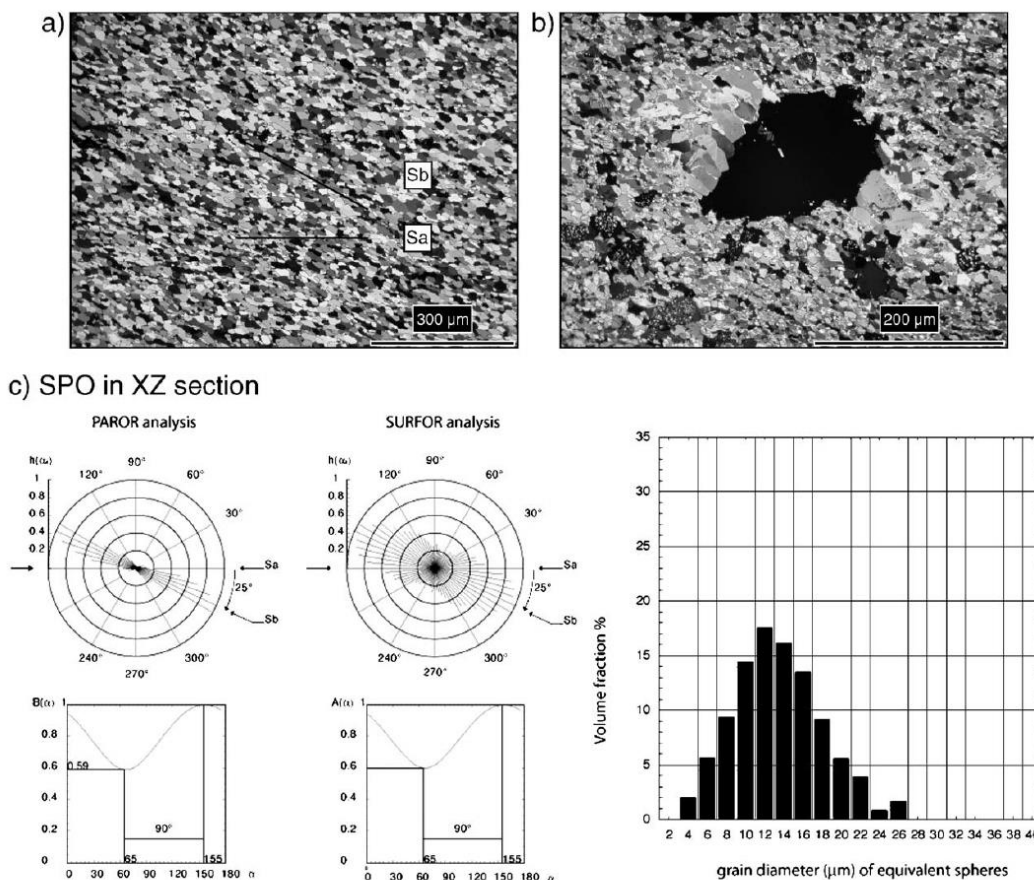


Fig. 14. Microstructure of sample Sa1a4 from locality 2. a, b) Photomicrographs of thin sections in cross-polarised light. Oblique grain shape preferred orientation and asymmetric calcite pressure fringes developed at the rim of detrital quartz grain are both indicative of sinistral shear. c) Microstructural analysis. Grain shape preferred orientation is oblique to *Sa* by 25° compatible with sinistral shearing of the rock. Grain size distribution is similar to that in *XZ* sections of samples MPY2 and MPY28.

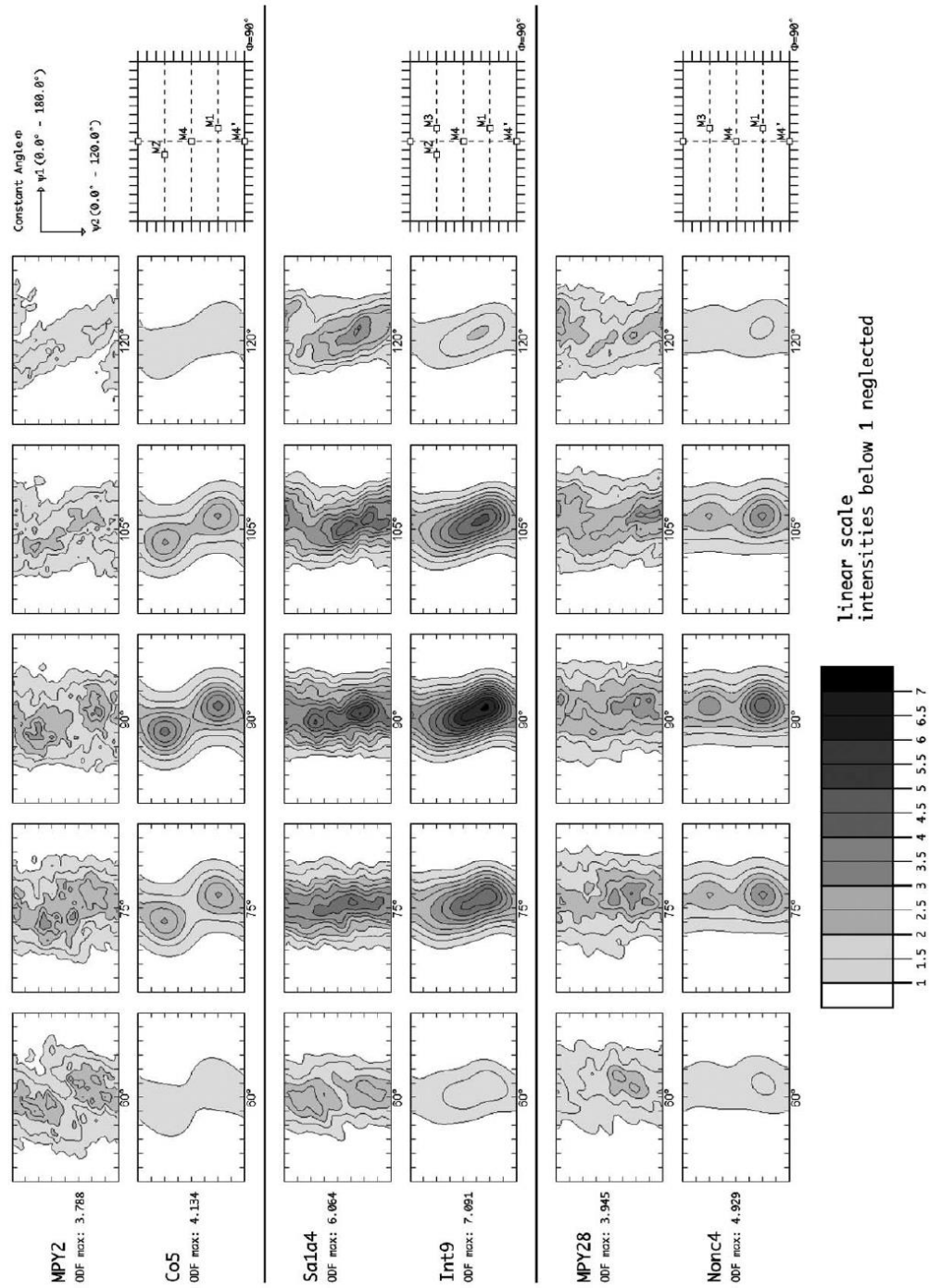


Fig. 15. ODF sections for constant ϕ between 60° and 120° for the three most recrystallised samples (MPY2 from profile 1, Sa1a4 from locality 2, MPY28 from profile 2) and for three corresponding idealized model distributions (co5, in9 and nonc4). The ideal crystal orientations M1, M2, M3, M4, M4' at $\phi=90^\circ$ are illustrated in Fig. 16.

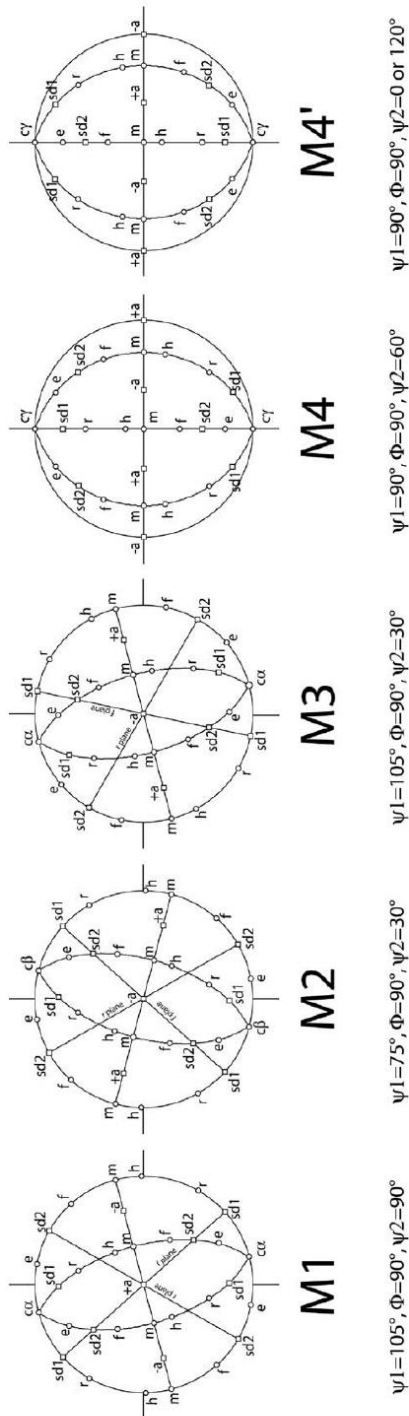


Fig. 16. Equal area projections (upper hemisphere) of ideal crystal orientations used as centres for model distributions. Relevant crystal directions (squares) and poles (circles) are marked.

inclined at 60° from it. The c -axis is tilted by 15° in the sense of shear, which is confirmed by the CIP pole figure (Fig. 9b).

Both microstructure and texture of the dynamically recrystallised matrix indicate a monoclinic symmetry, with the structural Y -direction as the two-fold symmetry axis.

4.4. SEM analysis of samples MPY2 and MPY28

The content in second phase particles of samples MPY2 (orthorhombic microfabric) and MPY28 (monoclinic microfabric) was analysed. Samples were prepared according to the two-step etching technique described by Herwegh (2000) and observed under a scanning electron microscope in backscattered electron mode (Fig. 13). Quartz and micas inclusions are distinguished on the basis of their shape and backscatter contrast. No systematic differences in density, size and distribution of second phase particles have been observed between samples MPY2 and MPY28.

4.5. Ultramylonite sample with asymmetric characteristics

Sample Sa1a4 was taken at locality 2 (Fig. 2), which is east of and along-strike from the outcrop of the two profiles at locality 1. It originates from the hinge of a fold that re-deformed previously formed calcite mylonites and separates two basement boudins including their Eocene cover. The grain size distribution is very similar to those found in samples MPY2 and MPY28, and likewise the dynamically recrystallised matrix covers more than 90% of the volume. The microstructure shows a clear grain shape foliation S_b oriented at 25° to the foliation (Fig. 14a). The grains show sharp extinction and no deformation twinning. Incipient S–C type structures are locally recognizable. Calcite pressure shadows at the rims of detrital quartz grains show an asymmetry and confirm a sinistral sense of shearing (Fig. 14b). Quantitative analysis (Fig. 14c) on the X – Z section yields an average aspect ratio of 0.59 with preferred elongation at 25° to the lineation, and a grain size mode of about $12 \mu\text{m}$.

This sample Sa1a4 shows a texture that is intermediate between that of samples MPY2 and MPY28 (Fig. 12, bottom): The c -axes form a broad and strong maximum roughly normal to the foliation. The r planes and the a directions are similarly oriented as in MPY28, whereas $sd1$ and $sd2$ are similar to the patterns in MPY2. The symmetry of the pole figures deviates visibly from monoclinic about the Y -axis of the actually inferred

Table 1
Volume fractions of orientation components in the three model distributions

Texture components [%]	Random	M1	M2	M3	M4	M4'
Model						
Co5	75	10	10	0	2.5	2.5
Int9	50	17.5	7.5	5	15	5
Nonco4	75	12.5	0	7.5	2.5	2.5

structural reference frame, but could be brought into approximate orthorhombic symmetry, if the reference axes X and Y would have been rotated within the foliation plane by 30° .

4.6. ODF sections and ideal crystal orientation models

In the following, the different texture types found in profiles 1 and 2 and at locality 2 will be discussed. Samples MPY2 and MPY28 are used to represent profiles 1 and 2, respectively, since they exhibit the most strongly developed textures in the two series of samples. Sample Sa1a4 from locality 2 represents a third texture type found repeatedly along the RYSZ.

All textures observed for the limestone mylonites have in common that the c -axes are preferentially oriented towards directions at the pole figure periphery and nearly normal to the foliation plane. Consequently, the ODF sections displayed in Fig. 15 are restricted to sections between $\Phi=60^\circ$ and 120° , where the highest

ODF densities occur along fibres for fixed Euler angles close to $\Phi=90^\circ$ and $\psi_1=90^\circ$ and variable ψ_2 .

Apart from this general similarity, the three sample textures occupy several orientations with different frequency. In an attempt to highlight these differences, model textures are constructed from a set of five ideal crystal orientation components M1, M2, M3, M4 and M4'. The orientations (defined in Fig. 16) and width (40°) of the components were fixed, and only their volume fraction, i.e. their relative weight, was varied, until a satisfying match to the sample textures was found by manual trial-and-error (Table 1). It is emphasized that all three model textures contain between 50 and 75% volume of grains with orientations drawn from a uniform distribution, which means that the visible ODF maxima are actually built of comparatively small volume portions of the sample. In all three cases, M1 is the strongest component, while the second strongest component is either M2 (profile 1) or M3 (profile 2) or M4 (locality 2).

Orientation M1 places the c -axis at an angle of 15° counter clockwise from the Z -direction of the sample. Two single poles of r and f planes are located at the periphery of the pole figure at angles of about 60° and 50° from Z in a conjugate geometry, respectively. These r and f planes contain one of the $sd2$ or one of the $sd1$ directions at the periphery of the pole figure. A second $sd2$ direction in the f plane is not far off the periphery of the pole figure.

Orientation M2 results from M1 by a rotation of 180° around either the X or Z -axis. Its projection looks like

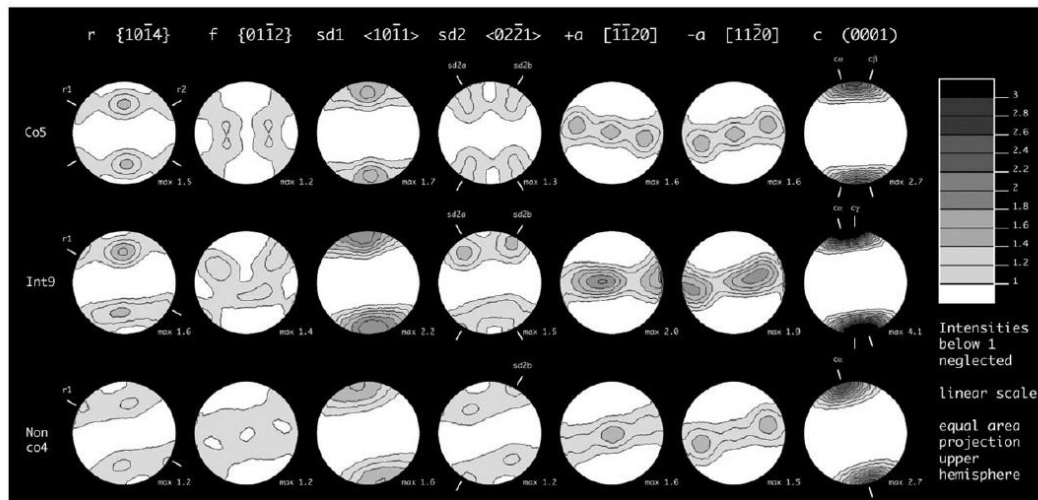


Fig. 17. Pole figures for the three idealized model distributions (co5, int9 and nonco4); same cases as in Fig. 15. Same representation as for the studied samples (Figs. 8 and 12).

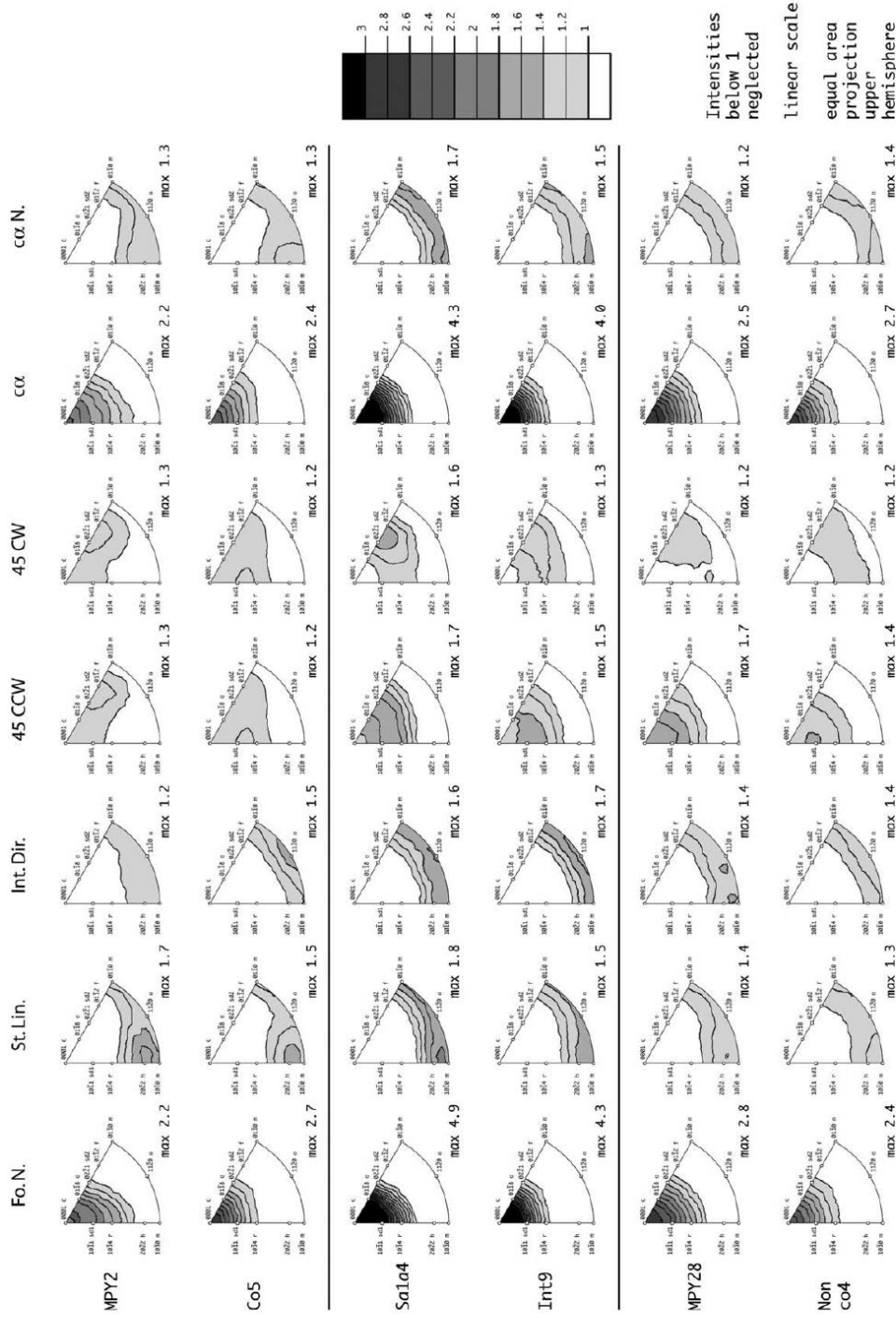


Fig. 18. Inverse pole figures for the three most recrystallized samples (MPY2 from profile 1, Sa1a4 from locality 2, MPY28 from profile 2) and for three idealized model distributions (co5, int9 and nonco4), same cases as in Fig. 15. Sample reference directions are foliation normal (Fo. N.), intermediate direction (Int. Dir.), stretching lineation (St. Lin.), two conjugate directions at 45° between lineation and foliation normal, the directions of c -axis maxima ($c\alpha$ and $c\beta$) and perpendicular to them ($c\alpha N$ and $c\beta N$) along the pole figure periphery. Contouring as in Fig. 8, equal area projection of upper hemisphere.

the mirror image of M1 with respect to either the Y – Z or X – Y plane, but with the sign of the a -axes inverted.

Orientation M3 is related to M1 by a 60° rotation around the c -axis at α . Both orientations place the basal plane at an angle of 15° counter clockwise from the plane normal to Z (foliation). Their projections appear as mirror positions with respect to the basal plane, again with sign inversion for the a -axes.

The orientations M1, M2 and M3 have a two-fold symmetry axis (crystal a -axis) parallel to Y . Thus a texture that only consists of any amount of these components has at least monoclinic symmetry with symmetry axis Y . A texture only with M1 and M2 in equally large portions possesses orthorhombic sample symmetry. If only M1 and M3 would be present in equal shares, then the texture would resemble hexagonal crystal (and sample) symmetry with respect to the crystal c - and a -axes.

The orientations M4 and M4' have their c -axis parallel to Z , and one of the a -axes parallel to X . They are mutually related by a 180° rotation around Y . If they are equally present then the texture preserves monoclinic symmetry, otherwise the two-fold symmetry around Y is broken.

The pole figures for the three models are shown in Fig. 17 to be compared with those for the samples of profile 1 (Fig. 8), profile 2 (Fig. 12) or locality 2 (Fig. 12, bottom). They resemble particularly the symmetry of the three texture types, which is orthorhombic for profile 1 (model co5), monoclinic for profile 2 (model nonco4), and asymmetric for locality 2 (model int9).

4.7. Inverse pole figures

Inverse pole figures (IPF) were calculated in order to show the preferential orientation of crystal planes and directions with respect to certain sample directions (Fig. 18). These are foliation normal (Z =FoN), stretching lineation (X =StLin), intermediate direction (Y =IntDir), two conjugate directions at 45° between X and Z (45° CCW and 45° CW), directions 15° counter clockwise (α) and 75° clockwise (α N) from Z around Y , directions 15° clockwise (β) and 75° counter clockwise (β N) from Z around Y .

Like the ODF and pole figures, the IPF show similar general characteristics. The IPF for Z and α have the sharpest concentrations, which are towards the c -axis. The IPF for X and Y show girdle distributions along directions in the basal planes, where the lineation (and similarly α N) is preferentially aligned normal to poles of m -prisms or h -rhombohedra, and the intermediate direction has a somewhat higher concentration of a -axes. The IPF for the two conjugate directions (45° CCW, 45°

CW) show maxima near r and f rhombohedral planes and $sd1$ and $sd2$ directions. Subtle differences are noticed, as only samples from profile 1 and from locality 2 show some shoulder towards r in the IPF for Z , and only for profile 1 the two IPF for 45° CCW and 45° CW are identical, as expected for symmetry reasons.

5. Discussion

5.1. Deformation mechanisms

The microfabric evolution shows the following characteristics with increasing distance to the basement along both profiles 1 and 2: (1) the extent of dynamic recrystallisation increases, (2) the dynamically recrystallised grains show an increasing degree of shape preferred orientation, and (3) increasingly stronger textures develop. These observations lead to the interpretation that the spatial gradient across the profiles also maps gradients in finite strain, and that deformation has most likely occurred by dominant dislocation creep accompanied by dynamic recrystallisation. While there is some evidence also for pressure solution and re-precipitation, grain boundary sliding and/or diffusion creep were presumably not the dominant deformation mechanisms in our samples, because those are expected to result in rocks with isotropic fabrics (Edington et al., 1976; Schmid et al., 1977; Padmanabhan and Davies, 1980; Schmid et al., 1987; Rutter and Brodie, 1988).

5.2. Kinematics of deformation: coaxial vs. non-coaxial

The samples from profile 1 exhibit microfabric characteristics, notably in terms of SPO and texture measurements, which possess orthorhombic sample symmetry with respect to the structural reference frame, defined by lineation X , foliation normal Z and intermediate strain axis Y . Fabrics are approximately symmetric with respect to rotations by 180° around these three axes, which is almost equivalent to mirror symmetries perpendicular to them. They do not indicate any preferred sense of shearing, i.e. do not contain any record of dominant non-coaxial (simple shear) deformation. We interpret these rocks to be deformed on a coaxial deformation path, where all three principal axes are distinct, which is presumably close to plane strain, i.e. pure shear. The inferred principal stress axes nearly coincide with the axes of the structural reference frame of profile 1, i.e. σ_1 is oriented about normal to the macroscopic foliation and σ_3 falls near the stretching lineation, which independently demonstrates conditions of coaxial strain.

The samples from profile 2 possess microstructures and textures that have no more than monoclinic sample symmetry with a single two-fold symmetry axis around the intermediate strain axis Y . It is emphasized that the fabric symmetry could not be raised just by redefinition of the reference frame, but that there are distinct features oriented relative to each other that break orthorhombic symmetry. These are S–C fabrics and asymmetric pressure fringes in the microstructures, and the position and weight of orientation components relative to each other as well as relative to primary and secondary foliation planes in the textures. Only the intermediate axes σ_2 of the inferred principal stress tensor roughly coincides with an axis (the Y -axis) of the structural reference frame of profile 2, while σ_1 and σ_3 are oriented at equally large angles to foliation and lineation. These observations are taken as evidence that deformation of these samples must have occurred on a non-coaxial deformation path with vorticity axis towards Y , i.e. simple shear in the idealized case of plane strain deformation.

In summary, the samples from the two profiles exhibit contrasting types of fabrics on a microscopic scale. The microstructural data independently confirms the conclusions made for the macroscopic scale (Fig. 3). All data suggest that the specimens of profiles 1 and 2, i.e. specimens with identical lithological compositions and strained under the same P–T conditions, deformed in contrasting kinematic regimes. As the deformation mechanisms have been identical, and since the influence of second phase particles has been ruled out in Section 4.4 we interpret the differences in texture as due to the different kinematics of deformation.

5.3. Asymmetric fabrics

The microstructure of sample Sa1a4 indicates that this rock was deformed by a significant amount of rotational deformation. Its texture shows similarities with the textures of sample MPY2 (profile 1, coaxial) as well as of sample MPY28 (profile 2, non-coaxial). It differs from both as it does not equally balance the orientation components around M_4 and M_4' . This means that none of the three structural reference axes is actually a two-fold symmetry axis anymore, and the strain path must have deviated from plane strain. It remains puzzling that the texture resembles nearly orthorhombic symmetry with respect to axes rotated by about 30° around Z , i.e. shifting X and Y within the foliation plane, because those apparent symmetry directions have no pendant in the field when back-projected into geographic coordinates.

5.4. Suitably oriented slip systems

The following slip systems have been confirmed as dominant slip systems for calcite in experiments of Turner et al. (1954), Griggs et al. (1960), Turner and Heard (1965), Weiss and Turner (1972), Braillon (1976), Spiers and Wenk (1980), and De Bresser and Spiers (1990, 1993, 1997):

r {10–14} sd_2 <02–21>	Turner et al., 1954 Griggs et al., 1960 Turner and Heard, 1965 Weiss and Turner, 1972 Braillon, 1976 Spiers and Wenk, 1980 De Bresser and Spiers, 1990 De Bresser and Spiers, 1993
f {01–12} sd_2 <02–21>	Turner et al., 1954 Griggs et al., 1960 Spiers and Wenk, 1980
f {01–12} sd_1 <10–11>	De Bresser and Spiers, 1990 De Bresser and Spiers, 1993 De Bresser and Spiers, 1997
c {0001} < a >	De Bresser and Spiers, 1997

Assuming ideal plastic rheology of an isotropic material, the maximum shear stress is resolved on two conjugate planes oriented at 45° between the two extreme principal stress directions, where the normal to one plane is also the shear direction on the other plane. In coaxial deformation, the principal directions of stress fall together with those of strain rate as well as finite strain, thus the maximum shear stress is expected on planes at 45° to X and Z . In simple shear as a special case of non-coaxial deformation, the principal directions are identical for stress and strain rate, but those of finite strain rotate with progressive deformation around the Y -axis and converge to a position, where σ_1 and σ_3 make equal angles of 45° both to X and Z . Given that deformation was dominated by simple shearing and has reached large shear strain, the angle between the shear zone boundary and the macroscopic foliation is very small, and it can be assumed that the σ_1 direction lies for sinistral shear near the upper-right/lower-left corners of the XZ -plane. In other words, the maximum shear stress is then resolved on the foliation plane and on the plane perpendicular to the lineation. While both positions are equally suited at a local scale, only shear on the foliation plane along lineation is geometrically feasible at the larger scale of a shear zone.

For any given crystal orientation, those slip systems are most likely to be activated on which the highest shear stress is resolved, i.e. which are closest to the above planes and directions of maximum resolved shear stress. Our paleostress analysis may have given some

indications for the principal directions of stress, but there is hardly any constraint on the magnitudes of the principal stresses. Therefore we restrict the following discussion on qualitative arguments instead of attempting to quantify the resolved shear stress by means of the Schmidt factor, which would require further assumptions on the complete stress tensor.

For coaxial deformation (e.g. pure shear) as inferred for the samples from profile 1, their ideal crystal orientations M1 and M2 (Figs. 14 and 15) both have a $r[sd2]$ and a $f[sd1]$ slip system suitably oriented, and to a lesser extent also a $f[sd2]$ system (Fig. 15). The a direction that is parallel to the Y -axis is geometrically disabled to slip, and the other two basal $[a]$ slip systems are rather unsuitably oriented. For the orientations M4 and M4' (Figs. 14 and 15), the resolved shear stress vanishes for all three basal slip systems, but slip on conjugate pairs of $r[sd2]$ and $f[sd2]$ is possible.

For non-coaxial deformation (e.g. simple shear) as inferred for the samples from profile 2, their main orientations M1 and M3 have r and f planes oriented at 60° and 50° to the foliation, which thus are not well oriented slip planes. The basal plane, inclined at 15° to the foliation “with the sense of shear”, is the only potential slip plane that is close to the orientation of the bulk shear plane, and which could have been activated by duplex slip along the two a -directions that are not parallel to Y . However, given the angle of 15° between basal plane and foliation, it appears that antithetic slip along the f or r planes would also be needed in order to maintain homogeneous simple shear deformation (Mancktelow, 1987; Schmid, 1994). Basal $[a]$ -slip systems are perfectly oriented for the orientations M4 and M4', which, however, do not constitute the primary orientation components in the textures along profile 2.

5.5. Textures in experimentally deformed samples

The pure shear textures are similar to the “high temperature type” textures obtained in pure shear experiments of micritic limestones performed by Wagner et al. (1982) in a testing apparatus with three independent stress actuators at 400°C . This experimentally produced texture consists of two stronger maxima at the periphery of the pole figure, 30° on either side of the σ_1 direction and a third weaker maximum parallel to the σ_3 direction. Our textures from profile 1 somewhat resemble the HT-type textures of Wagner et al. (1982), as far as both show orthorhombic texture symmetry with double c -axis maxima in the X - Z plane closer to Z than to X . Slip on the r and f planes was inferred to be the dominant deformation mechanism. The corresponding microstructures

(Kern and Wenk, 1983) show a strong SPO consistent with the imposed coaxial strain path and no twinning or dynamic recrystallisation. Twinning is also not observed in the case of our natural samples at Rocher de l'Yret. Hence the absence of twinning at higher temperatures appears to be an important criterion of distinction between “low” and “high temperature” deformation in the sense of Wagner et al. (1982), especially in the texture evolution (see also Schmid et al., 1987 their “twinning” vs. their “intracrystalline slip” regime). Twinning activity is further suppressed due to the small grain size in the limestone and in our mylonites, while a coarse grained marble would still easily twin under the same conditions. Model simulations of the texture evolution by dislocation glide are consistent with the observed textures in the absence of twinning (Wagner et al., 1982; Kern and Wenk, 1983; Wenk et al., 1987).

Since these pure shear experiments have not been carried out to large enough strains the role of dynamic recrystallisation for texture evolution could not be assessed experimentally. It is likely that recrystallisation by subgrain rotation and local boundary migration processes do not alter the texture type but strengthen the texture with progressive deformation similarly as observed in the RYSZ samples of profile 1.

None of the studies of texture evolution in experimental simple shear (Schmid et al., 1987; Pieri et al., 2001a,b) have produced exactly the same textures as those observed in the RYSZ. Schmid et al. (1987) observed similar textures in their 800°C “grain boundary migration regime” experiments with a distinct c -axis maximum rotated with the sense of shear relative to foliation, which they also inferred due to a dominating contribution of slip in the basal plane. Preferred orientations similar to M3 with c -axes inclined with the sense of shear developed in torsion experiments of Carrara marble at 500°C and 600°C after very large shear strain ($\gamma \geq 10$, Barnhoom et al., 2004). Twinning of the initially coarse grained marble controlled the texture formation at small strain and caused a c -axis maximum opposite to the sense of shear. Twinning was less important in the fine grained mylonite at large strain, which then caused the texture transition.

5.6. Texture evolution in naturally deformed limestones

One geometric assumption often made for texture interpretation is that during progressive simple shear deformation accompanied by dynamic recrystallisation, one or several distinct slip planes tend to align parallel or at small angles to the bulk shear plane and corresponding slip directions tend to align with the bulk shear direction of the rock (Nicolas, 1976; Etchecopar, 1977; Bouchez,

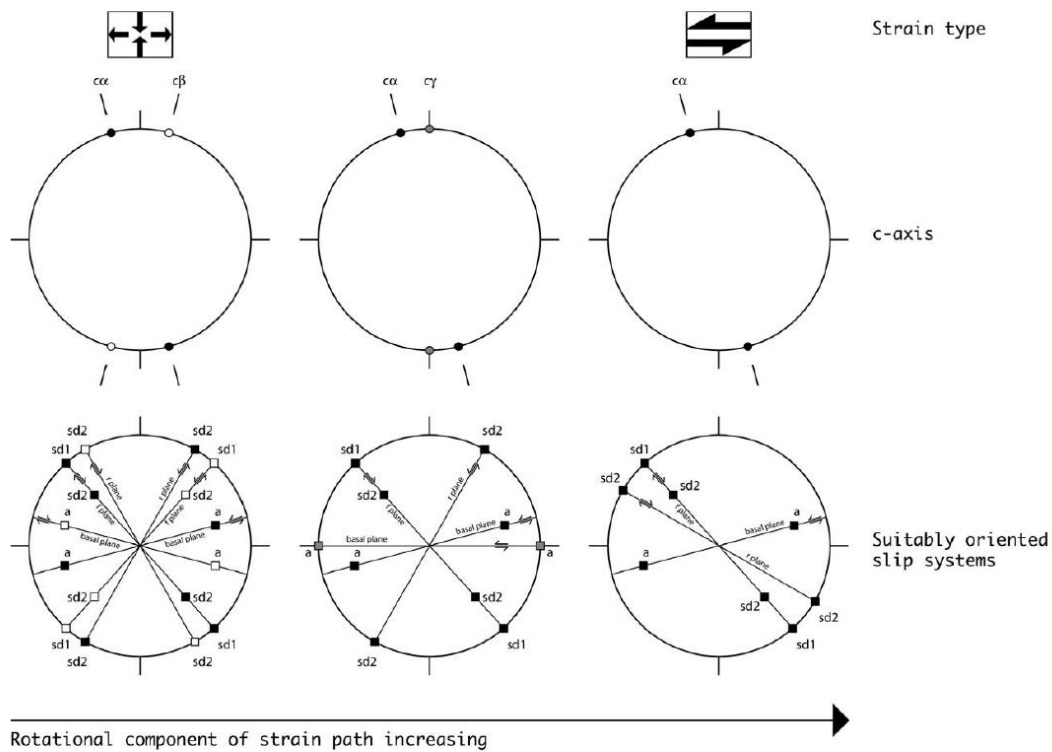


Fig. 19. Sketch summarizing the evolution of the calcite c -axis distribution during the transition from coaxial dominated to non-coaxial dominated deformation under conditions suppressing twinning. Poles and projections of slip planes and slip directions are reported for the main ideal orientation components, which are suitably oriented for slip under the assumed kinematics. Black symbols belong to orientations with c -axis at $c\alpha$ (M1, M3), white symbols at $c\beta$ (M2), grey symbols at $c\gamma$ (M4, M4').

1978; Schmid, 1994). Such an orientation of certain slip systems aligns the microscopic deformation scale (simple shear by crystal plastic slip on one slip system) with that of the macroscopic deformation. This alignment is only possible for simple shear kinematics.

The previous discussion points out that there seems to be a gradual shift from predominant rhomb slip (r and f slip) in pure shear to predominant basal slip in simple shear. This shift would imply that the kinematics of deformation has an influence on the activity of the slip systems. At first sight this appears intriguing, as the critical resolved shear stresses of the various slip systems should not depend on the kinematics of deformation. However, the texture evolution is also influenced by dynamic recrystallisation (Schmid, 1994; Wenk and Tome, 1999). In the case of simple shear, grains with their c -axis orientations inclined against the sense of shear are unsuitably oriented for basal slip and may hence be eliminated by nucleation and preferential growth of grains that are suitably oriented in terms of basal slip.

Provided that grains with orientations that are not suitably oriented for basal slip act as local stress raisers during simple shearing, they could preferentially be consumed by dynamic recrystallisation. Dynamic recrystallisation results in a stationary cycle of newly formed small grains (through subgrain rotation and/or bulging), which grow and deform by slip until they will be consumed again by their neighbours. While individual grains permanently change their size, shape and orientation, the microstructure and texture on average remain constant with strain after a certain initialisation. The rate of these recrystallisation cycles is largely affected by the impurity content at the micro- and nanoscale (Herwegh and Kunze, 2002). The nummulitic limestone of RYSZ must be considered a rather impure calcite rock in that sense, as it contains enough impurities to prevent grain growth and to decelerate the microstructural resetting.

In summary of our empirical observations, a texture transition as function of strain path is schematically

depicted in Fig. 19, following ideas proposed for quartz by Schmid and Casey (1986). We emphasize, however, that in case of calcite the simple-shear end-member does not involve slip along one single slip system only, namely the basal plane, but antithetical slip on r and f also contributed to deformation. Slip along a single slip system is only possible if this slip system is perfectly aligned with the shear zone boundary and no incompatibilities arise at grain boundaries. The obliquity between basal plane and foliation is too high (15°) in case of the ultramylonites, for which the foliation is expected to nearly coincide with the shear zone boundary.

To our knowledge most published oblique calcite c -axis textures (see for example Behrmann, 1983; Dietrich and Song, 1984; Schmid et al., 1987; Ratschbacher et al., 1991) exhibit maxima oriented “against the sense of shear”, as expected when calcite e -twinning is responsible for texture evolution (Schmid et al., 1987). In our samples, however, twinning was suppressed by the small grain size and elevated temperatures. The c -axis maxima oriented “with the sense of shear” correspond to what is consistently found for quartz mylonites (Lister and Price, 1978; Bouchez and Pecher, 1981; Malavieille and Etchecopar, 1981; Schmid and Casey, 1986; Bhattacharya and Weber, 2004), which are similarly attributed to dominant basal slip.

Two conditions need to be satisfied if the interpretation of the texture transition discussed so far is correct: (1) the slip systems involved (r , f and basal plane) need to have comparable critical resolved shear stresses at the temperature conditions of deformation, and (2) there must be very subordinate twinning during deformation. Condition (1) appears to be satisfied for the high temperature deformation regime (De Bresser and Spiers, 1997). Condition (2) appears to be satisfied in many experimentally and naturally deformed samples where dynamic recrystallisation dominates (Wagner et al., 1982; Schmid et al., 1987; Lafrance et al., 1994; Pieri et al., 2001a,b).

Whether calcite textures and their asymmetry can be used as unequivocal shear sense criteria remains an issue of further research and microstructural criteria such as oblique SPO are certainly more reliable criteria. If no twinning occurs, it appears that c -axis maxima are either normal to foliation or rotated synthetically with the sense of shear. If twinning is dominant during deformation, the c -axis maximum will be rotated antithetically to, i.e. “against” the shear sense. Then an asymmetry opposite to that observed for the samples from Rocher de l’Yret would be expected. Thus, for all practical purposes, calcite textures should only be used in conjunction with

shape fabric analyses and microstructural studies of twinning and dynamic recrystallisation.

6. Summary and conclusions

Two sample series from the Rocher de l’Yret shear zone were studied, which deformed at the same time under conditions of low anchizone metamorphic conditions. From the fabric analysis of both zones it is concluded that orthorhombic SPO symmetry is indicative of pure shear dominated deformation while monoclinic SPO symmetry is indicative of simple shear dominated deformation. The textures of these samples also show orthorhombic and monoclinic symmetries, respectively, and confirm the conclusion that the two profiles represent cases that are close to the pure and simple shear end members.

In general, the SPO and texture analysis of samples from the Rocher de l’Yret deformation zone indicates that the symmetry of calcite fabrics appears to indicate simple shear deformation for monoclinic fabrics. Orthorhombic fabric symmetry, however, may but does not necessarily has to indicate pure shear deformation, because the latter may also be produced by simple shear strain paths as documented in the literature (Schmid et al., 1987; Lafrance et al., 1994; Pieri et al., 2001a,b). The type of c -axis patterns observed in the simple shear samples shows some deviation from textures reported from other naturally deformed calcitic rocks, where an oblique c -axis maximum typically occurs opposite to the sense of shear due to e -twinning. A c -axis maximum rotated synthetically with the sense of shear may be also used as a shear sense indicator provided that it can be demonstrated that twinning in calcite was of subordinate importance compared to basal slip, which is often the case for fine grained calcite mylonites.

7. Software used

- [1] Tectonic VB 1.5a Ortner, H., 2001. <http://geopal.uibk.ac.at/tvb/front.html>.
- [2] NIH image public domain software <http://rsb.info.nih.gov/nih-image/download.html>.
- [3] Stripstar <http://www.unibas.ch/earth/micro/software/grainsize/grainsize.html>.
- [4] MENTEX Schaeben et al., 1990.
- [5] BEARTEX Wenk et al., 1998.

Acknowledgement

The authors wish to thank all colleagues from the tectonics group at Basel University for stimulating discussions, Pierre Dèzes for assistance in computer

programming, Willy Tschudin for preparing excellent ultrathin sections. Thorough reviews by Marco Herwegh, Bernd Leiss and a third anonymous reviewer significantly improved the manuscript. This study was funded by the Swiss National Science Foundation.

References

- Angelier, J., Mechler, P., 1977. Sur une methode graphique de recherche des contraintes principales egalement utilisables en tectonique et en seismologie: la methode des diedres droits. *Bulletin de la Societe Geologique de France* 19 (6), 1309–1318.
- Aprahamian, J., 1974. La cristallinite de l'illite et les mineraux argileux en bordure des massifs cristallins externes de Belledonne et du Pelvoux (variations et relations possibles avec des evenements tectoniques et metamorphiques alpins). *Geologie Alpine* 50, 5–15.
- Aprahamian, J., 1988. Cartographie du metamorphisme faible a tres faible dans les Alpes francaises externes par l'utilisation de la cristallinite de l'illite. *Geodinamica Acta* 2 (1), 25–32.
- Bagnoud, A., Wernli, R., Sartori, M., 1998. Decouverte de foraminiferes planctoniques paleogenes dans la zone de Sion-Courmayeur a Sion (Valais, Suisse). *Ecolgae Geologicae Helvetiae* 91 (3), 421–429.
- Barnhoorn, A., Bystrichy, M., Burlini, L., Kunze, K., 2004. The role of recrystallisation on the deformation behaviour of calcite rocks: large strain torsion experiments on Carrara marble. *Journal of Structural Geology* 26 (5), 885–903.
- Beach, A., 1981. Thrust structures in the eastern Dauphinois Zone (French Alps), north of the Pelvoux Massif. *Journal of Structural Geology* 3 (3), 299–308.
- Behrmann, J.H., 1983. Microstructure and fabric transitions in calcite tectonites from the Sierra Alhamilla (Spain). *Geologische Rundschau* 72 (2), 605–618.
- Bestmann, M., Kunze, K., Matthews, A., 2000. Evolution of a calcite marble shear zone complex on Thassos Island, Greece; microstructural and textural fabrics and their kinematic significance. *Journal of Structural Geology* 22 (11–12), 1789–1807.
- Bhattacharya, A.R., Weber, K., 2004. Fabric development during shear deformation in the Main Central Thrust Zone, NW-Himalaya, India. *Tectonophysics* 387, 23–46.
- Bouchez, J.L., 1978. Preferred orientations of quartz $\langle a \rangle$ axes in some tectonites; kinematic inferences. *Tectonophysics* 49 (1–2), T25–T30.
- Bouchez, J.L., Pecher, A., 1981. The Himalayan Main Central Thrust pile and its quartz-rich tectonites in central Nepal. *Tectonophysics* 78 (1–4), 23–50.
- Braillon, P.A.S.J., 1976. Deformation plastique de monocristaux de calcite en compression suivant $\langle 001 \rangle$. *Physica Status Solidi. A, Applied Research* 36, 637–646.
- Bunge, H.J., 1982. *Texture Analysis in Material Science — Mathematical Methods*. Butterworth, London.
- Bürgisser, J., Ford, M., 1998. Overthrust shear deformation of a foreland basin; structural studies south-east of the Pelvoux Massif, SE France. *Journal of Structural Geology* 20 (11), 1455–1475.
- Burlini, L., Marquer, D., Challandes, N., Mazzola, S., Zangarini, N., 1998. Seismic properties of highly strained marbles from the Splügenpass, central Alps. *Journal of Structural Geology* 20, 277–292.
- Butler, R.W.H., 1992. Thrust zone kinematics in a basement-cover imbricate stack; eastern Pelvoux Massif, French Alps. *Journal of Structural Geology* 14 (1), 29–40.
- Casey, M., 1981. Numerical analysis of X-ray texture data; an implementation in Fortran allowing triclinic or axial specimen symmetry and most crystal symmetries. *Tectonophysics* 78 (1–4), 51–64.
- Casey, M., Kunze, K., Olgaard, D.L., 1998. Texture of Solnhofen Limestone deformed to high strains in torsion. *Journal of Structural Geology* 20 (2–3), 255–267.
- Ceriani, S., Fuegenschuh, B., Schmid, S.M., 2001. Multi-stage thrusting at the “Penninic Front” in the Western Alps between Mont Blanc and Pelvoux massifs. *International Journal of Earth Sciences* 90 (3), 685–702.
- De Bresser, J.H.P., 1989. Calcite c -axis textures along the Gavarnie thrust zone, central Pyrenees. *Geologie en Mijnbouw* 68, 367–375.
- De Bresser, J.H.P., Spiers, C.J., 1990. High-temperature deformation of calcite single crystals by r (super+) and f (super+) slip. *Geological Society Special Publications* 54, 285–298.
- De Bresser, J.H.P., Spiers, C.J., 1993. Slip systems in calcite single crystals deformed at 300–800 degrees C. *Journal of Geophysical Research* 98 (4), 6397–6409.
- De Bresser, J.H.P., Spiers, C.J., 1997. Strength characteristics of the r , f , and c slip systems in calcite. *Tectonophysics* 272 (1), 1–23.
- Dietrich, D., Song, H., 1984. Calcite fabrics in a natural shear environment, the Helvetic nappes of western Switzerland. *Journal of Structural Geology* 6 (1–2), 19–32.
- Edington, J.W., Melton, K.N., Cutler, C.P., 1976. Superplasticity. *Progress in Materials Science* 21, 61–170.
- Erskine, B.G., Heidelbach, F., Wenk, H.R., 1993. Lattice preferred orientations and microstructures of deformed Cordilleran marbles; correlation of shear indicators and determination of strain path. *Journal of Structural Geology* 15 (9–10), 1189–1205.
- Etchecopar, A., 1977. A plane kinematic model of progressive deformation in a polycrystalline aggregate. *Tectonophysics* 39 (1–3), 121–139.
- Ford, M., 1996. Kinematics and geometry of early Alpine, basement-involved folds, SW Pelvoux Massif, SE France. *Ecolgae Geologicae Helvetiae* 89 (1), 269–295.
- Froitzheim, N., Schmid, S.M., Frey, M., 1996. Mesozoic paleogeography and the timing of eclogite-facies metamorphism in the Alps; a working hypothesis. *Ecolgae Geologicae Helvetiae* 89 (1), 81–110.
- Fuegenschuh, B., Schmid, S.M., 2003. Late stages of deformation and exhumation of an orogen constrained by fission-track data; a case study in the Western Alps. *Geological Society of America Bulletin* 115 (11), 1425–1440.
- Gidon, P., 1954. Les rapports des terrains cristallins et de leur couverture sedimentaire, dans les regions orientale et meridionale du massif du Pelvoux. *Travaux du Laboratoire de Geologie de la Faculte des Sciences de Grenoble* 31, 1–199.
- Gidon, M., 1979. Le role des etapes successives de deformation dans la tectonique alpine du massif du Pelvoux (Alpes occidentales). *Comptes Rendus Hebdomadaires des Seances de l'Academie des Sciences. Serie D, Sciences Naturelles* 288 (9), 803–806.
- Gignoux, M., Moret, L., 1938. Description geologique du bassin superieure de la Durance. *Travaux du Laboratoire de Geologie de la Faculte des Sciences de Grenoble* 21, 1–295.
- Griggs, D.T., Turner, F.J., Heard, H.C., 1960. Deformation of rocks at 500 degrees to 800 degrees C. *Geological Society of America* 39–104.
- Heilbronner, R.P., Pauli, C., 1993. Integrated spatial and orientation analysis of quartz c -axes by computer-aided microscopy. *Journal of Structural Geology* 15 (3–5), 369–382.
- Heilbronner, R.P., Pauli, C., 1994. Orientation and misorientation imaging: integration of microstructural and textural analysis. In: Bunge, H.J., Siegesmund, S., Skrotzki, W., Weber, K. (Eds.),

- Texture of Geological Materials. DGM Informationsgesellschaft Verlag, Oberursel, pp. 147–164.
- Helming, K., Geier, St., Heinitz, J., Leiss, B., Rauschenbach, B., Schwarzer, R.A., Ullemeyer, K., Wenk, H.-R., 1994. Texture estimates by means of components. *Zeitschrift für Metallkunde* 85, 545–553.
- Herwegh, M., 2000. A new technique to automatically quantify microstructures of fine grained carbonate mylonites; two-step etching combined with SEM imaging and image analysis. *Journal of Structural Geology* 22 (4), 391–400.
- Herwegh, M., Berger, A., 2003. Differences in grain growth of calcite; a field-based modeling approach. *Contributions to Mineralogy and Petrology* 145 (5), 600–611.
- Herwegh, M., Kunze, K., 2002. The influence of nano-scale second-phase particles on deformation of fine grained calcite mylonites. *Journal of Structural Geology* 24 (9), 1463–1478.
- Kern, H., Wenk, H.R., 1983. Calcite texture development in experimentally induced ductile shear zones. *Contributions to Mineralogy and Petrology* 83 (3–4), 231–236.
- Kurz, W., Neubauer, F., Unzog, W., Genser, J., Wang, X., 2000. Microstructural and textural development of calcite marbles during polyphase deformation of Penninic units within the Tauern Window (Eastern Alps). *Tectonophysics* 316, 327–342.
- Lafrance, B., White, J.C., Williams, P.F., 1994. Natural calcite *c*-axis fabrics; an alternate interpretation. *Tectonophysics* 229 (1–2), 1–18.
- Leiss, B., Molli, G., 2003. “High-Temperature” texture in naturally deformed Calcite marble from the Alpi Apuane, Italy. *Journal of Structural Geology* 25, 649–658.
- Leiss, B., Ullemeyer, K., 1999. Texture characterisation of carbonate rocks and some implications for the modeling of physical anisotropies, derived from idealized texture types. *Zeitschrift der Deutschen Geologischen Gesellschaft* 150 (2), 259–274.
- Leiss, B., Weiss, T., 2000. Fabric anisotropy and its influence on physical weathering of different types of Carrara marbles. *Journal of Structural Geology* 22, 1737–1745.
- Leiss, B., Siegesmund, S., Weber, K., 1999. Texture asymmetries as shear sense indicators in naturally deformed mono- and poly-phase carbonate rocks. *Textures and Microstructures* 33, 61–74.
- Lister, G.S., Price, G.P., 1978. Fabric development in a quartz–feldspar mylonite. *Tectonophysics* 49, 37–78.
- Malavieille, J., Etchecopar, A., 1981. Ductile shear deformation of quartzite in an alpine crustal thrust (Ambin massif). *Tectonophysics* 78, 65–71.
- Mancktelow, N.S., 1987. Quartz textures from the Simplon fault zone, Southwest Switzerland and North Italy. *Tectonophysics* 135 (1–3), 133–153.
- Merle, O., Brun, J.P., 1984. The curved translation path of the Parpaillon Nappe (French Alps). *Journal of Structural Geology* 6 (6), 711–719.
- Mosar, J., Stampfli, G.M., Girod, F., 1996. Western Prealpes Medianes Romandes; timing and structure; a review. *Eclogae Geologicae Helveticae* 89 (1), 389–425.
- Nicolas, A., 1976. Flow in upper-mantle rocks; some geophysical and geodynamic consequences. *Tectonophysics* 32, 93–106.
- Oesterling, N., Heilbronner, R., Stünitz, H., Barnhoorn, A., Molli, G., submitted for publication. Strain dependent variations of microstructure and texture in naturally deformed Carrara marble. *Tectonophysics*.
- Padmanabhan, K.A., Davies, G.J., 1980. Superplasticity. Springer. 312 pp.
- Panozzo, R.H., 1983. Two-dimensional analysis of shape-fabric using projections of digitized lines in a plane. *Tectonophysics* 95 (3–4), 279–294.
- Panozzo, R.H., 1984. Two-dimensional strain from the orientation of lines in a plane. *Journal of Structural Geology* 6 (1–2), 215–221.
- Passchier, C.W., Trouw, R.A.J., 1996. *Microtectonics*. Springer. 289 pp.
- Pieri, M., Burlini, L., Kunze, K., Stretton, I., Olgaard, D.L., 2001a. Rheological and microstructural evolution of Carrara Marble with high shear strain; results from high temperature torsion experiments. *Journal of Structural Geology* 23 (9), 1393–1413.
- Pieri, M., Kunze, K., Burlini, L., Stretton, I., Olgaard, D.L., Burg, J.P., Wenk, H.R., 2001b. Texture development of calcite by deformation and dynamic recrystallisation at 1000 K during torsion experiments of marble to large strains. *Tectonophysics* 330 (1–2), 119–140.
- Ratschbacher, L., Wenk, H.R., Sintubin, M., 1991. Calcite textures; examples from nappes with strain-path partitioning. *Journal of Structural Geology* 13 (4), 369–384.
- Rutter, E.H., Brodie, K.H., 1988. The role of tectonic grain size reduction in the rheological stratification of the lithosphere. *Geologische Rundschau* 77 (1), 295–308.
- Schaeben, H., Siemes, H., Hoefler, S., Will, G., 1990. Practical application of entropy optimization in quantitative texture analysis. *Geological Society Special Publications* 54, 375–381.
- Schmid, S.M., 1994. Textures of geological materials: computer model predictions versus empirical interpretations based on rock deformation experiments and field studies. In: Bunge, H.J., Siegesmund, S., Skrotzki, W., Weber, K. (Eds.), *Texture of Geological Materials*. DGM Informationsgesellschaft Verlag, Oberursel, pp. 279–301.
- Schmid, S.M., Casey, M., 1986. Complete fabric analysis of some commonly observed quartz *c*-axis patterns. *Geophysical Monograph* 36, 263–286.
- Schmid, S.M., Boland, J.N., Paterson, M.S., 1977. Superplastic flow in finegrained limestone. *Tectonophysics* 43 (3–4), 257–291.
- Schmid, S.M., Casey, M., Starkey, J., 1981. The microfabric of calcite tectonites from the Helvetic Nappes (Swiss Alps). *Geological Society of London Special Publication* 9, 151–158.
- Schmid, S.M., Panozzo, R., Bauer, S., 1987. Simple shear experiments on calcite rocks; rheology and microfabric. *Journal of Structural Geology* 9 (5–6), 747–778.
- Seward, D., Mancktelow, N.S., 1994. Neogene kinematics of the Central and Western Alps; evidence from fission-track dating. *Geology* 22 (9), 803–806.
- Seward, D., Ford, M., Bürgisser, J., Lickorish, H., Williams, E.A., Meckel, L.D., 1999. Preliminary results of fission-track analyses in the southern Pelvoux area, SE France. In: Gosso, G., Jadoul, F., Sella, M., Spalla, Maria I. (Eds.), 3rd workshop on Alpine Geological Studies. *Memorie di Scienze Geologiche*, 51(1), pp. 25–31.
- Spencer, S., 1992. A kinematic analysis incorporating incremental strain data for the frontal Pennine zones of the western French Alps. *Tectonophysics* 206 (3–4), 285–305.
- Spiers, C.J., Wenk, H.R., 1980. Evidence for slip on *r* and *f* in the positive sense in deformed calcite single crystals. *American Geophysical Union; 1980 fall meeting. Eos, Transactions* 61 (46), 1128.
- Tagami, T., Galbraith, R.F., Yamada, R., Laslett, G.M., 1998. Revised annealing kinetics of fission tracks in zircon and geological implications. In: Van den Haute, P., De Corte, F. (Eds.), *Advances in Fission-Track Geochronology*. Kluwer Academic Publishers, Dordrecht, pp. 99–112.
- Trullenque, G., 2005. Tectonic and microfabric studies along the Penninic Front between Pelvoux and Argentera massifs (Western Alps, France). PhD thesis, Basel University, 287 pp.

- Turner, F.J., Heard, H.C., 1965. Deformation in calcite crystals at different strain rates. *University of California Publications in Geological Sciences* 46, 103–126.
- Turner, F.J., Griggs, D.T., Heard, H.C., 1954. Experimental deformation of calcite crystals. *Geological Society of America Bulletin* 65 (9), 883–933.
- Wagner, F., Wenk, H.R., Kern, H., Houtte, P.V., Esling, C., 1982. Development of preferred orientation in plane strain deformed limestone; experiment and theory. *Contributions to Mineralogy and Petrology* 80 (2), 132–139.
- Weiss, L.E., Turner, F.J., 1972. Some observations on translation gliding and kinking in experimentally deformed calcite and dolomite, flow and fracture of rocks. *Geophysical Monograph* 16, 95–107.
- Wenk, H.R., Tome, C.N., 1999. Modeling dynamic recrystallisation of olivine aggregates deformed in simple shear. *Journal of Geophysical Research, B: Solid Earth and Planets* 104 (11), 25,513–25,527.
- Wenk, H.R., Takeshita, T., Bechler, E., Erskine, B.G., Matthies, S., 1987. Pure shear and simple shear calcite textures; comparison of experimental, theoretical and natural data. *Journal of Structural Geology* 9 (5–6), 731–745.
- Wenk, H.R., Venkatasubramanian, C.S., Baker, D.W., Turner, F.J., 1973. Preferred orientation in experimentally deformed limestone. *Contributions to Mineralogy and Petrology* 38 (2), 81–114.
- Wenk, H.R., Matthies, S., Donovan, J., Chateigner, D., 1998. BEARTEX, a Windows-based program system for quantitative texture analysis. *Journal of Applied Crystallography* 31, 262–269.
- Wyckoff, R.W.G., 1920. The crystal structures of some carbonates of the calcite group. *American Journal of Science* 50, 317–360.

Very low-grade metamorphism in the para-autochthonous sedimentary cover of the Pelvoux massif (Western Alps, France)

Sébastien Potel · Ghislain Trullenque

Received: 14 November 2011 / Accepted: 14 May 2012 / Published online: 19 August 2012
© Swiss Geological Society 2012

Abstract The metamorphic grade from the para-autochthonous cover of the Pelvoux massif (PM, western Alp, France) was investigated in Priabonian metamarls, through mineral assemblages, simultaneous measurements of illite and chlorite “crystallinity”, K-white mica *b* cell dimension and K-white mica polytypes content. Kübler (KI) and Árkai (ÁI) indexes display values characteristic for uppermost diagenetic to low anchizonal conditions. These results are supported by the incomplete transformation of K-white mica polytypes from $1M_d$ and $2M_1$ and are in line with the not annealed status of zircon fission tracks in the southeast zone of the Pelvoux massif (Seward et al. 1999). Our findings differ from previous results, which suggested epizonal conditions at several places in the northern part of our field area, but are coherent with the temperature estimation suggested by the mineral assemblage described in the literature. These results are further supported by

temperature values deduced from fluid inclusion investigations. A small decrease of KI and ÁI values is observed within the basal decollement level of the Priabonian cover, when going from the least deformed zones to the most deformed ones. K-white mica *b* cell dimensions in micas of the area are in the range 9.000–9.040 Å, which corresponds to an inferred geothermal gradient of 25–35 °C/km, similar to the values found further north in the Dauphinois domain (Ceriani et al. 2003). This indicates a long steady state heat flow corresponding to a long term metamorphic event like in the eastern Alps.

Keywords Illite crystallinity · Very low-grade metamorphism · Western Alps · External crystalline massif

1 Introduction

In the western Alps, the illite “crystallinity” method has been used in order to differentiate the anchizone from diagenesis and epizone domains according to Kübler (1968). The general trend of the metamorphic grade, increasing from W to E, from diagenesis to epizone, is perturbed by tectonic duplexes and the influence of crystalline basement (Desmons et al. 1999).

In the northern part of the Pelvoux massif, Ceriani et al. (2003) studied the low-grade metamorphism in the region of the Frontal Penninic units (FPU) of the Western Alps between the Arc and Isère Valleys (Fig. 1a, b). The results of the study allowed relating the metamorphism to the different stages of deformation.

Previous metamorphic studies described south of the Pelvoux massif a laumontite–prehnite–pumpellyite subfacies (zeolite facies) in the “grès de Champsaur” formation,

Editorial handling: Rafael Ferreira Mählmann and Edwin Gnos.

Present Address:

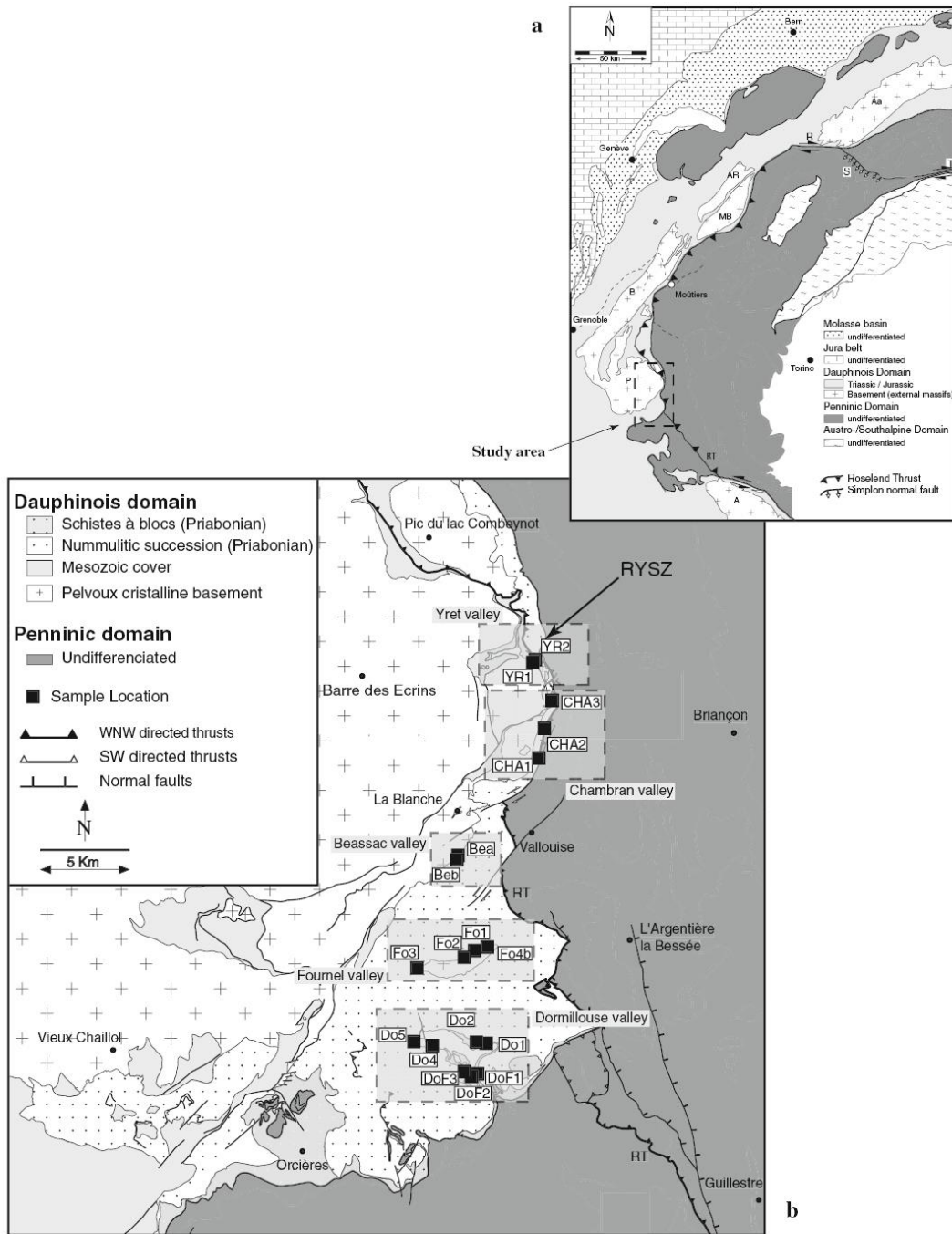
S. Potel (✉)
Institut Polytechnique LaSalle Beauvais-Equipe B2R,
19 rue Pierre Waguet, BP 30313, 60026 Beauvais Cedex, France
e-mail: sebastien.potel@lasalle-beauvais.fr

S. Potel
Insitut für Geowissenschaften und Lithosphärenforschung,
Universität Giessen, Giessen, Germany

Present Address:

G. Trullenque
Institut für Geowissenschaften, Geologie, Universität Freiburg,
Albertstrasse 23b, Freiburg, Germany

G. Trullenque
Institute of Geology and Paleontology, University of Basel,
Basel, Switzerland



◀ **Fig. 1** a Simplified geological overview of the arc of the western Alps (A Argentera massif, CM Combeynot massif, MB Mont Blanc massif, P Pelvoux massif, R Rhone-Simplon line, T Tonale line); after Ferreiro Mählmann (1996), Ceriani et al. (2001) and Ravenne et al. (1987, 2004). b Tectonic map along the eastern rim of the Pelvoux massif compiled from (1) geological maps BRGM (1/50,000): La Grave, Briançon, St Christophe en Oisans, Guillestre, Orcières and Embrun and (2) Tricart (1986). Points Yr, Fo, Be, Cha, Do and DoF refer to samples studied, collected at the eastern rim of the Pelvoux massif, in the Yret, Fournel, Beassac, Chambran, Dormillouse and Dormillouse-Fangeas valleys, respectively. RT Roselend Thrust, RYSZ Rocher de l'Yret shear zone

with rock-forming laumontite (Arahamian 1988) and pumpellyite–prehnite in veins (Waibel 1990). On the metamorphic map of the Alps (Frey et al. 1999) and the map of metamorphic structure of the Alps (Oberhänsli et al. 2004) the sub-greenschist facies (epizone) is found in the tiny basement of Fournel and Dormillouse valleys (ref. Fig. 1b).

The aim of this contribution is to present the results of a study on metamorphic grade in the southern footwall of the Penninic Basal Contact (PBC, Ceriani et al. 2001), within the Dauphinois cover of the southeastern rim of the Pelvoux massif, and to compare the results with those from Ceriani et al. (2003). The metamorphic grade was investigated in the globigerina metamarl level and in the Mesozoic cover by mineral assemblages, simultaneous measurements of illite and chlorite “crystallinity” using the KI- and Al -methods, K-white mica b cell dimension and K-white mica polytypes content. Within the Rocher de l'Yret shear zone (RYSZ, Fig. 1), results are completed by a fluid inclusion study. Quartz precipitates found along the strike slip fault planes dissecting the uppermost basement units from the RYSZ were analysed. All the methods were used for a better P–T estimate to get a higher precision on the metamorphic evolution in this region and to conclude better with some geodynamic implications. The results of this metamorphic study are compared to those from Ceriani et al. (2003) north of the Pelvoux massif, to the FT data available in the region (Seward et al. 1999; Fügenschuh and Schmid 2003) and previous studies describing mineral assemblage in the “grès de Champsaur” (Arahamian 1988; Waibel 1990).

2 Regional geology

The Dauphinois domain is part of the European margin and composed of Variscan basement carrying a thick Permian to Tertiary sedimentary cover. During Mesozoic rifting, the eastern margin of the European plate was substantially thinned. Formation of major tilted crustal blocks allowed for the deposition of thick Mesozoic sedimentary series in asymmetric half grabens intensively described in literature

(Tricart et al. 1988; Davies 1982; Gillcrist et al. 1987; Butler 1989; Coward et al. 1991; Huyghe and Mugnier 1995; Lazarre et al. 1996; Sue et al. 1997).

Mesozoic strata are discordantly overlain by a conglomerate formation (Gupta 1997), followed by the classical “Priabonian trilogy” (Ravenne et al. 1987; Apps et al. 2004), which comprises, from base to top: (1) shallow water nummulitic limestone of variable thickness (0–50 m), (2) hemipelagic globigerina marls (0–50 m), and (3) the “grès de Champsaur” formation, a regular alternance of turbiditic sandstones and shales (Perriaux and Uselle 1968; Waibel 1990), whose thickness varies from 700 to 1,200 m. In some areas immediately south of the Pelvoux massif, the siliciclastic deposits contain up to 50 % of volcanic detritus (Debrand-Passard et al. 1984; Bürgisser 1998).

Locally, three Alpine deformation phases (D_1 , D_2 and D_3) can be recognized (Trullenque 2005). D_1 , first phase of deformation that affected the Dauphinois units corresponds to the third phase of deformation described by Ceriani et al. 2001, i.e. Oligocene to lower Miocene out of sequence thrusting along the Roselend thrust (RT). It is the major deformation phase encountered in the investigated area since it is related to the thrusting along the RT (Ceriani et al. 2001). D_1 deformation structures constantly show WNW-directed kinematic indicators measured directly along tectonic contacts, i.e. consistent with activity along the RT.

The second D_2 deformation phase recorded within the investigated area results in SW-directed movements that overprint the top-WNW D_1 deformation features and which are missing N of the Pelvoux massif. Trullenque (2005) proposed that the D_2 top-SW deformation phase is linked to the formation of the Apennines chain, as a consequence of the opening of the Thyrenian basin during Langhian times.

D_3 structures, normal faults related to the Durance fault system (High Durance Faulted Zone, Tricart 2004) are the latest deformation features found in the investigated area. These normal faults are notably responsible for a strong geothermal gradient and seismicity recorded along the Durance valley. The timing of the onset of normal faulting, also recorded north of Pelvoux, remains a matter of debate (see Fügenschuh et al. 1999; Fügenschuh and Schmid 2003; Tricart et al. 2001). However, in this region, fission track data on zircon (Seward et al. 1999) reveal that maximum temperatures were well below greenschist facies conditions. Seward et al. (1999) interpreted the heating event as being due to the emplacement of internal thrust sheets, which thin out westwards.

3 Materials and methods

In marine pelites and carbonates, no diagnostic minerals and mineral assemblages form at conditions of very

low-grade field. In these rocks, the transitions from non-metamorphic to very low-grade and from very low-grade to low-grade metamorphic domains take place through the diagenetic zone, the anchizone and the epizone, each zone being characterized by specific values of the illite Kübler Index (KI; Árkai et al. 2003). The illite “crystallinity” (IC or KI; Kübler 1964) is defined as the full width at half maximum of the first illite basal reflection in XRD patterns (Frey 1987; Guggenheim et al. 2002). Guggenheim et al. (2002) recommended that the use of a “crystallinity index” should be avoided, although it may be placed within quotation marks when referring in a limited way to previously referenced work. They also recommended to refer to an index by relating it to the author describing the procedures necessary to define the value, regardless of what the index may actually be describing. Therefore, we will refer for K-white mica to the illite “crystallinity” for raw data and to KI after calibration against Kübler’s scale.

Illite “crystallinity” is considered to be a function of crystallite thickness, the number of lattice defects (Merriam et al. 1990). Temperature is thought to be the main factor controlling the illite “crystallinity”, but other parameters like lithology, time, tectonic stress and fluid/rock ratio may probably have important effect (see Frey 1987). Árkai (1991) and Árkai et al. (1995) proposed a similar index the chlorite “crystallinity” (ChC) or Árkai index (ÁI) to monitor the reaction’s progress.

Twenty-four metamarl samples were collected within the Priabonian and Mesozoic cover formations of the Dauphinois. Sampling was restricted to these formations in order to minimize the petrological effect on the IC. The outcrops density also limited sampling around the Dormillouse and Fournel valleys outcrops are poor. Moreover, westward the Selle Fault cut out the Priabonian formation. The nature, age and tectonic setting of this fault are poorly constrained leading to uncertainties on its effects on the metamorphic pattern. Therefore, samples were taken in the Dormillouse, Fournel, Beassac and Chambran valleys and in the Yret zone (Figs. 1, 2).

In the different samples, the main schistosity is related to the D₁ phase (Trullenque 2005), the D₂ phase only affects the area south of an E-W line of Beassac valley. The clay fraction analysed is generally related to D₁.

Samples with detrital mica visible in hand specimen and/or weathered specimens were avoided as far as possible to eliminate detrital contamination. Mineral abbreviations used are from Kretz (1983).

3.1 X-ray diffraction

Clay mineral separation was conducted using techniques described by Potel et al. (2006). Carbonate removal was done using a 5 % acetic acid (C₂H₄O₂) and washed after

with deionised water. To minimize the effect of possible detrital clay minerals, we avoided long grinding processes (<15 s) and repeated the settling procedure for the ≤2 μm fraction five times. Illite and chlorite crystallinity was measured at the University of Giessen on air-dried pre-preparates, using a D501 Bruker-AXS (Siemens) diffractometer, CuKα radiation at 40 kV and 30 mA and divergence slits of 0.5° with a secondary graphite monochromator. Two slices of each sample were prepared and each measured two times as air-dried and one time glycolated. The range of measurement, the time counting and the step size were as follow: for whole-rock paragenesis between 2 and 70 Δ°2Θ with 1 s and 0.02° step, for air-dried pre-preparate between 2 and 70 Δ°2Θ with 2 s and 0.01° step.

Illite “crystallinity” was calculated using the software DIFFRACPlus (evaluation/release 2001 by ©Bruker AXS) and MacDiff 4.25 (written by R. Petschick, 17 May 2001). IC measured in Giessen (IC_{Giessen}) values were transformed into KI values using a correlation with the SW standards (CIS standards) of Warr and Rice (1994) (KI_{CIS} = 1.2702 × IC_{Giessen} - 0.0314) (Table 1). The KI was used to define the limits of anchizone, and the transition values were chosen as follows: KI = 0.25 Δ°2Θ for the epizone to high anchizone boundary, KI = 0.30 Δ°2Θ for the high to low anchizone boundary and KI = 0.42 Δ°2Θ for the low anchizone to diagenetic zone. However, the use of the CIS standards is not universally accepted as giving Kübler-equivalent zone limits. Kisch et al. (2004) show that the CIS standard values are much broader than those obtained by all other laboratories and that the high- and low-grade boundaries of the anchizone of the raw values of Warr and Rice (1994) are much broader than the Kübler-equivalent. This discrepancy is likely to reflect errors in the conversion of the IC values into Kübler equivalent (Kisch et al. 2004; Ferreiro Mählmann and Frey this volume; Ferreiro Mählmann et al. this volume). Therefore, following the recommendations done by Kisch et al. (2004), we published in the Table 1 the IC_{Giessen} and ChC to allow comparison with other laboratories. The same experimental conditions were also used to determine chlorite “crystallinity” on the (002) peak of the second (7 Å) basal reflections of chlorite (Table 1). The ChC measurements were calibrated with those of Warr and Rice (1994) and expressed as the ÁI (Guggenheim et al. 2002): ÁI = 0.8775 × ChC + 0.0239. The anchizone boundaries for the ÁI were defined by correlation with the KI and are given as 0.24 Δ°2Θ for the epizone to anchizone boundary and 0.30 Δ°2Θ for the anchizone to diagenetic zone.

Randomly oriented samples for K-white mica *b* cell dimension and polytype determination of K-white mica were prepared using wood glue on quartz sample holder. The K-white mica *b* cell dimension is based on the d_{060,331} spacing and on the increasing celadonite substitution that

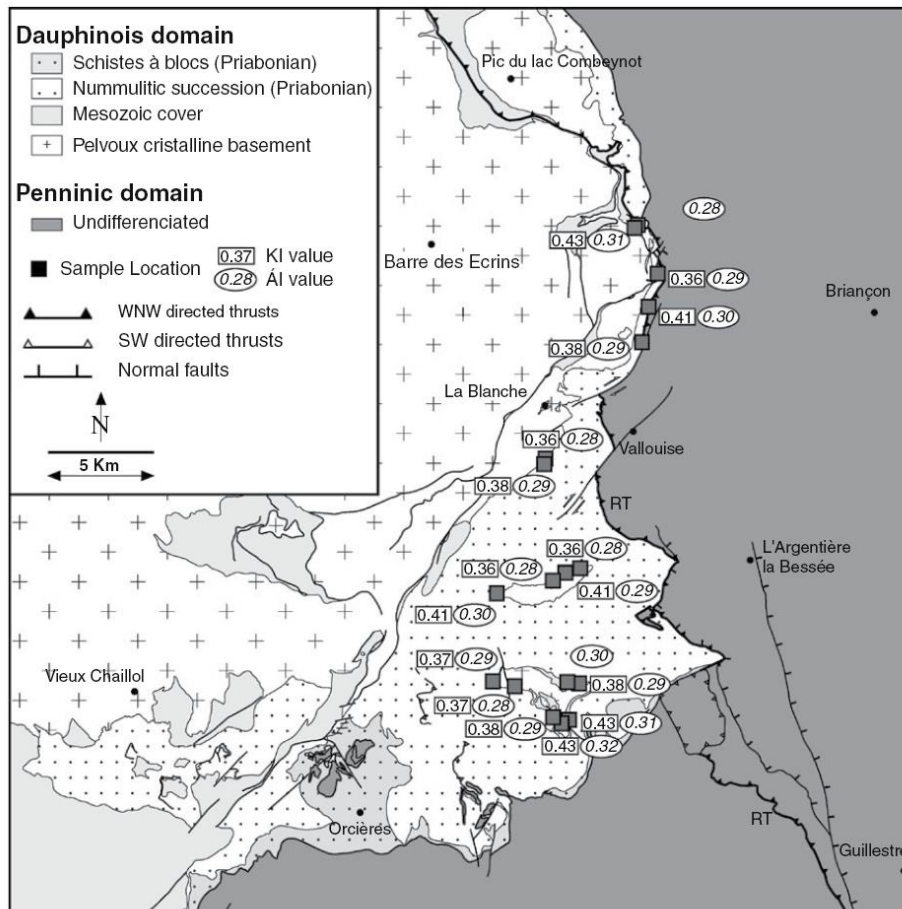


Fig. 2 Distribution and values of Kübler index (KI) and Årkai index (AI) in the studied area. Due to the proximity of the samples Do4,4a,4b; Do5a,c; DoFla,b; Fo1b,c,e; Fo2b,c and Fo3a,b,c the values are shown as averages. RT Roselend thrust

occurs with pressure increase in white mica (Ernst 1963; Guidotti et al. 1989). Guidotti et al. (1989) presented linear regression equations that quantify the changes in the K-white mica b cell dimensions of muscovite $2M_1$ that result from cation substitutions on the interlayer and octahedral sites. The K-white mica b cell dimension value was determined by measurement of the (060) peak of the potassic white mica, if present (Sassi and Scolari 1974), by using the cell-refinement program WIN-METRIC V.3.0.7 (©Bruker AXS).

Illite-muscovite polytype determination was done using a curve of $2M_1/(2M_1 + 1M)$ peaks ratio calibrated using different mixture of illite polytype following the technique described by Dalla Torre et al. (1994). Merriman and Peacor (1999) recognized that the wealth of data on

variations in white mica polytypism as a function of temperature is generally consistent with predictable trends. However, they recommended that polytype sequences should not be used other than as indicators of reaction progress.

3.2 Microthermometry

Quartz-calcite veins were sampled along the Rocher de l'Yret shear zone (RYSZ) (Figs. 1, 2), in order to substantiate P-T estimation and to reconstruct the fluid evolution history during metamorphism (Frey et al. 1980). Microthermometry investigations were done at the University of Giessen on double polished thin sections and performed using a Linkam THM 600/S/Geo heating-freezing

Table 1 Samples identification, stratigraphic age, Illite Kübler index and chlorite “crystallinity” values of the <2 μm grain-size fraction samples (data in $\Delta^\circ 2\theta$), percent of $2M_1$ polytypes and K-white mica b cell dimension data

Sample	Stratigraphic age	Elevation (m)	IC ^{Giessen} $\Delta^\circ 2\theta$	KI $\Delta^\circ 2\theta$	1σ $\Delta^\circ 2\theta$	ChC $\Delta^\circ 2\theta$	\acute{A} I $\Delta^\circ 2\theta$	1σ $\Delta^\circ 2\theta$	% $2M_1$	b (\AA)
Bea	Priabonian	1,350	0.31	0.36	0.004	0.30	0.28	0.004	92	9.024
Beb	Priabonian	1,370	0.33	0.38	0.004	0.30	0.29	0.007	87	9.009
CHA1	Priabonian	1,700	0.33	0.38	0.007	0.30	0.29	0.008	89	9.008
CHA2	Priabonian	1,710	0.36	0.41	0.004	0.32	0.30	0.010	72	9.015
CHA3	Priabonian	1,720	0.32	0.36	0.002	0.30	0.29	0.008	84	9.001
Do1	Mesozoic Cover	1,500	0.33	0.38	0.001	0.30	0.29	0.005	81	8.998
Do2	Mesozoic Cover	1,520	0.35	0.40	0.002	0.32	0.30	0.010	–	9.006
Do4a	Priabonian	1,835	0.33	0.38	0.004	0.30	0.29	0.012	–	9.026
Do4b	Priabonian	1,835	0.34	0.39	0.006	0.30	0.29	0.013	–	9.025
Do4	Priabonian	1,840	0.30	0.34	0.012	0.29	0.28	0.012	96	9.010
D05a	Mesozoic Cover	2,100	0.33	0.38	0.004	0.31	0.30	0.006	89	9.004
Do5c	Mesozoic Cover	2,105	0.32	0.37	0.008	0.31	0.29	0.010	79	9.007
DoF1a	Mesozoic Cover	1,700	0.35	0.41	0.003	0.32	0.30	0.007	–	–
DoF1b	Mesozoic Cover	1,700	0.38	0.45	0.001	0.33	0.32	0.019	73	–
DoF2	Priabonian	2,400	0.37	0.43	0.001	0.34	0.32	0.021	85	–
DoF3	Priabonian	2,200	0.33	0.38	0.004	0.30	0.29	0.004	84	9.025
Fo1b	Priabonian	1,800	0.32	0.37	0.002	0.30	0.28	0.011	88	9.018
Fo1c	Priabonian	1,740	0.31	0.35	0.004	0.29	0.28	0.021	90	9.010
Fo1e	Priabonian	1,740	0.33	0.38	0.003	0.30	0.28	0.009	–	–
Fo2b	Priabonian	1,760	0.32	0.37	0.001	0.30	0.28	0.005	95	9.017
Fo2c	Priabonian	1,760	0.31	0.36	0.004	0.30	0.29	0.006	90	9.019
Fo3a	Priabonian	2,100	0.31	0.35	0.002	0.29	0.28	0.009	82	9.028
Fo3b	Priabonian	2,100	0.36	0.42	0.004	0.32	0.31	0.007	81	9.025
Fo3c	Priabonian	2,100	0.39	0.46	0.017	0.32	0.31	0.010	70	–
Fo4b	Priabonian	1,640	0.35	0.41	0.004	0.31	0.29	0.005	90	9.016
YR1	Priabonian	2,700	0.37	0.43	0.006	0.33	0.31	0.003	81	9.021
YR2	Priabonian	2,700	0.34	0.39	0.006	0.29	0.28	0.010	–	–

IC illite “crystallinity” measured in Giessen, KI Kübler Index, ChC chlorite “crystallinity” of the 002 chlorite peak, \acute{A} I \acute{A} rkai Index, % $2M_1$ percent of $2M_1$ polytypes. b (\acute{A}) K-white mica b cell dimension

stage coupled to a TMS 94 temperature controller with an error of ± 1 $^\circ\text{C}$. The stage is mounted on an Olympus microscope with a $100\times$ Objective. The heating and cooling stage was calibrated using synthetic fluid inclusion calibration standard: CO_2 and H_2O from $^\circ\text{Bubbles}$ Incorporation.

Two-phase (consisting of vapour and liquid at room temperature) fluid inclusions were identified. No dissolved volatile phase was observed, either by melting of CO_2 at or below its triple point of -56.6 $^\circ\text{C}$, nor by formation or dissolution of clathrate or liquid–vapor equilibrium of a volatile component such as higher hydrocarbons (HHC), CH_4 , CO_2 , N_2 or H_2S . Thus, microthermometry was restricted to measuring the melting temperature of ice ($T_{\text{m,ice}}$) and the bulk homogenization temperature of the fluid inclusions (T_{h}). As none of the investigated fluid inclusions contained any observable gas component, salinity was derived from the ice melting temperature in NaCl-equivalence after Hall et al. (1988). Density for fluid inclusions with homogenisation temperatures less than

200 $^\circ\text{C}$ are from the equations of state given by Brown and Lamb (1989) and for temperatures greater than 200 $^\circ\text{C}$ are from Zhang and Frantz (1987). The isochores were calculated from the equation of state given by Zhang and Frantz (1987).

3.3 Raman microspectrometry

Gas, liquid and solid phases were investigated at the University of Frankfurt am Main using a Raman microprobe Leica/Renishaw and the software Renishaw WiRETM 2.0 and GRAMS. An Argon laser (green laser: $\lambda = 514.5$ nm) was used as excitation laser radiation. The Raman microspectrometry was used to identify the presence of CH_4 , CO_2 , HHC (C_2H_6 or C_3H_8) and N_2 in fluid inclusions. The relevant peak is positioned at $2,917$ cm^{-1} for CH_4 , $1,285$ and $1,388$ cm^{-1} for CO_2 , $2,890$ and $2,954$ cm^{-1} for C_2H_6 or C_3H_8 , respectively and $2,331$ cm^{-1} for N_2 (Burke 2001). The small size of most fluid inclusions (<10 μm) and the large vertical dimension of the laser beam focus (4 μm in diameter) cause the presence of Raman lines of the

enclosing quartz ($1,160\text{ cm}^{-1}$) in the spectra of fluids. This line does not interfere at all with the CH_4 , CO_2 and N_2 lines.

4 Results

4.1 Mineralogy

The mineralogy of the studied samples is given in Table 1.

In the Priabonian and Mesozoic meta-marls, the mineral assemblages consist of quartz + K-white micas + chlorite and calcite with minor amounts of albite. Gypsum is detected in some samples from the Fournel and Dormillouse valleys (Do2, Fo3a and Fo3c). In the fraction $<2\ \mu\text{m}$, illite-muscovite predominates, chlorite and quartz are significant, and feldspar, if detected, is only present in small quantities.

4.2 Characteristics of the phyllosilicates

Figure 2 shows the distribution of the KI data, the values of which are listed in Table 1.

The values in the Dormillouse valley vary between uppermost diagenetic conditions ($0.43\ \Delta^\circ 2\Theta$) in the south and low anchizonal values ($0.36\ \Delta^\circ 2\Theta$) in the north. In the Fournel, Beassac and Chambran Valleys, the KI data indicate low anchizonal conditions ($0.35\text{--}0.41\ \Delta^\circ 2\Theta$). In the Yret Zone, illite crystallinity values correspond to the diagenesis/anchizone boundary ($0.37\text{--}0.43\ \Delta^\circ 2\Theta$) (Fig. 2). No trend can be observed between KI and elevation of the sample. However, a trend can be observed in each valley or zone, with an increase from south to north of KI values. This is similar to that Aprahamian (1988) described.

The distribution of AI values are presented in Fig. 2. The pattern of very low-grade metamorphism shown by AI agrees well with the pattern of the KI (Fig. 2). A positive linear correlation ($R^2 = 0.64$) is found between KI and AI values (Fig. 3a). This gives confidence on the fact that illite and chlorite “crystallinities” actually refer to the same P–T conditions and thus the same experienced T–t history.

The percentage of $2M_1$ illite-muscovite polytype relative to the KI in the studied area shows a positive trend with increasing metamorphic grade (Fig. 3b).

Sassi and Scolari (1974) determined a semi quantitative relationship between the K-white mica b cell dimension and the metamorphic pressure gradient under greenschist facies condition. They plotted the K-white mica b -values as cumulative frequency curves in order to compare them with other metamorphic belts. Guidotti and Sassi (1986) collated published K-white mica b cell dimension data for greenschist and blueschist facies rocks. They presented a qualitative plot of b cell dimension as a family of curves in

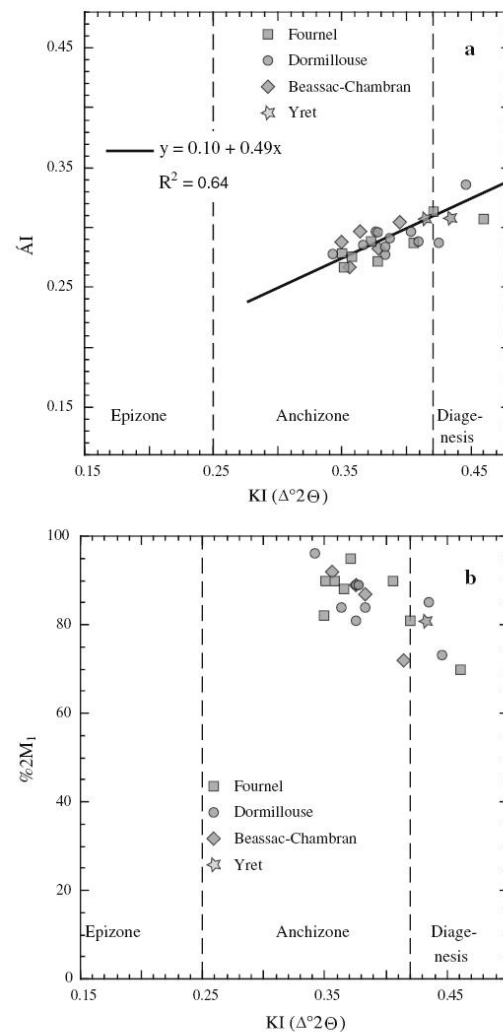


Fig. 3 Correlation between Kübler index (KI) and Arkaí index (AI) (a) and the $2M_1/1M_0$ illite polytype ratio (b), all derived from air-dried mounts

P–T space. The values presented by Guidotti and Sassi (1986) do not extend to the sub-greenschist facies. However, the considerable amount of K-white mica b cell dimension data from very low-grade metapelites accumulated in different metamorphic belt corroborate the groupings found by Guidotti and Sassi (1986), as shown by Merriman and Peacor (1999). K-white mica b cell dimensions were calculated for 21 samples from the anchizone (three samples were not integrated due to interferences and poor intensity signal), all fall in the same range with a

minimum 8.998 and a maximum 9.028 Å values (Table 1). Specimens from the Mesozoic cover have lower values (at around 9.000 Å), while Priabonian are centred around 9.020 Å. However, both value groups are in the intermediate pressure facies (between 9.000 and 9.040 Å) as shown in Fig. 4 (the curve obtained is similar to the reference curve from Ryoke), suggesting an inferred geothermal gradient of 25–35 °C/km (Guidotti and Sassi 1986).

4.3 Vein mineralogy, textural relationships and microthermometry

Samples were collected within the RYSZ, previously described by Butler (1992), and consisting in an imbricate of

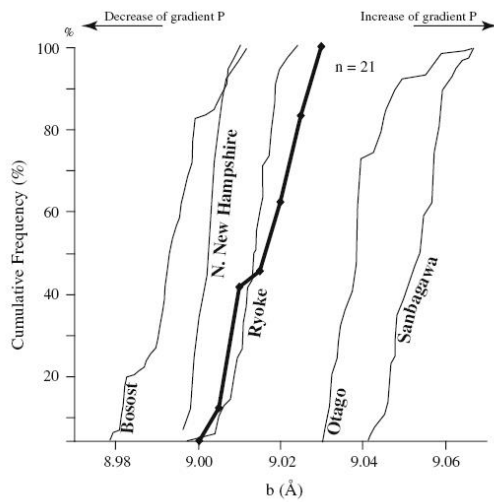


Fig. 4 Cumulative curves of K-white mica *b* cell dimensions for 21 anchizonal samples from our study area (*in bold*) with reference curves from Sassi and Scolari (1974) and Guidotti and Sassi (1986)

basement slices and para-autochthonous sedimentary cover. This shear zone, lying directly below the frontal penninic nappe stack, has been considered as the map trace of the RT in this area (Trullenque 2005). All kinematic indicators measured in the field or deduced from microfabric analysis of calcite ultramyonites (Trullenque et al. 2006), consistently show a WNW directed sense of transport, consistent with activity along the RT. No evidence of D₂ structures are found in this area.

Samples have been collected along strike slip fault planes dissecting basement slices and indicating a clear WNW directed sense of transport. These faults are clearly related to the first deformation phase D₁. The chronology of the different fluid inclusion populations (Table 2) is a relative one with respect to their host mineral and their overgrowth (Mullis 1976).

Veins are mainly composed of small quartz crystals associated sometimes with calcite crystals. Only two-phase fluid inclusions (consisting of vapour and liquid at room temperature) were identified with the microscope. Fibre quartz is observed in the sample F72. In F92, two fluid inclusion assemblages are identified. The first one is a two-phase type in the host quartz and probably of primary type, i.e. trapped during mineral growth. The second one is overprinting the first assemblage and probably of pseudo-secondary type. The true temperature of entrapment of the fluid inclusions, i.e. mineral growth, was constrained by intersecting the isochores of primary two-type phase fluid inclusions with the inferred geothermal gradient deduced from the K-white b cell dimension (Fig. 5). Isochores were calculated for the lower and upper homogenization temperature (*T_h*) with an average salinity of 5.6 and 13.8 wt. % NaCl equivalent for samples F72 and F92, respectively.

5 Discussion

The structural metamorphic map of the Alps (Oberhänsli et al. 2004) indicates lower sub-greenschist facies E of the

Table 2 Fluid inclusion data of two quartz samples from the Yret Zone, Western French Alps

1	2	3	4	5	6	7	8	9	10
Locality	FP	HM	IT	<i>n_f</i>	V %	<i>T_{mICE}</i>	<i>T_h</i>	H ₂ O mole %	NaCl mole %
F72	1	FQ	P	66	5	-3.5 ± 0.6	176.6 ± 18.3	94.5	5.6
F92	1	VQ	Ps II	22	5	-6.9 ± 0.9	182.4 ± 15.5	89.8	10.2
"	2	VQ	P	3	5–10	-9.6 ± 0.9	172.3 ± 10.0	87.2	13.8

(1) Locality number. (2) *FP* fluid inclusion population. (3) *HM* host mineral—*FQ* fibre quartz, *VQ* vein quartz. (4) *IT* inclusion type—*Ps II* pseudosecondary fluid inclusions, *P* primary fluid inclusions. (5) *n_f* number of measured fluid inclusions. (6) *V* % volume % of the volatile part estimated at room temperature. (7) *T_{mICE}* melting temperature of ice (°C)—First number = mean value, second number = standard deviation. (8) *T_h* homogenization temperature of fluid inclusions—First number = mean value, second number = standard deviation. (9) and (10) = approximate mole-% H₂O and NaCl (equivalents)

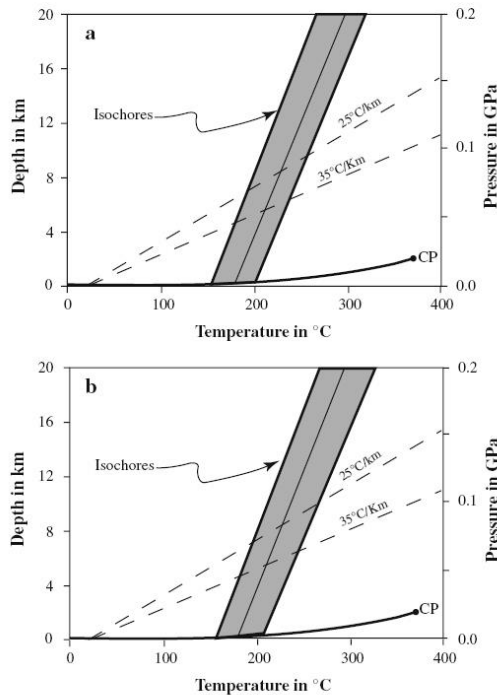


Fig. 5 Depth-temperature diagrams with isochores representing the higher and the lower calculated molar volumes for vapour-rich fluid inclusions and the mean isochores in samples F72 (a) and F92 (b) from the Yret zone. The *dashed lines* represent the range of geothermal gradients from 25 and 35 °C/km as deduced from the K-white mica *b* cell dimensions. The *thick curve* represents the liquid–gas reaction curve of water. *CP* critical point of water

RT and N of the Pelvoux massif. North of the Pelvoux massif, Ceriani et al. (2003) described an E–W metamorphic gradient on the E side of the RT. In the Briançonnais, they reported an increase from anchizonal to epizonal conditions from E to W. In the same area, the Dauphinois domain (in the footwall of the RT) shows epizonal metamorphic conditions. The Dauphinois domain in this area is only affected by one deformation phase, corresponding to the third deformation phase in the FPU (Ceriani 2001; Ceriani et al. 2001) and equivalent to D_1 in our studied area (Trullenque 2005). The K-white *b* cell dimensions obtained by Ceriani et al. (2003) in the Dauphinois Domain are ranging between 9.000 and 9.030 Å similar to those obtained in our study, indicating similar geothermal metamorphic gradient between the two areas.

Frey (1987) and Essene and Peacor (1995) showed that KI cannot be used as a precise geothermometer and only provide an approximate temperature range. In spite of this, attempts have been made to relate KI values to absolute

temperatures. This was done in different low-grade metamorphic units by comparing the KI data with other geothermometers (Ferreiro Mählmann 1994, 1996; Merriman and Peacor 1999; Mullis et al. 2002; Potel et al. 2006). Mullis et al. (2002) have suggested a diagenesis–anchizone boundary in the Alps on the basis of a comparison of IC versus FI data. This allows to better define the range of temperature that the SE of the Pelvoux massif was subjected during tectonic evolution.

The KI values indicate that the Dauphinois domain in the SE of the Pelvoux massif underwent up to low anchizonal metamorphic conditions (Table 1; Fig. 2). According to Mullis et al. (2002), the boundary is linked to a temperature of around 230–240 °C (similar to the compilation results from Ferreiro Mählmann (1994)). This can be compared to the temperature estimates obtained west of our studied area in the “grès de Champsaur” (W of Prapic). Waibel (1990) described quartz–prehnite ± calcite veins in the “grès de Champsaur”. The country rock is dark green in colour, enriched in pumpellyite of variable composition, and to a lesser extent prehnite, at the expense of laumontite. Aprahamian (1988) described also mottled sandstone (faciès moucheté), the pale-coloured mottles being enriched in laumontite as cement and as partial replacement product of albitized clastic plagioclase and the darker areas being relatively enriched in chlorite cement. According to Frey et al. (1991) and Potel et al. (2002), the coexistence of zeolites (laumontite in this case) and prehnite–pumpellyite is restricted to a rather small P–T area below 240 °C and therefore in the range obtained by using the correlation from Mullis et al. (2002).

Zircon FT data were gained from the turbiditic “grès de Champsaur” and the underlying Pelvoux crystalline basement (Seward et al. 1999). These data provide important information on the peak temperatures reached during Alpine metamorphism. For the zircon FT system, several estimates on the temperature range of the partial annealing zone exist (e.g. Yamada et al. 1995, 2007; Tagami et al. 1998). Tagami et al. (1998) suggested a temperature range between 200 and 320 °C to be appropriate, which covers the temperature range relevant to the metamorphic zonation based on illite “crystallinity” (e.g. Mullis et al. 2002). The combination of both methods therefore provides additional constraints on the maximum temperature reached to the SE of the Pelvoux massif. In the Glarus Alps, the comparison between fluid inclusion data and zircon FT data suggests that zircon FT annealing in the Taveyanne sandstone (a lateral equivalent of the “grès de Champsaur”) only becomes detectable above 250 °C (Rahn 2001). The measured K-white mica *b* cell dimension values inferred an intermediate geothermal gradient with 25–35 °C/km (Merriman and Peacor 1999). This gradient seems to be a very conservative approach, however the

result is similar to that found in the Dauphinois domain north of the Pelvoux massif (Ceriani et al. 2003). Combining this information with the fluid inclusion data obtained in the Yret zone, a trapping temperature for the fluid inclusions of 220 ± 10 °C can be obtained (Fig. 5a, b). Consequently, the comparison of KI, FT and fluid inclusion leads to the conclusion that the SE of the Pelvoux massif was subjected to temperatures higher than 200 °C, but lower than 250 °C. This is higher than the estimation of temperature by Seward et al. (1999) who estimated that the burial temperature of the “grès de Champsaur” was not higher than 200 °C. This implies metamorphic burial between 7 and 9 km. Neither our KI nor the FT data (Seward et al. 1999) reveal the presence of a metamorphic gradient from E to W in the SE of the Pelvoux massif as described by Aprahamian (1974). The absence of epizonal KI values in the Vallouise valley (Aprahamian 1974, 1988), moves the anchizone–epizone boundary to the N of the Pelvoux massif, where epizonal metamorphic conditions are observed (Ceriani et al. 2003). As mentioned by Ferreiro Mählmann and Frey (2012), one of the reasons of the lack of epizonal values, is that the KI values obtained by CIS calibration led to a broadening of the anchizone area.

The available metamorphic data from the south of the Pelvoux massif combined with the available deformation data allow us to deduce some conclusions concerning the tectono-metamorphic evolution in this area. A first important result provided by the KI, fluid inclusion and FT data is the fact that the Dauphinois domain exhibits lower metamorphic conditions compared to the Penninic domain. According to the metamorphic map of the Alps, the Penninic domain west of the RT is metamorphosed under lower greenschist facies (Oberhänsli et al. 2004). Field evidences SE of the Pelvoux massif (this paper; Trullenque 2005), indicate that D₁ corresponds to the first penetrative schistosity, marked by very fine-grained K-white mica, chlorite, quartz and albite. The metamorphic gradient observed and the formation of the fluid inclusions studied are related to this deformation phase and the burial heating (with a maximum of 9 km burial) was generated by the overthrust Penninic domain along the RT onto the Dauphinois domain. As mentioned above, the K-white mica *b* cell dimension values in our studied area SE of the Pelvoux massif, are similar to those obtained in the north by Ceriani et al. (2003). Therefore, the metamorphic gradient observed in the Penninic domain must be established before D₁, as observed by Ceriani et al. (2003) further to the N (the D₁ observed SE of the Pelvoux massif correspond to the D₃, see above). So, we have no trace of an older metamorphic event.

North of the Pelvoux massif, the metamorphic grade is higher with epizonal conditions and may be explained by

thicker Penninic units on top of the Dauphinois domain leading to higher degree of burial and therefore show a regional metamorphic gradient increasing from S to N. This is corroborated by the same pressure gradient observed north and south of the Pelvoux massif in the Dauphinois domain (same range of K-white mica *b* cell dimension).

Ferreiro Mählmann (2001) in the eastern Alps showed that in rocks submitted to a long metamorphic event (20 Ma) and a steady state heat flow, the smectite content in the anchizone is between 0 and 5 % (90 % of the samples without smectite), and that under stable thermal conditions (equilibrium), KI can be used as a thermometer. In this region, Henrichs (1993) reported K-white mica *b* cell dimension values between 9.000 and 9.022 Å and the compilation of the Ferreiro Mählmann et al. (2012) shows a normal to low geothermal gradient (30 °C/km). Comparison of our results with KI and K-white mica *b* cell dimension values will suggest that the Dauphinois Domain has been submitted to a relative long heating time like in the eastern Alps.

6 Conclusion

The tectono-metamorphic history of the Dauphinois domain in the SE of the Pelvoux is similar that described by Ceriani et al. (2003) in the north. Peak metamorphic conditions in the Dauphinois domain are reached during the overthrusting of the Penninic units during D₁ top-WNW directed thrusting along the RT. The metamorphism is characterized by temperatures below 250 °C and higher than 200 °C and a metamorphic gradient between 25 and 35 °C, and a long time event. This range of temperature is compatible with the FT data published by Seward et al. (1999) indicating that the burial temperature in the region was lower than 250 °C. Based on our KI values and the mineral paragenese observed in the W of the “grès de Champsaur”, no E–W metamorphic zonation as described by Aprahamian (1974, 1988) is observed. But, in the studied area, the grade of metamorphism in the Dauphinois Domain is lower than in the northern of the Pelvoux massif (Ceriani et al. 2003) confirming the N–S metamorphic zonation described by Aprahamian (1974, 1988). This is also outlined by the zircon FT ages indicating an increase in age primarily from the north to the south (Fügenschuh and Schmid 2003) and supports their hypothesis that the more southerly located areas were less deeply buried and hence less exhumed. Like proposed by Ceriani et al. (2001) and Fügenschuh and Schmid (2003), the overthrust along the RT of the Penninic units may caused burial and metamorphism in the external Dauphinois units.

Acknowledgments This manuscript benefited greatly from constructive and helpful reviews and comments from M. Rahn and R. Ferreiro Mählmann.

References

- Apps, G. M., Peel, F., & Elliott, T. (2004). The structural setting and palaeogeographical evolution of the Gres d'Annot Basin. Deep-water sedimentation in the Alpine Basin of SE France; new perspectives on the Gres d'Annot and related systems. *Geological Society Special Publication*, 221, 65–96.
- Aprahamian, J. (1974). La cristallinité de l'illite et les minéraux argileux en bordure des massifs cristallins externes de Belledonne et du Pelvoux. *Géologie Alpine*, 50, 5–15.
- Aprahamian, J. (1988). Cartographie du métamorphisme faible à très faible dans les Alpes françaises externes par l'utilisation de la cristallinité de l'illite. *Geodinamica Acta*, 2, 25–32.
- Árkai, P. (1991). Chlorite crystallinity: an empirical approach and correlation with illite crystallinity, coal rank and mineral facies as exemplified by Palaeozoic and Mesozoic rocks of northeast Hungary. *Journal of Metamorphic Geology*, 9, 723–734.
- Árkai, P., Faryad, S. W., Vidal, O., & Balogh, K. (2003). Very low-grade metamorphism of sedimentary rocks of the Meliata unit, Western Carpathians, Slovakia: implications of phyllosilicate characteristics. *International Journal of Earth Sciences*, 92, 68–85.
- Árkai, P., Sassi, F. P., & Sassi, R. (1995). Simultaneous measurements of chlorite and illite crystallinity: a more reliable tool for monitoring low- to very low grade metamorphism in metapelites. A case study from the Southern Alps (NE Italy). *European Journal Mineralogy*, 7, 1115–1128.
- Brown, P. E., & Lamb, W. M. (1989). P-V-T properties of fluids in the system $H_2O \pm CO_2 \pm NaCl$: new graphical presentations and implications for fluid inclusion studies. *Geochimica Cosmochimica Acta*, 53, 1209–1221.
- Bürgisser, J. (1998). *Deformation in foreland basins of the Western Alps (Pelvoux massif, SE France): significance for the development of the Alpine arc*. Zürich: ETH. 151 pp.
- Burke, E. A. J. (2001). Raman microspectrometry of fluid inclusions. *Lithos*, 55, 139–158.
- Butler, R. W. H. (1989). The influence of pre-existing basin structure on thrust system evolution in Western Alps. *Geological Society Special Publications*, 44, 105–122.
- Butler, R. W. H. (1992). Thrust zone kinematics in a basement-cover imbricate stack; eastern Pelvoux massif, French Alps. *Journal of Structural Geology*, 14, 29–40.
- Ceriani, S. (2001). A combined study of structure and metamorphism in the frontal Penninic units between the Arc and the Isère valleys (Western Alps): Implications for the geodynamics evolution of the Western Alps. Unpublished PhD thesis, Universität Basel, 196 pp.
- Ceriani, S., Fügenschuh, B., Potel, S., & Schmid, S. M. (2003). The tectono-metamorphic evolution of the Frontal Penninic units of the Western Alps: correlation between low-grade metamorphism and tectonic phases. *Schweizerische Mineralogische und Petrographische Mitteilungen*, 83, 111–131.
- Ceriani, S., Fügenschuh, B., & Schmid, S. M. (2001). Multi-stage thrusting at the “Penninic Front” in the Western Alps between Mont Blanc and Pelvoux massifs. *International Journal of Earth Sciences*, 90, 685–702.
- Coward, M. P., Gillcrist, R., & Trudgill, B. (1991). Extensional structures and their tectonic inversion in the Western Alps. *Geological Society Special Publications*, 5, 93–112.
- Dalla Torre, M., Stern, W. B., & Frey, M. (1994). Determination of white K-mica polytype ratios: comparison of different XRD methods. *Clay Minerals*, 29, 717–726.
- Davies, V. M. (1982). Interaction of thrusts and basement faults in the French external Alps. *Tectonophysics*, 88, 325–331.
- Debrand-Passard, S., Courbouleix, S., & Lienhardt, M.-J. (1984). Synthèse géologique du Sud-Est de la France. Mémoire du Bureau de recherches géologiques et minières, 126 pp.
- Desmons, J., Compagnoni, R., & Cortesogno, L. (1999). Alpine metamorphism of the Western Alps: II. High-P/T and related pre-greenschist metamorphism. In: Frey, M., Desmons, J., & Neubauer, F. (Eds.), *The new metamorphic map of the Alps. Schweizerische Mineralogische und Petrographische Mitteilungen*, 79 (pp. 111–134).
- Ernst, W. G. (1963). Significance of phengitic micas from low grade schists. *American Mineralogist*, 48, 1357–1373.
- Essene, E. J., & Peacor, D. R. (1995). Clay mineral thermometry—a critical perspective. *Clays Clay Mineral*, 43, 540–553.
- Ferreiro Mählmann, R. (1994). Zur Bestimmung von Diagenesehöhe und beginnender Metamorphose-Temperaturgeschichte und Tektonogenese des Austroalpins und Süppenninikums in Vorarlberg und Mittelbünden. Universität Frankfurt, *Frankfurter Geowissenschaftliche Arbeiten, Serie C 14*, 498 pp.
- Ferreiro Mählmann, R. (1996). The pattern of diagenesis and metamorphism by vitrinite reflectance and illite-“crystallinity” in Mittelbünden and in the Oberhalbstein. Part2: correlation of coal petrographical and of mineralogical parameters. *Schweizerische Mineralogische und Petrographische Mitteilungen*, 76, 23–46.
- Ferreiro Mählmann, R. (2001). Correlation of very low-grade data to calibrate a thermal maturity model in a nappe tectonic setting, a case study from the Alps. *Tectonophysics*, 334, 1–33.
- Ferreiro Mählmann, R., Bozkaya, O., Potel, S., Le Bayon, R., Šegvič, B., & Nieto García, F. (2012). The pioneer work of Bernard Kübler and Martin Frey in very low-grade metamorphic terranes: Paleo-geothermal potential of Kübler-Index/organic matter reflectance correlation – a review. *Swiss Journal of Geosciences*, this volume.
- Ferreiro Mählmann, R. & Frey, M. (2012). “Standardisation, calibration and correlation of the Kübler-Index and the vitrinite/bituminite reflectance: an inter-laboratory and field related study”. *Swiss Journal of Geosciences*, this volume.
- Frey, M. (Ed.). (1987). *Low temperature metamorphism*. Glasgow and London: Blackie & Son.
- Frey, M., de Capitani, C., & Liou, J. G. (1991). A new petrogenetic grid for low-grade metabasites. *Journal of Metamorphic Geology*, 9, 497–509.
- Frey, M., Desmons, J., & Neubauer, F. (Eds.) (1999). The new metamorphic map of the Alps. *Schweizerische Mineralogische und Petrographische Mitteilungen*, 79, 230 pp.
- Frey, M., Teichmüller, M., Teichmüller, R., Mullis, J., Künzi, B., Breitschmid, A., et al. (1980). Very low-grade metamorphism in external parts of the Central Alps: illite crystallinity, coal rank and fluid inclusion data. *Eclogae Geologicae Helveticae*, 73, 173–203.
- Fügenschuh, B., & Schmid, S. (2003). Late stages of deformation and exhumation of an orogen constrained by fission-track data: a case study in the Western Alps. *Geological Society of America Bulletin*, 115, 1425–1440.
- Fügenschuh, B., Loprieno, A., Ceriani, S., & Schmid, S. M. (1999). Structural analysis of the Subbrian çonnais and Valais units in the area of Moûtiers (Savoy, Western Alps): paleogeographic and tectonic consequences. *International Journal of Earth Sciences*, 88, 201–218.

- Gillcrist, R., Coward, M., & Mugnier, J. L. (1987). Structural inversion and its controls; examples from the Alpine Foreland and the French Alps. *Geodinamica Acta*, 1, 5–34.
- Guggenheim, S. Jr, Bain, D. C., Bergaya, F., Brigatti, M. F., Drits, V. A., Eberl, D. D., et al. (2002). Report of the association internationale pour l'étude des argiles (AIPEA) nomenclature committee for 2001: order, disorder and crystallinity in phyllosilicates and the use of the 'crystallinity index'. *Clays and Clay Minerals*, 50, 406–409.
- Guidotti, C. V., & Sassi, F. P. (1986). Classification and correlation of Metamorphic Facies Series by Means of Muscovite b_0 data from Low-Grade Metapelites. *Neues Jahrbuch Mineralogie Abteilung-Hefte*, 153, 363–380.
- Guidotti, C. V., Sassi, F. P., & Blencoe, J. G. (1989). Compositional controls on the a and b cell dimensions of $2M_1$ Muscovites. *European Journal of Mineralogy*, 1, 71–84.
- Gupta, S. (1997). Tectonic control on paleovalley incision at the distal margin of the early Tertiary Alpine foreland basin, southeastern France. *Journal of Sedimentary Research*, 67, 1030–1043.
- Hall, D. L., Sterner, S. M., & Bodnar, R. J. (1988). Freezing point depression of NaCl–KCl–H₂O solutions. *Economic Geology*, 83, 197–202.
- Henrichs, C. (1993). Sedimentpetrographische Untersuchungen zur Hochdiagenese in der Kössen-Formation (Ober Trias) der westlichen Ostalpen und angrenzenden Südalpengebiete. *Böcher geologische und geo-technische Arbeiten* 40, 206 pp.
- Huyghe, P., & Mugnier, J. L. (1995). A comparison of inverted basins of the southern North Sea and inverted structures of the external Alps. *Geological Society Special Publications*, 88, 339–353.
- Kisch, H. J., Árkai, P., & Brime, C. (2004). On the calibration of illite Kübler index (illite 'crystallinity'). *Schweizerische Mineralogische und Petrographische Mitteilungen*, 84, 323–331.
- Kretz, R. (1983). Symbols for rock-forming minerals. *American Mineralogist*, 68, 277–279.
- Kübler, B. (1964). Les argiles, indicateurs de métamorphisme. *Institut Français Pétrole*, 19, 1093–1112.
- Kübler, B. (1968). Evaluation quantitative du métamorphisme par la cristallinité de l'illite. Etat des progrès réalisés ces dernières années. *Bulletin Centre Recherche Pau, S.N.P.A.*, 2, 385–397.
- Lazarre, J., Tricart, P., Courrioux, G., & Ledru, P. (1996). Héritage téthysien et polyphasage alpin; réinterprétation tectonique du "synclinal" de l'aiguille de Morges (massif du Pelvoux, Alpes occidentales, France). *Comptes Rendus de l'Académie des Sciences, Série II. Sciences de la Terre et des Planètes*, 323, 1051–1058.
- Merriman, R. J., & Peacor, D. R. (1999). Very low-grade metapelites: mineralogy, microfabrics and measuring reaction progress. In M. Frey & D. Robinson (Eds.), *Low-Grade Metamorphism* (pp. 10–60). London: Blackwell Science.
- Merriman, R. J., Roberts, B., & Peacor, D. R. (1990). A transmission electron microscope study of white mica crystallite size distribution in a mudstone to slate transitional sequence, North Wales, U. K. *Contributions to Mineralogy & Petrology*, 106, 27–40.
- Mullis, J. (1976). Das Wachstumsmilieu der Quarzkristalle im Val d'Iliez (Wallis, Schweiz). *Schweizerische Mineralogische und Petrographische Mitteilungen*, 56, 219–268.
- Mullis, J. J., Rahn, M. K. W., Schwer, P., de Capitani, C., Stern, W. B., & Frey, M. (2002). Correlation of fluid inclusion temperatures with illite "crystallinity" data and clay mineral chemistry in sedimentary rocks from the external part of the Central Alps. *Schweizerische Mineralogische und Petrographische Mitteilungen*, 82, 325–340.
- Oberhänsli, R., Bousquet, R., Engi, M., Goffé, B., Gosso, G., Handy, M., Höck, V., Koller, F., Lardeaux, J.-M., Polino, R., Rossi, P., Schuster, R., Schwarz, S. & Spalla, M.I. (2004). Metamorphic structure of the Alps (1:1'000'000), Commission for the Geological Map of the World (UNSECO), Paris.
- Perriaux, J., & Uselle, J. P. (1968). Quelques données sur la sédimentologie des grès du Champsaur (Hautes-Alpes). *Géologie Alpine*, 44, 329–332.
- Potel, S., Ferreiro, Mähmann R., Stern, W. B., Mullis, J., & Frey, M. (2006). Very low-grade metamorphic evolution of pelitic rocks under high-pressure/low-temperature conditions, NW New Caledonia (SW Pacific). *Journal of Petrology*, 47, 991–1015.
- Potel, S., Schmidt, S Th, & de Capitani, C. (2002). Composition of pumpellyite, epidote and chlorite from New Caledonia—How important are metamorphic grade and whole-rock composition? *Schweizerische Mineralogische und Petrographische Mitteilungen*, 82, 229–252.
- Rahn, M. K. W. (2001). *The metamorphic and exhumation history of the Helvetic Alps, Switzerland, as revealed by apatite and zircon fission tracks. Unpublished Habilitation thesis.* Freiburg: Albert-Ludwigs-Universität. 140 pp.
- Ravenne, C., Vially, R., Riche, P., & Tremolieres, P. (1987). Sédimentation et tectonique dans le bassin marin Eocene supérieur-Oligocene des Alpes du Sud. *Revue de l'Institut Français du Pétrole*, 42, 529–553.
- Sassi, F. P., & Scolari, A. (1974). The b_0 of the potassic white micas as a barometric indicator in low-grade metamorphism of pelitic schists. *Contributions to Mineralogy and Petrology*, 45, 143–152.
- Schmid, S. M., Fügenschuh, B., Kissling, E., & Schuster, R. (2004). Tectonic map and overall architecture of the Alpine orogen. *Eclogae Geologicae Helveticae*, 97, 93–117.
- Seward, D., Ford, M., Bürgisser, J., Lickorish, H., Williams, E. A., & Meckel, L. D. I. I. (1999). Preliminary report on fission tracks studies in the Pelvoux area, SE France. *Memorie di Scienze Geologiche*, 51, 25–31.
- Sue, C., Tricart, P., Dumont, T., & Pecher, A. (1997). Raccourcissement polyphase dans le massif du Pelvoux (Alpes occidentales): exemple du chevauchement de socle de Villard-Notre-Dame. *Comptes Rendus de l'Académie des Sciences, Série II. Sciences de la Terre et des Planètes*, 324, 847–854.
- Tagami, T., Galbraith, R. F., Yamada, R. & Laslett, G. M. (1998). Revised annealing kinetics of fission tracks in zircon and geological implications. In P. Van den haute, & F. De Corte (Eds.), *Advances in fission-track geochronology*: Kluwer academic publishers, Dordrecht, The Netherlands, pp 99–112.
- Tricart, P. (1986). Le Chevauchement de la zone briannonnaise au Sud-Est du Pelvoux; clé des rapports zone externe—zones internes dans les Alpes occidentales. *Bulletin de la Société Géologique de France, Huitième Série*, 2, 233–244.
- Tricart, P. (2004). From extension to transpression during the final exhumation of the Pelvoux and Argentera massifs, Western Alps. *Eclogae Geologicae Helveticae*, 97, 429–439.
- Tricart, P., Bourbon, M., Chenet, P. Y., Cros, P., Delorme, M., Dumont, T., et al. (1988). Tectonique synsédimentaire triasico-jurassique et rifting téthysien dans la nappe briannonnaise de Peyre-Haute (Alpes occidentales). *Bulletin de la Société Géologique de France*, 4, 669–680.
- Tricart, P., Schwartz, S., Sue, C., Poupeau, G., & Lardeaux, J. M. (2001). La dénudation tectonique de la zone Ultra-dauphinoise et l'inversion du front Briançonnais au Sud Est du Pelvoux (Alpes Occidentales); une dynamique Miocène à actuelle. *Bulletin de la Société Géologique de France*, 172, 49–58.
- Trullenque, G. (2005). Tectonic and microfabric studies along the Penninic Front between Pelvoux and Argentera Massifs (Western Alps, France). Unpublished PhD thesis, Universität Basel, 301 pp.
- Trullenque, G., Kunze, K., Heilbronner, R., Stünitz, H., & Schmid, S. (2006). Microfabrics of calcite ultramylonites as records of

- coaxial and non-coaxial deformation kinematics: examples from the Rocher de l'Yret shear zone (Western Alps). *Tectonophysics*, 424, 69–97.
- Waibel, A.F. (1990). Sedimentology, petrographic variability, and very-low-grade metamorphism of the Champsaur sandstone (Paleogene, Hautes-Alpes, France). Evolution of volcanoclastic foreland turbidites in the external Western Alps. Unpublished PhD thesis, Université de Genève, 140 pp.
- Warr, L. N., & Rice, A. H. (1994). Interlaboratory standardization and calibration of clay mineral crystallinity and crystallite size data. *Journal of Metamorphic Geology*, 12, 141–152.
- Yamada, R., Galbraith, R. F., Murakami, M., & Tagami, T. (2007). Statistical modelling of annealing kinetics of fission-tracks in zircon: reassessment of laboratory experiments. *Chemical Geology*, 236, 75–91.
- Yamada, R., Tagami, T., Nishimura, S., & Ito, H. (1995). Annealing kinetics of fission tracks in zircon: an experimental study. *Chemical Geology (Isotope Geoscience Section)*, 122, 249–258.
- Zhang, Y., & Frantz, J. D. (1987). Determination of the homogenization temperatures and densities of supercritical fluids in the system NaCl-KCl-CaCl₂-H₂O using synthetic fluid inclusions. *Chemical Geology*, 64, 335–350.

4 Research activities in the framework of professional experience

The summaries of my DEA and PhD thesis have shown some of my expertise in geodynamics, structural geology and microtectonics. All these competences are needed in the lines of research I am following in my career.

By the end of my PhD thesis I wanted to deepen my knowledge in the field of texture analysis using Electron Back Scattered Diffraction (EBSD) techniques. This tool permits a local analysis of CPO and brings essential additional information to bulk X-ray texture analysis.

In order to better understand development of CPO as a function of strain I decided to implement an experimental rock deformation set-up. This laboratory approach allows to precisely control displacements imposed to a given sample. This monitoring is crucial as precise strain estimates in the field are often difficult.

This ambitious program was intended to better constrain deformation mechanisms affecting geological materials in both brittle and ductile fields. I was fully aware that intensive training was needed in order to master experimental deformation at a range of pressure and temperatures together with chemical and crystallographic characterization tools at mineral scale.

In addition, science funding being crucial, I considered that some engineering expertise was important as it was paving a way to applied research with associated potential investors.

4.1 Training mobility

At the end of my PhD thesis, I applied for a training mobility program in the form of a proposal funded at 50% by the Swiss national fund and 50% by the Freiwillige Akademische Gesellschaft Basel. I received during this project trainings on a Paterson-type deformation apparatus plus EBSD sample preparation techniques and analysis under the Scanning Electron Microscope (SEM). This training was first given at University of Minnesota Twin cities campus (Minneapolis, USA) under supervision of Prof. Kohlstedt and continued at University of Utrecht (Utrecht, The Netherlands) under supervision of Dr. De Bresser and Dr. Drury.

During this year of training, I participated to the discovery of a new intracrystalline glide system for calcite, namely glide in the a $\langle -12-10 \rangle$ direction along the r $\{10-14\}$ plane (De Bresser et al., 2008). This work was in the direct continuation of the texture analysis I performed during my PhD and dedicated to crystallographic response of calcitic rocks subjected to shear deformation.

I used a novel direct shear experimental set-up mounted in an axial loading uniaxial geometry using a gas pressure vessel at 300 MPa and 1000 K temperature. Oriented calcite single crystals were used as a starting material for a series of deformation tests up to a shear strain $\gamma = 1.5$ and a shear strain rate of $1.7 \times 10^{-4} \text{ s}^{-1}$. Our experiments have shown a nearly steady state creep in the stress-strain curve starting at $\gamma = 0.2$ indicating the onset of dominant slip on the r plane in the $\langle a \rangle$ direction.

The analysis of mechanical data indicated that the r $\langle a \rangle$ slip must be considered when dealing with interpretation of calcite textures although this new system as a Critical Resolved Shear Stress (CRSS) about 10% higher than the well-known r $\langle -2021 \rangle$.



Evidence for $r\langle a \rangle$ slip in calcite

J.H.P. De Bresser (1), G. Trullenque (2,3) and M.R. Drury (1)

(1) Department of Earth Sciences, P.O. box 80021, 3508 TA Utrecht, The Netherlands, (2) Institut für Geowissenschaften, Johannes Gutenberg Universität, Becherweg 21, D-55099 Mainz, Germany, (3) Now at Oxford Instruments GmbH Nanoanalysis, Otto-von-Gluericke-Ring 10, D-65205 Wiesbaden, Germany (j.h.p.debresser@geo.uu.nl, FAX: +31 30 2537725 / Phone: +31 30 2534973)

Torsion deformation experiments performed on Carrara marble a few years ago (Pieri et al., 2001; Tectonophysics 330, 119-140) have shown the development, at high strain, of a lattice preferred orientation with a sharp single orientation component with the calcite $r\{10\bar{1}4\}$ plane parallel to the shear plane and the direction $a\langle\bar{1}2\bar{1}0\rangle$ parallel to the shear direction. This suggested that the $r\langle a \rangle$ system is an important slip system in calcite, confirmed by results of plasticity models. However, the $r\langle a \rangle$ system thus far has not been demonstrated to be operative in calcite, while slip on the r -plane in the $\langle\bar{2}021\rangle$ direction is well established. We performed direct shear experiments on single crystals of calcite and now found unequivocal evidence for $r\langle a \rangle$. Square samples of size $8 \times 8 \times 0.5$ mm have been deformed in a direct shear piston configuration mounted in an axial loading set-up in a constant volume, internally heated argon gas medium deformation apparatus. Samples have been deformed to a shear strain of $\gamma = 1.5$, at a temperature of 1000 K, a confining pressure of 300 MPa and a shear strain rate of $1.7 \times 10^{-4} \text{ s}^{-1}$. The calcite samples were oriented such that either the $r\langle\bar{2}021\rangle$ or the $r\langle a \rangle$ system was activated, given that the latter actually exists. Stress-strain curves show a yield point at about $\gamma = 0.2$, followed by a quasi-steady state part up to $\gamma = 1.5$. We have used Electron Backscatter Diffraction (EBSD) to analyze the deformed calcite single crystals. Results clearly show evidence for activity of the $r\langle a \rangle$ system. At the conditions investigated, the $r\langle a \rangle$ system is about 10% stronger than the classical $r\langle\bar{2}021\rangle$ system. Detailed misorientation analysis also demonstrated the local development of small subgrains and recrystallized grains. We are currently analyzing rotation axes associated with the development of these subgrains.

4.2 Research assistant at Johannes Gutenberg University

The above-mentioned technical competences gave me the opportunity to present my candidature to a research assistant position opened at the Johannes Gutenberg University, Mainz, Germany. The position required some substantial technical and engineering skills and the working contract was on a fixed-term basis.

I was responsible for creating and ensuring maintenance of the EBSD sample preparation laboratory. I negotiated all orders in terms of polishing equipment and consumables and introduced a set of working practices at the SEM laboratory. I greatly appreciated this first laboratory management experience. I was in charge of texture measurements plus data interpretation in a large variety of materials and developed large-scale imaging plus EDS and EBSD mapping techniques.

Willing to keep some continuity in my publication record, I participated to an experimental mineralogy study dealing with experimental irradiation damage of silicon crystalline wafers implanted with Si⁺ ions at temperatures between 23°C and 225°C (Nasdala et al., 2007). I performed EBSD measurements on the different samples and could show that the initial crystalline order is progressively lost up to complete amorphization at temperatures below 130°C. Interestingly, the Back Scattered Electron signal is brighter in irradiated areas while the atomic number of the sample remains constant. Care must therefore be taken when assigning density variations to minerals using SEM imaging as the degree of crystallographic order influences signal strength.

During my stay at the University of Mainz, I obtained the “maître de conférences” accreditation in CNU sections number 35 and 36.

Willing to share experience in terms of SEM imaging and analytics with students, I proposed a set of lectures including SEM imaging and analytics to Bachelor and Master level.

LETTER

Effects of irradiation damage on the back-scattering of electrons: Silicon-implanted silicon

LUTZ NASDALA,^{1,*} ANDREAS KRONZ,² DIETER GRAMBOLE,³ AND GHISLAIN TRULLENQUE⁴

¹Institut für Mineralogie und Kristallographie, Universität Wien, A-1090 Wien, Austria

²Geowissenschaftliches Zentrum der Georg-August-Universität Göttingen, D-37077 Göttingen, Germany

³Forschungszentrum Dresden-Rossendorf, Institut für Ionenstrahlphysik und Materialforschung, D-01328 Dresden, Germany

⁴Institut für Geowissenschaften, Johannes Gutenberg-Universität, D-55099 Mainz, Germany

ABSTRACT

Radiation damage in a (initially crystalline) silicon wafer was generated by microbeam ion implantation with 600 keV Si⁺ ions (fluence 5×10^{14} ions/cm²). To produce micro-areas with different degrees of damage, 14 implantations at different temperatures (between 23 and 225 °C) were done. The structural state of irradiated areas was characterized using Raman spectroscopy and electron back-scatter diffraction. All irradiated areas showed strong structural damage in surficial regions (estimated depth <1 μm), and at implant substrate temperatures of below 130 °C, the treatment caused complete amorphization. Back-scattered electron (BSE) image intensities correlate with the degree of irradiation damage; all irradiated areas were higher in BSE than the surrounding host. Because there were no variations in the chemical composition and, with that, no Z contrast in our sample, this observation again supports the hypothesis that structural radiation damage may strongly affect BSE images of solids.

Keywords: Back-scattered electron images, Raman spectroscopy, electron back-scatter diffraction, radiation damage, silicon

INTRODUCTION

In a recent study, Nasdala et al. (2006) described that structural radiation damage may notably increase the back-scattering of electrons and, thus, affect the grayscale patterns observed in back-scattered electron (BSE) images of single crystals. In that study, the BSE intensity of zircon (ZrSiO₄) single crystals correlated with the degree of accumulated self-irradiation damage, with the average atomic number (i.e., Z contrast) being less significant for the BSE. Their assertion was supported by the demonstration of how dry thermal annealing of the radiation damage, which was claimed to have only minor effects on the chemical composition, leads to a clear decrease of the mean back-scatter coefficient (η). The authors attempted to explain their observation with decreased penetration depths of incident beam electrons in disordered structures, and assigned their observation as special case of electron channeling contrast.

In the meantime, not the interpretation but the observation has been questioned by several colleagues suspecting that the BSE intensity loss upon annealing might be due to changes in concentrations of elements that are not analyzed in the electron microprobe, such as loss of water. This aspect has already been discussed by Nasdala et al. (2006) who stated that if there was unrecognized loss of water, Z, and, with that, the BSE intensity should increase, whereas the opposite was observed. On the

other hand, it is clear that chemical changes of elements that are below the detection limit of the electron microprobe, or are not detectable, cannot be excluded from the outset.

In this paper, we present an unambiguous example for increased electron back-scattering caused by radiation damage. Structural damage has been produced by the local irradiation of a silicon wafer with silicon ions. This has produced a crystalline sample with several heavily damaged micro-areas, which uniformly consist of pure Si. Any Z contrast (Hall and Lloyd 1981; Lloyd 1987) can therefore be excluded in this case.

SAMPLES AND EXPERIMENTAL DETAILS

A synthetic silicon sample, polished parallel to the crystallographic (100) plane, was implanted with 600 keV Si⁺ ions. Irradiation experiments were done using the nuclear microprobe at the 3 MV tandem accelerator of the Forschungszentrum Dresden-Rossendorf (Herman and Grambole 1995). The sample chamber was evacuated to $\sim 10^{-8}$ mbar. To avoid notable ion channeling effects (e.g., Raineri et al. 1991; Dos Santos et al. 1995), the beam was irradiated with an angle of 7° to the surface normal. The beam was focused to a nearly square area 150 μm in size. The current density was 80 μA/cm², and the implantation fluence was 5×10^{14} ions/cm². To produce areas with different degrees of damage, 14 irradiation experiments under identical conditions but at different temperatures were done. In doing this, we used the well-known fact that the amorphization rate of ion-beam irradiated solids depends strongly on temperature (e.g., Wang et al. 1998a, 1998b). To avoid any damage annealing upon re-heating, experiments were done beginning with the highest temperature (225; 200, between 180 and 100 °C at 10° steps; 80; 34; 23 °C). Implanted areas were placed in a row with separations of 0.3 mm. Considering the high thermal conductivity of silicon and the small size of the focal-spot area, local heating of the sample as a result of the implantation is negligible (compare Melngailis 1987).

Micro-Raman measurements were done with a Renishaw RM1000 spectrom-

* E-mail: lutz.nasdala@univie.ac.at

eter equipped with Leica DMLM optical microscope, edge filter, a grating with 1200 grooves/mm, and Peltier-cooled CCD detector. Spectra were excited with the 632.8 nm emission (8 mW) of a He-Ne laser. Wavelength calibration was done using Ne lamp emissions. The wavenumber accuracy was better than 0.5 cm^{-1} and the spectral resolution was determined at 2.2 cm^{-1} .

Electron back-scatter diffraction (EBSD) Kikuchi patterns (Baba-Kishi 1990) were obtained on a Zeiss DSM 962 scanning electron microscope (SEM) with W filament. The accelerating voltage was 20 kV. The sample stage was tilted $\sim 70^\circ$ relative to the surface normal and the free working distance was set to 19 mm. Patterns of manually selected micro-areas were obtained using a Nordlys detector coupled with the Channel5 computer package (HKL Technology ApS). Accumulation times were 15 s per point.

Back-scattered electron (BSE) imaging, as well as cathodoluminescence (CL) and secondary electron (SE) imaging, was done using a JEOL 8900 RL electron microprobe. To obtain BSE images, a paired semiconductor-type detector was operated in additive mode, then displaying "compositional atomic number contrast" with a sensitivity of better than $0.1 \Delta Z$. The accelerating voltage was set to 25 kV and the beam current was chosen between 7 and 15 nA, measured on Faraday cup. Electron channeling patterns (ECP; Brooker et al. 1967; Wilkinson and Hirsch 1997) were obtained using the so-called pseudo-Kikuchi technique. Here, the electron beam rocks across a comparably large sample area while scanning under a low magnification (40 \times). This results in numerous angles (up to 4.29°) of the electron irradiation directions with respect to the surface normal, leading to variations of the total intensity of back-scattered electrons. For details see Brooker et al. (1967) and Baba-Kishi (2002). Prior to SEM-EBSD analysis and electron microprobe imaging, the sample was coated with a 150 Å thick carbon layer to avoid potential charging effects. Ultrapure carbon (less than 2 ppm impurities) was used for this, and the coating thickness was controlled with a Cressington MTM 10 oscillating quartz crystal detector.

CHARACTERIZATION OF THE IRRADIATION DAMAGE

We used Raman spectroscopy (Fig. 1A) to study the degree of damage produced in the sample by irradiation with 600 keV Si^+ ions. Structural damage was already studied in a nuclear microprobe using the micro Rutherford back-scatter (RBS)/Channeling technique, which uses changes in the stopping and back-scattering behavior of incoming ions to probe structural changes in the target; procedure and results have been described elsewhere (Grambole et al. 2007). Raman and RBS/Channeling spectra obtained in micro-areas that were implanted at temperatures below 140 °C (Raman) and 130 °C (RBS/Channeling), respectively, indicate complete amorphization. This is also seen from EBSD patterns (Fig. 2D); the absence of Kikuchi lines and bands indicates the complete loss of crystal order. Micro-areas implanted at temperatures of 130/140 °C and higher show gradually lower degrees of damage, however, significant irradiation damage (i.e., partial amorphization) is observed in all implantation areas up to 225 °C.

Monte Carlo simulations using the SRIM-2006 code (see Ziegler et al. 1985) predicted that irradiation with 600 keV Si^+ ions has damaged the Si target in a surficial layer of only $\sim 1 \mu\text{m}$ thickness, with the maximum density of vacancies generated through atomic displacements in the depth range 550–800 nm. We have observed that bands of crystalline Si are fully absent in Raman spectra of micro-areas that were implanted at temperatures of 130 °C and below (i.e., the underlying host wafer does not contribute to the Raman scattered light). This is explained by the low penetration depth of visible light in amorphous silicon. In fact, for amorphous Si the depth probed by Raman spectroscopy with 6328 Å excitation is close to 140 nm (De Wolf et al. 1998). In contrast, with the RBS/Channeling technique the entire damaged layer is probed.

Raman spectra indicate that probed surficial layers of micro-

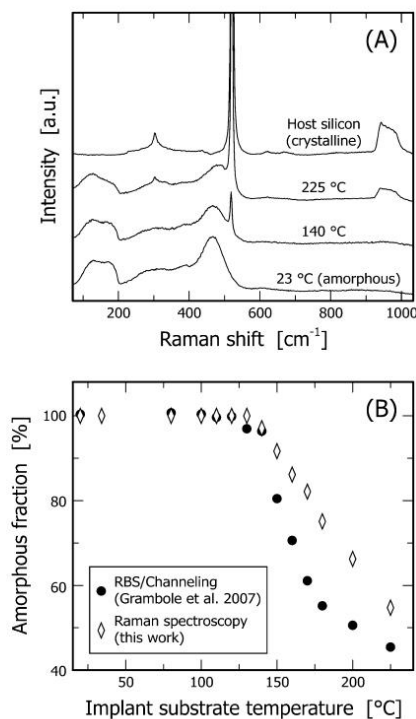


FIGURE 1. Analytical characterization of structural damage in Si^+ -implanted silicon. (A) Raman spectra (stacked) of the same four areas as above. (B) Plot of the amorphous fraction calculated from RBS/Channeling and Raman spectra vs. the implantation temperature.

areas irradiated at elevated temperatures in the range 140–225 °C consist of remnants of crystalline Si in a (dominating) volume fraction of amorphous Si. Amorphous fractions f_a were determined from Raman spectra to quantify the structural damage. Two estimates based on the area integral of the LO=TO band (at $\sim 521 \text{ cm}^{-1}$) of remnant crystalline Si, and the ratio of integrated Raman intensities in the wavenumber ranges 100–190 cm^{-1} (amorphous dominant) and 920–1000 cm^{-1} (crystalline dominant; see Fig. 1A), gave the same crystalline-to-amorphous ratios within an error of $\pm 1.5\%$. However, amorphous fractions calculated from RBS/Channeling (Grambole et al. 2007) and Raman spectra show notable differences for most partially amorphized micro-areas (Fig. 1B). We explain this by the consideration that the two micro-techniques probe different sample depths.

BACK-SCATTERED ELECTRON IMAGING

A BSE image of the Si-implanted silicon wafer is presented in Figure 2A. The host wafer itself did not yield uniform BSE brightness, as it would correspond to its uniform chemical composition and structural state; rather it shows a blurred but

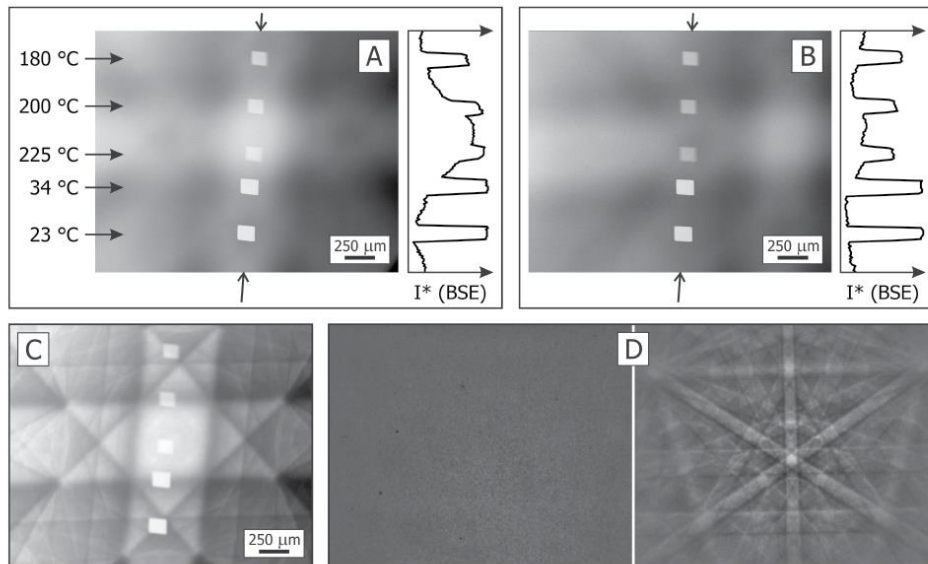


FIGURE 2. Electron microprobe and SEM images. (A) Back-scattered electron image of the silicon wafer. Five of the Si^+ -implanted areas are seen as slightly distorted, bright rectangles. Implantation temperatures are quoted at the left side. I^* = arbitrary grayscale values along the line marked with arrows. (B) Back-scattered image and grayscale plot of the same area after sample tilt. (C) Electron channeling (or pseudo-Kikuchi) pattern of the same area. The sample position (tilt) corresponds to A, i.e., view roughly along [100]. (D) An EBSD pattern obtained in the micro-area implanted at 80 °C (left) does not show any indication of diffraction (Kikuchi bands and lines are not seen) and, thus, it indicates amorphization. The corresponding EBSD pattern of the neighboring host (same experimental conditions; view roughly along [111]) is shown right.

somehow regular pattern of slightly brighter and darker patches. The phenomenon is related to the diffraction of back-scattered electrons. To verify this, an ECP (in early papers described as pseudo-Kikuchi or Kikuchi-like pattern) of the same area as shown in Figure 2A was obtained (Fig. 2C). This image suggests that the patchy appearance of the host silicon in Figure 2A can be described as an overlay of the “regular” BSE with a fuzzy Kikuchi pattern. The latter exhibits fourfold symmetry, which corresponds to the irradiation direction of the electron beam close to the [100] axis. The ECP (Fig. 2C) is not equivalent to the EBSD Kikuchi pattern (right part of Fig. 2D), even though both have been obtained from the same wafer. The EBSD pattern exhibits threefold symmetry because tilting the sample prior to SEM analysis has brought the [111] zone axis close to the center of the observation direction. Back-scattered electron images of geological samples are normally not affected by pseudo-Kikuchi patterns, because regular mechanical polishing does not produce surfaces whose quality is sufficient to observe these diffraction features.

The BSE image (Fig. 2A) shows five (out of a total of 14) irradiated micro-areas, which are easily recognized as bright, slightly distorted rectangular spots. This observation indicates that irradiation damage causes a significant increase of the back-scatter coefficient. The BSE intensity of partially amorphized areas (i.e., those that have been implanted at elevated tempera-

tures) correlates inversely with the implantation temperature and, thus, it correlates with the degree of damage. The area irradiated at 225 °C (which represents the lowest degree of damage; Fig. 1B) shows the lowest BSE intensity among all implantation areas seen in Figure 2A, however, even this spot appears significantly brighter than the neighboring, undamaged host wafer. Areas implanted at low temperatures (i.e., those that have experienced complete surficial amorphization) are exceptionally high in BSE (see two spots closest to the bottom of Fig. 2A).

Monte Carlo simulations using the electron trajectory simulation program CASINO v. 2.42 (for the theoretical background see Newbury and Myklebust 1995) were done to estimate sampling depths of BSE images. For an accelerating voltage of 25 kV, results predicted that only ~44.2% of detected electrons are back-scattered from a depth shallower than 1 μm whereas more than 50% of detected electrons are back-scattered from the depth range between 1 and 2 μm . We may therefore speculate that observed BSE differences between irradiated areas and host wafer would have been even more pronounced if damaged layers had thicknesses $>1 \mu\text{m}$.

Neither SE nor CL images of the same areas showed notable differences in signal intensity among implantation spots and host wafer. This excludes the possibility that high BSE intensities of implantation areas are due to enhanced quantities of secondary electrons and/or luminescence emission that, as analytical arti-

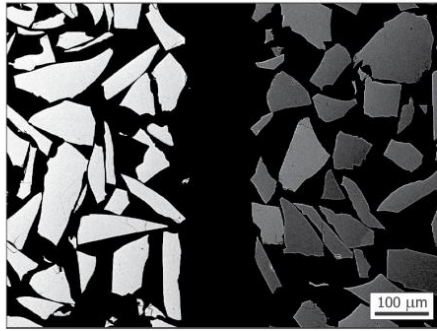


FIGURE 3. Back-scattered electron image of SiO_2 . The sample consists of randomly oriented chips of SiO_2 glass (left) and α -quartz (right) embedded in epoxy. The BSE intensity of the glass is generally higher than that of quartz.

fact, have been registered by the BSE detector.

It might be speculated that the enhanced electron back-scattering of radiation-damaged phases is related to their lower density. However, CASINO simulations predicted that a target's density has insignificant effects on η . Furthermore, it needs to be discussed critically whether the observed lower BSE intensity of the host crystal, when compared to the partially or fully amorphized implantation areas, might be simply due to crystal orientation contrast (Lloyd 1987), i.e., caused by enhanced channeling of incident beam electrons into the sample along [100]. If this was the case, the BSE intensity of the wafer should dramatically increase, and BSE differences between implanted areas on the one hand and host wafer on the other hand should decrease, after tilting the wafer. However, tilting the wafer a few degrees (Fig. 2B) caused insignificant changes in observed BSE intensities. This observation implies that different crystal orientations are less significant for the BSE than structural differences between a crystal and its amorphous analog. A similar observation is made when comparing the BSE intensities of SiO_2 glass and α -quartz (Fig. 3). The latter always yields lower BSE, with comparably minor BSE differences among α -quartz crystals with different orientations (i.e., the BSE phase contrast between crystalline and amorphous clearly exceeds the extent of the BSE crystal orientation contrast within the crystalline phase).

These observations imply that in the case of a randomly oriented crystalline target, compared to its amorphous analog, fewer electrons are back-scattered and/or back-scattered electrons have lower energies (recall that integral electron energies, not numbers of electrons, are registered by the BSE detector). This might be explained by the consideration that in crystalline materials, electrons penetrate on average deeper into the sample (for instance, along lattice planes after low-angle deflection). A sound interpretation, however, cannot be given at the present stage.

Our study reconfirms the observations of Nasdala et al. (2006); radiation-damaged solids do show higher BSE than their

crystalline analogs. This structural effect, however, is probably only of importance in BSE imaging if single crystals show only minor internal Z contrast. To sort out the causes of the decreased penetration and absorption and the increased back-scattering of electrons of radiation-damaged and other amorphous/disordered phases, more systematic studies are needed.

ACKNOWLEDGMENTS

We are indebted to T. Váci for experimental assistance and to B. Griffin for stimulating discussions. Constructive reviews of F. Corfu and an anonymous expert are gratefully acknowledged. Partial funding of this research was provided by the European Commission through contract no. MEXC-CT-2005-024878 and Research Infrastructures Transnational Access (RITA) contract no. 025646.

REFERENCES CITED

- Baba-Kishi, K.-Z. (1990) A study of directly recorded RHEED and BKD patterns in the SEM. *Ultramicroscopy*, 34, 205–218.
- (2002) Electron backscatter Kikuchi diffraction in the scanning electron microscope for crystallographic analysis. *Journal of Materials Science*, 37, 1715–1746.
- Brooker, G.R., Shaw, A.M.B., Whelan, M.J., and Hirsch, P.B. (1967) Some comments on the interpretation of the "Kikuchi-like reflection patterns" observed by scanning electron microscopy. *Philosophical Magazine*, 16, 1185–1191.
- De Wolf, I., Jiménez, J., Landesmann, J.-P., Frigeri, C., Braun, P., Da Silva, E., and Calvet, E. (1998) Raman and luminescence spectroscopy for microelectronics. Catalogue of optical and physical parameters. "Nostradamus" project SMT4-CT-95-2024. Office for Official Publications of the European Communities, Luxembourg.
- Dos Santos, J.H.R., Grande, P.L., Boudinov, H., Behar, M., Stoll, R., Klatt, C., and Kalbitzer, S. (1995) Electronic stopping power of (100) axial-channelled He ions in Si crystals. *Nuclear Instruments and Methods in Physics Research B*, 106, 51–54.
- Grambole, D., Herrmann, F., Heera, V., and Meijer, J. (2007) Study of crystal damage by ion implantation using micro RBS/Channeling. *Nuclear Instruments and Methods in Physics Research B*, 260, 276–280.
- Hall, M.G. and Lloyd, G.E. (1981) The SEM examination of geological samples with a semiconductor back-scattered electron detector. *American Mineralogist*, 66, 362–368.
- Herrmann, F. and Grambole, D. (1995) The new Rosendorf nuclear microprobe. *Nuclear Instruments and Methods in Physics Research Section B: Beam Interactions with Materials and Atoms*, 104, 26–30.
- Lloyd, G.E. (1987) Atomic number and crystallographic contrast images with the SEM: a review of backscattered electron techniques. *Mineralogical Magazine*, 51, 3–19.
- Melngailis, J. (1987) Focused ion beam technology and applications. *Journal of Vacuum Science and Technology B: Microelectronics and Nanometer Structures*, 5, 469–495.
- Nasdala, L., Kronz, A., Hanchar, J.M., Tichomirowa, M., Davis, D.D., and Hofmeister, W. (2006) Effects of natural radiation damage on back-scattered electron images of single-crystals of minerals. *American Mineralogist*, 91, 1738–1746.
- Newbury, D.E. and Myklebust, R.L. (1995) NIST Micro MC: A user's guide to the NIST microanalysis Monte Carlo electron trajectory simulation program. *Microbeam Analysis*, 4, 165–175.
- Raineri, V., Galvagno, G., Rimini, E., Biersack, J.P., Nakagawa, S.T., La Ferla, A., and Carnera, A. (1991) Channeling implants of B ions into (100) silicon surfaces. *Radiation Effects and Defects in Solids*, 116, 211–217.
- Wang, L.M., Wang, S.X., Gong, W.L., and Ewing, R.C. (1998a) Temperature dependence of Kr ion-induced amorphization of mica minerals. *Nuclear Instruments and Methods in Physics Research B*, 141, 501–508.
- Wang, L.M., Wang, S.X., Gong, W.L., Ewing, R.C., and Weber, W.J. (1998b) Amorphization of ceramic materials by ion beam irradiation. *Materials Science and Engineering*, A253, 106–113.
- Wilkinson, A.J. and Hirsch, P.B. (1997) Electron diffraction based techniques in scanning electron microscopy of bulk materials. *Micron*, 28, 279–308.
- Ziegler, J.F., Biersack, J.P., and Littmark, U. (1985) *The Stopping and Range of Ions in Solids*. Pergamon Press, New York.

MANUSCRIPT RECEIVED MARCH 22, 2007

MANUSCRIPT ACCEPTED MAY 29, 2007

MANUSCRIPT HANDLED BY BRYAN CHAKOUMAKOS

4.3 Application specialist at Oxford Instruments Nanoanalysis GmbH

In the framework of my position at the University of Mainz, I was often in contact with the Oxford Instruments company manufacturing EBSD, EDS and Wavelength Dispersive Spectrometry (WDS) detectors. My skills in terms of laboratory management, SEM analytical practice and teaching triggered some interest by the director of the company branch office situated in Wiesbaden (Germany). I was offered an EDS-WDS-EBSD application specialist position on an open-ended contract basis.

My activities within the company have been extremely diverse. Product demonstration gave me the opportunity to study a wide range of materials used by automotive industry, aerospace sector, nanocomposites developers or nuclear security agencies to cite just a few. I was in charge of installing and calibrating new systems while ensuring customer training and service. I was also representing the company in many exhibitions. I had a close and privileged link to SEM manufacturers and could train on a wide range of equipment.

Despite many difficulties related to confidentiality agreements in the industrial sector, and willing to continue research activities, I participated in some publishing of customers' results in international scientific journals (Kempe et al., 2018; van de Moortèle et al., 2010).

The contribution by van de Moortèle et al. (2010) was dedicated to the study of antigorite lattice preferred orientation measurements in a naturally deformed high pressure serpentinite. Antigorite is extremely challenging in terms of EBSD measurements due to the complexity of its crystallographic cell. Antigorite structure is a 1:1 laminar structure in which each layer is formed by tetrahedral and octahedral units in a laminar and wavy stack (Dódoný and Buseck, 2004; Evans et al., 2013; Liang et al., 2022). Fine tuning in terms of sample preparation, acquisition parameters and Kikuchi patterns analysis allowed to reach an indexing rate above 90%. Antigorite is considered as the main water source within subduction zones and its dehydration may in turn trigger melting of the mantle, induce seismicity and influence migration and distribution of chemical elements. Our results highlighted the presence of a strong crystallographic preferred orientation in the form of a *c* axis perpendicular to foliation and clustering of *a* axis. We interpreted this texture as a result of intra-crystalline deformation consistent with glide along the basal plane. Texture measurements by means of EBSD was proven feasible and potential applications were suggested in terms of antigorite bearing rocks petrophysical properties determination.

The contribution by Kempe et al. (2018) deals with a multidisciplinary approach of natural zircon crystals with a high degree of internal disorder according to Raman spectroscopy but a high degree of ordering according to optical birefringence. This apparent discrepancy could be explained by 1) the high content of yttrium, thorium and rare earth elements and 2) a re-interpretation of the physical meaning in band position and width in the Raman spectra. It was proposed that the zircon lattice is strained as a result of charge unbalance caused by substitution of trivalent elements being not fully compensated by coupled phosphorous, niobium or uranium substitutions. In our study, the high degree of disorder was not interpreted in terms of amorphization but in terms of high misorientation angles within the zircon crystal and observed by means of EBSD mapping.

Electron back-scattering diffraction (EBSD) measurements of antigorite lattice-preferred orientations (LPO)

B. VAN DE MOORTÈLE*, L. BEZACIER*, G. TRULLENQUE†
& B. REYNARD*

*Laboratoire de Sciences de la Terre, Université de Lyon, Ecole Normale Supérieure de Lyon, CNRS,
Lyon Cedex, France

†Oxford Instruments GmbH, Otto-von-Guericke-Ring 10, D-65205 Wiesbaden, Germany

Key words. Antigorite, anisotropy, deformation, EBSD, lattice preferred orientation, serpentine

Summary

Lattice preferred orientations of serpentines induce a strong anisotropy of various properties in serpentine bearing-rocks. Lattice preferred orientations had so far been obtained only by X-ray diffraction techniques. We have applied electron back-scattering diffraction to the measurement of the lattice preferred orientations of antigorite in a naturally deformed high-pressure serpentine. This technique is very sensitive to sample preparation that can lead to surface amorphization in the case of serpentine. A polishing procedure is described that avoids amorphization and allows accurate electron back-scattering diffraction measurements with optimized experimental conditions in a variable pressure scanning electron microscope. Results indicate that deformation leads to lattice preferred orientations characterized by extremely strong *c*-axis clustering perpendicular to the foliation, as expected for a layered silicate. In the foliation plane, a significant clustering of the *a*-axis is observed and tentatively attributed to intracrystalline deformation mechanisms. These data suggest that antigorite deforms mostly by gliding along the basal plane of the layered phyllosilicate structure, but that gliding may occur along directions favouring *a*-axis alignment. Electron back-scattering diffraction appears to be a reliable method for determining phyllosilicate lattice preferred orientations in deformed rocks, with potential applications for determining anisotropy of properties like seismic velocities or thermal and electrical conductivities.

Introduction

Antigorite-serpentinites are formed in subduction zones at the top of the subducting plate interface where fluids liberated

by dehydration interact with the mantle wedge (Schmidt & Poli, 1998). It has been proposed that they control the plate interface coupling because of their supposed low viscosity (Seno, 2005; Uchida *et al.*, 2009). Deformation experiments at high pressure have confirmed that they can deform plastically at subduction zone conditions (Hilairet *et al.*, 2007). Deformation of serpentinites induces lattice preferred orientations (LPO) that will be determined by the active deformation mechanisms. LPO will affect properties such as sound velocities (Kern *et al.*, 1997) or transport properties (heat and electrical conductivities, effective porosity, ...) by inducing potentially strong anisotropy. Determining LPO in naturally and experimentally deformed samples will help comparing the active deformation mechanisms, testing the validity of experimentally determined flow laws in natural contexts, and resolving anisotropy of serpentinites. Determinations of bulk LPO in serpentinites have so far been limited to the use of X-ray diffraction (Kern *et al.*, 1997). This technique has the disadvantage that measured preferred orientations cannot be linked to individual grain properties like size and shape. Electron back-scattering diffraction (EBSD) in scanning electron microscopy allows mapping of local LPO on rocks polished sections, linking the texture directly with the grain scale. It is thus desirable to apply such a technique to serpentinites, but its development may be impeded by preparation and observation problems inherent to the studied sample. We describe here a procedure that allows efficient EBSD mapping on antigorite-bearing natural serpentine from Cuba (Auzende *et al.*, 2002).

Sample and methods

We used antigorite from serpentine sample Cu12 from the high-pressure Escambray massif (Central Cuba). Antigorite has a structural formula $(Mg_{2.62}Fe_{0.16}Al_{0.15})(Si_{1.96}Al_{0.04})O_5(OH)_{3.57}$ (Auzende *et al.*, 2002, 2004). The lattice parameters at ambient conditions were refined from

Correspondence to: Bertrand Van de Moortèle, Laboratoire de Sciences de la Terre, Université de Lyon, Ecole Normale Supérieure de Lyon, CNRS, 46 Allée d'Italie, F-69364 Lyon Cedex 07, France. Tel: +33 (0)4 72 72 84 05; fax: +33 (0)4 72 72 86 77; e-mail: Bertrand.van.de.moortele@ens-lyon.fr

X-ray diffraction data as $a = 4.35852$ (0.00763) nm, $b = 0.92624$ (0.0017) nm, $c = 0.7246$ (0.0135) nm and $\beta = 91.160$ (0.024)°. Antigorite LPO were determined by the EBSD technique (Lloyd *et al.*, 1990). This technique is based on an indexation of diffraction patterns (Kikuchi bands) generated by the interaction between the electron beam and a crystal lattice.

The quality of the sample surface is critical for obtaining good indexation efficiency because only the first 10 to 50 nm below the sample surface contributes to the signal (depending essentially from material density and acceleration voltage). Artefacts at the grain surface can be generated during sample polishing (i.e. production of dislocation or amorphization) that alter the crystallinity of the sample surface and decrease the quality of the EBSD pattern (EBSP). In extreme cases, this leads to a decrease of the indexation efficiency and prevents a statistically reliable determination of LPO. Here the sample was first cut with a low-speed precision diamond saw, embedded in a graphite conductive resin (warm impregnation at $T = 150^\circ\text{C}$ and $P = 20$ MPa for 1 min) and then mechanically grinded using a semi-automatic metallographic machine (Ecomet Automet apparatus from the Buehler Company; Buehler GmbH, Düsseldorf, Germany) with SiC papers (grades P 400; 600 and 1200), Ecomet Automet apparatus with following conditions: basal plate rotation speed 300 r min^{-1} , individual pressure of 20 N, head rotation speed = 60 r min^{-1} , time = 1 min for each SiC paper grade. The mechanical polishing stage was achieved using a series of colloidal alumina suspensions with following grades: 5, 2, 0.3 and $0.05 \mu\text{m}$) for 2–3 min with a lower basal plate speed (150 r min^{-1}) and same force. The surface quality was then improved by vibration polishing on a colloidal silica suspension (particle size $0.05 \mu\text{m}$) using a Vibromet 2 apparatus (Buehler Company) for 12 h. At this step, we were able to obtain good enough EBSP (about 80% indexing after offline analysis) for LPO determination. However, we increased the rate of indexing with additional Ar^+ ion polishing (10 min at 3 kV, 30° incidence angle and a sample revolution of 30 rounds per minute) using a Precision Etching apparatus 680 PECS (Gatan Company; Gatan, Inc., Pleasanton, CA, U.S.A.). This increase of indexing rate was observed for the different accelerating voltages used and leads to about 90% of indexation at 30 kV.

As the sample itself is non-conductive electrically, classical scanning electron microscopy operation would require coating of the sample surface with a thin amorphous layer of either carbon or gold. A very accurate control of the coating thickness is required because a gold layer only 6 nm thick deposited on strong scatterers (like annealed nickel foil or a silicon single crystal) can prevent the formation of any EBSP. The use of a variable pressure scanning electron microscope could be a good alternative to the sample coating presented here. Scanning electron microscopy and EBSD observations were carried out using

an Ultra 55 VP Scanning Electron Microscope (Zeiss; Carl Zeiss SMT AG, Baden-Württemberg, Germany) coupled with a NordlysS camera (Oxford Instruments Company) with a maximal resolution of 1344×1024 pixels. The variable pressure mode allows working with no coating and the very low amount of nitrogen injected in the scanning electron microscope chamber (maximal chamber pressure 17 Pa) did not significantly deteriorate the EBSP quality. No charging or drifting of the measurement area has been observed even after several hours of uninterrupted measurement.

Another variable is the acceleration voltage that should be as low as possible to avoid charge effects, and high enough to maintain a small enough electron wavelength to avoid deterioration of the EBSP quality. In the case of antigorite an acceleration voltage below 20 kV leads to a drastic reduction of the EBSD indexing rate because the Kikuchi bands appear broader on the EBSD detector screen, decreasing the number of visible crystal zone axes. The best EBSPs were obtained using 30 kV accelerating voltage, a maximum of 3 nA probe current, 17 Pa pressure and 9 mm working distance (the desired minimum working distance value was limited by the size of the sample 30 mm diameter and 8 mm thickness).

We used the full camera resolution at the cost of longer measurement time because, even if the EBSP seem of excellent quality at 2×2 pixel binning the indexing process then results in systematic misorientation of 180° around the b -axis. EBSP at each analysed point were recorded on a PC, it takes about 6 h for a map of 37 083 points. We used the Channel 5 software (or-HKL) to post-process each EBSP offline (during 5 to 10 h, depending on the set of parameters and of the computer used). This method allows fine-tuning of the indexing parameters and increases the indexation efficiency. We used two polysomes of antigorite $m = 16$ or $m = 17$ described by Capitani & Mellini (2004, 2006) to index the EBSP. The best results were obtained with the polysome $m = 17$ and the following software-specific parameters: 5 to 7 band centre detected, Hough space resolution between 105 and 125, number of reflectors between 39 and 46, 0-lock mode level 2 and 10 to 15 frames per point. Noise reduction option was used at the end of the offline analysis and concerns only 3% of the data. The final indexation rate of above 90% is particularly good for such complex structure. Most of the non-indexed points are found along the grain boundaries and holes where some crystals were ripped off during polishing. The relative precision of crystal orientations measured from electron backscattering patterns is in average less than 1° (Krieger & Lassen, 1996) but in the present case we estimate the accuracy as $2\text{--}3^\circ$ due to the complex EBSP.

Results and discussion

The sample section was cut perpendicular to the foliation (Fig. 1). No lineation could be observed on the hand specimen.

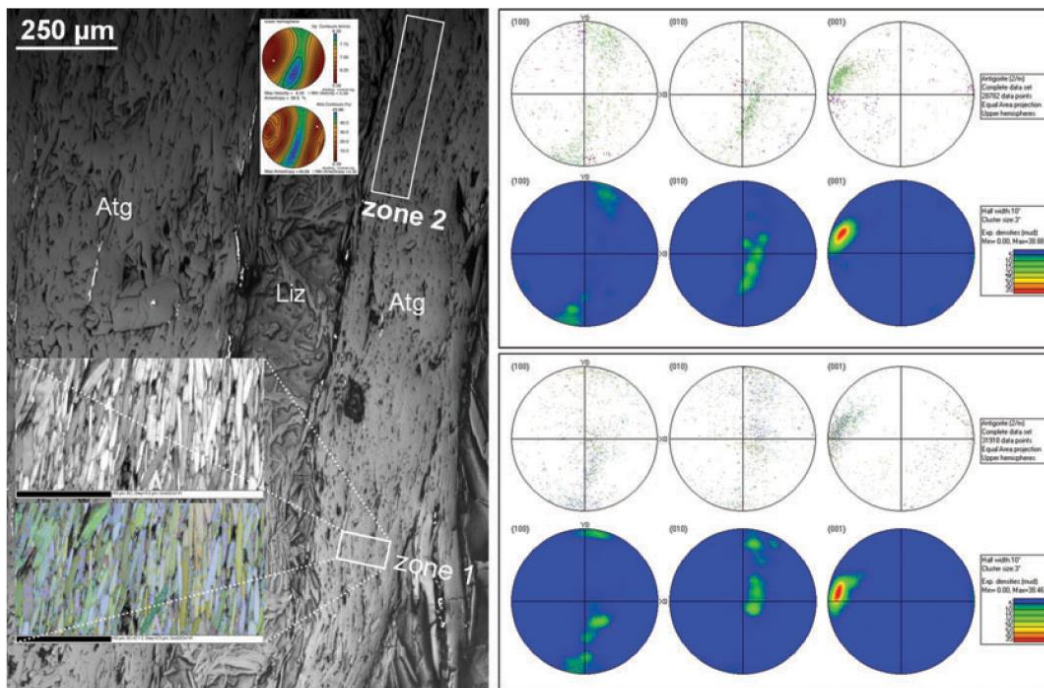


Fig. 1. Reflected light image (left) of the sample section perpendicular to the macroscopic foliation. Two textures are visible: (1) small antigorite grain (Atg) regions with antigorite platelets parallel to the foliation and (2) large lizardite areas (Liz) with randomly oriented antigorite platelets crosscutting it. LPO were measured by EBSD in two zones of the foliated areas defined by the rectangles. For zone 1, enlarged pictures show the band contrast image (black and white image where white areas correspond to the best quality of the indexing solution) and the orientation cartography (red blue green colour channels being linked to the three Euler angles of orientation). Note that dark areas correspond to holes or defects of the sample that appeared during polishing. Pole figures are shown for individual measurements as points and as density maps for zones 1 and 2. c -axes cluster perpendicular to the foliation, as expected for a layered structure, a - and b -axes tend to cluster around particular maxima in the foliation whose orientation varies from place to place. Two observations attest the quality of the EBSD maps: (1) they superimpose on the optical image notably along grain boundaries (no drifting or distortion of the measurement area) and (2) almost every grain observed lacks isolated wild spikes which is in favour of a correct indexing routine. In insert (top left), pole figure of V_p and ΔV_S (on the left side of zone 2) calculated from single-crystal elastic constants and LPO obtained by EBSD measurements using the CareWare software developed by D. Mainprice (Mainprice, 1990).

Two different types of texture could be observed firstly as zones with a well-defined alignment of the elongated antigorite grains along the macroscopic foliation, and secondly as large lizardite grains crosscut by randomly orientated antigorite platelets. Lizardite is interpreted as relict grains from early, possibly oceanic, serpentinization that persisted in weakly deformed areas and antigorite crystallization is coeval of eclogite facies deformation in the foliated parts of the sample (Auzende *et al.*, 2002). The foliated zones composed of small grains (about 10–100 μm in length and 1–20 μm in width) and were analysed by EBSD.

In both analysed zones, c -axes are clustered within 10° around the pole to the foliation. This corresponds to the expected orientation of the layered antigorite structure in

the maximum flattening plane that can be interpreted either as passive reorientation of platelets or as efficient dislocation glide along the weakest interlayer bonds. This is the dominant characteristic of the rock fabric. The a - and b -axes are thus mostly within the foliation where they are not randomly oriented. They cluster along broad maxima in both zones. These maxima have varied orientation between zones 1 and 2 in the rock, and they cannot be identified with any macroscopic feature such as lineation. Such maxima are difficult to attribute to morphological effect such as passive grain reorientation because there are little dimensional differences in antigorite platelets in the plane of the layers. They may thus well indicate that intracrystalline deformation mechanisms operated during LPO development, where dislocation glide in

the *ab*-plane are favoured along specific directions. Therefore we suggest that the stacking disorder be observed along [100] and not along [010] in these antigorite (Auzende *et al.*, 2002) may be related to deformation mechanisms that lead to the observed significant orientation of *a*-axes in the foliation.

The *c*-axis density observed here perpendicular to the foliation is larger than that observed in serpentinized peridotites used for ultrasonic measurements (Kern *et al.*, 1997), yet the measured sound velocity anisotropy in their sample was particularly high (about 30% and 40% for V_P and V_S , respectively). Stronger seismic velocity anisotropy is thus expected for the present Cuban sample in foliated areas. It was estimated using single-crystal elastic data measured on an antigorite picked up from the same rock (Bezacier *et al.*, submitted to EPSL) as an example of application of EBSD measurement. The resulting V_P and V_S anisotropy is 38% and 48%, respectively, as presented in Fig. 1 (on the left side of zone 2).

Acknowledgments

This study was supported by ANR project SUBDEF grant no. ANR-08-BLAN-0192 to B. Reynard, and INSU program SEDIT. We thank Damien Crozet (Buehler Company) and Andreas Höpner (Gatan Company) for assistance with the sample preparation. Electron microscopy in Lyon is supported by CLYM.

References

- Auzende, A.L., Devouard, B., Guillot, S., Daniel, I., Baronnet, A. & Lardeaux, J.M. (2002) Serpentinites from Central Cuba: petrology and HRTEM study. *Eur. J. Mineral.* **14**, 905–914.
- Auzende, A.L., Daniel, I., Reynard, B., Lemaire, C. & Guyot, F. (2004) High-pressure behaviour of serpentine minerals: a Raman spectroscopic study. *Phys. Chem. Miner.* **31**, 269–277.
- Capitani, G. & Mellini, M. (2004) The modulated crystal structure of antigorite: the $m = 17$ polysome. *Am. Miner.* **89**, 147–158.
- Capitani, G.C. & Mellini, M. (2006) The crystal structure of a second antigorite polysome ($m = 16$), by single-crystal synchrotron diffraction. *Am. Miner.* **91**, 394–399.
- Hilaret, N., Reynard, B., Wang, Y.B., Daniel, I., Merkel, S., Nishiyama, N. & Petitgirard, S. (2007) High-pressure creep of serpentine, interseismic deformation, and initiation of subduction. *Science* **318**, 1910–1913.
- Kern, H., Liu, B. & Popp, T. (1997) Relationship between anisotropy of P and S wave velocities and anisotropy of attenuation in serpentinite and amphibolite. *J. Geophys. Res.-Solid Earth* **102**, 3051–3065.
- Krieger Lassen, N.C. (1996) The relative precision of crystal orientations measured from electron backscattering patterns. *J. Microsc.-Oxf.* **181**, 72–81.
- Lloyd, G.E., Schmidt, N.H., Mainprice, D. & Prior, D.J. (1990) Crystallographic textures. *Meeting on Mineral Textures*. Mineralogical Society, Manchester, England.
- Mainprice, D. (1990) A FORTRAN program to calculate seismic anisotropy from the lattice preferred orientation of minerals *Comp. Geosci.* **16**.
- Schmidt, M.W. & Poli, S. (1998) Experimentally based water budgets for dehydrating slabs and consequences for arc magma generation. *Earth Planet. Sci. Lett.* **163**, 361–379.
- Seno, T. (2005) Variation of downdip limit of the seismogenic zone near the Japanese islands: Implications for the serpentinization mechanism of the forearc mantle wedge. *Earth Planet. Sci. Lett.* **231**, 249–262.
- Uchida, N., Nakajima, J., Hasegawa, A. & Matsuzawa, T. (2009) What controls interplate coupling? Evidence for abrupt change in coupling across a border between two overlying plates in the NE Japan subduction zone. *Earth Planet. Sci. Lett.* **283**, 111–121.

Substitution-induced internal strain and high disorder in weakly radiation damaged hydrothermal zircon from Mt. Malosa, Malawi

ULF KEMPE^{1,*}, GHISLAIN TRULLENQUE², RAINER THOMAS³, SERGEY SERGEEV^{4,6}, SERGEJ PRESNYAKOV⁴, NIKOLAI RODIONOV⁴ and CAMELIU HINCINSCHI⁵

¹ Institut für Mineralogie, TU Bergakademie Freiberg, Brennhausgasse 14, 09596 Freiberg, Germany

*Corresponding author, e-mail: kempe@mineral.tu-freiberg.de

² Oxford Instruments GmbH, Otto-von-Guericke-Ring10, 65205 Wiesbaden, Germany

³ Deutsches GeoForschung Zentrum GFZ Potsdam, Telegrafenberg, 14473 Potsdam, Germany

⁴ Centre of Isotopic Research, Karpinsky Russian Geological Research Institute (VSEGEI), Srednyi prospect 74, 199106 St. Petersburg, Russia

⁵ TU Bergakademie Freiberg, Institut für Theoretische Physik, Leipziger Straße 23, 09596 Freiberg, Germany

⁶ Institute of Earth Sciences, St. Petersburg State University, Universitetskaya nab. 7/9, 199034 St. Petersburg, Russia

Abstract: Characteristics of two types of zircon from a single rock sample from the Mt. Malosa Massif, Malawi, are presented. According to Raman spectroscopy, the structure of a yellow hydrothermal zircon grown within a miarolitic cavity seems to be highly disordered. However, the extent of radiation damage calculated from the Raman data exceeds the degree of disorder that can be ascribed to the maximum possible internal radiation dose received by the crystals since their formation. Optical birefringence suggests an ordering degree close to that of well-ordered zircon for most areas in the crystals as may be also concluded from the always sharp electron backscattered diffraction (EBSD) patterns. Brownish zircon crystals from the wall-rock of the cavity of the same sample are most probably magmatic in origin. These crystals display a high degree of order and common low contents of radioactive and other substituting elements (<0.5 wt% in total). The absolute ages and U and Th contents of both zircon types were verified by U–Pb sensitive high-resolution ion microprobe (SHRIMP) analysis and the magmatic zircon is found to be significantly older (292 ± 10 Ma) than the hydrothermal one (121 ± 9 Ma). The apparent discrepancies between the data obtained by various methods for the hydrothermal zircon may be explained taking into account the unusual chemical composition and structural particularities established as well as (re-)interpreting the physical meaning of the variations in band positions and band widths in the Raman spectra. Electron probe microanalysis (EPMA) shows relatively high contents of yttrium (up to 4.8 wt% Y_2O_3) and the rare earth elements (REE, up to 1.5 wt% oxides in total), occasionally also of thorium (up to 0.8 wt% ThO_2). The charge unbalance caused by the substitution of trivalent elements is not compensated by coupled substitution involving other elements like phosphorus, niobium or uranium. The unusual composition and substitution is reflected by the related cathodoluminescence (CL) spectra consisting of sharp and intense line emissions from Dy^{3+} , Sm^{3+} , Nd^{3+} and Tb^{3+} centers in zircon. The broad band emissions normally observed in well-ordered zircon are quenched. Orientation contrast imaging (OCI) and EBSD reveal textures consisting of relatively large strained orientation domains showing a distinct distribution pattern. We suggest that internal tensional strain induced by substitution, vacancy formation and related domain formation may explain the data. Possible consequences of these findings for the understanding of the formation of metamict zircon should be considered in future research.

Key-words: zircon; strain; EBSD; Raman; disorder; metamict; substitution.

1. Introduction

Due to the exceptional behavior and widespread occurrence of zircon, its U–Pb geochronology is of great importance for absolute age determination in geosciences (e.g., Davis *et al.*, 2003; Harley & Kelly, 2007). Another topic of long-lasting scientific interest is the use of zircon ceramics in the storage of radioactive waste (e.g., Gentry *et al.*, 1982; Ewing *et al.*, 1995; Ewing, 2001). Under both aspects, an understanding of the phenomenon of zircon

metamictization (occurrence of an isotropic state of secondary origin; Syme *et al.*, 1977) is crucial because metamict zircon may not retain the required original age information (e.g., Davis *et al.*, 2003; Kempe *et al.*, 2015) and is not always resistant to secondary alteration under hydrothermal conditions (e.g., Geisler *et al.*, 2003; Anderson *et al.*, 2008; Soman *et al.*, 2010; Wang *et al.*, 2014). It is now generally accepted that metamictization of natural zircon results from the accumulated α -recoil damage occurring during radioactive decay of U and Th

incorporated in the zircon structure (e.g., Ewing *et al.*, 2003).

Beginning from the pioneering work by Nasdala *et al.* (1995), a growing number of authors have made use of the Raman microprobe technique to evaluate the degree of metamictization of natural zircon on a local scale (see, e.g., Nasdala *et al.*, 2003). Advantages of this method are the high spatial resolution down to micrometer-scale and the virtual absence of any sample damage at low laser powers. Additionally, there is no need in sophisticated sample preparation.

According to the modern concepts of zircon metamictization, the loss of long-range order (periodicity of the structure according to the lattice model) on nano- to micro-scale accompanied by a loss of short-range order (fixed arrangement of the nearest neighbors around single atoms/ions) results from the growth of structural domains strongly affected by α -recoil damage and their transformation to a metamict (fully disordered) state (Murakami *et al.*, 1991; Ewing *et al.*, 2003). This concept implies that systematic changes in density (Holland & Gottfried, 1955; Özkan, 1976; Murakami *et al.*, 1991), hardness (Özkan, 1976; Chakoumakos *et al.*, 1991; Oliver *et al.*, 1994), birefringence (Holland & Gottfried, 1955; Sahama, 1981; Palenik *et al.*, 2003), and diffraction properties (Holland & Gottfried, 1955; Murakami *et al.*, 1991; Rios *et al.*, 2000b; Nasdala *et al.*, 2002b) as well as in infrared (IR; Akhmatova & Leonova, 1961; Wasilewski *et al.*, 1973; Delines *et al.*, 1977; Woodhead *et al.*, 1991; Zhang & Salje, 2001), Raman (Nasdala *et al.*, 1995; Zhang *et al.*, 2000; Nasdala *et al.*, 2001; Nasdala *et al.*, 2002b, 2003; Marsellos & Garvers, 2010), electron paramagnetic resonance (EPR; Nasdala *et al.*, 2003; Kempe *et al.*, 2010) and luminescence characteristics (Lenz & Nasdala, 2015) are correlated with each other and with the dose accumulated.

A zircon sample from Mt. Malosa, Malawi, investigated here in more detail, demonstrates that this is not always the case. Some natural zircon may display a high degree of disorder by one method but does not show it at the same extent when investigated by other techniques. As will be discussed in more detail below, such findings may indicate that other processes leading to high disorder in natural zircon besides irradiation damage should be considered.

Earlier, this Malawi sample was included into a sample set investigated by several spectroscopic techniques including optical absorption (OA), electron paramagnetic resonance (EPR), Raman, and time-resolved photoluminescence (TRL) spectroscopy (Kempe *et al.*, 2010; Kempe *et al.*, 2016). According to the Raman data and using the classification proposed by Nasdala *et al.* (1995, 1998), the disorder in the Mt. Malosa zircon should be estimated as “intermediate to metamict” (Kempe *et al.*, 2010). However, subsequent evaluation of thin sections of this material in transmitted light suggests that the order in these crystals is rather well preserved with the possible exception of some high-Th growth zones. This finding prompted additional studies.

Several facts reported in recent publications or found during our own research question the assumption that the

theory of zircon metamictization has already reached maturity. In particular, it was mentioned that the formation of disordered areas in zircon is sometimes related to hydrothermal alteration rather than to radioactive decay (Zhirov, 1952; Rudenko, 1968; Kempe *et al.*, 2004). Anderson *et al.* (2008) reported trace element-poor, nearly U- and Th-free zircon material in late cracks within altered, trace element-rich metamict zircon from Nova Scotia. The former areas were nearly amorphous according to the absence of TEM electron diffraction patterns while the latter showed a somewhat higher ordering degree.

Kempe *et al.* (2010) found a green natural zircon where the significant shift in the position of the Raman bands was not accompanied by related band broadening. Furthermore, an extremely U-rich, green zircon from Sri Lanka was found to be rather well-ordered (Kempe *et al.*, 2016). We also reported an apparently well-ordered, extremely U-rich zircon from Muruntau (Kempe *et al.*, 2015).

In the following text, we will restrict our self to the case of the Malawi zircon under consideration here. Additional work is needed to clarify the situation in all cases mentioned and to understand their relations to the general phenomenon of zircon metamictization.

2. Materials and methods

2.1. Geological background

The sample studied comes from a miarolitic cavity as typically observed in the roof zone of the alkaline granite massif at the Mt. Malosa, Zomba plateau, Chilwa alkaline province, southern Malawi (e.g., Eby *et al.*, 1995; Högdahl & Jonsson, 1999; Soman *et al.*, 2010). The Chilwa alkaline province is located at the southern extension of the East African rift system (Woolley & Platt, 1986; Woolley & Jones, 1987; Eby *et al.*, 1995). The intrusive rocks vary in composition from nepheline syenite and quartz syenite to granite and include also carbonatites (Platt & Woolley, 1986; Woolley & Platt, 1986; Woolley & Jones, 1987; Eby *et al.*, 1995). Obviously, the formation of the complex is related to rifting in this part of the continent (Woolley, 1987). At surface, the Zomba-Malosa complex forms a pear-shaped body in the northern part of the province. The central part is formed by syenite surrounded by rings of quartz-syenite and granite (Woolley & Jones, 1987; Eby *et al.*, 1995). The area around Mt. Malosa exhibits many pegmatite cavities carrying exotic Th-rich Zr-Nb-REE-Be mineralization (Högdahl & Jonsson, 1999; Guastoni & Pezzotta, 2007; Guastoni *et al.*, 2009). Several stages of hydrothermal activity close to each other in formation time were observed according to replacement relations within the pegmatites (Guastoni *et al.*, 2009; Soman *et al.*, 2010). Similar mineralization is also present elsewhere in the area (Platt *et al.*, 1987).

Three types of zircon may be distinguished in the pegmatites according to Högdahl & Jonsson (1999): (1) translucent reddish-brownish crystals with a complex of simple forms, (2) opaque short prismatic brownish zircon and (3) translucent prismatic yellow crystals. The zircon

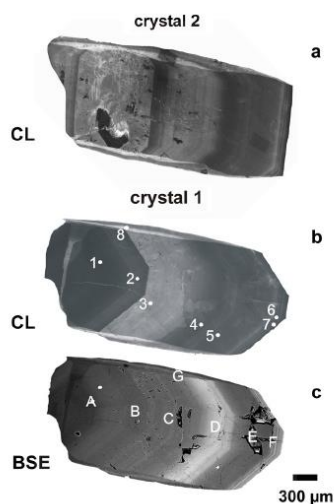


Fig. 1. Cathodoluminescence (CL) and BSE images of the two Type 1 yellowish crystals used for EMPA, CL spectroscopy, SHRIMP and Raman spectroscopy (crystal 1) and oriented-contrast (OC) imaging, EBSD and Raman spectroscopy (crystal 2), respectively. The numbers and locations of the spots in Fig. 1b correspond to the numbers of analyses obtained by EMPA, CL spectroscopy, SHRIMP and Raman spectroscopy in other figures, tables and in the text. SHRIMP spots are visible in the BSE image taken after SHRIMP analysis.

investigated in this work belongs to the first and third types. Earlier, Soman *et al.* (2010) have investigated a brownish, opaque zircon crystal of the second type displaying significant secondary alteration features.

2.2. Sample and sample preparation

The crystals of yellowish translucent hydrothermal zircon used in the present study were prepared from a single rock sample from the wall of a miarolitic cavity in the alkaline granite. Crystals formed in free space together with some quartz and riebeckite. The growth proceeded from the wall to the center of the cavity. All crystals exhibit simple combinations of the $\{100\}$ prism and the $\{101\}$ dipyrmaid and do not show any signs of deformation. We conclude that the zircon crystals experienced only fluid pressure and that only fluid-induced brittle but no plastic deformation could have occurred. As mentioned above, the degree of disorder in a yellow transparent crystal termination used in our previous work is intermediate to metamict according to Raman spectroscopy (*cf.* classification by Nasdala *et al.*, 1995, 1998) with an average full-width at half maximum (FWHM) of $18.3 \pm 1.0 \text{ cm}^{-1}$ for the ν_3 (B_{1g}) mode of the $[\text{SiO}_4]$ tetrahedral groups (Kempe *et al.*, 2010). Subsequent measurements on several other crystals yielded very similar results.

Examination of several dozens of grains under a binocular microscope showed that there is a common growth zoning which can be paralleled to the internal texture revealed in five crystals investigated in polished sections by scanning electron microscopy with back-scattered electron (BSE) and cathodoluminescence (CL) imaging irrespective of the variable crystal sizes (Fig. 1): (1) A core of yellow to greenish coloration with variable internal textures including sector zoning (zone A in Fig. 1c) is surrounded by an outer zone not clearly distinguishable under the optical microscope but clearly visible in CL and BSE images (zone B in Fig. 1c). (2) The next zone C is cloudy with many cracks and voids and displays yellowish-brownish coloration and normal growth zoning under BSE and CL. (3) The transparent yellow upper crystal termination consists of zone D exceptionally bright in the backscattered electron (BSE) contrast with normal growth zoning followed by the nearly homogeneous zone E darker in BSE and, finally, the thin zone F with distinct oscillatory growth zoning at the rim. Sector zoning is well expressed by thin sector G at the $\{100\}$ prism faces in BSE and CL images (Fig. 1c). In few crystals grown sub-parallel to the wall of the cavity, the same zoning may be also followed in the opposite direction from the crystal core.

One crystal of this hydrothermal zircon was oriented parallel to the c axis using a spindle stage and mounted into a polished thin section for optical microscopy. Two other crystals from the same sample were selected for detailed local analysis. One of these crystals was mounted together with other zircon in a polished section and gold coated for BSE and CL imaging and subsequent SHRIMP analysis. Following this procedure, the gold was removed and the section investigated by Raman spectroscopy. Prior to the following electron probe microanalysis and CL spectroscopy, the sample was carbon coated to prevent build-up of electrical charge.

The second crystal was polished with silica gel for orientation contrast (OC) and CL imaging, electron-backscattered diffraction (EBSD), and Raman spectroscopy. The sample was coated with a 2 nm thick platinum film. This film was later removed to allow subsequent Raman measurements.

The coarse-grained host rock of the sample around the cavity contained the second zircon type – brownish crystals of short-prismatic habit with a combination of a dominant $\{110\}$ prism (occasionally also with a weakly developed $\{100\}$ prism) and a $\{101\}$ dipyrmaid. These crystals display normal growth zoning, sector zoning and some recrystallisation features visible under the microscope and in BSE and CL images (Fig. 2). The mode of occurrence of this zircon type forming intergrowth with rock-forming minerals suggests a magmatic origin. To verify the genetic relationships between the two zircon types, two crystals of the brownish zircon were also analyzed. One was mounted together with one yellowish crystal of hydrothermal zircon in a polished section for the investigation procedure including BSE and CL imaging, U-Pb SHRIMP analysis, Raman spectroscopy, EMPA and

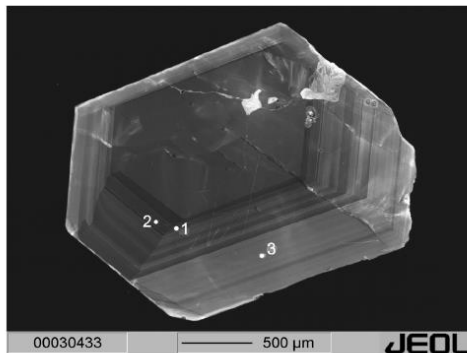


Fig. 2. CL image of the brownish Type 2 crystal of magmatic zircon from the host rock used for EMPA, CL spectroscopy, SHRIMP and Raman spectroscopy. The location numbers of the spots in the figure correspond to numbers of EMPA, CL, SHRIMP and Raman analyses in the figures, tables and in the text.

CL spectroscopy. The other brownish crystal was used for a thin section for optical microscopy with orientation of the *c* axis parallel to the sample surface.

2.3. Methods

Optical properties in transmitted light were investigated using a Carl Zeiss Axioskop 40. The birefringence was calculated from the interference colors as described by Palenik *et al.* (2003) except that the thickness of crystal section in the point of measurement of the thin section was determined using the micrometer drive of the microscope calibrated to a set of polished diamond slabs with known thicknesses determined by a micrometer. The estimated error in birefringence is about ± 0.002 , somewhat higher than in the work by Palenik *et al.* (2003).

For electron microscopy, a Jeol JSM 6400 equipped with a Tracor/Noran Series II energy dispersive X-ray detection system, an Oxford Mini-CL detector for CL imaging and a Mono-CL 1 mirror system combined with a transportable spectrograph for CL spectroscopy (Götte & Kempe, 2008) was used. For CL and BSE imaging, the SEM was operated at 20 kV and 0.6 nA; CL spectra were taken subsequent to SHRIMP measurements with a defocused electron beam (diameter about 20 μm adjusted to the diameter of adjacent spots from SHRIMP measurements) at 20 kV and 3.56 nA. Calibration was done using mercury and argon emission lines for the blue and red part of the spectrum, respectively. The acquisition time for the spectra was 100 s. Due to the low signal intensities, no CL spectra could be obtained with a focused beam from a particular Th-rich growth zone appearing bright in the BSE images of the crystal where no larger areas without cracks or voids could be found (cf. below). To display orientation contrast (OC), BSE imaging was performed at 3 kV and 3.4 nA with a working distance of 8 mm. Additional OC images were obtained using a cold field

emission JSM 7500F at the Jeol Demonstration Center in Garching near Munich (Germany). A large-angle BSE (LAGE) detector operated at 1 kV and 50 pA at a working distance of 4 mm yielded an increased stereographic contrast.

Four EBSD maps were acquired using a Nordlys S camera mounted on a ZEISS SUPRA 55VP operated in the high vacuum mode at 20 kV, 1.5 nA probe current and 13 mm WD with step sizes of 200 nm in variable grids. The sample tilt was 70°. The Channel 5 (Oxford Instruments) software was used for data acquisition and evaluation.

For SHRIMP measurements, the two chosen crystals – one yellow of the first type from the cavity and one brownish of the second type from the wall rock – were mounted in epoxy resin together with reference zircon TEMORA 1 (Middledale Gabbroic Diorite, New South Wales, Australia; Black *et al.*, 2003) and reference zircon 91500 (Wiedenbeck *et al.*, 1995), polished and gold coated. Before SHRIMP analysis, the grains were documented by reflected and transmitted light photographs as well as CL and BSE imaging. SHRIMP measurements were carried out at the Centre of Isotopic Research of the Karpinsky All-Russian Geological Research Institute (VSEGEI), St. Petersburg, Russia using SHRIMP II. The spot size was set at 20 μm and the beam current at 4 nA. Five mass scans were collected for each analysis. Mass resolution at the mass 254UO was 5200 at 1% peak height. Data reduction was performed using the procedure proposed by Williams (1998) applying the SQUID Excel Macro by Ludwig (2000). The Pb/U ratios were normalized relative to a $^{206}\text{Pb}/^{238}\text{U}$ value of 0.0668 for the TEMORA 1 reference equivalent to an age of 416.75 Ma (Black *et al.*, 2003). Reference zircon 91500 was used as concentration reference material (81.2 ppm U). Measured against the TEMORA 1 reference during the same session, it showed some enhanced isotope data scatter with a calculated Concordia age of 1062 ± 27 Ma ($n=5$; accepted value 1065.4 ± 0.4 Ma).

Subsequent Raman, EMPA and CL measurements were made as close as possible adjacent to the SHRIMP spots with locations carefully chosen within the same growth zones defined by optical, BSE and CL imaging. Additional locations were also checked, especially when fine zoning or voids and cracks in the crystal avoided SHRIMP measurements at a 20 μm scale (as in the Th-rich growth zone mentioned above and at the crystal rim). Some Raman measurements were also made within the SHRIMP spots but yielded essentially identical results as in the adjacent areas (cf. Nasdala *et al.*, 1998).

Microprobe analysis was performed with an SX-100 microprobe (CAMECA) applying the standard method used at the GeoForschungsZentrum, Potsdam (e.g., Anderson *et al.*, 2008). The acceleration voltage was 20 kV and the beam current 40 nA. Natural and synthetic zircon (Zr, Si), HfO₂ (Hf), Y and rare earth element (REE) phosphates (REE, Y, Sc, and P), pure metals (Ti, Nb, U, Th), hematite (Fe), corundum (Al), wollastonite (Ca), and vanadinite (Pb) were used as references. Counting times were 20 s for Si K α , Zr L α , Ca K α , and Al K α ; 30 s for Fe

$K\alpha$, $Y L\alpha$, $Sc K\alpha$, and $P K\alpha$ and 50 s for the other elements ($Hf L\beta$, $Ce L\alpha$, $Nd L\beta$, $Sm L\beta$, $Gd L\beta$, $Dy L\beta$, $Yb L\alpha$, $Ti K\alpha$, $Nb L\alpha$, $Th M\alpha$, $U M\beta$, and $Pb M\beta$) both on the peak and on the carefully chosen background positions on both sides of the peaks. Iron, Hf, Ce, Nd, Sm, Gd, Dy and Yb were measured on a LiF crystal while P, Ca, Sc, Ti, Th, U, and Pb were measured on PET and Si, Zr, Nb, Al and Y on a TAP crystal. The limits of detection were: Hf – 1900 ppm, Fe – 400 ppm, Al – 130 ppm, Ca – 180 ppm, Sc – 160 ppm, Nb – 200 ppm, Th – 640 ppm, U – 840 ppm, Pb – 1100 ppm, Y – 440 ppm, Ce – 630 ppm, Nd – 710 ppm, Sm – 720 ppm, Gd – 590 ppm, Dy – 600 ppm and Yb – 600 ppm. Phosphorus was not found in any analysis; the somewhat overestimated theoretical detection limit for this element was at about 340 ppm. A search for F was also not successful. Because of the rather high EMPA detection limits for Th, U and Pb, mainly results from SHRIMP measurements for these elements will be used in the following discussion.

Raman measurements were done with a Jobin Yvon LABRAM HR800 operated in the confocal mode (pinhole 100 μm) at room temperature using the 488 nm line of an Innova 70C Coherent Ar^+ laser (laser power 14 mW on the sample). The laser was focused on the sample surface using an Olympus microscope with a 100 \times objective. The spectral resolution of the system was 0.6 cm^{-1} .

2.4. Comparison of spatial resolution of Raman spectroscopy and EBSD

Because we will compare long-range order probed by EBSD with the short-range order checked by Raman spectroscopy, it is useful to recall and discuss here to some extent the spatial resolution of the two methods.

Raman spectroscopy probes a significantly larger volume compared to EBSD. In modern Raman microprobes, the focused beam may approach about 1 μm as a minimum diameter constraining the lateral resolution of the method (Bruneel *et al.*, 2002; Nasdala *et al.*, 2005). A cone of the laser light is penetrating further into the sample without sharp depth restrictions for samples transparent in the region of the laser wavelength used as in the present case for zircon. Depth resolution may be increased applying confocal optics (Puppels *et al.*, 1991; Nasdala *et al.*, 1998; Bruneel *et al.*, 2002; Nasdala *et al.*, 2003). It is sometimes believed that depth resolution may even reach 2 μm for crystalline materials (Nasdala *et al.*, 2003, 2005). However, closer evaluation shows that this is by far a too optimistic value. Normally, about 7 μm or more may be expected for transparent crystalline materials (Bruneel *et al.*, 2002; Kranert *et al.*, 2016). As outlined by Everall (2000), this is mainly due to the refraction at the air – sample interface when dry objectives are used. Clearly, this effect is pronounced for zircon with its high refraction indices (1.92–2.02 for crystalline and 1.75 for metamict material). We have further verified the sampling depth for our instrumental setup by a simple experiment using one and the same crystal of fluorite and zircon, respectively, to prepare a thin section (30 μm thickness)

from one half of the sample and a thick section (about 1 mm thickness for zircon and about 3 mm for fluorite limited by the sample sizes) from the other. The sample pairs were measured in the confocal mode (pinhole 100 μm) on a T64000 (fluorite) and a Jobin Yvon LABRAM HR800 (zircon) in one session under the same conditions with the beam focused on the polished surface. In both cases, the Raman signal of the fluorite and zircon modes increased by about 50% in intensity when going from the thin to the thick section indicating detection of some additional Raman scattering from sample areas even below 30 μm . Recently, Presser & Glotzbach (2009) reached very similar conclusions on local resolution and sampling depth for zircon and other transparent materials.

Compared to Raman spectroscopy, spatial resolution of EBSD mapping is exceptionally high. The EBSD signal derives entirely from a near-surface zone only some nm thick. Therefore, spatial resolution depends mostly on the electron probe diameter, acceleration voltage, and the average atomic number of the sample and is clearly below 40 nm in the given case, considering the relatively high average atomic number of zircon with $Z > 14$ (*cf.* Humphreys, 2001; Dingley, 2004).

3. Results

3.1. Polarized-light microscopy, optical absorption and cathodoluminescence spectra

The birefringence in yellowish Type 1 zircon is nearly constant over the whole grain (red, sometimes yellowish of second order for sample thicknesses of about 20 μm), mostly approaching 0.050 (0.048–0.050) indicative of well-ordered zircon. At the yellow transparent crystal termination, there is a zone with a distinct decrease in birefringence down to 0.031 (0.044–0.031). This zone coincides with the mentioned Th-rich zone D appearing bright in BSE images (Fig. 1). Palenik *et al.* (2003) found a linear correlation between birefringence and radiation dose for Sri Lanka zircons. This, in principle, opens the opportunity to estimate received radiation doses from birefringence measurements for samples from this location. It is, of course, dangerous to apply this relationship to other zircons with a different thermal history. Provided that our crystals and Sri Lanka zircons have not experienced significant re-heating after formation and that the indicated disorder is related to radiation damage only, an estimate of the received radiation dose may be attempted basing on the measured birefringence. For the zone under discussion, birefringence would correspond to a received radiation dose of 3.7×10^{18} α -events/g. Note, however, that at least Sri Lanka zircon experienced some kind of secondary annealing (Palenik *et al.*, 2003; Nasdala *et al.*, 2004). Therefore, such an estimate is certainly in error and can only be seen as a very rough approximation. At the crystal rim F, birefringence decreases down to 0.038 (0.046–0.038) in some of the fine, Th-rich oscillatory growth zones which would correspond to an estimated dose of 2.2×10^{18} α -events/g, respectively.

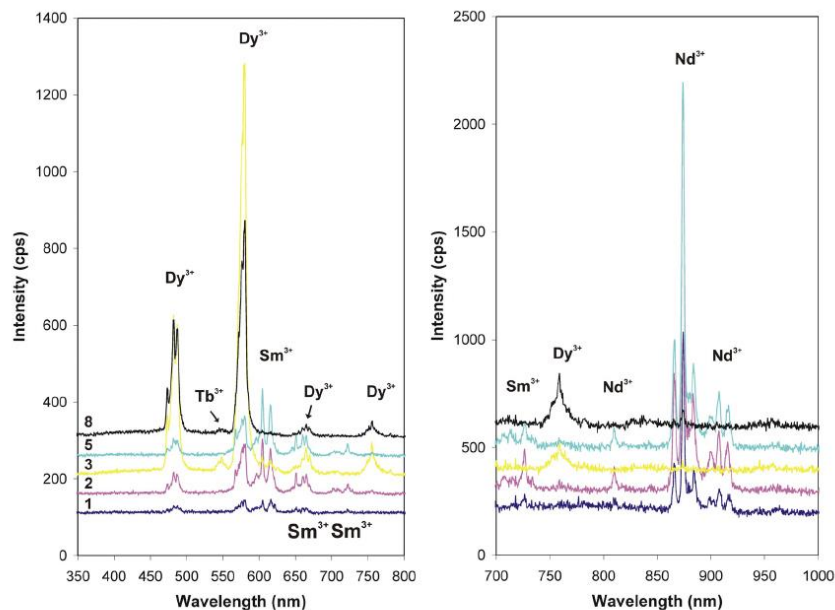


Fig. 3. CL spectra of Type 1 REE-rich yellowish hydrothermal zircon (crystal 1) from the cavity. Spot numbers correspond to those in Fig. 1b.

In the brownish Type 2 zircon from the wall rock, the birefringence is nearly constant around 0.054 indicating well-ordered zircon (Holland & Gottfried, 1955; Sahama, 1981). Note that the maximum birefringence suggested by the model proposed by Palenik *et al.* (2003) is 0.0486 at zero dose, somewhat below the expected value of 0.055.

According to optical absorption spectroscopy (Kempe *et al.*, 2010, 2016), the yellow color of the zircon crystals from the cavity is caused by an edge-like absorption appearing at about 450 nm. Probably, this absorption is related to charge transfer transitions involving REE that may have variable valance states in zircon as Ce, Pr, Eu and/or Tb. Another possible explanation is a “shift” of the absorption edge into the visible range due to lattice defects accumulated from radioactive irradiation (Kempe *et al.*, 2016). The sharp absorption lines appearing in the red part of the spectra are related to Nd^{3+} and Er^{3+} , but they have only negligible influence on the visible color. Remarkably, absorption lines from U^{4+} were not observed in the spectra (Kempe *et al.*, 2016).

Cathodoluminescence spectroscopy revealed that the light emitted from yellowish Type 1 zircon is, if detectable, exclusively related to sharp line emissions from REE^{3+} centers (Fig. 3). Identification of the emission lines was achieved using published luminescence spectra of synthetic zircon intentionally doped with single rare earth elements and considering the observed intensity relations and fine structures in these spectra besides line positions. Except general intensity variations, two principal types of

spectra can be distinguished in the yellow zircon: (1) CL spectra of the yellowish-green core region (central part and rim; zones A and B) and of the yellow crystal area E between the zone D with quenched luminescence on one side and the oscillatory growth zoning at the upper crystal rim F on the other are of the first type (spectra 1, 2 and 5 in Fig. 3). (2) The yellowish-brown intermediate region C between the core (A+B) and the zone D with quenched CL as well as the growth sectors G of the $\{100\}$ prism exhibit the second type (spectra 3 and 8 in Fig. 3).

For the second-type spectra, CL emission is dominated by four transitions occurring in Dy^{3+} , namely ${}^4\text{F}_{9/2} \rightarrow {}^6\text{H}_{15/2}$ centered at about 480 nm, ${}^4\text{F}_{9/2} \rightarrow {}^6\text{H}_{13/2}$ (575 nm), ${}^4\text{F}_{9/2} \rightarrow {}^6\text{H}_{11/2}$ (665 nm) and ${}^4\text{F}_{9/2} \rightarrow {}^6\text{H}_{9/2}$ (755 nm). Similar spectra for Dy^{3+} were reported by Votyakov & Samojlov (1981), Cesbron *et al.* (1995), Karali *et al.* (2000), Friis *et al.* (2010) and – for a part of the related spectral range – by Trofimov (1962), Gaft *et al.* (2000), Finch *et al.* (2004), Nasdala *et al.* (2003) and Lenz & Nasdala (2015). Our spectra are most similar to the spectrum published by Friis *et al.* (2010) obtained by photoluminescence spectroscopy, especially considering intensity relations and the resolved fine structure of the lines. Besides the intense emissions from Dy^{3+} , there are only weak lines from Sm^{3+} in these spectra at 610 nm (*cf.* below) and an additional line at 545 nm (Fig. 3). The latter signal may be interpreted to arise from Tb^{3+} or Er^{3+} . Spectra of Er^{3+} were published by Votyakov *et al.* (1985, X-ray luminescence), Cesbron *et al.* (1995, CL),

Karali *et al.* (2000, radio- and thermoluminescence), Gaft *et al.* (2000, time-resolved photoluminescence) and partly by Nasdala *et al.* (2003, photoluminescence), spectra for Tb^{3+} in Iacconi & Caruba (1980, thermoluminescence), Votyakov & Samojlov (1981, thermoluminescence), Votyakov *et al.* (1985), Iacconi (1995), Cesbron *et al.* (1995), Gaft *et al.* (2000) and, for a part of the relevant spectral range, in Trofimov (1962, photoluminescence). Considering published data, we assign the emission under question to the $^5D_3 \rightarrow ^7F_5$ transition in Tb^{3+} because: (1) the emission in Er^{3+} in this range is centered at somewhat higher wavelengths (about 550–555 nm); (2) the related emission in Tb^{3+} is by far the most intense in X-ray luminescence and thermoluminescence (normally exhibiting similar intensity relations and fine structures as in CL) while this is not the case for Er^{3+} .

The CL spectra of the first type differ significantly from the second type described above. In the first type of spectra, there is a strong decrease in the relative emission intensities of the Dy^{3+} lines and an increase in the intensity of the emission lines from Sm^{3+} . The latter show the typical intensity relations and fine structure transitions of the type $^4G_{5/2} \rightarrow ^6H_{7/2}$ centered at 605 nm, $^4G_{5/2} \rightarrow ^6H_{9/2}$ (660 nm), and $^4G_{5/2} \rightarrow ^6H_{11/2}$ (703–728 nm). Fine structure lines from the $^4G_{5/2} \rightarrow ^6H_{5/2}$ transition also occur but overlap with the Dy emission at 580 nm. Similar spectra were reported by Cesbron *et al.* (1995), Gaft *et al.* (2000), Karali *et al.* (2000), Nasdala *et al.* (2003), Friis *et al.* (2010) and Lenz & Nasdala (2015) and – for a part of the range – by Trofimov (1962). Our spectra of Sm^{3+} show a close similarity to the spectra reported by Nasdala *et al.* (2003), Friis *et al.* (2010) and Lenz & Nasdala (2015).

Dramatic changes occur in the red part of the first-type CL spectra where strong lines appear at 810.0, 865.9, 873.7 (strongest), 879.0 (weak), 883.4, 889.4, 907.2 and 915.6 nm. We assign these emissions to the $^4F_{5/2} \rightarrow ^4I_{9/2}$ (810 nm) and $^4F_{3/2} \rightarrow ^4I_{9/2}$ (865–916 nm) transitions in Nd^{3+} . Luminescence spectra of Nd^{3+} in natural zircon are rarely reported in the literature because the Nd content in the mineral is normally low to very low. The photoluminescence spectra published by Nasdala *et al.* (2003) and Lenz *et al.* (2013) are similar in the fine structure and line positions but the one by the first authors differs strongly in intensity relations from the spectrum published by Lenz *et al.* (2013) and the spectra obtained in the present work.

The CL signal obtained for the brownish Type 2 zircon from the wall rock differs from that of the yellow zircon (Fig. 4). It is dominated by broad bands with only weak signals from REE $^{3+}$ centers, in particular from Dy^{3+} and Er^{3+} . Remarkably, only the $^4F_{3/2} \rightarrow ^4I_{9/2}$ (404 nm) and $^4F_{5/2} \rightarrow ^4I_{9/2}$ (471 nm) transitions in Er^{3+} are of notable intensity, while the transitions from lower lying levels, especially at 530 and 558 nm, are very weak. The most intense broad band luminescence appears in the yellow spectral range (centered at 580 nm) while the short-living “blue” band at about 420 nm is suppressed in intensity. Such a CL behavior is typical of well-ordered zircon with low REE contents (Kempe *et al.*, 2000).

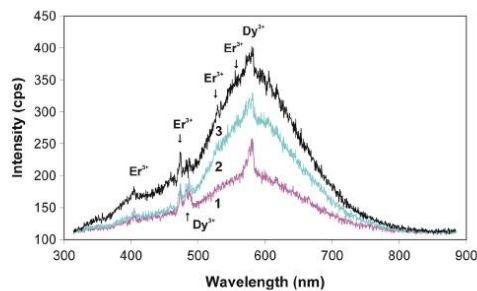


Fig. 4. CL spectra of Type 2 brownish magmatic zircon from the host rock. Spot numbers correspond to those in Fig. 2.

3.2. Chemical composition

The EMPA, EDX analysis in the SEM and the SHRIMP study revealed an unusual chemical composition for the yellow zircon from the cavity, but a common one for brownish zircon from the wall rock. Representative results of EMPA are listed in Table 1, the positions of related analytical spots is indicated in Fig. 1b and 2. Most remarkable are the very high contents of Y and the REE, occasionally including the light REE, in the yellow zircon. The Y contents are so high that they appear in the formula (0.01 atom per formula unit or more; Table 1).

The Th content is comparable to that of U in some areas, but may be significantly higher, reaching several thousands of ppm as in the broad zone D optically indistinguishable inside the yellow transparent crystal termination mentioned above. This zone D is clearly visible in the SEM because it appears bright in BSE images. In this Th-rich zone, Th is easily detected even by EDX. On the other hand, Fe, Ca and Al contents are always rather low to very low except some zones in the crystal core A. The Hf concentration around 1.5 wt% HfO₂ may be considered as typical of zircon in granitic rocks but is, in fact, a little enhanced compared to normal magmatic zircon from alkaline granites.

Although we have analyzed by EMPA only the even REE, pronounced fractionation of the REE is observed throughout the crystal as demonstrated by chondrite-normalized distribution patterns in Fig. 5. In the figure, Y is plotted instead of Ho; the absence of anomaly demonstrates that there was no significant Y/Ho fractionation (*cf.* Bau, 1996) during fluid evolution. The first REE distribution type (Fig. 5) is restricted to the core A. The distribution is concave with enrichment of the light (Ce) and heavy (Yb) REE and a relative depletion of the middle REE. The second type is observed for the zone B surrounding the core, the zone E in the outer yellow transparent crystal termination adjacent to the Th-rich zone and for a related narrow zone in the {100} growth sector G. Here, all REE including the light, middle and heavy groups are enriched although there is some relative depletion of Ce and some enrichment of Yb (Fig. 5). In all

Table 1. Selected EPMA data and relevant formulae for Type 1 yellowish hydrothermal zircon and Type 2 brownish magmatic zircon from Mt. Malosa (Malawi). Spot numbers are those shown in Figs. 1b and 2, respectively.

Point	Hydrothermal Type 1								Magmatic Type 2	
	1	2	3	4	5	6	7	8	1	2
SiO ₂	31.98	31.97	31.60	31.87	32.05	31.76	31.86	31.62	32.38	32.26
ZrO ₂	63.11	61.99	58.77	59.52	62.23	60.41	60.23	59.50	65.91	65.99
HfO ₂	1.49	1.41	1.45	1.46	1.62	1.41	1.36	1.36	0.99	1.19
Y ₂ O ₃	0.33	1.79	4.76	3.29	1.19	2.79	3.07	4.24	<0.05	<0.05
Ce ₂ O ₃	0.45	0.60	0.16	0.17	0.46	0.13	0.07	0.07	<0.07	<0.07
Nd ₂ O ₃	0.08	0.38	0.04	0.04	0.57	0.04	0.06	<0.04	<0.04	<0.04
Sm ₂ O ₃	<0.08	0.15	<0.08	0.08	0.18	<0.08	<0.08	<0.08	<0.08	<0.08
Gd ₂ O ₃	0.06	0.17	0.28	0.43	0.26	0.39	0.30	0.33	<0.06	<0.06
Dy ₂ O ₃	<0.05	0.14	0.44	0.52	0.19	0.37	0.32	0.41	<0.05	<0.05
Yb ₂ O ₃	0.07	0.15	0.44	0.24	0.13	0.25	0.33	0.59	0.05	<0.05
UO ₂	<0.08	<0.08	<0.08	0.10	<0.08	<0.08	<0.08	<0.08	<0.08	<0.08
ThO ₂	<0.05	<0.05	0.09	0.75	0.11	0.49	0.43	<0.05	<0.05	<0.05
Nb ₂ O ₅	0.28	0.24	0.13	0.23	0.23	0.17	0.13	0.03	0.02	0.02
TiO ₂	0.07	0.02	0.02	0.01	0.01	0.01	0.01	<0.01	<0.01	<0.01
Total	98.20*	99.01	98.18	98.71	99.23	98.15	98.22	98.17	99.35	99.46
Contents in wt%										
Formula units (apfu) calculated on a two-cation basis										
Zr	0.965	0.941	0.899	0.909	0.945	0.925	0.921	0.910	0.992	0.993
Hf	0.013	0.013	0.013	0.013	0.014	0.013	0.012	0.012	0.009	0.010
Y	0.006	0.030	0.079	0.055	0.020	0.047	0.051	0.071	<0.001	<0.001
Ce	0.005	0.007	0.002	0.002	0.005	0.002	0.001	0.001	<0.001	<0.001
Nd	0.001	0.004	0.001	<0.001	0.006	<0.001	0.001	<0.001	<0.001	<0.001
Sm	<0.001	0.002	<0.001	0.001	0.002	<0.001	<0.001	<0.001	<0.001	<0.001
Gd	0.001	0.002	0.003	0.005	0.003	0.004	0.003	0.003	<0.001	<0.001
Dy	<0.001	0.001	0.005	0.005	0.002	0.004	0.003	0.004	<0.001	<0.001
Yb	0.001	0.001	0.004	0.002	0.001	0.002	0.003	0.006	<0.001	<0.001
U	<0.001	<0.001	<0.001	0.001	<0.001	<0.001	<0.001	<0.001	<0.001	<0.001
Th	<0.001	<0.001	0.001	0.005	0.001	0.004	0.003	<0.001	<0.001	<0.001
Nb	0.004	0.003	0.002	0.003	0.003	0.002	0.002	<0.001	<0.001	<0.001
Ti	0.002	<0.001	<0.001	<0.001	0.001	<0.001	<0.001	<0.001	<0.001	<0.001
Zr position	0.998	1.004	1.008	1.001	1.002	1.003	1.000	1.007	1.001	1.003
Si	1.002	0.995	0.991	0.998	0.998	0.997	0.999	0.992	0.999	0.996

* Including 0.17 wt% FeO and 0.09 wt% CaO

other zones including C with a yellowish-brownish coloration, the related zone in the {1 0 0} growth sector G, the Th-rich zone D, and the rim zone F with narrow growth zoning, the light REE are relatively depleted and heavy REE are strongly enriched as normally found in natural zircon and favored by the zircon structure (Speer, 1982).

Table 2 compiles U and Th contents defined by SHRIMP. One EMPA analysis from the Th-rich zone D is also included. The U and Th contents and Th/U ratios of 0.6 found in the core (zones A + B) are in a range typical of magmatic zircon from granitic rocks (*cf.* Ahrens, 1965; Ahrens *et al.* 1967; Hoskin & Ireland, 2000; Hoskin & Schaltegger, 2003). In the other zones, however, there is a strong increase in Th and Th/U ratios up to 6.500 ppm and 7.5, respectively, indicating that the core and the rest of the crystal may have a different origin. On the other hand, the transition between these two ranges is relatively smooth, hinting for a common origin of the whole crystal. The magmatic zircon from the host rock also displays enhanced Th/U ratios (2.3–3.9) at normal Th contents possibly reflecting the Th enrichment in the alkaline rocks.

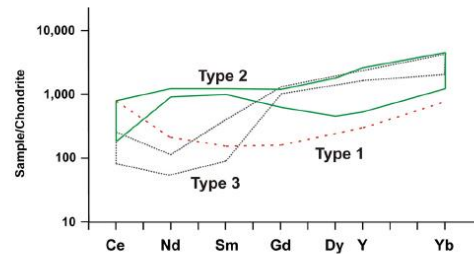


Fig. 5. REE+Y distribution patterns of yellowish hydrothermal zircon according to EMPA. Type 1 distribution is found in the greenish-yellowish core (analytical point 1 in Fig. 1b). Type 2 is typical of the rim zone of the core (point 2) and the zone preceding the oscillatory zoning at the rim (point 5). Type 3 distribution was found in the remaining zones (points 3, 4, 6, 7 and 8). Chondrite normalization according to Anders & Grevesse (1989) See text for discussion.

A conspicuous feature of the EMPA analyses of yellow zircon from the cavity are the low analytical totals ranging between 97.9 and 99.2 wt%. Totals for the wall-rock

Table 2. Contents of U and Th, U/Th ratios, calculated received radiation doses according to defined SHRIMP ages and line widths (FWHM) of the ν_3 (B_{1g}) Raman mode fitted with a single line for Type 1 (hydrothermal) and Type 2 (magmatic) zircon from Mt. Malosa (Malawi).

Point	Hydrothermal Type 1						Magmatic Type 2		
	1	2	3	4 ^{*1}	5	8	1	2	3
Element contents									
U	114	194	130	882	196	55	74	76	24
Th	67	110	393	6591	1452	176	291	230	55
Th/U	0.59	0.57	3.02	7.47	7.41	3.26	3.93	3.03	2.29
Calculated radiation dose									
(120 Ma)	0.05	0.09	0.09	0.96	0.21	0.04	0.06	0.05	0.01
(290 Ma)	0.13	0.20	0.21	2.34	0.52	0.09	0.14	0.12	0.04
Raman line broadening									
FWHM ^{*2}	6.2	13.9	18.1	20.3	13.4	19.2	3.7	3.4	2.9

U and Th in ppm. Dose in 10^{18} α -events per g.

*¹ Results for U and Th from EMPA.

*² FWHM (in cm^{-1}) of the ν_3 (B_{1g}) Raman mode fitted with one band and corrected for apparatus function. The error from the fits is between $\pm 1.2 \text{ cm}^{-1}$ (point 1) and $\pm 3.8 \text{ cm}^{-1}$ (point 4) for Type 1 and $\pm 0.8 \text{ cm}^{-1}$ for Type 2 zircon.

Table 3. Results of U–Pb SHRIMP analyses for Type 1 (yellowish hydrothermal) and Type 2 (brownish magmatic) zircon from Mt. Malosa (Malawi). Errors for calculated ages are one sigma. Th is calculated from the Th/U ratio.

Spot	U ppm	Th ppm	Th/U	Common Pb ²⁰⁶ %	²³⁸ U/ ²⁰⁶ Pb uncorrected	²⁰⁷ Pb/ ²⁰⁶ Pb uncorrected	²⁰⁶ Pb/ ²³⁸ U age Ma (²⁰⁴ Pb corr.)	²⁰⁶ Pb/ ²³⁸ U age Ma (²⁰⁷ Pb corr.)
Yellow hydrothermal zircon								
1	114	67	0.59	59.3	22.14 ± 0.35	0.4870 ± 0.0073		129.2 ± 4.5
2	194	110	0.57	14.9	50.46 ± 0.76	0.0867 ± 0.0024		120.5 ± 1.9
3	130	393	3.02	49.4	50.70 ± 1.00	0.0693 ± 0.0030		122.6 ± 2.5
5	196	1452	7.41	16.4	50.12 ± 0.80	0.0589 ± 0.0023		125.7 ± 2.1
8	54	176	3.26	91.0	48.10 ± 1.20	0.1288 ± 0.0067		119.2 ± 1.2
Brownish magmatic zircon								
1	74	291	3.93	4.5	21.53 ± 0.37	0.0536 ± 0.0020	279.7 ± 5.9	292.1 ± 4.8
2	76	230	3.03	3.1	21.34 ± 0.36	0.0607 ± 0.0021	292.1 ± 4.9	292.1 ± 4.9
3	24	55	2.29	6.1	22.01 ± 0.48	0.0587 ± 0.0033	269.5 ± 8.5	284.1 ± 6.3

zircon (99.4–99.7 wt%) and other zircons measured within the same session lie in the normal range between 99.5–100.1 wt%. The deficient results may be partly explained by the presence of other REE not measured during EMPA, especially La and Er. However, a calculation using the REE distribution patterns for rough estimation of the contents of all REE (excluding Eu) yields still too low analytical totals between 99.3 and 99.6 wt%. This phenomenon will be discussed in more detail below.

3.3. SHRIMP analysis and absolute age relations

The SHRIMP analysis was conducted to verify the age relationships between the two types of zircon and to obtain a data base for dosage calculations. The results are compared with the values obtained for birefringence and with data from EMP, Raman and CL measurements in one and the same crystal area. We have not aimed at a precise absolute age determination. Five points were analyzed in the hydrothermal zircon crystal from the cavity and three in the magmatic zircon from the wall rock. The results are listed in Table 3 and plotted in Fig. 6. Most of the

analytical points plot close to or on the Concordia. The data for the hydrothermal zircon are more discordant and there is considerable common lead which is an additional hint at its hydrothermal origin. If all five analytical points for this zircon are used for calculation without any assumptions for the composition of common lead, an age of 122 ± 2 Ma (MSWD 1.7) can be obtained (Fig. 6). When the common lead composition is “anchored” according to the model by Stacey & Kramers at $0.83^{207}\text{Pb}/^{206}\text{Pb}$ initial ratio, an age indistinguishable within error from the first one (125 ± 7 Ma; MSWD 1.8) is found. The Concordia age for the three most concordant points lies also in the same range (126 ± 5 Ma; MSWD 0.13). These data are in remarkable accordance with zircon ages reported by Högdahl & Jonsson (1999, 2002, cited in Soman *et al.*, 2010) and Soman *et al.* (2010) for zircon from the pegmatite cavities at Mt. Malosa ranging between 117 ± 1 Ma and 123 ± 4 Ma, and with the chemical age calculated by the latter authors for weakly altered thorite inclusions in zircon (122 ± 5 Ma). The K–Ar amphibole ages of 111 ± 3 and 115 ± 3 Ma reported earlier by Eby *et al.* (1995) are also similar though somewhat younger.

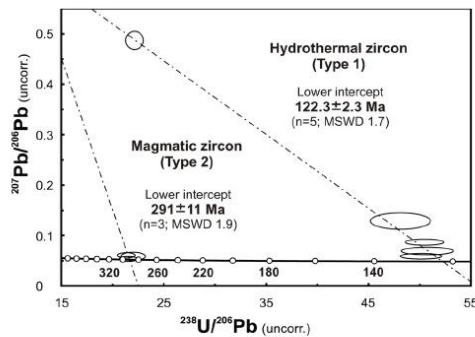


Fig. 6. Reverse Concordia plot of U–Pb SHRIMP data obtained for yellowish hydrothermal Type 1 zircon (crystal 1) and brownish magmatic Type 2 zircon from Mt. Malosa (Malawi). Error ellipses are two sigma. The strongly discordant point for Type 1 zircon corresponds to the core and displays high common Pb content. Nevertheless, calculations including or excluding this point with or without “anchored” common Pb composition yielded indistinguishable results for the calculated ages. See text for further discussion.

The few U–Pb data for the host-rock zircon studied here demonstrate that the formation age of that zircon and the related intrusion age of the granite should be significantly higher. The calculated U–Pb age for the crystal investigated is 291 ± 11 Ma (MSWD 1.9; Fig. 6). The age data obtained for both zircon types were used for radioactive dose calculations listed in Table 2.

3.4. Raman spectroscopy

As in our previous study (Kempe *et al.*, 2010), all Raman measurements on the two sections of Type 1 zircon yielded spectra with significantly broadened Raman bands. Another, previously unnoted feature is the appearance of an appreciable asymmetry for the ν_3 (B_{1g}) mode. The latter mode is commonly used to assess the degree of local disorder (Nasdala *et al.*, 1995, 2001, 2003). Significant asymmetry may also be seen for the neighboring ν_1 (A_{1g}) mode (Fig. 7). As demonstrated in Fig. 7, it was commonly not possible to fit these two peaks adequately with one band, respectively, in order to allow comparison to other work (*cf.* Palenik *et al.*, 2003). In the classical approach, such large Raman bandwidths (from 6.2 cm^{-1} in the core, but closer to the maximum value of 20.3 cm^{-1} in the rest of the crystal) clearly point to a high degree of radiation damage in the hydrothermal zircon. In contrast, Raman spectra of brownish Type 2 zircon show only very weak band broadening, typical of well-ordered zircon (Table 2).

Similar Raman measurements were conducted on the second sample of hydrothermal Type 1 zircon. Additionally,

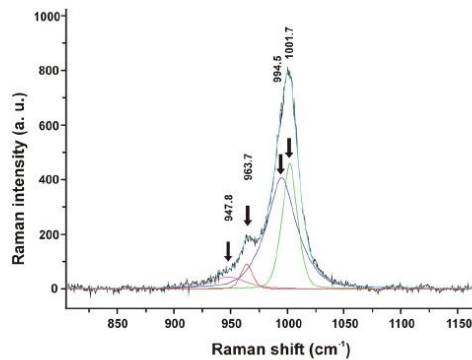


Fig. 7. Raman spectrum of yellowish hydrothermal Type 1 zircon with significant band asymmetry. Both the ν_3 (B_{1g}) and ν_1 (A_{1g}) modes cannot be adequately fitted with one band (999.7 ± 0.8 and $967.2 \pm 1.1 \text{ cm}^{-1}$ with FWHM 20.3 ± 4.2 and $25.6 \pm 4.5 \text{ cm}^{-1}$, respectively), especially at the peak flanks. This particular spectrum can be satisfactorily fitted with four bands (from the right to the left: 1001.7 ± 0.5 , FWHM 11.1 ± 2.1 ; 994.5 ± 0.5 , FWHM 24.0 ± 2.8 ; 967.2 ± 0.7 , FWHM 8.2 ± 2.5 and 947.8 ± 1.2 , FWHM $36.9 \pm 4.7 \text{ cm}^{-1}$). Note that despite the large uncertainties of the fit, the pairs of both modes at higher and lower wavenumbers show comparable bandwidths. The spectrum was taken in the area of point 5 in Fig. 1b. See text for further discussion.

two measurement series along profiles with a step width of $10 \mu\text{m}$ were made. As shown below, these profiles crossed two types of internal textures revealed by OCL. Results for the fits of the Raman spectra are plotted in Fig. 8 and the locations of the profiles are marked in Fig. 9b. The Raman measurements in this second crystal were made after EBSD. One profile (number 2) was partly located inside an area studied by EBSD while the other probed a “pristine” region. In general, the Raman results for the second crystal were very similar to that for the first except that the bandwidths tend to be somewhat lower in the second crystal. When the ν_3 (B_{1g}) mode is fitted with one band, the corrected FWHM varied between 8.3 and 14.3 cm^{-1} . However, the ν_3 (B_{1g}) mode of all spectra could be successfully fitted only with two bands as in crystal 1. Fit results for the two profiles in Fig. 8 show that in the “pristine” area (profile 1), the behavior of both fitted bands is similar with a clear change both in line position and band width when crossing from one types of texture to the other, indicating more “disordered” states in the pronounced texture closer to the core. Changes in the band width of the higher frequency band are less well pronounced, however. In the second profile, the bands are moved to lower wavenumbers and the bandwidths are increased compared to profile 1. The texture closer to the core was additionally affected by EBSD. As can be seen from Fig. 8, the trend inside this area is not as clear as in profile 1. This result demonstrates the influence of electron irradiation

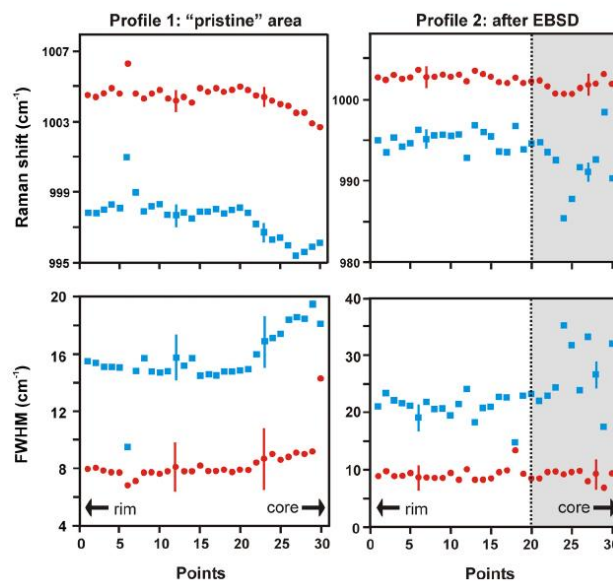


Fig. 8. Results of fits using two bands for the ν_3 (B_{1g}) mode in the Raman spectra taken along two profiles in crystal 2 of yellowish hydrothermal zircon. Comparison of the area closer to the crystal core affected by previous EBSD analysis (shaded gray) in profile 2 (right) to profile 1 (left) demonstrates that the clear trend visible for the “pristine” area in profile 1 was distorted by the electron beam. Error bars defined for the fit are 2σ . Locations of the profiles are shown in Fig. 9b.

(normally occurring at high doses during EMPA or EBSD because high beam currents focused in small spots are needed for these analyses) on the measured Raman characteristics of zircon. Similar effects were noted earlier by Nelson *et al.* (2000) and Nasdala *et al.* (2002b).

3.5. Orientation contrast imaging (OCI)

The OCI revealed a complex domain structure which shows no obvious relation to growth zoning visible in CL and BSE images (Fig. 9). The domain structure is well expressed in the central part of the crystal and weakens toward the prism faces and the crystal termination (Fig. 9b). Investigation with the cold field emission SEM revealed, however, that the domain structure is also present in these crystal areas (Fig. 9c), though it is not clearly discernible with conventional SEM (Fig. 9b). The domain size may reach several tens of micrometers. On the other hand, there is a “domain in domain” structure with the smallest visible domains measuring several dozens to hundreds of nanometers in size down to (or possibly below) the limit of resolution of the OC images (Fig. 9c). The orientation contrast commonly changes gradually within the domains, indicating high internal strain. In some places, domain walls are marked by abrupt contrast changes, which may be additionally outlined by cracks.

3.6. EBSD results

The location of the EBSD grids is shown in Fig. 10a. Two maps were obtained from the two areas shown in Fig. 9. Two additional areas were probed in the growth sector $\{100\}$ and the Th-rich zone, respectively. The EBSD analysis shows that the observed OC is related to gradual changes in the lattice orientation as well as to abrupt changes at small angle boundaries (Fig. 10b and c). Note that indexing of EBSD patterns failed only in pits and cracks although the local resolution of the method is of the order of a few tens of nanometers, just in the range assumed for the extent of α -recoil tracks in zircon (Ewing *et al.*, 2003). This result demonstrates that the long-range order in the crystal is well preserved. Misorientation angles at domain boundaries vary from the order of several tenths (mostly at the crystal termination) up to about 10° (in the central part of the crystal), occasionally reaching 20° . The main rotation axis may be defined along $[01\bar{3}]$ with some orientation distribution around it. Orientation distribution is more clearly seen for rotation angles below 5° .

Band contrast (BC; height of the diffraction peaks above the background signal in the Hough space) varies in a similar manner as the orientation contrast in the OC images. In general, the BC depends on crystal perfection, phase orientation and several experimental parameters

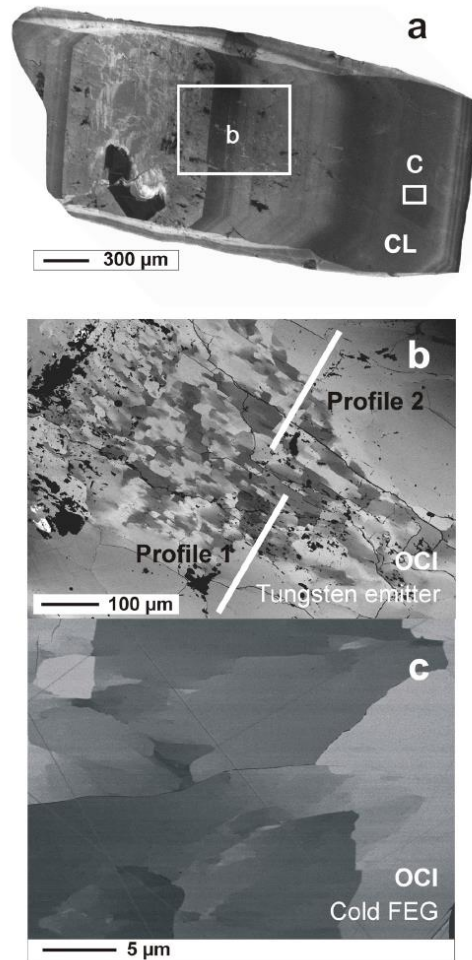


Fig. 9. Orientation contrast images (OCI) of the yellowish hydrothermal zircon (crystal 2): (a) CL image of the crystal with the location of the OCI (b and c). (b) OCI of a central region of the crystal obtained with conventional SEM (tungsten emitter). The locations of the two profiles investigated by Raman spectroscopy are marked on the figure. (c) OCI of a region closer to the crystal termination taken with a SEM equipped with a cold field emission gun and a large-angle BSE detector.

(Humphreys, 2001). Experimental parameters were kept constant in our case. The average BC value is the same in the central part of the crystal (map 1) and at the crystal termination (map 2) and in the other maps. On the other hand, variations in BC are much larger in the first case. We

may conclude that the long-range order is of about the same (high) degree in all areas probed and that variations in the BC are dominated by the orientation distribution.

The band slope (BS) parameter is determined by the width of the peaks in the Hough transform describing the maximum intensity gradient at the Kikuchi band margins. The band slope depends on the long-range order, crystallite size, internal strain and the same experimental parameters as BC. The BS parameter displays large variations in the central part of the crystal but only restricted distribution and higher average values at the crystal termination. Considering conclusions on BC, we interpret the variations in BS mainly as a result of distributions in internal strain and crystallite (domain) sizes rather than in long-range order.

4. Discussion

It is clear from the above results that the correlation between U and Th concentrations, age, birefringence, Raman spectroscopic behavior and structural changes normally reported for natural zircon and well explained by the radiation-damage model is not observed for the yellowish hydrothermal zircon from Malawi, although it holds for the well-ordered brownish magmatic zircon from the same rock sample. Several aspects of this apparent contradiction are discussed in more detail below.

4.1. Degree of disorder

The main problem arising with the interpretation of the data concerns the degree of disorder in the yellowish hydrothermal zircon. While a high degree of (short-range) disorder is indicated by Raman spectroscopy, birefringence suggests a high degree of short-range order (ordered orientation of covalent bonds) except for the Th-rich zones (Table 4). From dose calculations based on U+Th contents and U–Pb SHRIMP ages, only weak radiation damage is expected except for some enhanced values in the Th-rich zone (Table 4). No significant distortion of the long-range order is seen by EBSD in all areas investigated. We conclude from the data that there is a high degree of long-range order in both the magmatic and hydrothermal zircon crystals studied.

The Raman data, namely the FWHM defined for the ν_3 (B_{1g}) mode fitted with a single band, may be plotted in a diagram together with the dose (calculated here from the SHRIMP data; Fig. 11) as proposed by Nasdala *et al.* (2001). The diagram shows that the disorder indicated by Raman spectroscopy for the hydrothermal zircon is much higher than can be expected from internal radiation in any realistic time interval considering the U and Th contents. All but one data point (calculated for an unrealistic high age) plot well above the linear array defined by Nasdala *et al.* (2001) as a calibration line for zircon samples with no evidence for annealing after crystallisation. Deviations from this line are frequently observed for zircon that experienced annealing well after formation. In this case,

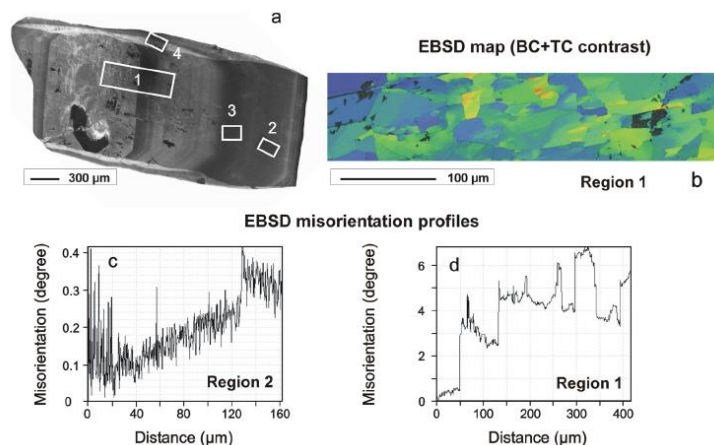


Fig. 10. Results of EBSD analysis of the yellowish hydrothermal zircon (crystal 2). (a) CL image of the crystal with the location of the mapped areas (1–4). (b) EBSD map of region 1 (band contrast+texture contrast) illustrating the orientation domain textures. (c) Misorientation profile through region 2. (d) Misorientation profile through region 1.

data points plot below the calibration line and projection on this line by recalculation to other ages is sometimes used to estimate the original dose and/or the (hydro-)thermal event responsible for recrystallisation (Nasdala *et al.*, 2001; Geisler *et al.*, 2003; Dziggel *et al.*, 2005; Tichomirowa *et al.*, 2005). However, this method is not applicable in our case. Other approaches are needed to explain the observed apparent discrepancies between the data obtained by various methods.

4.2. BSE contrast and CL intensity

In an earlier work, we noted two types of zircon considering BSE and CL contrast: (1) “normal” zircon with inverse behavior of BSE and CL intensity and (2) zircon with low CL signal paralleled by “anomalous” low BSE (Kempe *et al.*, 2000). These relations were further explored by Nasdala *et al.* (2006, 2009). The cited authors found for zircon of the first type analytical totals close to 100 % (Nasdala *et al.*, 2009). Surprisingly, the BSE intensity was found to correlate well with the broadening of the Raman peaks in their samples rather than with the average atomic number as normally assumed in electron microscopy (Nasdala *et al.*, 2006). The zircon of the second type showed low analytical totals but there was no clear correlation with the Raman characteristics (Nasdala *et al.*, 2009). In our case, the brownish zircon from the host rock belongs to the first group – CL and BSE contrast are inversely correlated, the BSE signal is at a “normal” level and all microprobe analyses show good analytical totals. The Raman peaks are rather sharp. However, the yellowish hydrothermal zircon does not fit into a “two-type” schema. Except for the core region A in some crystals (*e.g.*, in crystal 1), the CL and BSE signals are inversely correlated,

but the analytical totals are always low when the trace-element content is high. In general, the BSE signal intensity in the crystals is at the same level as in the brownish zircon crystal (*i.e.* as in “common” zircon). The Raman peaks in the spectra from the yellowish zircon are always considerably broadened as further discussed below. The core region in the first crystal studied in more detail is somewhat similar to zircon of the second type characterised by Nasdala *et al.* (2009) because the CL is quenched while the BSE signal is low (Fig. 1) and Fe and Ca appear in detectable quantities (Table 1). This conclusion is also supported by SHRIMP analysis indicating high common lead (Table 3) and a significant discordance of the U–Pb system (Fig. 6).

4.3. Element substitution, charge balance, stoichiometry, and analytical totals

A striking peculiarity of hydrothermal zircon from the cavity is the high contents of Y and the REE substituting for Zr as suggested by the microprobe analyses and formulae calculations shown in Table 1. It is well established that these elements substitute at the dodecahedral Zr site which is coordinated by eight oxygen atoms (Speer, 1982; Hoskin & Schaltegger, 2003). However, replacement of tetravalent Zr by trivalent Y and REE needs charge compensation. According to the literature, the most common compensation mechanism is the coupled substitution of P for Si in the tetrahedral site (see Speer, 1982; Finch *et al.*, 2001; Hoskin & Schaltegger, 2003 and Harley & Kelly, 2007 for summaries). This mechanism cannot be operative in our case because P could not be detected by EMPA. An alternative way of charge compensation is the coupled substitution of pentavalent

Table 4. Comparison of estimated doses (in 10^{18} α -events per g) for hydrothermal (Type1) and magmatic (Type2) zircon from Malawi according to (1) chemical composition and age, (2) Raman spectroscopy using the linear array defined by Nasdala *et al.* (2001) in the plot FWHM for the ν_3 (B_{1g}) Raman mode vs. dose calculated from chemical composition and age and (3) birefringence using the linear relation defined by Palenik *et al.* (2003) for Sri Lanka zircon.

Point	Dose calculated from age and U+Th (1)	Dose estimated from Raman spectroscopy (2)	Dose estimated from birefringence (3)
Yellowish hydrothermal Type 1 zircon (120 Ma)			
1	0.05	0.30	< 1.5
2	0.09	0.88	< 1.5
3	0.09	1.11	< 1.5
4	0.96	1.33	2.2–3.5
5	0.21	0.84	< 1.5
8	0.04	1.25	< 1.5
Brownish magmatic Type 2 zircon (290 Ma)			
1	0.14	0.14	< 1.5
2	0.12	0.12	< 1.5
3	0.04	0.07	< 1.5

(Note that the relationships obtained between calculated dose and Raman characteristics or birefringence, respectively, were originally not proposed for dose calculations. This is because such relationships would apply only for cases when the thermal history of the measured and the reference samples was the same after crystal formation. In the case of Raman, the linear array applies for zircon not re-heated after formation (Nasdala *et al.*, 2001) as found for magmatic zircon in our case. The linear relationship found for birefringence rests on measurements on Sri Lanka samples certainly re-heated after formation. See text for further explanations.)

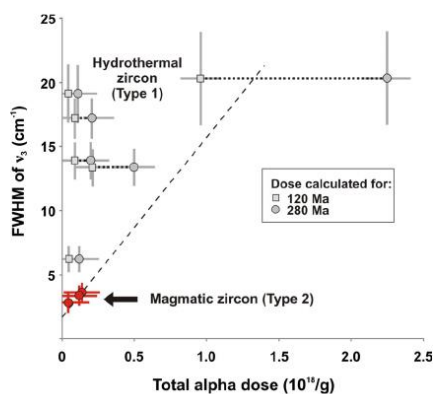


Fig. 11. Plot of the FWHM of the ν_3 (B_{1g}) mode in the Raman spectra versus dose calculated from SHRIMP data (*cf.* Table 2) according to Nasdala *et al.* (2001). For hydrothermal zircon, doses for both U–Pb SHRIMP ages (120 and 280 Ma) were calculated and plotted in the figure. The points of the magmatic zircon calculated for an age of 280 Ma plot on the calibration line defined by Nasdala *et al.* (2001) for zircons not annealed after formation.

Nb and Ta for tetravalent Zr and Hf (Vinokurov *et al.*, 1964; Solntsev & Shcherbakova, 1974; Di Gregorio *et al.*, 1980; Speer, 1982; Smith *et al.*, 1991; Hoskin & Schaltegger, 2003). Although Nb is present in measurable quantities in the zircon studied, the content is too low to compensate the charge unbalance from Y and the REE (see Table 1). A third possibility of charge compensation often overlooked is incorporation of pentavalent U at the zirconium position known from doping experiments (Vance & Mackey, 1978). The presence of pentavalent

U in natural zircon is well established by absorption spectroscopy in the near-IR range (Vance & Mackey, 1974; Zhang *et al.*, 2003). In our case, however, the U content is also by far too low to account for compensation although the lack of U^{4+} lines in the optical absorption spectra and of UO_2^{2+} in the luminescence spectra suggests that nearly all U in this zircon is present in the pentavalent state. Other suggestions for charge compensation not applicable in our case were reviewed by Speer (1982) and Smith *et al.* (1991) and include charge compensation by divalent elements (Ca, Fe) or by Al, replacement of oxygen by hydroxyl groups and formation of holes trapped on oxygen. Note that no water or OH could be found by Raman spectroscopy in our case. Finch *et al.* (2001), Ushikubo *et al.* (2008) and Soman *et al.* (2010) showed or assumed that Li is a possible compensator. It is still unclear which position Li should take in the zircon structure and we have no hints for Li mineralization at our sampling location as stated above. Note, however that Li is frequently present in enhanced concentrations in Zr–Nb–REE mineralisation. In the case of the Jack Hills zircon studied by Ushikubo *et al.* (2008), the Li was found in zircon in alteration zones apparently formed during weathering. Lithium together with P could not maintain charge balance in that case. Lithium was also noted by Smith *et al.* (1991) in zircon from Thor Lake (Canada) where its content has also been estimated to be too low for charge compensation. Although we assume that Li does not fit well into the zircon structure, the role of Li in zircon merits further investigation.

Summarising, charge unbalance from trivalent elements replacing Zr and Hf is apparently not compensated by coupled substitution with other cations in our zircon. In a comprehensive study on zircon from various localities in the Alps, Rizzo *et al.* (2000) have also found a significant number of cases, where Y+REE substitution was not

compensated by P or other elements measured. They concluded that significant distortions in the mineral structure should result. We assume here, considering the absence of measurable F, that one possible explanation is charge compensation by oxygen vacancies, a mechanism widely unnoticed or neglected (Finch *et al.*, 2001) in the literature.

There are also hints for further deviations from the ideal structure which cannot be, however, proven here due to the low precision level of the microprobe analysis. All non-formula elements detected (including U, Th and Ti; Solntsev & Shcherbakova, 1972; Speer, 1982; Harley & Kelly, 2007) substitute for Zr and Hf. It is, therefore, interesting to look whether or not stoichiometry is maintained between the Si and Zr sites. Apparently, there is a tendency for an increased deviation from stoichiometry with increasing contents of trivalent elements (Fig. 12). If this is not related to an analytical artefact (*e.g.*, to a systematic overestimation of the Y content for what we have presently no hint) this deviation from stoichiometry indicates the occurrence of some additional vacancies on the tetrahedral (Si) position which, in turn, should result in an increasing number of oxygen vacancies for charge compensation. Interestingly, similar non-stoichiometry effects were noted by Finch *et al.* (2001) for synthetic crystals doped with REE and P. We have noted earlier another type of deviation from zircon stoichiometry observed for Hf-rich zircon with an anomalous low BSE contrast and with low contents of other non-formula elements. In that case, reversely, a deficit on the Zr position was apparent (Kempe *et al.*, 1997).

As shown above, our analyses of the Y- and REE-rich zircon yielded analytical totals below 100 wt%. Similar low totals for trace-element rich zircon were reported by Černý & Siivola (1980) and Pointer *et al.* (1988) for hydrothermally altered zircon from the Tanco pegmatite (Canada) and the Ririwai granite (Nigeria), respectively, and by Smith *et al.* (1991) for hydrothermal zircon from Thor Lake (Canada). These authors assumed an additional presence of “water” and a role of sub-microscopic voids in their samples.

The problem of low analytical totals frequently met for natural zircon was explored by Pointer *et al.* (1988), Smith *et al.* (1991), Pérez-Soba *et al.* (2007) and is recently reviewed and further evaluated by Nasdala *et al.*, (2009, 2010). The conclusion by the first two authors favouring the incorporation of water or OH groups and/or the existence of sub-microscopic voids was corroborated by the data obtained by the latter authors. According to these models, voids and possible water uptake occur in zircon by recrystallisation of metamict crystal areas during hydrothermal alteration. In our case, however, low analytical totals cannot be explained by sub-microscopic voids partly filled with water. Although there are areas in the investigated crystals rich in such voids down to a few hundreds of nanometres or less in diameter which are often observed in high-resolution FE SEM imaging, large parts of the crystals lack such voids. No systematic relation between low analytical totals and the appearance of voids

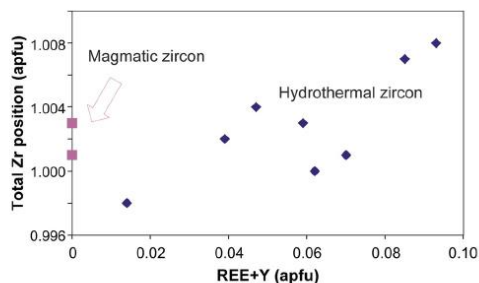


Fig. 12. Evaluation of results of EMPA (data from Table 1): comparison of apparent site occupancy on the Zr position with the content of REE + Y.

in the respective areas could be found. In general, areas with voids were avoided during our EMPA and SHRIMP measurements. This point merits further research.

4.4. Interpretation of Raman spectra

The original interpretation of line broadening and shift in the Raman spectra of zircon was based on the observation that changes in the spectra may be correlated with similar changes in the position and line widths in X-ray powder diffraction patterns measured for the same samples (Nasdala *et al.*, 1995). The weakness of this approach was in its purely empirical nature. In a later discussion, Nasdala *et al.* (2002a) suggested that line broadening observed for the internal ν_3 vibration results from irregular distortion and tilting of individual $[\text{SiO}_4]$ tetrahedra resulting from strain induced by point defects (produced by radioactive irradiation) and from the presence of an amorphous phase, while the Raman band shift reflects the lattice expansion established by XRD analysis. Similar conclusions were reached earlier by Woodhead *et al.* (1991) applying IR analysis and by Knittel & Williams (1993) after high-pressure Raman experiments, but they are in conflict with an XRD single-crystal study on moderately metamict zircon that demonstrated that changes in the $[\text{SiO}_4]$ tetrahedra are negligible (Rios *et al.*, 2000a).

As revealed by OCI and EBSD, the Raman laser probed heterogeneous crystal areas (domains) of the hydrothermal zircon from Malawi with distribution of (1) lattice orientation, (2) domain sizes, and (3) internal strain. In general, Raman spectra may be affected by all three factors (Burns & Scott, 1970; Sanjurjo *et al.*, 1983; Frey & Payne, 1996). However, orientation distribution cannot be accounted for band shifts here because Raman-active modes in zircon are not polarized. The influence from phonon confinement effects within the domains should also be negligible because the domain sizes are mainly well above the critical value of 20–30 nm (*e.g.*, Nasdala *et al.*, 2002a). We propose that the variations in the Raman spectra may be directly linked to internal strain, an effect well known from other crystalline materials (*e.g.*, De Wolf *et al.*, 1992). In this interpretation, the direction and extent of the line shifts are a measure of the kind and extent of the

strain while the line widths characterise strain distribution. As shown by De Wolf *et al.* (1992), tensional strain occurring *e.g.* at grain boundaries causes mainly line shifts to lower frequencies while compression shifts the lines to higher values excluding for “soft” modes. Shifts of Raman lines to higher values related to compression were previously reported from high-pressure experiments on zircon (Knittel & Williams, 1993; Nasdala *et al.*, 2008) and for zircon enclosed in sapphire (Wang *et al.*, 2006). We further note that changes in the band position and widths are also observed for external (lattice related) modes and are not restricted to the internal modes of the [SiO₄] tetrahedron (see also Nasdala *et al.*, 1995). We may conclude that line shifts to lower Raman frequencies observed in our case reflect tensional strain in the hydrothermal zircon under consideration as suggested by OC imaging and EBSD.

The internal tension may be explained in several ways. At least in part, the strain is simply related to the substitution of larger elements into the Zr site (Solntsev & Shcherbakova, 1974; Hoskin & Black, 2000; Finch *et al.*, 2001).

The influence of substitution into the Zr site on the Raman spectra of synthetic zircon was studied for the cases of Hf, Y and U by Hoskin & Rodgers (1996), Nasdala *et al.* (2003) and by Geisler *et al.* (2005) for Chernobyl “lava” zircon, respectively. For Hf, a weak increase in the Raman shift for internal stretching modes and some decrease for internal rotational and external modes was observed. No significant changes in the line widths were reported (Hoskin & Rodgers, 1996). Substitution of Y or U causes an increase in band widths and the occurrence of band asymmetry (Nasdala *et al.*, 2003) as well as a shift to lower wavelength numbers (Geisler *et al.*, 2005). Note, however, that the maximum spectral changes observed in synthetic zircon, even for a substitution of about 12 mol % USiO₄ as for the U-rich Chernobyl zircon, are well below the changes found in our study. To give an example, the FWHM in the U-rich Chernobyl zircon approaches 6.7 cm⁻¹ for the ν_3 (B_{1g}) mode, while up to 20.3 cm⁻¹ were found for Malawi zircon. We assume that the effect of line shift and broadening is further enhanced by vacancy formation and the problem to compensate for these structural changes by ordering processes, twinning etc. promoting local strain domain formation. Note that the zircon structure is very rigid as reflected by the unusually low thermal expansion and compressibility of zircon (Özkan & Jamieson 1978; Hazen & Finger, 1979; Speer & Cooper, 1982).

Reddy *et al.* (2006, 2009) assigned similar internal textures detected by EBSD to deformation events induced by external stress. Growth in open space and lack of any signs of deformation preclude such an interpretation in our case. Summarizing, we favour internal (structural) mechanisms to be responsible for the occurrence of tensional strain.

The suggestions made here on the role of internal strain are corroborated by the results obtained from the Raman measurements along the two profiles crossing two textural areas of orientation distribution in the second crystal

(Fig. 8 and Fig. 9b). The extent of domain misorientation measured by EBSD correlates with the extent of assumed tension and strain distribution indicated by the Raman spectra. Partial relaxation of strain between the two areas seen in the Raman spectra after intense electron irradiation during EBSD analysis (Fig. 8) may be explained by local heating effects and by electron trapping in the zircon structure, namely, oxygen vacancies can act as excellent electron traps.

Remarkably, the observed domain structure with related tensional strain distribution may also explain the band asymmetry observed in the Raman spectra. As shown above, the resolution of Raman spectroscopy and the domain sizes are of comparable order. That means that two or more domains may be present within a single Raman spot. The resulting effect leading to the appearance of asymmetric Raman bands in the spectra was earlier demonstrated by Nasdala *et al.* (2005) by an intentional measurement on a boundary between two areas with quite different degrees of metamictization in a single zircon grain. The asymmetry may be also related to strain distribution within single domains.

No asymmetry was observed in our previous study on single crystals of hydrothermal zircon from the Malawi sample (Kempe *et al.*, 2010). In that work, the volume probed by the Raman measurements was further enlarged by focusing the laser beam below the sample surface with a resulting signal averaged over a much greater number of domains. We assume that high statistics in strain distribution yielded symmetric broad bands in the resulting composite spectra.

Note that in a conventional study, the Raman spectroscopy of the hydrothermal zircon from Malawi would suggest a high degree of metamictization. Such samples are commonly avoided in geochronological studies. However, no general analytical problems except enhanced contents of common lead were met during our SHRIMP analysis.

4.5. CL spectroscopy

While the CL spectra of the magmatic zircon reflect the well-ordered structural state of this zircon with common broad-band emissions accompanied by some weak line emissions related to the REE³⁺, the CL spectroscopy of the yellow hydrothermal zircon underlines its unusual character. The strong REE³⁺ line emissions correspond to the high contents of the REE in the crystals. Remarkably, there are crystal areas with even more intense emissions from the light REE than from the heavy one. Comparable intense Nd³⁺ emission were not yet reported in the literature for natural zircon. Note that heavy REE fit easier into the zircon structure than light REE. Accordingly, higher local distortion may be expected from the very high light-REE contents. On the other hand, comparison of the Dy³⁺ emission in well-ordered brownish magmatic zircon and in the yellowish hydrothermal one does not show any significant line broadening (*cf.* Fig. 3 and Fig. 4). Although this may be related to some extent to the resolution of the fine structure in our spectra, this observation may also

indicate preservation of long-range order (resulting in only weak variations in the crystal field around the REE) in the hydrothermal zircon despite significant substitution of non-formula elements (*cf.* Lenz *et al.*, 2013; Lenz & Nasdala, 2015). However, the more sensitive, common broad-band emissions related to the defect structure in well-ordered zircon (Kempe *et al.*, 2000, 2010) are completely absent in the hydrothermal zircon indicating that some kind of disorder should be present. We assume here that the quenching of intrinsic broad band luminescence results mainly from the high vacancy concentration discussed above.

4.6. Possible consequences for the model of zircon metamictization

Although the yellowish hydrothermal zircon discussed above is certainly a very rare and extreme case, we assume that our findings may also contribute to the general understanding of the phenomenon of disorder in zircon and zircon metamictization. Besides the accepted model assuming radioactive decay as the leading process, there may be other mechanisms operative and resulting in the effects observed. One assumption made previously for metamict minerals in general was that metamictization may be related to the formation of very small, metastable and partially ordered domains with high defect densities within the crystals which show a misorientation distribution (Pyatenko, 1970; Graham & Thornber, 1974, 1975). The formation of such domains may or may not be accelerated by radioactive irradiation. It was further assumed that the formation of such domains may be induced by a complex composition, substitution of large cations and/or charge unbalances (Aleksandrov, 1960; Graham & Thornber, 1974). Note that metamictization most often occurs in complex oxides where ordering processes are complicated by the complex chemical composition and in structures with highly charged cations (Graham & Thornber, 1974, 1975). Meldrum *et al.* (1999) noted as a result of TEM investigations on zircon that a polycrystalline structure is observed in natural metamict zircon which is not reproduced by ion irradiation. Slightly misoriented microcrystallites about 100 nm in size were also found by Bursill & McLaren (1966) in a TEM study on another metamict zircon. In Fig. 13, we compare the orientation distribution in the EBSD pole figure [1 0 0] of our Malawi sample with the orientation distribution reported by Rios & Salje (1999) for diffuse X-ray scattering of the (4 0 0) reflection in the reciprocal space of a slightly metamict sample from Moroto (Uganda). The similarity is striking. The latter authors explained their results by an intrinsic mosaic of the sample and swelling of defective areas.

Note that according to our interpretation of the line broadening and shift, Raman spectroscopy of partly metamict zircon indicates always tensional strain for the damaged and undamaged crystalline parts present there along with amorphous regions, according to the accepted model for zircon amorphization (see Chakoumakos *et al.*, 1987; Salje *et al.*, 1999; Zhang *et al.*, 2000). In contrast,

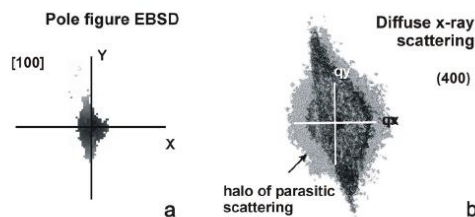


Fig. 13. Similarity in orientation distribution of (a) domains in the hydrothermal zircon from Malawi illustrated by the central part of the [1 0 0] EBSD pole figure (this work) and (b) for Moroto zircon (Rios & Salje, 1999) illustrated by diffuse X-ray scattering of the (4 0 0) reflection in the reciprocal space.

compression is expected according to the amorphization model in highly metamict zircon when the volume swelling is mainly related to the volume increase by formation of amorphous regions (Weber & Maupin, 1988), *i.e.* beyond the second percolation point (Salje *et al.*, 1999).

In conclusion of this discussion, we would stress the convergence between both mechanisms of amorphization, namely complex substitution and radioactive irradiation, because the α -recoil during the decay of U and Th produces mostly oxygen vacancies (Bursill & McLaren, 1966; Park *et al.*, 2001; Ewing *et al.*, 2003) which are responsible for strain and misorientation distribution in the present case of the Malawi zircon. In the Malawi zircon, however, oxygen vacancies were rather formed by charge compensation for trivalent elements substituting into the zirconium site.

4.7. Hydrothermal activity and cooling history of the Mt. Malosa complex

Our results may also shed some light on the magmatic and hydrothermal history of the Mt. Malosa complex. Although more geochronological work is needed, the age defined for the apparently magmatic zircon in our sample indicates that alkaline magmatism at least in the Zomba-Malosa massif may be significantly older than previously assumed (Eby *et al.*, 1995). As a consequence, K–Ar ages for amphibole and fission track ages for apatite and zircon reported by the latter authors may reflect hydrothermal reset ages rather than cooling ages.

5. Conclusion

The example of the unusual hydrothermal zircon from Mt. Malosa, Malawi suggests that Raman spectroscopy of partly or strongly disordered zircon may reflect internal strain due to misorientation domain structures of variable size. Changes in the spectra may not directly be linked to the damage of the long- and short-range order in the crystal caused by radioactive irradiation. This fact again raises the problem of the nature of the disorder frequently observed in natural zircon.

Acknowledgements: The authors thank Andreas Massanek (Freiberg) for providing access to samples from Malawi including the studied sample, Freiberg Mineral Collection #80504. Michael Magnus (Freiberg) is thanked for excellent preparation of the EBSD section and Dieter Dettmar (Bochum) for his efforts with the preparation of oriented thin sections of zircon crystals. We are indebted to Rune Gehrlein for providing access to the EBSD Oxford Instruments demonstration facility in Wiesbaden. Shunsuke Asahina (JEOL Europe) assisted with sample preparation for OC imaging and operation of the JSM 7500F. Dieter Rhede (Potsdam) carried out electron probe microanalyses. The manuscript greatly benefited from critical comments on earlier versions by Steve Reddy and Marion Tichomirrowa and from careful examination by two anonymous reviewers. S.V. Krivovichev is thanked for his editorial efforts.

References

- Ahrens, L.H. (1965): Some observations on the uranium and thorium distributions in accessory zircon from granitic rocks. *Geochim. Cosmochim. Acta*, **29**, 711–716.
- Ahrens, L.H., Cherry, R.D., Erlank, A.J. (1967): Observations on the Th-U relationship in zircons from granitic rocks and from kimberlites. *Geochim. Cosmochim. Acta*, **31**, 2379–2387.
- Akhmatova, M.V. & Leonova, L.L. (1961): Study of metamict decay of zircon using infrared absorption spectra. *Geokhimiya*, **5**, 401–414 (in Russian).
- Aleksandrov, V.B. (1960): Crystal structure of fersmite. *Dokl. Akad. Nauk SSSR*, **132**, 669–672 (in Russian).
- Anderson, A.J., Wirth, R., Thomas, R. (2008): The alteration of metamict zircon and its role in the remobilization of high-field-strength elements in the Georgeville granite, Nova Scotia. *Can. Mineral.*, **46**, 1–18.
- Anders, E. & Grevesse, N. (1989): Abundances of the elements: meteoric and solar. *Geochim. Cosmochim. Acta*, **57**, 197–214.
- Bau, M. (1996): Controls on the fractionation of isoivalent trace elements in magmatic and aqueous systems: Evidence from Y/Ho, Zr/Hf, and lanthanide tetrad effect. *Contrib. Mineral. Petrol.*, **123**, 323–333.
- Black, L.P., Kamo, S.I., Allen, C.M., Aleinikoff, J.M., Davis, D.W., Korsch, R.J., Foudoulis, C. (2003): TEMORA 1: a new zircon standard for Phanerozoic U-Pb geochronology. *Chem. Geol.*, **200**, 155–170.
- Bruneel, J.L., Lassègues, J.C., Sourisseau, C. (2002): In-depth analyses by confocal Raman microspectrometry: experimental features and modelling of the refraction effects. *J. Raman Spectr.*, **33**, 815–828.
- Burns, G. & Scott, B.A. (1970): Raman spectra of polycrystalline solids; application to the $\text{PbTi}_{1-x}\text{Zr}_x\text{O}_3$ system. *Phys. Rev. Lett.*, **25**, 1191–1194.
- Bursill, L.A. & McLaren, A.C. (1966): Transmission electron microscope study of natural radiation damage in zircon (ZrSiO_4). *Phys. Stat. Solidi*, **13**, 331–343.
- Černý, P. & Siivola, J. (1980): The Tanco pegmatite at Bernic Lake, Manitoba. XII. Hafnian zircon. *Can. Mineral.*, **18**, 313–321.
- Cesbron, F., Blanc, P., Ohnenstetter, D., Remond, G. (1995): Cathodoluminescence of rare earth doped zircons. I Their possible use as reference materials. *Scann. Micr. Suppl.*, **9**, 35–56.
- Chakoumakos, B.C., Murakami, T., Lumpkin, G.R., Ewing, R.C. (1987): Alpha-decay-induced fracturing in zircon: The transition from the crystalline to the metamict state. *Science*, **236**, 1556–1559.
- Chakoumakos, B.C., Oliver, W.C., Lumpkin, G.R., Ewing, R.C. (1991): Hardness and elastic modulus of zircon as a function of heavy-particle irradiation dose: I. *In situ* α -decay event damage. *Rad. Eff. Def. Sol.*, **118**, 393–403.
- Davis, D.W., Williams, I.S., Krough, T.E. (2003): Historical development of zircon geochronology. in “Zircon”, J.M. Hanchar & P.W.O. Hoskin, ed. Reviews in Mineralogy and Geochemistry, **53**, Mineralogical Society of America, Washington D.C., 145–181.
- Delines, M., Delhal, J., Tarte, P. (1977): Metamictization and U–Pb systematic – a study by infrared absorption spectrometry of Precambrian zircons. *Earth Planet. Sci. Lett.*, **33**, 331–344.
- De Wolf, L., Vanhellermont, J., Romano-Rodriguez, A., Norström, H., Maes H.E. (1992): Micro-Raman study of stress distribution in local isolation structures and correlation with transmission electron microscopy. *J. Appl. Phys.*, **71**, 898–906.
- Di Gregorio, S., Greenblatt, M., Pifer, J.H. (1980): ESR of Nb^{4+} in zircon. *Phys. Stat. Solidi (b)*, **101**, K147–K150.
- Dingley, D. (2004): Progressive steps in the development of electron backscatter diffraction and orientation imaging microscopy: *J. Micr.*, **213**, 214–224.
- Dziggel, A., Armstrong, R.A., Stevens, G., Nasdala, L. (2005): Growth of zircon and titanite during metamorphism in the granulite-gneiss terrane south of the Barberton greenstone belt, *S Afr. Mineral. Mag.*, **69**, 1019–1036.
- Eby, G.N., Roden-Tice, M., Krueger, H.L., Ewing, W., Faxon, E.H., Woolley, A.R. (1995): Geochronology and cooling history of the northern part of the Chilwa Alkaline Province, Malawi. *J. Afr. Earth Sci.*, **20**, 275–288.
- Everall, N.J. (2000): Modelling and measuring the effect of refraction on the depth resolution of confocal Raman microscopy. *Appl. Spectr.*, **54**, 773–782.
- Ewing, R.C. (2001): The design and evaluation of nuclear waste forms: clues from mineralogy. *Can. Mineral.*, **39**, 697–715.
- Ewing, R.C., Lutze, W., Weber, W.J. (1995): Zircon: A host-phase for the disposal of weapons plutonium. *J. Mater. Res.*, **10**, 243–246.
- Ewing, R.C., Meldrum, A., Wang, L.M., Weber, W.J., Corrales, L.R. (2003): Radiation effects in zircon. in “Zircon”, J.M., Hanchar & P.W.O. Hoskin, ed. Reviews in Mineralogy and Geochemistry, **53**, Mineralogical Society of America, Washington D.C., 387–425.
- Finch, R.J., Hanchar, J.M., Hoskin, P.W.O., Burns, P.C. (2001): Rare-earth elements in synthetic zircon: Part 2. A single-crystal X-ray study of xenotime substitution. *Am. Mineral.*, **86**, 681–689.
- Finch, A.A., Garcia-Guinea, J., Hole, D.E., Townsend, P.D., Hanchar, J.M. (2004): Ionoluminescence of zircon: rare earth emissions and radiation damage. *J. Phys. D: Appl. Phys.*, **37**, 2795–2803.
- Frey, M.H. & Payne, D.A. (1996): Grain-size effect on structure and phase transformations for barium titanate. *Phys. Rev. B*, **54**, 3158–3168.
- Friis, H., Finch, A.A., Williams, C.T., Hanchar, J.M. (2010): Photoluminescence of zircon (ZrSiO_4) doped with REE^{3+} ($\text{REE} = \text{Pr, Sm, Eu, Gd, Dy, Ho, Er}$). *Phys. Chem. Minerals*, **37**, 333–342.

- Gaft, M., Panczer, G., Reinfeld, R., Shinno, I. (2000): Laser-induced luminescence of rare-earth elements in natural zircon. *J. All. Comp.*, **300–301**, 267–274.
- Geisler, T., Burakov, B.E., Zirlin, V., Nikolaeva, L., Pöml, P. (2005): A Raman spectroscopic study of high-uranium zircon from the Chernobyl “lava”. *Eur. J. Mineral.*, **17**, 883–894.
- Geisler, T., Rashwan, A.A., Rahn, M., Poller, U., Zwingmann, H., Pidgeon, R.T., Schleicher, H., Tomaschek, F. (2003): Low-temperature hydrothermal alteration of natural metamict zircons from the Eastern Desert, Egypt. *Mineral. Mag.*, **67**, 485–508.
- Gentry, R.V., Sworski T.J., McKown, H.S., Smith, D.H., Eby, R.E., Christie, W.H. (1982): Differential lead retention in zircons: Implications for nuclear waste containment. *Science*, **216**, 296–298.
- Graham, J. & Thornber, M.R. (1974): The crystal chemistry of complex niobium and tantalum oxides. IV. The metamict state. *Am. Mineral.*, **59**, 1047–1050.
- , — (1975): The crystal chemistry of complex niobium and tantalum oxides. IV. The metamict state: Reply. *Am. Mineral.*, **60**, 734.
- Guastoni, A. & Pezzotta, F. (2007): REE-mineral phases replacing helvite, niobian-rutile, bastnäsite-(Ce) from alkaline pegmatites of Mount Malosa, Zoma District, Malawi. in “Granitic pegmatites: The state of the art”, International Symposium, Porto, Portugal (abstract), 42–43.
- Guastoni, A., Nestola, F., Giaretta, A. (2009): Mineral chemistry and alteration of rare earth element (REE) carbonates from alkaline pegmatites of Mount Malosa, Malawi. *Am. Mineral.*, **94**, 1216–1222.
- Harley, S.L. & Kelly N.M. (2007): Zircon tiny but timely. *Elements*, **3**, 13–18.
- Hazen, R.M. & Finger, L.W. (1979): Crystal structure and compressibility of zircon at high pressure. *Am. Mineral.*, **64**, 196–201.
- Högdahl, K. & Jonsson, E. (1999): Age and mineral assemblages in apatitic pegmatites in the Chilwa alkaline province, Malawi, SE Africa. *J. Conf. Abstr.*, **4**, 767
- Högdahl, K. & Jonsson, E. (2002): CL characteristics versus Th, U, Hf contents in alkaline pegmatite-hosted zircon. in “The 25th Nordic geological winter meeting”, S.S. Jonsson, ed. Reykjavik (Abstract), 27.
- Holland, H.D. & Gottfried D. (1955): The effect of nuclear radiation on the structure of zircon. *Act. Crystallogr.*, **8**, 291–300.
- Hoskin, P.W.O. & Black, L.P. (2000): Metamorphic zircon formation by solid-state recrystallization of protolith igneous zircon. *J. metamorphic Geol.*, **18**, 423–439.
- Hoskin, P.W.O. & Ireland, T.R. (2000): Rare earth element chemistry of zircon and its use as a provenance indicator. *Geology*, **28**, 627–630.
- Hoskin, P.W.O. & Rodgers, K.A. (1996): Raman spectral shift in the isomorphous series $(Zr_{1-x}Hf_x)SiO_4$. *Eur. J. Solid State Inorg. Chem.*, **33**, 1111–1121.
- Hoskin, P.W.O. & Schaltegger, U. (2003): The composition of zircon and igneous and metamorphic petrogenesis. in “Zircon”, J.M. Hanchar, P.W.O. Hoskin, ed. Reviews in Mineralogy and Geochemistry, **53**, Mineralogical Society of America, Washington D.C., 27–62.
- Humphreys, F.J. (2001): Grain and subgrain characterisation by electron backscatter diffraction. *J. Mat. Sci.*, **36**, 3833–3854.
- Iacconi, P. (1995): Thermoluminescence of zircon. *Scan. Micr. Suppl.*, **9**, 13–34.
- Iacconi, P. & Caruba, R. (1980): Trapping and emission centres in X-irradiated zircon. III. Influence of trivalent rare-earth impurities. *Phys. Stat. Solidi (a)*, **62**, 589–596.
- Karali, T., Can., N., Townsend, P.D., Rowlands, A.P., Hanchar, J.M. (2000): Radioluminescence and thermoluminescence of rare earth elements and phosphorus-doped zircon. *Am. Mineral.*, **85**, 668–681.
- Kempe, U., Gruner, T., Renno, A.D., Wolf, D. (1997): Hf-rich zircons in rare-metal bearing granites: Magmatic or metasomatic origin? in “Mineral deposits: Research and exploration. Where do they meet?”, H. Papunen, ed. Balkema, Rotterdam, 643–646.
- Kempe, U., Gruner, T., Nasdala, L., Wolf, D. (2000): Relevance of cathodoluminescence for interpretation of U-Pb zircon ages (with an example of application to a study of zircons from the Saxonian Granulite Complex, Germany). in “Cathodoluminescence in Geosciences”, M. Pagel, V. Barbin, P. Blanc, D. Ohnenstetter, ed. Springer, Berlin, 415–455.
- Kempe, U., Bombach, K., Matukov, D., Schlothauer, T., Hutschenreuter, J., Wolf, D., Sergeev, S. (2004): Pb/Pb and U/Pb zircon dating of subvolcanic rhyolite as a time marker for Hercynian granite magmatism and Sn mineralisation in the Eibenstock granite, Erzgebirge, Germany: Considering effects of zircon alteration. *Mineral. Dep.*, **39**, 646–669.
- Kempe, U., Seltmann, R., Graupner, T., Rodionov, N., Sergeev, S. A., Matukov, D.I., Kremensky A.A. (2015): Concordant U-Pb SHRIMP ages of U-rich zircon in granitoids from the Murantau gold district (Uzbekistan): Timing of intrusion, alteration ages, or meaningless numbers. *Ore Geol. Rev.*, **65**, 308–326.
- Kempe, U., Thomas, S.M., Geipel, G., Thomas, R., Plötze, M., Böttcher, R., Grambole, G., Hoentsch, J., Trinkler, M. (2010): Optical absorption, luminescence, and electron paramagnetic resonance (EPR) spectroscopy of crystalline to metamict zircon: Evidence for formation of uranyl, manganese, and other optically active centers. *Am. Mineral.*, **95**, 335–347.
- Kempe, U., Trinkler, M., Pöpl, A., Hincinschi, C. (2016): Coloration of natural zircon. *Can. Mineral.*, **54**, 635–660.
- Knittel, E. & Williams, Q. (1993): High-pressure Raman spectroscopy of $ZrSiO_4$: Observation of the zircon to scheelite transition at 300 K. *Am. Mineral.*, **78**, 245–252.
- Kranert, C., Sturm, C., Schmidt-Grund, R., Grundmann, M. (2016): Raman tensor formalism for optically anisotropic crystals. *Phys. Rev. Lett.*, **116**, 1–5.
- Lenz, C. & Nasdala, L. (2015): A photoluminescence study of REE³⁺ emissions in radiation-damaged zircon. *Am. Mineral.*, **100**, 1123–1133.
- Lenz, C., Talla, D., Ruschel, K., Skoda, R., Götze, J., Nasdala, L. (2013): Factors affecting the Nd³⁺ (REE³⁺) luminescence of minerals. *Mineral. Petrol.*, **107**, 415–428.
- Ludwig, K.R. (2000): SQUID 1.00: A User’s Manual. Berkeley Geochronology Center Special Publication No 2, 2455 Ridge Road, Berkeley CA 94709, USA.
- Marsellos, A.E. & Garvers, J.I. (2010): Radiation damage and uranium concentration in zircon as assessed by Raman spectroscopy and neutron irradiation. *Am. Mineral.*, **95**, 1192–1201.
- Meldrum, A., Boatner, L.A., Zinkle, S.J., Wang, S.X., Wang, L.M., Ewing, R.C. (1999): Effects of dose rate and temperature on the crystalline-to-metamict transformation in the ABO₄ orthosilicates. *Can. Mineral.*, **37**, 207–221.

- Murakami, T., Chakoumakos, B.C., Ewing, R.C., Lumpkin, G.R., Weber, W.J. (1991): Alpha-decay event damage in zircon. *Am. Mineral.*, **76**, 1510–1532.
- Nasdala, L., Irmer, G., Wolf, D. (1995): The degree of metamictization in zircon: A Raman spectroscopic study. *Eur. J. Mineral.*, **7**, 471–478.
- Nasdala, L., Pidgeon, R.T., Wolf, D., Irmer, G. (1998): Metamictization and U–Pb isotopic discordance in single zircons: a combined Raman microprobe and SHRIMP ion probe study. *Mineral. Petrol.*, **62**, 1–27.
- Nasdala, L., Wenzel, M., Vavra, G., Irmer, G., Wenzel, T., Kober, B. (2001): Metamictization of natural zircon: accumulation vs. thermal annealing of radioactivity-induced damage. *Contrib. Mineral. Petrol.*, **141**, 125–144.
- Nasdala, L., Irmer, G., Jonckheere, R. (2002a): Radiation damage ages: Practical concept or impractical vision? – Reply to two comments on “Metamictization of natural zircon: Accumulation versus thermal annealing of radioactivity-induced damage”, and further discussion. *Contrib. Mineral. Petrol.*, **143**, 758–765.
- Nasdala, L., Lengauer, C.L., Hanchar, J.M., Kronz, A., Wirth, R., Blanc, P., Kennedy, A.K., Seydoux-Guillaume, A.-M. (2002b): Annealing radiation damage and the recovery of cathodoluminescence. *Chem. Geol.*, **191**, 121–140.
- Nasdala, L., Zhang, M., Kempe, U., Panczer, G., Gaft, M., Andrut, M., Plötze, M. (2003): Spectroscopic methods applied to zircon. in “Zircon”, J.M. Hanchar, P.W.O. Hoskin, ed. Reviews in Mineralogy and Geochemistry, 53, Mineralogical Society of America, Washington D.C., 145–181.
- Nasdala, L., Rainers, P.W., Garver, J.I., Kennedy, A.K., Stern, R.A., Balan, E., Wirth, R. (2004): Incomplete retention of radiation damage in zircon from Sri Lanka. *Am. Mineral.*, **89**, 219–231.
- Nasdala, L., Hanchar, J.M., Kronz, A., Whitehouse, M.J. (2005): Long-term stability of alpha particle damage in natural zircon. *Chem. Geol.*, **220**, 83–103.
- Nasdala, L., Kronz, A., Hanchar, J.M., Tichomirowa, M., Davis, D. W., Hofmeister, W. (2006): Effects of natural radiation damage on back-scattered electron images of single crystals of minerals. *Am. Mineral.*, **91**, 1739–1746.
- Nasdala, L., Miletich, R., Ruschel, K., Váczi, T. (2008): Raman study of radiation-damaged zircon under hydrostatic compression. *Phys. Chem. Mineral.*, **35**, 597–602.
- Nasdala, L., Kronz, A., Wirth, R., Váczi, T., Pérez-Soba, C., Willner, A., Kennedy, A.K. (2009): The phenomenon of deficient electron microprobe totals in radiation-damaged and altered zircon. *Geochim. Cosmochim. Acta*, **73**, 1637–1650.
- Nasdala, L., Hanchar, J.M., Rhede, D., Kennedy, A.K., Váczi, T. (2010): Retention of uranium in complexly altered zircon: An example from Bancroft, Ontario. *Chem. Geol.*, **269**, 290–300.
- Nelson, D.R., Robinson, B.W., Myers, J.S. (2000): Complex geological histories extending for ≥ 4.0 Ga deciphered from xenocryst zircon microstructures. *Earth Planet. Sci. Lett.*, **181**, 89–102.
- Oliver, W.C., McCallum, J.C., Chakoumakos, B.C., Boatner, L.A. (1994): Hardness and elastic modulus of zircon as a function of heavy-particle irradiation dose: II. Pb-ion implantation damage. *Rad. Eff. Def. Solid.*, **132**, 131–141.
- Özkan H. (1976): Effect of nuclear radiation on the elastic moduli of zircon. *J. Appl. Phys.*, **47**, 4772–4779.
- Özkan, H & Jamieson, J.C. (1978): Pressure dependence of the elastic constants of nonmetamict zircon. *Phys. Chem. Minerals*, **2**, 215–224.
- Palenik, Ch.S., Nasdala, L., Ewing R.C. (2003): Radiation damage in zircon. *Am. Mineral.*, **88**, 770–781.
- Park, B., Weber, W.J., Corrales, L.R. (2001): Molecular-dynamics simulation study of threshold displacements and defect formation in zircon. *Phys. Rev. B*, **64**, 174108-1–174109-16.
- Pérez-Soba, C., Villaseca, C., González del Tánago, J., Nasdala, L. (2007): The composition of zircon in the peraluminous Hercynian granites of the Spanish Central System batholith. *Can. Mineral.*, **45**, 509–527.
- Platt, R.G. & Woolley, A.R. (1986): The mafic mineralogy of the peralkaline syenites and granites of the Mulanje complex, Malawi. *Mineral. Mag.*, **50**, 85–99.
- Platt, R.G., Wall, F., Williams, C.T., Woolley, A.R. (1987): Zirconolite, chevkinite and other rare earth minerals from nepheline syenites and peralkaline granites and syenites of the Chilwa Alkaline Province, Malawi. *Mineral. Mag.*, **51**, 253–263.
- Pointer, C.M., Ashworth, J.R., Ixer, R.A. (1988): The zircon-thorite mineral group in metasomatized granite, Ririwai, Nigeria. 2. Zoning, alteration and exsolution in zircon. *Mineral. Petrol.*, **39**, 21–37.
- Presser, V. & Glotzbach, C. (2009): Metamictization in zircon: Raman investigation following a Rietveld approach. Part II: Sampling depth implication and experimental data. *J. Raman Spectr.*, **40**, 499–508.
- Puppels, G.J., Colier, W., Olminkhof, J.H.F., Otto, C., de Mul, F.F., Greve, J. (1991): Description and performance of a highly sensitive confocal Raman microspectrometer. *J. Raman Spectr.*, **22**, 217–223.
- Pyatenko, Y.A. (1970): On the behaviour of metamict minerals during heating under respect of the general problem of metamictization. *Geokhimiya*, **9**, 1077–1083.
- Reddy, S.M., Timms, N.E., Trimby, P., Kinny, P.D., Buchan, C., Blake, K. (2006): Crystal-plastic deformation of zircon: A defect in the assumption of chemical robustness. *Geology*, **34**, 257–260.
- Reddy, S.M., Timms, N.E., Hamilton, P.J., Smyth, H.R. (2009): Deformation of microstructure in magmatic zircon and implications for diffusion. *Contrib. Mineral. Petrol.*, **157**, 231–244.
- Ríos, S. & Salje, E.K.H. (1999): Diffuse x-ray scattering from weakly metamict zircon. *J. Phys. Condens. Matt.*, **11**, 8947–8956.
- Ríos, S., Malcherek, T., Salje, E.K.H., Domeneghetti, C. (2000a): Localized defects in radiation-damaged zircon. *Acta Crystallogr. B*, **56**, 947–952.
- Ríos, S., Salje, E.K.H., Zhang, M., Ewing, R.C. (2000b): Amorphization in zircon: evidence for direct impact damage. *J. Phys.: Condens. Matt.*, **12**, 2401–2412.
- Rizzo, G., Spiess, R., Hanchar, J.M. (2000): Non xenotime-type substitution within zircon: implications for lattice distortion. in “Integrative geosciences solutions: A start for the new millennium”, American Geophysical Union 2000 Spring Meeting, Washington D.C. Program with Abstracts, GS31A-05.
- Rudenko, S.A. (1968): The phenomenon of metamict decay of minerals and its position in mineral formation processes. *Zap. Vses. Mineral. Obshch.*, **97**, 565–570 (in Russian).

- Sahama, T.G. (1981): Growth structure in Ceylon zircon. *Bull. Mineral.*, **104**, 89–94.
- Salje, E.K.H., Chrosch, J., Ewing, R.C. (1999): Is “metamictization” of zircon a phase transition? *Am. Mineral.*, **84**, 1107–1116.
- Sanjurjo, J.A., Lopez-Cruz, E., Burns, G. (1983): High-pressure Raman study of zone centre phonons in PbTiO₃. *Phys. Rev. B*, **28**, 7260–7268.
- Smith, D.G.W., de St. Jorre, L., Reed, S.J.B., Long, J.V.P. (1991): Zonally metamictized and other zircons from Thor Lake, Northwest Territories. *Can. Mineral.*, **29**, 301–309.
- Solntsev, V.P. & Shcherbakova, M.Y. (1972): Electron spin resonance of Ti³⁺ in α-quartz and zircon. *J. Struct. Chem.*, **13**, 859–861.
- (1974): Mechanism of charge compensation and substitution of Nb and Y in the zircon structure. *Neorg. Mater.*, **10**, 1834–1838 (in Russian).
- Soman, A., Geisler, T., Tomaschek, F., Grange, M., Berndt, J. (2010): Alteration of crystalline zircon solid solutions: a case study on zircon from an alkaline pegmatite from Zomba-Malosa, Malawi. *Contrib. Mineral. Petrol.*, **160**, 909–930.
- Speer, J.A. (1982): Zircon. in “Orthosilicates”, P.H. Ribbe, ed. Reviews in Mineralogy, 5, Mineralogical Society of America, Washington D.C., second edition, 67–112.
- Speer, J.A. & Cooper, B.J. (1982): Crystal structure of synthetic hafnon, HfSiO₄, comparison with zircon and the actinide orthosilicates. *Am. Mineral.*, **67**, 804–808.
- Syme, R.W.G., Lockwood, D.J., Kerr, H.J. (1977): Raman spectrum of synthetic zircon (ZrSiO₄) and thorite (ThSiO₄). *J. Phys. C: Solid State Phys.*, **10**, 1335–1348.
- Tichomirova, M., Whitehouse, M.J., Nasdala, L. (2005): Resorption, growth, solid state recrystallisation, and annealing of granulite facies zircon – a case study from the Central Erzgebirge, Bohemian Massif. *Lithos*, **82**, 25–50.
- Trofimov, A.K. (1962): The nature of the line luminescence spectra of zircon. *Geokhimiya*, **11**, 970–975 (in Russian).
- Ushikubo, T., Kita, N.T., Cavosie, A.J., Wilde, S.A., Rudnick, R.L., Valley, J.W. (2008): Lithium in Jack Hills zircons: Evidence for extensive weathering of Earth’s earliest crust. *Earth Planet. Sci. Lett.*, **272**, 666–676.
- Vance, E.R. & Mackey, D.J. (1974): Optical study of U⁵⁺ in zircon. *J. Phys. C: Solid State Phys.*, **7**, 1898–1908.
- (1978): Optical spectra of U⁴⁺ and U⁵⁺ in zircon, hafnon, and thorite. *Phys. Rev. B*, **18**, 185–189.
- Vinokurov, V.M., Zaripov, M.M., Stepanov, V.G., Chirkin, G.K., Shekun, L.Y. (1964): Paramagnetic resonance of Nb⁴⁺ ions in zircon single crystals. *Sov. Phys. Solid State*, **5**, 1487–1488.
- Votyakov, S.L. & Samojlov, M.V. (1981): Defects in zircon and its thermoluminescence. in “Crystallochemical peculiarities of silicate minerals from the Urals”, Ural Scientific Centre of the Academy of Sciences of the SSSR, 45–52 (in Russian).
- Votyakov, S.L., Krokhaliev, V.Y., Krasnobaev, A.A. (1985): Recombination luminescence in zircon. *Zhur. Priklad. Spekt.*, **42**, 928–935 (in Russian).
- Wang, X.L., Coble, M.A., Valley, J.W., Shu, X.J., Kitajima, K., Spicuzza, M.J., Sun, T. (2014): Influence of radiation damage on Late Jurassic zircon from southern China: Evidence from *in situ* measurements of oxygen isotopes, laser Raman, U–Pb ages, and trace elements. *Chem. Geol.* **389**, 122–136.
- Wang, W., Scarratt, K., Emmett, J.L., Breeding, C.M., Douthit, T.R. (2006): The effects of heat treatment on zircon inclusions in Madagascar sapphires. *Gems & Gemology*, **42**, 134–150.
- Wasilewski, P.J., Senftle, F.E., Vaz, J.A., Thorpe, A.N., Alexander, C.C. (1973): A study of the natural α-recoil damage in zircon by infrared spectra. *Rad. Eff.*, **17**, 191–199.
- Weber, W.J. & Maupin, G.D. (1988): Simulation of radiation damage in zircon. *Nucl. Instr. Meth. Phys. Res.*, **B32**, 512–515.
- Wiedenbeck, M., Alle, P., Corfu, F., Griffin, W.L., Meier, M., Oberli, F., von Quadt, A., Roddick, J.C., Spiegel, W. (1995): Three natural zircon standards for U–Th–Pb, Lu–Hf, trace element and REE analysis. *Geostand. Newslett.*, **19**, 1–3.
- Williams, I.S. (1998): U–Th–Pb geochronology by ion microprobe. in “Applications of Microanalytical Techniques to Understanding Mineralizing Processes”, M.A. McKibben, I.W.C. Shanks, W.J. Ridley, ed. Reviews in Economic Geology, 1–35.
- Woodhead, J.A., Rossman, G.R., Silver, L.T. (1991): The metamictization of zircon: Radiation dose-dependent structural characteristics. *Am. Mineral.*, **76**, 74–82.
- Woolley, A.R. (1987): Lithosphere metasomatism and the petrogenesis of the Chilwa Province of alkaline igneous rocks and carbonatites, Malawi. *J. Afr. Earth Sci.*, **6**, 891–898.
- Woolley, A.R. & Jones, G.C. (1987): The petrochemistry of the northern part of the Chilwa alkaline province, Malawi. in “Alkaline igneous rocks”, J.G. Fitton, B.G.J. Upton, ed. Geological Society Special Publication, London, **30**, 335–355.
- Woolley, A.R. & Platt, R.G. (1986): The mineralogy of nepheline syenite complexes from the northern part of the Chilwa Province, Malawi. *Mineral. Mag.*, **50**, 597–610.
- Zhang, M. & Salje, E.K.H. (2001): Infrared spectroscopic analysis of zircon: Radiation damage and the metamict state. *J. Phys.: Condens. Matt.*, **13**, 3057–3071.
- Zhang, M., Salje, E.K.H., Farnan, I., Graeme-Barber, A., Daniel, P., Ewing, R.C., Clark, A.M., Leroux, H. (2000): Metamictization of zircon: Raman spectroscopic study. *J. Phys.: Condens. Matt.*, **12**, 1915–1925.
- Zhang, M., Salje, E.K.H., Ewing, R.C. (2003): Oxidation state of uranium in metamict and annealed zircon: near-infrared spectroscopic quantitative results. *J. Phys.: Condens. Matt.*, **15**, 3445–3470.
- Zhirov, K.K. (1952): On the transition of zircon into the metamict state. *Dokl. Akad. Nauk SSSR*, **85**, 889–891 (in Russian).

Received 13 April 2017

Modified version received 26 September 2017

Accepted 30 January 2018

4.4 Assistant Professor at Albert Ludwig University

After several years of practice at professional level in SEM imaging and analytics, I decided to return to the academic community.

I obtained in 2011 an assistant Professor position within the geology department on the Albert Ludwig University in Freiburg im Breisgau (Germany). My contract was on a two years fixed-term basis.

I integrated the research team of Professor Kenkmann within a project focused on impact driven mechanical effects affecting a variety of earth crust materials. This discipline was totally new to me and therefore exciting plus challenging. Dynamic processes such as pressure and shock waves induce a specific set of material responses leading to failure (Melosh, 1989). These research activities enriched my earth sciences culture while using my multidisciplinary approach in terms of fieldwork, microfabric analysis and rock petrophysical plus mechanical properties characterization.

My activities within the research group and the MEMIN (Multidisciplinary Experimental and Modeling Impact Research Network, DFG – Research Unit FOR – 887 Experimental Impact Cratering) projects were multiple. I was in charge of putting back into service and upgrading a FORM+TEST Alpha 2-3000 S triaxial device, having a 3000 kN axial load, 150 MPa confining pressure and 200°C heating capacities. I also received the responsibility to develop the EBSD sample preparation facility and manage the SEM laboratory. I optimized the available EBSD system and participated to installation of an EDS Oxford Instruments X-Max EDS detector.

My experience in terms of microfabric analysis was used to characterize deformation features of a steel projectile during an impact experiment (Kenkmann et al., 2013). Hypervelocity cratering have been modeled using centimeter-size steel projectiles impacting sandstone targets at velocities ranging between 3400 and 5300 ms⁻¹. In this contribution, I have been interested in the deformation mechanisms active in the projectile itself using a combination of SEM imaging and EBSD analysis. Plastic deformation was dominant in the projectile and was accommodated by a combination of dislocation glide and climb. Some brittle fracturing and melting of both projectile and sandstone target were observed as well. At the highest speeds, a significant amount of grain annealing was noticed within the projectile.

I also participated to a research program dedicated to dynamic load of quartz crystals. I proposed to use both a diamond anvil cell and synchrotron radiation at PETRA III, DESY Hamburg (Germany). This setup permits to reach pressures in the GPa range, i.e. well above the values obtainable in the previously mentioned triaxial device while studying simultaneously phase transitions in the mineral. The goal was to investigate the development of high pressure α quartz polymorphs under dynamic and non-hydrostatic conditions. Our experiments revealed that α quartz did not transform to coesite as predicted from phase diagram during static experiments at equilibrium conditions but was instead amorphized and partially converted to stishovite between 20.7 and 28 GPa (Carl et al., 2017).

Besides my research and laboratory management activities, I was in charge of several lectures in the field of petrophysics, accretionary prism modeling in sand box apparatuses and general geology. I participated in several field camps in central Germany and organized a field trip in the Armorican massif in Brittany (France).

Deformation and melting of steel projectiles in hypervelocity cratering experiments

T. KENKMANN^{1*}, G. TRULLENQUE¹, A. DEUTSCH², L. HECHT³, M. EBERT³, T. SALGE⁴,
F. SCHÄFER⁵, and K. THOMA⁵

¹Institut für Geowissenschaften, Albert-Ludwigs-Universität Freiburg (ALU), Albertstr. 23-B, 79104 Freiburg, Germany

²Institut für Planetologie, Westfälische Wilhelms-Universität Münster (WWU), Wilhelm-Klemm-Str. 10, 48149 Münster, Germany

³Museum für Naturkunde (MfN), Leibniz Institut an der Humboldt-Universität Berlin, Invalidenstraße 43, 10115 Berlin, Germany

⁴Bruker AXS Microanalysis, Schwarzschildstrasse 12, 12489 Berlin, Germany

⁵Fraunhofer-Institut für Kurzezeitdynamik, Ernst-Mach Institut Freiburg (EMI), Freiburg, Germany

*Corresponding author. E-mail: thomas.kenkmann@geologie.uni-freiburg.de

(Received 15 March 2012; revision accepted 04 October 2012)

Abstract—We carried out hypervelocity cratering experiments with steel projectiles and sandstone targets to investigate the structural and mineralogical changes that occur upon impact in the projectile and target. The masses of coherent projectile relics that were recovered in different experiments ranged between 58% and 92% of their initial projectile masses. A significant trend between impact energy, the presence of water in the target, and the mass of projectile relics could not be found. However, projectile fragmentation seems to be enhanced if the target contains substantial amounts of water. Two experiments that were performed with 1 cm sized steel projectiles impacting at 3400 and 5300 m s⁻¹ vertically onto dry Seeberger sandstone were investigated in detail. The recovered projectiles are intensely plastically deformed. Deformation mechanisms include dislocation glide and dislocation creep. The latter led to the formation of subgrains and micrometer-sized dynamically recrystallized grains. In case of the 5300 m s⁻¹ impact experiment, this deformation is followed by grain annealing. In addition, brittle fracturing and friction-controlled melting at the surface along with melting and boiling of iron and silica were observed in both experiments. We estimated that heating and melting of the projectile impacting at 5300 m s⁻¹ consumed 4.4% of the total impact energy and was converted into thermal energy and heat of fusion. Beside the formation of centimeter-sized projectile relics, projectile matter is distributed in the ejecta as spherules, unmelted fragments, and intermingled iron-silica aggregates.

INTRODUCTION

Abundant extraterrestrial material has been delivered to Earth throughout its history via impact events; the physical and chemical processes that affect the composition and distribution of projectile matter upon impact, however, are not yet understood in sufficient detail (Kearsley et al. 2004; Koeberl 2007). Fragments of the projectile are preserved at young, simple impact craters, like Meteor (Barringer) Crater, USA (Buchwald 1975; Mittlefehldt et al. 2005); Wolfe Creek, Australia (Knox 1967); Wabar, Saudi Arabia, Monturaqui, Chile, Henbury, Australia (Gibbons et al. 1976); or Kamil, Egypt (Folco et al. 2010, 2011; D’Orazio et al. 2011).

Large craters only rarely contain projectile relics (Maier et al. 2006). Traces of the projectile occur in larger and older impact structures as chemical components (e.g., nickel, chromium, osmium isotopes, platinum group elements [PGEs]) in various settings, including impact melt rocks and breccias, and fractures in the crater floor (Grieve et al. 2006; Tagle and Hecht 2006; Tagle and Berlin 2008). This “meteoritic component” allows the deduction of the type of projectile via measurement of the element abundances and ratios of the PGEs, although interelement fractionation of the PGEs during emplacement or postimpact alteration may hamper a correct identification of the projectile type. The best-known example for a meteoritic component is the iridium

anomaly in the worldwide Cretaceous-Paleogene (former “K/T”) event bed that represents the distal ejecta of the approximately 200 km sized Chicxulub impact structure, Yucatán, Mexico. The Chicxulub impact event triggered the “K/T” mass extinction event (Hildebrand et al. 1991; Schulte et al. 2010).

The physical conditions during emplacement of projectile matter, modes of target-projectile mixing, and possible fractionation processes are not well constrained (e.g. Evans et al. 1994; Koeberl 1998). Projectile matter could be emplaced in condensates from a vapor phase, as melt droplets, as fine-grained solid material, or as spall fragments. Experimental cratering with well-defined projectile matter and sophisticated ejecta catcher arrangements is a good approach to study projectile dissemination (Shoemaker et al. 1963; Jammes et al. 1983; Rowan et al. 1996; Kearsley et al. 2007). Previous attempts to detect projectile matter in melt lithologies produced by hypervelocity experiments were made with scanning electron microscope (SEM) or electron microprobe (EMP) analysis (Hörz et al. 1983; Rowan and Hörz 1995). These experiments were performed with metal targets (e.g., Au, Cu, Al, Mo), and rocks (e.g., basalt glass, dunite) or Fe-Ni-PGE alloy (Evans et al. 1994) as projectiles. Only Shoemaker et al. (1963) and Jammes et al. (1983), who investigated projectiles, performed experiments in approximate analogy to nature by using quartz sand or sandstone as targets. Generally, only limited indications of mixing between projectile and target melts were reported in these experiments. For silicate projectiles, Hörz et al. (1983) and Rowan et al. (1996) observed fractionation between some major elements, which was attributed to selective oxidation/reduction and/or selective vaporization processes. Impact-related high-temperature vaporization of silicates and metals was also investigated by means of laser pulse experiments (Gerasimov et al. 2005).

The analysis of the deformation inventory of projectile relics has not been considered in detail so far and is a focus of this contribution. We present results of hypervelocity cratering experiments using steel projectiles (Figs. 1 and 2) and sandstone targets. We specifically focus on two experiments that were conducted as a pilot study (P1-2808) (Schäfer et al. 2006; Kenkmann et al. 2007, 2011) and test shot (3232) in the framework of the Multidisciplinary Experimental and Modeling Impact Research Network (MEMIN), but include for comparison recent MEMIN experiments. One major goal of this study is to reach a better understanding of the parameters that control the fate of projectiles in cratering events, i.e., their dissemination into the target by injection, and ejection, vaporization, and condensation. This study resulted in the selection of appropriate projectile materials (Ebert et al. 2013) for the recent series

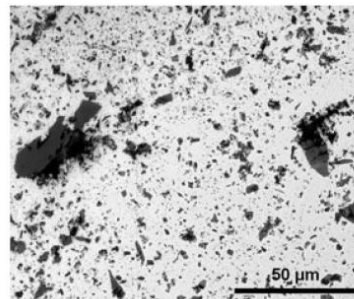


Fig. 1. Optical micrograph of steel SAE 4130 used as a projectile in the MEMIN cratering experiments P1-2808 and 3232: The homogeneous matrix is peppered with heterogeneously distributed Si-C-rich domains (dark to medium grey) of various sizes and compositions. Note that the SiC domains are primary and are not a relic of the sample grinding and polishing procedure. Reflected light, // nicols.

of impact experiments (Poelchau et al. 2013). The impact velocities of the experiments presented here are comparable to those typical for small iron projectiles decelerated by the Earth’s atmosphere and, hence, are applicable to small terrestrial craters like the Kamil crater (D’Orazio et al. 2011).

METHODS

Experimental Setup

Cratering experiments were conducted with a two-stage light-gas gun developed at the Ernst-Mach-Institute (EMI), Efringen-Kirchen, Germany (Schäfer et al. 2006). We fired steel spheres of 10 and 12 mm diameter and masses of 4.1–4.6 g with velocities ranging between 2500 and approximately 5300 m s⁻¹ vertically onto blocks of Seeberger Sandstein. Cratering and ejection processes were monitored by a high-speed framing camera (Fig. 3). Details of the experimental setup and the obtained craters are given in Kenkmann et al. (2011) and Poelchau et al. (2013).

Geochemical Analysis

Whole rock geochemical analysis of the target was carried out by X-ray fluorescence spectroscopy (XRF) on glass pellets at the Museum of Natural History Berlin (MfN). In addition, projectile and target materials were characterized by optical and electron microscopy. The deformed samples were analyzed using a scanning electron microscope (SEM, JEOL-JSM 6300 at MfN; LEO 1525 field emission gun microscope at Albert-Ludwigs-Universität Freiburg, ALU) in backscattered

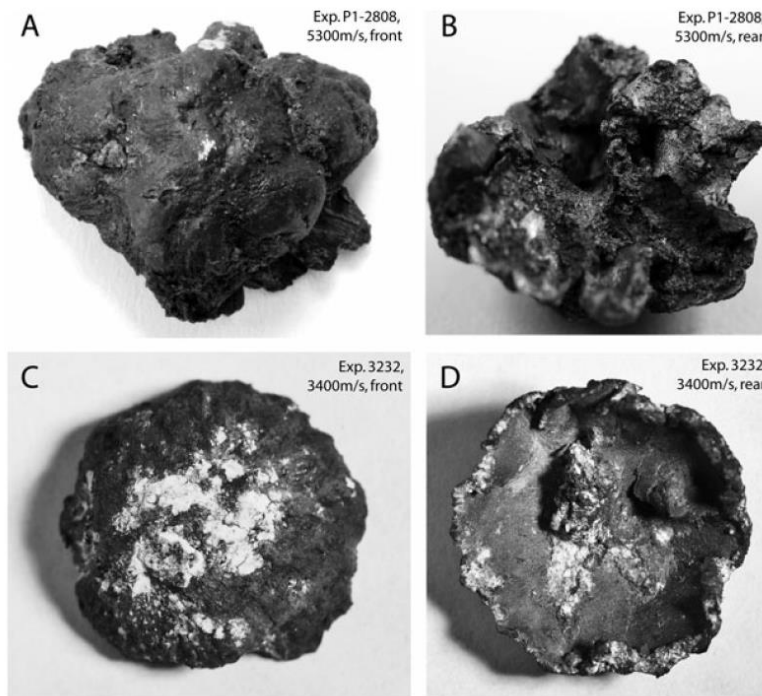


Fig. 2. Recovered steel projectiles. A) front, B) rear of the initially spherical projectile of experiment P1-2808. C) front, D) rear of the projectile relic of test shot 3232. Image width: approximately 2 cm.



Fig. 3. High-speed shadowgraph image of dry experiment P1-2808, showing a reflected projectile relic (black arrow indicates bright particle) as it overtakes the central plume. The brightness indicates a high temperature.

(BSE) and secondary electron mode (SE). High-resolution element mapping (4076×3072 pixels) was acquired with a Bruker AXS Quantax EDS system using a silicon drift detector that allows ultra-high resolution. The energy resolution of ≤ 125 eV at Mn-K α , resulting in ≤ 48 eV at C-K α worked at count rates of 100,000 cps.

Texture Analysis

For texture analysis of projectile relics, the technique of electron back scattered diffraction (EBSD) was applied. EBSD enables the measurement of the crystallographic orientation of minerals and metals, and the calculation of misorientation axes and angles between any two data points (Prior et al. 1999). Orientation contrast (OC) images allow the mapping of all misorientation boundaries in a specimen, and thus provide a location map for EBSD analyses. EBSD coupled to OC imaging in the SEM enables complete specimen microtextures to be determined (Prior et al.

1999). For the analysis of the texture, the projectile relic was fully impregnated in epoxy resin and sectioned using a 0.8 mm thick diamond blade mounted on a precision saw. A low rotation speed and sufficient cooling were used to minimize preparation-related deformation during cutting. Grinding and subsequent polishing were performed using silicon carbide lapping films and polycrystalline diamond suspension down to 3 μm grain size. A final surface treatment with aluminium oxide suspension was applied using a soft synthetic cloth under the sample's own weight for 15 min.

SEM-EBSD work at the LEO 1525 field emission gun microscope (ALU) was performed under high vacuum conditions with a 120 μm aperture. Sample charging due to surface oxidation was avoided by vapor-depositing a 2–3 nm thick carbon film on the polished surface. Prior to mounting in the SEM chamber, the sample was demagnetized using an electromagnetic coil to avoid image drift during acquisition. Orientation contrast images on steel were made at 12 kV acceleration voltage and a sample-to-backscatter detector distance of less than 2 mm. Atomic contrast images were taken using the same set-up, but longer working distances. EBSD analysis was performed using a commercial Oxford Crystal system with a modified detector. The SEM was operated at 18 kV and with a 27 mm working distance. Due to hardware limitations, the minimum electron back scattered pattern acquisition time was 150 milliseconds per point. EBSD maps were constructed via beam scanning with a step size of 0.15 μm . The crystal lattice of iron bcc (body-centered-cubic) was used for automatic indexation of the captured diffraction pattern.

RESULTS OF THE CRATERING EXPERIMENTS

Characterization of Projectile and Target

Our analysis mainly concentrated on the experiments P1-2808 and 3232. In these experiments, we used spherical projectiles of alloyed heat-treatable steel SAE 4130 (German Industry standard material number DIN 1.7218) whose composition is given in Table 1. Figure 1 illustrates the textural and chemical heterogeneities of this steel. The homogeneous matrix of this steel contains heterogeneously distributed Si-C-rich domains of various sizes and compositions (Si 25–70 wt%, C < 75 wt%). The melting temperature of SAE 4130 is approximately 1430 °C.

The target material is upper Triassic Seeberger Sandstein, a sandstone quarried at Seeberg near Gotha, Germany (Stück et al. 2011; TRACO-company). The bed chosen for the target block (bank 5) is an arenitic sandstone with grain size of 0.17 ± 0.01 mm (Kenkmann et al. 2011). It exhibits a centimeter-spaced layering with

Table 1. Chemical composition of the projectile matter in experiment P1-2808 and test shot 3232 used for this study (steel SAE).

(wt%)	Projectile steel SAE
C	< 0.33
Si	< 0.3
P	< 0.035
S	< 0.04
Cr	0.92 ± 0.17
Mn	0.51 ± 0.10
Fe	97.3–98.2
Co	0.14 ± 0.03
Ni	0.07 ± 0.02
Mo	0.16 ± 0.05

a porosity varying between 12 and 20 vol%. Quartz grains often contain thin coatings of iron oxides and clay minerals. Accessory minerals are feldspar, mica, zircon, and hematite. The rock has the following composition (XRF) [wt%]: 97.2 SiO₂, 0.11 TiO₂, 1.2 Al₂O₃, 0.25 Fe₂O₃, 0.08 CaO, 0.02 Na₂O, 0.12 K₂O, 0.6 LOI (loss on ignition).

In subsequent experiments, we also used the iron meteorite Campo del Cielo and the alloyed steel D290-1 as projectiles (Table 2) (Ebert et al. 2013; Poelchau et al. 2013).

Experiment

In experiment P1-2808, a 1 cm steel sphere (4.1 g) was launched into an air-dry sandstone block with an impact velocity of 5340 m s⁻¹. The impact energy was 58.4 kJ. A comprehensive description of the experiments is given in Kenkmann et al. (2011). Planar impact approximation using coefficients for iron and Coconino sandstone (Kieffer and Simonds 1980) yielded a peak shock pressure of 70 GPa (Poelchau et al. 2013). The air pressure in the target chamber was 500 mbar. The test shot 3232 was carried out under identical condition with an impact velocity of 3400 m s⁻¹ (23.7 kJ). For experimental details of the experiments listed in Table 2, we refer to Poelchau et al. (2013).

Recovered Projectile

In the experiment P1-2808, 2.84 g (69 wt%) of the projectile was recovered from a fiber board mounted approximately 55 cm adjacent to the target surface. The remaining 31 wt% of the projectile were melted or vaporized, or dispersed to very fine fragments. The soft-wood fiber building board surrounding this piece was burnt, documenting the high temperature of the steel fragment. This piece was traced in one shadowgraph image (Fig. 3) as it overtook the expanding central

Table 2. MEMIN experiments in which larger projectile relics were recovered. For experimental details, see Poelchau et al. (2013).

Experiment	Projectile material	Sphere diameter (mm)	Impact velocity (m s ⁻¹)	Projectile mass (g)	Impact energy (kJ)	Target conditions (sandstone)	Target dimension (cm)	Projectile relic mass (g) (%)		Projectile relic characteristics
P1-2808	SAE 4130 steel	10	5340	4.1	58.4	Dry	100 × 50 × 50	2.84	69.27	One large bowl-shaped fragment
P2-2809	SAE 4130 steel	10	5270	4.1	56.9	Wet – 44%	100 × 50 × 50	–	–	Tiny fragments < 1 mm
3232	SAE 4130 steel	10	3400	4.1	23.7	Dry	100 × 50 × 50	~3.0	~73	One large bowl-shaped fragment
E1-3382	D290-1 steel	12	4564	4.6	47.9	Dry	80 × 80 × 50	3.23	70.19	One mid-size bowl-shaped fragment and irregular-shaped fragments
E2-3383	D290-1 steel	12	4578	4.6	48.2	Wet – 50%	80 × 80 × 50	2.68	58.36	One small bowl-shaped fragment and irregular-shaped fragments
D4-3299	Iron meteorite	10	3507	4.12	25.3	Dry	50 × 50 × 50	2.95	71.71	One large bowl-shaped fragment
D5-3300	Iron meteorite	10	2503	4.14	13.0	Dry	50 × 50 × 50	3.24	78.33	One large bowl-shaped fragment
E3-3384	Iron meteorite	12	4590	4.6	48.5	Wet – 50%	80 × 80 × 50	4.25	92.32	Irregular-shaped fragments

plume at a speed of about 450 m s⁻¹ at 280 μs after the initial contact of the projectile with the target.

In the experiment 3232, 73% of the projectile was recovered. Projectiles were also recovered from other MEMIN experiments (Fig. 4; Table 2). The masses of coherent projectile relics range between 58% and 92% of their initial projectile masses. A significant trend between impact energy and mass of the recovered projectile relic could not be found (Fig. 5). Likewise, no systematic correlation could be determined between the water content of the target and the recovery rate of the projectile. However, the chance of fragmentation of the projectile is enhanced if target water is present. For instance, in experiment E3-3384 (Table 2; Fig 4D), numerous irregularly formed shrapnel fragments developed. In experiment P2-2809 (Table 2), no larger fragments could be collected.

Surface Features of the Deformed Projectile

The recovered projectile relics all have the shape of a deformed bowl with a convex outer and an irregularly

formed or concave inner side, a serrated, sometimes fragmented brim, and a knobby region in the center of the inner side (Figs. 2 and 4). The overall shape points to intense plastic deformation of the projectiles. The detailed surface analysis of the projectile relic of experiment P1-2808 shows that the serrated rim is formed by brittle fracturing under tensile stresses, yet the fracturing is intimately linked with melting (Figs. 6A–D). Bubbles and droplets (Figs. 6A, 6C, 7C, and 7D) indicate a temperature near the liquid–vapor transition of the steel. Delicate melt filaments bridge the open fissures (Figs. 6C and 6D). They indicate a rather low viscosity of the melt. The convex-shaped part of the projectile relic contains arrangements of parallel trending grooves and striae, which are similar to slickenside surfaces that develop on shear planes (Fig. 7A). The orientation of striae and grooves are perpendicular to the serrated brim. Some shear planes contain tiny spheroids (Fig. 7B). Foam textures of burst spheroids indicate boiling (Figs. 7C–D) as a result of shock and shear heating. The boiling temperature of iron at ambient pressure is approximately 2750 °C. The SEM analyses of

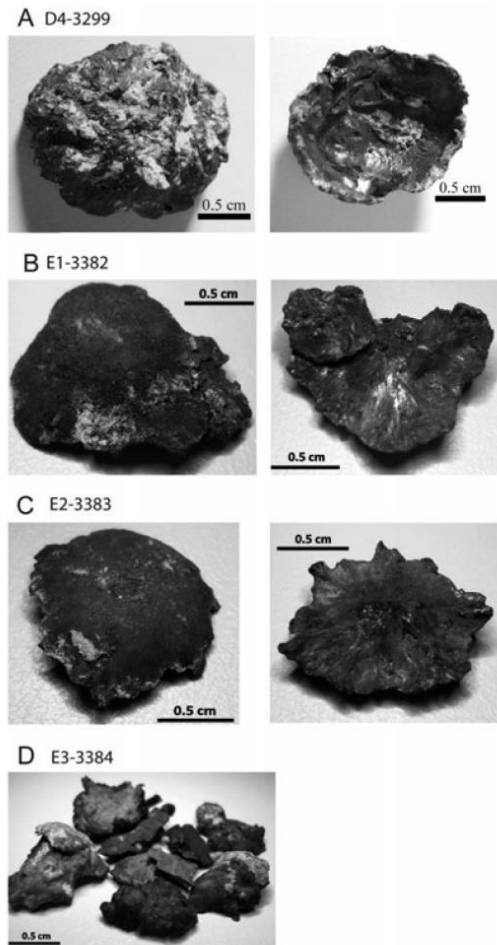


Fig. 4. Morphologies of recovered projectile relics of MEMIN experiments. Front and rear sides are shown for each projectile relic. Shrapnel-like splinters developed in experiment E3-3384 that was performed with a partly water-saturated target. Experimental details are listed in Table 2 and in Poelchau et al. (2013).

the composition of melt and spheroids suggest melting of projectile and target (Fig. 8). Mixing of iron and silica occurs in various proportions, although Fe analysis in Si-melt is complicated by the presence of tiny Fe-droplets (Ebert et al. 2013). A minor fraction of the Si-melt may have originated from the SiC-rich domains in the steel (Fig. 1). EDX analyses show that the Fe-spherules contain traces of Ca, Al, and Ti on their surfaces. Sources of these elements are likely the phyllosilicate

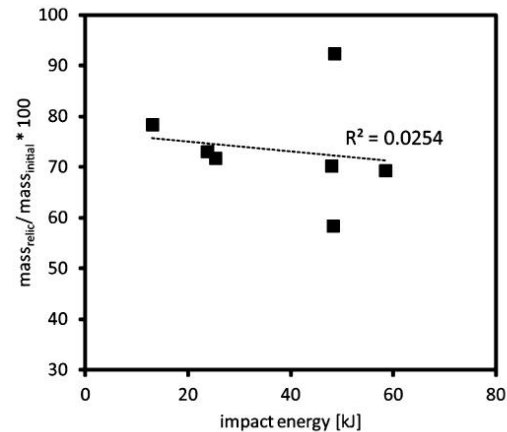


Fig. 5. The ratio of the projectile relic mass to the initial mass of the projectile strongly scatters and shows no significant correlation with the impact energy. Data are taken from Table 2.

coatings around the quartz grains and Ti-oxide minerals in the target sandstone. Deposition of these coatings may be due to selective absorption or condensation.

Mosaics of atomic contrast BSE images provide overviews of cross-sections of the projectile relics of experiment P1-2808 and 3232 (Figs. 9A and 9B). Their surfaces are partly covered by highly deformed discontinuous layers with thickness varying between a few micrometers and several millimeters. They occur along the convex and concave sides of the projectiles and, in the case of P1-2808, also along fractures within the main body of the projectile relic. In both experiments, these layers are composed of highly shocked and fragmented quartz crystals impregnated by a matrix consisting of a composite silica-oxide and steel melt (Fig. 9D) that was welded to the projectile surface. Evidence of melting is given by the presence of quenched Fe-droplets and a foam structure indicative of degassing in both experiments. The amorphous nature of the melt is confirmed by the absence of an electron diffraction pattern in these areas. In the case of experiment P1-2808 in which a higher level of shock was achieved, all quartz grains show multiple sets of planar deformation features (PDF) (Fig. 9D) and the grains are welded by lechatelierite. In experiment 3232, PDFs are less frequent.

In experiment 3232, a single crystal (80 μm) of zircon (Fig. 9C) was found in this outer layer. It shows intersecting planar to curvi-planar and lensoid microstructures of a few micrometer width. BSE orientation contrasts change abruptly and are either lower or higher than the host grain, suggesting that the lamellae

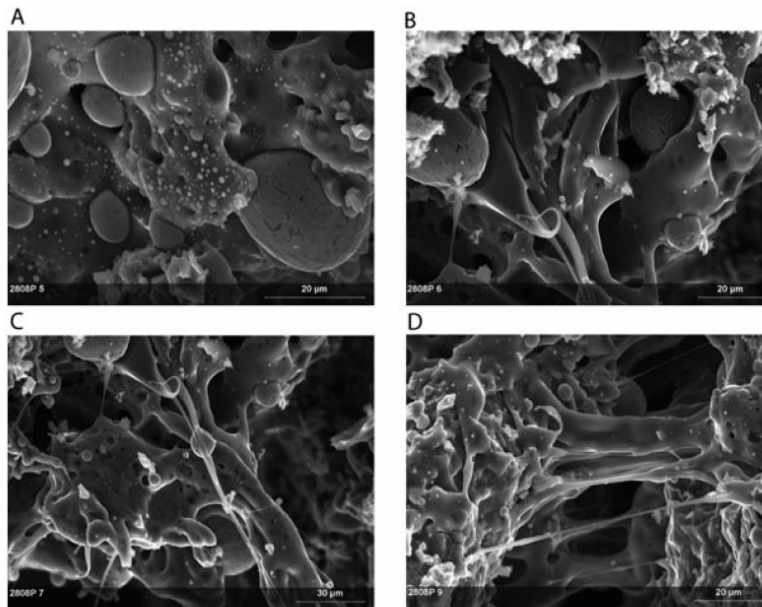


Fig. 6. A–D) SEM-SE micrographs of the surface of the recovered projectile relict (experiment P1-2808) showing bubbles of various sizes and amorphous films decorating the projectile surface. Thin filaments bridging tensile cracks indicate low viscosities of the melt films.

may represent micro-twins (Timms et al. 2012) or deformation bands. The diffraction patterns of the lamellae are weak and vanish with progressive radiation. This suggests that these areas are strongly deformed domains that locally lead to amorphization. Granular fabrics formed by amorphization and decomposition of $ZrSiO_4$ could not be detected (Fiske et al. 1994; Wittmann et al. 2006).

The two cross-sections of the projectile relics of experiments P1-2808 (Fig. 9A) and 3232 (Fig. 9B) display convex–concave sickle shapes. However, the projectile relict of P1-2808 (Fig. 9A) has a more complex geometry and is subdivided into several splinters. The projectile relict of experiment 3232 shows a knobby region near the center of its concave side. This is occupied by a mass of fragmented quartz grains and steel splinters that most likely were detached from the projectile relict during spallation at the rear of the projectile. A thin film of steel cements the individual elements together. Melting of quartz grains in this zone is rare.

Deformation of the Recovered Projectile

Orientation contrast imaging was carried out for the experiments 3232 and P1-2808 (Fig. 10). The

variable intensity of the contrast here does not depend on differences in the atomic masses, but on the orientation of the crystal lattice planes with respect to the incident electron beam due to the electron channeling mechanism. Orientation contrast within the recovered projectile of experiment 3232 reveals a strong grain shape preferred orientation (GSPO). Size, orientation, and shape of recrystallized grains correlate with their position within the deformed projectile and indicate that the microstructures are the result of impact deformation (Figs. 10A–C). In the vicinity of the convex side of the sample, grain long axes are parallel to the curvature of the rim. The diameters of the crystal domains are usually $< 2 \mu\text{m}$ and their aspect ratios (ratio of long and short axis) may exceed 10. In the concave portion of the projectile, and in the central area, a more irregular to chaotic pattern with no clear GSPO is found. Due to their extremely small size, several domains do not show a clear diffraction pattern. Orientation contrast imaging of the recovered projectile of experiment P1-2808 also displays domains with fine grain sizes and strong GSPO parallel to the curvature of the projectile surface (Fig. 10D). The grain sizes are even finer grained and range in the submicrometer size. However, these domains alternate with areas of large

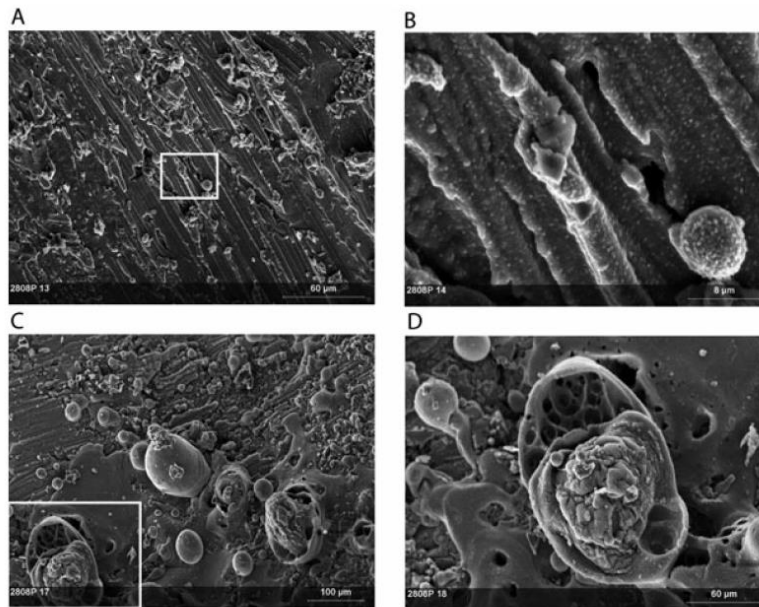


Fig. 7. A–D) SEM-SE micrographs of the surface of the recovered projectile relict (experiment P1-2808). A–B) The smooth and striated surface is interpreted as a shear plane. Tiny spherules indicate melting by shear heating. C–D) Boiling bubbles and melt films on a shear plane of the projectiles' surface.

uniform grain aggregates that are not strained and that formed perfectly equilibrated triple point networks (Figs. 10D–F). This is an unequivocal evidence for grain growth under static conditions and indicates postshock thermally induced annealing of the microstructure.

EBSD mapping of the projectile relict 3232 (Figs. 11A and 11B) shows that the GSPO correlates with a crystallographic preferred orientation (CPO) (Figs. 11C and 11D). The maxima of the pole figures suggest that several symmetrically equivalent glide planes along $\{111\}$ and (100) were activated and that slip occurred in the $[110]$ direction. The CPO indicates that deformation mechanisms involving dislocation glide and creep were active and that the projectile was plastically deformed during its collision with the target rock. Further evidence of plasticity is observable in the sub grain and grain boundaries maps shown in Figs. 11E and 11G. Some intensively elongated grains show an internal development of subgrain boundaries. The cumulated internal misorientations reach values up to 50° (Fig. 11F) as a result of elongation. The presence of low-angle grain boundaries indicates that dislocations have migrated into low-angle boundaries. Further grain deformation is

accommodated by subgrain rotation and leads to subgrain rotation recrystallization and the building of high angle boundaries. As a result of dynamic recrystallization, fine grains developed. Indications for subsequent annealing could not be found. In addition to plasticity, the projectile shows several internal spall fractures (Fig. 9A).

EBSD mapping of the projectile relict of experiment P1-2808 (Figs. 12A and 12B) is shown in Fig. 12. The extreme fine grain sizes ($< 1 \mu\text{m}$) do not allow a proper EBSD mapping and indexing of crystallographic orientations. Where grain sizes allow indexing, the GSPO also correlates with a CPO as in projectile relict 3232. In contrast, the domains with large grains and stable triple points do not show signs of a CPO. The grains are internally strain-free (Fig. 12C). The misorientation between adjacent grains is random (Fig. 12B). The selective annealing of the projectile relict of experiment P1-2808 is most likely a result of the heterogeneous distribution of SiC inclusions within the steel (Fig. 1). In domains where SiC inclusions occur, grain boundaries are pinned and grain growth is prohibited. In domains that are free of impurities, static grain growth could take place.

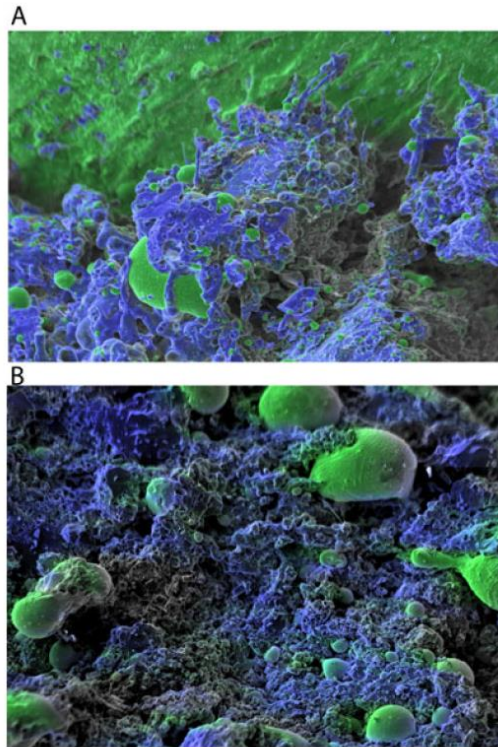


Fig. 8. Element mapping of the projectile surface (experiment P1-2808). Iron (green) of the projectile and silicon (blue) show intense mixing. Both phases indicate melting: iron forms spherules, whereas silicon forms a thin melt film and delicate apophyses. (Width of micrographs approximately 400 μm .)

Projectile Residues in the Crater Floor and Dispersed in the Ejecta

In addition to the large bowl-shaped projectile relics, fine-grained metallic particles were collected in the MEMIN experiments with a bar magnet from (1) the ejecta catcher, and (2) the pulverized material decorating the crater floor surface. The particles, which are interpreted as residues of the projectiles, comprise of (1) angular fragments, (2) spheroids that are similar in shape to spheres produced in gas welding, and (3) delicate carbon-rich paramagnetic apophyses (Fig. 13). The apophyses from experiment P1-2808 intensively pervade and impregnate the fine-grained sandstone target and weld the quartz grains (Fig. 13). Injection along early formed fracture planes would theoretically form two-dimensional injection planes. The dendroid shape appearance of these apophyses does not support the

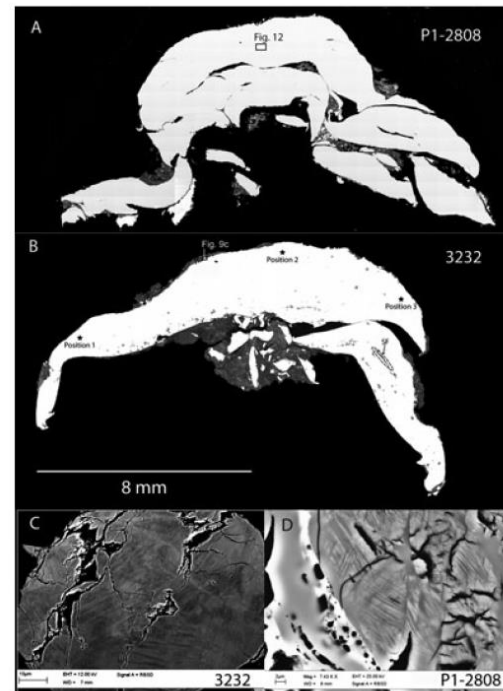


Fig. 9. A) BSE overview of the studied sample cross-section of the projectile relic P1-2808 (bright areas: steel, dark grey areas: sandstone remnants). B) 172 stitched BSE images display a cross-section of the projectile relic 3232. Note the discontinuous thin silicate layer at the outer rim of the sample and the rounded sandstone/steel imbricate next to the inner rim. Stars indicate areas investigated by means of Orientation Contrast imaging and EBSD mapping. SF is a spall fracture. C) Orientation contrast (OC) image of a deformed zircon single crystal adjacent to projectile relic 3232 (see B for location). D) BSE image of vesicular lechatelierite and shocked quartz grains with abundant planar deformation features. This type of shock metamorphism is typical in the matter that is glued to projectile P1-2808.

assumption that the metallic injections occurred along fracture planes. The compositional variety of the residues is large and exceeds the range defined by the compositional end-members steel, quartz, and phyllosilicate; carbon is locally enriched. A possible source of carbon could be the carbon-rich inclusions in the steel (Fig. 1) or carbon from the fiber board.

DISCUSSION

Planar impact approximation suggests that the peak shock pressure in experiment P1-2808 may have locally

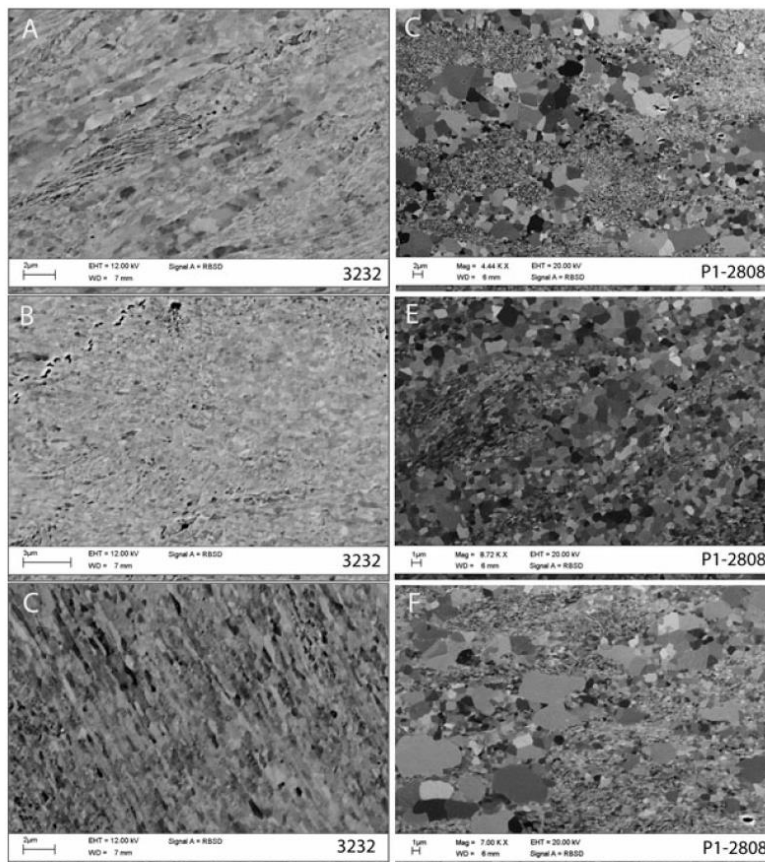


Fig. 10. EBSD coupled to OC imaging in the SEM enables complete specimen microtextures to be determined. Orientation contrast (OC) images of areas situated along the outer rim of the steel projectile (see location of positions in Fig. 9B). Note the intense grain shape-preferred orientation and grain elongation dipping NE/SW (A) for position 1, horizontal (B) for position 2, and dipping NW/SE (C) for position 3 in projectile relic 3232. Long grain axes are oriented parallel to the projectile surface indicating strain elongation. Orientation contrast images (D) through (F) were carried out on the projectile relic of experiment P1-2808. They display very fine-grained domains with a grain shape-preferred orientation alternating with annealed domains.

reached 70 GPa (Poelchau et al. 2013). The peak shock pressure in experiment 3232 may have reached 40 GPa. The dynamic response of steel and iron to shock wave loading was investigated, e.g., by Barker and Hollenbach (1974) or Brar and Rosenberg (1996). The Hugoniot elastic limit of almost pure iron was found to be 1.37 GPa. This provides a limit for the brittle response of the recovered projectile. At shock pressures > 13 GPa, the passage of the shock front causes iron-bcc to transform into a close-packed phase where most of the structure is isotropic hexagonal close-packed (hcp) and, depending on shock strength and grain orientation, some

fraction is austenite face-centered-cubic (fcc) (Kadau et al. 2007).

The observed melting and even vaporization of steel in experiment P1-2808 are in stark contrast to the expected shock and postshock heating of iron. For instance, iron shocked to 39 GPa experiences a volume compression of 19% and temperature rise of only approximately 320–340 °C (Kadau et al. 2007). The postshock temperature rise of steel upon unloading from a peak pressure of 60–70 GPa is on the order of only 400 °C. This temperature is clearly insufficient to melt considerable amounts of the steel projectile, which has a

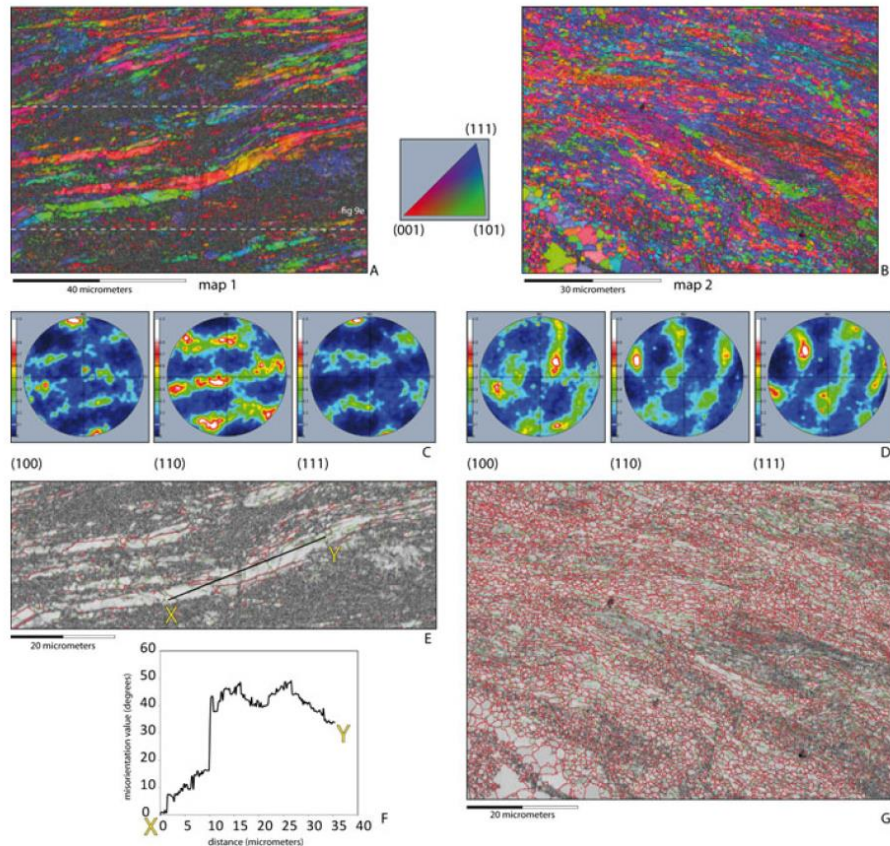


Fig. 11. A, B) EBSD maps from locations 1 and 3 (see Fig. 9B) of sample 3232 with step sizes of $0.15\ \mu\text{m}$. The color coding represents the preferential orientation of the horizontal direction in the given inverse pole figure look-up table. C, D) (100), (110), and (111) pole figure distributions; equal area projection, lower hemisphere, linear scale, and relative intensity. Orientation data extracted from maps 1 and 2, respectively. Note the strong CPO related to the plastic deformation of steel. E) Grain/subgrain boundary maps extracted from a selected region of map 1 (see location A). Image in the background is the EBSD pattern quality map. Green line: local misorientation between 5 and 10 degrees; red line: local misorientation higher than 10° . F) Misorientation profile across a highly elongated grain. The value of misorientation is calculated from the first orientation value calculated at point X. G) Grain/subgrain boundary map extracted from map 2. Same color coding as E).

melting temperature of $1430\ ^\circ\text{C}$. Significant differences in shock impedance between the iron phase and the $< 40\ \mu\text{m}$ -sized Si-C-rich domains (Fig. 1) may, however, explain the presence of solidified Si-rich shock-melt filaments. Multiple shock reverberation at the iron-SiC phase boundaries could lead to a shock pressure equilibration between iron and SiC and would cause a strong temperature increase in SiC.

A possible source for the strong projectile heating in addition to shock and postshock heating is the strong temperature increase in sandstone upon shock loading.

Porous sandstone achieves a shock temperature of $1000\ ^\circ\text{C}$ at shock pressures of 15 GPa (Ahrens and Gregson 1964; Stöffler and Langenhorst 1994). Extraordinary heat pulses in sandstone are caused by the high shock impedance contrasts between the quartz grains and the interstitial pores and the abrupt closure of pore space (Kieffer 1971). In dense quartz, 45 GPa are necessary to reach this temperature. The temperature pulse within the porous target may specifically affect the immediate projectile–target interface and its surrounding where the heat could be conducted. Shoemaker et al.

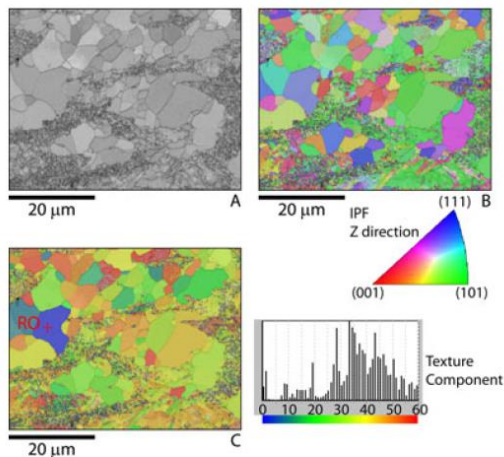


Fig. 12. EBSD mapping results obtained on sample P1-2808 (see Fig. 9A for map localization) using a beam acceleration voltage of 20 kV and a step size of 180 nm. A) Pattern quality map. The pattern quality depends on crystal perfection and phase orientation as well as on experimental parameters (Humphreys et al. 2001). B) Inverse pole figure map (Z direction, normal to the plane of measurement) overlain on the pattern quality map in semi-transparency mode. Note the color uniformity within the large grains indicating the lack of internal misorientations. C) Texture component map overlain on the pattern quality map in a semi-transparency mode. The rainbow color coding represents the deviation from an arbitrary reference orientation (RO; Euler angles: $\Psi_{11} = 21.93^\circ$, $\Phi_{11} = 40.32^\circ$, $\Psi_{12} = 32.29^\circ$). The blue color represents no deviation from the reference, the red color a maximal deviation of 60° . The large angular deviation spread visible in the histogram to the right of the map indicates the lack of any crystallographic-preferred orientation.

(1963) performed an impact experiment with a steel projectile and Coconino sandstone, and estimated that the total heat flow across the interface is about 4 J cm^{-2} leading to a net temperature increase of only $10\text{--}20^\circ\text{C}$ in the steel projectile. Thus, heat conduction from a hot target to the projectile is limited and cannot account for the high temperature within the projectile.

More important heat sources stem from dissipation of internal energy as heat during plastic deformation and frictional shearing (Kenkmann et al. 2000; Langenhorst et al. 2002; Van der Bogert et al. 2003; Spray 2010). Both processes can be observed in the investigated samples and are spatially separated. Whereas shear heating predominantly affected the surface of the projectiles and even led to localized boiling of iron at the immediate projectile–target interface, plastic deformation pervasively heated up the interior of the recovered projectile by crystal plasticity. The texture analysis of the projectile relics revealed that both dislocation glide and

dislocation creep played important roles for the ductile response, whereas twinning is of subordinate importance. Dislocation glide led to a strong grain shape and crystallographic-preferred orientation. In the projectile relic of experiment 3232, this is particularly observed near the convex outer part of the recovered projectile and the grain elongation is parallel to the surface (Figs. 10B and 11A–C). Dislocation creep resulted in dynamic recrystallization and the formation of fine grain sizes with low aspect ratios. In the projectile relic of experiment P1-2808, the dynamically recrystallized grain size is finer than in experiment 3232, indicating a larger amount of accommodated strain in experiment P1-2808. The creep behavior of iron alloys strongly depends on the C-content (Lesuer et al. 2001). High-temperature creep with dynamic recrystallization is expected at homologous temperatures T/T_M of 0.7 and higher, where T_M is the melting temperature. Dislocation creep and dynamic recrystallization are associated with atom diffusion through the crystal lattice. As diffusion is a rate-dependent process, the period of deformation plays a critical role. High-temperature creep is restricted to the period of the contact and compression phase that lasted approximately $1\text{--}2 \mu\text{s}$.

The presence of deformation features indicating high-temperature creep suggests that both projectile relics were heated to at least $900\text{--}1000^\circ\text{C}$. For the projectile relic of experiment P1-2808, the real temperature was most likely higher than this. The corresponding thermal energy Q , required for a temperature change ΔT of the projectile with mass m , is given by $Q = c_p m \Delta T$. The specific heat capacity c_p of steel SAE 4130 is $0.48 \text{ kJ kg}^{-1} \text{ K}^{-1}$. Thus, 2.3% of the total impact energy (P1-2808: 58.4 kJ) is consumed for heating the projectile. Assuming that the entire missing mass (1.26 g) of the projectile in experiment P1-2808 was melted (31%), a minimum thermal energy of 850 J is required to achieve this temperature and about 365 J to convert the solid at its melting point into a liquid without increase in temperature (latent heat of fusion of iron 288 J g^{-1}), equivalent to approximately 2.1% of the total impact energy. This value may represent an upper limit as it is not sure that the entire missing projectile was melted. Even boiling of iron was locally found to occur on shear planes at the projectile target interface and in residues. However, the quantity of vaporized iron and the input of heat for vaporization cannot be estimated here, but may counterbalance the overestimated thermal energy for melting. To summarize, heating plus melting of the projectile consumed about 4.4% of the total impact energy in the case of experiment P1-2808. The projectile experienced high temperatures for at least $250 \mu\text{s}$ (Fig. 3). However, high-temperature creep was restricted to the period of the contact and compression phase, as the differential stress required for dislocation motion may

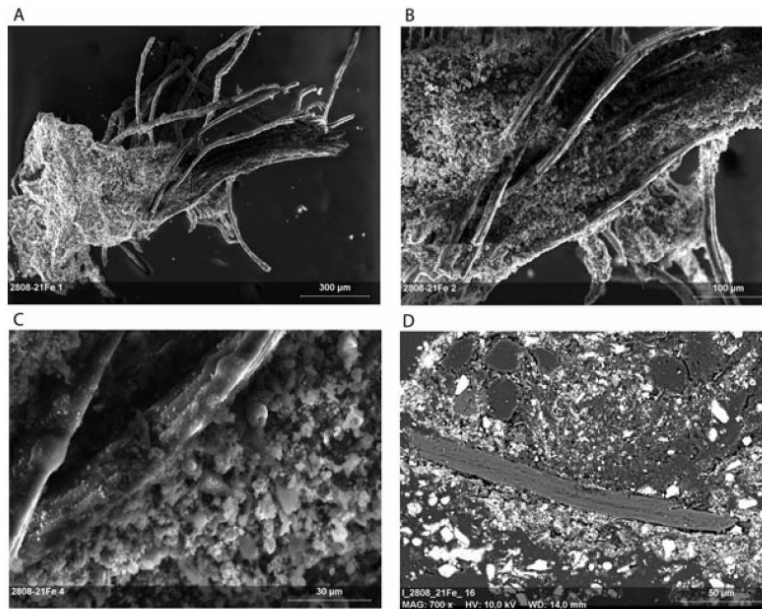


Fig. 13. SEM-SE micrographs of a paramagnetic fragment collected from the crater floor of the dry experiment P1-2808. A–C) Apophyses permeate a deformed sandstone aggregate. The branches are enriched in C, Fe, and Si. D) Polished cut surface of one of the apophyses (SEM-BSE micrograph).

have dropped to zero during the ejection process. After this time, the projectile relic left the presumably very hot central ejecta plume (Fig. 3). Static annealing of steel SAE 4130 occurs above approximately 850 °C. The observed annealing of the projectile relic of experiment P1-2808 indicates that this temperature must have persisted for a while after deformation, whereas in experiment 3232, the temperature should have rapidly dropped below 850 °C. In the smaller scale impact experiment of Shoemaker et al. (1963) who also used a steel projectile and a sandstone target (impact energy 3.7 kJ), about 10% of the projectile material was melted.

The recovered projectiles of our MEMIN experiments were strongly distorted. Their convex sides lined the growing crater cavity. The projectile relic of experiment P1-2808 was more severely stretched and strained. When the shock wave was reflected at the inner side of the projectile, the deformed projectile was subjected to brittle tensile fragmentation. Subsequently, the splinters were stacked and pushed together (Fig. 9A). To a lesser degree, this is also seen in the knobby and rough region in the inner part of the concave, bowl-shaped projectile relic of experiment 3232 that contains numerous steel splinters that were originally located at the rear of the projectile, but became intermingled with target material that most

likely intruded from the sides, when the projectile fully penetrated into the target. The recovered material shows a variety of complex textures and chemical peculiarities. For example, the origin of the silica in the recovered projectile matter cannot be constrained with certainty. Textural and chemical homogeneity of the projectile material are important to avoid unbalanced mass distribution, and a clear chemical distinction from the target sandstone. Ebert et al. (2013) give a detailed geochemical analysis of projectile–target interaction using Campo del Cielo iron meteorite material as a projectile.

CONCLUSIONS

Small terrestrial impact craters of several tens to hundreds of meters in diameter are often formed by iron meteoroids. While traversing the Earth’s atmosphere, iron meteoroids with sizes of a few meters to decameters are often capable of withstanding the aerodynamic stresses without complete fragmentation. The bodies decelerate to a few kilometres per second and finally form meteorite craters like Kamil, Egypt, or Wabar, Saudi Arabia. To study the fate of these projectiles, hypervelocity cratering experiments at impact velocities ranging between 2500 and approximately 5300 m s⁻¹ with centimeter-sized steel

projectiles and sandstone targets were carried out. The masses of coherent projectile relics that were recovered in different experiments ranged between 58% and 92% of their initial projectile masses. A systematic relationship between the impact energy and the relative proportion of projectile relic could not be found.

A detailed microstructural investigation of projectile relics showed that their surfaces indicate shearing and brittle fracturing. Melting and boiling of iron and silica are evident from the formation of bubbles, droplets, and melt filaments. For the experiment P1-2808 that was carried out at an impact velocity of 5300 m s⁻¹ and an impact energy of 58.4 kJ, it is estimated that at least 4.4% of the impact energy is dissipated by heating and melting of the projectile. Dislocation glide and creep along with dynamic recrystallization are the main deformation mechanisms during plastic deformation of the projectile, followed by a later annealing of the microstructure. Small-scale residues of the projectile are distributed in the ejecta as spherules, unmelted fragments, and intermingled iron-silica aggregates.

Acknowledgments—We thank R. T. Schmitt (MfN) and I. Domke (WWU) for providing selected geochemical data, M. Poelchau (ALU) for coordination, H. Knöfler (MfN) and H. Ickler (ALU) for technical support, and the other MEMIN group members for numerous fruitful discussions. The manuscript benefitted from constructive reviews by Dr. Axel Wittmann, Dr. C. Van der Bogert, and the associate editor Dr. N. Artemieva. This work is funded by the German Research Foundation DFG, Research Unit FOR-887, grants DE 401/23-1, HE-2893/8-1, KE-732/18-1.


Editorial Handling—Dr. Natalia Artemieva

REFERENCES

- Ahrens T. J. and Gregson V. G. 1964. Shock compression of crustal rocks. Data for quartz, calcite, and plagioclase rocks. *Journal of Geophysical Research* 69:4839–4874.
- Barker L. M. and Hollenbach R. E. 1974. Shock wave study of the α - ϵ phase transition in iron. *Journal of Applied Physics* 45:4872–4887.
- Brar N. S. and Rosenberg Z. 1996. Shock Hugoniot of 1215 steel. *AIP Conference Proceedings* 370, pp. 101–104.
- Buchwald V. F. 1975. *Handbook of iron meteorites*. Berkeley: University of California Press.
- D'Orazio M., Folco L., Zeoli A., and Cordier C. 2011. Gebel Kamil: The iron meteorite that formed the Kamil crater (Egypt). *Meteoritics & Planetary Science* 46:1179–1196.
- Ebert M., Hecht L., Deutsch A., and Kenkmann T. 2013. Chemical modification of projectile residues and target material in a MEMIN cratering experiment. *Meteoritics & Planetary Science* 48, doi: 10.1111/j.1945-5100.2012.1429.x.
- Evens N. J., Shainpoor M., and Ahrens T. J. 1994. Hypervelocity impact: Ejecta, angle, and composition. In *Large meteorite impacts and planetary evolution*, edited by Dressler B. O., Grieve R. A. F., and Sharpton V. L. GSA Special Paper 293. Boulder, Colorado: Geological Society of America, pp. 93–101.
- Fiske P. S., Nellis W. J., and Sinha A. K. 1994. Shock-induced phase transitions of ZrSiO₄, reversion kinetics, and implications for terrestrial impact craters. *EOS Transactions* 75:416–417.
- Folco L., Di Martino M., El Barkooky A., D'Orazio M., Lethy A., Urbini S., Nicolosi I., Hafez M., Cordier C., van Ginneken M., Zeoli A., Radwan A. M., El Khrepy S., El Gabry M., Gomaa M., Barakat A. A., Serra R., and El Sharkawi M. 2010. The Kamil crater in Egypt. *Science* 329:804, doi: 10.1126/science.1190990.
- Folco L., Di Martino M., El Barkooky A., D'Orazio M., Lethy A., Urbini S., Nicolosi I., Hafez M., Cordier C., van Ginneken M., Zeoli A., Radwan A. M., El Khrepy S., El Gabry M., Gomaa M., Barakat A. A., Serra R., and El Sharkawi M. 2011. Kamil crater (Egypt): Ground truth for small-scale meteorite impacts on Earth. *Geology* 39:179–182.
- Gerasimov M. V., Yakovlev O. I., Dikov Y. P., and Wlotzka F. 2005. Evaporative differentiation of impact-produced melts: Laser-simulation experiments and comparison with impact glasses from the Logoisk crater. In *Large meteorite impacts III*, edited by Kenkmann T., Hörz F., and Deutsch A. GSA Special Paper 384. Boulder, Colorado: Geological Society of America, pp. 351–366.
- Gibbons R. V., Hörz F., Thompson T. D., and Brownlee D. E. 1976. Metal spherules in Wabar, Monturaqui, and Henbury impactites. *Proceedings, 7th Lunar Science Conference*, pp. 863–880.
- Grieve R. A. F., Cintala M. J., and Tagle R. 2006. Planetary impacts. In *Encyclopedia of the solar system*, 2nd ed., edited by McFadden L. A., Weissman P., and Johnson T. Amsterdam: Academic Press, pp. 813–828.
- Hildebrand A. R., Penfield G. T., Kring D. A., Pilkington M., Camargo Z. A., Jacobsen S. B., and Boynton W. V. 1991. Chicxulub crater: A possible Cretaceous/Tertiary boundary impact crater on the Yucatán Peninsula, Mexico. *Geology* 19:867–871.
- Hörz F., Fechtig H., Janicke J., Schneider E., and Kuzcera H. 1983. The chemistry of projectile residue in experimental microcraters. *Proceedings, 14th Lunar and Planetary Science Conference*, pp. 327–328.
- Humphreys F. J., Bate P. S., and Hurley P. J. 2001. Orientation averaging of electron backscattered diffraction data. *Journal of Microscopy* 201:50–58.
- Jammes C., Stöffler D., Bischoff A., and Reimold W. U. 1983. Reduction of SiO₂ to Si and metallurgical transformations in Al by hypervelocity impact of Al-projectiles into quartz sand. *Proceedings, 14th Lunar and Planetary Science Conference*, pp. 347–348.
- Kadau K., Germann T. C., Lomdahl P. S., Albers R. S., Wark J. S., Higginbotham A., and Holian B.L. 2007. Shock waves in polycrystalline iron. *Physical Review Letters* 98:135701.
- Kearsley A. T., Graham G. A., McDonnell T., Bland P., Hough R., and Helps P. 2004. Early fracturing and impact residue emplacement: Can modelling help to predict their location in major craters? *Meteoritics & Planetary Science* 39:247–265.
- Kearsley A. T., Graham G. A., Burchell M. J., Cole M. J., Dai Z. R., Teslich N., Bradley J. P., Chater R., Wozniakiewicz P. A., Spratt J., and Jones G. 2007. Analytical scanning and transmission electron microscopy of laboratory impacts on

- Stardust aluminum foils: Interpreting impact crater morphology and the composition of impact residues. *Meteoritics & Planetary Science* 42:191–210.
- Kenkmann T., Hornemann U., and Stöffler D. 2000. Experimental generation of shock-induced pseudotachylites along lithological interfaces. *Meteoritics & Planetary Science* 35:1275–1290.
- Kenkmann T., Patzschke M., Thoma K., Schäfer F., Deutsch A., Hecht L., and MEMIN Team. 2007. Melting and vaporization of a steel projectile in meso-scale hypervelocity cratering experiments (abstract #1527). 38th Lunar and Planetary Science Conference. CD-ROM.
- Kenkmann T., Wünnemann K., Deutsch A., Poelchau M. H., Schäfer F., and Thoma K. 2011. Impact cratering in sandstone: The MEMIN pilot study on the effect of pore water. *Meteoritics & Planetary Science* 46:890–902.
- Kieffer S. W. 1971. Shock metamorphism of the Coconino sandstone at Meteor Crater, Arizona. *Journal of Geophysical Research* 76:5449–5473.
- Kieffer S. W. and Simonds C. H. 1980. The role of volatiles and lithology in the impact cratering process. *Reviews of Geophysics and Space Physics* 18:143–181.
- Knox R. 1967. Surviving metal in meteoritic iron oxide from the Wolfe Creek, Western Australia, meteorite crater. *Meteoritics* 3:235–238.
- Koerberl C. 1998. Identification of meteoritic component in impactites. In *Meteorites: Flux with time and impact effects*, edited by Grady M. M., Hutchinson R., McCall G. J. H., and Rothery R. A. Geological Society Special Publication 140. London: Geological Society London. pp. 133–153.
- Koerberl C. 2007. The geochemistry and cosmochemistry of impacts. In *Meteorites, comets, and planets*, edited by Davis A. Treatise of Geochemistry, Vol. 1. Amsterdam: Elsevier. pp. 1–5.
- Langenhorst F., Poirier J.-P., Deutsch A., and Hornemann U. 2002. Experimental approach to generate shock veins in single-crystal olivine by shear melting. *Meteoritics & Planetary Science* 37:1541–1553.
- Lesuer D. R., Syn C. K., Whittenberger J. D., Carsi M., Ruano O. A., and Sherby O. D. 2001. Creep behavior of Fe-C alloys at high temperatures and high strain rates. *Materials Science and Engineering* 317:101–107.
- Maier W. D., Andreoli M. A., McDonald I., Higgins M. D., Boyce A. J., Shukolyukov A., Lugmair G. W., Ashwal L. D., Graser P., Ripley E. M., and Hart R. J. 2006. Discovery of a 25-cm asteroid clast in the giant Morokweng impact crater, South Africa. *Nature* 441:203–206.
- Mittlefehldt D. W., Hörz F., See T. H., Scott E. R. D., and Mertzmann S. A. 2005. Geochemistry of target rocks, impact-melt particles, and metallic spherules from Meteor Crater, Arizona: Empirical evidence on the impact process. In *Large meteorite impacts III*, edited by Kenkmann T., Hörz F., and Deutsch A. GSA Special Paper 384. Boulder, Colorado: Geological Society of America. pp. 367–390.
- Poelchau M. H., Kenkmann T., Thoma K., Hoerth T., Dufresne A., and Schäfer F. 2013. The MEMIN research unit: Sealing impact cratering experiments in porous sandstones. *Meteoritics & Planetary Science* 48, doi: 10.1111/maps.12016.
- Prior D. J., Boyle A. P., Brenker F., Chaddle M. C., Day A., Lopez G., Peruzzo L., Potts G.J., Reddy S., Spiess R., Timms N. E., Trimby P., Wheeler J., and Zetterström L. 1999. The application of electron backscatter diffraction and orientation contrast imaging in the SEM to textural problems in rocks. *American Mineralogist* 84:1741–1759.
- Rowan L. R. and Hörz F. 1995. Deciphering projectile compositions of impact craters via shock recovery experiments on simple metal-silicate systems. Proceedings, 26th Lunar and Planetary Science Conference. pp. 1193–1194.
- Rowan L. R., Hörz F., and Zolensky M. 1996. Selective oxidation/reduction and impact melting in experimental metal-silicate craters. Proceedings, 27th Lunar and Planetary Science Conference. pp. 1109–1110.
- Schäfer F., Thoma K., Behner T., Kenkmann T., Wünnemann K., and MEMIN Team. 2006. Impact tests on dry and wet sandstone. Proceedings First International Conference on Impact Cratering in the Solar System. 6 p.
- Schulte P., Alegret L., Arenillas I., Arz J. A., Barton P. J., Bown P. R., Bralower T. J., Christeson G. L., Claeys P., Cockell C. S., Collins G. S., Deutsch A., Goldin T. J., Goto K., Grajales-Nishimura J. M., Grieve R. A. F., Gulick S. P. S., Johnson K. R., Kiessling W., Koerberl C., Kring D. A., MacLeod K. G., Matsui T., Melosh H. J., Montanari A., Morgan J. V., Neal C. R., Nichols D. J., Norris R. D., Pierazzo E., Ravizza G., Rebolledo-Vieyra M., Reimold W. U., Robin E., Salge T., Speijer R. P., Sweet A. R., Urrutia-Fucugauchi J., Vajda V., Whalen M. T., and Willumsen P. S. 2010. The Chicxulub impact and mass extinction at the Cretaceous-Paleogene boundary. *Science* 327:1214–1218. doi: 10.1126/science.1177265 2010.
- Shoemaker E. M., Gault D. E., Moore H. J., and Lugn R. V. 1963. Hypervelocity impact of steel into Coconino sandstone. *American Journal of Science* 261:668–682.
- Spray J. G. 2010. Frictional melting processes in planetary materials: From hypervelocity impact to earthquakes. *Annual Review of Earth and Planetary Sciences* 38:221–254.
- Stöffler D. and Langenhorst F. 1994. Shock metamorphism of quartz in nature and experiment: I. Basic observation and theory. *Meteoritics* 29:155–181.
- Stück H., Siegesmund S., and Rüdlich J. 2011. Weathering behaviour and construction suitability of dimension stones from the Drei Gleichen area (Thuringia, Germany). *Environmental Earth Sciences* 63:1763–1786.
- Tagle R. and Berlin J. 2008. A database of chondrite analyses including platinum group elements, Ni, Co, Au, and Cr: Implications for the identification of chondritic projectiles. *Meteoritics & Planetary Science* 43:541–559.
- Tagle R. and Hecht L. 2006. Geochemical identification of projectiles in impact rocks. *Meteoritics & Planetary Science* 41:1721–1735.
- Timms N. E., Reddy S. M., Healy D., Nemchin A. A., Grange M. L., Pidgeon R. T., and Hart R. 2012. Resolution of impact-related microstructures in lunar zircon: A shock-deformation mechanism map. *Meteoritics & Planetary Science* 47:120–141.
- Van der Bogert C. H., Schultz P. H., and Spray J. G. 2003. Impact-induced frictional melting in ordinary chondrites: A mechanism for deformation, darkening, and vein formation. *Meteoritics & Planetary Science* 38:1521–1531.
- Wittmann A., Kenkmann T., Schmitt R. T., and Stöffler D. 2006. Shock metamorphosed zircon in terrestrial impact craters. *Meteoritics & Planetary Science* 41:433–454.

High-pressure phase transitions of α -quartz under nonhydrostatic dynamic conditions: A reconnaissance study at PETRA III

Eva-Régine CARL^{1,2*}, Ulrich MANSFELD³ , Hanns-Peter LIERMANN⁴, Andreas DANILEWSKY²,
Falko LANGENHORST³, Lars EHM^{5,6}, Ghislain TRULLENQUE^{4,7}, and Thomas KENKMANN¹

¹Institut für Geo- und Umweltnaturwissenschaften, Geologie, Albert-Ludwigs-Universität, Albertstr. 23b, 79104 Freiburg, Germany

²Institut für Geo- und Umweltnaturwissenschaften, Kristallographie, Albert-Ludwigs-Universität, Hermann-Herder-Str. 5, 79104 Freiburg, Germany

³Institut für Geowissenschaften, Mineralogie, Friedrich-Schiller-Universität Jena, Carl-Zeiss-Promenade 10, 07745 Jena, Germany

⁴DESY, Notkestraße 85, 22607 Hamburg, Germany

⁵Stony Brook University, Mineral Physics Institute, Stony Brook, NY 11794-2100, USA

⁶National Synchrotron Light Source II, Brookhaven National Laboratory, Upton, NY 11973-500, USA

⁷Institut Polytechnique LaSalle Beauvais, Département GEOS, équipe B2R 19 rue Pierre Waguët – BP 30313, 60026 Beauvais Cedex, France

*Corresponding author. E-mail: eva-regine.carl@geologie.uni-freiburg.de

(Received 12 May 2016; revised 24 November 2016; revision accepted 19 December 2016)

Abstract—Hypervelocity collisions of solid bodies occur frequently in the solar system and affect rocks by shock waves and dynamic loading. A range of shock metamorphic effects and high-pressure polymorphs in rock-forming minerals are known from meteorites and terrestrial impact craters. Here, we investigate the formation of high-pressure polymorphs of α -quartz under dynamic and nonhydrostatic conditions and compare these disequilibrium states with those predicted by phase diagrams derived from static experiments under equilibrium conditions. We create highly dynamic conditions utilizing a mDAC and study the phase transformations in α -quartz in situ by synchrotron powder X-ray diffraction. Phase transitions of α -quartz are studied at pressures up to 66.1 and different loading rates. At compression rates between 0.14 and 1.96 GPa s⁻¹, experiments reveal that α -quartz is amorphized and partially converted to stishovite between 20.7 GPa and 28.0 GPa. Therefore, coesite is not formed as would be expected from equilibrium conditions. With the increasing compression rate, a slight increase in the transition pressure occurs. The experiments show that dynamic compression causes an instantaneous formation of structures consisting only of SiO₆ octahedra rather than the rearrangement of the SiO₄ tetrahedra to form a coesite. Although shock compression rates are orders of magnitude faster, a similar mechanism could operate in impact events.

INTRODUCTION

Quartz is an omnipresent mineral in near-surface rocks of the continental lithosphere and, therefore, among the best studied phases under equilibrium conditions. Its wide occurrence also makes it the most widely used shock barometer (Stöffler and Langenhorst 1994; French and Koeberl 2010) in impact studies.

High-pressure polymorphs of α -quartz such as coesite (Coes 1953) are known from different geologic

settings. For example, natural occurrences of coesite were first reported from impact craters, namely Meteor Crater, AZ, USA (Chao et al. 1960) and the Ries crater, Germany (Shoemaker and Chao 1961). Later on, coesite was found in mantle-derived kimberlites (e.g., Smyth and Hatton 1977) and in ultrahigh-pressure metamorphic rocks of continental collision zones (e.g., Chopin 1984).

The thermodynamic stability fields of high-pressure polymorphs of α -quartz have been experimentally and

theoretically investigated since 1953 (Coes 1953): α -quartz transforms to coesite with fourfold coordinated Si at 2 GPa and to stishovite with sixfold coordinated Si (Stishov and Popova 1961) at 8 GPa (Kirfel et al. 2001) and room temperature. At quasi-hydrostatic conditions and room temperature, the high-pressure polymorphs, coesite I and coesite II, have also been reported (Černok et al. 2014).

However, a great mismatch exists when the static stability field of high-pressure SiO₂ polymorphs is compared to the occurrence of these phases during shock metamorphism. In impact craters, coesite is found only in diaplectic SiO₂ glasses that were exposed to shock pressures in excess of 35 GPa, for example, Stöffler and Langenhorst (1994). Coesite is thought to crystallize exclusively upon shock pressure release from silica melt (Stöffler and Langenhorst 1994; Langenhorst and Deutsch 2012; Fazio et al. 2016). Stishovite, on the other hand, is believed to form via a solid–solid transition during shock compression at lower pressures than coesite (French and Koeberl 2010) and then reverts back to the amorphous state (Luo et al. 2003). Considering the high energy barrier of a solid–solid phase transition to stishovite, a nucleation of stishovite from hot spots of silica melt is also suggested as a further hypothesis for the formation of stishovite. The occurrence of stishovite in melt pockets (Kieffer et al. 1976; Mansfeld et al. 2017) or melt veins (Langenhorst and Poirier 2000) supports this hypothesis. Hence, the formation and preservation of coesite and stishovite depends on the specific pressure–temperature evolution during shock compression and decompression.

Furthermore, diamond anvil cell experiments reveal a complex behavior of α -quartz under compression (e.g., Dubrovinsky et al. 2004). Reconstructive phase transitions to the stable high-pressure polymorphs are often hindered by high kinetic barriers resulting in the formation of complex metastable phases if heating is not sufficient (e.g., Choudhury and Chaplot 2006). Here, we briefly review literature data of SiO₂ high-pressure polymorphs, which is relevant for the interpretation of our results.

Under dynamic compression, α -quartz undergoes a pressure-induced amorphization in the pressure range 18–35 GPa (McNeil and Grimsditch 1992; Kingma et al. 1993a, 1993b). Furthermore, theoretical investigations of the SiO₂ system predict a number of competing metastable postquartz phases that precede or coexist along the full amorphization (Teter et al. 1998; Wentzcovitch et al. 1998; Choudhury and Chaplot 2006) indicating that the structural transformation pathways are highly dependent on the precursor phase

and the degree of hydrostaticity (Haines et al. 2000; Ohtaka et al. 2001; Huang et al. 2006).

Quartz (P3₂21 space group) may transform to a monoclinic (P2₁/c space group) postquartz phase (Haines et al. 2001). Its structure is built of 3 × 2 kinked chains of edge-sharing SiO₆ octahedra. Theoretical calculations by Teter et al. (1998) and Martoňák et al. (2007) reveal that this phase transformation is diffusionless. The monoclinic postquartz phase (MQtz) has not been discovered in natural geological settings. This phase is closely related to stishovite (P4₂/mm space group) that is built of edge-sharing octahedra forming straight chains. These two structures are competing because of very similar activation energies (Teter et al. 1998). Furthermore, there are many analogous structures that feature chains of edge-sharing octahedra with different kinking sequences such as seifertite (2 × 2 kinked chains) or SnO₂-type SiO₂ (4 × 4 kinked chains). Besides the transition from α -quartz to the MQtz, the formation of intermediate and metastable phase quartz II was reported (Choudhury and Chaplot 2006). Quartz II forms above 16 GPa and coexists with the MQtz (Haines et al. 2001; Prakapenka et al. 2004). The structure of quartz II is calculated to be monoclinic (C2 space group) and characterized by mixed polyhedral building blocks: Two-thirds of the silicon atoms are in octahedral coordination, while the remaining one-third is tetrahedrally coordinated. This C2 structure is built up of edge-shared octahedral units with corner-shared silicate tetrahedra, which form a framework structure. Computations by Choudhury and Chaplot (2006) show that quartz II can form at 9 GPa with α -quartz persisting metastably up to 32 GPa.

Due to the great complexity (e.g., influence of the precursor phase) and to the metastability of high-pressure SiO₂ phases, previous investigations on α -quartz at high pressure have left many unanswered questions concerning the behavior of the material and the evolution of high-pressure phases.

Here, we present time-resolved X-ray diffraction experiments under dynamic compression that provide insights into the kinetics of high-pressure phase transitions of α -quartz, making use of fast data acquisition, now available at synchrotrons. Although the compression rates are much higher and temperatures are elevated in the context of impact cratering, these in situ investigations of phase transitions are a necessary first step to understand the behavior of SiO₂ under the much faster compression rates of impact events. The obtained diffraction patterns are compared to transmission electron microscopy (TEM) observations of recovered samples.

Table 1. The experimental conditions of the nine selected experiments SiO₂_RT_01 – SiO₂_RT_09.

SiO ₂ _RT_x	P_{start} (GPa)	Compression rate (GPa s ⁻¹)	P_{max} (GPa)	Hold at P_{max} (min)	Decompression rate (GPa s ⁻¹)	P_{end} (GPa)	Wavelength (Å)
01	0.0001	0.14	59.2	60	0.08	16.4	0.28985
02	0.0001	0.20	26.7	120	0.005	11.5	0.48374
03	6.4	0.34	57.1	10	0.13	43.0	0.29135
04	0.0001	0.55	37.5	120	0.15	26.4	0.48374
05	1.2	0.79	46.4	10	0.10	36.7	0.29135
06	3.0	1.02	51.0	10	0.10	44.1	0.29135
07	0.0001	1.02	50.4	120	^a	^a	0.48374
08	0.0001	1.69	36.6	120	0.15	8.5	0.48374
09	7.1	1.96	66.1	10	0.15	41.8	0.29135

^aDiamonds were broken during compression.

EXPERIMENTAL METHODS

The experiments were conducted in a membrane-driven diamond anvil cell (mDAC), which was equipped with diamonds of a culet size of 0.3 mm. The culets indented 0.25 mm Re-gaskets to 0.020–0.035 mm thickness before a 0.1 mm hole was drilled at its center. A mixture of α -quartz powder (Alfa Aesar, 99.5%, –400 Mesh, 2 μm , LOT: L01W019) and Au flakes as an internal pressure calibration (about 1 wt%) was filled into the gasket hole without a pressure medium.

Monochromatic X-ray powder diffraction experiments were carried out at the Extreme Conditions Beamline (ECB) P02.2 at PETRA III, DESY, Hamburg, Germany (Liermann et al. 2015). The wavelength was tuned to 0.28985 Å for the experiment SiO₂_RT_01 and to 0.29135 Å for the four experiments SiO₂_RT_03, 05, 06, and 09. The recorded diffraction patterns were too weak for an unambiguous identification of the high-pressure phases. In order to improve the quality of the diffraction patterns, the energy of the beam was switched from 42.7 to 25.6 keV. These experiments SiO₂_RT_02, 04, 07, and 08 were carried out at a wavelength of 0.48374 Å (Table 1). The sample to detector distance was calibrated using the CeO₂ standard (NIST 687) and varied between 369.13 mm (SiO₂_RT_01), 449.81 mm (SiO₂_RT_03, 05, 06, and 09), and 431.12 mm (SiO₂_RT_02, 04, 07, and 08). The X-ray beam was focused with either Kirkpatrick–Baez mirrors ($2 \times 2 \mu\text{m}^2$ focus) or Compound Refractive Lens systems ($8 \times 3 \mu\text{m}^2$ focus). The compression and decompression was achieved by pumping He gas into or out of the membrane after activation of the membrane pressure controller. Identical rates for compression and decompression were defined, but friction between the piston and cylinder of the mDAC caused slower rates on the sample during decompression. During compression and decompression, diffraction images were taken every 1 (fast compression)–10 (slow compression) s. They were recorded on a Perkin Elmer area detector (model XRD

1621) and were subsequently converted to one-dimensional diffraction diagrams using the software Fit2D (Hammersley et al. 1996).

The experimental data were surveyed using the P02 Processing Tool (Konopkova et al. 2015; Rothkirch, personal communication). This software provided an online tool to quickly process and plot the one-dimensional diffraction patterns as a function of frame number and, thus, time to create two- and three-dimensional contour plots. The tool was essential to get an overview of the compression experiment to define the onset of phase transitions. For a detailed analysis of the diffraction patterns including the identification of phases and the determination of cell parameters, we used the program package FullProf (Rodríguez-Carvajal 1993).

The LeBail analysis (LeBail et al. 1988) was carried out from 3 to 15° 2 θ for all diffraction patterns. The LeBail method extracts integrated intensities from powder diffraction data. Therefore, the structural factor and associated structural parameters are not needed to be known for a LeBail analysis. The algorithm involves the refinement of the unit cell, profile parameters, and intensities of the reflections to match the experimental diffraction pattern. For each phase, the lattice parameters and the width of the reflections at half maximum (FWHM) were refined using the split pseudo-Voigt function. Given that each experiment consists of between 1,500 and 3,690 diffraction patterns, a sequential fitting was carried out if possible.

The 100 and 101 reflections of α -quartz were fitted independently using the Rietveld method (Rietveld 1967, 1969) in order to obtain the integrated intensities of the reflections. These integrated intensities were used to determine the start and progress of the amorphization of the sample during compression. A decrease in the integrated intensity defines the start of the amorphization. An increase in the background or the typical “glass” hump at low diffraction angles

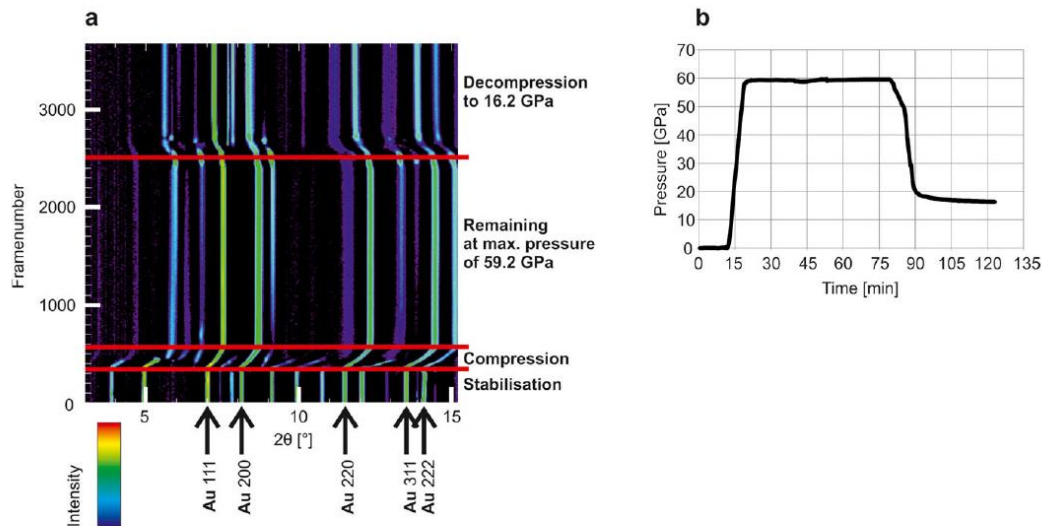


Fig. 1. a) 3D diffraction plot of experiment SiO₂_RT_01: After stabilization at ambient conditions, the compression of the material starts with a rate of 0.14 GPa s⁻¹. Then, the maximum pressure of 59.2 GPa is maintained for 60 min. The final decompression of the material reaches 16.4 GPa. The pressure is obtained with respect to gold (Au). b) The pressure–time path of experiment SiO₂_RT_01 is shown. (Color figure can be viewed at wileyonlinelibrary.com.)

cannot be observed in high-pressure experiments due to the dominant background arising from the DAC.

The transition pressures of the phase transitions are determined with respect to the appearance of the strongest reflection of the phase for all experiments. For stishovite, this is the 110 reflection.

After inspection of the X-ray diffraction pattern, three phases were further considered: α -quartz, MQtz, and stishovite. The starting lattice parameters were $a = 4.91239 \pm 4e-05$ Å and $c = 5.40385 \pm 7e-05$ Å for α -quartz (Will et al. 1988), $a = 4.1773$ Å and $c = 2.6655$ Å for stishovite (Hill et al. 1983), and $a = 7.66$ Å, $b = 4.10$ Å, $c = 5.03$ Å and $\beta = 117.9^\circ$ for the MQtz (Haines et al. 2001). The unit cell dimensions computed from the 111, 200, 220, and 311 diffraction lines of gold were used to calculate the pressure using a third-order Birch–Murnaghan Equation of State (Birch 1952) with the bulk modulus from Anderson et al. (1989).

The parameters of the compression cycle of nine experiments are listed in Table 1. The compression rates increased from 0.14 to 1.96 GPa s⁻¹ with increasing number of experiments. In some experiments, the compression started at elevated pressure P_{start} due to too strong closing of the mDAC. The maximum pressure P_{max} ranged between 26.7 GPa (SiO₂_RT_04) and 66.1 GPa (SiO₂_RT_05), and was held constant for up to 2 h (Table 1). Decompression did not reach

ambient pressures but stopped at P_{end} due to the friction between the piston and the cylinder of the mDAC. The error in pressure is 0.5 GPa.

The identification of phases in the experiments was difficult because the nonhydrostatic compression caused high stresses on the grains that result in broadening of the reflections. Moreover, the weak scattering of α -quartz and the strong Compton scattering of the diamonds decreased the signal-to-noise ratio. Consequently, a LeBail analysis reached its limit and the position of the low-intensity reflections could not be determined precisely. They differed strongly from one refinement step to the next or remained at positions where no reflection was observed.

For TEM investigations, the recovered sample of SiO₂_RT_4 was pushed out of the gasket with a needle. Fragments were then ground between two glass substrates and subsequently dispersed on a lacey carbon grid. TEM imaging and electron diffraction were carried out using a 200 kV FEI Tecnai G² (University of Jena).

RESULTS

Figure 1a depicts a representative dataset of a slow-compression experiment (SiO₂_RT_01) as a contour plot of integrated diffraction patterns. The corresponding pressure–time curve is shown in Fig. 1b.

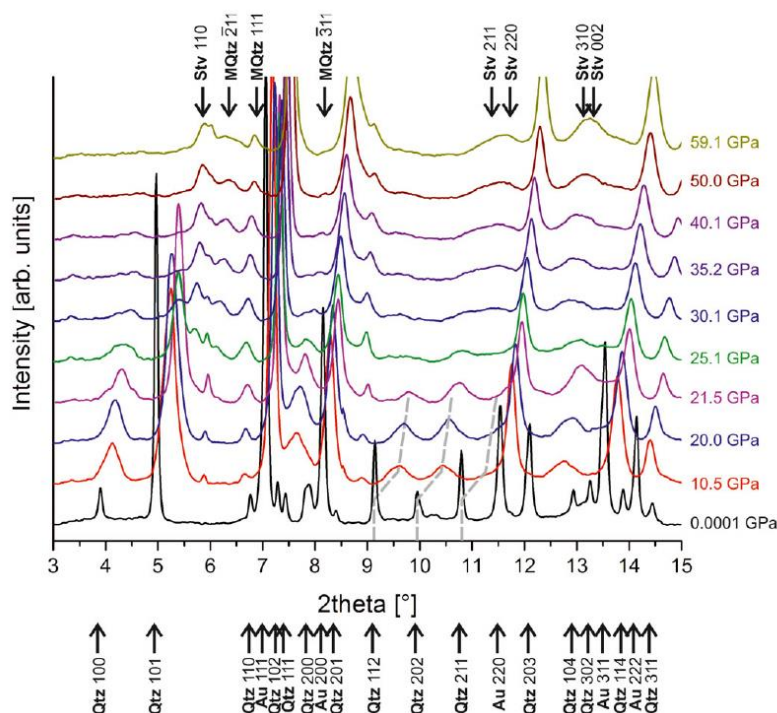


Fig. 2. The evolution of the silica phases during compression in experiment SiO₂_RT_01 (compression rate: 0.14 GPa s⁻¹): The amorphization of α -quartz (Qtz) starts at around 10 GPa. Reflections of stishovite (Stv) occur at 20.7 GPa. At low pressures, two reflections are observed which could be interpreted as the 211 and 111 reflections of the monoclinic postquartz phase (MQtz). The pressure is obtained with respect to gold (Au). (Color figure can be viewed at wileyonlinelibrary.com.)

No diffraction signal of coesite was observed in any of the compression experiments. The main feature observed in all experiments is the significant drop of the integrated intensity of the reflections of α -quartz between 10 and 15 GPa until complete disappearance. This is attributed to the amorphization of α -quartz. During amorphization, we also observe broadening of the reflections due to a reduction in the crystallite size and/or an increase in lattice distortion of α -quartz. Above 20 GPa, α -quartz transforms to the high-pressure phase stishovite as evident by the appearance of the 110, 211, 220, 310, and 002 reflections (Fig. 2).

Besides these major phase changes, we observe the appearance of additional diffraction lines that cannot be explained by contamination (e.g., Re-gaskets) and seem to be a feature of the compressed sample. In all runs, we see at low 2θ values from 3° to 8° two reflections that can be indexed with the strongest 111 and 211 reflections of the MQtz (Fig. 2). These reflections appear at low pressures. Between 19 and 20 GPa,

another weak reflection becomes visible in runs SiO₂_RT_01_07, and _08 at 2θ values of 4–5° (Fig. 2). It is noteworthy that the appearance of the 111 and 211 reflections goes along with an intensity drop in the Au 111 diffraction line indicating the compaction of the sample at the onset of the compression cycle. The 111 and 211 reflections of the MQtz are present in all runs at highest pressure of the compression cycle.

Figure 3a features a diffraction pattern collected at the highest pressure of 59.2 GPa. Gold, stishovite, and the MQtz can be identified. The broad nature of the diffraction lines and their low intensity in comparison to the background indicate the large degree of amorphization and the limited long-range order of the sample. After remaining at maximum pressure for 60 min, there are no significant changes observed in the diffraction pattern (Fig. 3b).

During decompression, no further phase transition is observed (Fig. 4a). The reflections of stishovite and of the MQtz are observed down to the lowest minimum

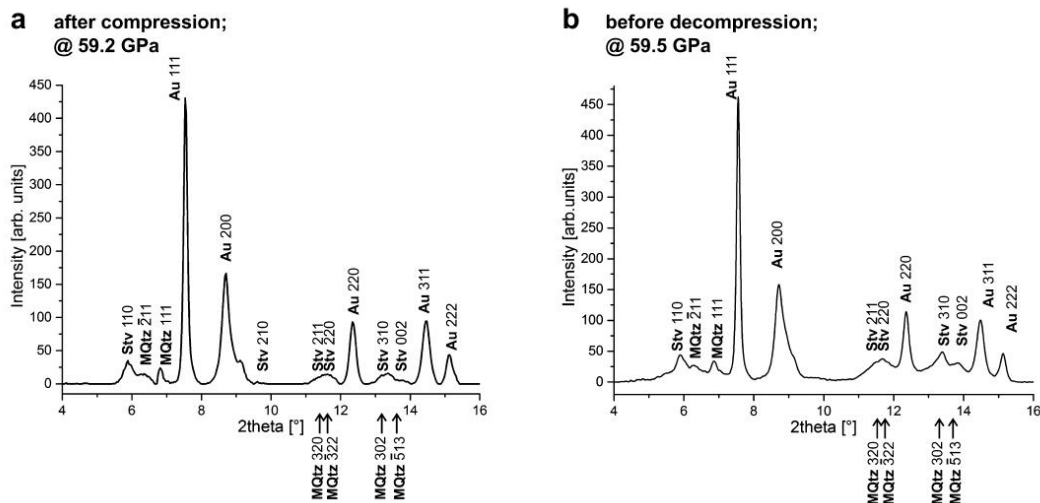


Fig. 3. The evolution of the silica phases while remaining at the maximum pressure of 59.2 GPa. The pressure is obtained with respect to gold (Au). a) After reaching maximum pressure, reflections of two silica phases are observed: stishovite (Stv) and the monoclinic postquartz phase (MQtz). b) After 60 min at maximum pressure, no changes are observed in the diffraction pattern. Collection time per diffraction pattern: 2 s.

pressure of 16.5 GPa. Decompression did not reach ambient pressures because of the friction between the piston and the cylinder of the mDAC. Due to a rearrangement of the powder and the movement of the gasket, additional reflections of the two silica phases and rhenium that originate from the gasket are observed (Fig. 4b).

The recovered sample of SiO₂_RT_04 was investigated by means of transmission electron microscopy (TEM). The microstructural investigation of a large number of fragments from the crushed specimen reveals that the vast majority of material was transformed to amorphous silica. Nonetheless, few regions contain small crystallites of stishovite embedded in the predominant amorphous silica as can be seen in Fig. 5. Using selected area electron diffraction (SAED), stishovite could be unambiguously identified on the basis of different zone axis patterns as shown in the insets in Fig. 5. In the center image, linear alignments of crystallites indicate a solid-state transition into stishovite. This is supported by the texturing of reflections in all electron diffraction patterns that were taken from numerous crystallites in a certain area indicating a preferred orientation of the crystallites. No other high-pressure phase of silica could be found by the TEM investigation of 20–30 fragments of five samples each. However, the predominant observation of amorphous silica suggests that most of the α -quartz is

transformed to glass during the pressure evolution, while only a small amount of stishovite is formed which is in accordance with the low-intensity reflections of stishovite compared to the starting reflections of α -quartz in the synchrotron experiments. The MQtz could not be found.

DISCUSSION

The presented compression experiments on α -quartz clearly indicate a complex phase transition history. At low pressures, small parts of the sample seem to transform immediately to the MQtz, while it seems that the bulk of the sample does not transform until above 20 GPa. During the compression between 10 and 15 GPa, the bulk of the sample seems to amorphize as indicated by the broadening and drop of the intensities of the α -quartz diffraction lines as well as the increase in the background signal. This is further supported by the analysis of the recovered samples with the TEM. The analysis reveals small crystallites of stishovite in an amorphous matrix, underlining that the mixture of amorphous portions and the MQtz phase transforms directly to stishovite at higher pressures above 22 GPa, bypassing the stability field of coesite. The transition from α -quartz to the MQtz in the pressure range from 21 to 35 GPa has been observed in very slow (static) compression experiments at room temperatures by

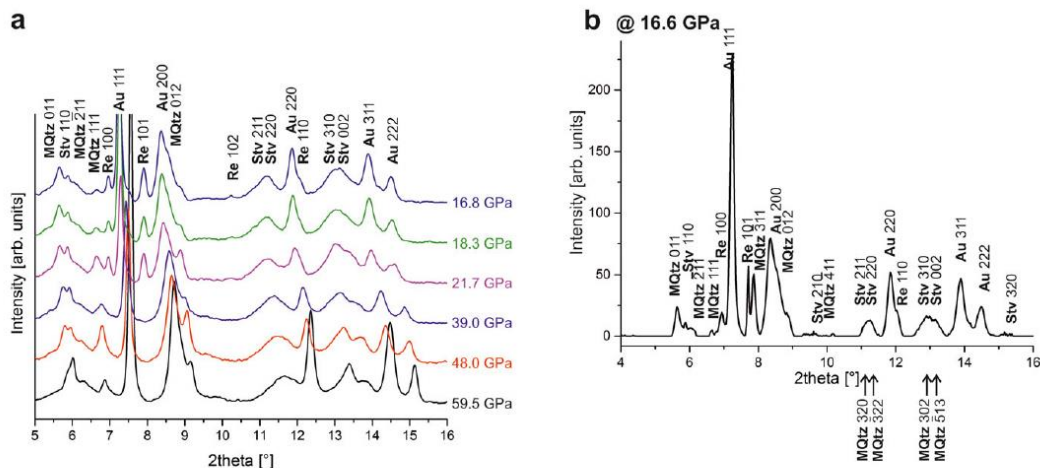


Fig. 4. The evolution of the silica phases during decompression (decompression rate: 0.03 GPa s^{-1}). The pressure is obtained with respect to gold (Au). Due to a shift of the sample, reflections of rhenium (Re) from the gasket are also observed. a) Stishovite (Stv) and the monoclinic postquartz phase (MQtz) remain stable, while α -quartz does not reappear. At 49.9 GPa, the 011 reflection of the MQtz occurs. With the end of decompression, new reflections of the MQtz are observed. b) A single diffraction pattern (collection time: 2 s) reveals the present phases at minimum pressure at 16.6 GPa. Stishovite and the MQtz are indicated. The overall intensity of the reflections of the silica phases has dropped. (Color figure can be viewed at wileyonlinelibrary.com.)

Kingma et al. (1993b) and Haines et al. (2001) and, thus, matches well with our observations of the transition of the bulk sample. The transformation of smaller portions of the sample at a much lower pressure is somewhat puzzling. However, taking into account the fact that the appearance of the 111 and 211 diffraction lines go along with a significant drop in diffraction intensity of gold could indicate that at the beginning, the sample in the chamber is not well compressed and moves during the initial compaction. During this process, it could very well be that few larger grains are birthing between the diamonds and experiencing much higher pressures than indicated by the pressure standard of gold and, consequently, transforming much earlier to the MQtz than the bulk of the sample. The MQtz could not be found by subsequent TEM analysis. Nevertheless, it is conceivable that the phase is metastable and, thus, did not survive the preparation of the recovered samples as their reflections were observed under ambient conditions after the experiments. The transition from the amorphous phase or portion of the MQtz to stishovite has never been observed at ambient conditions. Stishovite formation has only been observed at elevated temperatures, for example, at 1000 K and 55 GPa by Prakapenka et al. (2004). However, simulations by Martoňák et al. (2007) showed that a direct transition from α -quartz to stishovite may be possible via the metastable phase quartz II that is

thought to be the first phase whose structure contains SiO_6 octahedra forming between 16 and 20 GPa (e.g., Haines et al. 2001; Prakapenka et al. 2004). Thus, it is conceivable that the MQtz can be seen as another intermediate state aiding the formation of SiO_6 octahedra and helping to induce the transition to stishovite.

In all experiments, up to three additional reflections were observed that could not be attributed to stishovite, the MQtz, or possible contaminations. A distinct indexing of these reflections was not possible because the reflections could be attributed to more than one additional high-pressure phase of α -quartz such as seifertite or SnO_2 -type SiO_2 . Moreover, the low signal/noise ratio and the circumstance that the reflections of gold might overlap with important reflections make the identification of the phases even more difficult. However, taking the different kinking of SiO_6 octahedra between the high-pressure phases into account, the occurrence of these reflections may resemble a disordering in the MQtz. On the other hand, the weak reflection between 4 and $5^\circ 2\theta$ might be the 001 reflection of quartz II, although no other observed reflections can be indexed for this phase. In general, these observations show the complexity of the nonhydrostatic compression in the mDAC.

The pressure-induced amorphization of α -quartz starts between 10 and 15 GPa, which is below the

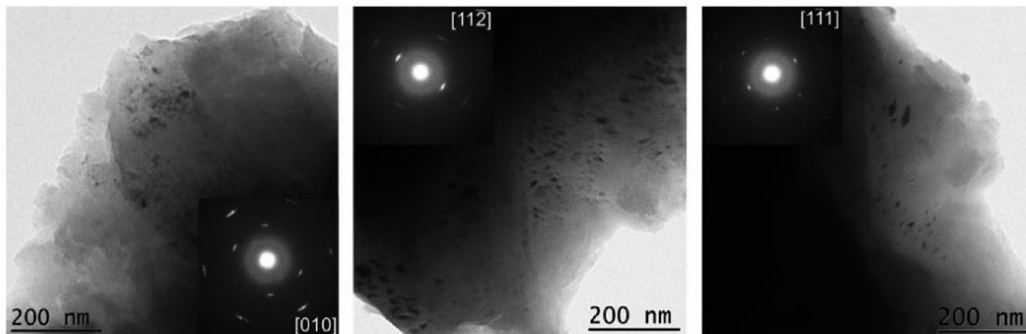


Fig. 5. Transmission electron microscopy (TEM) images of the recovered sample of $\text{SiO}_2\text{-RT-04}$ show regions that contain crystallites of stishovite embedded in the predominant amorphous silica. The insets show diffraction patterns with characteristic zone axes of stishovite. The linear alignment of crystallites represented in the center image points to a solid-state transition into stishovite. This is supported by the texturing of reflections in the diffraction patterns taken over numerous crystallites indicating a preferred orientation of the crystallites.

range of 18–35 GPa, as obtained in earlier studies (McNeil and Grimsditch 1992; Kingma et al. 1993a, 1993b). We suggest that increased strains in a nonhydrostatic compressed sample result in amorphization at lower pressures, especially when considering that McNeil and Grimsditch (1992) and Kingma et al. (1993a, 1993b) used pressure-transmitting media for their experiments.

To conclude, we conducted nine compression experiments at various compression rates indicating a transition of α -quartz to stishovite via an intermediate MQtz. Recent in situ laser shock experiments on silica glass showed the formation of stishovite as well, and are thus in line with this interpretation (Gleason et al. 2015). During decompression, stishovite and the MQtz stay stable under minimum pressure of the compression experiment, while α -quartz does not recrystallize. In literature, however, α -quartz was reported to recrystallize (e.g., Kingma et al. 1993b; Haines et al. 2001). Haines et al. (2001) discovered the monoclinic post-quartz phase and quartz in their recovered samples. Their assumption that quartz II recrystallizes to α -quartz during decompression helps us exclude the formation of quartz II in our experiments because reflections of α -quartz were not observed under ambient conditions after the experiment.

SUMMARY

We use a combination of a mDAC and in situ powder X-ray diffraction to study the phase transitions of α -quartz at pressures up to 66.1 GPa at room temperature and different compression rates up to

2.0 GPa s^{-1} . The collection time of one diffraction pattern is down to 1 s.

The nonhydrostatic compression experiments reveal that α -quartz transforms even at room temperature directly to stishovite, skipping the stability field of coesite. This observation suggests that stishovite could possibly directly form during shock compression, which is much shorter but takes place at an enhanced temperature. This phase transition to stishovite occurs in our experiments between 20.7 and 28.0 GPa during compression and slightly increases with an increasing compression rate. Stishovite remains stable upon reaching maximum pressure and during the time while the maximum pressure is kept for more than 1 h. During decompression, stishovite reflections remain observable, while no reflections of α -quartz appear in the patterns. The formation of stishovite was confirmed by an analysis of the recovered samples in the TEM.

In the course of compression, new reflections can be observed up to 19.8 GPa, which might be assigned to the MQtz, although an independent proof of this phase by TEM analysis was not successful. These new reflections remain detectable until the maximum pressure is reached. The reflections are not influenced by the phase transition of α -quartz to stishovite. Upon decompression, these reflections do not vanish.

Furthermore, an amorphization of α -quartz starts between 10 and 15 GPa during compression. The material becomes more and more amorphized with proceeding compression until α -quartz transforms to stishovite. The amount of stishovite formed is very small and its long range order decreases as shown by the weak and broad reflections of this phase. After the phase transition, the amorphization only progresses slightly

forward as revealed by diffraction patterns taken at maximum pressures between 26.7 and 66.1 GPa. There are no other changes with respect to the phases of silica observed in these diffraction patterns.

Our dynamic compression experiments provide insight into the kinetics of high-pressure phase transitions of α -quartz: The experiments indicate that a meteorite impact causes an instantaneous formation of structures consisting only of SiO_6 octahedra rather than the rearrangement of the SiO_4 tetrahedra to form coesite. Although the compression rates are much higher and temperatures are elevated in the context of impact cratering, these present in situ investigations of phase transitions are a necessary first step to understand the behavior of SiO_2 under the much faster compression rates of impact events. The latter is envisaged to be studied with a laser shock-compressed sample at X-ray-free electron lasers (XFELs) in the future (Gleason et al. 2015).

Acknowledgment—This study was conducted in the framework of the DFG research unit FOR-887 Experimental Impact Cratering – The MEMIN II Program (Multidisciplinary Experimental and Modeling Impact Research Network), project KE 732/23-1 “Dynamic loading and unloading of SiO_2 aggregates. Real-time phase transformation monitored by means of synchrotron beam diffraction.” FL is grateful to the Deutsche Forschungsgemeinschaft for funds provided by the Leibniz program (LA 830/14-1) and project LA830/17-1 within the MEMIN II program. The authors thank the reviewers Prof. Dr. Alex Deutsch and Prof. Dr. Fred Hörz for their useful comments and suggestions, which helped to improve the manuscript.

Editorial Handling—Prof. Alexander Deutsch

REFERENCES

- Anderson O. L., Isaak D. G., and Yamamoto S. 1989. Anharmonicity and the equation of state for gold. *Journal of Applied Physics* 65:1534–1543.
- Birch F. 1952. Elasticity and constitution of the Earth's interior. *Journal of Geophysical Research* 57:227–286.
- Černok A., Bykova E., Ballaran T. B., Liermann H. P., Hanfland M., and Dubrovinsky L. 2014. High-pressure crystal chemistry of coesite-I and its transition to coesite-II. *Zeitschrift für Kristallographie* 229:761–773.
- Chao E. C. T., Shoemaker E. M., and Madsen B. M. 1960. First natural occurrence of coesite. *Science* 132:220–223.
- Chopin C. 1984. Coesite and pure pyrope in high-grade blueschists of the Western Alps: A first record and some consequences. *Contributions to Mineralogy and Petrology* 86:107–118.
- Choudhury N. and Chaplot S. L. 2006. Ad initio studies of phonon softening and high-pressure phase transitions of α -quartz SiO_2 . *Physical Review B* 73:094304.
- Coes L. 1953. A new dense crystalline silica. *Science* 118:131–132.
- Dubrovinsky L. S., Dubrovinskaia N. A., Prakapenka V., Seifert F., Langenhorst F., Dmitriev V., Weber H. P., and Le Bihan T. 2004. A class of new high-pressure silica polymorphs. *Physics of the Earth and Planetary Interiors* 143–144:231–240.
- Fazio A., Mansfeld U., and Langenhorst F. 2016. Coesite in suevite from the Ries impact structure (Germany): From formation to post-shock evolution. *Meteoritics & Planetary Science*, doi:10.1111/maps.12849.
- French B. M., and Koeberl C. 2010. The convincing identification of terrestrial meteorite impact structures: What works, what doesn't, and why. *Earth-Science Reviews* 98:123–170.
- Gleason A. E., Bolme C. A., Lee H. J., Nagler B., Galtier E., Milathianaki D., Hawreliak J., Kraus R. G., Eggert J. H., Fratantuono D. E., Collins G. W., Sandberg R., Yang W., and Mao W. L. 2015. Ultrafast visualization of crystallization and grain growth in shock-compressed SiO_2 . *Nature Communications* 6:8191.
- Haines J., Léger J. M., and Chateau C. 2000. Transition to a crystalline high-pressure phase in α - GeO_2 at room temperature. *Physical Review B* 61:8701–8706.
- Haines J., Léger J. M., Gorelli F., and Hanfland M. 2001. Crystalline post-quartz phase in silica at high pressure. *Physical Review Letters* 87:155503.
- Hammersley A. P., Svensson S. O., Hanfland M., Fitch A. N., and Häusermann D. 1996. Two-dimensional detector software: From real detector to idealized image or two-theta scan. *High Pressure Research* 14:235–248.
- Hill R. J., Newton M. D., and Gibbs G. V. 1983. A crystal chemical study of stishovite. Locality: Synthetic. *Journal of Solid State Chemistry* 47:185–200.
- Huang L., Durandurdu M., and Kieffer J. 2006. Transformation pathways of silica under high pressure. *Nature Materials* 5:977–981.
- Kieffer S. W., Phakey P. P., and Christie J. M. 1976. Shock processes in porous quartzite; transmission electron microscope observations and theory. *Contributions to Mineralogy and Petrology* 59:41–93.
- Kingma K. J., Meade C., Hemley R. J., Mao H., and Veblen D. R. 1993a. Microstructural observations of α -quartz amorphization. *Science* 259:666–669.
- Kingma K. J., Hemley R. J., Mao H., and Veblen D. R. 1993b. New high-pressure transformation in α -quartz. *Physical Review Letters* 70:3927–3930.
- Kirfel A., Krane H. G., Blaha P., Schwarz K., and Lippmann T. 2001. Electron-density distribution in stishovite, SiO_2 : A new high-energy synchrotron-radiation study. *Acta Crystallographica Section A* 57:663–677.
- Konopkova Z., Rothkirch A., Singh A. K., Speziale S., and Liermann H. P. 2015. In situ x-ray diffraction of fast compressed iron: Analysis of strains and stress under non-hydrostatic pressure. *Physical Review B* 91:144101.
- Langenhorst F. and Deutsch A. 2012. Shock metamorphism of minerals. *Elements* 8:31–36.
- Langenhorst F. and Poirier J. P. 2000. Anatomy of black veins in Zagami: Clues to the formation of high-pressure phases. *Earth and Planetary Science Letters* 184:37–55.
- LeBail A., Duroy H. and Fourquet J. L. 1988. Ab initio structure determination of LiSbWO_6 by x-ray powder diffraction. *Material Research Bulletin* 23:447–452.

- Liermann H.-P., Konôpková Z., Morgenroth W., Glazyrin K., Bednarcik J., McBride E. E., Petitgirard S., Delitz J. T., Wendt M., Bican Y., Ehnes A., Schwark I., Rothkirch A., Tischer M., Heuer J., Schulte-Schrepping H., Kracht T., and Franz H. 2015. The extreme conditions beamline P02.2 and the extreme conditions science infrastructure at PETRA III. *Journal for Synchrotron Radiation* 22:908–924.
- Luo S. N., Ahrens T. J., and Asimov P. D. 2003. Polymorphism, superheating, and amorphization of silica upon shock wave loading and release. *Journal of Geophysical Research B* 108:2421.
- Mansfeld U., Langenhorst F., Ebert M., Kowitz A., and Schmitt R. T. 2017. Microscopic evidence of stishovite generated in low-pressure shock experiments on porous sandstone: Constraints on its genesis. *Meteoritics & Planetary Science*, doi:10.1111/maps.12867.
- Martonoák R., Donadio D., Oganov A. R., and Parrinello M. 2007. From four- to six-coordinated silica: Transformation pathways from metadynamics. *Physical Review B* 014120:1–11.
- McNeil L. E. and Grimsditch M. 1992. Pressure-amorphized SiO₂ α -quartz: An anisotropic amorphous solid. *Physical Reviews Letters* 68:83–85.
- Ohtaka O., Yoshiasa A., Fukui H., Murai K., Okube M., Katayama Y., Utsumi W., and Nishihata Y. 2001. Structural changes of quartz-type GeO₂ under pressure. *Journal for Synchrotron Radiation* 8:791–793.
- Prakapenka V. P., Shen G., Dubrovinsky L. S., Rivers M. L., and Sutton S. R. 2004. High pressure induced phase transformation of SiO₂ and GeO₂: Difference and similarity. *Journal of Physics and Chemistry of Solids* 65:1537–1545.
- Rietveld H. M. 1967. Line profiles of neutron powder-diffraction peaks for structure refinement. *Acta Crystallographica* 22: 151–152.
- Rietveld H. M. 1969. A profile refinement method for nuclear and magnetic structures. *Journal of Applied Crystallography* 2:65–71.
- Rodríguez-Carvajal J. 1993. Recent advances in magnetic structure determination by neutron powder diffraction. *Physica B* 192:55–69.
- Shoemaker E. P. and Chao E. C. T. 1961. New evidence from impact origin of Ries basin, Bavaria, Germany. *Journal of Geophysical Research* 66:3371–3378.
- Smyth J. R. and Hatton C. J. 1977. A coesite-sanidine grosspyrite from the Roberts Victor kimberlite. *Earth and Planetary Science Letters* 77:284–290.
- Stishov S. M. and Popova S. V. 1961. A new dense modification in silica. *Geokhimiya* 10:837–880.
- Stöfler D. and Langenhorst F. 1994. Shock metamorphism of quartz in nature and experiment: I. Basic observation and theory. *Meteoritics & Planetary Science* 29:155–181.
- Teter D. M., Hemley R. J., Kresse G., and Hafner J. 1998. High-pressure polymorphs in silica. *Physical Review Letters* 80:2145–2148.
- Wentzcovitch R. M., da Silva C., Chelikowsky J. R., and Binggeli N. 1998. A new phase and pressure induced amorphization in silica. *Physical Review Letters* 80:2149–2152.
- Will G., Parrish W., and Hart M. 1988. Crystal structures of quartz and magnesium germanate by profile analysis of synchrotron-radiation high-resolution powder data. *Journal of Applied Crystallography* 21:182–191.
- Wünnemann K. and Ivanov B. A. 2003. Numerical modelling of impact crater depth-diameter dependence in an acoustically fluidized target. *Planetary and Space Science* 51:831–845.

4.5 Structural geologist at UniLaSalle

I obtained a permanent position at UniLaSalle Beauvais campus in February 2013.

My teaching duties include lectures at all levels from the engineer and technician curriculum. A complete list of these activities is given in section 5. I am a member of the Basin Reservoir and Resources (B2R, URR 7511) research team headed by Dr. Sébastien Potel. I contribute to some subcontracting activities provided by UniLaSalle and participate to several student's exhibitions plus international representations at local, national and international scales.

I wish to first explain the reasons for applying to a position in an engineering school and will then summarize my main ongoing projects in terms of research and education.

4.5.1 The choice of a candidature at UniLaSalle

The different positions I held after my PhD allowed me to obtain a panel of scientific and technical competences plus a solid laboratory management experience. I could enlarge my domains of research and acquire a good practice in terms of teaching and student supervision. My activities within the private sector gave me the opportunity to discover several examples of possible collaborations between the public academic sector and different applied research and development departments within the industrial sector.

The structural geologist position within the geoscience department at UniLaSalle was perfectly adapted to my profile. At first, I am a member of the Basin Reservoir Resources (B2R) research unit. This research

activity is my career priority. I propose my own research subjects dealing with reservoir geology and I am invited to participate to the research activities and publications of my colleagues like the results presented by Potel et al. (2016). Concerning education, UniLaSalle proposes several study tracks in a varieties of earth science specialties at engineer and technician levels. My teaching experience is profitable and I provide an average of 250 hours of lectures per year. UniLaSalle puts forward an intensive training in the field, promotes international mobility and encourages internships in the private sector. This approach is in line with my conception of teaching activities.

I am grateful to the UniLaSalle institute who accepted my candidature and specials thanks are expressed to the Language International and Culture (LINC) for developing my international network. Obtaining a permanent academic position offered me the possibility to implement for the first time in my career my own research and teaching projects on the long term. I can use and share my interdisciplinary experience, together with my international professional network in order to develop some sectors of activity and existing infrastructures. In terms of teaching, I further enhance the existing curriculum and create new courses of study. I pay particular attention to include the last research findings within my lectures and promote international internships in a variety of research laboratories.

4.5.2 The choice of geothermal plus carbon capture and storage

4.5.2.1 General context

The planet earth is facing since several decades a global warning likely enhanced by human activities related greenhouse gases emissions. The European community has launched a series of measures and investments to prospect and utilize a variety of renewable energy resources and lower its dependency to fossil fuels. This political willingness is further motivated by the complexity of the world's present geopolitical context in which access to conventional energy resources is subjected to political crises and associated restrictions. Energy independence of the European continent is considered as a strategic issue of primary importance in order to ensure economic and societal prosperity while keeping energy costs under control. Energy transition policies and environment protection measures have a broad societal impact, they trigger the need of a collective effort in terms of training, development plus project funding at international scale.

Geologists are at the forefront when dealing with the search multiple resources from the earth's underground. Besides the oil and gas plus mining industry to cite only two of them, increasing interest is noticed in the fields of geothermal utilization and Carbon Capture and Storage (CCS). The European commission, countries' governments and private investors have launched a multitude of initiatives in both these fields. Education is also concerned as an increasing number of lectures dealing with renewable energy production and means to lower green gases concentration in the earth atmosphere are given at University and schools of engineering.

Geothermal presents a series of advantages compared to other renewable energy sources: the resource is virtually inexhaustible, environmental impact is low, energy production is constant and independent from weather conditions. At present-day, geothermal reservoir utilization is possible in a variety of geological settings and brine temperature.

Geological sequestration of CO₂ implies a CO₂ injection at supercritical stage in a chosen highly permeable geological formation at great depth with a non-permeable cap unit. The targets are generally chosen within depleted oil reservoirs, unmineable coal seams or deep saline formations. The storage must last for millions of years and is strongly dependent on reservoir structure, rock petrophysical properties, fluid rock interaction processes and associated reaction kinetics.

It is evident that in the present state of knowledge, the European-scale utilization of geothermal and geological sequestration of CO₂ are not reaching their full potential. This delay has multiple explanations like 1) the lack of direct underground data combined to 2) difficulties in geophysical data interpretation, 3) a missing global understanding of dual porosity reservoirs, 4) a scarce number of comprehensive training programs for researchers, engineers and technicians together with 5) a poor communication strategy to general public, policy makers and stakeholders. For all these reasons multidisciplinary, intersector and international research and training initiatives are needed.

4.5.2.2 The concept of reservoir analogue

Gaining a global understanding of a reservoir at depth is a challenging task. At best, the only data available to the geologist usually consist in an expensive combination of cores and downhole geophysics plus imaging combined with indirect geophysical data acquired at surface. A quantified geological and petrophysical characterization of the whole reservoir is therefore subjected to large amount of uncertainties. A common method designed to populate a statistically relevant database in terms of structural organization of the reservoir, sample petrophysical properties characteristics, level of fracture connectivity is to work on naturally exhumed paleo-reservoirs with approaching geological setting at depth compared to the chosen active reservoir. These exhumed systems are called reservoir analogues.

Many criteria come into play when selecting the reservoir analogue. It is evident that a perfect copy at surface of a poorly known reservoir at depth is not possible to find and it is important to precisely define the concept of analogy itself. The analogy between a fossil and an active reservoir consists in chosen similar characteristics between both objects and a precise determination of these characteristics must be made at first. It is conceivable that a single reservoir analogue will not permit to cover the whole range of key parameters needed to design an exploration strategy and information from several analogues are then needed. Another issue when dealing with reservoir analogue is the inherent tectonic overprint and retrograde metamorphism during exhumation combined to weathering at surface. Nevertheless, the analogue-based approach is cost effective and as proven to be extremely valuable especially when correlated to the active reservoir by wells.

The use of reservoir analogue is usual in the oil and gas sector to outline for example petrophysical properties evolution controlling the flow of hydrocarbons (Alsop et al., 2014; Barbier et al., 2012; Giuffrida et al., 2020; Howell et al., 2014; Pranter et al., 2014). Analogue investigations have been applied as well to eolian (Clemmensen, 1987; Mountney et al., 1999) and fluvial depositional systems (Fielding and Crane, 1987; Gibling, 2006; Keogh et al., 2014).

4.5.2.2.1 Geothermal reservoir analogues

Geothermal analogues can potentially be found from all geological settings where geothermal energy can be gained from. These are namely 1) intra-cratonic sedimentary basins which are in general porous reservoirs with fluid temperatures ranging between 50°C and 150°C, 2) fractured plutonic or metamorphic basement with fluid temperature ranging between 150°C and 250°C plus 3) volcanic provinces presenting fluids in a supercritical stage (above 400°C). The use of geothermal reservoir analogues is relatively recent and data are available for the upper Rhine graben (Bär, 2012; Bär et al., 2011; Bauer et al., 2015; Bossennec et al., 2022, 2021; Kushnir et al., 2018; Meier et al., 2015; Sass et al., 2011; Schmidt et al., 2015), the North German basin (Barth et al., 2014; Reyer, 2014), the Thuringian syncline in central Germany (Beyer et al., 2014), the molasse basin in southern Germany (Homuth et al., 2014), the Harz massif (Peacock et al., 2022) considered as an analogue to the Leinegraben basement below the city of Göttingen (Lower Saxony,

Germany), the Death Valley area (Chabani et al., 2021b, 2021a; Klee et al., 2021b, 2021a) used as an analogue to the Soultz sous Forêts (SSF) and Rittershoffen (RH) reservoir (URG, France) and the Acoculco caldera complex located within the Trans Mexican Volcanic Belt (Avellán et al., 2020; Hiriart et al., 2011; Lepillier et al., 2020) to cite only a few.

4.5.2.2.2 CCS reservoir analogues

CCS reservoir analogues are classically divided between natural and industrial analogues. They are both defined as case studies that permit to identify features either effective or to be avoided for a successful storage of CO₂. These analogues permit to improve both technical know-how and its application. Natural analogues relevant for the CCS concept are either accumulations that remain stable over geological time scale or accumulations where evidences of leaking can instead be found. Even if counterintuitive at first sight, studying the reasons for a leakage permits to outline characteristics to be avoided when selecting specific sites for geological CO₂ storage. A vast number of references are found the literature compiling natural occurrences of CO₂ (Morgan, 2007; Naruk et al., 2019; Stevens et al., 2005) and natural leakage of CO₂ (Annunziatellis et al., 2008; Beaubien et al., 2008; Holloway et al., 2005; Klusman, 2002; Pearce et al., 2004). CCS industrial analogues consist in Enhanced Oil Recovery (EOR) projects and natural gas storage. EOR implies the injection of CO₂ into depleted reservoirs forcing mobility of oil from the injection well towards the production well. The technique is used from many decades and well-mastered. Natural gas storage in the underground is also commonly put into practice using depleted oil and gas fields plus aquifers (Benson, 2005; Perry, 2005).

4.5.2.3 Outline of my research approach at UniLaSalle

Considering the analogue dedicated literature, I realized that the multidisciplinary set of fundamental research competences that I acquired during my education and professional experience could, when combined, find direct applications in terms of reservoir utilization. These are namely 1) field mapping and multiscale domain structural analysis, 2) fluid rock interaction processes, 3) microfabric analysis of highly strained rocks in both brittle and ductile field and 4) rock mechanical properties. The study of reservoir analogues allows me to achieve research using and combining the disciplines I am competent in.

My present research is applied to geothermal utilization in fractured basement reservoir with fluid temperatures between 150°C and 250°C and related analogue studies. I also recently entered the field of CCS studies investigating its feasibility within fractured reef constructions. My investigations are dealing with 1) a reconstruction of the tectonic and metamorphic evolution of reservoir analogues, 2) a 3D representation and statistical analysis of fracture network, 3) a study of chemical and physical processes responsible of the interaction between the brine and the host rock, 4) the influence of strain and grain comminution on the kinetics of alteration minerals development, 5) the study of anisotropy development within strain related alteration zones and 6) the influence of this anisotropy on fault mechanical and petrophysical behavior. I propose to combine these different research lines in order to participate in a realistic conceptual modeling of mechanical, petrophysical, microstructural and microtextural fractured systems' properties change upon development of alteration minerals drastically impacting fluid circulation within the reservoir.

In terms of geothermal energy utilization, my approach gives inputs to model reservoir permeability and mechanical stability evolution during both stimulation and injection phases. These two parameters are essential as their precise understanding is used to design reservoir exploitation strategies dedicated to 1)

maintain both a constant flow rate and fluid temperature and 2) avoid the development of induced seismic events. My work participates in lowering the risks of geothermal reservoir utilization both in terms of engineering and societal acceptance of geothermal projects.

In terms of CCS feasibility within fractured carbonates, my research aims at gaining a precise reconstruction of the reservoir anisotropy. This anisotropy is related to the formation process of the carbonate reef itself the architecture of which is being overprinted by tectonic deformation. I am using multi-scale data, namely seismic lines, borehole and core imaging plus sample thin sections. I plan to perform petrophysical measurements in terms of porosity and permeability estimations on core samples gained from the above-mentioned borehole. Reservoir architecture and host rock petrophysical data are used as inputs for Thermo Hydraulic Mechanical (THM) simulations in order to outline possible CO₂ migrations in time within the reservoir. Reaction kinetics between the brine and the host rock and related to the acidizing effect of the gas injection will be modeled separately. My work participates in ensuring CO₂ storage on the long term and deciphering potential leakage hazard.

In summary, I am willing to use and develop my scientific expertise in order to bring input used by the reservoir engineering community.

4.5.3 Research activities

I have been establishing over the years a cooperation network with a variety of Universities, research centers and industrial partners. Participants are found in the United States, Europe, Turkey and Asia. This network is of primary importance in terms of knowledge and facilities sharing plus access to reservoir exploitation data.

My research funds are mainly granted by highly competitive European projects in the framework of H2020, Horizon Europe and Erasmus + programs. An additional PhD funding dedicated to exploration of a potential CCS site is provided by the Technical University of Petronas (Malaysia).

In this section, I am giving a summary of the different research grants I obtained, emphasizing on my research outcomes.

4.5.3.1 The MEET research, development and demonstration project

The UniLaSalle candidature to H2020 Low Carbon Energy 2017 call was decided under my instigation. I obtained some financial support from both UniLaSalle and “Fonds Regional d’Aide aux Porteurs de Projets Européens” (FRAPPE) in order to prepare the proposal under guidance of a consulting company. I was the scientific coordinator of the Multidisciplinary and multi-context demonstration of EGS exploration and Exploitation Techniques and potentials (MEET) project (Trullenque et al. 2018). I ensured its proper functioning in terms of strategy (opportunities and risk analysis) and operation (project internal animation plus communication and deliverable review). I was also responsible from a work package dealing with communication and dissemination to stakeholders of project’s results. A letter certifying my role within the project is found in appendix to the present candidature. In terms of research, I was supervising one PhD and two post-doctoral fellows plus one research engineer.

MEET was a demonstration project with a Technical Readiness Level equal to 8 aiming at developing EGS (Enhanced Geothermal Systems) at European scale. The consortium included 16 European partners with a variety of industrial partners, research institutes and Universities together. The project had several demonstration and reservoir analog sites worldwide.

The main objective of MEET was to enable EGS techniques on existing geothermal power plans and oil boreholes over a wide range of temperatures. It was proposed to produce electricity using small scale mobile ORC power units. These represent a lower investment compared to larger scale infrastructures, and can be deployed at large scale over the European territory. Geothermal brines co-produced during oil and gas extraction were also valorized in terms of district heating in the framework of the project.

MEET aimed at optimize reservoir productivity and stimulation techniques benefiting from operators' expertise. A better understanding of geological settings is needed in order to transfer EGS technology in various environments. MEET demonstrated EGS applications in different geological settings: granitic basement, Variscan metamorphic provinces, sedimentary basins and volcanic areas taking into account their various deformation related characteristics.

The project included a series of feasibility studies as a function of technical, economic and environmental data. The most promising sites were registered in a GIS database available to potential future investors. MEET participated to economic model simulations in order to prepare future creation of new power plans.

In terms of research I participated to 1) geological investigations carried out in several reservoir analogues, 2) microfabric analysis of scales developing in power plans pipes and heat exchangers (Ledésert et al., 2021) and 3) the development of a techno economic decision-making tool for future investors (Raos et al., 2019).

Besides technological and scientific value, MEET gave to me the opportunity as a work package leader to consider the importance of communication to a broad audience and investors in order to develop new renewable energy sources.

The MEET project results have been published in a series of international scientific reviews with various thematic (geological, material science, economic feasibility) and a special issue entitled "Enhanced Geothermal Systems and other Deep Geothermal Applications throughout Europe: the MEET Project" (ISSN 2076-3263) is available in the Geoscience journal. I am coeditor of this volume and actively participated to a series of A ranking articles related to geology and transverse disciplines (Chabani et al., 2021b, 2021a; Klee et al., 2021b, 2021a; Ledésert et al., 2021; Pavlis and Trullenque, 2021; Raos et al., 2019).

4.5.3.1.1 Reservoir analogues studies

As a demonstration project, MEET gave emphasis to a variety of geological settings from which geothermal utilization could be planned. Demonstration sites were found in sedimentary basins with conversion of oil wells to geothermal wells, Variscan rocks units widely distributed across Europe and volcanic provinces in Iceland. Among Variscan formations MEET made a distinction between metasediments plus metavolcanics basement and granitic basement. Both metasediments plus metavolcanics and granites can be affected or not by post Variscan extensional tectonics (Figure 1).

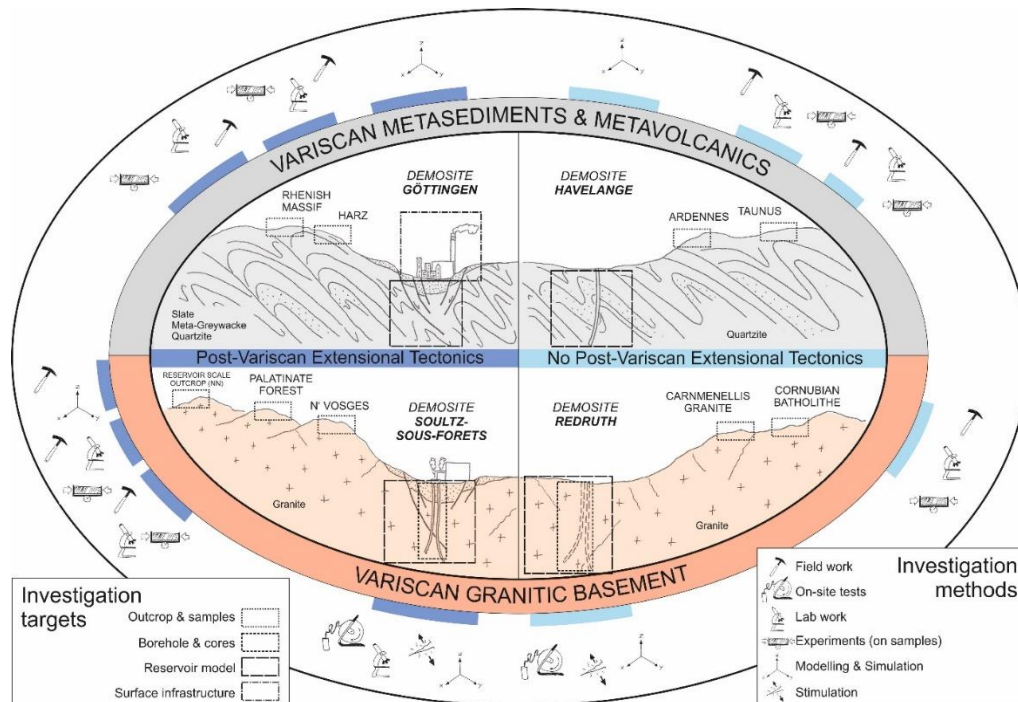


Figure 1: Overview of the four MEET demonstration sites within Variscan reservoirs (after Trullenque et al. 2018).

Considering the classification presented in Figure 1, my research activities were dedicated to the context presented in the lower left quarter namely Variscan granitic basement affected by post Variscan extensional tectonics. I coordinated a team in order to study alteration processes and fracture network development in granitic basement rocks subjected to progressive deformation using exhumed reservoir analogues. I have applied a multidisciplinary approach involving structural geology, petrographic characterization of alteration processes and statistical analysis of fracture networks.

The reference demonstration site for the context of Variscan reservoirs affected by post Variscan tectonics is the SSF reservoir located in northern Alsace (France), within the Upper Rhine Graben (URG). Other data from geothermal wells are available from the RH power plan and the Illkirch geothermal project. The SSF power plan consists of several wells drilled down to 5 km depth in fractured granitic crystalline basement. The SSF production well brings 30kg/s of a geothermal brine with a temperature of 160°C at surface and a salt concentration of around 100g/L. The site produces 1.7 MWe gross power (Mouchot et al., 2019) using an ORC unit. The SSF site was intensively studied as a scientific pilot project during two decades with about 60 PhD thesis and more than 250 publications in peer review journals.

The URG constitutes the central segment of a vast rift system crossing western Europe (Figure 2) and extending from the Mediterranean to the North sea, called the European Cenozoic Rift System (ECRIS, Prodehl et al., 2006; Ziegler, 1994, 1992). The URG is about 300 km long and 40 km wide and is bordered by the Rhenish massif to the North, the front of the Jura mountains to the South, the Variscan Vosges Massif (VM) to the West, and by the Variscan Odenwald and Black Forest massifs (BFM) to the East. The maximum crustal extension has been estimated between 5 and 7 km (Illies, 1965; Ziegler, 1994; Ziegler and Dèzes, 2005).

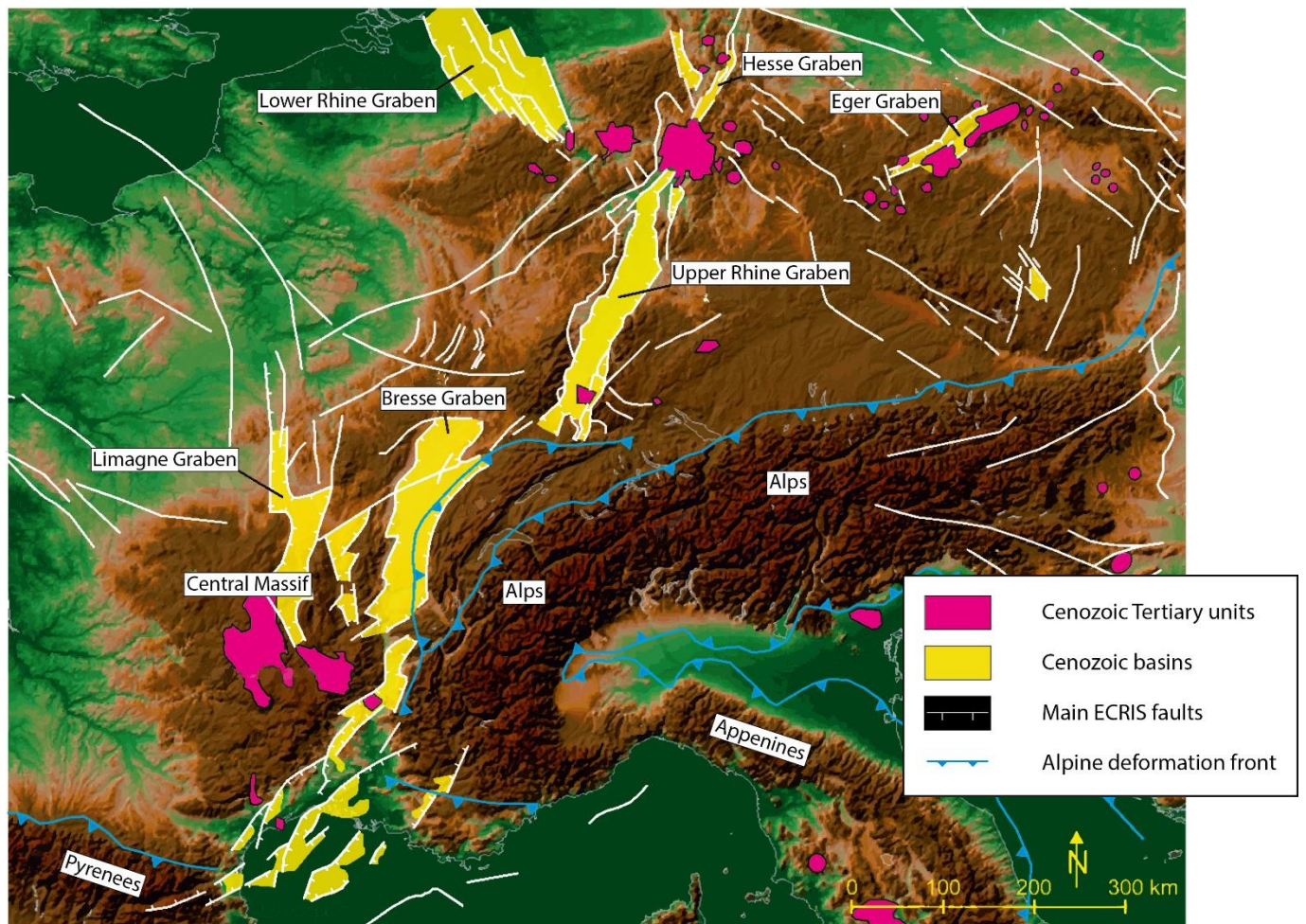


Figure 2: Overview of the European Cenozoic Rift System (ECRIS). Graphic illustration by Christian Röhr (<https://www.oberrheingraben.de/index.htm>).

The URG consists of three segments of about 100 km long and 30 to 40 km wide and widens to 60 km in the South and 80 km to its northern termination (Grimmer et al., 2017). The URG has been extensively studied in terms of both its tectonics (Bergerat, 1985; Dèzes et al., 2005, 2004; Illies, 1978, 1977, 1974; Illies et al., 1967; Villemin and Bergerat, 1987) and sedimentary sequences (Bartz, 1974; Doebbl, 1970, 1967; Illies, 1977; Lutz and Cleintuar, 1999; Schumacher, 2002; Sissingh, 1998; Ziegler, 1994).

The presence of the URG and its structural organization being intimately related to reactivation of inherited Variscan faults and shear zones in a polyphase geological context with varying stress-field (Edel et al., 2007; Frey et al., 2022; Grimmer et al., 2017; Schumacher, 2002), I propose at first to outline the main features of the Variscan orogeny in Western Europe.

The Variscan orogen is composed of several domains, namely the Northern Phyllite zone, the Mid German Crystalline High, the Saxo Thuringian and the Moldanubian (Figure 3) (Anderle et al., 1995; Behr, 1966; Boigk and Schöneich, 1970; Franke, 2014, 2000, 1995, 1992, 1989; Franke et al., 2017; Oncken et al., 1995; Winchester et al., 2002). These units have been imbricated during Middle Paleozoic convergence between Laurussia and Gondwana (Behr et al., 1984; Franke, 2000; Giese, 1995; Kroner et al., 2008; Zeh and Gerdes, 2010).

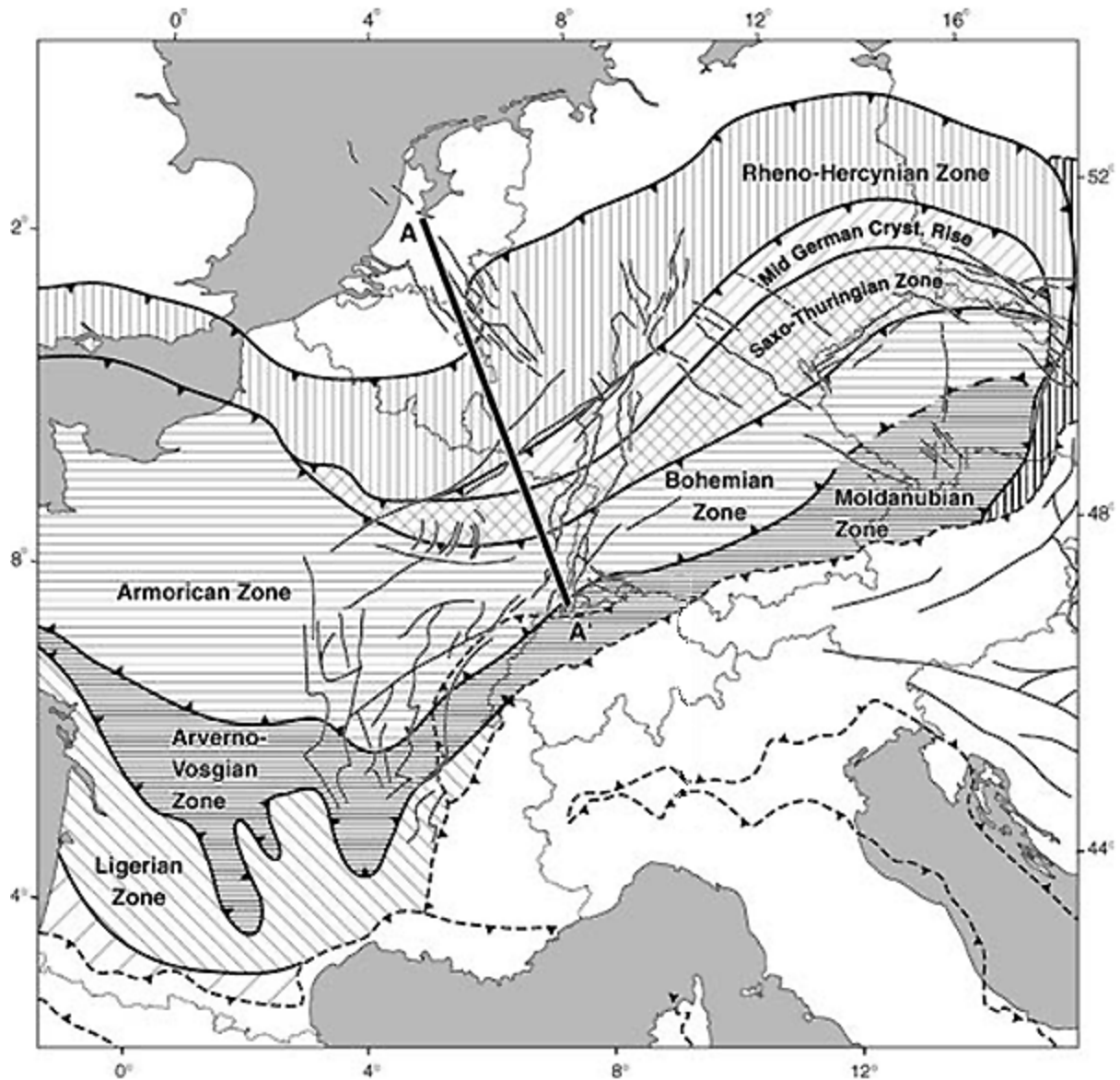


Figure 3: Variscan tectonic framework of ECRIS (redrawn after Ziegler and Dèzes, 2005).

Three Variscan sutures are observable in Figure 3 namely 1) a south dipping suture between the Rheno Hercynian zone and the Saxo Thuringian zone, 2) a south dipping suture between the Saxo Thuringian zone and the Bohemian zone (Lalaye Lubin and Baden Baden zone) and 3) a north dipping suture (Badenweiler Lenzkirch zone) between the Moldanubian zone and the Bohemian zone (Eisbacher et al., 1989; Franke, 2000; Hegner et al., 2001). As presented in Figure 4a, a reconstruction of the Variscan orogeny during the Westphalian (313 to 304 Ma) shows an Armorican Terrane Assemblage, i.e. micro terranes and marine basins separated during the Cambrian from the northern margin of Gondwana (Crowley et al., 2000; Franke et al., 2017; Kemnitz et al., 2002).

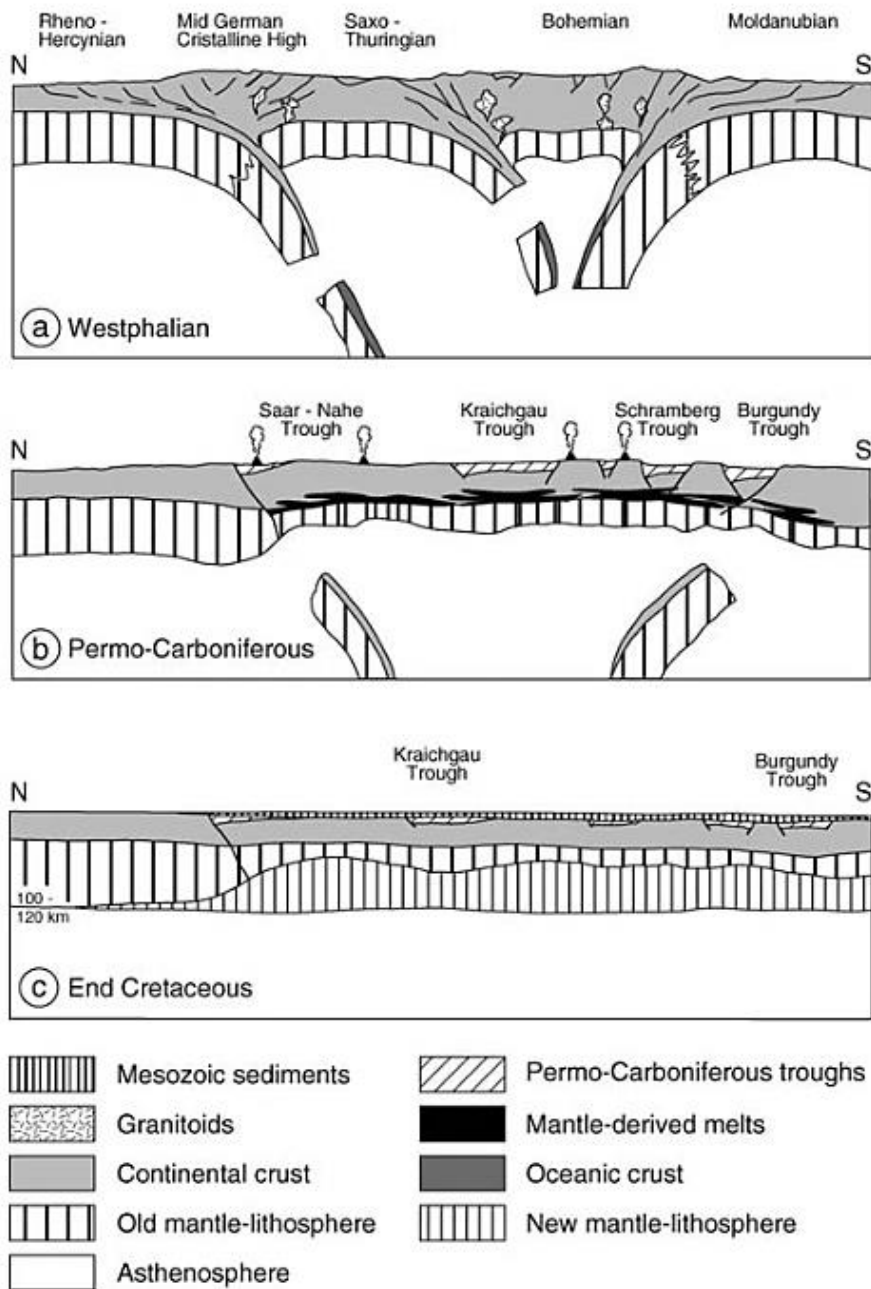


Figure 4: Geodynamic evolution along the AA' transect in figure 3 (redrawn after Ziegler and Dèzes, 2005).

Ongoing shortening accommodated by opposed subduction zones led to intense volcanic arc activity and magmatism (Figure 4b). The remnants of the widespread granitic magmatisms are exposed in the Odenwald, BFM, VM (Okrusch, 1995; Stein, 2001; Timmermann, 2008) and Massif Central (Thiery et al., 2009). This widespread magmatism thermally destabilized the orogenically thickened lithosphere. During this period slab detachment and asthenosphere upwelling contribute to the delamination of the lithosphere and disruption of the Variscan orogen. Mantle derived melts accumulate at the base of the continental crust and anatexis occurs within the lower crust (von Seckendorff et al., 2004). The collapse of the orogen is observed and a series of ENE-WSW transtensional pull-apart basins like the Saar-Nahe basin form (Henk,

1993a, 1993b; Scheck-Wenderoth et al., 2008; Weber, 1995) and Sillon Houiller in Massif Central (Edel et al., 2013). These basins accumulate thick continental clastics deposits (Figure 4c) up to 10 km (Henk, 1992; Schäfer, 2011, 1989). The formation of these basins involved the reactivation of Variscan structures in dextral shear which was coeval with a sinistral reactivation of Variscan shear zones outlining the Hessian graben, the URG (Boigk and Schöneich, 1970; Eisbacher et al., 1989; Schumacher, 2002; Weber, 1995; Ziegler and Dèzes, 2005) and Sillon Houiller in Massif central (Edel et al., 2013).

From early Permian, the magmatic activity decays inducing thermal subsidence of the lithosphere. Erosion reduces the Variscan topography until isostatic equilibrium is met (Ziegler et al., 2004; Ziegler and Dèzes, 2005) (Figure 4c).

Major dextral translation between Gondwana and Laurussia induced disruption and exhumation of the Variscan orogen (Ziegler and Dèzes, 2005). Based on gravity and magnetic maps Edel and Weber (1995) argue that during Devonian – Early Carboniferous times large scale displacements are accommodated by a combined along 1) dextral NW-SE striking South Armorican, Bray, Bavarian, Elbe and Vistula faults and 2) sinistral activity along NE-SW striking Sillon Houiller and URG (see Figure 5).

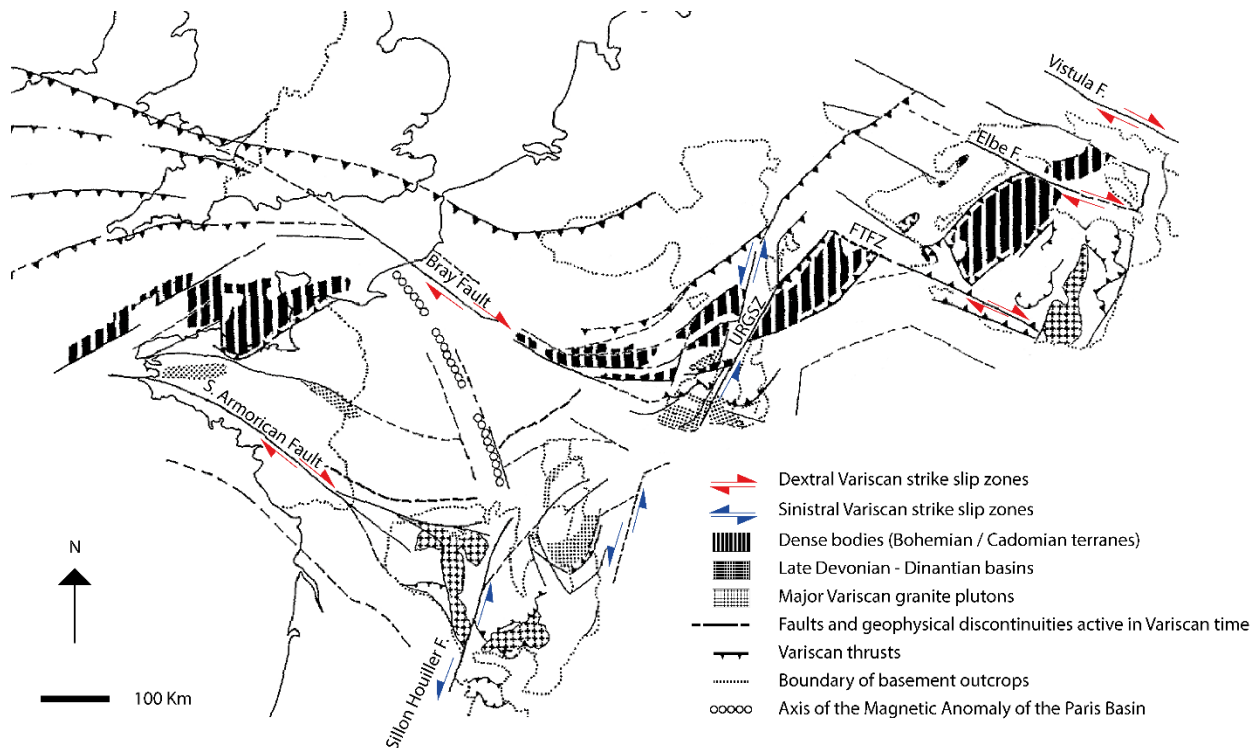


Figure 5: Structural sketch map of Variscan structures in western Europe (redrawn after Edel and Weber, 1995).

The Sillon Houiller Fault (SHF) has been intensively studied in the literature and its tectonic history has been long debated. There is a general agreement for a dominant sinistral activity along the SHF (Castaing, 1982; Grolier and Letourneur, 1968; Lerouge, 1987; Letourneur, 1953; Rolin, 1987; Thiery et al., 2009). The SHF strikes in a NNE-SSW direction, has a length of around 270 km and is interpreted as crustal scale structure. Sinistral activity along the SHF and the Sainte Marie aux Mines Faults (SMMF) in the VM is coeval in time to dextral shearing along the above mentioned South Armorican, Bray, Bavarian, Elbe and Vistula faults.

Thiery et al. (2009) argue that activity along the SHF consists in a first phase of sinistral wrenching resulting in a left lateral displacement of 70 km between the base of Middle Visean and Upper Visean. This first phase of movements along the so-called Proto SHF is accommodated by ductile deformation along steeply inclined mylonitic zones. The last transtensional deformation increments favor emplacement of granite intrusives until middle Namurian. A second tectonic episode is responsible Proto SHF reactivation during Stephanian and opening of pull-apart coal basins i.e. formation of the Sillon Houiller. This reactivation occurs under brittle deformation conditions and evidenced by numerous breccia and cataclastics deformation zones.

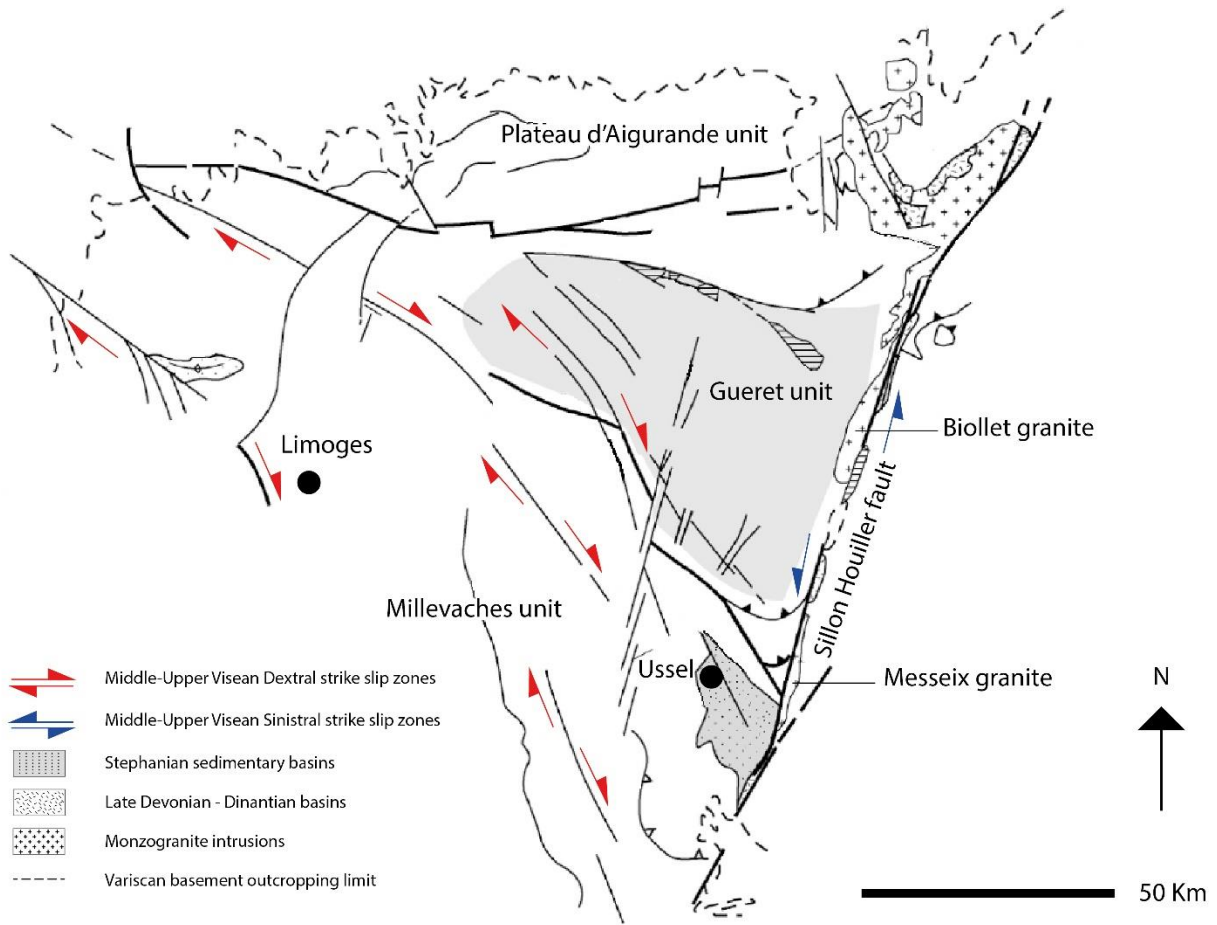


Figure 6: Structural scheme of Variscan domain in French Massif Central (redrawn after Thiery et al., 2009).

Further North Est, in the present location of the URG, Edel et al. (2007) have proposed that during the Visean a lithospheric scale discontinuity was active in the form of a 40km wide and 400 km long shear zone (Upper Rhine Graben Shear Zone, URGSZ) trending NE-SW and offsetting in a sinistral sense pre-Variscan and early Variscan structures (Figure 7). The URGSZ offsets at present low grade terrains from Proterozoic and/or Early Paleozoic between the Northern Vosges and Northern Black Forest by about 40 km (Edel and Fluck, 1989; Rousset et al., 1993).

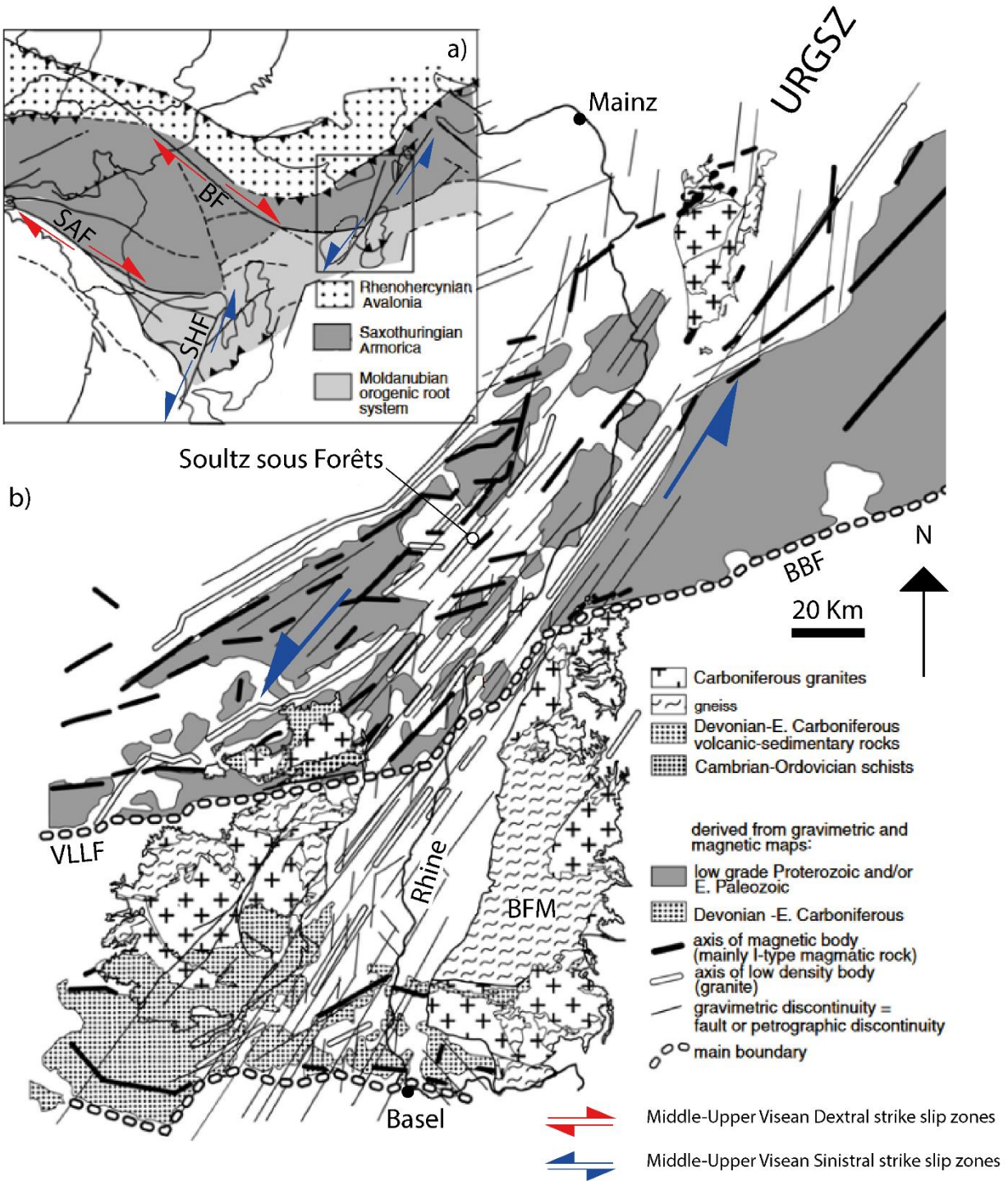
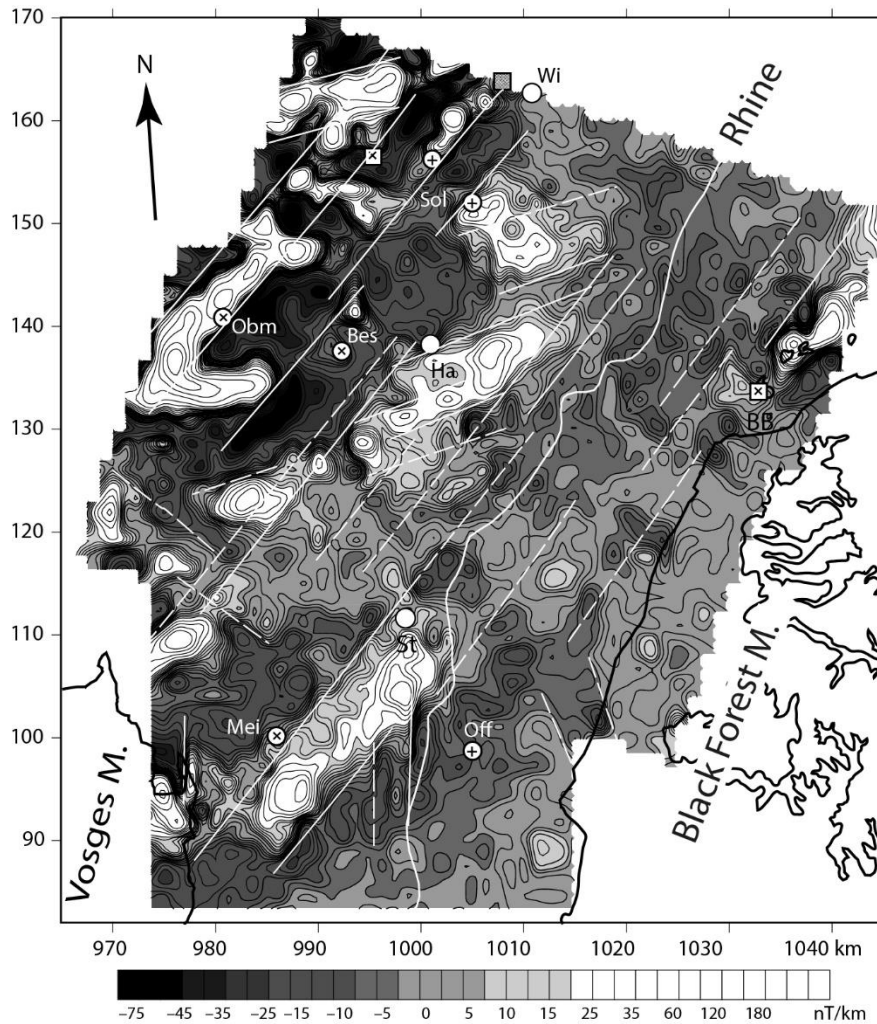


Figure 7: a) structural scheme of the west European Variscan domain, b) structural map of the Upper Rhine Graben area with extrapolated geophysical data (redrawn after Edel et al., 2007).

During late Visean granitoids like the ones of SSF intruded the lithosphere while being ductile along this sinistral wrench zone system. As presented in the distribution of magnetic anomalies (Figure 8), the SSF

granites and other plutonic intrusions from similar age form lenses oriented in a NE-SW direction possibly bounded by steep faults.



deep borehole: ⊕ granite ⊗ granodiorite ● Dévonian
 outcrop: ⊠ granodiorite ■ Dévonian

Figure 8: First vertical derivation of the magnetic anomaly (redrawn after Edel et al., 2007).

The Variscan wrench tectonics has produced in the URG area numerous sinistral strike-slip structures, oriented NE-SW, which have accumulated large amounts of strain. Given the thermally weakened state of the lithosphere during Devonian to Carboniferous and the fact that the URGSZ is considered as a lithospheric-scale structure (Edel et al., 2007) it can be envisaged, like in the SHF, that differential movements along NE-SW structures were accommodated by ductile deformation processes. Evidences of ductile shearing of Variscan origin are ubiquitous along the strike of the SMMF and also within the central part of the BFM showing a dominant NE-SW oriented gneiss foliation. Interestingly the granitoid fabric shows a similar NE-SW preferential orientation of biotite crystals interpreted as an initial magmatic fabric

acquired during syn-kinematic pluton emplacement under ductile conditions and still preserved at present-day (Schulmann et al., 2002).

During the Cenozoic the URG formation is related to a polyphase complex stress-field produced during Pyrenean and Alpine orogens with a possible contribution of mantle uplift (Illies, 1975, 1974; Illies et al., 1967; Monninger, 1985; Ziegler, 1994, 1990).

The main phases of the Cenozoic URG formation can be summarized as follow:

- Rifting in the URG area started in the late Eocene as a result of N-S compression which origin is to be found in both Alpine and Pyrenean collision zones (Dèzes et al., 2004).
- Starting in the Oligocene the Alpine orogenic wedge was thrust onto the European plate towards the NW (Ceriani et al., 2001; Trullenque, 2005) and the main E-W extension in URG occurred as a result of Northwards compression related to Alpine and Pyrenean collision.
- In the late Oligocene NE-SW compression reactivates the border faults with a dextral shear sense (Schumacher, 2002; Villemin and Bergerat, 1987)
- During the Miocene, URG was subjected to W and NW directed compressional stresses due to frontal Alpine collision within the external crystalline massifs (Dèzes et al., 2004).
- Since Miocene, the URG acts as a sinistral strike-slip zone (Ahorner, 1975; Bergerat, 1985; Bonjer, 1997; Bonjer et al., 1984; Buchmann and Connolly, 2007; Delouis et al., 1993; Edel et al., 2007; Homuth et al., 2014; Illies, 1977; Illies and Greiner, 1979; Plenefisch and Bonjer, 1997; Rotstein et al., 2005; Villemin and Bergerat, 1987) as a response to a far-field stress imposed by the convergence between Africa and Europe.

The above literature review outlines the importance of strike-slip tectonics within the URG itself and at European scale since Variscan times. Several phases of NE-SW oriented Variscan fault reactivation are observed and strike-slip structures accommodating varying amounts of strain are ubiquitous. Such reactivations have also been proposed within the SSF reservoir (Glaas, 2021; Illies, 1972; Rotstein et al., 2006; Villemin and Bergerat, 1987). **My research interest within the MEET project was in turn dedicated to a precise characterization of 1) progressive microfabric evolution and 2) coeval increasing rock alteration along a strain gradient imposed on granitic rocks deformed in a strike-slip regime within the brittle field.** Investigations of rock alteration processes occurring during deformation are important as they drastically influence both 1) mechanical, hydraulic and petrophysical properties of fault zones (Bartier et al., 2008; Charléty et al., 2007; Ledésert et al., 2010) and 2) reservoir response to production and stimulation activities. In the geothermal industry, this last topic is sensitive as it may trigger mechanical instabilities leading to induced seismicity (Dorbath et al., 2009; Groos et al., 2013; Häring et al., 2008). Induced seismicity causes a dramatic effect in terms of societal acceptance of geothermal projects (Kraft and Deichmann, 2014) and it is therefore important to lower this risk. In order to achieve these goals, I have been coordinating a team with a cluster of expertise covering the fields of regional geology understanding and structural analysis of a chosen reservoir analogue province, petrographic and geochemical investigation of alteration processes affecting deformed granitic rocks and statistical analysis of fracture patterns. My approach contributes to the understanding of the coupled activity of alteration and strain within fault zones. Data from a large-scale exhumed reservoir analogue deformed in a strike-slip setting provide are compared with fluid-rock interaction models proposed to date from an active geothermal site using limited borehole data.

I define an analogue as a site to gain input in understanding the evolution of given key processes at depth on certain types of geological structures. I believe that one of these processes are fluid-rock interactions and their evolution depending on deformation amounts in transcurrent structures

affecting the crystalline basement. Under these circumstances a perfect copy of the URG is not needed and the analogue should satisfy the three following conditions:

- 1) Present an array of converging similarities with the URG in terms of large-scale tectonic setting,
- 2) Have similar crystalline basement rock petrographic characteristics,
- 3) Allow access to exceptionally outcropping conditions where deformation gradients and fluid rock interaction processes are particularly well-developed and preserved.

I have chosen the Noble Hills range structural high, situated along the Southern Death Valley Fault Zone (SDVFZ), as reservoir analogue to the SSF demonstration site. The NH area fulfills the three above-mentioned prerequisites and is ideal for studying under virtually 100% outcrop exposure the complete microfabric and petrographical evolution of granitic rocks from a pristine to ultracataclastic state along a strike-slip wrench zone.

The Death Valley (DV) area is situated in California in between the SW termination of the Basin and Range province and the NW termination of the Mojave block (Figure 9). DV lies in the core of the Eastern California Shear zone which accommodates more than 10% of Pacific-North America plate motion. DV is a transtensional system forming a typical pull-apart basin bounded by dextral strike-slip zones, the Northern and Southern Death Valley Fault zones (NDVFZ and SDVFZ respectively).

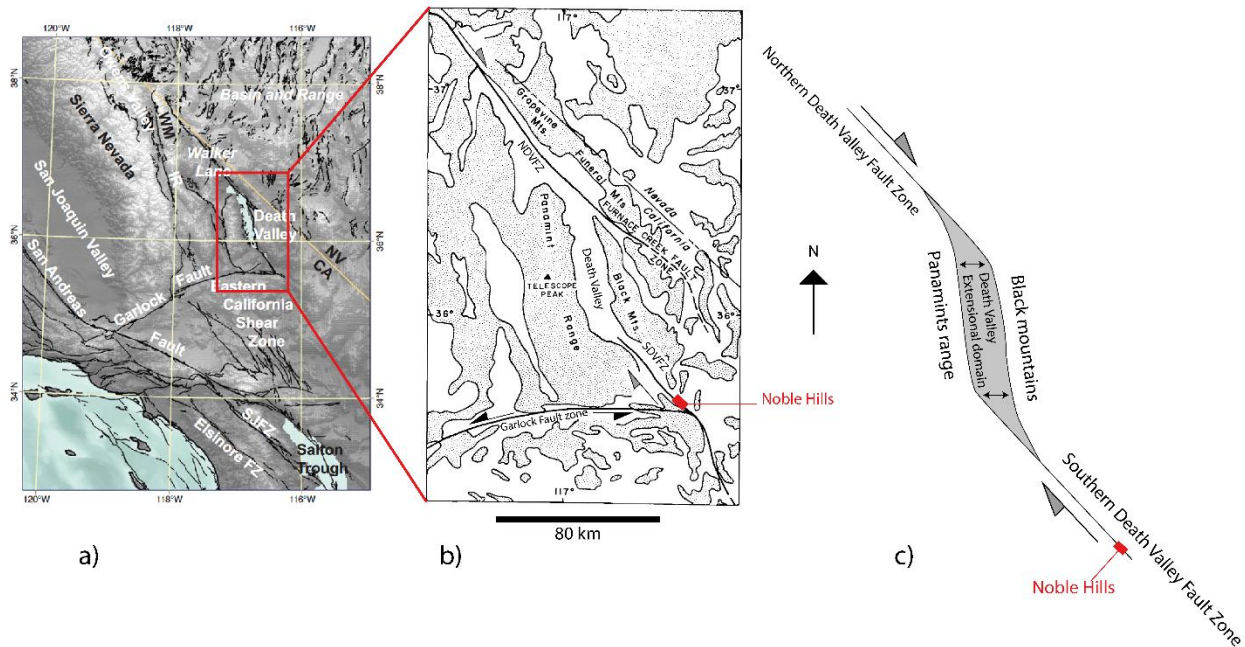


Figure 9: a) large scale structural map of western USA (Norton, 2011), b) Simplified structural scheme of the Death Valley area and localization of the NH (redrawn from Burchfiel and Stewart, 1966), c) pull-apart schematic representation of the Death valley area and localization of the NH range (redrawn from Burchfiel and Stewart, 1966).

Based on geometrical reconstructions and facies correlations between units found on each side of the SDVFZ Pavlis and Trullenque (2021) have demonstrated a net dextral lateral offset of around 40 km along strike of this structure. The NH are interpreted as a slice of Proterozoic basement intruded by Mesozoic granites dragged along the SDVFZ and recording a net cumulated slip lower than the total fault trace. In addition, the authors propose that much of the dextral slip occurred during the main extension of the DV basin i.e. from 12 to 6 Ma. The results by Pavlis and Trullenque (2021) have been used for the organization of a field excursion and publication of the associated field excursion guide (Fleming et al., 2022).

Evidence for 40–41 km of dextral slip on the southern Death Valley fault: Implications for the Eastern California shear zone and extensional tectonics

Terry L. Pavlis¹ and Ghislain Trullenque²

¹Department of Geological Sciences, University of Texas at El Paso, El Paso, Texas 79968, USA

²UniLaSalle, GEOS Department, B2R team, 19 rue Pierre Waguet, 60000 Beauvais, France

ABSTRACT

Recognition of a pair of pre-Neogene markers together with analysis of published data indicate ~40 km of dextral slip across the southern Death Valley fault zone, California, USA. Stratigraphic overlaps on fault rocks indicate much of the dextral slip predates the late Miocene, placing a significant fraction of the dextral slip in the same time window as regional extension and challenging interpretations that the modern strike-slip system became active post-6–3 Ma. However, these results are consistent with regional evidence that dextral transension began by ca. 12 Ma.

INTRODUCTION

Death Valley (California, USA) is the archetypical pull-apart basin (Burchfiel and Stewart, 1966), yet there is controversy on slip estimates for the bounding strike-slip faults. Discrepancies in strike-slip motion are partially due to complex deformation in a distributed transensional system that evolved over the last ~12 m.y. (e.g., Serpa and Pavlis, 1996; Snow and Wernicke, 2000; Renik and Christie-Blick, 2013), but scarcity of markers has handicapped resolution of slip.

We present results from detailed mapping in the Noble Hills (Fig. 1) where the southern Death Valley fault system (SDVF) is well exposed and show that these exposures closely match an exposure in the Owlshhead Mountains ~40 km to the northwest. We then compare this result to previous estimates and assess the implications of this conclusion.

REGIONAL GEOLOGIC SETTING AND THE SLIP ESTIMATE PROBLEM

The Death Valley region has been a centerpiece for Neogene extensional/transensional tectonic studies in the southern United States Cordillera. Stewart (1967, 1983) and Wernicke et al. (1988) emphasized that there is a rich pre-Neogene record that can be exploited to reconstruct this late Cenozoic history. This record includes stratigraphic markers, Mesozoic contractional structures, and Neogene depos-

its. Both stratigraphic variations and Mesozoic structures trend northeast at nearly right angles to Neogene structures (Fig. 1), potentially providing high-resolution piercing lines to constrain reconstructions (Wernicke et al., 1988).

Stewart (1967) first attempted to reconstruct the Neogene system using stratigraphic markers to infer strike-slip offsets of ~80 km across the Death Valley region. Wright and Troxel (1967) countered this interpretation using stratigraphic details in Death Valley to estimate dextral offset of less than 10 km on SDVF. This low slip estimate stands in marked contrast to relatively robust, large slip estimates for the northern Death Valley fault (NDVF) system. These include Stewart's (1967, 1983) estimate, and that by Snow and Wernicke (1989, 2000), who proposed a displacement of 68 ± 4 km. More recent efforts by Renik and Christie-Blick (2013) emphasized differential slip along the fault but estimated <50 km across what is now Death Valley proper.

The low slip estimate (<10–35 km) for the SDVF has tended to persist in many reconstructions through hypotheses that either transfer slip onto other strike-slip structures (e.g., Wright et al., 1991; Serpa and Pavlis, 1996) and/or onto the extensional complex and transensional structures (e.g., Wernicke et al., 1988, 1989; Serpa and Pavlis, 1996; Snow and Wernicke, 2000), with different interpretations of timing on the SDVF. This distinction has led

to hypotheses that the Death Valley pull-apart basin is a young (6 Ma to <3 Ma) superposition on an extensional system (e.g., Stewart, 1983; Norton, 2011).

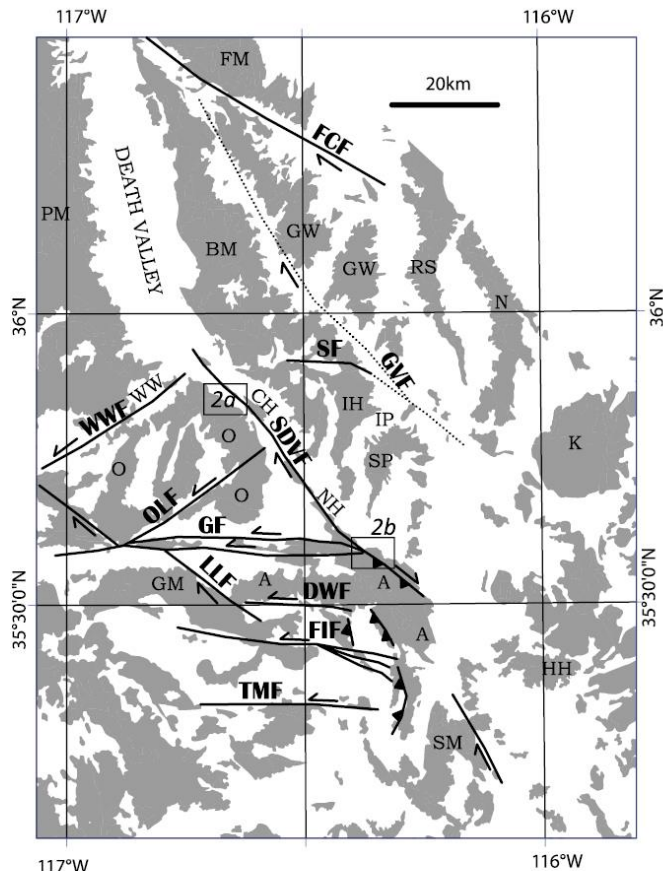
GEOLOGY OF THE SOUTHERN DEATH VALLEY FAULT ZONE IN THE NOBLE HILLS

Recent work by Trullenque et al. (2018) and Klee et al. (2020) using high-resolution digital mapping techniques similar to that of Pavlis et al. (2010) in the vicinity of the SDVF-Garlock intersection, together with previous mapping, provides strong evidence that the low slip estimate for the SDVF is incorrect.

Studies in the Noble Hills have focused on Neogene rocks exposed along the SDVF (Brady, 1984; Brady and Troxel, 1999; Butler et al., 1988; Niles, 2016). Those studies demonstrated that Quaternary deformation of the Noble Hills is dominated by the complex interactions of the sinistral Garlock fault and the dextral SDVF, which produce contractional structures in an area otherwise dominated by extensional tectonics.

In our work, we concentrated on deformation in a structural high within the Noble Hills (Fig. 2B). This effort revealed that this pre-Neogene basement complex was intensely deformed by brittle deformation at low temperatures (Klee et al., 2020). The complex is composed of Proterozoic gneiss and the nonconformably overlying Crystal Springs Formation, and both were intruded by Mesozoic granite. The complex is cut by arrays of faults that range from discrete slip surfaces to broad cataclastic shear zones up to 100 m across. Near-vertical faults are dominant with ubiquitous dextral shear sense indicators, both at the margins of the structural high as well as on faults interior to the structural high. Our studies support the conclusion of Niles

CITATION: Pavlis, T.L., and Trullenque, G., 2021, Evidence for 40–41 km of dextral slip on the southern Death Valley fault: Implications for the Eastern California shear zone and extensional tectonics: *Geology*, v. 49, p. 767–772, <https://doi.org/10.1130/G48528.1>



Geographic Abbreviations: A=Avawatz Mountains, BM=Black Mountains, FM=Funeral Mountains, HH=Holloran Hills, GM=Granite Mountains, GW=Greenwater Range, IH=Ibex Hills, IP=Ibex Pass, K=Kingston Range, N=Nopah Range, O=Owlshead Mountains, PM=Panamint Mountains, RS=Resting Spring Range, SM=Soda Mountains, SP=Saddle Peak Hills, WW=Wingate Wash. Fault Abbreviations: DWF=Drinkwater Lake; FCF=Furnace Creek; FIF=Fort Irwin; GF=Garlock; GVF=Grandview; LLF=Leach Lake; OLF=Owl Lake; SF=Sheephead; SDVF=Southern Death Valley; TMF=Tiefort Mountain Fault; WWF=Wingate Wash. Figure is drawn from GIS files for the California Geologic map: maps.conservation.ca.gov/cgs/gmc.

Figure 1. Regional map of the Death Valley–northeast Mojave Desert region, California, USA. Major Pliocene–Pleistocene strike-slip and thrust faults are shown but normal faults are omitted for clarity. GIS—geographic information system.

(2016), who noted that the Neogene section is depositional on granite at the northern tip of the basement high (Fig. S1 in the Supplemental Material¹), but the margins are strike-slip faults that overprint the unconformity. These observa-

tions indicate that significant faulting postdates the Neogene nonconformity, but that significant motion had also occurred well before deposition of the Neogene cover. The overlapping rocks have not been directly dated, but Niles (2016) showed that they were no younger than ca. 3.5 Ma. Based on lithology and stratigraphic position, Brady and Troxel (1999) correlated the unit with the Owlhole Spring Formation dated at 6–8 Ma, an estimate we accept here.

¹Supplemental Material. Supplemental figure of the Noble Hills. Please visit <https://doi.org/10.1130/GEOL.S.14120396> to access the supplemental material, and contact editing@geosociety.org with any questions.

At map scale (Fig. 2B), we observed that to the southeast, the distinctive cataclastic granites of the bedrock high can be traced into a broad fault zone well inboard of the Avawatz Mountains front. This cataclastic zone is clearly part of the SDVF but merges with cataclastic rocks (fr in Fig. 2B) developed along the eastern trace of the Garlock/Mule Springs fault (Brady, 1984). This geometry shows that the SDVF *sensu stricto* lies east of this intersection, and, therefore, rocks to the east of the line labeled Fault A in Figure 2B have been transported by most, or all, of the dextral motion on the SDVF. This fault block contains north-facing units that are truncated against the fault, including, from southeast to northwest: exposure of coarse-grained Mesozoic granite; Proterozoic basement; and the Crystal Springs Formation with its characteristic Mesoproterozoic mafic intrusions. The Crystal Springs Formation strikes ENE and dips uniformly through this section at moderate to steep angles of 50°–90°. Across the fault to the west (Fig. 3), the Avawatz Mountains contain very different rocks, including Triassic diorite, minor younger granites, and roof pendants of Proterozoic to Mesozoic rocks engulfed in diorite (Brady, 1984; Spencer, 1990; Pavlis et al., 1998).

This fault block at the Avawatz Mountains front is significant because it is similar to an exposure at the northeast tip of the Owlshead Mountains, just west of the SDVF (Figs. 1 and 2A). The match between these two exposures is striking (see arrows for reference in Fig. 2): (1) the basic orientation and facing of the basement–Crystals Springs assemblage match across the fault, and (2) the positions of the granite intrusions into basement also match closely. In the Owlshead locality, the orientation of the rocks is demonstrably pre-ca. 14 Ma, as signified by a nearly flat-lying unconformity (Fig. 2A). Although only Quaternary deposits provide an equivalent constraint at the Avawatz Mountains front (Fig. 2B), it is likely the bedding has not been rotated significantly because bedding is nearly perpendicular to likely rotation axes from young contraction. Using the offset positions of either the basement–cover contact (base of the Crystal Springs Formation) or the granite–basement contact (arrows in Figs. 2A and 2B) indicates a net dextral offset of 40.5 km (straight-line distance) to 41.5 km (along-fault distance).

Further support for this offset marker pair is provided by the geology of the Noble Hills bedrock high. Because of structural position, these rocks must be a slice picked up somewhere along the fault trace, with less net slip than the total fault slip. Lithologically, however, the slice is closely akin to the offset markers: Crystal Springs Formation, basement, and granite, albeit with a much higher percentage of granite. Examination of the geology along the SDVF trace (Fig. 3A) suggests the slice was

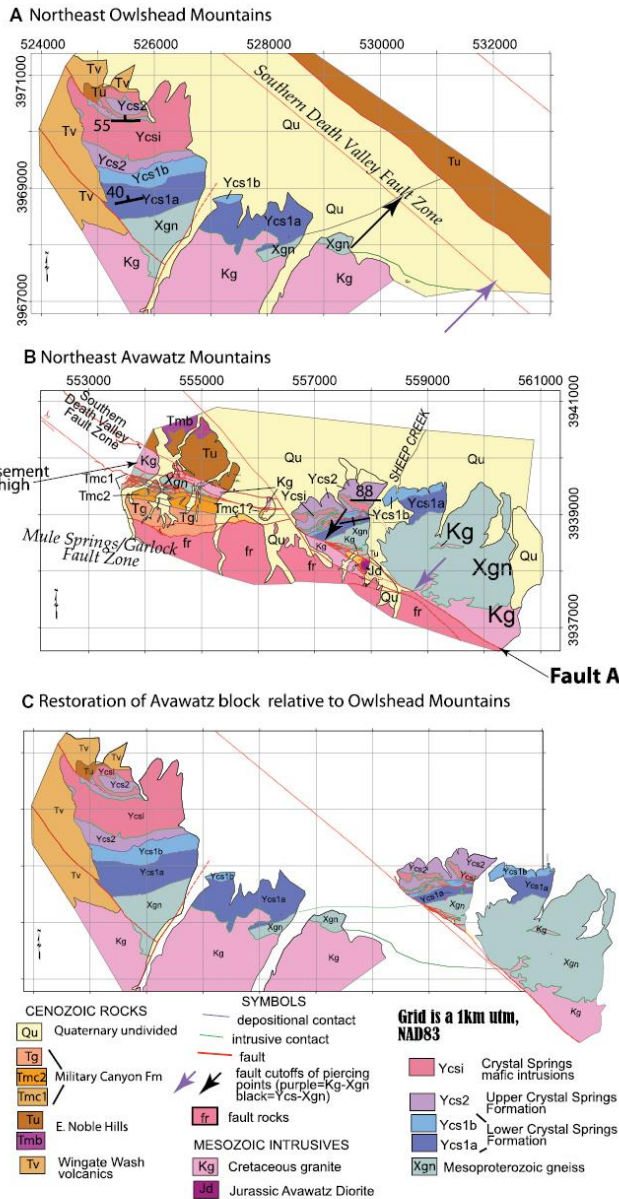


Figure 2. Geologic maps of the area of offset markers proposed in this study (California, USA): (A) geologic map modified from Pavlis et al. (2012) with some additions in the southeast corner; (B) geologic map from this study; (C) map showing proposed restoration of slip on the southern Death Valley fault (SDVF). UTM—Universal Transverse Mercator; NAD83—North American Datum 1983.

derived from along the Owshead Mountains front, but close to Crystal Springs Formation exposures, because roof pendants farther south are all high-grade marbles (m in Fig. 3A). Similarly, it cannot be locally derived basement from the Avawatz Mountains because all rocks west of the SDVF and south of the Garlock fault are dominated by mafic granitoids (e.g., Spencer, 1990; Brady, 1984; Pavlis et al., 1998).

DISCUSSION

Additional Evidence for ~40 km of Offset

Brady (1984) and Brady and Troxel (1999) showed that conglomerates west of the SDVF (THH in Fig. 3A) had clasts with no known source directly to the east, across the fault. Rather, the clasts had close affinity with rocks now exposed to the south and east in the Halloran Hills (Figs. 1 and 3). This marker is blunt, but restoration of 40 km of the slip on the SDVF would place these Neogene sediments directly southwest of their interpreted source (Fig. 3C). Similarly, Butler et al. (1988) tied Neogene gravels in the Noble Hills to an Owshead Mountain source (labeled G in Fig. 3), leading to an estimate of ~35 km of offset on the fault. Bennie W. Troxel (deceased) later questioned the conclusion based on field details (unpublished field observations by B. Troxel and T. Pavlis), and Caskey et al. (2010) and Niles (2016) questioned other details. Nonetheless, Butler et al.'s (1988) conclusion is fully consistent with our slip estimate here.

Farther north, Serpa and Pavlis (1996) used the northern limit of Mesozoic plutonism as a marker for reconstruction, which, together with a similar marker, indicated that the northern limit of subjacent granitoids is consistent with 30–40 km of slip (Fig. 3). Similarly, Luckow et al. (2005) and Canalda (2009) suggested that middle Miocene volcanics in Wingate Wash (Fig. 1) were dextrally offset from volcanic rocks near Ibox Pass (Fig. 1). This correlation is a coarse marker because the volcanics cover large areas on either side of the SDVF, but if the northern limit of known exposures is mapped (Fig. 3A), the resultant offset is also ~40 km. Note, that an outlier of these volcanics lies well north of our line in the Amargosa Chaos (blue asterisk in Fig. 3), and this issue is considered further below.

Finally, Stewart (1967) mapped multiple stratigraphic trends that indicate ~80 km of dextral displacement across the southern Death Valley region (Fig. 3). We note here that the main evidence for the low slip interpretation on the SDVF is the analysis of the Neoproterozoic section by Wright and Troxel (1967). Their work showed multiple stratigraphic pinch-outs extending WSW from the Kingston Range to the Ibox Hills (Fig. 1) and then northwestward through the Amargosa Chaos to the Panamint Mountains (Fig. 3A). Note, however, that the

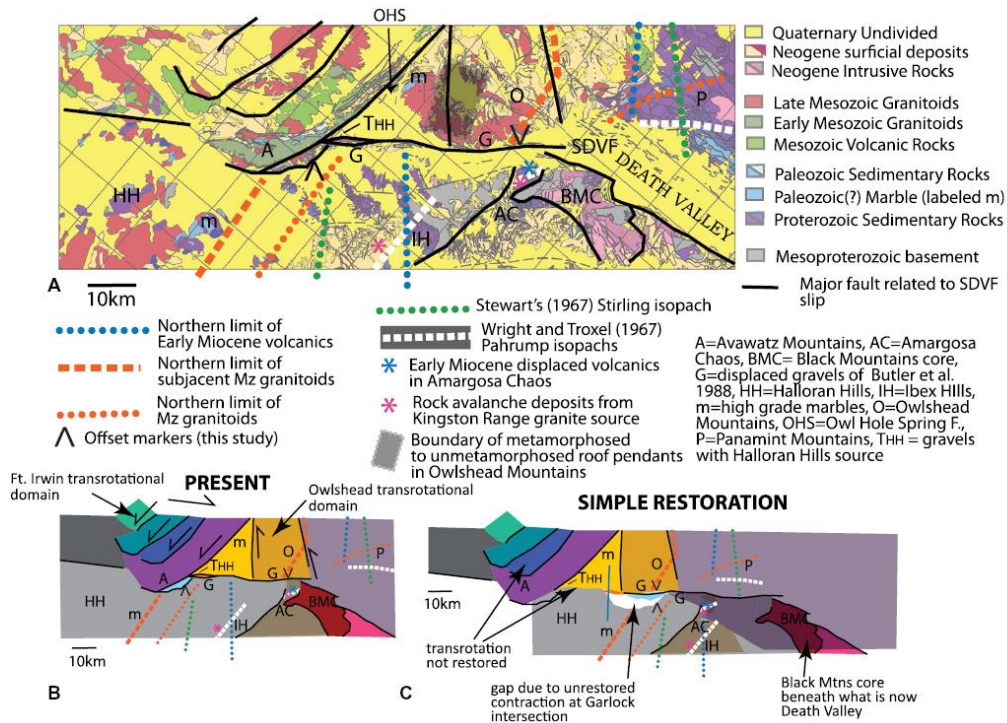


Figure 3. (A) Geologic map along the southern Death Valley fault (SDVF; California, USA) with offset markers discussed in the text (from geographic information system files in Workman et al. [2002] merged with California geologic map: maps.conservation.ca.gov/cgs/gmcc/). Figure is rotated with motion along the SDVF vertical. Mz—Mesozoic. (B) Simplified fault blocks from A. (C) Rigid body restoration of 40 km of slip on the SDVF transferred to the Black Mountains frontal fault in simple pull-apart assumption. See text for details.

Amargosa Chaos and its Neogene cover (Amargosa Chaos basin of Topping, 1993) are detached and displaced to the northwest along a low-angle normal fault system (Amargosa fault). Thus, these displaced rocks are not a meaningful marker constraining strike-slip motion on the SDVF because they were carried along a separate fault system. Indeed, if the Amargosa Chaos rocks are excluded from the Wright and Troxel (1967) map (Fig. 3), these markers are similar to the northern limit of the Neogene volcanic rocks. This observation also explains the seeming outlier of Neogene volcanics at the base of the Amargosa Chaos basin (blue asterisk in Fig. 3) because they were displaced along with underlying rocks.

Figure 3C shows a simple restoration of 40 km of slip on both the SDVF and the Amargosa fault system. This restores the northern limit of early Miocene volcanics and the Pahrump Group pinch-outs of Wright and Troxel (1967) to their equivalent positions in the Ibex

Hills (Fig. 3C), and pre-extensional markers other than Stewart's restore to within 1–5 km—a close correlation given the crude positions for some of these markers. The offset gravels recognized by Butler et al. (1988) over-restore in this reconstruction (G in Fig. 3), which is expected for a syntectonic deposit. A feature that is not taken into account in Figure 3C is the well-documented transrotation south of the Garlock fault (e.g., Schermer et al., 1996). Slip estimates that constrain the transrotation vary (e.g., Schermer et al., 1996; Pavlis et al., 1998) but predict rotations less than the paleomagnetic data. Nonetheless, contraction at the ends of the transrotational blocks is well documented (Fig. 1), including the faults at the eastern Avawatz Mountains front, which accounts for gaps in our reconstruction (Fig. 3C). Similarly, rock avalanche deposits in the Amargosa Chaos basin (pink asterisk in Fig. 3C) do not restore close to their Kingston Range source, indicating extensional and/or strike-slip faults to the east have displaced

these markers as well as Stewart's markers. Additional work is needed to fully integrate our slip estimate with these known issues.

Broad-Scale Implications for Transensional Systems

Our findings have implications for transtensional mechanics as well as the plate-tectonic evolution of southwestern North America. The Death Valley area is one of the best-documented transtensional systems on Earth, yet uncertainties in how slip is distributed among strike-slip versus extensional structures remain, complicating understanding of the driving process(es) for extension. Geodetic studies (e.g., Lifton et al., 2013) demonstrate that Death Valley now lies in the core of a distributed dextral system, the Eastern California shear zone/Walker lane belt (ECSZ/WL), which takes up more than 10% of Pacific–North American plate motion. To the south, this motion is taken up primarily by transrotational panels, but north of the Garlock fault,

the westerly motion of the Sierra Nevada relative to the Mojave produces a broad, transtensional system (e.g., Dokka and Travis, 1990).

Ages of synextensional strata (e.g., Holm et al., 1994) show that modern Death Valley is relatively young (ca. 6 Ma), but slip histories of other faults allow a range of interpretations pre-6 Ma. Studies of the NDVF/Furnace Creek fault show that the fault system initiated during middle Miocene extension (e.g., Renik and Christie-Blick, 2013), but this link has been elusive for the SDVF. Our ~40 km slip estimate for the SDVF is consistent with the estimate by Renik and Christie-Blick (2013) of <50 km for strike-slip motion at the northern margin of the basin (Renik and Christie-Blick, 2013), and our timing constraints suggest both fault systems moved throughout the main extensional event. This result, together with other recent work (e.g., Renik and Christie-Blick, 2013; Pavlis et al., 2014), suggests a new family of reconstructions is needed that account for these new observations. When completed, reconstructions could be used in an integrated geodynamic model to evaluate the mechanics of interactions among pull-apart basins, regional extension, and transrotation.

Any geodynamic analysis of the region needs to consider that our result suggests that strike-slip motion was prominent throughout the regional extension, implying the system was plate driven, with gravitational effects being secondary. This conclusion is consistent with evidence that strike-slip motion was prominent to the north in the Walker Lane from 14 to 12 Ma onward (e.g., Oldow et al., 2008; Busby, 2013) and driven by plate motion (Lee et al., 2020). This suggests the ECSZ/WL represents a long-lived plate-boundary process linked to the evolving transform margin. Serpa and Pavlis (1996) emphasized this plate-driven hypothesis with interpretations that transrotation played a major role during the extension, and synextensional folds in the system were produced by distributed dextral shear. Our observations here suggest distributed shear models of this type need to be reconsidered for the entire span of the extension from ca. 12 Ma to present.

CONCLUSIONS

New studies in southern Death Valley suggest that the net dextral slip on the SDVF is 40–41 km. Previous estimates of <10 km used markers that are themselves displaced by detachment faults, indicating those markers are minimum slip estimates. Evidence showing that 8–6 Ma Neogene sediments onlap SDVF catclases suggests that much of the dextral slip occurred during the main extension from 12 to 6 Ma. This challenges interpretations that the Death Valley pull-apart is a post-6 Ma structural feature, but it is consistent with regional evidence that dextral transension in the ECSZ/WL belt began in the middle Miocene.

ACKNOWLEDGMENTS

This project received funding from the European Union's Horizon 2020 research and innovation program under grant agreement no. 792037. We thank Brian Wernicke, Nick Christie-Blick, and an anonymous reviewer for suggestions on improving the manuscript.

REFERENCES CITED

- Brady, R.H., III, 1984, Neogene stratigraphy of the Avawatz Mountains between the Garlock and Death Valley fault zones, southern Death Valley, California: Implications as to the late Cenozoic tectonism: *Sedimentary Geology*, v. 38, p. 127–157, [https://doi.org/10.1016/0037-0738\(84\)90077-0](https://doi.org/10.1016/0037-0738(84)90077-0).
- Brady, R.H., III, and Troxel, B.W., 1999, The Miocene Military Canyon Formation: Depocenter evolution and lateral faulting, southern Death Valley, California, in Wright, L.A., and Troxel, B.W., ed., *Cenozoic Basins of the Death Valley Region: Geological Society of America Special Paper 333*, p. 277–288, <https://doi.org/10.1130/0-8137-2333-7-277>.
- Burchfiel, B.C., and Stewart, J.H., 1966, "Pull-apart" origin of the central segment of Death Valley, California: *Geological Society of America Bulletin*, v. 77, p. 439–442, [https://doi.org/10.1130/0016-7606\(1966\)77\[439:POOTCS\]2.0.CO;2](https://doi.org/10.1130/0016-7606(1966)77[439:POOTCS]2.0.CO;2).
- Busby, C.J., 2013, Birth of a plate boundary at ca. 12 Ma in the ancestral Cascade arc, Walker Lane belt of California and Nevada: *Geosphere*, v. 9, p. 1147–1160, <https://doi.org/10.1130/GES00928.1>.
- Butler, P.R., Troxel, B.W., and Verosub, K.L., 1988, Late Cenozoic history and styles of deformation along the southern Death Valley fault zone, California: *Geological Society of America Bulletin*, v. 100, p. 402–410, [https://doi.org/10.1130/0016-7606\(1988\)100<0402:LCHASO>2.3.CO;2](https://doi.org/10.1130/0016-7606(1988)100<0402:LCHASO>2.3.CO;2).
- Canalda, S.M., 2009, Magnitude of Right-Lateral Offset on the Southern Death Valley Fault Zone from Miocene Volcanic Assemblages [M.S. thesis]: El Paso, Texas, University of Texas at El Paso, 155 p.
- Caskey, S.J., Goodman, J.T., Green, H., Niles, J.H., Wan, E., Wahl, D.B., and Olsen, H.A., 2010, Constraints on post-middle-Pleistocene offsets and new perspectives on Plio-Pleistocene tectonism along the southern Death Valley fault zone: *Geological Society of America Abstracts with Programs*, v. 42, no. 4, p. 55.
- Dokka, R.K., and Travis, C.J., 1990, Role of the Eastern California shear zone in accommodating Pacific–North American plate motion: *Geophysical Research Letters*, v. 17, p. 1323–1326, <https://doi.org/10.1029/GL017i009p01323>.
- Holm, D.K., Fleck, R.J., and Lux, D.R., 1994, The Death Valley turtlebacks reinterpreted as Miocene–Pliocene folds of a major detachment system: *The Journal of Geology*, v. 102, p. 718–727, <https://doi.org/10.1086/629715>.
- Klee, J., Trullenque, G., Ledser, B., Potel, S., Hebert, R., and Genter, A., 2020, Petrographic and petrophysical analyses of fractured granites used as an analogue of the Soultz-sous-Forêts Geothermal Reservoir: Noble Hills, CA, USA, in *Proceedings of the World Geothermal Congress 2020: Reykjavik, Iceland* (in press).
- Lee, J., Hoxey, A.K.R., Calvert, A., and Dubyoski, P., 2020, Plate boundary trench retreat and dextral shear drive intracontinental fault-slip histories: Neogene dextral faulting across the Gabbas Valley and Gillis Ranges, central Walker Lane, Nevada: *Geosphere*, v. 16, p. 1249–1275, <https://doi.org/10.1130/GES02240.1>.
- Lifton, Z.M., Newman, A.V., Frankel, K.L., Johnson, C.W., and Dixon, T.H., 2013, Insights into distrib-

uted plate rates across the Walker Lane from GPS geodesy: *Geophysical Research Letters*, v. 40, p. 4620–4624, <https://doi.org/10.1002/grl.50804>.

- Luckow, H.G., Pavlis, T.L., Serpa, L.F., Guest, B., Wagner, D.L., Snee, L., Hensley, T.M., and Korjenkov, A., 2005, Late Cenozoic sedimentation and volcanism during transtensional deformation in Wingate Wash and the Owlhead Mountains, Death Valley: *Earth-Science Reviews*, v. 73, p. 177–219, <https://doi.org/10.1016/j.earscirev.2005.07.013>.
- Niles, J.H., 2016, Post-Middle Pliocene Tectonic Development of the Noble Hills, Southern Death Valley, California [M.S. thesis]: San Francisco, California, San Francisco State University, 91 p.
- Norton, L., 2011, Two-stage formation of Death Valley: *Geosphere*, v. 7, p. 171–182, <https://doi.org/10.1130/GES00588.1>.
- Oldow, J.S., Geissman, J.W., and Stockli, D.F., 2008, Evolution and strain reorganization within late Neogene structural stepovers linking the central Walker Lane and northern Eastern California shear zone, western Great Basin: *International Geology Review*, v. 50, p. 270–290, <https://doi.org/10.2747/0020-6814.50.3.270>.
- Pavlis, T.L., Serpa, L., Troxel, B., Dean, M., Hartman, T., and Rodosta, T., 1998, Late Cenozoic deformation in eastern Fort Irwin and its significance for the tectonic history of the Garlock fault system, in Calzia, J.P., and Reynolds, R.E., eds., *Finding Faults in the Mojave: 1998 Mojave Desert Quaternary Research Center Field Trip Guide and Volume: San Bernardino County Museum Association Quarterly*, v. 45, p. 77–83.
- Pavlis, T.L., Langford, R., Hurtado, J., and Serpa, L., 2010, Computer-based data acquisition and visualization systems in field geology: Results from 12 years of experimentation and future potential: *Geosphere*, v. 6, p. 275–294, <https://doi.org/10.1130/GES00503.2>.
- Pavlis, T.L., Guest, B., Golding-Luckow, H., Serpa, L., and Wagner, D., 2012, Geologic Map of the Wingate Wash Area, Death Valley National Park, California and Nevada: Geological Society of America Digital Map and Chart Series 11, scale 1:25,000, <https://doi.org/10.1130/2012.DMCH011>.
- Pavlis, T.L., Rutkofsky, J., Guerrero, F., and Serpa, L.F., 2014, Structural overprinting of Mesozoic thrust systems in eastern California and its importance to reconstruction of Neogene extension in the southern Basin and Range: *Geosphere*, v. 10, p. 1–25, <https://doi.org/10.1130/GES00993.1>.
- Renik, B., and Christie-Blick, N., 2013, A new hypothesis for the amount and distribution of dextral displacement along the Fish Lake Valley–northern Death Valley–Furnace Creek fault zone, California–Nevada: *Tectonics*, v. 32, p. 123–145, <https://doi.org/10.1029/2012TC003170>.
- Schermer, E.R., Luyendyk, B.P., and Cisowski, S., 1996, Late Cenozoic structure and tectonics of the northern Mojave Desert: *Tectonics*, v. 15, p. 905–932, <https://doi.org/10.1029/96TC00131>.
- Serpa, L., and Pavlis, T.L., 1996, Three-dimensional model of the late Cenozoic history of the Death Valley region, southeastern California: *Tectonics*, v. 15, p. 1113–1128, <https://doi.org/10.1029/96TC01633>.
- Snow, J.K., and Wernicke, B., 1989, Uniqueness of geological correlations: An example from the Death Valley extended terrain: *Geological Society of America Bulletin*, v. 101, p. 1351–1362, [https://doi.org/10.1130/0016-7606\(1989\)101<1351:UO GCAE>2.3.CO;2](https://doi.org/10.1130/0016-7606(1989)101<1351:UO GCAE>2.3.CO;2).
- Snow, J.K., and Wernicke, B.P., 2000, Cenozoic tectonism, in the central Basin and Range: Magnitude, rate, and distribution of upper crustal strain: *American Journal of Science*, v. 300, p. 659–719, <https://doi.org/10.2475/ajs.300.9.659>.

- Spencer, J.E., 1990, Geologic Map of the Southern Avawatz Mountains, Northeastern Mojave Desert Region, San Bernardino County, California: U.S. Geological Survey Miscellaneous Field Studies Map 2117, scale 1:24,000, <https://doi.org/10.3133/mf2117>.
- Stewart, J.H., 1967, Possible large right-lateral displacement along fault and shear zones in the Death Valley–Las Vegas area, California and Nevada: Geological Society of America Bulletin, v. 78, p. 131–142, [https://doi.org/10.1130/0016-7606\(1967\)78\[131:PLRDAF\]2.0.CO;2](https://doi.org/10.1130/0016-7606(1967)78[131:PLRDAF]2.0.CO;2).
- Stewart, J.H., 1983, Extensional tectonics in the Death Valley area, California: Transport of the Panamint Range structural block 80 km north-westward: Geology, v. 11, p. 153–157, [https://doi.org/10.1130/0091-7613\(1983\)11<153:ETITDV>2.0.CO;2](https://doi.org/10.1130/0091-7613(1983)11<153:ETITDV>2.0.CO;2).
- Topping, D.J., 1993, Paleogeographic reconstruction of the Death Valley extended region: Evidence from Miocene large rock-avalanche deposits in the Amargosa Chaos basin, California: Geological Society of America Bulletin, v. 105, p. 1190–1213, [https://doi.org/10.1130/0016-7606\(1993\)105<1190:PROTDV>2.3.CO;2](https://doi.org/10.1130/0016-7606(1993)105<1190:PROTDV>2.3.CO;2).
- Trullenque, G., Genter, A., Leiss, B., Wagner, B., Bouchet, R., Leoutre, E., Malnr, B., Bar, K., and Rajs, I., 2018, Upscaling of EGS in different geological conditions, a European perspective, in Proceedings of the 43rd Workshop on Geothermal Reservoir Engineering: Stanford, California, Stanford University, abstract SGP-TR-213.
- Wernicke, B., Axen, G.J., and Snow, J.K., 1988, Basin and Range extensional tectonics at the latitude of Las Vegas, Nevada: Geological Society of America Bulletin, v. 100, p. 1738–1757, [https://doi.org/10.1130/0016-7606\(1988\)100<1738:BA RETA>2.3.CO;2](https://doi.org/10.1130/0016-7606(1988)100<1738:BA RETA>2.3.CO;2).
- Wernicke, B.P., Snow, J.K., Axen, G.J., and Burchfiel, B.C., 1989, Extensional Tectonics in the Basin and Range Province between the Southern Sierra Nevada and the Colorado Plateau: American Geophysical Union Field Trip Guidebook 138, 80 p., <https://doi.org/10.1029/FT138>.
- Workman, J.B., Menges, C.M., Page, W.R., Taylor, E.M., Ekren, E.B., Rowley, P.D., Dixon, G.L., Thompson, R.A., and Wright, L.A., 2002, Geologic Map of the Death Valley Ground-Water Model Area, Nevada and California: U.S. Geological Survey Miscellaneous Field Studies Map MF-2381-A, scale 1:250,000, <https://doi.org/10.3133/mf2381A>.
- Wright, L.A., and Troxel, B.W., 1967, Limitations on right-lateral, strike-slip displacement, Death Valley and Furnace Creek fault zones, California: Geological Society of America Bulletin, v. 78, p. 933–950, [https://doi.org/10.1130/0016-7606\(1967\)78\[933:LORSDD\]2.0.CO;2](https://doi.org/10.1130/0016-7606(1967)78[933:LORSDD]2.0.CO;2).
- Wright, L., Thompson, R., Troxel, B., Pavlis, T., DeWitt, E., Otton, J., and Serpa, L., 1991, Cenozoic magmatic and tectonic evolution of the east-central Death Valley region, California, in Walanwender, M.J., and Hanan, B.B., eds., Geological Excursions in Southern California and Mexico: San Diego, California, Geological Society of America, Annual Meeting Field Trip Guidebook, p. 93–127.

Printed in USA

Unraveling the multi-phase history of southern Death Valley geology

Zachariah Fleming*

Department of Geology, Occidental College, Los Angeles, California 90041, USA

Terry Pavlis*

Department of Geological Sciences, University of Texas at El Paso, El Paso, Texas 79968

Ghislain Trullenque*

UniLaSalle, GEOS Department, B2R team, 19 rue Pierre Waguet, 60000 Beauvais, France

ABSTRACT

This field trip is designed to highlight recent findings in regard to the tectonic history of the southern Death Valley region. During the first day, stops will take place in the Ibex Hills and adjacent Ibex Pass area. These stops were chosen to emphasize recent work that supports multiple phases of extension in the region, and is recorded by the interactions of complexly overprinted normal faults. Mapping of the Ibex Hills revealed an older set of normal faults that have a down-to-the-SW sense of movement and are cross-cut by down-to-the-NW style normal faults. Additionally, the Ibex Pass basin poses a number of questions regarding its stratigraphy and how it relates to the timing and kinematics of the region. Multiple stops within the basin will show the variation of volcanic and sedimentary units across Ibex Pass. The second day of the field trip is focused more so on the more recent transtensional and strike-slip history of southern Death Valley. In particular, recent mapping has correlated features in the Avawatz and Owshead Mountains that indicate ~40k m of offset along the Southern Death Valley Fault Zone (SDVfZ). Stops will take place along traces of the SDVfZ in the Avawatz Mountains and the Noble Hills. The final stop of the trip is in the Mormon Point turtleback, where the implications of the SDVfZ offset are discussed, alongside the metamorphic rocks at the stop, suggesting the restoration of the Panamint Range partially atop the Black Mountains.

INTRODUCTION

The Death Valley region (Fig. 1) has long been used as a “natural laboratory” for the field of extensional tectonics, owing to its rich geologic history and prolific rock exposure. Notably, Death Valley is the type area for the concept of a pull-apart basin,

formed between the Northern Death Valley Fault Zone–Furnace Creek Fault Zone and the Southern Death Valley Fault Zone (SDVfZ) (Burchfiel and Stewart, 1966). However, the history of the region is much more complex and fraught with overprinting structures that have been interpreted in a variety of ways (Snow and Wernicke, 1989; Miller and Pavlis, 2005; Norton, 2011).

*Emails: z Fleming@oxy.edu; tpavlis@utep.edu; ghislain.trullenque@unilasalle.fr

Fleming, Z., Pavlis, T., and Trullenque, G., 2022, Unraveling the multi-phase history of southern Death Valley geology, in Jiang, G., and Dehler, C., eds., Field Excursions from Las Vegas, Nevada: Guides to the 2022 GSA Cordilleran and Rocky Mountain Joint Section Meeting: Geological Society of America Field Guide 63, p. 67–83, [https://doi.org/10.1130/2022.0063\(04\)](https://doi.org/10.1130/2022.0063(04)). © 2022 The Geological Society of America. All rights reserved. For permission to copy, contact editing@geosociety.org.

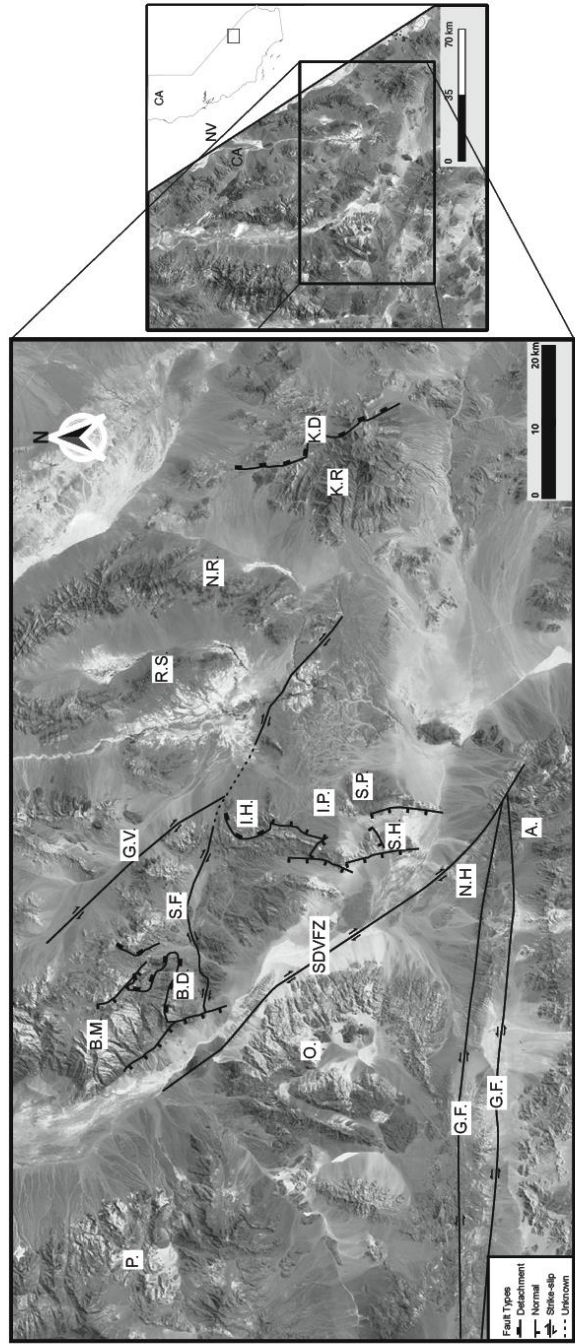


Figure 1. Map showing the general locality of the study area along with nearby structures and geographic areas referred to in the text. Right portion shows the location of the Death Valley region within the context of California. The black inset shows the southern Death Valley region. On the left is southern Death Valley with major structures and localities identified. A.—Avawatz Mountains, B.M.—Black Mountains, B.D.—Black Mountains detachment, G.F.—Garlock fault, G.V.—Grandview fault, I.H.—Ibex Hills, I.P.—Ibex Pass, K.R.—Kingston Range, K.D.—Kingston Range detachment, N.H.—Noble Hills, N.R.—Nopah Range, O.—Owlshead Mountains, P.—Panamint Range, R.S.—Resting Springs Range, S.P.—Saddle Peak Hills, S.H.—Saratoga Hills, S.F.—Sheephead fault, SDVfZ—Southern Death Valley Fault Zone. CA—California; NV—Nevada.

Understanding the mechanisms behind the deformation seen in the Death Valley region can provide valuable insight into continental extension as a whole, and in particular, the Basin and Range Province. Southern Death Valley in particular has sparked debate over the offset along both normal and strike-slip faults in the region (Troxel, 1999; Wernicke, 1999; Miller and Prave, 2002), and this field guide emphasizes locales that have recently shed light on the area's kinematic history, particularly in the context of Cenozoic extension and transtension (Pavlis and Trullenque, 2021; Fleming et al., 2021).

Southern Death Valley exhibits a complex interaction of multi-phase deformation, ranging from Mesozoic contraction to Cenozoic extension to present-day transtension (Norton, 2011). In southern Death Valley, the overprinting that resulted from such interactions has led to a kinematic history that is not easily resolved, leading to various interpretation of piercing lines, and, thus, offsets in the region. For some time, emphasis was placed upon the existence of a single, large-scale detachment fault that accommodated significant extension with an offset of as much as ~80 km in the southern Death Valley region (Snow and Wernicke, 2000). The detachment, referred to as Black Mountain detachment or Amargosa detachment, was generally linked to the concept of the "rolling-hinge" model (Wernicke and Axen, 1988), and unroofed the cores of the turtlebacks along the southeastern flank of the Black Mountains (Fig. 1). In some models, this detachment would have displaced the Panamint Mountains from atop the Black Mountains (Stewart, 1983); however, others suggested that the Panamint and Black Mountains were adjacent features, separated later by the opening of the Death Valley basin in line with the pull-apart model (Burchfiel and Stewart, 1966). In either case, there is little doubt surrounding the existence of a detachment that exhumed the southeastern Black Mountains. Tracing that detachment surface up-dip to the south and east, however, is less clear. A commonly cited interpretation was to have the Black Mountain detachment fault extend into the Ibex Hills (Fig. 1), where the Pahrump Group and younger rock lie in fault contact with basement rock (e.g., Holm et al., 1994). Recent mapping, however, indicates that, while the presence of the proposed Black Mountain detachment fault is possible, it is difficult to resolve the interpreted fault offset with the more significant extensional models (Fleming et al., 2021). In addition, such mapping has also revealed evidence for an older, unrecognized phase of extension in the range, which further complicates extensional models of the region (Fleming et al., 2021).

The hypothesis of a large-scale regional detachment has been challenged in the literature by work that emphasizes the role of strike-slip faulting in the region (Miller and Prave, 2002; Miller and Pavlis, 2005). These models suggest that the broader extension of the Death Valley region is accommodated along various discrete extensional zones bounded by strike-slip motion, instead of a single detachment surface. For example, Pavlis (1996) and Miller and Pavlis (2005) emphasized that the Death Valley turtlebacks recorded two distinct levels of detachment within the extensional terrane: one at the level of the brittle faults bounding

the turtlebacks, and a second, structurally lower level along the floor of a syn-extensional pluton. In the southern Death Valley region, a number of strike-slip faults exist that could potentially accommodate the motion required by these models, including the SDVFZ, Sheephead fault, and Grandview fault (Fig. 1) (Topping, 1993; Fleming et al., 2021). However, there is no consensus on the amount of offset recorded by these faults, and, in the case of the Sheephead fault, the sense of slip is also up for debate, with some authors citing evidence for a sinistral slip along the fault (Topping, 1993; Serpa and Pavlis, 1996), whereas others support a dextral slip (Renik and Christie-Blick, 2013). While correlations in the Ibex Hills to areas in the east have provided some insight into the sense of slip and magnitude of the Sheephead fault and Grandview fault, a more substantial inquiry is needed. Farther to the south, along the SDVFZ, a study by Pavlis and Trullenque (2021) showcases evidence for ~40 km of slip along the fault zone. This is in contrast to previous studies that had suggested more modest amounts of offset, ~10–30 km (Wright et al., 1991; Niles, 2016).

This guide was assembled to highlight key localities that have been influential in recent work related to the issues discussed above, namely the normal and strike-slip fault distribution and offsets that produced the current geometry of southern Death Valley. In the following sections, a summary of the recent evidence and interpretations that have been made in the region is provided.

NORMAL FAULTING IN THE SOUTHERN DEATH VALLEY REGION

Following Mesozoic–Paleogene contraction in the region, Death Valley has largely undergone extension, beginning in the Miocene, with the development of the modern pull-apart basin during the past ca. 3 Ma (Norton, 2011) with suggestions of distributed transtension back to the early phase of extension at ca. 12 Ma (Serpa and Pavlis, 1996). The earliest Miocene extension in the region has been interpreted by top-to-the-southwest structures, most notably the Kingston Range detachment, which extends from the Kingston Range in the north to the Halloran Hills in the south (Fig. 1) (Burchfiel et al., 1983; Fowler and Calzia, 1999). The timing of the Kingston Range detachment is provided by cross-cutting plutons that constrain movement from ca. 13.5–12 Ma (Ramo et al., 2002). Until recently, however, evidence for other structures associated with southwest-northeast extension has not been published extensively. Troxel (1999) recognized northwest-trending dikes in the Saddle Peak Hills, presumed to have been coincident with nearby ca. 12 Ma volcanic deposits, supporting such southwest-northeast extension. Further work by Mahon and Link (2013) mapped out currently low-angle normal faults in the Saddle Peak Hills (Fig. 1), which have a down-to-the-west sense of displacement as well as northwest-trending, down-to-the-southwest normal faults, in line with the interpretations of Troxel (1999) and Troxel et al. (1992).

Recent work by Fleming et al. (2021) identified map relationships of currently low-angle normal faults that supports

down-to-the-southwest movement, presumably related to southwest-northeast extension and concurrent with the events discussed above (Troxel, 1999; Mahon and Link, 2013) in the Ibex Hills (Fig. 1). These faults are primarily in the northern Ibex Hills and are curved along a northeast-trending axis that gives the gen-

erally synformal outcrop pattern to that section of the range. Previous interpretation of the Ibex Hills incorporated the low-angle faults as an up-dip portion of the Black Mountain detachment; however, given the evidence for an earlier, kinematically distinct episode of extension, that interpretation is at least partially incorrect. Two primary down-to-the-southwest normal fault surfaces were identified in the northern Ibex Hills, where they carry the Crystal Springs Formation and Horse Thief Springs Formation in their hanging-walls, and juxtapose them on top of 1.7 Ga basement rock and the Crystal Springs Formation, respectively (Fleming et al., 2021). Map patterns support the interpretation of these structures as the fault traces cut up-section to the north and east. Collectively, the down-to-the-southwest faults of the Ibex Hills were interpreted to accommodate a minimum of ~1.5 km of heave based upon simple 2-dimensional cross-section reconstructions (Fleming et al., 2021). Additionally, stratigraphic relationships also support the interpretation of northeast to southwest displacement in the Ibex Hills. In parts of the northern Ibex Hills, the Noonday Dolomite sits directly upon the Horse Thief Springs Formation, with only small lenses of the Kingston Peak Formation in between the two (Fig. 2); however, in some areas the Beck Springs Dolomite does appear but it is within the hanging-walls of structurally higher faults linked to a later, distinct kinematic event. This unconformable relationship between the Kingston Peak and overlying units follows a broadly northwest-southeast

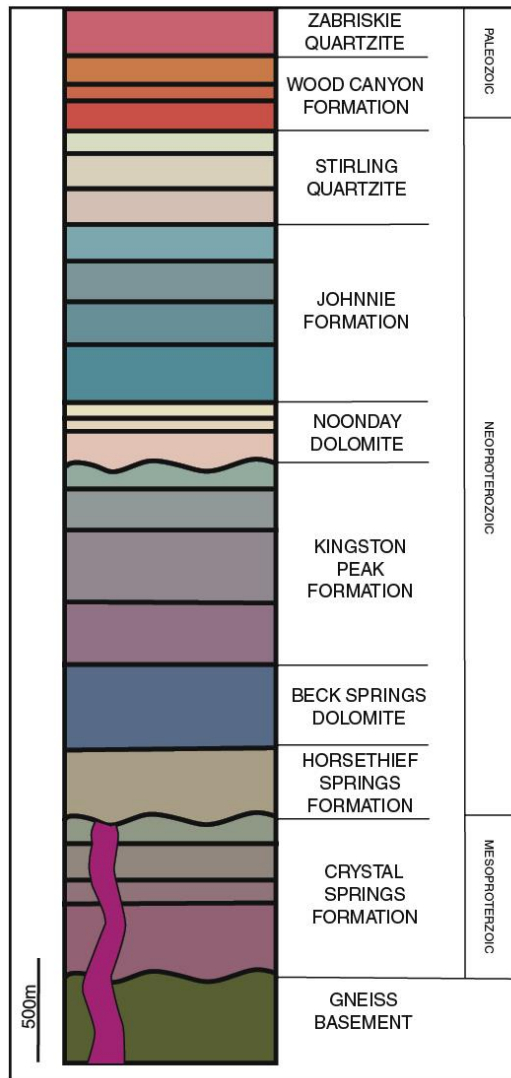


Figure 2. Stratigraphic column of the bedrock units in the areas of the field trip. Formations are divided by thick black lines.

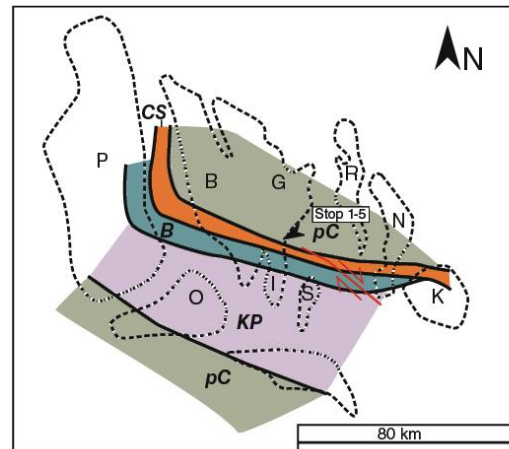


Figure 3. Map showing southern Death Valley ranges and the units that directly underlie the Noonday Dolomite (shown as bold and italicized). A—Avawatz Mountains, B—Beck Springs Dolomite, B—Black Mountains, CS—Crystal Springs Formation, G—Grapevine Mountains, I—Ibex Hills, K—Kingston Peak, KP—Kingston Peak Formation, N—Nopah Range, O—Owlshead Mountains, P—Panamint Mountains, pC—Precambrian basement, R—Resting Springs Range, S—Saddle Peak Hills. Red line indicates the approximate trace of the Grand View Fault. Modified from Wright et al. (1976).

trough, the Amargosa Autoclone of Wright et al. (1976). Following the trend of the unconformity (Wright et al., 1976), if the low-angle faults of the Ibex Hills recorded southeast to northwest displacement, one would expect to see the Kingston Peak Formation in the hanging-wall (Fig. 3). This is especially true if we assume any appreciable dextral offset along the Grand View fault; i.e., the modern isopach pattern, as mapped by Wright et al. (1976), is partially the consequence of younger fault displacement. Therefore, it is likely that the Ibex Hills were in a more southwesterly position relative to the ranges to the east, e.g., the Nopah Range, previous to dextral Grand View fault offset, rather than nearly due east as it is today (Fig. 3). Based upon those assumptions, the fault most likely displaced material from another source, north of the upper Kingston Peak isopach, toward the south and southwest before being displaced along the Grand View fault (Fig. 3) (Fleming et al. 2021). One potential source would be the southern Nopah Range, with the offset between that range and the Ibex Hills potentially providing a piercing line for constraint on strike-slip offset along the Grand View fault (Figs. 1 and 3).

More recent extension in southern Death Valley is recorded by generally northeast-striking, down-to-the-northwest normal faults (Mahon and Link, 2013; Fleming et al., 2021). The evidence and extent of this extension are much more abundant than the older phase, with the most notable feature being the Black Mountain detachment mentioned in the previous section (Fig. 1) (Holm et al., 1992). Clear cross-cutting relationships are found in the Saddle Peak Hills and Ibex Hills, which demonstrate this transition to faulting associated with northwest-southeast extension (Troxel, 1999; Mahon and Link, 2013; Fleming et al., 2021). This later phase of extension has also been argued in light of thermochronologic data in the area (Holm et al., 1992; Holm and Dokka, 1993). However, others have pointed out that the data published in Holm et al. (1992) is not necessarily indicative of a singular, top-to-the-northwest detachment, as they argued, and can potentially be explained by multiple generations of faulting (Miller and Pavlis, 2005). Mapping in the Ibex Hills revealed the presence of both moderate and currently low-angle normal faults, with a down-to-the-northwest sense of movement, which align with this northwest-southeast phase of extension (Fleming and Pavlis, 2015; Fleming et al., 2021). The low-angle normal faults that display a top-to-the-northwest sense of motion indicate that previous models that place the Black Mountain Detachment in the Ibex Hills may be partially correct; however, given the high structural position of these faults in the range, the breakaway zone is likely to be proximal to the Ibex Hills.

The structures mapped in bedrock units extend into Cenozoic cover between the Ibex Hills and Saddle Peak Hills (Fig. 1). These deposits record a composite stratigraphy with an older volcanic section below an angular unconformity overlain by younger sedimentary deposits that include large megabreccia sheets (Fleming et al., 2021). These deposits are crucial to unraveling the relative timing of the extensional structures with the older deposits strongly affected by the southwest-directed extensional structures, while the younger deposits are not extensively

deformed. During this field trip, we will visit these deposits and discuss their significance to the extensional history.

TRANSTENSION AND STRIKE-SLIP FAULTING IN SOUTHERN DEATH VALLEY

As part of a detailed study of fault rock development along the southern Death Valley fault, Pavlis and Trullenque (2021) made a serendipitous discovery that has important implications for Death Valley tectonics. They recognized that a well-known exposure of Crystal Springs Formation and underlying basement along the Avawatz Mountain front (Fig. 1) was invaded by granites that were similar to granites seen in the Owlshead Mountains. Specifically, a very similar association of units occurred west of the Death Valley fault zone in the NE Owlshead Mountains, ~40 km to the north. This similarity led Pavlis and Trullenque (2021) to an interpretation that these two exposures represented markers that were offset along the SDVFZ, indicating the net dextral slip on the fault was 40–41 km (Fig. 3). They argued further that this offset was consistent with a series of more blunt markers, but all indicated offsets on the same order, supporting their higher-precision interpretation.

During this field trip, we will visit several sites critical to Pavlis and Trullenque's (2021) interpretations, centered on exposures of a bedrock high within the core of the SDVFZ in the Noble Hills, a range of low hills just north of the Avawatz Mountains (Fig. 1). The original study was undertaken as a detailed study of fault-rock development in granitic rocks as an analog for geothermal reservoirs in shattered granites (Trullenque et al., 2017; Chabani et al., 2021). We will highlight some of the observations on the fault-rock development and the implications of field relationships for the history of the fault system. In particular, we will focus on exposures that show the following:

(1) The internal structure of the bedrock high in the Noble Hills is complex due to a fault network that formed progressively with time, and broad zones of cataclasis associated with intense, relatively low-*T* (temperature) hydrothermal alternation (Klee et al., 2021). Individual faults range from discrete slip surfaces to a few major slip zones marked by 0.5–2-m-thick clay gouge zones that can be mapped as distinct faults within granites. Most of the faults within this network are high-angle faults with ubiquitous dextral shear sense indicators. Perhaps the clearest example of a dextral fault is a broad cataclastic zone with foliated fault gouge that forms the eastern boundary of the bedrock high along most of its map trace. A second zone, potentially with even more slip, is recognized entirely within the altered granite. We will visit both the bounding fault and internal strike-slip faults of the bedrock during this field trip.

(2) Pavlis and Trullenque (2021) had limited data on the absolute age of Cenozoic units that flank the bedrock high of the Noble Hills, but based on correlations suggested by Brady and Troxel (1999), they concluded that a significant part of the cataclasis in the Noble Hills basement rocks occurred prior to deposition of ca. 10–8 Ma sediments. Their interpretation differs

somewhat from the Niles (2016) interpretation of contact relationships, but both studies agree that significant deformation predated the unconformity at the base of these sediments. This is an interpretation we will examine on this field trip. This interpretation is also supported by direct dating of fault rocks and thermochronology studies of the exhumed rocks in the bedrock high (Trullenque, 2021, personal commun.).

(3) Structures within the Noble Hills bedrock high, as well as contacts that bound the bedrock high to the west, suggest that a late phase of the deformation is recorded as contraction related to the arrival of the bedrock high in the contractional “corner” where the sinistral Garlock fault meets the dextral Death Valley system (Fig. 1). We will examine evidence that a distinct bedrock slice is present in the southern Noble Hills, and that it represents a thrust slice carrying basement depositionally overlain by Tertiary Military Canyon Formation. This inference suggests the bedrock high is a composite feature, with this basement slice bounding a block that has insignificant dextral offset from granitic rocks that themselves have been displaced at least 20 km from their original position, along what is now the eastern Owlshhead Mountains.

Based upon the observations and correlations of Pavlis and Trullenque (2021), alongside previous estimates (e.g., Stewart, 1967; Wright and Troxel, 1967; Butler *et al.*, 1988), the SDVfz has likely seen an offset of ~40 km, comparable to the Northern Death Valley Fault Zone—Furnace Creek Fault to the north. Additionally, the timing constraints for both fault systems suggest that movement along them has persisted since the mid- to late Miocene (Renik and Christie-Blick, 2013; Pavlis and Trullenque, 2021). This timing for both of the Death Valley fault zones indicates that strike-slip faulting has played a significant role in the evolution of the region since the onset of Miocene extension. Some previous piercing lines, for example deposits of the Amargosa Basin (Topping, 1993), still require further offset, however, which is likely accommodated by faults to the east of the SDVfz (Pavlis and Trullenque, 2021). The Grandview fault and/or Sheephead fault are likely candidates, and insight into their offset may be found by correlating the Noonday unconformity (Fig. 3) discussed in the previous section, and this possibility will be a point of discussion for the stop in the northern Ibex Hills.

IMPLICATIONS OF IBEX AND NOBLE HILLS FOR THE CENTRAL DEATH VALLEY BASIN: WHERE WERE THE PANAMINT MOUNTAINS PRIOR TO EXTENSION?

Together, our work in the Ibex Hills and Noble Hills suggests that the net slip on the Amargosa detachment system in the core of the Black Mountains (Fig. 1) is on the order of 40 km. This slip is primarily indicated by the interpretation that dextral slip on the SDVfz was transferred to the detachment system that unroofed the Black Mountains. We have no new data bearing on issues of single detachment versus composite features complicated by block rotation versus multiple detachment levels (e.g., see discussion in Miller and Pavlis, 2005). It should be noted, however, that

Castonguay (2013) and Castonguay and Miller (2018) recently presented evidence that the Black Mountain detachment within the Amargosa Chaos also shows multi-phase deformation inconsistent with a single detachment system. This conclusion, when taken with the interpretations of the northern Ibex Hills, raises the question whether extensional nappes of distinct kinematic histories gave rise to the Amargosa Chaos—a topic for discussion on the field trip. Additionally, the new slip estimates of the region suggest reassessments of relationships with the core of the extensional terrane in Death Valley itself. For example, in the model of Stewart (1983), the Black Mountains detachment system accommodated ~80 km of slip, which, when restored along the NW extension direction, would place the Panamint Range directly above the Black Mountains and what is now Death Valley atop areas now far east of the Black Mountains. In contrast, Pavlis and Trullenque’s (2021) estimate of approximately half this slip (i.e., ~40 km) would place the Panamint Range atop the Black Mountains, but with the eastern edge of what is now the Panamint Mountains atop the eastern edge of the Black Mountains (Fig. 4). We suggest this restoration, shown in Figure 4, which includes transrotation inferred by Pavlis *et al.* (1998), is far more consistent with the known geology of both the Black Mountains and the Panamint Mountains.

The Black Mountains have been the focus of some of the most detailed studies in North America, beginning with the pioneering work of Wright *et al.* (1973) and Wright and Troxel (1984) and continuing with extensive studies in the 1990s and early 2000s (Holm and Wernicke, 1990; Holm *et al.*, 1992; Holm and Dokka, 1993; Mancktelow and Pavlis, 1994; Serpa and Pavlis, 1996; Miller and Prave, 2002; Miller, 2003; Miller and Pavlis, 2005). The area has seen less work in the last ~10 yr, but a reconnaissance geochronology study by Lima *et al.* (2018) and preliminary metamorphic petrology studies from the turtlebacks provide important new insights to be discussed on this field trip. Specifically, Lima *et al.* (2018) showed that migmatites in the Copper Canyon and Mormon Point turtlebacks contained leucosomes that record zircon growth over an extended period from late Mesozoic to Neogene (ca. 10 Ma) time. This conclusion has historical significance in the context of Black Mountains geology, because the migmatitic rocks of the turtlebacks were long assumed to be Precambrian migmatites, arising from their interpretation as Proterozoic basement. Lima *et al.*’s (2018) study demonstrates that assumption was very wrong and suggests that parts of the migmatitic complex may be simply high-grade metasedimentary rocks (e.g., the Pahrump Group). Their data also explain the early Cenozoic pegmatites at Badwater turtleback recognized by Miller and Friedman (1999) as products of prolonged anatexis in the turtlebacks. These new geochronology data also support an old interpretation by Pavlis (1996) and Miller and Pavlis (2005) that the Copper Canyon and Mormon Point turtlebacks were heated to very high temperatures in the Neogene when a large mafic pluton, the ca. 12 Ma Willow Springs diorite (Asmerom *et al.*, 1990), was emplaced as an ~2-km-thick sill-like pluton above the turtlebacks; i.e., the turtlebacks are the floor to that pluton.

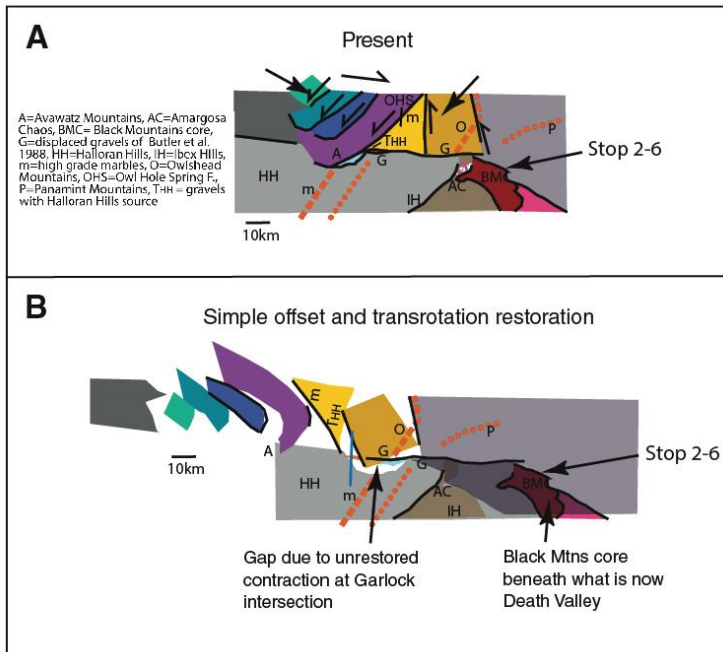


Figure 4. Implication of inferred 40 km of offset along the SDVFZ. (A) The present geology, simplified, along the fault. (B) A simple restoration of 40 km of dextral offset, as well as a simplified addition of inferred transrotation in the northeastern Mojave, as per Pavlis et al. (1998). Dashed and dotted thick lines indicate the upper and lower extent of the Mesozoic granitic rocks, respectively. Figure modified from Pavlis and Trullenque (2021).

The very young zircon rims reported by Lima et al. (2018) are consistent with that interpretation with reheating of the complex to high- T in the Neogene on the pluton floor (e.g., Pavlis, 1996). Similarly, preliminary thermobarometric work reported by Pavlis et al. (2018) and Tracy et al. (2019) is consistent with the geochronologic evidence, with evidence for an early, relatively high- P (pressure) (~7 kb), very high- T (~700 °C) history in the Mesozoic followed by decompression to ~5–6 kb and a second thermal peak at ~660–685 °C. Note that these temperature estimates are all above $Mu + qtz$ breakdown temperatures, consistent with the absence of muscovite and ubiquitous sillimanite in the Copper Canyon and Mormon Point turtlebacks, and consistent with the migmatitic textures suggestive of melting. Indeed, these metamorphic assemblages are suggestive of restites from crustal anatexis. In addition, the younger pressure estimate suggests the Mormon Point and Copper Canyon turtlebacks were at depths of ~15–20 km prior to onset of extension. Thus, if the ~40 km slip estimate for the Amargosa fault system, and inference of a breakaway zone in the Ibex Hills, is correct, the average initial dip of the detachment system was ~20–27 degrees. We will discuss these data and field relationships consistent with the data when observing high-grade metamorphic rocks of the Mormon Point turtleback.

The new data from the Death Valley turtlebacks can be synthesized with work in progress in the Panamint Mountains to

the west of Death Valley. In all tectonic scenarios, the Panamint Mountains were at higher structural levels than the Black Mountains prior to extension, either lying beside to somewhat atop the Black Mountains (e.g., Miller and Pavlis, 2005) or fully atop to even east of the Black Mountains (Fig. 4) (e.g., Holm and Wernicke, 1990; Snow and Wernicke, 2000; Norton, 2011). Thus, the structural history of the Panamint Mountains is critical in assessing alternative hypotheses for the Black Mountains history.

In that context, one of us (Pavlis) has conducted detailed studies in parts of the western Panamint Mountains metamorphic complex as part of a series of ongoing experiments developing 3D mapping techniques (e.g., see Brush et al., 2018). During this field trip, we do not have time to visit key exposures in the Panamint Mountains, but we will visit some sites virtually on the first evening, using 3D visualizations from the ongoing work. The key observations from the Panamint Mountains that will be discussed at the Black Mountains stop include:

(1) The western Panamint escarpment exhumed a partial crustal section that is largely unbroken across ~20–30 km horizontally with a Tertiary unconformity at the eastern edge of the range. Note that the 20–30 km range depends on the direction the measurement is made and assumptions about slip on higher-level faults. The intact rocks lie beneath a very low-angle normal fault system that dips west at 5–30 degrees. With a little trigonometry, and assuming the fault system originally dipped west at

~45 degrees, this generalization suggests the deepest levels of the Panamint Mountains crustal section were exhumed to the surface from depths of ~15–20 km.

(2) This crude estimate of the structural relief across the range is consistent with the observed low-*P*, high-*T* Mesozoic metamorphism reported by Labotka (1981), which is exemplified by ubiquitous andalusite and sillimanite with the absence of kyanite in the metamorphic assemblages. Note also that this crude estimate is also consistent with the observed Neogene metamorphism in the turtlebacks, based on the new *P-T* estimates that assume the Panamints lay atop/beside the Black Mountains prior to extension, i.e., depth estimates of 15–20 km. Note, however, that the metamorphic assemblages in the Panamint Mountains are unequivocally Mesozoic; thus, direct comparisons with *P-T* estimates in the Black Mountains require an assessment of the entire metamorphic history, a topic for discussion on this field trip.

(3) Finally, new mapping in the Panamint Mountains leaves no doubt that previous descriptions of the structural history in the metamorphic complex are a gross oversimplification. Brush et al. (2018) provided a partial description of the history and work in progress (Pavlis, 2021, personal commun. and in virtual visit as part of this field trip) will provide more details. The key structural observation from the complex is that the entire metamorphic complex shares a three-phase ductile deformational history similar to that described by Hodges et al. (1987) at Tucki Mountain in the northern Panamints, with the caveat that all of the structure is demonstrably Mesozoic to Paleogene in age. Specifically, structures in the Panamint metamorphic complex record a three-phase fabric development associated with three phases of folding. The two oldest, D1 and D1a, represent superimposed isoclinal folding events that generated the main continuous cleavage in the rocks. D1a is cryptic due to intense overprinting by D1 structures, and both phases are demonstrably older than Late Cretaceous, shown by two mica granites dated by U-Pb zircon at ca. 85 Ma (Cobb, 2015). Finite strain associated with D1-D1a superposition is well recorded in coarse clastic rocks of the Kingston Peak Formation, and LS fabrics mimic the finite strain with prominent N-S stretching. F1 and F1a fold axes are subparallel to lineation consistent with folds with axes developed parallel to stretching or formation of sheath folds, with either possible given the observed high finite strains. The main continuous cleavage is in turn folded about horizontal to gently plunging, upright to steeply inclined folds (F3) associated with a domainal crenulation cleavage of S3. These F3 folds are the only folds shown on regional maps of the central Panamint Mountains (Albee et al., 1981), but represent relatively low-strain components in the assemblage. They are demonstrably younger than the Late Cretaceous plutons of the assemblage but their minimum age is less clear, constrained only as pre-Eocene by Ar/Ar cooling ages reported by Labotka et al. (1985) and zircon He dates reported by Bidgoli et al. (2015). F3 folds may correlate to younger folds in the Black Mountains given similarities in style and orientation, yet the younger folds in the Black Mountains are clearly, at least partly, of Neogene age (e.g., Mancktelow and Pavlis, 1994), a topic for discussion

on this field trip. In any case, the metamorphic structural history of the Panamint Mountains must be directly linked to the higher-grade rocks of the Black Mountains, but exactly how is not yet known and will require more extensive fieldwork and geochronology to be fully unraveled.

FIELD STOPS

The following section provides travel directions and field stop descriptions. Day 1 of the trip highlights extensional faulting and Tertiary basin deposits, whereas Day 2 is centered on offset along the SDVFZ. The exact locations for the stops are provided in Table A1 and shown on the Figure 5 map.

Day 1

Travel: Coming south from the town of Shoshone, California, from the Route 127–178 intersection, turn right off the highway after 14.1 mi and proceed along the dirt road toward the Ibex Hills to the west. As you drive along the road, on your left are flat-topped hills capped by a carbonate megabreccias. These megabreccias lie on gravels that are part of the upper succession in the Tertiary basin, a topic of discussion throughout today's stops. We interpret these carbonates as Beck Springs Dolomite, suggestive of a Kingston Range source analogous to the granite megabreccias we will see later. After driving 3.2 mi down the dirt road, park along the flank of the range.

Stop 1-1: Central Ibex Hills, below Comet Mine (35.8209° N, 116.383° W)

At this stop, we will see the trace of the Eastern Boundary fault of the Ibex Hills along with landslide features associated with movement along that fault. In addition, there are gravels that lie atop various bedrock units flanking the Ibex Hills, providing insight into the basin stratigraphy, which is significantly thinner than locales to the south and east. From here we can also see an overview of the area for later stops in the Tertiary basin, just north of the Saddle Peak Hills and at the southern extent of the Ibex Hills.

Immediately southeast of the parking location is the notable Johnnie oolite, marking the upper Johnnie Formation that lies in the hanging wall of the Eastern Boundary fault. On the north and west side of the fault is the Crystal Springs Formation. The Crystal Springs Formation in this locality is nearly complete and well exposed, making it an ideal spot to analyze the section. Continuing south-southwest along the Eastern Boundary fault, we find Crystal Springs Formation on the eastern side of the fault, lying below the Tertiary gravels, indicating faulting that predates gravel deposition and fault movement.

Farther north along the Eastern Boundary fault, ~600 m, is the first in a series of landslides composed primarily of Beck Springs and Noonday Dolomites. These landslides overlie the gravels in the Tertiary basin, which in turn overlie Johnnie and Stirling Formations, and are cross-cut themselves by the Eastern Boundary fault.

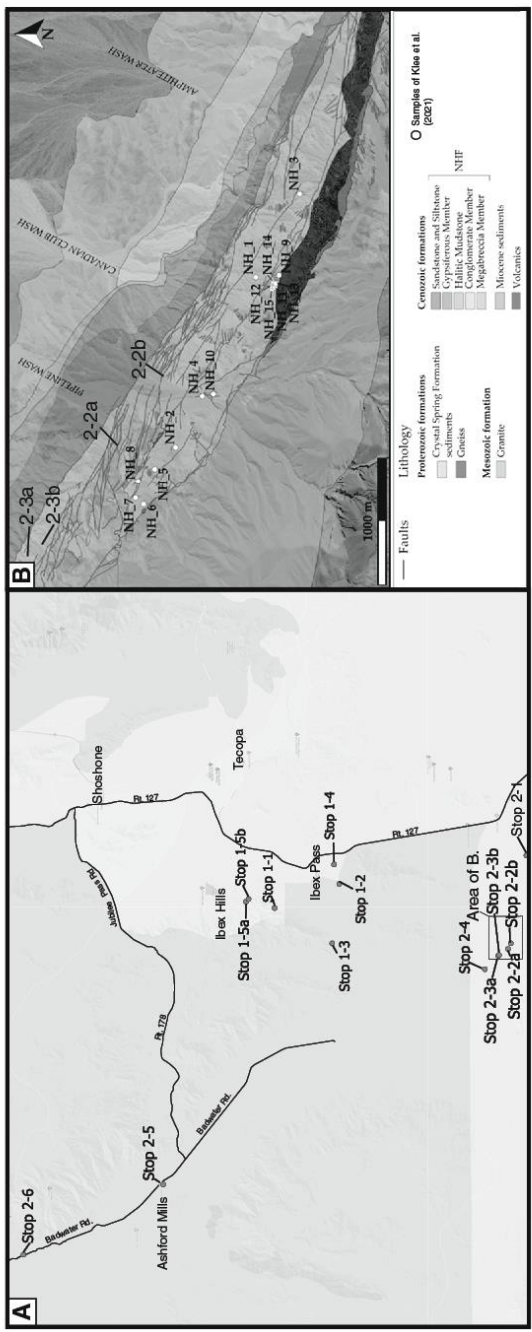


Figure 5. (A) Google road map imagery overlain with the locations of field-trip stops and local place names. For exact stop positions, consult Table A1. (B) Zoomed-in view of the Stops for 2-2 and 2-3 in the Noble Hills. Overlain on the geologic map of Klee et al. (2021).

Travel: Proceed back to the highway and turn right toward Ibx Pass. Drive 2.0 mi and turn right onto the gravel road toward the microwave station, continuing down the road to a rusty oil drum. Walk up the wash to the left and take the first right fork of the wash; proceed ~200 m and you will see the angular unconformity beneath the Tertiary volcanics.

Stop 1-2: Basal Tertiary Unconformity

(35.764° N, 116.3569° W)

At this site, we can see a massive, porphyritic, andesitic flow that was deposited on steeply east-dipping Johnnie Formation. In addition, the unconformity is exposed with a thin lag of ash containing Johnnie clasts, overlain by the massive flow unit. At this locality, there is also a small fault that offsets the unconformity in a dextral sense—indicating either dextral slip or west-side-up. From the stop you can see the shallowly dipping unconformity, which can be easily traced across the countryside. To the east, the next major gully exposes the unconformity with a thin section of gravels just above the contact. The gravels along that unconformity contain Johnnie clasts derived from immediately underlying rocks.

Travel: Continue down the dirt road in the wash to a turn off (to the right) just before the “deep sand” sign. After the turn, continue 3.4 mi west on the dirt (very bad) road and take a left immediately after passing the old Ibx Mine housing, onto another equally bad dirt road. Drive and then park the car 0.5 mi from the turn, a total of 5.9 mi from the original turnoff from the main road.

Stop 1-3: Basal Tertiary Gravels and Ash Deposits

(35.770166° N, 116.421436° W)

Walk northwest from the parking location along the desert pavement. After walking ~250 m, we arrive at an exposure in the gully of a red gravel (Fig. 6). The clasts within the gravel are predominately red to light-colored quartzite, with some clasts of dark-colored shales. Our original interpretation of this gravel was as a basal sequence above the unconformity containing clasts of Crystal Springs Formation; however, we acknowledge that the lack of distinctive clasts types leaves this open for interpretation.

Heading ~100 m northeast from the gravel deposit, we encounter outcrops of a tuff unit, similar to an outcrop we will see at the next stop. This tuff unit can be used as a potential tie-line between the two sections, and doing so reveals a much more abbreviated volcanics section underlying the tuff in the southern Ibx Hills, than to the Ibx Pass area to the east. Following down the wash, to the east, containing the tuffs, we find a red gravel similar to the one seen in earlier outcrops within the volcanic sequence, potentially indicating a possible channel flow through the volcanics.

To the south of this stop the ridge lines are made up of bedrock units ranging from lower Johnnie Formation to the upper Noonday Dolomite. This sequence is relatively continuous; however, it is complexly faulted by mostly NW-SE-striking normal faults that disrupt the section. Immediately between the volcanic rocks of the current stop and the bedrock units to the south is an

~E-W-striking fault that drops the southern bedrock units down. This fault ultimately runs into and cross-cuts faults that flank the front of the range, adjacent to, and west of, the basin we are currently in. Farther north-northeast of the current stop are more faults, striking NW-SE, that bound the northern part of the basin, as well as the talc mine on the ridge. These faults clearly displace the Crystal Springs Formation and the overlying unconformity, but are presumably cross-cut by the Eastern Boundary fault.

Travel: After 5.2 mi backtracking from Stop 1-3, park vehicle and walk north toward dark outcrops.

Stop 1-4: Top of Ibx Pass Tertiary Section

(35.768478° N, 116.335809° W)

At this stop, we will see the top of the Tertiary volcanic section and the angular unconformity that separates these rocks from overlying megabreccias. In preparing for this field trip, we examined these outcrops that were outside our recent mapping, and this exposure reveals some interesting features worth discussing.

Walk up the wash to the first dark outcrops and examine the volcanic rocks, then walk east to find the unconformity with overlying megabreccias. Note the tiny exposure of ash deposits just below the unconformity. Also note the clast compositions and lack of rounding in the clasts in the megabreccias. In particular, note scattered clasts of purple shales, presumably from the Crystal Springs Formation, and the porphyritic texture of the igneous rocks in the megabreccias as well as the rapakivi texture of the phenocrysts.

After examining this outcrop, we will walk ~200 m up the wash and re-examine the section. Note the significant difference in rocks below the unconformity, including a thick white ash that served as a marker bed in our mapping, as well as the basaltic pyroclastic rocks below the ash. This volcanic section is strikingly similar in physical stratigraphy to the section to the north and west, across southern Death Valley in Wingate Wash. We



Figure 6. Field photograph of the basal gravel in the basin of the southern Ibx Hills at Stop 1-3. Garmin GPS unit for scale.

will discuss this issue on Day 2, Stop 5, in reference to slip on the southern Death Valley fault. After examining the volcanics, note the tuff is the same tuff we saw at the earlier outcrop, but it is much thicker because it is truncated to the south along an angular unconformity.

After examining the volcanic deposits, proceed up section along the outcrop to examine the megabreccias. Note the distinction in the composition with abundant clasts of quartzite and purple shale that we again interpret as Crystal Springs Formation. This observation is unique to this eastern exposure of the basal landslide assemblage, because just to the west, these Crystal Springs megabreccias are absent and granite megabreccia lies directly on the volcanics.

If time permits, we will walk north around the small hill, and head east and down the next gully to see the overlying granite megabreccia and a fault contact that repeats the entire section. A topic for discussion is a hypothesis we developed when we found this outcrop: Do the differences we see in the section, both vertically and laterally, represent the unroofing of Kingston Range pluton from initial Crystal Springs with porphyritic border rocks of the pluton proceeding to unroofing of the deeper level of the pluton?

Travel: After returning to Route 127, turn left to head north 7 mi. At that point, take a left onto the dirt road that leads to the final stop of the day. Follow the road for 4.5 mi and park just east of the Eclipse Mine.

Stop 1-5: Northern Ixex Hills

Stop 1-5a (35.846043° N, 116.37618° W). Walk up the nearby hill ~200 m to the northwest to overlook the ridge of Noonday Dolomite to the north. In this locality, the Noonday Dolomite is sitting atop a thin layer of Kingston Peak Formation, which in turn sits on Horse Thief Springs Formation (Fig. 7A). It is important to note the lack of significant Kingston Peak or Beck Springs Formations in the stratigraphy here, as would be expected if the rocks were transported from the southwest. The absence of that stratigraphy makes for a good discussion of extensional models that rely on such NW-SE kinematics, as well as potential correlations of the northern Ixex Hills to areas to the W-NW, for example, the southern Nopah Range (Fig. 3). The sequence below the Noonday ridge is then in fault contact with the gabbro intrusive upon which the current stop is located. Looking to the south, toward the Eclipse Mine, there is the first in a series of NE-SW–striking normal faults that repeat the Crystal Springs and Horse Thief Springs Formations. On the distant southwest horizon an exposure of Beck Springs Dolomite is visible; this is sitting in the hanging-wall of a low-angle normal fault that juxtaposes it against lower Crystal Springs. This low-angle fault, along with others carrying Beck Springs Dolomite, are interpreted as sitting structurally higher than those that carry the Noonday outcrop at this stop and represent kinematically distinct extensional events. This is in line with interpretations of the unconformity below the Noonday (Fig. 3); that is, if the faults displace material to the northwest, we would expect to see the Beck Springs below the Noonday, as we do.

Stop 1-5b (35.843873° N, 116.373346° W). Now head ~225 m east, down the dirt road, until the intersection and turn right. Walk ~325 m along this road. Now in the bend of the dirt road we see the damage zone of the Eastern Boundary fault exposed (Fig. 7B). Here the Crystal Springs Formation lies in the foot-wall, to the west, and the Stirling Quartzite is in the hanging-wall. The damage zone continues for ~25 m on the roadcut and can also be seen in the adjacent gully. Looking back to the north, past where we just came from, and along strike of the Eastern Boundary fault, it is interesting to note that the fault would be expected to cut through the ridges of Noonday Dolomite; however, there is no clear indication of this. In fact, the trace of the fault is difficult to find beyond the first Noonday ridge. Potential avenues for the fault trace, along with its implications, will be prime for discussion.

On the way back to the vehicle, after walking back to the main dirt road, we can overlook the gully to the north of the road where we see the last clear exposure of the Eastern Boundary fault, placing Johnnie Formation against Crystal Springs Formation. Just to the east of that exposure are faults, clearly cross-cut by the Eastern Boundary fault, that repeat sections of Johnnie and Stirling Quartzite.

Day 2

Travel: From Shoshone, California, head south on Route 127 across Ixex Pass and into southern Death Valley. Just past the sand dunes on your left, take a right onto Saratoga Springs Road/Wade Road. Proceed along this dirt road 1.8 mi to the Sheep Creek Springs Road, and turn left onto that road. Proceed up this very rough road to just past the large talc waste piles, ~4 mi.

Stop 2-1: Sheep Creek (35.592669° N, 116.359897° W)

This quick overview stop shows the large exposure of steeply dipping, north-facing Crystal Springs Formation that Pavlis and Trullenque (2021) correlated to exposures to the NW, and served as the main basis for their inferred 40–41 km of dextral offset on the SDVFZ. As we came up the long bumpy road, we crossed the Avawatz frontal fault, which is an active thrust system developed here in the zone where the sinistral Garlock and dextral Death Valley fault systems merge. The contraction has long been recognized as a geometric incompatibility as these two fault systems merge. Just to the south along the Avawatz mountain front, you can find localities where the crystalline rocks of the Avawatz mountains are thrust onto Quaternary gravels.

Looking north from the stop, we can see a full section of the Crystal Springs Formation lying on basement. The talc mines are in the Crystal Springs carbonates that were intruded by gabbroic plutons—similar to what we saw yesterday along the front of the Ixex Hills (Fig. 8). To the west, we can see fault gouges on the hillsides along the Avawatz front. These gouges were generated along the Garlock/Mule Spring fault. The Mule Spring fault is the name given to the structure by Brady (1984) to distinguish it

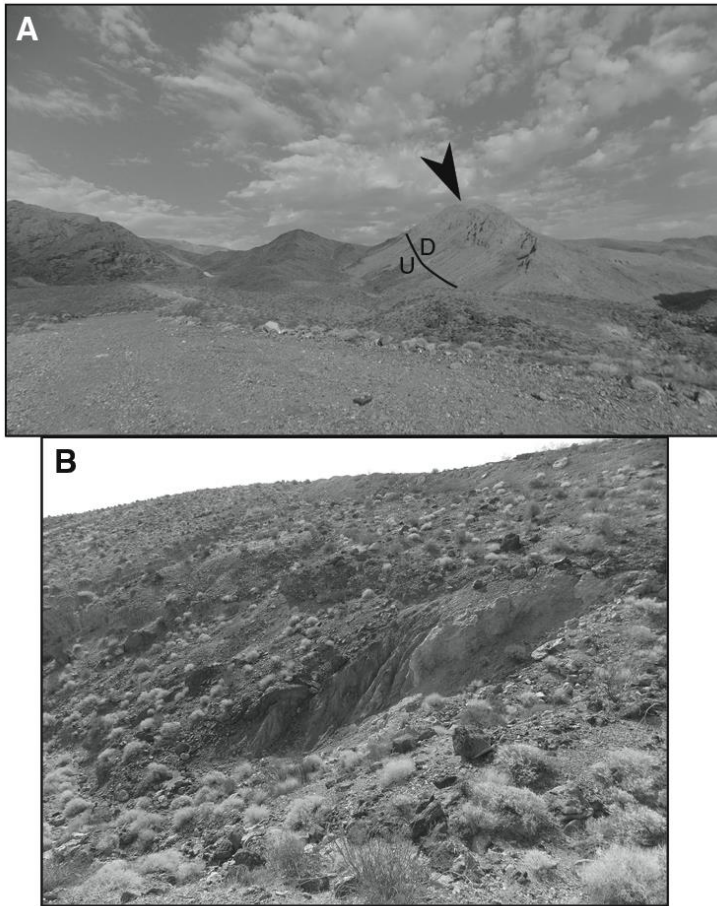


Figure 7. (A) Looking west from Stop 1-5a toward the Ibex Hills. Right arrow shows the ridge of Noonday Dolomite that lies atop small lenses of Kingston Peak Formation; the line indicates the fault at the base of the Horse Thief Springs Formation along with sense of offset. D—down; U—up. (B) Outcrop of the fault zone along the Eastern Boundary fault at Stop 1-5b.

as the contractional structure here along the Avawatz front that is the eastern continuation of the sinistral Garlock. Presumably the gouges are a composite fault rock generated initially along the Garlock system and dragged into this position as they were brought up along the Mule Spring thrust system. Not visible here is the second piercing point described by Pavlis and Trullenque (2021), where a granite intrudes into Precambrian basement over the hill to the south and west.

Travel: Leave Sheep Creek and return to the main Saratoga Springs road, then head northwest 4.7 mi toward Death Valley. Just past the marked turn to Saratoga Springs, a dirt road will turn off to your left. Turn onto this road and continue until it intersects with a road that parallels the mountain front. Turn right on that road, follow it until it turns northwest up a wash, then follow it

up the wash until the road makes a sharp right toward a gap in the rocks and park.

Stop 2-2: Slice and Dice within the Basement High

Stop 2-2a (35.615002° N, 116.427508° W). In addition to the offset markers at the last stop, Pavlis and Trullenque (2021) argued that structural relationships within the Noble Hills indicated that a structural high within the hills was a highly faulted slice of rock that was plucked from the eastern Owlshhead Mountains and transported along with, but with slightly less displacement than, the slice we saw at the last stop. During this and the next two stops, we will examine rocks in the structural high to look at its deformation and the cross-cutting relationships between structures within the “basement high” and adjacent



Figure 8. Field photograph looking northwest at Stop 2-1. The arrow indicates the steeply dipping Crystal Springs Formation, adjacent to the talc deposits.

Tertiary sediments originally described by Brady (1984), and later referred to as the Noble Hills assemblage by Niles (2016).

From the vehicles, walk up the wash ~200 m, then take the right fork off the main wash, which continues back behind the basement high into the Avawatz Mountains. On your right will be highly deformed Tertiary beds composed of interbedded gypsum and shale. This deformation is demonstrably driven by motion on the Southern Death Valley fault system, but has led to some controversy, because the latest deformation in the Noble Hills is characterized by significant contraction related to the Garlock–Death Valley fault intersection. As you walk up the right fork, in about another 100 m you will cross the Eastern Boundary fault of the basement high, but the contact is completely buried here. Proceed up the wash and you will see extensive exposures of Crystal Springs Formation (Fig. 5B). However, unlike the beautiful sections of Crystal Springs you saw yesterday, here you immediately run into variable orientations, mixing of rock types (including large slices of basement gneiss), and extensive cataclasis, including some spectacular breccias. As you walk up the wash, you’ll see continuous exposures of this slice and dice, cut by complex fault arrays. Note the extensive brecciation and chaotic appearance of the blocks, reminiscent of *mélange* and a clear demonstration that this is a broad fault zone.

As we continue up the wash, we ultimately find extensive slices of granite that are classic “Owlshead type” or “Tutonia type” typical of Late Cretaceous granitoids in this area, particularly the Owlshead Mountains. This is the same lithologic association we saw at Sheep Creek: evidence this is a slice of rock plucked from the eastern side of the Owlshead Mountains. The

lack of significant metamorphism of the Crystal Springs Formation also suggests these rocks came from near the rocks we saw at Sheep Creek, and our inferred correlatives in the northern Owlshead Mountains. That is, just to the north of us here, across the SDVF in the southeast Owlshead, carbonate rocks are amphibolite facies marble very different from these rocks. We will turn around about halfway across the basement high, but to the west the Crystal Springs slices become scarce and the rocks are almost entirely granite and basement.

Stop 2-2b (35.613488° N, 116.425687° W). Optional stop (time permitting, or can be visited virtually). As we walk back down the wash toward the vehicles, climb out of the wash to the north as we get to the eastern-bounding fault in the bedrock high. Several burro paths allow us an easy climb to avoid loose gravel slopes. As we crest the hill, you can look north and see a large expanse of exposed rock that includes a complex mix of Crystal Springs Formation, basement rock, and Mesozoic granite. Where we stand is the same slice and dice of these rocks we saw in the wash, but as you look farther north, you can see a large homoclinal section of Crystal Springs and Horsethief Springs (?) Formations intruded by granites. This is the most intact slab of Crystal Springs in the bedrock high. We will discuss some uncertainties here about pre-faulting structure, as well as evidence that the “slice and dice” relationships we saw in the wash originate from slicing and dextral displacement of this assemblage.

Travel: From the stop, continue on the road through the gap in outcrops down the wash where you will see a cabin. We will drive past the cabin ~100 m down the wash, then the road turns back up the wash around an outcrop. Keep on that road about

another 100 m, and park at the bottom of a large wash coming out of the reddish Tertiary sediments.

Stop 2-3: Eastern Fault Contact of the Noble Hills

At this stop, we will look at spectacular exposures of the fault rocks along the eastern boundary of the basement high within the Noble Hills (Fig. 5B). We will discuss evidence that these outcrops show evidence of faulting and partial overlap of cataclasite by Tertiary sediments.

Walk up the major wash toward the Noble Hills. Stay in the main wash through spectacular exposures of highly folded gypsum beds interbedded with shale (part of the Noble Hills assemblage of Niles, 2016). Stay in the main wash until you reach a major fork in the drainage, ~150 m east of the contact with the gray cataclastic granites of the basement high. Here, we will go up both forks of the creek, but start by taking the right fork (main drainage) and follow it until we reach cataclastic granites.

Stop 2-3a (35.623637° N, 116.435132° W). You will reach a conspicuous fault contact between cataclastic granite and red shale and siltstone of the Noble Hills assemblage. Here you see an unequivocal fault contact between the Noble Hills sediments and cataclastic granite. The fault contact is indicated by clear truncation of beds in the sediments, as well as extensive cataclasis of rocks on both sides of the fault. Depending on how kind the winter rains have been to us, we should be able to see very clear shear sense indicators in the cataclasites showing dextral strike slip. Take a little time looking at the exposures, noting the pervasive cataclasis and alteration of the granites—i.e., you could use a shovel to sample much of this granite, and in fact, sampling on the project here required lots of epoxy resin.

After examining these rocks, walk back down the wash to the fork, and walk back toward the fault contact in the left fork.

Stop 2-3b (35.622961° N, 116.434076° W). At this stop, you will see contradictory evidence for the nature of this contact. Like the exposure in Stop 2-3a, you see spectacular cataclastic structures in the granite with shear sense indicators showing dextral shear. What is odd here, however, is if you look on the slope above the wash to the north, you can see apparent onlap of sediments across the cataclastic granites. We debated this outcrop in our group, but ultimately concluded it was an indication that the Noble Hills assemblage was deposited upon already cataclastic granite—a critical age relationship suggesting that a great deal of slip had occurred prior to deposition of these sediments.

Travel: After returning to the vehicles, continue on the road toward the north to Denning Springs Wash. At the T-intersection in the wash, turn left and proceed up the wash (road) about a mile to exposures of the cataclastic granite. As we drive up the wash, we first pass granitic megabreccias mixed with Pahrump rocks that are interpreted as landslides into the Miocene basin (Brady, 1984). These megabreccias are overlain by folded gypsum and shale beds of the Noble Hills assemblage—we can discuss if the base of these sediments is structural or depositional. As we go farther up the wash, we get back into the sediments before reaching our objective, the tip of the bedrock high.

Stop 2-4: Tip of the Bedrock High

(35.635438° N, 116.449478° W)

At this stop, we will look at the northern limit of the bedrock high we saw at Stops 2-2 and 2-3. This outcrop contains a critical exposure where the structural high plunges beneath sedimentary cover.

Begin by examining the cataclastic granite outcrops on the north side of the wash. Look at the cliff above and consider what the layered rocks we see at the top represent—Tertiary sediments versus older rocks sliced into the assemblage. Then, walk to the north, around the west side of the granite exposures to the ridge top.

Here, we can see clear deposition of gravels, now steeply dipping to the northeast, directly onto the cataclastic granite. There is no doubt this is an unconformity given the prevalent clasts of granite in the conglomerate. The only question here is: Is this a basal gravel of the Noble Hills sediments we saw at previous stops, or is it a younger gravel? Our interpretation is it is part of the Noble Hills assemblage, based on the steep dip and observations like we saw at Stop 2-3b.

Optional stop (time permitting): After leaving Stop 2-4, we will drive back down Denning Springs Wash, and at the mouth of the canyon we will see gray gravels along the mountain front that contrast with the yellowish brown gypsiferous deposits. The gravels have near vertical dips, and the color arises from their lithology—they are comprised entirely of Owlshhead granite type clasts. Wright and Troxel (1967) used these rocks to infer significant slip of these gravels relative to the Owlshheads, and it was a major player in the interpretation of Butler et al. (1988) for more than 30 km of slip on the SDVF. Niles (2016) interpreted this as a depositional contact, an interpretation we reject based on work we did here many years ago and reanalyzed more recently. That is, we concur with Troxel that these gravels have been displaced dextrally from their original deposition along the eastern flank of the Owlshhead Mountains. We will share a virtual model of the outcrops to the north as a potential discussion point for this issue.

Travel: At Saratoga Springs Road, turn left and proceed up the southern Death Valley road toward the heart of Death Valley. Hopefully this road will be in good shape after winter rains, but it can be slow going, and in *heavy rain years it can be impassable* because the Amargosa River crosses the road. When we reach the pavement, continue north into Death Valley until you see the turnoff for the Ashford Mill site, and take a left into the parking area.

Stop 2-5: Ashford Mill

(35.918975° N, 116.683283° W)

At this stop, we have a vista looking west at the Owlshhead Mountains and Confidence Hills, to the east the Black Mountains with exposures of the Amargosa low-angle normal fault system and to the northwest, the Panamint Mountains, including Wingate Wash.

From here, as we look west to the northwestern Owlshhead Mountains, we see exposures of the Crystal Springs Formation

that were used by Pavlis and Trullenque (2021) as offset markers from the rocks we saw at Sheep Creek to infer 40–41 km of slip on the SDVFEZ. (We chose not to visit this site during the field trip because it is a seriously long hike.)

To the north of the Crystal Springs exposures, the dark exposures on the northern flank of the Owlsheads are the Wingate Wash volcanics that have been dated at 14–12 Ma (Luckow et al., 2005). The northern limit of these volcanics in the southern Panamint Mountains (visible from here to the NW) was considered a secondary marker constraining SDVF offset by Pavlis and Trullenque (2021). A part of that story, however, can be seen just to our east, in the Black Mountains where 14–12 Ma volcanics lie directly above the Amargosa fault. These outcrops are the northern limit of the Miocene volcanics east of Death Valley, but they are only ~20 km from the exposures in the Panamints. This observation seemingly defies use of these volcanics as a marker, but recall these rocks were carried with other rocks along the Amargosa fault, and thus would show less slip than the total slip, consistent with their position seen here.

Also, from here we can see the trace of the active strands of the SDVFEZ, where they pass through the Confidence Hills through Shoreline Butte and into the valley where the fault famously offsets the “split cinder cone.” Note the split cinder cone has a poorly known age with no published data constraining the age. Original reports suggested it was as old as 750 ka (e.g., Wright et al., 1991), but later work by Pavlis, Serpa, and Snee (2021, personal commun.) showed the original K-Ar dates were plagued by extraneous ^{40}Ar due to numerous xenoliths of Precambrian basement. Therefore, the 750 ka age estimate is too old. Using isochron plots to constrain the actual age, their analysis indicates the cinder cone is between 100 and 200 ka. That makes the observed offset consistent with GPS estimates for the slip rate.

Travel: Proceed north on the road toward Mormon Point turtleback. As we drive along the road, we will see numerous fault scarps where the SDVF steps over toward the mountain front, forming the southern part of the classic Death Valley pull-apart basin. Just south of the tip of the turtleback, stop short of the location where the playa lake laps essentially onto bedrock. We'll walk a short distance to the mountain front to examine the high-grade metamorphic rocks at this site.

Stop 2-6: Mormon Point Turtleback

(36.041832° N, 116.759535° W)

At this stop, we will take a short hike over a rocky fan to look at the high-grade metamorphic rocks of the Mormon Point turtleback. The main point of this stop is to illustrate the very high- T metamorphic assemblages and ductile structures seen in the turtlebacks, and to serve as a summary point to discuss the implications of the slip magnitude of the southern Death Valley fault system for reconstructing the system. Specifically, if the ~40 km of slip estimated for the southern Death Valley fault was transferred onto the Black Mountains fault systems, the Panamints would restore atop the Black Mountains, with the central Pana-

mint Range approximately above us at this stop (Fig. 4) (Pavlis and Trullenque, 2021). Based on the metamorphic assemblages and structures seen in the Panamint Mountains (described above and shown in virtual visualizations), the structure and metamorphism here is at least partially Mesozoic but is also clearly partially Neogene.

As you walk up the wash east of the road, you're initially within exposure of fault rock from brittle deformation along the Mormon Point turtleback fault. As we walk up the wash, we will do some bottom-feeding petrology by examining the rocks in float that have come off the turtleback. You will see several indicators that these are very high-grade rocks: (1) the abundance of migmatites and the absence of muscovite with abundant sillimanite. Early studies here noted the presence of migmatites, but assumed this was irrelevant to the Mesozoic–Cenozoic history because the migmatites were thought to just be Precambrian basement assemblages. We now know, however, that the rocks reached temperatures approaching 700° C as recently as 10 Ma (Lima et al. 2018; Pavlis et al., 2018). Thus, it is now uncertain which, if any, of the migmatites are actually basement and which are high-grade metasedimentary units derived from miogeoclinal stratigraphy. (2) Marbles here contain spectacular calc-silicate assemblages. As you walk up the wash, you'll see boulders containing garnets the size of baseballs, plus high-grade assemblages like garnet + diopside + calcite ± epidote and locally, forsterite-bearing marbles. (3) The structures here are indicative of extreme ductile deformation. In the upper part of the wash, we come to a wall in intact metasedimentary rocks where you can see marbles isoclinally folded into the schists/gneiss complex. When we thought all of the schists/gneiss assemblage was reworked basement, we interpreted these structures as total remobilization of basement. However, given the possibility that these rocks may include metasedimentary assemblages that are part of the marble stratigraphic sequence, this could be isoclinal folding of the metasedimentary assemblage. Nonetheless, the structure shows that these rocks contain extremely high strain, presumably from accumulated finite strains from Mesozoic through Neogene time.

We hope this site will allow a discussion of the tectonic reconstructions for this region. Specifically, can we explain the observations in the Panamint metamorphic assemblages together with the Black Mountains assemblage to surmise a crustal section, or are the observations incompatible and require alternative explanations?

End of field trip.

ACKNOWLEDGMENTS

The authors would like to acknowledge the efforts of reviewer Marli Miller, whose input resulted in an improved paper, as well as those of the editors. In addition, we would like to thank the Death Valley Natural History Association's co-sponsorship of the trip.

TABLE 1. NAMES AND COORDINATES (WORLD GEODETIC SYTEM 84) OF THE FIELD-TRIP STOPS

Stop no.	Latitude (°N)	Longitude (°W)
Stop 1-1	35.8209	116.383
Stop 1-2	35.764	116.3569
Stop 1-3	35.770166	116.421436
Stop 1-4	35.768478	116.335809
Stop 1-5a	35.846043	116.37618
Stop 1-5b	35.843873	116.373346
Stop 2-1	35.592669	116.359897
Stop 2-2a	35.615002	116.427508
Stop 2-2b	35.613488	116.425687
Stop 2-3a	35.623637	116.435132
Stop 2-3b	35.622961	116.434076
Stop 2-4	35.635438	116.449478
Stop 2-5	35.918975	116.683283
Stop 2-6	36.041832	116.759535

REFERENCES CITED

- Albee, A.L., Labotka, T.C., Lanphere, M.A., and McDowell, S.D., 1981, Geologic Map of the Telescope Peak Quadrangle, California: U.S. Geological Survey Geologic Quadrangle 1532, scale 1:62,500.
- Asmerom, Y., Snow, J.K., Holm, D.K., Jacobsen, S.B., Wernicke, B.P., and Lux, D.R., 1990, Rapid uplift and crustal growth in extensional environments: An isotopic study from the Death Valley region, California: *Geology*, v. 18, p. 223–226, [https://doi.org/10.1130/0091-7613\(1990\)018<0223:RUACGI>2.3.CO;2](https://doi.org/10.1130/0091-7613(1990)018<0223:RUACGI>2.3.CO;2).
- Bidgoli, T.S., Amir, E., Walker, J.D., Stockli, D.F., Andrew, J.E., and Caskey, S.J., 2015, Low-temperature thermochronology of the Black and Panamint mountains, Death Valley, California: Implications for geodynamic controls on Cenozoic intraplate strain: *Lithosphere*, v. 7, p. 473–480, <https://doi.org/10.1130/L406.1>.
- Brady, R.H., 1984, Neogene stratigraphy of the Avawatz Mountains between the Garlock and Death Valley fault zones, southern Death Valley, California: Implications as to late Cenozoic tectonism: *Sedimentary Geology*, v. 38, p. 127–157, [https://doi.org/10.1016/0037-0738\(84\)90077-0](https://doi.org/10.1016/0037-0738(84)90077-0).
- Brady, R.H., III, and Troxel, B.W., 1999, The Miocene Military Canyon Formation: Depocenter evolution and constraints on lateral faulting, southern Death Valley, California, in Wright, L.A., and Troxel, B.W., eds., *Cenozoic Basins of the Death Valley Region*: Geological Society of America Special Paper 333, p. 277–288, <https://doi.org/10.1130/0-8137-2333-7.277>.
- Brush, J.A., Pavlis, T.L., Hurtado, J.M., Jr., Mason, K.A., Knott, J.R., and Williams, K.E., 2018, Evaluation of field methods for 3-D mapping and 3-D visualization of complex metamorphic structure using multiview stereo terrain models from ground-based photography: *Geosphere*, v. 15, p. 188–221, <https://doi.org/10.1130/GES01691.1>.
- Burchfiel, B.C., and Stewart, J.H., 1966, "Pull-apart" origin of the central segment of Death Valley, California: *Geological Society of America Bulletin*, v. 77, p. 439–442, [https://doi.org/10.1130/0016-7606\(1966\)77<439:POOTCSJ>2.0.CO;2](https://doi.org/10.1130/0016-7606(1966)77<439:POOTCSJ>2.0.CO;2).
- Burchfiel, B.C., Walker, D., Davis, G.A., Wernicke, B., and Anonymous, 1983, Kingston Range and related detachment faults: a major "breakway" zone in the southern Great Basin: *Geological Society of America Abstracts with Programs*, v. 15, p. 536.
- Butler, P.R., Troxel, B.W., and Verosub, K.L., 1988, Late Cenozoic history and styles of deformation along the southern Death Valley fault zone, California: *Geological Society of America Bulletin*, v. 100, p. 402–410, [https://doi.org/10.1130/0016-7606\(1988\)100<0402:LCHASO>2.3.CO;2](https://doi.org/10.1130/0016-7606(1988)100<0402:LCHASO>2.3.CO;2).
- Castonguay, S.R., 2013, Structural evolution of the virgin spring phase of the Amargosa Chaos, Death Valley, California, USA [Ph.D. thesis]: Eugene, University of Oregon, 164 p., <http://adsabs.harvard.edu/abs/2013PhDT.....212C> (accessed October 2016).
- Castonguay, S.R., and Miller, M.B., 2018, Amargosa Chaos: a product of multiphase deformation: *Geological Society of America Abstracts with Programs*, v. 50, no. 5, paper no. 2-3, <https://doi.org/10.1130/abs/2018RM-314267>.
- Chabani, A., Trullenque, G., Ledésert, B.A., and Klee, J., 2021, Multiscale characterization of fracture patterns: A case study of the Noble Hills Range (Death Valley, CA, USA): Application to Geothermal Reservoirs: *Geosciences*, v. 11, p. 280, <https://doi.org/10.3390/geosciences11070280>.
- Cobb, J., 2015, Understanding the contractional history of Surprise Canyon, California through digital field mapping, 3d modeling, and U-Pb zircon geochronology [M.S. thesis]: El Paso, Texas, University of Texas at El Paso, 134 p.
- Fleming, Z.D., and Pavlis, T.L., 2015, Multiple phases of low-angle normal faulting from the Precambrian to the Neogene in the Ibox Hills and Saratoga Hills, CA: *Geological Society of America Abstracts with Programs*, v. 47, no. 1, p. 149.
- Fleming, Z.D., Pavlis, T.L., and Canalda, S., 2021, Superposition of two kinematically distinct extensional phases in southern Death Valley: Implications for extensional tectonics: *Geosphere*, v. 17, no. 5, p. 1534–1562, <https://doi.org/10.1130/GES02354.1>.
- Fowler, T.K., and Calzia, J.P., 1999, Kingston Range detachment fault, southeastern Death Valley region, California: relation to Tertiary deposits and reconstruction of initial dip, in Wright, L.A., and Troxel, B.W., eds., *Cenozoic Basins of the Death Valley Region*: Geological Society of America Special Paper 333, p. 245–257, <https://doi.org/10.1130/0-8137-2333-7.245>.
- Hodges, K.V., Walker, J.D., and Wernicke, B.P., 1987, Footwall structural evolution of the Tucki Mountain detachment system, Death Valley region, southeastern California, in Coward, M.P., Dewey, J.F., and Hancock, P.L., eds., *Continental Extensional Tectonics*: Geological Society, London, Special Publication 28, p. 393–408, <https://doi.org/10.1144/GSL.SP.1987.028.01.24>.
- Holm, D.K., and Dokka, R.K., 1993, Interpretation and tectonic implications of cooling histories: An example from the Black Mountains, Death Valley extended terrane, California: *Earth and Planetary Science Letters*, v. 116, p. 63–80, [https://doi.org/10.1016/0012-821X\(93\)90045-B](https://doi.org/10.1016/0012-821X(93)90045-B).
- Holm, D.K., and Wernicke, B., 1990, Black Mountains crustal section, Death Valley extended terrain, California: *Geology*, v. 18, p. 520–523, [https://doi.org/10.1130/0091-7613\(1990\)018<0520:BMCSDV>2.3.CO;2](https://doi.org/10.1130/0091-7613(1990)018<0520:BMCSDV>2.3.CO;2).
- Holm, D.K., Snow, J.K., and Lux, D.R., 1992, Thermal and barometric constraints on the intrusive and unroofing history of the Black Mountains: Implications for timing, initial dip, and kinematics of detachment faulting in the Death Valley Region, California: *Tectonics*, v. 11, p. 507–522, <https://doi.org/10.1029/92TC00211>.
- Holm, D.K., Fleck, R.J., and Lux, D.R., 1994, The Death Valley turtlebacks reinterpreted as Miocene-Pliocene folds of a major detachment surface: *The Journal of Geology*, v. 102, p. 718–727, <https://doi.org/10.1086/629715>.
- Klee, J., Trullenque, G., Ledésert, B., Potel, S., Herbert, R., Chabani, A., and Genter, A., 2021, Petrographic analyzes of fractured granites used as an analogue of the Soultz-Sous-Forêts Geothermal Reservoir: Noble Hills, CA, USA, in *Proceedings of the World Geothermal Congress 2020+1*, Reykjavik, Iceland, 24–27 October 2020.
- Labotka, T.C., 1981, Petrology of an andalusite-type regional metamorphic terrane, Panamint Mountains, California: *Journal of Petrology*, v. 22, p. 261–296, <https://doi.org/10.1093/petrology/22.2.261>.
- Labotka, T.C., Warasila, R.L., and Spangler, R.R., 1985, Polymetamorphism in the Panamint Mountains, California: A ³⁹Ar-⁴⁰Ar study: *Journal of Geophysical Research—Solid Earth*, v. 90, p. 10,359–10,371, <https://doi.org/10.1029/JB090iB12p10359>.
- Lima, R.D., Prior, M.G., Stockli, D.F., and Hayman, N.W., 2018, Protracted heating of the orogenic crust in Death Valley, California, USA: *Geology*, v. 46, p. 315–318, <https://doi.org/10.1130/G39865.1>.
- Luckow, H.G., Pavlis, T.L., Serpa, L.F., Guest, B., Wagner, D.L., Snee, L., Hensley, T.M., and Korjenkov, A., 2005, Late Cenozoic sedimentation and volcanism during transtensional deformation in Wingate Wash and the Owlhead Mountains, Death Valley: *Earth-Science Reviews*, v. 73, p. 177–219, <https://doi.org/10.1016/j.earscirev.2005.07.013>.

- Mahon, R.C., and Link, P.K., 2013, EdMap geologic map of the Saddle Peak Hills 7.5' quadrangle, Death Valley National Park, San Bernardino County, California: Geological Society of America Abstracts with Programs, v. 45, no. 7, p. 372, <https://gsa.confex.com/gsa/2013AM/webprogram/Paper231464.html>.
- Mancktelow, N.S., and Pavlis, T.L., 1994, Fold-fault relationships in low-angle detachment systems: *Tectonics*, v. 13, p. 668–685, <https://doi.org/10.1029/93TC03489>.
- Miller, M.B., and Pavlis, T.L., 2005, The Black Mountains turtlebacks: Rosetta stones of Death Valley tectonics: *Earth-Science Reviews*, v. 73, p. 115–138, <https://doi.org/10.1016/j.earscirev.2005.04.007>.
- Miller, M.G., 2003, Basement-involved thrust faulting in a thin-skinned fold-and-thrust belt, Death Valley, California, USA: *Geology*, v. 31, p. 31–34, [https://doi.org/10.1130/0091-7613\(2003\)031<0031:BITFIA>2.0.CO;2](https://doi.org/10.1130/0091-7613(2003)031<0031:BITFIA>2.0.CO;2).
- Miller, M.G., and Friedman, R.M., 1999, Early Tertiary magmatism and probable Mesozoic fabrics in the Black Mountains, Death Valley, California: *Geology*, v. 27, p. 19–22, [https://doi.org/10.1130/0091-7613\(1999\)027<0019:ETMAPM>2.3.CO;2](https://doi.org/10.1130/0091-7613(1999)027<0019:ETMAPM>2.3.CO;2).
- Miller, M.G., and Prave, A.R., 2002, Rolling hinge or fixed basin?: A test of continental extensional models in Death Valley, California, United States: *Geology*, v. 30, p. 847–850, [https://doi.org/10.1130/0091-7613\(2002\)030<0847:RHOFA>2.0.CO;2](https://doi.org/10.1130/0091-7613(2002)030<0847:RHOFA>2.0.CO;2).
- Niles, J., 2016, Post-Middle Pliocene tectonic development of the Noble Hills, Southern Death Valley, California [M.S. thesis]: San Francisco, California, San Francisco State University, 103 p.
- Norton, I., 2011, Two-stage formation of Death Valley: *Geosphere*, v. 7, p. 171–182, <https://doi.org/10.1130/GES00588.1>.
- Pavlis, T.L., 1996, Fabric development in syn-tectonic intrusive sheets as a consequence of melt-dominated flow and thermal softening of the crust: *Tectonophysics*, v. 253, p. 1–31, [https://doi.org/10.1016/0040-1951\(95\)00049-6](https://doi.org/10.1016/0040-1951(95)00049-6).
- Pavlis, T.L., and Trullenque, G., 2021, Evidence for 40–41 km of dextral slip on the southern Death Valley fault; implications for the Eastern California shear zone and extensional tectonics: *Geology*, v. 49, p. 767–772, <https://doi.org/10.1130/G48528.1>.
- Pavlis, T.L., Serpa, L., Troxel, B., Dean, M., Hartman, T., and Rodosta, T., 1998, Late Cenozoic deformation in eastern Fort Irwin and its significance for the tectonic history of the Garlock fault system, in Calzia, J.P., and Reynolds, R.E., eds., *Finding Faults in the Mojave: The 1998 Desert Research Symposium Field Trip and Volume & Abstracts of Proceedings: San Bernardino Country Museum Association Quarterly*, v. 45, p. 77–83.
- Pavlis, T.L., Tracy, R.J., Hollister, L., Chadwick, J., and Anonymous, 2018, Reappraisal of the Death Valley turtlebacks from analysis of metamorphism and ductile deformation in the turtlebacks and Panamint Mountains: *Geological Society of America Abstracts with Programs*, v. 50, no. 5, paper no. 18-4, <https://doi.org/10.1130/abs/2018RM-314071>.
- Ramo, O.T., Calzia, J.P., and Kosunen, P.J., 2002, Geochemistry of Mesozoic plutons, southern Death Valley region, California: Insights into the origin of Cordilleran interior magmatism: *Contributions to Mineralogy and Petrology*, v. 143, p. 416–437, <https://doi.org/10.1007/s00410-002-0354-9>.
- Renik, B., and Christie-Blick, N., 2013, A new hypothesis for the amount and distribution of dextral displacement along the Fish Lake Valley–northern Death Valley–Furnace Creek fault zone, California–Nevada: *Tectonics*, v. 32, p. 123–145, <https://doi.org/10.1029/2012TC003170>.
- Serpa, L., and Pavlis, T.L., 1996, Three-dimensional model of the late Cenozoic history of the Death Valley region, southeastern California: *Tectonics*, v. 15, p. 1113–1128, <https://doi.org/10.1029/96TC01633>.
- Snow, J.K., and Wernicke, B., 1989, Uniqueness of geological correlations: An example from the Death Valley extended terrain: *Geological Society of America Bulletin*, v. 101, p. 1351–1362, [https://doi.org/10.1130/0016-7606\(1989\)101<1351:UOGCAE>2.3.CO;2](https://doi.org/10.1130/0016-7606(1989)101<1351:UOGCAE>2.3.CO;2).
- Snow, J.K., and Wernicke, B.P., 2000, Cenozoic tectonism in the central Basin and Range: magnitude, rate, and distribution of upper crustal strain: *American Journal of Science*, v. 300, p. 659–719, <https://doi.org/10.2475/ajs.300.9.659>.
- Stewart, J.H., 1967, Possible large right-lateral displacement along fault and shear zones in the Death Valley–Las Vegas Area, California and Nevada: *Geological Society of America Bulletin*, v. 78, p. 131–142, [https://doi.org/10.1130/0016-7606\(1967\)78\[131:PLRDAF\]2.0.CO;2](https://doi.org/10.1130/0016-7606(1967)78[131:PLRDAF]2.0.CO;2).
- Stewart, J.H., 1983, Extensional tectonics in the Death Valley area, California: Transport of the Panamint Range structural block 80 km northward: *Geology*, v. 11, p. 153–157, [https://doi.org/10.1130/0091-7613\(1983\)11<153:ETITDV>2.0.CO;2](https://doi.org/10.1130/0091-7613(1983)11<153:ETITDV>2.0.CO;2).
- Topping, D.J., 1993, Paleogeographic reconstruction of the Death Valley extended region: Evidence from Miocene large rock-avalanche deposits in the Amargosa Chaos Basin, California: *Geological Society of America Bulletin*, v. 105, p. 1190–1213, [https://doi.org/10.1130/0016-7606\(1993\)105<1190:PROTDV>2.3.CO;2](https://doi.org/10.1130/0016-7606(1993)105<1190:PROTDV>2.3.CO;2).
- Tracy, R.J., Caddick, M.J., Pavlis, T.L., Hollister, L.S., and Anonymous, 2019, Metamorphic paths record the contraction and the extension that led to formation of the Death Valley turtlebacks: *Geological Society of America Abstracts with Programs*, v. 51, no. 5, paper no. 77-7, <https://doi.org/10.1130/abs/2019AM-337283>.
- Troxel, B., 1999, Geology of the Saddle Peak Hills 7.5' Quadrangle, southernmost Death Valley, California, in Slate, J.L., ed., *Proceedings of Conference on Status of Geologic Research and Mapping, Death Valley National Park: U.S. Geological Survey Open-File Report 99-153*, p. 83–84.
- Troxel, B.W., Calzia, J.P., and Pavlis, T.L., 1992, SW-directed extensional features and related magmatism, southern Death Valley region and the Kingston Range: *Geological Society of America Abstracts with Programs*, v. 24, no. 5, p. 87.
- Trullenque, G., Parashar, R., Delcourt, C., Collet, L., Villard, P., and Potel, S., 2017, Properties of a pair of fracture networks produced by triaxial deformation experiments; insights on fluid flow using discrete fracture network models: *Hydrogeology Journal*, v. 25, p. 813–827, <https://doi.org/10.1007/s10040-016-1468-x>.
- Wernicke, B., 1999, Tectonic evolution of the Death Valley Region, in Slate, J.L., ed., *Proceedings of Conference on Status of Geologic Research and Mapping, Death Valley National Park: U.S. Geological Survey Open-File Report 99-153*, p. 10–18.
- Wernicke, B.P., and Axen, G.J., 1988, On the role of isostasy in the evolution of normal fault systems: *Geology*, v. 16, p. 848–851, [https://doi.org/10.1130/0091-7613\(1988\)016<0848:OTROIL>2.3.CO;2](https://doi.org/10.1130/0091-7613(1988)016<0848:OTROIL>2.3.CO;2).
- Wright, L.A., and Troxel, B.W., 1967, Limitations on right-lateral, strike-slip displacement, Death Valley and Furnace Creek fault zones, California: *Geological Society of America Bulletin*, v. 78, p. 933–950, [https://doi.org/10.1130/0016-7606\(1967\)78\[933:LORSDD\]2.0.CO;2](https://doi.org/10.1130/0016-7606(1967)78[933:LORSDD]2.0.CO;2).
- Wright, L., and Troxel, B., 1984, Geology of the Northern Half of the confidence Hills 15-Minute Quadrangle, Death Valley Region, Eastern California; the Area of the Amargosa Chaos, Scale 1:24,000: Sacramento, California, California Department of Conservation, Division of Mines and Geology Map Sheet 34, 1977.
- Wright, L.A., Troxel, B.W., DeJong, K.A., and Scholten, R., 1973, Shallow-fault interpretation of basin and range structure, southwestern Great Basin, in DeJong, K.A., and Scholten, R., eds., *Gravity and Tectonics: New York, John Wiley and Sons*, p. 397–407.
- Wright, L.A., Troxel, B.W., Williams, E.G., Roberts, M.T., and Diehl, P.E., 1976, Precambrian sedimentary environments of the Death Valley region, eastern California: Shoshone, California, Death Valley Publishing Company, in Troxel, B.W., and Wright, L.A., eds., *Geologic features, Death Valley, California: California Division of Mines and Geology Special Report 106*, p. 7–18 <http://www.npshistory.com/publications/geology/state/ca/cdmg-sr-106/sec1.htm> (accessed January 2022).
- Wright, L.A., Thompson, R.A., Troxel, B.W., Pavlis, T.L., DeWitt, E., Otton, J.K., Ellis, M.A., Miller, M.G., and Serpa, L.F., 1991, Cenozoic magmatic and tectonic evolution of the east-central Death Valley region, California, in Walawender, M.J., and Hanan, B., eds., *Geological Excursions in Southern California and Mexico: Department of Geological Sciences, San Diego State University, Geological Society of America Annual Meeting Guidebook*, p. 93–127.

MANUSCRIPT ACCEPTED BY THE SOCIETY 27 DECEMBER 2021







The NH are used with a twofold aim and the results have been obtained in the frame of the PhD dissertation from Dr. Klee and the Post-Doctoral fellowships of Dr. Fleming and Dr. Chabani I have been mentoring (see supervision section). Klee et al. (2021b, 2021a) investigated fluid rock interaction processes from the petrographic and geochemical point of view in terms of pervasive alteration 1) away from fracture zones and 2) at low to moderate strain. Chabani et al. (2021b, 2021a) characterized multiscale fracture patterns, fracture spacing variability and distribution of fracture patterns within the NH.

In their part 1, Klee et al. (2021b) have characterized the pervasive alteration of granitic rocks found within the NH and compared to the initial protolith found along strike of the SDVFZ about 40 km to the North. They used a combination of petrographic, geochemical and petrophysical analyses and completed their study by a metamorphic grade study. The authors showed a progressive increase of temperature along strike of the NH range towards the south that they relate to a possible differential exhumation. Klee et al. (2021b) could evidence three stages of alteration: 1) a pervasive propylitic alteration present in both the protolith and NH range, 2) an argillic alteration only present in the NH and 3) a negligible weathering type alteration in both the protolith and the NH range. In terms of chronology, the local argillic alteration postdates the pervasive propylitic alteration.

In their part 2, Klee et al. (2021a) found evidences in favor of a polyphase circulation of fluids through the reservoir. The authors observe an increase of alteration degree, porosity and calcite contents when approaching the fracture zones but could not find a direct link between the degree of alteration and fracture density.

Article

Fluid-Rock Interactions in a Paleo-Geothermal Reservoir (Noble Hills Granite, California, USA). Part 1: Granite Pervasive Alteration Processes away from Fracture Zones

Johanne Klee ^{1,*} , Sébastien Potel ¹ , Béatrice A. Ledésert ² , Ronan L. Hébert ² , Arezki Chabani ¹ , Pascal Barrier ¹ and Ghislain Trullenque ¹ 

¹ B2R, Geosciences Department, Institut Polytechnique UniLaSalle Beauvais, 19 Rue Pierre Waguët, F-60026 Beauvais, France; sebastien.potel@unilasalle.fr (S.P.); arezki.chabani@unilasalle.fr (A.C.); pascal.barrier@unilasalle.fr (P.B.); ghislain.trullenque@unilasalle.fr (G.T.)
² Geosciences and Environment Cergy, CY Cergy Paris Université, 1 Rue Descartes, F-95000 Neuville-sur-Oise, France; beatrice.ledesert@cyu.fr (B.A.L.); ronan.hebert@cyu.fr (R.L.H.)
* Correspondence: johanne.klee@unilasalle.fr; Tel.: +33-6-06-93-90-07



Citation: Klee, J.; Potel, S.; Ledésert, B.A.; Hébert, R.L.; Chabani, A.; Barrier, P.; Trullenque, G. Fluid-Rock Interactions in a Paleo-Geothermal Reservoir (Noble Hills Granite, California, USA). Part 1: Granite Pervasive Alteration Processes away from Fracture Zones. *Geosciences* 2021, 11, 325. <https://doi.org/10.3390/geosciences11080325>

Academic Editors: Chris Clark and Jesus Martinez-Frias

Received: 18 June 2021

Accepted: 27 July 2021

Published: 31 July 2021

Publisher's Note: MDPI stays neutral with regard to jurisdictional claims in published maps and institutional affiliations.



Copyright: © 2021 by the authors. Licensee MDPI, Basel, Switzerland. This article is an open access article distributed under the terms and conditions of the Creative Commons Attribution (CC BY) license (<https://creativecommons.org/licenses/by/4.0/>).

Abstract: Only few data from geothermal exploited reservoirs are available due to the restricted accessibility by drilling, which limits the understanding of the entire reservoir. Thus, analogue investigations are needed and were performed in the framework of the H2020 MEET project. The Noble Hills range, located along the southern branch of the Death Valley pull-apart (CA, USA), has been selected as a possible granitic paleo-reservoir. The aim is to characterize the pervasive alteration processes affecting this granite, away from the influence of the faults, in terms of mineralogical, petrophysical and chemical changes. Various methods were used as petrographic, geochemical and petrophysical analyses. Mineral changes, clay mineralogy, bulk rock chemical composition, calcite content and porosity were determined on different granite samples, collected in the Noble Hills granite, far from the faults and in the Owlshhead Mountains, north of the Noble Hills, considered as its protolith. In order to complete the granite characterization, the metamorphic grade has been studied through the Noble Hills granite body. This complete characterization has allowed distinguishing the occurrence of three stages of alteration: (1) a pervasive propylitic alteration characterized by calcite-corrensite-epidote-K-white mica assemblage, (2) a more local one, only present in the Noble Hills granite, producing illite, kaolinite, illite/smectite, calcite and oxides, characteristic of the argillic alteration, which overprints the propylitic alteration and (3) weathering evidenced by the presence of montmorillonite in the Owlshhead Mountains, which is considered as negligible in both granites. Alteration was also outlined by the correlation of the loss on ignition, representing the hydration rate, to porosity, calcite content and chemical composition. Moreover, the Kübler Index calculated from illite crystals allowed to identify a NW-SE temperature gradient in the Noble Hills.

Keywords: Noble Hills granite; Owlshhead Mountains granite; metamorphic grade; fluid/rock interactions; newly formed minerals; element variations; geothermal reservoir

1. Introduction

Geothermal systems occur in different geological settings such as active volcanic fields, plutonic provinces, extensional domains, intracratonic basins and orogenic belts, i.e., anywhere with heat and fluids that are able to flow through the rocks [1]. The exploitation of geothermal energy is expanding worldwide due to the abundant resources and the progress of the technology that lead to Enhanced Geothermal Systems (EGS). EGS (1) defines a reservoir where the natural permeability of the rocks needs to be enhanced through stimulations in order to obtain a sufficient temperature/flow rate ratio [2] and (2) aims at transforming efficiently the geothermal resource into heat and electricity for human consumption [3].

The present study is part of the MEET H2020 project (Multidisciplinary and multi-context demonstration of EGS exploration and Exploitation Techniques and potentials) [4]. One aim of this project is to provide a characterization method of a geothermal granitic reservoir in a geological extensive context, such as the Great Basin region (USA), where normal fault zones also act as the most favorable structural setting for geothermal fluid flow [5]. In the Great Basin, other notable structural settings control fluid flow such as the intersection between normal faults and other structures like strike-slip faults (~22%), as well as pull-apart structures (4%) [5]. The fluid-rock interaction along and inside fracture zones results in hydrothermal alterations. They lead to geochemical, mineralogical and petrophysical (porosity and permeability) modifications of the rocks [6]. In granitic rocks, fluid circulations usually occur through the fracture network at different scales [6,7] involving a pervasive alteration which may influence up to cubic kilometers of rock [8]. Thus, an intense fluid/rock interaction [9] can significantly change the mineralogy, the chemistry and the texture of the bulk-rock [7] among which the common formation of clay minerals, including illite. Exploited geothermal reservoirs are located at depth, and the only and limited available data come from drillings (cores, cuttings) and seismic surveys. Studying exhumed geothermal reservoirs allows better understanding of the 3D features of the reservoir. To do so, the Noble Hills range (NH, Death Valley, CA, USA) has been selected as a possible granitic geothermal reservoir in a trans-tensional context. The NH are located in the southwestern part of the Great Basin region along the Southern Death Valley Fault Zone (SDVFZ), which constitutes the southern branch of the Death Valley pull-apart [10]. They extend over an area of 7 km long and 2 km wide and contain a part of the Cretaceous granitic pluton (~95 Ma) forming the Owlshead Mountains (OM) [11]. The arid climate prevents from a thick vegetal cover and the deep canyons that crosscut the range allow a thorough 3D investigation in order to characterize the evolution of the granite at the kilometer scale.

This paper aims at characterizing the pervasive alteration processes affecting the NH granite. This massif is considered as a possible paleo-geothermal reservoir. The study is based on the analysis of (1) rock mineralogical and related petrophysical properties changes and (2) associated chemical transfers between host rock and percolating fluids. All samples have been collected away from fractures described by [12] (this issue) in order to avoid the influence of strain and massive fluid flow. This sampling strategy ascertains the preservation of the protolith initial magmatic texture and mineralogy. A second paper (Klee et al., this issue) focusses on the role of deformation on hydrothermal alteration close to fractures. Data collected from the NH granite samples are directly compared to those obtained for the granite samples collected in the OM pluton, which is considered as the protolith. Analyses performed on targeted areas include macroscopic and microscopic petrographic studies, mineralogical characterization by X-ray diffraction (XRD) on whole rock and clay minerals, bulk rock chemical characterization by Inductively Coupled Plasma (ICP)—Mass Spectrometry (MS) and—Atomic Emission Spectrometry (AES), Scanning Electron Microscopy coupled with Energy Dispersive Spectrometry (SEM-EDS) for structural observation and local chemical analyses, as well as calcimetry and porosimetry analyses. To help at the granite characterization, the metamorphic evolution can be estimated through the Kübler Index (KI). Indeed, the temperature range of illite formation can be estimated thanks to the KI [13,14] based on illite “crystallinity” (IC). Temperature is thought to be the main factor controlling the IC evolution, but the lithology also has important effects [15–18]. Working at constant lithology, here granitic rock, allows us to avoid this effect. During the NH range formation, minerals could be transformed similarly as diagenetic reactions observed in feldspathic sandstones [19]. Inoue (1995) [9] has also shown that the rock alteration resulting from hot fluid storage during a long geological period, heated in-situ and in equilibrium with the surrounding rock is usually considered as diagenesis or metamorphism. Therefore, the terms defined by [13] for each diagenetic and metamorphic zones are considered in this study as eligible for granitic context.

2. Geological Setting

2.1. Death Valley

The area of interest for this study is the southern part of the Death Valley (DV) region, which extends for about 200 km. It is located southwest of the Basin and Range province [20], in the Eastern California Shear Zone/Walker Lane Belt (ECSZ/WLB) [21–23] (Figure 1a). DV is considered as one of the youngest regions where strike-slip deformation contemporaneously occurs with large-scale crustal extension within the Basin and Range province [24–26]. This extensional basin formation accompanying normal and associated strike-slip faulting would be active since 15 Ma according to [24]. It corresponds to a structural depression between the Panamint Range and the Black and Funeral Mountains [27] (Figure 1b), generally NNW-SSE oriented. This depression is related to tension along a segment of two strike-slip faults. Those two strike-slip faults consisting in the Northern Death Valley Fault Zone (NDVFZ) and the Southern Death Valley Fault Zone (SDVFZ), are characterized by en echelon traces [28] (Figure 1b). They have a general right-lateral movement, NW-SE oriented, from which results a “pull-apart” structure forming a N-S oriented basin [10] (Figure 1b).

The SDVFZ is composed of several branches. The SDVFZ formed the NH, at its southernmost part, by vertical displacement [29,30] (Figure 2a). It intersects the east-trending left lateral Garlock Fault Zone (GFZ), which ends at its western termination by the northwest-striking San Andreas fault zone [28] (Figure 1a). Recently, [11] suggested a net dextral slip along the SDVFZ of 40–41 km based on the offset positions of the granite-basement contact from the OM to the Avawatz Mountains. Much of the dextral slip, occurring before the deposition of the 6–8 Ma Neogene cover, is indicated by stratigraphic overlaps on fault rocks. This suggests an occurrence of the dextral slip during the main extension. The authors challenge the young feature of the DV pull-apart [25], by opting to a long-lived pull-apart which is consistent with regional evidence of the initiation in the middle Miocene of the dextral trans-tension in the ECSZ/WLB [31].

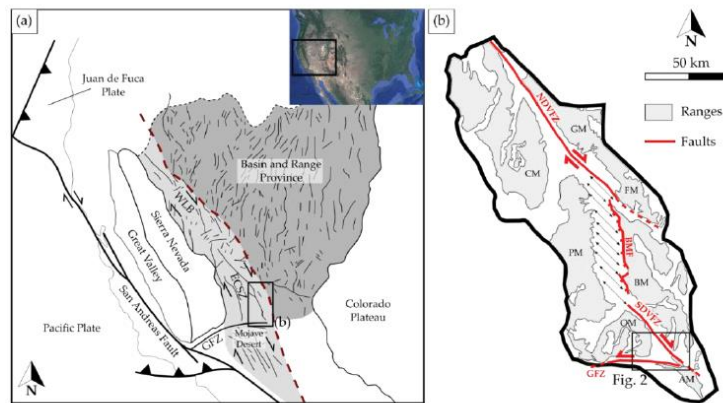


Figure 1. (a) Simplified tectonic map of the Great Basin region (western U.S. Cordillera) showing the tectonic provinces (modified after [32]). WLB—Walker Lane Belt; ECSZ—Eastern California Shear Zone; GFZ—Garlock Fault Zone. The Basin and Range Province is represented in dark grey and the WLB/ECSZ in light grey. The red dashed line marks the limit between these both domains. The dark lines within the Basin and Range Province and in the WLB-ECSZ zone represent the main faults. (b) Structural setting of the Death Valley region (modified after [33,34]). AM—Avawatz Mountains; BM—Black Mountains; BMF—Black Mountains Fault; CM—Cottonwood Mountain; FM—Funeral Mountains; GM—Grapevine Mountains; OM—Owlshead Mountains; PM—Panamint Mountains; GFZ—Garlock Fault Zone; NDFVZ—Northern Death Valley Fault Zone; SDVFZ—Southern Death Valley Fault Zone.

2.2. Noble Hills

The NH extend 14 km northwest of the northern Avawatz Mountains [30] (Figure 2a,b). A first general geological map of the NH was provided by [35], and later completed by [29,36–38]. They show that Precambrian gneiss covered by Crystal Spring Formation (CSF), a siliclastic-carbonate unit [39] of the Pahrump Group, were first intruded by 1.1 Ga diabase sills then by Mesozoic granitic rocks. All of these facies form the axial crystalline ridge defined by [29].

The NH granite was poorly studied previously. It is part of the calc-alkaline granitoid intrusion related to the emplacement of the Sierra Nevada batholith, which was formed due to the eastward dipping subduction of the Pacific plate under the North American continent [40]. It was only defined as both quartz monzonite [35] and leucocratic adamellite [41]. Brady (1986) [29] completed the description as a medium to coarse equigranular grained to slightly porphyritic leucocratic rock containing few biotite and little or no hornblende. The presence of sporadic mineralization due to hydrothermal alteration was also raised by [38]. After the emplacement of the granite and its exhumation, ~3.34 Ma Pliocene sediments of the Noble Hills Formation (NHF) were deposited [38]. The NHF consists in interbedded fine-grained clastic and evaporitic rocks, alluvial conglomerates, minor limestone and megabreccia. Recent work done by [42] in the NH has shown a more complex geometry of the axial ridge than described until now (Figure 2c). The undifferentiated Precambrian and Paleozoic rocks facies were described by [42] as a stacking of different CSF series, intruded by the Mesozoic granite. They seem to be dragged and stretched southeastward against the granite following the SDVFZ trend. Tertiary volcanism was also highlighted at the back of the range.

Based on the geology along the SDVFZ trace, Pavlis and Trullenque (2021) [11] suggests that the NH axial crystalline ridge must be a transported part of the Cretaceous granitic pluton (~95 Ma), forming the OM [34], which is relatively weakly deformed internally at its southern part [26]. This piece would have moved a minimum of 8 km according to [29,37] and around 28 km according to [43] along the SDVFZ (Figure 2b). Brittle shearing and large-scale *boudinage* characterize a brittle deformation, showing generally subhorizontal axes, which is prevalent within the Cretaceous granitic intrusion and Precambrian roof pendants (Figure 2c). Contractual deformation involving all members of the NHF is characterized along the NH and increases in intensity southeast toward the intersection with the GFZ [38].

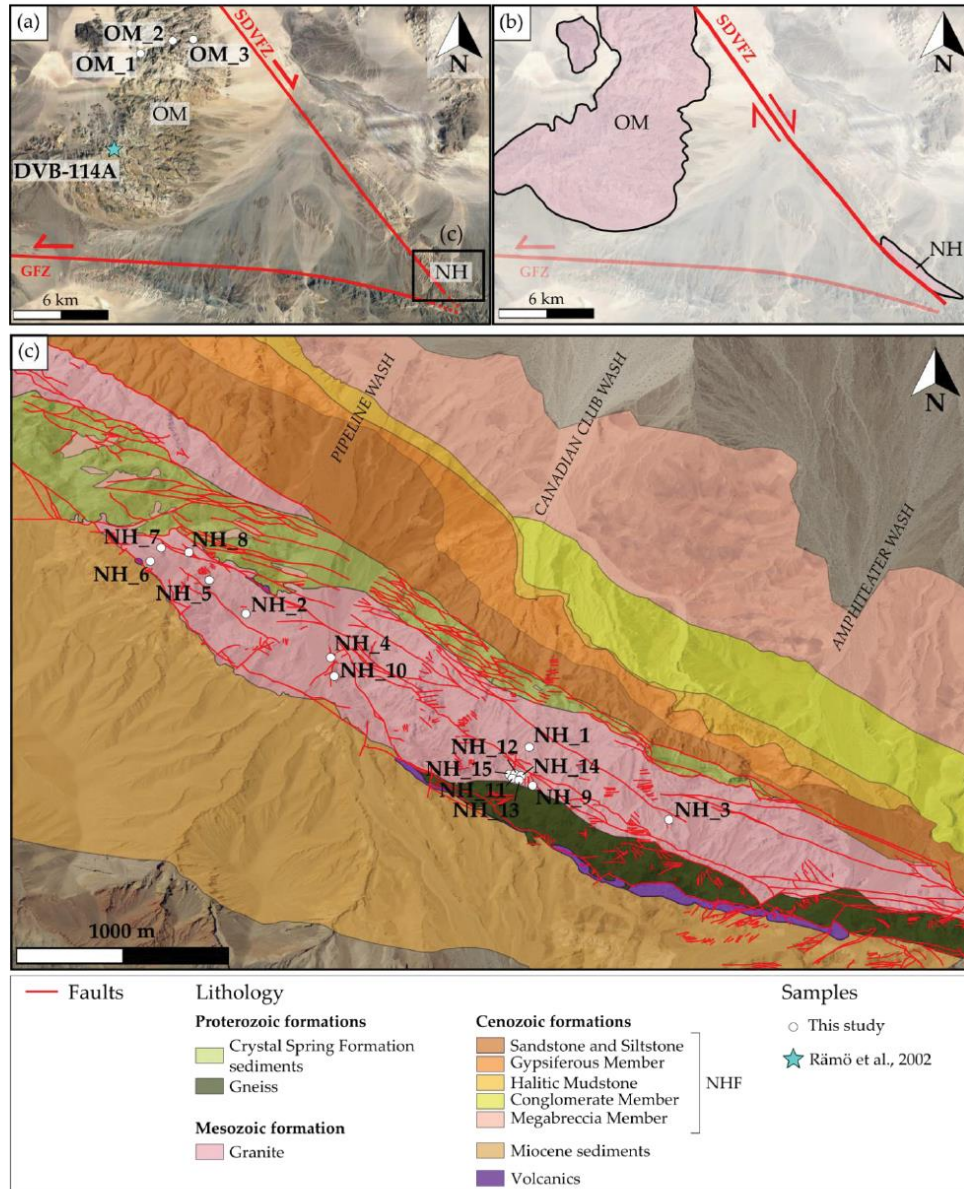


Figure 2. (a) Map presenting the structural setting of the southern part of the Death Valley region and the location of the Noble Hills range (NH) and the location of samples in the Owlshead Mountains (OM) represented by the white dots. (b) A scheme showing the displacement of the NH granite from the OM along the SDVZF described by [11]. (c) The geological map of the Noble Hills range, modified after [38,42]. The quaternary is not displayed but available on [38] map. In (a,b), samples location for this study are represented by the white dots; the blue star corresponds to a sample from [34]. NHF—Noble Hills Formation.

3. Material and Methods

3.1. Material and Sampling Strategy

Fifteen samples from the NH granite and three samples from the OM granite (Figure 2) were collected in order to perform petrographical, mineralogical and geochemical characterizations. Hand specimens of centimetric size were collected in the two granite bodies (OM and NH) in order to characterize their mineralogical changes.

The selection of those samples through the NH was done under one scope, consisting of target zones away from the faults in order to avoid their influence. In that case, the magmatic texture is preserved. These faults are striking mainly NW/SE (SDVFZ direction) ([12], this issue). In order to be more precise in the sample selection, this latter was also based on the degrees of microfracturing defined by [44], from microscopical observations. This scale was improved by attributing a value of fracture density, based on scanlines realized on thin section mosaics, for each degree of microfracturing, which is described in the Methods section.

All the samples are georeferenced for database supply as well as located precisely (Figure 2). The OM being considered as the same batholith as the NH granite [11], samples were collected in an area unaffected by the SDVFZ activity in order to have a reference protolith of the studied area. Thin sections as well as powders were prepared to perform the following analyses.

3.2. Methods

3.2.1. Microscopic Observations

A petrographical study performed on covered and polished thin-sections of 15 samples from the NH and two samples from the OM (OM_1 and OM_3), was realized at Institut Polytechnique UniLaSalle in Beauvais, using a Leica DM4500-P optical microscope equipped with a Leica DFC450C camera. Images were acquired thanks to the software Leica Application Suite (LAS) v4.11.0. The system is also equipped with a multistep acquisition program to perform thin section mosaics. It consists in the acquisition of several photos that follow each other in order to scan the whole thin section. At the end, the pictures are merged to obtain the mosaic. All the mineral abbreviations used in this paper refer to mineral symbols defined by [45]. The degree of mineral transformation into secondary minerals was defined based on optical observations.

3.2.2. Fractures Density

The studied samples were selected away from fracture zones, but also according to a certain degree of microfracturing based on the scale defined by [44]. For this study, fractures density values were calculated for each degree of microfracturing by using thin section mosaics. For each mosaic, two scanlines [46,47] perpendicular to the main fractures were realized by digitalizing fractures along both lines. The P_{10} [46] has been calculated for each scanline. It consists in the number of fracture intersects per line length of scanline. The average was calculated to obtain a value of fracture density attributed to each thin section mosaic and corresponding to each microfracturing degree defined by [44]:

$F_d0 < 1687$ fracs/m—no to very low microfracturing

$F_d1 = 1687$ fracs/m—microfracturing of order less than the grain size

$F_d2 = 2694$ fracs/m, with a multiplier factor of 1.6—microfracturing of grain size order with interconnections

$F_d3 = 3549$ fracs/m, with a multiplier factor of 1.3—abundant microfracturing

$F_d4 \geq 5140$ fracs/m ([12] this issue), with a multiplier factor of 1.4—very abundant microfracturing

Samples selected for this study have so a fracture density lower or equal to F_d2 .

3.2.3. SEM-EDS

Scanning Electron Microscope (Hitachi S-3400N SEM) equipped with a Thermo Ultrady Energy Dispersive X-ray Spectrometer (EDS) probe was used on two polished

thin sections and one hand specimen at Institut Polytechnique UniLaSalle in Beauvais. It aimed at analyzing the microstructure characteristics and to perform qualitative and semi-quantitative chemical analyses of various selected mineral phases.

A NORAN-type correction (©Thermo Fisher Scientific, Waltham, MA, USA) procedure was used for all data and all Fe was assumed to be ferrous for simplification. Polished thin sections were analyzed using a 50 μ A beam current, an accelerating voltage of 20 kV and an acquisition time of 30 s.

3.2.4. X-ray Diffraction (XRD)

Experimental Conditions

XRD analyses were performed at Institut UniLaSalle Beauvais on the 15 samples from the NH and one sample from the OM (OM_2) using a D8-Advance Bruker-AXS (Siemens, Munich, Germany) diffractometer with a Ni-filtered $\text{CuK}\alpha$ radiation at 40 kV and 40 mA, a primary soller slit of 2.5° , divergence slit of 0.6 mm and a secondary soller slit of 2.5° , with a detector slit of 0.1 mm and an antiscattering slit of 0.6 mm. Samples were crushed with an agate pestle and mortar. Quantitative phase analysis based on Reference Intensity Ratio values were performed on randomly oriented bulk rock powders with a step length of 0.5° and a scan speed of $0.014^\circ/\text{s}$ over the range 3° – $70^\circ 2\theta$ for bulk rocks composition. The uncertainty is estimated to be around 5%.

Determination of Illite Crystallinity and Kübler Index

XRD investigations were carried out on bulk rock powder specimens and clay fractions of 16 samples in order to identify and determine the relative abundance of mineral phases (semi-quantitative, around 3–5%) observed upstream under the optical microscope and the SEM. Clay mineral separation was conducted using techniques described by [48], following the recommendations of [49], and according to the standard techniques suggested by [50]. It consists into the collection of the $<2\ \mu\text{m}$ and 2 – $6\ \mu\text{m}$ fractions from the sample powders put in suspension into water in decantation tubes. Oriented slides were then prepared by pipetting suspension onto glass slides ($5\ \text{mg}/\text{cm}^2$) and air-drying. XRD measurements were then performed at air dried, solvated with ethylene glycol, and after heating ($550\ ^\circ\text{C}$) conditions with a step length of 0.5° and a speed of $0.01^\circ/\text{s}$ per step over the range 3° – $35^\circ 2\theta$. The clay minerals identification, which is based on d-values and the relative intensity of their 00l peak reflections, was undertaken referring to [51,52]. The illite “crystallinity” (IC), defined as the full width at half maximum (FWHM) of the $10\ \text{\AA}$ (001) peak of illite, was calculated using the software DIFFRAC EVA v 4.2 (by ©Bruker AXS, Billerica, MA, USA). The obtained values were standardized using the crystallinity index-standard (CIS) samples of [53] in order to calculate the Kübler Index (KI). The KI values of raw data expressed in $\Delta^\circ 2\theta$, were measured into three slots, corresponding to different campaigns, inducing the three following standardizations:

$$\text{KI}_{(\text{ULS1})} = 1.6987 \times \text{IC}_{\text{measured}} - 0.0842 \quad (R^2 = 0.9724) \quad (1)$$

$$\text{KI}_{(\text{ULS2})} = 1.5501 \times \text{IC}_{\text{measured}} - 0.0512 \quad (R^2 = 0.9944) \quad (2)$$

$$\text{KI}_{(\text{ULS3})} = 1.5337 \times \text{IC}_{\text{measured}} - 0.0498 \quad (R^2 = 0.9975) \quad (3)$$

KI was used to define the limits of metamorphic zones [54], following the recommendations for Kübler-Index calibration of [50] and the CIS-KI transformation formalism of [55]. In siliciclastic rocks, the transitions from non-metamorphic to low-grade (referring to the term greenschist facies [56]) and from the very low-grade (chlorite zone [57]) to low-grade metamorphic zone (biotite zone [58]) take place through three zones defined by [13]: the diagenetic zone, the anchizone and the epizone. The zone boundary values are presented in Table 1. The smallest FWHM able to be measured by our diffractometer (limit detection) is $0.08\Delta^\circ 2\theta$.

Table 1. Metamorphic zone boundaries [59] for Kübler Index (KI) values [55] and temperatures [60].

Metamorphic Zone	KI ($\Delta^{\circ}2\theta$)	Temperature ($^{\circ}$ C)
Low Diagenesis	>1	~100
High Diagenesis	0.42–1	~200
Low Anchizone	0.30–0.42	
High Anchizone	0.25–0.30	~300
Epizone	<0.25	

3.2.5. ICP-MS—ICP-AES

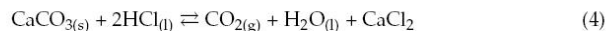
The analyses of major, trace and rare earth elements were completed on five selected samples from the NH (NH_1, NH_2, NH_3, NH_4 and NH_12) and one from the OM (OM_3) by Bureau Veritas Minerals (Vancouver, Canada) using ICP-ES and ICP-MS.

Samples were crushed and mixed with $\text{LiBO}_2/\text{LiB}_4\text{O}_7$ flux. Crucibles were fused in a furnace at 980°C . Then, the cooled bead was dissolved in ACS grade nitric acid and analyzed by ICP-AES and/or ICP-MS. Loss on ignition (LOI) was determined by igniting the samples split then measuring the weight loss.

3.2.6. Manocalcimetry

Calcite contents were determined using an OFITE 152-95 manocalcimeter. The analyses were performed on 15 samples from the NH and one sample from the OM at CY Cergy Paris University in the Geosciences and Environment Cergy (GEC) laboratory. It provides an indication of the total carbonate content in a sample and allows to assess the influence of calcite on permeability of the fluid pathways. This is achieved by measuring the rate of response of 10% hydrochloric acid on the samples. Calcimetry has also proved to be an efficient, easy and low-cost method to better understand the hydrothermal sealing of a reservoir [61].

Manocalcimetry consists into the measurements of CO_2 partial pressure when calcite is dissolved by HCl. The reaction that occurs is:



The calcimeter, composed of a glass flask and a high precision manometer calibrated with pure calcite reduced into fine powder. This allows us to determine the calcimeter coefficient. Variation of temperature and pressure can cause uncertainty on measurements, which was considered to obtain high quality results with a precision around 0.5 wt.%.

Prior to measurements, sample preparation was done according to [61]. The samples were reduced into powder in an agate mortar and put in the oven at 60°C for 24 h. Then, 1.000 g of each sample was weighed and put in a sample holder, itself put in the calcimeter with a little glass filled with HCl. The amount of HCl is in excess in order to dissolve all the calcite present in the sample. The maximum value reached during the measurement was read on the manometer and the CaCO_3 percentage was determined as follows:

$$\% \text{CaCO}_3 = (\text{Measured value} \times 100) / \text{Calcimeter coefficient} \quad (5)$$

Two replicates were performed for each sample in order to check the reproducibility of the results, which is considered as good when the difference between the two results is lower than 0.5 wt.%, corresponding to the precision interval mentioned above.

3.2.7. Ethanol Saturation Porosimetry

The estimation of available volume for fluid storage is fundamental and can be quantified by porosity measurements [62]. The connected porosity was measured on 6 samples from the NH and one from the OM by the triple weighing method [63] defined by the RILEM standard (test n $^{\circ}$ L.1, 1978). It consists in the saturation of the samples after

vacuum degassing. The measurements were carried out at CY Cergy Paris University in the Laboratory of Mechanics and Materials for Civil Engineering (L2MGC).

In this study, ethanol has been chosen instead of water, as used in classical methods, in order to avoid possible clay swelling [64], which could lead to the destruction of the sample and biased results. Even though ethanol (0.469 nm) is a molecule larger than that of water (0.343 nm), the pore volume is not estimated to be under-evaluated, as the pore size is much larger than that of ethanol molecules. The samples were first oven-dried at approximately 40 °C until obtaining a constant weight (W1). Samples were then soaked by capillary action with ethanol after staying for 12 h under a vacuum. When the samples were completely immersed, the vacuum was stopped and the samples left in the ethanol for 24 h. Finally, they were weighted twice: (1) weighing of saturated samples, W2; and (2) weighing of samples under “ethanostatic” conditions (suspended into ethanol under the balance), W3. The connected porosity ϕ is then calculated:

$$\phi(\%) = (W2 - W1/W2 - W3) \times 100 \quad (6)$$

4. Results

4.1. Petrographic Description

4.1.1. The Owlshead Granite

Samples of the OM granite appear rather fresh, meaning that primary minerals seem not transformed into secondary ones and present no sign of deformation. They show a light grey/whitish and yellowish granite (Figure 3a) with equant medium-size grains (0.1–1 cm). Primary assemblage is composed of plagioclase, quartz, K-feldspar and biotite. Biotite is generally surrounded by a yellowish oxide halo, showing its incipient alteration.

OM granite microscopic observations (Figure 3b,c, Table 2) confirm the freshness of the rock as well as the very low to absent microfracturing. Figure 3b shows a microfracturing around F_{d1} (Table 2). Most of the fractures are open and a few of them are filled by calcite. Calcite is also present at the grain boundaries (Figure 4a,b).

Regarding mineralogical composition, plagioclase (35%, modal composition) occurs subautomorphous crystals, up to 5 mm, of oligoclase composition with an oscillatory zonation [65] (Figure 3b). Quartz (35%) forms up to 2 cm polycrystalline clusters of anhedral crystals which range up to 1 cm and present a slight rolling extinction. K-feldspar (25%) occurs as centimetric subautomorphous crystals of microcline and orthoclase with a Carlsbad twin, rich in perthites (albite vein or braid/patch shape [65] (Figure 4a,b). K-feldspar crystals can contain plagioclase and biotite inclusions. Biotite (5%) of around 2 mm in length is euhedral. Primary opaque minerals (<1%) are also found in this granite.

The core of plagioclase is slightly transformed into K-white mica (Figures 3c and 4c,d). They will be represented as Wm. Quartz and K-feldspar are not affected by the alteration and are only little undeformed as seen on quartz showing undulatory extinction (Figure 4a). Biotite can be slightly altered. Few epidotes are present nearby the biotite (Figure 4e,f).

Microscopic observations of samples OM_3 and OM_1 are consistent with whole rock XRD analyses performed on the sample OM_2 from the OM granite. The three samples have a similar mineralogical composition and are grouped together in Table 2.

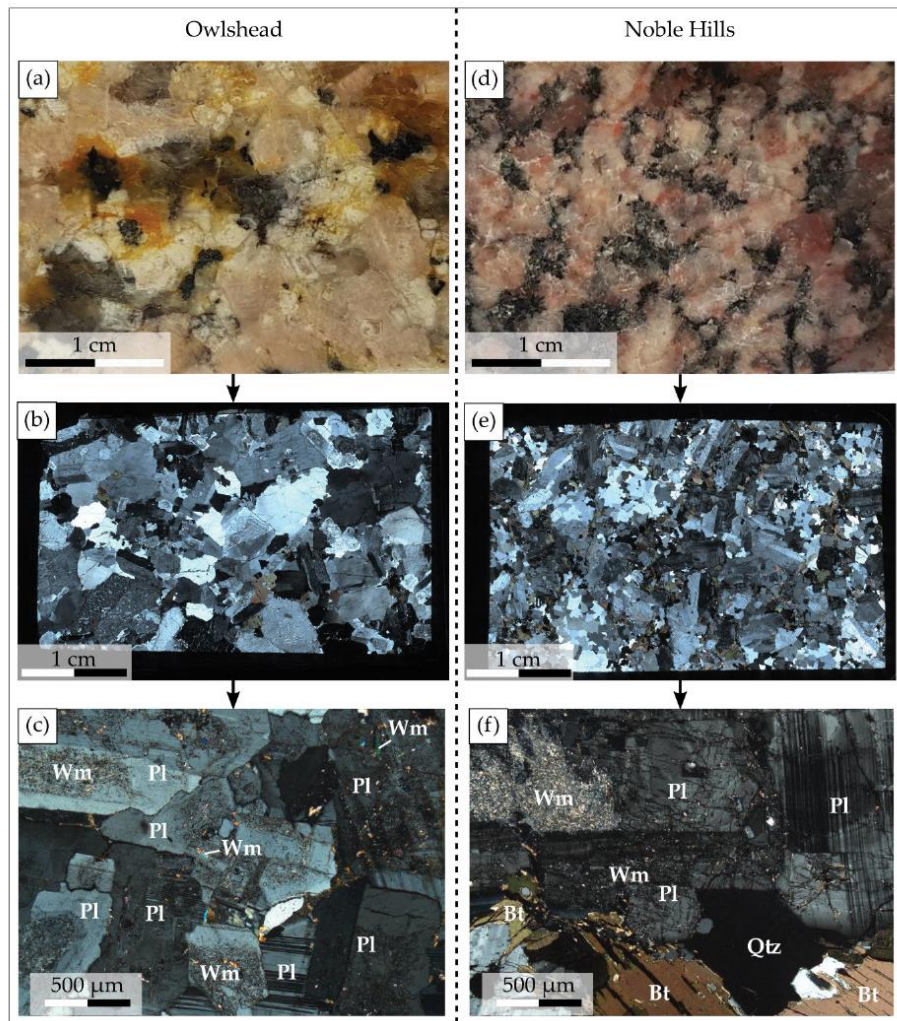


Figure 3. Macroscale to microscale photographs illustrating (a–c) the Owshead and (d–f) the Noble Hills granites. (a,d) Hand specimens for each granite showing their different aspects. (b,e) Thin section mosaics realized for each granite under optical microscope in polarized—analyzed light and showing the difference in terms of grain size and microfracturing. (c,f) Thin sections zooms of each granite mosaic in polarized—analyzed light showing the difference in terms of alteration degree. Abbreviations (except for “Wm”) after [45]: Bt—Biotite, Kfs—K-feldspar, Wm—K-white mica, Pl—Plagioclase, Qtz—Quartz.

Table 2. List of samples collected in the field with their mineralogical composition determined after microscopic observations and XRD analysis (primary minerals, alteration phases for plagioclase, biotite and K-feldspar, other secondary minerals and microfissuring after Castaing and Rabu scale). Abbreviations (except for “Ox and Wm”) after [45]: Qz—Quartz, Pl—Plagioclase, Mc—Microcline, Or—Orthoclase, Bt—Biotite, Kln—Kaolinite, Ep—Epidote, Ox—Oxide (when it could not be determined precisely), Wm—K-white mica, Cal—Calcite, Dol—Dolomite, Hem—Hematite, Gp—Gypsum, Fd—Fracture density.

Sample ID	Primary Minerals			Major Secondary Phases Within				Other Secondary Minerals		Microfracturing
	Wm	Pl	Kln	Cal	Wm	Bt	Ox	Kfs	Wm	
OM_1_2_3	Qz, Pl, Mc, Or, Bt, Ox									Fd1
NH_1	Qz, Pl, Mc, Or, Bt, Ox	✓	✓		✓		✓			Fd1
NH_2	Qz, Pl, Or, Bt, Ox	✓	✓				✓			Fd1
NH_3	Qz, Pl, Or, Bt, Ox	✓	✓				✓			Fd1-2
NH_4	Qz, Pl, Or, Bt, Ox	✓	✓				✓			Fd0-1
NH_5	Qz, Pl, Or, Bt, Ox	✓	✓				✓			Fd0-1
NH_6	Qz, Pl, Or, Bt, Ox	✓	✓	✓			✓			Fd1-2
NH_7	Qz, Pl, Or, Bt, Ox	✓	✓				✓			Fd1
NH_8	Qz, Pl, Or, Bt, Ox	✓	✓	✓			✓			Fd1-2
NH_9	Qz, Pl, Or, Bt, Ox	✓	✓				✓			Fd0-1
NH_10	Qz, Pl, Or, Bt, Ox	✓	✓	✓			✓			Fd2
NH_11	Qz, Pl, Or, Bt, Ox	✓	✓	✓			✓			Fd1-2
NH_12	Qz, Pl, Mc, Or, Bt, Ox	✓	✓	✓			✓			Fd0-1
NH_13	Qz, Pl, Mc, Or, Bt, Ox	✓	✓	✓			✓			Fd0-1
NH_14	Qz, Pl, Mc, Or, Bt, Ox	✓	✓	✓			✓			Fd0-1
NH_15	Qz, Pl, Or, Bt, Ox	✓	✓	✓			✓			Fd1-2

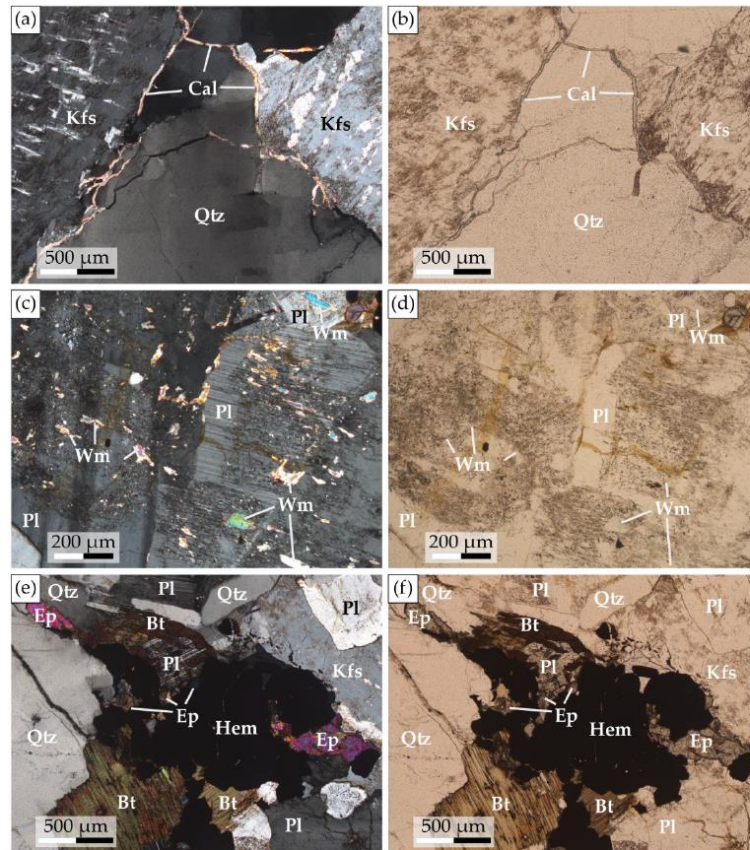


Figure 4. Photomicrographs of the Owlshead granite in polarized-analyzed and polarized—non-analyzed light showing (a,b) perthitic and unaltered orthoclase, unaltered quartz presenting a slight undulatory extinction and calcite veinlets at grain boundaries. (c,d) Plagioclase alteration with the formation of K-white mica. (e,f) Incipient biotite alteration associated to hematite and epidote formation. Abbreviations (except for “Wm”) after [45]: Bt—Biotite, Cal—Calcite, Ep—Epidote, Hem—Hematite, Kfs—K-feldspar, Wm—K-white mica, Pl—Plagioclase, Qtz—Quartz.

4.1.2. The Noble Hills Granite

Far from the major faults, the NH granite appears, as a whole, microfractured and altered, with preserved “fresh” zones. The collected hand specimens (Figure 2b) are equant to slightly porphyritic and display a pinkish color (Figure 3d) or a whitish color for the samples with evidences of alteration. Primary assemblage, as for the OM granite, is made of plagioclase, quartz, K-feldspar and biotite.

At the microscale, the degree of microfracturing ranges from F_{d0-1} to F_{d2} (Table 2). As for the OM granite, the microfractures can be opened or filled by carbonates. As regards mineralogical composition, plagioclase (~35%, oligoclase in composition) occurs as sub-anhedral to euhedral crystals (up to 5 mm in length) showing growth zonation (see Figure 3f and [65]). Quartz (~30%) forms polycrystalline euhedral clusters of around 1 cm in size made of 3-mm-wide crystals with sometimes a slight undulatory extinction linked to low deformation. K-feldspar (~25%) is made of sub-anhedral to euhedral orthoclase

(up to 1 cm in length) with vein shaped perthites [65]. Microcline is only present in the samples NH_12 and NH_14, in the southern part of the range (Figure 2 and Table 2). Some K-feldspar crystals contain inclusions of plagioclase or/and biotite. Depending on the samples, the amount of plagioclase can be equivalent to that of K-feldspar (~30% each), but most of the time, plagioclase dominates. Myrmekite can be observed at the interface between plagioclase and K-feldspar. Biotite (~10%) appears euhedral with crystals ~2 mm in length. Accessory minerals (<1%) as apatite are also observed. More rarely, primary muscovite, as well as primary opaque minerals (oxides) are observed in the granite. A comparison between the NH and the OM granites highlights a grain size difference. Quartz and K-feldspar crystals are smaller in the NH granite (up to 3 mm and 1 cm respectively, Figure 3e) than in the OM granite (up to 1 cm and centimetric crystals respectively, Figure 3b).

Primary minerals, function of their sensitivity to alteration [65], recrystallized into secondary minerals which are shown in Table 2. This is related to differences into chemical properties [66]. In the plagioclase, which is the most altered mineral (Figure 5), recrystallization propagates from the core of the crystal to the more albitic rim (Figure 5a) [67]. When alteration is intense, plagioclase is entirely replaced by newly formed minerals leaving only the pseudomorph of the plagioclase to subsist (Figure 5d). The newly formed minerals are the following:

- Illite is the most frequent and occurs as tiny flakes or needles 0.5 to 8 µm width and up to 40 µm long [68] (Figure 5b,c).
- Kaolinite is present as fan shape (Figure 5e,f) of 25 µm to 40 µm in diameter. Under SEM (Figure 5f), well crystallized kaolinite presents a porous structure which can contribute to the porosity of the rock. It is only present in the NH granite (Table 3) indicating that the NH granite has undergone a different alteration from that of the OM granite.
- Calcite, which occurs as small spots, is mainly associated with kaolinite (Figure 5d,e). It crystallizes in the porosity created by plagioclase dissolution.

Illite and kaolinite can be present together in the same sample (Figure 5d).

The K-feldspar remains always unaffected (Figure 5d), but when the alteration is relatively pronounced, perthites can be altered as well as the mineral inclusions like in sample NH_3 (Table 2). Biotite is progressively replaced by K-white mica (illite) as compared to the biotite in the OM granite (Table 2). K-white mica crystallizes along the cleavages and can be associated to the crystallization of oxides, as hematite, also along the cleavages (Figure 6).

Table 3. List of samples with their respective clay minerals composition, FWHM and Kübler Index (KI) for the fractions < 2 µm and 2–6 µm. Abbreviations (except for “Cor”) after [45]: Ill—Illite, Kln—Kaolinite, Cor—Corrensite, I/S—Illite/Smectite, Vrm—Diocahedral Vermiculite, Bt—Biotite, Mnt—Montmorillonite, AD—Air-dried.

Sample ID	<2 µm					2–6 µm						<2 µm (AD)		2–6 µm (AD)	
	Ill	Kln	Cor	I/S	Bt	Ill	Kln	Cor	I/S	Mnt	Bt	FWHM	KI	FWHM	KI
OM_2	no material					–	–	–	–	–	–	–	–	0.18	0.22
NH_1	+	–	–	–	++	–	+	–	–	–	++	0.48	0.69	0.34	0.46
NH_2	–	–	–	–	++	–	–	–	–	–	++	0.31	0.43	0.32	0.44
NH_3	+	+	++	–	–	+	+	++	–	–	–	0.63	0.92	0.59	0.87
NH_4	++	+	–	–	–	++	+	–	–	–	–	0.81	1.29	0.73	1.16
NH_5	+	–	–	–	–	–	–	–	–	–	+	0.69	1.09	0.37	0.55
NH_6	+	++	–	–	–	+	++	–	–	–	–	1.37	2.25	1.15	1.87
NH_7	+	+	–	–	–	+	+	–	–	–	+	1.01	1.63	0.71	1.13
NH_8	+	+	+	–	–	+	++	+	–	–	–	1.10	1.79	1.18	1.93
NH_9	+	+	++	–	–	+	+	++	–	–	–	0.85	1.36	0.56	0.87
NH_10	+	–	–	–	++	+	–	–	–	–	++	0.46	0.65	0.51	0.73
NH_11	++	–	+	–	–	++	+	+	–	–	–	0.67	1.05	0.62	0.97
NH_12	++	+	–	–	–	++	+	–	–	–	–	0.57	0.89	0.46	0.69
NH_13	+	–	+	–	–	+	–	+	–	–	–	0.46	0.69	0.38	0.56
NH_14	+	–	–	–	+	+	–	–	–	–	+	0.59	0.92	0.44	0.66
NH_15	+	–	+	–	–	+	–	–	–	–	–	0.69	1.08	0.50	0.77

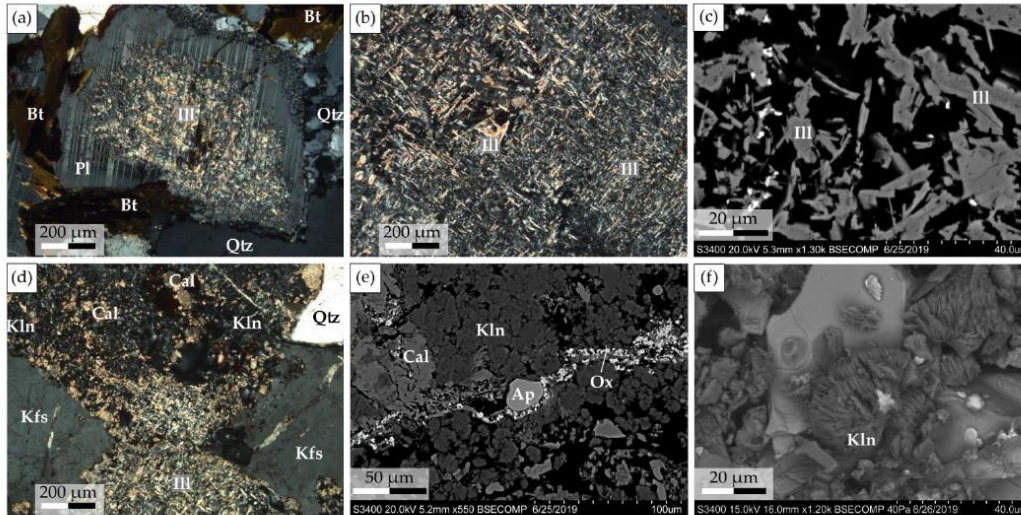


Figure 5. Photomicrographs showing the plagioclase transformation progress in the Noble Hills granite. (a) Progressive illitization of plagioclase initiating in the core of the mineral under optical microscope in polarized—analyzed light. (b) Needles shape illite replacing plagioclase in polarized—analyzed light under optical microscope. (c) Back-scattered electron image of needles/flakes shape illite replacing plagioclase. (d) Plagioclase completely replaced by illite, kaolinite and calcite and non-altered K-feldspar under optical microscope in polarized—analyzed light. (e) Back-scattered electron image showing a fan shape kaolinite, calcite and oxide veinlet. (f) Back-scattered electron image showing a magnified view of a single mineral of kaolinite under SEM. Abbreviations (except for “Ox”) after [45]: Ap—Apatite, Bt—Biotite, Cal—Calcite, Ill—Illite, Kln—Kaolinite, Kfs—K-feldspar, Ox—Oxides, Pl—Plagioclase, Qtz—Quartz.

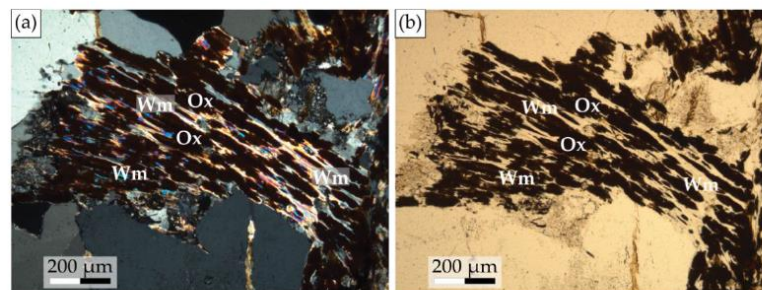


Figure 6. Photomicrographs showing a biotite completely altered and replaced by oxides and K-white mica (essentially illite) according to the cleavage planes (a) in polarized—analyzed light under optical microscope and (b) in polarized—analyzed light under optical microscope. Abbreviations (except for “Ox and Wm”) after [45]: Bt—Biotite, Cal—Calcite, Kfs—K-feldspar, Wm—K-white mica, Ox—Oxides, Pl—Plagioclase, Qtz—Quartz.

All the samples are plotted in the Streckeisen ternary diagram (Figure 7) [68]. The OM and NH granites of this study are both defined as monzogranites. The OM sample analyzed by [34] (Figure 2a, blue star) shows a different composition (Figure 7, blue star). It is rather a monzonite, as defined by [34], than a monzogranite, as defined in this study.

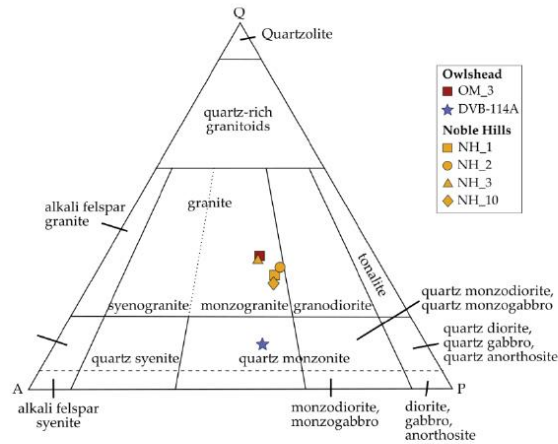


Figure 7. Normative composition of one sample from the OM and 4 samples from the NH in a QAP (Quartz-Alkali-feldspar-Plagioclase) ternary diagram [68].

4.1.3. Clay Minerals Identification and Kübler INDEX

Clay minerals from the <2 μm and 2–6 μm fractions were separated. The clay composition of both fractions of each studied sample (OM and NH) is given in Table 3, based on [51].

Owlshead Mountains

The OM sample clay analyses confirm the presence of illite observed under optical microscope. They also reveal the pattern of montmorillonite (Mnt) [51], a common smectite (Figure 8). Its very intense 001 peak allows the determination of its amount representing 15% of the clay fraction. This peak is characterized by a shift from 14.87 Å (air-dried) to 16.90 Å after glycol solvation and it collapses at 10.09 Å after heating. After glycol solvation, new peaks appear at 5.61 Å and 8.46 Å. After glycol solvation, new peaks appear at 5.61 Å and 8.46 Å.

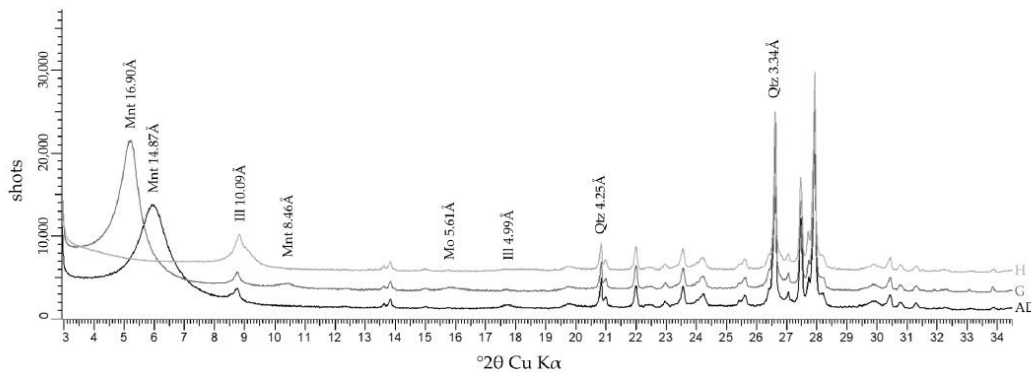


Figure 8. XRD result obtained for the clay fraction < 2 μm in Air-Dried (AD), Glycolated (G) and Heated (H) of the samples in the OM granite and showing a montmorillonite (Mnt) pattern.

Noble Hills

Two typical XRD patterns of clay minerals are identified in the NH samples for the <2 μm fraction (Figure 9):

- Corrensite, kaolinite and illite are identified in the first pattern, where corrensite is well known as the trioctahedral variety of regular 50:50 mixed-layer chlorite/smectite [69] (Figure 9a). It is characterized by (1) the peak at 13.60 \AA in air-dried conditions, shifting to 15.62 \AA after glycol solvation and collapses to 11.72 \AA after heating, and (2) new peaks at 7.78 \AA , 5.15 \AA and 3.44 \AA appear after glycol solvation and disappear after heating. The corrensite found in the NH granite is considered as a low charge corrensite after [51].
- Illite/smectite (I/S) mixed-layer, kaolinite and illite (Figure 9b) are identified in the second pattern, where I/S is illite-rich (R3), with more than 90% of illite and R representing the Reichweite parameter [70]. I/S is characterized by a large peak at 10.08 \AA in air-dried, becoming narrower when it collapses to 9.93 \AA after glycol solvation and by a peak at 5 \AA swelling after glycol solvation.

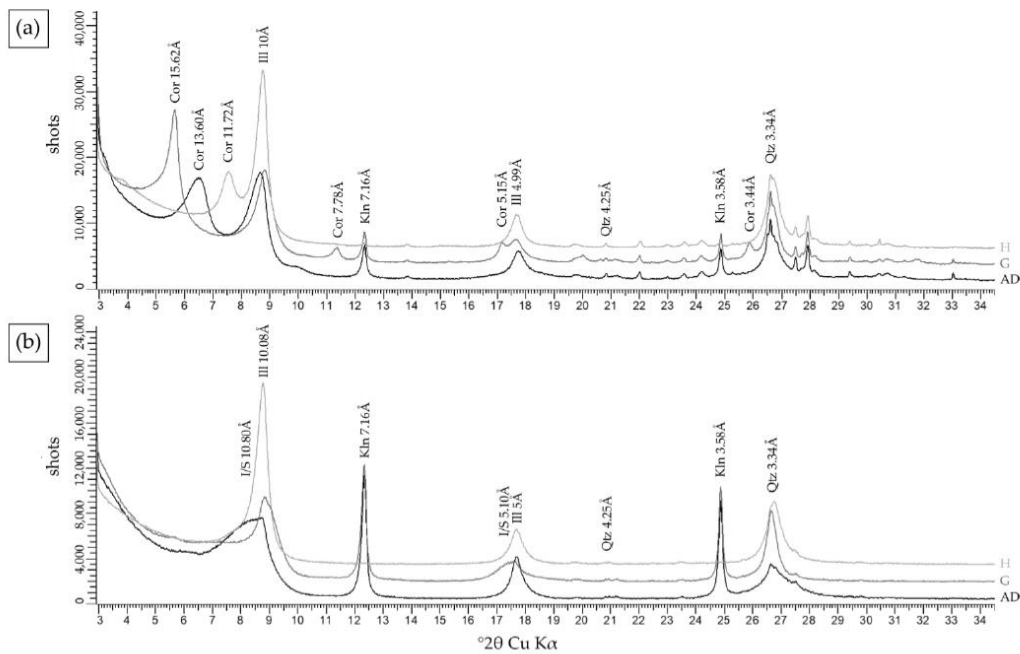


Figure 9. XRD patterns obtained for the clay fraction <2 μm in Air-Dried (AD), Glycolated (G) and Heated (H) for the NH granite and showing the clay composition of the samples in the NH granite: (a) corrensite (Cor), a chlorite/smectite mixed-layer, and (b) illite/smectite mixed-layer (I/S). Abbreviations (except for “Cor and I/S”) after [45]: Bt—Biotite, Kln—Kaolinite, Qtz—Quartz, Ill—Illite.

In the NH KI values range from $2.25\Delta^{\circ}2\theta$ to $0.43\Delta^{\circ}2\theta$ for the <2 μm fraction and from $1.93\Delta^{\circ}2\theta$ to $0.44\Delta^{\circ}2\theta$ for the 2–6 μm fraction (Table 3). The spatial distribution of the samples and the KI values are shown in Figure 10. A NW to SE decrease in KI values in the main granitic body is distinguishable in the <2 μm fraction (Figure 10a) and confirmed in the 2–6 μm fraction (Figure 10b).

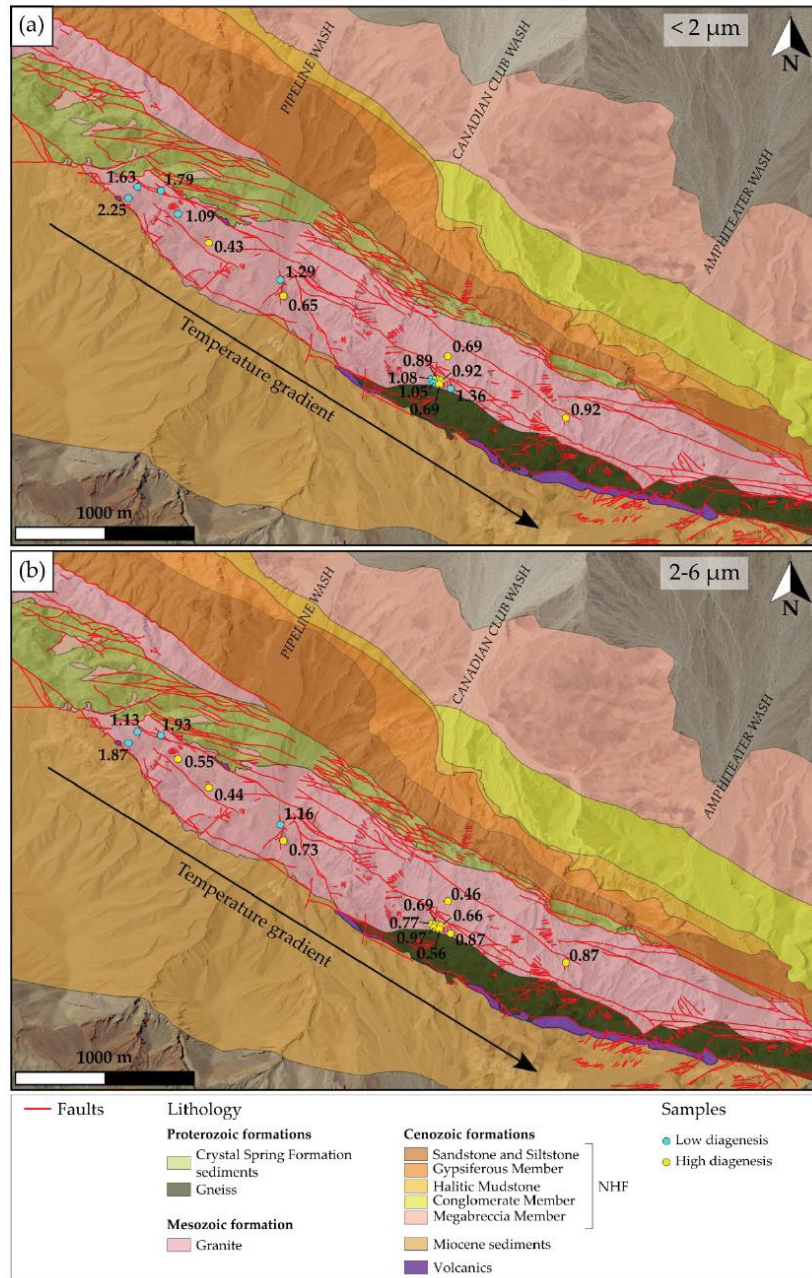


Figure 10. Geological map (see Figure 2b) representing the Kübler Index (KI) in air dried conditions of each sample and the corresponding metamorphic zone showed by the color of the dots for (a) the fraction <math>< 2 \mu\text{m}</math> and (b) the fraction $2-6 \mu\text{m}$.

4.2. Geochemical Analyses

4.2.1. Major Element Bulk Rock Chemistry

Major element geochemistry (Table 4) allows classifying the granite samples in different diagrams (Figures 11 and 12).

Table 4. Major elements of the Owlshead and Noble Hills granites.

Sample ID	OM_3	NH_10	NH_1	NH_2	NH_3
		Oxides (weight %)			
SiO ₂	74.65	68.54	69.56	68.69	68.78
Al ₂ O ₃	12.90	15.36	14.93	14.53	14.99
Fe ₂ O ₃	1.83	3.02	2.83	4.29	2.95
MgO	0.31	0.57	0.56	1.15	0.78
CaO	1.09	2.62	2.20	2.50	1.99
Na ₂ O	3.51	3.31	3.42	3.19	2.78
K ₂ O	4.43	4.31	4.10	3.60	4.22
TiO ₂	0.20	0.29	0.26	0.46	0.28
P ₂ O ₅	0.07	0.14	0.13	0.20	0.14
MnO	0.08	0.09	0.08	0.12	0.08

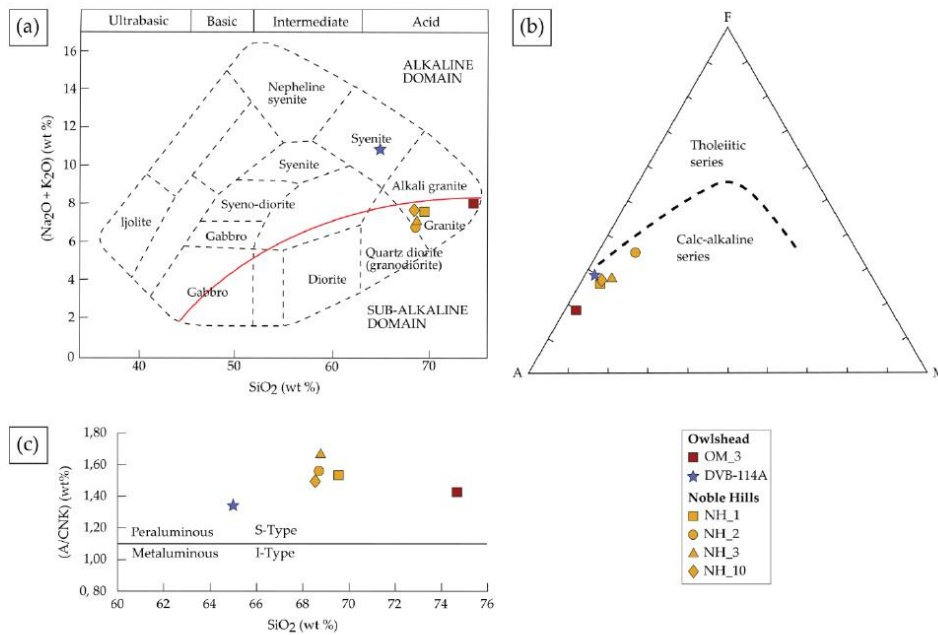


Figure 11. (a) Total alkali versus silica diagram ([71] adopted for plutonic rocks by [72]). (b) AFM (Alkali-Fe₂O₃-MgO) classification diagram established by [73]. (c) A/CNK (Al₂O₃/(CaO + Na₂O + K₂O)) versus silica diagram. The blue star corresponds to a sample from the OM analyzed by [34].

In the Na₂O + K₂O versus SiO₂ classification (called TAS) diagram of [71], modified after [72] for plutonic rocks, all the samples plot in the sub-alkalic domain. They all have a granite composition close to the granodiorite zone (Figure 11a). However, the sample from [34] plots in the syenite field, while it plots in the monzonite field in the Streckeisen diagram (Figure 7). The AFM triangular plot classifies all the samples as calc-alkaline

(Figure 11b). The silica content of the OM granite 74.65 wt.% is higher than that of the NH granite which ranges from 68.54 to 69.56 wt.%. According to the SiO₂ versus A/CNK diagram (Figure 11c) [74], all the samples are peraluminous rocks, and are found rather far from the boundary with metaluminous S-type granites, with a A/CNK between 1.4 and 1.6 wt.%. Harker diagrams complete the information by showing a high content of K₂O ranging from 3.6 to 4.43 wt.%, and plot the samples in the high-K calc-alkaline domain (Figure 12a) which limits were defined by [75]. However, the OM sample has a lower Al₂O₃ content (12.9 wt.%) than the NH samples (14.53–15.36 wt.%) forming a separate cluster (Figure 12b). Again, the sample from [45] (DVB-114A—blue star) shows a large difference in composition compared to OM₃.

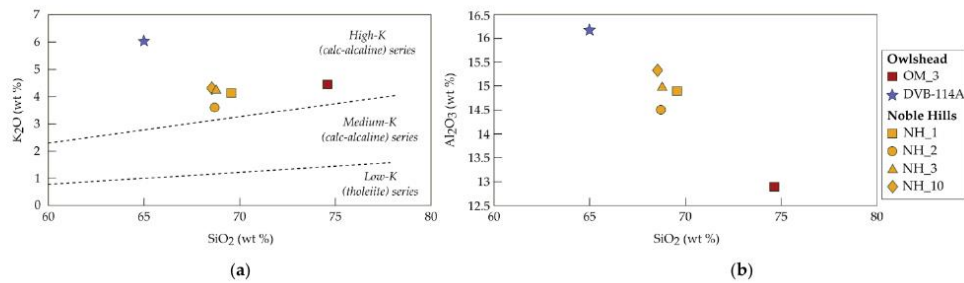


Figure 12. Harker diagrams showing the variation of (a) K₂O [75] and (b) Al₂O₃ in the OM and NH granites. A sample from the OM analyzed by [34] is represented by the blue star.

The loss on ignition (LOI) is of 0.7 wt.% for the OM granite and ranges from 1.1 to 2.8 wt.% for the NH granite (Table 5), showing that the OM granite contains less volatile elements than the NH granite, even for the freshest samples (NH₁₀, NH₁ and NH₂). By comparing the alteration degree of each sample estimated from optical observations of plagioclase and biotite (Table 5) and the LOI values, we note that a low LOI corresponds to a slight alteration, e.g., OM₃ or NH₂ and a high LOI corresponds to a more pronounced alteration, e.g., NH₃.

Table 5. Loss on ignition values compared to the alteration degree of plagioclase and biotite estimated under optical microscope.

Sample ID	OM ₃	NH ₁₀	NH ₁	NH ₂	NH ₃
Loss on ignition (LOI) (wt.%)	0.7	1.5	1.7	1.1	2.8
Alteration degree (%)	2	10	9	4	18
Plagioclase alteration (%)	5	20	20	10	40
Biotite alteration (%)	0	15	10	0	20

In diagrams representing selected major elements versus the LOI (Figure 13), LOI values of NH samples show a positive correlation with K₂O and a negative correlation with Na₂O and CaO. SiO₂ and Al₂O₃ contents are approximately constant, 68.54–69.56 wt.% and 14.53–15.36 wt.% respectively. MgO content varies a lot (0.56–1.15 wt.%) showing no clear correlation with the LOI. K₂O and Na₂O contents of the OM granite are equivalent to those of the freshest NH granites (NH₂, NH₁₀ and NH₁). However, the OM granite sample presents a higher amount of SiO₂ and a lower amount of Al₂O₃, CaO and MgO. The chemistry of the OM granite seems different from that of the NH granite regarding Figures 12 and 13 even though, according to [11], the NH granite derived from the OM granite.

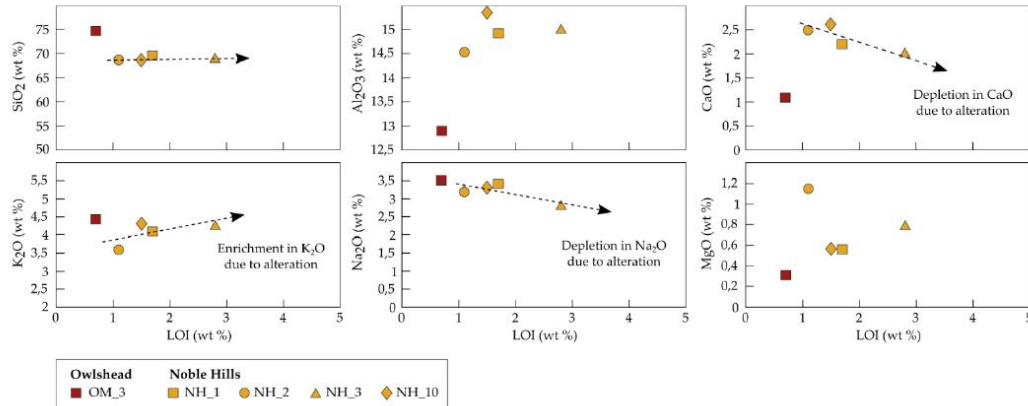


Figure 13. Plot of selected major element oxides (SiO₂, K₂O, Al₂O₃, Na₂O, CaO and MgO) versus LOI (loss on ignition).

4.2.2. Trace Element and REE Bulk Chemistry

Trace elements and Rare Earth Elements (REE) (Table 6) analyses were performed on the same samples as for major elements.

Table 6. Trace elements chemical composition of the Owlshead and Noble Hills granites.

Sample ID	OM_3	NH_10	NH_1	NH_2	NH_3
Trace elements (ppm)					
Be	2	2	2	3	2
Co	1.5	4.2	2.9	6.4	3.5
Cs	1.6	2.4	1.1	3.4	1.8
Ga	15.6	16.7	16.0	17.2	14.1
Hf	4.3	3.6	4.1	4.6	4.6
Nb	22.3	13.8	11.4	18.9	10.5
Rb	154.7	144.9	103.0	139.9	115.7
Sn	2	1	<1	2	<1
Sr	116.2	275.2	237.5	268.2	182.7
Ta	1.6	0.9	0.7	1.3	0.6
Th	19.3	11.4	10.2	9.0	11.0
U	1.8	2.2	1.5	1.4	1.5
V	16	33	22	40	25
W	<0.5	<0.5	0.7	<0.5	<0.5
Zr	139.8	134.2	156.6	180.6	159.0
Y	19.7	22.5	17.5	21.4	17.0
Ba	554	1009	845	704	772
Ni	<20	<20	<20	<20	<20
Sc	4	5	4	8	4
Cr ₂ O ₃	<0.002	<0.002	<0.002	<0.002	<0.002
Be	2	2	2	3	2

Table 6. Cont.

Sample ID	OM_3	NH_10	NH_1	NH_2	NH_3
Rare Earth Elements (ppm)					
La	52.1	28.3	26.2	21.7	26.8
Ce	97.0	53.0	48.1	40.8	52.2
Pr	9.97	5.93	5.31	4.59	5.62
Nd	31.7	20.6	18.8	16.6	19.5
Sm	5.29	3.82	3.51	3.56	3.48
Eu	0.53	0.89	0.89	0.81	0.81
Gd	4.24	3.66	3.14	3.60	3.22
Tb	0.65	0.59	0.51	0.59	0.51
Dy	3.66	3.63	3.05	3.65	2.96
Ho	0.69	0.78	0.62	0.73	0.59
Er	2.05	2.25	1.87	2.18	1.81
Tm	0.30	0.33	0.28	0.33	0.27
Yb	2.08	2.32	1.77	2.16	1.86
Lu	0.33	0.37	0.28	0.36	0.28
TOT/C	0.02	0.14	0.21	0.04	0.26
TOT/S	<0.02	<0.02	<0.02	<0.02	<0.02

Chondrite-normalized REE patterns (Figure 14a) present enriched samples in light rare earth elements (LREE) relative to heavy rare earth elements (HREE) in both granites. However, the OW granite shows a higher abundance of LREE and a stronger negative Eu anomaly than the NH samples. In spite of different degrees of mineral alteration, all the NH samples follow the same trend. The primitive mantle-normalized multi-element diagram (Figure 14b) is characterized by distinct negative anomalies for Nb and Sr and high Th and U contents, typical for upper crustal composition [76]. They also show variable but high Cs, Rb and Ba contents. More generally, samples are relatively rich in large-ion lithophile elements (LILEs) such as Rb, Ba, Th and U, with Sr having the greatest depletion relative to the LILEs. High field strength elements (HFSEs) such as Ta, Nb, Zr and Hf are depleted compared to the LILEs. The OW granite shows, once again, a different trend compared to the NH samples. It has higher Th, Ta, Nb, La, Ce, Nd and Sm contents and a lower Ba content. On both diagrams of Figure 14, the sample DVB-114A [34] shows a different pattern compared to OM_3.

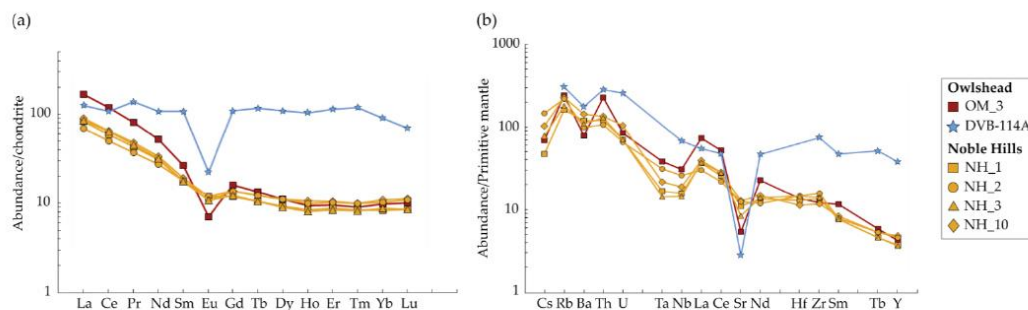


Figure 14. (a) Chondrite-normalized (values from [77]) rare earth element (REE) patterns of samples from the OM and the NH. (b) Primitive mantle-normalized (values from [78]’s slight revision of [79]) multi-element diagram showing trace element patterns of samples from the OM and the NH.

4.3. Calcimetry and Porosimetry

Calcite is present in all the samples, essentially linked to the alteration of the plagioclase. The calcite content is of 0.55% for the OM granite and ranges from 0.55 to 6.53% for the NH granite, with an average of 2.2% and a standard deviation of 1.64%. The porosity is of 2.28% for the OM granite and ranges from 2.21 to 5.17% for the NH granite. A clear positive correlation can be seen between the calcite content and the LOI (Figure 15a). Positive correlations are also visible between the porosity and the LOI and between the porosity and the calcite content (Figure 15b,c). However, the sample NH₇ in Figure 15c is different. Having a low calcite content, it presents a higher porosity compared to the others. Those diagrams show that a low LOI corresponds to a low amount of calcite and a low porosity and that a low amount of calcite fits with a low porosity except for NH₇.

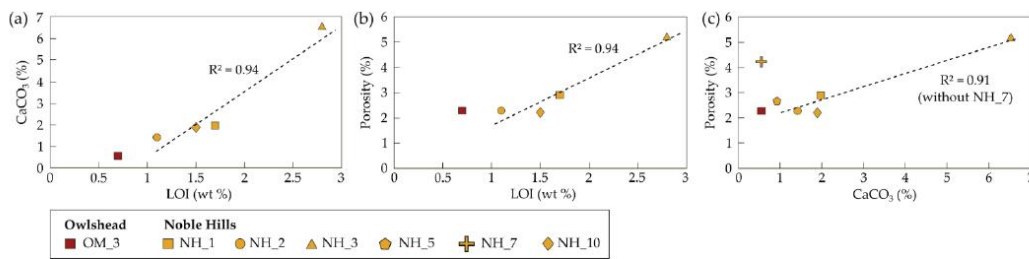


Figure 15. (a) Plot of the porosity versus the calcite content. (b) Plot of calcite content versus LOI (Loss on ignition). (c) Plot of porosity versus LOI.

5. Discussion

5.1. Petrogenesis of the OM and NH Granites

Bulk rock analyses of the OM and NH granites indicate for both of them a calc-alkaline, monzogranite composition, S-type in character (Figure 11). Rämö et al. (2002) [34] also investigated the OM in the same batholith, but south of our sampling area (blue star in Figure 2a). The comparison of geochemical data from their sample with the samples studied here, shows differences in terms of chemical composition (Figures 7, 11, 12 and 14). The OM seems to be a heterogeneous pluton.

Chondrite-normalized REE patterns for the NH granite samples show the same trend (Figure 14a), but are different from the OM granite one. REE are relatively immobile during low-grade metamorphism and hydrothermal alteration [76]. The enrichment of the LREE and the depletion of Eu indicate the degree of magmatic differentiation the rock underwent. The Eu negative anomaly is attributed to the plagioclase fractionation involved in the setting of granites [80]. However, the breakdown of plagioclase and biotite can release some REE except Eu, which can be accommodated by illite formation [81].

The same observations were done through the primitive mantle-normalized spider diagrams, which shows variations in Ta and Nb contents of the NH samples (Figure 14b). Those variations are in good correlation with the LOI: the higher the LOI, the lower the Nb and Ta contents. Li et al. (2013) [82] observed Nb/Ta ratios in altered domains in granitic rocks due to the Nb and Ta decreasing content during the illitization stage. The LOI is directly related to the percentage of alteration, the same phenomenon is observed in our samples. The depletion of Sr in the NH granite might be due to the alteration of magmatic primary plagioclase [82]. However, Sr content in OM is relatively low.

Those diagrams show and confirm the difference in terms of chemical composition between the NH and the OM, which was suspected during thin sections observations. A comparison between our own chemical data within the OM and the data presented by [34] show substantial differences meaning that the OM granite is not homogeneous. Given the fact that the NH granite is considered as a transported part of the OM [11], it is therefore

not surprising that the NH granite presents local composition variations. The OM samples are considered as representing the protolith prior to the mineral transformations identified in the NH granite.

Microcline was identified in the OM granite and only in the southern part of the NH indicating that this part of the range might have undergone a slower cooling than the northern part of the range or a warming.

5.2. Thermal Evolution of the NH Granite

Petrographic investigations have shown that plagioclase and sometimes biotite are replaced by illite. A recent study from [83] has confirmed that IC provides a useful method for characterizing regional grades of diagenesis and low-grade metamorphism. As already mentioned, in some conditions the alteration of a granite, resulting from fluid circulation, shows similarities with diagenetic reactions present in feldspathic sandstones [19], meaning that it is possible to characterize a regional grade by using the KI values obtained in granitic rocks.

As shown in Figure 2, the NH range is a structure stretched NW-SE. The KI values display a trend following this direction with decreasing values towards the south-east (Figure 10). KI values can be associated to different metamorphic zones corresponding to ranges of temperature (Table 1, [60]). The northwestern part of the range, characterized by high KI values, reveals mostly low-grade diagenesis tending progressively to high-grade diagenesis roughly toward the SE. A decrease of KI values indicates an increase in temperature [59]. Thus, this tendency reflects a temperature gradient increasing from the NW toward the SE. The elevation being higher in the south-east, with a higher temperature in this zone might indicate that the southern part of the range was more buried than the rest of the range and has been exhumed. A northeast-vergent contractional deformation is well expressed along the NH range in addition to the strike-slip deformation. It increases in intensity where the NH range converges with the Avawatz mountains ([38] and references therein), at the intersection between the SDVFZ and the GFZ [30]. Chabani et al. (2021) [12] have identified E-W structures in this area and they suppose that these structures are linked to the activity of the GFZ and the convergence of the Avawatz and the NH range. It is tempting to propose that this convergence implied the elevation of the topography at the southern part of the NH range. A work is in progress about exhumation history reconstruction by means of isotopic dating.

5.3. Alteration Parageneses

The OM and NH granites characterization reveals the presence of various secondary minerals as oxides, epidote, corrensite, K-white mica, calcite, kaolinite, illite/smectite mixed-layer and montmorillonite. Those minerals are well known as being the product of alteration processes due to the interaction of a circulating fluid with the surrounding rock. They are in equilibrium with the new environment in response to temperature, pressure and composition of the altering fluid [6,84–86]. In the OM and the NH granites, only plagioclase and biotite are affected. In the case of intense circulation, some primary minerals like plagioclase or biotite may be completely replaced. The newly formed minerals consist mainly in clay minerals [9]. According to optical observations, SEM-EDS and XRD analyses, two types of alteration processes have been identified in the OM and NH granites which are classified as (1) propylitic alteration and (2) argillic alteration. The characterization of the paragenesis and the alteration processes of the granites investigated in this study help to refine a part of the history of the OM and NH granitic basements (Figure 16).

PARAGENESIS	IGNEOUS STAGE	PROPYLITIC ALTERATION	ARGILLIC ALTERATION
Quartz	-----		
K-feldspar	-----		
Plagioclase	-----		
Biotite	-----		
Oxide 1	-----		
Corrensite		-----	
Epidote		-----	
K-white micas		-----	
Calcite			-----
Kaolinite			-----
Illite/Smectite			-----
Oxide 2			-----

Figure 16. Paragenesis sequence and alteration evolution in the OM and NH granite.

5.3.1. Propylitic Alteration

The newly formed minerals depend on the composition of the host mineral. Corrensite, epidote, K-white micas, calcite and iron oxides were identified in the OM and NH granites (Figure 16) by means of optical observations, SEM-EDS and XRD analyses:

1. The calcite as in the OM granite occurs as infills of the microcracks without interacting with the surrounding rock, as well as at grain boundaries.
2. Mixed-layer clay minerals are the intermediate products of reactions involving end-member clays [87]. Corrensite, a chlorite/trioctahedral smectite mixed-layer phyllosilicate is considered as a stable mineral and also as an indicator of propylitic alteration [86,88,89]. It replaces partially biotite and occurs between 160–250 °C in geothermal fields [6,84,90].
3. Epidote crystallization occurs around 220 °C [86]. It is also one major indicator of the propylitic alteration with corrensite [89].
4. The presence of K-white mica flakes allows to fix temperatures around 230 °C up to 350 °C [84,91].

All those secondary minerals occur at temperatures between approximately 160 °C and 350 °C. The presence of corrensite and epidote is the major indicator of a stage of propylitic alteration. The propylitic alteration (Figure 17b) is considered as an earlier pervasive alteration stage. It is common at the margins of alteration zones produced at low fluid/rock ratio [6] and it takes place at the end of the crystallization of the granite [92]. The propylitic alteration results in the partial recrystallization of primary minerals (biotite and plagioclase) in secondary propylitic assemblages by interstitial fluids trapped into the grain boundaries during the cooling of the pluton [88]. Its effects are discrete, but both the OM and NH massifs are affected.

5.3.2. Argillic Alteration

Other newly formed mineral assemblages were identified only in the NH granite. They consist in illite + kaolinite + mixed-layers as illite/smectite (I/S) + calcite and oxide (Figure 16):

1. Illitic minerals are well known to be indicators of fluid circulation as well as paleo-circulation systems [93]. [19,94] show that illite crystallization episodes can occur, for example, in a temperature range of 120 to 160 °C, corresponding to the argillic alteration facies. The illitization process mainly develops in plagioclase and biotite. It is a form of alteration product found extensively in granitoids, and felsic rocks, whereas K-feldspar remains relatively unaltered [8,67,85].
2. According to [84], the presence of kaolinite in alteration paragenesis indicates a fluid temperature lower than 200–150 °C. Kaolinite is stable under more acidic conditions than illite, with pH values ranging from about 4.5 to 6. It also represents a more

- advanced product of hydrolysis reaction due to a high H^+ activity in hydrothermal fluids.
- The illite-rich (R3) I/S mixed-layer form around 150 °C [84,87], with more than 90% of illite based on [51].
 - Plagioclase, oligoclase in composition, presents patches of calcite. Those patches are interpreted as a product of Ca release due to plagioclase alteration.
 - Oxides can be present along the cleavages of the altered biotite. They are interpreted as the result of Mg and Fe release during biotite alteration.

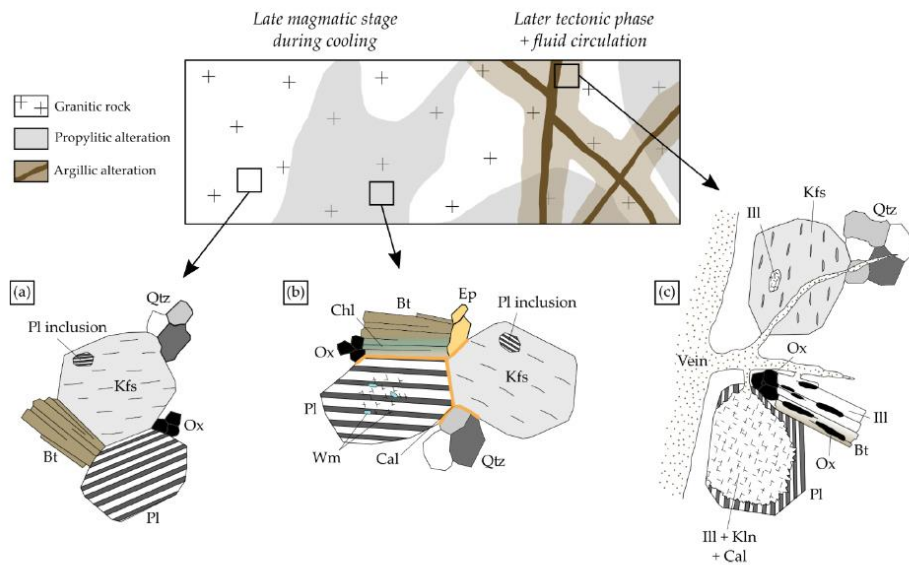


Figure 17. Schematic representation of the different alteration processes which can be observed in the OM and NH granites. (a) Fresh granite non-affected by alteration. (b) Granite affected by the propylitic alteration showing the slight chloritization of biotite and the crystallization of K-white micas in the core of plagioclase. (c) Granite affected by the argillic alteration and localized along fractures where fluid has circulated. Biotite are locally completely transformed into illite and plagioclase into illite, calcite and/or kaolinite. Perthites and inclusions in K-feldspars can also be altered. Abbreviations (except for “Ox and Wm”) after [45]: Bt—Biotite, Cal—Calcite, Chl—Chlorite, Ep—Epidote, Ill—Illite, Kln—Kaolinite, Kfs—K-feldspar, Ox—Oxide, Pl—Plagioclase, Qtz—Quartz, Wm—K-white mica.

Plagioclase and quartz form an interconnected skeleton through the texture. The difference of physical and chemical behaviors between both minerals results in different types of porosity. Quartz shows microcracks and plagioclase shows dissolution pits (Figure 18). Ref. [95] observed the same in the Soultz-sous-Forêts granite. They also showed that the exchange surface between plagioclase and a fluid is around 20 times higher than in quartz. As a consequence, they assume that all the pores are interconnected in plagioclase. They considered this mineral as the main path for fluid flow. Thus, this can be also available in the NH granite. K-feldspar is not affected by the alteration, but perthites and mineral inclusions present in the K-feldspars can be dissolved.

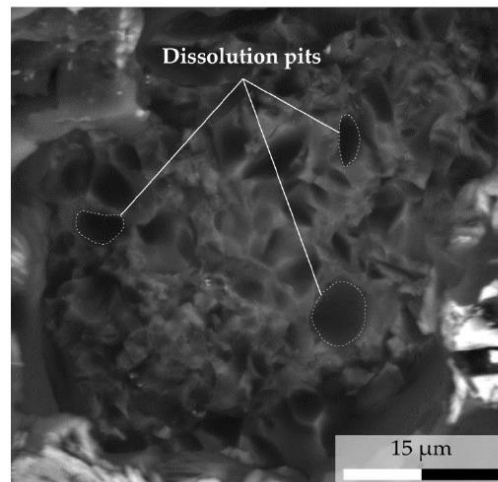


Figure 18. Back-scattered image showing a magnified view of plagioclase dissolution pits under SEM (15 kV 5.3 mm × 1.7 k BSECOMP).

The crystallization of these minerals occurs at temperature between 130 and 200 °C. This range of temperature corresponds to the stage of argillic alteration [84]. The argillic alteration (Figure 17c) consists into the chemical leaching and clay enrichment processes produced at lower temperatures [19,88,96]. This alteration is known as a vein alteration organized in the vicinity of fractures where fluids have circulated [86,88].

5.3.3. Evidences of Weathering

XRD analyses on an oriented sample of the clay fraction from the OM reveal the presence of Montmorillonite (Mnt) (Figure 8). Mnt, a common smectite pattern, results either from argillic (vein) alteration [84,89] or from weathering [97,98]. As described above, the OM granite appears as “fresh” from (1) field observations: no veins were observed at outcrop scale and macro-scale and the granite appears competent, (2) thin-section analyzes: no veins or veinlets, calcite crystallizations are only present at grain boundaries, and (3) geochemical analyzes, which indicate a very low LOI (0.7 wt.%). No vein was observed at any scale and secondary minerals are all characteristic of propylitic alteration. Those data show that the Mnt cannot result from argillic alteration. In the case of the OM granite, the Mnt is interpreted as a signature of weathering. As its amount is low (15% of the clay fraction), the global alteration of the granite is considered as being dominated by the propylitic alteration. With the OM being considered as the protolith, weathering can be considered negligible in both OM and NH granites.

5.3.4. Alteration Stage Occurrences

The OM granite presents evidence of propylitic alteration only, while the NH granite presents both propylitic and argillic facies. The argillic facies seems most of the time to overprinting the propylitic facies. However, some samples present only evidence of argillic alteration. In those cases, either the propylitic facies have either completely disappeared, or some zones were not initially affected by the propylitic alteration. Some minerals, such as illite and kaolinite, crystallize during the argillic alteration under different conditions [84]. This suggests that several episodes of alteration could have occurred in the NH granite. Afterward, weathering can occur at ambient temperature, when the granite was exhumed. These alteration overprints result also in a retrograde evolution in terms of temperature (T) with $T_{\text{propylitic}} > T_{\text{argillic}} > T_{\text{weathering}}$.

In the NH granite, the argillic alteration seems to be associated to fracturing. A fresh granitic rock is not permeable enough to allow fluid circulation [6]. This suggests that the development of fractures is an important factor allowing fluid to circulate [6], the observation that the freshest NH granite is more altered than the one from the OM (Figure 3) can be related to the fact that the NH lie along an important shear corridor. None of NH samples considered in the present study are fracture free, even though they were collected far from the faults, and each of them shows evidences of argillic alteration. In spite of the low fracture density the existing number of microfractures is enough to allow fluid to significantly percolate through the host rocks and chemically interact with it. A second paper (PART 2, this issue) focusses on the role of the fracture system on the granite alteration processes.

5.4. Effects of Alteration on Petrographic and Petrophysical Behaviour

Petrographic observations and the range of LOI (0.7–4.1 wt.%) values confirm that the NH granite experienced alteration. LOI is so directly related to the degree of mineral alteration as done by [99,100]. Mineral changes being related to the propylitic and argillic alterations, the LOI can be defined in this study as a monitor for alteration processes. The effects of alteration on element transfers can be evaluated thanks to the diagrams plotting SiO_2 , Al_2O_3 , CaO , K_2O , Na_2O and MgO against LOI (Figure 13). In Figure 13, the K_2O , Na_2O , CaO and MgO define a broad correlation with LOI, indicating that they may have been mobile during alteration [99]. The NH granite shows that Na_2O and CaO have a negative correlation which can be related to the alteration of the plagioclase (oligoclase initial composition). Indeed, plagioclase can be depleted in Na and Ca mobile elements when it interacts with a fluid [101]. Likewise, the K_2O is observed in alteration products of plagioclase as illite and shows an enrichment with the LOI increase. Newly formed minerals, as presented above, are related to the recrystallization of the plagioclase as a result of its interaction with the fluid. As for the CaO and MgO contents, they remain high compared to the OM granite. This can be linked to an external contribution. In a whole, the NH granite was affected by an alkali alteration, which results in major compositional changes. Thus, all the elements, Si and Al excepted, have partly left the system, meaning that the system is open. Their content differences in the NH granite compared to the OM granite could be explained by the depletion of the most mobile elements during the alteration of the NH granite. This can so influence the percentage of each element. Otherwise, it can be suggested that the visible variations of SiO_2 and Al_2O_3 were controlled by protolith composition rather than alteration processes.

Link alteration degree and amount of calcite is difficult since petrographic analyses of the samples is qualitative. However, Figure 15a shows a positive correlation between LOI and calcite content. Ledésert et al. (2009) [61] show that calcite can be encountered in high amount in altered zones. Thus, in the NH, the correlation shows that the higher the calcite content, the higher the degree of alteration and vice versa. In the same way, LOI can be related to porosity (Figure 15b) with a low LOI linked to low porosity (NH_1, NH_2 and NH_10) and high LOI linked to as high porosity (NH_3). Therefore, the increase of porosity is also linked to the increase of alteration. Studies [102,103] showed that the porosity increases from unaltered to altered granite. Figure 15c shows a similar correlation between the calcite content and the porosity. Samples having a low calcite content (NH1, NH_2, NH_5 and NH_10) present a low porosity, while NH_3 has a high calcite content associated with a high porosity. One exception can be observed. The sample NH_7 presents a low calcite content for a high porosity. This can be explained by the presence of larger microfractures compared to the other samples, which increase the porosity. Thus, it is not always possible to link the porosity to the calcite content. According to [104], the average calcite content of a fresh granite is 0.252 wt.%, and does not exceed 1.8 wt.%. As a consequence, measurements over this last value can be regarded as a calcite anomaly, and so are representative of a granite affected by argillic alteration, which may be a sign of paleo fluid flow [94]. Ten samples out of fifteen from the NH have a calcite content higher

than 1.8 wt.%. This suggests that the OM and some zones of the NH were not affected by the argillic alteration, but only by the propylitic one. By considering the calcite content average of 2.2% for the NH, those data also indicate that even if the samples were collected far from the major faults, the granite can be affected by argillic alteration.

5.5. The NH: A Paleo-Geothermal Reservoir?

In the present contribution we have given numerous pieces of evidences for a pervasive alteration of the NH granite. Ubiquitous argillic alteration affecting plagioclase and biotite is present. The K-feldspar being unaltered, potassium enrichment by incoming fluids is necessary to produce abundant amount of illite. The high concentration of calcite, in some samples, requires an external input of Ca, which cannot come only from the plagioclase alteration. Due to this alteration, the rock porosity was drastically enhanced by dissolution of the plagioclase. Porosity is also enhanced by the microfracturing well visible in quartz and K-feldspar, which is related to the activity of the SDVFZ. It is believed that this microfracturing drastically enhanced interaction surfaces between minerals and fluids allowing chemical elements exchanges between hydrothermal fluids and the granite. The strain is not homogeneously distributed in the NH. The NH granite is affected either by non-localized deformation (samples from this study) or by strain concentrations along fault zones that will be presented in the accompanying contribution (PART 2, this issue).

Our results have shown that an alteration of vast volumes of rocks is thus possible, even outside localized high strain zones. All these data are in favor of a hydrothermal fluid percolation, which is encountered in an exploited geothermal reservoir [6,19]. A geothermal reservoir consisting into a flow system where a high amount of hot fluid is stored and circulates through the rock, and our results encourage to consider the NH as a paleo-geothermal reservoir.

6. Conclusions

The NH were chosen in the framework of the H2020 MEET project as being an opportunity to characterize a granitic paleo-geothermal reservoir in a trans-tensional context. Arid conditions and a 3D exposure were important criteria allowing the thorough characterization of the granite. The aim of this study was to characterize the granite pervasive alteration processes, away from the fractures, in terms of changes of mineralogical, geochemical and related petrophysical properties.

Illite was identified by XRD in all the NH samples, allowing to obtain KI values which revealed a NW-SE temperature gradient through the range. This gradient might be considered as a sign of a possible exhumation of the southern part of the range due to the interaction with the Avawatz Mountains.

The partial recrystallization of plagioclase and biotite into newly formed minerals, due to fluid/rock interactions, was identified as reflecting three types of alteration:

1. A pervasive propylitic alteration. This alteration is present in the OM granite (the freshest one considered as the protolith) and in the NH granite and characterized by the presence of corrensite and/or epidote.
2. A local argillic alteration. This alteration was identified only locally in the NH granite by the occurrence of clay minerals such as kaolinite, illite/smectite mixed-layers and illite, all of which crystallize at a lower temperature than the propylitic alteration. Kaolinite and illite might reflect a different amount of leaching or different pH, meaning that several fluids have circulated.
3. Weathering identified in the OM granite by the presence of montmorillonite, thus formed at surface temperature.

The NH granite alteration was highlighted by optical observations. In addition, geochemistry also provided data to support them. Indeed, depletion of Na and Ca was observed with the increase of LOI, considered as a good indicator of the amount of alteration of plagioclase alteration. At the same time, K enrichment was observed with the increase of LOI, and linked to illite crystallization. Calcimetry performed on the NH granite

samples showed a calcite content often higher than the 1.8% value, admitted as being the maximum in a fresh granite. These values tend to increase with the LOI, confirming that the NH granite underwent alteration. Porosity also shows a positive correlation with the LOI indicating that the porosity increases with the amount of alteration. However, its correlation with the calcite content is less obvious, as calcite might crystallize in the porosity and thus reduce it.

The NH granite underwent up to two stages of alteration before being exposed to surface conditions, showing a retrograde evolution. It was observed petrographically that the argillic alteration overprinted the propylitic alteration, until its signature is lost. The weathering signal is low (~15% of the clay fraction) and considered as negligible in the OM. The OM being considered as the protolith of the NH, the contribution of weathering is also considered as negligible in the NH granite, where no montmorillonite was found. The newly formed minerals are thus considered as being the product of hydrothermal alteration and not of weathering.

This study provides multiple evidence allowing the consideration of the NH granite as a paleo-geothermal reservoir.

The activity of a geothermal reservoir is a combination of pervasive circulation within nearly strain-free zones (as shown in the present contribution), as well as fractured domains where high strain is accumulated. Our study is therefore completed by a PART 2 (this issue), in which the same investigation approach is dedicated to samples taken within visibly fractured zones.

Author Contributions: Conceptualization, J.K., S.P., B.A.L., R.L.H., A.C. and G.T.; methodology, J.K., S.P., B.A.L., R.L.H., A.C. and G.T.; software, J.K.; validation, S.P., B.A.L., R.L.H., A.C., P.B. and G.T.; formal analysis, J.K.; investigation, J.K., S.P., B.A.L., R.L.H. and G.T.; resources, J.K.; data curation, J.K., S.P., B.A.L., R.L.H., A.C. and G.T.; writing—original draft preparation, J.K.; writing—review and editing, S.P., B.A.L., R.L.H., A.C., G.T. and P.B. and H2020 MEET consortium; visualization, S.P., B.A.L., R.L.H., A.C., G.T. and P.B.; supervision, J.K.; project administration, G.T.; funding acquisition, G.T. and H2020 MEET consortium. All authors have read and agreed to the published version of the manuscript.

Funding: This project has received funding from the European Union’s Horizon 2020 research and innovation program under grant agreement No 792037 (H2020 MEET project).

Data Availability Statement: Not applicable.

Acknowledgments: This manuscript was prepared as a contribution to the PhD thesis (Institut Polytechnique UniLaSalle Beauvais) of Johanne Klee, which was funded by the European Union’s Horizon 2020 research and innovation program under grant agreement No 792037 (H2020 MEET project). The authors are grateful to Terry Pavlis for his knowledge and helpful discussions about the regional geology of Death Valley and the Noble Hills. We also acknowledge Albert Genter for the fruitful exchanges about granite alteration processes. We thank Thi Tuyen Nguyen, Elena Pavlovskaia, Carl Tixier and Chloé Gindrat for their help for analyses. Helpful comments and the validation of the manuscript by the H2020 MEET consortium are gratefully acknowledged. We finally would like to thank Catherine Lerouge and the anonymous reviewer for their help and remarks to improve this manuscript.

Conflicts of Interest: The authors declare no conflict of interest.

References

1. Williams, C.F.; Reed, M.J.; Anderson, A.F. Updating the classification of geothermal resources. In Proceedings of the Thirty Sixth Workshop on Geothermal Reservoir Engineering Stanford University, Stanford, CA, USA, 31 January–2 February 2011.
2. Moeck, I.S. Catalog of geothermal play types based on geologic controls. *Renew. Sustain. Energy Rev.* **2014**, *37*, 867–882. [[CrossRef](#)]
3. Olasolo, P.; Juárez, M.C.; Morales, M.P.; D’Amico, S.; Liarte, I.A. Enhanced Geothermal Systems (EGS): A Review. *Renew. Sustain. Energy Rev.* **2016**, *56*, 133–144. [[CrossRef](#)]
4. Trullenque, G.; Genter, A.; Leiss, B.; Wagner, B.; Bouchet, R.; Leoutre, E.; Malnar, B.; Bär, K.; Rajšl, I. Upscaling of EGS in different geological conditions: A European perspective. In Proceedings of the 43rd Workshop on Geothermal Reservoir Engineering Stanford University, Stanford, CA, USA, 12–14 February 2018; p. 10.

5. Faulds, J.E.; Hinz, N.H.; Dering, G.M.; Siler, D.L. The hybrid model—The most accommodating structural setting for geothermal power generation in the Great Basin, Western USA. *Geotherm. Resour. Coun. Trans.* **2013**, *37*, 3–10.
6. Nishimoto, S.; Yoshida, H. Hydrothermal alteration of deep fractured granite: Effects of dissolution and precipitation. *Lithos* **2010**, *115*, 153–162. [[CrossRef](#)]
7. Dezayes, C.; Lerouge, C. Reconstructing paleofluid circulation at the hercynian basement/mesozoic sedimentary cover interface in the Upper Rhine Graben. *Geofluids* **2019**, *2019*, 1–30. [[CrossRef](#)]
8. Plumper, O.; Putnis, A. The complex hydrothermal history of granitic rocks: Multiple feldspar replacement reactions under subsolidus conditions. *J. Petrol.* **2009**, *50*, 967–987. [[CrossRef](#)]
9. Inoue, A. Formation of clay minerals in hydrothermal environments. In *Origin and Mineralogy of Clays*; Velde, B., Ed.; Springer: Berlin/Heidelberg, Germany, 1995; pp. 268–329. ISBN 978-3-642-08195-8.
10. Burchfiel, B.C.; Stewart, J.H. “Pull-apart” origin of the central segment of Death Valley, California. *GSA Bull.* **1966**, *77*, 439–442. [[CrossRef](#)]
11. Pavlis, T.L.; Trullenque, G. Evidence for 40–41 km of dextral slip on the Southern Death Valley fault: Implications for the Eastern California shear zone and extensional tectonics. *Geology* **2021**, *49*, 767–772. [[CrossRef](#)]
12. Chabani, A.; Trullenque, G.; Ledésert, B.A.; Klee, J. Multiscale Characterization of fracture patterns: A case study of the Noble Hills Range (Death Valley, CA, USA), application to geothermal reservoirs. *Geosciences* **2021**, *11*, 280. [[CrossRef](#)]
13. Kisch, H.J. Correlation between indicators of very low-grade metamorphism. In *Low Temperature Metamorphism*; Frey, M., Ed.; Chapman & Hall: London, UK, 1987; pp. 227–300.
14. Árkai, P.; Sassi, F.; Desmons, J. Very low- to low-grade metamorphic rocks. In *Metamorphic Rocks A Classification and Glossary Terms*; Cambridge University Press: Cambridge, UK, 2007.
15. Frey, M. Very low-grade metamorphism of clastic sedimentary rocks. In *Low Temperature Metamorphism*; Chapman & Hall: London, UK, 1987; pp. 9–58.
16. Árkai, P.; Maehlmann, R.; Suchy, V.; Balogh, K.; Sykorová, I.; Frey, M. Possible Effects of Tectonic Shear Strain on Phyllosilicates: A Case Study from the Kandersteg Area, Helvetic Domain, Central Alps, Switzerland. *TMPM Tschermaks Mineral. Petrogr. Mitt.* **2002**, *82*, 273–290.
17. Mullis, J.; Máhlmann, R.F.; Wolf, M. Fluid Inclusion Microthermometry to Calibrate Vitrinite Reflectance (between 50 and 270 °C), Illite Kübler-Index Data and the Diagenesis/Anchizone Boundary in the External Part of the Central Alps. *Appl. Clay Sci.* **2017**, *143*, 307–319. [[CrossRef](#)]
18. Ferreiro Máhlmann, R.; Bozkaya, Ö.; Potel, S.; le Bayon, R.; Šegvič, B.; Nieto, F. The Pioneer Work of Bernard Kübler and Martin Frey in Very Low-Grade Metamorphic Terranes: Paleo-Geothermal Potential of Variation in Kübler-Index/Organic Matter Reflectance Correlations. A Review. *Swiss. J. Geosci.* **2012**, *105*, 121–152. [[CrossRef](#)]
19. Ledésert, B.; Berger, G.; Meunier, A.; Genter, A.; Bouchet, A. Diagenetic-Type Reactions Related to Hydrothermal Alteration in the Soultz-Sous-Forets Granite, France. *Eur. J. Mineral.* **1999**, *11*, 731–741. [[CrossRef](#)]
20. Wernicke, B.; Axen, G.J.; Snow, J.K. Basin and Range Extensional Tectonics at the Latitude of Las Vegas, Nevada. *GSA Bull.* **1988**, *100*, 1738–1757. [[CrossRef](#)]
21. Wright, L. Late Cenozoic Fault Patterns and Stress Fields in the Great Basin and Westward Displacement of the Sierra Nevada Block. *Geology* **1976**, *4*, 489–494. [[CrossRef](#)]
22. Wernicke, B.; Spencer, J.E.; Burchfiel, B.C.; Guth, P.L. Magnitude of Crustal Extension in the Southern Great Basin. *Geology* **1982**, *10*, 499–502. [[CrossRef](#)]
23. Stewart, J.H. Extensional Tectonics in the Death Valley Area, California: Transport of the Panamint Range Structural Block 80 Km Northwestward. *Geology* **1983**, *11*, 153–157. [[CrossRef](#)]
24. Calzia, J.P.; Rämö, O.T. Late Cenozoic Crustal Extension and Magmatism, Southern Death Valley Region, California. *GSA Field Guides* **2000**, *2*, 135–164. [[CrossRef](#)]
25. Norton, I. Two-Stage Formation of Death Valley. *Geosphere* **2011**, *7*, 171–182. [[CrossRef](#)]
26. Luckow, H.; Pavlis, T.; Serpa, L.; Guest, B.; Wagner, D.; Snee, L.; Hensley, T.; Korjenkov, A. Late Cenozoic Sedimentation and Volcanism during Transtensional Deformation in Wingate Wash and the Owlshead Mountains, Death Valley. *Earth Sci. Rev.* **2005**, *73*, 177–219. [[CrossRef](#)]
27. Hill, M.L.; Troxel, B.W. Tectonics of Death Valley Region, California. *GSA Bull.* **1966**, *77*, 435–438. [[CrossRef](#)]
28. Butler, P.R.; Troxel, B.W.; Verosub, K.L. Late Cenozoic History and Styles of Deformation along the Southern Death Valley Fault Zone, California. *GSA Bull.* **1988**, *100*, 402–410. [[CrossRef](#)]
29. Brady, R.H., III. Cenozoic Geology of the Northern Avawatz Mountains in Relation to the Intersection of the Garlock and Death Valley Fault Zones, San Bernardino County, California. Ph.D. Thesis, University of California, Berkeley, CA, USA, 1986.
30. Brady, R.H.; Clayton, J.; Troxel, B.W.; Verosub, K.L.; Cregan, A.; Abrams, M. Thematic Mapper and Field Investigations at the Intersection of the Death Valley and Garlock Fault Zones, California. *Remote Sens. Environ.* **1989**, *28*, 207–217. [[CrossRef](#)]
31. Lifton, Z.M.; Newman, A.V.; Frankel, K.L.; Johnson, C.W.; Dixon, T.H. Insights into Distributed Plate Rates across the Walker Lane from GPS Geodesy. *Geophys. Res. Lett.* **2013**, *40*, 4620–4624. [[CrossRef](#)]
32. Nagorsen-Rinke, S.; Lee, J.; Calvert, A. Pliocene Sinistral Slip across the Adobe Hills, Eastern California-Western Nevada: Kinematics of Fault Slip Transfer across the Mina Deflection. *Geosphere* **2013**, *9*, 37–53. [[CrossRef](#)]







33. Miller, M.B.; Wright, L.A. *Geology of Death Valley National Park*, 3rd ed.; Kendall Hunt Publishing Company: Dubuque, IA, USA, 2015.
34. Rämö, T.O.; Calzia, J.P.; Kosunen, P.J. Geochemistry of Mesozoic Plutons, Southern Death Valley Region, California: Insights into the Origin of Cordilleran Interior Magmatism. *Contrib. Mineral. Petrol.* **2002**, *143*, 416–437. [[CrossRef](#)]
35. Troxel, B.W.; Butler, P.R. *Rate of Cenozoic Slip on Normal Faults, South-Central Death Valley, California*; Department of Geology, University of California: Berkeley, CA, USA, 1979.
36. Butler, P.R. *Geology: Structural History and Fluvial Geomorphology of the Southern Death Valley Fault Zone, Inyo and San Bernardino Counties, California*. Ph.D. Thesis, University of California, Davis, CA, USA, 1984.
37. Brady, R.H.; Troxel, B.W. Stratigraphy and Tectonics of the Northern Avawatz Mountains at the Intersection of the Garlock and Death Valley Fault Zones, San Bernardino County, California. In *Quaternary Tectonics of Southern Death Valley, California—Field Trip Guide: Shoshone, California, Friends of the Pleistocene, Pacific Cell*; USGS: Shoshone, CA, USA, 1986; pp. 1–12.
38. Niles, J.H. Post-Middle Pliocene Tectonic Development of the Noble Hills, Southern Death Valley, California. Ph.D. Thesis, San Francisco State University, San Francisco, CA, USA, 2016.
39. Mahon, R.C.; Dehler, C.M.; Link, P.K.; Karlstrom, K.E.; Gehrels, G.E. Detrital Zircon Provenance and Paleogeography of the Pahump Group and Overlying Strata, Death Valley, California. *Precambrian Res.* **2014**, *251*, 102–117. [[CrossRef](#)]
40. DeCelles, P.G. Late Jurassic to Eocene Evolution of the Cordilleran Thrust Belt and Foreland Basin System, Western USA. *Am. J. Sci.* **2004**, *304*, 105–168. [[CrossRef](#)]
41. Stamm, J.F. *Geology at the Intersection of the Death Valley and Garlock Fault Zones, Southern Death Valley, California*. Ph.D. Thesis, Pennsylvania State University, State College, PA, USA, 1981.
42. Klee, J.; Trullenque, G.; Ledésert, B.; Potel, S.; Hébert, R.; Chabani, A.; Genter, A. Petrographic analyzes of fractured granites used as an analogue of the soultz-sous-forêts geothermal reservoir: Noble Hills, CA, USA. In Proceedings of the Extended Abstract, Reykjavik, Iceland, 26 May 2021.
43. Troxel, B.W. Right-Lateral Offset of ca. 28 Km along a Strand of the Southern Death Valley Fault Zone. *Calif. Geol. Soc. Am. Abstr. Programs* **1994**, *26*, 99.
44. Castaing, C.; Rabu, D. Apports de La Géologie à La Recherche et à l'Exploitation de Pierres de Taille (Roches Ornamentales et de Construction). Available online: <https://hal.archives-ouvertes.fr/hal-01860154> (accessed on 12 July 2021).
45. Kretz, R. Symbols for Rock-Forming Minerals. *Am. Mineral.* **1983**, *68*, 277–279.
46. Bisdorn, K.; Gauthier, B.D.M.; Bertotti, G.; Hardebol, N.J. Calibrating Discrete Fracture-Network Models with a Carbonate Three-Dimensional Outcrop Fracture Network: Implications for Naturally Fractured Reservoir Modeling. *AAPG Bull.* **2014**, *98*, 1351–1376. [[CrossRef](#)]
47. Gillespie, P.A.; Howard, C.B.; Walsh, J.J.; Watterson, J. Measurement and Characterisation of Spatial Distributions of Fractures. *Tectonophysics* **1993**, *226*, 113–141. [[CrossRef](#)]
48. Schmidt, D.; Schmidt, S.T.; Mullis, J.; Ferreira Mählmann, R.; Frey, M. Very Low Grade Metamorphism of the Taveyanne Formation of Western Switzerland. *Contrib. Mineral. Petrol.* **1997**, *129*, 385–403. [[CrossRef](#)]
49. Kisch, H.J. Illite Crystallinity: Recommendations on Sample Preparation, X-ray Diffraction Settings, and Interlaboratory Samples. *J. Metamorph. Geol.* **1991**, *9*, 665–670. [[CrossRef](#)]
50. Ferreira Mählmann, R.; Frey, M. Standardisation, Calibration and Correlation of the Kübler-Index and the Vitrinite/Bituminite Reflectance: An Inter-Laboratory and Field Related Study. *Swiss J. Geosci.* **2012**, *105*, 153–170. [[CrossRef](#)]
51. Moore, D.M.; Reynolds, R.C. X-ray diffraction and the identification and analysis of clay minerals. In *X-ray Diffraction and the Identification and Analysis of Clay Minerals*; Oxford University Press: Oxford, UK, 1989.
52. Starkey, H.C.; Blackmon, P.D.; Hauff, P.L. *The Routine Mineralogical Analysis of Clay-Bearing Samples*; United States Government Publishing Office: Washington, DC, USA, 1984.
53. Warr, L.N.; Rice, A.H.N. Interlaboratory Standardization and Calibration of Day Mineral Crystallinity and Crystallite Size Data. *J. Metamorph. Geol.* **1994**, *12*, 141–152. [[CrossRef](#)]
54. Kübler, B. La Cristallinité de l'illite et Les Zones Tout a Fait Superieures Du Metamorphisme. In *Etages Tectoniques*; van Bemmelen, R.W., Chapman, C.A., Watznauer, A., Eds.; La Baconniere: Boudry, Switzerland, 1981; pp. 105–121.
55. Warr, L.N.; Mählmann, R.F. Recommendations for Kübler Index Standardization. *Clay Minerals* **2015**, *50*, 283–286. [[CrossRef](#)]
56. Winkler, H.G.F. Anatexis, Formation of Migmatites, and Origin of Granitic Magmas. In *Petrogenesis of Metamorphic Rocks*; Winkler, H.G.F., Ed.; Springer Study Edition; Springer: New York, NY, USA, 1979; pp. 283–339. ISBN 978-1-4757-4215-2.
57. Tilley, C.E. A Preliminary Survey of Metamorphic Zones in the Southern Highlands of Scotland. *Q. J. Geol. Soc.* **1925**, *81*, 100–112. [[CrossRef](#)]
58. Barrow, G. On an Intrusion of Muscovite-Biotite Gneiss in the South-Eastern Highlands of Scotland, and Its Accompanying Metamorphism. *Q. J. Geol. Soc.* **1893**, *49*, 330–358. [[CrossRef](#)]
59. Merriman, R.J.; Frey, M. Patterns of very low-grade metamorphism in metapelitic rocks. In *Low-Grade Metamorphism*; Frey, M., Robinson, D., Eds.; Blackwell Publishing Ltd.: Oxford, UK, 1998; pp. 61–107. ISBN 978-1-4443-1334-5.
60. Abad, I. Physical meaning and applications of the Illite Kübler index: Measuring reaction progress in low-grade metamorphism. In *Diagenesis and Low-Temperature Metamorphism, Theory, Methods and Regional Aspects*; Sociedad Española de Mineralogía: Jaén, Spain, 2007; pp. 53–64.

61. Ledésert, B.; Hébert, R.L.; Grall, C.; Genter, A.; Dezayes, C.; Bartier, D.; Gérard, A. Calcimetry as a Useful Tool for a Better Knowledge of Flow Pathways in the Soultz-Sous-Forêts Enhanced Geothermal System. *J. Volcanol. Geotherm. Res.* **2009**, *181*, 106–114. [\[CrossRef\]](#)
62. Dullien, F.A.L. *Porous Media: Fluid Transport and Pore Structure*; Academic Press: San Diego, CA, USA, 1979; ISBN 978-0-323-13933-5.
63. Navelot, V.; Géraud, Y.; Favier, A.; Diraison, M.; Corsini, M.; Lardeaux, J.-M.; Verati, C.; Mercier de Lépinay, J.; Legendre, L.; Beauchamps, G. Petrophysical Properties of Volcanic Rocks and Impacts of Hydrothermal Alteration in the Guadeloupe Archipelago (West Indies). *J. Volcanol. Geotherm. Res.* **2018**, *360*, 1–21. [\[CrossRef\]](#)
64. Gates, W.P.; Nefiodovas, A.; Peter, P. Permeability of an Organo-Modified Bentonite to Ethanol-Water Solutions. *Clays Clay Miner.* **2004**, *52*, 192–203. [\[CrossRef\]](#)
65. Bard, J.P. *Microtextures des Roches Magmatiques et Métamorphiques*; Masson: Paris, France, 1980.
66. Goldich, S.S. A Study in Rock-Weathering. *J. Geol.* **1938**, *46*, 17–58. [\[CrossRef\]](#)
67. Que, M.; Allen, A.R. Sericitization of Plagioclase in the Rosses Granite Complex, Co. Donegal, Ireland. *Mineral. Mag.* **1996**, *60*, 927–936. [\[CrossRef\]](#)
68. Streckeisen, A.; Le Maître, R.W. A Chemical Approximation to Modal QAPF Classification of the Igneous Rocks. *Neues Jahrb. Mineral. Abh.* **1979**, *136*, 169–206.
69. Beaufort, D.; Baronnat, A.; Lanson, B.; Meunier, A. Corrensite; a Single Phase or a Mixed-Layer Phyllosilicate in Saponite-to-Chlorite Conversion Series? A Case Study of Sancerre-Couy Deep Drill Hole (France). *Am. Mineral.* **1997**, *82*, 109–124. [\[CrossRef\]](#)
70. Jagodzinski, H. Eindimensionale Fehlordnung in Kristallen und ihr Einfluss auf die Röntgeninterferenzen. I. Berechnung des Fehlordnungsgrades aus den Röntgenintensitäten. *Acta Cryst.* **1949**, *2*, 201–207. [\[CrossRef\]](#)
71. Cox, K.G. *The Interpretation of Igneous Rocks*; Springer Science & Business Media: London, UK, 1979; ISBN 978-94-017-3373-1.
72. Wilson, M. Review of Igneous Petrogenesis: A Global Tectonic Approach. *Terra Nova* **1989**, *1*, 218–222. [\[CrossRef\]](#)
73. Jensen, L.S. A New Plot for Classifying Subalkalic Volcanic Rocks. *Ont. Div. Mines Misc. Pap.* **1976**, *66*, 1–22.
74. White, A.J.R.; Chappell, B.W. Granitoid types and their distribution in the Lachlan Fold Belt, southeastern Australia. In *Geological Society of America Memoirs*; Geological Society of America: Boulder, CO, USA, 1983; Volume 159, pp. 21–34, ISBN 978-0-8137-1159-1.
75. Le Maître, R.W.; Bateman, P.; Dudek, A.; Keller, J.; Lameyre Le Bas, M.J.; Sabine, P.A.; Schmid, R.; Sorensen, H.; Streckeisen, A.; Woolley, A.R.; et al. *A Classification of Igneous Rocks and Glossary of Terms*; Blackwell: Oxford, UK, 1989.
76. Rollinson, H.R. *Using Geochemical Data: Evaluation, Presentation, Interpretation*; Routledge: Abingdon, UK, 1993; ISBN 978-1-317-89819-1.
77. Boynton, W.V. Cosmochemistry of the rare earth elements: Meteorite studies. In *Developments in Geochemistry*; Elsevier: Amsterdam, The Netherlands, 1984; Volume 2, pp. 63–114. ISBN 978-0-444-42148-7.
78. McDonough, W.; Sun, S.-S.; Ringwood, A.; Jagoutz, E.; Hofmann, A. Potassium, Rubidium, and Cesium in the Earth and Moon and the Evolution of the Mantle of the Earth. *Geochim. Cosmochim. Acta* **1992**, *56*, 1001–1012. [\[CrossRef\]](#)
79. Sun, S.; McDonough, W.F. Chemical and Isotopic Systematics of Oceanic Basalts: Implications for Mantle Composition and Processes. *Geol. Soc. Lond. Spec. Publ.* **1989**, *42*, 313–345. [\[CrossRef\]](#)
80. Koljonen, T.; Rosenberg, R.J. Rare Earth Elements in Granitic Rocks. *Lithos* **1974**, *7*, 249–261. [\[CrossRef\]](#)
81. Alderton, D.H.M.; Pearce, J.A.; Potts, P.J. Rare Earth Element Mobility during Granite Alteration: Evidence from Southwest England. *Earth Planet. Sci. Lett.* **1980**, *49*, 149–165. [\[CrossRef\]](#)
82. Li, X.-C.; Fan, H.-R.; Santosh, M.; Hu, F.-F.; Yang, K.-F.; Lan, T.-G. Hydrothermal Alteration Associated with Mesozoic Granite-Hosted Gold Mineralization at the Sanshandao Deposit, Jiaodong Gold Province, China. *Ore Geol. Rev.* **2013**, *53*, 403–421. [\[CrossRef\]](#)
83. Warr, L.N.; Cox, S.C. Correlating Illite (Kübler) and Chlorite (Árkai) “Crystallinity” Indices with Metamorphic Mineral Zones of the South Island, New Zealand. *Appl. Clay Sci.* **2016**, *134*, 164–174. [\[CrossRef\]](#)
84. Fulignati, P. Clay Minerals in Hydrothermal Systems. *Minerals* **2020**, *10*, 919. [\[CrossRef\]](#)
85. Creasey, S.C. Hydrothermal alteration. In *Geology of the Porphyry Copper Deposits Southwestern North America*; Titley & Hicks: Tucson, AZ, USA, 1966; pp. 51–74.
86. Traineau, H.; Genter, A.; Cautru, J.P.; Fabriol, H.; Chevremont, P. Petrography of the Granite Massif from Drill Cutting Analysis and Well Log Interpretation in the Geothermal HDR Borehole GPK1 (Soultz, Alsace, France). *Geotherm. Sci. Technol.* **1991**, *3*, 1–29.
87. Środoń, J. Nature of Mixed-Layer Clays and Mechanisms of Their Formation and Alteration. *Annu. Rev. Earth Planet. Sci.* **1999**, *27*, 19–53. [\[CrossRef\]](#)
88. Genter, A. Géothermie Roches Chaudes Sèches: Le Granite de Soultz-Sous-Forêts (Bas-Rhin, France): Fracturation Naturelle, Altérations Hydrothermales et Interaction Eau-Roche. Ph.D. Thesis, Université d’Orléans, Orléans, France, 1989.
89. Burnham, C.W. Facies and Types of Hydrothermal Alteration. *Econ. Geol.* **1962**, *57*, 768–784. [\[CrossRef\]](#)
90. Velde, B. *Clays and Clay Minerals in Natural and Synthetic Systems*; Development in Sedimentology; Elsevier: Amsterdam, The Netherlands, 1977; ISBN 978-0-08-086933-9.
91. Steiner, A. Clay Minerals in Hydrothermally Altered Rocks at Wairakei, New Zealand. *Clays Clay Miner.* **1968**, *16*, 193–213. [\[CrossRef\]](#)
92. Ledésert, B.; Hébert, R.; Genter, A.; Bartier, D.; Clauer, N.; Grall, C. Fractures, Hydrothermal Alterations and Permeability in the Soultz Enhanced Geothermal System. *Comptes Rendus Geosci.* **2010**, *342*, 607–615. [\[CrossRef\]](#)

93. Vidal, J.; Patrier, P.; Genter, A.; Beaufort, D.; Dezayes, C.; Glaas, C.; Lerouge, C.; Sanjuan, B. Clay Minerals Related to the Circulation of Geothermal Fluids in Boreholes at Rittershoffen (Alsace, France). *J. Volcanol. Geotherm. Res.* **2018**, *349*, 192–204. [[CrossRef](#)]
94. Ledésert, B.A.; Hébert, R.L. How Can Deep Geothermal Projects Provide Information on the Temperature Distribution in the Upper Rhine Graben? The Example of the Soultz-Sous-Forêts-Enhanced Geothermal System. *Geosciences* **2020**, *10*, 459. [[CrossRef](#)]
95. Sardini, P.; Ledésert, B.; Touchard, G. Quantification of microscopic porous networks by image analysis and measurements of permeability in the Soultz-Sous-Forêts Granite (Alsace, France). In *Fluid Flow and Transport in Rocks: Mechanisms and Effects*; Jamtveit, B., Yardley, B.W.D., Eds.; Springer: Dordrecht, The Netherlands, 1997; pp. 171–189. ISBN 978-94-009-1533-6.
96. Glaas, C.; Patrier, P.; Vidal, J.; Beaufort, D.; Genter, A. Clay Mineralogy: A Signature of Granitic Geothermal Reservoirs of the Central Upper Rhine Graben. *Minerals* **2021**, *11*, 479. [[CrossRef](#)]
97. Meunier, A.; Velde, B.D.; Dudoignon, P.; Beaufort, D. Identification of Weathering and Hydrothermal Alteration in Acidic Rocks: Petrography and Mineralogy of Clay Minerals. *Sci. Géologiques Bull. Mémoires* **1983**, *72*, 93–99.
98. Tardy, Y.; Paquet, H.; Millot, G. Trois modes de genèse des montmorillonites dans les altérations et les sols. *Bull. Groupe Français Argiles* **1970**, *22*, 69–77. [[CrossRef](#)]
99. Liu, Y.; Xie, C.; Li, C.; Li, S.; Santosh, M.; Wang, M.; Fan, J. Breakup of the Northern Margin of Gondwana through Lithospheric Delamination: Evidence from the Tibetan Plateau. *GSA Bull.* **2018**, *131*. [[CrossRef](#)]
100. Chambeffort, I.; Moritz, R.; von Quadt, A. Petrology, Geochemistry and U-Pb Geochronology of Magmatic Rocks from the High-Sulfidation Epithermal Au–Cu Chelopech Deposit, Srednogie Zone, Bulgaria. *Miner. Depos.* **2007**, *42*, 665–690. [[CrossRef](#)]
101. Garrels, R.M.; MacKenzie, F.T. Origin of the Chemical Compositions of Some Springs and Lakes. In *Equilibrium Concepts in Natural Water Systems*; Advances in Chemistry; American Chemical Society: Washington, DC, USA, 1967; Volume 67, pp. 222–242. ISBN 978-0-8412-0068-5.
102. Rosener, M.; Géraud, Y. Using Physical Properties to Understand the Porosity Network Geometry Evolution in Gradually Altered Granites in Damage Zones. *Geol. Soc. Lond. Spec. Publ.* **2007**, *284*, 175–184. [[CrossRef](#)]
103. Cassiaux, M.; Proust, D.; Siitari-Kauppi, M.; Sardini, P.; Leutsch, Y. Clay Minerals Formed during Propylitic Alteration of a Granite and Their Influence on Primary Porosity: A Multi-Scale Approach. *Clays Clay Miner.* **2006**, *54*, 541–554. [[CrossRef](#)]
104. White, A.F.; Schulz, M.S.; Lowenstern, J.B.; Vivit, D.V.; Bullen, T.D. The Ubiquitous Nature of Accessory Calcite in Granitoid Rocks: Implications for Weathering, Solute Evolution, and Petrogenesis. *Geochim. Cosmochim. Acta* **2005**, *69*, 1455–1471. [[CrossRef](#)]

Article

Fluid-Rock Interactions in a Paleo-Geothermal Reservoir (Noble Hills Granite, California, USA). Part 2: The Influence of Fracturing on Granite Alteration Processes and Fluid Circulation at Low to Moderate Regional Strain

Johanne Klee ^{1,*} , Arezki Chabani ¹ , Béatrice A. Ledésert ² , Sébastien Potel ¹ , Ronan L. Hébert ²  and Ghislain Trullenque ¹ 

¹ B2R, Geosciences Department, Institut Polytechnique UniLaSalle Beauvais, 19 Rue Pierre Waguet, F-60026 Beauvais, France; arezki.chabani@unilasalle.fr (A.C.); sebastien.potel@unilasalle.fr (S.P.); ghislain.trullenque@unilasalle.fr (G.T.)

² Geosciences and Environment Cergy, CY Cergy Paris Université, 1 Rue Descartes, F-95000 Neuville-sur-Oise, France; beatrice.ledesert@cyu.fr (B.A.L.); ronan.hebert@cyu.fr (R.L.H.)

* Correspondence: johanne.klee@unilasalle.fr; Tel.: +33-6-06-93-90-07



Citation: Klee, J.; Chabani, A.; Ledésert, B.A.; Potel, S.; Hébert, R.L.; Trullenque, G. Fluid-Rock Interactions in a Paleo-Geothermal Reservoir (Noble Hills Granite, California, USA). Part 2: The Influence of Fracturing on Granite Alteration Processes and Fluid Circulation at Low to Moderate Regional Strain. *Geosciences* **2021**, *11*, 433. <https://doi.org/10.3390/geosciences11110433>

Academic Editors: Michael G. Pettersson and Jesus Martinez-Frias

Received: 23 September 2021

Accepted: 18 October 2021

Published: 20 October 2021

Publisher's Note: MDPI stays neutral with regard to jurisdictional claims in published maps and institutional affiliations.



Copyright: © 2021 by the authors. Licensee MDPI, Basel, Switzerland. This article is an open access article distributed under the terms and conditions of the Creative Commons Attribution (CC BY) license (<https://creativecommons.org/licenses/by/4.0/>).

Abstract: Fracture connectivity within fractured granitic basement geothermal reservoirs is an important factor controlling their permeability. This study aims to improve the understanding of fluid–rock interaction processes at low to moderate regional strain. The Noble Hills range (Death Valley, CA, USA) was chosen as a naturally exhumed paleo geothermal reservoir. A series of petrographic, petrophysical, and geochemical investigations, combined with a fracture distribution analysis, were carried out on samples collected across fracture zones. Our results indicate that several generations of fluids have percolated through the reservoir. An increase of (1) the alteration degree; (2) the porosity values; and (3) the calcite content was observed when approaching fracture zones. No correlation was identified among the alteration degree, the porosity, or the calcite content. At a local scale, samples showed that the degree of alteration does not necessarily depend on the fracture density or on the amount of the strain. It is concluded that the combined influence of strain and coeval fluid–rock interaction processes drastically influence the petrophysical properties of fracture zones, which in turn impact geothermal production potential.

Keywords: fracturing processes; fluid circulation; granite alteration; low to moderate regional strain; geothermal reservoir

1. Introduction

Long-term exploitation of geothermal resources is closely linked to reservoir rock petrophysical properties and regional geological settings [1]. Due to the low matrix porosity and permeability of granitic rocks, underground granitic units are considered as a reservoir only when fractures are present. These fractures provide the essential reservoir permeability and porosity for fluid flow [2,3] and are therefore of primary importance regarding geothermal exploitation [4–8]. These structures control the deep flow at the reservoir scale, in case of good connectivity [2,3,9–11], which is one of the most important controls on the permeability [12]. Several granitic reservoirs, as Soultz-sous-Forêts in the Upper Rhine Graben, France [6,13] or the Cooper Basin in Australia [14], give invaluable experience in terms of exploration and exploitation feedback. In addition to these datasets gained from data limited to boreholes and indirect geophysical methods, studies of surface reservoir analogues are common [15–17]. The MEET H2020 project (Multidisciplinary and multi-context demonstration of EGS exploration and Exploitation Techniques and potentials) [18] aims to develop enhanced geothermal systems throughout Europe. Within this project, the Noble Hills (NH) range, located in the southern termination of the Death

Valley (DV, CA, USA), has been chosen as an analogue of fractured granitic basements in a context of transtensional deformation [19]. Klee et al. (2021) [19] highlighted numerous evidences of hydrothermal alterations: (1) a propylitic alteration affecting pervasively a large volume of rock during the cooling of the pluton and (2) an argillic alteration, also called vein alteration [19–23], inducing changes of the bulk-rock chemical and mineralogical compositions and of physical properties [7,24].

A vast amount of literature [9,11,25] has proven that increasing amounts of strain within fault zones drastically change their petrophysical properties. The present paper focuses on the influence of fractures on the fluid circulation and alteration processes at low to moderate regional strain.

The present study aims to:

1. Characterize the relations among the varying amounts of strain, fracture densities, and alteration degrees at the NH scale, as well as the sample scales through the case studies.
2. Characterize the variations in (1) chemical elements concentrations; (2) calcite content; (3) porosity; and (4) temperature condition variations when approaching fracture zones.
3. Identify the different fluid circulation episodes through the granite body.

Macroscopic and microscopic petrographic studies, XRD mineralogical characterization of whole rock and clay minerals, bulk rock chemical analyses by inductively coupled plasma (ICP), mass spectrometry (MS), atomic emission spectrometry (AES), scanning electron microscopy coupled with energy dispersive spectrometry (SEM-EDS) for structural observation and local chemical analyses, mass balance calculations, fracture density calculations, calcimetry, and porosimetry, were performed on samples collected in the vicinity of fracture zones within areas of the NH affected by low to moderate regional transcurrent strains. The results will be discussed and compared with the protolith studied by [19].

2. Geological Setting

The Death Valley (DV, Figure 1a) is located in the core of a Cenozoic distributed system of dextral strike-slips, about 700 km long, comprising the Walker Lane Belt and the Eastern California Shear Zone (ECSZ/WLB) [26–29]. This narrow northwest-trending system, lying between the Basin and Range region to the east and the Sierra Nevada batholith to the west [28], today accommodate ~25% of the Pacific-North America relative motion [26,30]. DV is a structural depression, NNW-SSE oriented, bounded by the Black and Funeral Mountains to the west and by the Panamint Range to the east [31]. It has been formed by a right-lateral movement giving a pull-apart structure [32].

The area of interest for this study is the Noble Hills range (NH, Figure 1b). It is located in the southernmost part of the DV region and trends parallel to the NW-striking SDVFZ at its southern end. Geological markers along the SDVFZ trace [33] suggest that the NH correspond to a transported fragment of the frontal part of the Owlshhead Mountains (OM), a Cretaceous (~95 Ma, [34]) granitic pluton at a 40–41 km distance to the SE. Several attempts have been made and discussed in the literature to give insight to the geological setting of the NH and structural relationships between SDVFZ and GFZ [35–37]. Particular emphasis has been given to a detailed description of sedimentary sequence deposits on each side of the NH Crystalline Bedrock Slice (CBS) [38,39]. The CBS is composed of Proterozoic sediments with upward younging direction the Crystal Spring (CS) quartzite, CS dolomite, detrital flysh, and carbonate sequences possibly part of the Pahrump Group, intruded by 1.1 Ga diabase sills, the whole intruded by Mesozoic granite [40]. However, a detailed structural analysis of the CBS itself is missing. Thus, Section 4.1 of this study will give new elements, improving the observations made by [38,41] concerning the NH structure. A precise fracture pattern characterization of the NH was performed by [42], through a wide-ranging analysis scale from the microscopic scale to the regional scale. These authors showed that the NH fracture network geometry has been controlled by the SDVFZ and the GFZ.

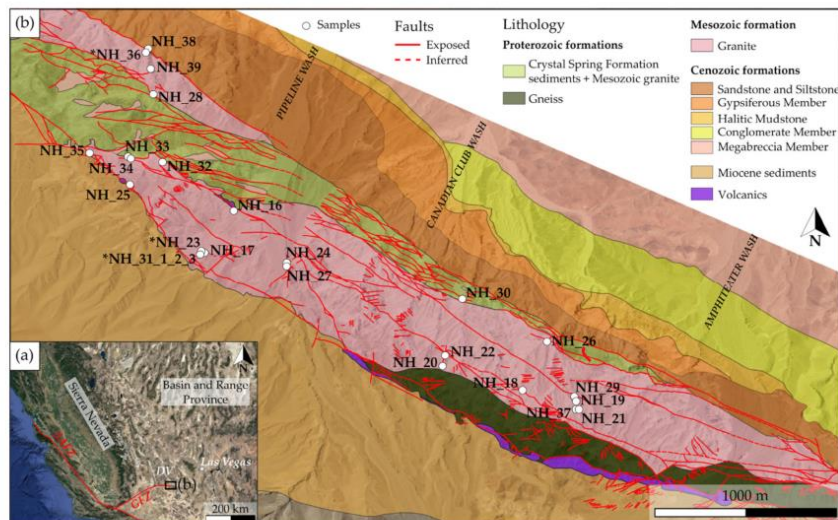


Figure 1. (a) Location of the Noble Hills on the western USA satellite map. SAFZ—San Andreas Fault Zone, GFZ—Garlock fault zone, and DV—Death Valley. (b) The geological map of the Noble Hills range, modified after [19,38,41]. The quaternary is not displayed, but available on the map provided by [38]. Sample locations are represented by the white dots. The asterisk shows the samples used as case studies in this work. NHF—Noble Hills Formation.

The NH granite was poorly studied in terms of microstructure, petrography, and geochemistry. A recent study conducted by Klee et al. (2021) [19] characterized the granite as a leucocratic equigranular monzogranite (S-type), ranging in the high-K calc-alkaline and peraluminous domains. The NH granite is composed of primary plagioclase, quartz, K-feldspar, and biotite. Klee et al. (2021) [19] have also shown that the NH granite underwent two alteration stages, forming secondary minerals that recorded the chemical and paleo-thermal conditions of the system: (1) a pervasive, propylitic alteration linked to the cooling of the pluton; and (2) a more local alteration corresponding to the argillic alteration (illitization and sometimes kaolinitization), which overprints the propylitic alteration. Among the primary minerals, optical observations and geochemical data show that only plagioclase and biotite are affected by those alteration processes.

3. Materials and Methods

3.1. Material and Sample Selection

Digital field mapping techniques have been used in the field; these include the use of portable rugged tablet laptop with internal GPS. The QGIS software has been used for sample location, geological digitization, and structural data acquisition. Georeferenced topographic maps and ortho-imagery were the initial input of the database.

A detailed petrographic, mineralogical, geochemical, and petrophysical characterization was conducted on 25 samples from the NH granite, based on fieldwork and laboratory analyses.

Samples were selected by targeting fracture zones located in CBS areas that have been affected by low to moderate strain, aimed at characterizing the influence of fracturing on fluid circulations and the associated argillic alteration, mentioned only by [19] until now. Thus, the collected samples consisted of altered granite presenting open fractures, veins, reactivated veins, and breccias. All samples were georeferenced for precise locations as well as database supply (Figure 1b). The selection took into account ranges of fracture density (F_d) defined by [19] from scanlines realized on thin sections, based on [43]:

$F_d 0 < 1687$ fracs/m—no to very low microfracturing;
 $F_d 1 = 1687$ fracs/m—microfracturing of order less than the grain size;
 $F_d 2 = 2694$ fracs/m, with a multiplier factor of 1.6 compared to $F_d 1$ —microfracturing of grain size order with interconnections;
 $F_d 3 = 3549$ fracs/m, with a multiplier factor of 1.3 compared to $F_d 2$ —abundant microfracturing;
 $F_d 4 \geq 5140$ fracs/m ([42] this issue), with a multiplier factor of 1.4 compared to $F_d 3$ —very abundant microfracturing.

Samples selected for this study had a fracture density higher than 2694 fracs/m, meaning they fell into categories from $F_d 2$ to $F_d 4$. $F_d 4$ corresponds to highly strained zones in which granite becomes a breccia. In order to correlate the fracture density with the amount of alteration, three hand specimens and seven thin sections, located in the granite body, were used for fracture extraction and analysis. These fracture characterizations are based on the scanline method, described in Section 3.1. Data from Chabani et al. (this issue, under review) [44] will be used to complete the characterization.

3.2. Methods

3.2.1. Fracture Network Parameters

Fracture networks can be characterized by their spatial arrangements [45]. The fracture network geometry is used to predict fluid circulation [45] and evidence of structural growth processes [46]. Spacing measurements through the 1D-scanline method are widely used to characterize arrangements [47–50]. They consist of the digitization of fractures along those lines, in order to calculate the linear fracture density P_{10} characterized by the number of fractures per length calculated along the scanline [47,48]. The Terzaghi correction has been applied [51]. Two parallel scanlines were performed on the hand specimens, perpendicular to a major fracture. For each oriented thin section mosaic, two scanlines were realized perpendicular to the main structures. For each scanline, stick plots and cumulative frequency diagrams were realized to describe the fractures spatial distribution [50]. A coefficient of variation C_v was computed for each scanline in order to quantify the fracture distribution [48]: $C_v < 1$ indicates a regular fracture spacing, $C_v \sim 1$ indicates a random distribution, and $C_v > 1$ indicates a clustered distribution. Fracture density data obtained by [42] on selected samples will be used in this study.

3.2.2. Petrographic Characterization

Twenty-four samples were selected to prepare thirty-one covered and polished thin sections, for petrographic observations. Optical microscopy was used to study the mineralogical assemblage, the alteration paragenesis, the microfabric, and the degree of microfracturing. The thin sections were observed under a Leica DM4500-P optical microscope, equipped with a Leica DFC450C camera at Institut Polytechnique UniLaSalle (ULS, Beauvais, France). Large field area imaging under polarized-analyzed and polarized-non-analyzed light was conducted using Leica automatized stage facility and Leica Application Suite (LAS) v4.11.0 software [19].

Based on optical microscopical observations, microsites were selected on 9 thin sections for energy dispersive X-ray spectrometry (EDS) analyses [52] performed at ULS. These were conducted with a Hitachi S-3400N scanning electron microscope (SEM) equipped with a Thermo Ultradry EDS [53] and associated with NSS thermal scientific software. These analyses aimed to obtain qualitative and semi-quantitative chemical compositions and to characterize the microstructure of different selected phases. The analytical conditions consisted of a 50 μ A beam current, an accelerating voltage of 20 kV, and an acquisition time of 30 s. A NORAN-type correction procedure was used.

In addition, cathodoluminescence (CL) analyses [54] was performed on 8 thin sections from 4 samples. CL imaging was performed (1) at the University of Göttingen using a “hot-cathode” cathodoluminescence microscope HC3-LM apparatus and (2) at CY Cergy Paris University in the Geosciences and Environment Cergy (GEC) laboratory, using a

cathodoluminescence Olympus BX50. CL of minerals is predominantly a “defect luminescence”. This allowed the detection of distribution patterns of certain trace elements, such as iron (Fe), which is the most efficient quencher element and manganese (Mn), which is the most important activator element. Many minerals show visible CL colors like quartz (blue-purple), K-feldspar (blue when fresh and brownish when weathered), plagioclase (green and blue-purple when highly affected by hydrothermal alteration), calcite (yellow or yellow-orange when resulting from hydrothermal alteration), dolomite (orange-red), magnesite (red), apatite (yellow), kaolinite (dark blue) [54,55]. Illite shows no luminescence [54,55].

Most of the mineral abbreviations used in this paper refer to [56] mineral symbols and only a few others were defined by the authors.

3.2.3. X-ray Diffraction (XRD)

XRD analyses were carried out to identify and determine the mineral phases (semi-quantitative, around 3–5%). The analyses were performed at (1) ULS using a D8-Advance Bruker-AXS (Siemens) diffractometer with a Ni-filtered $\text{CuK}\alpha$ radiation at 40 kV and 40 mA, a primary Soller slit of 2.5° , divergence slit of 0.6 mm, and a secondary Soller slit of 2.5° , with a detector slit of 0.1 mm and an anti-scattering slit of 0.6 mm; and (2) the University of Göttingen, using a PHILIPS PW1800 diffractometer with a Cu-anode and an automatic divergence slit. Whole rock powders and oriented clay fractions (2–6 μm and <2 μm) analyses were performed on 12 samples. Quantitative phase analysis based on reference intensity ratio values were performed on randomly oriented whole-rock powders with a step length of 0.5° and a scan speed of $0.014^\circ/\text{s}$ over the range 3° – $70^\circ 2\theta$ for whole rocks composition. The uncertainty is estimated to be $\pm 5\%$. Clay mineral separation was conducted using a technique described by [19], based on [57,58], according to the standard techniques suggested by [59]. For the XRD analyses of both fractions, oriented specimens were measured at air-dried (AD), solvated with ethylene glycol (G), and after heating at 550°C (H) conditions. These three analytical steps were routinely used to better determine clay minerals content and swelling properties [7]. The clay minerals identification, which is based on d-values and the relative intensity of their 00l reflections, was undertaken, referencing [60,61]. These measurements were performed with a step length of 0.5° and a speed of $0.01^\circ/\text{s}$ per step over the range 3° – $35^\circ 2\theta$. The interpretations of the data obtained at ULS were performed using the DIFFRAC EVA v4.2 (©Bruker AXS) software. Two fractions were collected in order to (1) separate the last produced or neoformed clay minerals (fraction <2 μm), which could be assimilated to the result of the last fluid circulation event, from the fraction 2–6 μm assimilated to old grain recrystallization or to a possible mix between detrital and neoformed clay mineral; (2) obtain the respective clay composition; and (3) obtain the temperature conditions.

Kübler Index and Kaolinite Crystallinity Index determination

The Kübler Index (KI) was used to define the limits of metamorphic zones (diagenetic zone, anchizone, and epizone) [19,62], following the recommendations for Kübler Index calibration of [59] and the CIS-KI transformation formalism of [63], as well as the temperature of illite formation [64,65]. The KI was calculated from the illite crystallinity (IC), which is defined as the full width at half maximum (FWHM) of the (001) 10Å peak of illite, on the AD oriented clay fractions. A recent study [66] has confirmed that IC provides a useful method for characterizing regional grades of diagenesis and low-grade metamorphism. Temperature is thought to be the main factor controlling IC, but other parameters, such as lithology, also have important effects [67–69]. Working at constant lithology allows this effect to be avoided. In some conditions, an altered granite shows similarities with diagenetic reactions present in feldspathic sandstones [20]. Thus, it is possible to characterize temperature ranges by using the KI values obtained for granitic rocks. The values obtained by IC were thus standardized using the crystallinity index-standard (CIS) samples provided by [70] in order to calculate the KI. The KI values of raw data expressed in $\Delta^\circ 2\theta$,

were measured into three slots, corresponding to different campaigns, which induced three standardizations given by [19]. The Kaolinite Crystallinity Index (KCI) was calculated and put in parallel with the KI in order to identify any correlation between both, and to determine temperature evolution as an indicator for samples free of illite. The KCI is defined as the FWHM of the (001) 7Å peak of kaolinite on the AD oriented clay fraction.

3.2.4. Manocalcimetry

Manocalcimetry is used as an indicator of the total calcite content in a rock sample and to assess its possible influence on permeability and consequently better understand the hydrothermal sealing of a reservoir [71]. Calcite content was determined using an OFITE 152–95 manocalcimeter composed of a glass flask and a high precision manometer. The analyses were performed on 15 samples at CY-GEC. High quality results were obtained with an accuracy of ± 0.5 wt.%. Prior to measurement, sample preparation was conducted according to [71]. Two replicates were performed for each sample, following the protocol described by [19], in order to check the reproducibility of the results. This procedure was considered to be good when the difference between the two results was lower than 0.5 wt.%, corresponding to the precision mentioned above. The CaCO₃ percentage was calculated according to [19]. The average calcite content of a fresh granite is 0.252 wt.% and does not exceed 1.8 wt.% [72]. As a consequence, measurements above this last value can be regarded as a calcite anomaly [71], due to hydrothermal alteration.

3.2.5. Ethanol Saturation Porosimetry

Porosity measurement quantify the available volume for fluid storage [73]. The connected porosity was measured on three samples by the triple weighing method [19,74] defined by the RILEM standard (test n°1.1, 1978). The measurements were carried out at CY Cergy Paris University in the Mechanics and Material for Civil Engineering laboratory (L2MGC). They consist in the saturation of the samples after vacuum degassing. The analyses and calculations were conducted using the technique described by [19]. Ethanol has been chosen instead of water in classical methods, in order to avoid possible clay swelling [75], which could lead to the destruction of the sample and bias to porosity values. Even though ethanol (0.469 nm) is a larger molecule than water (0.343 nm), the pore volume is not estimated to be under-evaluated, because the pore size is likely much larger than that of ethanol molecules.

3.2.6. Bulk Rock Geochemical Analyzes

Chemical analyzes of the major element oxides, rare earth elements, and trace elements were conducted on five samples, selected as case studies in this paper. Analyzes were performed at the Bureau Veritas Minerals (Vancouver, BC, Canada) using inductively coupled plasma emission spectrometry or mass spectrometry (ICP-ES and ICP-MS, respectively). Samples were crushed and mixed with LiBO₂/LiB₄O₇ flux. Crucibles were fused in a furnace at 980 °C. The obtained cooled bead was dissolved in ACS grade nitric acid and analyzed. Loss on ignition (LOI) was determined by igniting the samples split then measuring the weight loss. These chemical analyzes were performed in order to determine the element transfers and the degree of alteration.

3.2.7. Mass-Balance Using Gresens' Method

Bulk-rock mass-balance were used to establish element transfers during hydrothermal alteration by applying Gresens' mass-balance procedure [76], consisting of the quantification of gains and losses of major elements by comparing unaltered and altered samples. NH_2 is considered as the reference because it is the freshest sample collected in the area by [19] and 3 altered samples were selected from this study (NH_20, NH_28, NH_32_3, and NH_37). The following equation defined by [76] relates the composition and volume of altered rocks to unaltered/fresh rocks:

$$X_n = F_v \times (d_A/d_F) \times C_n^A - C_n^B \quad (1)$$

With X_n corresponding to the gain or loss of a considered element n (absolute mobility (%)), F_v the volume factor, d_A and d_F the density (in g/cm^3) of the altered (A) and the fresh (F) rocks, respectively, and C_n^A and C_n^B , the oxide percentage of the element n for the altered (A) and the fresh (F) rocks, respectively, which were given by the bulk geochemical analyses, recalculated without the LOI. The densities were calculated from the sample masses obtained during the porosity measurements. The F_v was calculated for each altered sample by considering $X_{\text{Al}_2\text{O}_3} = 0$ following the analysis of the values. X_n was calculated for each element. Then, the obtained F_v values being very close to 1, the X_n values were recalculated by considering $F_v = 1$ (constant volume). Hence, X_n values > 0 (positive values) represent the gains and X_n values < 0 (negative values) represent the losses for the considered elements. This calculation was applied for the major elements in each sample.

4. Results

4.1. Noble Hills Structural Overview

We investigated the geometry of outcropping Proterozoic sequences between Pipeline and Cave Spring washes (Figure 2a) and confirm at first the plutonic nature of the contact at the base of the Proterozoic sequence with the underlying Mesozoic granite by metamorphic halos [40]. The whole architecture of the NH presents signs of deformation affecting both Proterozoic and granitic units. Proterozoic units present much evidence of deformation with (1) several tectonically induced duplications of the stratigraphic sequence (Figure 2b) and (2) a lateral bending, stretching, and boudinage of this Proterozoic cover nappe stack [41]. Boudinage was identified in the field and in map view where progressive dismantling of stratigraphic markers is observed. (Figure 2b,c). Development of synthetic, oblique dextral shears (Figure 2c), offsetting along the CBS strike and accommodating the deformation, have also been identified. The age and tectonic significance of the nappe stack described in (1) is still unclear at present and possibly predates Mesozoic magmatic intrusion, as it does not appear intensively deformed along the basal contacts of the nappes. Lateral bending and stretching mentioned in (2) and depicted in Figure 2b,c are related to SDVFZ activity, since all kinematic indicators are consistent with progressive southeast oriented dextral shearing. This feature is ubiquitous within the NH as described by [33]. Given these new findings dealing with internal CBS structural organization, it is expected that areas along the rear southern limit of the CBS have recorded less transcurrent shear compared to areas situated along its northern front. Thus, the CBS gives an opportunity to study the effects of progressive transcurrent shearing within a granitic geothermal analogue. The above considerations have important implications regarding strain distribution within the NH and, in turn, concerning the sampling strategy. Given the above-mentioned findings, we consider the CBS as an exceptional example of large-scale cataclastic flow in which rock masses of the northern domain are dragged as a continuous body into a transcurrent deformation corridor (Figure 2a). No signs of a discrete, large-scale deformation structure appear on the map presented in Figure 2, where yellow dashed lines show instead a continuous flow accommodated by brittle deformation processes.

4.2. Petrographic Description

As described by [19], the primary assemblage of the NH granite is made of plagioclase (mainly oligoclase in composition), quartz, K-feldspar (perthitic orthoclase and sometimes microcline), and biotite. The granitic samples collected for this study show strong evidence of intense alteration, especially on plagioclase and biotite. Plagioclase transformed into illite, kaolinite and/or calcite and biotite into illite and oxides. In rare samples, K-feldspar perthite could be partially altered into illite. However, the magmatic texture is almost preserved, except in the case of breccias, which are not necessarily highly altered. For all samples, the alteration product is always the same, but the relative proportions of the different secondary phases might vary. The mineralogical composition and the degree of fracturing of each sample is given in Table 1.

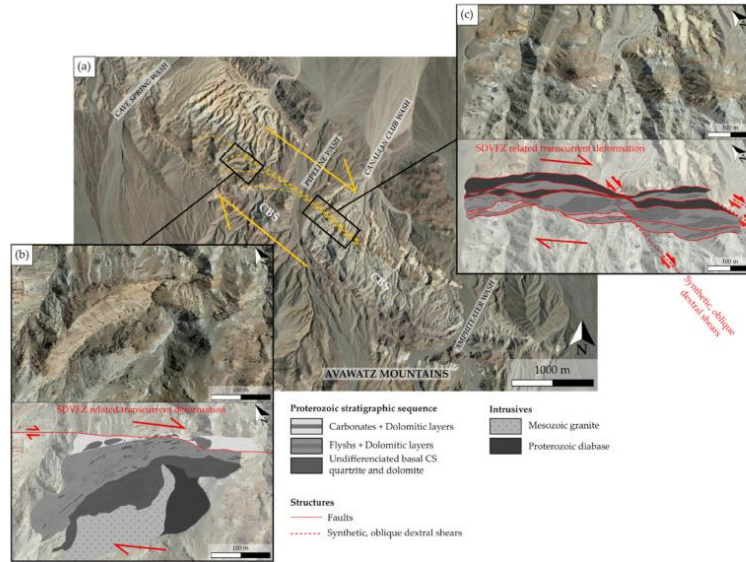


Figure 2. (a) Satellite view of the NH range showing a deformation gradient increasing southeastward, represented by the yellow dashed lines. (b,c) Map view zooms on the Proterozoic units along the NH strike showing the strain increase from (b) to (c), where basal CS sedimentary sequence appears increasingly stretched and boudinated.

The clay mineral composition of some samples has been precisely determined for the $<2\ \mu\text{m}$ and $2\text{--}6\ \mu\text{m}$ (Table 1). It reveals the presence of illite/smectite (I/S) mixed-layers in three samples (NH_17, NH_24, and NH31_1_2) in both fractions when it was measurable. The I/S identified is always illite-rich (R3), with more than 90% of illite [60], where R represents the Reichweite parameter [60]. A small amount of corrensite (trioctahedral variety of regular 50:50 chlorite/smectite mixed-layer (C/S) [77]) was also identified in the samples NH_16, NH_27, and NH_32. Both mixed-layers (I/S and C/S) were already identified by [19] in the sampled granite away from the fracture zones. Two new patterns were identified in this study (Figure 3):

- The first pattern (Figure 3a) shows illite characterized by peaks at $10.1\ \text{\AA}$ and $4.99\ \text{\AA}$, which support the previous results [19]. Illite is present in almost all the samples except NH_28, NH_36, NH_38, and NH_39. Kaolinite is also present and could be associated to illite or not.
- The second pattern (Figure 3b) shows the presence of dioctahedral vermiculite. It is characterized by a peak at $14.32\ \text{\AA}$ in air-dried condition, which slightly swells up to $14.59\ \text{\AA}$ after glycol solvation and slightly collapses to $12.26\ \text{\AA}$ after heating. It was identified only in samples NH_24, NH_26, and NH_33, where it is associated to illite and kaolinite.

Table 1. List of samples collected in the field with their mineralogical composition determined after microscopic observations (optical-microscope and SEM-EDS) and XRD analysis (primary minerals and secondary minerals), their degree of microfracturing after [43], and their clay mineral composition for the fractions <2 µm and 2–6 µm. Abbreviations after [56], except for the following: Olg—oligoclase, Ox—oxide, I/S—illite/smectite, C/S—corrensite, n.m.—not measured, n.a.—not analyzed.

Sample Name	Primary Minerals	Secondary Minerals	Clay Fraction < 2 µm					Clay Fraction 2–6 µm					Microfracturing		
			Ill/Ms	Kln	C/S	I/S	Vrm	Bt	Ill/Ms	Kln	C/S	I/S		Vrm	Bt
NH_16	Qtz, Or, Bt, Olg	Cal, Clays	+	-	-	n.m.	-	+	-	-	-	-	-	-	Fd2
NH_17	Qtz, Or, Ab, Ap	Gp, Clays													Fd2
NH_18	Qtz, Or, Olg, Bt	Clays	++	-				++	-						Fd2
NH_19	Mc, Or, Olg, Bt, Qtz, Ms	Dol, Cal, Clays	+					+							Fd2-3
NH_20	Qtz, Or, Olg, Bt	Cal, Ox, Clays				n.a.				n.a.					Fd2-3
NH_21	Qtz, Or, Olg	Cal, Dol, Sd, Ox, Clays				n.a.				n.a.					Fd3
NH_22	Qtz, Or, Bt, Olg	Cal, Hem, (Dol), Clays	+	-				+							Fd3
NH_23	Qtz, Or, Olg, Bt	Cal, Ox, Clays	++	+				++	+						Fd3
NH_24	Qtz, Or, Olg, Bt	Cal, Clays	++	+				++	+						Fd3
NH_25	Qtz, Or, Bt, Ep	Cal, Ox, Clays	-	++				-	++						Fd3
NH_26	Qtz, Or, Bt, Olg, Mc	Clays	+	++				+	++						Fd3
NH_27	Qtz, Or, Bt	Ank, Cal, Clays		++					++						Fd3
NH_28	Qtz, Or, Mc, Olg, Bt, Ms	Cal, Ox, (Dol), Clays		++					++						Fd3
NH_29	Qtz, Or, Olg, Ab, Bt	Cal, Dol, Clays		++		n.a.			++						Fd3
NH_30	Qtz, Or, Mc, Olg, Ab, Bt, Ms	Cal, (Ox, Dol), Clays		++		n.a.			++						Fd3
NH_31_1_2	Qtz, Or, Olg, Bt	Clays	+	+				+	+						Fd3
NH_31_3	Qtz, Or, Ab, Bt	Gp, Cal, Clays		++		n.m.			++						Fd3
NH_32	Qtz, Or, Bt	Cal, Ox, (Dol), Clays	+	++				+	++						Fd3
NH_33	Qtz, Or, Bt, Ab	Cal, Clays	-	++				-	++						Fd4
NH_34	Qtz, Or, Mc, Ab, Ap, Bt	Gp, Cal, Hem, Clays		++		n.m.			++						Fd4
NH_35	Qtz, Or, Mc, Bt	Cal, Clays		++		n.a.			++						Fd4
NH_36	Qtz, Or, Bt, Olg	Cal, Gp, Hl, Clays		+					+						Fd4
NH_37	Qtz, Or	Cal, Dol, Ank, Ox, Clays		++		n.a.			++						Fd4
NH_38	Qtz, Or, Mc, Olg, Bt	Cal, Clays		++					++						Fd4
NH_39	Qtz, Or, Mc, Olg, Bt	Cal, Clays		++					++						Fd4

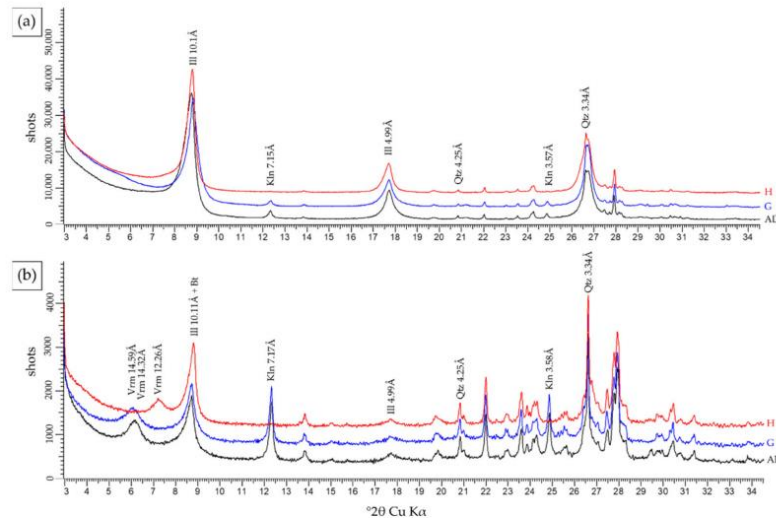


Figure 3. Two examples of XRD patterns obtained for the clay fraction $<2 \mu\text{m}$ in air-dried (AD–dark), after glycol solvation (G–blue) and heated (H–red) conditions for the NH granite, which were not identified in the fresh granite described by [19], and showing different clay compositions. (a) Illite, kaolinite, and quartz. (b) Vermiculite, illite, kaolinite, and quartz.

The high proportions of illite and kaolinite are characteristic of the argillic alteration [19]. Argillic alteration is prevalent in the vicinity of fracture zones (Table 1). Vermiculite can be interpreted as either hydrothermal alteration or weathering. This will be discussed in Section 5.1.

Microscopic observations and SEM-EDS analyses have shown that, in almost all the samples, carbonates (dolomite, siderite, ankerite, and calcite) and oxides were present as veins and/or in replacement of plagioclase. Moreover, XRD analyses revealed the presence of gypsum and/or halite in minor amounts in few samples (Table 1). Halite only occurred in sample NH_36 and gypsum was found in samples NH_17, NH31_3, NH_34, and NH_36.

4.3. Fracturing and Fluid Circulation

The NH granite presents ubiquitous signs of both fracturing and alteration, due to its location along the SDVFZ major fault corridor. The area lies along a deformation corridor governed by transcurrent deformation along the SDVFZ. In addition to the present contribution, Klee et al. [41] argue in favor of a deformation gradient affecting the CBS. At low to moderate strains, the system presents fracture zones composed of a fault core in which fractures are branching and where most of the displacement is concentrated (Figure 4a). These fracture zones affect the surrounding rock, creating an important fracture network (the damage zone, DMZ). Open fractures and veins are observed in this DMZ (Figure 4b).

Fault zones may act as a channel when connected and open fractures are present or as a barrier when fracture are sealed by mineralization. The distinction is made between (1) zones of opening related structures (i.e., where no signs of displacement are recognized between the two borders of the vein, Figure 4b); and (2) zones of lateral displacement (i.e., indicative of a shear displacement is observable) through three samples used as case studies (NH_31 (Figure 5a), NH_36, and NH_23 (Figure 5b)). Note that these samples are spaced at 2 m and are almost perpendicular to each other.

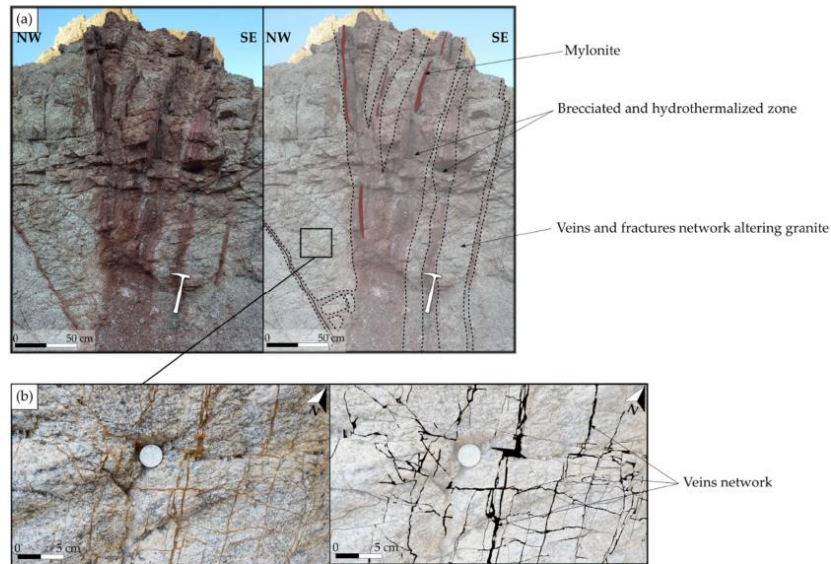


Figure 4. (a) Photograph and digitization showing representative hydrothermalized fracture zones observed on the field. (b) Photograph and digitization of granite crosscutting by multiple carbonate veins (veins network) altering pervasively the rock.

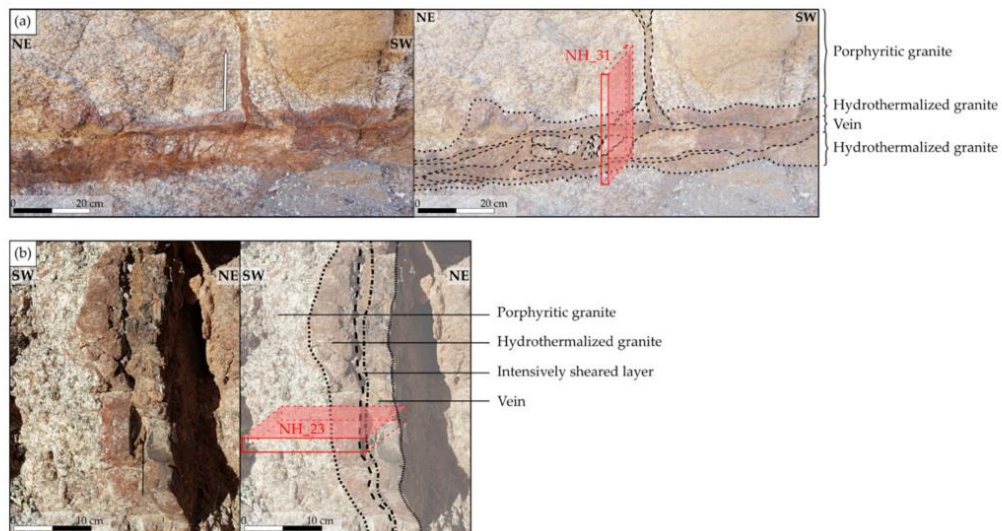


Figure 5. (a) Photograph and digitization of a brecciated and recrystallized vein also developing a gradient of alteration. Location of the sample NH_31 used as a case study in this section. (b) Photograph and digitization of a mylonitic vein developing a gradient of alteration. Location of the sample NH_23 used as a case study in this section.

4.3.1. Opening Related Structures with Minimum Shear Displacement

A significant number of veins, veinlets, and microfractures were identified in the different samples and outcrops investigated. Veinlets of various mineralization natures ($\leq 100 \mu\text{m}$ wide) were also identified in the samples. This variety of fracture infills shows different fluid circulation episodes. Rare veinlets of quartz were observed and intersected by illite veinlets (Figure 6a), which can be contemporaneous to kaolinite veinlets. Illite development is dependent on host mineral properties in terms of mechanical resistance and chemical stability. In that sense, quartz and K-feldspar, which remains unaltered, presents sharp open fractures in which illite precipitates (Figure 6b). Plagioclase, which is altered, presents blurred vein borders and start to spread out pervasively, due to the secondary porosity created by the alteration process (Figure 6b). These veinlets are generally intersected by carbonate veins (Figure 6c). These veins, the sizes of which range from 500- μm widths up to centimetric scales, are composed of dolomite, siderite, ankerite, and calcite. Most of the time, dolomite and ankerite appear contemporaneous. When siderite is present, it alters dolomite borders and crystallizes in it or crosscut it (Figure 6d). Then, calcite veins intersect the dolomite/ankerite and siderite veins (Figure 6d). Calcite can crystallize around angular clasts arranged in a fan shape characteristic of hydraulic fracturing (Figure 6e). Open microfractures present in the samples can show altered walls with kaolinite (Figure 6f) and/or illite (Figure 6g) indicating an influence of microfractures on mineral alteration.

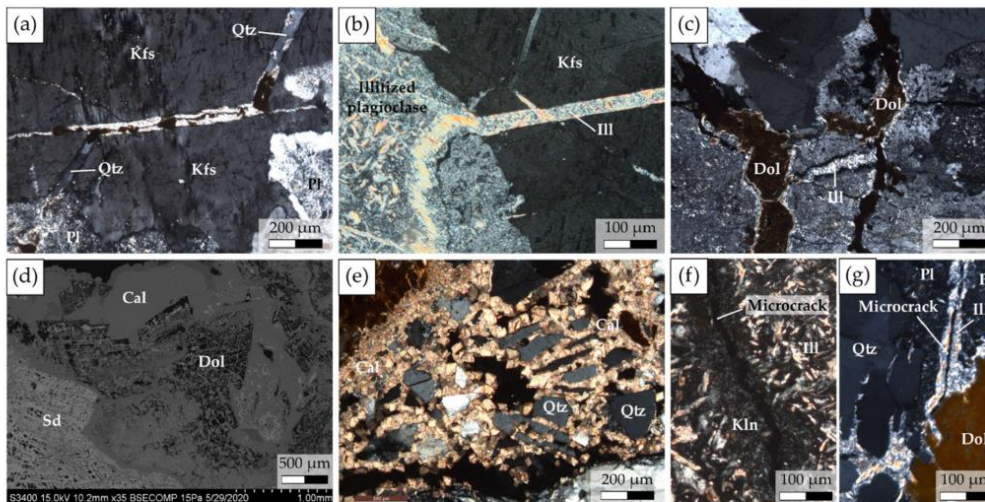


Figure 6. (a) Photomicrograph of a quartz veinlets intersected by an illite veinlets under optical microscope in polarized-analyzed light. (b) Photomicrograph showing an illite vein crosscutting K-feldspar and illitized plagioclase under optical microscope in polarized-analyzed light. (c) Back-scattered image showing the different phases presented in (b). (c) Photomicrograph showing dolomite intersecting illite under optical microscope in polarized-analyzed light. (d) Back-scattered image of a dolomite, siderite, and calcite showing their chronology. (e) Hydraulic fracturing with calcite precipitating around clasts of quartz placed like a fan under optical microscope in polarized-analyzed light. (f) Photomicrograph under optical microscope in polarized-analyzed light of a microfracture intersecting an altered plagioclase which borders are made of pure kaolinite, whereas the plagioclase was recrystallized into kaolinite and illite. (g) Photomicrograph under an optical microscope in polarized-analyzed light, showing illite developing on the walls of an open microfracture and dolomite filling this open space.

4.3.2. Infill of Fractures Developed with a Confirmed Lateral Shear Displacement

The previous section shows that all of the samples in the area present many fractures where fluid has circulated, precipitating or not various secondary minerals. However, the area is constrained by a shear component. Three samples were selected in order to describe the relationship between the amount of the strain and fluid circulation.

Sample NH_31

The outcrop of the sample NH_31 (Figure 5a) presents a vein around 10 cm thick crosscutting the granite and with a pinkish halo developed on each border. This halo represents the hydrothermalized zone of the granite. The sample NH_31 (Figure 7a) is composed of (1) a brecciated vein presenting brecciated quartz remnants, which were overprinted by a carbonate matrix and granitic clasts transported by the carbonate matrix; (2) a hydrothermalized zone, which corresponds to the pinkish halo; and (3) the porphyritic granite crosscut by veinlets filled by carbonates coming from the brecciated vein. Quartz veins are scarce in the NH granite. Fractures are dominantly rich in carbonates. It can be observed through this sample that carbonates crosscut the quartz.

- Spatial fracture distribution: two scanlines were realized in the granitic part of the sample (Figure 7a), from the brecciated vein towards the host rock, in order to evaluate the evolution of the fracture density along those two profiles. The spatial analysis is summarized in Table 2.

The cumulative frequency plotted against the fracture-projected position is presented in Figure 7b. The fracture frequency regularly and slowly increases over the first half part of the diagram curve, then increases regularly but more significantly. The C_v of 0.67 and 0.60 for each scanline shows a regular to random fracture arrangement, which is confirmed by the stick plots in Figure 7c. Both scanlines present an equivalent fracture density of 829 and 882 fracs/m.

Moreover, three thin sections were gained from the sample and one scanline was realized for each thin section (Figure 8a,b). As for the sample scanlines, the thin section scanlines were realized perpendicular to the vein and towards the host rock (Figure 8c).

SL_NH_31_1 shows a fracture frequency that increases following a random arrangement ($C_v = 1.03$) (Figure 8c,d).

The SL_NH_31_2, parallel to the previous scanline, also presents an irregular distribution. The frequency increases slowly at the beginning, followed by a high fracture density zone around 0.7–1.05 (fracture cluster), then a more significant increase comprising a new fracture cluster around 2–2.2 (Figure 8c). The slightly higher C_v compared to the previous scanline ($C_v = 1.07$) and the fracture distribution (Figure 8c) indicate a random to clustered arrangement of the fractures.

The last scanline SL_NH_31_3, which is the furthest from the vein, shows a greater overall increase of the fracture frequency compared to the two previous scanlines (Figure 8c). Only one fracture cluster was identified around 1.7–1.9 cm even if the C_v is higher ($C_v = 1.11$). The fracture arrangement is again considered as random to clustered.

C_v values, as well as fracture density values, increase from the vein towards the host rock, from 1.03 to 1.11 and from 2997 to 5084 fracs/m, respectively (Figure 8d).

By comparing fracture analyses between sample scale and thin section scale, a clear difference is observed among P_{10} , the mean spacing, and C_v values (Table 2). At thin section scale, the fracture density is significantly higher ($\times 4.7$) than at sample scale and the mean spacing is six times lower. At sample scale, the C_v is lower than 1 indicating an almost regular spacing between the fractures, even if there is a change of the slope (Figure 7c). Whereas, at the thin section scale, the C_v is around 1 or slightly higher, indicating a global random distribution of the fractures along the scanlines with the appearance of a few clusters (Figure 7c). For both, differences in the fracture distribution can be linked to a subjective bias during the data collection [78], but also to the image resolution, which

prevents from seeing all the fractures and so induced a bias. Thin section fracture analyses are, thus, more precise.

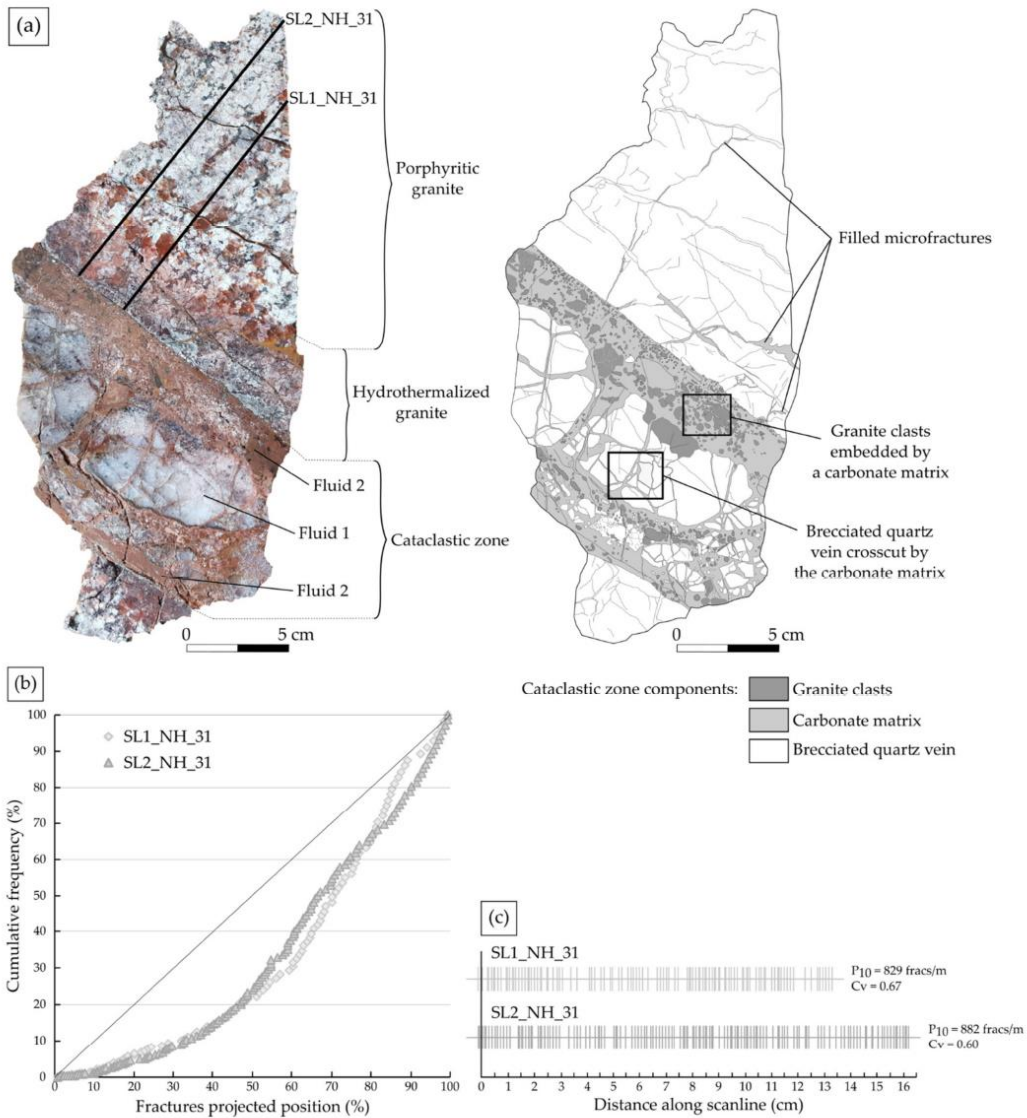


Figure 7. (a) Photo and the respective digitalization of the sample NH₃₁, gathering NH₃₁_1_2 and NH₃₁_3, showing the different compartments that compose it, as well as the two scanlines realized in the host rock of the vein. (b) Plots of the cumulative frequency percentage against distance percentage for both scanlines. The diagonal represents a uniform distribution. (c) Stick plots showing the fracture position along the scanlines and for which the fracture density (P₁₀) and the coefficient of variation (C_v) are given.

Table 2. Spatial fractures analysis. Scanline length: total length of each scanline; fracture number, mean spacing, P_{10} , and Cv value by scanline and fracture distribution tendency by scanline.

Sample Name	Scale	Scanline Name	Scanline Length (cm)	Fracture Number	Mean Spacing (cm)	P_{10} (fracs/m)	Cv	Fracture Distribution
NH_31	Sample	SL1_NH_32	13.51	111	0.12	829	0.67	Regular—Random
		SL2_NH_32	16.44	144	0.11	882	0.60	Regular—Random
	Thin sections	SL_NH_32_1	1.60	47	0.03	2997	1.03	Random
		SL_NH_32_2	2.21	87	0.02	3988	1.07	Random—Clustered
NH_36	Samples	SL_NH_36	15.8	53	0.3	342	1.03	Random
		SLH_NH_36_1	2.87	153	0.02	4636	1.49	Clustered
	Thin sections	SLV_NH_36_1	2.06	133	0.02	6312	1.01	Random
		SLH_NH_36_2	3.35	184	0.02	5231	1.11	Random—Clustered
		SLV_NH_36_2	1.88	74	0.03	3930	0.92	Regular—Random
NH_23	Sample	SL1_NH_24	14.33	197	0.07	1382	0.68	Regular—Random
		SL2_NH_24	12.93	170	0.07	1322	0.66	Regular—Random
	Thin sections	SL_NH_24_1	2.48	117	0.02	4798	0.77	Regular—Random
		SL_NH_24_2	2.37	91	0.02	3879	1.19	Random—Clustered

- Petrographic and petrophysical characterization: the brecciated vein presents a large variety of mineralogical phases. As shown in Figure 7a, this zone shows a carbonate matrix containing clasts of granite, which overprints a brecciated quartz vein remnant showing an undulatory extinction but no evidence of dynamic recrystallization. The carbonate matrix is complex, composed of several phases (Figure 9a–g).

Focusing on the veins crosscutting the quartz porphyroclasts, three phases are identified (Figure 9a–e):

1. Phase 1 is composed of calcite veins crosscutting the quartz. These veins, appearing as a single phase under SEM and optical microscope (Figure 9a,c), present two phases under cathodoluminescence (CL): a dark phase (Cal A) in the center of the vein and an orange bright phase (Cal B) (Figure 9b,d). Cal B phase seems to dissolve or corrode the Cal A phase (Figure 9b,d). A zonation corresponding to calcite growth halos are visible in the phase A, which are used as weakness zones in which the phase B can penetrate by dissolving the phase A.
2. Phase 2 is composed of a matrix rich in carbonates (calcite, dolomite, ankerite) transported clasts of quartz, K-feldspars and few biotite, but also presents barite precipitation patches (Figure 9e). This phase crosscuts the quartz and the calcite veins.
3. Phase 3 consists again of calcite veins. However, they crosscut the whole rock, and appear as a dark single phase (Cal C) under CL (Figure 9b).

Evidence of hydraulic fracturing, as presented in Figure 6e, have also been observed in this part of the sample.

By focusing in the carbonate matrix, at the contact with the granite, a new phase is observed, composed of dolomite embedding small clasts (mainly quartz). This phase is intersected by the phase 2, which is intersected by the phase 3 (Figure 9e,f). Examining the hydrothermalized granite along the brecciated vein (NH_31_1 and NH_31_2), the granite shows a preserved magmatic texture with plagioclase fully altered into illite, \pm kaolinite, and calcite, completely altered biotite into illite and oxides, and unaltered perthitic K-feldspar (Figure 9h,i). Hematite and numerous dolomite/ankerite and calcite veinlets are present. Moving away from the brecciated vein (NH_31_3), the granite appears less affected by the alteration. Plagioclase and biotite are only partially altered and K-feldspar and quartz are unaltered (Figure 9j,k). Unlike the hydrothermalized zone, the granite presents only a few veinlets of calcite.

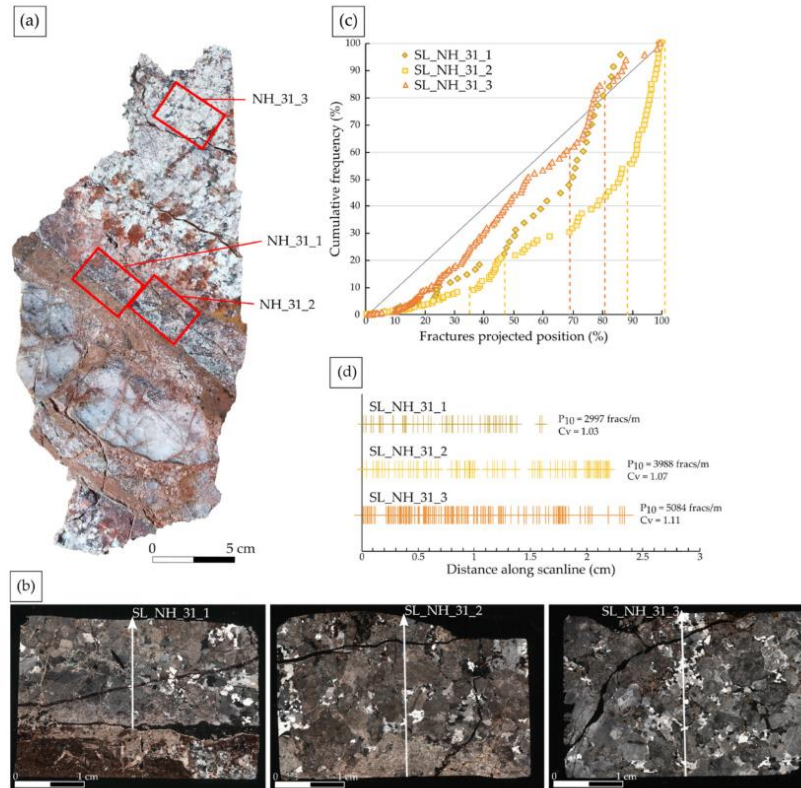


Figure 8. (a) Thin sections location on the sample NH_31. (b) Thin section mosaics showing the position and orientation of the scanlines. (c) Plots of the cumulative frequency percentage against distance percentage for each scanline. The diagonal represents a uniform distribution. Dashed lines indicate a zone where a rapid increase of the number of fractures is observed (slope threshold >2). (d) Stick plots showing the position of the fracture along the scanlines and for which the fracture density (P_{10}) and the coefficient of variation (Cv) are given.

Bulk chemical analyses were performed on the granitic part of the sample and show a low LOI of 2.5%, a porosity of 10.1%, and a calcite content of 1.86%, close to the brecciated vein (NH_31_1_2), and a calcite content of 1.37% away from it (NH_31_3).

Sample NH_36

This sample (Figures 1b and 10a) shows a fractured granite with a preserved magmatic texture intersected by brecciated zones. As for sample NH_31, the fracture distribution analyses, as well as a petrographic description, were realized.

- Spatial fracture distribution: the spatial fracture distribution analysis was realized based on data from [42]. One scanline was realized through the sample in order to evaluate the evolution of the fracture distribution and density (Table 2, Figure 10a). The cumulative frequency against the fractures projected position presented in Figure 10b shows a fracture frequency slowly increasing, as well as a fracture cluster. The Cv of 1.03 indicates a random arrangement of the fractures along the scanline (Figure 10c). A fracture density of 342 fracs/m was compiled (Figure 10c).

Two thin sections were made from the sample (Figure 10a,d). Two perpendicular scanlines were realized on each thin section (Figure 10d).

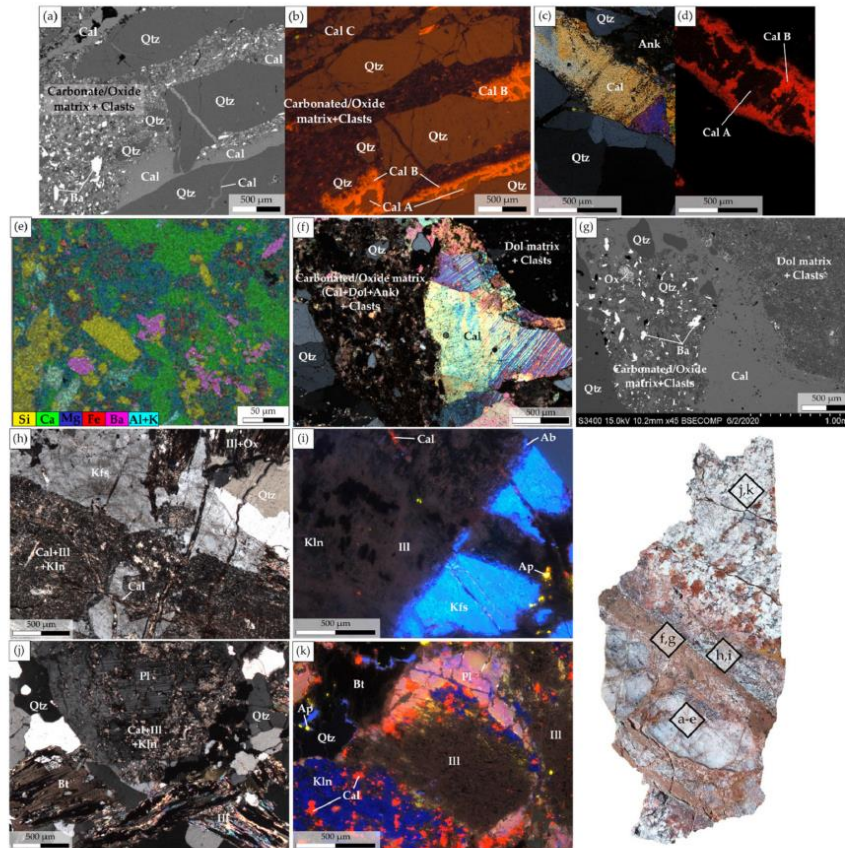


Figure 9. Photomicrographs of the different compartments of the sample NH₃₁ and their locations in the sample. (a,b) Respectively back-scattered image and CL images of calcite veins composed of two phases (Cal A and Cal B) cross-cutting quartz, crosscut by a phase made of a carbonate/oxide matrix (calcite, dolomite, ankerite) with barium patches and transported clasts of quartz, K-feldspars, and few biotites, crosscut by later calcite veins (Cal C). (c,d) Zoom on the first generation of calcite vein and crosscutting quartz under optical microscope in polarized–analyzed light and showing two phases under CL. (e) A chemical quantification map realized under SEM of the carbonate/oxide matrix with barium and clasts. Different colors show a relative abundance of specific chemical elements (counts). (f,g) A photomicrograph under optical microscope in polarized–analyzed and under SEM, respectively, of the contact with the granite showing a dolomite matrix with transported clasts intersected by a calcite vein, the whole intersected by a carbonate/oxide matrix with transported clasts and barium precipitation patches. (h) The altered granite close to the brecciated vein showing a completely altered plagioclase replaced by calcite, kaolinite, and illite, a completely altered biotite replaced by illite and oxides and non–altered K-feldspar and quartz under an optical microscope in polarized–analyzed light. (i) The altered granite close to the brecciated vein presented in (h) under CL showing illite with no luminescence, in light blue an unaltered K-feldspar, in red some calcite and apatite in yellow. (j) The altered granite, away from the brecciated vein, showing a plagioclase partially replaced by calcite, kaolinite, and illite, biotites partially replaced by illite, and oxides, and unaltered quartz under optical microscope in polarized–analyzed light. (k) The altered granite away from the brecciated vein presented in (j) under CL showing kaolinite in dark blue, calcite in red, apatite in yellow and illite, quartz and biotite with no luminescence.

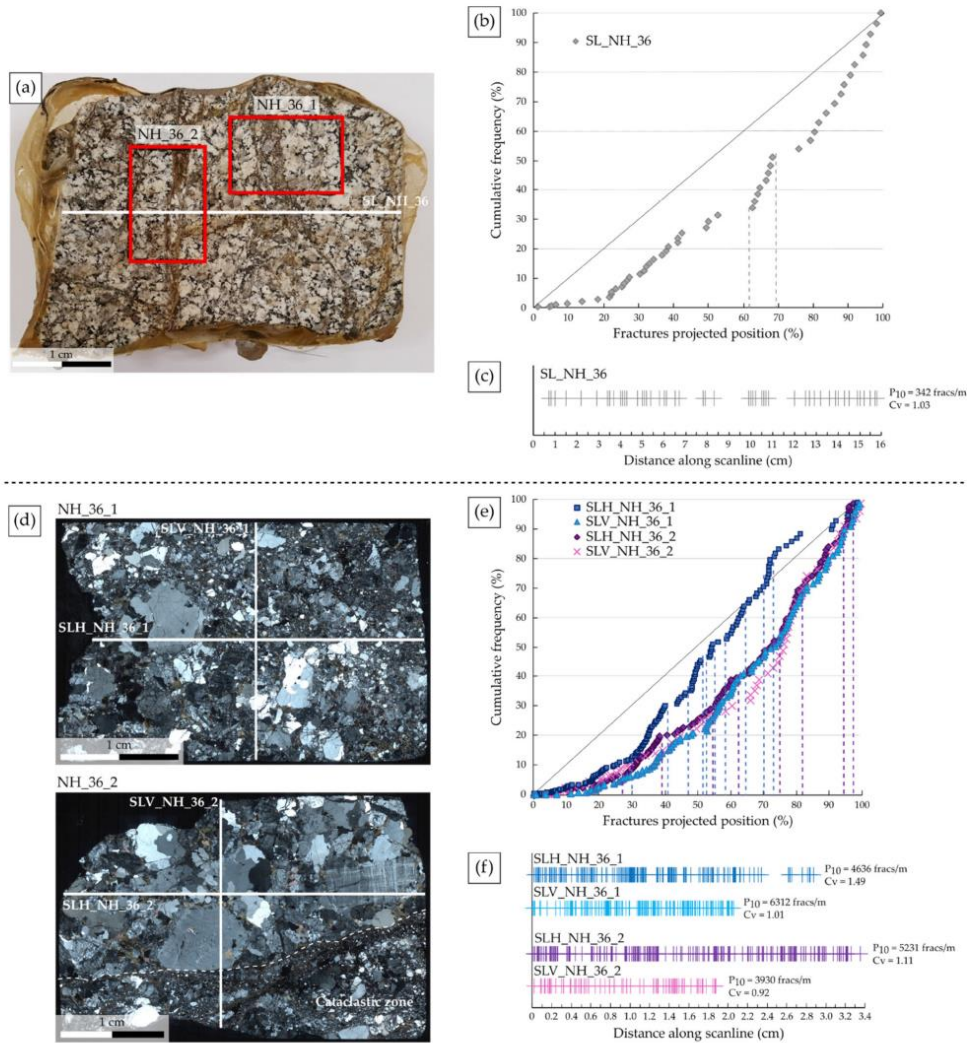


Figure 10. (a) Photograph of the sample NH₃₆ showing the scanline and the emplacement of the two thin sections made in the sample. (b) Plot of the cumulative frequency percentage against distance percentage for the scanline. The diagonal line represents a uniform distribution. Dashed lines indicate a cluster, meaning a zone where a rapid increase of the number of fractures is observed (slope threshold >2). (c) Stick plot showing the fracture position along the scanline and for which the fracture density (P₁₀) and the coefficient of variation (C_v) are given. (d) Thin section mosaics showing the position and the orientation of the scanlines. (e) Plots of the cumulative frequency percentage against distance percentage for each scanline. The diagonal line represents a uniform distribution and the dashed lines delimit a fracture cluster. (f) Stick plot showing the fracture position along the scanline and for which the fracture density (P₁₀) and the coefficient of variation (C_v) are given. Data were provided by [42].

Regarding the thin section NH_36_1, the scanline SLH_NH_36_1, perpendicular to the main fractures, shows a fracture frequency increases slowly the first 30%, then increases more strongly by presenting five fracture clusters (Figure 10e). This fracture distribution is highlighted by a $C_v = 1.49$, confirming a clustered arrangement of the fractures (Figure 10f). The fracture clusters are respectively comprised between, 0.9–1.2 cm, 1.4–1.5 cm, 1.55–1.6 cm, 1.7–1.85 cm, and 2.05–2.1 cm intervals (Figure 10e,f). The scanline SLV_NH_36_1, parallel to the main fractures, shows a different trend. The fracture frequency increases slowly and irregularly (Figure 10e). This distribution is highlighted by a $C_v = 1.01$, indicating a random arrangement of the fractures (Figure 10f). Considering both scanlines, the average fracture density is of 5474 fracs/m.

Regarding thin section NH_36_2, the scanline SLH_NH_36_2, parallel to the main fractures shows a fracture frequency trending similarly to SLV_NH_36_1. Four fracture clusters were identified (Figure 10e), also visible in the stick plot between 0.95–1.3 cm, 1.85–2.05 cm, 2.5–2.7 cm, and 3.1–3.2 cm (Figure 10f). The $C_v = 1.11$ confirmed a random to clustered arrangement of the fractures. The scanline SLV_NH_36_2, perpendicular to the main fractures, crosscut the magmatic preserved texture of the granite and a breccia. A change of the curve inclination is visible around 65% of the scanline, where the fracture frequency strongly increases (Figure 10e). It corresponds to the limit between both zones (Figure 10d). The $C_v = 0.92$ indicates a global regular to random fracture arrangement along this scanline (Figure 10f). Considering both scanlines, the average fracture density is of 4581 fracs/m.

Because fractures are difficult to recognize in the breccia of the sample NH_36_2, the fracture density calculated for both thin sections may be underestimated.

As for sample NH_31, an important difference between the P_{10} values of the sample and the thin sections is observed. However, a global random arrangement of the fractures at both scales is observed. Only SLH_NH_36_1 presents a clustered distribution.

- Petrographic and Petrophysical Characterization

The two thin sections (Figure 11a–c) allow petrographic characterization of the sample. The first thin section, NH_36_1 (Figure 11a,b), shows a breccia of the granite with significant variations of the grain size. No crystallographic preferential orientation (CPO) is observed. Some zones show brecciated minerals with small precipitation of carbonates as calcite and dolomite in the microfractures (Figure 11d). Primary minerals are only slightly altered but intensively deformed. Quartz shows a pronounced undulatory extinction and starts to dynamically recrystallize by means of sub-grain rotation processes (Figure 11d). Other zones show preserved minerals, but also a significant amount of carbonate, mainly calcite, between the clasts (Figure 11e). The second thin section, NH_36_2 (Figure 11c), shows a granite with a preserved magmatic texture, but fractured, and a breccia composed of a carbonate matrix and transported clasts coming from the granite with no CPO. The preserved granite part shows a low alteration degree. Quartz, K-feldspars (orthoclase and microcline), and biotite are fractured and unaltered. Plagioclase is fractured, slightly altered, and replaced by kaolinite (Figure 11f). The breccia shows a matrix composed of dolomite and calcite flowing through transported clasts of unaltered quartz and feldspar and lenses of kaolinite (Figure 11g).

Bulk analyses show a low LOI (2.6%), a calcite content of 5.95%, and a porosity of 11.5%. XRD bulk and clay fraction analyses also reveal the presence of gypsum and halite.

Sample NH_23

At outcrop (Figure 5b) and sample (Figure 12a) scales (Figure 1b), three compartments were identified: (1) a vein composed of a microcrystalline quartz-feldspathic unit, showing signs of foliation with clear shear sense indicators, bordered by a calcium rich mylonite and containing clasts of it, (2) a hydrothermalized zone in the granite along the vein, represented by a pinkish halo and (3) the porphyritic granite (Figure 12a).

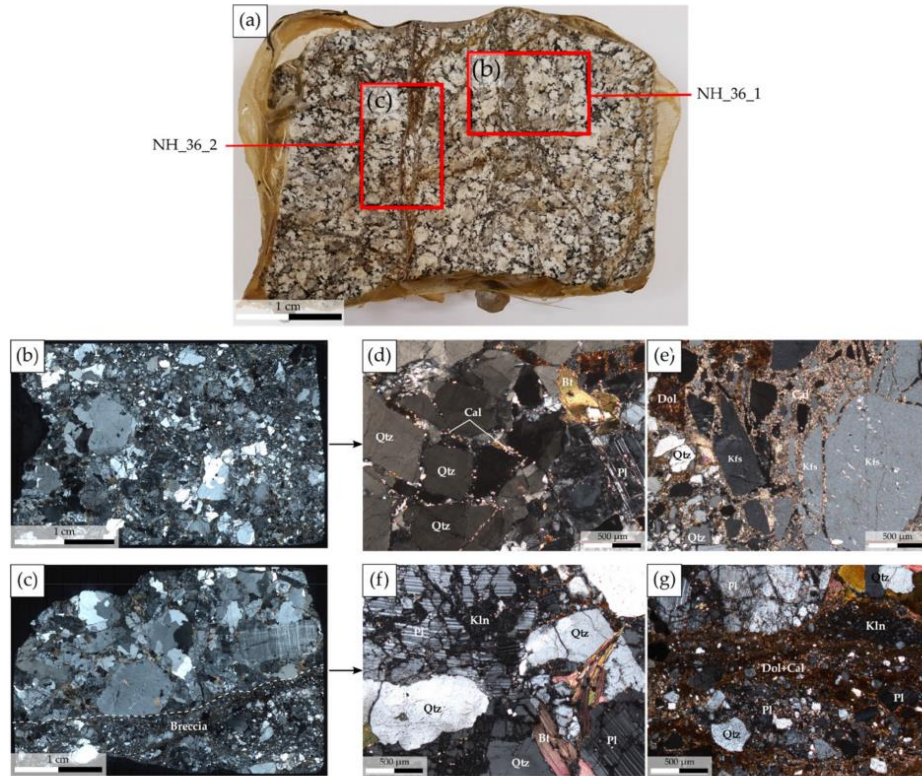


Figure 11. (a) Sample NH₃₆ collected close to a fault zone showing the location of the two thin sections. (b) A mosaic of the thin section NH_{36_1} showing a breccia. (c) A mosaic of the thin section NH_{36_2} showing the limit between a breccia and the almost preserved granite. (d) A microphotograph of the NH_{36_1} thin section showing a brecciated and slightly altered plagioclase, a brecciated quartz with a significant undulatory extinction, starting to recrystallize into subgrains, a brecciated biotite, and calcite crystallizing in the microfractures. (e) A micrograph of thin section NH_{36_1} showing brecciated and non-altered K-feldspar and quartz with dolomite and calcite deposits between the clasts. (f) A microphotograph zooming in the preserved granitic zone visible of the thin section NH_{36_2} and showing a brecciated and partially replaced plagioclase into kaolinite and brecciated, but unaltered, quartz and biotite. (g) A microphotograph zooming in the brecciated part of the thin section NH_{36_2} and showing a carbonate matrix composed of dolomite and calcite transported clasts from the granite.

- Spatial fracture distribution: two scanlines were realized in the granitic part of the sample NH₂₃ to evaluate the fracture arrangement from the vein towards the host rock (Figure 12a). The spatial analysis is summarized in Table 2. Fracture distributions presented in Figure 12b,c for each scanline show an evolution in two steps of the fracture cumulative frequency (Figure 12b).

Along the SL1_NH₂₃ scanline, the frequency slowly increases and shows a regular fracture distribution. At 40% of the scanline, the frequency slightly increases, with a regular arrangement of the fractures. The stick plot Figure 12c highlights this distribution. The SL2_NH₂₃ scanline presents a similar evolution as SL1_NH₂₃ scanline, with an increase in the frequency at 3/4 of the scanline. This slope change is expressed at the end by a fracture cluster around 8.7–10 cm, clearly visible on the stick plot (Figure 12c). The Cv of 0.68 and 0.67 for each scanline shows a regular to random arrangement of the fractures

along both scanlines (Figure 12c, Table 2). Both scanlines fracture densities are equivalent, with respectively 1382 and 1322 fracs/m (Figure 12c, Table 2).

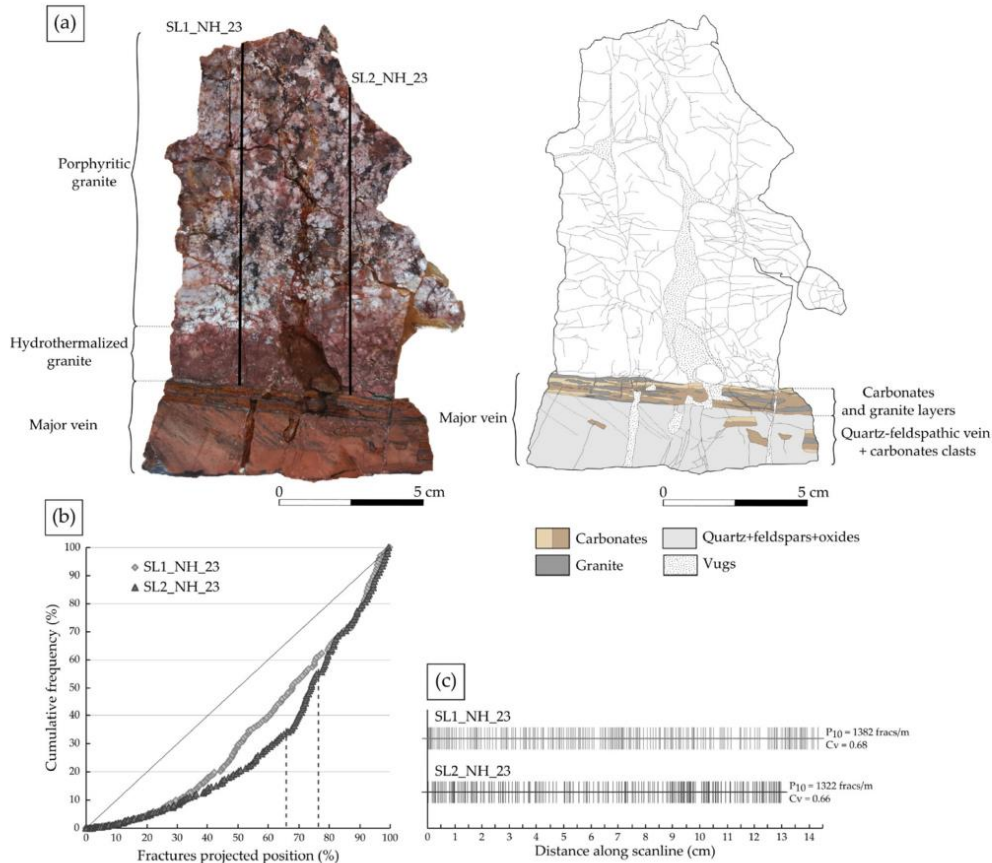


Figure 12. (a) A photo and the corresponding digitalization of the sample NH₂₃ showing the different compartments that compose it, as well as the two scanlines realized in the host rock of the vein. (b) Plots of the cumulative frequency percentage against distance percentage for both scanlines. The diagonal represents a uniform distribution. Dashed lines indicate a zone where a rapid increase of the number of fractures is observed (slope threshold >2). (c) Stick plots showing the fracture position along the scanlines and for which the fracture density (P_{10}) and the coefficient of variation (C_v) are given.

In order to complete the dataset, the method was repeated on two thin sections from the granite. One is at the border of the vein (NH_{23_1}) and the second away from it (NH_{23_2}) (Figure 13a). A scanline was realized in both thin sections (Figure 13b), perpendicular to the major vein. The spatial analysis is presented in Table 2.

Along the SL_NH_{23_1} scanline (Figure 13c), a low fracture density zone is present at the beginning of the scanline, then there is an increase of frequency between 0.9–1.4 cm (fracture cluster, Figure 13d), followed by an irregular fracture distribution until the 0.4 last cm where a fracture cluster was identified. Three fracture clusters are present in the SL_NH_{23_2} scanline around 1.5 cm, between 1.7–2.1 cm, and around 2.3 cm. From the first fracture cluster, the frequency increases significantly and irregularly. The scanline SL-NH_{23_1}, with the $C_v = 0.77$, shows a regular to random arrangement of the fractures,

while the $C_v = 1.19$ of the scanline SL_NH_23_2 indicate a random to clustered arrangement (Figure 13c). The fracture distribution varies with the position of the scanline and shows a P_{10} slightly higher close to the vein (4798 fracs/m) than away from it (3879 fracs/m) (Figure 13d).

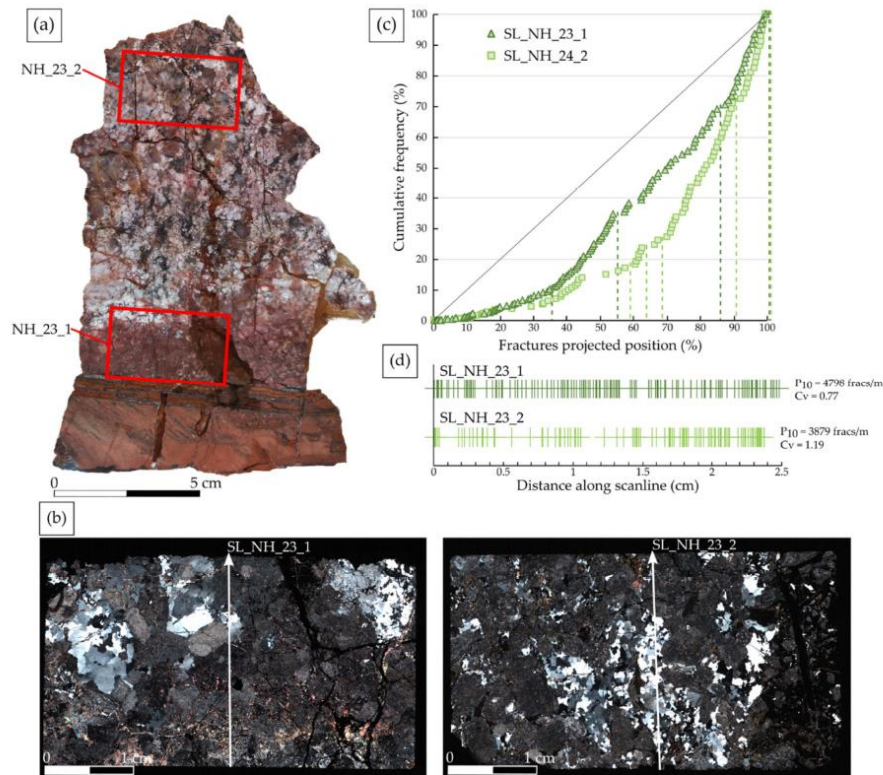


Figure 13. (a) Thin section location on the sample NH_23. (b) Thin section mosaics showing the position and orientation of the scanlines. (c) Plots of the cumulative frequency percentage against distance percentage for each scanline. The diagonal represents a uniform distribution. Dashed lines indicate a zone where a rapid increase of the number of fractures is observed (slope threshold >2). (d) Stick plots showing the position of the fractures along the scanlines and for which the fracture density (P_{10}) and the coefficient of variation (C_v) are given.

- Petrographic and petrophysical characterization: the vein of the sample NH_23 consists of two parts. The major part is mainly composed of quartz, few feldspars, and oxide minerals having no CPO. Ankerite veinlets crosscut it, and are also intersected by calcite veinlets (Figure 14a,b). This vein includes clasts of carbonates having the same characteristics as the carbonate vein at the contact with the granite (Figure 12b). This thin carbonate vein is composed of ankerite layers and granite lenses (Figure 14c). By zooming in on the ankerite layer, some part of it appears as lenses with automorphic crystals in the swell, which are crushed and stretched through the pinches (Figure 14d). Granite is pinched between these ankerite layers. Quartz clasts present in the granite lenses show an undulatory extinction, as well as some evidences of subgrain rotation phenomena. Carbonates can deform plastically and accumulate

large amount of strain at relatively low P–T conditions, from a minimum temperature of 180 °C [78–81]. Quartz crystal plastic deformation is dominant from 600 °C [82]. Hence, in the present situation, carbonates accommodate large amounts of deformation by means of crystal plasticity, while granite is being deformed by cataclastic flow, i.e., a process accommodated by brittle processes. A localized and significant amount of deformation occurred in this vein. The major vein of this sample is thus composed of (1) a highly deformed zone made of ankerite and granite lenses and (2) a siliceous vein, which contains clasts of similar composition to the carbonate vein. We suggest that the carbonate vein was the first event, which was intensively deformed, and then intersected by the siliceous vein, tearing off pieces of the carbonate vein. Calcite and ankerite veins identified in Figure 14a,b intersect the carbonate vein and the siliceous vein.

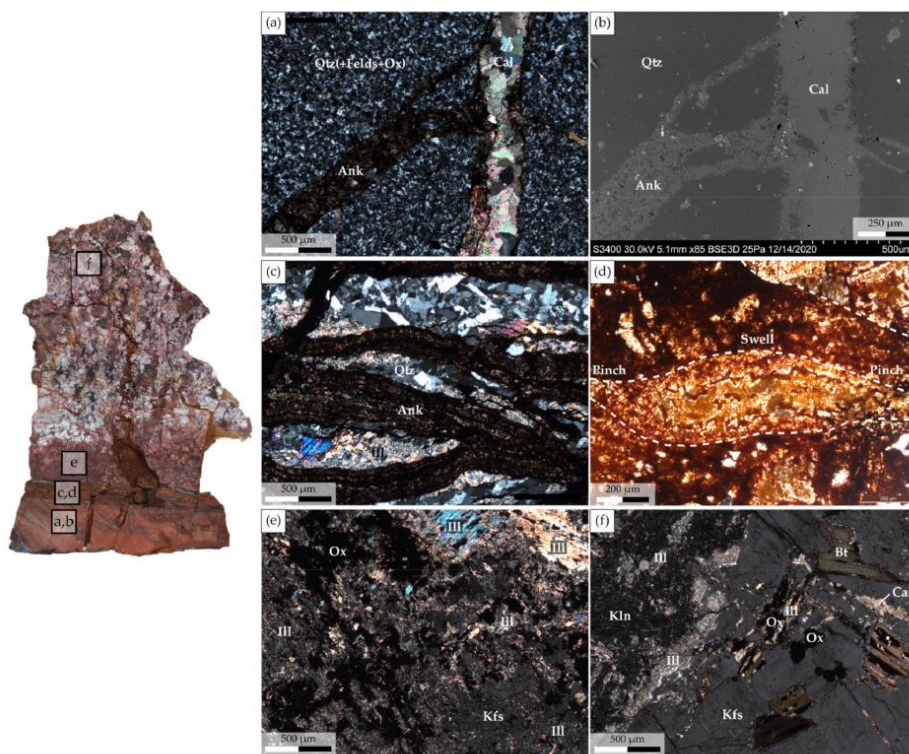


Figure 14. Photomicrographs of the different compartments of the sample and their location in the sample. (a) Veins of ankerite and calcite crosscutting the major quartzitic/feldspathic vein of the sample under optical microscope in polarized–analyzed light. (b) Back-scattered electron image of the photomicrograph (a). (c) Photomicrograph of the ankerite–granite interlayering zone under optical microscope in polarized–analyzed light. (d) A zoom image of the ankerite vein, under optical microscope in polarized–analyzed light, presented in (c) and showing a sigmoid of ankerite with a swell of automorphic crystals crushed and stretched in the pinches. (e) The altered granite close to the vein showing a completely altered plagioclase and biotite both replaced by illite and oxides and partially altered K-feldspar under optical microscope in polarized–analyzed light. (f) The altered granite away from the vein showing a completely altered plagioclase replaced by illite and kaolinite, biotite partially replaced by illite and oxides, an unaltered K-feldspar, and calcite veinlets under optical microscope in polarized–analyzed light.

As presented above, the magmatic texture of the granitic part of the sample is preserved. However, a color change of the granite is observed close to the vein. At a sample scale, the granitic part along the vein (NH_23_1) shows a pronounced pinkish color (Figure 13a). In the thin section, the granite appears almost completely altered. Plagioclase and biotite are no longer recognizable and are replaced by illite and oxides. Perthitic K-feldspar are not completely affected by the alteration, but are partially replaced by illite (Figure 14e). Away from the vein (NH_23_2), the granite appears whitish at a sample scale (Figure 13a). Compared to NH_23_1, plagioclase are completely replaced by illite and kaolinite, but biotite are only partially altered and K-feldspar are unaltered (Figure 14f). This indicates that the granite is more affected by the alteration along the vein, in the hydrothermally altered zone. Bulk analyses performed on the granitic part of the sample show a LOI of 5.2%. In all the granite, calcite veinlets are observed coming from the major vein.

4.4. Geochemical Analyses

The geochemistry of major elements, presented in Table 3, allows establishing diagrams representing selected elements versus LOI (Figure 15) in order to study the alteration degree of the selected samples.

Table 3. Major elements and loss on ignition (LOI) weight percentage (wt%) for the NH granite.

Sample ID	NH_19	NH_23	NH_27	NH_31_3	NH_36
SiO ₂	67.18	60.84	56.26	69.29	66.67
Al ₂ O ₃	15.03	17.31	14.05	15.42	15.30
Fe ₂ O ₃	2.93	4.61	3.17	2.69	3.65
MgO	0.71	1.06	0.89	0.24	0.97
CaO	1.81	2.83	9.10	2.34	3.80
Na ₂ O	2.20	2.45	0.27	2.89	3.12
K ₂ O	5.45	4.69	4.48	4.05	3.05
TiO ₂	0.23	0.39	0.29	0.24	0.34
P ₂ O ₅	0.12	0.18	0.14	0.13	0.17
MnO	0.11	0.23	0.23	0.06	0.12
LOI	4.10	5.20	10.90	2.50	2.60
Sum	99.91	99.88	99.90	99.88	99.87

The LOI ranges from 2.50 to 10.90 wt% with an average around 5 wt%. The LOI values show a negative correlation with Na₂O and SiO₂ and a positive one with K₂O. The CaO content varies slightly between 1.81 wt% and 3.12 wt%, except for the sample NH_27, which CaO content is about 9.10 wt%. Al₂O₃, MgO, and Fe₂O₃ content vary more widely in the ranges 14.05–17.31 wt%, 0.24–1.06 wt%, and 2.69–4.61 wt%, respectively. However, a positive correlation is observed between Al₂O₃ and LOI if the sample NH_27 is rejected. These diagrams show that carbonate (represented by Ca and Mg) and oxide (represented by Fe) precipitations do not depend on the LOI.

4.5. Calcite Content

Calcite is present in the majority of the samples. Samples homogeneously distributed in the studied area were selected for calcite content analyses. The calcite content is represented on the map in Figure 16 by the white dots and figures. The values range between 1.2% and 8.7%. Fracture zones, as well as the surrounding granite, present variable calcite content. However, the calcite content appears higher in the southeastern part of the range than in the northwest. All of the samples, except NH_17, NH_26, and NH_31_3, have a calcite content higher than 1.8%, meaning that they were affected by hydrothermal alteration, according to White et al. (2005) [72].

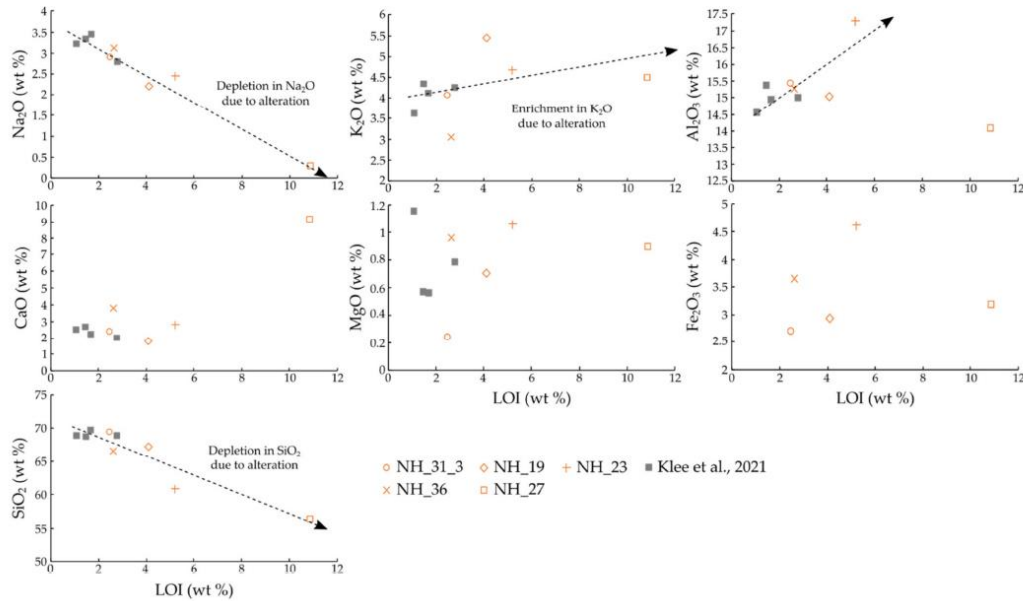


Figure 15. Plot of selected major element oxides (Na_2O , K_2O , Al_2O_3 , CaO , MgO , Fe_2O_3 , and SiO_2) versus loss on ignition (LOI) of samples from this study in orange and from [19] in grey. The dashed arrows show the different trends observed.

4.6. Porosity and Mass-Balance

Porosimetry measurement was only performed on samples NH_27, NH_31_3, and NH_36 (Table 4). NH_36 is the closest to a fracture zone and has the highest porosity (11.5%). This suggests that the porosity increases with proximity to fracture zones. Porosity measurements were used to better decipher the petrophysical properties of the rock for geothermal purpose and to realize mass-balance calculations. The chemical compositions recalculated after suppression of the LOI, the densities, and volume factors (F_v), assuming $X_{\text{Al}_2\text{O}_3} = 0$ of the rock samples used for mass balance calculations, are given in Table 4. The F_v shows values very close to 1, indicating a small change in volume between the freshest sample and the altered ones.

The results of mass-balance calculations, corresponding to the absolute mobility values of each element for each sample, are given in Table 5, by considering a constant volume, $F_v = 1$, as exposed by [76]. Positive values represent the gains and negative values the losses of the considered elements. Absolute mobility values indicate almost immobility of Al_2O_3 , TiO_2 , and MnO . They also show losses of SiO_2 and Na_2O , which are three times more important in NH_27 than in NH_31-3, and twice that of NH_36. The losses of Fe_2O_3 and MgO are more important in NH_31_3 and less important in NH_36. CaO losses are observed in NH_31_3, whereas CaO gains are observed in NH_36 and a high gain is observed in NH_27. Finally, the results show a gain of K_2O in samples NH_27 and NH_31_3 and a loss in NH_37.

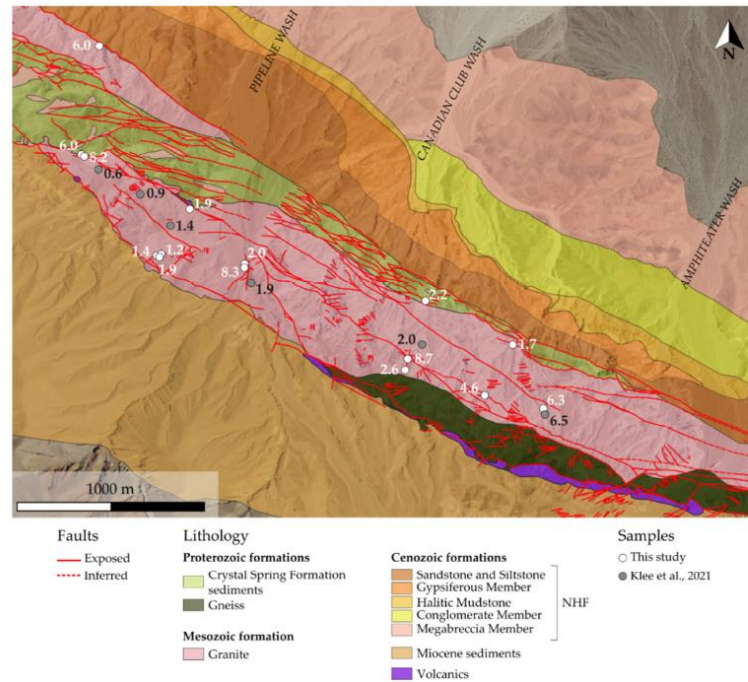


Figure 16. NH geological map showing the location and the associated calcite content of samples from this study represented by the white dots and of samples from [19] by the grey dots.

Table 4. Porosity values, recalculated bulk-rock major element weight percentage, altered rock density/fresh rock density ratio, volume factor (F_v) assuming the immobility of Al_2O_3 ($X_{Al_2O_3} = 0$).

Sample ID	NH_2 ¹	NH_27	NH_31_3	NH_36
Porosity (%)	2.29	10.1	10.1	11.5
Oxides (weight %)				
SiO ₂	69.57	63.3	71.18	68.6
Al ₂ O ₃	14.72	15.81	15.84	15.74
Fe ₂ O ₃	4.35	3.57	2.76	3.76
MgO	1.16	1	0.25	1
CaO	2.53	10.24	2.4	3.91
Na ₂ O	3.23	0.3	2.97	3.21
K ₂ O	3.65	5.04	4.16	3.14
TiO ₂	0.47	0.33	0.25	0.35
MnO	0.12	0.26	0.06	0.12
Density ratio (d_A/d_F)		0.93	0.92	0.92
F_v ($X_{Al_2O_3} = 0$)	1.00	1.00	1.01	1.02

¹ Geochemical data recalculated from [19].

Table 5. Results of mass-balance calculations assuming $F_v = 1$.

Sample ID	NH_27	NH_31_3	NH_36
Absolute mobility (%)			
SiO ₂	−10.39	−3.54	−5.32
Al ₂ O ₃	0.06	−0.18	−0.29
Fe ₂ O ₃	−1.01	−1.77	−0.82
MgO	−0.23	−0.92	−0.22
CaO	7.04	−0.30	1.10
Na ₂ O	−2.95	−0.47	−0.22
K ₂ O	1.06	0.20	−0.70
TiO ₂	−0.16	−0.24	−0.14
MnO	0.12	−0.06	−0.01

4.7. Temperature Conditions

The clay composition of the fractions <2 μm and 2–6 μm was given in Table 1. For some of the samples containing enough illite, Kübler Index (KI) was measured for both fractions (Table 6). The fraction <2 μm likely is supposed to represent neoformed clay minerals, thus corresponding to the youngest event. By contrast, the fraction 2–6 μm might contain either more developed illite crystals by inherited grains recrystallization, or a mix of detrital and neoformed minerals. The KI gives information concerning the degree of metamorphism for each fraction. In some fraction, it was not possible to measure the KI due to the too low amount of illite.

Table 6. List of samples with their respective FWHM and Kübler Index (KI) values in air-dried (AD) conditions for the fractions <2 μm and 2–6 μm . n.m.—not measured.

Sample ID	Illite Peak (10) <2 μm		Illite Peak (10) 2–6 μm	
	FWHM AD	KI AD	FWHM AD	KI AD
NH_16	0.62	0.97	0.43	0.65
NH_17		n.m.	0.80	1.27
NH_18	0.41	0.61	0.34	0.49
NH_19	0.52	0.75	0.51	0.74
NH_22	0.53	0.78	0.58	0.84
NH_24	0.83	1.32	0.70	1.11
NH_25	0.59	0.59	0.63	0.63
NH_27	0.65	0.96	0.55	0.80
NH_31_1_2	0.72	1.14	0.64	1.01
NH_31_3		n.m.	0.34	0.50
NH_32	0.29	0.29	0.21	0.21
NH_34		n.m.	0.28	0.39

KI values range from $1.32\Delta^{\circ}2\theta$ to $0.29\Delta^{\circ}2\theta$ for the <2 μm fraction and from $1.27\Delta^{\circ}2\theta$ to $0.21\Delta^{\circ}2\theta$ for the 2–6 μm fraction (Table 6). The spatial distribution of the samples and their associated KI values are shown in Figure 17 by the dots. In both fractions, most of the samples present KI values corresponding to the diagenetic zone, except for two samples (NH_32 and NH_34). These samples are located in the northwestern part of the main granitic body (Figure 7a,b), at the contact with the Proterozoic basement. They present lower KI values of low anchizone and epizone. No significant variations in KI or trends are observed between both fractions.

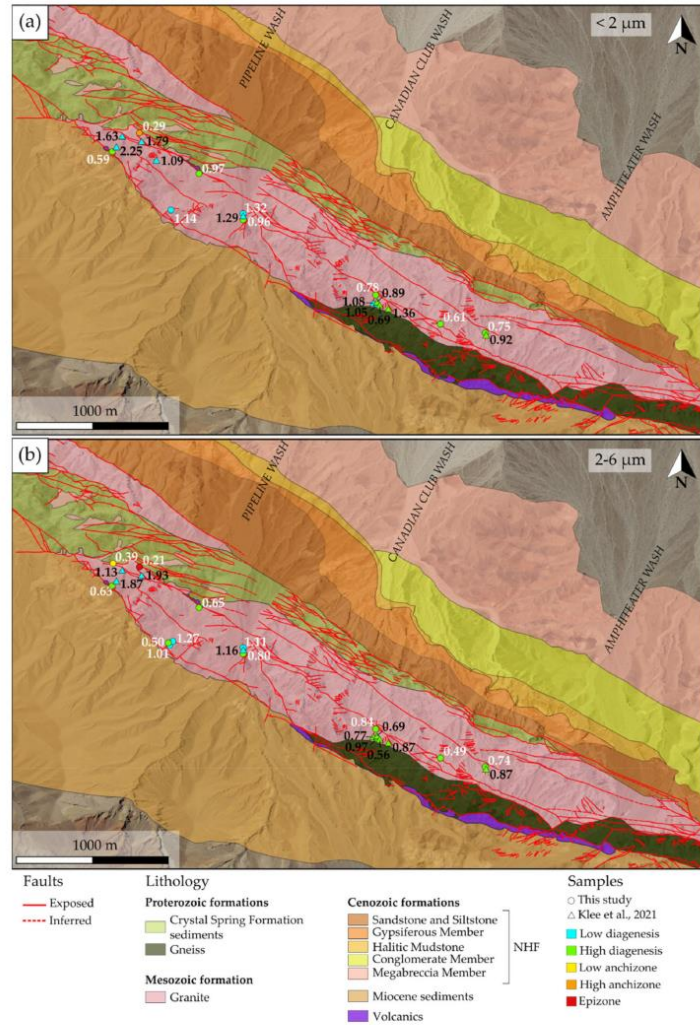


Figure 17. Geological map representing the Kübler Index (KI) in air-dried conditions of each sample from this study (dots) and from [19] (triangles) and the corresponding metamorphic zone represented by the different colors indicated in the legend for (a) the fraction $< 2 \mu\text{m}$ and (b) the fraction $2-6 \mu\text{m}$.

Some samples contain only kaolinite and no illite. Positive trends have been identified between KI and KCI for both clay fractions $< 2 \mu\text{m}$ and $2-6 \mu\text{m}$ (Figure 18). Samples NH_6, NH_8, and NH_31_1_2, with out of range values, due to the presence of I/S and/or corrensite interfering with the 7\AA peak, were excluded from the correlation. The trends observed in the two different fractions are similar and give more confidence into the concomitant evolution of KI and KCI. The correlation provides temperature indications for illite-free samples. Thus, samples NH_26, NH_33, and NH_36 show values equivalent to diagenetic zone and anchizone conditions.

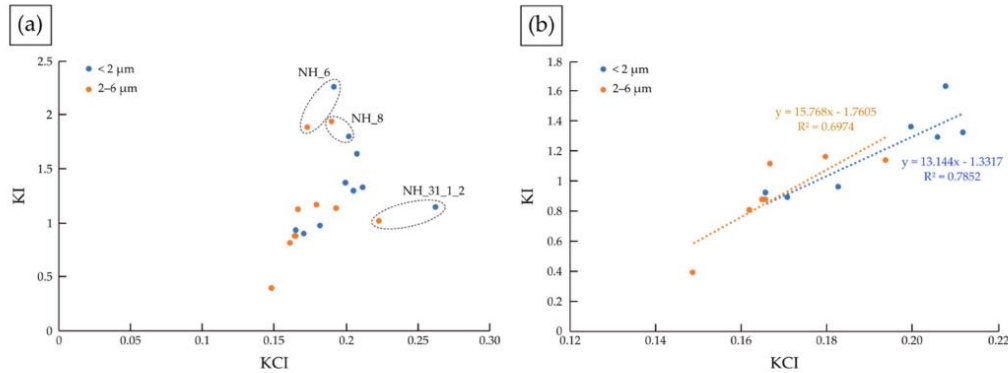


Figure 18. (a) Diagrams showing Kübler Index (KI) values versus the Kaolinite Crystallinity Index (KCI) for the clay fractions <2 μm and 2–6 μm. (b) Diagram showing positive correlations between KI and KCI for the clay fractions <2 μm and 2–6 μm, excluding samples NH_6, NH_8, and NH_31_1_2.

5. Discussion

5.1. Argillic Alteration Dominance

The characterization of the NH granite alteration processes in the vicinity of fracture zones reveals the presence of various secondary minerals, such as clay minerals (kaolinite, illite, I/S mixed layer, corrensite, and vermiculite), carbonates (calcite, dolomite, ankerite, siderite), and oxides. Thus, two successive types of hydrothermal alteration events, characterized by [19] in the protolith, were observed:

1. The propylitic alteration, which is an early stage of alteration affecting pervasively the granite during the cooling of the pluton [83]. It involves mainly the formation of corrensite and epidote considered as the major indicators of the propylitic alteration [19,22,84]. Only plagioclase and biotite are partially affected.
2. The argillic alteration, associated with fluid circulation through a fracture network. Thus, the argillic alteration is also called “vein” alteration [13,21,85]. It is characterized by (1) a high water/rock ratio in the fractures/veins walls, due to fluid circulating within the fracture network [20,21,24,86–89]; and (2) illite + kaolinite + illite/smectite mixed layers + carbonates + oxides replacing plagioclase, biotite and, more rarely, partially K-feldspar [19]. Fractures enhance the fluid circulation and, thus, the fluid–rock interaction. Alteration gradients are visible, increasing toward the fracture (Figure 7a, Figure 9h–k, Figures 12a and 14e,f). An alteration zoning around microfractures is also presented in Figure 6f,g, which could correspond to a time dependent process controlled by a sequence of interrelated mineral reactions [15].

However, compared to [19], the samples are more altered and corrensite is not as evident as in the samples from this study. Kaolinite and illite are the prevailing clay minerals. This confirms a significant fluid–rock interaction near fractures and a predominant argillic alteration, which has overprinted almost completely the propylitic alteration. Kaolinite, being the dominant clay mineral, indicates either a more important leaching of the rock or the circulation of a more acidic fluid [90].

The samples NH_24, NH_26, and NH_33 contain a small amount of vermiculite, which can be associated to hydrothermal alteration at low temperature or to weathering. It is commonly thought that most of the vermiculite is formed under supergene conditions [91,92]. In these samples, the amount of vermiculite is low and the weathering contribution already discarded by [19].

5.2. Thermal Evolution toward Fracture Zones

Studied samples present KI values characteristic of the diagenetic zone, meaning temperatures lower than 200 °C [93]. However, KI values of samples NH_32 and NH_34 have lower KI values with anchizonal to epizonal conditions, meaning temperatures around 300 °C [93]. These two samples present the highest fracture density (Fd4) suggesting that shear heating could contribute to a local increase of temperature [94]. Moreover, KI values are similar between both clay fractions indicating the predominance of neoformed illite crystallization close to fracture zones. It is highlighted by the presence of illite veins observed microscopically. By comparing KI values from this study and from [19], the KI tends to decrease approaching fracture zones. Thus, the greater the fracturing, the higher was the temperature, except for NH_31_1_2 and NH_24. These two samples present higher KI values, meaning lower temperatures. It can be explained by the presence of I/S and vermiculite, forming at lower temperature than illite and kaolinite [91,92,95]. The samples NH_26, NH_33, and NH_36 present only kaolinite. KCI values correlating with KI values, these samples show temperatures estimated to be around 200 °C or less, which correspond to the temperature obtained for the other samples. Likewise, the presence of kaolinite in hydrothermal alteration paragenesis indicates temperature lower than 200 °C [90].

5.3. A Multi-Stage Paleo-Fluid Circulation

Hydrothermal alteration in crystalline basement rocks induces the precipitation of secondary minerals that can seal the fractures [2]. The argillic facies, described above, is also characterized by fractures filled by various kinds of secondary minerals, as a result of different fluid generations. Veins are formed from fluids that had reacted with granite [96] and transported various chemical elements. Through the petrographic analyses of the whole samples, a relative chronology between the different veins can be determined. Six vein generations, following each other, were identified (Figures 6 and 9):

1. Quartz veins resulting in the precipitation of secondary quartz due to primary silicate partial dissolution.
2. Illite veinlets, which have different behaviors, according to the mineral crossed. Indeed, as presented by [19,97], plagioclase is the main pathway for fluid flow due to their abundance in the rock and to dissolution pit porosity, allowing the interconnection between the pores. In quartz and K-feldspar; however, only microfractures create the porosity allowing the fluid to circulate. This explains why veinlets look like straight lines in quartz and K-feldspar and are twisted and blurred lines in altered plagioclase. Illite veinlets can be contemporary to kaolinite veinlets.
3. A dolomitic brecciated vein embedding essentially quartz clasts, such as in sample NH_31.
4. Carbonate veins with different compositions: contemporary ankerite/dolomite veins, intersected by siderite veins and the whole intersected by later calcite veins. They are preferentially oriented NW–SE, according to the direction of the NH. It is suggested that the fluids, having precipitated these carbonate veins, have circulated through the fracture network formed by the activity of the SDVFZ.
5. A carbonate brecciated vein that is likely to have transported clasts of quartz, K-feldspar, and biotite, and is presenting precipitations of barite. This phase, but also barite itself, is only present in sample NH_31. This phase was probably due to a later event that reactivated the main fracture composing the sample and let a new fluid circulate.
6. Calcite veins, as shown in the sample NH_31, which are of a different compositions from generation 4.

Two types of calcite veins and the carbonate vein of phase 5 were, thus, identified through the sample NH_31, allowing the definition of two generations of calcite. However, they do not allow a decision on if the calcite veins identified in the other samples correspond to the generation 4 or 6. CL analyses are ongoing to identify the type of calcite generation. Sample NH_31 and the multiple vein generations show how complex the fluid circulation history was in this area.

5.4. Fluid Circulation and Argillic Alteration Effects on Petrographic and Petrophysical Behavior

The effects of the alteration on the element transfers are described by the diagrams plotting major element oxides against LOI (Figure 15) and by mass-balance calculations (Table 5) using the Gresens method [76] to quantify the losses and gains of elements during hydrothermal alteration. To this end, data from this study and from [19] were used. LOI has been defined as an indicator of the alteration degree [19,98,99] supporting optical observations. In this study, LOI values range from 2.5% to 10.9% (Table 3), whereas, Klee et al. (2021) [19] obtained values from 1.1% to 2.8% for the protolith. These values confirm a more pronounced alteration of the granite in the vicinity of fracture zones.

Concerning element transfers, only minor variations of Al_2O_3 were observed compared to the LOI, also confirmed through mass-balance calculations. Al is thus considered as immobile. This study has shown a significant SiO_2 negative correlation with LOI. This loss is confirmed by mass-balance calculations. It indicates the partial silicate alteration, explaining the presence of quartz veins and veinlets through the granite. A negative correlation with LOI was observed for Na_2O , confirmed by the loss of Na_2O obtained by mass-balance calculation. Indeed, altered plagioclase are depleted in Na_2O . No Na-bearing newly formed minerals (except a little I/S and C/S) was encountered. It is likely that Na was exported out of the alteration zone. When the alteration of plagioclase is less pronounced, as in samples NH_31_3 and NH_36 (Table 3), the Na_2O depletion is lower. However, a global enrichment of K_2O is observed linked to illite crystallization. A positive correlation is observed between the amount of alteration and illite formation. K-feldspar being rarely altered, chemical modelling would be necessary to determine whether the amount of K release by biotite alteration would be sufficient to allow the rather important formation of illite. MgO and Fe_2O_3 present no clear correlation with LOI. However, low depletion of Fe_2O_3 and MgO compared to the protolith were identified by mass-balance calculations. It is suggested that these depletions are linked to the alteration of biotite but they are compensated by their precipitation as oxides or in carbonates. Thus, it is likely that no Fe or Mg is exported out of the alteration zones. CaO and calcite content present no correlation with the LOI. Samples NH_19, NH_36 (this study), and NH_3 (in [19]) present a similar calcite content, respectively, of 6.3%, 6.0%, and 6.5%, whereas they present different LOI values (4.1%, 2.6%, and 2.8%, respectively). The case of a high calcite content associated to a low LOI can be explained by (1) physicochemical fluid composition bringing Ca, and not allowing a complete alteration of plagioclase and biotite into clay minerals [100]; (2) the residence time of the fluid not being sufficient [101]; or (3) a non-sufficient amount of fluid to allow the transformation of plagioclase and biotite into clay minerals. CaO losses are attributed to the alteration of plagioclase. However, the amount of Ca released by the alteration of plagioclase is certainly not sufficient to explain the crystallization of large amounts of carbonate into the granite veins. We infer that Ca is related to an external source as it is gained by the system (open system). As carbonate veins are related to the SDVFZ activity, we suggest that the source of the Ca is the Proterozoic series, which contain dolomite and carbonate sequences.

Fracture zones created porosity through microfractures and spaces between secondary minerals (Figure 6f) precipitated during primary mineral alteration. When fracturing increases, alteration increases too, as well as porosity [10]. However, the subsequent mineralization and chemical alteration can either decrease or increase the porosity of the rock [2]. For a similar LOI, porosity values vary significantly (e.g., NH_3 [19], NH_23, and NH_31_3). No correlation is visible between porosity and alteration or calcite content.

5.5. Relation among Fluid Circulation, Alteration, and Fracture Density

It is expected that areas along the rear southern limit of the CBS have recorded less transcurent shear than areas situated along its northern front (Section 4.1). Recent work by Chabani et al. (2021) [42] has shown a structural compartmentalization occurring at the NH scale with a varying intensity that may influence fluid flow through the fracture network. Likewise, they identified a complex network of joints at outcrop scale, also

encountered in this study at the sample and thin section scales, playing a key role in the fracture connectivity. The authors identified several fracture sets, among which, the NW/SE and the E/W oriented sets are predominant. The NW/SE trend, following the SDVFZ direction, controls the geometry in the whole range, whereas the E/W set, characterized by several short fractures, is mostly present in the central and southeastern part of the NH. The geometrical analysis of both fracture sets showed that the connectivity is ruled by fractures of different sizes. Regarding the fracture distribution, the highest fracture density is recorded within the rear southern part with values five times higher than in the northern part. This can be explained by the complex tectonic setting and the gradient of deformation observed in the entire NH range, with evidence of extreme shearing in the southern part as already presented. Moreover, through scanline analyses along drone photogrammetric outcrop profiles and ground outcrop profiles, Chabani et al. (this issue, under review) [44] show a clear correlation between fracture density and distance from a fault zone. The closer the fault zone, the greater the fracture density. There is no straightforward correlation between amounts of deformation and fracture density. Fracture density depends on a series of parameters notably rock competence, anisotropy of units and possible presence of detachment zones concentrating deformation in narrow areas.

This study, together with that of Klee et al. (2020) [19], confirm the increase of fracture density towards fault zones through several samples collected at different distances from the faults. Moreover, at the NH scale, the LOI increases as the fracture zones are approached (Section 5.4). The more intense the fracturing, the higher the alteration. Likewise, porosity values obtained for samples from Klee et al. (2021) [19] range from 2.2% to 5.2%, whereas, porosity values for this study samples range from 10.1% to 14.0%. Close to fracture zones, samples have more than twice the porosity than the samples away from them. Calcite content (Figure 16) also show higher values near to fracture zones, highlighting the importance of the presence of fractures allowing fluid circulations and thus carbonate precipitation, which mainly filled and sealed the fractures [71,102]. Carbonate veins are present in the whole range, preferentially orientated following the NH strike, probably related to the SDVFZ activity. However, calcite content is generally higher in the southeastern part of the range. This part is characterized by a high fracture density due to complex tectonic setting, related to the GFZ activity [42]. The connectivity within this part is ruled by the small and large fractures, and an additional complex joint network leading the fluid supply toward the fault zone.

The comparison of the data from Klee et al. (2021) [19] with those in this study at the NH scale shows that the increase in fracture density is correlated with the increases in alteration degree, porosity, and calcite content, respectively. However, no correlation is observed between alteration, porosity, and calcite content all together. The sample NH_36 (Figure 11) has shown that calcite content is not related to the intensity of alteration (Section 5.4). This highly fractured sample has been characterized by a specific fracture arrangement, composed mainly of fracture clusters, following the SDVFZ direction. It allows the fluid to circulate following these clusters, and then creating a flow anisotropy. However, only a low alteration degree is observed, which can either be due to (1) specific physicochemical fluid composition [100]; (2) an equilibrium between the fluid and the surrounding rock; (3) an insufficient residence time of the fluid [101]; or (4) a non-sufficient amount of fluid. Fracture density increase does not necessarily induce the increase of alteration (Figure 19a,b), whereas at the NH scale, a general correlation between fracture density and alteration was shown. Sample NH_36 shows that fluid can circulate through a highly fractured granite without necessarily producing alteration (Figure 19b).

Numerous fractures and veins, showing a high fluid–rock ratio, crosscut the granite altering it consequently (Figure 20a,b). Faulkner et al. (2010) [11] have shown that within crystalline rocks, the flow can be ruled by a small number of fractures within the rock surrounding a fracture zone. The fracture interconnections constitute the main parameter, which can enhance the fluid circulation. Samples NH_31 and NH_23 showed the relation between fracturing and alteration at local scale (Section 4.3.2). Thin section fracture analyses

showed that the fracture density average is similar in both samples. NH_31 consists of a brecciated vein developing an alteration gradient but no fracturing gradient (Figure 20c), while NH_23, perpendicular to NH_31, consists of a mylonite developing an alteration and a fracturing gradient (Figure 20d). Regarding the stress axis orientation, it is suggested that the main stress axis σ_3 is at a very high angle to the NH_31 initial quartz vein. The close to normal angle between the initial quartz vein and the stress axis σ_3 was favorable to reactivation, inducing a brecciated vein without developing a significant additional fracture gradient in the surrounding rock (Figure 20c). It has been shown that remnants of a quartz vein composed the NH_31 brecciated vein. This quartz vein, developed during a past event of unknown age and origin, possibly magmatic (last crystallization fluids). It is suggested that this vein was reactivated, letting a new fluid rich in Ca circulates. Then carbonates crystallized giving a brecciated vein as a final product. The alteration gradient observed in the wall rock is especially pronounced at the borders of the brecciated vein. The proximity with the main fluid pathway induced an important leaching by the fluid. Within NH_23 (Figure 20d), it is supposed that the quartz-feldspathic unit was initially a dyke crosscutting the granitic pluton. Such dykes have been observed in the surroundings. During SDVFEZ activity, reactivation of this zone of weakness permitted percolation of a Ca-rich fluid. An intensive shearing induced dynamic recrystallization developing a mylonite in the borders and its associated fracturing gradient in the wall rock. In that case, the main stress axis σ_1 would be characterized by an intermediate angle to the shear plane. A fracturing gradient is observed in the surrounding rock. The fracture density induced in the surrounding rock does not further increase. Asymmetric clasts and shear bands are observed within this mylonitic layer.

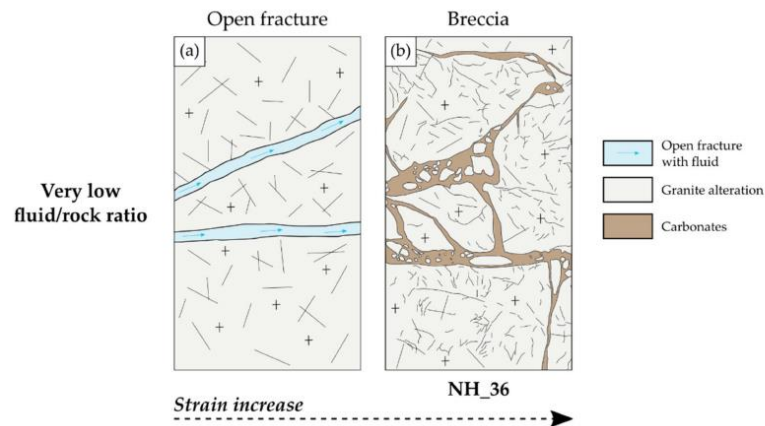


Figure 19. Synthetic scheme showing, from low to moderate strain, the interaction between the fluid and the granite in the cases of a very low fluid/rock ratio. (a) Open fractures with an incipient alteration of the surrounding rock. (b) Brecciated zones with a carbonated matrix and no change of alteration degree. No scale is given for this scheme, because it can represent fracture zones of several order of magnitude.

Fluid circulation and induced fracturing have promoted fluid–rock interactions and the granite alteration, which is more pronounced in NH_23 than in NH_31 (Figures 9h–k and 14e,f). Those two samples showed that at sample and outcrop scales, fracturing and alteration are heterogeneous, but also that the alteration degree is not always related to the fracture density (Figure 20c,d).

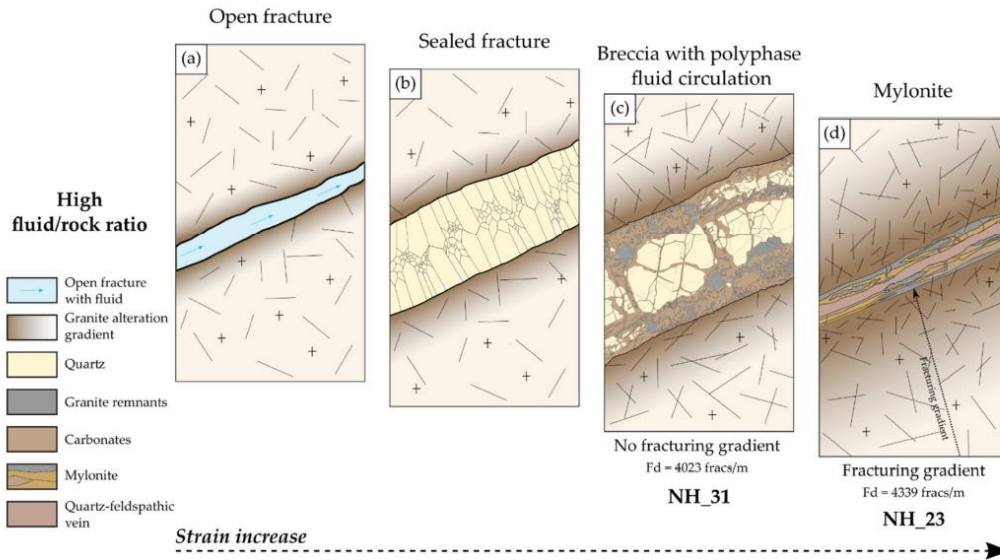


Figure 20. Synthetic scheme showing, from low to moderate strain, the interaction between the fluid and the granite in the cases of a high fluid/rock ratio observed in the field. (a) An open fracture with an incipient alteration gradient at the border. (b) A sealed fracture with a slight alteration gradient. (c) A brecciated vein induced from fracture reactivation and showing an alteration gradient, but no fracturing gradient. (d) A mylonite made of carbonates and granitic lenses showing an alteration gradient and a fracturing gradient. NH₃₁ and NH₂₃ show a similar fracture density (Fd). No scale is given for this scheme, because it can represent fracture zones of several order of magnitude.

These sample analyses allowed us to study a fault zone development depending on strain, fluid–rock ratio, and material rheology. It is shown that at low to moderate regional strain, incipient local high strain concentration is present (Figure 20). It has been observed that:

1. The fluid interacts with the surrounding rock, altering it pervasively, and fractures are sealed by secondary minerals (Figure 20a,b). Those veins can be reactivated by shearing [103]. Thus, it creates a brecciated vein (e.g., NH₃₁) or even a mylonite (e.g., NH₂₃), developing an alteration gradient. Sample NH₂₃ shows that mylonitic deformation appears at low to moderate regional strain when carbonates are involved. Fault reactivation tends to cause a mineral fill breakage and reopens the fracture [2,104].
2. Open fractures let fluid circulate without interaction with the surrounding rock. Shearing creates a breccia without further alteration within the granite, such as in NH₃₆ (Figure 19).

At any scales, fracture density promotes fluid flow through the fracture network provided a fluid is present [5,11]. However, the alteration degree is not correlated to the fracture density.

5.6. Implication of Alteration in Terms of Geothermal Reservoir Properties

Fresh granite has a very low initial matrix porosity (<1%), which “does not allow” the fluid circulation, hence inducing a low permeability [9]. A granitic geothermal reservoir is considered as exploitable when it presents a connected fracture network increasing the permeability and in which a sufficient amount of hot fluid circulates [2,3,9,11]. By flowing through fractures, the fluid interacts with the rock, increasing the matrix porosity and

permeability promoted by the dissolution of the primary minerals and crystallization of newly-formed phases [13]. However, newly-formed minerals can also crystallize in the fractures and seal them, reducing the porosity and the permeability [105,106]. Thus, sealed fractures are transformed from conduits into barriers to fluid flow [83,107,108] and impact the geothermal production by decreasing the connectivity between the fractures and hence the permeability [2,109].

The NH altered granite shows an important fracture network and a high matrix porosity, which allowed fluids to circulate and to interact with the surrounding rock. Indeed, numerous veins with various infills crosscut the granite indicating several successive fluid circulation events. Carbonates occupy a prominent part of the fracture system, which can be easily dissolved thanks to acid injections in order to connect the boreholes to major conductive fractures for geothermal exploitation. It is suggested that, when NH were an active reservoir at depth, fractures were only partially filled, and the fluid could flow through the fracture network. It has been seen that the stress field has a major impact on the fluid circulation. Indeed, drilling into fractures at a very high angle from the main stress axis σ_1 , such as exposed by sample NH_31, is favorable to allow fluid to circulate. In the event of geothermal exploitation, only minor chemical stimulation, if any, would have been necessary [13,71,110]. Moreover, the alteration amount is not necessarily related to the degree of fracturing and, therefore, the fracture network influence on fluid circulation is hardly predictable. Thus, due to the conduit-barrier role, the deformation gradient, the degree of fracturing, the alteration processes, and the relationship between them, have a large impact on geothermal production [109].

6. Conclusions

Noble Hills (NH) is a newly studied area, in terms of an exhumed granitic geothermal reservoir. It provides an excellent opportunity to give fundamental scientific input in 3D, allowing for better understanding of granitic reservoir behavior in a trans-tensional context. This analogue shows how complex a granitic reservoir can be, in terms of structures, fluid circulation, and fluid–rock interactions. This study proposes a geometric, petrographic, petrophysical, and geochemical description in order to characterize the influence of fracturing on fluid circulation and alteration processes.

Approaching fracture zones at large scale, the NH granite shows signs of several generations of fluid circulations resulting in successive veins of various mineralization. Fluid circulation being more important in the vicinity of fracture zones, a stronger fluid–rock interaction is observed. Thus, argillic alteration prevails compared to in the protolith. It is highlighted by the increase of the LOI correlated to a Na depletion due to plagioclase alteration and a K enrichment associated to illite precipitation. Likewise, the porosity, the calcite content, and the temperature increase nearer to fracture zones. However, no correlation exists among LOI, porosity, and calcite content altogether. Moreover, a high fracture density does not necessarily imply a strong alteration (e.g., sample NH_36).

This relation among fluid circulation, alteration, and fracturing is also visible at a sample scale. The higher the fracture density, the more pronounced the alteration. However, samples NH_31 and NH_23 showed how complex this relation could be:

- NH_31 shows a reactivated vein giving a brecciated vein (quartz and granitic clasts in a carbonate matrix), which induced no fracture gradient in the surrounding porphyritic granite, but developed an alteration gradient.
- NH_23 shows a carbonate mylonite creeping around deformed granite lenses, which induced a fracture gradient, as well as an alteration gradient in the surrounding porphyritic granite.

These two samples, showing different deformation features as a result of a different orientation within the stress field, present a similar fracture density. Strain was accumulated within a carbonate mylonite within sample NH_23. The alteration gradient is more pronounced in this sample, but the fracture density does not change. Sample NH_36, consisting of a granite composed of a cohesive breccia, whose matrix is made of dolomite,

shows a low alteration. Even locally, alteration does not always depend on the deformation gradient or on the fracture density.

This study shows that the deformation gradient observed at a large scale is also visible locally in the context of a low to moderate strain. It also highlights the importance of mineral crystallization in a geothermal reservoir. Fluid flow depends on a connected network of open and permeable fractures. In reservoirs at depth, fractures can be sealed and act as a barrier. Stimulation techniques are needed in order to reopen them so that a drain allowing a new fluid circulation is created. The influence of fracture zones on fluid flow and alteration is difficult to predict and yet impacts the production from the reservoir.

In order to complete this work, a future study will focus on the influence of a fault zone on fluid circulation and alteration processes, in the NH, at high strain conditions. Moreover, laboratory investigations could be performed to better understand the controlling parameters of the ongoing processes and fracturing of rocks.

Author Contributions: Conceptualization, J.K., A.C., B.A.L., S.P., R.L.H. and G.T.; methodology, J.K., A.C., B.A.L., S.P., R.L.H. and G.T.; software, J.K.; validation, A.C., B.A.L., S.P., R.L.H. and G.T.; formal analysis, J.K.; investigation, J.K., A.C., B.A.L., S.P., R.L.H. and G.T.; resources, J.K.; data curation, J.K., A.C., B.A.L., S.P., R.L.H. and G.T.; writing—original draft preparation, J.K.; writing—review and editing, A.C., B.A.L., S.P., R.L.H. and G.T.; and H2020 MEET consortium; visualization, A.C., B.A.L., S.P., R.L.H. and G.T.; supervision, J.K.; project administration, G.T.; funding acquisition, G.T. and H2020 MEET consortium. All authors have read and agreed to the published version of the manuscript.

Funding: This project has received funding from the European Union’s Horizon 2020 research and innovation program under grant agreement no. 792037 (H2020 MEET project).

Data Availability Statement: Not applicable.

Acknowledgments: This manuscript was prepared as a contribution to the PhD thesis (Institut Polytechnique UniLaSalle Beauvais) of Johanne Klee, which was funded by the European Union’s Horizon 2020 research and innovation program under grant agreement no. 792037 (H2020 MEET project). The authors greatly thank Terry Pavlis for his support and helpful exchanges about the regional geology of Death Valley and the Noble Hills. Albert Genter is thanked for the helpful discussions and knowledge about fractured granitic reservoirs. We are grateful to Klaus Wemmer for his help on XRD analyses and the fruitful discussions. We also thank Graciela Sosa and Alphonse M. Van den Kerkhof for their help on cathodoluminescence observations and acquisitions. We thank Mahdi Chettabi, Thi Tuyen Nguyen, Elena Pavlovskaya, Carl Tixier, and Chloé Gindrat for their help with the analyses. We acknowledge the H2020 MEET consortium for their helpful comments and the validation of the manuscript. We would like also to thank the Hauts-de-France region for its help in setting up the MEET project, in particular the FRAPPE (Fonds Regional d’Aide aux Porteurs de Projets Européens). We finally would like to thank the two anonymous reviewers and the editors for their help and remarks in improving this manuscript.

Conflicts of Interest: The authors declare no conflict of interest.

References

- Williams, C.F.; Reed, M.J.; Anderson, A.F. Updating the Classification of Geothermal Resources. In Proceedings of the Thirty Sixth Workshop on Geothermal Reservoir Engineering Stanford University, Stanford, CA, USA, 31 January–2 February 2011.
- Gillespie, P.A.; Holdsworth, R.; Long, D.; Williams, A.; Gutmanis, J. Introduction: Geology of fractured reservoirs. *J. Geol. Soc.* **2021**, *178*, 2020–2197. [[CrossRef](#)]
- Gentier, S.; Hopkins, D.; Riss, J. Role of fracture geometry in the evolution of flow paths under stress. In *Geophysical Monograph Series*; Faybishenko, B., Witherspoon, P.A., Benson, S.M., Eds.; American Geophysical Union: Washington, DC, USA, 2000; Volume 122, pp. 169–184, ISBN 978-0-87590-980-6.
- Curewitz, D.; Karson, J.A. Structural settings of hydrothermal outflow: Fracture permeability maintained by fault propagation and interaction. *J. Volcanol. Geotherm. Res.* **1997**, *79*, 149–168. [[CrossRef](#)]
- Dezayes, C.; Lerouge, C. Reconstructing Paleofluid Circulation at the Hercynian Basement/Mesozoic Sedimentary Cover Interface in the Upper Rhine Graben. Available online: <https://www.hindawi.com/journals/geofluids/2019/4849860/abs/> (accessed on 21 June 2019).

6. Vidal, J.; Genter, A. Overview of naturally permeable fractured reservoirs in the central and southern Upper Rhine Graben: Insights from geothermal wells. *Geothermics* **2018**, *74*, 57–73. [[CrossRef](#)]
7. Callahan, O.A.; Eichhubl, P.; Olson, J.E.; Davatzes, N.C. Fracture Mechanical Properties of Damaged and Hydrothermally Altered Rocks, Dixie Valley–Stillwater Fault Zone, Nevada, USA. *J. Geophys. Res. Solid Earth* **2019**, *124*, 4069–4090. [[CrossRef](#)]
8. Bauer, J.F.; Meier, S.; Philipp, S. Architecture, fracture system, mechanical properties and permeability structure of a fault zone in Lower Triassic sandstone, Upper Rhine Graben. *Tectonophysics* **2015**, *647–648*, 132–145. [[CrossRef](#)]
9. Géraud, Y.; Rosener, M.; Surma, F.; Place, J.; Le Garzic, E.; Diraison, M. Physical properties of fault zones within a granite body: Example of the Soultz-sous-Forêts geothermal site. *Comptes Rendus Geosci.* **2010**, *342*, 566–574. [[CrossRef](#)]
10. Géraud, Y.; Surma, F.; Rosener, M. *Porosity Network of Soultz-Sous-Forêts Granite: The Importance of the Damaged Zone around Faults and Fractures*; Ecole et Observatoire des Sciences de la Terre: Strasbourg, France, 2005.
11. Faulkner, D.; Jackson, C.; Lunn, R.; Schliske, R.; Shipton, Z.; Wibberley, C.; Withjack, M. A review of recent developments concerning the structure, mechanics and fluid flow properties of fault zones. *J. Struct. Geol.* **2010**, *32*, 1557–1575. [[CrossRef](#)]
12. Long, J.C.S.; Witherspoon, P.A. The relationship of the degree of interconnection to permeability in fracture networks. *J. Geophys. Res. Space Phys.* **1985**, *90*, 3087–3098. [[CrossRef](#)]
13. Ledéser, B.; Hebert, R.; Genter, A.; Bartier, D.; Clauer, N.; Grall, C. Fractures, hydrothermal alterations and permeability in the Soultz Enhanced Geothermal System. *Comptes Rendus Geosci.* **2010**, *342*, 607–615. [[CrossRef](#)]
14. Kuncoro, G.B. Fluid-Rock Interaction Studies on an Enhanced Geothermal System in the Cooper Basin, South Australia. Ph.D. Thesis, University of Adelaide, Adelaide, SA, Australia, 2015.
15. Turpault, M.-P.; Berger, G.; Meunier, A. Dissolution-precipitation processes induced by hot water in a fractured granite Part I: Wall-rock alteration and vein deposition processes. *Eur. J. Miner.* **1992**, *4*, 1457–1476. [[CrossRef](#)]
16. Dezayes, C.; Lerouge, C.; Innocent, C.; Lach, P. Structural control on fluid circulation in a graben system: Constraints from the Saint Pierre Bois quarry (Vosges, France). *J. Struct. Geol.* **2021**, *146*, 104323. [[CrossRef](#)]
17. Dalmais, E.; Genter, A.; Trullenque, G.; Leoutre, E.; Leiss, B.; Wagner, B.; Mints, A.C.; Bär, K.; Rajsl, I. MEET Project: Toward the Spreading of EGS across Europe. In Proceedings of the European Geothermal Congress, Den Haag, The Netherlands, 11–14 June 2019.
18. Trullenque, G.; Genter, A.; Leiss, B.; Wagner, B.; Bouchet, R.; Leoutre, E.; Malnar, B.; Bär, K.; Rajsl, I. Upscaling of EGS in Different Geological Conditions: A European Perspective. In Proceedings of the 43rd Workshop on Geothermal Reservoir Engineering Stanford University, Stanford, CA, USA, 12–14 February 2018.
19. Klee, J.; Potel, S.; Ledéser, B.; Hébert, R.; Chabani, A.; Barrier, P.; Trullenque, G. Fluid-Rock Interactions in a Paleo-Geothermal Reservoir (Noble Hills Granite, California, USA). Part 1: Granite Pervasive Alteration Processes away from Fracture Zones. *Geosciences* **2021**, *11*, 325. [[CrossRef](#)]
20. Ledéser, B.; Berger, G.; Meunier, A.; Genter, A.; Bouchet, A. Diagenetic-type reactions related to hydrothermal alteration in the Soultz-sous-Forêts granite, France. *Eur. J. Miner.* **1999**, *11*, 731–742. [[CrossRef](#)]
21. Genter, A. Géothermie Roches Chaudes Sèches: Le Granite de Soultz-Sous-Forêts (Bas-Rhin, France): Fracturation Naturelle, Altérations Hydrothermales et Interaction Eau-Roche. Ph.D. Thesis, Université d'Orléans, Orléans, France, 1989.
22. Traineau, H.; Genter, A.; Cautru, J.P.; Fabriol, H.; Chevremont, P. Petrography of the Granite Massif from Drill Cutting Analysis and Well Log Interpretation in the Geothermal HDR Borehole GPK1 (Soultz, Alsace, France). *Geotherm. Sci. Technol.* **1991**, *3*, 1–29.
23. Meunier, A. Hydrothermal Alteration by Veins. In *Origin and Mineralogy of Clays: Clays and the Environment*; Velde, B., Ed.; Springer: Berlin/Heidelberg, Germany, 1995; pp. 247–267. ISBN 978-3-662-12648-6.
24. Bonorino, F.G. Hydrothermal alteration in the front range mineral belt, Colorado. *GSA Bull.* **1959**, *70*, 53–90. [[CrossRef](#)]
25. Caine, J.S.; Bruhn, R.L.; Forster, C.B. Internal structure, fault rocks, and inferences regarding deformation, fluid flow, and mineralization in the seismogenic Stillwater normal fault, Dixie Valley, Nevada. *J. Struct. Geol.* **2010**, *32*, 1576–1589. [[CrossRef](#)]
26. Norton, I. Two-stage formation of Death Valley. *Geosphere* **2011**, *7*, 171–182. [[CrossRef](#)]
27. Dokka, R.K.; Travis, C.J. Role of the Eastern California Shear Zone in accommodating Pacific-North American Plate motion. *Geophys. Res. Lett.* **1990**, *17*, 1323–1326. [[CrossRef](#)]
28. Stewart, J.H.; Ernst, W.G. Tectonics of the Walker Lane Belt, Western Great Basin: Mesozoic and Cenozoic Deformation in a Zone of Shear. *Metamorph. Crustal Evol. West. United States* **1988**, *7*, 683–713.
29. Lifton, Z.M.; Newman, A.V.; Frankel, K.L.; Johnson, C.W.; Dixon, T.H. Insights into distributed plate rates across the Walker Lane from GPS geodesy. *Geophys. Res. Lett.* **2013**, *40*, 4620–4624. [[CrossRef](#)]
30. Miller, M.M.; Johnson, D.J.; Dixon, T.H.; Dokka, R.K. Refined kinematics of the eastern California shear zone from GPS observations, 1993–1998. *J. Geophys. Res. Space Phys.* **2001**, *106*, 2245–2263. [[CrossRef](#)]
31. Hill, M.L.; Troxel, B.W. Tectonics of Death Valley region, California. *GSA Bull.* **1966**, *77*, 435–438. [[CrossRef](#)]
32. Burchfiel, B.C.; Stewart, J.H. “Pull-Apart” Origin of the Central Segment of Death Valley, California. *GSA Bull.* **1966**, *77*, 439–442. [[CrossRef](#)]
33. Pavlis, T.L.; Trullenque, G. Evidence for 40–41 km of dextral slip on the southern Death Valley fault: Implications for the Eastern California shear zone and extensional tectonics. *Geology* **2021**, *49*, 767–772. [[CrossRef](#)]
34. Rämö, T.O.; Calzia, J.P.; Kosunen, P.J. Geochemistry of Mesozoic plutons, southern Death Valley region, California: Insights into the origin of Cordilleran interior magmatism. *Contrib. Miner. Pet.* **2002**, *143*, 416–437. [[CrossRef](#)]

35. Reinert, E. Low-Temperature Thermochronometry of the Avawatz Mountains, California: Implications for the Inception of the Eastern California Shear Zone. Ph.D. Thesis, University of Washington, Seattle, WA, USA, 2004.
36. Chinn, L.D. *Low-Temperature Thermochronometry of the Avawatz Mountains*; Implications for the Eastern Terminus and Inception of the Garlock Fault Zone; University of Washington: Seattle, WA, USA, 2013; 48p.
37. Spencer, J.E. Chapter 15: Late Cenozoic extensional and compressional tectonism in the southern and western Avawatz Mountains, southeastern California. In *Geological Society of America Memoirs*; Geological Society of America: Boulder, CO, USA, 1990; Volume 176, pp. 317–334.
38. Niles, J.H. Post-Middle Pliocene Tectonic Development of the Noble Hills, Southern Death Valley, California. Ph.D. Thesis, San Francisco State University, San Francisco, CA, USA, 2016.
39. Brady, R.H. Neogene stratigraphy of the Avawatz Mountains between the Garlock and Death Valley fault zones, southern Death Valley, California: Implications as to late Cenozoic tectonism. *Sediment. Geol.* **1984**, *38*, 127–157. [[CrossRef](#)]
40. Troxel, B.W.; Butler, P.R. *Rate of Cenozoic Slip on Normal Faults, South-Central Death Valley, California*; Department of Geology, University of California: Berkeley, CA, USA, 1979.
41. Klee, J.; Trullenque, G.; Ledésert, B.; Potel, S.; Hébert, R.; Chabani, A.; Genter, A. Petrographic Analyses of Fractured Granites Used as An Analogue of the Soultz-Sous-Forêts Geothermal Reservoir: Noble Hills, CA, USA. In Proceedings of the World Geothermal Congress 2020+1, Reykjavik, Iceland, 24–27 October 2020.
42. Chabani, A.; Trullenque, G.; Ledésert, B.; Klee, J. Multiscale Characterization of Fracture Patterns: A Case Study of the Noble Hills Range (Death Valley, CA, USA), Application to Geothermal Reservoirs. *Geoscience* **2021**, *11*, 280. [[CrossRef](#)]
43. Castaing, C.; Rabu, D. Apports de La Géologie à La Recherche et à l'exploitation de Pierres de Taille (Roches Ornamentales et de Construction). *BULL BRGM* **1981**, *3*, 1.
44. Chabani, A.; Trullenque, G.; Klee, J.; Ledésert, B.A. Fracture Spacing Variability and the Distribution of Fracture Patterns in Granitic Geothermal Reservoir: A Case Study in the Noble Hills Range (Death Valley, CA, USA). *Geosciences* **2021**, *11*, 280. [[CrossRef](#)]
45. Laubach, S.; Lamarche, J.; Gauthier, B.; Dunne, W.; Sanderson, D. Spatial arrangement of faults and opening-mode fractures. *J. Struct. Geol.* **2018**, *108*, 2–15. [[CrossRef](#)]
46. Olson, J.E. Joint pattern development: Effects of subcritical crack growth and mechanical crack interaction. *J. Geophys. Res. Space Phys.* **1993**, *98*, 12251–12265. [[CrossRef](#)]
47. Bisdom, K.; Gauthier, B.; Bertotti, G.; Hardebol, N. Calibrating discrete fracture-network models with a carbonate three-dimensional outcrop fracture network: Implications for naturally fractured reservoir modeling. *AAPG Bull.* **2014**, *98*, 1351–1376. [[CrossRef](#)]
48. Gillespie, P.; Howard, C.; Walsh, J.; Watterson, J. Measurement and characterisation of spatial distributions of fractures. *Tectonophysics* **1993**, *226*, 113–141. [[CrossRef](#)]
49. Priest, S.; Hudson, J. Discontinuity spacings in rock. *Int. J. Rock Mech. Min. Sci. Géoméch. Abstr.* **1976**, *13*, 135–148. [[CrossRef](#)]
50. Sanderson, D.J.; Peacock, D.C. Line sampling of fracture swarms and corridors. *J. Struct. Geol.* **2019**, *122*, 27–37. [[CrossRef](#)]
51. Terzaghi, R.D. Sources of Error in Joint Surveys. *Géotechnique* **1965**, *15*, 287–304. [[CrossRef](#)]
52. Zhou, W.; Wang, Z.L. *Scanning Microscopy for Nanotechnology: Techniques and Applications*; Springer Science & Business Media: Berlin/Heidelberg, Germany, 2007; ISBN 978-0-387-39620-0.
53. Kanda, K. Energy Dispersive X-Ray Spectrometer. U.S. Patent 5,065,020, 1991.
54. Götze, J. Cathodoluminescence in Applied Geosciences. In *Cathodoluminescence in Geosciences*; Pagel, M., Barbin, V., Blanc, P., Ohnenstetter, D., Eds.; Springer: Berlin/Heidelberg, Germany, 2000; ISBN 978-3-662-04086-7.
55. Götze, J. Application of Cathodoluminescence Microscopy and Spectroscopy in Geosciences. *Microsc. Microanal.* **2012**, *18*, 1270–1284. [[CrossRef](#)] [[PubMed](#)]
56. Kretz, R. Symbols for Rock-Forming Minerals. *Am. Mineral.* **1983**, *68*, 277–279.
57. Schmidt, D.; Schmidt, S.T.; Mullis, J.; Mählmann, R.F.; Frey, M. Very low grade metamorphism of the Tavayanne formation of western Switzerland. *Contrib. Miner. Pet.* **1997**, *129*, 385–403. [[CrossRef](#)]
58. Kisch, H.J. Illite crystallinity: Recommendations on sample preparation, X-ray diffraction settings, and interlaboratory samples. *J. Metamorph. Geol.* **1991**, *9*, 665–670. [[CrossRef](#)]
59. Mählmann, R.F.; Frey, M. Standardisation, calibration and correlation of the Kübler-index and the vitrinite/bituminite reflectance: An inter-laboratory and field related study. *Swiss J. Geosci.* **2012**, *105*, 153–170. [[CrossRef](#)]
60. Moore, D.M.; Reynolds, R.C. *X-ray Diffraction and the Identification and Analysis of Clay Minerals*; Oxford University Press: New York, NY, USA, 1989.
61. Starkey, H.C.; Blackmon, P.D.; Hauff, P.L. *The Routine Mineralogical Analysis of Clay-Bearing Samples*; U.S. G.P.O.: Washington, DC, USA, 1984.
62. Kübler, B. La Cristallinité de l'illite et Les Zones Tout a Fait Superieures Du Metamorphisme. In *Etages Tectoniques*; La Baconniere: Boudry, Switzerland, 1967; pp. 105–121.
63. Warr, L.; Mählmann, R.F. Recommendations for Kübler Index standardization. *Clay Miner.* **2015**, *50*, 283–286. [[CrossRef](#)]
64. Kisch, H.J. Correlation between indicators of very low-grade metamorphism. In *Low-Temperature Metamorphism*; Frey, M., Ed.; Blackie and Son Ltd.: Glasgow, UK, 1987; pp. 227–300.

65. Árkai, P.; Sassi, F.; Desmons, J. Very Low- to Low-Grade Metamorphic Rocks. In *Metamorphic Rocks A Classification and Glossary Terms*; Cambridge University Press: Cambridge, UK, 2003.
66. Warr, L.N.; Cox, S.C. Correlating illite (Kübler) and chlorite (Árkai) “crystallinity” indices with metamorphic mineral zones of the South Island, New Zealand. *Appl. Clay Sci.* **2016**, *134*, 164–174. [[CrossRef](#)]
67. Frey, M. Very low-grade metamorphism of clastic sedimentary rocks. In *Low-Temperature Metamorphism*; Frey, M., Ed.; Blackie: Glasgow, UK, 1987; pp. 9–58.
68. Árkai, P.; Maehlmann, R.; Suchy, V.; Balogh, K.; Sykorová, L.; Frey, M. Possible Effects of Tectonic Shear Strain on Phyllosilicates: A Case Study from the Kandersteg Area, Helvetic Domain, Central Alps, Switzerland. *TMPM Tschermaks Mineral. Petrogr. Mitt.* **2002**, *82*, 273–290.
69. Mullis, J.; Máhlmann, R.F.; Wolf, M. Fluid inclusion microthermometry to calibrate vitrinite reflectance (between 50 and 270 °C), illite Kübler-Index data and the diagenesis/anchizone boundary in the external part of the Central Alps. *Appl. Clay Sci.* **2017**, *143*, 307–319. [[CrossRef](#)]
70. Warr, L.N.; Rice, A.H.N. Interlaboratory standardization and calibration of day mineral crystallinity and crystallite size data. *J. Metamorph. Geol.* **1994**, *12*, 141–152. [[CrossRef](#)]
71. Ledésert, B.; Hébert, R.L.; Grall, C.; Genter, A.; Dezayes, C.; Bartier, D.; Gérard, A. Calcimetry as a useful tool for a better knowledge of flow pathways in the Soultz-sous-Forêts Enhanced Geothermal System. *J. Volcanol. Geotherm. Res.* **2009**, *181*, 106–114. [[CrossRef](#)]
72. White, A.F.; Schulz, M.S.; Lowenstern, J.B.; Vivit, D.V.; Bullen, T.D. The ubiquitous nature of accessory calcite in granitoid rocks: Implications for weathering, solute evolution, and petrogenesis. *Geochim. Cosmochim. Acta* **2005**, *69*, 1455–1471. [[CrossRef](#)]
73. Dullien, F.A.L. *Porous Media: Fluid Transport and Pore Structure*; Academic Press: San Diego, CA, USA, 1979; ISBN 978-0-323-13933-5.
74. Navelot, V.; Géraud, Y.; Favier, A.; Diraison, M.; Corsini, M.; Lardeaux, J.-M.; Verati, C.; de Lépinay, J.M.; Legendre, L.; Beauchamps, G. Petrophysical properties of volcanic rocks and impacts of hydrothermal alteration in the Guadeloupe Archipelago (West Indies). *J. Volcanol. Geotherm. Res.* **2018**, *360*, 1–21. [[CrossRef](#)]
75. Gates, W.P.; Nefiodovas, A.; Peter, P. Permeability of an Organo-Modified Bentonite to Ethanol-Water Solutions. *Clays Clay Miner.* **2004**, *52*, 192–203. [[CrossRef](#)]
76. Gresens, R.L. Composition-volume relationships of metasomatism. *Chem. Geol.* **1967**, *2*, 47–65. [[CrossRef](#)]
77. Beaufort, D.; Baromet, A.; Lanson, B.; Meunier, A. Corrensite; a single phase or a mixed-layer phyllosilicate in saponite-to-chlorite conversion series? A case study of Sancerre-Couy deep drill hole (France). *Am. Miner.* **1997**, *82*, 109–124. [[CrossRef](#)]
78. Andrews, B.J.; Roberts, J.J.; Shipton, Z.K.; Bigi, S.; Tartarello, M.C.; Johnson, G. How do we see fractures? Quantifying subjective bias in fracture data collection. *Solid Earth* **2019**, *10*, 487–516. [[CrossRef](#)]
79. Bestmann, M.; Kunze, K.; Matthews, A. Evolution of a calcite marble shear zone complex on Thassos Island, Greece: Microstructural and textural fabrics and their kinematic significance. *J. Struct. Geol.* **2000**, *22*, 1789–1807. [[CrossRef](#)]
80. Burkhard, M. Ductile deformation mechanisms in micritic limestones naturally deformed at low temperatures (150–350 °C.). *Geol. Soc. London Spéc. Publ.* **1990**, *54*, 241–257. [[CrossRef](#)]
81. Schmid, S.; Panozzo, R.; Bauer, S. Simple shear experiments on calcite rocks: Rheology and microfabric. *J. Struct. Geol.* **1987**, *9*, 747–778. [[CrossRef](#)]
82. Stipp, M.; Kunze, K. Dynamic recrystallization near the brittle-plastic transition in naturally and experimentally deformed quartz aggregates. *Tectonophysics* **2008**, *448*, 77–97. [[CrossRef](#)]
83. Glaas, C.; Patrier, P.; Vidal, J.; Beaufort, D.; Genter, A. Clay Mineralogy: A Signature of Granitic Geothermal Reservoirs of the Central Upper Rhine Graben. *Minerals* **2021**, *11*, 479. [[CrossRef](#)]
84. Burnham, C.W. Facies and types of hydrothermal alteration. *Econ. Geol.* **1962**, *57*, 768–784. [[CrossRef](#)]
85. Dubois, M.; Ledesert, B.; Potdevin, J.-L.; Vançon, S. Détermination des conditions de précipitation des carbonates dans une zone d’altération du granite de Soultz (soubassement du fossé Rhénan, France): L’enregistrement des inclusions fluides. *Comptes Rendus l’Académie Sci. Ser. II A Earth Planet. Sci.* **2000**, *331*, 303–309. [[CrossRef](#)]
86. Marqués, J.M.; Matias, M.J.; Basto, M.J.; Carreira, P.M.; Aires-Barros, L.A.; Goff, F.E. Hydrothermal alteration of Hercynian granites, its significance to the evolution of geothermal systems in granitic rocks. *Geothermics* **2010**, *39*, 152–160. [[CrossRef](#)]
87. Pauwels, H.; Fouillac, C.; Fouillac, A.-M. Chemistry and isotopes of deep geothermal saline fluids in the Upper Rhine Graben: Origin of compounds and water-rock interactions. *Geochim. Cosmochim. Acta* **1993**, *57*, 2737–2749. [[CrossRef](#)]
88. Parneix, J.; Petit, J. Hydrothermal alteration of an old geothermal system in the Auriat granite (Massif Central, France): Petrological study and modelling. *Chem. Geol.* **1991**, *89*, 329–351. [[CrossRef](#)]
89. Berger, G.; Velde, B. Chemical parameters controlling the propylitic and argillic alteration process. *Eur. J. Miner.* **1992**, *4*, 1439–1456. [[CrossRef](#)]
90. Fulignati, P. Clay Minerals in Hydrothermal Systems. *Minerals* **2020**, *10*, 919. [[CrossRef](#)]
91. Fordham, A.W. Weathering of Biotite into dioctahedral Clay Minerals. *Clay Miner.* **1989**, *25*, 51–63. [[CrossRef](#)]
92. Kajdas, B.; Michalik, M.; Migoń, P. Mechanisms of granite alteration into grus, Karkonosze granite, SW Poland. *Catena* **2017**, *150*, 230–245. [[CrossRef](#)]
93. Abad, I. Physical Meaning and Applications of the Illite Kübler Index: Measuring Reaction Progress in Low-Grade Metamorphism. In *Diagenesis and Low-Temperature Metamorphism, Theory, Methods and Regional Aspects, Seminarios, Sociedad Espanola: Sociedad Espanola Mineralogia*; University of Jaen: Jaen, Spain, 2007; pp. 53–64.




94. Camacho, A.; McDougall, I.; Armstrong, R.; Braun, J. Evidence for shear heating, Musgrave Block, central Australia. *J. Struct. Geol.* **2001**, *23*, 1007–1013. [[CrossRef](#)]
95. Środoń, J. Nature of mixed-layer clays and mechanisms of their formation and alteration. *Annu. Rev. Earth Planet. Sci.* **1999**, *27*, 19–53. [[CrossRef](#)]
96. Bruhn, R.L.; Parry, W.T.; Yonkee, W.A.; Thompson, T. Fracturing and hydrothermal alteration in normal fault zones. *Pure Appl. Geophys.* **1994**, *142*, 609–644. [[CrossRef](#)]
97. Sardini, P.; Ledesert, B.; Touchard, G. Quantification of Microscopic Porous Networks By Image Analysis and Measurements of Permeability in the Soultz-Sous-Forêts Granite (Alsace, France). In *Fluid Flow and Transport in Rocks*; Springer: Berlin/Heidelberg, Germany, 1997; pp. 171–189, Chapter 10.
98. Liu, Y.; Xie, C.; Li, C.; Li, S.; Santosh, M.; Wang, M.; Fan, J. Breakup of the northern margin of Gondwana through lithospheric delamination: Evidence from the Tibetan Plateau. *GSA Bull.* **2019**, *131*, 675–697. [[CrossRef](#)]
99. Chambefort, L.; Moritz, R.; von Quadt, A. Petrology, geochemistry and U–Pb geochronology of magmatic rocks from the high-sulfidation epithermal Au–Cu Chelopech deposit, Srednogie zone, Bulgaria. *Miner. Deposita* **2007**, *42*, 665–690. [[CrossRef](#)]
100. Glassley, W.; Crossey, L.; Montañez, I. Fluid–Rock Interaction. In *Encyclopedia of Geochemistry*; Springer International Publishing: Cham, Switzerland, 2016.
101. Kadko, D.; Butterfield, D.A. The relationship of hydrothermal fluid composition and crustal residence time to maturity of vent fields on the Juan de Fuca Ridge. *Geochim. Cosmochim. Acta* **1998**, *62*, 1521–1533. [[CrossRef](#)]
102. Hebert, R.L.; Ledesert, B.; Bartier, D.; Dezayes, C.; Genter, A.; Grall, C. The Enhanced Geothermal System of Soultz-sous-Forêts: A study of the relationships between fracture zones and calcite content. *J. Volcanol. Geotherm. Res.* **2010**, *196*, 126–133. [[CrossRef](#)]
103. Dhansay, T.; Navabpour, P.; de Wit, M.; Ustaszewski, K. Assessing the reactivation potential of pre-existing fractures in the southern Karoo, South Africa: Evaluating the potential for sustainable exploration across its Critical Zone. *J. Afr. Earth Sci.* **2017**, *134*, 504–515. [[CrossRef](#)]
104. Moir, H.; Lunn, R.; Shipton, Z.; Kirkpatrick, J. Simulating brittle fault evolution from networks of pre-existing joints within crystalline rock. *J. Struct. Geol.* **2010**, *32*, 1742–1753. [[CrossRef](#)]
105. Laubach, S.E. Practical approaches to identifying sealed and open fractures. *AAPG Bull.* **2003**, *87*, 561–579. [[CrossRef](#)]
106. Woodcock, N.H.; Dickson, J.A.D.; Tarasewicz, J.P.T. Transient permeability and reseal hardening in fault zones: Evidence from dilation breccia textures. *Geol. Soc. London, Spéc. Publ.* **2007**, *270*, 43–53. [[CrossRef](#)]
107. Vidal, J.; Patrier, P.; Genter, A.; Beaufort, D.; Dezayes, C.; Glaas, C.; Lerouge, C.; Sanjuan, B. Clay minerals related to the circulation of geothermal fluids in boreholes at Rittershoffen (Alsace, France). *J. Volcanol. Geotherm. Res.* **2018**, *349*, 192–204. [[CrossRef](#)]
108. Liotta, D.; Brogi, A.; Ruggieri, G.; Rimondi, V.; Zucchi, M.; Helgadóttir, H.M.; Montegrossi, G.; Friðleifsson, G. Ómar Fracture analysis, hydrothermal mineralization and fluid pathways in the Neogene Geitafell central volcano: Insights for the Krafla active geothermal system, Iceland. *J. Volcanol. Geotherm. Res.* **2020**, *391*, 106502. [[CrossRef](#)]
109. Griffiths, L.; Heap, M.; Wang, F.; Daval, D.; Gilg, H.; Baud, P.; Schmittbuhl, J.; Genter, A. Geothermal implications for fracture-filling hydrothermal precipitation. *Geothermics* **2016**, *64*, 235–245. [[CrossRef](#)]
110. Ito, H. Inferred role of natural fractures, veins, and breccias in development of the artificial geothermal reservoir at the Ogachi Hot Dry Rock site, Japan. *J. Geophys. Res. Space Phys.* **2003**, *108*. [[CrossRef](#)]

Chabani et al. (2021b) have proposed a multiscale geometric description of fractures within the NH range based on a combination of satellite imagery, aerial and ground photogrammetric models, outcrop scan lines, hand specimens and rock thin sections. Based on this combination of data they could propose a model outlining the structuration of the NH and used this model to discuss the connectivity of the fracture network and its potential influence on fluid flow. Using an approach combining facies variability and change in fracture trend orientation the authors outlined the presence of three different domains within the NH and concluded that connectivity was ruled by both small and large fractures. In addition, fracture orientation within the NH shows a dependence to the scale of observation which is not the case for fracture length.

In a second contribution, Chabani et al. (2021a) used numerous scanlines to characterize fracture spacing variability, distribution of fracture patterns and impact of the major faults on fracture distribution and fluid circulation. The authors could identify three different fracture sets and argue that 1) clustering of fracture distribution is dependent on fracture orientation and 2) clustering intensity is higher close to high strain zones. It is concluded that high strain induces clustering of fracture patterns while at moderate deformation fracture pattern distribution tends to random or regular. Such distributions having an important impact on flow must be taken into account when dealing with numerical simulations.

Article

Multiscale Characterization of Fracture Patterns: A Case Study of the Noble Hills Range (Death Valley, CA, USA), Application to Geothermal Reservoirs

Arezki Chabani ^{1,*} , Ghislain Trullenque ¹, Béatrice A. Ledésert ²  and Johanne Klee ¹ 

¹ UniLaSalle, UPJV, B2R UMR 2018.C100, U2R 7511, 19 rue Pierre Waguet, F-60026 Beauvais, France; ghislain.trullenque@unilasalle.fr (G.T.); johanne.klee@unilasalle.fr (J.K.)

² Geosciences and Environnement Cergy, CY Cergy Paris Université, 1 rue Descartes, F-95000 Neuville sur Oise, France; beatrice.ledesert@cyu.fr

* Correspondence: arezki.chabani@unilasalle.fr; Tel.: +33-6-58-07-14-14

Abstract: In the basement fractured reservoirs, geometric parameters of fractures constitute the main properties for modeling and prediction of reservoir behavior and then fluid flow. This study aims to propose geometric description and quantify the multiscale network organization and its effect on connectivity using a wide-ranging scale analysis and orders scale classification. This work takes place in the Noble Hills (NH) range, located in the Death Valley (DV, USA). The statistical analyses were performed from regional maps to thin sections. The combination of the length datasets has led to compute a power law exponent around -2 , meaning that the connectivity is ruled by the small and the large fractures. Three domains have been highlighted in the NH: (1) domain A is characterized by a dominance of the NW/SE direction at the fourth order scale; (2) domain B is characterized by a dominance of the E/W and the NW/SE directions at respectively the fourth and third order scales; (3) domain C is also marked by the E/W direction dominance followed by the NW/SE direction respectively at the fourth and third order scale. The numerical simulations should consider that the orientation depends on scale observation, while the length is independent of scale observation.

Keywords: fracture network; Death Valley; Noble Hills; power law distribution; multiscale analysis; geothermal reservoir characterization



Citation: Chabani, A.; Trullenque, G.; Ledésert, B.A.; Klee, J. Multiscale Characterization of Fracture Patterns: A Case Study of the Noble Hills Range (Death Valley, CA, USA), Application to Geothermal Reservoirs. *Geosciences* **2021**, *11*, 280. <https://doi.org/10.3390/geosciences11070280>

Academic Editors: Jesus Martinez-Frias and Gianluca Groppelli

Received: 10 June 2021

Accepted: 30 June 2021

Published: 3 July 2021

Publisher's Note: MDPI stays neutral with regard to jurisdictional claims in published maps and institutional affiliations.



Copyright: © 2021 by the authors. Licensee MDPI, Basel, Switzerland. This article is an open access article distributed under the terms and conditions of the Creative Commons Attribution (CC BY) license (<https://creativecommons.org/licenses/by/4.0/>).

1. Introduction

Fluid flow in fractured rocks of very low matrix permeability is localized mainly in few fractures [1]. The complex geometry of fracture and fault patterns is the main cause of the complexity of fluid flow. In that case, numerous studies have been undertaken worldwide to show the control of the fracture network on the fluid circulations especially in hydrocarbon and aquifers reservoirs [2–5], in heat transfer [6], and thus also in geothermal reservoirs [7–9].

A fracture system is characterized by geometrical parameters as fracture lengths, spacings, orientations, and relations between them [1,10–12]. In order to access hierarchical and mechanical relationships between fracture systems, many authors undertook a multi-scale approach, in sedimentary [2,12–15], and in Crystalline [16–20] rocks. This approach allows to model and predict hydraulic reservoir properties, by studying several geometric attributes, such as the distribution of orientations, lengths, widths, spacings and densities classically considered in spatial arrangement analysis [21–24].

The geometric parameters are commonly collected for (1) explicitly constructing deterministic models (Discrete Fracture Network: DFNs, [2]) or (2) ensuring inputs of stochastic simulations by determining fracture distribution functions from sampled fracture networks [23,25–27]. The main goal is to better understand the fracture network connectivity and then the fluid flow patterns [3,22,28]. Subsequently, the main question is whether

data correspond to scale-limited lognormal or exponential distributions, or scale-invariant power laws, corresponding to fractal patterns? Several orders of magnitude based on length and spacing characteristics are thus mandatory to establish scaling laws from statistical distributions [29]. These orders of magnitude have been widely described in the literature in extensional [17,20,30] and trans-tensional [17] contexts. It consists of: (1) first order scale related to the crustal faults larger than 100 km length, (2) second order scale refers to the faults comprised between 20 and 30 km length, (3) third order scale refers to faults around 10 km length, (4) and the fourth order refers to faults under 1 km length [20]. In the extensional regime, [30] having defined a spacing characteristic for the two first order scales, with a 10 to 15 km spacing for first order and 3 to 8 km for the second order scale; while [20] have defined 0.8 to 1.5 km spacing for the third order scale. However, the fourth order spacing characteristic is not defined in the literature.

Fracture networks impact the fluid flow in reservoirs [23]. The 2D/3D seismic lines and 1D borehole data cannot detect respectively the fracture geometries and the spatial arrangement at the reservoir scale due to the lack of information [31]. Then, the spatial arrangement of fracture networks are widely studied from field analogues [16,23,29,32], as they give access to 2D and 3D distributions. In geothermal basement setting, the analogues are chosen according to the lithology and geological context to get closer to the reservoir conditions. Sometimes, the analogue is chosen in desert conditions, without vegetation, perfectly suited for realistic multiscale fracture network reconstructions in 2D, and in 3D in case of modeling canyons with photogrammetric [33] or lidar [34] approaches.

The present work is part of the MEET project (Multidisciplinary and multi-context demonstration of EGS exploration and Exploitation Techniques and potentials, [35]), which aims to develop geothermal exploitation at European scale by applying Enhanced Geothermal System (EGS) technology to different geological contexts. This study aims to propose geometric description and quantify the multiscale network organization and its effect on connectivity. A wide-ranging scale analysis from the microscopic scale to the regional scale was conducted in the desert environment of Noble Hills (NH) fractured granitic basement. It is located in the southern termination of Death Valley (DV, California, USA) and assimilated to a paleo geothermal analogue. The NH range is considered as analogue to the Soultz-sous-Forêts (SsF) geothermal electricity producing system, due to the granitic nature, the alteration and the trans-tensional tectonic setting of the DV region [36,37].

Measurements have been performed at various scales using the DV regional map [38] at 1:250,000, NH regional map based on previous studies undertaken by [37,39] and orthophoto images taken for the present day. At outcrop scale, fractures are digitized thanks to the photogrammetric models. Several 2D fracture maps are also used, as well as additional scales on samples and in thin sections. This allows to integrate fracture lengths ranging from micrometer to kilometer scales.

In this study, the multiscale approach is used to better understand the spatial arrangement of the fracture networks which aims at producing the necessary data for DFN modeling. This helps to better characterize reservoirs in response to the developing geothermal exploration and exploitation by EGS. This study is conducted through:

1. a 2D characterization of the NH fracture network;
2. a multiscale evolution of length distributions;
3. evaluate the fracture system in the complex tectonic and geometrical setting;
4. present a conceptual scheme of the NH fracture network organization, and the role of each fracture order of magnitude on the connectivity.

2. Geological Setting

The present study takes place in the NH fractured granitic zone, located at the southern termination of the Death Valley (DV, California, USA) (Figure 1a). The NH range is assimilated to a paleo geothermal analogue [37]. Indeed, Reference [37] confirmed the analogy between the DV region and Soultz-sous-Forêts reservoir (Rhine graben, East of France), with many similarities, especially: (1) the trans-tensional tectonic setting of the DV,

and (2) the granitic nature and hydrothermal alteration of the central part of the NH range. Furthermore, the desert conditions of the NH range make this analogue perfectly suited for multiscale characterization of fracture networks dedicated to the global understanding of the spatial arrangement in granitic reservoir affected by trans-tensional tectonics [35].

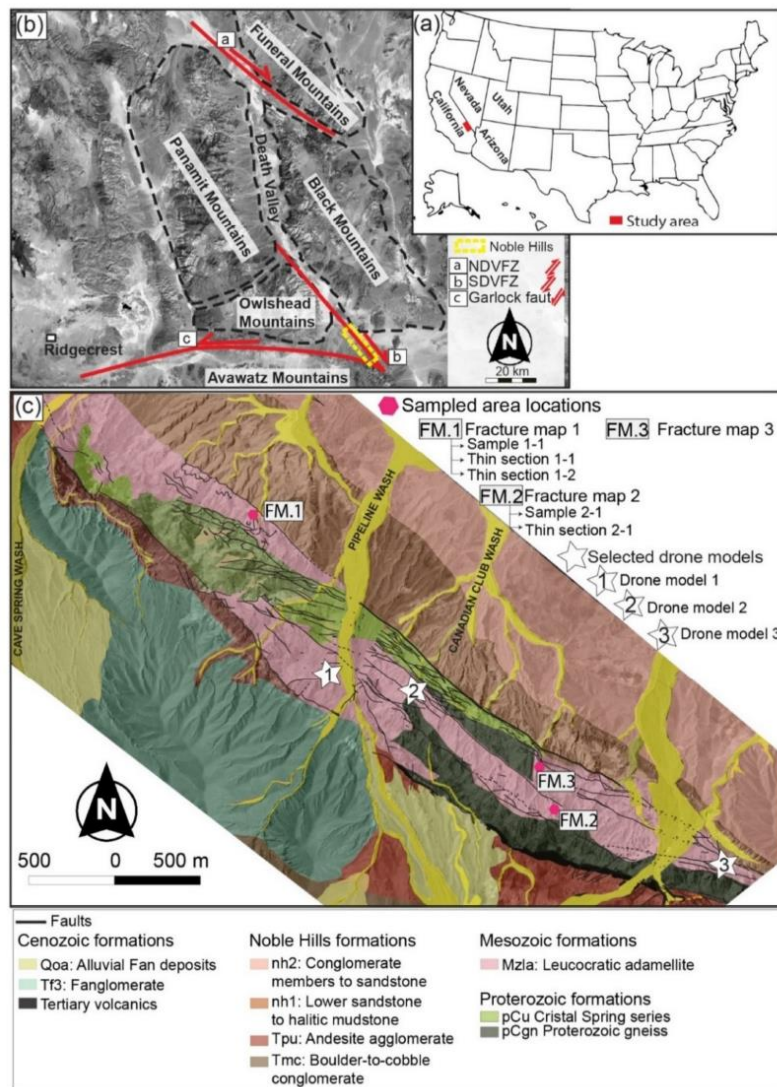


Figure 1. (a,b) Location and geological setting of DV, NDVFEZ: Northern Death Valley Fault Zone, SDVFEZ: Southern Death Valley Fault Zone; (c) Structural scheme of the NH range built using high-resolution digital mapping techniques modified after [37,39]. Additional digitized fractures were performed using orthophotos. The aerial picture in (b) was extracted from Google Earth®. The samples location was reported in the structural scheme. FM: fracture map.

The DV region has been characterized by a complex structural and tectonic history which includes the overprinting of Mesozoic to early Cenozoic contractional structures by late Cenozoic extensional and trans-tensional features [40–42]. The northwest trending contractional structures of the DV are at the origin of the Cordilleran orogenic belt of North America, which extends more than 6000 km from southern Mexico to the Canadian Arctic and Alaska [43]. Their age is estimated around 100 Ma and coincides with the Sevier orogenic belt [43,44]. The northeast trend is related to a thrust faults system [41].

The Mesozoic period was marked by the beginning of pluton emplacement in DV along the development of contractional structures. Then, during the Cenozoic period, the DV extension episode occurred [45,46], but there is no general agreement about its timing, e.g. [45,47]. The Miocene period was characterized by a trans-tensional regime. The opening of the DV region as a pull-apart basin began around 5 Ma [41,48–50]. A recent study done by [51] challenges this, mentioning that the opening of DV region into pull-apart basin started around 12 Ma ago.

Located in the southernmost part of the DV, the NH range trends parallel to, and then forms, the main topographic features aligned with components of the right-lateral Southern Death Valley Fault Zone (SDVZFZ) [37] (Figure 1b). This SDVZFZ is part of the Death Valley fault system (DVFS) [52], and its net dextral strike-slip displacement has been estimated around 40–41 km [51]. The northeast-vergent contractional deformation has been characterized along the length of the NH and constitutes the dominant structural style [48,53,54]. In the NH foreland basin, compressional structures have been characterized by [39] near the Canadian Club Wash (Figure 1c). An entire compressional region has also been created by the interaction between the SDVZFZ and the GF zone, which is responsible for shortening within the Avawatz Mountains [55,56]. Furthermore, the reverse displacement of the GF was identified in the front of the Avawatz [57]. The E/W fractures observed mainly in the southeast end of the NH show an identical orientation to GF. Given this similarity in orientation and the close vicinity to the GF, it is tempting to relate the E/W trending fracturing to GF zone activity.

Recent work by [37] using high-resolution digital mapping techniques reveals the dominance of basement rocks in the central part of the NH (Figure 1c). Indeed, the granitic rocks are mostly represented and related to the Mesozoic granitic intrusion (Mzla, Figure 1c) [58]. Proterozoic formations characterized by gneiss in the bottom have been defined in the center part and the southeast end of the NH (pCgn, Figure 1c). The Proterozoic Crystal Spring sedimentary series defined in the northwestern part of the NH are mainly composed of carbonates and quartzites facies (pCu, Figure 1c). Some tertiary volcanic series have also been mapped in the southeastern end of the NH.

Outside the center part, Reference [39] has widely studied the Cenozoic NH formations mainly composed of Fanglomerate and alluvial fan deposits.

3. Materials and Methods

3.1. Materials

3.1.1. Large Scale Characterization

The analysis of large scale fracture attributes was performed on fractures digitized from DV regional map at 1:250,000 scale (geological map of California, Trona Sheet [38]) (Figure 2a). In the central part of the NH range, the main structures were mapped during 2018 and 2019 field campaigns published by Klee et al. [37]. In addition, in this present study, orthophoto images of 1 m resolution were used to digitalize and then complete the fractures sampling (Figure 2b).

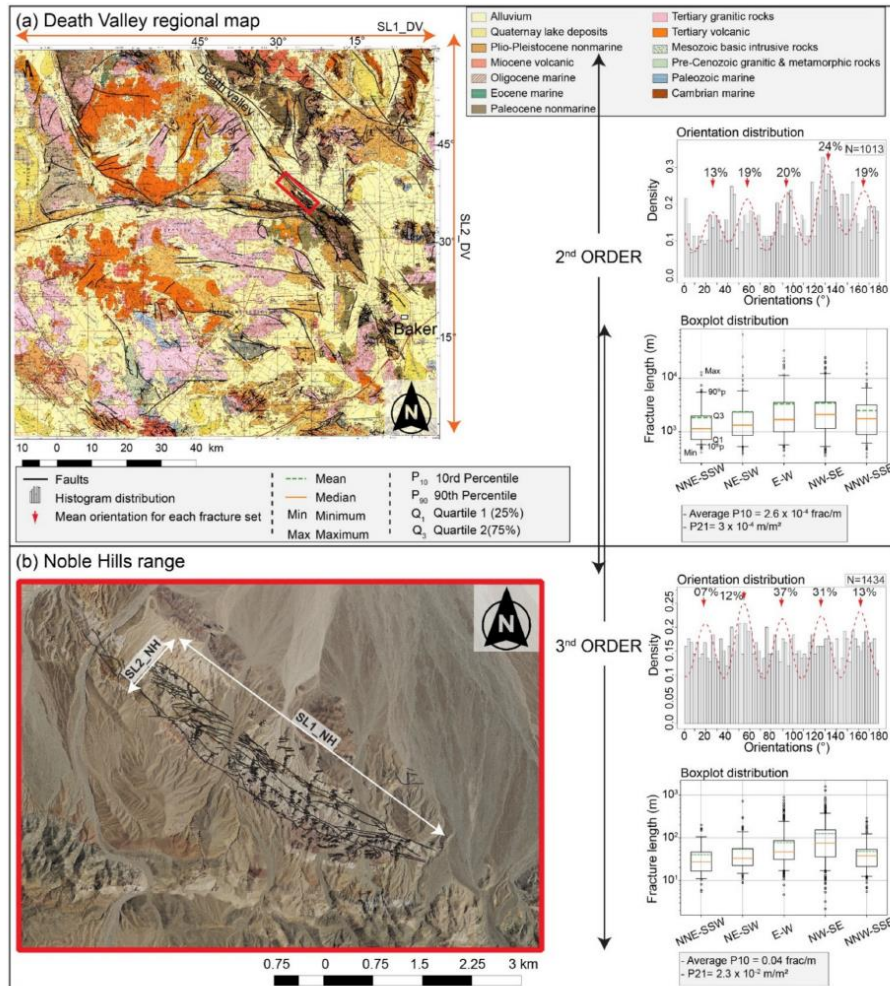


Figure 2. Fracture traces, orientation, and boxplot distributions from (a) DV geological map and (b) NH range map (in red rectangle for large scale location). The order of fractures magnitude were referred to the classification detailed in [30]. The first order referred to the faults larger 100 km length is not detected in this study. Each fracture map dataset is expressed in histogram for orientation distribution, and into boxplot for length distribution, according to the fracture orientations. Two scanlines (SL) were taken for every map.

With the aim of pinpointing the likely fracture variability, the NH range map has been divided into three domains (Figure 3). The sampling strategy along domains is detailed below. In total, 1013 fractures are extracted from the DV geological map, 1434 fractures from the NH map with 306 from domain A, 522 from domain B, and 606 from domain C.

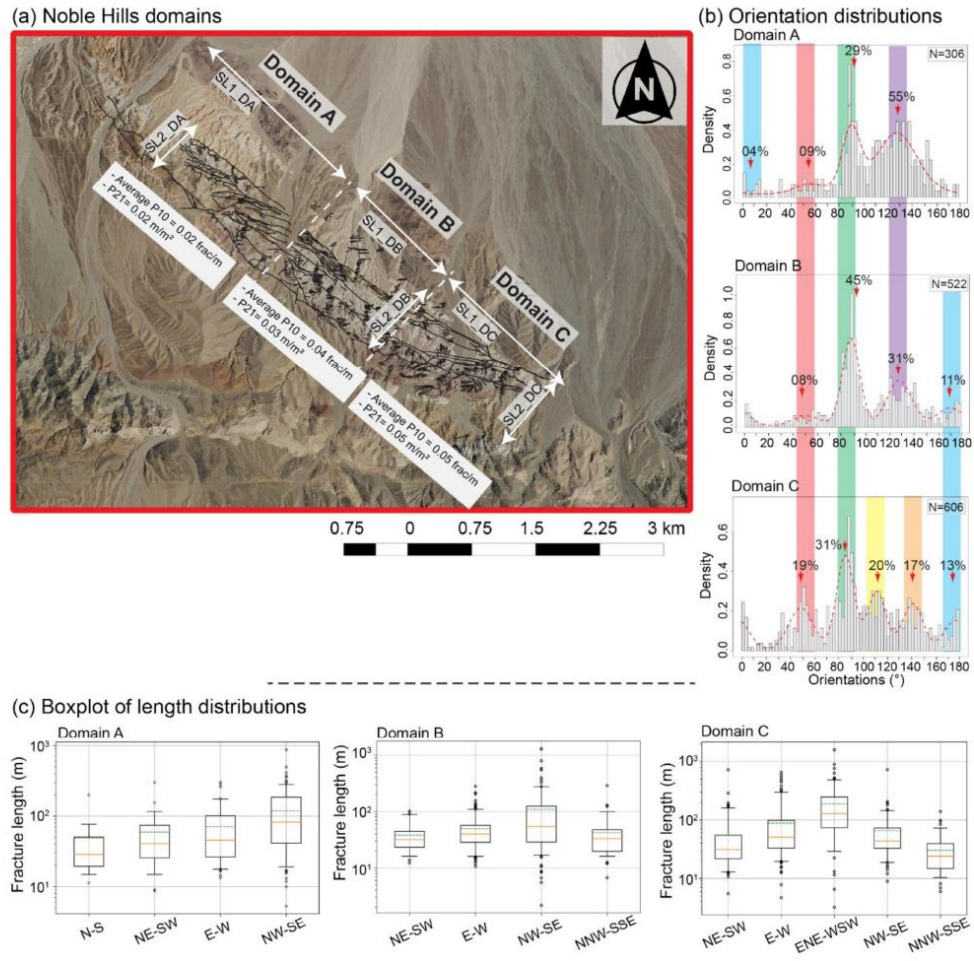


Figure 3. Fracture traces from the NH range divided into 3 domains. (a) NH domains: A, B, and C, (b) orientation distributions, and (c) boxplot of length distributions according to the fracture orientations. Two scanlines (SL) were taken for every domain. For boxplot and orientation distribution legend, see Figure 2.

Orientation and length distributions were collected and 1D/2D densities were calculated from them. All of these data are summarized in Table 1.

Table 1. Spatial statistics of 2D samples acquired at large scale (DV and NH regional maps) and outcrop scale (Drone models). Two Scanlines (SL) at least were generated for calculating the fracture density (P10). The length average is provided.

	Nb of Fractures	Mean Orientation	Average SL Length (m)/Area (m ²)	Fracture Density (P10) (frac/m)	Fracture Density (P21) (m/m ²)
DV regional map	133	N025	10 ⁵ /1.3 × 10 ¹⁰	2 × 10 ⁻⁴	3 × 10 ⁻⁴
	188	N058			
	199	N096			
	248	N132			
	197	N167			
NH regional map	97	N020	4.7 × 10 ³ /4.4 × 10 ⁶	2.6 × 10 ⁻⁴	3 × 10 ⁻⁴
	168	N054			
	535	N090			
	441	N126			
	192	N163			
NH domain A	13	N010	1.5 × 10 ³ /1.9 × 10 ⁶	2 × 10 ⁻²	2 × 10 ⁻²
	26	N055			
	89	N091			
	168	N132			
NH domain B	43	N050	1.7 × 10 ³ /1.2 × 10 ⁶	4 × 10 ⁻²	3 × 10 ⁻²
	233	N088			
	164	N128			
	59	N171			
NH domain C	113	N049	2 × 10 ³ /1.2 × 10 ⁶	5 × 10 ⁻²	5 × 10 ⁻²
	191	N085			
	119	N111			
	103	N141			
	77	N177			
Drone model 1	235	N025	3.5 × 10 ² /1.4 × 10 ⁴	6.5 × 10 ⁻¹	2 × 10 ⁻¹
	208	N055			
	183	N085			
	112	N115			
	281	N142			
	214	N174			
Drone model 2	681	N022	1.7 × 10 ² /5.8 × 10 ³	1.28	7 × 10 ⁻¹
	767	N043			
	642	N085			
	616	N108			
	722	N142			
	637	N171			
Drone model 3	2968	N018	2.8 × 10 ² /1.7 × 10 ⁴	9 × 10 ⁻¹	1
	2531	N038			
	1993	N079			
	2127	N109			
	2232	N140			
	3084	N169			

3.1.2. Photogrammetric Study/Analysis

In order to combine the widest fracture network analysis, three photogrammetric models, localized only in the granitic facies and alongside the major faults that structure the NH range (see Figure 1 for the location), are considered in this study to extract the fractures ranging approximatively from 10⁻² m to 20 m. A photogrammetric campaign was carried out in October 2018 with a high-resolution 3D point cloud and large collection of photographs.

Drone model 1 is sized approximately 350 m per 46 m and is located in the granitic facies (Figure 1); 1271 fractures are traced. Drone model 2 is located in the granitic facies

within a high deformation zone, and is sized approximately 172 m per 44 m (Figure 1). In total, 4196 fractures are traced. Finally, drone model 3 is located in the southeast termination of NH, and is sized approximately 280 m per 70 m. 15,594 fractures are traced.

The main statistical characteristics are summarized in Table 1.

3.1.3. Fracture Map Characterization

To complete the multiscale analysis with the small fractures, fracture maps were created with a resolution of 2×10^{-4} m. The fracture map 1 (see Figure 1c for location) is sized at 3.4 m per 3.1 m and is located between the granitic facies and the tertiary sediments, near the influence of the SDVFZ (see Figure 1b for the SDVFZ location). It is composed of quartzite boudin facies (part of Crystal Spring series) and granitic rocks, which respectively represent approximately 20% and 80% of occurrences.

In order to include the very small fractures in this study, additional fracture sets were collected from this fracture map with sample 1-1 sized 17 cm per 12 cm (resolution of 10^{-4} m) and thin sections 1-1 and 1-2 (resolution of 10^{-5} m), both sized 3.5 per 2.5 cm (see Figure 1c for location). Both sections are composed mainly of Plagioclase, Quartz, K-Feldspar, and Biotite representing respectively 35%, 30%, 25%, and 10% of occurrences.

Fracture map 2 (Figure 1c) is sized 1.7 m per 1.6 m and is located in the granitic facies, near the SDVFZ deformation corridor. This map includes sample 2-1 and thin section 2-1 which size respectively 15 cm per 5.2 cm and 3.5 cm per 2.5 cm. Thin section 2-1 represents the same mineral composition as thin sections 1-1 and 1-2 with approximately the same occurrences. Fracture map 3 (Figure 1c) is sized 1.8 m per 1.7 m and is located also in the granitic facies.

Table 2 summarizes the main statistical characteristics.

Table 2. Spatial statistics of 2D samples acquired from outcrop scale (fracture maps) to thin section scale. Two Scanlines (SL) at least were generated for calculating the fracture density (P10); the length average is provided.

	Nb of Fractures	Mean Orientation	Average SL Length (m)/Area (m ²)	Fracture Density (P10) (frac/m)	Fracture Density (P21) (m/m ²)
Fracture map 1	1133 631	N005 N083	3.1/7.94	12	12
Sample 1-1	104 115 117 51	N018 N053 N090 N126	$15 \times 10^{-2}/2.2 \times 10^{-2}$	184	118
Thin section 1-1	723 754 751 730	N018 N053 N090 N126	$3 \times 10^{-2}/8 \times 10^{-4}$	5140	715
Thin section 1-2	612 659 444 512 623	N020 N051 N088 N128 N162	$3 \times 10^{-2}/8 \times 10^{-4}$	4525	702
Fracture map 2	36 34 98 32 83	N005 N038 N070 N110 N145	1.7/1.91	18	13

Table 2. Cont.

	Nb of Fractures	Mean Orientation	Average SL Length (m)/Area (m ²)	Fracture Density (P10) (frac/m)	Fracture Density (P21) (m/m ²)
Sample 2-1	75	N017	$10^{-1}/10^{-2}$	177	240
	145	N057			
	101	N092			
	116	N130			
	135	N157			
Thin section 2-1	201	N014	$3 \times 10^{-2}/8 \times 10^{-4}$	517	1064
	213	N059			
	170	N097			
	221	N140			
Fracture map 3	149	N009	1.7/3	20	12
	88	N033			
	119	N071			
	70	N104			
	146	N149			

3.2. Methods

3.2.1. Fractures Acquisition

In this study, fracture digitization was performed manually by tracing every fracture segment from entire 2D maps in QGIS[®] software v.2.18.17. Only fractures reported as full solid lines on the DV geological map were considered for statistical analysis (Figure 2a).

Regarding the procedure of fracture digitization, the fractures extending out of the sampling domain were considered as one continuous feature [16,23,59] (Figure 2b). The digitization of fractures consists of an extraction of the end point coordinates of each fracture using the QGIS[®] software v.2.18.17. Each extracted fracture is characterized by the X and Y coordinates of each of the two end points, which help to compute the orientations and the length of segments. In case of curved fractures, a straight segment line was automatically traced between the end of point coordinates, and then the mean directions and lengths were computed.

As described above, the NH fracture data were acquired during the field mapping campaign and then completed by orthophoto image analysis. The data were analyzed in the entire area (Figure 2b). However, the complexity in loading history within NH widely discussed in the literature [48,54,60] makes the analysis of the fracture geometries difficult. Furthermore, the field observations and the new geological map done by [37] reveal additional complexities inside this area, and show a stacking of different Crystal Spring series (pCu, Figure 1c), intruded by the Mesozoic granite (Mzla, Figure 1c). This observation was highlighted in the northwest part of the NH. In center part, Crystal Spring series thicknesses were reduced, dragged, and stretched against the granite due to the SDVZ activity (pCu, Figure 1c). The southeast of the NH is characterized by the absence of the Crystal Spring series. To better characterize the fracture variability, it is prime of interest to consider the facies variability and the deformation intensity within NH, because they influence the fracture evolution [23,59]. In this sense, we decided to divide the NH range into three domains according to the facies variability and change in range trend orientation variation (Figure 3): (1) Domain A is located northwestward, highlighted by thick Crystal Spring sediments and granitic rocks; (2) Domain B is in the central part of NH, highlighted by reduced thickness of Crystal Spring sediments, granitic and gneissic rocks, and (3) Domain C is located in the southeastern part of the NH and is characterized by granite, gneiss, and Tertiary volcanism. Note that Domain B and C are composed approximately of the same facies. However, range orientation in domain B is NW/SE, while in domain C it is toward E/W. This general E/W trend is puzzling as it is similar to the GF (see Figure 1b for location). Therefore, this difference in orientation constitutes an additional argument to better delimitate domain B and C. Figure 3 shows the fracture

distributions within each domain. Some more work based on field analyses could more precisely delimitate the domains.

The photogrammetric models undertaken in this work were performed using a 3DR Solo drone with 4k cameras and DJI Phantom drone provided by University of Texas at El Paso (UTEP), Texas, USA. The videos were recorded between the late morning and the early afternoon during seven days with a manual mode camera setting to reduce the effects of lighting condition. Pictures were then extracted every second from the recorded drone videos using ffmpeg software v.4.5. The extracted pictures with a sufficient overlapping were aligned in Agisoft Metashape software (2020, Version 1.6.5). The obtained 3D models are georeferenced and then imported in CloudCompare software (version 2.9.1; [GPL software] (2017)) to begin the fracture extraction process. A workflow explaining the procedure of the models construction and the fractures extraction is detailed in [36]. In this study, the digitized fractures are projected on a 2D map to make the work only in 2D in order to keep data homogenous at different scales.

The 2D fracture maps at outcrop scale were performed in the field using a DSLR high resolution camera provided by UniLaSalle (Beauvais, France), with a 50 mm focal lens to minimize distortion. Pictures were taken vertically, with the same distance, and in the absence of sunlight to avoid the light effects in the fracture digitization [12]. From each fracture map, several pictures were taken with a sufficient overlapping. Then, pictures were aligned using the Agisoft Metashape software with the same procedure detailed in [36]. The maps are georeferenced and then used to extract the fractures in QGIS® with the same technique as for large scale maps.

Additional fracture datasets are used in this study by adding samples. These samples were taken directly from fracture maps. Then, a high-resolution picture was taken for each sample using a DSLR camera. With the same procedure as large-scale fractures acquisition, the sample was added in QGIS® to extract the fractures.

Thin section mosaics are also added to this study, made from samples as described earlier to keep a consistent sampling strategy. These mosaics were taken under an optical microscope Leica DM4500-P provided also by UniLaSalle (Beauvais, France), using a $\times 5$ magnification and polarized non-analyzed light mode. A Leica DFC450C high resolution camera provided also by UniLaSalle (Beauvais, France) and Leica application Suite v.4.11.0 were used to take pictures. Every mosaic was relatively oriented using the corresponding sample. Then, with the same fracture digitization procedure described earlier, fracture parameters were extracted under QGIS® v.2.18.17.

3.2.2. Fractures Analysis

Different geometrical parameters were then collected from each fracture database at different scales. Detailed orientation distributions and classification into fracture sets were performed using the mixture of von Mises distribution (MvM) [61]. This approach consists of a semi-automated procedure based on appraisal tests in order to avoid any subjectivity in fracture sets analysis. For each fracture set, three output parameters were considered: (1) mean orientation (μ) around which the distribution is centered, (2) kappa (κ) which controls the concentration of the orientation's values around the mean, and (3) weight (ω) corresponding to the relative contribution of each fracture set to the model. Then, we are able to check the best number of fracture sets from the distributions using the goodness of fit parameters (e.g., Likelihood). For more details, see [62] who describe and adapt the methodology for structural data. The standard of deviation of $\pm 10^\circ$ was calculated for each given mean orientation value in this study.

Fracture length is the most used geometrical parameter to characterize the spatial organization in the natural fracture networks [4,25,63]. This characterization is performed using a statistical distribution as the Power law distributions widely used in structural data from field analogue [4,25,26,63,64]. The power law is often used to describe the distribution of fracture parameters such as length and aperture [25]. It is recognized that power law and fractal geometry provide widely applicable descriptive tools for fracture system

characterization. This is due to the absence of characteristic length scales in the fracture growth process. The power law exponent α provides a real significance on the fracture connectivity. Indeed, for an exponent comprised between 2 and 3, fracture connectivity is ruled by both small and large fractures [65]. In addition, fractal analyses using Cantor's dust method allow the quantification of fracture distribution in clusters or, in the opposite, with a homogeneous distribution [66] and prediction of the fracture occurrence [7]. The exponential law is also used to describe the size of discontinuities in rocks [67–69], and to incorporate a characteristic scale that reflects a physical length in the system, such as thickness of a sedimentary layer [70].

However, fitting the geometric attributes to the statistical distributions suffers from a lot of biases, such as truncation and censoring biases [25]. Truncation effects are caused by resolution limitations of a field observation such as from satellite images, the human eye, or microscopes [63]. Censoring effects are associated with the probability that a long fracture intersecting the boundary of the sampling area is not sampled, and to the subjective choice of the sampling area which tends to exclude very long fractures [63,71]. Then, censoring effects cause an overestimation of fracture density. In this study, the truncation and censoring effects were automatically excluded from the distributions. Length distribution in Figure 4 shows the data excluded from the distribution (grey color) due to the impact of truncation and censoring effects.

The fracture length distributions are analyzed using the cumulative distribution. Statistical distributions used in this study were adjusted after corrections from the truncated and censoring effects. Research for truncation and censoring thresholds was performed using the « *powerLaw: Analysis of Heavy Tailed Distributions* » package from Rstudio® v.1.3.1056 [72]. We also used the coefficient of determination (R^2) to estimate the goodness of fit of the power law to the length distribution. This coefficient is comprised between 0 and 1. A high R^2 for a given number of degrees of freedom means that the regression is a statistically meaningful description of the data.

Fracture densities are computed in this study. They consist of fracture density (P_{10}), defined as the number of fracture intersections along a 1D virtual scanline traced on every analyzed 2D map [59,73]. The scanline methodology is widely used to describe the fracture variability in 1D [73]. In this study, the linear fracture density P_{10} was obtained from two virtual scanlines, orientated perpendicular to the main structures.

Finally, the surface fracture density (P_{21}) is defined as the total sum of fracture lengths within the area [59,73].

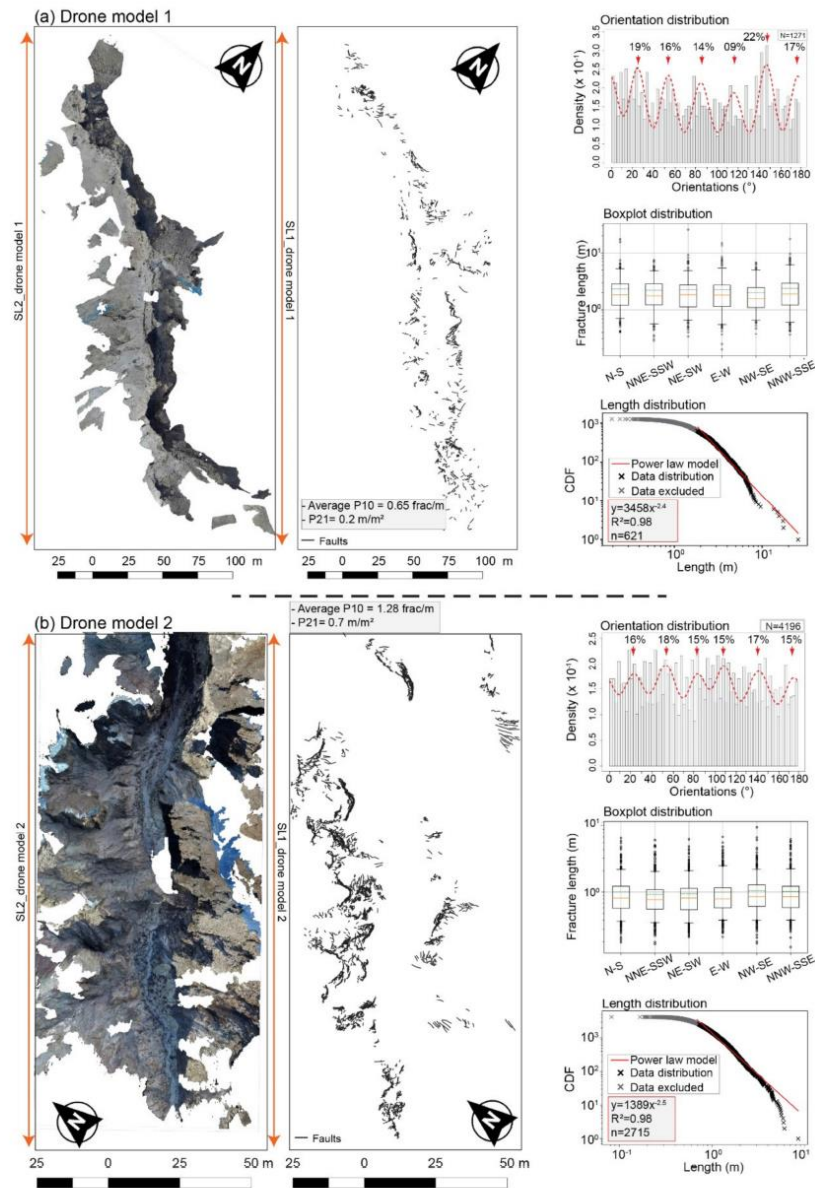


Figure 4. Fracture traces, orientation, boxplot length distributions from (a) drone model 1 and (b) drone model 2. Each fracture map data is expressed into histogram for orientation distribution, boxplot of length distribution according to the fracture orientations, and cumulative distribution function (CDF) of lengths. Two scanlines (SL) were taken along the left and the right side of the canyon. For the boxplots and orientation distributions legend, see Figure 2.

4. Results

4.1. Large Scale Domains

The mean orientation (μ) N095° (E/W trend) and N132° (NW/SE trend) trending fractures occur at the largest length scale, with a 20 and 24% of whole fractures, and about 3300 to 4400 m mean length (Figure 2a). Both directions are well expressed following the DV and Garlock strike slip trend faults (See Figure 1b for location) [39,48]. The largest fracture length is recorded within the NE/SW fracture set with 65 km length. The other recorded fracture sets are relatively equivalent (around 20%), except for the N025° fracture set which is less dominant, with 13% and 1900 m mean length.

At NH scale, the same dominance of N090° and N126° fracture sets with respectively 37% and 31% are observed (Figure 2b). The other fracture sets are poorly expressed (<15%). The boxplot distribution in Figure 2b showed also the dominance of the E/W and NW/SE fracture sets with respectively 80 m and 125 m mean length. The other fracture sets did not exceed the 50 m mean length.

The occurrence of two prominent fracture sets is shown in the NH domains A and B (Figure 3a,b). Domain A is characterized by two main fracture sets striking N091° and N132° representing respectively 29% and 55% of occurrences (Figure 3b). The N091° fracture set lengths range from 30 m to 300 m, while the N132° fracture set length ranges from 5 m to 800 m, meaning that the NW/SE is the most dominant fracture set in domain A (Figure 3b).

Orientation and length data of domain B shows an equivalent distribution as in domain A (Figure 3b). Indeed, two main fracture sets striking also N088° and N128° are mostly representative with respectively 45% and 31%. The fractures are much longer within NW/SE trend, ranging from 2 m to 1300 m (mean is of 108 m). The other fracture sets show an intermediate length with a 50 m mean value.

Fracture geometry in Domain C shows immediately a different distribution with four main fracture sets striking N050° (19%), N085° (31%), N111° (20%), and N141° (17%) (Figure 3b). The NW/SE fracture set mainly sampled and representative in the domain A and B is split into N111° and N141° fracture sets in domain C, with respective lengths ranging from 3 to 1600 m (mean is 190 m) and from 8 m to 730 m (mean is 65 m).

The fracture densities are increasing considerably from domain A to C with $2 \times 10^{-2}/3 \times 10^{-2}$ m/m² in the domain A and B, and 5×10^{-2} m/m² in the domain C.

4.2. Photogrammetric Models

NH canyons modeled with photogrammetric method provide fractures from centimetric to decametric scale. Fracture distributions are displayed by drone model 1 for both sides of the canyon walls (Figure 4a). Six fracture sets are recorded and strike N025°, N055°, N085°, N115°, N142°, and N174°. The N142° is also the most dominated fracture set with 22%. The E/W fracture set is the less expressed (14%) at outcrop scale. An equivalent mean length of fractures is shown by the boxplot distribution graphic with 2.3 m, whatever the fracture set (Figure 4a).

The exponent of power law (red line in the length distribution, Figure 4) is of $\alpha = -2.4$ for length distribution of the drone model 1, outside lengths affected by truncation and censoring bias (data mentioned in the length distribution graphic with grey color, Figure 4). The range of length values performed by the power law is 1.85 m to 25 m.

Finally, fracture densities P_{21} and P_{10} are of respectively 2×10^{-1} m/m² and 6.5×10^{-1} frac/m.

Fractures from drone model 2 are mainly distributed along the left side of the canyon (Figure 4b). The same fracture sets as drone model 1 are recorded with an equivalent percentage (between 15 and 18%) (Figure 4b). Fracture lengths are highlighted by the boxplot distribution and are also equivalent with 1 m mean length, whatever the fracture set. The largest fractures are recorded within the NW/SE fracture set (maximum of 8.5 m), and then confirm the consistency of the NW/SE direction at outcrop scale.

The fracture length range modeled by the power law is of 0.69 m to 8.5 m, for exponent $\alpha = -2.5$ and $R^2 = 0.97$ (Figure 4b). Fracture lengths under 0.69 m are excluded automatically from the distribution (truncation effects).

Fracture densities are quite high in comparison with Drone model 1, with $7 \times 10^{-1} \text{ m/m}^2$ and 1.28 frac/m for respectively P_{21} and P_{10} .

Drone model 3 is the largest studied model with 15594 traced fractures (Figure 5). Six fracture sets are highlighted also in this canyon. Their proportions range from 13% (N079° and N109°), 14–16% (N140° and N038°), to 19–20% (N018 and N169°). The fracture lengths are equivalent, once again, with a 1.2 m mean length.

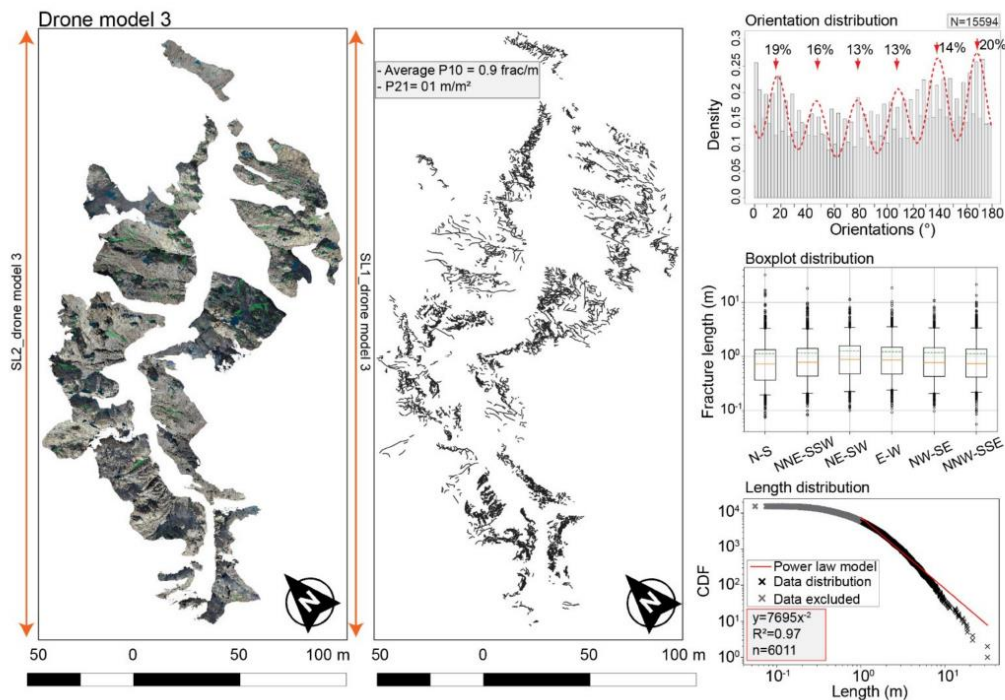


Figure 5. Fracture traces, orientation, boxplot length distributions from drone model 3. Different Datasets are expressed into histogram for orientation distribution, boxplot of length distribution according to the fracture orientations, and cumulative distribution function (CDF) of lengths. Two scanlines (SL) were taken along the left and the right side of the canyon. For Boxplot and orientation distribution legend, see Figure 2.

The power law exponent for drone model 3 length distribution is of $\alpha = -2$, outside lengths affected by truncation and censoring effects (Figure 5). R^2 value is of 0.97, indicating a good fit of the power law to the data. Fracture density P_{21} is of 1 m/m^2 , increasing by a factor 5 compared to drone model 1 fracture density.

4.3. Fracture Maps

Fracture map 1 is characterized by intense fracture areas, especially along the center part (Highly fractured area, Figure 6). The high fracture density is located mainly in the quartzite boudin, while the less fractured zone is related to the granitic rocks.

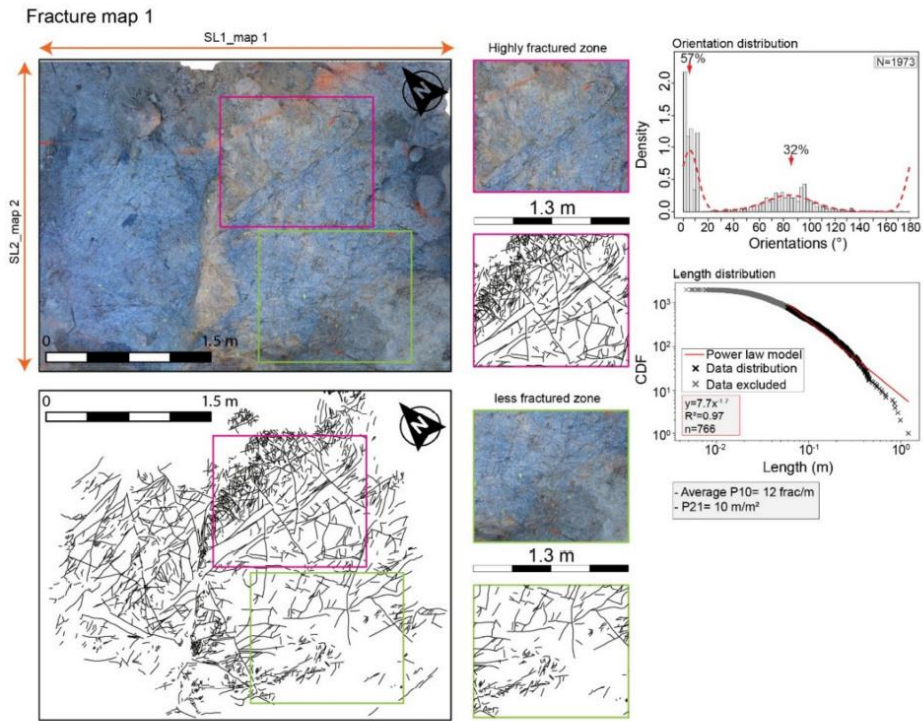


Figure 6. Fracture traces, orientation and length distributions from fracture map 1. Different datasets are expressed into histogram for orientations distribution, and into cumulative distribution function (CDF) of lengths. Two scanlines (SL) were taken for every domain. For orientation distribution legend, see Figure 2.

For the rest of the fracture map, average P_{10} of 12 frac/m is computed from two scanlines (SL1_map1 and SL2_map 2, Figure 6), while P_{21} is of 10 m/m². Two main fracture sets are highlighted: N005° and N083°, with respectively 57% and 32% (Figure 6). Outside fracture lengths affected by truncation and censoring bias, the power law exponent is of $\alpha = -1.7$ for values ranging from 6×10^{-2} m to 1.2 m.

Sample 1-1 is characterized by homogeneous fracture distribution with four main fracture sets: N018°, N053°, N090°, and N126° representing respectively 27%, 30%, 30%, and 13% (Figure 7a). The largest veins visible in the sample map are characterized by carbonate mineralizations in two directions: N053° and N126°. P_{10} and P_{21} fracture densities are of 184 frac/m and 118 m/m² respectively. Regarding the length distribution, the power law exponent is of $\alpha = -1.43$, with thresholds of 3×10^{-3} m and 7×10^{-2} m.

Four main fracture sets are highlighted in thin section 1-1: N018°, N053°, N090°, and N126° with a comparable fracture proportion (around 25%). Additional fracture set is detected in thin section 1-2: N162°. Regarding the densities, P_{21} is of 715 m/m² and 702 m/m², while P_{10} is of 5140 frac/m and 4525 frac/m respectively for thin section 1-1 and 1-2 (Figure 7b,c). The power law exponents are quite higher with $\alpha = -1.95$ (modeled range from 2.2×10^{-4} m to 4.63×10^{-3} m) and $\alpha = -1.7$ (modeled range from 2.2×10^{-4} m to 7×10^{-3} m) respectively for thin section 1-1 and 1-2.

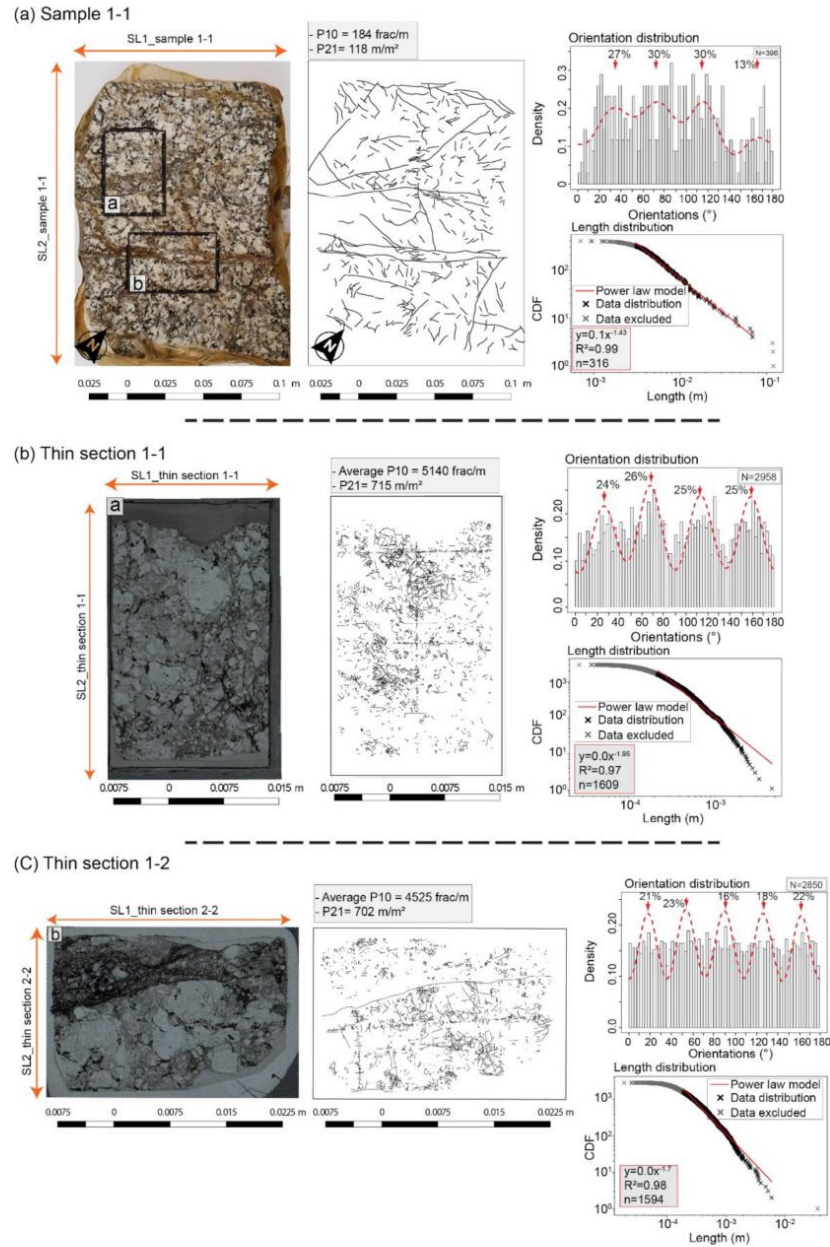


Figure 7. Fracture traces, orientation and length distributions from (a) sample 1-1, (b) thin section 1-1, and (c) thin section 1-2 sampled from fracture map 1. Different datasets are expressed into histograms for orientations distribution, and into cumulative distribution function (CDF) of lengths. Two scanlines (SL) were taken for each map. For orientation distribution legend, see Figure 2.

Fracture densities of fracture map 2 are comparable with fracture map 1 with average $P_{10} = 18 \text{ frac/m}$ and $P_{21} = 13 \text{ m/m}^2$ (Figure 8a). Five fracture sets are highlighted: N005°, N038°, N070°, N110°, and N145°. The N070° and N145° are the most recorded fracture sets with respectively 32% and 27%.

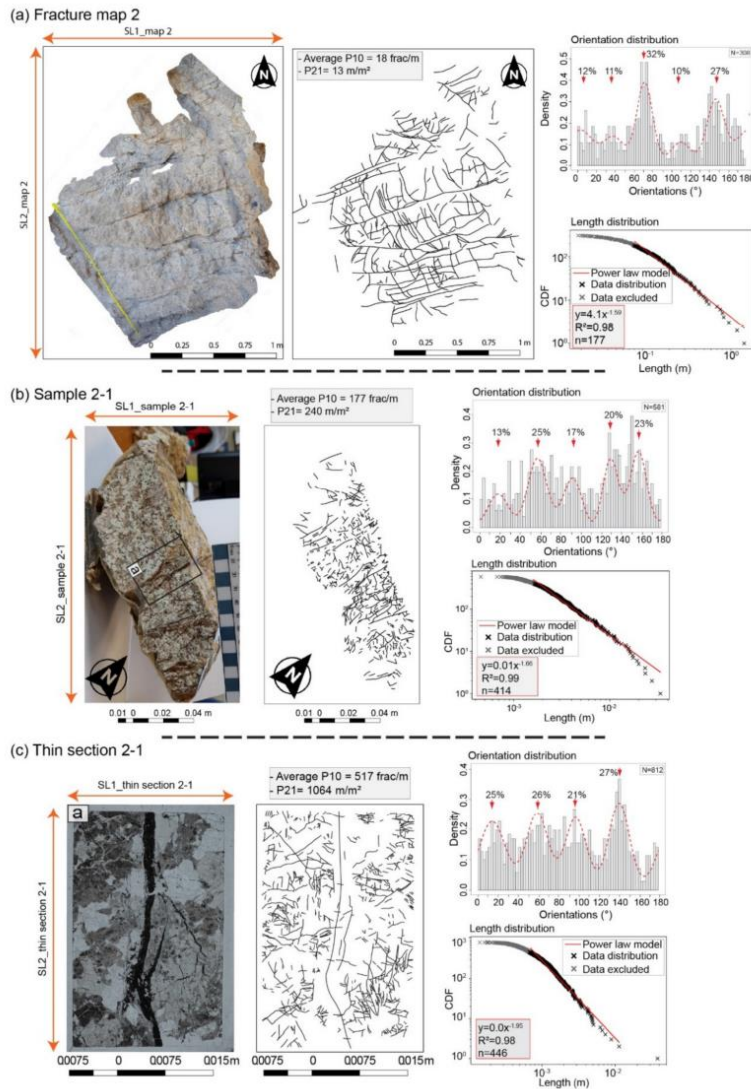


Figure 8. Fracture traces, orientation, and length distributions from (a) fracture map 2, (b) sample 2-1, and (c) thin section 2-1, located in sample 2-1. Different datasets are expressed into histogram for orientations distribution, and into cumulative distribution function (CDF) of lengths. Two scanlines (SL) were taken for each map. For orientation distribution legend, see Figure 2.

The power law exponent is also comparable to that of fracture map 1 ($\alpha = -1.59$), with the thresholds of 8×10^{-2} m and 1.43 m (Figure 8a).

Sample 2-1 is characterized by a fracture density of $P_{10} = 177$ frac/m and $P_{21} = 240$ m/m² (Figure 8b). In total, five fracture sets are highlighted: N017°, N057°, N092°, N130°, and N157°. Three fracture sets are the most recorded: N057°, N130° and N157°, with 20% to 25%. The power law exponent is of $\alpha = -1.66$, thresholds from 1.6×10^{-3} m to 3.33×10^{-2} m.

Thin section 2-1 trans-cutting a large carbonate vein in the central part (Figure 8c), is characterized by a fracture density $P_{21} = 1064$ m/m² higher than in thin section 1-1 and 1-2. Only four fracture sets are highlighted: N014°, N059°, N097° and N140°, with an equivalent fracture proportion. Outside the lengths affected by sampling bias, the exponent is of $\alpha = -2$, thresholds of 7×10^{-4} m to 3.5×10^{-2} m.

Finally, fracture map 3 is characterized by a comparable fracture density as in fracture map 2 with $P_{10} = 20$ frac/m and $P_{21} = 12$ m/m² (Figure 9). Five fracture sets are also detected with a high proportion of 26% for N009° and N149°. Fracture sets N033°, N077°, N104° showed an abundance of 15%, 21%, and 12% respectively. The power law exponent is of $\alpha = -1.53$ for lengths data ranging from 4×10^{-2} m to 1.21 m.

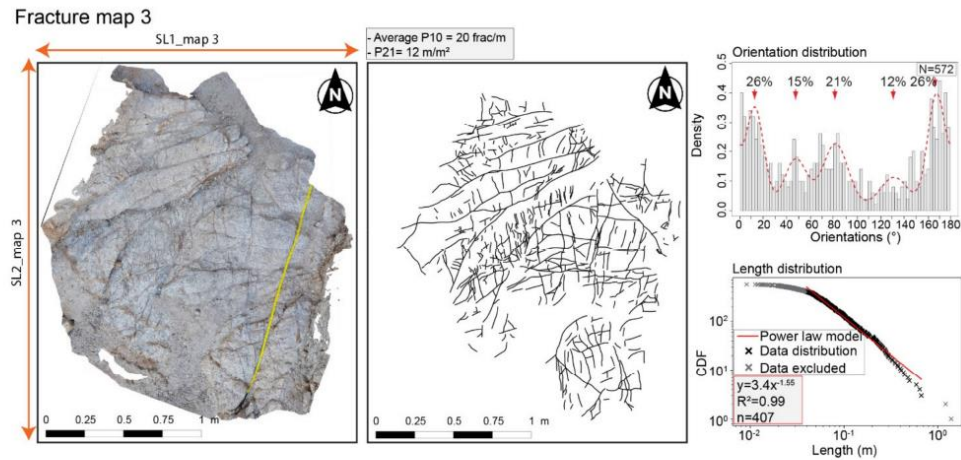


Figure 9. Fracture traces, orientation and length distributions from fracture map 3. The computed dataset is expressed into histogram for orientations distribution, and into cumulative distribution function (CDF) of lengths. Two scanlines (SL) were taken. For orientation distribution legend, see Figure 2.

5. Discussion

The combination of data at various scales in this study allowed to propose a new interpretation of the fracture network in the NH range, based on multiscale evolution of fractures length and orientation. A conceptual scheme of the NH structuration is created and discussed in terms of fracture network connectivity and its influence of fluid flow.

5.1. Multiscale Length Characterization

The cumulative length distributions of each fracture map from the DV regional map scale to thin section scale are plotted in Figure 10. All length datasets have been fitted to the power law distribution, outside lengths affected by truncation and censoring bias.

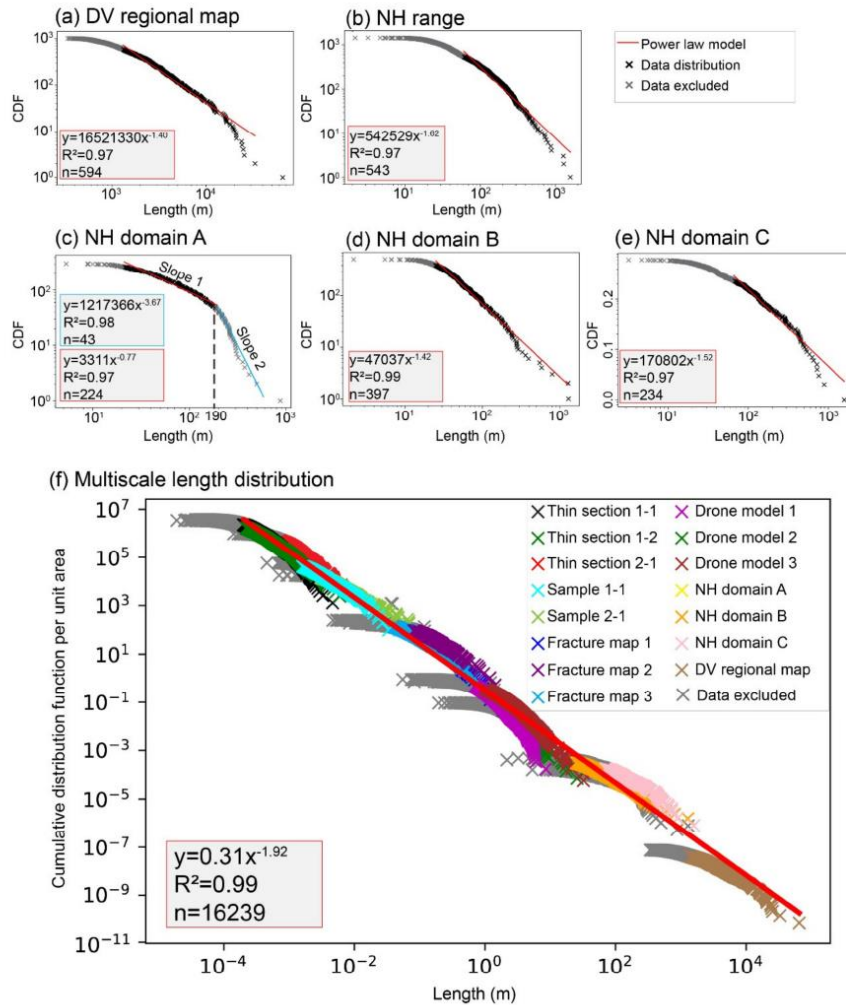


Figure 10. Fracture length distribution from (a) DV geological map, (b) NH range, (c) NH map domain A, (d) NH map domain B, and (e) NH map domain C, and (f) Multiscale length distribution obtained from the combination of the whole data.

DV regional map exponent is quite low, around $\alpha = -1.40$, and gradually increase to around $\alpha = -1.62$ in NH map (Figure 10a,b). The division of the NH into 3 domains according to the facies variability and the change in range trend orientation showed a disparity in power law exponent values. Indeed, the exponent $\alpha = -0.83$ in the domain A (values ranging from 21 m to 230 m), while $\alpha = -1.42$ (values ranging from 25 m to 1283 m) and $\alpha = -1.52$ (values ranging from 70 m to 1500 m) respectively in domain B and C (Figure 10c–e). The lowest α value in domain A can be explained by the dependence of fracture lengths on scale of observation for fractures ranging from 5 m to 870 m. In addition, the domain A is composed of granitic rocks and Crystal Spring sedimentary series with carbonates and quartzites (Figure 1), meaning that the sedimentary rocks can

have a different behavior from that of basement rocks during the fracture growth and propagation process.

Cumulative distribution of fracture lengths in the domain A showed also two different trend slopes (Figure 10c), with a failure slope quantified around 230 m. Distribution into two slopes has been largely discussed in the literature [25,67,70], and can be explained by the fracture growth process which has been divided into two trends. However, this result and interpretation cannot allow to determine if these two trends correspond to a single or to two different regional directions. Cumulative distribution of fracture lengths according to their orientations and the nature of rocks could help to resolve the episodes of deformation challenge, together with some more work in the field (e.g., looking for evidences of displacement).

The cumulative fracture length from all maps has been plotted in a single graphic, normalized by surface area of each map [63] (Figure 10f). The power law distribution included fracture lengths from 2.2×10^{-4} m to 65 km scale. Power law distribution was performed over 6 orders of magnitude. Two length ranges were not represented in this study. The first one corresponds to the fracture lengths over 100 km and related to the first order fracture defined by [30]. This absence can be explained by: (1) a different evolution stage and opening mechanism of faults [30,74], (2) a structural heritage which controls the reactivation during the DV trans-tensional tectonic setting. The second one corresponds to the length ranging from 1 km to 5 km length (Figure 10f). The Basin and Range regional map and the geological map at 1:25,000 scale could help to resolve both gaps.

The power law distribution gives an exponent $\alpha = -2$ for the whole 2D fracture lengths analyzed in this study (Figure 10f), which suggests the 2D representation is self-similar [4,16,23,26]. The probability to detect fracture of the size of the sampling window is the same at all scales. Then, the fracture connectivity is ruled by the small and large fractures [65], meaning that the large fractures detected and studied at large scale in the NH play the same role as any fracture at millimeter scale in fracture network connectivity.

5.2. Spatial Organization of NH Fracture Network

The fracture densities and the main dominant orientations on the regional maps show the control of NH geometry by NW/SE and E/W trends. Both trends are associated to the second order scale faults over 20 km length, well expressed in terms of abundance (DV regional map, Figure 11). The third order scale detected along NE/SW trend is characterized by faults around 10 km length. Spacing values were computed and correspond to 5 km and 1 km respectively for the second and the third order scale (Figure 12a). The same geometrical characteristics (detailed in the introduction) were approved in the extensional regime [20,30], meaning that the second and third order scale spacing classification can be generalized to the trans-tensional regime studied in the present work.

At NH scale, the fracture densities and the main dominant orientations approve the separation of the NH into three domains:

1. The first domain referred to the NH domain A is characterized by a specific spatial arrangement with a NW/SE direction dominance (Domain A, Figure 11). This direction is marked by the SDVFZ bordering fault of the strike-slip corridor, and is mostly dominated the NH fracture network in terms of length and abundance. It approved the importance of the NW/SE deformation episode at the fourth order scale. These fractures are the longest ones and also control the internal structuration inside the domain (Figure 12b). The E/W direction is less represented in comparison with domains B and C (Figure 11), but still the second most dominated fracture set, with less control on the NH geometry. Regarding the spacing characteristics, the NW/SE fractures set are regularly spaced from 0.1 to 0.2 km, while the E/W fractures set did not exceed 0.1 km spacing (Figure 12b).
2. The central domain (domain B, Figure 3) is characterized by several short segments of fractures. Indeed, the E/W direction is also dominated by short fractures with 60 m mean length, while the NW/SE direction is the second dominated system with long

- fracture of 100 m mean length (Figure 11). Then, NW/SE and E/W directions control the NH geometry respectively following the third and fourth order scale length. In this case, the spacing related to the third order scale is around 1 km between the SDVFZ bordering faults and regularly spaced at 0.2 km (Figure 12b). A spacing of 0.05 km is defined along the E/W fracture set (Figure 12b).
3. The southeastern end area corresponding to the domain C (Figure 3) highlights a specific spatial arrangement with an additional fracture set (yellow color, Figure 11), the longest one with 200 m mean length. Indeed, the NW/SE direction is split into N111° and N141° fracture sets thus highlighting the influence of both NW/SE and E/W deformation episodes in this area. Once again, the E/W direction is more expressed, with a 100 m mean length (Figure 11). The ENE/WSW, E/W and also NW/SE directions control the NH geometry and structuration respectively following the third and fourth order scale. The spacing of 0.3 km defined for the third order scale in domain C between the SDVFZ bordering faults is under the third order spacing characteristic. Indeed, the NW/SE direction has been deviated and then the relative spacing is reduced. Regarding the internal organization, the NW/SE and E/W fractures are also regularly spaced with 0.1–0.2 km and 0.05 km, respectively (Figure 12b).

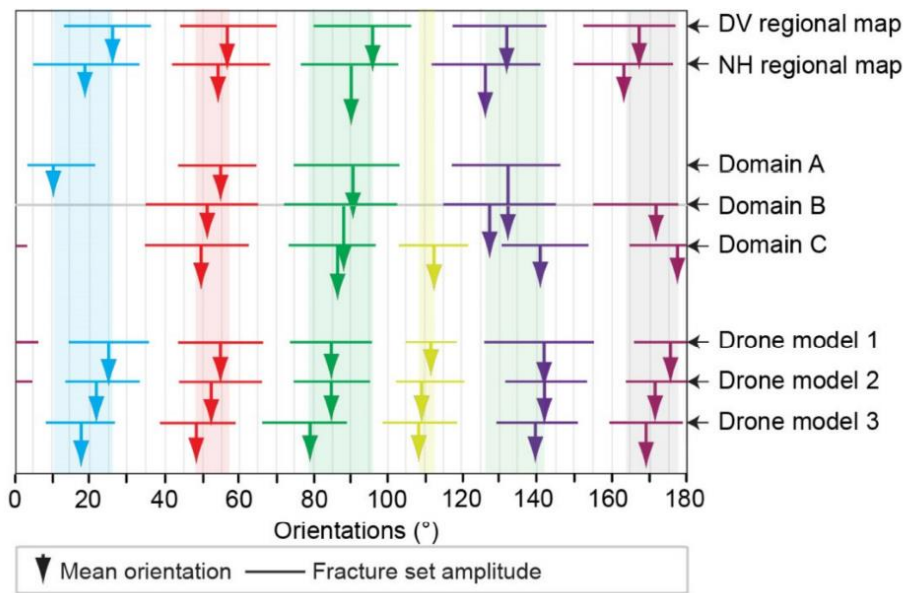


Figure 11. Orientation plot representing mean orientation of each fracture set from DV regional map, NH regional map, NH domains and drone models at outcrop scale. Each arrow corresponds to the mean orientation. The length of each arrow corresponds to the fracture set abundance. The horizontal line above each arrow corresponds to the fracture set standard deviation within an interval of confidence of 75% (see [62] for more explanations). Each color arrow corresponds to fracture set: Blue arrow corresponds to NNE/SSW fracture set, red arrow corresponds to the NE/SW fracture set, green arrow corresponds to the E/W fracture set, yellow arrow corresponds to the NNW/SSE fracture set, purple arrow corresponds to the NW/SE fracture set, and maroon arrow corresponds to the N/S fracture set.

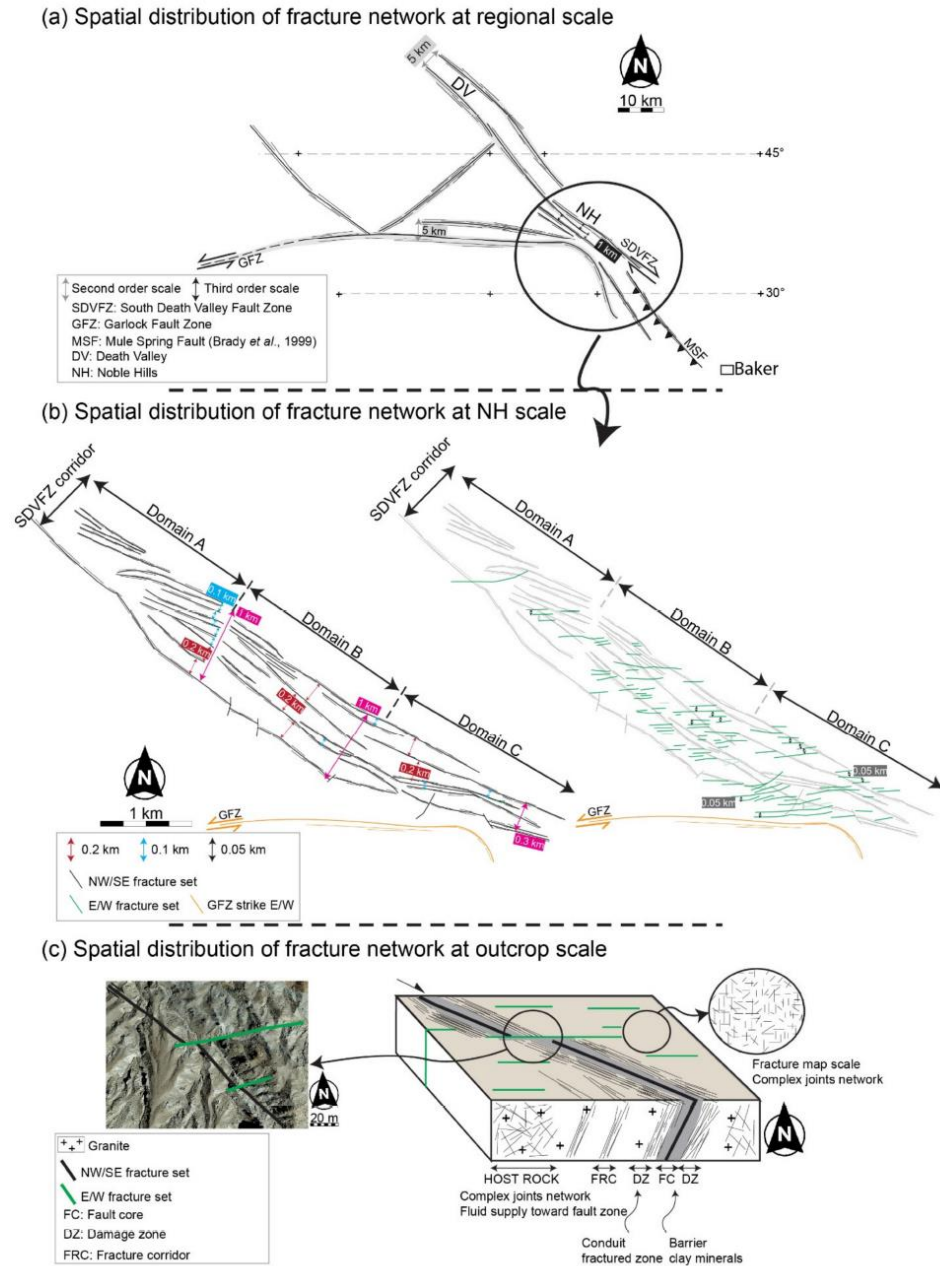


Figure 12. Conceptual scheme presenting the spatial arrangement of the NH fracture network at (a) regional scale, (b) NH scale, and (c) outcrop scale. The organization is based on scale orders referring to the [16,17,20,30] classification, and their associated spacing characteristics referring to [20,30]. The picture presented in (c) is provided by GoogleEarth®.

In the present work, the spacing characteristics of 0.05 km to 0.1–0.2 km computed in the three internal domains are attributed to the fourth order scale (Figure 12b). These values vary according to their directions and also lengths. Two spacing characteristics can be highlighted from this study: (1) spacing of 0.05 km corresponding to the fractures comprised between 0.1 and 0.35 km (percentile 90 values), (2) spacing of 0.1–0.2 m corresponding to the fractures comprised between 0.35 and 0.5 km. Further work on the fourth order scale spacing characteristics will obviously be needed in order to generalize them to the trans-tensional regime.

At outcrop scale, the drone models highlighted the reproducibility and the consistency of the whole fracture sets defined at large scale (Figure 11). However, N111° fracture set, detected only in domain C, is less expressed in domain A (drone model 1, 9%) (Figure 11). The E/W direction trend is more expressed in the drone models 2 and 3 respectively in the domain B and C. This observation is confirmed by the fracture maps 2 and 3, sample 2-1 and thin section 2-1 (Figures 8 and 9), highlighting a consistent fracturing episode. In the previous works, [39,55–57] mentioned the presence of the compression signature at the southeastern end of the NH and the front of the Avawatz mountains. According to these studies and our current observations, a hypothesis of fracturing intensity which affected up to the internal domain can explain the consistency of the E/W direction.

A special fracture arrangement was observed in fracture map 1 (Figure 6). The length distribution is characterized by a high density of short fractures in the quartzite boudin rocks, while the granitic part is characterized by a lower density of long fractures. This leads to a change in the power law and orientation distributions and then makes a bias. Indeed, only N/S and E/W directions are recorded, while the sample 1-1, thin sections 1-1 and 1-2 have recorded the whole fracture sets.

Fractures are organized along SDVFZ direction as fault zone segments with a highly mineralized (clay minerals) fault core (FC) which can act as a barrier and damage zone (DZ), acting as a conduit (Figure 12c). A complex joint network that can play a key role in the fracture connectivity is highlighted in the host rock. A petrographic study focusing on these fault zones is required to better characterize the fluid circulation potential.

The N/S to NNE/SSW and the NE/SW fracture sets are less expressed and are attributed to the fourth order scale with 40 m mean length on NH map, while they are still very important and consistent at outcrop, sample, and thin section scales, regardless of domain (Figures 2–5). These trends are highly dependent on the scale of observation and have no influence on the NH geometry.

To summarize, a new spatial organization of the NH range based on second, third, and fourth order scales has been proposed with length, spacing, density, and orientation distributions. Each NH domain shows its own internal organization. Variability in between recorded fracture sets from different areas is a marker of a complex tectonic and geometrical setting. One main deformation episode played a key role in the NH structuration: SDVFZ trending NW/SE affected whole NH and then controlled its geometry. The second main deformation episode is in the GF system trending E/W, likely responsible for E/W fracturing episode, and controlled the NH geometry mostly in its internal part and the southeastern end.

The identical orientation of GF and the E/W structures could suggest that the GF was responsible for the E/W fracturing in the internal and southeastern end domains (Figure 12b). Furthermore, the E/W structures are characterized by a sinistral strike-slip displacement, highlighted by the movement of the tertiary volcanic blocks in the back of the NH. This sinistral strike-slip movement has been characterized along the GF zone, widely described in the literature [55,57]. The similarities on the strike-slip nature can help to consider that the E/W fractures are related to GF activity which plays a key role on the NH geometry. In addition, the lower dominance of the NW/SE direction in the central and the southeastern end of the NH can be explained by the overprinting of the E/W fracturing, highlighting that these structures are posterior to the SDVFZ system (Figure 12c).

Regarding the fracture distributions, the fracture density is higher in the domain C with a factor 2.5 and 1.5, in comparison respectively with domain A and B (Figure 3). At outcrop scale, fracture densities raise from domains A and B to domain C with a factor 05 and 1.4, approving the localization of the fracture intensity in this area due to the complex tectonic setting [39]. Furthermore, a gradient of deformation has been observed in the field along the entire NH length with evidence of extreme shearing, notably in the internal domain. Boudinage structures and brittle shearing are prevalent within Crystal Spring series. A future publication will be planned to better characterize this deformation.

5.3. Fracture Network Impact on Flow

The deformation occurred with a different intensity at the whole NH scale. This can influence the fluid circulation through the fracture network following the domains. Even if the connectivity in the reservoir analogue is ruled by the large and small fractures (Figure 10f), some domains, such as domain A, had a different behavior insofar as the connectivity was ruled by only the large fractures. A complex joint network is highlighted at outcrop scale in the host rock and plays a key role in the fracture connectivity leading the fluid supply toward the fault zone.

The fluid flow modeling in this reservoir analogue should consider that the orientation parameter depends on scale observation and then should be modeled differently at each scale, while the length parameter is independent of the observation scale in the case of NH geothermal reservoir analogue.

Flow simulations will be planned in the future publications, based on photogrammetric models acquired from different NH domains. This study can help to approve the sensitivity of the fluid circulations to the gradient of strike-slip deformation and the spatial arrangement of NH fracture network. The sensitivity of the deterministic models on resulting permeability will be tested according to the directional dependence and their corresponding length distribution.

6. Conclusions

This study is part of the MEET project (Multidisciplinary and multi-context demonstration of EGS exploration and Exploitation Techniques and potentials), aiming at developing geothermal exploitation at European scale by applying Enhanced Geothermal System (EGS) technology to different geological settings. NH range, assimilated to a paleo geothermal reservoir analogue, gives an opportunity to study the basement rocks in trans-tensional context. This study proposes geometric description and quantifies the multiscale network organization and its effect on connectivity using a wide-ranging analysis scale from the microscopic scale to the regional scale. We used 2D fracture maps at different scales. We have shown a power law distribution for six orders of scales. Then, a power law exponent of $\alpha = -2$ was computed by combining the whole datasets, meaning that the connectivity is ruled by the small and the large fractures.

A new spatial arrangement of the fracture network at different scales has been proposed for the NH range, based on densities, spacings, orientations, and length distributions. The SDVFZ controls the NH geometry at large scale within the second order scale, while the E/W directions—whose origin remains to be determined—controls the NH geometry within the third order scale. The spacing characteristics are of 5 and 1 km for respectively the second and the third order scale, and correspond to the spacings highlighted in the extensional regime.

The division into three domains according to the facies variability and the change in range trend orientation has been approved by statistical analysis. Indeed, domain A is characterized by a dominance of the NW/SE direction in terms of length and abundance at the fourth order scale with a regular fracture spacing of 0.1–0.2 km. Then, NW/SE direction controls the internal structuration of this domain. Domain B is structured by the second and third orders of fractures scales following the E/W and NW/SE direction with regular spacing of 0.2 km and 0.005 km, respectively. Domain C was also characterized by

the structuration of a specific spatial arrangement with the dominance of short fractures following E/W direction, which highlight the persistence of the E/W fracturing episode. The ENE/WSW, E/W, and also NW/SE directions control the NH geometry and structuration in this area. A regular spacing of 0.2 km and 0.005 km is computed inside the domain at fourth order scale. Therefore, two spacing characteristics have been highlighted in this study at fourth order scale: 0.1–0.2 km and 0.05 km spacing for fractures length of 0.1–0.35 km and 0.005 km, respectively.

Each internal domain described in this study proposes its own spatial arrangement of fracture network. Indeed, two main deformation episodes referring to the SDVFZ striking NW/SE and fractures system striking E/W play a key role in the structuration of the NH range. However, the SDVFZ deformation affected the whole NH, whereas the E/W fracturing affected only the central and the southeastern area.

Fluid flow modeling will be planned and will take into consideration that orientation parameters should be modelled differently at each scale, while length parameters modelled by the power law should be considered as homogenous at different scales.

Author Contributions: Conceptualization, A.C., G.T. and B.A.L.; methodology, A.C.; software, A.C.; validation, G.T., B.A.L. and J.K.; formal analysis, A.C.; investigation, A.C., G.T., B.A.L. and J.K.; resources, A.C.; data curation, A.C.; writing—original draft preparation, A.C.; writing—review and editing, G.T., B.A.L. and H2020 MEET consortium; visualization, G.T., B.A.L. and J.K.; supervision, G.T.; project administration, G.T.; funding acquisition, G.T. and H2020 MEET consortium. All authors have read and agreed to the published version of the manuscript.

Funding: This project has received funding from the European Union’s Horizon 2020 research and innovation program under grant agreement No 792037 (MEET project).

Data Availability Statement: Not applicable.

Acknowledgments: This work is part of postdoctoral contribution, prepared at Institut Polytechnique UniLaSalle Beauvais, which was funded by European Union’s Horizon 2020 research (H2020 MEET project). We are grateful to Armand Pomart and Ruben Attali for their help for analyses. We also wish to thank the H2020 MEET consortium for their helpful comments and manuscript validation. We also thank the Assistant Editor Sorin Hadrian Petrescu and the anonymous reviewers for the relevant remarks that significantly approved the article.

Conflicts of Interest: The authors declare no conflict of interest.

References

1. Bour, O.; Davy, P. Connectivity of Random Fault Networks Following a Power Law Fault Length Distribution. *Water Resour. Res.* **1997**, *33*, 1567–1583. [[CrossRef](#)]
2. Gillespie, D.T. Approximate Accelerated Stochastic Simulation of Chemically Reacting Systems. *J. Chem. Phys.* **2001**, *115*, 1716–1733. [[CrossRef](#)]
3. Berkowitz, B. Characterizing Flow and Transport in Fractured Geological Media: A Review. *Adv. Water Resour.* **2002**, *25*, 861–884. [[CrossRef](#)]
4. Odling, N.E.; Gillespie, P.; Bourgin, B.; Castaing, C.; Chiles, J.P.; Christensen, N.P.; Fillion, E.; Genter, A.; Olsen, C.; Thrane, L. Variations in Fracture System Geometry and Their Implications for Fluid Flow in Fractured Hydrocarbon Reservoirs. *Pet. Geosci.* **1999**, *5*, 373–384. [[CrossRef](#)]
5. Johnston, J.D.; McCaffrey, K.J.W. Fractal Geometries of Vein Systems and the Variation of Scaling Relationships with Mechanism. *J. Struct. Geol.* **1996**, *18*, 349–358. [[CrossRef](#)]
6. Geiger, S.; Emmanuel, S. Non-Fourier Thermal Transport in Fractured Geological Media. *Water Resour. Res.* **2010**, *46*, W07504. [[CrossRef](#)]
7. Ledéser, B.; Dubois, J.; Genter, A.; Meunier, A. Fractal Analysis of Fractures Applied to Soultz-Sous-Forêts Hot Dry Rock Geothermal Program. *J. Volcanol. Geotherm. Res.* **1993**, *57*, 1–17. [[CrossRef](#)]
8. Dezayes, C.; Genter, A.; Valley, B. Structure of the Low Permeable Naturally Fractured Geothermal Reservoir at Soultz. *Comptes Rendus Géosciences* **2010**, *343*, 517–530. [[CrossRef](#)]
9. Valley, B.; Dezayes, C.; Genter, A.; Maqua, E.; Syren, G. Main Fracture Zones in GPK3 and GPK4 and Cross-Hole Correlations. In Proceedings of the EHDRA Scientific Conference, Soultz-sous-Forêts, France, 17–18 March 2005.
10. Bour, O.; Davy, P. On the Connectivity of Three-dimensional Fault Networks. *Water Resour. Res.* **1998**, *34*, 2611–2622. [[CrossRef](#)]




11. Darcel, C.; Bour, O.; Davy, P.; de Dreuzy, J.R. Connectivity Properties of Two-Dimensional Fracture Networks with Stochastic Fractal Correlation: Connectivity of 2D Fractal Fracture Networks. *Water Resour. Res.* **2003**, *39*, 1272. [[CrossRef](#)]
12. Odling, N.E. Scaling and Connectivity of Joint Systems in Sandstones from Western Norway. *J. Struct. Geol.* **1997**, *19*, 1257–1271. [[CrossRef](#)]
13. Castaing, C.; Halawani, M.A.; Gervais, F.; Chilès, J.P.; Genter, A.; Bourguine, B.; Ouillon, G.; Brosse, J.M.; Martin, P.; Genna, A. Scaling Relationships in Intraplate Fracture Systems Related to Red Sea Rifting. *Tectonophysics* **1996**, *261*, 291–314. [[CrossRef](#)]
14. Marrett, R.; Ortega, O.J.; Kelsey, C.M. Extent of Power-Law Scaling for Natural Fractures in Rock. *Geology* **1999**, *27*, 799–802. [[CrossRef](#)]
15. Soliva, R.; Schultz, R.A.; Benedicto, A. Three-dimensional Displacement-length Scaling and Maximum Dimension of Normal Faults in Layered Rocks. *Geophys. Res. Lett.* **2005**, *32*, L16302. [[CrossRef](#)]
16. Bertrand, L.; Géraud, Y.; Le Garzic, E.; Place, J.; Diraison, M.; Walter, B.; Haffen, S. A Multiscale Analysis of a Fracture Pattern in Granite: A Case Study of the Tamariu Granite, Catalunya, Spain. *J. Struct. Geol.* **2015**, *78*, 52–66. [[CrossRef](#)]
17. Bertrand, L.; Jusseaume, J.; Géraud, Y.; Diraison, M.; Damy, P.-C.; Navelot, V.; Haffen, S. Structural Heritage, Reactivation and Distribution of Fault and Fracture Network in a Rifting Context: Case Study of the Western Shoulder of the Upper Rhine Graben. *J. Struct. Geol.* **2018**, *108*, 243–255. [[CrossRef](#)]
18. Ehlen, J. Fractal Analysis of Joint Patterns in Granite. *Int. J. Rock Mech. Min. Sci.* **2000**, *37*, 909–922. [[CrossRef](#)]
19. Genter, A.; Castaing, C. Effets d'échelle Dans La Fracturation Des Granites. *Comptes Rendus de l'Académie des Sci. Ser. IIA Earth Planet. Sci.* **1997**, *325*, 439–445. [[CrossRef](#)]
20. Le Garzic, E.; de L'Hamaide, T.; Diraison, M.; Géraud, Y.; Sausse, J.; De Urreiztieta, M.; Hauville, B.; Champanhet, J.-M. Scaling and Geometric Properties of Extensional Fracture Systems in the Proterozoic Basement of Yemen. Tectonic Interpretation and Fluid Flow Implications. *J. Struct. Geol.* **2011**, *33*, 519–536. [[CrossRef](#)]
21. De Dreuzy, J.-R.; Davy, P.; Bour, O. Hydraulic Properties of Two-dimensional Random Fracture Networks Following Power Law Distributions of Length and Aperture. *Water Resour. Res.* **2002**, *38*, 12-1–12-9. [[CrossRef](#)]
22. Davy, P.; Le Goc, R.; Darcel, C.; Bour, O.; de Dreuzy, J.R.; Munier, R. A Likely Universal Model of Fracture Scaling and Its Consequence for Crustal Hydromechanics. *J. Geophys. Res.* **2010**, *115*, B10411. [[CrossRef](#)]
23. Hardebol, N.J.; Maier, C.; Nick, H.; Geiger, S.; Bertotti, G.; Boro, H. Multiscale Fracture Network Characterization and Impact on Flow: A Case Study on the Latemar Carbonate Platform. *J. Geophys. Res. Solid Earth* **2015**, *120*, 8197–8222. [[CrossRef](#)]
24. McCaffrey, K.J.W.; Sleight, J.M.; Pugliese, S.; Holdsworth, R.E. Fracture Formation and Evolution in Crystalline Rocks: Insights from Attribute Analysis. *Geol. Soc. Lond. Spec. Publ.* **2003**, *214*, 109–124. [[CrossRef](#)]
25. Bonnet, E.; Bour, O.; Odling, N.E.; Davy, P.; Main, I.; Cowie, P.; Berkowitz, B. Scaling of Fracture Systems in Geological Media. *Rev. Geophys.* **2001**, *39*, 347–383. [[CrossRef](#)]
26. Bour, O.; Davy, P.; Darcel, C.; Odling, N. A Statistical Scaling Model for Fracture Network Geometry, with Validation on a Multiscale Mapping of a Joint Network (Hornelen Basin, Norway). *J. Geophys. Res. Solid Earth* **2002**, *107*, ETG 4-1–ETG 4-12. [[CrossRef](#)]
27. Bonneau, F.; Caumon, G.; Renard, P.; Sausse, J. Stochastic Sequential Simulation of Genetic-like Discrete Fracture Networks. *Proceeding 32nd Gocad Meeting, Nancy, France*. 2012. Available online: <https://www.ring-team.org/component/liad/?view=pub&id=2214> (accessed on 3 July 2021).
28. de Dreuzy, J.-R.; Méheust, Y.; Pichot, G. Influence of Fracture Scale Heterogeneity on the Flow Properties of Three-Dimensional Discrete Fracture Networks (DFN): 3D Fracture Network Permeability. *J. Geophys. Res.* **2012**, *117*, B11207. [[CrossRef](#)]
29. Chabani, A. Analyse Méthodologique et Caractérisation Multi-Échelle Des Systèmes de Fractures à l'interface Socle/Couverture Sédimentaire Application à La Géothermie (Bassin de Valence, SE France). These de Doctorat, Paris Sciences et Lettres (ComUE), Paris, France, 2019. Available online: <http://www.theses.fr/2019PSLEM046> (accessed on 3 July 2021).
30. Morellato, C.; Redini, F.; Doglioni, C. On the Number and Spacing of Faults. *Terra Nova* **2003**, *15*, 315–321. [[CrossRef](#)]
31. Bourbiaux, B.; Basquet, R.; Daniel, J.M.; Hu, L.Y.; Jenni, S.; Lange, G.; Rasolofosaon, P. Fractured Reservoirs Modelling: A Review of the Challenges and Some Recent Solutions. *First Break* **2005**, *23*. [[CrossRef](#)]
32. Gillespie, P.; Monsen, E.; Maerten, L.; Hunt, D.; Thurmond, J.; Tuck, D.; Martinsen, O.J.; Pulham, A.J.; Haughton, P.D.W.; Sullivan, M.D. Fractures in Carbonates: From Digital Outcrops to Mechanical Models. *Outcrops Revital.—Tools Tech. Appl. Tulsa Okla. SEPM Concepts Sedimentol. Paleontol.* **2011**, *10*, 137–147.
33. Vollgger, S.A.; Cruden, A.R. Mapping Folds and Fractures in Basement and Cover Rocks Using UAV Photogrammetry, Cape Liptrap and Cape Paterson, Victoria, Australia. *J. Struct. Geol.* **2016**, *85*, 168–187. [[CrossRef](#)]
34. Biber, K.; Khan, S.D.; Seers, T.D.; Sarmiento, S.; Lakshminantha, M.R. Quantitative Characterization of a Naturally Fractured Reservoir Analog Using a Hybrid Lidar-Gigapixel Imaging Approach. *Geosphere* **2018**, *14*, 710–730. [[CrossRef](#)]
35. Trullenque, G.; Genter, A.; Leiss, B.; Wagner, B.; Bouchet, R.; Léoutre, E.; Malnar, B.; Bär, K.; Rajšl, I. Upscaling of EGS in Different Geological Conditions: A European Perspective. In Proceedings of the Proceedings 43rd Workshop on Geothermal Reservoir Engineering, Stanford, CA, USA, 12–14 February 2018.
36. Chabani, A.; Trullenque, G.; Rishi, P.; Pomart, A.; Attali, R.; Sass, I. Modelling of Fractured Granitic Geothermal Reservoirs: Use of Deterministic and Stochastic Methods in Discrete Fracture Networks and a Coupled Processes Modeling Framework. In Proceedings of the Extended Abstract, Reykjavik, Iceland, 2 May 2021.

37. Klee, J.; Trullenque, G.; Ledésert, B.; Potel, S.; Hébert, R.; Chabani, A.; Genter, A. Petrographic Analyzes of Fractured Granites Used as An Analogue of the Soultz-Sous-Forêts Geothermal Reservoir: Noble Hills, CA, USA. In Proceedings of the Extended Abstract, Reykjavik, Iceland, 26 May 2021.
38. Jennings, C. Geologic Map of California, Scale 1: 250,000. Olaf P. Jenkins Edition, Long Beach Sheet. *Calif. Div. Mines Geol, Serie No 33, List No 6347.033*; CA, USA, 1962. Available online: https://www.davidrumsey.com/luna/servlet/detail/RUMSEY~8~1~324920~90093990:Geologic-Map-of-California,-Long-Be?sort=Pub_List_No_InitialSort%2CPub_Date%2CPub_List_No%2C-Series_No (accessed on 3 July 2021).
39. Niles, J.H. Post-Middle Pliocene Tectonic Development of the Noble Hills, Southern Death Valley, California. Doctoral Dissertation, San Francisco State University, San Francisco, CA, USA, 2016.
40. Miller, M.; Pavlis, T. The Black Mountains Turtlebacks: Rosetta Stones of Death Valley Tectonics. *Earth-Sci. Rev.* **2005**, *73*, 115–138. [[CrossRef](#)]
41. Pavlis, T.L.; Rutkofske, J.; Guerrero, F.; Serpa, L.F. Structural Overprinting of Mesozoic Thrust Systems in Eastern California and Its Importance to Reconstruction of Neogene Extension in the Southern Basin and Range. *Geosphere* **2014**, *10*, 732–756. [[CrossRef](#)]
42. Snow, J.K.; Wernicke, B. Uniqueness of Geological Correlations: An Example from the Death Valley Extended Terrain. *Geol. Soc. Am. Bull.* **1989**, *101*, 1351–1362. [[CrossRef](#)]
43. DeCelles, P.G. Late Jurassic to Eocene Evolution of the Cordilleran Thrust Belt and Foreland Basin System, Western U.S.A. *Am. J. Sci.* **2004**, *304*, 105–168. [[CrossRef](#)]
44. Walker, J.D.; Burchfiel, B.; Davis, G.A. New Age Controls on Initiation and Timing of Foreland Belt Thrusting in the Clark Mountains, Southern California. *Geol. Soc. Am. Bull.* **1995**, *107*, 742–750. [[CrossRef](#)]
45. Stewart, J.H. Possible Large Right-Lateral Displacement along Fault and Shear Zones in the Death Valley-Las Vegas Area, California and Nevada. *Geol. Soc. Am. Bull.* **1967**, *78*, 131–142. [[CrossRef](#)]
46. Stewart, J.H. Extensional Tectonics in the Death Valley Area, California: Transport of the Panamint Range Structural Block 80 Km Northwestward. *Geology* **1983**, *11*, 153–157. [[CrossRef](#)]
47. Snow, J.K. Cenozoic Tectonism in the Central Basin and Range; Magnitude, Rate, and Distribution of Upper Crustal Strain. *Am. J. Sci.* **2000**, *300*, 659–719. [[CrossRef](#)]
48. Brady, R. Cenozoic Geology of the Northern Avawatz Mountains in Relation to the Intersection of the Garlock and Death Valley Fault Zones, San Bernardino County, California. Doctoral Dissertation, University of California, Davis, CA, USA, 1987.
49. Norton, I. Two-Stage Formation of Death Valley. *Geosphere* **2011**, *7*, 171–182. [[CrossRef](#)]
50. Burchfiel, B.C.; Stewart, J.H. “Pull-Apart” Origin of the Central Segment of Death Valley, California. *Geol. Soc. Am. Bull.* **1966**, *77*, 439–442. [[CrossRef](#)]
51. Pavlis, T.L.; Trullenque, G. Evidence for 40–41 Km of Dextral Slip on the Southern Death Valley Fault: Implications for the Eastern California Shear Zone and Extensional Tectonics. *Geology* **2021**, *49*, 767–772. [[CrossRef](#)]
52. Machette, M.N.; Klinger, R.E.; Knott, J.R.; Wills, C.J.; Bryant, W.A.; Reheis, M.C. *A Proposed Nomenclature for the Death Valley Fault System. Quaternary and Late Pliocene Geology of the Death Valley Region: Recent Observations on Tectonics, Stratigraphy, and Lake Cycles (Guidebook for the 2001 Pacific Cell—Friends of the Pleistocene Fieldtrip)*; US Department of the Interior, US Geological Survey: Reston, VA, USA, 2001; p. 173.
53. Troxel, B.W.; Butler, P.R. Rate of Cenozoic Slip on Normal Faults, South-Central Death Valley, California. Doctoral Dissertation, Department of Geology, University of California, Office of Scholarly Communication (OSC), Irvine, CA, USA, 1979.
54. Brady III, R.H. Neogene Stratigraphy of the Avawatz Mountains between the Garlock and Death Valley Fault Zones, Southern Death Valley, California: Implications as to Late Cenozoic Tectonism. *Sediment. Geol.* **1984**, *38*, 127–157. [[CrossRef](#)]
55. Reinert, E. Low Temperature Thermochronometry of the Avawatz Mountains, California: Implications for the Inception of the Eastern California Shear Zone. Doctoral Dissertation, University of Washington, Washington, DC, USA, 2004. Available online: https://www.ess.washington.edu/content/people/student_publications_files/reinert-erik/Reinert_2004.pdf (accessed on 3 July 2021).
56. Spencer, J.E. *Late Cenozoic Extensional and Compressional Tectonism in the Southern and Western Avawatz Mountains, Southeastern California. Basin and Range Extensional Tectonics near the Latitude of Las Vegas, Nevada: Geological Society of America Memoir*; Geological Society of America: Las Vegas, NV, USA, 1990; Volume 176, pp. 317–333. [[CrossRef](#)]
57. Chinn, L.D. *Low-Temperature Thermochronometry of the Avawatz Mountains; Implications for the Eastern Terminus and Inception of the Garlock Fault Zone*; University of Washington: Washington, DC, USA; Available online: https://www.ess.washington.edu/content/people/student_publications_files/chinn-logan/chinn-logan_ms_2013.pdf (accessed on 3 July 2021).
58. Rämö, T.O.; Calzia, J.P.; Kosunen, P.J. Geochemistry of Mesozoic Plutons, Southern Death Valley Region, California: Insights into the Origin of Cordilleran Interior Magmatism. *Contrib. Mineral. Petrol.* **2002**, *143*, 416–437. [[CrossRef](#)]
59. Bisdom, K.; Gauthier, B.D.M.; Bertotti, G.; Hardebol, N.J. Calibrating Discrete Fracture-Network Models with a Carbonate Three-dimensional Outcrop Fracture Network: Mpllications for Naturally Fractured Reservoir Modeling. *AAPG Bull.* **2014**, *98*, 13511376. [[CrossRef](#)]
60. Brady, R.H.; Troxel, B.W.; Wright, L.A. The Miocene Military Canyon Formation: Depocenter Evolution and Constraints on Lateral Faulting, Southern Death Valley, California. *Spec. Pap. Geol. Soc. Am.* **1999**, *277*–288. [[CrossRef](#)]
61. von Mises, R. Über Die “Ganzzahligkeit” Der Atomgewicht Und Verwandte Fragen. *Physikal. Z.* **1918**, *19*, 490–500.

62. Chabani, A.; Mehl, C.; Cojan, I.; Alais, R.; Bruel, D. Semi-Automated Component Identification of a Complex Fracture Network Using a Mixture of von Mises Distributions: Application to the Ardeche Margin (South-East France). *Comput. Geosci.* **2020**, *137*, 104435. [[CrossRef](#)]
63. Pickering, G.; Bull, J.M.; Sanderson, D.J. Sampling Power-Law Distributions. *Tectonophysics* **1995**, *248*, 1–20. [[CrossRef](#)]
64. Pickering, G.; Peacock, D.C.; Sanderson, D.J.; Bull, J.M. Modeling Tip Zones to Predict the Throw and Length Characteristics of Faults. *AAPG Bull.* **1997**, *81*, 82–99.
65. Davy, P.; Bour, O.; De Dreuzay, J.-R.; Darcel, C. Flow in Multiscale Fractal Fracture Networks. *Geol. Soc. Lond. Spec. Publ.* **2006**, *261*, 31–45. [[CrossRef](#)]
66. Ledéser, B.; Dubois, J.; Velde, B.; Meunier, A.; Genter, A.; Badri, A. Geometrical and Fractal Analysis of a Three-Dimensional Hydrothermal Vein Network in a Fractured Granite. *J. Volcanol. Geotherm. Res.* **1993**, *56*, 267–280. [[CrossRef](#)]
67. Cruden, D.M. *Describing the Size of Discontinuities*; Elsevier: Amsterdam, The Netherlands, 1977; Volume 14, pp. 133–137.
68. Priest, S.D.; Hudson, J.A. *Estimation of Discontinuity Spacing and Trace Length Using Scanline Surveys*; Elsevier: Amsterdam, The Netherlands, 1981; Volume 18, pp. 183–197.
69. Priest, S.D.; Hudson, J.A. Discontinuity Spacings in Rock. *Int. J. Rock Mech. Min. Sci. Geomech. Abstr.* **1976**, *13*, 135–148. [[CrossRef](#)]
70. Cowie, P.A.; Sornette, D.; Vanneste, C. Multifractal Scaling Properties of a Growing Fault Population. *Geophys. J. Int.* **1995**, *122*, 457–469. [[CrossRef](#)]
71. Priest, S.D. *Discontinuity Analysis for Rock Engineering*; Springer Science & Business Media: Berlin/Heidelberg, Germany, 1993.
72. Gillespie, C.S. The PoweRlaw Package: A General Overview. Newcastle, UK. Available online: https://cran.r-project.org/web/packages/poweRlaw/vignettes/a_introduction.pdf (accessed on 3 July 2021).
73. Gillespie, P.A.; Howard, C.B.; Walsh, J.J.; Watterson, J. Measurement and Characterisation of Spatial Distributions of Fractures. *Tectonophysics* **1993**, *226*, 113–141. [[CrossRef](#)]
74. Bertrand, L. *Etude Des Réservoirs Géothermiques Développés Dans Le Socle et à l'interface Avec Les Formations Sédimentaires*. Doctoral Dissertation, Université de Lorraine, Lorraine, France, April 2017; p. 492.

Article

Fracture Spacing Variability and the Distribution of Fracture Patterns in Granitic Geothermal Reservoir: A Case Study in the Noble Hills Range (Death Valley, CA, USA)

Arezki Chabani ^{1,*}, Ghislain Trullenque ¹, Johanne Klee ¹ and Béatrice A. Ledésert ²

¹ UniLaSalle, UPJV, B2R UMR 2018.C100, U2R 7511, 19 Rue Pierre Waguet, F-60026 Beauvais, France; ghislain.trullenque@unilasalle.fr (G.T.); johanne.klee@unilasalle.fr (J.K.)

² Geosciences and Environnement Cergy (GEC), CY Cergy Paris Université, 1 Rue Descartes, F-95000 Neuville-sur-Oise, France; beatrice.ledesert@cyu.fr

* Correspondence: arezki.chabani@unilasalle.fr; Tel.: +33-6-58-07-14-14



Citation: Chabani, A.; Trullenque, G.; Klee, J.; Ledésert, B.A. Fracture Spacing Variability and the Distribution of Fracture Patterns in Granitic Geothermal Reservoir: A Case Study in the Noble Hills Range (Death Valley, CA, USA). *Geosciences* **2021**, *11*, 520. <https://doi.org/10.3390/geosciences11120520>

Academic Editors: Giovanni Barreca and Jesus Martinez-Frias

Received: 21 September 2021

Accepted: 12 December 2021

Published: 17 December 2021

Publisher's Note: MDPI stays neutral with regard to jurisdictional claims in published maps and institutional affiliations.



Copyright: © 2021 by the authors. Licensee MDPI, Basel, Switzerland. This article is an open access article distributed under the terms and conditions of the Creative Commons Attribution (CC BY) license (<https://creativecommons.org/licenses/by/4.0/>).

Abstract: Scanlines constitute a robust method to better understand in 3D the fracture network variability in naturally fractured geothermal reservoirs. This study aims to characterize the spacing variability and the distribution of fracture patterns in a fracture granitic reservoir, and the impact of the major faults on fracture distribution and fluid circulation. The analogue target named the Noble Hills (NH) range is located in Death Valley (DV, USA). It is considered as an analogue of the geothermal reservoir presently exploited in the Upper Rhine Graben (Soulz-sous-Forêts, eastern of France). The methodology undertaken is based on the analyze of 10 scanlines located in the central part of the NH from fieldwork and virtual (photogrammetric models) data. Our main results reveal: (1) NE/SW, E/W, and NW/SE fracture sets are the most recorded orientations along the virtual scanlines; (2) spacing distribution within NH shows that the clustering depends on fracture orientation; and (3) a strong clustering of the fracture system was highlighted in the highly deformed zones and close to the Southern Death Valley fault zone (SDVFZ) and thrust faults. Furthermore, the fracture patterns were controlled by the structural heritage. Two major components should be considered in reservoir modeling: the deformation gradient and the proximity to the regional major faults.

Keywords: fracture network variability; Death Valley; granite; spacing distribution; fracture intensity P_{10} ; geothermal reservoir characterization

1. Introduction

In deep geothermal systems, many studies have been undertaken to better understand the importance of the natural fractures in various contexts [1,2]. In granitic basement rocks, the permeability is mostly increased by the fracture network and faults [3–7], while the porosity is increased by both the alteration (e.g., dissolution of primary minerals) and the proximity to fracture zones ([8], this issue). The low rock matrix permeability and porosity allow the fluid flow within fracture networks [9–11]. The understanding of the spatial arrangement of the fracture network constitutes the main issue in fractured reservoirs [1,3,7,12,13].

A fracture network is characterized by geometrical parameters such as lengths, spacings, widths, orientations, fracture distributions, and the relationships between them significantly affect the connectivity within the reservoir [9,14–17]. Among these parameters, spacing between fractures is a well-considered parameter, because it controls the probability of intersecting fractures during drilling [18]. Statistic parameters that describe fracture spacing include: (1) The mean, which characterizes the global expected frequency of fracture intersection, and (2) the standard deviation, which describes the distribution of the fractures around the mean.

Regarding the spacing distribution, fractured zones can be classified into: (1) Fracture corridor, a term usually used for a dominant set of fractures displaying an important variation of fracture intensity. It can represent the main drains for fluid circulation in various reservoir contexts such as geothermal fields [19]; (2) fracture arrays, a term generally used to define a dominant set of fractures which forms an angle to the swarm (area in which any kind of fracture appears) [20]; (3) shear zone, which is defined as a continuous deformed zone with a high strain [21], accommodated by a cataclastic process in granitic rocks and crystalline plasticity in (e.g., carbonate rocks); and (4) fault zone characterized by a fault and its associated damage zone which can act as a barrier or a drain for flow, depending on its intrinsic properties [5,20,22]. In crystalline basement rocks, the fracture distribution within the damage zone is influenced by the distance from the fault core and its displacement along the fault plane [23]. Indeed, the strong variation in fracture distribution (fracture densities) is commonly observed near active faults. Ostermeijer et al. [23] add that the pattern is mainly ruled by the distribution of macro-damage induced on shear-accommodating subsidiary fractures.

Spatial organization of fracture systems became an important studied topic in the recent decades because of the necessity to better understand the architecture of fractured reservoirs [7,24–26]. The spatial arrangement can be quantified using statistical laws (e.g., power law, log normal, and exponential law) [24,27,28] or statistical parameters, such as the coefficient of variability (Cv) along 1D [20] and the normalized correlation count method [27]. The main goal is to enhance the fracture distribution understanding (clustered, random, or uniform distribution) and its effects on connectivity [29]. In that case, many studies are focused on fracture networks characterization in various settings and at different scales [3,12,16,20,30,31]. They commonly used field analogues at surface to resolve the challenge of lack of sub-surface information in reservoirs [32]. The characterization of heterogeneity of the fracture spacing and the fracture abundance at any scale may be performed using line sampling method along one dimension (1D) named scanline (e.g., [26]). The present study combines the spacing data of joints (opening-mode fractures), veins (partially or fully filled), and faults to highlight the spatial arrangement of the fracture patterns in granitic rocks and the influence of the regional major faults. In the present study, the measured fractures, whatever their filling have been classified according to their orientation.

The present work is part of the European MEET project (multidisciplinary and multi-context demonstration of EGS exploration and exploitation techniques and potentials, [33]). This study proposes to (1) describe fracture system distribution at outcrop scale, based on fracture network parameters; (2) shows the role of the regional major faults proximity on the fracture patterns evolution in the basement rocks; and (3) highlights the impact of the deformation at outcrop scale. The present study was performed in the desert environment of Noble Hills (NH) fractured granitic basement, located in the southern termination of Death Valley (Death Valley, CA, USA), and is considered as a paleo geothermal analogue of the Upper Rhine Graben (URG, Alsace area situated in the eastern of France) ([25,34,35], this issue) geothermal systems producing electricity, because of the similarities in the basement rock nature (granite), hydrothermal alterations and the trans-tensional tectonic setting [25,34–36]. However, the geological history of the NH range is rather different from that of those in the URG, but numerous pieces of evidence of analogy have been highlighted by recent work of Klee et al., [37], which addressed a list of similarities between the URG reservoir targets (exploited geothermal present-day reservoir) and the NH ranges:

- Pervasive alteration of the NH granite;
- Ubiquitous argillic alteration affecting plagioclase and biotite is present;
- Unaltered K-feldspar;
- Porosity is enhanced by the alteration and microfracturing;
- Evidence of the hydrothermal fluid percolation, as identified in an exploited geothermal reservoirs;
- Fluid circulation in open system such as in EGS systems (input of potassium and carbonates).

Based on scanline methodology (e.g., [26]), this work has been performed using a spacing measurement, compiled from four different canyons located in the central part of NH. This central part has been characterized as having a distinct spatial arrangement of fractures at different scales in comparison with the northeast and southeast parts (for additional explanations, see [25]). The scanlines are located in the granitic part of the NH range, the so called crystalline basement slice (CBS) according to Brady et al. [38]. Some of the measures were acquired directly from the field and others from virtual scanlines (method detailed in Section 3.2). Apertures of fractures have also been measured directly in the field. Numerous fractures were filled by newly formed minerals such as carbonates, oxides, and sometimes barite.

In this study, scanline methodology and statistical tools are used to better understand the fracture spacing variability and the distribution of fracture patterns at depth. This allows better characterizing reservoirs in response to the developing geothermal exploration and exploitation by EGS in basement rock context. This study was conducted:

1. Through a description of the fracture system using orientation, density, spacing and aperture parameters;
2. By highlighting the role of the proximity to the regional major faults on the fracture patterns;
3. By highlighting the role of the deformation gradient and structural heritage at outcrop scale.

2. Geological Setting

The NH structurally belongs to the DV region (Figure 1a), which is characterized by a complex tectonic history (e.g., [39]), starting with late Cenozoic extensional and trans-tensional structures which overprint the Mesozoic to Early Cenozoic contractional structures [39–41]. The extensional regime of the DV has begun around 16 Ma [42,43], and is shifted to a trans-tensional regime around 5 Ma [39,44–46]. Recent work by Pavlis and Trullenque, [36] reconsider the age of the transcurrent deformation in DV around 12 Ma.

The NH ranges forms the principal physiographic feature aligned with segments of the right-lateral Southern Death Valley Fault Zone (SDVFZ) [25,47] (Figure 1b). The SDVFZ net dextral strike-slip displacement has been estimated around 40–41 km [36]. A whole compressional region was created by the interaction between the SDVFZ and the Garlock Fault (GF) system (see Figure 1b for location), which leads to shortening within the Avawatz Mountains (Figure 1b) [48–50].

The exhumation history of NH range is poorly described in the literature. Based on KI/temperature of illite crystals, recent work by Klee et al. [37] highlighted that the southeastern of NH is much elevated, with a higher temperature which could indicate that the south-eastern part of NH was buried deeper than its north-western part and has been exhumed.

Recent work by Chabani et al., [25] highlights the structural organization of the NH range according to the orders of fault magnitude classification by analyzing 2D maps at different scales. These orders consist in (1) second order scale, referring to the faults comprised between 20 and 30 km length; (2) third order scale, referring to faults around 10 km length; and (3) fourth order, referring to the faults under 1 km length. The first order referring to the crustal faults (higher than 100 km length) is not observed within the NH range.

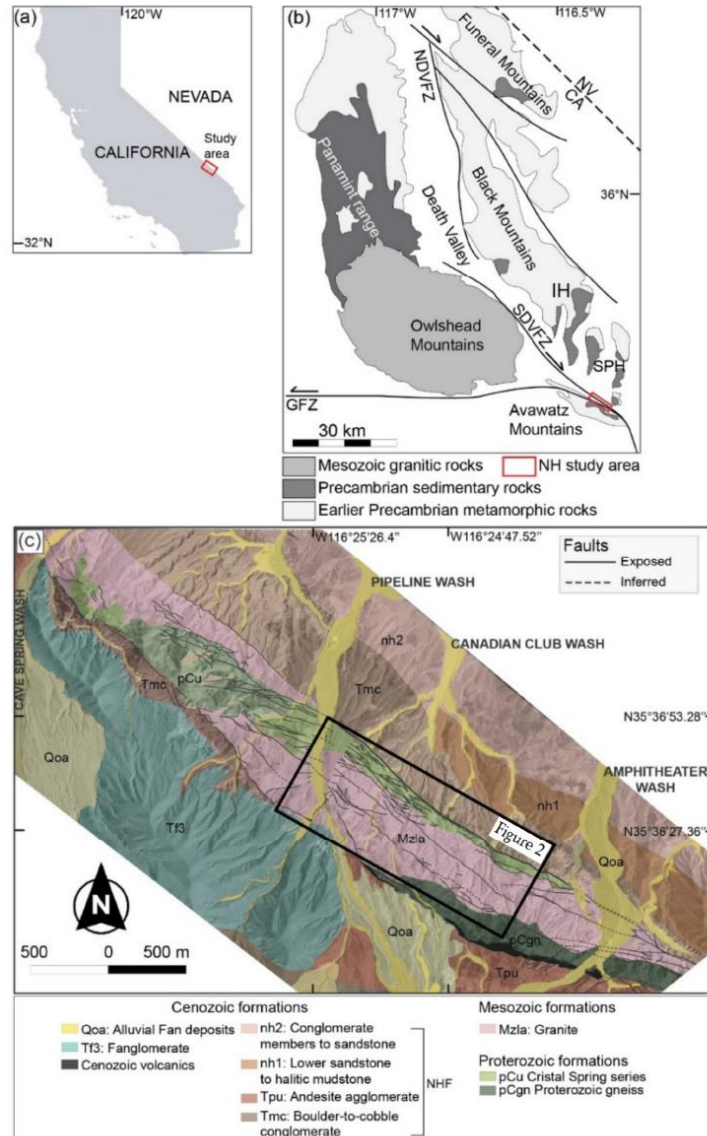


Figure 1. (a,b) Location and geological setting of DV and NH studied area modified after [50], NDVZF: Northern Death Valley Fault Zone, SDVZF: Southern Death Valley Fault Zone, GFZ: Garlock fault zone, CA: California, NV: Nevada, IH: Ibex Hills, SPH: Saddle Peak Hills. (c) Structural scheme of the NH range performed thanks to high-resolution digital mapping techniques (see below) modified after [34,47]. Additional digitized fractures were obtained using orthophotos. NHFs: Noble Hills formations.

The SDVFZ trending NW/SE and the GFZ trending E/W controlled NH range geometry. Indeed, the SDVFZ controls the NH geometry at large scale within the second order scale, while the GFZ trending E/W controls the NH geometry within the third order scale. Chabani et al., [25] add that the NH are divided into three internal structural domains: (1) Domain A, to the north, is characterized by the dominance of the NW/SE direction at the fourth order scale; (2) domain B, central, is marked by the dominance of the E/W and the NW/SE directions at respectively the fourth and third order scales; and (3) domain C, to the south, is also characterized by the E/W and NW/SE directions dominance but at the third and fourth order scales, respectively.

Numerous episodes of deformations have been highlighted during the fieldwork campaigns. Indeed, the SDVFZ fault segments act with a dextral movement (black lines in Figure 2b), highlighting an intense deformation with local evidences of extreme shearing. These structures are contemporaneous with the syn-kinematic dextral strike faults (orange lines in Figure 2b), highlighted in the recent work done by Klee et al. [8]. In addition, compressional structures like thrust faults crosscut outcrops 6 and 8 (red lines in Figure 2b). A clear overprinting has been recognized between SDVFZ (which also crosscut the OT2, OT6, and OT7) and the compressive structures are due to the GFZ, which acts with a sinistral movement. Furthermore, the thrusting highlighted in the present study postdates the activity of the SDVFZ. According to Chabani et al. [25], it is tempting to relate the thrust structures to the activity along the frontal termination of GFZ. Furthermore, the compressive structures are related to the interaction of the NH ranges with the Avawatz mountains during the GFZ movement.

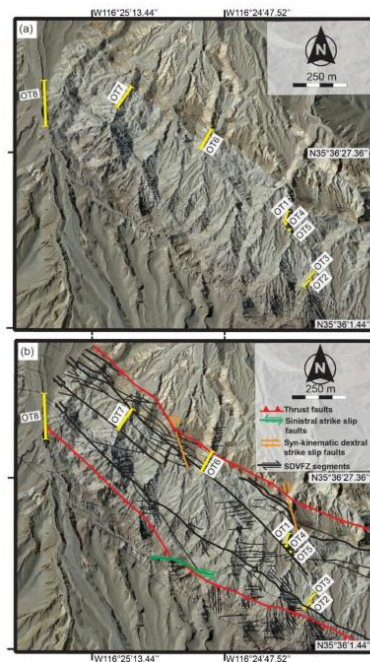


Figure 2. (a) Map highlighting the structural position of the central part of NH, including the outcrops (OT) location and (b) SDVFZ segments position in black, syn-kinematic dextral strike slip faults in orange, sinistral strike-slip faults in green lines, and thrust faults in red. Dextral strike slip faults are syn-kinematic with SDVFZ episode, those systems are followed by thrust faults, which are contemporaneous with the GFZ orientated globally E/W.

A gradient of deformation has been highlighted in the central part of NH, with evidence of extreme shearing, close to OT6 and OT7. Boudinage structures and brittle shearing are highlighted within the Crystal Spring series (pCu, Figure 1c). In that case, the new geological map (Figure 1c) built using the high-resolution mapping techniques on the ground, using a tablet and QGIS software by Klee et al. [34] revealed a stacking of the Crystal Spring series, intruded by the Mesozoic granite (Mzla, Figure 1c). Laterally, the thickness of Crystal Spring series was reduced, as they were dragged and stretched against the granite due to the SDVZ activity, especially in OT6 to OT8 areas.

Cenozoic volcanic series have also been highlighted in the southeastern end of the NH [47]. Cenozoic formations have been characterized by Niles, [47] outside the center part of the NH. They are mainly composed of fanglomerate, alluvial fan deposits, lacustrine deposits, sabkha, evaporitic rocks, carbonate units, and megabreccia.

3. Methodology

Scanlines are commonly used to describe the reservoir properties and the fracture systems from analogues of hydrocarbon and groundwater reservoirs [20,30,51–54], and of geothermal reservoirs [55]. The scanline methodology, widely described in the literature [2,26,54,56], helps the understanding of the fractured reservoir geometry.

3.1. Scanline Data Acquisition

In the present work, the geometrical parameters of fractures, such as orientation, spacing, and aperture, were acquired directly from scanlines in the field. A decameter was installed horizontally along the outcrop (Figure 2a). Note that data about every fracture (e.g., joint, vein or fault) intersected by the scanline were collected, whatever its orientation class or filling. The cross-cutting relationships between the studied fractures are difficult to observe in the field, as intersections rarely occur along the scanline. Then, the fracture parameters were acquired by reporting the successive position of each fracture along the scanline. The projected positions were then collected and reported in Excel software v.2019. The spacing between two consecutive fractures is given by [20]:

$$S_A = P_n - P_{n-1} \quad (1)$$

S_A is the apparent spacing of fractures calculated from the fracture positions measured from field, P_n refers to the position of fracture n , and P_{n-1} refers to the position of fracture $n-1$, both expressed in meters, the location of the beginning of the measurement line being the reference. During the data analysis step, the fractures were filtered by orientation classes in order to discuss the effect of the regional directions on the local fracturing heterogeneity.

One to two scanlines were acquired from each outcrop. Five scanlines were performed along the outcrops OT 1, OT2, and OT3.

Fracture spacings were also calculated from virtual scanlines based on photogrammetric models and on fracture maps. The photogrammetric models were performed using two drones: 3DR Solo drone and DJI Phantom. These drones were loaned by University of Texas at El Paso (UTEP), TX, USA. The videos were recorded between the late morning and the early afternoon during seven consecutive days using a manual mode camera setting to reduce the effects of lighting condition. Then, pictures were extracted from the recorded videos. To provide a sufficient overlapping, pictures were extracted every second using ffmpeg software v.4.5 (Grenoble, France). The alignment of the pictures was done in Agisoft Metashape software 2020, v.1.6.5. (Saint Petersburg, Russia). Regarding the picture resolution, we ensured that every picture had a resolution of 300 dpi (300 pixels per 300 pixels). That permitted us to digitize the maximum number of fractures of decimeter length. The size of the pixel is 10 cm per pixel.

Several processing steps were needed to build the 3D models, starting by sky removal to reduce the noises, and the creation of different picture chunks (Figure 3). The 3D models were georeferenced and then imported in open access QGIS® software 2018, v.2.18.17 (Beaverton, OR, USA) to start the fracture extraction process. To improve the accuracy,

ground control points (GCP) put in the field, using differential global positioning system (DGPS) and global positioning system (GPS) integrated directly in the drones, have been used. The georeferencing of each outcrop was realized independently using DGPS. The extraction of fractures was done manually by tracing every plane from the 3D outcrop. The orientation of every extracted trace plane was done automatically, and then compiled. For further explanation, the methodology of the modeling and the fracture extraction is detailed in Chabani et al. [35]. The digitized fractures were projected on a 2D map in order to keep data consistent among the whole datasets.

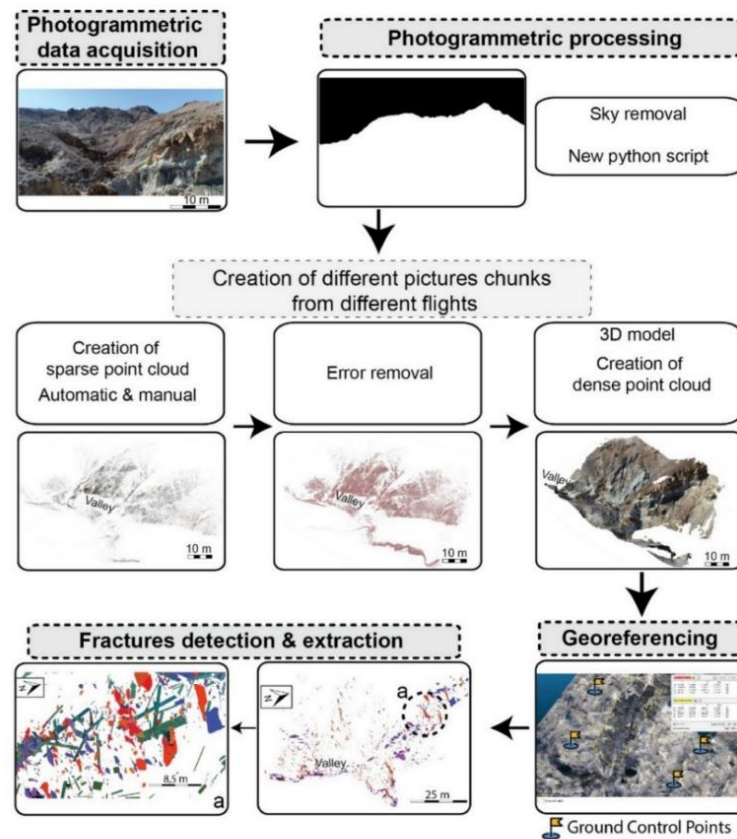


Figure 3. Workflow illustrating the different steps to build the 3D photogrammetric models, georeferencing, and fractures detection and extraction. Modified after Chabani et al. [35].

Two-dimensional fracture maps OT4 and OT5 (Figure 2) were performed from the field using a DSLR high resolution camera, with fixed focal (50 mm) in order to reduce the distortion. Furthermore, to avoid light effects, pictures were taken in the absence of direct sunlight (e.g., [16]). Several pictures were taken vertically, with the same distance, and with a sufficient overlapping. These pictures were then aligned using Agisoft Metashape software 2020 v.1.6.5 with the procedure detailed in Chabani et al. [35]. Outcrops OT6 to OT8, also located in the central part of NH, were analyzed by photogrammetric technology, and are also located in the central part of NH. In total, five scanlines were performed (Figure 4e–i).

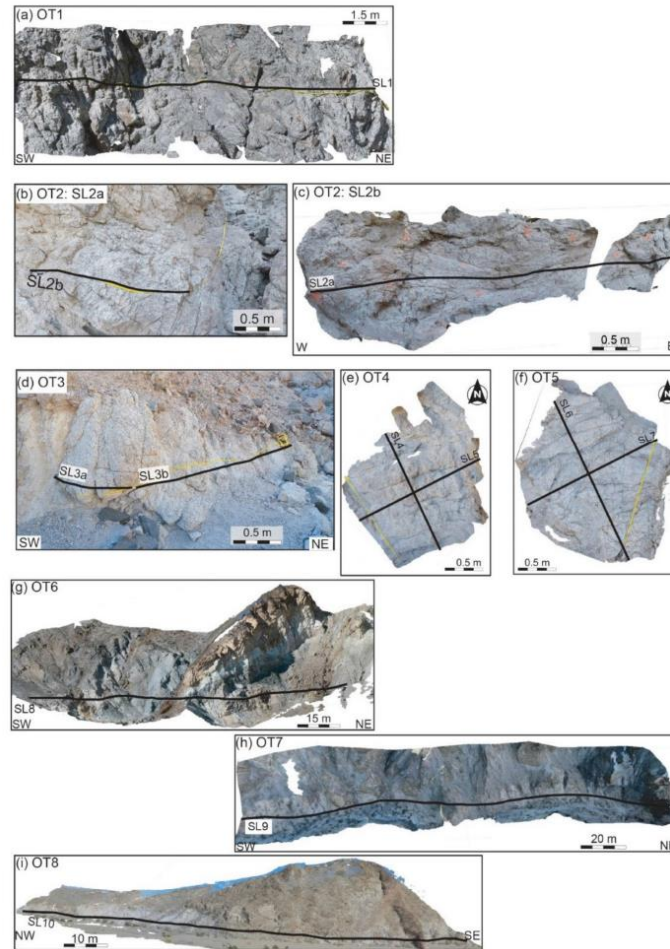


Figure 4. Visualization of the eight outcrops studied in this work, including the scanlines (SL) location. (a) Outcrop 1 trending SW/NE shows heterogeneity of fracture orientation distribution. (b,c) Outcrop 2 trending E/W shows large NE/SW and NW/SE fracture planes crosscut by SL2a and SL2b. (d) Outcrop 3 trending NW/SE shows large E/W fracture planes crosscutting SL3a and SL3b. (e) Outcrop 4 consists in a fracture map; 2 scanlines were traced perpendicular to the main structures, recording then large E/W and N/S fracture planes for SL4 and SL5 respectively. (f) Outcrop 5 also consists in a fracture map; 2 scanlines were traced perpendicular to the main structures, crosscutting mainly fracture planes orientated NW/SE for SL6 and E/W for SL7. (g) Outcrop 6 consists in a canyon perpendicular to the SDVФЗ segments, which crosscuts a large E/W fracture plane. This outcrop shows the transition between granitic basement and Crystal Spring sedimentary rocks. (h) Outcrop 7 trending NE/SW records a several fracture plane orientations. (i) Outcrop 8 trending NW/SE highlights mainly NE/SW and E/W fracture planes. SDVФЗ: Southern Death Valley Fault Zone. For outcrops location, see Figure 2. Note that the OT6, 7 and 8 cross some major talus slopes. These outcrops have been modeled in 3D, making the fracture digitation possible to do in CloudCompare software. Then, the planes have been projected in 2D to keep data homogeneous from all fracture sets.

The fracture maps and the photogrammetric models were georeferenced and then used to extract the fractures in QGIS[®] software 2018, v.2.18.17. In this study, the fracture digitization was performed manually by tracing every detected fracture because of insufficient contrast between the fractures and the surrounding rock. Each digitized fracture became a georeferenced lineament in QGIS[®]. In the case of fracture maps, note that the fractures extending out of the sampling area were considered as one continuous feature [57–59] (Figure 2b). In QGIS[®], the procedure of digitization consisted in an extraction of the end point coordinates of each fracture. Each fracture contained X and Y coordinates of each of the two end points, which helped to compute the spacings along a virtual scanline according to the following procedure:

1. Digitized fractures are loaded in shapefile format (e.g., shp format);
2. Virtual lines are traced along the georeferenced outcrop, and the intersection between the digitized fractures and the virtual line are collected. Note that, the intersection point ID must be the same as that of digitized fractures;
3. X and Y coordinates are added to the intersection points file, computed directly in QGIS[®];
4. Values are classified according to X coordinate in Excel software, to ensure the right position of each intersected fracture;
5. Spacings are computed following [17]:

$$||AB|| = \sqrt{(x_b - x_a)^2 + (y_b - y_a)^2} \quad (2)$$

The calculated spacing in Equation (2) is not adjusted by Terzaghi correction. According to the scanline orientation, fracture orientations, and the position of scanline intersections for each fracture set, the fractures spacing were adjusted by applying the Terzaghi correction following [60]:

$$S = S_A \times \cos \theta \quad (3)$$

S is the true mean spacing of fractures in a set, S_A is the apparent mean spacing of fractures in a set and θ is the acute angle between the direction normal to fractures and the scanline.

Orientation bias can be minimized by drawing a scanline parallel to the normal to a fracture set, such that θ is close to 0° . All fractures intersected by scanlines were acquired. Then, all measured fractures were filtered by orientations during the analysis in order to describe the patterns of spacing according to each fracture set.

3.2. Fracture Orientation Analysis

In this study, the orientation is the first parameter analyzed to classify the fractures into fracture sets. As described before, from virtual scanlines, the fracture dip was not obtained from virtual scanlines, while it was measured for each fracture on field scanlines. The fracture dip has been measured for each fracture. Here, the classification into fracture sets is based only on strike orientation without considering the variation in dip to preserve data homogeneity. Note that, from field scanlines, the dip direction for each fracture is however provided in the Schmidt canvas.

Several software packages such as Win-tensor [61], Stereonet [62], and Digifrac [63] have been developed in order to project the structural data. Fisher distribution [64], Fisher-Bingham distribution [65], and von Mises distribution [66] are commonly used to describe symmetrical distributions of orientations in 2D, and sometimes in 3D in case of Fisher distribution. However, these distributions do not describe complex asymmetrical data. Then, the classification was performed using the mixture of von Mises distribution (MvM) [67], which is adapted to describe complex circular data and then seem relevant to model larger complex fracture networks. The methodology consists in a semi-automated approach based on appraisal tests to avoid any subjectivity in fracture set analysis. This distribution is based on three parameters: (1) Mean orientation (μ°), around which the

distribution is centered; (2) kappa (κ), which controls the concentration of the orientation values around the mean; and (3) weight (ω), corresponding to the relative contribution of each fracture set to the model. In addition, the best number of fracture sets is approved using the goodness of fit parameters (e.g., likelihood). The degree of precision of each mean fracture orientation is computed using the standard deviation (SD), which is of $\pm 10^\circ$. For further explanations, see Chabani et al., [68], which described and adapted the MvM methodology for structural data. To plot the orientation data in the current study, we used a rose diagram for describing data which only contain dip direction measurements, and Schmidt canvas for describing data which contain strike and dip measurements.

3.3. Analysis of Spacing

Numerous statistical tools have been developed in the recent decades specially to analyze the fracture parameters such as spacing, width, length, orientation [26,51–53], and its spatial distribution (e.g., clustered, random, or uniform distribution) [26]. For spacing parameter, a coefficient of variability (Cv) has been widely described in the literature, that provides an indication of the fracture distribution [20,26,54,69]. It is given as:

$$Cv = \sigma_s / S \quad (4)$$

σ_s and S represent, respectively, the standard deviation and the mean spacing. When $Cv \approx 1$, the fractures intersected by the scanline are distributed randomly. When $Cv < 1$, fractures are more regularly spaced, while $Cv = 0$ represents uniformly spaced fractures, and $Cv > 1$ indicates fractures that are more irregularly spaced. Each Cv value can provide information about the degree of fracture clustering [26].

The heterogeneity of fracture distribution based on cumulative distribution has also been quantified using the V' statistic of [70], applied to structural geology by [20,30,31]. Indeed, the heterogeneity of distribution of the fractures and associated parameters (aperture, spacing, thickness, etc.) may be characterized from the cumulative frequency using the method described by [70]. Then, V' is defined as the measure of the heterogeneity within the scanline, which is given as:

$$V' = |D_{\max}| + |D_{\min}| / A \quad (5)$$

D_{\max} and D_{\min} are the cumulative frequency at that point if the fracture parameter was uniformly distributed [30]. D_{\max} and D_{\min} are positive and negative respectively. A is the total cumulative frequency of the analyzed parameter. In the present study, the V' will be used on aperture parameter in order to evaluate the strain heterogeneity. This strain heterogeneity depends on the amount of displacement (aperture or heave) and the spatial distribution of the fractures [31]. Analogical tests have been illustrated by Putz-Perrier and Sanderson [31] for two examples of the same population of extensional fractures, with different spatial arrangement, but with same strain. They obtained a fracture network uniformly distributed for the first example, and strongly clustered for the second one. Then, aperture parameter helps us to better characterize the degree of heterogeneity of every analyzed area. A perfect regular fracture distribution produces a $V' \approx 0$ as fracture sizes decrease, while the maximum heterogeneity of fractures distribution would produce a $V' = 1$ value. For further explanations, see Putz-Perrier and Sanderson [31].

3.4. Fracture Density P_{10}

The position and spacing of a set of fractures are considered whatever of their type (e.g., normal, reverse, etc.) [20]. A scanline normal to a set of fractures would intersect N fractures (number of fractures) over a length. The fracture density (P_{10}) is defined as the number of fracture intersections (N) per unit length (L) [58], following:

$$P_{10} = N/L \quad (6)$$

3.5. Cumulative Frequency Diagrams

The spacing distribution and arrangement were analyzed by using cumulative frequency. As recommended by [20,26], stick plots were used, in which the location of each fracture intersected by the scanline is mentioned. This allows to better visualize the fracture distribution. Furthermore, a plot of cumulative frequency versus distance along the scanline (from the beginning to the end) was used, in which P_{10} is proportional to the slope of the cumulative curve. The cumulative plot is normed by the maximum value, expressed in percentage (%) and it always starts at the origin (0, 0) and ends at $(d_N - d_1)$, $(N - 1)$. The parameters d_1 and d_N represents respectively the first and the last fracture. The cumulative frequency (%) against distance along the scanline provides a rapid visual comparison between datasets for each scanline and between those scanlines whatever their lengths [71].

4. Results

4.1. Description of Fracture Systems Acquired from NH Range

The studied outcrops reported in the Figure 2 were distributed homogenously within the entire central part of the NH (CBS). The structural position of each outcrop is described below.

4.1.1. Fieldwork Scanlines

The fracture network parameters were compiled from the field (Figure 2). The measurements were performed within OT1 using a scanline 1 (SL1 orientated N010) of 13.45 m length (Figure 4a), intersecting a total of 324 fractures, with a mean space of 0.04 m (Table 1). The orientation, spacing and aperture data were acquired along two scanlines with different orientations in OT2 (Figure 4b,c). The SL2a (orientated N160) of 7.5 m length intersected 109 fractures, with a mean space of 0.07 m, while the SL2b (orientated N070) of 1.64 m length intersected 37 fractures, with a mean space of 0.04 m. Within OT3, the fracture spacing and aperture were also acquired along two different orientation scanlines: SL3a and SL3b orientated N055 and N160 respectively (Figure 4d). Both scanlines intersected respectively 31 and 47 fractures, with a mean space of 0.03 and 0.06 m.

Table 1. Characteristics of the fractures acquired from each studied outcrop, along the scanlines. Outcrop 1 to 3 (without asterisk) show the characteristics of the fractures acquired directly from field scanlines. Outcrop 4 to 8 (with asterisk) show the data extracted from aligned photographs using Metashape Software v.1.6.5, with a virtual scanline. For each outcrop, number of scanlines are indicated with: Number of fractures intersected, orientation and length of scanlines, mean fractures space, density (frac/m), coefficient of variability (Cv), and V' statistic fom [70]. The proximity to the major faults is mentioned. Mean spacing and Cv are computed with Terzaghi correction. Sgmt: segments.

Outcrop	SL	Number of Fractures	Proximity to Major Fault Segments	SL Orientation	Length (m)	Mean Spacing (m)	Density (frac/m)	Cv	V' (95%)
1	SL1	261	10 m to SDVFZ sgmt	N010	13.45	0.04	19.4	1.2	0.29
2	SL2a	80	Crosscut by SDVFZ sgmt	N160	7.50	0.07	10.6	14.4	0.42
	SL2b	32	Crosscut by SDVFZ sgmt	N070	1.64	0.04	19.5	1.1	0.50
3	SL3a	27	40 m to SDVFZ sgmt	N055	0.85	0.03	31.8	0.7	0.32
	SL3b	38	42 m to SDVFZ sgmt	N160	4.50	0.06	8.4	1.7	0.57
4*	SL4	28	6 m to SDVFZ sgmt	N163	0.80	0.02	42.1	0.82	/
	SL5	46	6 m to SDVFZ sgmt	N073	1.72	0.04	26.7	0.84	/
5*	SL6	26	4 m to SDVFZ sgmt	N074	1.50	0.05	17.2	0.93	/
	SL7	31	4 m to SDVFZ sgmt	N157	0.70	0.02	44	0.89	/
6*	SL8	171	Crosscut by SDVFZ sgmt and thrust fault	N020	109	0.64	1.55	3.22	/
7*	SL9	188	Crosscut by SDVFZ sgmt	N132	82.22	0.5	2	3.26	/
8*	SL10	258	Crosscut by SDVFZ sgmt and thrust fault	N154	97.50	0.4	2.66	1.67	/

4.1.2. Virtual Scanlines

The fracture variability analysis was further conducted by creating fracture maps with a resolution of 2×10^{-4} m, OT4 and OT5. OT4 is sized 1.7 m per 1.6 m and is located in the granitic facies close to the SDVFZ segments (Figure 4e). Two scanlines: SL4 and SL5, orientated, respectively, N163 and N073, were traced perpendicular to each other in order to intersect the maximum number of fractures and avoid angular bias (e.g., [26]). In total, 28 fractures were intersected along SL4 of 0.80 m length, with a mean space of 0.02 m. Regarding the SL5, 46 fractures were intersected, with a mean space of 0.04 m (Table 1). OT5 is sized 1.8 per 1.7 m and is also located in the granitic facies, close to the SDVFZ segments (Figure 4f). Here again, two scanlines: SL6 and SL7 were traced, orientated respectively N074 and N157. They intersected, respectively, 26 and 31 fractures. The mean spacing is of 0.05 and 0.02 m for SL6 and SL7, respectively.

To perform the fracture variability study in 1D, three photogrammetric models localized only in the granitic facies were added to the present work. They are located close to the major fault segments. The fractures extracted from these models ranged from 10^{-2} to 20 m in length.

The drone photogrammetric model displayed in OT6 is sized approximately 110 per 45 m (Figure 4g); 171 fractures were traced and are intersected by the SL8. Note that OT6 presents various lithologies including granitic rocks, gneiss, gabbro, and sedimentary rocks. This may influence the spatial variability of the fractures in this area, as it will be discussed below. The drone photogrammetric model presented in OT7 is sized approximately 82 per 45 m. In this model, 188 fractures were traced and intersected by the SL9 (Figure 4h). Finally, drone photogrammetric model displayed in OT8 is sized approximately 100 per 25 m. In total, 258 fractures were traced and intersected by SL10 (Figure 4i).

4.2. Fracture Orientation Distributions

The data acquired from scanlines in the central part of the NH show a heterogeneous fracture distribution. SL1 is located near (around 10 m) a SDVFZ major segment (bold black line in Figure 2b), which acts following dextral strike-slip movement. Several lineaments are identified from the high-resolution field mapping, striking E/W (GFZ signature) to NW/SE (SDVFZ signature). From the SL1, the mean fracture orientations (μ) are striking N026, N062, N092, N130, and N171 (Figure 5a, Table 2). Fracture abundances for each fracture set are characterized by a slight dominance of the N062 and N092 fracture set with, respectively, 21% and 37% (Table 2). N026, N130, and N171 fracture sets represent, respectively, 17%, 15%, and 10% of the whole fracture set. Then, NE/SW trend appears at outcrop scale and is equivalent to E/W fractures in term of density. However, SL2a crosscut by SDVFZ major segment and close to thrust fault (Figure 2b), and a significant difference was observed in terms of fracture abundance with respectively 80 fractures in comparison with SL1 (261 fractures). The most recorded fracture sets are striking N014, N025, and N102 with, respectively, 18%, 46%, and 27%. The other fracture sets do not exceed 10% (Figure 5b, Table 2). N152 is the most dominant fracture orientation highlighted along the SL2b, representing 38%. N003 and N112 both represent 31% (Figure 5c, Table 2). Both SL3 scanlines are located far from the influence of the SDVFZ segments, thrust faults and sinistral strike-slip faults (Figure 2b). Then, SL3a, much smaller in length, intersected three fracture sets: N077, N098, and N135 with, respectively, 49%, 25%, and 26% abundances (Figure 5d, Table 2). Three fracture sets were also highlighted from the SL3b striking N040 (24%), N081 (65%), and N150 (11%). The orientations of fractures detected in SL3 scanlines are less heterogeneous than in SL2 and SL1. The structural position of SL3 far from major faults (around 40 m in distance) very likely impacts the fracturing at outcrop scale.

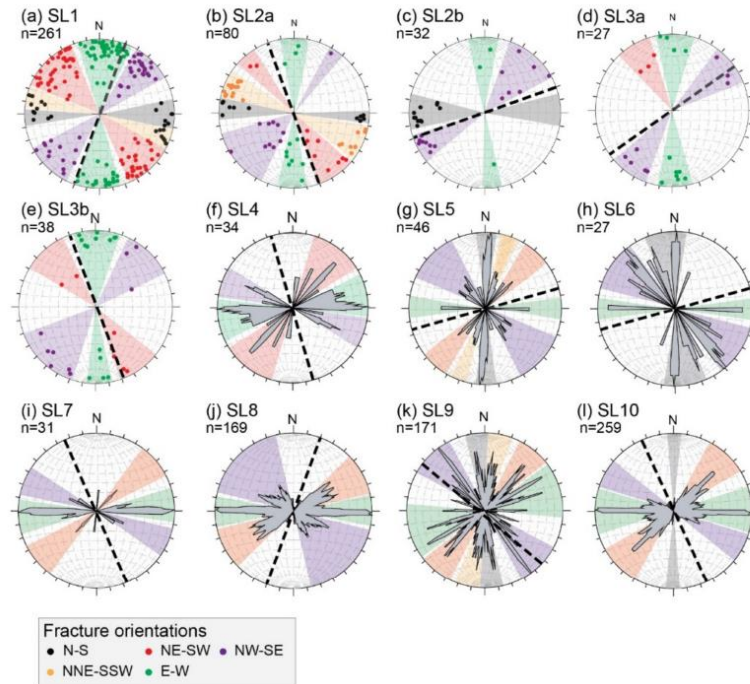


Figure 5. Fracture orientation distributions of the NH studied outcrops (a–l). (a–e) The fracture orientation distributions are represented into Schmidt canvas, lower hemisphere because they contain strike and dip measurements. (f–l) Fracture orientation distributions are represented by rose diagrams because they contain only dip direction measurements. Each direction rose diagram of direction is expressed with classes of 5°. The dashed lines indicate the direction of the scanline. n: Number of data. See legend in the figure for colors.

Regarding the virtual scanlines, the structural position of SL4 (OT4 orientated N163) and SL5 (orientated N073) is the same as SL1. Indeed, both scanlines are located near SDVFZ major segment (around 6 and 4 m in distance, respectively), highlighted by dominance of NW/SE and E/W structures. SL4 intersected much less fractures in comparison with the perpendicular SL5 (Table 1). SL4 displayed three fracture sets striking N034 (34%) and N086 (53%), and N123 (13%), while SL5 highlighted five fracture sets striking: N001 (39%), N018 (12%), N040 (14%), N113 (9%), and N144 (26%) (Figure 5f,g, Table 2). SL6 and SL7 orientated, respectively, N074 and N157, acquired from OT5, showed a heterogeneous fracture set, and are located near SDVFZ segments (4 m distance). Indeed, SL6 highlighted three fracture sets striking N004, N100, N161 with, respectively, 35%, 49%, and 16%, while SL7 highlighted N053, N087, and N116 fracture sets with, respectively, 13%, 81%, and 6% (Figure 5h,i, Table 2).

Table 2. Output parameters obtained from the MvM distribution fitting to fracture orientation data. Each scanline dataset was analyzed separately. Each simulation provides the number of fracture sets with their corresponding mean orientation μ ($^{\circ}$), kappa (κ) which corresponds to the orientation variance around the mean, and weight (ω) corresponding to the proportion of each fracture set. Cv: Coefficient of variability.

Number of Fractures in Each Set	Parameters				Number of Fractures in Each Set	Parameters			
	μ ($^{\circ}$)	k	ω (%)	Cv		μ ($^{\circ}$)	k	ω (%)	Cv
SL1					SL5				
44	N026	5.07	17	1.03	18	N001	44.83	39	0.79
55	N062	11.30	21	0.53	6	N018	57.7	13	0.79
97	N092	5.73	37	1.44	6	N040	31.58	13	0.86
39	N130	6.77	15	1.43	4	N113	4.95	9	0.74
26	N171	5.11	10	1.37	12	N144	15.13	26	0.95
SL2a					SL6				
14	N014	27.98	18	1.97	10	N004	23	35	0.54
35	N025	1.19	46	1.67					
8	N050	29.67	8	1.26					
18	N102	4.21	27	1.12					
5	N143	8.91	1	1.35					
SL2b					SL7				
10	N003	11.4	31	1.05	4	N053	3.54	13	0.88
10	N112	0.09	31	1	22	N087	46.2	81	0.83
12	N152	18	38	0.9	5	N116	33.5	6	0.84
SL3a					SL8				
13	N077	12.06	49	1.07	54	N058	10.09	32	1.3
6	N098	14.22	25	0.6	61	N090	21.05	36	3.45
8	N135	14.1	26	0.8	54	N132	3.1	32	2.82
SL3b					SL9				
9	N040	4.57	24	1.23	34	N029	7.17	20	2.97
25					46	N060	10.45	27	1.93
4					15	N096	6.25	9	3.83
					38	N132	9.85	22	2.31
				38	N176	5.38	22	2.62	
SL4					SL10				
11	N034	2.18	34	0.82	8	N004	75	3	0.81
18	N086	11.4	53	0.85	18	N040	75	7	1.68
5	N123	11	13	0.7	189	N091	43.23	73	1.7
					44	N118	35.3	17	1.35

Crosscutting the NW/SE thrust faults (in red lines, Figure 2b) and SDVFZ segment faults (in black bold lines, Figure 2b), the OT6 to OT8 displayed heterogeneous fracture orientation distribution from scanline measurements. SL8 scanline acquired within OT6 is characterized by a special geological setting. Indeed, compressional structures like thrust faults crosscut this outcrop (Figure 2b), close to the Canadian Club Wash (Figure 1c). SL7 is however crosscut by 2 SDVFZ major segments. Regarding the orientation distributions, SL8 of 109 m length, orientated N020, recorded three fracture sets, striking N058, N090, and N132 with an equivalent fracture abundance (between 32% and 36%) (Figure 5j, Table 2). However, five fracture sets were highlighted from SL9, striking N029 (20%), N060 (27%), N096 (9%), N132 (22%), and N176 (22%) (Figure 5k,l). SL10 recorded N004 (3%), N040 (7%),

N091 (73%), and N118 (17%) fracture sets. This scanline crosscut a thrust fault and several secondary SDVFZ segments (Figure 2b).

4.3. Spatial Distribution of Fractures

The spatial organization of fractures was highlighted from scanlines, whatever the fracture orientation, and is summarized in Table 1. In addition, the spatial organization was also studied following the fracture orientations in order to determine the impact of some regional directions on the NH structural organization.

From SL1, fracture density (P_{10}) and C_v are around, respectively, 19.4 frac/m and 1.2, indicating a random fracture distribution. Equivalent P_{10} and C_v were measured from SL2b with, respectively, 19.5 frac/m and 1.1, also indicating a random distribution. While SL2a recorded a P_{10} of 10.6 frac/m and C_v of 14.4, indicating a less abundant and highly clustered fracture system. Values of P_{10} of 31.8 and of 8.4 frac/m, C_v of 0.7 and 1.7 were highlighted from SL3a and SL3b, respectively, (Table 1), indicating very abundant fractures with a random distribution.

Three different spacing organizations were identified from fracture sets in SL1 (Table 2):

- Fractures distributed randomly in fracture set N026 with $C_v = 1.03$;
- Fractures uniformly spaced in fracture set N062 with $C_v = 0.53$;
- Fractures more irregularly spaced or clustered in fracture sets N092, N0130, and N171 with, respectively, $C_v = 1.44$, 1.43, and 1.37.

The fracture distribution presented in Figure 6 shows the layout of fractures and their location along each scanline. For SL1, the fracture distribution is showed using a cumulative frequency plot against the position of fractures along the scanline for each fracture set (Figure 6a). Two major trends are distinguished: (1) Regular fracture distribution from the beginning to the end of the scanline especially for fracture sets N026 and N171 (respectively in black and orange colors with diamond and square symbols in Figure 6a); and (2) a regular fracture distribution at the beginning, then clustered (increased frequency), followed by another regular distribution at the end for fracture sets N062, N092, and N130 (respectively in red, green and purple colors in Figure 6a). Three fracture clusters having a slope higher than 2 are highlighted in N062 fracture set, around 5.5, 8, and 10 m (Figure 6a), highlighting a clustered spacing. Note that, this slope corresponds to the shape of the cumulative frequency compared to the uniform distribution highlighted in the plots below (Figure 6). The cumulative frequency plot highlighted one fracture cluster around 12–13 m in the N092 fracture set. Within the N130 fracture set, two fracture clusters are characterized around 3–4 and 10 m.

SL1 is in moderate deformation zone, affected mainly by SDVFZ major segment and some E/W fault segments. The position of SL1 close to SDVFZ major segment, trending NW/SE creates these irregularities in fracture distribution. Indeed, the NW/SE (N130) fracture set is one of the most clustered fracture sets. The intermediate (in term of length) E/W segments shown in the Figure 2b have a strong impact on N092 fracture set distribution, making it the more clustered distribution with $C_v = 1.44$.

A high fracture density is observed in the central part of the SL2a profile (Figure 6b). Indeed, five fracture clusters were identified in which the fracture density is increased around 3–4 m in N143 fracture set (purple color in Figure 6b), 4.5 m in N014 and N025 fracture sets (black and orange colors, respectively, for N014 and N025 in Figure 6b), and around 6 m in N014 and N050 fracture sets, displayed, respectively, in black and red colors for N014 and N050 in Figure 6b. The SDVFZ crosscuts the SL2a profile and introduces some irregularities in fracture distribution since the beginning, mainly in N143 and N014 fracture sets, highlighting then an anisotropy following some directions.

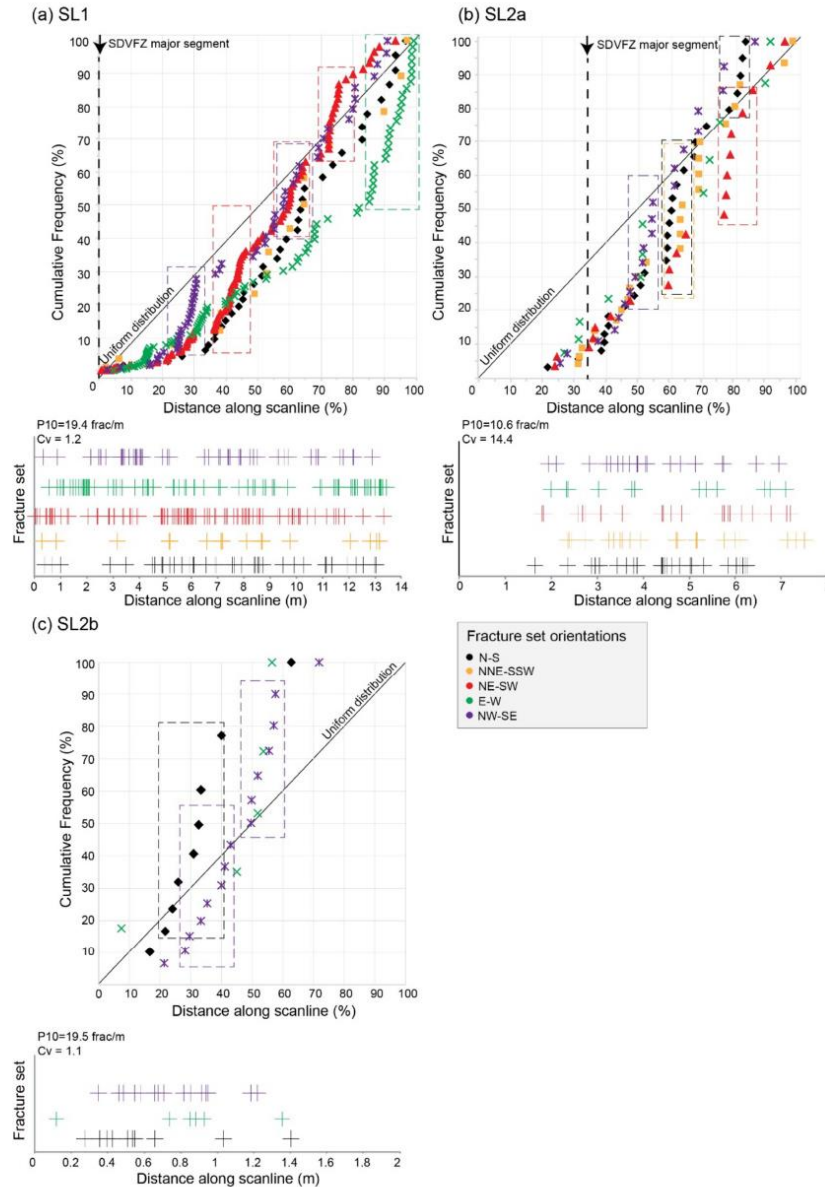


Figure 6. Cumulative frequency diagram along each scanline and following each fracture set (in colors). Plot of cumulative frequency expressed in % versus distance along scanline for: (a) SL1, (b) SL2a, and (c) SL2b. Dashed lines indicate a potential cluster for each fracture distribution, indicating a rapid increase in the number of fractures with slope threshold > 2. The diagonal line in each plot of cumulative frequency defines a uniform or regular distribution. Visual location of fractures expressed in stick plots for each fracture set distribution, highlighting the fracture position along the scanline, including the fracture density (P_{10}) and the coefficient of variation (C_v) values. The structural position is done in each diagram. See the color legend for the orientation of fracture sets.

Fractures intersected by the SL2b are distributed randomly whatever the direction with C_v close to 1 (Table 2). N098 and N0135 fracture sets intersected by SL3a displayed a C_v of 0.6 and 0.8, indicating a uniform spacing organization, while C_v of 1.07 measured from the N077 fracture set indicates a clustered organization. However, the beginning and the end of the SL2a profile showed a regular fracture distribution. Along SL2b, a random fracture distribution was observed whatever the fracture orientation with C_v around 1 (Figure 6c). Three fracture clusters are, however, detected within N003, N112, and N152 fracture sets (displayed respectively in black, green, and purple colors), respectively, around 0.4–0.6, 0.8–1, and 1.2 m (Figure 6c).

A regular fracture distribution was highlighted within fracture orientations N098 and N135 along SL3a profile, with C_v of 0.6 and 0.8, respectively (Figure 7a). For N077 fracture set (red color with triangle symbol), a clustered distribution was shown with two fracture clusters around 0.3–0.4 and 0.7–0.8 m. However, along SL3b scanline profile, one fracture cluster which corresponds to an increase in fracture density was shown around 2 and 2.25 m, respectively, in N040 and N150 fracture sets (respectively in red and purple colors in Figure 7b). Only three fracture clusters were identified around 1.5, 2.5–3, and 4 m in N081 fracture set (green color). A regular fracture distribution was characterized outside these fracture clusters. Located away from major fault segments, around 40 m distance, the SL3a and SL3b profiles displayed a very poor fracture system organization and fracture density. In addition, these profiles are in a moderate deformation zone, which can impact drastically the fracture distribution and density. Boudinage structures and brittle shearing are not observed within this area.

OT4 and OT5 are in a moderate deformation zone, affected mainly by SDVFZ major segment and some E/W fault segments. From virtual scanlines, three fracture sets were recorded in SL4. The N034 fracture set highlighted one fracture cluster around 0.5–0.6 m (red rectangle in Figure 8a). However, four fracture clusters were highlighted at the beginning and at the end of the SL4 profile within N086 fracture set (green color with cross mark symbol in Figure 8a), around 0.01, 0.25, 0.65, and 0.7–0.8 m. The rest of the intervals are characterized by a regular fracture distribution. The SL5 scanline recorded five fracture sets and are characterized by a regular fracture distribution whatever the fracture set (Figure 8b). An increased fracture density is identified within the N001 fracture set (black color) around 0.7 and 1.2 m.

Fractures detected within SL6 are mainly distributed regularly for N004 and N161 fracture sets (displayed respectively in black and purple colors in Figure 8c), with C_v of 0.88 and 0.84, respectively. C_v of 1.35 was, however, computed from the N090 fracture orientation (green color with cross mark symbol, Figure 8c), indicating highly clustered fractures. Then, one fracture cluster was identified around 0.5–0.6 m (Figure 8c). The three fracture sets striking N053, N087, and N132 are recorded mainly with fractures regularly distributed along the SL7, with C_v ranging from 0.83 to 0.84 (Figure 8d). Two fracture clusters are then identified within the N087 fracture set (green color with cross mark symbol in Figure 8d) around 0.5 and 0.6–0.7 m.

The influence of the regional directions was observed on E/W fractures orientation, with a higher density and clustering within this fracture set (Table 2). However, the NW/SE direction is less expressed in comparison with SL1 and SL2. The small length of OT4 and OT5 scanlines may influence the result and then introduce some bias to the analysis.

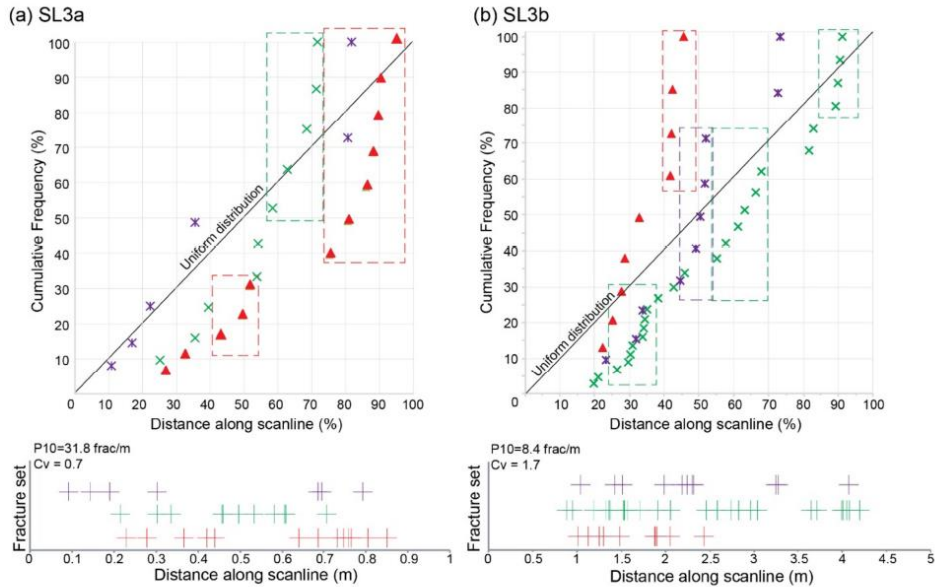


Figure 7. Cumulative frequency diagram along each scanline and following each fracture set (in colors). Plot of cumulative frequency expressed in % versus distance along scanline for: (a) SL3, and (b) SL3a. Dashed lines indicate a potential cluster for each fracture distribution, indicating a rapid increase in the number of fractures with slope threshold > 2. The diagonal line in each plot of cumulative frequency defines a uniform or regular distribution. Visual location of fractures expressed in stick plots for each fracture set distribution, highlighting the fracture position along the scanline, including the fracture density (P_{10}) and the coefficient of variation (C_v) values. See the color legend in Figure 6.

Near the Canadian wash (see Figure 1c for location), OT6 is located close to the highly deformed zone (for location, see Figure 2). Two major faults crosscut this outcrop: SDVFZ major fault segment and thrust fault. SL8 intersected three fracture sets with a high fracture density interval (Figure 9a). Three fracture clusters were identified in N058 fracture sets, respectively, around 10–20, 40, and 75 m (red color with triangle symbol legend, Figure 9a). The fracture clusters in N090 fracture set (green color with cross mark symbol, Figure 9a) are around 40, 50–60, 75, and 80 m. Finally, within N132 fracture set (purple color with strikethrough cross, Figure 9a), two fracture clusters comprised between 10–15 and 50–70 m were identified. We are fully aware that the canyon presents a complex structuration due to various lithologies and the overprinting faults.

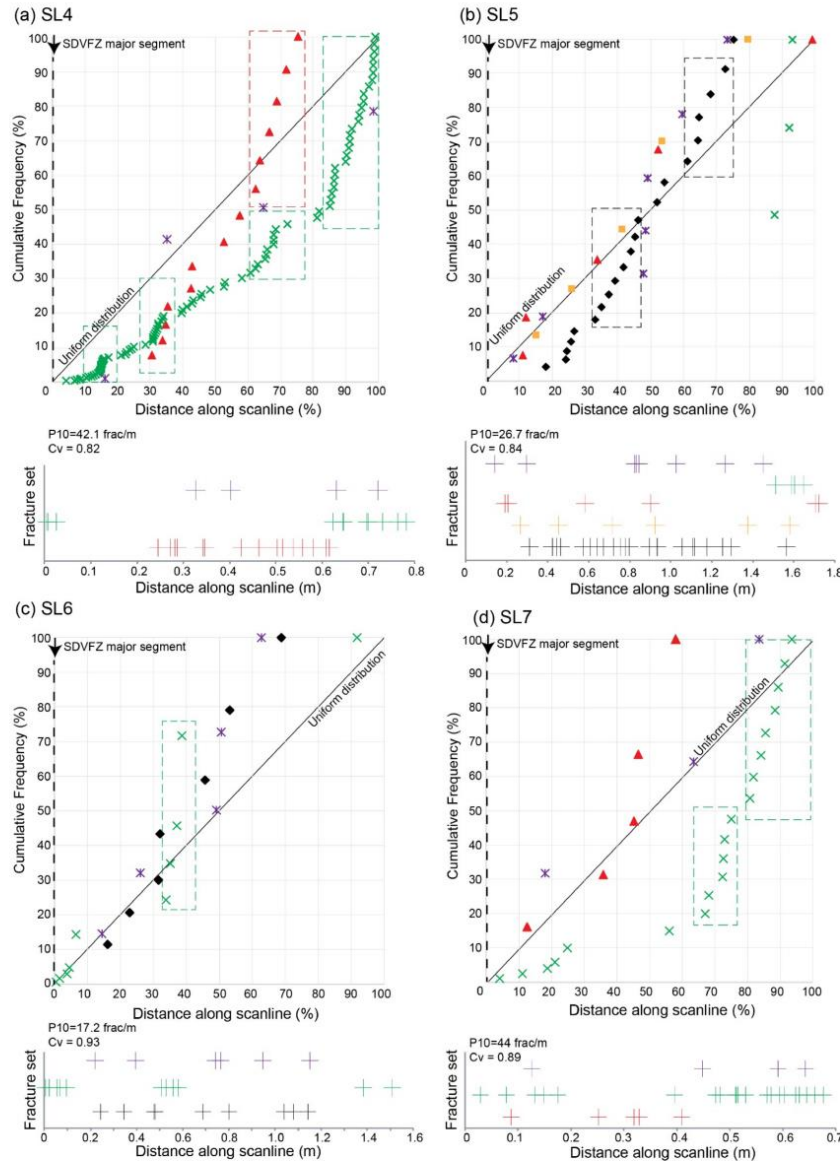


Figure 8. Cumulative frequency diagram along each scanline and following each fracture set (in colors). Plot of cumulative frequency expressed in % versus distance along scanline for: (a) SL4, (b) SL5, (c) SL6, and (d) SL6. Dashed lines indicate a potential cluster for each fracture distribution, indicating a rapid increase in the number of fractures with slope threshold > 2. The diagonal line in each plot of cumulative frequency defines a uniform or regular distribution. Visual location of fractures expressed in stick plots for each fracture set distribution, indicating the fracture position along the scanline, including the fracture density (P_{10}) and the coefficient of variation (Cv) values. The structural position is done in each diagram. See the color legend in Figure 6.

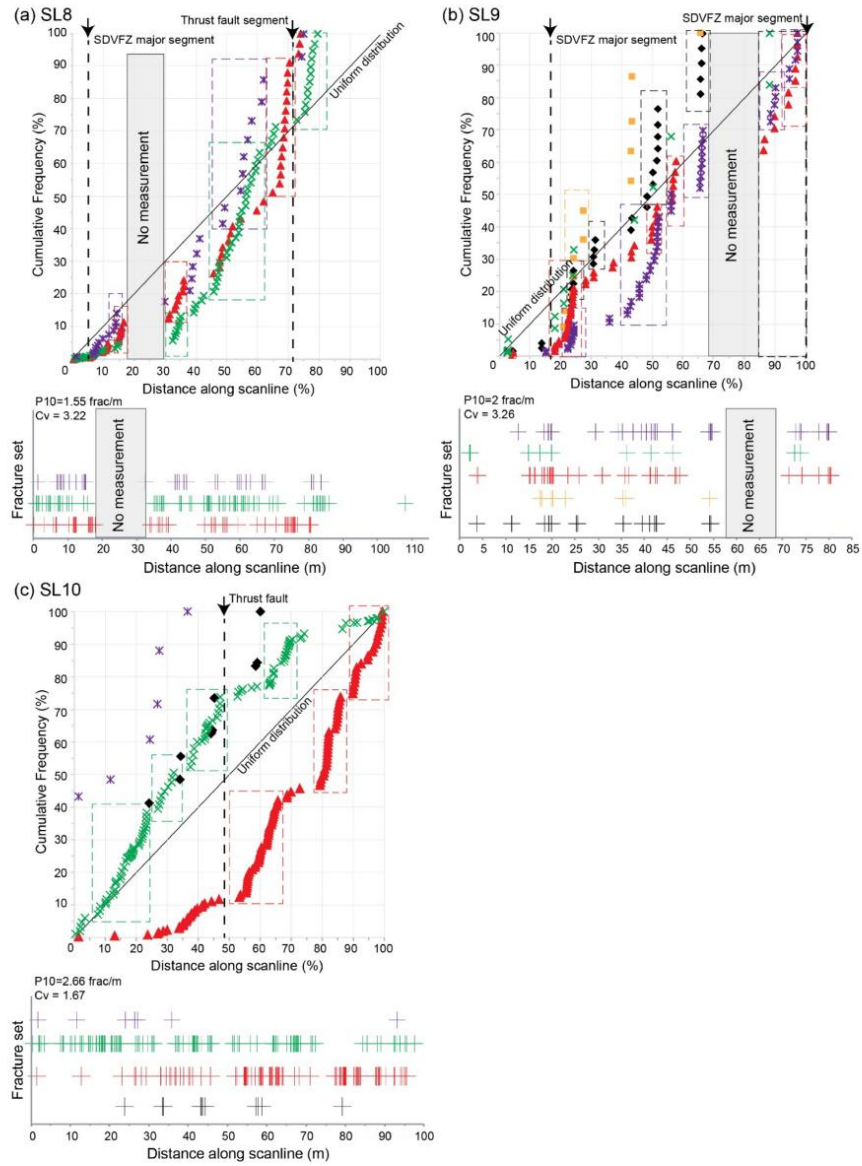


Figure 9. Cumulative frequency diagram along each scanline and following each fracture set (in colors). Plot of cumulative frequency expressed in % versus distance along scanline for: (a) SL8, (b) SL9, and (c) SL10. Dashed lines indicate a potential cluster for each fracture distribution, indicating a rapid increase in the number of fractures with slope threshold > 2. The diagonal line in each plot of cumulative frequency defines a uniform or regular distribution. Visual location of fractures expressed in stick plots for each fracture set distribution, showing the fracture position along the scanline, including the fracture density (P_{10}) and the coefficient of variation (Cv) values. See the color legend in Figure 6.

Additionally located in the highly deformed zone, SL9 is crosscut by two SDVFZ major segments. Several fracture clusters are observed as following (Figure 9b):

- N029 fracture set with one fracture cluster identified around 20 m;
- N060 fracture set with four fracture clusters characterized around 20, 42, 47, and 80 m;
- N096 fracture set with one fracture cluster identified around 15–20 m;
- N132 fracture set with five fracture clusters identified around 15–20, 35, 40–45, 55, and 80 m;
- N176 fracture set with four fracture clusters identified around 20, 25, 35–40, and 55 m.

SL10 scanline crosscuts several secondary SDVFZ segments and a thrust fault, in moderate deformation domain. A regular distribution of fractures was encountered in N004 fracture set (black color with diamond symbol legend in Figure 9c). Three fracture clusters were detected around 30–40, 55–65, and 80–90 m in N040 fracture set (data in red with triangle symbol legend, Figure 9c), while in N091 fracture set, the fracture clusters are around 10–20, 28, 40, 60–70, and 90 m (green color with cross mark symbol, Figure 9c). The E/W and NE/SW fractures orientations are more expressed in terms of fracture density which can be enhanced by the position of the major faults in this area.

4.4. Fracture Aperture Distribution

The heterogeneity of the fractures distribution and associated parameters (e.g., aperture, spacing, etc.) can be determined using the Kuiper's method [20,30,31,70]. In this study, the V' is used to better precise the degree of heterogeneity of aperture distribution along scanlines. V' values are summarized in Table 1 for only data acquired from the fieldwork. Confidence interval of 95% was used to compile V' . Then, a cumulative aperture was plotted against fracture location along the scanline (Figure 10). Application of the Kuiper test shows $V' = 0.29$ for SL1, meaning that the apertures are distributed randomly (Figure 10a). For SL2a and SL2b, V' is, respectively, 0.42 and 0.50 despite the difference in term of scanline length and orientation (Table 1, Figure 10b,c). These values indicate that the apertures are distributed randomly along each scanline. The same result of aperture distribution is shown along the SL3a and SL3b (Figure 10d,e), with V' of 0.32 and 0.57, respectively. The fracture aperture distribution is more heterogeneous in SL3b and SL2b, than in SL1, SL2a, and SL3a.

The possibility of any correlation between the fracture orientation and the aperture was tested using a plot of aperture against fracture set for each scanline (Figure 11). The mean fracture aperture in SL1 is about 2.5 mm and, therefore, lower than in fractures of SL2a and SL2b at, respectively, 2 and 1.7 mm. In SL1, the widest fracture apertures are around 10 mm, and occurred in fractures orientated N092 (Figure 11a). The most common observed fractures in the field were affected by mineralization of carbonates mostly (Figure 12). The widest fracture apertures detected in fracture orientation N092 are classified as fully sealed by carbonates (Figure 12a). In SL2a, the maximum fracture aperture is also 10 mm and belongs to the N050, N150, and N170 striking sets (Figure 11b). The widest fracture apertures are classified as fully sealed by carbonates and oxides (Figure 12a,b). In SL2b, the maximum fracture aperture does not exceed 8 mm, and occurred in fractures striking N009 and N090 (Figure 11c) and classified as fully sealed by carbonates and oxides.

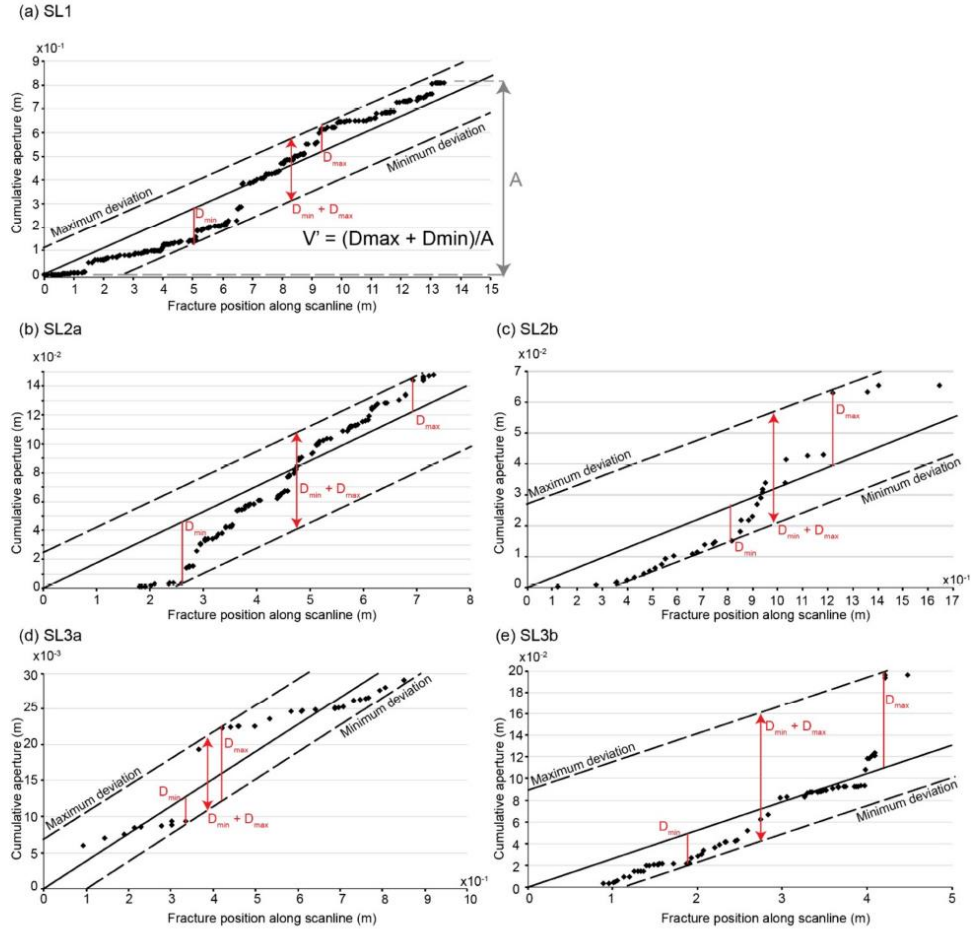


Figure 10. Plot of the sum of all apertures (cumulative fracture aperture) intersected along a scanline to show V' for (a) SL1, (b) SL2a, (c) SL2b, (d) SL3a, and (e) SL3b. The diagonal of each plot (black line) represents the uniform distribution linking the origin to the cumulative aperture to the end of the scanline (for further explanations, see [20,30]). D_{max} and D_{min} correspond to the maximum and minimum difference between the cumulative aperture and the uniform strain line, respectively. V' quantifies the heterogeneity of the strain distribution, varying from 0 (uniform distribution) to 1 (maximum possible heterogeneity).

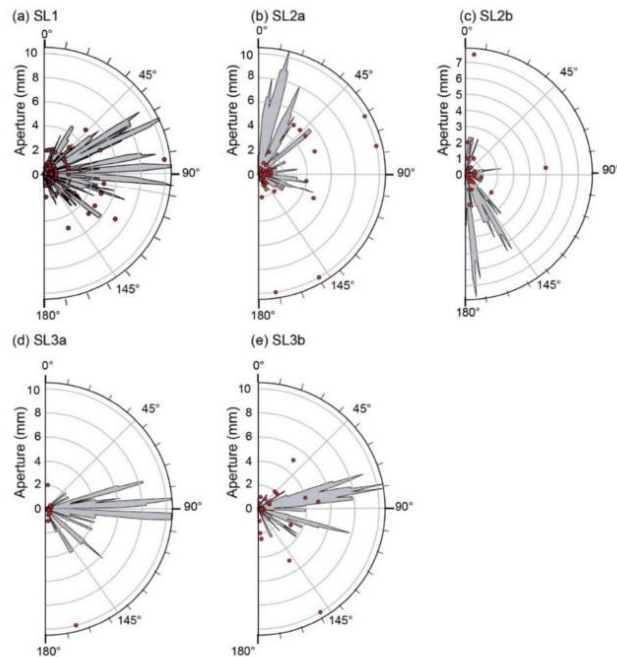


Figure 11. Half circular diagram showing the relation between fracture strike and apertures. (a) SL1, (b) SL2a, (c) SL2b, (d) SL3a, and (e) SL3b. Apertures from SL4 to SL10 are not available. Rose diagram scaled for mean aperture with classes of 5°.

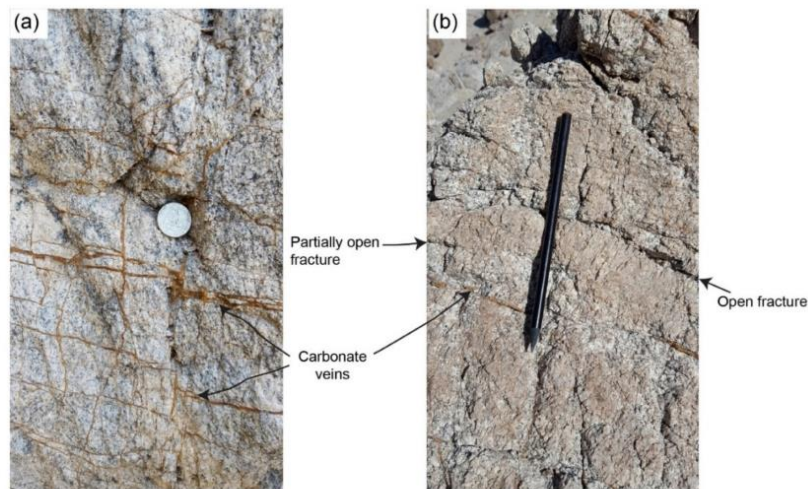


Figure 12. Illustration of the observed fractures observed in the field, mostly affected by mineralization. (a) Picture taken near OT6 illustrating veins fully sealed by carbonates. (b) Picture taken near the Canadian Wash illustrating open and partially open fractures. The carbonates are ubiquitous following SDVFZ trend (i.e., NW/SE). The fractures striking E/W have been observed with a wider aperture and were filled by barite and oxides.

The mean fracture aperture in SL3a and SL3b is about 0.9 and 2.8 mm, respectively. The maximum fracture apertures are around 10 mm. They occur in fractures striking N162 and N150 for SL3a and SL3b, respectively (Figure 11d,e). The maximum fracture apertures identified in SL3a occurred in fractures classified as partially open (Figure 12b), while in SL3b, the maximum fracture apertures occurred in fractures classified as fully sealed by carbonates and oxides. The fracture aperture distribution are more heterogenous in SL3b than in SL3a, in which apertures are generally lower than 2 mm.

As a summary, the distribution of the apertures in the central part of NH is ruled by a random behavior. Regarding the relationship between apertures and the orientations, an anisotropy was observed following E/W trend, which presents fractures with a wider aperture.

5. Discussion

5.1. Representativeness of the Fieldwork and Virtual Scanlines

The present study covers a sampled fracture network from fieldwork and virtual scanlines obtained from photogrammetry. The moderate linear density compiled from the virtual scanlines, especially in SL8, SL9, and SL10, does not exceed 3 frac/m. The highest linear density is detected in SL4 and SL7 with, respectively, 42.1 and 44 frac/m. From fieldwork scanlines, the linear densities ranged between 8.4 frac/m in SL3b and 31.8 frac/m in SL3a.

Regarding the sampling resolution, in case of virtual scanlines, the shorter fracture measurement is around the decimeter to meter and depends on the photogrammetric image resolution, while in the case of fieldwork scanlines, the measurement resolution is around the millimeter. The difference in resolution strongly impacts the fracture density and its representativeness. The low density of the fractures detected from virtual scanlines might not be fully considered as representative of the whole granitic rock. However, it is very useful in zones with difficult access.

In the case of sampling in 1D, a scanline perpendicular to the fractures will detect a maximum of sub-set of all fractures. Then, the probability that a fracture is detected within a scanline is proportional to the fracture surface area [72]. In basement rocks, fractures that span the sampling study area limits whatever its lengths and heights will reflect 3D sampling. The same case is observed in sedimentary rocks when fractures span the layers and the limits of the studied area [72].

5.2. Consistency of the Recorded Fracture Sets

The main dominant orientations recorded from the different scanlines displayed in the central part of the NH highlight the fact that NH geometry is controlled by NE/SW, E/W, and NW/SE trends (Figure 13). From fieldwork scanlines, the E/W and NW/SE fracture sets are the most consistent orientations whatever the scanline. The N/S, NNE/SSW, and NE/SW fracture sets are only recorded in the SL1 and SL2a fieldwork scanlines (Figure 13). SL2b, SL3a, and SL3b detected mostly E/W and NW/SE directions with a heterogeneous recording (Figure 13). The E/W is the most dominant trend within SL3b, while the NW/SE trend dominates within SL2b, and constitutes the second and third dominant fracture sets within SL3a and SL3b, respectively. The variability in fracture orientation may be related to the influence of the major faults. Indeed, as showed in Figure 2, the position of SL1 and SL2a close to the SDVFZ segment interfering with the thrust fault induces an additional complexity in the structural signature. As mentioned before, a clear overprinting has been recognized between primary SDVFZ and syn-kinematic dextral strike slip faults related to the transcurrent movements followed in time by compressive structures. Thrusting is postdating the activity of the SDVFZ, and it is tempting to relate the thrust structures to activity along the frontal termination of GFZ which acts with a sinistral strike slip movement.

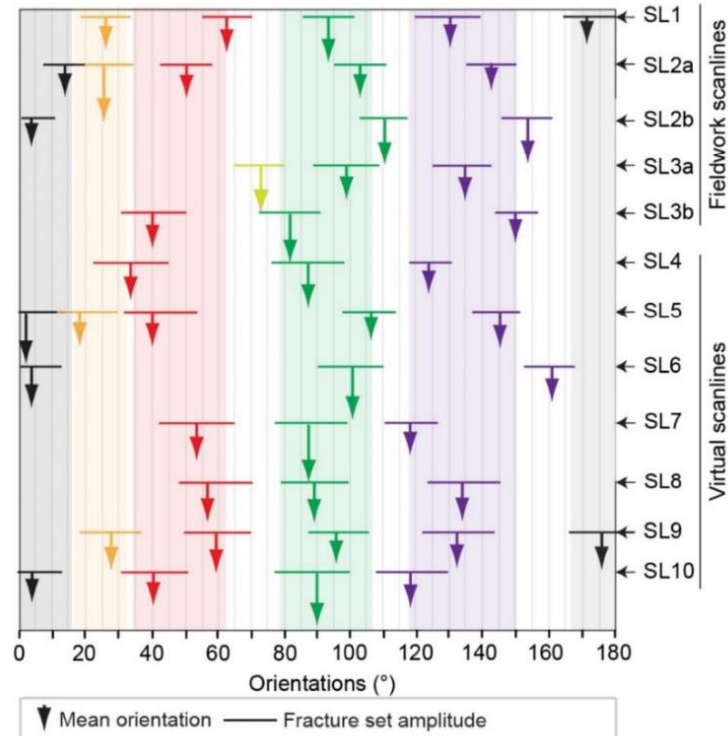


Figure 13. Plot displaying the mean orientation with arrows of each collected fracture set from NH scanlines. Each arrow was characterized by its own length, which corresponds to the fracture set abundance. The horizontal line above each arrow corresponds to the standard deviation of each fracture set, using an interval of confidence of 75% (see [68] for more explanations). Each color arrow corresponds to a fracture set. Orange arrow: NNE/SSW fracture set, red arrow: NE/SW fracture set, green arrow: E/W fracture set, yellow arrow: NNW/SSE fracture set, purple arrow: NW/SE fracture set, and black arrow: N/S fracture set.

In the southern end of the NH central area, E/W trending structures showing evidences of compression again possibly related to GFZ activity are even clearer.

Regarding the fracture orientations highlighted from the virtual scanlines, a reproducible and consistent NE/SW, E/W, and NW/SE fracture sets are encountered (Figure 13). The GFZ is confirmed as a major fault which influences the NH geometry and induces the E/W fractures which are more expressed in SL4, SL6, SL7, SL8, and SL10. According to Chabani et al. [25], who describe the spatial organization of a NH fracture network at different scales from 2D maps and previous works [47–49,73], the compression episode at the southeastern end of the NH and at the front of the Avawatz mountains plays a key role in the increase of the fracture intensity in the central domain of NH, and can explain the consistency of the E/W direction in the whole internal NH domain.

The NW/SE direction is the second most reproducible direction recorded along the internal part of NH (Figure 13), related to SDVFZ activity, which acts with a dextral movement. This direction is more expressed especially near the Canadian wash, where the deformation is important, following a second order scale as described by Chabani et al. [25].

The N/S and NE/SW fracture sets are also highlighted from the virtual scanlines but are less consistent than the E/W and NW/SE directions. These directions are heterogeneous with more than 25° (dispersion of the mean orientation) of variability in case of the NE/SW fracture set (Figure 13). These trends are highly dependent on the scale of observation and have no influence on the NH geometry [25].

As mentioned before, a recent study by Chabani et al., [25] revealed the same influence of the E/W and NW/SE fracture sets in the central part of NH. Indeed, E/W and NW/SE trends control the NH geometry within the third and fourth order scale. In addition, the major faults played a key role in the fracture density increase following different areas inside the central part of NH. The gradient of deformation shown in Klee et al. [34] and Chabani et al. [25] induced fracturing notably near OT6 and OT7, in which the strain gradient is the highest.

5.3. Clustering of Fractures in Central Part of NH

Figure 14a highlighted the C_v for the relative spaces between adjacent fractures for each studied scanline, by plotting the values against the overall fracture intensity. This correlation helps to better compare the C_v values and assess the spatial organization of the fractures. A large range of behaviors were observed. A regular spacing distribution ($C_v < 1$) was highlighted especially from SL3a, SL4, SL5, SL6, and SL7 (Figure 14a, Table 1). However, a more clustered distributions ($C_v > 1$) was observed in the SL1, SL2a, SL2b, SL8, SL9, and SL10. This large variation is probably related to the prominent influence of the thrust faults and the SDVFZ major segments close to SL8, SL9, and SL10, and only the influence of the SDVFZ major segments in the case of SL1 and SL2 profiles. However, the location in moderate deformation zone and away from major faults of SL3 scanlines highlight the absence of any organization in the fracture systems. They confirm the key role of the structural heritage (regional directions) in fracture patterns at outcrop scale. Recent study by Franklin et al. [74] highlighted and confirmed that the clustered spacing distribution is pronounced at the outcrop scale and is related to the influence of the major faulting.

From all the analyzed datasets, note that the outcrops with the greatest numbers of fractures are most usually characterized by random patterns. This observed relationship could be interpreted as the result of the increasing spatial heterogeneity of the fracture pattern with increasing strain. In that case, OT6 to OT8 highlighted that the greatest number of fractures, the fracture density, and the strong clustering within fracture sets can be related to the intensity of deformation in this area and the proximity to the SDVFZ major segments and thrust faults. Indeed, the new geological map displayed in Figure 2b highlighted a stacking of the Crystal Spring series, intruded by the Mesozoic granite. In addition, the thickness of Crystal Spring series was reduced, as they were dragged, and stretched laterally against the granite due to the SDVFZ activity, especially in OT6 to OT8 areas. This intense deformation affected the entire NH range with local evidences of extreme shearing. However, we are aware that the presence of several different lithologies with varying competences within OT6 may bias the fracture distribution and its interpretation. In addition, the structural architecture of this area is the most complex within NH range as it includes overprinting deformation phases. A future publication dedicated to these overprinting issues is in preparation.

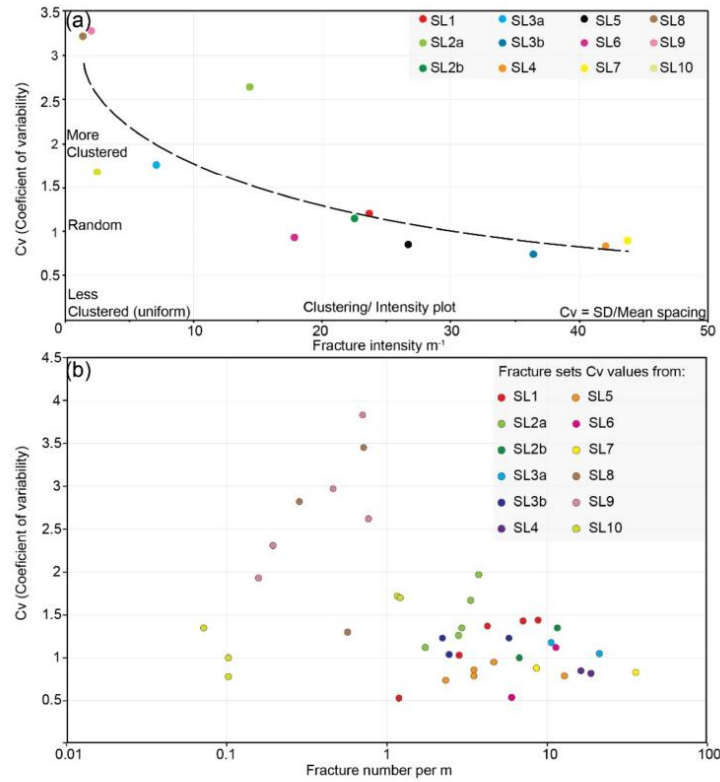


Figure 14. (a) Coefficient of variability (Cv) plotted against fracture intensity (P_{10}) of the NH studied outcrops. SD: Standard of deviation of spacing measured from each scanline; mean: Mean spacing measured from each scanline. (b) Coefficient of variability (Cv) plotted against fracture number normalized by the scanline length.

Another approach approved by Hooker et al. [30] consists of cross-examining the low number N of datasets. Cv values are commonly indistinguishable from random for low-N sets. Then, Cv increases with increasing fracture abundance (Figure 14b). This observation reflects an increase in fracture clustering with fracture abundance only in case of fracture sets detected from virtual scanlines (SL8, SL9, and SL10, Figure 14b). In case of fractures detected from fieldwork scanlines, the trend is more unclear since the Cv evolution is still comprised between 0.5 and 1.5, whatever the fracture abundance (Figure 14b). Once again, the proximity to major faults in case of SL8, SL9, and SL10 may play a key role in the fracture patterns growth. For SL1 to SL7, the fracture organization may be perturbed by the abundance of the E/W fracture orientation, which can increase drastically the fracture abundance following E/W fracture set trend. This may be related to the scanline orientation which cannot intersect the rest of the fracture sets. From SL1 to SL7, fracture set trending E/W is more expressed than the rest of the sets except for SL2a, SL2b, and SL5 (Table 2). Then, the complexity in fracture orientation recording has a strong impact on the spacing variability and fracture patterns evolution, evolving a random state. In case of SL8, SL9, and SL10, the fractures are distributed homogeneously following the orientations outside the fracture clusters (see Table 2 for proportion).

Regarding the clustering, relative spacing analysis shows that fracture clusters have been detected in the whole profiles, except for SL3 profiles, in which very few clusters were detected (Figure 8). Clustering depends on the fracture orientation. Two major factors are responsible for this clustering:

- Crosscutting or location close to major faults segments: This observation is supported essentially by OT1, OT6, OT7 and OT8 fracture distribution, in which SDVFZ and a thrust fault proximity enhance the considerably clustering and fracture density of each fracture set.
- The deformation gradient: Based on fieldwork observations, the most deformed zone is located close to OT6 and OT7 and strongly impacts the fracture distribution. Indeed, the fracture density is much higher in these areas, and the fracture patterns is arranged into clusters following E/W and NW/SE directions.

The regular spacing distribution exist whatever the analyzed direction. This observation is more highlighted within SL4, SL5, and SL7 profiles (Figure 8a,b,d). In these cases, clustering depends on the orientation. Few fracture clusters were detected within the E/W direction (data in green color with cross mark symbol, Figure 8).

However, the lower fracture density compiled from SL8, SL9, and SL10, due to the sampling bias relative to the virtual scanlines, nuances the real influence of this clustering on the anisotropy of the possible flow.

To summarize, clustering is mostly observed for scanlines orthogonal to the observed fractures close to the major faults, such as SDVFZ and thrust faults, except for SL3 profiles which can be biased due to their small length and their location away from major faults (Figure 14a). In contrast, scanlines sub-parallel to the main trend of the major faults have a rather random distribution pattern (Figure 14a).

5.4. Conceptual Model of NH Paleo Geothermal Analogue

In fractured reservoirs, the main challenge is to understand the fracture variability from only 1D data obtained from wells. The 3D fracture networks commonly show a strong spatial heterogeneity, related in several cases to geological features, such as faults, folds, stress fields, or lithological trends, which impact large scale fracture networks [75]. The central part NH studied here is an appropriate case study to test these assumptions, such as size distribution (e.g., length, spacing, aperture etc.), fracture trends record, and the relationship between them. In the present study, the 1D measurements which can be assimilated to synthetic well data revealed the same density results as those obtained by 2D measurements in the central part of NH. Note that, the 2D study has been published in previous work [25] for the entire NH range. This previous study concluded that the center part of NH is ruled by fracture networks dominated by E/W (GFZ trend) and NW/SE (SDVFZ trend) directions. This result is also observed in this present study based on 1D measurements. Indeed, the main dominant directions (e.g., E/W and NW/SE) are also recorded at outcrop scale, meaning that independently of well measurement, whatever any sampling bias and statistic uncertainties resulting from the data measurements, the well (in case of a reservoir) or the scanline (in case of an analogue) is representative of the heterogeneity at outcrop scale and reservoir scale.

The main directions that follow the regional trend and then control the NH geometry are commonly characterized by clustered fractures. Close to the major faults, the fracture network arrangement is more clustered, especially in the high strain zone near OT6, OT7, and OT8. Then, the fracture system is marked by a strong clustering within its organization following most of the recorded fracture sets, except for NW/SE and N/S fracture sets of OT8. This clustering impacts the reservoir behavior in that fluid circulation is influenced by the role of the major faults. Outside these major faults and their associated fracture clusters, a secondary fracture network was characterized by a random distribution, which plays a key role in the fracture connectivity leading to the fluid supply toward the fractured zone.

Evidences of fluid circulations have been identified by Klee et al. (2021a) [37] and Klee et al., 2021b [8] through (1) the alteration processes that occurred in the whole granite

body (propylitic and argillic), and (2) the fracture infills. Among the different natures of fractures infills that have been identified in the granite, carbonates are omnipresent [8]. They mainly filled the fracture following the SDVFZ direction (i.e., NW/SE), which is the main fracture orientation in the area. However, as presented above, E/W-oriented fractures have also been observed with a wider aperture. These fractures, related to the activity of the GFZ [25], are often filled with barite and oxides, especially at the southern rear part of the range, close to the Avawatz Mountains. This difference of infills according to two different fracture sets shows two different episodes of fluid circulation through the granite body.

Furthermore, fluid–rock interactions investigations through the NH area, by collecting samples according to profiles approaching major fault segments, have been conducted in recent previous works [8,37]. These major segments consist of the SDVFZ segments, the same ones considered in this present study, since we considered the same faults interpretation in both works based on fieldwork mapping. Porosity measurements were realized on five samples away from fracture zones and on three samples in the vicinity of fracture zones. It aimed at evaluating a possible correlation with the amount of alteration. The authors showed that the porosity increases with proximity to fracture zones. It is known that alteration can create some porosity by the dissolution of primary minerals like plagioclase and biotite. However, these studies have shown that porosity does not always correlates with the amount of alteration. Indeed, microfracturing also creates porosity.

The argillic alteration related to hydrothermal fluid circulations through the fracture network affects dominantly the NH granite [8,37]. During this fluid–rock interaction process, plagioclase and biotite are replaced by secondary minerals, such as illite and kaolinite, which crystallize between 120 and 200 °C [8]. Such temperatures are also confirmed by the Kübler Index measured from the illite crystallinity. To know more precisely the fluid temperature that has circulated, fluid inclusions measurements are required, which will be published in the future work.

As introduced before, NH is considered as an exhumed analogue for Soultz-sous-Forêts and Rittershoffen geothermal reservoirs. Both sites display a similar alteration and hydrothermal activity [8,76]. For example, the reservoir volume in Soultz-sous-Forêts is around 12 km³ [77], and is crosscut by regional faults following the second and third orders scale according to Morrelato et al. [78] classification. The order of faults magnitude highlighted in the central part of NH is the same as that detected in the subsurface reservoirs at Soultz-sous-Forêts and Rittershoffen. Indeed, the second and third order scales control the geometry of the internal part of NH [25]. Then, the reservoir volume in case of NH paleo geothermal analogue can be equivalent to that at those of Soultz-sous-Forêts reservoir. Furthermore, during the Rittershoffen reservoir stimulation, a repercussion has been recorded in the Soultz-sous-Forêts reservoir and confirmed the kilometer faults orders (personal communication).

To further characterize a geothermal reservoir, it is important to determine the geothermal gradient and temperature at the targeted exploitation depth. However, the geothermal gradient in the NH context is difficult to highlight. Some additional data likely provided by fluid inclusion micro-thermometry and stable isotope analyses are needed to determine this gradient. In addition, it would be important to take in consideration the present-day stress field according to their orientation, the fractures might be open or closed and thus favorable or not to fluid circulation.

6. Conclusions

The present work is part of MEET project and focused on the NH range, considered as a paleo geothermal reservoir analogue, which offers a general overview of the structural organization of the fracture networks at outcrop and wider scales. This study aims at understanding the fracture spacing variability and the distribution of fracture patterns in granitic rocks, and the impact of the proximity of major faults on fracture distribution and fluid circulation. In the NH case study, the fracture patterns are controlled by the

structural heritage. This heritage results from the activity of the SDFVZ and GFZ faults, which strongly control the geometry of the entire ranges. The evidence of fluid circulations has been highlighted in previous studies and consist in the granite hydrothermal alteration (propylitic and argillic), and the fracture infills. The carbonate infill is associated to the fractures striking NW/SE (SDVFZ direction), while the barite infill is related to the fractures striking E/W (GFZ direction). Hence, at least, two episodes of fluid circulation have occurred within NH ranges.

From fieldwork scanlines, the main dominant trends within the central part of NH are the NW/SE and the E/W directions, well expressed whatever the scanline. The variability between fracture orientations was probably related to the influence of the major faults. From virtual scanlines, NE/SW, E/W, and NW/SE fracture sets were the most consistent orientations. However, some sampling bias previously discussed, such as the absence of dip in case of virtual scanlines and image resolution, which can impact the fracture detection should be reconsidered in the methodological development of the future work.

The spatial organization of the NH fracture network reveals that fracture clustering increases with fracture abundance only in the case of fracture sets detected from virtual scanlines (SL8, SL9, and SL10) due to the proximity of major faults. However, from fieldwork scanlines, the correlation seems not so clear. Furthermore, clustering depends on the strike of the fractures:

- Three configurations (uniform, random and clustered distribution) were shown for SL1 spacing fractures: Regular distribution within N062, uniform distribution within N026, and clustered distribution within N092, N130, and N171 fracture sets;
- For SL3a and SL6, two configurations were identified: Uniform distribution within respectively N077 and N100 trends, clustered distribution within N098 and N135 for SL3a, and N004 and N161 fracture sets for SL6;
- SL2b, SL4, SL5, and SL7 profiles showed only one configuration, which consists in uniform distribution, not dependent on the direction;
- SL2a and SL3b, SL8, SL9, and SL10 showed a high C_v whatever the direction, which indicates a stronger clustering in the fracture system.

The most reproducible trends in the NH range are characterized by a clustered spacing distribution. The most clustered systems were identified close to or crosscutting the major faults which control the NH geometry. These faults are SDVFZ major segments and thrust faults. In addition, the deformation gradient impacts strongly the fracture patterns. The present paper highlighted that in a high deformation context, the spatial distribution of fracture become clustered, while in moderate deformation context, the fracture patterns are distributed randomly or regularly. These distributions considerably impact the fluid flow within the reservoir. The forthcoming reservoir modeling should consider the deformation gradient and the evolution of fracture patterns toward to major fault zones, as well as present-day stress field.

Author Contributions: Conceptualization, A.C., G.T., J.K. and B.A.L.; methodology, A.C.; software, A.C.; validation, G.T., B.A.L. and J.K.; formal analysis, A.C.; investigation, A.C., G.T., J.K., B.A.L.; resources, A.C.; data curation, A.C.; writing—original draft preparation, A.C.; writing—review and editing, G.T., B.A.L. and H2020 MEET consortium; visualization, G.T., B.A.L. and J.K.; supervision, G.T.; project administration, G.T.; funding acquisition, G.T. and H2020 MEET consortium. All authors have read and agreed to the published version of the manuscript.

Funding: This project has received funding from the European Union’s Horizon 2020 research and innovation program under grant agreement No 792037 (MEET project).

Institutional Review Board Statement: Not applicable.

Informed Consent Statement: Not applicable.

Data Availability Statement: Not applicable.

Acknowledgments: This work is part of postdoctoral contribution, prepared at Institut Polytechnique UniLaSalle Beauvais, which was funded by European Union's Horizon 2020 research (H2020 MEET project, grant agreement No 792037). We are grateful to Terry Pavlis for fruitful discussions. We also wish to thank the H2020 MEET consortium for helpful comments and manuscript validation.

Conflicts of Interest: The authors declare no conflict of interest.

References

- Torabi, A.; Ellingsen, T.S.S.; Johannessen, M.U.; Alaei, B.; Rotevatn, A.; Chiarella, D. Fault Zone Architecture and Its Scaling Laws: Where Does the Damage Zone Start and Stop? *Geol. Soc. Lond. Spec. Publ.* **2020**, *496*, 99–124. [CrossRef]
- Sanderson, D.J.; Nixon, C.W. The Use of Topology in Fracture Network Characterization. *J. Struct. Geol.* **2015**, *72*, 55–66. [CrossRef]
- Dezayes, C.; Lerouge, C.; Innocent, C.; Lach, P. Structural Control on Fluid Circulation in a Graben System: Constraints from the Saint Pierre Bois Quarry (Vosges, France). *J. Struct. Geol.* **2021**, *146*, 104323. [CrossRef]
- Barton, C.A.; Zoback, M.D. Self-Similar Distribution and Properties of Macroscopic Fractures at Depth in Crystalline Rock in the Cajon Pass Scientific Drill Hole. *J. Geophys. Res. Solid Earth* **1992**, *97*, 5181–5200. [CrossRef]
- Caine, J.S.; Evans, J.P.; Forster, C.B. Fault Zone Architecture and Permeability Structure. *Geology* **1996**, *24*, 1025–1028. [CrossRef]
- Callahan, O.A.; Eichhubl, P.; Olson, J.E.; Davatzes, N.C. Fracture Mechanical Properties of Damaged and Hydrothermally Altered Rocks, Dixie Valley–Stillwater Fault Zone, Nevada, USA. *J. Geophys. Res. Solid Earth* **2019**, *124*, 4069–4090. [CrossRef]
- Laubach, S.E.; Lamarche, J.; Gauthier, B.D.M.; Dunne, W.M.; Sanderson, D.J. Spatial Arrangement of Faults and Opening-Mode Fractures. *J. Struct. Geol.* **2018**, *108*, 2–15. [CrossRef]
- Klee, J.; Chabani, A.; Ledésert, B.A.; Potel, S.; Hébert, R.L.; Trullenque, G. Fluid-Rock Interactions in a Paleo-Geothermal Reservoir (Noble Hills Granite, California, USA). Part 2: The Influence of Fracturing on Granite Alteration Processes and Fluid Circulation at Low to Moderate Regional Strain. *Geosciences* **2021**, *11*, 433. [CrossRef]
- Bour, O.; Davy, P. Connectivity of Random Fault Networks Following a Power Law Fault Length Distribution. *Water Resour. Res.* **1997**, *33*, 1567–1583. [CrossRef]
- Genter, A.; Traineau, H.; Ledésert, B.; Bourguin, B.; Gentier, S. *Over 10 Years of Geological Investigations within the HDR Soultz Project, France*; International Geothermal Association: Reykjavik, Iceland, 2000; pp. 3707–3712.
- Renshaw, C.E. Influence of Subcritical Fracture Growth on the Connectivity of Fracture Networks. *Water Resour. Res.* **1996**, *32*, 1519–1530. [CrossRef]
- Laubach, S.E.; Lander, R.H.; Criscenti, L.J.; Anovitz, L.M.; Urai, J.L.; Pollyea, R.M.; Hooker, J.N.; Narr, W.; Evans, M.A.; Kerisit, S.N.; et al. The Role of Chemistry in Fracture Pattern Development and Opportunities to Advance Interpretations of Geological Materials. *Rev. Geophys.* **2019**, *57*, 1065–1111. [CrossRef]
- Lamarche, J.; Chabani, A.; Gauthier, B.D. Dimensional Threshold for Fracture Linkage and Hooking. *J. Struct. Geol.* **2018**, *108*, 171–179. [CrossRef]
- Bour, O.; Davy, P. On the Connectivity of Three-dimensional Fault Networks. *Water Resour. Res.* **1998**, *34*, 2611–2622. [CrossRef]
- Darcel, C.; Bour, O.; Davy, P.; de Dreuzy, J.R. Connectivity Properties of Two-Dimensional Fracture Networks with Stochastic Fractal Correlation: Connectivity of 2D fractal fracture networks. *Water Resour. Res.* **2003**, *39*. [CrossRef]
- Odling, N.E. Scaling and Connectivity of Joint Systems in Sandstones from Western Norway. *J. Struct. Geol.* **1997**, *19*, 1257–1271. [CrossRef]
- Chabani, A. Analyse Méthodologique et Caractérisation Multi-Échelle Des Systèmes de Fractures à l'interface Socle/Couverture Sédimentaire—Application à La Géothermie (Bassin de Valence, SE France). These de doctorat, Paris Sciences et Lettres (ComUE). 2019. Available online: <http://www.theses.fr/2019PSLEM046> (accessed on 21 September 2021).
- Narr, W. Estimating Average Fracture Spacing in Subsurface Rock. *AAPG Bull.* **1996**, *80*, 1565–1585. [CrossRef]
- Haffen, S.; Géraud, Y.; Diraison, M.; Dezayes, C. Determination of Fluid-Flow Zones in a Geothermal Sandstone Reservoir Using Thermal Conductivity and Temperature Logs. *Geothermics* **2013**, *46*, 32–41. [CrossRef]
- Sanderson, D.J.; Peacock, D.C. Line Sampling of Fracture Swarms and Corridors. *J. Struct. Geol.* **2019**, *122*, 27–37. [CrossRef]
- Fossen, H.; Cavalcanti, G.C.G. Shear Zones—A Review. *Earth Sci. Rev.* **2017**, *171*, 434–455. [CrossRef]
- Kim, Y.-S.; Peacock, D.C.P.; Sanderson, D.J. Mesoscale Strike-Slip Faults and Damage Zones at Marsalforn, Gozo Island, Malta. *J. Struct. Geol.* **2003**, *25*, 793–812. [CrossRef]
- Ostermeijer, G.A.; Mitchell, T.M.; Aben, F.M.; Dorsey, M.T.; Browning, J.; Rockwell, T.K.; Fletcher, J.M.; Ostermeijer, F. Damage Zone Heterogeneity on Seismogenic Faults in Crystalline Rock; a Field Study of the Borrego Fault, Baja California. *J. Struct. Geol.* **2020**, *137*, 104016. [CrossRef]
- Marrett, R.; Gale, J.F.W.; Gómez, L.A.; Laubach, S.E. Correlation Analysis of Fracture Arrangement in Space. *J. Struct. Geol.* **2018**, *108*, 16–33. [CrossRef]
- Chabani, A.; Trullenque, G.; Ledésert, B.A.; Klee, J. Multiscale Characterization of Fracture Patterns: A Case Study of the Noble Hills Range (Death Valley, CA, USA). Application to Geothermal Reservoirs. *Geosciences* **2021**, *11*, 280. [CrossRef]
- Gillespie, P.A.; Howard, C.B.; Walsh, J.J.; Watterson, J. Measurement and Characterisation of Spatial Distributions of Fractures. *Tectonophysics* **1993**, *226*, 113–141. [CrossRef]
- Wang, Q.; Laubach, S.E.; Gale, J.F.W.; Ramos, M.J. Quantified Fracture (Joint) Clustering in Archean Basement, Wyoming: Application of the Normalized Correlation Count Method. *Pet. Geosci.* **2019**, *25*, 415–428. [CrossRef]

28. Pavičić, I.; Dragičević, I.; Vlahović, T.; Grgasović, T. Fractal Analysis of Fracture Systems in Upper Triassic Dolomites in Žumberak Mountain, Croatia. *Rud. Geološko-Naft. Zb.* **2017**, *32*, 1–13. Available online: <https://hrcak.srce.hr/ojs/index.php/rgn/article/view/4894/pdf> (accessed on 21 September 2021). [[CrossRef](#)]
29. Shiri, Y.; Hassani, H. Two-Component Fluid Front Tracking in Fault Zone and Discontinuity with Permeability Heterogeneity. *Rud. Geol. Naft. Zb.* **2021**, *36*, 19–30. [[CrossRef](#)]
30. Hooker, J.N.; Laubach, S.E.; Marrett, R. Microfracture Spacing Distributions and the Evolution of Fracture Patterns in Sandstones. *J. Struct. Geol.* **2018**, *108*, 66–79. [[CrossRef](#)]
31. Putz-Perrier, M.W.; Sanderson, D.J. Spatial Distribution of Brittle Strain in Layered Sequences. *J. Struct. Geol.* **2008**, *30*, 50–64. [[CrossRef](#)]
32. Bourbiaux, B.; Basquet, R.; Daniel, J.M.; Hu, L.Y.; Jenni, S.; Lange, G.; Rasolofosaon, P. Fractured Reservoirs Modelling: A Review of the Challenges and Some Recent Solutions. *First Break* **2005**, *23*, 33–40. [[CrossRef](#)]
33. Trullenque, G.; Genter, A.; Leiss, B.; Wagner, B.; Bouchet, R.; Léoutre, E.; Malnar, B.; Bär, K.; Rajšl, I. Upscaling of EGS in Different Geological Conditions: A European Perspective. In Proceedings of the 43rd Workshop on Geothermal Reservoir Engineering, Stanford, CA, USA, 12–14 February 2018; p. SGP-TR-213.
34. Klee, J.; Trullenque, G.; Ledésert, B.; Potel, S.; Hébert, R.; Chabani, A.; Genter, A. Petrographic Analyses of Fractured Granites Used as An Analogue of the Soultz-Sous-Forêts Geothermal Reservoir: Noble Hills, CA, USA. In Proceedings of the Extended Abstract, Reykjavik, Island, 26 May 2021.
35. Chabani, A.; Trullenque, G.; Rishi, P.; Pomart, A.; Attali, R.; Sass, I. Modelling of Fractured Granitic Geothermal Reservoirs: Use of Deterministic and Stochastic Methods in Discrete Fracture Networks and a Coupled Processes Modeling Framework. In Proceedings of the Extended Abstract, Reykjavik, Island, 2 May 2021.
36. Pavlis, T.L.; Trullenque, G. Evidence for 40–41 Km of Dextral Slip on the Southern Death Valley Fault: Implications for the Eastern California Shear Zone and Extensional Tectonics. *Geology* **2021**, *49*, 767–772. [[CrossRef](#)]
37. Klee, J.; Potel, S.; Ledésert, B.A.; Hébert, R.L.; Chabani, A.; Barrier, P.; Trullenque, G. Fluid-Rock Interactions in a Paleo-Geothermal Reservoir (Noble Hills Granite, California, USA). Part I: Granite Pervasive Alteration Processes Away from Fracture Zones. *Geosciences* **2021**, *11*, 325. [[CrossRef](#)]
38. Brady III, R.H. Neogene Stratigraphy of the Avawatz Mountains between the Garlock and Death Valley Fault Zones, Southern Death Valley, California: Implications as to Late Cenozoic Tectonism. *Sediment. Geol.* **1984**, *38*, 127–157. [[CrossRef](#)]
39. Pavlis, T.L.; Rutkofske, J.; Guerrero, F.; Serpa, L.F. Structural Overprinting of Mesozoic Thrust Systems in Eastern California and Its Importance to Reconstruction of Neogene Extension in the Southern Basin and Range. *Geosphere* **2014**, *10*, 732–756. [[CrossRef](#)]
40. Miller, M.; Pavlis, T. The Black Mountains Turtlebacks: Rosetta Stones of Death Valley Tectonics. *Earth-Sci. Rev.* **2005**, *73*, 115–138. [[CrossRef](#)]
41. Snow, J.K. Cenozoic Tectonism in the Central Basin and Range; Magnitude, Rate, and Distribution of Upper Crustal Strain. *Am. J. Sci.* **2000**, *300*, 659–719. [[CrossRef](#)]
42. Calzia, J.; Rämö, O. Late Cenozoic Crustal Extension and Magmatism, Southern Death Valley Region, California. *GSA Field Guides* **2000**, *2*, 135–164. [[CrossRef](#)]
43. Calzia, J.; Ramo, O. Miocene Rapakivi Granites in the Southern Death Valley Region, California, USA. *Earth-Sci. Rev.* **2005**, *73*, 221–243. [[CrossRef](#)]
44. Brady, R. Cenozoic Geology of the Northern Avawatz Mountains in Relation to the Intersection of the Garlock and Death Valley Fault Zones, San Bernardino County, California. Ph.D. Thesis, University of California, Davis, CA, USA, 1987.
45. Norton, I. Two-Stage Formation of Death Valley. *Geosphere* **2011**, *7*, 171–182. [[CrossRef](#)]
46. Burchfiel, B.C.; Stewart, J.H. “Pull-Apart” Origin of the Central Segment of Death Valley, California. *Geol. Soc. Am. Bull.* **1966**, *77*, 439–442. [[CrossRef](#)]
47. Niles, J.H. Post-Middle Pliocene Tectonic Development of the Noble Hills, Southern Death Valley, California. Ph.D. Thesis, San Francisco State University, San Francisco, CA, USA, 2016.
48. Reinert, E. Low Temperature Thermochronometry of the Avawatz Mountains, California: Implications for the Inception of the Eastern California Shear Zone. Ph.D. Thesis, University of Washington, Seattle, WA, USA, 2004. Available online: https://www.ess.washington.edu/content/people/student_publications_files/reinert--erik/Reinert_2004.pdf (accessed on 21 September 2021).
49. Spencer, J.E. Late Cenozoic Extensional and Compressional Tectonism in the Southern and Western Avawatz Mountains, Southeastern California. In *Basin and Range Extensional Tectonics Near the Latitude of Las Vegas, Nevada: Geological Society of America Memoir*; Geological Society of America: Boulder, CO, USA, 1990; Volume 176, pp. 317–333. [[CrossRef](#)]
50. Mahon, R.C.; Dehler, C.M.; Link, P.K.; Karlstrom, K.E.; Gehrels, G.E. Geochronologic and Stratigraphic Constraints on the Mesoproterozoic and Neoproterozoic Pahrup Group, Death Valley, California: A Record of the Assembly, Stability, and Breakup of Rodinia. *Bulletin* **2014**, *126*, 652–664. [[CrossRef](#)]
51. Pickering, G.; Bull, J.M.; Sanderson, D.J. Sampling Power-Law Distributions. *Tectonophysics* **1995**, *248*, 1–20. [[CrossRef](#)]
52. Odling, N.E.; Gillespie, P.; Bourguin, B.; Castaing, C.; Chiles, J.P.; Christensen, N.P.; Fillion, E.; Genter, A.; Olsen, C.; Thrane, L.; et al. Variations in Fracture System Geometry and Their Implications for Fluid Flow in Fractured Hydrocarbon Reservoirs. *Pet. Geosci.* **1999**, *5*, 373–384. [[CrossRef](#)]

53. Bonnet, E.; Bour, O.; Odling, N.E.; Davy, P.; Main, I.; Cowie, P.; Berkowitz, B. Scaling of Fracture Systems in Geological Media. *Rev. Geophys.* **2001**, *39*, 347–383. [CrossRef]
54. Priest, S.D. *Discontinuity Analysis for Rock Engineering*; Springer Science & Business Media: Berlin/Heidelberg, Germany, 1993.
55. Ledésert, B.A.; Hébert, R.L. How Can Deep Geothermal Projects Provide Information on the Temperature Distribution in the Upper Rhine Graben? The Example of the Soultz-Sous-Forêts-Enhanced Geothermal System. *Geosciences* **2020**, *10*, 459. [CrossRef]
56. Priest, S.D.; Hudson, J.A. *Estimation of Discontinuity Spacing and Trace Length Using Scanline Surveys*; Elsevier: Amsterdam, The Netherlands, 1981; Volume 18, pp. 183–197. [CrossRef]
57. Hardebol, N.J.; Maier, C.; Nick, H.; Geiger, S.; Bertotti, G.; Boro, H. Multiscale Fracture Network Characterization and Impact on Flow: A Case Study on the Latemar Carbonate Platform. *J. Geophys. Res. Solid Earth* **2015**, *120*, 8197–8222. [CrossRef]
58. Bisdom, K.; Gauthier, B.D.M.; Bertotti, G.; Hardebol, N.J. Calibrating Discrete Fracture-Network Models with a Carbonate Three-dimensional Outcrop Fracture Network: Implications for Naturally Fractured Reservoir Modeling. *AAPG Bull.* **2014**, *98*, 13511376. [CrossRef]
59. Bertrand, L.; Géraud, Y.; Le Garzic, E.; Place, J.; Diraison, M.; Walter, B.; Haffen, S. A Multiscale Analysis of a Fracture Pattern in Granite: A Case Study of the Tamariu Granite, Catalunya, Spain. *J. Struct. Geol.* **2015**, *78*, 52–66. [CrossRef]
60. Terzaghi, R.D. Sources of Error in Joint Surveys. In *Geotechnique*; Road Research Laboratory: Crowthorne, UK, 1965; Volume 15, pp. 287–304. Available online: <http://worldcat.org/issn/00168505> (accessed on 21 September 2021).
61. Delvaux, D.; Sperner, B. Stress Tensor Inversion from Fault Kinematic Indicators and Focal Mechanism Data: The TENSOR Program. *New Insights Struct. Interpret. Model.* **2003**, *212*, 75–100. [CrossRef]
62. Cardozo, N.; Allmendinger, R.W. Spherical projections with OSXStereonet. *Comput. Geosci.* **2013**, *51*, 193–205. [CrossRef]
63. Hardebol, N.J.; Bertotti, G. DigiFract: A Software and Data Model Implementation for Flexible Acquisition and Processing of Fracture Data from Outcrops. *Comput. Geosci.* **2013**, *54*, 326–336. [CrossRef]
64. Fisher, R. Dispersion on a Sphere. *Proc. R. Soc. Lond. Ser. A Math. Phys. Sci.* **1953**, *217*, 295–305. Available online: http://palaeo.spb.ru/pmlibrary/pmpapers/fisher_1953.pdf (accessed on 21 September 2021). [CrossRef]
65. Kent, J.T. The Fisher-Bingham Distribution on the Sphere. *J. R. Stat. Soc. Ser. B* **1982**, *44*, 71–80. Available online: <http://www.jstor.org/stable/2984712> (accessed on 21 September 2021). [CrossRef]
66. Von Mises, R. Über Die “Ganzzahligkeit” Der Atomgewicht Und Verwandte Fragen. *Physikal. Z* **1918**, *19*, 490–500.
67. Lark, R.M.; Clifford, D.; Waters, C.N. Modelling Complex Geological Circular Data with the Projected Normal Distribution and Mixtures of von Mises Distributions. *Solid Earth* **2014**, *5*, 631–639. [CrossRef]
68. Chabani, A.; Mehl, C.; Cojan, I.; Alais, R.; Bruel, D. Semi-Automated Component Identification of a Complex Fracture Network Using a Mixture of von Mises Distributions: Application to the Ardeche Margin (South-East France). *Comput. Geosci.* **2020**, *137*, 104435. [CrossRef]
69. Gillespie, D.T. Approximate Accelerated Stochastic Simulation of Chemically Reacting Systems. *J. Chem. Phys.* **2001**, *115*, 1716–1733. [CrossRef]
70. Kuiper, N.H. Tests Concerning Random Points on a Circle. In *Proceedings of the Koninklijke, Nederlandse Akademie van Wetenschappen*: Amsterdam, The Netherlands, 1960; Volume 63, pp. 38–47. [CrossRef]
71. Sanderson, D.J.; Roberts, S.; Gumiel, P.; Greenfield, C. Quantitative Analysis of Tin-and Tungsten-Bearing Sheeted Vein Systems. *Econ. Geol.* **2008**, *103*, 1043–1056. [CrossRef]
72. Ortega, O.J.; Marrett, R.A.; Laubach, S.E. A Scale-Independent Approach to Fracture Intensity and Average Spacing Measurement. *AAPG Bull.* **2006**, *90*, 193–208. [CrossRef]
73. Chinn, L.D. Low-Temperature Thermochronometry of the Avawatz Mountains; Implications for the Eastern Terminus and Inception of the Garlock Fault Zone. 2013. Available online: https://www.ess.washington.edu/content/people/student_publications_files/chinn--logan/chinn--logan_ms_2013.pdf (accessed on 21 September 2021).
74. Franklin, B. Characterising Fracture Systems within Upfaulted Basement Highs in the Hebridean Islands: An Onshore Analogue for the Clair Field. Ph.D. Thesis, Durham University, Durham, UK, 2013. Available online: <http://etheses.dur.ac.uk/7765/> (accessed on 21 September 2021).
75. Bourbiaux, B.; Basquet, R.; Cacas, M.-C.; Daniel, J.-M.; Sarda, S. An Integrated Workflow to Account for Multi-Scale Fractures in Reservoir Simulation Models: Implementation and Benefits. In Proceedings of the Abu Dhabi International Petroleum Exhibition and Conference, Abu Dhabi, United Arab Emirates, 13–16 October 2002.
76. Ledésert, B.; Hébert, R.; Genter, A.; Bartier, D.; Clauer, N.; Grall, C. Fractures, Hydrothermal Alterations and Permeability in the Soultz Enhanced Geothermal System. *Comptes Rendus Geosci.* **2010**, *342*, 607–615. [CrossRef]
77. Dorbath, L.; Cuenot, N.; Genter, A.; Frogneux, M. Seismic Response of the Fractured and Faulted Granite of Soultz-Sous-Forêts (France) to 5 Km Deep Massive Water Injections. *Geophys. J. Int.* **2009**, *177*, 653–675. [CrossRef]
78. Morellato, C.; Redini, F.; Doglioni, C. On the Number and Spacing of Faults. *Terra Nova* **2003**, *15*, 315–321. [CrossRef]

Klee (2021) presented and discussed the mineralogical and petrophysical similarities between the NH analogue and the geothermal reservoirs exploited at present in the URG. From a petrographic point of view the granitic rocks found in both localities have a similar monzogranite composition. At both places, evidences of alteration are present and consist in an early pervasive stage (so-called propylitic alteration) followed by an alteration stage which occurred along fractures having channeled fluid flow. This second stage of alteration is called argillic alteration (Klee et al. 2021b and references therein). This argillic alteration produces a secondary mineral infill in both the SSF (Genter, 1989; Glaas et al., 2021; Klee et al., 2021b; Komninou and Yardley, 1997) and NH granites (Klee et al., 2021a). In both NH and SSF the argillic alteration is later than the propylitic alteration and this second alteration stage can become largely dominant in the vicinity of fracture zones (Klee et al., 2021b, 2021a; Vidal et al., 2018). Taking as a reference the 6 grades of granitic rocks alteration grades used by Glaas (2021) and Vidal (2017), Klee (2021) could produce a similar ranking in three grades. Many similarities between the SSF plus RH and NH granites are found in terms of progressive development of clay minerals approaching fracture zones. Fractures fillings at SSF are heterogeneous and many indications lead to propose a polyphase tectonic history with a possible reactivation of inherited Variscan structures during the Mesozoic and Cenozoic. A multistage paleofluid circulation has also been proposed for the NH fractures by Klee et al. (2021a) since many similarities are found in terms of paleofluid composition with the SSF reservoir. For the NH, quartz veins are interpreted as evidence of a first phase of brine circulation followed by a second circulation responsible of illite formation. A third circulation phase induces carbonates precipitation and a fourth phase leads to baryte deposits.

From a petrophysical point of view Chabani et al. (2021a) concluded that connectivity within the NH reservoir analogue was ruled by both small and large fractures. The presence of high amounts of calcite within both the NH and SSF can be only explained if both systems are similarly opened and if brine circulation is in both case controlled by the fracture network.

As a conclusion, a converging array of arguments confirm the working hypothesis namely that the NH are considered as a naturally exhumed domain having been affected by a polyphase fluid flow coeval with strike-slip activity along the SDVFZ. The validity in terms of reservoir analogue is confirmed.

4.5.3.1.2 Scalings development studies

In order to produce a constant amount of energy the geothermal industry needs to understand reservoir properties and gain from geologists precise models of its architecture and an in-depth characterization of rock properties. These data are important to predict reservoir evolution through time, minimize seismic hazard during stimulation and production phases and ensure a proper well positioning and orientation. Besides reservoir geology, surface infrastructures dimensioning and material resistance to corrosion are of primary importance. Given the aggressivity of highly saline geothermal brines, and their change of pressure and temperature during exploitation, scalings might develop in pipe lines and heat exchangers lowering plant efficiency.

Given my past expertise as application engineer within the Oxford Instruments company, I have participated to a characterization of sulfides precipitates developing in a small heat exchanger tested in the framework of MEET. Ledésert et al. (2021) have shown that the shape of galena precipitates is strongly dependent on flow turbulence. Portions of the heat exchanger having a turbulent flow show dendritic crystals as a result of quick growth while laminar flow present in the tubes induces a slower crystallization leading to well-developed faces.

Article

Scaling in a Geothermal Heat Exchanger at Soultz-Sous-Forêts (Upper Rhine Graben, France): A XRD and SEM-EDS Characterization of Sulfide Precipitates

Béatrice A. Ledésert ^{1,*}, Ronan L. Hébert ¹, Justine Mouchot ², Cléo Bosia ², Guillaume Ravier ², Olivier Seibel ², Éléonore Dalmais ², Mariannick Ledésert ^{3,†}, Ghislain Trullenque ⁴, Xavier Sengelen ¹ and Albert Genter ²

¹ CY Cergy Paris Université, Géosciences et Environnement Cergy, 1 Rue Descartes, 95000 Neuville-sur-Oise, France; ronan.hebert@cyu.fr (R.L.H.); xavier.sengelen@cyu.fr (X.S.)

² Électricité de Strasbourg Géothermie, 26 Boulevard du Président Wilson, 67000 Strasbourg, France; justine.mouchot@arverne.earth (J.M.); cléo.bosia@es.fr (C.B.); guillaume.ravier@es.fr (G.R.); olivier.seibel@es.fr (O.S.); eleonore.dalmais@es.fr (É.D.); albert.genter@es.fr (A.G.)

³ Cristallography Laboratory, 14000 Caen, France; ledesert@cyu.fr

⁴ UnilaSalle, Collège Géosciences, équipe B2R, 19 Rue Pierre Waguet, 60000 Beauvais, France; ghislain.trullenque@unilasalle.fr

* Correspondence: beatrice.ledesert@cyu.fr; Tel.: +33-134257357

† Retired.



Citation: Ledésert, B.A.; Hébert, R.L.; Mouchot, J.; Bosia, C.; Ravier, G.; Seibel, O.; Dalmais, É.; Ledésert, M.; Trullenque, G.; Sengelen, X.; et al. Scaling in a Geothermal Heat Exchanger at Soultz-Sous-Forêts (Upper Rhine Graben, France): A XRD and SEM-EDS Characterization of Sulfide Precipitates. *Geosciences* **2021**, *11*, 271. <https://doi.org/10.3390/geosciences11070271>

Academic Editors:
Jesus Martinez-Frias and
Matteo Alvaro

Received: 5 May 2021
Accepted: 23 June 2021
Published: 28 June 2021

Publisher's Note: MDPI stays neutral with regard to jurisdictional claims in published maps and institutional affiliations.



Copyright: © 2021 by the authors. Licensee MDPI, Basel, Switzerland. This article is an open access article distributed under the terms and conditions of the Creative Commons Attribution (CC BY) license (<https://creativecommons.org/licenses/by/4.0/>).

Abstract: The Soultz-Sous-Forêts geothermal site (France) operates three deep wells for electricity production. During operation, scales precipitate within the surface installation as (Ba, Sr) sulfate and (Pb, As, Sb) sulfide types. Scales have an impact on lowering energy production and inducing specific waste management issues. Thus scaling needs to be reduced for which a thorough characterization of the scales has to be performed. The geothermal brine is produced at 160 °C and reinjected at 70 °C during normal operation. In the frame of the H2020 MEET project, a small heat exchanger was tested in order to allow higher energy production, by reinjecting the geothermal fluid at 40 °C. Samples of scales were analyzed by XRD and SEM-EDS, highlighting that mostly galena precipitates and shows various crystal shapes. These shapes can be related to the turbulence of the flow and the speed of crystal growth. Where the flow is turbulent (entrance, water box, exit), crystals grow quickly and mainly show dendritic shape. In the tubes, where the flow is laminar, crystals grow more slowly and some of them are characterized by well-developed faces leading to cubes and derived shapes. The major consequence of the temperature decrease is the increased scaling phenomenon.

Keywords: Soultz-Sous-Forêts; geothermal site; heat exchanger; scales; sulfates; sulfides; As and Sb-bearing galena; crystal growth; crystal shapes

1. Introduction

Geothermal power production is a very attractive resource with characteristics such as low cost, little environmental pollution and worldwide distribution [1–3]. In addition, it is available all the time, whatever climatic conditions and day/night alternation, as opposed to wind- or solar-derived energy. Geothermal power plants take their energy from deep underground water that is pumped to the surface. During its residence time in the ground at sometimes high temperature (150–300 °C), the water acquires specific properties by interaction with the rock reservoir, generally resulting in high salinity and acidity. These characteristics are responsible for corrosion and scaling (deposition) issues in wells and in surface installations. Those phenomena are known from the very beginning of industrial high-temperature geothermal operations and are identified to be responsible for economic issues [4,5]. Scaling is encountered in both low enthalpy [6] and high enthalpy [5,7] geothermal systems. According to [8], among the most abundant scales are silica, carbonates, sulfates, sulfides, and native metals such as antimony (Sb). It is also

known that metal sulfide scaling frequently occurs in volcanic geological context or high Cl environments [9].

Among all the geothermal geological contexts, grabens present specific characteristics. In the Upper Rhine Graben (URG; at the border between France and Germany) hydrothermal fluids percolate within fault zones and are brought relatively close to the surface, favoring the development of high-energy geothermal plants. These are dedicated to the production of either electricity (e.g., Soultz-Sous-Forêts, called Soultz in the following) or heat (e.g., Rittershoffen). The URG deep ground water system is characterized by a brine with high salinity (99–107 g/L at Soultz) and moderate low pH (around 5) [10] responsible for strong corrosion of geothermal surface installations (pipes, heat exchangers) and also deposition of minerals within these installations [11,12].

The Soultz geothermal production plant is based on three 5000 m-deep wells, GPK-2, GPK-3 and GPK-4 (Figure 1) penetrating the granitic basement. GPK-2 is the production well while the total reinjection of the geothermal fluid is performed through GPK-3 and GPK-4. In industrial operation conditions, the brine is produced at 160 °C and is reinjected at 70 °C [13], showing no difference in its chemical composition when the temperature decreases. In the framework of the H2020 MEET European program [14,15], an additional small heat exchanger (SHEX) has been installed temporarily in order to assess the optimization of energy production by lowering the temperature of the reinjected fluid from 70 °C to 40 °C [16]. This SHEX received 10% of the total flow and was tested over 3 months. It was designed with six alloys in order to test their reaction to corrosion and scaling. Only scaling phenomena are described here and several points are addressed: (1) determination of the chemical and mineralogical composition of the scales, (2) impact of temperature lowering on the scaling processes (composition/morphology/thickening of the deposits), (3) influence of alloys on scaling development. An X-ray diffraction (XRD) and scanning electron microscopy coupled with energy dispersive spectrometry (SEM-EDS) survey was performed to answer those questions.

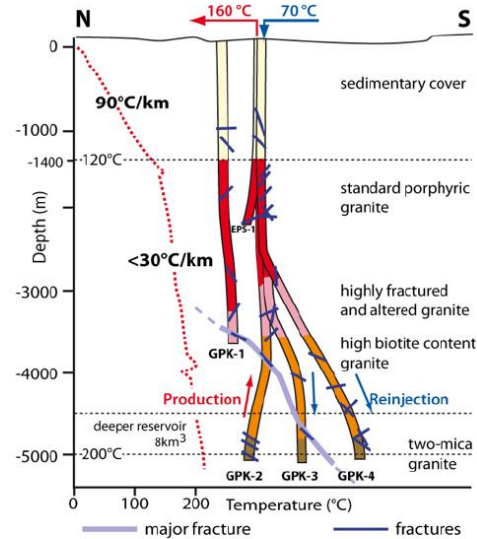


Figure 1. The Soultz Enhanced Geothermal System with its 5 wells among which the 3 deepest ones (GPK-2, GPK-3 and GPK-4) are used for electricity production. The brine is produced at 160 °C in GPK-2 well and reinjected at 70 °C in GPK-3 and GPK-4 in normal operation. The temperature gradient recorded at Soultz (red dashed line) and key figures are indicated on the left. Figure modified after [17,18]; size of the deep reservoir from [19].

2. Technical Context

2.1. Scaling Phenomenon in Geothermal Power Plants Worldwide

Scaling is a common phenomenon in geothermal power plants worldwide. Specific site analyses on scaling issues occurring in various geothermal plant types are reported in abundant literature [12,20–30], showing the importance of this topic for the plant operation. Scales act as insulators and thus lower the thermal exchanges. They also reduce the diameter of the pipes and inside volume of the exchangers which lowers the overall productivity of the geothermal power plants. Scales may also trigger the accumulation of toxic chemical elements, inducing additional risk and cost issues during the operational phase. In addition, scale formation is generally linked to degassing process, which has a major impact in terms of corrosion on the surface installation of geothermal power plants. Reducing the formation of scales is a challenge for operators who thus use inhibitors in their industrial process in order to prevent their formation [2,21,31].

2.2. Scaling Phenomenon at Soultz Geothermal Power Plant

At Soultz, surface installations are composed of several parts among which pipes and heat exchangers in which the natural geothermal fluid provides its thermal energy to an industrial fluid. An Organic Rankine Cycle (ORC) allows the production of electricity. The temperature of the brine lowers within the exchangers and the chemical equilibrium changes, resulting in the precipitation of minerals. The geochemistry of the brine provided by [10,13] shows a high salinity due to a great abundance of Na, K and Ca as major cations and Cl and SO₄ as major anions. It is summarized in Table 1, for the elements found in the scales. Li, Zn, Ba and other minor elements are also present in significant abundance. In addition, the geothermal fluid is characterized by a high CO₂ content, and natural anoxic conditions [10,13].

Table 1. Chemical composition of the brine after [10,13] from 22 brine samples collected in GPK-1, and the three deep wells at Soultz. Sb is not given in [13] (ng: not given), the only data about Sb comes from [10]. MRCC: most representative chemical composition of the native geothermal brine, in [13].

	Na (g/L)	K (g/L)	Ca (g/L)	Mg (mg/L)	Cl (g/L)	SO ₄ (mg/L)	SiO ₂ (mg/L)	As (mg/L)	Sb (µg/L) in [10]	Pb (µg/L)
Min-max values [13]	21–28.2	2.38–3.38	3.46–7.30	75–411	32.6–61	150–255	63–409	0.6–11	ng	181–782
MRCC [13] except for Sb	27.5	3.25	6.90	125	59	159	427	6	57.4	300

From this brine, sulfates of barite type ((Sr, Ba)SO₄) and minor sulfides of galena type ((Pb, As, Sb)S) precipitate during the lowering of the temperature in surface installations when no antiscalants are used [27,30]. The same phenomenon is also encountered in German geothermal plants located in the URG [12]. In the URG, and at Soultz in particular where the geothermal brine circulates within a granitic basement, those scales are known to accumulate radionuclides, ²²⁶Ra for sulfates and ²¹⁰Pb for sulfides [30], and are thus to be disposed of as Naturally Occurring Radioactive Material waste (NORM classification, [32]). In such conditions when no inhibitors were used, the Soultz power plant needed to be stopped and cleaned three times a year, inducing high maintenance cost, loss of energy production and waste management issues [33].

For safety reasons and power plant healthy operation, the formation of barite needs to be inhibited continuously [31,33]. Antiscalants are well known from the oil and gas industry and mainly consist of phosphonates and polycarboxylates when preventing barite formation [34]. The scaling phenomenon being closely linked with corrosion phenomena described by [35–37], both an antiscalant and a corrosion inhibitor are currently used at Soultz. The corrosion inhibitor agent is based on amines. Each type of mineral scale has an antiscalant which is more suitable for lowering its deposited amount. Antiscalants are

either inhibitors of crystallization known to be very powerful to control barite deposition or dispersants that better control metal sulfide scaling [33], or even a mixture of both. When sulfate production is made impossible thanks to antiscalants, sulfides precipitate as observed by [12] in geothermal power plants of the URC. In the following, chemicals used to prevent the deposition of scales will be simply called inhibitors.

2.3. The Tested Small Heat Exchanger (SHEx; Soultz)

In a geothermal exchanger, the natural hot brine provides its thermal energy to a working fluid and then is reinjected. Both flows are totally independent of one another and never mix. The SHEx was installed as bypass on the reinjection line [17]. It was tested over three months (late January to April 2019) in the presence of inhibitors, after which it was dismantled to allow scaling and corrosion studies. The SHEx consists of a tubular heat exchanger made with tubes of six different alloys (Figure 2), an entrance, an exit, and one water box at each end with different designs (Figure 2A) made of a seventh alloy. The west water box is separated into three compartments, while the east one is made of only two parts (Figure 2B). The cross-section of the shell and the included tubes with their alloy is shown in Figure 2C. The tubes are organized in three parallel layers. The hot fluid comes into the SHEx through the entrance and flows through the three layers of tube with a constant decrease of the temperature: around 65–70 °C at the entrance, ~60 °C in the upper layer of tubes, 50 °C in the intermediate layer, then 40 °C in the lower layer and the exit (Figure 2B). Each water box is closed by a flange (Figure 2D).

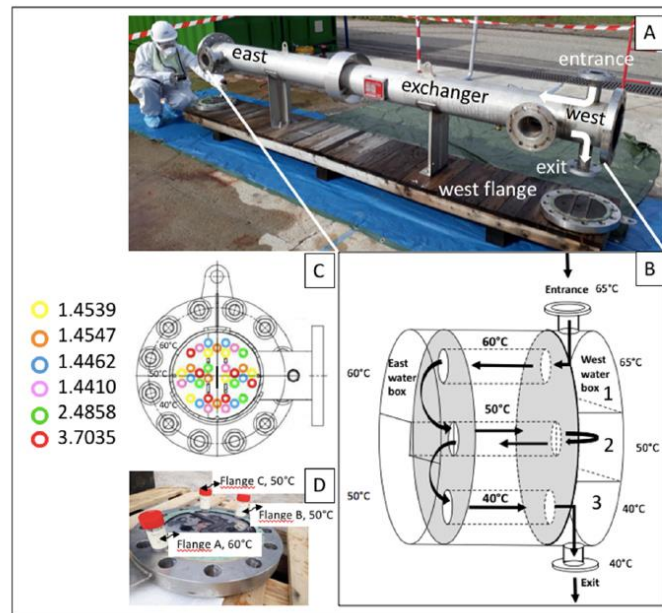


Figure 2. (A) overview of the SHEx; (B) schematic section of the cooling-down loop with 4 passes; (C): schematic front view with the tested alloys after [17]; (D): location of samples on flange closing the east water box. Note that only one tube is represented in (B) for each temperature (see Figure 2C for exact front representation of the location of tubes, after [17]). The intermediate layer of tubes is separated vertically in two parts (Figures 2B,C and 3) as can be seen in the east water box. Only the circulation of the geothermal brine is schematized.

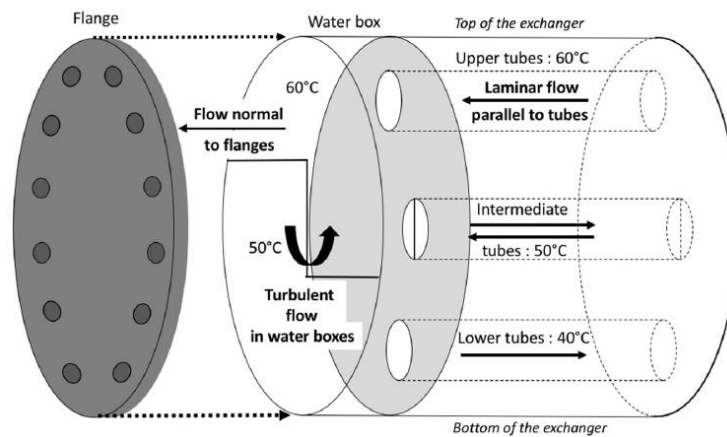


Figure 3. Temperature and flow inside the exchanger. Note that only one tube is represented for each temperature (see Figure 2C for exact cross section representation of the location and alloy of tubes). The intermediate layer of tubes is separated in two parts by a vertical panel. Thus, the flow occurs in both directions but in separate tubes. The west water box is not represented.

The path followed by the geothermal fluid within the SHEx and the flow regime is shown in Figure 3: turbulent in the entrance and in water boxes, laminar into the tubes, and perpendicular to the flanges, hence allowing to examine the likely influence of the flow regime on the scales. The three layers of tubes allow the examination of the likely impact of temperature on the scaling phenomenon. The six tested alloys are 1.4539 (904 L), 1.4547 (254 SMO), 1.4462 (DX 2205), 1.4410 (SDX 2507), 2.4858 (Alloy 825) and 3.7035 (TiGr2) [17] as visible in Figure 2C. The potential influence of the alloys on the scales will also be discussed. Mundhenk (2012) [26] proposed a ranking of metals as regards corrosion in geothermal brine conditions of the URG. The industrial exchangers currently operated at Soultz and Rittershoffen are made of 1.4410 (SDX 2507).

3. Material and Methods

3.1. Scales

In this fluid circulation test performed with the use of inhibitors, scales occur as black deposits, either as a powder (for example in water boxes, Table 2), or as a continuous plating forming a thin solid layer (like in tubes, Figure 4).

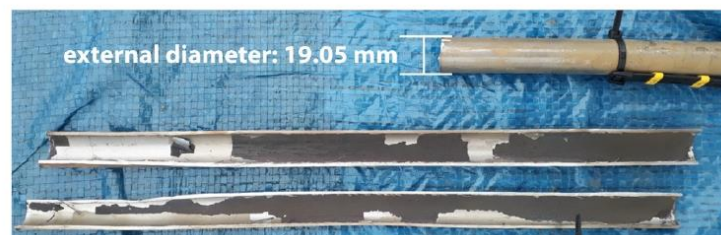


Figure 4. Macroscopic view of continuous scales while still in contact with a metal tube during dismantling of the SHEx in April 2019. The tube has been cut all along for the recovery of scales.

3.2. Preparation of Samples

The SHEx was only drained and not rinsed before dismantling. Thirty-five samples were collected in the SHEx and one in the operated industrial plant for SEM-EDS analyses (Table 2). They were collected in order to be representative of hydrodynamic and thermal conditions for each alloy. They were neither rinsed with clear water nor ground. They were simply dried at ambient temperature. The industrial sample was collected in 2017 in the operated power plant at the exit of the industrial heat exchanger, just before the reinjection line, where the geothermal fluid is circulating at a temperature of 75–65 °C in contact with a 1.4410 steel.

Millimeter-size fragments of continuous solid scales were collected and glued on metal stubs with carbon lacquer (Figure 5) for observation by reflection optical microscopy (ROM) and scanning electron microscopy (SEM) coupled with energy dispersive spectrometry (EDS) for local chemical analyses. For each sample, the side in contact with the metal (called metal side, MS in the following), the side in contact with the fluid (called fluid side, FS in the following) and the cross-section were prepared systematically (Figure 5). The MS surface looks bright and smooth while FS surface is velvety and rough (Figures 4 and 5). The cross-section was prepared in order to study the thickness of the deposits, but the preparation frequently failed. It is to be noted that on alloy 1.4462, the scales separated systematically into two layers (MS and FS) during sampling, which is the reason why three samples were collected for each temperature (MS, FS and total). Scales from industrial sample, entrance and water boxes of the SHEx occur as a powder (Figure 6) and they were just spread over carbon lacquer (Figure 6).

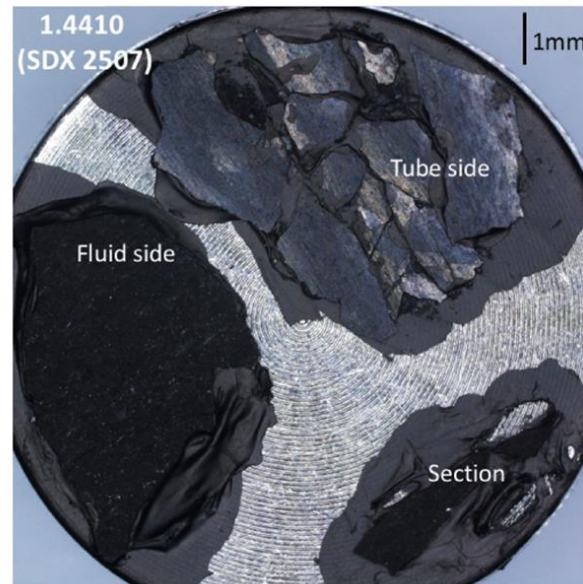


Figure 5. ROM view of tiny samples of continuous scales with smooth MS (tube side), velvety rough FS and section of samples collected in a tube made of 1.4410 super duplex steel, at 60 °C, glued with carbon lacquer on a metal stub for SEM-EDS analysis.

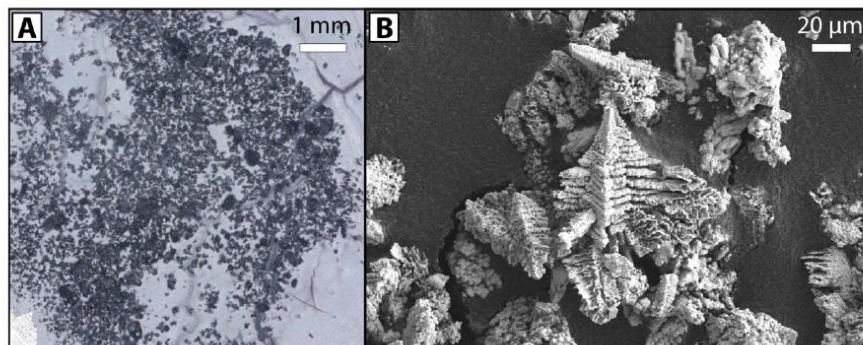


Figure 6. Powder collected in the entrance of the SHEX made of 1.4307, (A) as viewed by ROM and (B) by SEM.

3.3. X-ray Diffraction

More than 1 g of scales being necessary for X-ray diffraction (XRD), the amount of scales was insufficient in any tube of the SHEX. Only entrance, exit and water boxes 1 and 3, all of them made of 1.4307, provided 4 samples. XRD was performed by ORANO company with a Panalytical diffractometer using Co K α radiation ($\lambda = 1791 \text{ \AA}$) in order to avoid potential Fe fluorescence. Neither internal nor external standards were used. The results were compared to JCPDS files for the determination of the mineral phases present in the samples.

3.4. Scanning Electron Microscopy Coupled with Energy Dispersive Spectrometry (SEM-EDS)

The SEM used in this study, a Zeiss GeminiSEM 300 coupled with a Bruker EDS, belongs to the IMAT analysis facility of CY Cergy Paris Université. No metal coating was necessary prior to observation. Observation was performed with a secondary electron detector by using a chosen acceleration voltage (between 10 and 15 kV) at a working distance between 6 and 8 mm that allowed EDS analyses in high vacuum mode. A low acceleration voltage was deliberately chosen in order to lower the beam/sample interaction volume size and to ascertain that the X-ray pulses came exclusively from the scale particles. This modest acceleration voltage presents a second advantage as it reduces significantly charging phenomena. However, this induces a poor quality of analyses enhanced by the marked topography of samples which is not ideal in terms of quantification as the beam/sample interaction volume might be truncated or shadowed. Thus, the analyses can only be used for relative abundance of the elements within and between the different scale samples.

4. Results

Results obtained by XRD and SEM-EDS are presented below and discussed in Section 5.

4.1. X-ray Diffraction (XRD)

XRD patterns that were obtained for the four samples are provided in Figure 7. Entrance and exit of the SHEX show the same diffractograms, indicating the presence of galena (PbS), and likely minor dufrénoysite (Pb₂As₂S₅) as regards the weak intensity of the peaks, over the whole range of temperatures (65 °C and 40 °C). The water boxes also show the presence of galena and likely dufrénoysite, together with that of halite (NaCl) for the two temperatures under concern (65 °C and 40 °C). The samples not being reduced into powder it was possible to determine hkl diffraction planes for galena, namely 111, 200, 220, 311 and 222 (Figure 7).

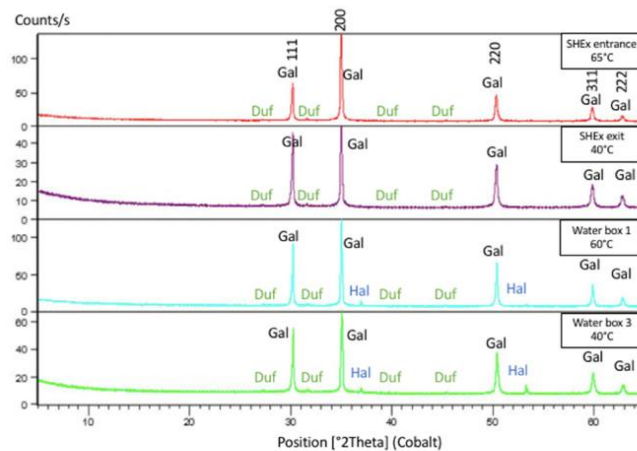


Figure 7. X-ray diffraction diagrams obtained for scales collected in the entrance, the exit and water boxes 1 and 3 of the SHEx. They show galena (Gal; As and Sb bearing PbS), additional halite (Hal; NaCl) in the water boxes, and likely traces of dufrénoysite (Duf; Pb₂As₂S₅), all of these sites being made of 1.4307 alloy. The numbers indicated vertically represent the hkl diffraction planes of galena crystals.

4.2. Scanning Electron Microscopy coupled with Energy Dispersive Spectrometry (SEM-EDS)

The observation by SEM allows to distinguish several features.

4.2.1. Structure of the Scales

As indicated before, scales occur as a continuous solid deposit (Figure 5) or as a powder (Figure 6, Table 2). In that first case, the deposit shows a rough FS in contact with the geothermal brine (Figure 8A,B) and a smooth MS in contact with the metal (Figure 8C,D).

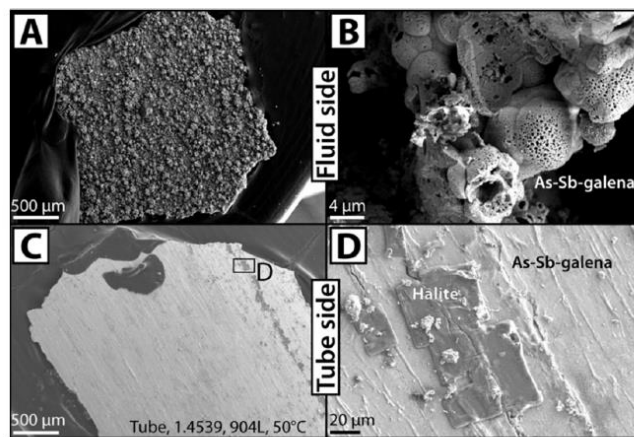


Figure 8. Sample 1.4539, 50 °C, surface of the scales: rough in contact with the brine (A and zoom in B), smooth in contact with the metal (C and zoom in D), showing As-Sb-galena and halite on MS and only galena on FS in this example.

Table 2. Summary of sampling points, performed analyses and observation by SEM. Industrial: industrial heat exchanger. All other sampling points are within the SHEX. FS: fluid side, MS: metal side, Total: FS+MS sampled at the same time when they separate. The alloys are from [17]. The analyses performed on each sample are indicated. Wwb: West water box. (co): cuboctahedron. (oct): octahedron. Underlined figures are for 1.4410 alloy for comparison between three temperatures.

Sampling Points	Alloy	Temperature (°C)	Structure of scales	Analyses	Whole Thickness of Scales (µm)	Thickness of Smooth Zone (µm)	Dendrite	Needle	Coral	Cube	Fibro-Radiated
Industrial Entrance	1.4410	65–75	Powder	SEM			x				
Exit	1.4307	65	Powder	XRD, SEM			x				
Wwb 1 (top)	1.4307	40	Powder	XRD						x	
Wwb 2 (Middle)	1.4307	65	Powder	XRD, SEM			x				
Wwb 3 (Bottom)	1.4307	55	Powder	SEM					x		
Flange A (East)	1.4307	40	Powder	XRD, SEM							x
Flange B (East)	1.4307	60	Continuous	SEM	-	15	x				
Flange C (East)	1.4307	50	Continuous	SEM	30	12					
Tube	1.4307	50	Continuous	SEM	110	15					
Tube	1.4539	60	Continuous	SEM					x	x (co)	
Tube	1.4547	60	Continuous	SEM					x		
Tube (FS)	1.4462	60	Continuous	SEM					-		
Tube (MS)	1.4462	60	Continuous	SEM					-		
Tube (Total)	1.4462	60	Continuous	SEM					x?		
Tube	1.4410	60	Continuous	SEM	22	5					
Tube	2.4858	60	Continuous	SEM	50	10					
Tube	3.7035	60	Continuous	SEM	15	6					
Tube	1.4539	50	Continuous	SEM							x
Tube	1.4547	50	Continuous	SEM	270	-					x
Tube (FS)	1.4462	50	Continuous	SEM							
Tube (MS)	1.4462	50	Continuous	SEM							
Tube (Total)	1.4462	50	Continuous	SEM							
Tube	1.4410	50	Continuous	SEM	80	10					x
Tube	2.4858	50	Continuous	SEM	50	30					x
Tube	3.7035	50	Continuous	SEM	200	10					
Tube	1.4539	40	Continuous	SEM	270	25					
Tube	1.4547	40	Continuous	SEM							
Tube (FS)	1.4462	40	Continuous	SEM							
Tube (MS)	1.4462	40	Continuous	SEM							
Tube (Total)	1.4462	40	Continuous	SEM							
Tube	1.4410	40	Continuous	SEM	220	10					x
Tube	2.4858	40	Continuous	SEM	60	30					x
Tube	3.7035	40	Continuous	SEM							

The scales are composed of several superimposed layers (Figure 9A) and the smooth layer in contact with the metal is generally divided in several parallel sub-layers (Figure 9B).

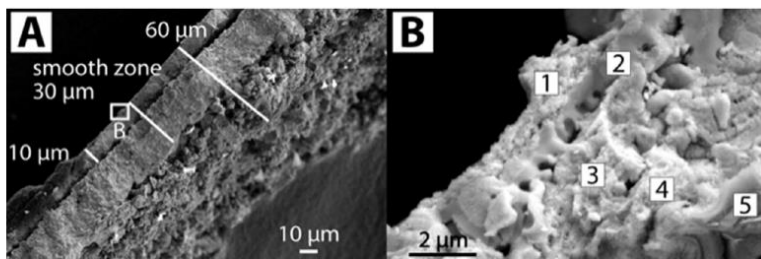


Figure 9. Sample of scales collected in a tube made of 2.4858 at 40 °C. (A) Cross-section of the scales divided into several layers, (B) the very first one (in contact with the metal) being itself composed of several micro-porous sub-layers. B is a focus on the white rectangle in A and shows five successive sub-layers that deposited on the top of one another. Sub-layer 1 is the oldest, in direct contact with the metal.

4.2.2. Thickness of the Scales

The thickness of scales was measured whenever it was possible, which was not very frequent. It could be measured systematically only for scales deposited in tubes made of 1.4410 (Figure 10) at decreasing temperatures. One has to note that measuring the thickness by SEM provides values with a non-negligible uncertainty as the measurement was sometimes not exactly normal to the deposit. However, the magnitude of the measurement remains true. The thickness observed in tubes of 1.4410 after the 3-month test was around 50 μm at 60 °C, 80 μm at 50 °C and locally up to 220 μm at 40 °C (Table 2, Figure 10), thus representing a deposition rate of about 17 μm/month at 60 °C to 73 μm/month at 40 °C, considering a constant deposition rate. The same trend of increasing thickness with decreasing temperatures tends to be seen on other alloys (Table 2): small at 60 °C (22, 50, and 15 μm, in tubes made of 1.4462, 1.4410, 3.7035 respectively), generally greater at 50 °C (270, 80, and 50 μm, in tubes made of 1.4547, 1.4410, 2.4858 respectively) and in general the biggest at 40 °C (200, 270, 220, 60 μm, in tubes made of 1.4539, 1.4547, 1.4410, 2.4858 respectively).

Wherever it could be measured, the smooth zone always shows a thickness smaller than or equal to 30 μm, while the whole thickness of the deposit reaches 270 μm. Nothing much can be said about the thickness of scales deposited on the east flange as it could not be measured as a whole at 60 °C and varies from 30 to 110 μm at 50 °C. No sample is available at 40 °C as the flange is separated in only two zones: 60 °C and 50 °C.

4.2.3. SEM-EDS Chemistry of the Samples

Whatever the location (water box, entrance, exit and tubes), either on MS or FS of the scales when they are continuous, or in powder, and whatever the alloy on which they deposited, SEM-EDS spectra and maps show the presence of Pb, S ± As and Sb compounds of galena type (Figures 11 and 12). Halite (NaCl) is also frequently observed. Both of these two phases were encountered on the XRD patterns (Figure 7). Because of the analytical limitations exposed in the Methods section and their likely small size, crystals of sulfosalts such as dufrénoyite were not identified by SEM-EDS.

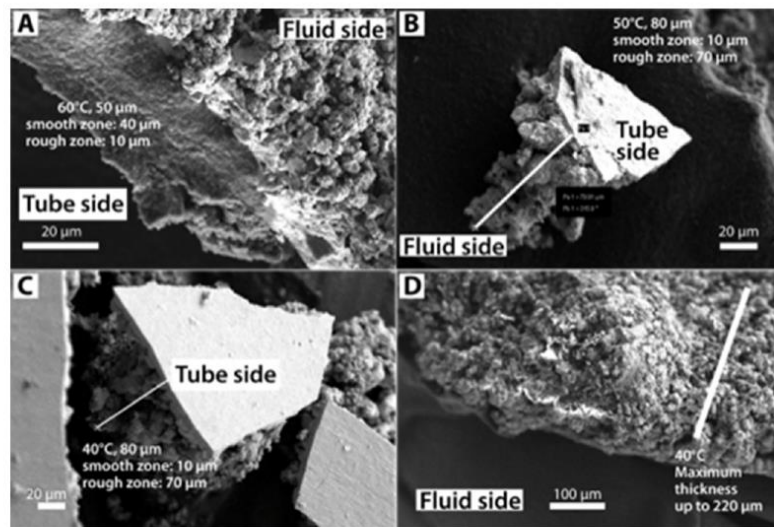


Figure 10. Tubes made of 1.4410, thickness as a function of temperature. The deposit in contact with the metal is smooth while it is rough when in contact with the brine. The thickness of the scales tends to increase when the temperature decreases within the SHEx, from 50 µm at 60 °C to 220 µm at 40 °C. (A) 60 °C, (B) 50 °C, (C,D) 40 °C.

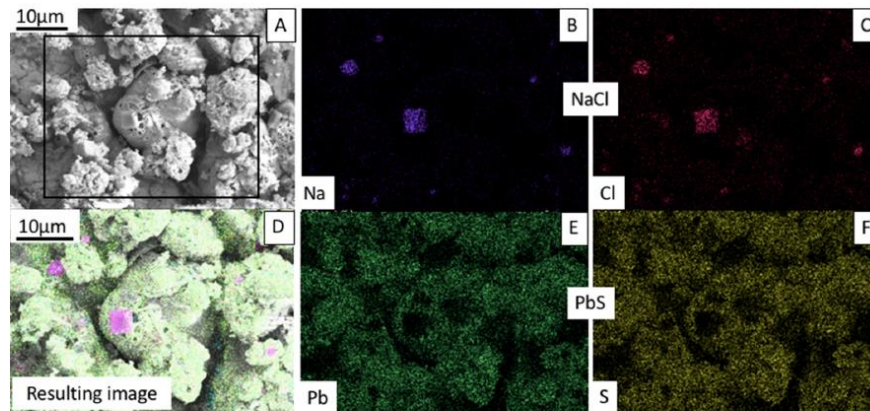


Figure 11. EDS map of FS of scales collected in a tube made of 2.4858, at 40 °C (A–F) showing (A) the SEM image and the black rectangle in which the elementary maps were performed, (B,C) maps of elementary concentration for Na and Cl characteristic of halite (NaCl) with its common cubic shape, (D) resulting map with all elements, (E,F) maps of elementary concentration for Pb and S characteristic of galena (PbS). As and Sb were also encountered together with Pb and S but in such a small amount that the images are not contrasted enough to be included.

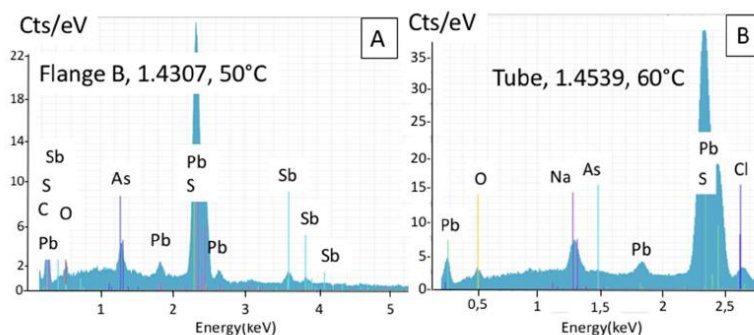


Figure 12. EDS spectra obtained on FS of scales collected (A) on a flange at 50 °C and (B) in a tube made of 1.4539, at 60 °C.

Table 3 shows examples of semi-quantitative analyses. The same elements (Pb, As, Sb, S) are present in each of the studied samples (analyses 1, 2 and 3), but in varying relative abundance. Sb is sometimes quite abundant (analyses 2 and 3) but no Sb-bearing sulfosalts were discovered either on XRD diagrams (Figure 7) or by SEM. Na and Cl are also locally detected in the samples.

Table 3. Three normalized semi-quantitative analyses obtained by SEM-EDS. Note the limitations of accuracy due to the low acceleration voltage, the topography of samples and their low thickness. The analyses can only be used for relative abundance of the elements within and between the different scale samples and mostly indicate the elements present in the samples.

	1	2	3
	Tube	Tube	Tube
	3.7035	2.4855	2.4855
	60 °C	60 °C	40 °C
Elements	Content (wt.%)	Content (wt.%)	Content (wt.%)
S	11.75	16.28	15.00
As	3.89	8.57	3.70
Sb	11.46	25.08	17.82
Pb	72.90	50.07	63.48
Total	100	100	100

From these semi-quantitative results, no difference appears in the chemistry of the scales, whatever the alloy on which they deposited or the temperature of the brine from which they precipitated.

4.2.4. Shapes of Galena Crystals

Various galena crystal shapes were observed thanks to SEM on the tiny fragments described in Section 3 (Materials and Methods). The crystals are of micrometer size in millimeter-sized samples. Thus, these observations might not be exhaustive but give an overview of the crystal shapes of galena.

1. Dendrites

Dendritic crystal shape was observed in the scales collected in the industrial installation (reference sample), as well as in the entrance of the SHEX, and on the upper part of the eastern flange (Figure 13). The industrial sample and that collected at the entrance of the SHEX are made of only dendrites (Figure 13A,B). The only dendrite observed on the flange (Figure 13C) seems to have been deposited by the flow as it is free and not embedded in the matrix. No dendrites were found in any of the tubes, whatever the temperature.

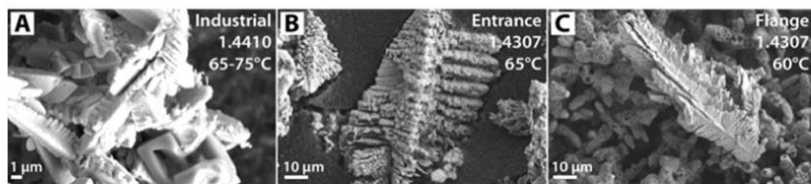


Figure 13. Dendritic shapes of galena crystals (A) in the industrial sample (1.4410 alloy), (B) in the entrance of the SHEX and (C) on the upper part of the eastern flange (both made of 1.4307). No dendrites were found in any of the tubes.

2. Needles

Needle shape is found in tubes of 1.4462 (50 °C and 40 °C), 1.4539 (60 °C and 50 °C), and 2.4858 (50 °C), in water boxes (1.4307 alloy, at 65 °C, 55 °C and 40 °C), and on a flange (1.4307 alloy, 50 °C), thus at various temperatures (from 65 °C to 40 °C, Figure 14) and alloys. Needles were not observed on other samples. Needles can be parallel to each other (A) or perpendicular (B to H) and sometimes in three orthogonal directions (C). Needles have a square section as visible mostly in B and F. They were observed in zones where the flow is rather laminar (tubes) or turbulent (water boxes and flanges).

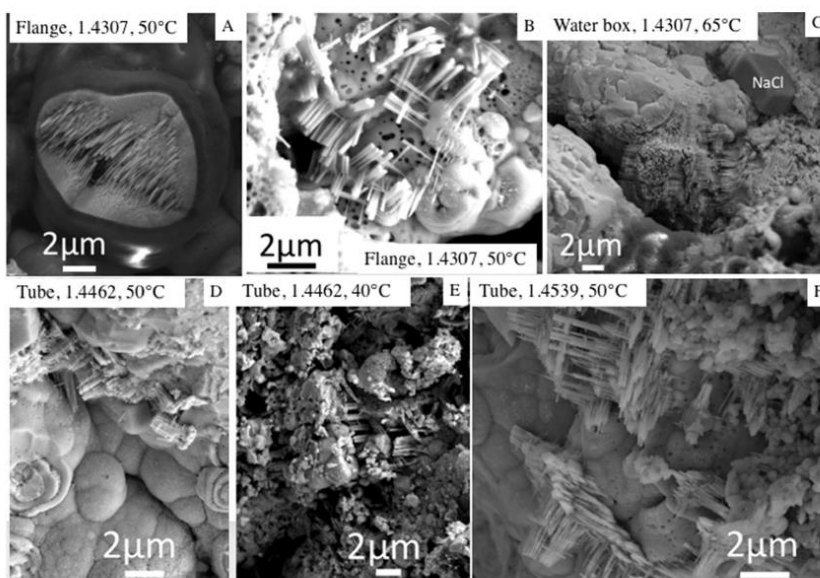


Figure 14. Needle shapes of galena crystals (A,B) on a flange and (C) in water box and (D–F) in tubes, at different temperatures and on three different alloys (1.4307, 1.4462, 1.4539). (A) needles parallel to each other, (B–F): needles grew in perpendicular directions. (B,F): Note that the needles are monocrystals with square section.

3. Coral Shapes

Coral-like shapes are of various types (Figure 15) that all show an important internal porosity. They are the most common shapes encountered in the exchanger (Table 4). They were observed in different zones of the SHEX (entrance, 1.4307 alloy; water box, 1.4307

alloy; flange, 1.4307 alloy) and in tubes of all alloys, and at temperatures varying from 65 °C (entrance and water box) to 40 °C (water box and tubes).

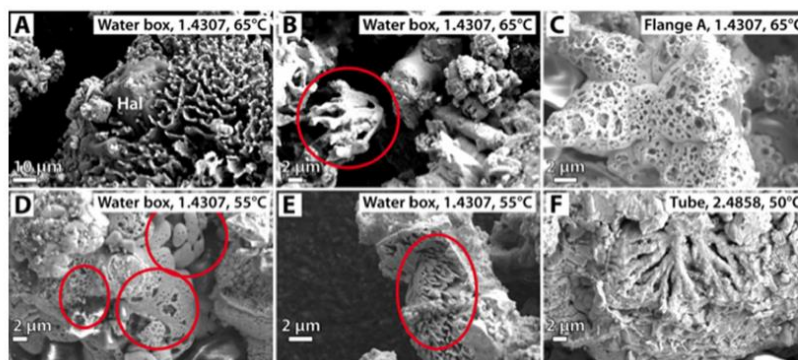


Figure 15. PbS coral shapes of different kinds. All of them show an important internal porosity. The zones to be observed are highlighted by red ellipses. Hal: halite. (A) halite crystal embedded in coral shape galena, water box, 1.4307, 65 °C, (B) 3D view of coral shape galena, water box, 1.4307, 65 °C, (C) coral shape made of botryoids with abundant porosity, flange A, 1.4307, 65 °C, (D) coral shape made of botryoids with abundant porosity, water box, 1.4307, 55 °C, (E) coral shape made of numerous contiguous needles, water box, 1.4307, 55 °C, (F) cross section of coral shape galena.

4. Cube and Cubic-Derived Shapes

Several cubic or cubic-derived shapes were observed in the samples. Cubes were found in a tube at 60 °C (1.4539) where it shows exactly the same hollow shape as on a flange (1.4307, 40 °C; Figure 16A). Cubes were also observed in a water box (1.4307, 40 °C; Figure 16B,C) where they occur either as massive structures (Figure 16B) or as a kind of skeleton made of needles oriented in the three directions of space (Figure 16C), those two features being in close contact in the same sample. Cubes are thus found on at least two different alloys (1.4307 and 1.4539) and at temperatures from 60 °C to 40 °C.

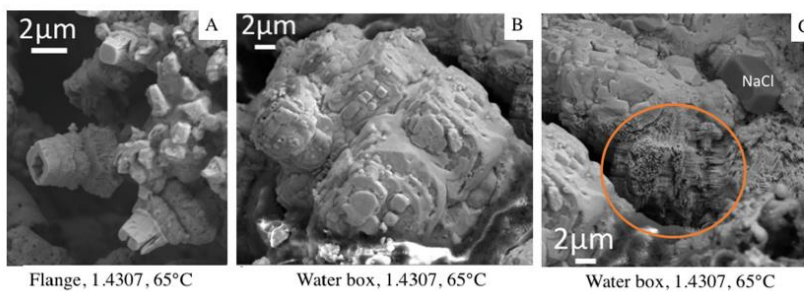


Figure 16. Cubic-derived shape of PbS crystals, occurring as (A) hollow cubes, (B) massive cubes, or (C) skeleton made of needles in three orthogonal directions inside the orange ellipse. The massive cube (B) is seen in the lower left-hand corner of (C).

Other PbS shapes derived from the cube were locally observed in tubes, as shown in Figure 17, such as a cuboctahedron (Figure 17A) and an octahedron (Figure 17B), on two different alloys and at 60 °C and 40 °C respectively. The octahedron (Figure 17B) is found in the vicinity of orthogonal needles not visible on the photograph.

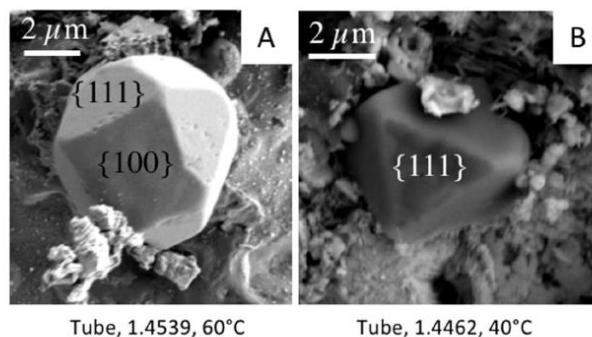


Figure 17. PbS cuboctahedron (A) and PbS octahedron (B) with their indexed faces, observed in two tubes made of 1.4539, at 60 °C (A) and 1.4462, at 40 °C (B).

Thus, cubes and cubic-derived shapes were observed on three different alloys and at temperatures from 65 to 40 °C (Table 4).

5. Fibro-Radiated Botryoidal Shape

The fibro-radiated botryoidal type (Figure 18A) is made of needles organized in 3D fan shape (Figure 18B,C) with several superimposed layers (Figure 18B,C). No to minor porosity is observed as opposed to coral shape. These three examples were observed occurred at a 50 °C temperature, on three different alloys. Table 2 shows all the locations where botryoids were observed, from 65 °C to 40 °C.

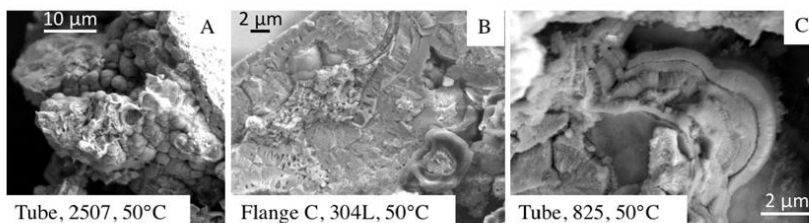


Figure 18. Fibro-radiated botryoidal shape from three different samples collected on a flange, and in two tubes of different alloys. All of the examples presented here were observed for a 50 °C temperature, but they also occurred at 65 °C and 40 °C (see Table 2). (A) general view, on a tube made of 2507 at 50 °C, (B,C) close view of a cross-section of botryoid on a flange and on a tube, at 50 °C.

Table 2 recapitulates all of the shapes that were observed by SEM, as a function of the location inside the SHEx, the alloy type and the temperature. Some samples do not show any characteristic crystal shapes, because of their poor quality (tubes of 1.4462 and 3.7035 alloys, Table 4). In the other samples, the coral shape is the most widely observed, whatever the alloy and the temperature. Other crystal shapes are frequently found in association with it in samples collected in tubes. Cubes are associated with coral shape in the west water box and on a flange, and in association with needles in both water boxes and in some tubes. Dendrites were observed in great abundance and not in association with other shapes in the industrial installation and in the entrance. The only dendrite found on a flange appears to be free on the surface of the scale and not embedded in the deposit. The various shapes were observed whatever the temperature and the alloy, except for dendrites which were observed only at the highest temperature.

5. Discussion

Galena is studied in ore deposits for scientific and economical purposes [38–40], and because of its toxicity in mining environments [41–43]. Galena is also well known in the industry, in particular for its semi-conductor properties and is thus thoroughly studied [44–46]. Natural galena is rarely a pure PbS component and frequently contains arsenic [47] and antimony [40,48]. Various galena shapes and chemical compositions are reported in natural environments [49]. Laboratory growth experiments show that the shape and chemistry of galena crystals can be controlled by several factors among which time, temperature and concentration of elements in the solvent [44–46,50]. All these previous studies might be useful for understanding the growth process in the SHEX at Soultz, even though the chemistry of the solution and other parameters are different. As regards shapes of PbS crystals, the literature reports laboratory growth of hopper (skeletal) crystals [51], dendrites, nanocubes, and truncated nanocubes [50], dendrites with different shapes [52], nanocoral [53], and many others.

5.1. Structure and Chemistry of Scales

In the SHEX, scales occur either as a powder or as layered deposits (Table 4).

Table 4. Structure of the scales sampled in the SHEX.

Structure	Location	Flow
Powder	Industrial Entrance Exit	Turbulent
Layers	Water boxes Tubes Flange	Laminar Perpendicular

Where the flow is turbulent, the scales deposit as a powder. Layered deposits are structured into sub-layers likely related to the operation of the power plant. In tubes made of 1.4462, the scales occurred as two major layers which were difficult to extract together and fell into small pieces during sampling, inducing a poor quality of samples. Scales deposited in 3.7035 tubes were strongly attached to the metal and were difficult to collect, resulting also in a bad quality of samples. This explains the lack of information about crystal shapes for those two alloys (Table 2). The micro-porosity observed in the superimposed thin layers, as well as between and inside the crystals (coral-shape for example) might be due to local turbulence of the flow.

The deposits that formed in the SHEX indeed contain galena, whatever the occurrence (entrance, water boxes or exit), as indicated by XRD diagrams (Figure 7) when compared to [50] who also used Cobalt anticathod. Their characteristics are summarized in Table 5.

Table 5. Characteristics of galena crystals determined from XRD.

Sharp Peaks	Location of Peaks	Preferential Growth
Well-crystallized [52]	Face-centered cubic structure, Fm3 m space group [50] Based on JCPDS, 5-592 [51] or ASTM file card No. 030660020 [53]	Strong intensity of (200) reflection peak [50,51], thus, preferential growth in the <100> direction

XRD analyses of the scales indeed show the presence of galena but give no information about its chemistry which was surveyed by SEM-EDS. It is homogeneous with the systematic presence of As and Sb in varying abundance, in addition to Pb and S, which is a well-known phenomenon in natural ore systems [40,47,48]. The chemistry of scale surveyed by SEM-EDS is summarized in Table 6.

Table 6. Summary of the chemistry of scales as surveyed by SEM-EDS.

Location	Elements	Phases	Shapes
All samples	Pb, As, Sb, S	Galena As, Sb sulfosalts (e.g., dufrénoysite, Figure 7)	Various (Table 2) Undetermined
All samples	Na, Cl	Halite	Cubes (Figures 8, 11 and 14)

Other sulfosalts might also occur given the high relative amount of As and Sb given by EDS analyses, but their small abundance did not allow us to see them on the diffractograms. In addition, the semi-quantification performed thanks to SEM-EDS did not allow to determine either their presence or their amount in the samples.

Halite was detected by XRD neither in the SHEX entrance, nor in its exit, probably because of its too small abundance, but it was seen by SEM-EDS. Indeed, the intensity of the peaks related to halite in the water boxes is weak on the XRD patterns (Figure 7).

To summarize, the composition of scales is homogeneous whatever the metal on which they formed and whatever the temperature of deposition (from 65 °C to 40 °C). Thus, it appears that these two parameters (alloy and temperature) do not influence the chemistry of scales.

5.2. Thickness of Scales

It is to be noted that the measurement of the deposit thickness (Table 2) might be considered as only semi-quantitative. Indeed, it could not always be performed strictly perpendicular to the deposit, which induced an uncertainty in the obtained value. However, a general tendency is observed: the thickness increases (e.g., from 50 to 220 µm for 1.4410 tubes) when the temperature decreases (from 60 °C to 40 °C). The deposition of scales in an exchanger has several effects, some of them positive, such as protection against corrosion, others negative, such as insulation reducing the heat exchange and hence energy production, or the decrease of the diameter of tubes which reduces the fluid flow. The thicker the deposit, the better the protection against corrosion but the lower the energy production. The thickness of scales has thus to be carefully monitored and controlled by addition of inhibitors to the process and maintenance when necessary, in order to allow optimal energy production.

5.3. Conditions of Scale Formation

It is likely that halite crystals developed when the SHEX was dismantled, during its draining and drying, as they are not embedded in the scales and sometimes grew on the MS of the scales (Figure 8A).

The conditions for scale formation during the geothermal process are summarized in Table 7 which shows the changes undergone by the deposit through time, with a decreasing influence of metal.

Table 7. Summary of conditions for scale formation.

Order of Layer Formation	Layer Structure	Location	Influence of Metal
1st	Smooth (Figures 8D, 9A and 10)	Contact with metal	Strong
2nd	Smooth to rough (Figures 9 and 10)	Contact with 1st layer	Low to none
3rd	Smooth to rough	Contact with 2nd layer	Low to none
4th and more	Rough (Figures 8A,B and 10)	Contact with previous layer	None

The influence of alloy nature on the shape of galena crystals being eliminated, the likely influencing parameters that remain to explain the crystal shapes are the chemical composition of the brine, its temperature and the flow regime.

Dendrites were observed exclusively at the exit of the industrial installation and in the entrance of the SHEx. Indeed, dendrites are known to crystallize quickly [31], which is permitted by the highest temperature (75–65 °C) and the turbulence in these locations.

Abundant recent literature presents the conditions of galena synthesis in laboratory and the shapes of crystals obtained [44,45,51–56]. Shapes identical to those found in the SHEx are encountered in conditions described as hydrothermal, meaning with water as a solvent and maintained at a temperature of, for example, 80 °C [50] to 200 °C [45], with durations of 2 h [45] to 48 h [50]. Song et al. (2012) [44] report that the concentration of the solution and reaction time (24 h at 170 °C) are key parameters for obtaining controlled PbS crystal shapes. In those conditions, they report cubes, dendrites, stars, and wires. These various shapes are required for specific industrial uses where the optical, magnetic and electronic properties of semi-conductors are of high importance [45]. Other authors [52] conducted solvothermal syntheses meaning with organic solvents and imposed temperature conditions leading to PbS dendrites. Nanocoral shape was obtained by [53], by vapor-solid deposition at high temperature (1050 °C) and thus at conditions drastically different from ours. [51] provide examples of various shapes obtained at a constant temperature (120 °C) but for various synthesis durations (3 to 24 h). [57] report various shapes of PbS nanoparticles (cubic, needle-like, spherical) due to the use of a number of capping agents. Wang et al. (2003) [52] who conducted their syntheses at the constant 120 °C temperature with various starting agents and several solvents, including water, obtained various types of PbS dendrites and other shapes. Hence, all these experiments show that there is no clear relationship between the parameters of the synthesis and the shapes obtained.

At Soultz, the solvent of the brine is water, but the inhibitors that are injected in the process are composed of organic molecules which play a role in the crystallization of galena. In fact, when no such agent is used, mostly sulfates (barite group (Ba,Sr,Ca)SO₄ solid-solution) are produced in the URG [12] and at Soultz in particular [27,31,33].

In the case of galena crystallization (use of inhibitors), when it occurs as cubes or derived shapes it results from a preferential growth along $\langle 111 \rangle$ direction inducing {100} faces to develop, which is not consistent with the major growth in $\langle 100 \rangle$ direction deduced from XRD. However, this is not abnormal since cubes and cubic-derived shapes are rarely found. Indeed, [54] proposed relations between crystal structure and crystal morphology on an energy basis. According to [54] the morphology of a crystal is governed by chains of strong bonds running through the structure, called periodic bond chain (P.B.C.) vectors. Crystal faces are divided into three classes. Flat faces (F) contain two or more coplanar P.B.C. vectors and are the most important faces. Stepped faces (S) are parallel to only one P.B.C. vector and are of medium importance. Kinked (K) faces are parallel to no P.B.C. vector and are very rare or do not occur at all. For PbS crystals that belong to the fcc structure, F faces are {100}, S faces are {110} and K faces are {111}. According to Hartmann's and Perdok's theory [54] only F faces should appear at equilibrium, giving cubes as in Figure 16. In fact, during crystal growth, impurities such as the inhibitors used in the geothermal industrial process at Soultz, or As and Sb ions present in the geothermal brine, are adsorbed on K faces ({111} in this case) which promotes their development, together with that of cube (faces {100}), inducing the formation of cuboctahedrons (Figure 17A). In other cases (Figure 17B), only faces {111} develop, leading to octahedral crystals. Crystals with such planar faces (cubes, cuboctahedron, octahedron) appear in conditions of small growth rate, here in laminar flow, as opposed to dendrites which are obtained by a high growth rate in a single direction, here in the hottest and most turbulent flow. As seen in Figure 19, when a crystal grows, the faces which are kept at the end are those where the setting up of atoms is the slowest (faces {100} in the case of galena cubes). Indeed [55] indicates that the faster the growth in a given direction, the smaller the area of the face developed perpendicular to that direction (Figure 19, face {111}).

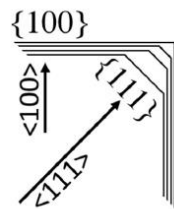


Figure 19. Schematic growth of a crystal face {xxx} as a function of the atom setting up rate in the direction perpendicular to that face <xxx>.

Hence, F faces are visible in the final crystal. Changes in morphology are related to F faces showing a different (higher) growth rate. As a consequence, dendrites and needles that develop in a preferential direction grow very quickly (turbulence and/or high temperature) while cubes and derived shapes grow slowly, in laminar flow and at temperatures which can be low (down to 40 °C). In Figure 14C, needles developed in three perpendicular directions grow on a preexisting 30µm wide galena cube. This succession of shapes might be controlled by very local changes in the parameters of the surrounding medium.

Table 8 summarizes the occurrence of galena crystal shapes.

Table 8. Occurrence of galena crystal shapes as a function of their location, the temperature and the flow.

Crystal Shape	Abundance among Location Samples	Temperature (°C)	Flow	
Dendrite	+	Industrial, Entrance(flange)	75–65	Turbulent
Needle	++	Water box, flange, tubes	65–40	Turbulent, laminar
Coral	+++	Water box, flange, tubes	65–40	Turbulent, laminar
Cube	+	Water box, flange, tubes	65–40	Turbulent, laminar
Fibro-radiated	++	Water box, flange, tubes	65–40	Turbulent, laminar

Thus, except for dendrites, the location and hence turbulence degree of the place, nature of alloy and temperature are not controlling the shape of PbS crystals that formed in the SHEx, which can be found mixed at given places (Table 2) as opposed to what is described in the literature for syntheses in the laboratory. This might be due to the fact that in the SHEx, the parameters are not controlled as in the laboratory, which allows various shapes to crystallize at the same place. In addition, the temperature range is low, from 65 °C to 40 °C and is probably not discriminating for promoting specific crystal shapes.

The presence of As sulfosalts such as dufrénoyite, and maybe others containing Sb as indicated by the EDS semi-quantitative analyses (Table 5), might also be responsible for some of the shapes that were encountered during this study. However, it was not possible to identify them during SEM-EDS survey.

6. Conclusions and Outlook

One way to improve the energy production of geothermal power plants in the URG is to decrease the reinjection temperature. This might induce several problems in the power plants including cooling of the rock reservoir, promotion of a chemical disequilibrium into it, and increase of scaling phenomenon as observed for the samples collected in the SHEx at Soultz. When inhibitors are used, those scales are mostly composed of lead sulfide (galena, PbS) together with minor sulfosalts. The galena crystals collected at the interface between the metals from which the SHEx was made and the geothermal fluid, after three months of operation, show a homogeneous chemical composition including As and Sb, whatever the alloy on which the scales deposited and whatever the temperature (65 °C to

40 °C). Thus, there is no influence of the alloy on the scaling phenomenon, as opposed to what is observed for corrosion. Those galena crystals show several shapes that cannot be evidently connected to the alloy, the temperature or the large-scale flow regime, except for dendrites. Indeed, the alloy is insulated from the fluid by the very first layers of deposit, the temperature does not vary drastically from the entrance to the exit of the SHEx (25 °C gradient only, at rather low temperatures), the chemical composition of the brine is constant during the industrial process (Ravier, personal communication), and after three months of operation, the scales are rough at the contact with the fluid and the flow is certainly very slow because of this rugosity, allowing the slow growth of crystals with various shapes including cubes and derived shapes. Dendrites are the only shape to be found exclusively at the highest temperature (65–75 °C) and in a turbulent environment. To go further, investigation could be performed with Raman to characterize the sulfosalts likely present in the samples, and with XANES to assess the oxidation state of As, Pb and Sb. In addition, statistics of the various shapes encountered at the different locations ought to be performed to pinpoint likely influencing parameters at the micro-scale. Furthermore, one could also conduct laboratory experiments with the brine produced from the geothermal reservoir, and with varying parameters such as temperature, alloy, speed of flow rate, type and amounts of inhibitors, etc. Finally, at present, scales produced at Soultz have to be disposed of as waste due to their toxicity. One can rather imagine an industrial valorization, especially for those deposited at the entrance and exit of the exchangers where mostly dendrites are formed, which is a sought-after shape for the industry [52].

Author Contributions: Conceptualization, B.A.L. and M.L.; methodology, G.R., O.S., B.A.L., É.D., A.G., X.S.; validation, J.M., C.B., É.D., A.G., Ayming and H2020 MEET partners; formal analysis, B.A.L.; investigation, B.A.L.; resources, G.R., O.S., J.M., C.B., É.D.; data curation, B.A.L. and M.L.; writing—original draft preparation, B.A.L. and M.L.; writing—review and editing, R.L.H., J.M., C.B., G.R., O.S., É.D., G.T., X.S., A.G.; supervision, B.A.L., A.G., G.T.; project administration, A.G., É.D., G.T.; funding acquisition, all the co-authors and H2020 MEET consortium. All authors have read and agreed to the published version of the manuscript. Authorship is limited to those who have contributed substantially to the work reported.

Funding: This project has received funding from the European Union’s Horizon 2020 research and innovation program under grant agreement No 792037 (MEET project).

Acknowledgments: The authors thank the Soultz-Sous-Forêts site owner, GEIE Exploitation Minière de la Chaleur, for giving access to their geothermal installation. Valérie Granger (Orano) is acknowledged for XRD analysis and its interpretation. We gratefully thank Jean Hérisson (Ayming) for reviewing this paper as well as relationship with European Commission and overview of the H2020 MEET project. We gratefully acknowledge the two reviewers for their helpful review which greatly helped us to improve the manuscript.

Conflicts of Interest: The authors declare no conflict of interest. The funders had no role in the design of the study; in the collection, analyses, or interpretation of data; in the writing of the manuscript, or in the decision to publish the results.

References

1. Assad, M.E.H.; Bani-Hani, E.; Khalil, M. Performance of Geothermal Power Plants (Single, Dual, and Binary) to Compensate for LHC-CERN Power Consumption: Comparative Study. *Geotherm. Energy* **2017**, *5*, 17. [[CrossRef](#)]
2. Spinthaki, A.; Kamaratou, M.; Skordalou, G.; Petratos, G.; Tramaux, A.; David, G.; Demadis, K.D. A Universal Scale Inhibitor: A Dual Inhibition/Dispersion Performance Evaluation under Difficult Brine Stresses. *Geothermics* **2021**, *89*, 101972. [[CrossRef](#)]
3. van der Zwaan, B.; Dalla Longa, F. Integrated Assessment Projections for Global Geothermal Energy Use. *Geothermics* **2019**, *82*, 203–211. [[CrossRef](#)]
4. Shannon, D.W. Economic Impact of Corrosion and Scaling Problems in Geothermal Energy Systems. Master’s Thesis, Battelle Pacific Northwest Labs, Richland, WA, USA, 1975.
5. Tardiff, G.E. Using Salton Sea Geothermal Brines for Electrical Power: A Review of Progress in Chemistry and Materials Technology, 1976 Status. In Proceedings of the Twelfth Intersociety Energy Conversion Engineering Conference, Washington, DC, USA, 28 August–2 September 1977.

6. Criaud, A.; Fouillac, C. Sulfide Scaling in Low Enthalpy Geothermal Environments: A Survey. *Geothermics* **1989**, *18*, 73–81. [[CrossRef](#)]
7. Scheiber, J.; Nitschke, F.; Seibt, A.; Genter, A. Geochemical and Mineralogical Monitoring of the Geothermal Power Plant in Soultz-Sous-Forêts (France). In Proceedings of the 37th Workshop on Geothermal Reservoir Engineering, Stanford, CA, USA, 30 January–1 February 2012; pp. 1033–1042.
8. Ngothai, Y.; Yanagisawa, N.; Pring, A.; Rose, P.; O'Neill, B.; Brugger, J. Mineral Scaling in Geothermal Fields: A Review. In Proceedings of the 2010 Australian Geothermal Energy Conference, Adelaide, Australia, 17–19 November 2010; pp. 405–409.
9. Skinner, B.J.; White, D.E.; Rose, H.J.; Mays, R.E. Sulfides Associated with the Salton Sea Geothermal Brine. *Econ. Geol.* **1967**, *62*, 316–330. [[CrossRef](#)]
10. Sanjuan, B.; Millot, R.; Innocent, C.; Dezayes, C.; Scheiber, J.; Brach, M. Major Geochemical Characteristics of Geothermal Brines from the Upper Rhine Graben Granitic Basement with Constraints on Temperature and Circulation. *Chem. Geol.* **2016**, *428*, 27–47. [[CrossRef](#)]
11. Baticci, F.; Genter, A.; Huttenloch, P.; Zorn, R. Corrosion and Scaling Detection in the Soultz EGS Power Plant, Upper Rhine Graben, France. In Proceedings of the World Geothermal Congress, WGC2010, Bali, Indonesia, 25–30 April 2010.
12. Haas-Nüesch, R.; Heberling, F.; Schild, D.; Rothe, J.; Dardenne, K.; Jähnichen, S.; Eiche, E.; Marquardt, C.; Metz, V.; Schäfer, T. Mineralogical Characterization of Scalings Formed in Geothermal Sites in the Upper Rhine Graben before and after the Application of Sulfate Inhibitors. *Geothermics* **2018**, *71*, 264–273. [[CrossRef](#)]
13. Mouchot, J.; Genter, A.; Cuenot, N.; Scheiber, J.; Seibel, O.; Bosia, C.; Ravier, G. First Year of Operation from EGS Geothermal Plants in Alsace, France: Scaling Issues. In Proceedings of the 43rd Workshop on Geothermal Reservoir Engineering, Stanford, CA, USA, 12–14 February 2018.
14. Dalmais, E.; Genter, A.; Trullenque, G.; Leoutre, E.; Leiss, B.; Wagner, B.; Mints, A.C.; Bär, K.; Rajsl, I. MEET Project: Toward the Spreading of EGS across Europe. In Proceedings of the European Geothermal Congress, Den Haag, The Netherlands, 11–14 June 2019.
15. Trullenque, G.; Genter, A.; Leiss, B.; Wagner, B.; Bouchet, R.; Léoutre, E.; Malnar, B.; Bär, K.; Rajsl, I. Upscaling of EGS in Different Geological Conditions: A European Perspective. In Proceedings of the 43rd Workshop on Geothermal Reservoir Engineering, Stanford, CA, USA, 12–14 February 2018.
16. Ravier, G.; Seibel, O.; Pratiwi, A.S.; Mouchot, J.; Genter, A.; Ragnarsdóttir, K.R.; Sengelen, X. Towards an Optimized Operation of the EGS Soultz-Sous-Forêts Power Plant (Upper Rhine Graben, France). In Proceedings of the European Geothermal Congress, Den Haag, The Netherlands, 11–14 June 2019.
17. Ledéser, B.A.; Hébert, R.L. How Can Deep Geothermal Projects Provide Information on the Temperature Distribution in the Upper Rhine Graben? The Example of the Soultz-Sous-Forêts-Enhanced Geothermal System. *Geosciences* **2020**, *10*, 459. [[CrossRef](#)]
18. Cuenot, N.; Charléty, J.; Dorbath, L.; Haessler, H. Faulting Mechanisms and Stress Regime at the European HDR Site of Soultz-Sous-Forêts, France. *Geothermics* **2006**, *35*, 561–575. [[CrossRef](#)]
19. Gunnarsson, I.; Arnórsson, S. Impact of Silica Scaling on the Efficiency of Heat Extraction from High-Temperature Geothermal Fluids. *Geothermics* **2005**, *34*, 320–329. [[CrossRef](#)]
20. Haklıdır, F.S.T.; Balaban, T.Ö. A Review of Mineral Precipitation and Effective Scale Inhibition Methods at Geothermal Power Plants in West Anatolia (Turkey). *Geothermics* **2019**, *80*, 103–118. [[CrossRef](#)]
21. Hardardóttir, V.; Árnannsson, H.; Þórhallsson, S. Characterization of Sulfide-Rich Scales in Brine at Reykjanes. In Proceedings of the World Geothermal Congress 2005, Antalya, Turkey, 24–29 April 2005.
22. Jamer, J.; Zarrouk, S.J.; Mroczek, E. Mineral Scaling in Two-Phase Geothermal Pipelines: Two Case Studies. *Geothermics* **2018**, *72*, 1–14. [[CrossRef](#)]
23. Köhl, B.; Grundy, J.; Baumann, T. Rippled Scales in a Geothermal Facility in the Bavarian Molasse Basin: A Key to Understand the Calcite Scaling Process. *Geotherm. Energy* **2020**, *8*, 1–27. [[CrossRef](#)]
24. Kristmannsdóttir, H. Types of Scaling Occurring by Geothermal Utilization in Iceland. *Geothermics* **1989**, *18*, 183–190. [[CrossRef](#)]
25. Mundhenk, N. Corrosion and Scaling in Utilization of Geothermal Energy in the Upper Rhine Graben. Ph.D. Thesis, Karlsruher Institut für Technologie (KIT), Karlsruhe, Germany, 2013. [[CrossRef](#)]
26. Nitschke, F.; Scheiber, J.; Kramar, U.; Neumann, T. Formation of Alternating Layered Ba-Sr-Sulfate and Pb-Sulfide Scaling in the Geothermal Plant of Soultz-Sous-Forêts. *Neues Jahrb. Für Mineral. Abh. J. Mineral. Geochem.* **2014**, *191*, 145–156. [[CrossRef](#)]
27. Raymond, J.; Williams-Jones, A.E.; Clark, J.R. Mineralization Associated with Scale and Altered Rock and Pipe Fragments from the Berlin Geothermal Field, El Salvador; Implications for Metal Transport in Natural Systems. *J. Volcanol. Geotherm. Res.* **2005**, *145*, 81–96. [[CrossRef](#)]
28. Reyes, A.G.; Trompeter, W.J.; Britten, K.; Searle, J. Mineral Deposits in the Rotokawa Geothermal Pipelines, New Zealand. *J. Volcanol. Geotherm. Res.* **2003**, *119*, 215–239. [[CrossRef](#)]
29. Genter, A.; Cuenot, N.; Melchert, B.; Moeckes, W.; Ravier, G.; Sanjuan, B.; Sanjuan, R.; Scheiber, J.; Schill, E.; Schmittbuhl, J. Main achievements from the multi-well EGS Soultz project during geothermal exploitation from 2010 and 2012. In Proceedings of the European Geothermal Congress, Pisa, Italy, 3–7 June 2013.
30. Scheiber, J.; Seibt, A.; Birner, J.; Genter, A.; Cuenot, N.; Moeckes, W. Scale Inhibition at the Soultz-Sous-Forêts (France) EGS Site: Laboratory and on-Site Studies. In Proceedings of the World Geothermal Congress 2015, Melbourne, Australia, 16–24 April 2015.

31. Sanjuan, B.; Millot, R.; Dezayes, C.; Brach, M. Main Characteristics of the Deep Geothermal Brine (5 Km) at Soultz-Sous-Forêts (France) Determined Using Geochemical and Tracer Test Data. *Comptes Rendus Geosci.* **2010**, *342*, 546–559. [CrossRef]
32. Cuenot, N.; Goerke, X.; Guery, B.; Bruzac, S.; Sontot, O.; Meneust, P.; Maquet, J.; Vidal, J. Evolution of the Natural Radioactivity within the Soultz Geothermal Installation. In Proceedings of the Soultz Geothermal Conference 2011, Soultz-Sous-Forêts, France, 5–6 October 2011; Volume 5, p. 19.
33. Mouchot, J.; Scheiber, J.; Florencio, J.; Seibt, A.; Jähnichen, S. Scale and Corrosion Control Program, Example of Two Geothermal Plants in Operation in the Upper Rhine Graben. In Proceedings of the European Geothermal Congress 2019, Den Haag, The Netherlands, 11–14 June 2019.
34. He, S.; Oddo, J.E.; Tomson, M.B. The Inhibition of Gypsum and Barite Nucleation in NaCl Brines at Temperatures from 25 to 90 °C. *Appl. Geochem.* **1994**, *9*, 561–567. [CrossRef]
35. Karlsdottir, S.N.; Ragnarsdottir, K.R.; Thorbjornsson, I.O.; Einarsson, A. Corrosion Testing in Superheated Geothermal Steam in Iceland. *Geothermics* **2015**, *53*, 281–290. [CrossRef]
36. Karlsdottir, S.N.; Thorbjornsson, I.O.; Ragnarsdottir, K.R.; Einarsson, A. Corrosion Testing of Heat Exchanger Tubes in Steam from the IDDP-1 Exploratory Geothermal Well in Krafla, Iceland. In Proceedings of the CORROSION 2014, San Antonio, TX, USA, 9–13 March 2014.
37. Ravier, G.; Huttenloch, P.; Scheiber, J.; Perrot, V.; Sioly, J.L. Design, Manufacturing and Commissioning of the ECOGI's Heat Exchangers at Rittershoffen (France): A Case Study. In Proceedings of the European Geothermal Conference, Strasbourg, France, 19–24 September 2016.
38. Apopei, A.I.; Damian, G.; Buzgar, N.; Buzatu, A. Mineralogy and Geochemistry of Pb–Sb/As–Sulfosalts from Coranda-Hondol Ore Deposit (Romania)—Conditions of Telluride Deposition. *Ore Geol. Rev.* **2016**, *72*, 857–873. [CrossRef]
39. Martínez-Abad, I.; Cepedal, A.; Arias, D.; Fuertes-Fuente, M. The Au–As (Ag–Pb–Zn–Cu–Sb) Vein-Disseminated Deposit of Arcos (Lugo, NW Spain): Mineral Paragenesis, Hydrothermal Alteration and Implications in Invisible Gold Deposition. *J. Geochem. Explor.* **2015**, *151*, 1–16. [CrossRef]
40. Pitcairn, I.K.; Olivo, G.R.; Teagle, D.A.; Craw, D. Sulfide Evolution during Prograde Metamorphism of the Otago and Alpine Schists, New Zealand. *Can. Mineral.* **2010**, *48*, 1267–1295. [CrossRef]
41. Medunić, G.; Bucković, D.; Crnić, A.P.; Bituh, T.; Srček, V.G.; Radošević, K.; Bajramovic, M.; Zgorelec, Z. Sulfur, Metal (Loid) s, Radioactivity, and Cytotoxicity in Abandoned Karstic Raša Coal-Mine Discharges (the North Adriatic Sea). *Rud. Geološko Naft. Zb.* **2020**, *35*. [CrossRef]
42. Majzlan, J.; Drahota, P.; Filippi, M. Parageneses and Crystal Chemistry of Arsenic Minerals. *Rev. Mineral. Geochem.* **2014**, *79*, 17–184. [CrossRef]
43. Karakaya, N.; Karakaya, M.C. Toxic Element Contamination in Waters from the Massive Sulfide Deposits and Wastes around Giresun, Turkey. *Turk. J. Earth Sci.* **2014**, *23*, 113–128. [CrossRef]
44. Song, C.; Jiang, L.; Zhang, Y.; Pang, L.; Wang, D. Shape Controllable Growth of PbS Polyhedral Crystals. *Cryst. Res. Technol.* **2012**, *47*, 1008–1013. [CrossRef]
45. Ding, B.; Shi, M.; Chen, F.; Zhou, R.; Deng, M.; Wang, M.; Chen, H. Shape-Controlled Syntheses of PbS Submicro-/Nano-Crystals via Hydrothermal Method. *J. Cryst. Growth* **2009**, *311*, 1533–1538. [CrossRef]
46. Ni, Y.; Wei, X.; Hong, J.; Ma, X. Hydrothermal Preparation of PbS Crystals and Shape Evolution. *Mater. Res. Bull.* **2007**, *42*, 17–26. [CrossRef]
47. Radosavljević-Mihajlović, A.S.; Stojanović, J.N.; Radosavljević, S.A.; Pačevski, A.M.; Vuković, N.S.; Tošović, R.D. Mineralogy and Genetic Features of the Cu–As–Ni–Sb–Pb Mineralization from the Mlakva Polymetallic Deposit (Serbia)—New Occurrence of (Ni–Sb)-Bearing Cu–Arsenides. *Ore Geol. Rev.* **2017**, *80*, 1245–1258. [CrossRef]
48. Adamczyk, Z.; Nowińska, K.; Melaniuk-Wolny, E.; Szweczenko, J. Variation of the Content of Accompanying Elements in Galena in Pyrometallurgical Process of Zinc and Lead Production. *Acta Montan. Slovaca* **2013**, *18*, 158–163.
49. Hagni, R.D. Platy Galena from the Viburnum Trend, Southeast Missouri: Character, Mine Distribution, Paragenetic Position, Trace Element Content, Nature of Twinning, and Conditions of Formation. *Minerals* **2018**, *8*, 93. [CrossRef]
50. Singh, K.; McLachlan, A.A.; Marangoni, D.G. Effect of Morphology and Concentration on Capping Ability of Surfactant in Shape Controlled Synthesis of PbS Nano- and Micro-Crystals. *Colloids Surf. A Physicochem. Eng. Asp.* **2009**, *345*, 82–87. [CrossRef]
51. Zhu, J.; Duan, W.; Sheng, Y. Uniform PbS Hopper (Skeletal) Crystals Grown by a Solution Approach. *J. Cryst. Growth* **2009**, *311*, 355–357. [CrossRef]
52. Wang, D.; Yu, D.; Shao, M.; Liu, X.; Yu, W.; Qian, Y. Dendritic Growth of PbS Crystals with Different Morphologies. *J. Cryst. Growth* **2003**, *257*, 384–389. [CrossRef]
53. Obaid, A.S.; Mahdi, M.A.; Hassan, Z. Nanocoral PbS Thin Film Growth by Solid-Vapor Deposition. *Optoelectron. Adv. Mater. Rapid Commun.* **2012**, *6*, 422–426.
54. Hartman, P.; Perdok, W.G. IUCr On the Relations between Structure and Morphology of Crystals. Available online: <https://scripts.iucr.org/cgi-bin/paper?a01327> (accessed on 11 December 2020).
55. Pandey, G.; Shrivastav, S.; Sharma, H.K. Role of Solution PH and SDS on Shape Evolution of PbS Hexagonal Disk and Star/Flower Shaped Nanocrystals in Aqueous Media. *Phys. E Low Dimens. Syst. Nanostruct.* **2014**, *56*, 386–392. [CrossRef]

56. Esmaeili, E.; Sabet, M.; Salavati-Niasari, M.; Saberyan, K. Synthesis and Characterization of Lead Sulfide Nanostructures with Different Morphologies via Simple Hydrothermal Method. *High. Temp. Mater. Process.* **2016**, *35*, 559–566. [[CrossRef](#)]
57. Patel, A.A.; Wu, F.; Zhang, J.Z.; Torres-Martinez, C.L.; Mehra, R.K.; Yang, Y.; Risbud, S.H. Synthesis, Optical Spectroscopy and Ultrafast Electron Dynamics of PbS Nanoparticles with Different Surface Capping. *J. Phys. Chem. B* **2000**, *104*, 11598–11605. [[CrossRef](#)]


4.5.3.1.3 Decision Making Tool development

Besides reservoir geology and scalings development within heat exchangers, I have also been involved in the development of a multiple criteria decision making tool for assessment of geothermal projects (Raos et al., 2019). This tool is designed to help investors and decision makers in terms of risk mitigation and is available for download at no charge (<https://www.meet-h2020.com/project-results/decision-making-support-tool/>).

The algorithm uses technical specifications, geological characteristics, spatial data, energy and heat price plus social and environment impact as input. My role within this project was to check consistency of the available geological data.

Article

Multiple-Criteria Decision-Making for Assessing the Enhanced Geothermal Systems

Sara Raos ^{1,*} , Perica Ilak ¹, Ivan Rajšl ¹, Tena Bilić ¹ and Ghislain Trullenque ²

¹ Faculty of Electrical Engineering and Computing, University of Zagreb, Unska 3, 10000 Zagreb, Croatia; perica.ilak@fer.hr (P.I.); ivan.rajsl@fer.hr (I.R.); tena.bilic@fer.hr (T.B.)

² Département GEOS UniLaSalle, Équipe B2R, 19 rue Pierre Waguet, 60000 Beauvais, France; ghislain.trullenque@unilasalle.fr

* Correspondence: sara.raos@fer.hr

Received: 1 April 2019; Accepted: 24 April 2019; Published: 26 April 2019



Abstract: This paper presents the main features of a multiple-criteria decision-making tool for economic and environmental assessment of enhanced geothermal systems projects. The presented holistic approach takes into account important influencing factors such as technical specifications, geological characteristics, spatial data, energy and heat prices, and social and environmental impact. The multiple-criteria decision-making approach uses a weighted decision matrix for evaluating different enhanced geothermal systems alternatives based on a set of criteria which are defined and presented in this paper. The paper defines and quantifies new criteria for assessing enhanced geothermal systems for a particular site. For evaluation of the relative importance of each criterion in decision making, the weight is associated with each of the listed criteria. The different scenarios of end-use applications are tested in the case study. Finally, in the case study, the data and statistics are collected from real geothermal plants. The case study provides results for several scenarios and the sensitivity analysis based on which the approach is validated. The proposed method is expected to be of great interest to investors and decision makers as it enables better risk mitigation.

Keywords: enhanced geothermal systems; economic assessment; environmental assessment; optimization; levelized cost of energy

1. Introduction

The growing concern around rising energy costs, the dependence on fossil fuels, and the environmental impact of energy supply makes it necessary to find economical and environment-friendly energy alternatives. The largest share in newly-installed power capacities around the world is covered by wind and solar plants. Besides those two renewables, geothermal energy also represents large untapped renewable potential and low environmental impact, especially regarding greenhouse gas emissions. Despite many other advantages, like a reliable, constant baseload electricity or direct heat usage and a small land area footprint, geothermal energy is nowadays still a small contributor to the primary energy consumption. Its worldwide installed capacity is estimated at 12.9 GW [1] and share in total electricity generation of less than 1%. The main reasons are related to the risks and uncertainties of sustained fluid provision from the reservoirs and large upfront costs associated with exploration, well drilling and stimulation [2]. Furthermore, the traditional hydrothermal systems, based on mature and well-known technology, enable the exploitation of mainly high-enthalpy reservoirs, whereas a huge geothermal potential is present in low permeable, low porosity and low to medium enthalpy bedrock. In order to enhance reservoir productivity in low permeable rocks, Enhanced Geothermal Systems (EGS) technology has been developed. The EGS technique consists of creating a fracture system in the targeted geological formation through which geothermal fluid can circulate. Hydraulic

and chemical stimulations are used to create these fractures. The thermal energy stored in the hot rock mass gets extracted by circulating the fluid through the reservoir. The circulation of the fluid is obtained with different extraction technologies, among which the most prominent are so-called injector-producer doublets or borehole heat exchangers.

Aside from exploiting the geothermal heat from low permeable bedrock, additional energy can be recovered from thousands of mature or abandoned oil wells. Mature oil fields have been used for production for a long time, but their production has reached its peak and has started to decline. The typical production pattern of most oil producing wells displays an increase of water with time, from 0% initially to a point, typically above 95%, when it is not economic to produce the remaining oil. Mature oil fields account for more than 70% of world's oil and gas production, and regarding European oil fields, it is expected that wells are nowadays producing much more water than oil, with average water to a fluid ratio of 90% and with temperature up to 90 °C and sometimes higher. This remaining heat is currently usually wasted, as it is simply re-injected into the reservoir for pressure maintenance or sweep purpose. There are several studies concentrating on energy recovery from mature or abandoned oil fields. In Reference [3] a preliminary assessment of the potential for geothermal exploitation of the co-produced water from wells in the Villafortuna-Trecate oil field in Italy was made by comparing three different implementation scenarios for the possible use of the co-produced hot water: direct use district heating (DH), electric power generation through Organic Rankine Cycle (ORC) plant, and co-generation of heat and power. In Reference [4] energy from abandoned oil and gas reservoirs is used by oxidizing the residual oil with the injected air. In Reference [5] a simulation for the determination of geothermal power production from abandoned oil wells by injecting and retrieving a secondary fluid is performed. Technical feasibility study of acquiring geothermal energy from existing abandoned oil and gas wells is conducted in Reference [6]. Computational results indicate that the geothermal energy produced from abandoned wells depends largely on the flow rate of the fluid and the geothermal gradient. Moreover, the results also indicate that the distance of the two proposed wells should not be less than 40 m to avoid their interrelationships. A Poland case study on the usage of abandoned oil and gas wells for recovering geothermal heat is given in Reference [7]. Some important aspects of power generation using the co-produced hot oil and liquid, with temperatures around 120 °C, from Huabei oil field were studied in Reference [8]. Study on the geothermal power generation using abandoned oil wells is done in Reference [9] with isobutane as working fluid. Also, some interesting insights are given regarding how to increase obtained heat. The results in Reference [10] show that it is necessary to consider the oil and gas saturation while estimating geothermal reserve in oil and gas reservoirs. In Reference [11] the Croatian case of the binary power plant installed in Velika Ciglina is described and in Reference [12] the economic feasibility of this power plant is presented. Moreover, the thermodynamic cycle optimization of Velika Ciglina power plant is conducted in Reference [13]. The explorations in Croatia for the national oil company showed a very high temperature of geothermal water in the oil negative well (about 170 °C). Nowadays, the power plant at Velika Ciglina is the largest ORC geothermal power plant in Europe, with design conditions that allow for a 15 MWe installed capacity. The power plant is ORC using the isopentane as a working fluid and an air-cooling system that was chosen for the condensing process. Currently, the plant is producing electricity but there is still enough potential capacity for a DH, for which studies are currently being carried out. Furthermore, in Reference [14] a global review of 18 significant EGS sites and technologies that have been applied in the EU, Japan, South Korea, Australia, and the USA was given. The results from this study show that the site characteristics are a key factor of successful EGS development. It was concluded that for sites suitable for EGS, the local geological conditions (stress field, temperature field, rock composition, the range of existing permeability, reservoir properties, etc.) mostly determining the amount of recovered geothermal heat by means of EGS techniques.

Many previous studies have focused either on economic assessment [15,16] or environmental assessment based on the life cycle environmental impact of geothermal power generation as studied in References [17,18]. A review in Reference [19] presents an analysis of existing software packages

for estimating and simulating costs, conventionally used in studying EGS facilities. The focus of the review is the top European software EURONAUT and the US GEOPHIRES package. EURONAUT is implemented based on the studies conducted at the EGS plant in Soultz-sous-Forêts. The root of the program is economic estimation via discontinuous cash flows, and all other calculations are developed as separate modules that can be joined together via various interfaces [19]. GEOPHIRES, however, is a software tool that combines reservoir, wellbore, and power plant models with capital and operating costs, correlations, and financial levelized cost model to assess the technical and economic performance of EGS. This software differs from the Geothermal Energy Technology Evaluation Model (GETEM) [20] and Hot Dry Rock economic model (HDRec) [21], which are two examples of technological/economic models initially used to simulate the operation of EGS plant. The distinction is mainly due to the fact that the currently available packages do not permit the simulation of not only electricity production but also direct-use-heat production and a combined heat and power (CHP) production, which was implemented in GEOPHIRES software.

The rate of geothermal development and implementation has been conditioned not only by mentioned geological conditions, drilling, and stimulation technologies, but also by legal frameworks, and regulative and social constraints. An overview of legislative and socio-economic issues of geothermal energy is available in References [22,23]. More on public and political acceptance issues could be found in Reference [24]. Establishing functional legal frameworks remains a challenge for countries seeking to develop their first geothermal projects to this day.

EGS technology enables exploitation of geothermal energy at a wide range of temperature and on a large geographic scale. However, EGS technology is not yet mature enough to be commercially competitive with other renewable resources. Almost all the EGS pilot plants, currently operating, need to be jointly funded by governments in order to operate or/and develop. Finally, the risks, uncertainties, and costs related to EGS projects mean that it is essential to conduct exhaustive studies involving modelling and simulation of EGS geothermal reservoirs and above-ground power plant facility at any location where it is desired to develop this kind of technology. This requires a holistic approach which should consider different scenarios and various influencing factors, from choosing the right extraction technology to the analysis of the energy prices and market signals. Given the fact that a taken decision will trigger financial consequences over a long period of time, the software for estimating and simulating the costs is an essential tool in order to successfully choose and face an EGS project. This paper presents the concept of such multi-scale Decision-Making Support Tool for Optimal Usage of Geothermal Energy (DMS-TOUGE) and multiple-criteria decision-making (MCDM) matrix that will be fully developed as part of the Horizon 2020 project: Multidisciplinary and multi-context demonstration of EGS exploration and Exploitation Techniques and potentials (MEET, GA No 792037).

The main objective of this work is to present the MCDM matrix and selected weighted criteria used to evaluate and compare different EGS sites and technologies and to demonstrate this MCDM matrix as a means of conducting a rapid preliminary evaluation of the technical and economic feasibility of an EGS project with related environmental and social impact. The MCDM matrix is used in this work for assessment of four different geothermal sites, and by using real data for each of the selected sites the comparison between sites was enabled.

The contribution of this work in relation to other selection matrices is that it provides expanded and detailed criteria related to environmental and social impact giving the necessary emphasis on so far neglected important aspects for successful completion of geothermal projects. Moreover, the novelty of this work is that by combining technical, economic, environmental, and social aspects of geothermal projects, the MCDM presented in this work gives a comprehensive assessment of EGS projects. Namely, since the EGS related projects are high-insensitive investments, for a DM interested in sustainably operate an EGS-plant close to densely populated areas, it is imperative to include many different aspects in techno-economic analysis and decision-making process. It is, however, challenging to predict all possible scenarios and influencing factors. Therefore, the process of developing a DMS-TOUGE and related MCDM matrix is a multiple-stage process. At this stage of the

development and modelling process, the tool is intended for an evaluation of an EGS project at early development stage, meaning that a great number of the variables should be approximatively forecasted and estimated. Using optimization, the adequate evaluation of the production for chosen site and technology can be displayed. With progress in time, the tool will be useful for upgrade or extension of an already existing chosen geothermal site. In that case, the DM can provide more detailed information about EGS power plant operating cycle since the plant has already been generating electricity or heat for direct usage.

The rest of paper is organised as follows. Methodology, background, and main components of DMS-TOUGE are explained in Section 2. In the same chapter one of the main component of DMS-TOUGE, the MCDM is presented in more detail. Section 3 describes in detail the MCDM matrix and its criterions used in this paper for the evaluation of different EGS sites. Section 4 describes the case study examples, presents the scenario results, and gives the sensitivity analysis based on these results. The obtained results are discussed. Section 5 concludes the paper and gives the main directions for future development and research.

2. Background

2.1. Decision-Making Support Tool for Optimal Usage of Geothermal Energy (DMS-TOUGE)

The DMS-TOUGE represents a holistic approach for economic and environmental assessment of EGS sites that provides the capability of simultaneous site-specific environmental and economic analysis, among others considering low-enthalpy energy from co-produced hot water during oil fields exploitation. It considers existing infrastructure with possible extension or upgrades, the possible costs of future facilities, co-use/re-use of existing mature or abandoned oil fields boreholes, and other different geological contexts. Furthermore, the DMS-TOUGE will be useful for the decision makers (DM) involved in activities associated with: applications of EGS techniques to currently unexploited reservoir types (such as Variscan orogenic belt) by means of injector-producer doublets, increasing the productivity of existing power plants by reinjection of geothermal fluids with a colder temperature combined with the generation from the small-scale ORC units, and usage of hot fluids from mature and abandoned oil fields for electricity or heat production.

The DMS-TOUGE tool will use both external data entered directly by DM and internal data from database, depending on the quantity and quality of input data entered by a DM, such as: water temperature, geothermal capacity, electricity and heat prices, injection water flow rate values, turbine technology specifications, generator type, heat exchangers, working fluid, type of extraction technology (injector-producer doublets, deep borehole heat exchanger), risk analysis (thermal effect, possible appearance of scaling, radioactive deposits, mechanical evolution of casing) or environmental data (CO₂ emission schemes, security of energy supply issues). In order to better anticipate and include future events, different possible scenarios are evaluated and accounted and accordingly the tool can use forecasted data (load, prices, etc.) which can occur over the operation lifetime of EGS technology. Some of the most important environmental (external) factors that are integrated into the tool are: proximity of nearest suitable power system grid and/or nearest suitable district heating system where EGS could be integrated into, proximity and availability of water for water cooling mechanism, possibility for different usage of geothermal energy for agricultural, industrial and district heating needs, and geopolitical environment and relevant legislative framework. The DMS-TOUGE relies on optimization algorithms to value/quantify different technologies. It will be used to quantify environmental and social impacts and calculate system levelized cost of energy (sLCOE) of technology in order to find the best-suited option for a given site. Moreover, when assessing the best-suited option and technology for a given site, malicious and faulty components should be taken into account since, in reality, it is illusory to expect that all components of the geothermal system are functioning without problems. An example of addressing this issue is presented in Reference [25]. Therefore, it is mandatory to include any possible risks involved with different components of the system. As an integral part of

the DMS-TOUGE, any possible risks will be analyzed, such as market (price) risks and technical issues: thermal effects, scaling effect, radioactive deposits, and mechanical effect of the casing through the conditional value-at-risk (CVaR) measure [26–28]. Technical issues and risk of escalating costs need to be managed and hedged because of the potential damages likely to take place on an operational plant. The DMS-TOUGE will be verified and validated based on the comparison between tool output and real-life expert analyses on existing operating EGS sites and also historical data related to existing EGS sites. Output data of DMS-TOUGE will be available as raw data or in a form of directives and suggestions that are suitable for decision makers and investors. The raw data will be processed by a special subprocess, a separate MCDM, into a decision. The MCDM will be further discussed in Section 3. The schematic depiction of the main features of the DMS-TOUGE is shown in Figure 1. It should be emphasized that DMS-TOUGE as a whole is still in the development phase, and some parts have been modelled, including MCDM described later.

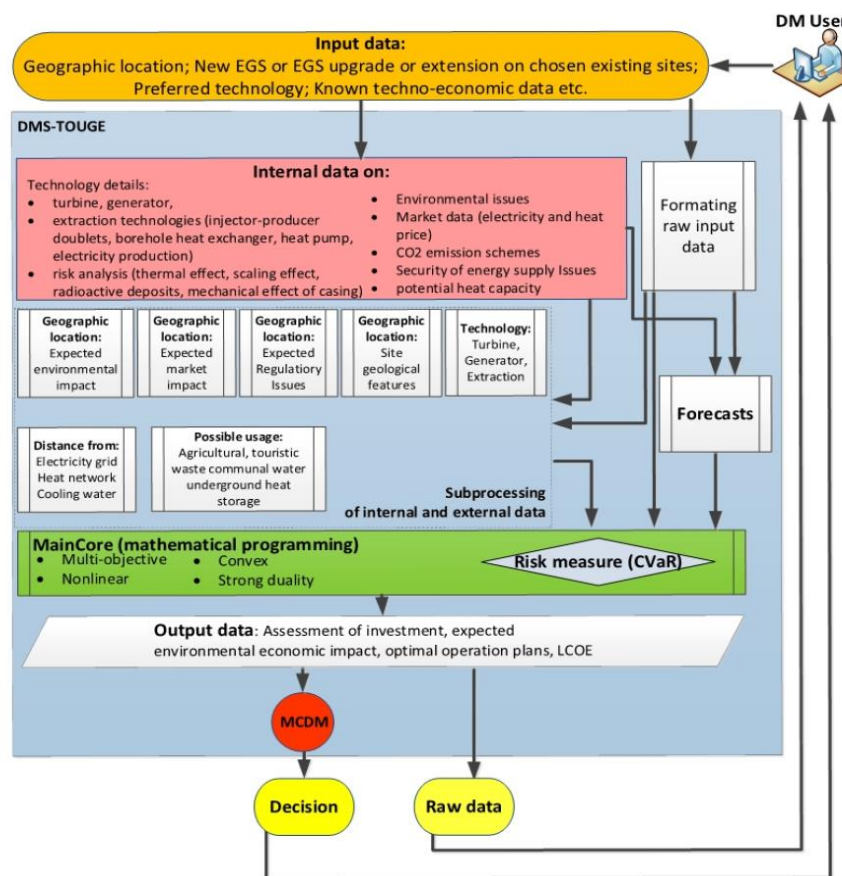


Figure 1. Schematic description of the main processes in Decision-Making Support Tool for Optimal Usage of Geothermal Energy (DMS-TOUGE).

2.2. Geothermal Project Development Phases

The geothermal project development occurs in various phases, with a unique duration of each phase. There is a series of seven key development steps before the actual operation and maintenance phase

commences: (i) a preliminary survey, (ii) exploration, (iii) test drilling, (iv) project review and planning, (v) field development, (vi) construction, and (vii) start-up and commissioning. The development of a typical utility size geothermal project will usually take between 5 to 10 years [29], depending on the country’s geological conditions, information available about the resource, institutional and regulatory climate, access to suitable financing, and other factors. All seven-key development steps could be compressed in the first three following phases, followed by the fourth operation and maintenance (O&M) phase:

1. Discover and establish a viable resource;
2. Develop the project to the point necessary to obtain the power purchase agreement (PPA);
3. Complete the project development once the PPA is obtained, and
4. Operate the power plant facility.

Each phase includes activities and elements that incur different related costs, which in DMS-TOUGE can be estimated or inputted by a decision maker. These costs, along with the estimated power generation over a project’s lifetime, are the basis for the sLCOE calculation for a defined scenario. The number of the activities in each phase, and consequently the capital and O&M costs of the project, depend also on the state of the project, i.e., is it a greenfield project representing a new EGS site or a brownfield project representing an existing EGS site with possible upgrade, or co-production and/or conversion of mature or abandoned oil fields. DMS-TOUGE will be able to calculate necessary costs for sLCOE estimation according to the input data regarding the above-mentioned steps and phases. Capital costs are present in the first three phases, and O&M cost in the fourth phase. All possibly occurring capital costs that will be estimated and calculated with DMS-TOUGE for defined EGS project are summarized in Figure 2. Furthermore, for brownfield project with existing infrastructure the drilling part is omitted and thereby approximately 40–60% of capital expenditure (CAPEX) is avoided, meaning that all the activities related to drilling process depicted in Figure 2. are omitted in that case.

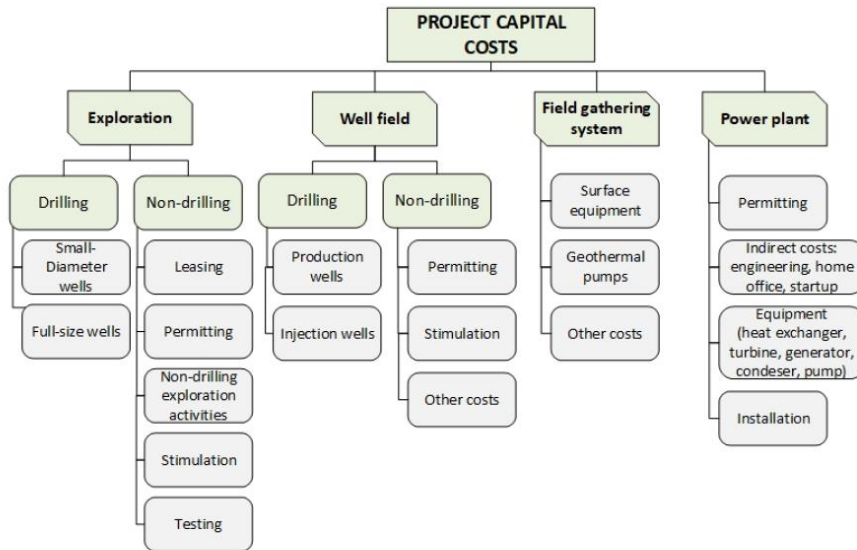


Figure 2. Capital costs included in Decision-Making Support Tool for Optimal Usage of Geothermal Energy (DMS-TOUGE) determination of a system levelized cost of energy (sLCOE).

2.3. Extraction Technology

Different extraction technologies need to be compared when assessing EGS sites, such as the producer-injector doublet and deep borehole heat exchanger. The production system, which consists of a production well, a surface heat exchanger, and a reinjection well, with all produced and cooled thermal water, returned to the aquifer is the so-called doublet system (Figure 3a). The production and the reinjection well must be drilled to the same geological horizon, i.e., reservoir. Consequently, the geofluid circulates in a closed loop: from the reservoir through the production well to the heat exchanger and back to the reservoir through reinjection wells. It is worth noting that pumping the fluid back in the reservoir maintains its hydrostatic pressure. (In the reservoir, around the bottom of the injection well, the permanently inflowing cooled water forms a cold front which propagates toward the production well). Borehole heat exchanger for shallower depths consists of single (Figure 3b) or double U-tubes (Figure 3c). In deeper wellbores, the presence of a liner will entail a coaxial-type solution (Figure 3d), which better optimises thermal and hydraulic behaviour. Injection takes place through the annulus and production (or heat delivery) through a centred co-axial pipe.

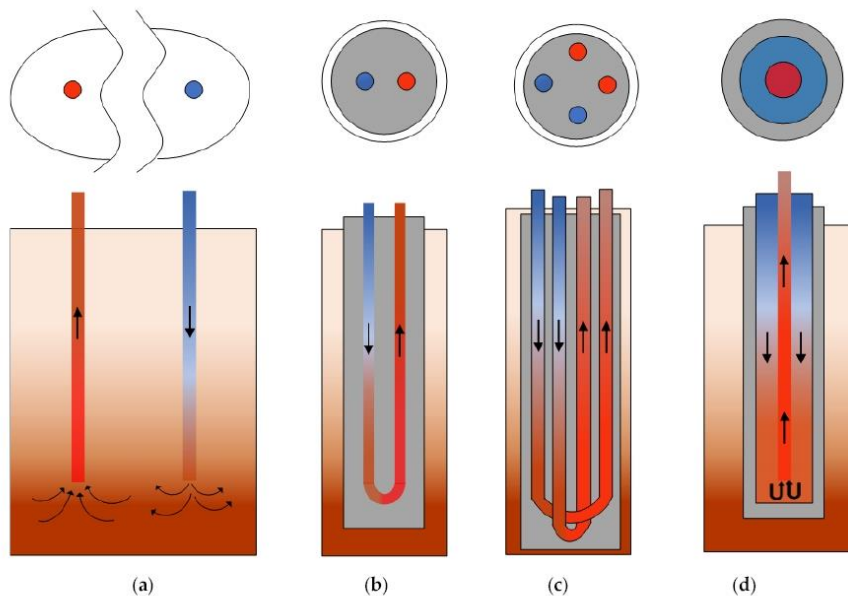


Figure 3. Extraction technologies: (a) producer-injector doublet, (b) borehole heat exchanger single U-tube, (c) borehole heat exchanger double U-tube, (d) coaxial borehole heat exchanger.

2.4. Geothermal Facility Arrangement

Different end-user options need to be compared with the simulation and optimization of three different end-user scenarios; (i) only direct-use heat production; (ii) only electricity production, and (iii) CHP production. The geothermal heat can be delivered to a nearby DH network and/or power plant via heat exchangers. Figure 4 presents a schematic description of possible end-user options. In the case of direct use option, (Figure 4a) the thermal energy from the geothermal fluid is transferred to the working fluid, usually water or steam, in DH network via heat exchanger. In the case of electricity production, the thermal energy is transferred to the working fluid circulating in the secondary system, ORC, also via heat exchanger, as depicted in Figure 4b. For the third end-user option (CHP) two configurations of the CHP plant are proposed: series and parallel, respectively. For the series configuration (Figure 4c)

the brine (geothermal water) delivers the heat to the ORC at a higher temperature and subsequently to the DH system or other direct use application at a lower temperature. The flow rate of the brine is constant and equal for both systems. In the case of the parallel configuration (Figure 4d), geothermal heat is delivered to both the DH system and the ORC at a high temperature but with lower flow rate compared to a series configuration. The selection of the configuration depends on the features of the selected geothermal site and its surrounding, as well as on heat characteristics needed in the connected DH system.

A default power plant type is based on the resource temperature [30] and since the focus of the research are low enthalpy resources, i.e., medium and low-temperature geothermal fields with temperatures of 200 °C and lower, the binary power plants show good performance and therefore will be modelled in DMS-TOUGE. The concept of the binary power plant is based on the ORC. In the ORC system, the fluid flow is divided into four steps. The working fluid is heated up and vaporized in a hot heat exchanger (the evaporator), and at this point, the temperature of the working fluid is the highest. This saturated steam drives the turbine, which enables electricity production by lowering the fluid pressure to its low level. The fluid is then condensed in a cold heat exchanger (condenser) and pumped again into the evaporator, increasing thereby the fluid's pressure. As for the condensers, the most commonly used heat rejection equipment at binary geothermal power plants are the air-cooled condensers. The use of air eliminates the requirement for makeup water. However, compared to water cooling towers, air-cooled condensers require more space and represent a larger parasitic power load on the plant.

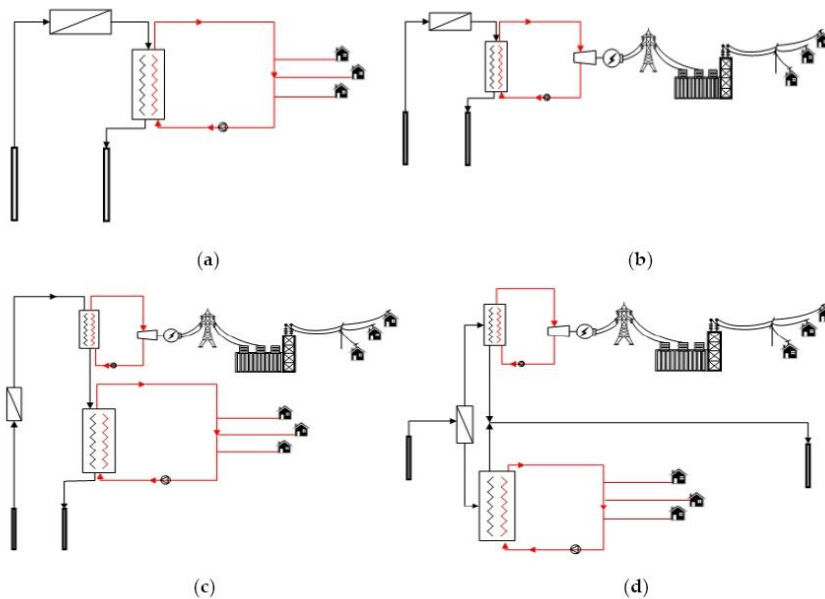


Figure 4. Schematic description of the possible end-user options: (a) direct use, (b) only electricity production, (c) combined heat and power (CHP)–series configuration, (d) CHP–parallel configuration.

The geothermal fluid, the hot source of the heat, is circulated in another loop on the other end of the evaporator. Therefore, for the binary plants, the major equipment components estimated are turbine-generator, air-cooled condenser, geothermal heat exchangers, and working fluid pumps, as depicted in Figure 5.

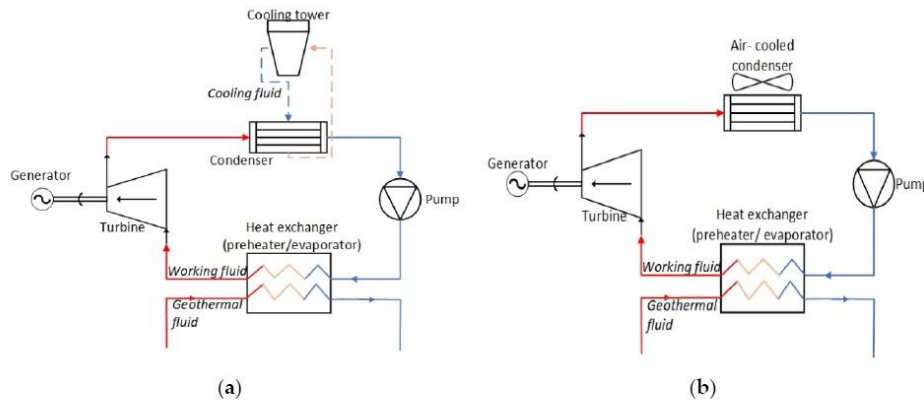


Figure 5. Schematic diagram of a basic binary cycle geothermal power plant: (a) water-cooled condenser and (b) air-cooled condenser.

3. Multiple-Criteria Decision-Making Analysis

As a subprocess in the DMS-TOUGE, an MCDM analysis will be used and performed using the weighted decision matrix (WDM). For evaluating different EGS options, a set of criteria is defined and presented in this subsection. For evaluation of the relative importance of each criterion in decision making, the weight is associated with each of the listed criteria. Performance, x_{ij} , of option i on criterion j is arbitrarily defined with a numerical value from 1 to 5, whose higher value means better performance, $x_{ij} \in \{1, 2, 3, 4, 5\}$. Finally, total performance, X_i , of i th EGS option on all criteria, $\forall j$, is assessed by summing all performance values, x_{ij} , multiplied by its weight as defined in Equation (1).

$$X_i = \sum_j^J w_j \cdot x_{ij}, \quad (1)$$

where X_i is the total performance of i th EGS option, $i \in I$, where I is a total number of EGS options. The w_j is weight i.e., relative importance in the decision making of criterion j , $j \in J$, where J is a total number of criteria. The x_{ij} is the performance of option i on criterion j . To use WDM successfully while assessing EGS options for a specific geothermal site, a set of well-defined criteria is needed. The criteria on which EGS option will be evaluated is listed below in Sections 3.1–3.12. It should be noted that, although the Equation (1) shows a simple summation, the actual calculation of total performance for a selected site was performed as an average mean of X_i performances of each criterion. Also, in this work every criterion j , is assumed to have equal relative importance in the decision making. Thereby, all criteria are evaluated assuming all w_j to be equal and valued with 1. It is worth mentioning that the actual range for w_j has not been yet precisely defined, as it is a sensitive part of the MCDM matrix. Therefore, such a range must be chosen that will adequately and meaningfully reflect the relative importance of certain criteria in relation to others. In the future work and through a process of validation and verification of the MCDM matrix and DMS-TOUGE, the discrete sequential values for w_j will be chosen.

3.1. First Criterion: Installed Power, $x_{i,1}$

When considering energy investment, installed power (capacity) is the first and most important parameter [31]. It later determines both costs (CAPEX, OPEX-O&M) and revenues (power output). According to Reference [30], performance $x_{i,1}$ of option i on 1st criterion should be determined by P/P_r ratio in p.u. (ratio of installed power, P , of ORC technology in i th option to the reference installed power, P_r , e.g., according to Reference [31] for ORC technology reference installed power ranges from 1 MW to 5 MW depending on site features) (Table 1).

Table 1. Performance values $x_{i,1}$ for 1st criterion.

Ratio (p.u.)	$0 \leq P/P_r < 0.3$	$0.3 \leq P/P_r < 0.6$	$0.6 \leq P/P_r < 0.9$	$0.9 \leq P/P_r < 1.2$	$1.2 \leq P/P_r < \infty$
$x_{i,1}$	1	2	3	4	5

3.2. Second Criterion: Fluid Heat Flow, $x_{i,2}$

Expected heat flow, Q (W), for the two main extraction technologies, a traditional doublet with fluid extraction and reinjection, and wellbore heat exchanger, a closed loop system, is defined with Equation (2):

$$Q = q \cdot \rho \cdot c_p \cdot (T_H - T_C), \quad (2)$$

where q is the fluid flow rate (m^3/s), ρ is fluid density (kg/m^3), c_p is specific heat capacity of fluid at constant pressure ($\text{J}/\text{kg}\cdot\text{K}$). T_H is the fluid temperature at the wellhead ($^\circ\text{C}$), T_C is the fluid temperature at the exit of the steam turbine ($^\circ\text{C}$).

Heat flow as a criterion was first proposed in Reference [31] and is used here with modifications in means of corresponding ranges for temperature. The idea is to emphasize the importance of flow rate and temperature of the produced fluid, and the impact of selected technology on flow rate and temperature. Reference [31] proposes criterion, here referred to as the $x_{i,2}$, whose value is based on the ratio between the fluid flow rate, q , and flowing temperature at the wellhead, T_H . According to [31] best suited ranges for valuing performance $x_{i,2}$ in heat flow criterion are defined by flow rates between $0 \text{ m}^3/\text{h}$ and $100 \text{ m}^3/\text{h}$ and when temperatures are between $80 \text{ }^\circ\text{C}$ and $160 \text{ }^\circ\text{C}$, since those ranges correspond to operative conditions for an ORC plant. For this criterion, the temperature range is modified for the values between $60 \text{ }^\circ\text{C}$ and $160 \text{ }^\circ\text{C}$, since one of the focus of the ongoing H2020 MEET project is to make those temperatures also exploitable (Table 2).

Table 2. Performance values $x_{i,2}$ for 2nd criterion.

Ratio	$1.67 \leq \frac{q}{T_H} < \infty$	$0.679 \leq \frac{q}{T_H} < 1.67$	$0.357 \leq \frac{q}{T_H} < 0.679$	$0.056 \leq \frac{q}{T_H} < 0.357$	$0 \leq \frac{q}{T_H} < 0.056$
$x_{i,2}$	1	2	3	4	5

3.3. Third Criterion: Theoretical Maximum Efficiency, $x_{i,3}$

In this paper, the ORC based power plants are proposed for exclusively electricity generation. It is mainly due to the low-to-medium temperature range of the produced geothermal fluid. The thermal efficiency evaluated at the heat exchanger of the conversion plant in such fields is usually less than 10%, and for the binary power plants, according to Reference [32] could be calculated with Equation (3).

$$\eta_{max} = 6.9681 \cdot \ln(T_H) - 29.713, \quad (3)$$

where the T_H represents the temperature of the produced fluid at the wellhead in ($^\circ\text{C}$) and η_{max} is expressed in (%).

However, in case of power plants different from ORC, meaning other types of conversion plants, the thermal exchanged cycle between the two fluids, one circulating in the primary cycle (geofluid) and other circulating in the secondary circle (working fluid), can be assessed using the Carnot's ideal efficiency. In those cases, the expected theoretical maximum efficiency of conversion, η_{max} expressed in (%), is evaluated using the Equation (4) as according to Reference [33].

$$\eta_{max} = (1 - T_C/T_H) \cdot 100\%, \quad (4)$$

and it depends on the geological site features (the T_H part, where T_H in (K) is the outlet temperature from the borehole at the wellhead), technology and environment features (the T_C part, where T_C in (K)

is the inlet temperature at the wellhead). The performance is valued as shown in Table 3. Depending on the end-user option the Equations (3) or (4) are used for assessment of the selected site.

Table 3. Performance values $x_{i,3}$ for 3rd criterion.

Efficiency of Conversion for ORC Plant (%)	$\eta_{max} < 4$	$4 \leq \eta_{max} < 6$	$6 \leq \eta_{max} < 10$	$10 \leq \eta_{max} < 12$	$\eta_{max} \geq 12$
$x_{i,3}$	1	2	3	4	5
Efficiency of Conversion for Other Cases (%)	$\eta_{max} < 30$	$30 \leq \eta_{max} < 40$	$40 \leq \eta_{max} < 50$	$50 \leq \eta_{max} < 60$	$\eta_{max} \geq 60$
$x_{i,3}$	1	2	3	4	5

3.4. Fourth Criterion: Geothermal Gradient, $x_{i,4}$

When setting the starting point of the geothermal plant feasibility analysis the geological factors should be considered. The efficiency of the heat transfer through the wellbore is highly dependent on the reservoir's initial temperature, which is a function of the well depth. Also, high thermal conductivity is required, so that the heat stored in the rocks could be transferred to the wellbore fluid. According to Reference [34], these two influencing factors could be collectively combined and represented with geothermal gradient, G_T ($^{\circ}\text{C}/100\text{ m}$). The paper also suggested a range of geothermal gradient based on measured gradients for several analyzed oil fields across the world, which was taken for evaluating the performance $x_{i,4}$ in the geothermal gradient criterion (Table 4).

Table 4. Performance values $x_{i,4}$ for 4th criterion.

Geo.gra. ($^{\circ}\text{C}/100\text{ m}$)	$G_T < 0.5$	$0.5 \leq G_T < 2$	$2 \leq G_T < 4$	$4 \leq G_T < 6$	$G_T \geq 6$
$x_{i,4}$	1	2	3	4	5

3.5. Fifth Criterion: The Fluid Temperature at Wellhead, $x_{i,5}$

According to Reference [31] the outlet temperature of the fluid from the wellhead is one of the main features of the geological site. It later determines installed power, technology, efficiency, revenues, and costs. Namely, this criterion has been defined to emphasize the relevance of this temperature, since it has a great impact on the conversion cycle in the power plant. The higher the fluid temperature at the wellhead, the higher the amount of the heat that can potentially be transferred to the secondary working fluid (depending of course on the heat exchanger technology). Performance $x_{i,5}$ of option on 5th criterion increases linearly depending on fluid temperature, T_H (Table 5). Here, the focus is on the utilization of temperatures from $60\text{ }^{\circ}\text{C}$ to $160\text{ }^{\circ}\text{C}$ (although upper bound for analyzed geo sites in the scope of this research is expected to be $90\text{ }^{\circ}\text{C}$) for cases of smart ORC units. This approach is adapted and modified from the work [31].

Table 5. Performance values $x_{i,5}$ for 5th criterion.

Temp. ($^{\circ}\text{C}$)	$T_H \leq 60$	$60 < T_H \leq 90$	$90 < T_H \leq 120$	$120 < T_H \leq 150$	$150 < T_H \leq \infty$
$x_{i,5}$	1	2	3	4	5

3.6. Sixth Criterion: Global Efficiency, $x_{i,6}$

Aside from the geological setting and wellbore conditions, the supply of heat or/and electricity is directly related to the performance of the plant energy conversion. Therefore, a global efficiency criterion should be established to evaluate the multi-stage heat (energy) loss within the energy conversion cycle and the impact of the ambient temperature on stored heat (Table 6). According to

Reference [33] the total heat loss is addressed by means of coefficients of the different stages of the conversion cycle resulting in an overall evaluation for plant conversion. Equations (5)–(7) defines those coefficients, where Equation (5) represents the heat loss due to Non-Condensable Gases (NCG), where C [%] is the estimates of NCG weight, because the presence of NCG can negatively impact the operation of the plant turbine. The Equation (6) represents the parasitic load heat loss, including well pumps, cooling tower, condenser, where P_{TPL} is total parasitic load and P_{gross} gross thermal power. Moreover, Equation (7) defines the parasitic loss during the working fluid transport where the L_p is the pipe length in km.

$$\eta_{NCG} = 1 - 0.0059 \cdot C \tag{5}$$

$$\eta_{TPL} = 1 - P_{TPL} / P_{gross} \tag{6}$$

$$\eta_{pipe} = 1 - 0.003 \cdot L_p \tag{7}$$

Overall plant efficiency is then calculated according to the Equations (8)–(10), where Equation (8) represents evaluation of the electricity generation, Equation (9) is used to evaluate combined heat-electricity production (CHP), where the second heat exchanger is required to exploit the remaining thermal energy of geothermal water into another district heating fluid, and Equation (10) represents the evaluation of direct usage of heat only in DH systems. Moreover, to measure the operational performance of the turbine and the generator efficiency, η_t and η_g , respectively, were included.

$$\eta_{G(E)} = \eta_{max} \cdot \eta_{NCG} \cdot \eta_t \cdot \eta_g \cdot \eta_{TPL} \cdot \eta_{pipe} \tag{8}$$

$$\eta_{G(CHP)} = \eta_{max1} \cdot \eta_{NCG} \cdot \eta_t \cdot \eta_g \cdot \eta_{TPL} \cdot \eta_{pipe} \cdot \eta_{max2} \tag{9}$$

$$\eta_{G(DH)} = \eta_{max} \cdot \eta_{pipe} \cdot \eta_{TPL} \tag{10}$$

where η_{max1} in the equation related to the CHP represents the efficiency of conversion in ORC for electricity production and η_{max2} is the efficiency of conversion of the remaining heat from the geothermal fluid for direct heat usage.

Table 6. Performance values $x_{i,6}$ for 6th criterion.

Global Efficiency	$\eta_G < 0.2$	$0.2 \leq \eta_G < 0.3$	$0.3 \leq \eta_G < 0.4$	$0.4 \leq \eta_G < 0.6$	$\eta_G \geq 0.6$
$x_{i,6}$	1	2	3	4	5

3.7. Seventh Criterion: Corrosion and Scaling Hazard, $x_{i,7}$

The corrosive or scaling tendency of the geothermal site is evaluated with the Langelier Saturation Index (LSI) (Table 7). The LSI later determines O&M costs. The less the LSI, the better the performance of the option will be (see Reference [31]).

Table 7. Performance values $x_{i,7}$ for 7th criterion.

LSI	$1.5 < LSI \leq 2$	$1 < LSI \leq 1.5$	$0.5 < LSI \leq 1$	$0 < LSI \leq 0.5$	$LSI = 0$
$x_{i,7}$	1	2	3	4	5

3.8. Eighth Criterion: Distance from Power/Heating Grid, $x_{i,8}$

Construction of power lines and substations for plant connection to the grid imposes significant costs and should be addressed accordingly. Therefore, the distance between the geothermal plant production site and the nearest power and/or district heating system connection point must be addressed. Depending on that distance, d (km), the investment costs and also sLCOE vary. Apart from the distance, considering that the grid connection costs are site-specific, there are many other factors that have an impact on the investment costs. Due to the complexity if all the factors were included,

the main influencing factor, namely the distance, was taken for the evaluation of the performance $x_{i,8}$. The range is shown in Table 8, finishing with the most favored onsite use, i.e., a very small distance between the plant facility and the connection point.

Table 8. Performance values $x_{i,8}$ for 8th criterion.

Distance (km)	$d > 4$	$3 \leq d < 4$	$2 \leq d < 3$	$1 \leq d < 2$	$d < 1$
$x_{i,8}$	1	2	3	4	5

3.9. Ninth Criterion: Load Factor, $x_{i,9}$

Generally, combined heat and electricity production increases the net efficiency of the power plant, which in turn improves power plant economics. This is even more important in the case of geothermal plants, where thermodynamic efficiencies are typically much lower compared to conventional power plants, due to the lower working fluid temperatures. Considering direct-use systems, heat is only supplied to the process, like greenhouse or district heating, when it is needed. As a result, according to Reference [34], the load factor, f_L , can vary from 15% to 75% depending on the application. Reference [34] examined the costs of the delivered heat as a function of a load factor for U.S. climates. Knowing that industrial applications can have a load factor of 0.30 to 0.75, the space heating only application 0.15 to 0.30, aquaculture 0.50 to 0.80 and greenhouses 0.18 to 0.24, the results showed that the high load factor correlates with lower cost of delivered heat and consequently affects the project’s economic feasibility and sLCOE. As for electricity production, the load factor is typically 0.8 and higher. For combined heat and electricity production, the load factor is higher than in the case of only heat production. Based on forenamed results, the range for performance $x_{i,9}$ of alternative is determined and showed in the Table 9.

Table 9. Performance values $x_{i,9}$ for 9th criterion.

Load Factor	$f_L \leq 0.2$	$0.2 < f_L \leq 0.4$	$0.4 < f_L \leq 0.6$	$0.6 \leq f_L \leq 0.8$	$0.8 < f_L \leq 1$
$x_{i,9}$	1	2	3	4	5

3.10. Tenth Criterion: sLCOE, $x_{i,10}$

The average cost of the project over the lifetime will be addressed by the sLCOE (system LCOE, depending on the end-user option) in (€/MWh) which also accounts for the costs of integration. This sLCOE will be calculated from all the available external data provided from DM and/or internal data from the internal database of the DMS-TOUGE, and according to Equation (13). Performance $x_{i,10}$ of option i on sLCOE criterion is determined by $sLCOE/\bar{\pi}$ ratio in p.u. (ratio of sLCOE of ORC technology in i th option to the average market price, $\bar{\pi}$, in different forecasts and for different horizons) shown in Table 10.

Table 10. Performance values $x_{i,10}$ for 10th criterion.

Ratio	$1 \leq \frac{sLCOE}{\bar{\pi}} < \infty$	$0.8 \leq \frac{sLCOE}{\bar{\pi}} < 1$	$0.6 \leq \frac{sLCOE}{\bar{\pi}} < 0.8$	$0.4 \leq \frac{sLCOE}{\bar{\pi}} < 0.6$	$0 \leq \frac{sLCOE}{\bar{\pi}} < 0.4$
$x_{i,10}$	1	2	3	4	5

3.11. Eleventh Criterion: Social Impact, $x_{i,11}$

According to Reference [22], the social acceptability is conditioned by the deviation from the regular condition in the area and utility of the affected parties from the project. As geothermal technologies are site-specific (the geology is different all over Europe and knowledge of the local geological setting is essential) and capital-intensive, the needs regarding exploration, resource development, construction, and O&M are covered by the local workforce. According to Reference [35], the costs of social acceptance

could be presented as the external costs of a geothermal project. Depending on the site, type, and size of the project the amount of those external costs range, on the average, 0.5–2% and 1.5–4% of the total construction costs, i.e., approximately 17,000–220,000 € and 265,000–7,040,000 €, for direct use and multi-purpose projects, respectively. Moreover, employment potential could be divided into direct, indirect, and induced employment effect and quantified in terms of full-time jobs/MW (FT) and person × years of construction and manufacturing employment (Table 11). Total direct, indirect, and induced employment ratio is a ratio of the installed capacity, $P_{inst.}$ (MW) and full-time jobs calculated from the Equation (11) (shown in Figure 6). Equation (12) represents construction and manufacturing employment (C&M), where those jobs are expressed as full-time positions over one year (person × year) as a function of installed capacity, $P_{inst.}$ (MW). However, those C&M jobs are spread over several years taking into account the development time frame for the new projects. The social impact criterion will be obtained by the average of performances of the following sub-criteria: $x_{i,11,1}$ social acceptance costs of direct use or electricity production sub-criterion, $x_{i,11,2}$ social acceptance costs of combined heat-electricity production sub-criterion, $x_{i,11,3}$ FT employment sub-criterion, $x_{i,11,4}$ C&M employment sub-criterion. Each sub-criterion will be evaluated with a weight in a range from 1 to 5. Figure 5 shows the full-time jobs function as a defined in Equation (11).

$$FT\ jobs = \log_{1.068}(P_{inst.}) \tag{11}$$

$$C\&M\ jobs = 22.4 \cdot P_{inst.} \tag{12}$$

Table 11. Performance values $x_{i,11}$ for 11th criterion.

Social Acceptance Costs of Direct Use or Electricity Production ($\cdot 10^3$)	$sac_{DU} > 295$	$145 < sac_{DU} \leq 295$	$30 < sac_{DU} \leq 145$	$4.5 < sac_{DU} \leq 30$	$sac_{DU} \leq 4.5$
$x_{i,11,1}$	1	2	3	4	5
Social Acceptance Costs of Combined Heat – Electricity ($\cdot 10^3$)	$sac_{CHP} > 6155$	$2640 < sac_{CHP} \leq 6155$	$880 < sac_{CHP} \leq 2640$	$350 < sac_{CHP} \leq 880$	$sac_{CHP} \leq 350$
$x_{i,11,2}$	1	2	3	4	5
Employment FT ($\frac{dFT}{dP_{inst.}}$)	$e_{FT} < 1$	$1 \leq e_{FT} < 1.5$	$1.5 \leq e_{FT} < 2$	$2 \leq e_{FT} < 4$	$e_{FT} \geq 4$
$x_{i,11,3}$	1	2	3	4	5
Employment C&M (<i>person × year</i>)	$e_{C\&M} \leq 50$	$50 < e_{C\&M} \leq 150$	$150 < e_{C\&M} \leq 250$	$250 < e_{C\&M} \leq 350$	$e_{C\&M} > 350$
$x_{i,11,4}$	1	2	3	4	5
Total Social Impact	$AV \leq 1$	$1 < AV \leq 2$	$2 < AV \leq 3$	$3 < AV \leq 4$	$4 < AV \leq 5$
$x_{i,11}$	1	2	3	4	5

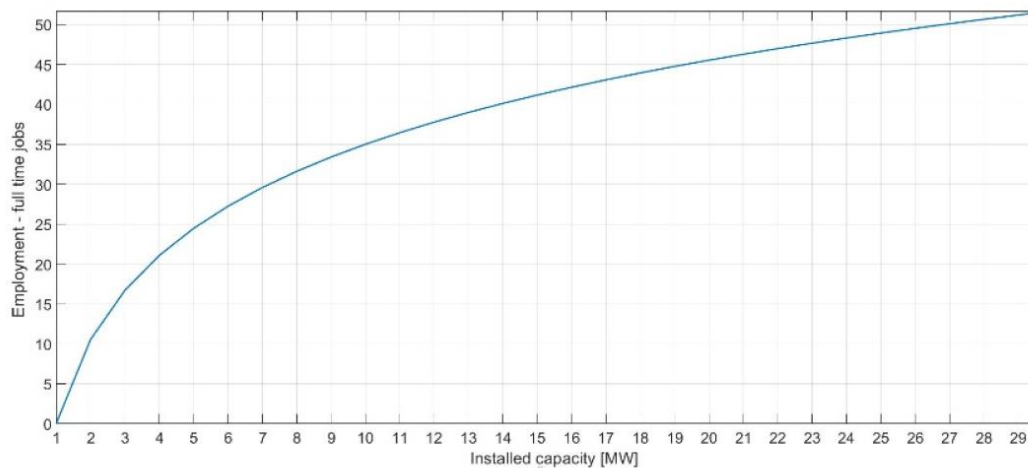


Figure 6. Total employment – full-time jobs function depending on the installed capacity of the project

3.12. Twelfth Criterion: Environmental Impact, $x_{i,12}$

According to Reference [24], the environmental impact should account for the impact on sustainability, landscape, subsidence, and potentially induced micro-seismicity, and account for the level of noise, atmospheric emissions, potential water contamination, and production of radioactive scaling. The fluid extraction could cause subsidence because of reservoir pressure decline and uplift during borehole drilling activities. This is measured in mm/year of soil decay. Moreover, the pore pressure reduction in production and increase in reinjection operations have been associated with increased induced seismicity, often microseisms of low energy (<2–3 M Richter scale) [31]. According to Reference [36] the ranges for this sub-criterion were assigned. The impact on the landscape is measured as land use intensity (LUI) for installed power in m^2/kW , and the range was estimated according to Reference [37]. The noise impact during routine operation is mainly caused by cooling towers and electrical transformers, and according to Reference [38], typical acceptable levels are 71–83 dB at 900 m distance from the facility. When considering atmospheric emissions, closed cycles, such as binary plants, have no gaseous emissions or they are close to zero and so do not contribute to air pollution. Considering objects of interest in this research (Figure 3), the impact on surface waters can be excluded. Groundwater contamination may occur if the casings in reinjection wells should fail, allowing fluid to leak. According to WHO, the range of total dissolved solids (TDS) and pH values was determined for the quantification of this sub-criterion. Radioactivity is mainly caused by interaction between the geothermal fluid and certain formations containing radioactive elements. As emphasized in Reference [39], the content of radionuclides in acidic magmatic rocks is generally higher compared to sedimentary rocks. Furthermore, uranium (U) and thorium (Th) are the most common radioactive elements found in granites. As defined in Reference [39], different types of rocks can contain different radioelements. Therefore, this sub-criterion is defined with the ranges of the forenamed most common radioactive elements but also taking into account the type of the rock – granitic rocks, shales, basaltic rocks, sandstones, and carbonates - in ascending order of the weights. The environmental impact criterion will be obtained by the average of performances of the following sub-criteria shown in Table 12: $x_{i,12,1}$ subsidence sub-criterion, $x_{i,12,2}$ potential seismicity sub-criterion, $x_{i,12,3}$ land use sub-criterion, $x_{i,12,4}$ noise sub-criterion, $x_{i,12,5}$ potential water contamination sub-criterion, and $x_{i,12,6}$ radioactivity sub-criterion. Each sub-criterion will be evaluated with a weight in a range from 1 to 5.

Table 12. Performance values $x_{i,12,j}$ for 12th criterion are defined according to values available in References [31,36–39].

Subsidence v_h (mm/year)	$v_h \geq 100$	$100 > v_h \geq 60$	$60 > v_h \geq 40$	$40 > v_h \geq 20$	$v_h < 20$
$x_{i,12,1}$	1	2	3	4	5
Potential Seismicity PGV (cm/s) PGA (cm/s ²)	$0.5 \leq \text{PGV} \leq 1.6$ $9 \leq \text{PGA} \leq 43$	$0.2 \leq \text{PGV} \leq 0.6$ $4 \leq \text{PGA} \leq 18$	$0.07 \leq \text{PGV} \leq 0.23$ $1.5 \leq \text{PGA} \leq 7.3$	$0.03 \leq \text{PGV} \leq 0.09$ $0.6 \leq \text{PGA} \leq 3$	$0.01 \leq \text{PGV} \leq 0.02$ $0.2 \leq \text{PGA} \leq 1.2$
$x_{i,12,2}$	1	2	3	4	5
Land Use (m ² /kW)	LUI > 40	40 ≥ LUI > 30	30 ≥ LUI > 20	20 ≥ LUI > 10	LUI ≤ 10
$x_{i,12,3}$	1	2	3	4	5
Noise (dB)	dB ≥ 100	100 > dB ≥ 90	90 > dB ≥ 80	80 > dB ≥ 70	dB < 70
$x_{i,12,4}$	1	2	3	4	5
Potential Water Contamination TDS (mg/L); (pH)	TDS ≥ 1200 ; pH ≤ 3 or pH > 8.5	900 ≤ TDS < 1200 ; 3 < pH < 4	600 ≤ TDS < 900 ; 4 ≤ pH < 5	300 ≤ TDS < 600 ; 5 ≤ pH < 6.5 or 7.5 < pH ≤ 8.5	TDS < 300 ; 6.5 ≤ pH ≤ 7.5
$x_{i,12,5}$	1	2	3	4	5
Radioactivity (ppm)	$2 \leq K^{40} < 6$ $1 \leq \text{Th} \leq 25$ $1 \leq \text{U} \leq 7$	$8 \leq \text{Th} \leq 18$ $1.5 \leq \text{U} \leq 5.5$	$0.2 \leq K^{40} < 2$ $0.5 \leq \text{Th} \leq 10$ $0.2 \leq \text{U} \leq 0.4$	$0.7 \leq K^{40} < 3.8$ $0.7 \leq \text{Th} \leq 3.8$ $0.2 \leq \text{U} \leq 0.6$	$0 \leq K^{40} < 2$ $0.1 \leq \text{Th} \leq 7$ $0.1 \leq \text{U} \leq 9$
$x_{i,12,6}$	1	2	3	4	5
Total Environmental Impact	AV ≤ 1	1 < AV ≤ 2	2 < AV ≤ 3	3 < AV ≤ 4	4 < AV ≤ 5
$x_{i,12}$	1	2	3	4	5

4. Results

In this section, the purpose of the MCDM matrix is discussed and decision-making results are presented. The matrix is used to rank four different geothermal projects for two given end uses mentioned in Section 2.4, only electricity production and direct heat use, respectively. For a successful comparison, the geothermal projects being compared should be targeting the same end use, so that the comparison considers how key technical and economic factors are being utilised. Therefore, the two main scenarios are considered separately for all the projects (four sites in Table 13). In order to be able to execute an overall comparison, all the criteria mentioned in Section 3 are assessed. As stated before, relative importance in the decision making of each criterion is considered equal, meaning each criterion is equally influential on the final decision and therefore $w_j, \forall j$ is set as 1. Final evaluation of chosen sites that includes all criteria is calculated as the average mean of 12 criteria. Moreover, the extraction technology examined in this analysis is doublet producer-injector technology, described in Section 2.3. For the four geothermal sites, the input parameters used for Equations (1)–(12) are presented in Table 13.

These input parameters represent realistic geothermal sites. Some of the observed sites are currently in usage for electricity production, aquaculture, agriculture, and food industry. The observed sites are not in the same geological and environmental area so the MCDM tool could be properly used, because it evaluates and compares different geothermal sites at various geological settings for two scenarios.

Table 13. Input parameters for the multiple-criteria decision-making (MCDM) matrix for four selected geothermal sites.

Parameter	Unit	Site 1	Site 2	Site 3	Site 4
Brine flow rate, q	L/s	83.33	20	5.5	77.1
Inlet temperature, T_H	°C	170	80	140	80
Outlet temperature, T_C	°C	70	32	70	40
Geothermal gradient	°C/100 m	6.18	6.1	3	6
Number of wells	No.	1	1	1	1
Specific heat capacity, c_p	J/kgK	4185.5	4185.5	4185.5	4185.5
Corrosion and scaling	LSI	1.5	0.5	0.5	0.5
Fluid	kg/m ³	897.3	971.76	925.9	971.76
Th. efficiency, $\eta_{max,ele}$	%	6.18	6.1	3	6
Max. efficiency, $\eta_{max,heat}$	%	76.47	62.5	78.57	53.33

¹ Density of the geothermal water changes with the temperature according to Reference [40].

4.1. Economic Parameters

The problems encountered with the development of geothermal energy systems are mostly related to the high upfront costs and the related finances. The high upfront costs are usually caused by the costs involved with the drilling of the wells, as mentioned in Section 2.2. The drawback with financing geothermal projects relates to the substantial uncertainties in the performance of the wells. Namely, EGS technology is still in an R&D phase since only a handful of projects have been realized. With estimated CAPEX and OPEX values, the LCOE of each site is calculated (Table 14), according to Equation (13) and passed on to the MCDM matrix. For analysis in this study, 55% of the CAPEX is excluded, since all the selected geothermal sites do not require drilling phase, i.e., the geothermal injector-producer doublet exist. Moreover, CAPEX is represented with specific investment costs in €/MW and OPEX is calculated as the percentage of the CAPEX in the range between 7–20%, depending on the year of operation.

$$LCOE = \frac{\sum_{t=1}^T \frac{CAPEX_t + OPEX_t}{(1+r)^t}}{\sum_{t=1}^T \frac{E_t}{(1+r)^t}}, \quad (13)$$

where E_t represents the amount of the electricity or heat produced in the year t . r represents the discount rate. T is the lifetime of the project.

Table 14. Economic parameters used for levelized cost of energy (LCOE) calculations.

Parameter	Unit	Value
Specific costs	€/MW	4,500,000; 6,750,000 ¹ ; 9,000,000
OPEX	€/MWh	10; 20 ¹ ; 30
Discount	%	6; 7 ¹ ; 8.7
Lifetime	years	20; 30 ¹ ; 40
Energy produced, E_t	MWh (annual)	Calculated ²

¹ Base case values are used in the base case scenario, left values represent decreased and right values increased values compared to the base case scenario that is used in the sensitivity analysis; ² The annual produced electricity or heat is calculated as a product of Equation (2) and (3) or Equation (4).

4.2. First Scenario—Electricity Production Only

This scenario includes the end user option for only electricity production. The results of running the modelled MCDM matrix on the four selected geothermal sites to rank their feasibility according to economic-environment-social assessment are illustrated in Table 15. To estimate each criterion, the parameters from Table 13 and from Table 14 the base case values are used.

Table 15. Ranking of the selected geothermal sites in this study for electricity production.

Criterion	Site 1	Site 2	Site 3	Site 4
$x_{i,1}$	4	1	1	1
$x_{i,2}$	1	2	4	1
$x_{i,3}$	3	1	2	1
$x_{i,4}$	5	5	3	5
$x_{i,5}$	5	2	4	2
$x_{i,6}$	1	1	1	1
$x_{i,7}$	1	4	4	4
$x_{i,8}$	4	5	4	5
$x_{i,9}$	5	5	5	5
$x_{i,10}$	3	3	3	3
$x_{i,11}$	5	5	5	5
$x_{i,12}$	5	5	5	5
Final	3.5	2.83	3	2.75

4.3. Second Scenario—Heat Production Only

This scenario includes the end user option for only heat production, for direct use applications. The results of running the modelled MCDM matrix on the four selected geothermal sites for this scenario to rank their feasibility according to economic-environment-social assessment are illustrated in Table 16. To estimate each criterion, the parameters from Table 13 and from Table 14 base case values are used. Load factor for specified sites is defined according to the application of the heat and as follows. It is modelled that all the sites use the obtained heat for district heating and accordingly the load factor is set to 0.3.

Table 16. Ranking of selected geothermal sites in this study for heat production.

Criterion	Site 1	Site 2	Site 3	Site 4
$x_{i,1}$	4	5	4	4
$x_{i,2}$	1	2	3	1
$x_{i,3}$	5	5	5	5
$x_{i,4}$	5	5	3	5
$x_{i,5}$	5	2	4	2
$x_{i,6}$	4	4	4	4
$x_{i,7}$	1	4	4	4
$x_{i,8}$	3	4	3	4
$x_{i,9}$	2	2	2	2
$x_{i,10}$	1	1	1	1
$x_{i,11}$	4	5	4	5
$x_{i,12}$	5	5	5	5
Final	3.33	3.67	3.5	3.5

4.4. Sensitivity Analysis

Sensitivity analysis was carried out to see how the change of independent variables (CAPEX, discount rate, OPEX, lifetime) affects the dependent variable, i.e., system LCOE, under certain conditions. A sensitivity analysis makes it possible to distinguish between high-leverage variables, whose values have a significant impact and low-leverage variables, whose values have minimal impact.

Site 1 and scenario of only electricity production were chosen for sensitivity analysis for the system LCOE. Values of observed input parameters used in the sensitivity analysis are shown in Table 17.

Table 17. The sensitivity of the system levelized cost of energy (LCOE) to input parameters.

Input Parameter	Unit	Decrease	Base	Increase
CAPEX	€/MW	4,500,000	6,750,000	9,000,000
Discount rate	%	6	7	8
OPEX	€/MWh	20	30	40
Lifetime	years	20	30	40

Tornado plot showing the sensitivity of calculated LCOE to changes in a selection of parameters is shown in Figure 7. The central value of the plot represents the calculated LCOE for the base case with the amount of 93 €/MWh. It could be seen that the most influence on system LCOE has CAPEX, followed by OPEX, discount rate and the lifetime of the project, respectively. Lowering the CAPEX, which consist mostly of the drilling costs, is crucial for making the EGS geothermal sites commercially available and competitive with other renewable sources.

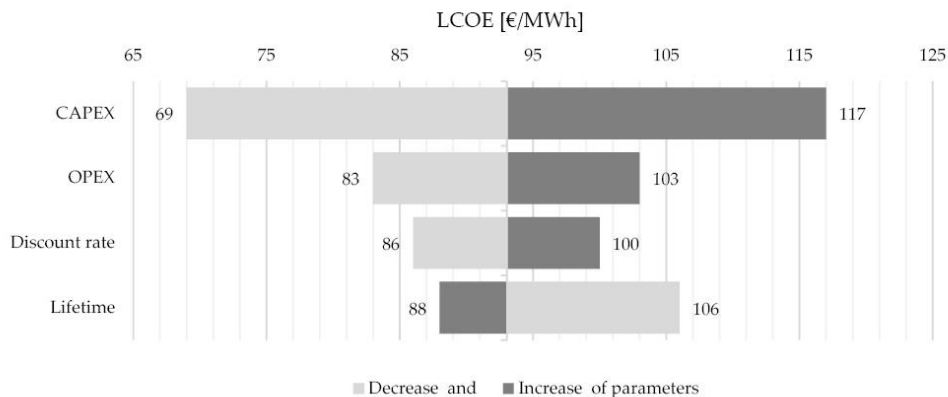


Figure 7. Tornado plot showing the sensitivity of the calculated levelized cost of energy (LCOE) to changes in a selection of parameters.

4.5. Discussion

The presented MCDM as a subprocess of the DMS-TOUGE will enable a comprehensive understanding of the interaction between economic, geological, social, and technical uncertainty. The analysis conducted in this paper is a first order analysis and will benefit from additional work gained from the MEET project. It is expected that the model will receive several modifications in order to make it more accurate and impactful. As it can be seen from the final evaluation of each site in Table 15, the temperature and the flow rate are one of the most important constraints for development of an EGS project, especially in the case of electricity production only. Site 1 presents the highest temperature of the produced geothermal brine, and the highest flow rate. These conditions lead to the greater installed power at this site, compared to the others, and thereby the largest amount of electricity produced. When comparing the results obtained for two given scenarios of end-use, it is clear that the electricity generation is a better solution for the Site 1, since the final evaluation for this scenario is 3.5, compared to the scenario of heat production with a final evaluation of 3.33. The selected site is built to produce electricity instead of heat. It can be concluded that in most cases, higher reservoir temperature and hence higher temperature at the wellhead are suitable and economically

viable for electricity production. Sometimes, specific end-user requirements, for example, heat load for industry regardless of the very expensive pipeline system, may determine final end user application. This can be manipulated by DM via weight factors settings. Moreover, for Site 2 in the scenario of electricity production, the evaluation is 2.83, that is, significantly lower than for the scenario of heat production with evaluation of 3.67. The decision for this site between the two scenarios is in favour of direct use heat production since, as it can be seen from the parameters from Table 13, the inlet temperature, as well as the difference between inlet and outlet temperature, is smaller than that for Site 1 or Site 3. In addition to this, the fluid flow rate for Site 2 is notably lower compared to Site 1 and Site 3. Therefore, the results obtained with the proposed MCDM matrix demonstrate that using low-to-moderate-temperature geothermal resources in the direct-heat applications, given the right conditions, is an economically feasible business as stated in Reference [41]. As stated before, practical results can be altered according to end user needs. For Site 3, the final evaluation for the electricity generation is 3 and 3.5 for the heat production scenario. Although the inlet temperature is quite high, the lowest fluid flow rate of all selected sites affects the final evaluation, especially in the scenario of electricity production. Site 4 has the lowest evaluation of 2.75 in the scenario of electricity generation. Namely, this site has the closest difference between the temperature of the produced geothermal fluid and the injection temperature, leaving thereby a small amount of heat that can be transferred to the secondary working fluid. The smaller the difference between those temperatures, the smaller the amount of produced electricity. However, in the case of the second scenario of heat production, it is visible that this site has a better final performance indicator. Therefore, lower reservoir temperature and a smaller difference between wellhead inlet and outlet temperature are more suitable for direct heat use applications. Social and environmental impact of selected EGS sites are favorable for both scenarios and therefore have high-performance indicators for those criteria. Namely, the installed power of the selected sites imposes modest land-use intensity, considering that technical characteristics of the EGS systems atmospheric emissions are zero. Moreover, selected air-cooled systems do not require additional cooling water, leading to no surface water exploitation. The social impact is positive, since the selected projects are relatively small to medium size projects, and represent more benefits than disadvantages at the local level since the balance between power plant size and local impact and benefits in terms of FT and C&M jobs is established.

5. Conclusions

This paper presents the concept of multi-scale Decision-Making Support Tool for Optimal Usage of Geothermal Energy (DMS-TOUGE) and one of its main features, the multiple-criteria decision-making. These features are used for economic and environmental assessment of enhanced geothermal systems projects. The paper contributes with expanded and detailed criteria related to environmental and social impact giving the necessary emphasis on so far neglected important aspects for successful completion of geothermal projects. Moreover, by combining technical, economic, environmental, and social aspects of geothermal projects, the multiple-criteria decision-making presented in this work gives a comprehensive assessment of enhanced geothermal systems projects. The multiple-criteria decision-making (MCDM) matrix is tested on the case of four operating demonstration geothermal sites where it is used for assessment and comparative analysis. In the application of MCDM matrix, the choice of the weight to assign to the different criteria affects the evaluation of the project. In this work, it is considered that each criterion has equal relative importance in decision making, therefore the weights, w_j , $\forall j$, associated with each criterion, are considered identical and are valued with unitary weight. It is, however, important to highlight that the weights assigned to each criterion can vary depending on the DM's standpoint. Therefore, the results of the final evaluation of the project will vary if a greater weight is assigned to specific criteria according to DM's assessment. Further steps in tool development are the incorporation of many other relevant decision-making input parameters, not included in the analysis made in this study, testing its capabilities and subsequent verification and validation of the tool. Its proper function is of key importance for work packages and several

deliverables of H2020 project such as generation of several layers for mapping (of the main promising European sites where EGS can or should be implemented in a near future) in different resolutions: EU wide layer, layer considering different geologic features, and pilot site layer. The multi-scale Decision-Making Support Tool for Optimal Usage of Geothermal Energy (DMS-TOUGE) will be fully developed as part of the Horizon 2020 project: Multidisciplinary and multi-context demonstration of EGS exploration and Exploitation Techniques and potentials (MEET, GA No 792037). The developed tool will be useful for the decision makers involved in enhanced geothermal system projects associated with applications to nearly unexploited reservoir types (Variscan orogenic belt). This will provide valuable information to decision makers and investors for assessment of enhanced geothermal systems projects considering site-specific environmental, techno-economic and geological features.

Author Contributions: S.R., P.I. and I.R. have contributed to developing the concept, formulation and validation of the methodology. S.R. and P.I. have been involved in the implementation of the problem, and analysis of the results. I.R., T.B. and G.T. have been involved in investigation, supervision and project administration. All the authors are involved in preparing the manuscript.

Funding: This project has received funding from the European Union’s Horizon 2020 research and innovation programme under grant agreement No 792037 and support from Department of Energy and Power Systems of University of Zagreb Faculty of Electrical Engineering and Computing.

Conflicts of Interest: The authors declare no conflict of interest.

References

- IRENA (International Renewable Energy Agency). Renewable Capacity Statistics 2018. Available online: <https://www.irena.org/publications/2018/Mar/Renewable-Capacity-Statistics-2018> (accessed on 20 December 2018).
- Beckers, K.F.; Lukawski, M.Z.; Anderson, B.J.; Moore, M.C.; Tester, J.W. Levelized costs of electricity and direct-use heat from Enhanced Geothermal Systems. *J. Renew. Sustain. Energy* **2014**, *6*. [[CrossRef](#)]
- Alimonti, C.; Falcone, G.; Liu, X. Potential for Harnessing the Heat from a Mature High-Pressure-High-Temperature Oil Field in Italy. In Proceedings of the SPE Annual Technical Conference and Exhibition, Amsterdam, The Netherlands, 27–29 October 2014; pp. 3763–3775. [[CrossRef](#)]
- Zhang, L.; Yuan, J.; Liang, H.; Li, K. Energy from Abandoned Oil and Gas Reservoirs. In Proceedings of the SPE Asia Pacific oil and gas Conference and Exhibition, Perth, Australia, 20–22 October 2008; pp. 404–503.
- Davis, A.P.; Efstathios, E.; Michaelides, E. Geothermal power production from abandoned oil wells. *Energy* **2009**, *34*, 866–872. [[CrossRef](#)]
- Bu, X.; Ma, W.; Li, H. Geothermal energy production utilizing abandoned oil and gas wells. *Renew. Energy* **2012**, *41*, 80–85. [[CrossRef](#)]
- Barbacki, A.P. The use of abandoned oil and gas wells in Poland for recovering geothermal heat. In Proceedings of the World Geothermal Congress, Kyzshu-Tohoku, Japan, 28 May–10 June 2000.
- Xin, S.; Liang, H.; Hu, B.; Li, K. Electrical Power Generation from Low Temperature Co-Produced Geothermal Resources at Huabei Oilfield. Proceedings Thirty-Seventh Workshop on Geothermal Reservoir Engineering, Stanford, USA, 2012. Available online: <https://pangea.stanford.edu/ERE/pdf/IGAstandard/SGW/2012/Xin.pdf> (accessed on 26 April 2019).
- Cheng, W.; Li, T.; Nian, Y.; Wang, C. Studies on geothermal power generation using abandoned oil wells. *Energy* **2013**, *59*, 248–254. [[CrossRef](#)]
- Zhang, L.; Liu, M.; Kewen, L. Estimation of Geothermal Reserves in Oil and Gas Reservoirs. In Proceedings of the SPE Western Regional Meeting, San Jose, CA, USA, 24–26 March 2009.
- Guercio, M.; Bonafin, J. The Velika Ciglena Geothermal Binary Power Plant. In Proceedings of the 6th African Rift Geothermal Conference, Addis Ababa, Ethiopia, 2–4 November 2016.
- Tipurić, D.; Bruketa, N.; Čenan, D. *Izvodljivost Programa Gospodarske uporabe Geotermalne Energije na Lokaciji Velika Ciglena*; Sveučilište u Zagrebu, Ekonomski fakultet Zagreb: Zagreb, Croatia, 2007.
- Golub, M.; Kurevija, T.; Koščak-Kolin, S. Thermodynamic cycle optimization in the geothermal energy production. *Rud.-Geol.-Naft. Zagreb* **2004**, *16*, 81–84.
- Lu, S.M. A global review of enhanced geothermal systems (EGS). *Renew. Sustain. Energy Rev.* **2017**, *81*, 2902–2921. [[CrossRef](#)]

15. Sanyal, S.K.; Morrow, J.W.; Butler, S.J.; Robertson-Tait, A. Is EGS Commercially Feasible? *GRC Trans.* **2007**, *31*. Available online: <https://catalog.data.gov/dataset/is-egs-commercially-feasible/resource/6dde9e1b-8cfl-4b4c-96ab-28a8ed25eba9> (accessed on 26 April 2019).
16. Sanyal, S.K.; Morrow, J.W.; Butler, S.J.; Robertson-Tait, A. Cost of electricity from enhanced geothermal systems. In Proceedings of the Thirty-Second Workshop on Geothermal Reservoir Engineering, Stanford, CA, USA, 22–24 January 2017.
17. Clark, C.; Sullivan, J.; Harto, C.; Han, J.; Wang, M. Life cycle environmental impacts of geothermal systems. *J. Renew. Sustain. Energy* **2013**, *5*. [[CrossRef](#)]
18. Bayer, P.; Rybach, L.; Blum, P.; Brauchler, R. Review of life cycle environmental effects of geothermal power generation. *Renew. Sustain. Energy Rev.* **2013**, *26*, 446–463. [[CrossRef](#)]
19. Olasolo, P.; Juárez, M.C.; Olasolo, J.; Morales, M.P.; Valdani, D. Economic analysis of Enhanced Geothermal Systems (EGS). A review of software packages for estimating and simulating costs. *Appl. Therm. Eng.* **2016**, *104*, 647–658. [[CrossRef](#)]
20. Office of Energy Efficiency and Renewable Energy, Geothermal Electricity Technology Evaluation Model (GETEM). Available online: <https://www.energy.gov/eere/geothermal/geothermal-electricity-technology-evaluation-model> (accessed on 15 October 2018).
21. Heindinger, P.; Dornstadter, A.; Fabritius, A. HDR economic modelling HDRec software. *Geothermics* **2006**, *28*, 71–683. [[CrossRef](#)]
22. De Jesus, A.C. Environmental benefits and challenges associated with geothermal power generation. In *Geothermal Power Generation: Developments and Innovation*; R. DiPippo; Woodhead Publishing, 2016; pp. 477–498. [[CrossRef](#)]
23. Cataldi, R. Social Acceptability of Geothermal Energy: Problems and Costs. 1997, pp. 343–351, Ankara. Available online: <https://www.geothermal-energy.org/pdf/IGAstandard/ISS/2001Romania/cataldi.pdf> (accessed on 26 April 2019).
24. Popovski, K. Political and Public Acceptance of Geothermal Energy. IGC2003. Reykjavik, Iceland, September 2003. Available online: <https://orkustofnun.is/gogn/unu-gtp-report/UNU-GTP-2003-01-03.pdf> (accessed on 26 April 2019).
25. Shang, Y. Resilient Multiscale Coordination Control against Adversarial Nodes. *Energies* **2018**, *11*, 1844. [[CrossRef](#)]
26. Rockafellar, R.T.; Uryasev, S. Conditional value-at-risk for general loss distribution. *J. Bank. Financ.* **2002**, *26*, 1443–1471. [[CrossRef](#)]
27. Ilak, P.; Rajšl, I.; Đaković, J.; Delimar, M. Duality Based Risk Mitigation Method for Construction of Joint Hydro-Wind Coordination Short-Run Marginal Cost Curves. *Energies* **2018**, *11*, 1254. [[CrossRef](#)]
28. Ilak, P.; Krajcar, S.; Rajšl, I.; Delimar, M. Pricing Energy and Ancillary Services in a Day-Ahead Market for a Price-Taker Hydro Generating Company Using a Risk-Constrained Approach. *Energies* **2014**, *7*, 2317–2342. [[CrossRef](#)]
29. Gehringer, M.; Loksha, V. *Geothermal Handbook: Planning and Financing Power Generation (English)*. ESMAP technical report; no. 002/12. 2012. Available online: https://www.esmap.org/sites/esmap.org/files/DocumentLibrary/FINAL_Geothermal%20Handbook_TR002-12_Reduced.pdf (accessed on 7 January 2019).
30. Mengying, L.; Noam, L. Comparative Analysis of Power Plant Options for Enhanced Geothermal Systems (EGS). *Energies* **2014**, *7*, 8427–8445. [[CrossRef](#)]
31. Soldo, E.; Alimonti, C. From an oilfield to a geothermal one: use of a selection matrix to choose between two extraction technologies. In Proceedings of the World Geothermal Congress 2015, Melbourne, Australia, 19–25 April 2015.
32. Moon, H.; Zarrouk, S.J. Efficiency of geothermal power plants: A worldwide review. In Proceedings of the New Zealand Geothermal Workshop 2012, Auckland, New Zealand, 19–21 November 2012.
33. AL-Mahrouqi, J.; Falcone, G. An Expanded Matrix to Scope the Technical and Economic Feasibility of Waste Heat Recovery from Mature Hydrocarbon Fields. In Proceedings of the 41st Workshop on Geothermal Reservoir Engineering, Stanford, CA, USA, 22–24 February 2016.
34. Rafferty, K. Industrial Processes and the Potential for Geothermal Applications. Report. GHC Bulletin: Oregon, 2003. Available online: https://oregontechstatic.azureedge.net/sitefinity-production/docs/default-source/geoheat-center-documents/quarterly-bulletin/vol-24/art21683ee4362a663989f6ff0000ea57bb.pdf?sfvrsn=8b258d60_4 (accessed on 26 April 2019).

35. Cataldi, R. Social Acceptability of Geothermal Energy: Problems and Costs. EC International Geothermal Course. Oradea, Romania, 2001; pp. 343–351. Available online: <https://www.geothermal-energy.org/pdf/IGAstandard/ISS/2001Romania/cataldi.pdf> (accessed on 26 April 2019).
36. Zang, A.; Oye, V.; Jousset, P.; Deichmann, N.; Gritto, R.; McGarr, A.; Majer, E.; Bruhn, D. Analysis of induced seismicity in geothermal reservoirs—An overview. *Geothermics* **2014**, *52*, 6–21. [CrossRef]
37. Johansson, T.B.; Patwardhan, A.; Nakicenovic, N. Gomez-Echeverri, Land-use and Energy Systems. In *L. Global Energy Assessment: Toward a Sustainable Future*; Cambridge University Press: Cambridge, UK, 2012; pp. 232–234.
38. DiPippo, R. Geothermal energy Electricity generation and environmental impact. *Energy Policy* **1997**, *19*, 798–807. [CrossRef]
39. Johnson, S. Natural radiation. *Va. Miner.* **1991**, *37*, 9–16.
40. Zongjun, G.; Yonggui, L.; Yaun, G. The Principle of Density Differences Drive Geothermal Water to Move and the Short-Range Recharge Model of Geothermal Water in Hilly Area. In Proceedings of the Thirty-Ninth Workshop on Geothermal Reservoir Engineering PROCEEDINGS, Stanford, CA, USA, 24–26 February 2014.
41. Lund, J.W. Direct Utilization of Geothermal Energy. *Energies* **2010**, *3*, 1443–1471. [CrossRef]



© 2019 by the authors. Licensee MDPI, Basel, Switzerland. This article is an open access article distributed under the terms and conditions of the Creative Commons Attribution (CC BY) license (<http://creativecommons.org/licenses/by/4.0/>).

4.5.3.2 My present research

4.5.3.2.1 Ongoing studies at the Noble Hills analogue (CA, USA)

4.5.3.2.1.1 Geodynamic evolution of the Eastern California Shear Zone

Pavlis and Trullenque (2021) have shown that the NH were transported along strike of the SDVFZ. Right lateral drag and intensive stretching of the Proterozoic basement and Mesozoic granitoids leading to formation of cataclastic shear zones and boudinage (Figure 10) have been described by Klee et al. (2021a). The authors evidence a strain gradient across the NH, with lower amount of deformation at the back of the range compared to the front. This deformation started around 12 Ma ago (Pavlis and Trullenque, 2021) and produced an internal anisotropy within the NH with a dominant NW-SE fractures direction in domains A and B (Figure 11) defined by Chabani et al. (2021b).

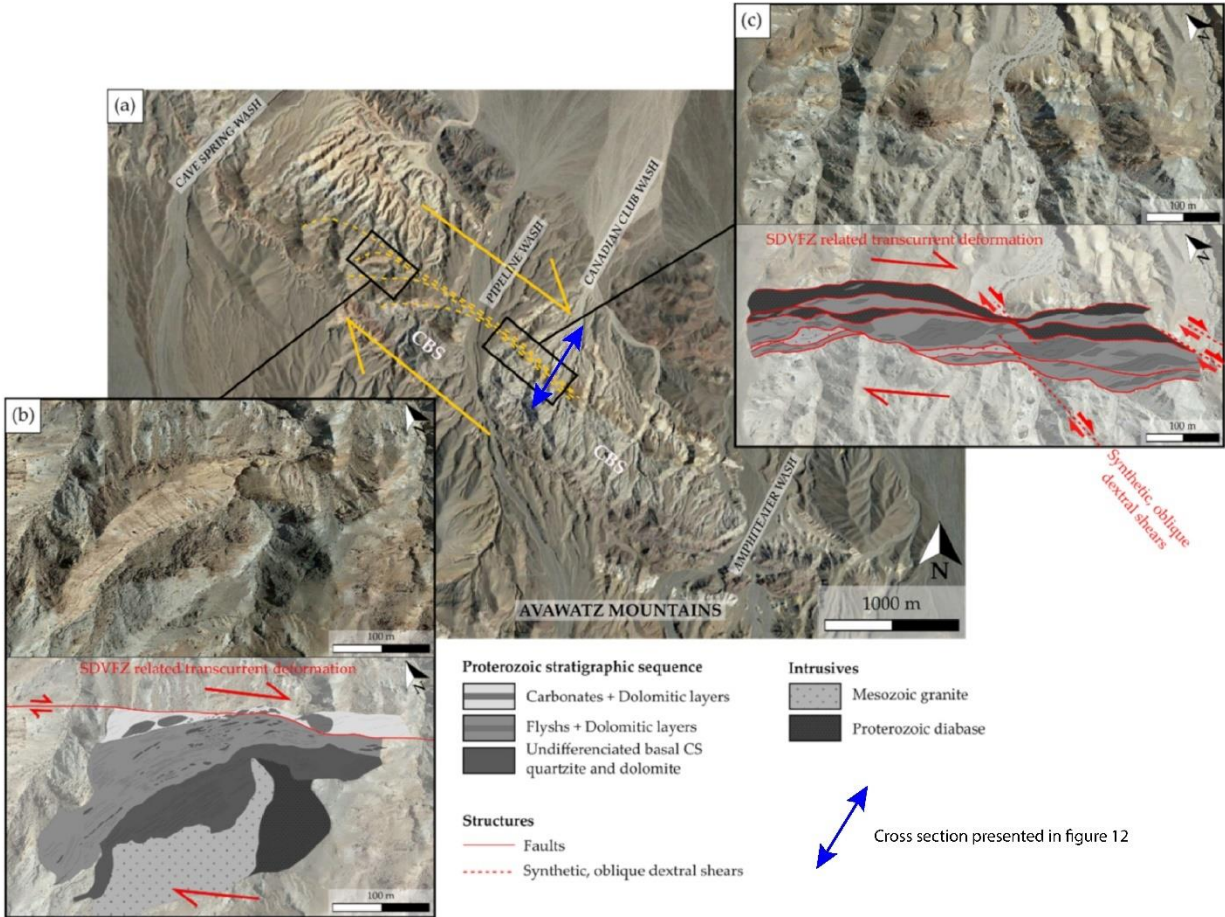
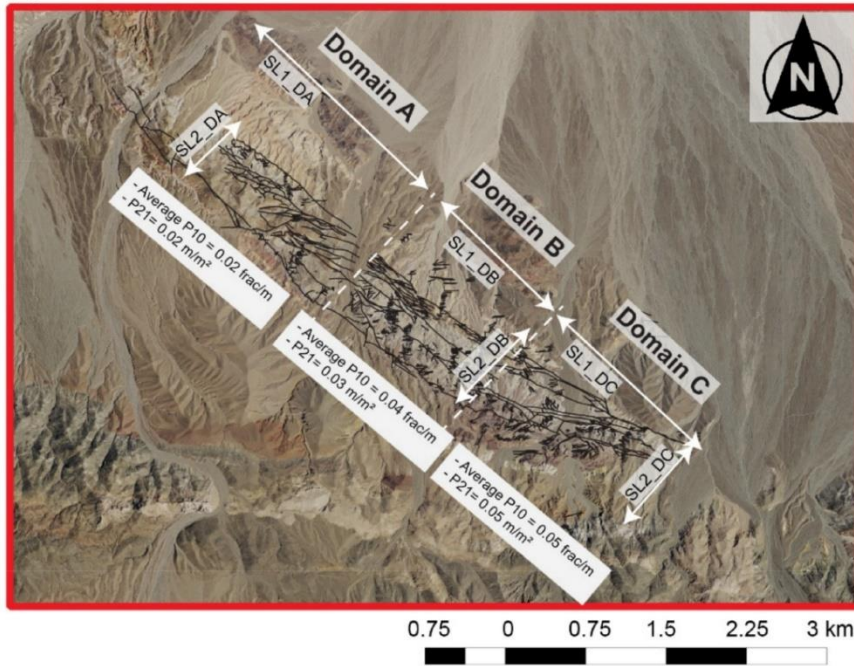


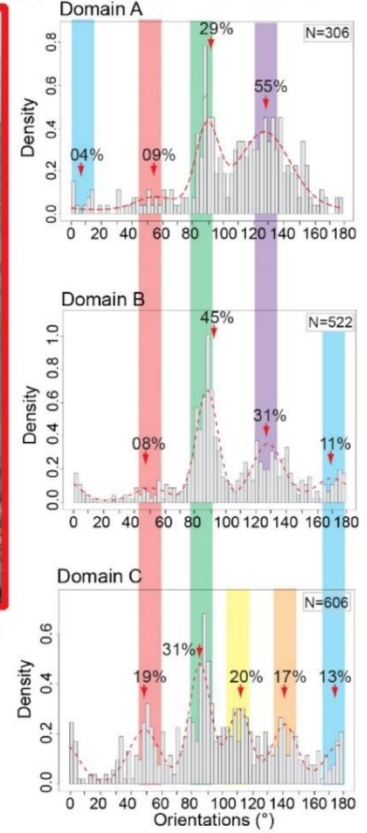
Figure 10: NH satellite image with inserts showing dextral transcurrent deformation at the front of the range (figure taken from Klee et al., 2021a).

Klee et al. (2021b) have documented a temperature gradient along strike of the NH, higher temperatures being found towards the SE and concluded that the south eastern termination of the NH have been buried deeper than the north western part. These findings implicitly suggest a differential uplift along strike of the NH which explains the observed topography steepening leading to higher erosion and disappearance of the Proterozoic basement and Crystal Springs sedimentary sequence towards the SE. This differential cannot be solely explained by means of dextral strike-slip activity along the SDVFZ in an overall transtensional setting within the DV area. Niles (2016) has documented south of the Canadian Club Wash (Figure 12) a compressive deformation at the front of the NH. I confirm compression in the southeastern part of the NH and add that this compressive phase passively transports inherited SDVFZ strike-slip structures towards the NE.

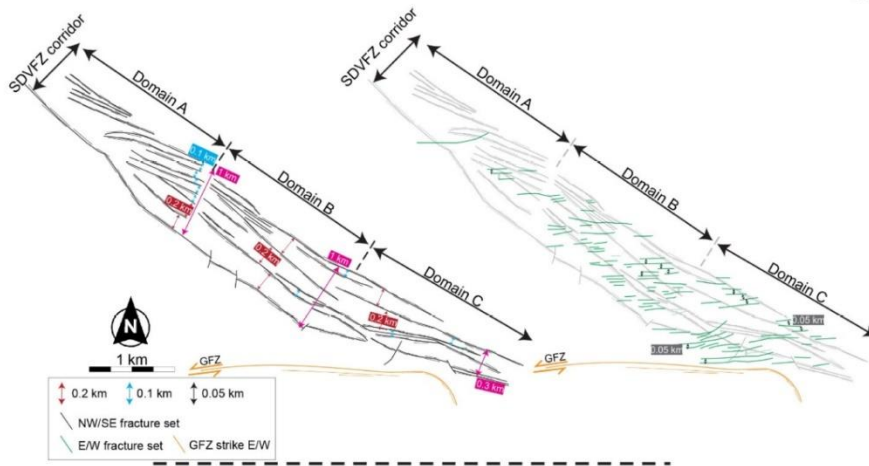
(a) Noble Hills domains



(b) Orientation distributions



(b) Spatial distribution of fracture network at NH scale



(c) Spatial distribution of fracture network at outcrop scale

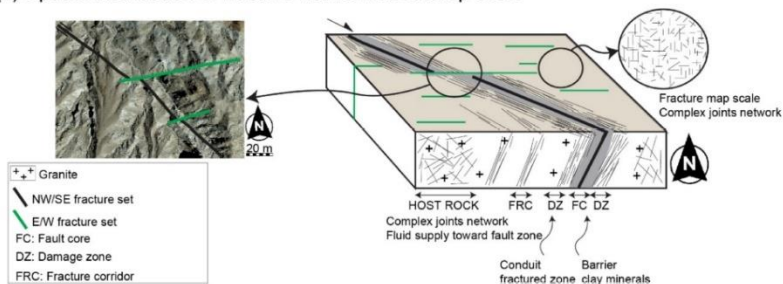


Figure 11: a) fracture traces found within the NH and subdivision of the range in three domains, b) orientation distributions, c) geological interpretation showing that NW-SE fractures are overprinted by the E-W fracture set (figures taken from Chabani et al., 2021b).

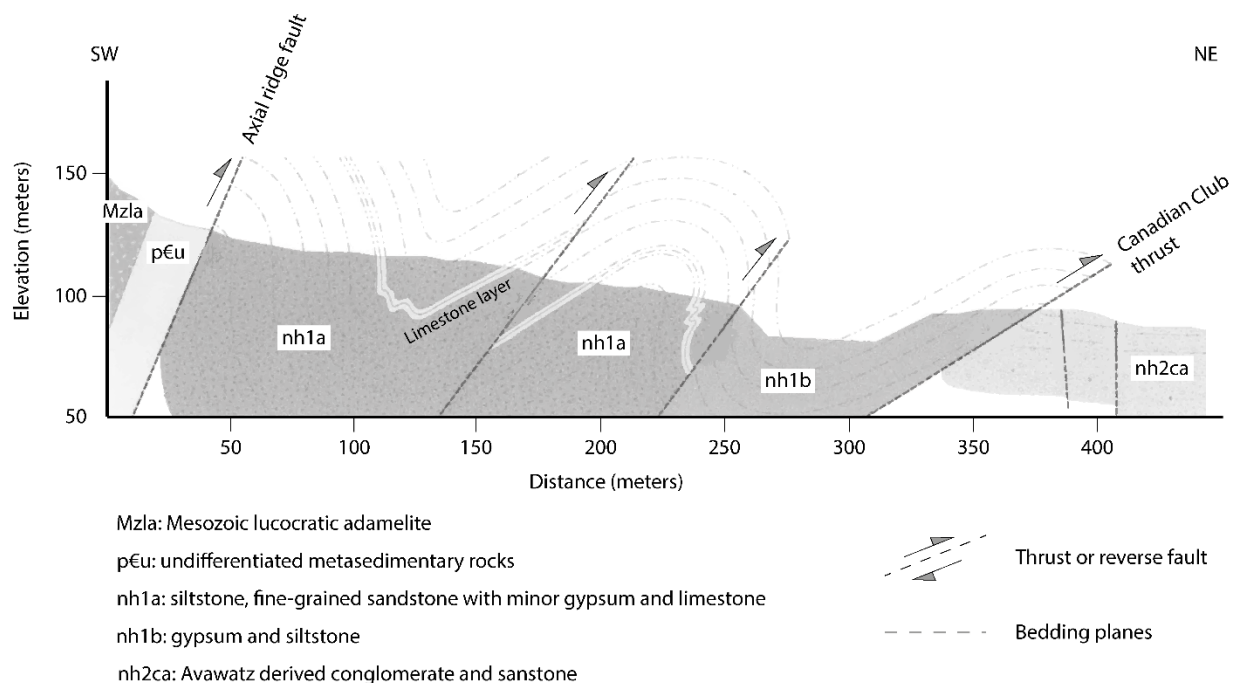


Figure 12: Cross-section at the frontal part of the Noble Hills range (simplified after Niles, 2016).

The observed compression postdates activity along the SDVFZ and is responsible of the wedging out and progressive curvature in map view of the NH in the southeast. This progressive curvature is accommodated by a combined sinistral activity along E-W (green distribution in Figure 11b) and NE-SW (red distribution in Figure 11b) fractures measured by Chabani et al. (2021b) in their domain B and domain C. The authors demonstrate that the E-W structures are offsetting in a left lateral sense the NW-SE fault zones inherited from activity along the SDVFZ (Figure 11c) and must therefore correspond to a later deformation phase. The NE-SW oriented structures are also postdating activity of the SDVFZ as they are also offsetting the NW-SE inherited anisotropy.

My ongoing research at NH combines high resolution field mapping with radiometric dating of fault rocks found along strike of SDVFZ and Garlock Fault Zone (GFZ). I confirm the hypothesis by Chabani et al. (2021b) namely that activity along GFZ is postdating movements along the SDVFZ. I am working on the publication of these results in the Geology journal (Trullenque et al. *in prep*).

4.5.3.2.1.2 Influence of inherited structures on later fluid flow

The above-described late E-W and NE-SW fractures are particularly well-developed at the back of the NH range where they occasionally form meter thick veins of baryte. These baryte veins do not penetrate across the whole NH and sinistral movements are then accommodated by broad cataclastic zones. It is interesting to note that vein opening seems restricted to the back part of the NH where 1) the rocks have suffered lower strain compared the front of the range and 2) anisotropy inherited from SDVFZ activity is less pronounced. On one hand, it could be argued that the late compressional overprint accommodated by both E-W and NE-SW sinistral strike-slip structures is of minor importance. Thrusting of SDVFZ inherited structures on top of Neogene units found at the front of the NH associated to thrusting of the whole Avawatz range on top of NH (Trullenque et al. *in prep*.) is not in favor of this hypothesis. On the other hand it is more conceivable

that penetrative cataclastic deformation associated to argillic alteration described by Klee et al. (2021a) in the vicinity of high strain zones induces a different mechanical response of the reservoir to renewed brittle deformation in a novel stress regime.

The intersection between the SDVFZ and GFZ represents an unique opportunity to investigate the role of late deformation phases on a pre-structured reservoir in terms of fluid flow in a varying stress regime. The response in terms of either 1) opening of sharp fractures or 2) distribution of movements within a diffuse zone which prevents to form a sharp flow channel will be further developed in the perspectives session.

4.5.3.2.2 Influence of inherited clay rich zones in reservoir fluid circulation. Combined geochemical and mechanical approach at the Schauinsland mining district

Our investigations along the southern termination of the SDVFZ have confirmed that the NH range can be considered as an exhumed geothermal reservoir. This reservoir shows many evidences in favor of a coeval fluid circulation during progressive straining of granitic rocks in a strike-slip regime. Klee et al. (2021a) have shown that argillic alteration is becoming dominant in the vicinity of high strain zones. This alteration leads to the formation of Clay Rich Zones (CRZ) which drastically influence the properties of the reservoir rocks. CRZ are generally associated to highly fractured zones of varying orientations. Clay mineral formation is responsible of a drastic friction coefficient diminution which prevents elastic stress accumulation within the structure. CRZ act therefore as decoupling zones and their petrophysical properties in terms of porosity and permeability are extremely variable which in turn influence flow pathways and fluid quantities within the reservoir. The mechanical influence of CRZ and the relation to induced seismicity during EGS operations has been discussed by Meller and Ledéser (2017). The authors show that seismic events induced during stimulation phases at the SSF reservoir are observed within unaltered granitic rocks while altered zones with a significant amount of clays only show little or no seismicity. Besides geothermal, the response to strain of rock alteration products leading to formation of CRZ along large scale faults influence the mechanical response of the whole system (Schleicher et al., 2010) and in turn its potential natural seismic hazard.

I am interested in the role of these CRZ and structural heritage in general on subsequent deformation phases affecting a given geological environment. My research contribution is here focusing on the perturbation of brittle mechanical vein opening process when approaching a highly anisotropic and mechanically weak inherited CRZ.

In the URG example, many inherited NE-SW oriented Variscan structures are found nowadays in the massifs bordering the graben, in Germany (Rhenish, Odenwald and BFM) and France (Southern VM) plus basement below the tertiary sedimentary infill of the graben. We have seen that these structures are associated with a 40 km wide and 400 km long crustal scale strike-slip system, the URGSZ, active during Viséan (Edel et al., 2007). From a large-scale geodynamic point of view, sinistral wrenching along the URGSZ is contemporaneous to dextral activity along NW-SE Thuringian, Bray and South Armorican fault zones (Figure 5).

Edel et al. (2007, 2002), Grimmer et al. (2017), Illies (1978) and Schumacher (2002) have insisted on the role of inherited NNE-SSW to WSW-ENE Variscan anisotropy on present-day structuration of the URG and also on the role this anisotropy had during URG opening in a varying stress-field.

The NE-SW structures have been reactivated during the Alpine cycle, at least during the Mesozoic and Cenozoic periods and still play a role in the present seismicity of the area. Thermal cooling of the

lithosphere between Paleozoic and Mesozoic lead Edel et al. (2007) to consider that post-Variscan reactivation of these structures occurred exclusively in the brittle field.

The first major phase of Variscan structures reactivation occurred in the Mesozoic.

During Trias, the new Alpine rifting cycle began and several rift systems initiating the breakup of Pangea developed in Europe (Ziegler and Stampfli, 2001). Continued Mesozoic extension is responsible of the opening of the Alpine Tethys during the late Middle Jurassic and Mid-Cretaceous opening of the Valais Ocean. The preferential alignment of URG Permian (Boigk and Schöneich, 1970) and Tertiary (Doehl, 1970, 1967; Schumacher, 2002) sediment sub-basins and isopaches along NE-SW directions is a first sign that inherited Variscan anisotropy might have influenced sedimentation within the graben.

The Mesozoic imprint is also noticeable within the VM in the form of hydrothermal activity within Triassic sandstones from the URG (Clauer et al., 2008; Liewig, 1993; Liewig et al., 1987) and Northern VM (Tournier et al., 1999). Edel (1997) and Fluck (1992) have discussed the presence of polymetallic veins found within the VM and distributed along NE-SW oriented structures. These veins are interpreted by Edel et al. (2007) as a sign of reactivation of Variscan structures during the Late Triassic, Early Jurassic break up of Pangea. Schleicher et al. (2006b) have documented Jurassic and Cretaceous episodes of Illite clays characterizing injections of hydrothermal fluids within altered SSF granite. When combining these evidences of hydrothermal fluid circulations to paleomagnetic data to paleostress reconstructions using ore veins from the southern VM, Edel et al. (2007) have suggested a first reactivation of some Variscan structures consistent with an extensional stress-field during Lias.

During the Cenozoic extension related to URG opening reactivated again the Variscan structures.

Based on data from Gentier et al. (2013) and Valley (2007), Armandine Les Landes et al. (2019) define four main set of faults within the URG: Inherited Variscan structures NE-SW (set 1) and NW-SE (set 2) striking are observed at regional scale.

Oligocene structures are ordered in two sets:

- N-S striking and W dipping (set 3). This set could be interpreted as reactivation of 1) lower Carboniferous to Permian sinistral faults during the late Eocene (Schumacher, 2002) or 2) N170° sinistral strike-slip faults from late Miocene up to present-day in a NW-SE compression regime as a strike-slip system.
- NNW-SSE striking as E dipping (set 4). This set could be considered as Variscan N20° sinistral strike-slip and Variscan N135° dextral strike-slip reactivated during late Eocene and to N170° sinistral strike-slip faults.

Another example of possible Cenozoic reactivation of Variscan structures is found in Glaas (2021) in their review of 8 geothermal wells in the central URG. The authors notice that the geometry of permeable fractures strikes NNW-SSE for SSF, N-S for RH and NNW-SSE for Illkirch and suggest that these nearly vertical fractures could represent an heritage from the Sudete Variscan phase possibly reactivated during the Pyrenean compression. Large scale present-day convective transport along the inherited NE-SW oriented Variscan structures has also been postulated by Sanjuan et al. (2016) outlining again the influence of inherited structures in the present-day fluid circulation within the URG.

Inherited Variscan structures still play a role in the present-day geological framework of the URG. The present stress-field in the URG area is consistent with a NW-SE orientation of σ_1 and is constrained by both earthquakes focal mechanisms (Ahorner, 1975; Bonjer, 1997; Bonjer et al., 1984; Plenefisch and Bonjer, 1997) and in situ measurements (Illies and Greiner, 1979). This orientation is consistent with late Miocene compression observed in the Jura as a result of Africa Europe convergence (Bergerat, 1985;

Giamboni et al., 2004; Laubscher, 2001; Schumacher, 2002; Villemin and Bergerat, 1987). Seismic activity is dominantly recorded in the southern part of the URG and is consistent with sinistral strike-slip motions along N-S to NNE-SSW structures though several focal mechanisms do not follow this trend and show a N-S to NNW-SSE σ_1 direction (Ahorner, 1975; Plenefisch and Bonjer, 1997; Rouland et al., 1983). These earthquakes are located on N30-N35° inherited Variscan structures and show dominant strike-slip mechanisms. The reactivation of these Variscan structures outlines their importance in the present stress distribution in the URG.

The above literature review shows that reactivation of Variscan, dominantly strike-slip, structures is evident through the whole history of the URG outlining the importance of structural heritage on its present-day position and tectonic evolution. This structural heritage plays a role in the location of structures from large scale tectonics down to local fracture or schistosity development. This anisotropy influences both heat and fluid flow within the geological environment inducing possible host rock alteration and regional stress-field perturbations. This overall complexity challenges reservoir utilization in terms of ore vein mining, geothermal well positioning or long-term storage capacity of CO₂.

The well-constrained geological framework coupled to polyphase deformation and associated brines transport makes the URG an ideal natural laboratory to investigate fluid flow perturbations in a complex structural setting. The challenge is to find in this area some outcrops with a preserved record of Variscan structures and evident signs of reactivation in both Mesozoic and Cenozoic. I am using the well-constrained models and associated outcrops at the Schauinsland and Freiamt Sexau (Figure 13) described by Werner et al. (2004) and Werner and Franzke (2001) as all the structures they present are found in a restricted environment. This precludes the necessity of large-scale extrapolations and inherently associated uncertainties. I am using as well some exposures found in an ore mine at Gabe Gottes (GG) (Figure 13) in the VM and described by (Hafeznia et al., 2015).

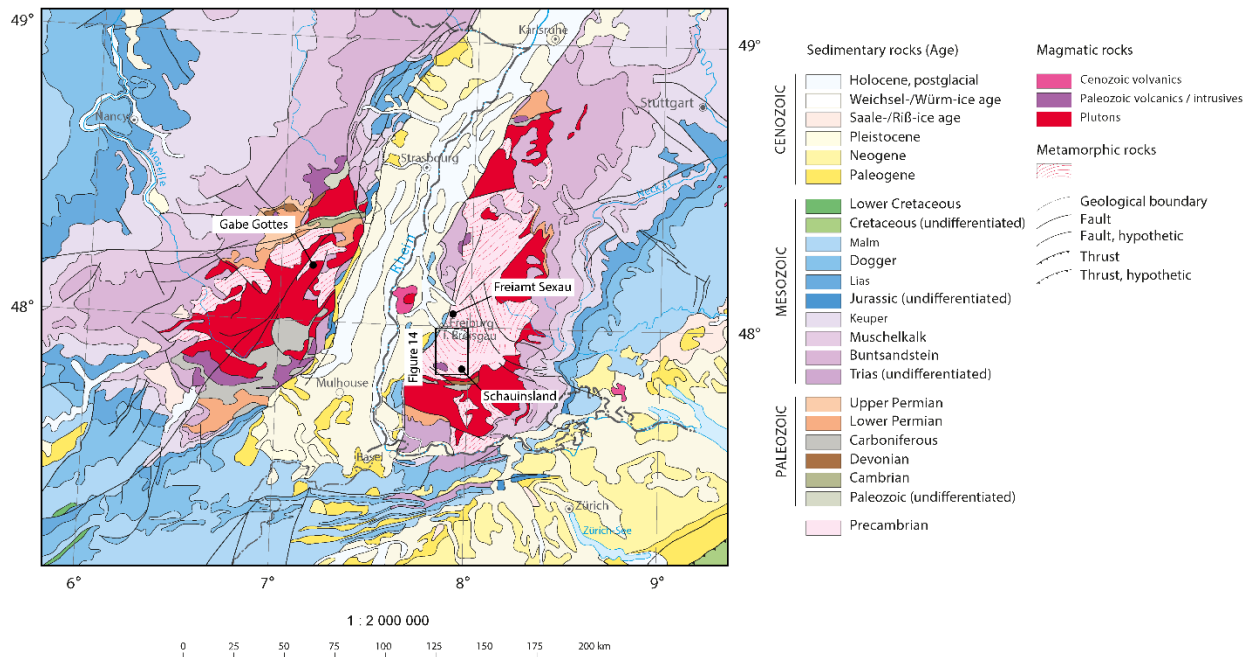


Figure 13: Geological map of the Upper Rhine Graben area (Voges et al., 2004).

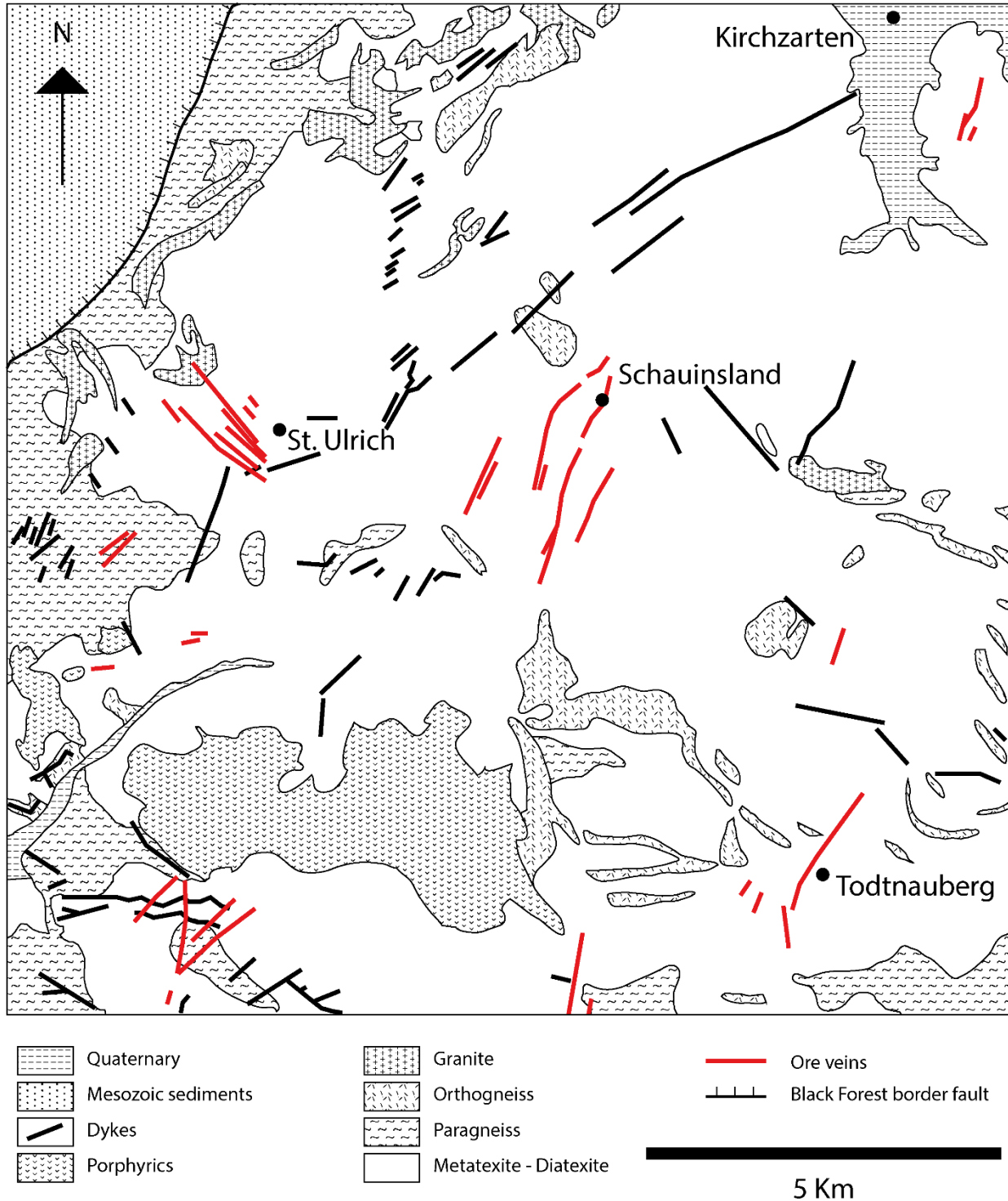


Figure 14: Simplified geological map around the Schauinsland massif (after Werner et al., 2004).

The vast majority of ore veins from the Schauinsland and Freiamt Sexau district (Figure 13 and Figure 14) have formed during the Cenozoic and the large majority of veins is oriented in a NNE-SSW to NE-SW direction.

The model of geological evolution proposed by Werner and Franzke (2001) at the Freiamt Sexau district can be summarized as follow (Figure 15).

- 1: Granitic intrusives are emplaced during late Variscan tectonic along dominantly sinistral strike-slip zones. From a geodynamic point of view, these granites are equivalent to the syn-wrenching plutonic activity described by Edel et al. (2007).
- 2: Strike-slip reactivation of the inherited NE-SW structural directions and formation of meter thick CRZ during late lower Cretaceous as a result of a far-field stress propagation linked to opening of Tethys and Atlantic oceans. Mankopf and Lippolt (1997) could date these CRZ and obtained ages between 290 and 240 Ma (Permian to Lower Trias boundary) using U/He dating method.
- 3: Second strike-slip reactivation of inherited NE-SW structural directions and deposits of Siderite and Baryte ore veins.
- 4: Post Oligocene third strike-slip reactivation of NE-SW structural directions and deposits of a second generation of Baryte veins.

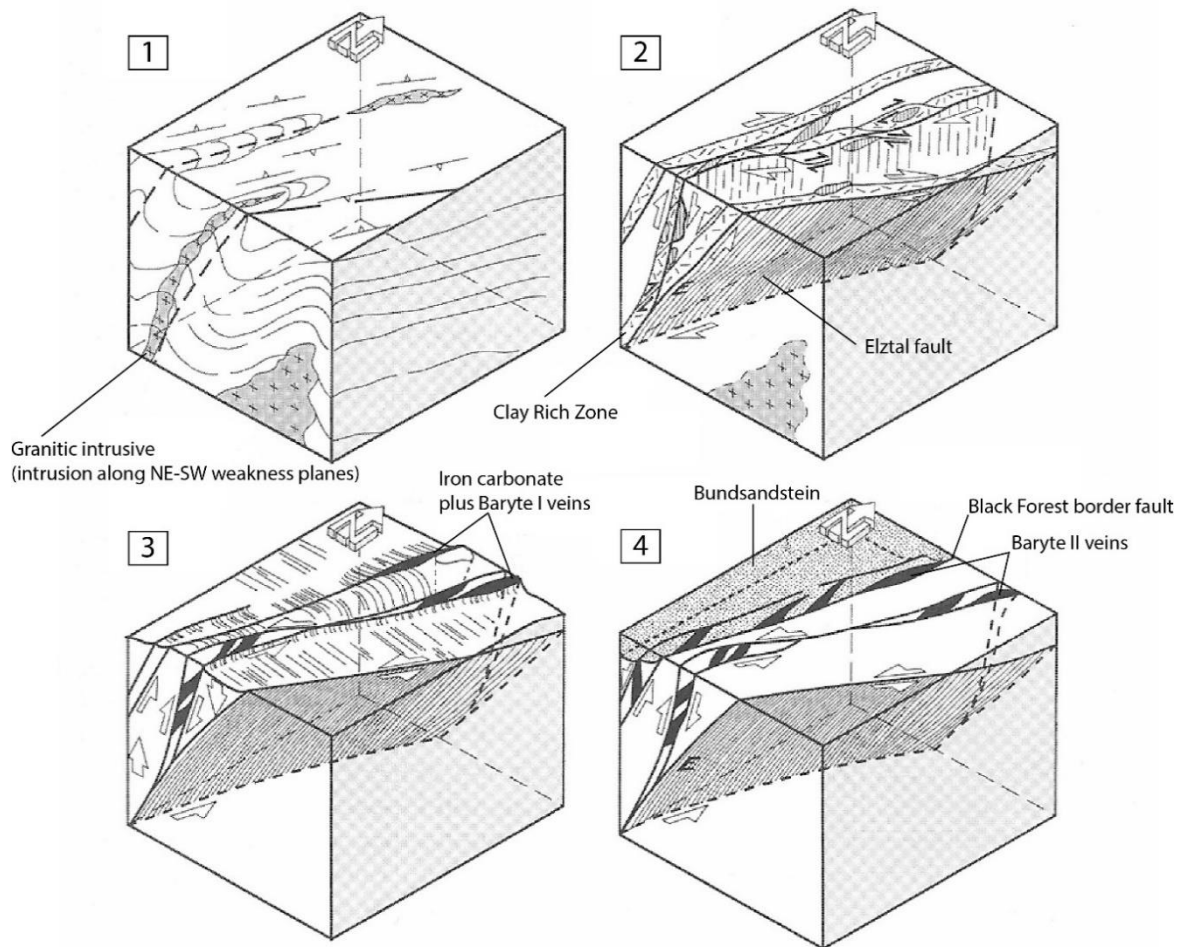


Figure 15: Geological reconstruction of the Freiamt – Sexau mining district (figure translated from Werner and Franzke, 2001).

The model of geological evolution proposed by Werner et al. (2004) at the Schauinsland district can be summarized as follow (Figure 16).

- 1: during upper Carboniferous, final stages of Variscan shortening and presence of North dipping thrusts belonging to the suture between Moldanubian and Bohemian terranes (so called Badenweiler Lenzkirch zone).
- 2: granitic and lamprophyres intrusions during Upper Carboniferous to Permian, along NE-SW directions (Lippolt and Siebel, 1991). These intrusions occur in a timeframe comparable to the granitic intrusives along the SHF, and the numerous granitic bodies from the VM and SSF (Cocherie et al., 2004). It is proposed that these intrusions are occurring at the end of the sinistral wrench tectonic found in the geographical position of the URG at that time.
- 3: In the lower Jurassic to Upper Cretaceous period, E-W Variscan structures are reactivated as a result of a far-field stress propagation linked to opening of Tethys and Atlantic oceans. This reactivation produced intense alteration of the host rock and forms meter thick CRZ.
- 4: During early Cenozoic, a trans-tensive reactivation of the NE-SW inherited structures lead to the formation of ore veins, offsetting the previously formed CRZ.

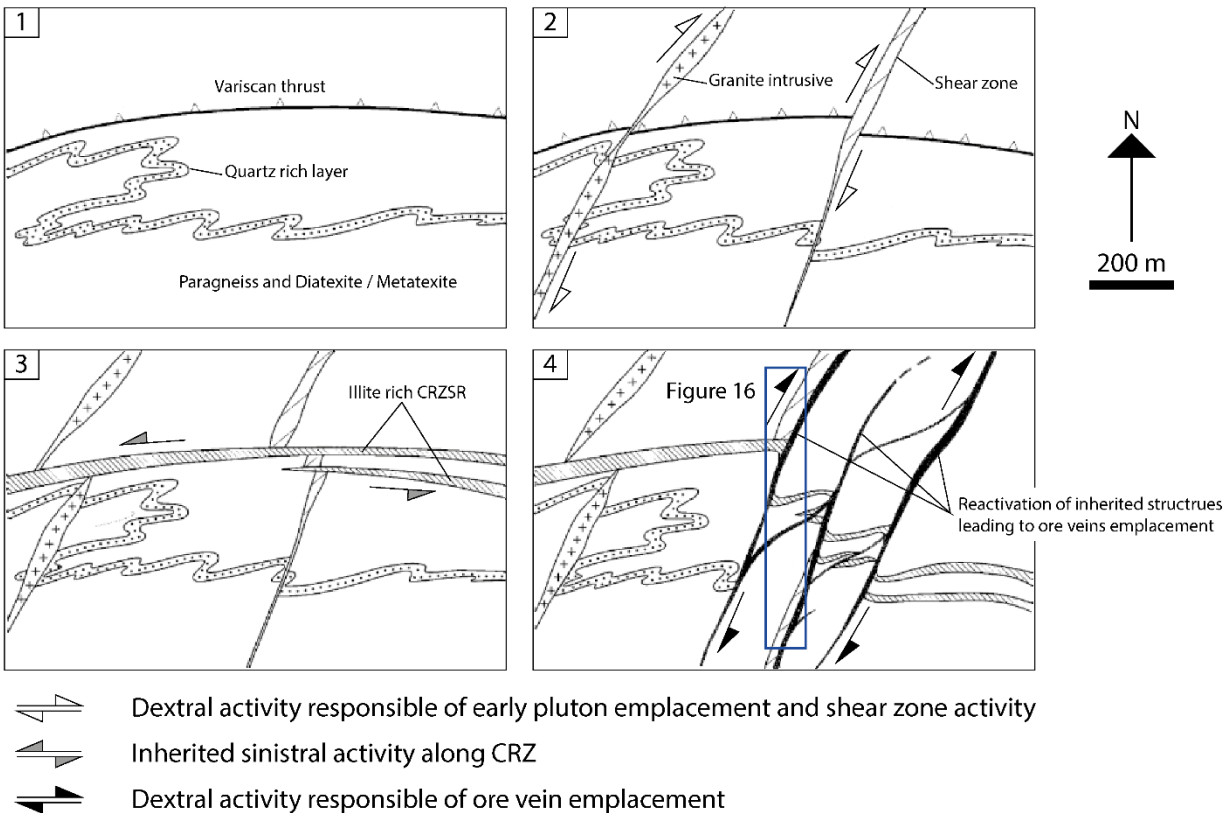


Figure 16: Geological reconstruction of the Schauinsland mining district (figure translated from Werner et al., 2004).

The structural map presented in Figure 17 (see location in Figure 16) shows an example of two ore veins running nearly parallel to each other in a NE-SW direction. These are connected by contemporaneous Riedel shear type structures (“Diagonalstruktur 2” and “Diagonalstruktur 3”) and paleo-stresses reconstructions show a main compressive direction oriented NE-SW with an extension direction of N130°-N150° (Werner and Franzke, 2001).

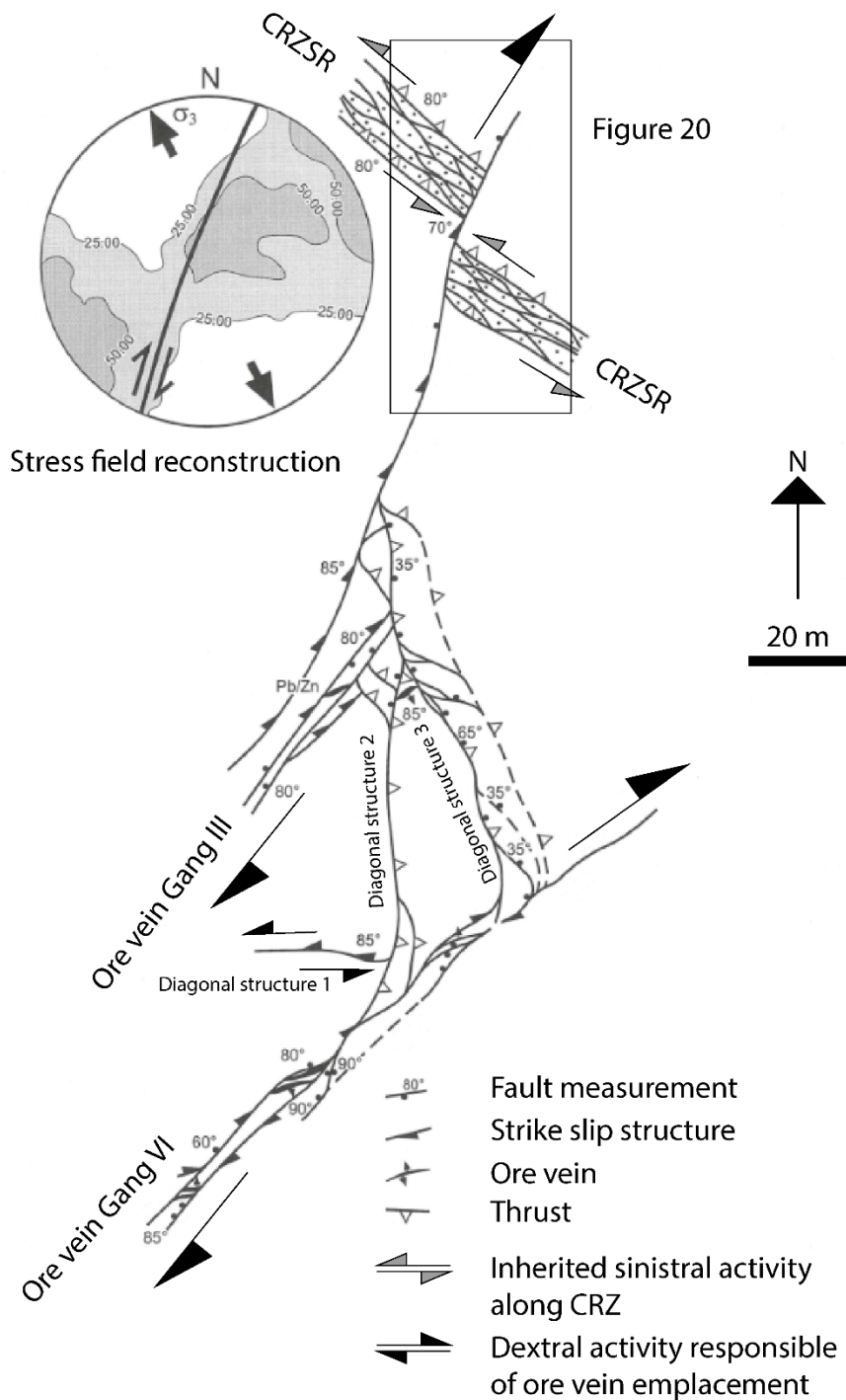


Figure 17: Structural map and stress-field reconstruction within the Schuainland mining district. Dextral offset of the CRZSR by ore vein Gang III is depicted (figure translated from Werner et al., 2004).

The CRZ Schumacher Ruschel (CRZSR) is interpreted as an inherited thrust active during Variscan convergence and reactivated as a sinistral strike-slip structure in Mesozoic. The origin of this reactivation is a possible far-field stress propagation related to opening of Tethys and Atlantic ocean (Werner et al.,

2004; Werner and Franzke, 2001). The CRZSR is oriented at N100-N110° and presents a subvertical dip angle.

A profile across the CRZSR shows all domains described by Choi et al. (2016) with a symmetric organization consisting is about 10 m of damage zone on each side of a 1 m thick clayish fault core. Within the damage zone, the gneiss host rock is increasingly brecciated and hydrothermally altered when approaching the fault core and formation of an incipient penetrative schistosity subparallel to both initial foliation and strike of fault core is observed (Huttner and Wimmenauer, 1967). Progressive development of clay seams is also noticed when approaching fault core. The fault core is dominated by a total amount of at least 60% clays and altered brecciated gneiss clasts. No high temperature ductile stretching is present within the gneiss clasts and Werner et al. (2004) have documented in thin section that quartz crystals were brecciated with numerous of undulatory extinction. Werner and Franzke (2001) conclude that shearing activity along the CRZSR has occurred close to the brittle/ductile transition for quartz at around 300°C. Composition of the fault core matrix shows dominant Illite, Illite-Smectite and Chlorite plus some minor Kaolinite and Montmorillonite (Werner et al., 2004). From a microstructural point of view CRZ at Schauinsland show an anastomosing network of micro shear zones (Figure 18). Boudinated and non-continuous layers of weakly consolidated gneiss cataclasites of centimeter thickness are found within the main CRZ foliation.

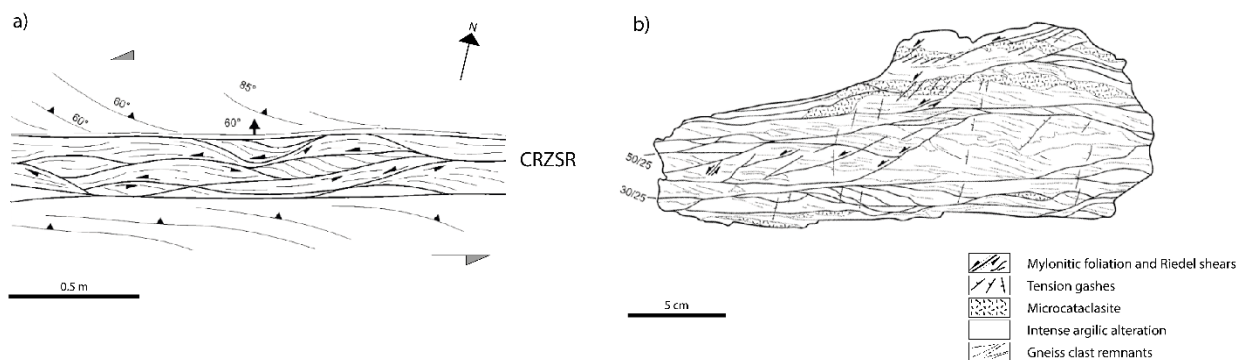


Figure 18: Schematic representation from the CRZSR a) at outcrop scale, b) hand specimen (figure translated from Werner et al., 2004).

Five features of particular interest for the purpose of my research interest are found when dealing with ore veins and CRZ at the Schauinsland mining district:

- Ore veins encountered within the Schauinsland massif always develop at a very high angle or perpendicular to the gneiss foliation, along inherited Variscan NE-SW directions (Figure 19).
- Ore veins wedge out when approaching CRZ (Figure 19).
- CRZ are locally thinned and offset in a dextral sense when in contact with the termination of an ore vein (Figure 20).
- Ore concentrations are barely found within the CRZ and only minor occurrences have been locally described in nearby districts by Franzke and Werner (1994), Garcia-Gonzales and Wimmenauer (1975) and Hofmann and Eikenberg (1991).
- Mine galleries cutting through CRZ are dry. CRZ are a natural barrier to present-day aquifer or meteoric fluid flow within the reservoir. At the opposite, ore veins are often guiding this water flow.

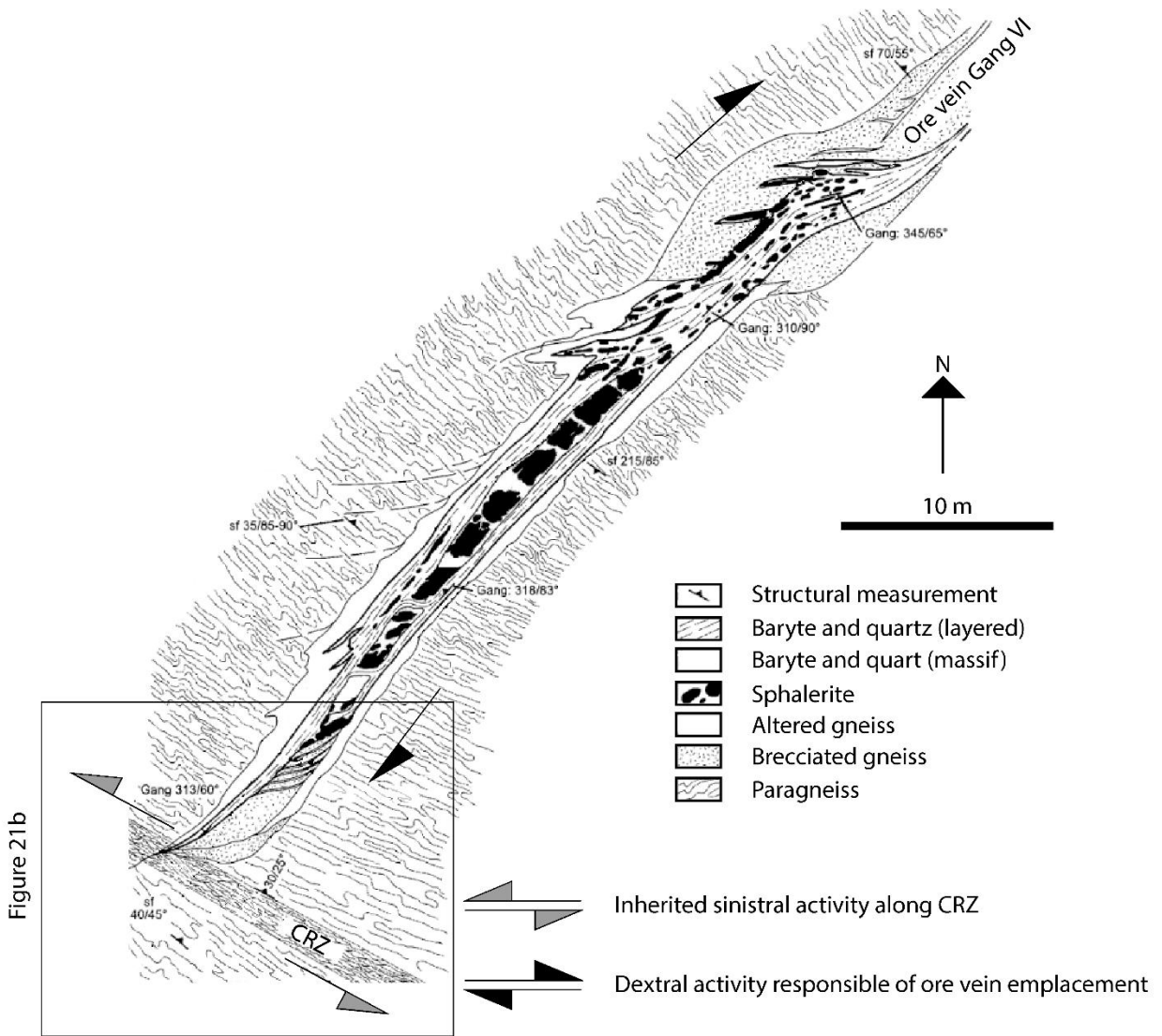


Figure 19: High resolution mapping alor ore vein Gang VI (figure translated from Werner et al., 2004).

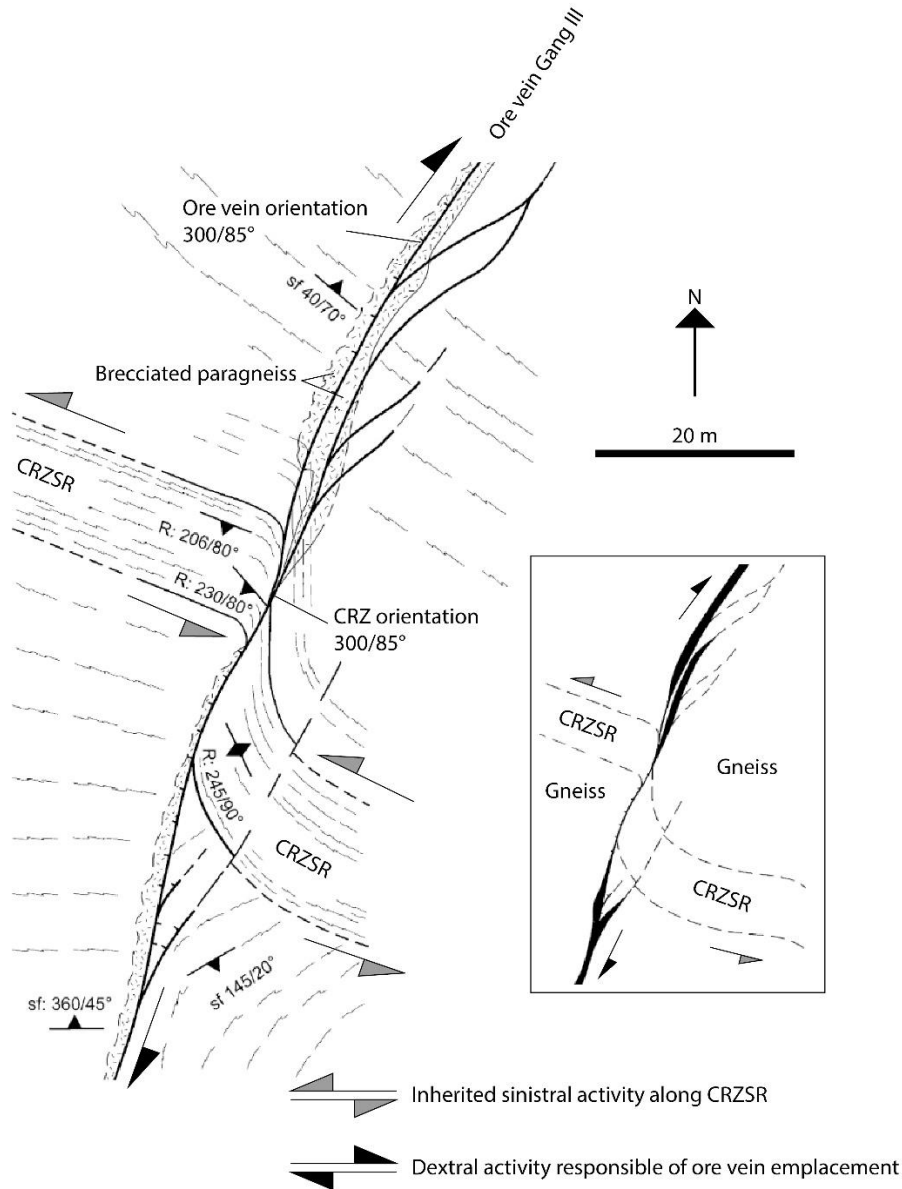


Figure 20: Detailed structural mapping showing dextral offset of the CRZSR, related to emplacement of ore vein Gang III. (figure translated from Werner et al., 2004). See position in figure 17.

In my opinion, these five features outline once more the importance of both inherited anisotropy and alteration on fracture development and associated fluid flow when a given stress-field is applied to a pre-structured system. The Schauinsland mining district has an early record of two coeval NW-SE and NE-SW shear directions developed during the Variscan orogeny. This structuration at local scale is analogue to large scale plate tectonics described in session 4.5.3.1.1 with a coeval activity from Bray plus South Armorican Shear Zone and Proto SHF plus URGSZ. Mesozoic reactivation of the NW-SE / E-W structural directions induced a pronounced argillic alteration leading to the formation of CRZ. Tertiary deformation during development of the URG at pressure and temperature conditions well within the brittle field for the gneiss host rock. This brittle rheology is prone to elastic strain accumulation on the non-highly altered NE-SW structures up to reactivation. In contrast, the mechanical response of the prominent Mesozoic CRZ to the Cenozoic stress-field can only be drastically different than the surrounding competent gneiss host rock

as temperatures are still high enough to trigger clay plasticity. Strain is therefore accommodated within the CRZ by means of bulk shearing with no discrete failure nor void opening which precludes the arrival of massive brine flow. Any brittle failure propagating within the competent host rock is stopped when encountering a CRZ as elastic strain cannot then be further accumulated. This process can be regarded as a switch from brittle to ductile deformation. Void opening within the CRZ is further prevented by 1) their unfavorable orientation in the imposed stress-field and 2) the intrinsic non-permeable nature of the clays preventing present-day meteoric and aquifer water flow in the galleries.

The CRZSR is to be considered as an end-member representative of a mature fault system having accumulated vast amounts of strain. The mining literature has precisely documented this type of CRZ for economic and technical reasons as their presence 1) precludes the development of large exploitable ore veins and 2) triggers gallery instability and potential collapse hazard. Less attention has been given to inherited fault zones which have not developed a thick clay rich core. The lack of a core process zone can be interpreted as a sign of either lower amounts of strain and/or fluid flow along the fault which in turn leads to moderate argillic alteration and intrinsic anisotropy development. The role of faults with a non-continuous clay core in terms of potential barrier to ore-saturated brines and present-day aquifer and meteoric flow remains poorly constrained. Klee (2021) has documented an outcrop (Figure 21) found at the GG mine in the VM at the entrance of the Gallery P-west described by Hafeznia et al. (2015).

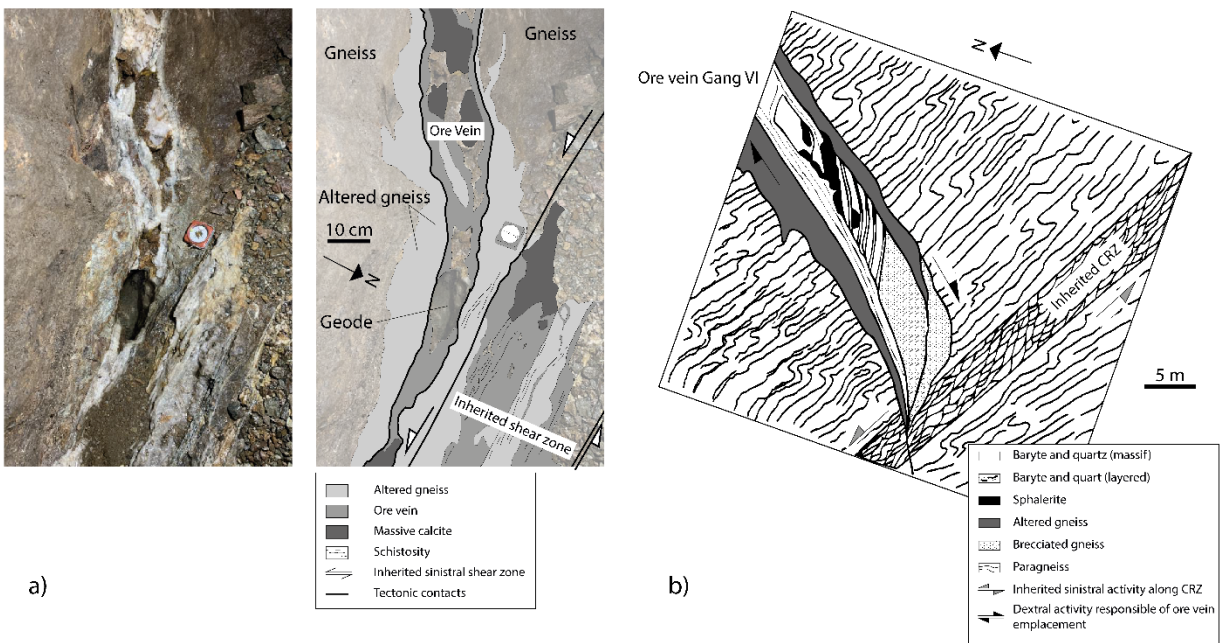


Figure 21: a) ore vein deviation when approaching the contact with an inherited high strain zone (figure redrawn after Klee, 2021), b) zoom on the termination of ore vein Gang VI (Werner et al., 2004), note the similar apparent drag and vein thinning.

The outcrop shows an intersection between a geodic ore vein and a mylonitic shear zone affecting the gneiss host rock. As observed in the Schauinsland mining district, the ore vein 1) cuts at a near right angle the gneiss foliation and 2) thins when approaching the mylonitic shear zone. The geodic appearance of the ore vein is interpreted as a sign of development at relatively shallow levels, i.e. moderate hydrostatic pressure, in order for voids to remain opened along strike of the fracture. The mylonitic nature of the shear zone with ubiquitous signs of crystal plastic mechanisms in quartz indicates that the shear zone is inherited from an earlier high temperature deformation phase having affected the reservoir. Incipient argillic alteration is

observed along the foliation and schistosity planes but no continuous CRZ is developed along strike of this inherited strained zone.

This outcrop presents two interesting features:

- 1) Centimeter-scale, ore mineral partially filled, geodes and tensile bridges are found along strike of the inherited shear zone. These form an interconnected, continuous flow pathway which uses the inherited schistosity as a preferential route.
- 2) The main geodic ore vein re-appears about 15 m away on the other side of the inherited shear zone forming a 30 cm thick geodic vein again cross cutting the gneiss foliation at a near right angle.

This outcrop at GG illustrates the influence of inherited strained zones in the absence of massive argillic alteration. In the present case, the inherited strained zone is affected by minor Riedel type brittle offsets, and foliation/schistosity is mechanically prone to reactivation allowing fluid injections parallel to its strike. As a working hypothesis I suspect that, as in Schauinsland, the mechanical behavior of the inherited strained zone substantially differs from the host rock at a given distance, introducing a local stress-field variation with possible reactivation along the foliation and schistosity planes. In the given stress-field, fractures that would have propagated for long distances parallel to each other deviate from their initial strike when encountering an inherited strained zone. In this peculiar case, the inherited strained zone permits a physical connection and brine circulation between fractures that would have remained unconnected otherwise. A brine flow deviation occurs along the inherited strained zone in the absence of large lateral shearing displacements (Figure 22). The flow-deviation role of inherited structures challenges ore mining activities but also well positioning and stimulation designs for the geothermal industry.

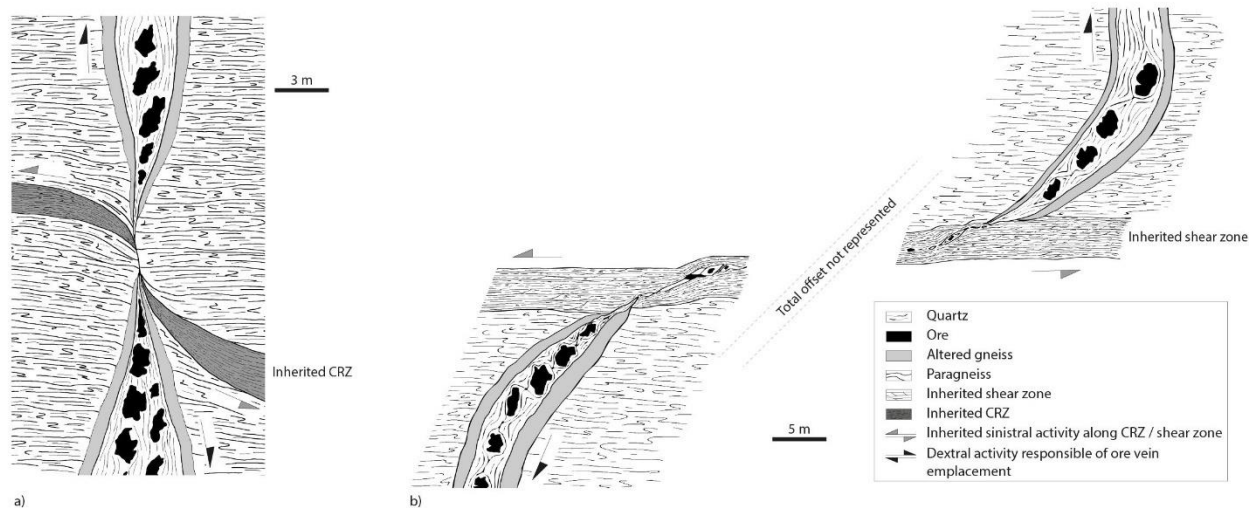


Figure 22: Conceptual model showing the observed interactions between late ore veins and a) inherited CRZ, b) high strain zones (inspired from Klee, 2021).

In summary, CRZ are common within the BFM and inherited strained zones were found in the VM. Both have influenced the distribution of exploitable ore veins in the different mining districts. As the present-day distribution of ore veins reflects a past circulation of saturated brines it is obvious that the distribution and mechanical plus petrophysical properties of CRZ and other strained zones must be documented in order to produce realistic flow models in a given reservoir.

I am presently working in enhancing the model by Klee (2021) by means of geochemical, mechanical and microfabric characterization plus numerical modeling. In order to do so, I have established a cooperation

with the GeoLab department of numerical sciences and modeling at UniLaSalle in order to simulate in the near future fluid flow within outcrops previously modeled by means of photogrammetric analysis. I have obtained investment funds in order to equip the UniLaSalle SEM laboratory with a combined EBSD and EDS system. As described in my perspectives session, this tool is essential to characterize clay phases and active deformation mechanisms in CRZ and reservoir host rocks.

The ongoing PhD thesis by Mr. Avakian in the framework of the Eutopia program is dealing with a high-resolution characterization of chemical element distribution along a profile perpendicular to the Schauinsland CRZSR and parallel to the strike of the Tertiary ore veins. By means of geochemistry we intend to trace fluid pathways and map the alteration fronts between the two distinct structures. The approach participates to the reconstruction of the geological evolution of the outcrop with a particular emphasis on 1) outlining potential permeable zones and 2) link permeability to microtextural and microstructural rock characteristics.

Regarding rock mechanics, preliminary experimental testing of samples taken along a profile perpendicular to the CRZSR by Muhl et al. (2022) show 1) a general decrease of both tensile strength and elastic modulus when approaching the CRZ and 2) cohesion plus Poisson ratio values much higher than expected in the core zone.

This ongoing research aims to pursue with themes addressed during the MEET project i.e. 1) alteration processes characterization in time and space and 2) influence of alteration processes on mechanical and petrophysical properties of reservoir rocks during polyphase tectonic evolution. Besides geothermal, this research finds direct applications in the field of CCS. It is evident that further work is needed and I will present my approach in the perspectives session.

Influences of pre-structuration of a reservoir on permeability evolution in fracture zones Insights from mechanical testing on an alteration profile

Lena Muhl¹, Benjamin Avakian², Ghislain Trullenque³, Ingo Sass¹, Beatrice Ledésert².

¹ Helmholtz Centre Potsdam GFZ Potsdam German Research Centre for Geosciences, Section: Geoenery, Telegrafenberg, 14473, Potsdam, Germany

² Geosciences and Environment Cergy, CY Cergy Paris Université, 1 rue Descartes, F-95000 Neuville sur Oise, France

³ B2R, Geosciences Department, Institut Polytechnique UniLaSalle Beauvais, 19 Rue Pierre Waguët, F-60026 Beauvais, France

lmuhl@gfz-potsdam.de

Keywords: Geothermal, Black Forest, analogue, fault zone, mechanical testing.

ABSTRACT

In the international energy transition, geothermal energy plays a role as a renewable energy which almost does not emit CO₂ and allows the reduction of dependency on fossil fuels. Geothermal energy in a crystalline basement is part of the different deep geothermal sources which can be used for heating or electricity production. In 2018, the heating generated from deep geothermal plants was up to 2.6 Twh in France and is planned to increase. For the upcoming 2030, the objective in France is to have 38% of renewable energy in the final heat consumption, where geothermal energy has its place (French energy transition law for green growth n°2015-992).

Geothermal production in crystalline basement relies on the presence of fractures and sometimes stimulation techniques. In France, such exploited sites are located in Alsace (Upper Rhine Graben, URG) where a hot brine is harvested in the granitic basement to produce electricity (Soulz-sous-Forêts) or heat (Rittershoffen). However, recent unexpected seismic events occurred during the stimulation of new sites and lead to stop deep geothermal exploration in Alsace.

For the resource development of geothermal reservoirs, the understanding of the properties of fractures and fracture networks has to be investigated.

Uniaxial compression strength, triaxial compression strength and brazilian disk tests measurements were performed on samples collected along a fault zone from Schauinsland mine in the Black Forest. These samples are considered as analogues of the deep geothermal reservoir of Soulz-sous-Forêts in the URG. A decrease of the tensile strength and elastic modulus was measured along the fault zone while the cohesion value

is much higher than expected in the core zone. The Poisson ratio is the highest in the damage zone which indicates that the samples are heterogeneous and need to be investigated at a smaller scale.

1. INTRODUCTION

Geothermal energy allows the production of a local and permanent source of energy for electricity or heating system with almost no CO₂ emission. This is the case in Alsace (France) at Soulz-sous-Forêts and Rittershoffen exploitation sites where a geothermal brine is collected in a crystalline fractured basement and used for energy production. In this context, the fracture network is the main fluid pathway in the reservoir. The permeability can be increased by stimulations (thermal, hydraulic and/or chemical) to enhance the connectivity between the fractures or enlarge them. The understanding of how fluid circulates in such a reservoir is a key parameter to consider, for a safe and efficient geothermal installation.

The deformation of a reservoir plays a role in fluid circulation pathways by creating fractures and fault zones. The pre-structuration induced by deformation during previous geological events may affect later fluid circulations in fault zones. This may change the behaviour of a fault core to act as a barrier or as a conduit (Glaas, 2021; Klee, 2021). Mechanical testing and geological investigations will give a better understanding of the role of the pre-structuration of a basement reservoir and its influence on later fluid circulation and a potential reason for induced seismicity. Such events occurred recently in France (Schmittbuhl et al., 2021) where shear zones were reactivated during geothermal stimulation.

A surface analogue of a fractured geothermal reservoir was investigated in the Black Forest mines in the URG to be in the same geological context as in the deep

exploited basement but to allow a wider view than in boreholes. This gives access to a 3D view of the structures where a sampling profile was established from a non-deformed gneiss to a high-strain fault core zone rich in clay minerals, through a well-developed damage zone. This study is focused on understanding the differences in the mechanical behaviour of the core zone and damage zone sampled in the mines by realizing mechanical tests.

2. GEOLOGICAL CONTEXT

2.1 THE UPPER RHINE GRABEN AND BLACK FOREST

The URG is a part of the European Cenozoic Rift system (Fig.1) with an NNE orientation, a length and a width of respectively 300 km and 30–40 km (Ziegler, 1992). Its formation took place in an extensional context and is contemporaneous of the Alpine and Pyrenean orogenesis (Schumacher, 2002). The URG is filled with Mesozoic and Cenozoic sediments (Ziegler, 1992) and lies on Hercynian basement rocks. This structure is bordered by major normal faults which delimitate the Vosges massif on the Western side and the Black Forest on the Eastern side. The Black Forest thus corresponds to a shoulder of the graben and is composed of crystalline basement rocks. Mesozoic and

Cenozoic sedimentary rocks are covering the massif (Werner and Dennert., 2004).

2.2 THE SCHAUNSLAND MASSIF

The Schauinsland massif was chosen as a surface analogue of a fractured geothermal system of the URG to understand the role of fault zones in fluid pathways. This massif located in the Black Forest is made of Precambrian gneiss with various compositions, (Witterbrink, 1999). The massif has recorded deformation events since the Variscan in various directions and is crosscut by a high strain fault zone with an E-W direction called the “Ruschel” in the miner language (Fig.2). This fault zone was reactivated several times, illite and cataclasite can be found inside. The fault zone was most active during the Jurassic (Werner et al., 2002). The interest of this massif is the presence of ore and mineral veins that are almost perpendicular to the Ruschel as it can be transposed to an actual geothermal reservoir where brines encounter shear zones.

From the 13th to the 20th century, the Schauinsland mine was exploited for various materials like lead, zinc and silver. Various ore veins were exploited and can be observed in the mine. These are markers of fluid circulation inside the mine.

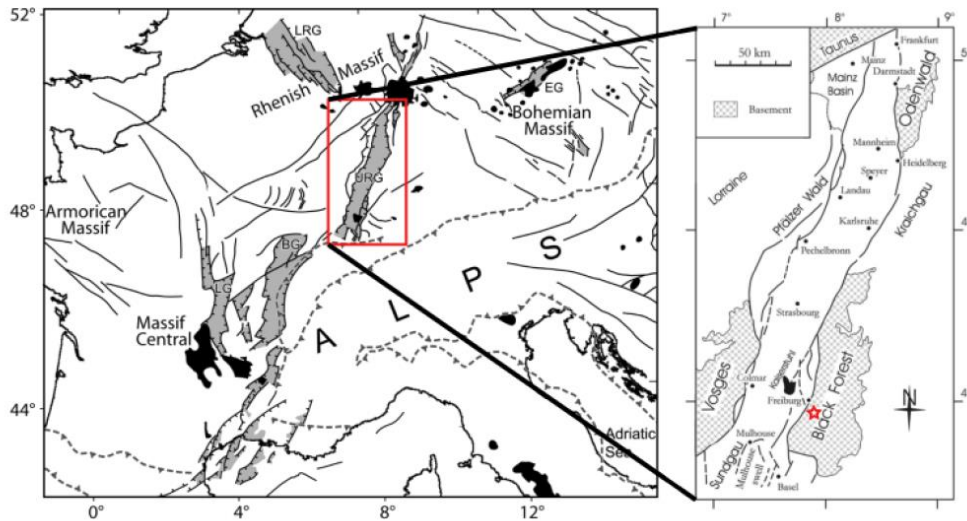


Figure 1: Structural map of the European Cenozoic rift system (on the left part) modified by (Lustrino et Carminati., 2007) after (Dèzes et al., 2004). The Cenozoic faults are represented in black lines, the sedimentary rift in light grey and the volcanic field in black. The dashed lines correspond to the Alpine deformation front. BG—Bresse Graben; EG—Eger Graben; LG—Limagne Graben; LRG—Lower Rhine Graben; URG—Upper Rhine Graben. The tectonic map of the Upper Rhine Graben (on the right part) which has NNE-SSW normal border faults, the Schauinsland massif is located by the red star on the map, modified after (Schumacher, 2002).

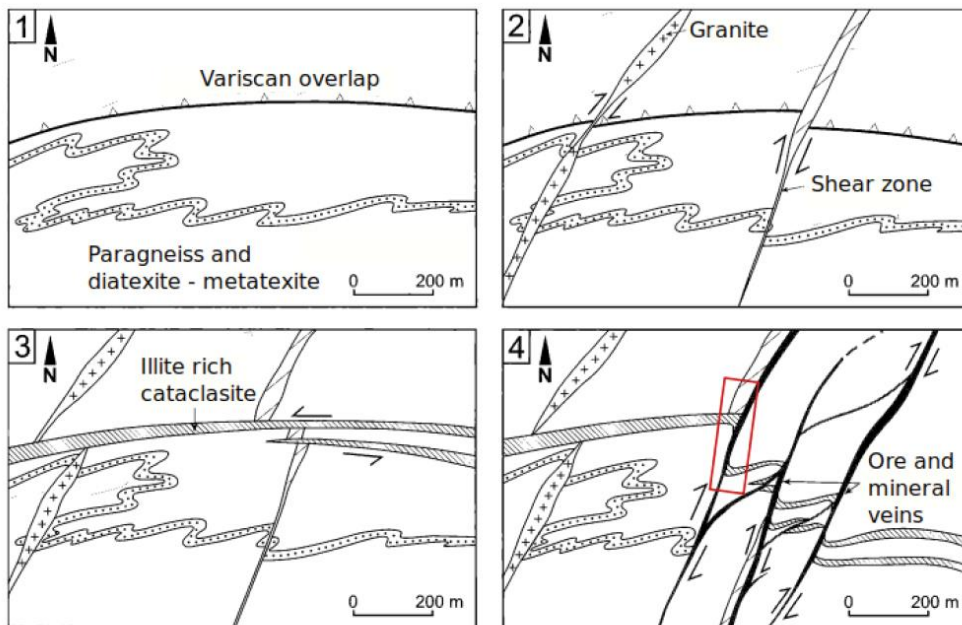


Figure 2: Representation of the tectonic evolution of the Schauinsland massif since the Variscan orogenesis. Here is the tectonic situation at the Upper Carboniferous (1). Afterwards, granitic intrusion and development of shear zones from the Upper Carboniferous to the Permian occurred (2). An E-W shearing of the massif and the creation of the highly sheared zone called the “Ruschel” took place. Cataclasite was developed and illitisation occurred during the Jurassic to the Cretaceous (3). Deposition of ore and mineral veins happened with a NNE-SSW shearing during the Cenozoic (4). The red rectangle corresponds to the geological setting that is investigated as an analogue of a geothermal reservoir, modified after (Werner et al., 2002).

2.3 SCHAUINSLAND MINE

A specific N-S gallery in the mines was investigated, representing the geological context depicted in the Fig.2 in the red rectangle. It follows a decimetric ore vein mostly composed of barite that developed in a paragneiss. This vein vanishes in the vicinity of the high strain zone rich in clay minerals, the Ruschel (Fig.3). As described by Werner et al (2002), this high strain zone was shifted during a late phase of deformation allowing the ore mineral deposition. Ductile deformation and clay smearing features are observed in the gallery, especially in the core of the fault zone (Fig.4). However, the vein (Fig.5) which was deposited later than the E-W fault zone does not crosscut this pre-structuration.

To develop such ore veins in a paragneiss, the host rock may have accumulated elastic stress and was fractured leading to the formation of breccia (Fig.5). However, the same stress conditions applied to a rock rich in clay minerals may not induce the same response and clay smearing occurs instead of accumulating stress. This

difference in mechanical response may not let the fluid propagates and develop in the fault core.

These observations highlight the importance of pre-structuration in the case of brine circulation in a pre-structured reservoir. To better understand the system, mechanical testing of samples taken from the core of the fault zone to the less deformed gneiss was performed.

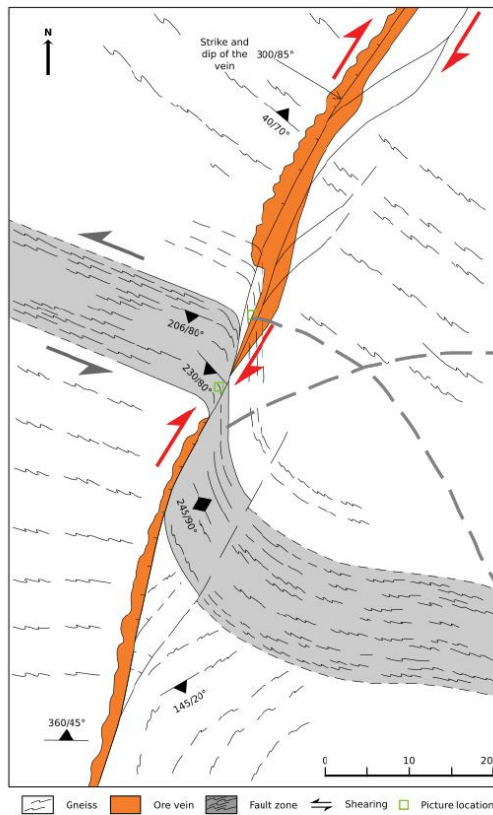


Figure 3: Geological scheme of the Schauinsland gallery (schematic map view), modified after (Werner et al., 2002). The mine has recorded multiple shearing episodes. The first visible one created the highly sheared zone, called the “Ruschel” in mining language (in grey) with a sinistral movement and an E-W direction. The second one crosscuts the Ruschel with a dextral movement and a NNE-SSW direction. The ore vein deposited after the Ruschel shearing. It vanishes close to the

fault zone and reappears on the other side. The green squares indicate the location of photographs of the fault core (Fig.4) and the ore vein (Fig.5).

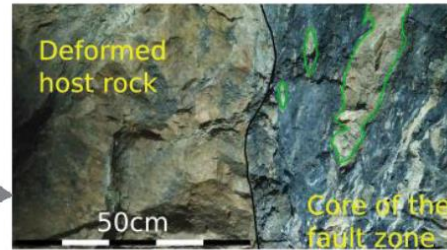


Figure 4: Picture of the deformed host rock and the core of the fault zone. The fault core (“Ruschel”) is rich in clay minerals (grey color) and contains clasts of the host rock 10 (green shapes in the figure). An alternation between the deformed host rock and a high-strain zone rich in clay minerals can be observed multiple times on the gallery wall.

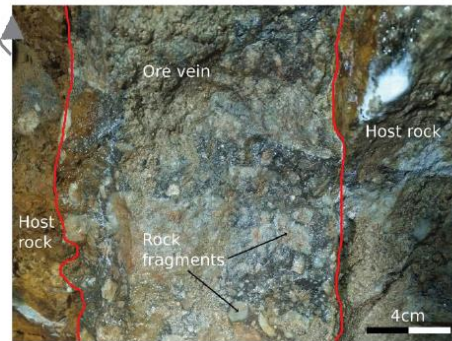


Figure 5: Picture of the ore vein (delimited by the red lines on the figure) developed in the host rock, filled with galena containing some small host-rock fragments. The ore vein is visible when leaving the fault zone and increases in width.

2. METHODS

The rock mechanical behaviour was analysed by a series of brazilian disk, uniaxial compression strength and triaxial compression strength tests. The samples were collected in the Schauinsland mine from where the extraction and transportation of rock materials are difficult. Therefore, only a minor amount of samples was investigated. Moreover, the rocks were difficult to extract due to the high-strain zone they had overcome during their history. Hence, the tested cylindrical samples had small dimensions with a diameter of 30 mm and a length of 60 or 15 mm for all mechanical tests.

The brazilian disk (BD) test was conducted at the Mechanical Testing System (MTS) of GFZ Potsdam with a loading rate of 0.001 mm/s until failure (Fig.6). In total 53 samples were investigated.

The uniaxial compression strength (UCS) test was executed in the same device. Hereby, the samples were covered by a shrink tube and two LVDT extensometers for lateral and vertical strain measurements were applied. The constant loading rate was identical to the Brazilian Disk test. In total three samples were analysed.

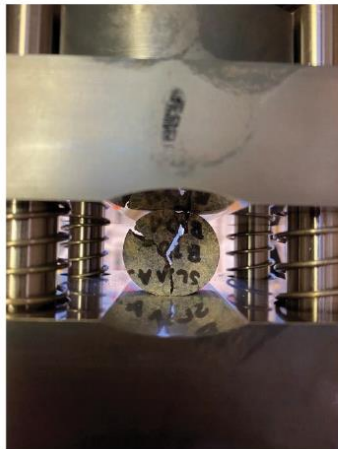


Figure 6: The setup of the brazilian disk test in the MTS of GFZ Potsdam.

The triaxial compression strength (Triax) test was conducted with a loading rate of 0.5 MPa/min and the same setup as in the UCS test was utilized. For the confining pressure, 20 MPa, 40 MPa and 60 MPa were applied in single measurements until the failure. In addition, two multiple failures were applied with all three confining pressure maxima. Hereby, the axial loading was stopped shortly before the failure occurred and the next higher confining pressure was applied. At 60 MPa confining pressure the axial loading was

increased until failure. In total, ten samples were investigated.

3. RESULTS

The results of the mechanical testing are divided into the three different experiments BD, UCS and Triax. The results of the tests are displayed for the three different zones of the profile (Fig.7, Table 1).

Table 1: Results of the brazilian disk test, Zone 1 describes the basement, Zone 2 transition zone and Zone 3 close to the inner core of the damage zone with the tensile strength (TS in MPa)

Zone	TS [MPa]	amount
1	9.48	16
2	7.07	22
3	4.93	15

The three samples of the UCS experiments are shown in Table 2.

Table 2: Results of the UCS with the elastic modulus (E-Modul) and the maximum compressive strength (Co)

Zone	E-Modul [GPa]	Co [MPa]
1	42.9	112.1
1	41.0	96.4
2	30.9	87.5

For the Triax experiments, the results are provided for the different confining pressure values and for the single and multiple triaxial failure tests (Table 3).

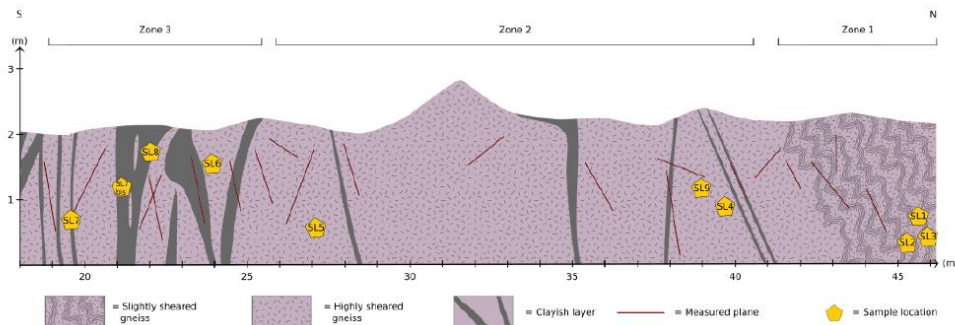


Figure 7: Cross-section of the studied gallery indicating the location of the samples (in yellow) and the delimitation of the Zones. Zone 1 corresponds to the less deformed gneiss, the basement. Zone 2 is the transition zone of the fault zone and Zone 3 to the inner core of the damage zone. Samples in the fault zone are more sheared and the presence of clay-rich bands is represented in grey. Planes were measured along the profile (in red). The foliation on the right represents the limit where it was no longer visible on the outcrop but is not represented with the right strike/dip directions.

Table 3: Results of the triax test under a confining pressure of 20, 40 and 60 MPa with the elastic modulus, the maximum compressive strength and the Poisson ratio (ν), $m =$ multiple tests

20 MPa confining pressure			
Zone	E-Modul [GPa]	Co [MPa]	ν [-]
1	37.6	159.3	0.12
1 (m)	47.3	160.8	0.1
2	33.7	148.3	0.15
2 (m)	31.7	148.9	0.14
3	18.1	169.2	0.06

40 MPa confining pressure			
Zone	E-Modul [GPa]	Co [MPa]	ν [-]
1	50.1	252.1	0.12
1 (m)	-	290.9	0.08
2	41.6	197.5	0.15
2 (m)	-	187.2	0.2
3	22.0	218.3	0.08

60 MPa confining pressure			
Zone	E-Modul [GPa]	Co [MPa]	ν [-]
1	47.7	262.7	0.17
1 (m)	-	340.8	0.11
2	36.5	230.3	0.17
2 (m)	-	229.5	0.21

The results of the BD showed a decrease in tensile strength from Zone 1 to Zone 3. The UCS tests were only executed in Zone 1 and 2 due to the small number of samples. Hereby, the same trend was visualized as in the BD test. It has to be highlighted that Zone 1 already shows two quite different Co values. For the elastic modulus, the results were more distinct between the two zones. The triaxial results presented for the elastic modulus had the same trend as the UCS results. For the Co, the results of Zone 3 were higher than Zone 1 and Zone 2 by 20 MPa confining pressure. For 40 MPa confining pressure the value of Zone 3 was still higher than Zone 2. The Poisson ratio displayed no clear difference between the Zones. Zone 2 has the highest values in all three Tables and Zone 3 has the smallest. For Zone 1 they are in between Zone 2 and Zone 3 but the two measured values show great differences.

The post-failure analysis displayed a brittle to a tendency of ductile behaviour, especially for the Zone 3. At the maximum confining pressure already Zone 1 demonstrated a slower decrease in pressure after failure but comparatively small to the Zone 3 at lower confining pressure values. The post failures occurred along previous existing structures. Compared to other mechanical tests led on gneiss, these results give a lower value of the TS, E-modulus and Poisson ratio than those obtained by Eloranta (2006).

3. CONCLUSIONS

From the results of the Mechanical testing, it can be seen that there is a decrease in tensile strength over the profile from Zone 1 to Zone 3. It is similar for the elastic modulus from the UCS and Triax tests. The Co and Poisson ratio are not that clear. For Co, Zone 3 demonstrates higher strength than expected and shows similar or even higher than Zone 1. For the Poisson ratio, Zone 2 shows the highest values and differences in each Zone are quite large. These differences in one Zone show that the declared zones are quite heterogeneous and have to be analysed at a smaller scale with more experiments. The post-failure analysis presents a similar picture to the calculated parameters. Hereby, no clear behaviour can be detected concerning the type of failure. Some samples show a tendency of ductile behaviour while other samples have a clear brittle failure. Therefore, the extent of the Zones has to be questioned and may be changed after a more detailed analysis of the whole profile including geochemical and petrographical analysis. The results of the mechanical testing showed that there are clear changes over the profile length e.g. the tensile strength and for other cases, it can be highlighted that possible changes are smaller than expected or due to the complex geological past more differentiated than assumed. There might be a transition from brittle behaviour in Zone 1 to plasticity in Zone 3. The comprehension of fluid pathways which vanishes to the fault zone is still not clear.

The ongoing research goes into detail for geochemical and petrographical analysis at a narrow scale to find answers for questions raised. In this next step, processes of hydrothermal alteration will be taken into account as the pre-structuration might have changed the properties of the host rock, enhancing the heterogeneity and differences in mechanical behaviour between the Zones.

REFERENCES

- Dèzes, P., Schmid, S.M., and Ziegler, P.A.: Evolution of the European Cenozoic Rift System: Interaction of the Pyrenean and Alpine orogens with the foreland lithosphere, *Tectonophysics*, **389**, (2004), p. 1–33.
- Eloranta, P.: Laboratory testing of gneissic rocks in Olkiluoto borehole OL-KR24, working report, Finland, (2006).
- Glaas, C., Vidal, J., Genter, A.: Structural characterization of naturally fractured geothermal reservoirs in the central Upper Rhine Graben, *Journal of Structural Geology*, **148**, (2021).
- Klee, J., Chabani, A., Ledéser, B.A., Potel, S., Hébert, R.L., Trullenque, G.: Fluid-rock Interactions in a Paleo-Geothermal Reservoir (Noble Hills Granite, California, USA). Part 2: The Influence of Fracturing on Granite Alteration Processes and Fluid Circulation at Low to Moderate Regional Strain, *Geosciences*, **11**, (2021).

- Lustrino, M. and Caminati, E.: Phantom plumes in Europe and the circum-Mediterranean region. Special paper, *Geological Society of America*, **430**, (2007), p.723-745
- Schmittbuhl, J., Lambotte, S., Lengliné, O., Grunberg, M., Jund, H., Vergne, J., Cornet, F., Doubre, C., Masson, F.: Induced and triggered seismicity below the city of Starsbourg, France from November 2019 to January 2021. *Comptes Rendus. Géosciences*, **353**, (2021), p. 561-584.
- Schumacher, M.E.: Upper Rhine Graben: Role of preexisting structures during rift evolution. *Tectonics*, **21**, (2002).
- Werner, W. and Dennert, V.: Lagerstätten und Bergbau im Schwarzwald: ein Führer unter besonderer Berücksichtigung der für die Öffentlichkeit zugänglichen Bergwerke, *Landesamt für Geologie, Rohstoffe und Bergbau Baden-Württemberg*, Freiburg im Breisgau, (2004).
- Werner, W., Franzke, H.J., Wirsing, G., Jochum, J., Lüders, V., Wittenbrink, J., Steiber, B.: Die Erzlagerstätte Schauinsland bei Freiburg im Breisgau: Bergbau, Geologie, Hydrogeologie, Mineralogie, Geochemie, Tektonik und Lagerstättenentstehung. Aedificatio-Verlag. Ed. *Naturforschende Gesellschaft zu Freiburg im Breisgau c/o Institut für Geo- und Umweltnaturwissenschaften*, (2002).
- Wittenbrink, J.: Diplomkartierung (Teil A) Petrographische und tektonische Kartierung des Zentralschwarzwälder Gneiskomplexes im Bereich der Blei – Zink – Lagerstätte Schauinsland bei Freiburg i. Br./Schwarzwald, Master thesis, Technische Universität Clausthal, (1999).
- Ziegler, P.A.: European Cenozoic rift system. *Tectonophysics*, **208**, (1992), p.91–111.

4.5.3.2.3 CO₂ storage potential in fractured carbonate reservoir via Thermo Hydro Mechanical Chemical simulations

My research work triggered some attention at the Faculty of Science and Information Technology of Universiti Teknologi Petronas (UTP) in Malaysia where I was invited to give some lectures in summer 2022. Members of the Department of Geosciences involved in a CCS research project paid a great attention to my multidisciplinary approach in geothermal as it could be easily transferred to CCS.

As mentioned earlier, geological CO₂ sequestration has been proposed to reduce greenhouse gas emission in the earth's atmosphere. A variety of targets have been identified like salt mining cavities, depleted oil and gas fields and unmineable coal seams. In any case, great attention must be paid to fault and fractures as these have a great impact on the dynamics of injection and sequestration potential of the reservoir on the long term.

Naturally fractured carbonate reservoirs (NFCRs) in Malaysia can serve as underground storage of CO₂ to help mitigate climate change and greenhouse effect. Little attention has been given to the NFCRs as potential CO₂ storage sites due to 1) the high conductivity of the fractures that may lead to increase in spatial spreading of the CO₂ plume and increase of capillary forces in the fractures and 2) the potential reactivity between carbonates and carbonic acid.

The area of investigation lies in the South China Sea within the Luconia province offshore of the Borneo island (Figure 23).

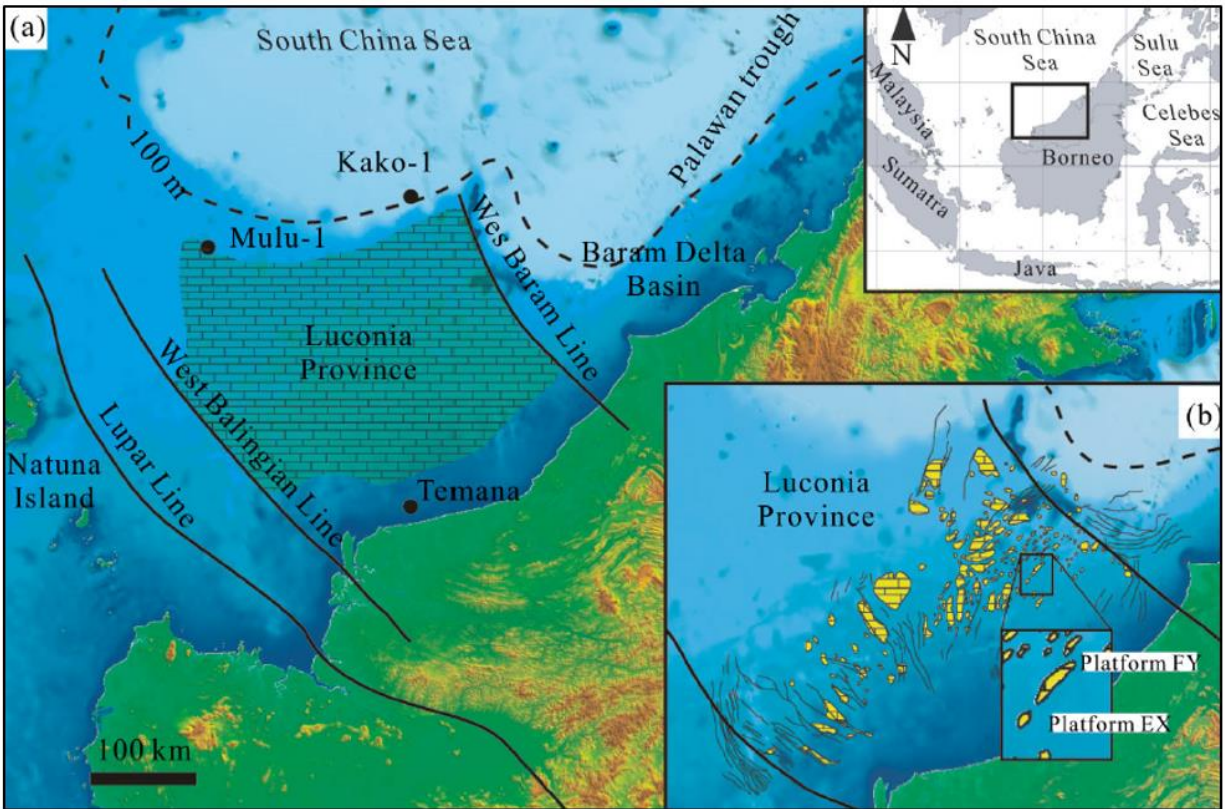


Figure 23: a) location and geological framework of the Luconia province, b) zoom on the EX platform (after Jamaludin et al., 2021).

The Luconia shelf is composed by several hundred of Oligocene to recent carbonate platforms which have been identified as a gas-dominated province (Cullen, 2014), bounded by the West Balingian line and the West Baram line (Jamaludin et al., 2021).

Jamaludin et al. (2021) have evidenced a series of three tectonic events from the Upper Cretaceous to Pliocene associated to episodes of limestone growth in Luconia province. This polyphase tectonic history starts by formation of compressional structures during the period Upper Cretaceous to Lower Oligocene and closure of the Proto South China Sea (event 1) followed by rifting of the South China Sea until Lower Miocene (event 2). This second event triggered the main phase of carbonate growth used as potential targets for the CCS project. The third and last event (event 3) is related to renewed regional compression responsible of the uplift of the Borneo hinterland which is in turn responsible of a massive clastic sedimentation onlapping the previously formed carbonates (see Figure 24).

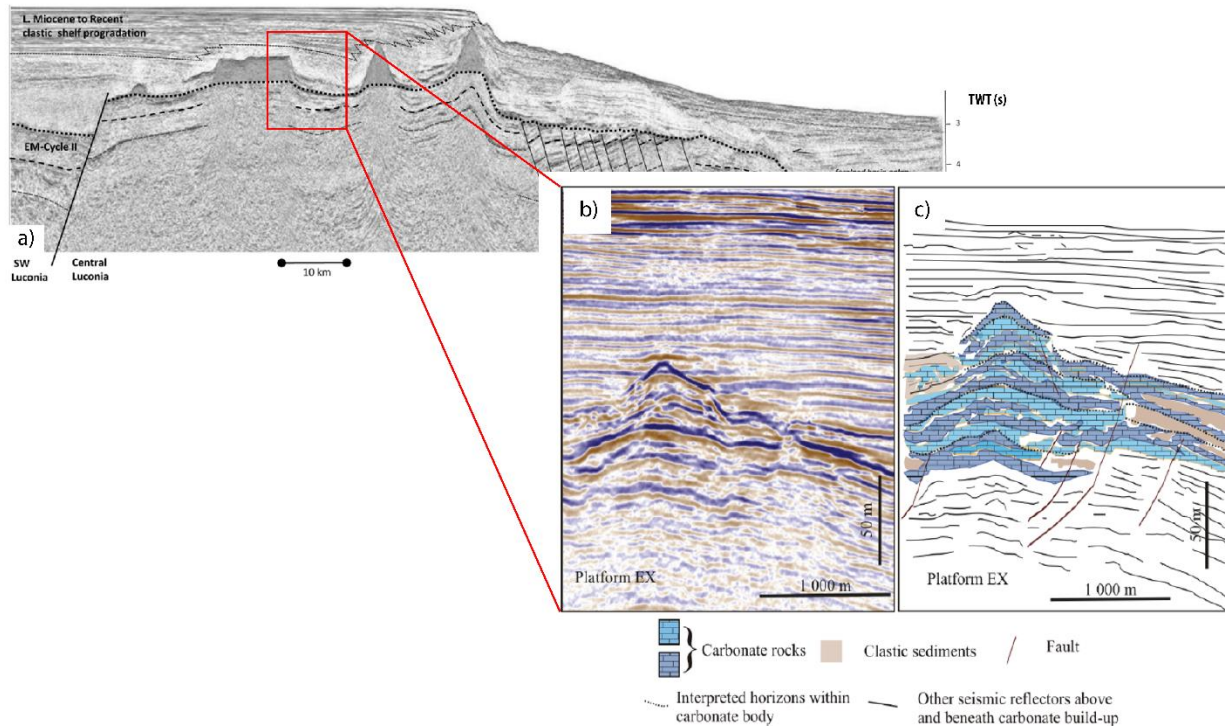


Figure 24: a) SW-NE seismic line from SW and central Luconia (Cullen, 2014), b) and c) high resolution seismic record and interpretation of platform EX (Jamaludin et al., 2021).

Overall, the project will focus at first on analyzing the structural orientation, connectivity and petrophysical plus mechanical properties of the fracture networks inherited from the 3 previously described events. In a second step, CO₂ flow simulations into fractured pores and faults in the reservoir are planned in order to evaluate its sequestration potential on the long term.

In order to achieve this goal, the project is constructed in three major steps:

- Individual fractures will be studied and characterized using a multidisciplinary approach. The access to the hierarchical and mechanical relationships between fracture systems can be led by multi-scale approach, which helps the modeling and prediction of the hydraulic reservoir properties. This approach is based on studying several geometric fracture attributes such as the distribution of orientations, lengths, widths, spacings and fracture densities largely considered in spatial organization analysis, from large scale (e.g, fractured reservoir) to micro scale (e.g, thin section scale). A detailed multi-scale study is planned using seismic data, well data, well samples, and large-scale maps to (1) analyze the fracture connectivity related to the CO₂ injection process, (2) evaluate the fracture system in the complex tectonic setting, and (3) understand the fluid flow patterns at the whole fractured reservoir.
- Sample investigation in the laboratory will on one hand concentrate of petrophysical characteristics at UTP and on the other hand in petrographic and microfabric analysis at UniLaSalle. The petrophysical investigations will include porosity, permeability, lithological, fluid identification and capillary analysis using tools and software in UTP laboratories. Sample analysis will consist in bulk X-ray composition determination and micro analysis by means of EDS spectrometry under the SEM. High resolution imaging and EBSD characterization will

- allow to characterize the degree of rock anisotropy as this parameter play a crucial role in fault mechanical behavior and on fluid draining capacities.
- Flow rates simulations and Thermal-Hydraulic-Mechanical-Chemical (THMC) models are planned to examine the CO₂ injection rate in the fracture networks and predict the effects of fluid rock interactions fractures mechanical and petrophysical properties related to the injection process. A fully coupled THMC model based on finite element methods is planned to analyze the transient stress, pressure, temperature and chemical solute concentration changes simultaneously around an injection well and within the whole reservoir.

Within this recently started project, I am field supervisor of a PhD student, Mrs. Ong (see letter in appendix) and I supervise the Master Thesis of Mr. Lubrez. I am involved in the study of reservoir architecture representation, fluid rock interaction processes characterization and strain related anisotropy development in fault core rocks investigations.

5 Summary of supervision and teaching activities

5.1 Supervision

5.1.1 Mentoring of Early Stage Researchers

1. Mrs. Lena Muhl

Study engineer, fixed-term contract within the MEET project (September 2021 – January 2022)

Subject: Influence of tectonic heritage on fault zone permeability. Mechanical testing on samples collected across an altered deformation zone

Mrs. Muhl presented an extended abstract (Muhl et al. 2022) and prepares a A ranking publication in order to present her results.

2. Dr. Arezki Chabani (2019-2021)

Postdoctoral fellow within the MEET project.

Research subject: Multiscale characterization of a fracture network within a reservoir analogue. Insights on deep geothermal reservoir fluid circulation understanding.

Dr. Chabani published two A ranking papers (Chabani et al. 2021a, 2021b) and an extended abstract (Chabani et al. 2020).

3. Dr. Zachariah Fleming (2018-2019)

Postdoctoral fellow within the MEET project.

Research subject: 3D visualization of a fractured granitic massif at the southern termination of Death Valley, CA, USA. Input from photogrammetric techniques to the understanding of structural organization on an exhumed geothermal reservoir.

5.1.2 PhD supervision

1. Mr. Benjamin Avakian

Subject: Fluid circulation within highly sheared granitic bodies. Applications in terms of sustainable geothermal energy production.

The subject is part of a cooperation between UniLaSalle Beauvais campus (France), CY Cergy Paris University (France) and Vrije University Brussels (Belgium).

Thesis started on November 1st 2021 and financed for a duration of four years by the EUTOPIA program.

2. Mrs. Ong Poh Yee

Subject: Assessment of CO₂ storage potential in naturally fractured carbonate (NFC) reservoir through discrete fracture network (DFN) and dual-porosity model (DPM).

The subject is part of a cooperation between UniLaSalle Beauvais campus (France) and Universiti Teknologi Petronas (Malaysia).

Thesis started on July 1st 2022 and financed for a duration of three years.

3. Dr. Johanne Klee (2018-2021)

Subject: Influence of fluid-rock interaction processes and strain on strike-slip zones properties: an analogue-based multidisciplinary approach. Fractured granitic geothermal reservoirs applications.

Thesis started on October 15th 2018, presented to EDSTS 585 Doctoral school – Sciences, technology and health, Picardie Jules Vernes University and defended on November 26th 2021 at UniLaSalle Beauvais campus.

Thesis funded within the MEET project.

Dr. Klee published two A ranking articles (Klee et al. 2021a, 2021b) and an extended abstract (Klee et al. 2020).

5.1.3 Master thesis, UniLaSalle (France)

1. Yaiche Mohamed. Modélisation de circulation fluids au sein d'un analogue de reservoir géothermique. 2023
2. Aurélien Lubrez. Study of the fracture network system on Miocene carbonate reservoirs in Central Luconia Province, Malaysia for fluid flow model in CO₂ storage assessment. 2022.
3. Pek Hung Beh. Microfabric analysis of basement rocks sampled across a deformation profile. Insights on alteration processes. 2022. ERASMUS + International Credit Mobility (grant number 2019-1-FR01-KA107-060920).
4. Mahdi Chettabi. Petrographic characterization of a granitic analogue: a fluid inclusion study. 2021.
5. Elena Pavlovskaja. Combined tectonometamorphic studies along a deformation gradient within the Noble Hills range, Death Valley, CA, USA. 2020. International Credit Mobility ERASMUS + (Projet 2018-1-FR01-KA107-046923).
6. Thi Tuyen Nguyen. Mineralogical characterization of fractured zones in Noble Hills (Death Valley, USA) as a surface analogous system of the Soultz sous Forêts granite. 2019.
7. Sabine Lor. Ingénierie d'affaire, valorisation géothermique de puits pétroliers. 2019.

5.1.4 5th year Engineering graduation thesis, UniLaSalle (France)

1. Armand Pomard. Accompagnement à la structuration de la filière française de géothermie: Mise en place d'outils d'aide à la décision et d'aide à l'animation régionale. MFE Cycle Ingénieur. 2021.
2. Marc Fargeau. Assessment of the hydrocarbon potential in north African mature basins through play analysis. MFE Cycle Ingénieur. 2021.
3. Valentin Mendes. Etude de la fiabilité de l'essai: détermination des références de compactage d'un matériau (essai PROCTOR normal et modifié, norme NF P 094-093). MFE Cycle Technicien Supérieur Professionnel. 2018.
4. Valentin Carrie. Rôle du technicien géologue dans la gestion des sites et sols pollués. MFE Cycle Technicien Supérieur Professionnel. 2018.
5. Clément Delcourt. Spatial variability of the spectral albedo of an alpine snowpack (Col du Lautaret, French Alps): comparison between in situ measurements and remote sensing data. MFE Cycle Ingénieur. 2018.
6. Marion Berger. Etude des flux thermiques du massif central. MFE Cycle Ingénieur. 2017.
7. Marie-Sophie Daly. La réalisation de diagnostics initiaux de l'état des milieux en théorie et en pratique. MFE Cycle Technicien Supérieur Professionnel. 2016.
8. Romain Maire. Investigation of thermo-physical and mechanical parameters of crystalline geothermal reservoir rocks of the Upper Rhine Graben (Germany). MFE Cycle Ingénieur. 2014.

5.1.5 4th year Engineering project, UniLaSalle (France)

1. Ruben Attali. Structural characterization of a granitic reservoir analogue based on photogrammetrical data. 2020.
2. Armand Pomart. Characterization of the tectonic settings of an abandoned mine situated at the East of the Upper Rhine Graben border (Schauinsland). 2019.
3. Maylis Casteleyn. Modeling of coastal karstic aquifers. 2017.
4. Florent Dutheillet de Lamothe. Petrophysical characterization of rocks and correlation of these properties with mineralogical composition. 2016.
5. Marion Berger. Numerical modeling of fluid flow in a fracture network. 2015.
6. Clément Delcourt. Simulation and numerical modeling of flow in fractured gabbro samples. 2015.
7. Morgane Douezy. Analyses goniométriques de marbres provenant de la zone axiale des Pyrénées Orientales. 2015.
8. Clément Crayssac. Investigation of Petrology and Geochemistry properties of crystalline geothermal reservoir rocks of the Upper Rhine Graben. 2015.
9. Pauline Villard. Numerical modelling of polycrystalline aggregates in the field of elasticity. 2014.

5.1.6 3rd year engineering project, UniLaSalle (France)

1. Théo Berthelin et Marie Collignon. Interprétation géologique par approche photogrammétrique. 2018.
2. Sapha Laaraj et Pauline Lesecq. Traitement de modèles photogrammétriques à des fins de géologie structurale. 2018.
3. Lorraine Coudert de Ceris et Julien Floch. Etude tectono-métamorphique d'un bassin polyphasé varisque (Harz, Allemagne). 2018.
4. Nathan Bliscaux et Thimoté De Tonquédec. Etude tectonique et microstructurale des déformations D2 et D3 du Cap de Creus (Pyrénées Espagnoles). 2016.
5. Etude et caractérisation des déformations D1 et D2, Cap de Creus, Espagne. 2015.
6. Florient Dutheillet de Lamothe. Etude de la déformation D3 du Cap de Creus (Espagne). 2015.
7. Lucille Collet et Pauline Villard. Etude des variations de la géométrie d'une zone de fracture expérimentale en fonction de la contrainte différentielle appliquée. 2014.
8. Baptiste Beyrie et Morgane Douëzy. Etude des nappes de Coustouged et de Bac Grillera : Problème de datation des séries rouges. 2014.
9. Matthieu Cedou et Thomas Tabary. Etude du gradient thermobarométrique et relations tectono-métamorphiques. 2014.
10. Sara Drachenberg et Matthieu Hequet. Etude de la fracturation du granite de Malsburg (Forêt Noire, Allemagne). 2013.
11. Camille Minière, Camille Mounier, Nassivera Laura. Caractérisation des filons de microgranite et de leur encaissant sédimentaire dans le bassin du Markstein (Vosges du Sud). 2013.
12. Chloé Lazizi et Yugo Yamada. Influence des circulations de fluides sur la validité des marqueurs thermobarométriques au sein d'une zone de fracture dans le granite de Malsburg (Forêt Noire, Allemagne). 2013.
13. William Fresser et Ludivine Mathieu. Caractérisation pétrologique et structurale de filons tardi-varisques intrusifs dans les granites varisques de l'association des crêtes dans le secteur de La Bresse (Vosges, France). 2013.

5.1.7 3rd year apprentice project, UniLaSalle (France)

1. Chloé Boiledieu et Charlotte Vassort. Etude d'un analogue de réservoir géothermique: la carrière de Malsburg. 2019.
2. Théo Berthelin. Interprétation par approche photogrammétrique des couloirs failles de la terminaison Sud de la vallée de la Mort (Californie, USA). 2018.

3. Armand Pomard et Enzo Armand Lorne. 3D representation of the fracture network in the Upper Rhine Graben. 2018.

5.1.8 Technician application project, UniLaSalle (France)

1. Alison Fry et Stephen Zimny. Etude structurale et microtectonique de marbres mylonitiques paléozoïques de la zone axiale des Pyrénées. Création d'un outil pour l'analyse de la zone d'étude et analyse de lames minces. 2016.
2. Tiffany Durand et Marie-Sophie Daly. Etude structurale et microtectonique de marbres mylonitiques paléozoïques de la zone axiale des Pyrénées. Etudes de lames minces, construction de coupes géologiques, cartographie SIG, photogrammétrie et interprétation de données de goniométrie texturale à rayons X. 2015.

5.1.9 Bachelor thesis, University of Freiburg im Breisgau (Germany)

1. Christoph Blümmel. Der Malsburg Granit. 2012.
2. Bernadette Bastian. Mantle Plumes, Hotspots und Supervulkane. Eine Evaluierung existierender Theorien am Beispiel des Yellowstone. 2012.
3. Annika Hartung. Geländeaufnahme und Strontiumisotopenanalyse Steinbruch Dieburg, Mainzer Berg, Odenwald. 2012.
4. Tatiana Kalytta. Deformation mechanisms active during catastrophic rock unloading. 2012.
5. Michael Rudolf. Influence of dehydration reactions on catastrophic rock failure. 2012.

5.2 Teaching activities

5.2.1 UniLaSalle (France) (2013- 2022)

Responsible of teaching modules in engineering and technician curriculum: geodynamics, tectonics, Alpine field trip, regional geology.

The tables below present all lectures I have given at UniLaSalle since my arrival in 2013. L1 to L3: Bachelor level, M1 and M2: Master level, CM: Cours Magistral (lecture), TD: Travaux Dirigés (exercises), TP: Travaux Pratiques (practice), AF: Auto Formation (self-training).

5.2.1.1 UniLaSalle Beauvais Campus

2022-2023

Level	Module	CM	TD	TP	AF
L1	Géologie de la France, géologie descriptive	12			
L1	Système terre	22			
L1	Cycle interne	10			
L2	Tectonique et sédimentation	8		40	

L2	Tectonique quantitative	8			
L2	Photo-interprétation			40	
L3	Camp de terrain: Alpes	8			
L3	MEB, EDS et EBSD	6		8	
M2	MEB, EDS et EBSD	6		8	
M2	Modélisation structurale	8			

2020-2022

Level	Module	CM	TD	TP	AF
L1	Géologie de la France, géologie descriptive	12			
L1	Système terre	22			
L1	Cycle interne	10			
L2	Tectonique quantitative	8			
L2	Tectonique et sédimentation	8			
L3	Camp de terrain: Alpes	8		40	
M2	Modélisation structurale	8			

2017-2019

Level	Module	CM	TD	TP	AF
L1	Géodynamique interne	22			
L2	Tectonique de couverture	6	12		
L2	Pétrologie du métamorphisme	12			
L3	Initiation recherche acquisition des données			144	
L3	Communication scientifique				8
L3	Synthèse géologique des orogènes	2		6	
M1	Camp de terrain: Alpes			40	

M1	Mécanique des roches et stabilité des versants rocheux	8	4
M2	Modélisation structurale	8	

2013-2016

Level	Module	CM	TD	TP	AF
L1	Géologie de la France, Géologie descriptive	12			
L1	Cartographie			16	
L1	Géodynamique interne	22			
L1	Camp de terrain, Bassin de Paris			36	
L1	Cycle interne	12			
L2	Photointerprétation			24	8
L2	Pétrologie du métamorphisme	12			
L2	Tectonique descriptive			20	
L2	Camp de terrain, Alpes			80	
L2	Camp de cartographie semi-autonome, Pyrénées			36	
L3	Initiation recherche et acquisition de données			24	
L3	MIR synthèse et rédaction				70
L3	MIR présentation orale				42
M1	Caractérisation multiparamètres des roches	4			
M1	Mécanique des roches et stabilité des versants	8		4	
M1	Communication scientifique				8
M2	Modélisation structurale	6			
M2	Encadrement stage, rédaction de rapport	4			

5.2.1.2 UniLaSalle Intensive Study Program Geo3En (2022)

The MEET project has highlighted a lack of young qualified engineers and technicians dedicated to geothermal. I initiated some actions in order to fill this gap and obtained an ERASMUS + strategic partnership grant. The Geo3En project (Geothermal Energy European Education Network) was a consortium of three Universities, namely Technical University of Darmstadt (Germany), University of Zagreb (Croatia) and University of Reykjavik (Iceland) plus the UniLaSalle school of engineering at Beauvais and Amiens campuses. I was coordinator of this pioneering project and received organizational support from the LINC department at UniLaSalle.

Geo3En targeted the construction of an international Master-level curriculum of excellence. The competence matrix covered all engineering expertise necessary to increase the contribution of geothermal within the renewable energies market. The panel of competences included disciplines in geology, material science, mechanical engineering, energy network management, reservoir modeling, economic intelligence, project management, entrepreneurship and legal plus environmental aspects.

In order to fulfill the industrial needs, several stakeholder consultations in the form of questionnaire and program presentation during online live events have been organized in France, Germany, Croatia and Iceland. The program integrated the latest research and innovation results in the curriculum in order for this last one to remain competitive at all time. Many internships in research laboratories have been proposed to students in order to give them the possibility to enlarge their professional networks within academic society and continue their education as PhD candidates.

Some of the planned Geo3En lectures have been tested during the spring 2022 season. Candidates from the different involved institutions have received a grant for participation to a series of four intensive study programs (ISP), each program being under leadership of a partner. The ISP were organized in two parts, namely four weeks of online lectures in the field of geology (UniLaSalle), energy engineering (University of Zagreb), petrophysics (TU Darmstadt) and economics (University of Reykjavik) followed by four weeks of site visits. At the end of the program students have delivered a report dealing with a virtual feasibility study and used data from the different sites visits.

The Geo3EN program has been presented at the New Zealand Geothermal Workshop in the form of an extended abstract (Newson et al., 2022).

Graduate Geothermal training in the European Economic Area

J. A. Newson¹, G. Trullenque², C. Bossennec³, I. Sass⁴, S. Šadek⁵, B. Gautason⁶ and R. M. Greene¹

¹ Iceland School of Energy, Reykjavik University, Menntavegur 1, 102 Reykjavik, Iceland

² UniLaSalle - Beauvais campus 19, rue Pierre Waguet – BP 30313 60026 BEAUVAIS, France

³ Institute of Applied Geosciences, Geothermal Science and Technology, Technische Universität Darmstadt, Schnittspahnstraße 9, 64287 Darmstadt, Germany

⁴ Helmholtz Centre Potsdam-GFZ German Research Centre for Geosciences, Telegrafenberg, 14473 Potsdam, Germany

⁵ University of Zagreb, Faculty of Electrical Engineering and Computing, Unska 3, 10000 Zagreb, Croatia

⁶ Iceland Geosurvey (ÍSOR), Rangárvöllum 2, hús 8, 603 Akureyri, Iceland

julietn@ru.is

Keywords: *geothermal engineering education, EU strategic partnership and Erasmus Mundus programmes, student mobility, international training, applied sciences, renewable energies utilization, geothermal training, geothermal energy*

ABSTRACT

Intensive graduate courses in geothermal energy have traditionally been the remit of nations with a long tradition of high temperature geothermal utilization: Iceland, Italy, Japan, and New Zealand. In addition, El Salvador has had a Spanish language Geothermal Diploma Course for Latin America since 2010, courses in Indonesia, taught in Indonesian, and African geothermal training is under development. However, increasing impacts of climate change, geopolitical conflict and related refugee movement has drawn attention to the need for clean, renewable and sustainable energy worldwide. This attention has created interest in geothermal research and utilization in many countries that do not have high temperature, tectonic margin or volcano-related, geothermal systems. This paper discusses the ongoing development of an EU-funded European Erasmus + Strategic Partnership dealing aiming at the construction of a geothermal course curriculum for international students, involving Iceland France, Germany and Croatia.

1. INTRODUCTION

This paper discusses the forerunner intensive course program, called Geo3EN (Geothermal Energy European Education Network), to the development of an Erasmus Mundus Master's degree, which can be funded by the EU. This Master's degree is taught in English by a consortium of higher education institutions (HEIs) from different countries; in this case from Croatia, France, Germany and Iceland.

This paper presents first the European context of geothermal energy in terms of resource utilization, research and teaching funding, and then discusses the implementation of some Geo3EN test courses.

2. EUROPEAN CONTEXT

This section is intended to give context to Geo3EN, the geothermal training programme that is the subject of the paper. The section contains a brief description of geothermal energy in Europe, followed by an outline of the main European research funding programme, Horizon Europe, and the youth training programme, Erasmus+ and how the Geo3EN programme fits into this funding regime.

2.1 Utilization of Geothermal Energy in Europe

Utilization of geothermal energy for electricity in Europe ('Europe' is defined as countries in the EU and EEA) is currently 20,881 GWh/yr. The majority of electrical generation is within three countries of Iceland (6,010 GWh/yr), Italy (6,100 GWh/yr) and Turkey (8,168 GWh/yr) (Huttrer, 2020). These countries have geothermal systems related to volcanic areas. However, Figure 1 (Dalla Longa et al, 2020) shows that there is so far un-utilized geothermal potential all across Europe, for instance at more than 2 km depth in sedimentary basins such as the Pannonian, as well as in fractured basement in rift systems within the Rhine Graben. The producing power plants of Velika 1 in Croatia, Soutz sous Forêts and Rittershofen in France, Insheim in Germany are already-operating examples.

Direct use of geothermal heat in Europe amounts to 264,843 TJ/yr, including use by heat pumps. Sweden, Turkey and Iceland (Lund & Toth, 2020) lead this growth in direct use for space heating. Much of Europe has suitable resources for direct geothermal heat applications in agriculture, industry and the built environment in reservoirs at depths of less than 2 km (Figure 1).

The pandemic slowed geothermal development in Europe, but the energy crisis associated with the 2022 war in Ukraine rushed the European Union to develop renewable heating systems. Half of new geothermal projects have been in heating and cooling (Figure 2). In particular, there is strong growth of geothermal heat pump installation, and 13 new district heating systems have added more than 154 MWth of new capacity. 75% of new growth in district heating came from France, Poland and Iceland (EGEC, 2022).

In European heating and cooling projects there is a decentralized energy system approach, and a large effort with respect to technology, system integration and 'non-technical' issues (i.e. policies, building standards, risk management and social acceptance issues) (EGEC, 2020).

The availability of low temperature geothermal resources, the need for renewable energy sources, and a recent focus on geothermal as part of a local-scale energy system, means that use of shallow, lower temperature geothermal resources will continue to support Europe's energy transition and independence in the future.

Proceedings 44th New Zealand Geothermal Workshop
23 - 25 November, 2022
Auckland, New Zealand
ISSN 2703-4275

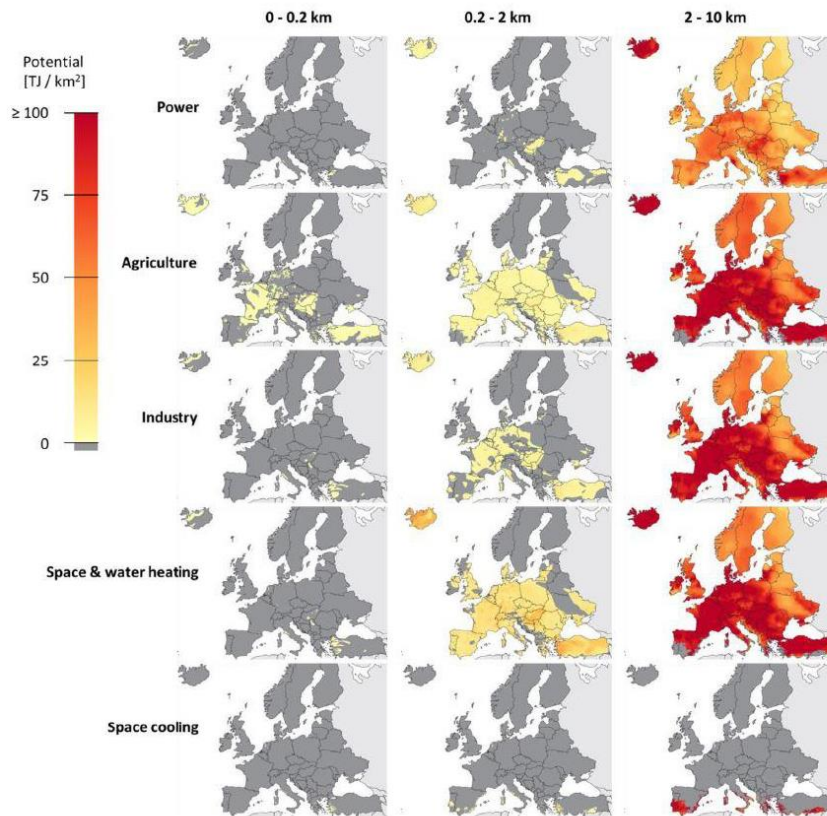


Figure 1: Long-term economic potentials for various geothermal applications in Europe at three different depth ranges. Adapted from Dalla Longa et al, 2020.

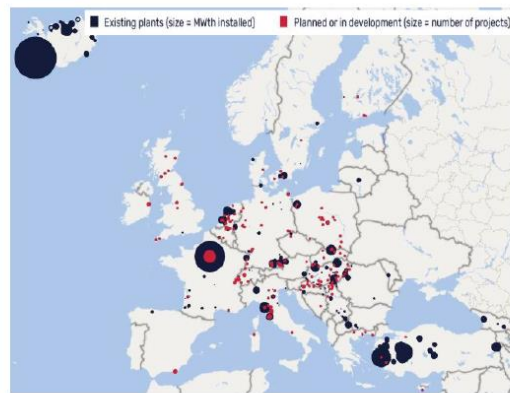


Figure 2. Location of existing and planned geothermal district heating and cooling systems in Europe (from EGEC, 2022).

2.2 Horizon Europe Funding Programme

Horizon Europe and the Erasmus Programme are the funding sources for the project under discussion in this paper (Geo3EN). Hence a brief description of these programmes is included here.

Horizon 2020 was the EU Research and Innovation funding programme, with a budget of € 80 billion, from 2014 to 2020. This has been followed by the new Horizon Europe (budget € 95.5 billion), running from 2021 to 2027.

2.3 Erasmus+ Funding Programme

Erasmus+ is the EU programme for education, training, youth, and sport. There are 3 Key Actions (KA's):

- KA1 Learning mobility of individuals, promoting student and teacher exchange programmes all over Europe, and (albeit with less opportunities) with the rest of the world. .
- KA2 Cooperation among organizations and institutions. This Programme funded the classes described in this paper.
- KA3: Support to policy development and cooperation.

2.4 KA2 and Geo3EN

The Geothermal Energy European Education Network (Geo3EN) has been funded by the Erasmus+ Programme (KA2) of the EU under the project number 2019-1-FR01-KA203-062936.

The higher education priorities of KA2 are:

1. Tackling skills gaps and mismatches
2. Promoting and rewarding excellence in teaching and skills development
3. Promoting internationalization

The Geo3EN programme aims to remedy the lack of qualified junior graduates in Europe available to master all elements of the geothermal energy value chain. Hence it is most closely related to the first KA2 priority of tackling skills gaps.

Geo3EN originated as academic spin-off of the H2020 research project MEET on Enhanced Geothermal Systems (Trullenque et al. 2018; Dalmais, 2020; Ledésert et al. 2022, Raos et al., 2022). The aim of MEET was to demonstrate the lower cost of small-scale production of electricity and heat in wider areas with various geological environments, in order to support a large increase of geothermal-based production sites in Europe in a near future.

In terms of the future, Geo3EN is intended to be the forerunner to an international multi-site MSc in geothermal science and engineering. This will provide students with competencies in geology, material sciences, mechanical engineering, power system management, modelling, and energy economics but also project management, entrepreneurship and intercultural awareness to successfully lead and design complex geothermal energy projects. All the Geo3EN and the proposed MSc programme will be entirely taught in English. The proposed degree will be operated

under a programme known as the Erasmus Mundus Joint Master.

2.5 Erasmus Mundus Joint Master Degree

The aim of the Geo3EN project is the creation of Erasmus Mundus Joint Master Degree (EMJM). The Erasmus Mundus programme supports high-level integrated transnational Master's study that is taught by a consortium of higher education institutions (HEIs) from different countries worldwide, with specific expertise and interest in the concerned study areas/professional domains. The programme provides a predetermined number of full scholarships for the particular EMJM course and students may apply from anywhere in the world. The students must study at a minimum of two HEIs, and earn either a joint degree or a dual degree, depending on the original agreement between institutions. These agreements between institutions depend on the fundamental degree-granting rules of each institution, and may be the controlling factor in the final designation of the Erasmus Mundus degree.

4. THE GEO3EN PROJECT

4.1 Background

The Geo3EN programme was under development since 2019, with an implementation period over March to July of 2022. This paper describes the background, development and implementation of the course. This period unfortunately was concurrent with the most drastic effects of COVID 19 on the world education system and society, with restricted mobility, online teaching and widespread stress. For a programme built on the concept of mobility this period was a challenge, and ultimately the mobility activity was compressed into the final nine months of the project.

4.2 Need for the Geo3EN Project

The objective of Geo3EN is to contribute to making Europe the leader in geothermal energy education and geothermal energy applications by creating a multi-site European MSc of Excellence in Geothermal Engineering. The need for such a qualification has been expressed by geothermal industry stakeholders (as represented by the 19 associated partners of Geo3EN). Their feedback as players of the European geothermal energy sector (industry, energy agencies, clusters, electricity operators, etc.) makes it clear that they face difficulties in finding suitable profiles for developing their activities.

The employment study of the GEOELEC project (funded by the EU, www.geoelec.eu) evaluated that in 2013 around 3000 jobs were directly related to geothermal electricity in the EU-28. The total number of geothermal power jobs (heat + electricity) between 2013 and 2030 is expected to grow from 10,000 to 100,000. The biggest industry challenges will be (EGEC, 2016):

- Finding the right combination of technical and soft skills, and shortage of people at the feasibility stage
- Development of drilling expertise, energy storage, solutions against scaling, efficient communication, and legal and financial framework
- Finding competencies such as flexibility to adapt to the changing environment and clients' needs, reservoir engineering, project and plant management.

Proceedings 44th New Zealand Geothermal Workshop
23 - 25 November, 2022
Auckland, New Zealand
ISSN 2703-4275

These are the challenges that Geo3EN begins to address.

Geo3EN is a truly international project since the education of geothermal engineers requires a multidisciplinary set of competencies that are not available in a single university programme. Geo3EN aims to use the knowledge of its consortium partners to provide their students with the required competencies and skill sets, i.e. to be able to understand geology, material science, geothermal energy storage, energy production and transmission, energy economics, and to have excellent project management and entrepreneurial skills to successfully lead and design complex geothermal energy projects.

Similarly, Geo3EN aims at increasing the mobility of its students to benefit from the different competencies of the consortium partners and to test the curriculum of the future MSc programme. Moreover, boosting mobility will help students to be acquainted with different working techniques, pedagogic techniques and working methods, to master different equipment, experience another working environment and study designs.

4.3 Institutions

The lead applicant for the project was Institut Polytechnique UniLaSalle of France. This is a private higher education establishment founded in 1854. UniLaSalle hosts 4050 students on four campuses in Beauvais, Amiens, Rouen and Rennes and has been emerging as one of France's leading knowledge hub in applied sustainable development. UniLaSalle trains generalist engineers to hold high-level executive and top management positions in the following sectors: agriculture, food industry, food and health, geosciences and the environment, and is an accredited Engineering school. The leader of the Geo3EN project application is Dr Ghislain Trullenque.

TU Darmstadt (Technische Universität Darmstadt), founded in 1877, is a public higher education and research institution. It belongs to the TU9, which is the alliance of leading Universities of Technology in Germany. TU Darmstadt offers 111 degree programmes to 25,840 students. The Geothermal Science and Technology research group is led by Prof Dr Ingo Sass, and is part of the Darmstadt Graduate School of Energy Science and Engineering.

The University of Zagreb (Sveučilište u Zagrebu) is a public university, and the largest university in Croatia. The status of university was formally recognized in 1669. The University of Zagreb offers education programmes in all scientific fields and a wide range of courses at all study levels, from undergraduate to postgraduate for more than 70,000 students. The Technical College, which included engineering, was established in 1918, and today the Faculty of Electrical Engineering and Computing (FER) is the largest technical faculty and R&D institution in the fields of electrical engineering, information and communication technology and computing in the Republic of Croatia. The present research and educational staff comprises more than 190 professors, 202 teaching and research assistants and around 3300 undergraduate and graduate students. Izv. Prof. Dr. Sc. Siniša Šadek, Department of Energy and Power Systems was the FER representative on the Geo3EN programme.

Nýsköpunarmiðstöð Íslands (the Innovation Centre of Iceland) was the original Icelandic institution involved in this grant, however by 2021 this organization was failing, and

Reykjavik University (Háskólinn í Reykjavík) was asked to be the Icelandic partner. Reykjavik University is a small private university in Reykjavik, Iceland. The University is ranked 53rd in the Times Higher Education young universities rankings, and has around 3800 students. Reykjavik University teaches Law, Computer Science, Engineering, Business and Sports Science. The Engineering Department hosts the Iceland School of Energy, which is the school involved in the Geo3EN programme.

4.4 Logistics and the Budget Component of Geo3EN

The project primarily supported academic staff working time dedicated to curriculum construction, building of a competence matrix, financing transnational project meetings plus project management and communication. Extra funds were available to test some of the proposed lectures and site visits in the form of an intensive study program for two academics and six students per institution, including costs for international travel. There were some events that had to be modified or cancelled due to COVID 19, and thus cost less than budgeted. The nature of these EU funded projects is such that funds are not generally transferrable between categories, so the final total spend of €191,000 was around €60,000 less than the original budget.

The project logistics include coordination of activity times and degree regulations between four universities in four different countries. The complexities are not discussed further in this paper, which is focused on academic matters, but nonetheless management is an important and time-consuming part of the project.

4.5 Academic component of Geo3EN

4.5.1 Stakeholder Consultations

As already mentioned in section 2.4, Geo3EN originated from the Innovation Action MEET demonstration project during which the lack of young, qualified, multi and interdisciplinary geothermal engineers appeared. Members of the consortium produced a preliminary version of a competence matrix needed for future engineers. To ensure that the imagined profile corresponds exactly to the needs of the industry and research at present and in the near future, stakeholder consultations were carried out prior to the curriculum development in WP1. The stakeholders were first consulted via a questionnaire to be filled online and four Multiplier Events were later organized online due to COVID 19 restrictions in Zagreb, Beauvais, Darmstadt and Reykjavik. Feedback was carefully analyzed and the competence matrix was adapted several times accordingly. This process ensures that clear guidelines from both industry, academia and R&D organisms are given to the competence matrix. The competence requirements are a key feature to determine the exact design and selection of courses plus the mobility tracks to be followed by the students.

4.5.2 Intensive Study Program (ISP)

One of the main challenges when dealing with the Geo3EN concept is to develop tools and methodology that will enable students from different thematic backgrounds to gain the same level of base competencies in geothermal topics. The tools and methods should ensure that students acquire basic knowledge in all fields of geothermal engineering in order to be able to follow classes in unrelated fields. The challenge is in bringing a multi-disciplinary approach to a group of students with diverse academic backgrounds. In order to test

the reachability of this goal an ISP has been organized between 23 students and several academic staff. The concept of the program was dealing with a geothermal energy utilization feasibility study. Students had to acquire and treat data from a given reservoir, study rock properties in the laboratory, plan surface installations and take into accounts a given investment budget plus energy price. The students were introduced to concepts used in multi-parameter decision-making processes, with application to geothermal energy usage optimization. The teaching methods originally included classroom instruction, field and laboratory work. The results were evaluated in the form of group projects. Ongoing COVID 19 restrictions and differences in availability between institutions meant that courses were delivered online, and eventually in a very short time period, which was an unfortunate restriction; material had to be compressed, and group interaction and learning time reduced. The courses from each university are described below.

UniLaSalle: Geodynamics and rock rheology related to reservoir properties

1. 3D outcrop visualization
2. Metamorphism and fluid-rock interaction
3. Large-scale geodynamic processes
4. Rock rheology (stress & strain in geologic materials)
5. Brittle deformation processes
6. Ductile deformation processes

TU Darmstadt: Resource Characterization & Utilization

1. Introduction to petrothermal systems and reservoir characteristics.
2. Geological and geothermal models
3. Resource assessment.
4. Quantification and identification of deep geothermal potentials.
5. Introduction to EGS reservoir utilization assessment.

University of Zagreb: Power engineering

1. Introduction to power engineering
2. Power plant operation
3. Fluid machinery
4. Geothermal power plants
5. Electric machines and transformers
6. Transmission and distribution of electric energy
7. Heat exchangers and heat pumps
8. High voltage technology

Reykjavik University: Economics of geothermal energy

1. Conceptual models of high temperature geothermal systems.
2. Geothermal Power Plant configurations.
3. Energy Financial Assessment.
4. Environmental and resource impact of utilization, extracting maximum value from a project.
5. Economics of geothermal utilization.

4.5.3 Site visits

Each taught course was followed, some weeks later by fieldwork, site visits and practical laboratory work. These visits were finally able to go ahead after most COVID 19 restrictions were lifted, although visits to some industrial facilities were limited. The resulting trips still encompassed an interesting variety of reservoir analogue sites, active

geothermal areas, and power stations, power developments adjacent to protected environments (Thjórsá in Iceland), and the protected historic areas with old mines which now give us valuable information on adjacent basement reservoirs.

The first country visit was to Croatia. The visits were somewhat restricted by COVID 19, but the group had access to EL-TO Zagreb thermal power plant, the 16.5 MW Velika 1 Geothermal Binary Plant (Figure3), and the Varaždin Hydro Plant on the Drava River.



Figure 3. The Geo3EN class on a study visit to the Velika 1 geothermal binary power station in Croatia.

Visits to geothermal power plants within the Upper Rhine Graben were able to go ahead and consisted of Soultz-sous-Forêts, Rittershoffen, and the Insheim Power Plants.

Several reservoir analogues were visited in the Upper Rhine Graben border massifs, namely in the Black Forest (Teufelsgrund and Schauinsland mines, shown in Figures 4, 5 & 6) and Vosges (Gabe Gottes Mine). The excursion led by UniLaSalle consisted of a transect across the graben and several paleo geothermal reservoir systems containing hydrothermal ore deposits were investigated.



Figure 4. Geological overview presentation to students within the Schauinsland mine.



Figure 5. The Geo3EN class at the Rhine Graben reservoir analogue site – the Teufelsgrund (Devilground) underground mine.



Figure 6. It was a long descent (~99 m) into the Schauinsland mine.

Field visits in Iceland consisted of Seltún and Reykjanes active thermal areas, the 2021 Fagradalsfjall volcano (Figure 7) and the Hellisheiði Geothermal Heat and Power Station. In addition, the class visited Thjórsádalur (the valley of the river of bulls) which is the location of Iceland's longest and second most voluminous river. More than half (1035 MW) of Iceland's hydro capacity is in the Thjórsá area, which also hosts extensive fractured basalt flow (geothermal reservoir analogue) outcrops. The overnight trip to the Highlands took the class to Landmannalaugar thermal area on the northern margin of the Torfajökull caldera, the largest silicic volcanic area in Iceland, and a very popular tourist destination and protected area within the Fjallabak National Park.



Figure 7. Part of the Geo3EN class at the recently active Fagradalsfjall volcano.

The TU Darmstadt section of site visits consisted of petrophysical investigations in the laboratory, and proved very popular with the students. During this week of laboratory work, students had the opportunity to follow the complete process of petrophysical property measurements on representative facies rock samples from the different geothermal reservoirs.

The hydrothermikum platform accessible at the TU Darmstadt provides high-tech analytics and an interdisciplinary laboratory concept for a broad spectrum of investigation options (Figure 8). It consists of a thermophysical laboratory, containing facilities to determine permeability and porosity, and other thermopetrophysical properties of rocks relevant for geothermal reservoir characterization. Participants were also introduced to a thermo-triax facility, which allows an experimental characterization of rock properties in in-situ conditions (high temperature, high pressure, variable pH of brines).

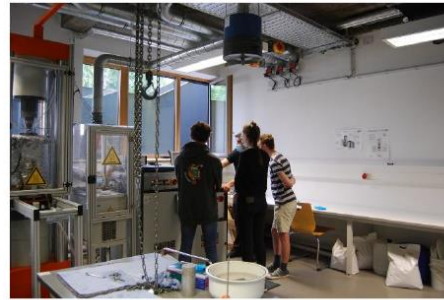


Figure 8. ISP Students performing experiments with mentoring in the Thermo-triax facility necessary for optimal permeabilities for geothermal reservoir rocks samples

5. CONCLUSION

This Geo3EN programme was the forerunner to implementation of an Erasmus Mundus Joint Master Degree in Geothermal Engineering. It occurred over the period of the COVID 19 pandemic, and was affected by this, although there were many other important learnings from this project.

The main lessons are:

- When there are four groups of students from four different countries, it is better to have more in-person contact for fruitful discussions.
- The students and teachers felt that the country visits occurred too close together. This was due to the limited time when limited international travel began to open up but in any case, care has been taken to sufficiently separate events of this type in the curriculum
- Students with no initial geological education background have passed on their difficulties working in the field, analyzing outcrops and investigating geological structures. This was expected by the consortium as it is possibly related to the short duration of the ISP program. A substantial number of intensive basic geology lectures are planned for students in question here. These lectures are available within a pool of Base Line Courses provided by Reykjavik University, TU Darmstadt and UniLaSalle Beauvais.

Topics that should receive more focus in the curriculum are:

- Geothermal resource management
- Natural resource policy
- Integration of geothermal energy with other energy sources.
- Coordination between different universities with respect to the pre-and co-requisites for courses, the course requirements for the degree; also the semester start and finish times are a challenge. This point will require an intensive and precise planning.

The Geo3EN program permitted the construction of a solid base for an application to the EMJD program. The current worldwide geopolitical situation and increasing public awareness regarding environmental concerns are factors in favour of the Geo3EN consortium initiative. Multi and interdisciplinary engineers able to lead the energy transition process are highly needed and it is expected that the employment market in this field will be exponentially growing.

The next steps are the design of a full Erasmus Mundus Joint International Master's degree, considering our Geo3EN experience. All consortium members are highly motivated in bringing their expertise to this novel and innovative training program.

ACKNOWLEDGEMENTS

Special thanks to Ghislain Trullenque whose energy propelled our group from start to finish, and the UniLaSalle International Project Manager Kimberly Couchy for gently keeping us all under control. Thanks to all the other teachers and Teaching Assistants, and finally to all our great students who were the experimental subjects for this project.

REFERENCES

- Dalla Longa, F., Nogueira, L. P., Limberger, J. van Wees, J.-D., van der Zwaan, B. *Scenarios for geothermal energy deployment in Europe*. Energy 206 (2020) 118060.
- Dalmais, E., Genter, A., Trullenque, G., Leoutre, E., Leiss, B., Bär, K., Míntsa, A., Olafson, D. I., Rasl, I., Wagner, B. *Meet Project: Toward Large Scale Deployment of Deep Geothermal Energy in Europe*. Proceedings World Geothermal Congress 2020+1, Reykjavik, Iceland, April - October 2021.
- Dumas, P., Bogi, A., Garabetian, T. *Research, Innovation and Competitiveness of the Geothermal Sector in Europe*. Proceedings World Geothermal Congress 2020+1, Reykjavik, Iceland, April - October 2021.
- Erasmus+ Programme Guide Version 2(2022): 26-01-2022 <https://erasmus->

plus.ec.europa.eu/sites/default/files/2022-01/2022-erasmusplus-programme-guide-v2_en_0.pdf

European Geothermal Energy Council (EGEC). *KnowRes Geothermal Sector Report, 2016* <https://www.egec.org/studies-on-employment-in-the-geothermal-sector/>

European Geothermal Energy Council (EGEC). *Strategic research innovation agenda for geothermal heating*. www.rhc-plattform.org (2020).

Huttrer, G. W. *Geothermal Power Generation in the World 2015-2020 Update Report*. Proceedings World Geothermal Congress 2020+1, Reykjavik, Iceland, April - October 2021.

Ledésert, B. A., Hébert, R. L., Trullenque, G., Genter, A., Dalmais, E., Hérisson, J. *Enhanced Geothermal Systems and other Deep Geothermal Applications through-out Europe: The MEET Project*. Geosciences Special Issue (in press) 2022. <https://www.mdpi.com/si/72997>

Lund, J. W. & Toth, A. N. *Direct Utilization of Geothermal Energy 2020 Worldwide Review*. Proceedings World Geothermal Congress 2020+1, Reykjavik, Iceland, April - October 2021.

Raos, S., Hranic, J., Rajsl, I., Bär, K. *An extended methodology for multi-criteria decision-making process focused on enhanced geothermal systems*. Energy Conversion and Management, Volume 258,15 April 2022.

Trullenque, G., Genter, A., Leiss, B., Wagner, B., Bouchet, R., Léoutre, E., Malnar, B., Bär, K., Rajsl, I. *Upscaling of EGS in different geological conditions: a European perspective*. Proceedings, 43rd workshop on geothermal reservoir engineering Stanford university, Stanford, California, sgp-tr-213, 2018.

5.2.1.3 UniLaSalle, invited lecturer at Technical University Petronas, Perak (Malaysia) (2022)

Stress and strain (Master level, 8 hours lecture).

Fluid rock interaction processes within active geothermal reservoirs. Insights from reservoir analogues (Master level, 8 hours lecture).

5.2.1.4 UniLaSalle, invited lecturer at University of Goettingen (Germany) (2018)

3D numerical techniques of reservoir visualization (Master level, 40 hours lecture).

5.2.2 University of Freiburg im Breisgau (Germany) (2011-2013)

Petrophysical properties of geological materials (Bachelor and Master levels, 40 hours lecture).

Geophysical methods in laboratory and in the field (12 hours lecture and practice in the field).

Sandbox analogue modeling (Bachelor and Master level, 6 days lectures and practice in the laboratory).

Field mapping camp (Bachelor and Master levels, 3 hours lecture plus two field camps per year).

Field excursion in the Armorican Variscan massif (Bachelor and Master levels, 10 days field camp).

5.2.3 University of Mainz (Germany) (2005-2007)

SEM imaging techniques and EBSD/EDS analytics (Bachelor and Master levels, 40 hours lecture and practice at SEM).

5.2.4 University of Basel (Switzerland) (2001-2004)

Field course assistant (Bachelor level, 7 days of excursion).

Structural geology lectures assistant (Bachelor level, 12 hours lectures).

6 Perspectives

I presented in section 4.5.2 the reasons why I oriented my lines of research and my teaching programs towards applied geosciences. I am willing to continue in this way and bring my contribution in order to deepen understanding of reservoir systems. Efforts must be continued in terms of fundamental research and development plus education in order to face societal challenges, increase the economic competitiveness of renewable energy systems and increase the social perception of reservoir utilization.

6.1 Research perspectives

Interpreting the role of inherited anisotropy in the structural evolution of a given domain requires in my mind a deep understanding of mechanical properties evolution of rocks involved in a strain zone knowing that coeval chemical interactions with fluids are occurring. Chemical reactions lead to the formation of new minerals having different mechanical properties than the initial host rock. These new minerals induce in turn a different mechanical response to loading. de Ronde et al. (2005) have for example described reaction-induced weakening of plagioclase-olivine composites using an experimental approach in a Griggs apparatus at temperatures of 900°C and 1000-1600 MPa. The authors observe weakening when solid-solid reaction between anorthite and forsterite occurs. Weakening is interpreted in terms of a switch from dislocation creep to grain size sensitive deformation mechanisms, imposed strain being localized and accommodated by interconnected layers of fine-grained reaction products.

The reservoir analogue studies I perform are based on data gained from indirect geophysical methods and structural analysis of outcrops having suffered polyphase deformation. Fault reactivation is deduced from geometrical criteria like structure offsets and superposition of kinematic indicators. The geological history is reconstructed step by step and is further completed by radiometric dating and thermobarometric modeling. In the future, I am willing to gain a deeper understanding of processes active during fault reactivation. I will investigate three different subjects:

- 1) Microfabric analysis of inherited magmatic foliations and their role in the guidance of fractures upon loading,
- 2) Alteration products microfabric analysis and role of alteration products in the mechanical plus petrophysical properties evolution of fault zones,
- 3) Coupled stress strain and flow simulations.

These three subjects are strongly coupled and require both my field and laboratory expertise.

6.1.1 Microfabric analysis of inherited magmatic foliations and their role in the guidance of fractures upon loading

Trullenque et al. (2017) have argued that loading conditions play a role in the geometry of fracture patterns. Their study is based on an experimental deformation approach of gabbro samples using a triaxial apparatus. Fracture networks have been digitalized to obtain a Discrete Fracture Network (DFN) model used as input for a fluid flow simulation. Figure 25 depicts a large thin section gained from an entire deformed core sample, the picture being obtained by stitching a series of transmitted light photographs using a motorized and computer-controlled stage optical microscope in polarized, non-analyzed light. Fractures with a non-measurable aperture at optical resolution have been manually digitalized as polylines. Fractures with a visible opening are treated as polygonal surfaces. The polyline-type fracture orientation distribution relative to σ_1 is consistent with a dominant NW-SE orientation. The polygon-type fractures show a N30° strike relative to σ_1 . The density of polylines being about one order of magnitude higher than the density of

polygons, it is conceivable that small-scale fractures do participate to the overall brine flow within the reservoir. The presence of these abundant small-scale fractures may 1) trigger large scale fracture connectivity, 2) enhance heat exchange between the brine and the host rocks and 3) facilitate fluid rock interaction processes leading to host rock propylitic alteration.

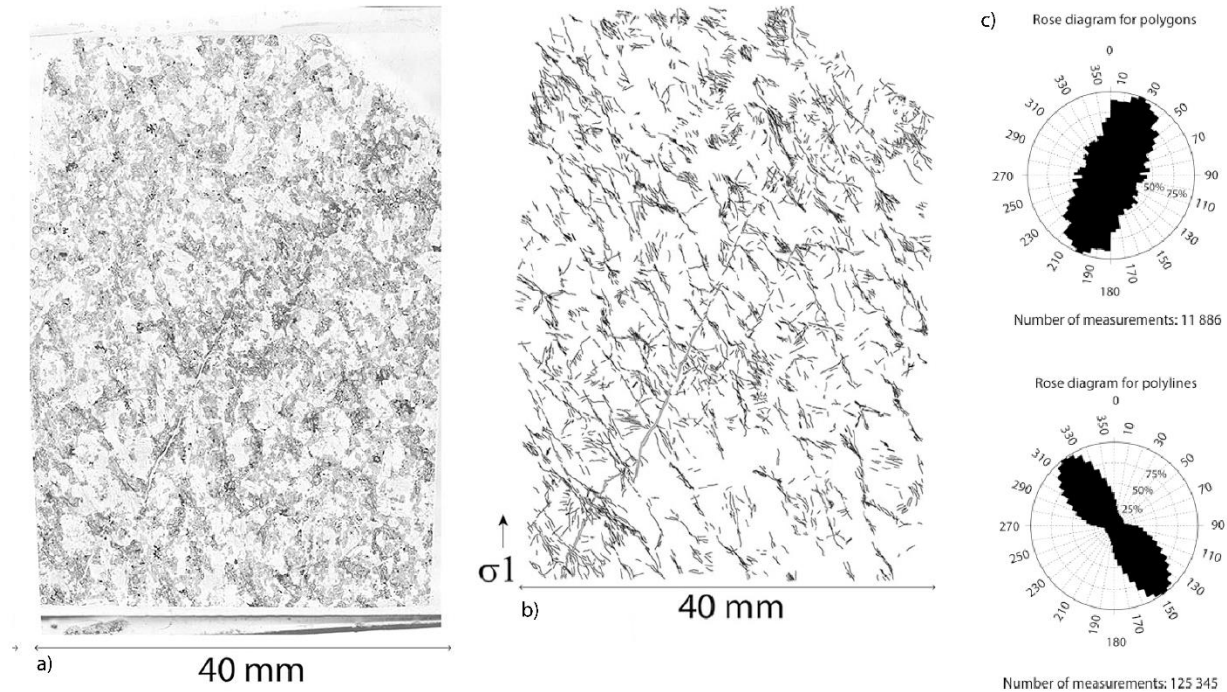


Figure 25: a) thin section overview, b) and c) fracture mapping and orientation from an experimentally deformed sample presented in Trullenque et al., 2017).

A closer view in the mineral distribution within the thin section shows a clinopyroxene Grain Shape Preferred Orientation (GSPO). This GSPO is oblique to the thin section and forms an angle of about 30° to σ_1 (Figure 26). The clinopyroxene crystals tend to form a connected network and present many contact points on both sides of their elongated crystals. I interpret this alignment as evidence of a preserved magmatic pseudo-foliation, frozen during final cooling of the pluton. The elongated shape of the clinopyroxene crystals is related to the intrinsic crystallographic nature of the mineral which is in turn passively transported with a preferential alignment of the grain long axis in the direction of magma flow.

A comparison between the experimental fracture pattern and clinopyroxene GSPO (Figure 26) shows two features of prime interest: 1) the average orientation of polyline-type fractures is parallel to the bulk GSPO and 2) fractures tend to dominantly develop within the clinopyroxene and olivine crystals. The plagioclase crystals are comparatively less fractured than clinopyroxene and olivine. This feature is striking as bulk elastic modulus of plagioclase is lower compared to clinopyroxene and olivine.

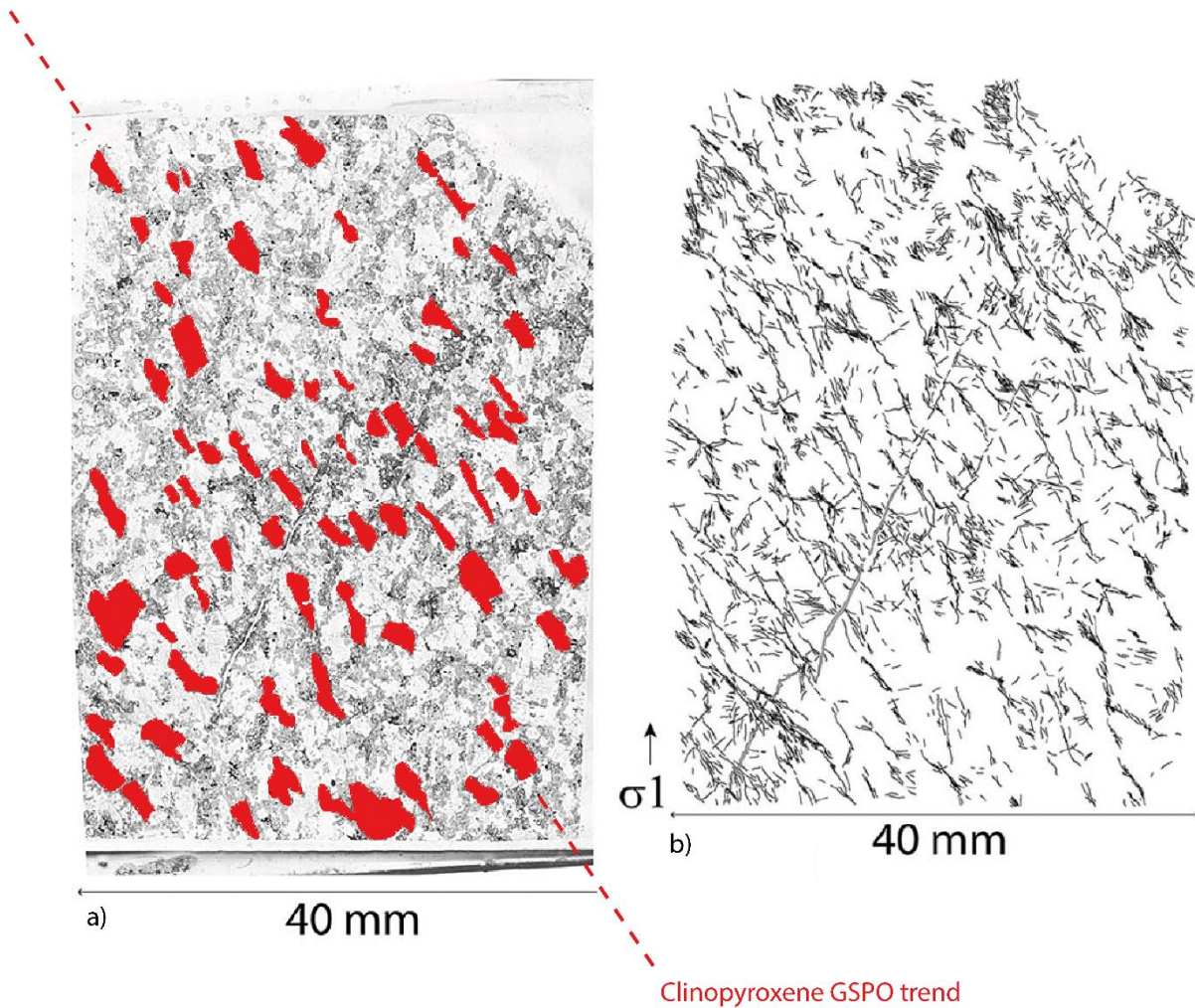


Figure 26: a) outline of the main diagonal clinopyroxene GSPO, b) fracture pattern (after Trullenque et al., 2017).

The rock samples used by Trullenque et al. (2017) have been drilled in an abandoned quarry in the Unit 1 from Odenwald massif in the so-called Frankenstein complex (Barth, 1970; Kirsch et al., 1988; Kreher, 1994; Stein and Dietl, 2001). Kirsch et al. (1988) indicate that this gabbro unit has been emplaced in the time frame 359 ± 3 Ma and 362 ± 9 Ma along the Rhenic suture marking the suture between Avalonia and Armorica microplates (Franke, 2000; Linnemann et al., 2007, 2004; Siebel et al., 2012; Stampfli et al., 2002). These gabbros are older than intrusives found in the Vosges (Boutin et al., 1995; Schaltegger et al., 1996) and SSF granite (Alexandrov et al., 2001). At outcrop scale, the gabbro unit appears massive, and no signs of fracturing nor alteration are present. Hand specimens are homogeneous with no obvious evidence of any compositional layering making these samples an ideal material for experimental testing.

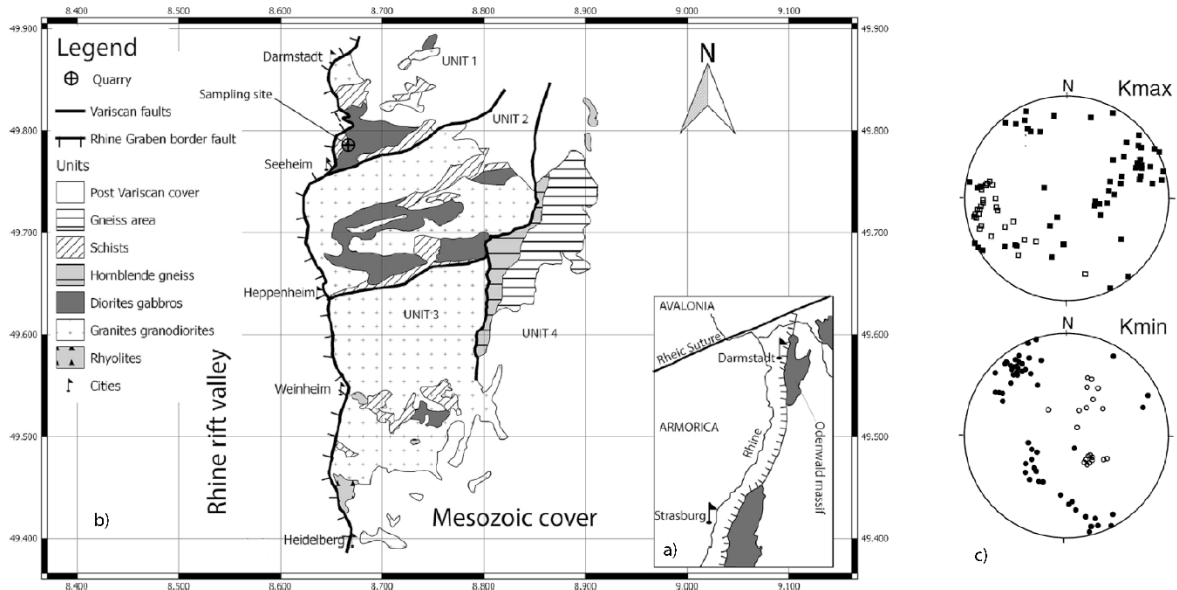


Figure 27: a) localization of the Odenwald massif within the URG, b) simplified geological map from the Odenwald massif (Trullenque et al., 2017), c) AMS distribution (data from Greiling and Verma, 2001).

Greiling and Verma (2001) have studied microstructure of granodiorite-granite intrusions from the nearby Unit III (Krohe, 1992; Stein, 2001) in the southern Odenwald massif. The authors notice the presence of a penetrative foliation related to syn-emplacement deformation of the pluton in a ENE-WSW trending strike-slip corridor. The age of this intrusion is estimated at 326-338 Ma (Kreuzer and Harre, 1975; Schubert et al., 2001) consistent with sinistral wrenching activity along the URGSZ (Edel et al., 2007). In addition to microstructural analysis, Greiling and Verma (2001) studied the Anisotropy of Magnetic Susceptibility (AMS) of their samples and find a similar ENE-WSW trending magnetic foliation and lineation. ENE-WSW magnetic fabrics has been reported in other intrusives within the VM (Edel et al., 2013) and in the cores of the SSF granitic reservoir (Schulmann et al., 1997) as well. All together these data indicate that a geometrical relationship exists between the orientation of magnetic fabric and the strike of the main Variscan structures. AMS studies are therefore highly relevant in order to further characterize inherited Variscan anisotropy related to early pluton emplacement well before subsequent tectonic reactivation of Variscan structures

AMS fabric is usually discussed in terms of Crystallographic Preferred Orientation (CPO) acquired in the deforming magma before its full crystallization (Bouchez, 2000). **If the apparent geometrical relationship between the inherited magmatic foliation and orientation of subsequent fractures (Figure 26) is confirmed then AMS fabric could also be integrated in fracture development modeling upon subsequent loading in the brittle field. In order to test this hypothesis, I am planning to 1) couple AMS fabrics to CPO data in reservoir rocks and 2) investigate the possible relationship between the AMS fabric and the geometry of fracture patterns in plutonic rocks.** I am willing here to use my experience in the field of texture analysis on the same samples used by Trullenque et al. (2017) and obtain at first local CPO data by means of EBSD measurements from the thin sections presented in Figure 26. These CPO data will be used to model the rock magnetic anisotropy using the same approach and database as presented by Biedermann (2018) and Biedermann et al. (2020). In a second stage the AMS data derived from CPO analysis will be compared to AMS laboratory measurements on remaining intact cores in order to check AMS fabric consistency and potential deviations between both approaches as discussed by

Biedermann et al. (2020). In a third stage the AMS pattern is to be compared to a multiscale fracture pattern analysis in order to possibly confirm a systematic relationship between orientation of both fractures and magnetic ellipsoid axes. This fracture analysis will be performed in the field along well-investigated fault zones like the SMMF in the VM and on experimentally deformed samples loaded in a given direction to the previously measured magnetic fabric.



Properties of a pair of fracture networks produced by triaxial deformation experiments: insights on fluid flow using discrete fracture network models

Ghislain Trullenque¹ · Rishi Parashar² · Clément Delcourt³ · Lucille Collet³ · Pauline Villard³ · Sébastien Potel¹

Received: 25 April 2016 / Accepted: 22 August 2016 / Published online: 2 September 2016
© Springer-Verlag Berlin Heidelberg 2016

Abstract Results of a series of deformation experiments conducted on gabbro samples and numerical models for computation of flow are presented. Rocks were subjected to triaxial tests ($\sigma_1 > \sigma_2 = \sigma_3$) under $\sigma_3 = 150$ MPa confining pressure at room temperature, to generate fracture network patterns. These patterns were either produced by keeping a constant confining pressure and loading the sample up to failure (conventional test: CT), or by building up a high differential stress and suddenly releasing the confining pressure (confining pressure release test: CPR). The networks are similar in overall density but differ primarily in the orientation of smaller fractures. In the case of CT tests, a conjugate fracture set is observed with one dominant fracture zone running at about 20° from σ_1 . CPR tests do not show such a conjugate pattern and the mean fracture orientation is at around 35° from σ_1 . Discrete fracture network (DFN) methodology was used to determine the distribution of flow and hydraulic head for both fracture sets under simple boundary conditions and uniform transmissivity values. The fracture network generated by CT

and CPR tests exhibit different patterns of flow field and hydraulic head configurations, but convey approximately the same amount of flow at all scales for which DFN models were simulated. The numerical modelling results help to develop understanding of qualitative differences in flow distribution that may arise in rocks of the same mineralogical composition and mechanical properties, but under the influence of different stress conditions, albeit at similar overall stress magnitude.

Keywords Fractured rocks · Geographic information systems · Discrete fracture network modelling · Distribution of flow · Experimental deformation

Introduction

Flow of fluids through fractured rocks is a phenomenon that concerns several domains of the geosciences. For many years, one of the primary fields in which research was conducted on this process was oil and gas extraction; however, in recent years, other motivations have prompted interest in simulating flow in different examples of fractured media such as in the field of geothermal energy extraction and sustainable water resources development. The efficacy of such applications is often tied to the pattern of flow field arising in faults and networks of fractures. Many studies have placed emphasis on the distribution and scaling pattern of fluid flow through fractures that have implications for geothermal and other related fields (Odling et al. 1999; Taylor et al. 1999; Klimczak et al. 2010; Reeves et al. 2012; Rutqvist et al. 2012). The fluid flow is strongly linked to the degree of connectivity and pattern of connected fractures, among many other properties of the fractured media. The study presented in this paper seeks to demonstrate the qualitative differences in flow response of fracture networks that are generated in similar rocks, with similar stress

The original version of this article was revised: The author names were presented incorrectly. The author names should be presented as above and the citation should be: Trullenque, G., Parashar, R., Delcourt, C., Collet, L., Villard, P., and Potel, S. Hydrogeol J (2016). doi:10.1007/s10040-016-1468-x.

✉ Ghislain Trullenque
ghislain.trullenque@lasalle-beauvais.fr

¹ Département GEOS, Institut Polytechnique LaSalle, équipe B2R, 19 Rue Pierre Waguët, 60000 Beauvais, France

² Division of Hydrologic Sciences, Desert Research Institute, 2215 Raggio Parkway, Reno, NV, USA

³ Institut Polytechnique LaSalle, 19 Rue Pierre Waguët, 60000 Beauvais, France

magnitude, but under different mechanisms of stress application. The change in the stress conditions causes the fracture network to develop dissimilar connectivity patterns when many other properties (including the fracture density) are similar for a pair of networks being compared. By developing a more in-depth understanding of how stress conditions influence localization or further spreading of the flow field in fractured media, it is hoped that improvements can be made toward those fractured-media-related applications where natural or artificially induced stress is an important factor in the determination of the outcome (e.g., enhanced geothermal systems).

Computation of flow in a fracture network can be performed using different conceptual models and approaches which either rely on a grid-based continuum method, or techniques based on geometrical attributes of network connectivity (see Neuman (2005) for a descriptive comparison). A discrete fracture network (DFN) approach, where hydraulic head is computed for all intersection points of fractures in a network, was used in this study to solve for flow in each individual fracture on a two-dimensional (2D) plane. The DFN-based numerical model designed to compute fluid flow in fractured rock samples is applied to the experimental data of the network structure collected from laboratory tests under different stress conditions. Both geometrical and hydraulic properties of fracture networks are impacted greatly by stress conditions resulting in changes to flow and transport behavior in the fractured formations (Henriksen and Braathen 2006; Zhao et al. 2013; Liu et al. 2013). By conducting a numerical study of flow for fracture networks generated from laboratory tests, it is expected that the results will help to understand important differences in the flow pattern for network types produced by changes in the stress environment. Deformation experiments were performed on small gabbro samples in order to study variations of fracture length, orientation, and network geometry in two dimensions as a function of the applied differential stress. DFN simulations under simple boundary conditions were then conducted for the fracture networks that appear during the deformation tests. Results obtained allow for assessment of the influence of the fracture networks' geometry and its hydraulic properties on the amount of fluid that is able to run through the fractured medium and on the flow distribution.

Geological setting of the sampling area

The samples investigated here come from the Odenwald massif located directly south of the city of Darmstadt in SW Germany (Figs. 1 and 2). The Odenwald massif, a Variscan basement unit lying about 250 km north of the Alpine deformation front and 50 km south of the Rhenic suture, is bordered to the west by the Rhine rift valley, a graben part of the European Cenozoic Rift

System (Dèzes et al. 2004 and references therein) and covered by discordant Mesozoic sediments in the east.

The Rhenic suture zone represents the map trace of a southward oriented subduction of the Rhenic Ocean that ended during Lower Carboniferous times in a collision between Avalonia and Ammorica microplates (Franke 2000; Stampfli et al. 2002; Linneman et al. 2004, 2007; Siebel et al. 2012). During this subduction process, intense magmatism developed in the upper lying Ammorica microplate for a period ranging between Late Devonian to Early Carboniferous. The resulting intrusive plutons are now exposed within the Odenwald massif which is classically interpreted as a magmatic arc mid- to late Variscan in age (Henes-Klaiber 1992; Kreher 1994). This massif is divided into four units according to changes in rock composition and age of the plutons (see Fig. 2b).

Unit 1: Mainly composed of gabbro (Frankenstein Complex, Barth 1970; Kirsch et al. 1988; Kreher 1994; Stein and Dietl 2001) and granite. Radiometric studies by Kirsch et al. (1988) indicate an emplacement of the Frankenstein complex at 362 ± 9 Ma deduced from $^{207}\text{Pb} / ^{206}\text{Pb}$ zircon age and 363 ± 7 Ma or 359 ± 3 Ma based on $^{40}\text{Ar} / ^{39}\text{Ar}$ dating on hornblende and plagioclase respectively. According to the same authors, the intrusions took place at shallow crustal levels with pressures ranging between 1 and 3 kbars.

Unit 2: Also called Flasergranitoid Zone (Nickel and Maggetti 1974; Stein 2000). It is composed of diorites, granodiorites, tonalities and granites.

Unit 3: Also called southern Bergsträsser Odenwald, is composed of granodiorites and granites. Ages of emplacement of units 2 and 3 are younger compared to Unit 1—338–330 Ma and 336–326 Ma, based on K-Ar dating on hornblende and biotite, Kreuzer and Harre (1975); Schubert et al. (2001)—while pluton emplacement depth is higher (with estimated pressures in the range of 4–6 kbars (Altherr et al. 1999), Henes-Klaiber 1992) and Willner et al. 1991).

Unit 4: Corresponds to the easternmost part of Odenwald massif and is mainly composed of gneisses.

All samples presented in the following come from unit 1, i.e. the Frankenstein Complex. The samples have been drilled directly on blocks from an abandoned artisanal (10 m in size) quarry (see Fig. 2b) using a diamond tool cooled down with water. The blocks piled up on top of each other at the entrance of the quarry did not show any sign of deformation. The samples have been chosen for their apparent lack of anisotropy with no evidence of alteration. A total of 25 rods of 42 mm diameter and about 20 cm length were gained within 4 h of drilling. Given the poor outcropping conditions at the quarry itself and its surroundings, intensively covered by vegetation, no detailed mapping and structural analysis of the area has been performed.

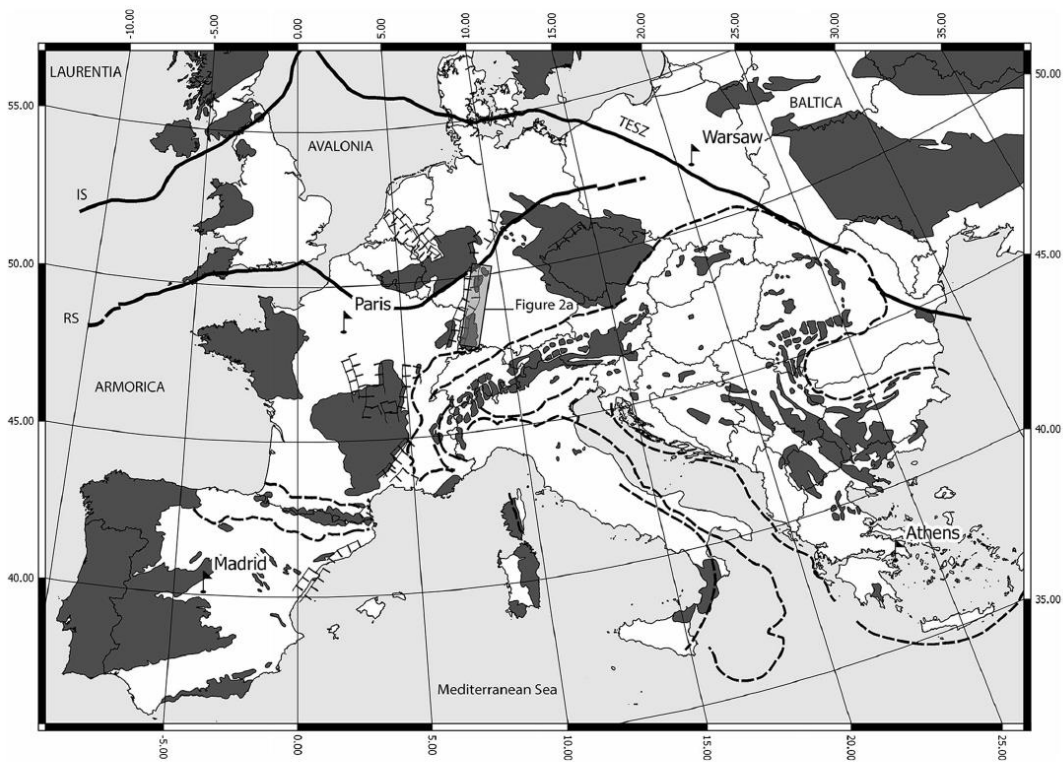


Fig. 1 General tectonic overview of Europe showing pre-alpine massifs (grey), major Hercynian structures (thick black lines), alpine deformation front (black stippled line), and Cenozoic rift-related normal faults (thin barbed lines). IS Iapetic Suture, RS Rheic Suture, TESZ: Trans European Suture Zone. Grey semi-transparent box shows the location of Fig. 2a.

Georeferencing coordinate system: EPSG: 54027, World Equidistant Conic. Reference grid: EPSG: 4326, WGS84, decimal units. Modified from Linneman et al. (2000), Dézes et al. (2004), Carrigan et al. (2006) and Siebel et al. (2012)

Experimental setting of the deformation experiments

The data presented here are taken from the work of Collet and Villard (2014). Three kinds of tests were performed on gabbro samples from the Odenwald massif: uniaxial testing, Brazilian testing, and triaxial testing. In the following, σ_1 will refer to the main axial compressive load, σ_2 to the intermediate stress, and σ_3 to the confining pressure; σ_1 , σ_2 and σ_3 are mutually perpendicular.

The deformation apparatus used in this study consists of a servo-controlled triaxial device with a maximum loading force capacity of 3 mega Newtons and 150 MPa confining pressure. The whole pressure vessel can be heated externally up to a temperature of 150 °C. Silicon oil is used as a confining pressure medium. The intermediate stress σ_2 is equal to σ_3 as a result of using fluid as a confining medium. Sample loading was obtained by a constant loading rate of 5 kN/s. For uniaxial and triaxial testing both faces of the cylinder were grinded in order to obtain flat parallel

faces within a maximum tolerance of 0.02 mm from perfect parallelism.

Uniaxial testing ($\sigma_1 > 0$, $\sigma_2 = \sigma_3 = 0$): Large cylindrical samples, 100 mm in diameter and 200 mm in length, were used for uniaxial testing. Samples are placed directly between the loading pistons of the device up to the failure point. This test allows determination of the uniaxial compressive strength, i.e. the stress at which the sample fails with no confining pressure.

Brazilian tests ($\sigma_1 = \sigma_2 = 0$, $\sigma_3 < 0$): Disks of 20 mm thickness and 100 mm diameter were used in a Brazilian unit mounted between the loading pistons of the device up to the failure point. This test allows an indirect determination of the tensile stress, i.e. the stress at which the sample fails under tension load (Claesson and Bohlooli 2002).

Triaxial testing ($\sigma_1 > \sigma_2 = \sigma_3$): Samples of 42 mm diameter and 70 mm length were mounted in an aluminium

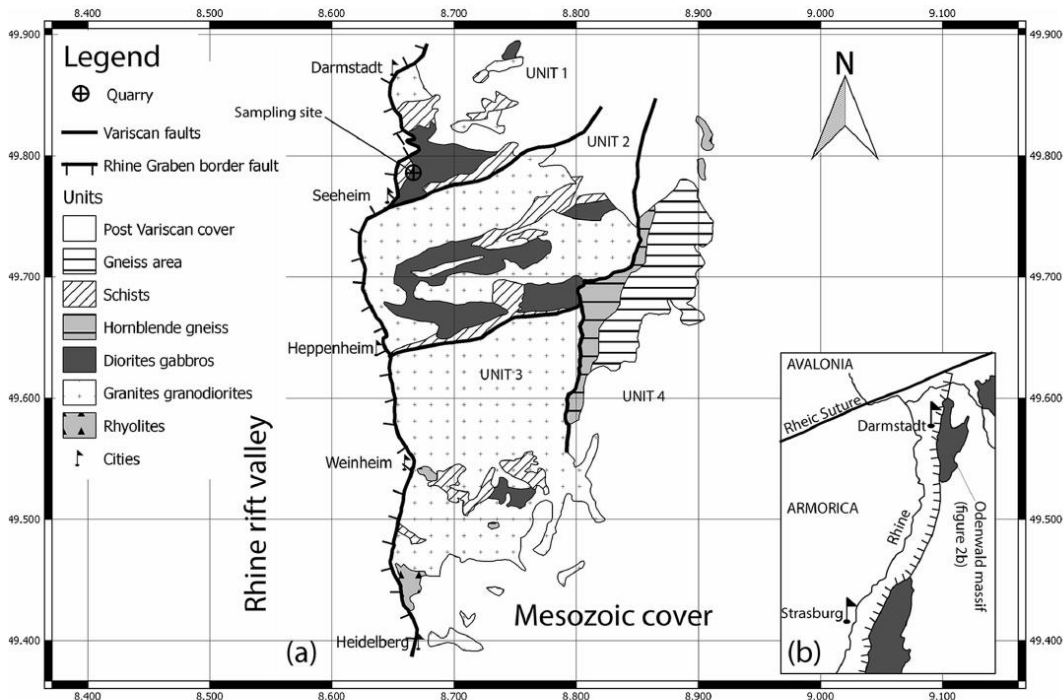


Fig. 2 a Simplified scheme of the northeastern border of the Rhine Graben showing pre-alpine massifs (grey) and Cenozoic rift-related fault zone (thin barbed line). Grey semi-transparent box: location of Fig. 2b. Modified from Kirsch et al. (1988). b Geological map from the Odenwald

massif. Georeferencing coordinate system and reference grid: EPSG: 4326, WGS84, decimal units. Modified from Barth (1970), Kirsch et al. (1988) and Siebel et al. (2012)

jacket (1 mm thick) and welded at both ends using 1-mm thick plate from the same aluminium alloy (Alloy AlMgSi_{0.5}). Welding was operated using a pulsed AC electric arc operated at 70 A using a TIG apparatus and pure Tungsten electrodes. Argon gas was injected around the electrode during the welding process in order to prevent oxidation of the molten alloy. Sample jackets were cooled down by circulating water at 0 °C in a copper pipe (3-mm inner diameter and 1-mm wall thickness) wrapped around the whole sample length during the welding time. This process is intended to minimize excessive heat conduction to the sample.

Once welded at both ends, the jackets were pressed in non-hardened steel adaptors in order to produce a complete radial (Hawkes and Mellor 1970; and Gramberg 1965) restraint at the end of the samples. A scheme of sample assembly is presented in Fig. 3. The choice of aluminium jackets, instead of rubber, was decided after a series of unsuccessful experiments during which the rubber jackets were systematically perforated upon sample failure and contaminated with the silicon oil-confining medium.

Confining pressure (σ_3) was raised in 30 MPa steps in order to build up lithostatic confinement up to 150 MPa. Differential stress was obtained once the 150 MPa confining pressure had been built by continuing to move the loading

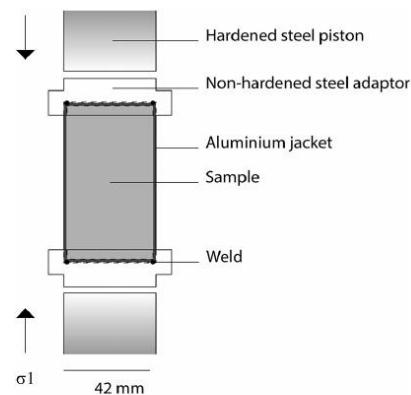


Fig. 3 Scheme of a typical sample assembly mounted between hardened-steel loading pistons. σ_1 is applied parallel to the cylinder long axis

piston at the same displacement speed. Upon sample failure, piston displacement was immediately stopped and confining pressure fully evacuated. Samples were examined to make sure that no post failure displacement on the fractures was produced.

Two different types of triaxial tests were performed at room temperature: conventional tests (CT) and confining pressure release (CPR) tests. The CT test consists of building up a differential stress at 150 MPa confining pressure up to the sample failure. The typical stress vs time curve for CT tests is presented in Fig. 4a. The sample fails while confining pressure is kept constant at 150 MPa (see zoom in Fig. 4b).

The CPR test consists of reaching a differential stress close to the sample failure and then fully releasing the confining pressure in a sudden way. This method has been described by Weiss and Wenk (1983) as a way to use a Griggs deformation apparatus as a dynamic loading device able to quasi-instantaneously produce exceptional differential stresses on a sample that would have failed otherwise under conventional loading conditions.

The typical stress vs time curve for CPR tests is presented in Fig. 5a. Even though both figures appear very similar it can clearly be seen that sample is brought to a sudden catastrophic failure in the case of a CT test at about 2,350 kN. In the case of

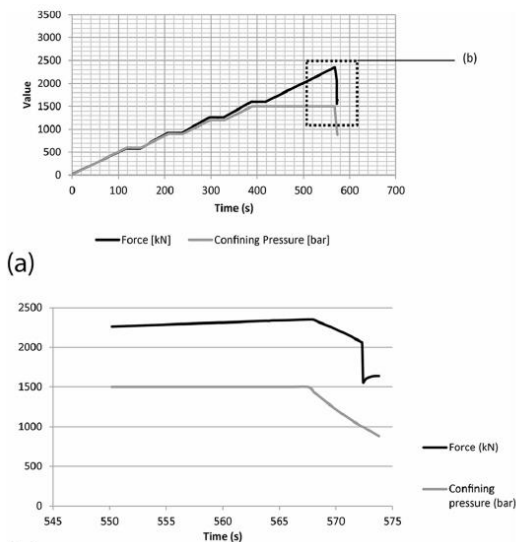


Fig. 4 a Typical time vs force (black curve) and confining pressure (grey curve) of a CT deformation test. Note that force and confining pressure are raised in steps at 60, 90, 120 and 150 MPa confining pressure. Black-stippled rectangle: portion of the curves zoomed in b. Note that upon sample failure confining pressure is released quasi instantaneously. b Zoom in the final portion of the time vs. force and confining pressure diagram of a CT test. Note that sample failure occurs while confining pressure remains constant at 150 MPa

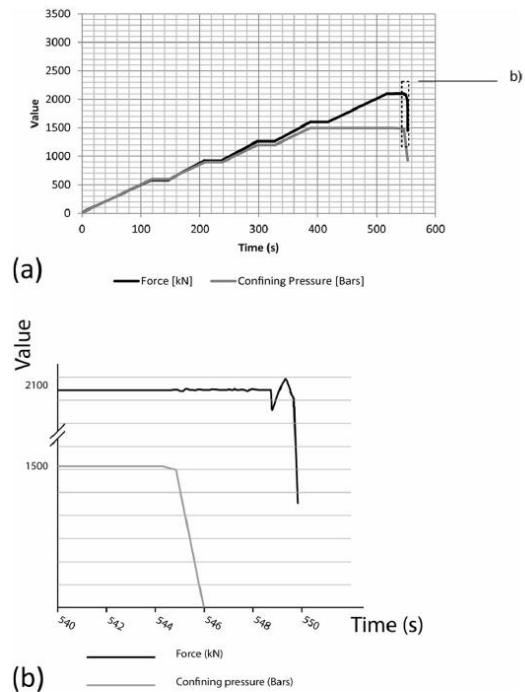


Fig. 5 a Typical time vs force (black curve) and confining pressure (grey curve) of a CPR deformation test. Note that force and confining pressure are raised in steps at 60, 90, 120 and 150 MPa confining pressure. Black-stippled rectangle: portion of the curves zoomed in Fig. 5b. b Zoom in the final portion of the time vs. force and confining pressure diagram of a CT test. Note that sample failure occurs some tenths of a second after confining pressure is released

a CPR test, the axial load is kept constant at 2,100 kN, i.e. building a large differential stress on the sample but not large enough to produce failure. Upon release of the confining pressure, the sample fails within a few seconds as shown in the zoomed portion of the diagram (see Fig. 5b).

The range of stresses reachable with the device used in the present study is several orders of magnitude smaller compared to the ones obtained by Weiss and Wenk (1983). However the device used in this study presents the following advantages: (1) the use of a fluid as a confining medium warrants a quasi-instantaneous release of the confining pressure compared to salt in a Griggs apparatus, (2) the large sample size (42 mm diameter and 70 mm length) offers a better sample representation compared to a Griggs machine (samples typically smaller than a centimetre) especially for coarse-grained rocks as in the present case (millimetric crystal size), and (3) in case of experiments performed at high temperature the use of a heating system external to the vessel prevents furnace failure which has often been observed in Griggs experiments leading to large temperature gradients within the sample.

Microstructural investigations of samples

Rock content determination

The mineralogical paragenesis of the sample was investigated by microscopic investigation on a thin section and completed by X-ray diffraction analysis on powder for whole-rock composition. X-ray diffraction analyses were performed using a D8-Advance Bruker-AXS (Siemens) diffractometer, Ni-filtered $\text{CuK}\alpha$ radiation at 40 kV and 40 mA, and primary soller slit of 2.5° and divergence slit of 0.6 mm; there was a secondary soller slit of 2.5° , with detector slit of 0.1 mm and antiscattering slit of 0.6 mm. Samples were crushed using an agate mortar and pestle mill. Analyses of the relative content of minerals were performed with a step length of 0.02° and a scan speed of $1.2^\circ/\text{min}$ over the range $2\text{--}70^\circ 2\theta$ for whole rocks composition.

Fracture geometry characterization

Extra-large thin sections covering the whole area of a surface running through the deformed rock cylinder long axis and perpendicular to the main fracture trace (so-called axial sections) were produced. In order to avoid collapse of the rock cylinder, the aluminium jacket was not completely removed but peeled off on both sides of the fracture trace. The cylinder was then impregnated in epoxy resin under vacuum and dried at 60°C for 24 h before cutting with a diamond saw. In spite of careful preparation some material loss at the top and bottom of the deformed cylinders could not be avoided, resulting in a maximum thin section size of $40\text{ mm} \times 60\text{ mm}$.

A series of 340 pictures at a resolution of $2,592 \times 1,944$ pixels using a 40X objective lens and a digital camera were obtained from the aforementioned axial sections using a fully automatized motorized stage mounted on an optical microscope. Nonpolarized transmitted light was then used to visualize the fractures. The axial thin section's long axis was mounted parallel to the Y axis of the stage, while the short axis was mounted parallel to the stage's X axis. Stage step-size in both X and Y directions was calculated in a way such that some overlaps were present from one picture to the other. An in-house computer code takes this overlap into account and replaces all pictures in an XY reference frame to reconstruct a single high resolution image file.

Fracture geometry analysis was performed by digital mapping on the obtained mosaic using geographic information systems (GIS)-based vectorization software. When an opening was visible in the picture, a polygon (i.e. a closed surface) was mapped over the opening, when no opening could be seen, the fracture traces were outlined by a line. This method is a somewhat crude approximation as the choice of drawing a polygon or a line might change according to the level of magnification on the microscope. Furthermore, the use of optical

microscopy in itself prevents recognition of cracks under a certain dimension which is below the resolution of the technique; however, these drawbacks are compensated by an excellent mapping statistic all over the thin section, and by the ease of use of an optical microscope compared to scanning electron microscopy for instance.

Once the mapping is complete, GIS is used to decompose every line and polygon into segments, and calculates the orientation of each segment with respect to the long axis (parallel to σ_1) of the thin section. The orientation values are collected in an attribute table, and each segment is colour coded according to a maximum angular deviation from σ_1 .

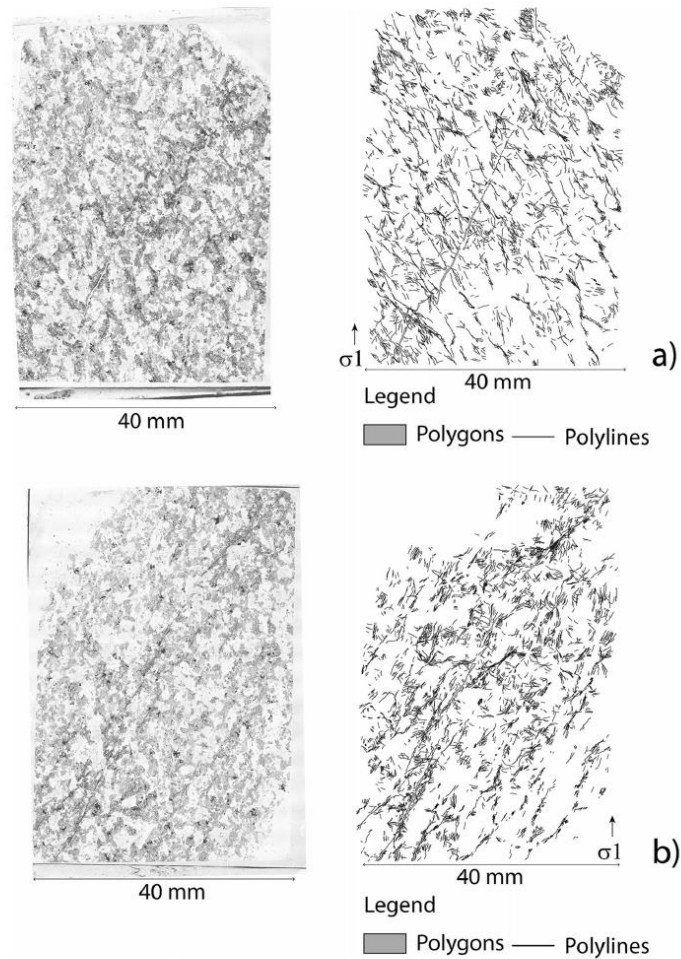
Note that coordinates of fractures when mapped into GIS are in meters, while the height and the diameter of the rock samples measure only a few tens of millimetres, due to the code used in GIS for the vectorization step. The resolution of the mosaic obtained was so high that the code-converted length units with a magnification of about 1.74×10^5 . This change in scale however does not affect the goals of the numerical exercise here which is to study the pattern of fracture connectivity produced experimentally under different test conditions, and to investigate the main flow-paths and distribution of flow field for such connected networks for constant boundary head conditions. A typical mapping of both CT and CPR related thin sections is presented in Fig. 6.

Numerical modelling of flow

Fractures mapped were examined for a set of elements providing a continuous connection between the top and the bottom boundary. The mapped fractures (see Fig. 6a,b) were seen to be just under the threshold for a completely connected hydraulic backbone between the top and the bottom boundary.

To ensure that the fracture network generated during experiments provides a connected pathway for fluid between the top and the bottom boundaries of the domain, a fixed linear extension of 145 m is numerically added to both ends of each fracture in the CT network. The linear extension added to the length of each fracture is chosen by first starting with a smaller value of extension, and then incrementally increasing it until the network appears to be well connected between the top and the bottom boundaries. It can be argued that this numerical extension to the fracture lengths represents (and therefore is a way to account for) the end portion of fractures in the sample which are often difficult to image because of very small aperture values at fracture extremities. It should however also be noted that the numerical model presented in this paper treats all fractures as a constant aperture feature thus allowing for an analysis mainly focused on the differences arising out of the geometrical nature of fracture networks generated in CT and CPR experiments. The extension needed to change the CPR experimental data into a well-connected network was found to

Fig. 6 Overview in polarized non-analysed light of the thin section obtained for a a CT sample and b CPR sample, and associated fracture mapping. The thin section pictures correspond to a mosaic of 340 digital images and are perpendicular to the main macroscopic fracture. The main loading direction (σ_1) is parallel to the long axis of the thin section



be 100 m, which is less than the extension applied to the CT fractures. Recall that the unit of meters (instead of smaller length units) for extension is an artificial construct because of the very large magnification that occurred during digitization of the laboratory data in GIS. These extension values only equate to about 1 % of the total domain height for either of the two fracture sets. This application of fracture extension allows for investigation of the main flow paths and distribution within the flow field as water percolates through the CT and the CPR systems.

A DFN approach in a fractured medium is designed to solve for flow in each individual fracture of the network by computing values of hydraulic head at all fracture intersection points. The boundary conditions are interpolated to assign value of hydraulic head to the boundary nodes (intersection points of fracture segments and boundary of the computational domain).

The head values at boundary nodes is then used to compute values of hydraulic head at all internal nodes by solving a set of linear equations representing conservation of mass (incoming flow equals outgoing flow at a node) for the entire system. Once the set of linear equations is solved to obtain values of hydraulic head at all internal nodes, the Darcy equation is utilized to compute the flow in each fracture segment and the value of global flow for the entire network. Note that the governing equation for flow (Darcy's equation) is built on the assumption that the fractures are fully saturated and that the aperture is uniform throughout the length of a fracture. This simpler conceptualization of fractures does not consider the role of fracture surface roughness which invariably reduces the hydraulic aperture in comparison to the mechanical aperture. The effect of surface roughness on the hydraulic aperture has been found to have a strong impact on the flow and

transport properties of fractured rocks (Zhao et al. 2014; Luo et al. 2016). Additionally, hydraulic properties of fractures are also known to be affected by stress conditions (Zhao et al. 2013), but for the study presented here, no distinction has been made in aperture and transmissivity values used for the CT and CPR fracture sets. The idealization of fractures as the void space between two parallel plates is a primary assumption in this study that helps keep the DFN model less complex and allows for examining the results mainly from the perspective of network pattern and connectivity structure.

Results from DFN models can further be used to compute permeability tensors and understand how the elements of the tensor are related to the properties of the fracture networks. Computation and evaluation of the permeability tensor is a useful tool in many fractured media problems (Min et al. 2004; Pan et al. 2010; Liu et al. 2016). The permeability tensors are however an effective tool at large scales and/or at high fracture density so that the tensor elements are not highly sensitive to one or two dominant fracture elements in the network. For the length scales of problems investigated in this study, the direct results from DFN modelling are analysed without putting the numerical results in the framework of a tensor. Investigation into properties of permeability tensors are planned for similar future studies at larger scales.

Since DFN models are computationally intensive, it is beneficial to reduce the number of unknowns (intersection points of fractures) by identifying and deleting non-conductive fractures. This is achieved by sequentially numbering end-points (nodes) of all fracture segments and then scanning the domain to filter out segments that have an end-point unconnected to any other node in the domain. A fracture segment is defined here as the span of an individual fracture between two successive intersection points; therefore, a long fracture intersected by many other fractures is modelled as a collection of many smaller segments. The aforementioned process of identifying non-conductive fractures, which can either be an isolated fracture or a dead-end segment, is iterative. This is because the deletion of a dead-end segment can turn other segments in the network into an isolated fracture or a new dead-end segment. Careful application of this identification and deletion process results in a simpler network with significantly less number of intersection points (internal nodes). More simplified networks can be further obtained as a by-product of the flow solution by identifying segments with negligible amount of flow and deleting those elements from the rest of the network.

Flow (Q) in fracture segments on a 2D plane is modelled using the simple Darcy equation:

$$Q = -T \left[\frac{h_1 - h_2}{L} \right] \quad (1)$$

where T is the transmissivity, L is the length and h_i ($i = 1, 2$) is the value of hydraulic head at ends of a fracture segment.

Incoming flow is equated to outgoing flow at each of the N internal nodes which results in a set of N linear algebraic equations in h . The equations can be cast in matrix form as $AX = B$ where A is an $N \times N$ diagonally dominant sparse matrix representing the connectedness of internal nodes, X is the vector of unknowns (value of hydraulic head at the internal nodes), and B is the known vector defining the connection between the boundary nodes and the internal nodes. The sparsity pattern of the coefficient matrix is irregular with usually more than 99.9 % of the matrix elements equal to zero for a moderate size network. The eigenvalues of such matrices are spread over several orders and lack the clustering necessary for fast convergence of iterative techniques for linear systems. A detailed analysis of the structure of the coefficient matrices in DFN solution, and performance comparison of various iterative methods available to solve such linear systems is available in Parashar and Reeves (2012). A DFN code built using the minimum residual method of solving large linear systems iteratively (Parashar and Reeves 2012) and used for some recent applications (Reeves et al. 2013, 2014) is employed here to conduct simulations for the CT and CPR fracture sets.

Results and discussion

Mineralogical composition

The percentages of different phases were estimated from macroscopic and X-ray diffraction analysis. The texture of a sample is phaneritic with minerals of millimetric size. The main component phase with 65–70 % is the plagioclase, with a composition between labrador and bytownite. The pyroxene present is a clinopyroxene like augite, which represents around 15 % of the sample. Hornblende and olivine have been also identified with 8–6 % in proportion, respectively. The olivine is in some places rimmed by pyroxene. At least, opaque minerals and titanite are present and cover almost 2 % of the sample; therefore, the gabbro appears to be a pyroxene hornblende gabbro after the classification of Steckeisen (1976).

Mechanical properties of the samples

A total of 21 deformation tests were investigated and the following average values for uniaxial compressive strength, tensile stress and compressive stress at 150 MPa confining pressure were obtained:

Average uniaxial compressive strength values: between 160 and 165 MPa

Average tensile stress values: between 17 and 19 MPa

Average compressive strength at 150 MPa confining pressure: between 320 and 330 MPa

Fracture pattern orientation description

A detailed fracture analysis of two axial thin sections (see section ‘Fracture geometry characterization’) representative for CT and CPR tests was performed. This representativeness was checked by a careful visual inspection of each axial section. In addition, automatic fracture mapping, using image-analysis detection algorithms, was performed for each section. The results of this mapping show no large difference between the samples within the CT set or within the CPR set. The fracture analysis performed using computer algorithms presents the advantage to compare several samples and to check how representative they are of the mean behavior; however, time-consuming mapping is better appropriated for higher data precision. The digitization of fractures was therefore performed for two samples only. The rose diagrams presented in Figs. 7 and 8 show the orientation of the polygons and lines mapped from the CT and CPR test. All diagrams show clear trends of orientations and some divergence from them that might reach 10–15°.

CT tests

The polygons representing the larger fractures show a dominant orientation at 20° from σ_1 and run oblique to the sample. From a macroscopic point of view, this fracture is the main fracture along which the initial rock cylinder is split. The lines (i.e. the smaller fracture) are oriented at 145° from σ_1 and branch on the main fracture.

CPR tests

The polygons and lines are respectively oriented at 35° and 30° to σ_1 (see Fig. 8). As in the CT tests, the polygons

represent the main fracture running oblique through the whole sample.

The underlying mechanisms for difference in the geometry of fractures noticed between CT and CPR samples is not yet fully understood and it is not the objective of the present paper to further investigate this point. The fractures in the CT network however appear to be more broadly distributed in 2D space and exhibit more disperse values of fracture orientation (comparing Fig. 6a to Fig. 6b, and comparing Fig. 7 to Fig. 8). This is likely caused by the application of constant confining pressure in the CT experiments which results in more variability in locations and orientations of the developed cracks. The sudden release of confining pressure in the CPR experiments likely reduces the variability in orientations of newly developed cracks. A first step to better visualize fracture development is currently under investigation and consists of modeling stress field distributions by means of finite element models down to the grain-scale depending on a CT versus CPR experimental setup. Results from this study will be presented in a future paper.

Flow simulations

The fractures generated by CT and CPR experiments were extended and the resulting network solved for flow to study how the pattern of network connectivity, fracture orientation, clustering of fractures, and distribution of fracture lengths influence the flow field. The DFN simulations were performed under a vertical hydraulic gradient of 0.01 where the left and right boundaries are made no-flow. For the purpose of this study, all fractures are assumed to have identical aperture values. A fixed value of 10^{-5} m³/s is used for transmissivity of all individual elements for both CT and CPR fracture sets. Even with this simpler model of uniform hydraulic attributes,

Fig. 7 Rose diagrams showing orientations of polygons (large opened fractures) and polylines (fracture opening non visible at the resolution used) of the map presented in Fig. 6a (CT sample)

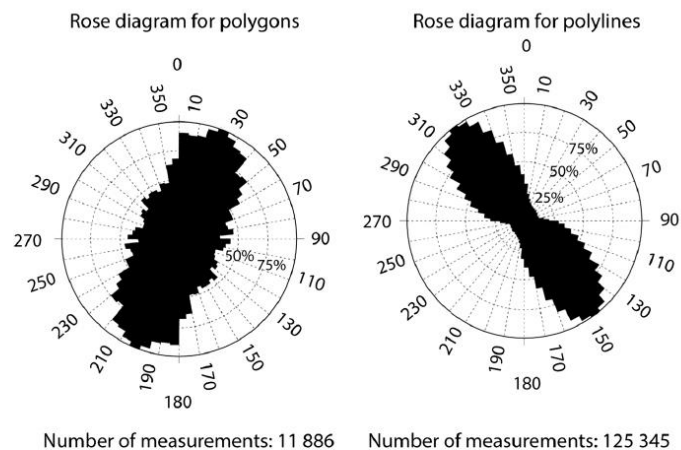
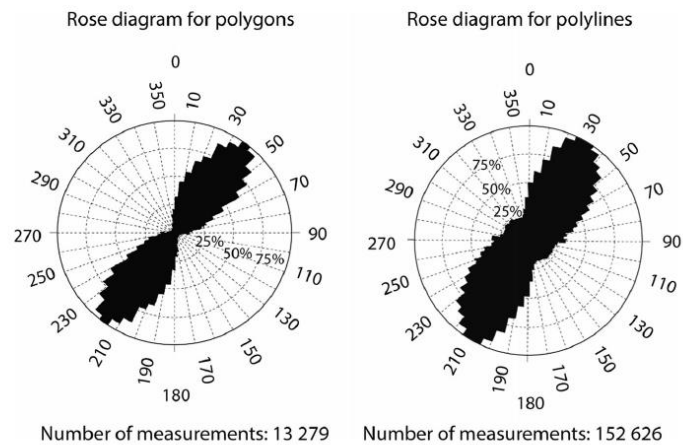


Fig. 8 Rose diagrams showing orientations of polygons (large opened fractures) and polylines (fracture opening non visible at the resolution used) of the map presented in Fig. 6b (CPR sample)



the DFN simulations can help reveal important information about a flow field such as areas of localization of flow and ranges of flow values throughout the domain of the network.

To study and compare the numerical results obtained via DFN simulations, flow computations were performed for five domain sizes of increasing length and height (see Fig. 9). The length and height of five domain sizes for the CPR fracture set was slightly more than that used for the CT fracture sets (see Figs. 10 and 11 for details). To avoid repetition of similar looking figures, the domain sizes map of only the CT fracture network is presented here. Larger domain sizes were chosen to study CPR fracture sets as the network in this case appeared to be better connected near the boundaries compared to the CT fracture sets. Selecting larger domain sizes to study CPR networks does not affect the main objectives of the numerical

exercise which is to examine flow patterns through experimentally generated fractures. The height to length ratio of all constructed rectangular domains is equal to 1.4. By performing computations at varying spatial scale, it is expected that the results will help understand presence or lack of homogenization of flow field and characteristics of any scaling relations.

Distribution of flow and hydraulic head

The flow field distribution and the hydraulic head distribution obtained from conducting DFN computations for the domain sizes shown in Fig. 9 are presented in Figs. 10 and 11. Results from only three (smallest, medium, and largest) of the five domains are shown to keep the number of plots to a reasonable limit. The flow field plots in Figs. 10 and 11 shows the main flow-paths and spatial distribution of flow as the area of study reduces by a factor of more than 10 (largest domain is $5,500 \times 7,700$ m for CT test and $7,000 \times 9,800$ m for CPR test; the smallest domain is $1,500 \times 2,100$ m for CT test and $3,000 \times 4,200$ m for CPR test). The hydraulic head distribution is illustrated by a three-dimensional (3D) plot where the rate of reduction in the z (head) values is useful in analysing zones of high or low flow.

The flow distribution plots show that in spite of the uniform value of transmissivity used to parametrize fractures in the network, both CT and CPR sets exhibits flow values ranging by about four orders of magnitude. This wide-ranging distribution in flow values applies for all three domain sizes shown in Figs. 10 and 11. The main flow-path runs close to the diagonal (i.e., along the principal oblique feature of the specimen) and provides a nearly continuous connection between the top and the bottom face. There is localized concentration of high flow occurring in clusters around the main flow-path, but the flow value drops dramatically (by 3–4 orders of

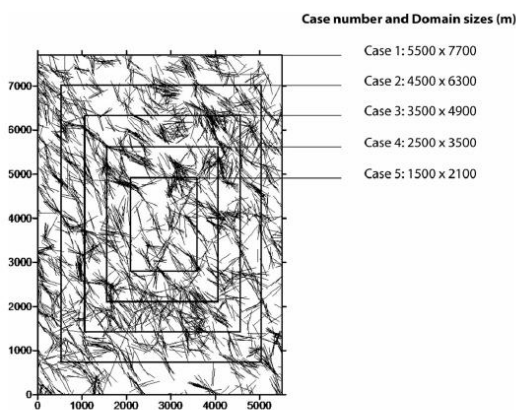


Fig. 9 Fractures of the CT experiment after applying extension to both ends of all individual elements, and placement of domains of varying sizes for computation of flow using DFN approach. The axes are shown here in meters as the network is magnified from the actual experimental image because of the way digitization is performed. Case numbers refer to Table 1

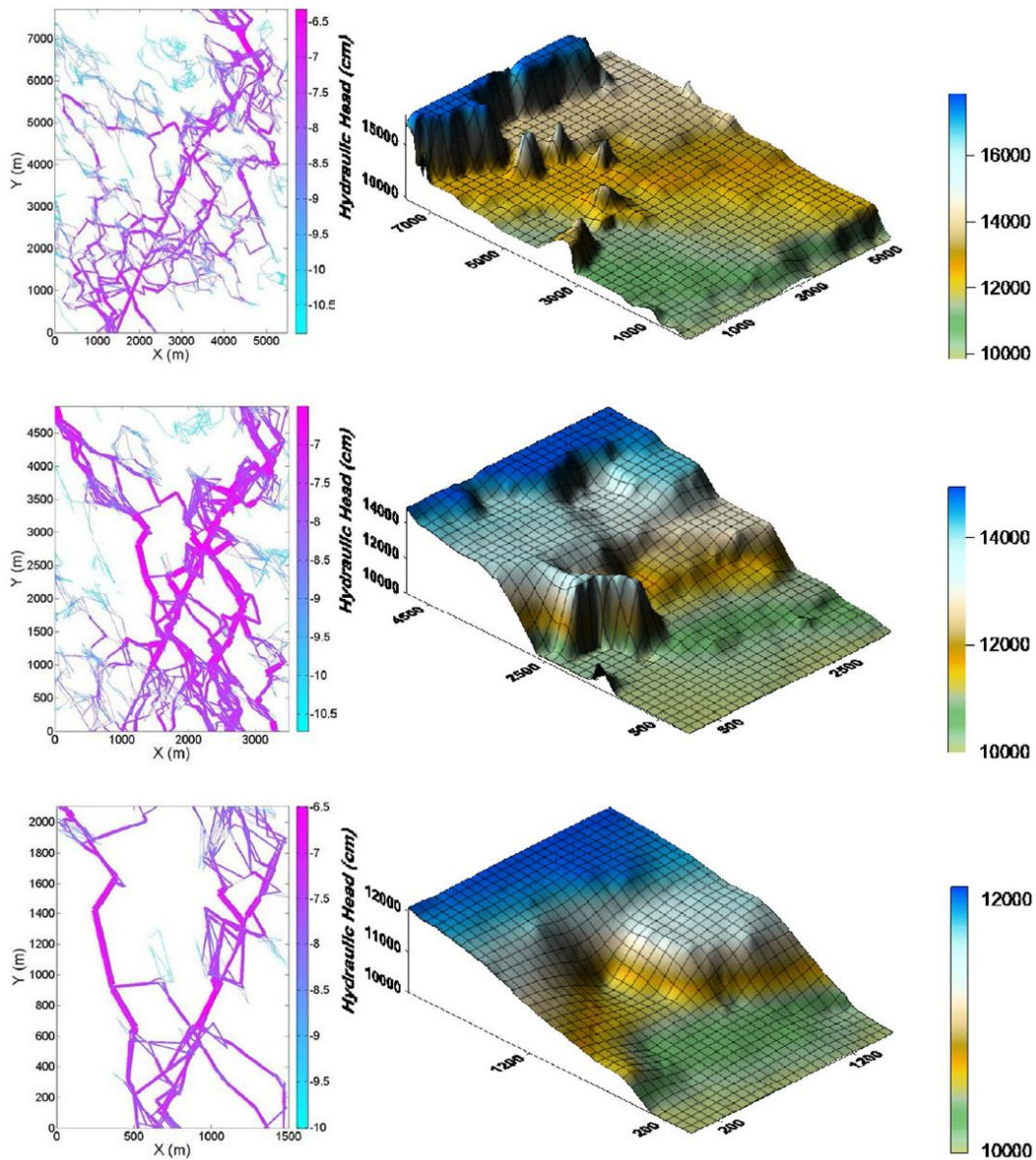


Fig. 10 Depiction of flow configuration (left column) and hydraulic head distribution (right column) for three sizes (1,500 × 2,100, 3,500 × 4,900, and 5,500 × 7,700) of domain of study of CT fracture sets. The flow values in fractures are shown both by the color and thickness of the lines, whereas the color bar is labelled by the logarithm of flow (showing a range of almost four orders of magnitude for all three domain sizes). The hydraulic head values are shown in centimeters where the boundary condition imposes a net hydraulic gradient of 0.01 between the top and the bottom face

magnitude) in areas at greater distances. Flow in the CPR fracture network (see Fig. 11) is much more concentrated

along the main flow path compared to the CT results (see Fig. 10). The flow field associated with CT experiments are

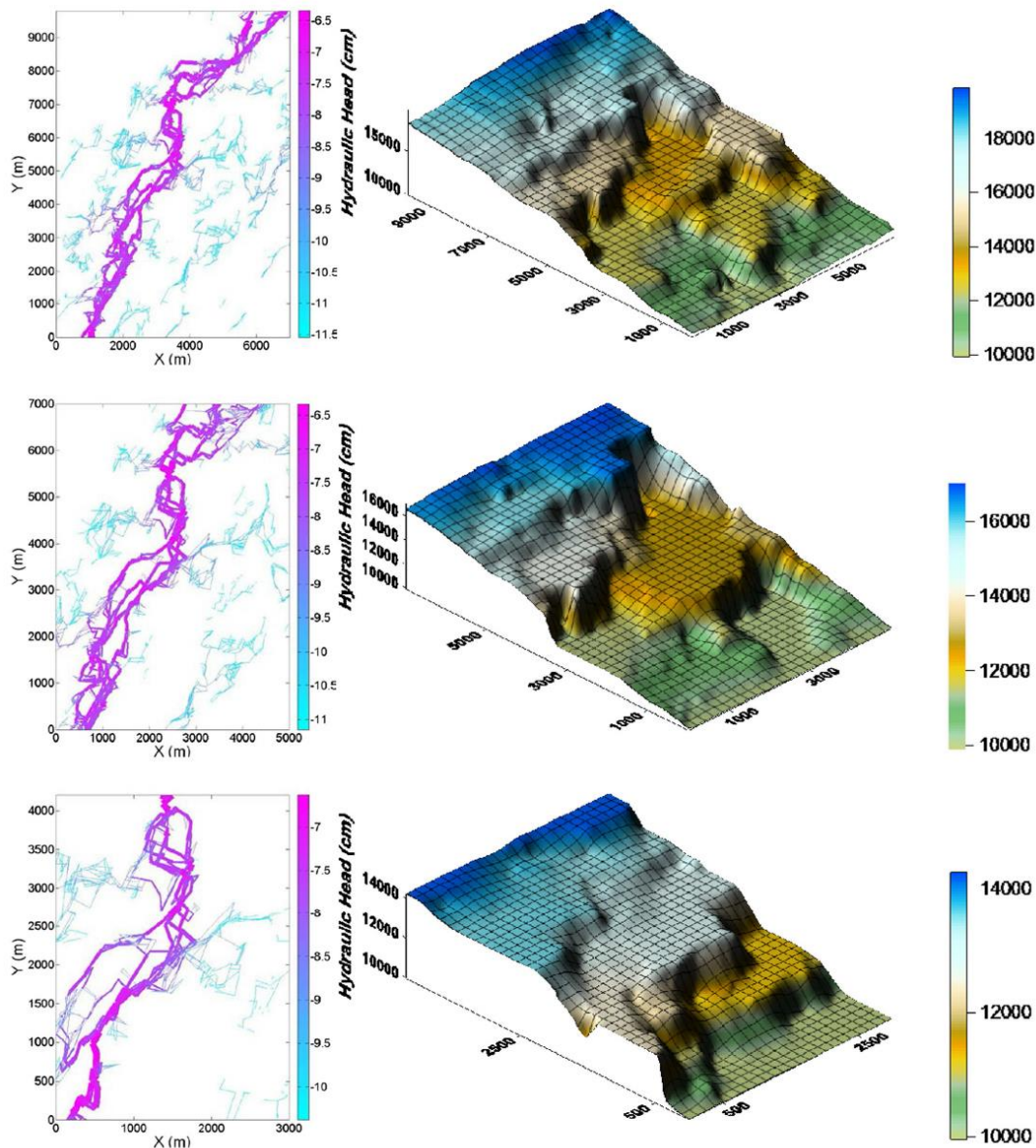


Fig. 11 Depiction of flow configuration (*left column*) and hydraulic head distribution (*right column*) for three sizes ($3,000 \times 4,200$, $5,000 \times 7,000$, and $7,000 \times 9,800$) of domain of study of CPR fracture sets. The flow values in fractures are shown both by the color and thickness of the lines, whereas the *color bar* is labeled by the logarithm of flow (showing a

range of almost four orders of magnitude for all three domain sizes). The hydraulic head values are shown in centimeters where the boundary condition imposes a net hydraulic gradient of 0.01 between the top and the bottom face

more spread out spatially pointing to the higher likelihood of presence of water in randomly located areas of the domain. Such distribution of flow field is significant in applications

like geothermal energy extraction where fluid can potentially come in contact with a larger volume of heat source. The more dispersed flow field of CT experiments is also a direct result of

Table 1 Domain sizes for the five CT DFN simulations, number of fractures inside the domain, and the computed flow values.

$$\text{Normalized Flow} = \frac{\text{Global Flow}}{\text{Domain Length}}$$

CaseNo.	Domain length (m)	Domain height (m)	Number of fractures	Global flow (m ³ /m/s)	Normalized flow (m ³ /m ² /s)
1	5,500	7,700	3,595	5.01E-07	9.11E-11
2	4,500	6,300	2,663	1.06E-06	2.35E-10
3	3,500	4,900	1,801	9.96E-07	2.84E-10
4	2,500	3,500	920	7.83E-07	3.13E-10
5	1,500	2,100	301	4.69E-07	3.13E-10

the conjugate pattern of orientation between the main and the smaller fractures which leads to a higher degree of network connectivity.

Examining the hydraulic head plots, one can see that the distribution is uniform for a large portion of the largest domain (5,500 × 7,700 m) for CT fracture sets (see Fig. 10). It should be noted that for the purpose of plotting, hydraulic head values were interpolated for areas that are unoccupied by any fractures. There is a sharp reduction in head values close to the top face pointing to concentrated flow in a very small number of fractures at large scales in the CT network. The flow then quickly distributes in the fractures located at short distances from the main flow-path. The hydraulic head distribution shows a different trend for the medium and smallest domain sizes where the reduction in values of head is more gradual, pointing to fewer occurrences of high concentration of localized flow. The hydraulic head plot for the medium domain size in the CT network (see Fig. 10) does show a large reduction around the center of the domain, which occurs because of two dominant flow-paths joining to form a more concentrated pathway towards the exit (bottom) boundary. Compared to the hydraulic head distribution of CT fracture networks, the CPR plots (see Fig. 11) show a more gradual and uniform reduction in values between the top and the bottom face of all three domain sizes. The rate of reduction in head values at various scales approximates very closely to the applied hydraulic gradient of 0.01. The amount of flow carried by the main pathway of CPR fracture sets does not vary significantly with location as there is less branching of flow due to lower degree of network connectivity generated as a result of both the main fracture and the secondary fractures trending approximately in the same direction.

Scaling relations

It is worthwhile to investigate changes in overall amount of flow as both the CT and the CPR fracture sets are subjected to a linear vertical hydraulic head gradient of 0.01 across varying domain sizes. Flow computations in fractured media are marked with a very high degree of heterogeneity where a representative elementary volume often does not exist (Klimczak et al. 2010). One would also expect the total amount of water conveyed by a fracture network to have some functional dependence on the size of the domain. In this study however, it is observed that the global flow (overall flow passing through the network) varied over a small range for the five domains for which DFN computations were performed for both of the fracture sets (see Tables 1 and 2). The flow field and hydraulic head distribution are impacted by changes in the domain size as discussed in the previous section, but these shifts do not appear to influence the total volume of water conveyed in a significant way. As the domain size is reduced from the largest to the smallest rectangular area, the flow field reconfigures to channelize about the same amount of water through the main diagonal flow-path. When the global flow is normalized with respect to the domain length, the values show a gradually increasing trend with reduction in the domain size. This behaviour is expected as the diagonal pathway carrying the majority of flow passes through domains of all sizes at an oblique angle. As the domain length reduces, the channelized flow gets distributed over a smaller section leading to the increasing trend in the last column of Tables 1 and 2. An exception occurs for case No. 5 in Table 2 when the extent of reduction in length precludes the rectangular domain to fully capture the principal oblique channel of flow.

Table 2 Domain sizes for the five CPR DFN simulations, number of fractures inside the domain, and the computed flow values.

$$\text{Normalized Flow} = \frac{\text{Global Flow}}{\text{Domain Length}}$$

Case No.	Domain length (m)	Domain height (m)	Number of fractures	Global flow (m ³ /m/s)	Normalized flow (m ³ /m ² /s)
1	7,000	9,800	5,118	4.59E-07	6.56E-11
2	6,000	8,400	4,409	4.84E-07	8.07E-11
3	5,000	7,000	3,471	4.90E-07	9.80E-11
4	4,000	5,600	2,416	4.65E-07	1.16E-10
5	3,000	4,200	1,425	2.35E-07	7.83E-11

Conclusions and perspectives

The data obtained from a series of deformation experiments conducted on Variscan homogeneous gabbro rock samples are discussed in detail. The triaxial device that has been used in this study appears perfectly suited for both (1) conventional tests (CT), which consisted of building up a differential stress at 150 MPa up to the sample failure, and (2) confining pressure release tests (CPR), where a sudden increase of the differential stress leading to catastrophic failure of the sample is produced. These different configurations have an apparent strong influence on the geometry of the fracture pattern that has been described using GIS-based vectorization techniques. The difference in fracture pattern geometry, if systematically confirmed, will be of crucial importance in the modelling of fractured reservoirs and associated fluid circulations.

Numerical results obtained by using DFN models for computing flow through experimentally produced fracture networks helps in understanding the extent by which flow field might differ for fracture sets generated under different stress regimes. The fracture networks produced by CT tests result in a flow field showing a higher degree of spread compared to the flow field associated with CPR tests. As the hydraulic properties of the network are identical (by keeping transmissivity value constant at $10^{-5} \text{ m}^3/\text{s}$ for all fractures in both network types), any observed difference in the flow behavior between CT and CPR fracture sets is solely because of their geometrical attributes. Flow values for both fracture sets show a high degree (almost 4 orders of magnitude) of variation and oblique channel of high concentration of flow within the small area of numerical study. Modeling flow through the networks at different spatial scales resulted in insignificant changes in the overall amount of flow. This occurs mainly because of the role the main diagonal flow pathway plays in channelizing the flow. The fracture networks generated by both CT and CPR tests have a single dominant feature which control the net conductance at all scales.

The distribution of flow field and spatial variations of hydraulic head at different scales are important tools in understanding response of fracture networks generated under different stress conditions. The insights gained by the experimental and numerical methods presented here could help in understanding performance of fractured systems where specific stress conditions are utilized to induce fracture networks having certain geometrical properties.

Acknowledgements We are grateful to Anne Combaud for writing the computer routine in GIS for fracture characterisation, Francois Xavier Joanny for helping in map georeferencing and Julien Duquennoy for writing the computer routine in order to build up the image mosaic. We are indebted to Marie Lummerzheim for establishing contact with University of Reno and to Scott Tyler for allowing Clément Delcourt to access his laboratory. Damien Painsel produced excellent thin sections.

References

- Altherr R, Henes-Klaiber U, Hegner E, Satir M, Langer C (1999) Plutonism in the Variscan Odenwald (Germany): from subduction to Collision. *Int J Earth Sci* 88:422–443
- Barth H (1970) Quarzdiorit und Granodiorit des Felsberg-Zuges im Bergsträßer Odenwald [Quartzdiorite and granodiorite of Felsberg-Zuges in Bergsträßer Odenwald]. PhD Thesis, Univ. Heidelberg, 144 pp
- Carrigan CW, Mukasa SB, Haydoutov I, Kolcheva K (2006) Neoproterozoic magmatism and Carboniferous high-grade metamorphism in the Sredna Gora Zone, Bulgaria: an extension of the Gondwana-derived Avalonian-Cadomian belt? *Precambrian Res* 147:404–416
- Claesson J, Bohloli B (2002) Brazilian test: stress field and tensile strength of anisotropic rocks using an analytical solution. *Int J Rock Mech Min* 39:991–1004
- Collet L, Villard P (2014) Etude des variations de la géométrie d'une zone de fracture expérimentale en fonction de la contrainte différentielle appliquée [Study of variations in the geometry of an experimental fracture zone as a function of the applied differential constraint]. BSc Thesis, Institut Polytechnique LaSalle Beauvais, France
- Dèzes P, Schmid SM, Ziegler PA (2004) Evolution of the European Cenozoic Rift System: interaction of the Alpine and Pyrenean orogens with their foreland lithosphere. *Tectonophysics* 389:1–33
- Franke W (2000) The mid European segment of the Variscides: tectonostratigraphic units, terrane boundaries and plate tectonic evolution. In: Franke W, Haak V, Oncken O, Tanner D (eds) *Orogenic processes: quantification and modelling in the Variscan belt*. Geol Soc London Spec Publ 179:35–62
- Gramberg J (1965) Axial cleavage fracturing, a significant process in mining and geology. *Eng Geol* 1(1):31–72
- Hawkes I, Mellor M (1970) Uniaxial testing in rock mechanics laboratories. *Eng Geol* 4:177–285
- Henes-Klaiber U (1992) Zur Geochemie der Variscischen Granitoide des Bergsträsser Odenwaldes [Geochemistry of Variscan Bergsträsser granitoides, Odenwald massif]. PhD Thesis, Univ Karlsruhe, Germany, 264 pp
- Henriksen H, Braathen A (2006) Effects of fracture lineaments and in-situ rock stresses on groundwater flow in hard rocks: a case study from Sunnfjord, western Norway. *Hydrogeol J* 14(4):444–461
- Kirsch H, Kober B, Lippolt HJ (1988) Age of intrusion and rapid cooling of the Frankenstein gabbro (Odenwald, SW-Germany) evidenced by $^{40}\text{Ar} / ^{39}\text{Ar}$ and single-zircon $^{207}\text{Pb} / ^{206}\text{Pb}$ measurements. *Geol Rundsch* 77(3):693–711
- Klimeczak C, Schultz RA, Parashar R, Reeves DM (2010) Cubic law with aperture-length correlation: implications for network scale fluid flow. *Hydrogeol J* 18(4):851–862
- Kreher B (1994) Petrologie und Geochemie der Gabbrointrusionen des Frankensteins (Odenwald) [Petrology and geochemistry of the gabbro intrusions of Frankensteins (Odenwald)]. *Geol Jb Hessen* 122: 81–122
- Kreuzer H, Harre W (1975) K/Ar Altersbestimmungen an Hornblenden und Biotiten des kristallinen Odenwaldes [K/Ar age determinations of hornblende and biotites in the crystalline Odenwald]. *Aufschluss* 27:71–78
- Linneman U, Gehmlich M, Tichomirova M, Buschmann B, Nasdala L, Jonas P, Lützner H, Bombach K (2000) From Cadomian subduction to Early Paleozoic rifting: the evolution of Saxo-Thuringia at the margin of Gondwana in the light of single zircon geochronology and basin development (Central European Variscides, Germany). In: Franke W, Haak V, Oncken O, Tanner D (eds) *Orogenic processes: quantification and modeling in the Variscan Belt*. Geol Soc Lond Spec Publ 179:131–153

- Linneman U, McNaughton N, Romer R, Gehmlich M, Drost K, Tonk C (2004) West African provenance for Saxo-Thuringia (Bohemian Massif): did Ammorica ever leave pre-Pangean Gondwana? U/Pb-SHRIMP zircon evidence and the Nd-isotopic record. *Int J Earth Sci* 93:683–705
- Linneman U, Gerdes A, Drost K, Buschmann B (2007) The continuum between Cadomian orogenesis and opening of the Rheic Ocean: constraints from LA-ICP-MS U-Pb zircon dating and analysis of plate-tectonic setting (Saxo-Thuringian zone, northeastern Bohemian Massif, Germany). *Geol Soc Am Spec Pap* 423:61–96
- Liu H-H, Wei M-Y, Rutqvist J (2013) Normal-stress dependence of fracture hydraulic properties including two-phase flow properties. *Hydrogeol J* 21(2):371–382
- Liu R, Yu L, Jiang Y (2016) Fractal analysis of directional permeability of gas shale fracture networks: a numerical study. *J Nat Gas Sci Eng*. doi:10.1016/j.jngse.2016.05.043
- Luo S, Zhao Z, Peng H, Pu H (2016) The role of fracture surface roughness in macroscopic fluid flow and heat transport in fractured rocks. *Int J Rock Mech Min Sci* 87:29–38
- Min K-B, Jing L, Stephansson O (2004) Determining the equivalent permeability tensor for fractured rock masses using the stochastic REV approach: method and application to the field data from Sellafeld, UK. *Hydrogeol J* 12:497–510
- Neuman S (2005) Trends, prospects and challenges in quantifying flow and transport through fractured rocks. *Hydrogeol J* 13(1):124–147
- Nickel E, Maggetti M (1974) Magmengenese und Dioritbildung im synorogen konsolidierten Grundgebirge des Bergsträßer Odenwaldes [Magma genesis and diorite formation in synorogenic consolidated basement of Bergsträßer Odenwald]. *Geol Rundsch* 63:618–654
- Odling NE, Gillespie P, Bourguin B, Castaing C, Chilés J-P, Christensen NP, Fillion E, Genter A, Olsen C, Thrane L, Trice R, Aarseth E, Walsh JJ, Watterson J (1999) Variations in fracture system geometry and their implications for fluid flow in fractured hydrocarbon reservoirs. *Pet Geosci* 5(4):373–384
- Pan J-B, Lee C-C, Lee C-H (2010) Application of fracture network model with crack permeability tensor on flow and transport in fractured rock. *Eng Geol* 116(1–2):166–177
- Parashar R, Reeves DM (2012) On iterative techniques for solving flow in large two-dimensional discrete fracture networks. *J Comput Appl Math* 236(18):4712–4724
- Reeves DM, Parashar R, Zhang Y (2012) Hydrogeologic characterization of fractured rock masses intended for disposal of radioactive waste. In: Rahman RA (ed) *Radioactive waste*. InTech Publishing. doi:10.5772/33168
- Reeves DM, Parashar R, Pohl G, Carroll R (2013) The use of discrete fracture network simulations in the design of horizontal hillslope drainage networks in fractured rocks. *Eng Geol* 163:132–143. doi:10.1016/j.enggeo.2013.05.013
- Reeves DM, Parashar R, Pohlmann K, Russell C, Chapman J (2014) Development and calibration of dual-permeability flow models with discontinuous fault networks. *Vadose Zone J* 13(8):1–23. doi:10.2136/vzj2013.10.0183
- Rutqvist J, Leung C, Hoch A, Wang Y, Wang Z (2012) Linked multicontinuum and crack tensor approach for modeling of coupled geomechanics, fluid flow and transport in fractured rock. *J Rock Mech Geotech Eng* 5:18–31
- Schubert W, Lippolt HJ, Schwarz W (2001) Early to middle Carboniferous hornblende $^{40}\text{Ar}/^{39}\text{Ar}$ ages of amphibolites and gabbros from the Bergsträsser Odenwald. *Mineral Petrol* 72:113–132
- Siebel W, Eroglu S, Shang CK, Rohrmüller J (2012) Zircon geochronology, elemental and Sr-Nd isotope geochemistry of two Variscan granitoids from the Odenwald-Spessart crystalline complex (mid-German crystalline rise). *Mineral Petrol* 105:187–200
- Stampfli GM, Von Raumer JF, Borel GD (2002) Paleozoic evolution of pre-Variscan terranes: from Gondwana to the Variscan collision. *Geol Soc Am Spec Pap* 364:263–280
- Steckesen AL (1976) Classification of the common igneous rocks by means of their chemical composition: a provisional attempt. *Neues JB Mineral* 1:1–15
- Stein (2000) Zur Platznahme von Granitoiden: vergleichende Fallstudien zu Gefügen und Platznahmemechanismen aus den White-Inyo Mountains, California, USA, und dem Bergsträßer Odenwald [Emplacement of granitoids: comparative case studies on structures and mechanisms in the White-Inyo Mountains, California, USA, and the Bergsträßer Odenwald]. *Geotekton Forschung* 93:1–344
- Stein E, Dietl C (2001) Hornblende thermobarometry of granitoids from the Central Odenwald (Germany) and their implications for the geotectonic development of the Odenwald. *Mineral Petrol* 72:185–207
- Taylor W, Pollard D, Aydin A (1999) Fluid flow in discrete joints sets: field observations and numerical simulations. *J Geophysics Res* 104:28983–29006
- Weiss LE, Wenk HR (1983) Experimentally produced pseudotachylite: like veins in gabbro. *Tectonophysics* 96:299–310
- Willner AP, Massonne HJ, Krohe A (1991) Tectonothermal evolution of a part of a Variscan magmatic arc: the Odenwald in the mid-German crystalline rise. *Geol Rundsch* 80:369–389
- Zhao Z, Rutqvist J, Leung C, Hokr M, Liu Q, Neretnieks I, Hoch A, Havlíček J, Wang Y, Wang Z, Wu Y, Zimmerman R (2013) Impact of stress on solute transport in a fracture network: a comparison study. *J Rock Mech Geotech Eng* 5(2):110–123
- Zhao Z, Li B, Jiang Y (2014) Effects of fracture surface roughness on macroscopic fluid flow and solute transport in fracture networks. *Rock Mech Rock Eng* 47:2279–2286

6.1.2 Microfabric analysis of strained reaction-induced alteration products. Mechanical and petrophysical properties evolution of fault zones

Deformation processes in CRZ have been largely documented in the literature. It has been argued that the presence of clays contributes to the weakness of faults (Carpenter et al., 2011; Shimamoto and Logan, 1981; Wang et al., 1980; Wu et al., 1975; Wu, 1978) which in turn may trigger aseismic slip (Schleicher et al., 2012, 2010). Haines et al. (2013) review the influence of CRZ on permeability and permeability anisotropy on faults and argue that this influence is related to 1) an increased number of fine grains produced by cataclastic processes and filling pore throats (Morrow et al., 1984; Takahashi et al., 2007), 2) shear induced fabric elements development (Brown et al., 1994) and 3) presence of interlayered porous clastic layers (Faulkner et al., 2010; Faulkner and Rutter, 1998). The presence of CRZ influences geothermal reservoir utilization as noticed by Meller and Kohl (2014). The authors notice that the formation of CRZ has two major effects: 1) hydrothermal alteration lowers the host rock mechanical resistance as evidenced by an increased number of borehole breakouts when crossing enriched clay zones and 2) stress-field re-orientation up to 90° across CRZ. The authors argue as well that CRZ, besides being mechanically weak, are forming decoupling horizons rotating the principal stress component. These two effects challenge reservoir simulations both for the geothermal industry and CCS projects. CRZ weakness has also been correlated to the crystallographic structure of clay minerals. On one hand, (001) planes present a relatively low CRSS due to weak interlayered bonds which facilitates plane slip (Moore and Lockner, 2004; Wu, 1978). On the other hand, weakly bonded water molecules adsorbed in clays (like smectites and vermiculites) can be released during shearing creating some pore pressure which in turn lowers frictional strength (Bird, 1984; Colten-Bradley, 1987; Ikari et al., 2007; Wu, 1978). Haines et al. (2013, 2009) have investigated fabric development in natural and artificial fault gouges and documented relatively weak CPO in CRZ by means of X-ray texture goniometry. CPO intensity strengthens with increasing shear strain and normal stress but the overall fabric intensity remains low. This observation challenges the above interpretations in which the weakness of clay rich fault zones is explained by means of anisotropic crystal structure. According to Haines et al. (2013), CRZ mechanical weakness is due to a combination of grain size sensitive mechanisms, particle morphology and polymodal grain size distribution. In their deformation experiments, the authors observe the rapid development with applied strain of thin B and R1 Riedel-type Shear zones (RS) along which deformation is rapidly localized (nomenclature after Chester et al. 1985). The development of RS in a CRZ influences both its mechanical plus petrophysical properties and triggers changes in terms of indirect geophysical signal (Haines et al., 2013). RS dissecting the CRZ could act as possible fluid pathways depending on their microfabric characteristics.

The conceptual model presented in Figure 28, shows a set of important information regarding CRZ evolution with strain:

- A linear elastic behavior is recorded in the friction / strain mechanical data diagram upon reaching a peak stress.
- Work softening occurs upon formation of incipient RS. With increasing strain, B and R1 RS increase their length and R1 RS dissect the whole sample. At this stage, the material exhibits a stable sliding behavior in the friction / strain record.
- With ongoing sample deformation, the angle between the R1 and the shear zone boundary is becoming smaller and microlithons back rotate in a position where the (001) planes are perpendicular to the main compressive stress (see Figure 28). This rotation is accommodated by internal deformation in the microlithons.

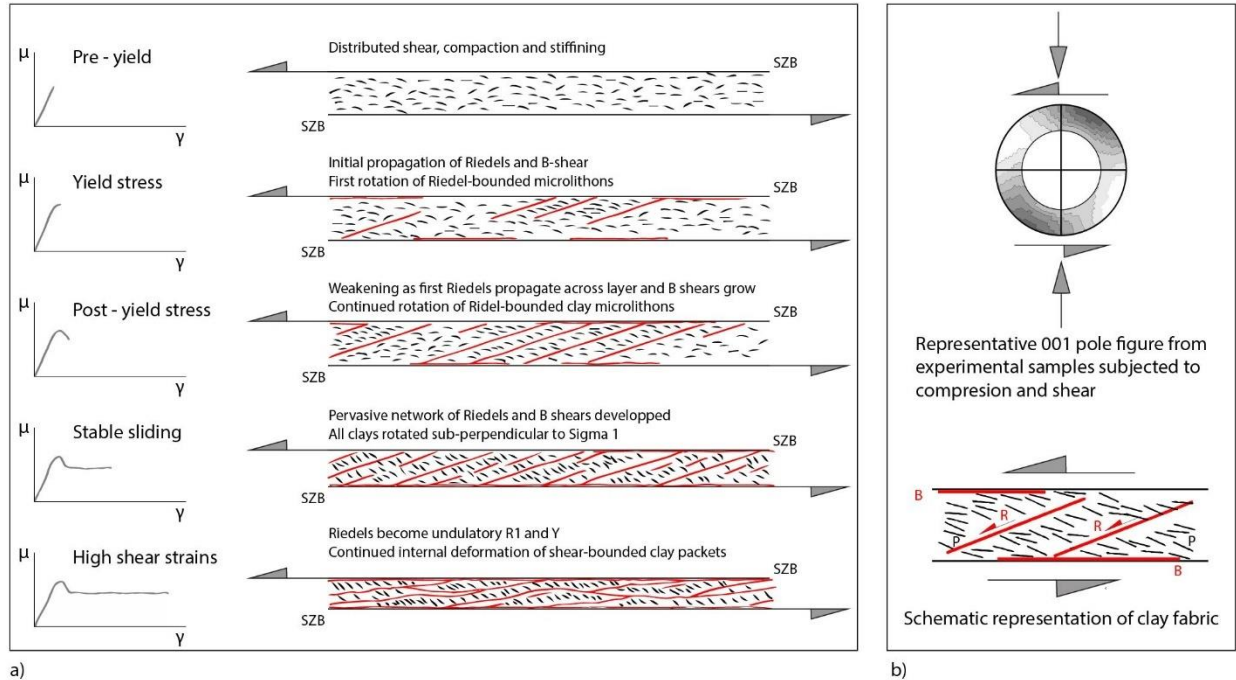


Figure 28: a) clay fabric elements evolution during increasing strain (redrawn after Haines et al., 2013), b) representative (001) pole figure from experimentally deformed samples in compression and shear (Haines et al., 2009). Shear plane terminology according to Chester et al. (1985).

It is important to deepen the microfabric analysis of CRZ with emphasis on deformation mechanisms operating both in the microlithons and RS. I will perform a study on natural CRZ found within the SDVFZ analogue and within the CRZSR at the Schauinsland mining district. Both these places have a well-constrained geodynamic setting and deformation gradients can be sampled along exceptional outcrop exposures. The CRZSR presents the additional advantage to be sheared again during a later event so that inherited potential texture is reworked in an orthogonal direction. Two orthogonal deformation gradients are present at CRZSR and the mechanisms active during such reworking were never investigated. Other drill core samples from the Luconia province are also available as CRZ represent a potential CO₂ leakage hazard when dealing with CCS projects in a faulted carbonate environment.

The similarity in terms of geometrical characteristics between the experimentally produced and natural samples from the CRZSR is striking (see Figure 29). Both samples present a comparable penetrative foliation dissected by oblique RS. Foliation is seen to be laterally dragged along highly localized sinistral R1 structures in which Haines et al. (2013) suggested the activity of cataclastic deformation processes. This proposition is based on SEM imaging only as the width of these deformation zones is too small to be measured by means of X-ray texture goniometry measurements. Due to the difficulty in focusing the X-ray beam on a single microlithon, deformation processes in this domain remain as well poorly constrained.

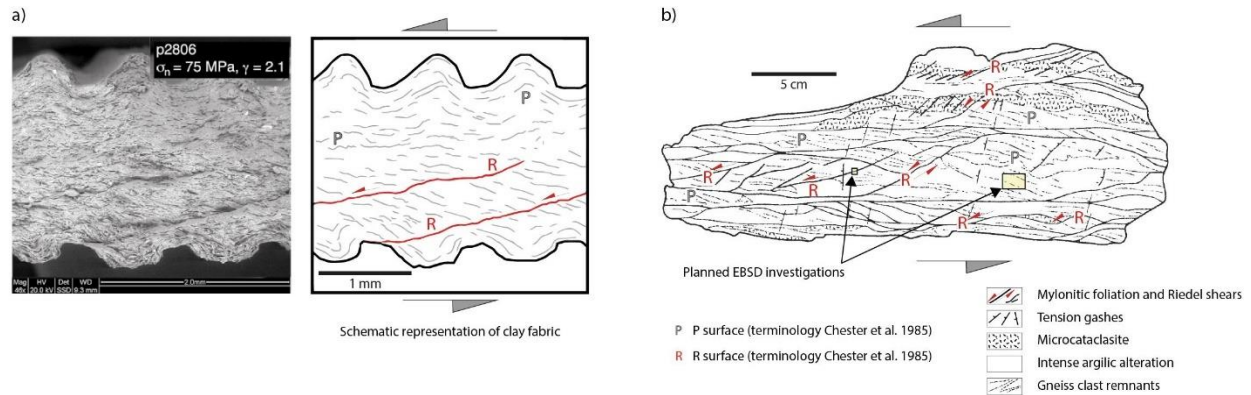


Figure 29: a) interpretation of an experimentally produced clay shear zone (Haines et al., 2013), b) note the striking similarity with field sampled taken along the CRZSR (modified after Werner et al., 2004).

The experiments by Haines et al. (2013) have been performed under dry conditions using high purity illite, montmorillonite and chlorite as a starting material. Under such circumstances, new mineral nucleation is not possible and the analogy with natural CRZ in which neo-crystallization of alteration clay minerals are observed (Schleicher et al., 2006a, 2009, 2010, 2012) is not straightforward. It is conceivable that neo-formed alteration minerals accommodate shear movements by grain size sensitive processes like grain boundary sliding assisted by fluids as inferred on fine grained limestones (Schmid et al., 1977) provided that their growth remains limited by second phase particles (Brodhag and Herwegh, 2010). In case of grain growth, crystal plasticity on favorably oriented slip planes could in turn occur (De Bresser et al., 2001). **To my knowledge, a study dealing with active deformation mechanisms in neo-formed clay crystals within a progressively strained CRZ is not available at present and I propose to fill this gap.** I am willing to use a combination of synchrotron tomography and bulk texture measurements, EBSD plus Transmission Electron Microscopy (TEM) to do so.

High energy synchrotron radiation is ideal to measure bulk rock texture within a rock volume. In addition, the fine spot size can be focused on individual domains like microlithons while preserving an acceptable statistic compared to X-ray goniometry. Besides texture, tomography imaging gives a volumetric distribution of the RS while imaging in 3D pore and voids shape plus phases distribution. Such information is needed to characterize CRZ anisotropy in space.

The EBSD technique presents the advantage to measure crystallite orientation under the SEM at a resolution at least equal to the electron beam diameter. This approach is needed to map the progressive development of misorientations across the R1 RS and within the microlithons themselves (see proposed study domains in Figure 29). Orientation maps can be used to outline active deformation processes like possible grain boundaries migration, subgrain rotation or grain bulging and in turn infer the onset of crystal plasticity instead of cataclasis. In combination with EDS, it is then possible to characterize at micron scale both crystallographic and chemical changes occurring on natural RS. Chemical changes and possible nucleation of new phases are ruled out in the experiments by Haines et al. (2013) as the procedure was performed in dry conditions but can be expected in natural CRZ as clays are considered as progressive alteration products from a given host rock (granite at SDVFZ, gneiss at Schauinsland). Precise EBSD mapping gives in addition the true grain size distribution by means of misorientation angle between neighboring grains with a much finer resolution compared to laser diffraction granulometers. Seismic anisotropy being related to the preferential alignment of minerals, I am planning as well to use both bulk and local texture information in order to build models of seismic anisotropy to be compared with ultrasonic wave measurements on bulk centimeter size samples. These models will permit to correlate the progressive contribution of RS

development along a natural strain gradient with a possible decrease of V_p and V_s wave velocity as proposed by Haines et al. (2013). The authors interpreted these lower velocities as an effect of crack opening and shear localization along RS but in the absence of a precise characterization of deformation mechanisms, this concept remains to be verified.

When even higher resolution is needed, clay crystallographic nature and orientation will be studied using TEM facilities available within my network. TEM lamellae are gained using a Focused Ion Beam facility mounted on a high-resolution Field Emission Gun SEM in order to sample directly within a microlithon and a RS. By means of TEM, I plan to investigate the crystallographic d-spacing value on a crystallite in order to decipher its nature, orientation relationship between neighboring crystals and other physical parameters like internal stress (by means of densities of dislocations measurements) and degree of crystallinity.

This second line of research participates to the fundamental understanding of CRZ evolution depending on strain with possible implications for natural fault mechanical understanding. The study finds a direct application in terms of reservoir flow modeling and prediction of both induced seismicity during geothermal activities and CO_2 leakage hazard when planning CCS projects.

6.1.3 Coupled stress, strain and flow simulations

The discussion proposed in section 4.5.3.2.2 plus the lines of research given in sections 6.1.1 and 6.1.2 outline the need of a deeper mechanical understanding of stress and strain distribution within 1) anisotropic reservoir rocks and 2) pre-structured reservoirs with occurrences of inherited CRZ.

6.1.3.1 Stress distribution and fracture propagation in crystalline basement rocks

A striking similarity is observed when comparing the orientation of experimentally produced fracture patterns and clinopyroxene plus olivine spatial distribution while plagioclase crystals are comparatively less fractured. This observation is puzzling as plagioclase have a lower bulk and shear elastic modulus compared to clinopyroxene and olivine.

I am willing to test an hypothesis dealing with the concept of force chain as commonly described for granular materials (Majmudar and Behringer, 2005; Peters et al., 2005; Sun et al., 2010; Zhang et al., 2017). It is obvious that no direct comparison can be proposed between a packed aggregate of loose particles and a magmatic rock with all minerals being sintered. Nevertheless, **I find conceivable that contact points between mechanically hard crystals showing a preferred long axis alignment as a result of magmatic flow may induce a heavy stress concentration upon elastic rock loading. The local high stress on contact point might be sufficient to induce failure of these minerals. This incipient failure is in turn guided by the intrinsic anisotropic nature of the mineral along a preferential family of crystallographic planes or cleavage. I propose that fracture coalescence, leading to catastrophic sample failure, is being triggered by force chains developed within the connected network of mechanically hard minerals.** In order to test this force chain and load-bearing frame concept leading to stress concentration between neighboring minerals and crack inception, I am willing to use a numerical approach and have established a cooperation involving colleagues from the GeoLab department at UniLaSalle and LSPM laboratory, University Sorbonne Paris Nord (France) and FachHochschule Augsburg (Germany). I propose to use a combination of crystallographic orientation measurements and nanoindentation tests. The nanoindentation technique is a common practice in material science (Merson et al., 2008; Müller et al., 2009; Villain et al., 2007) and applications have also been proposed in earth sciences

(Mukherjee and Misra, 2023). Indentation tests allow to locally measure the hardness and calculate the Young's modulus of a given mineral depending on its crystallographic orientation. Combining nanoindentation to EBSD measurements allows to extrapolate the Young's modulus for all crystal orientations present in a given thin section. The grain distribution map, in which each grain is assigned a Young's modulus value is then directly imported in a numerical simulator and a stress distribution upon loading is computed. This numerical modeling permits a direct visualization of stress concentrations to be compared with the magmatic foliation orientation.

I propose to study pristine crystalline rocks from the type presented in section 6.1.1 (gabbros) plus granitic rocks to be sampled in the VM and gneiss rocks available within the Schauinsland mine, away from the CRZSR and ore veins.

6.1.3.2 Stress distribution and decoupling horizons within a pre-structured reservoir

Besides inherited magmatic foliation I have discussed in session 4.5.3.2.2 the role of inherited CRZ and high strain zones in the guidance of fracture opening within the reservoir.

I want to investigate a working hypothesis dealing with a possible short-lived reservoir connectivity upon fracture propagation in a pre-structured reservoir. Figure 22a clearly shows the present lack of connectivity between the ore vein north of CRZSR and the ore vein south of it. It is evident that the CRZSR must not be considered as an endless constant barrier and that fractures within the gneiss have possibilities to find connections with depth. **Nevertheless, I want to investigate the possibility of a short-lived connection across CRZ upon fracture propagation within the reservoir and brutal arrival of the brine. Plastic deformation being strain rate dependent, it is conceivable that a transient opening phase affecting the whole outcrop allowed brine flow. Due to the plastic nature and mechanical weakness of the CRZ, this opening subsequently closed as a result of stress release and bulk clay shearing.** The outcrop at the GG mine (Figure 22b) is considered as intermediate in the sense that the inherited shear zone did not reach a full argillic alteration and inherited schistosity, along altered but still competent host rocks, acted as a combination of plastic flow and elastic driven space opening. The result is a deviation of later brine flow along the strike of the inherited shear zone.

I propose to perform a set of numerical simulations with a geometry consisting in a weak plastic layer deforming by bulk shearing pinched between two rigid blocks able to accommodate elastic strain. The use and development of numerical codes dedicated to the mechanics of fracture propagation is a challenging task especially when dealing with anisotropic domains. This line of research will require some substantial development of simulator solutions applied to material fatigue, but I am confident that the team I mentioned in session 6.1.3.1 is willing to invest the effort.

This project will trigger valuable output in the field of reservoir stimulation design and understanding the processes involved in hydraulic stimulations. Possibly, the migration of seismic clusters along the Robertsau fault in the Strasbourg Vendenheim area (Schmittbuhl et al., 2022) could be in part explained by a transient fluid flow upon opening of an initial flow barrier domain.

6.2 Teaching perspectives

The European union shows a clear willingness in terms of investments dedicated to the development of renewable energy resources.

I have described in the previous section my future lines of research participating in a better understanding of reservoirs in order to exploit them in a secure and sustainable manner. This research finds direct applications in terms of reservoir utilization like geothermal and CCS projects development.

It is however clear that research and development alone will not be sufficient to reach this ambitious goal and applied reservoir science is only conceivable when establishing industrial partnerships favoring employment of young researchers, engineers and technicians. Based on my preparatory Geo3EN program I now propose to create an applied training curriculum in the form of an Erasmus Mundus Joint Degree (EMJD) targeting these three career profiles. Given its international and networking-oriented nature, EMJD gives the best chances of rapid employment in key sectors of the geothermal energy business.

The first pillar of the training program I propose deals with the study of low, medium to high and high to superhigh temperature geothermal reservoirs. Students are proposed a lecture catalog in order to gain a high-end expertise in terms of field geological data acquisition, petrophysical multi-parameters characterization, database treatment, fluid flow and heat transfer modeling plus risk mitigation measures in terms of potential mechanical instabilities development.

The second pillar is dedicated to surface installations engineering in terms of energy production, conversion and transport, turbine engineering, heating network, material resistance to corrosion and encompassing measures to prevent excessive scaling formation within equipment.

The third pillar concerns a variety of transverses competences which are necessary in terms of both professional integration and cooperation with research and development departments within the industrial sector and academics. These competences exceed by far the reservoir and surface installation engineering. I propose for example to 1) share and develop professional networks in participating to a series of international events and creation of working groups, 2) insist on project proposal writing and application to competitive grants, 3) give entrepreneurship project management and market analysis lectures, 4) learn how to establish a successful communication and dissemination strategy and 5) present some aspects dealing with ethics, intellectual property rights and open science.

Student mobility is placed at the forefront with the opportunity for them to obtain double or triple degrees and follow common study semesters between schools of engineering and partner Universities.

6.3 Future projects

In order to reach my goals in terms of research and teaching I have applied to a first series of grants proposed by the European commission.

6.3.1 The MININGHEAT project

Program MSCA Doctoral Networks 2021/2022, Call HORIZON-MSCA-2021/2022-DN-01, Topic HORIZON-MSCA-2021/2022-DN-01-01, Type of Action HORIZON-TMA-MSCA-DN.

Project acronym: MININGHEAT (Multidisciplinary Integration and Networking for Increased sustainability of Geothermal HEAT).

First submission on November 15th 2021: 86.6/100 (Excellence 4.2/5 ; Impact 4.5/5 ; Implementation 4.4/5).

Second submission on November 15th 2022, results expected in April 2023.

The Multidisciplinary Integration and Networking for Increased sustainability of Geothermal HEAT (MININGHEAT) project is a Doctorate Network training program aiming to bring a pool of highly qualified Early Stage Researchers (ESR) on the employment market. The consortium is constituted by a panel of 16 partners (11 Universities, 1 school of engineering, 3 industrials) in Iceland, United Kingdom, the Netherlands, France, Germany, Switzerland, Italy and Turkey.

From a research point of view, the PhD thesis subjects are interdependent and aim at 1) enhancing fluid circulation modeling within geothermal reservoirs of various geological settings, 2) preventing the development of mechanical instabilities during stimulation and exploitation phases, 3) lowering environmental, economic risks and 4) increasing societal perception of geothermal.

Besides research activities the program is willing to train ESR to a large panel of theoretical and applied disciplines in order for them to acquire a set of transverse skills. MININGHEAT offers the possibility to transfer research knowledge to successful industrial strategies.

I am going to be the coordinator of MININGHEAT in terms of scientific coordination and administrative coordination and training plus dissemination. From a more specific point of view, I will be in charge of a PhD thesis supervision aiming to establish a link between rock microfabrics and petrophysical properties. The chosen approach consists in a combination of petrographic investigations dedicated to host rock alteration processes and strain related anisotropy development. This research participates to a more realistic upscaling of laboratory data to natural conditions present within the reservoir. In order to achieve this research work, the chosen technical approach relies on both X-ray diffraction, EBSD, EDS and synchrotron radiation (P21.2 beamline, PETRA III, DESY Hamburg, Germany) analytics plus SEM and TEM imagery.

6.3.2 The GEMINI project

The Geothermal Engineering (GEMINI) project is a planned EMJD program constructed using the different outputs from Geo3EN.

GEMINI aims at training a pool of geothermal engineers at a level of excellence, directly employable in key sectors from the geothermal business.

The GEMINI curriculum is divided in two main tracks dedicated to “above surface” and “below surface” engineering. The curriculum covers the fields of geosciences, energy production, conversion and transport, economic intelligence and communication. Students with initial geological competences will be oriented towards reservoir engineering at depth while students with no initial educational background will in turn be encouraged to follow lectures dealing with surface installations, marketing, entrepreneurship and energy science engineering. The GEMINI novelty is to establish transverse competences between surface and reservoir engineers as the consortium is convinced that successful worldwide development of geothermal energy is conditioned to teamwork and activities understanding between these two communities.

I am going to be the coordinator of GEMINI, ensuring day to day management of the program and reporting to the European Commission. I am involved in a set of lectures and field excursions on geothermal reservoir analogues.

7 Conclusions

I have presented a summary of my career and have emphasized on the plurality of my competences. I have insisted on both by interdisciplinary approach and international mobility that I consider mandatory in terms of research and teaching. I gained so far a large professional network and I am grateful to all colleagues participating to the different projects I am coordinating at present and wish to lead in the future. I am willing to repeat that my fundamental approach in geosciences has direct industrial applications.

A steadily growing professional network offers to me the possibility to establish new cooperation ventures leading to success of several European projects. I achieve fundamental research and share experience with engineers at international level while developing new curriculum demanded by both students and industry.

In the future, I plan to contribute to scientific progress in terms of reservoir understanding in a large variety of geological settings with applications in geothermal and carbon capture and storage. Science and education are needed in these relatively new applied fields and to cover societal challenges and needs in general.

My lines of research participate to the understanding of fault mechanics and rock deformation processes active in a variety of geodynamic contexts.

In order to conclude, my career perspectives show the willingness to bring knowledge, develop a variety of educational programs and to participate to a global effort in terms of fundamental and applied research, climate protection and green energy production.

8 Résumé

Ce mémoire rassemble l'ensemble de mes activités et perspectives de recherche en matière de géodynamique à grande échelle, analyses tectoniques et de microfabriques, déformation expérimentale, analyses par microscopie électronique à balayage et modélisation. Je considère qu'une approche multidisciplinaire est nécessaire afin de comprendre la complexité d'un système géologique donné en termes d'évolution structurale, de circulation de fluides et de processus d'interaction fluide/roche. Ma ligne de recherche est partagée au sein d'une communauté internationale de chercheurs et d'industriels et j'accorde une grande importance à la publication de mes travaux dans des revues scientifiques, à la communication avec le public, à l'enseignement aux élèves, à l'encadrement de thèses de Doctorat ainsi qu'au parrainage de jeunes chercheurs.

Je désire consacrer mes futures recherches à la compréhension 1) du rôle combiné de la déformation et des processus d'interaction fluide/roche sur la cinétique de réaction conduisant au développement de minéraux d'altération et 2) l'influence de ces produits d'altération et du développement d'une anisotropie sur les propriétés mécaniques et pétrophysiques des zones de faille, le tout dans une large gamme de conditions de température et de pression. Ces deux domaines sont intimement corrélés et leur étude permet de mieux appréhender les paramètres clé, chimiques et physiques, contrôlant les propriétés de transport de fluide au sein de systèmes fracturés.

Mes activités ont des applications directes en termes d'utilisation sécurisée et durable des réservoirs géologiques tant pour l'exploitation géothermique que pour la capture et le stockage du carbone dans divers contextes géologiques. Mes travaux participent aux défis sociétaux en termes de préservation de l'environnement ainsi qu'à la compétitivité économique des énergies renouvelables.

9 Abstract

This thesis summarizes my research activities and perspectives which cover a variety of domains namely large-scale geodynamics, tectonic and microfabric analysis, experimental deformation, SEM based analytics and modelling. I am considering that a multidisciplinary approach is necessary in order to understand the complexity of a given geological system in terms of structural evolution, fluid circulation and fluid rock interaction processes. My line of research is shared within both a community of international researchers plus a pool of industrials and I give an utmost importance to present the results within scientific journals, communicate to public, teach students, supervise PhDs and mentor young researchers.

I am planning to dedicate my future research activities to the understanding at a wide range of temperature and pressure conditions of 1) the interplay between increasing strain and fluid rock interaction processes on alteration mineral reaction kinetics and 2) the influence of rock alteration products plus anisotropy development on fault mechanical and petrophysical properties. These two domains are intrinsically correlated and studying them aims to better constrain chemical and physical key processes governing fluid transport properties in fractured systems.

My research line finds a direct application in the safe and sustainable utilization of geological reservoirs in terms of geothermal energy plus carbon capture and storage in a variety of geological conditions. It participates to global societal challenges like environmental protection while ensuring economic competitiveness of renewable energy systems.

10 References

- Ahorner L. Present-day stress field and seismotectonic block movements along major fault zones in Central Europe. *Tectonophysics* 1975; 29: 233–49.
- Alexandrov P, Royer J.J, Deloule E. 331 ± 9 Ma emplacement age of the Soultz monzogranite (Rhine Graben basement) by U/Pb ion-probe zircon dating of samples from 5 km depth. *Comptes Rendus de l'Académie des Sciences - Series IIA - Earth and Planetary Science* 2001; 332: 747–54. [https://doi.org/10.1016/S1251-8050\(01\)01594-4](https://doi.org/10.1016/S1251-8050(01)01594-4).
- Alsop D.B, Al Ghammari M, Al Abri A, Al Mahrooqi A, Al Rawahi H, Salem H. Reservoir architecture of the Gharif Formation outcrops in the Southern Huqf area, Sultanate of Oman. *Geological Society, London, Special Publications* 2014; 387: 111–33. <https://doi.org/10.1144/SP387.8>.
- Anderle H.J, Franke W, Schwab M. Rhenohercynian foldbelt: metamorphic units (Northern Phyllite Zone), III.C.1 - stratigraphy. In: Dallmeyer RD, Franke W, Weber K, editors. *Pre-Permian Geology of Central and Eastern Europe*, Berlin, Heidelberg: Springer Berlin Heidelberg; 1995, p. 99–107. https://doi.org/10.1007/978-3-642-77518-5_9.
- Annunziatellis A, Beaubien S, Bigi S, Ciotoli G, Coltella M, Lombardi S. Gas migration along fault systems and through the vadose zone in the Latera caldera (central Italy): Implications for CO₂ geological storage. *International Journal of Greenhouse Gas Control* 2008; 2: 353–72. <https://doi.org/10.1016/j.ijggc.2008.02.003>.
- Armandine Les Landes A, Guillon T, Peter-Borie M, Blaisonneau A, Rachez X, Gentier S. Locating Geothermal Resources: Insights from 3D Stress and Flow Models at the Upper Rhine Graben Scale. *Geofluids* 2019; 2019: 1–24. <https://doi.org/10.1155/2019/8494539>.
- Avellán D.R, Macías J.L, Layer P.W, Sosa-Ceballos G, Gómez-Vasconcelos M.G, Cisneros-Máximo G, Sánchez-Núñez J.M, Martí J, García-Tenorio F, López-Loera H, Pola A, Benowitz J. Eruptive chronology of the Acoculco caldera complex – A resurgent caldera in the eastern Trans-Mexican Volcanic Belt (México). *Journal of South American Earth Sciences* 2020; 98: 102412. <https://doi.org/10.1016/j.jsames.2019.102412>.
- Bär K. Untersuchung der tiefeingethermischen Potenziale von Hessen. Dissertation, Technische Universität Darmstadt 2012.
- Bär K, Arndt D, Fritsche J.G, Götz A.E, Kracht M, Hoppe A, Sass I. 3D-Modellierung der tiefeingethermischen Potenziale von Hessen-Eingangsdaten und Potenzialausweisung. *Zeitschrift Der Deutschen Gesellschaft Für Geowissenschaften* 2011: 371–88.
- Barbier M, Hamon Y, Callot J.P, Floquet M, Daniel J.M. Sedimentary and diagenetic controls on the multiscale fracturing pattern of a carbonate reservoir: The Madison Formation (Sheep Mountain, Wyoming, USA). *Marine and Petroleum Geology* 2012; 29: 50–67. <https://doi.org/10.1016/j.marpetgeo.2011.08.009>.
- Barth G, Franz M, Heunisch C, Kustatscher E, Thies D, Vespermann J, Wolfgramm M. Late Triassic (Norian-Rhaetian) brackish to freshwater habitats at a fluvial-dominated delta plain (Seinstedt, Lower Saxony, Germany). *Palaeobio Palaeoenv* 2014; 94: 495–528. <https://doi.org/10.1007/s12549-014-0168-6>.
- Barth H. Quarzdiorit and Granodiorit des Felsberg-Zuges im Bergsträßer Odenwald. Dissertation, Universität Heidelberg, 1970.
- Bartier D.L, Meunier A, Liewig N, Morvan G, Addad A. Hydrothermal alteration of the Soultz-sous-Forets granite (Hot Fractured Rock geothermal exchanger) into a tosudite and illite assemblage. *European Journal of Mineralogy* 2008; 20: 131–42. <https://doi.org/10.1127/0935-1221/2008/0020-1787>.

- Bartz J. Die Mächtigkeit des Quartärs im Oberrheingraben. *Approaches to Taphrogenesis* 1974; 8: 78–87.
- Bauer J.F, Meier S, Philipp S.L. Architecture, fracture system, mechanical properties and permeability structure of a fault zone in Lower Triassic sandstone, Upper Rhine Graben. *Tectonophysics* 2015; 647–648: 132–45. <https://doi.org/10.1016/j.tecto.2015.02.014>.
- Beaubien S, Ciotoli G, Coombs P, Dictor M, Kruger M, Lombardi S, Pearce J, West J. The impact of a naturally occurring CO₂ gas vent on the shallow ecosystem and soil chemistry of a Mediterranean pasture (Latera, Italy). *International Journal of Greenhouse Gas Control* 2008; 2: 373–87. <https://doi.org/10.1016/j.ijggc.2008.03.005>.
- Behr H.J. Das metamorphe Grundgebirge im Thüringer Becken. *Berichte Deutsche Gesellschaft Für Geologische Wissenschaften, A (Geol-Paläonto)* 1966; 11: 39–56.
- Behr H.J, Engel W, Franke W, Giese P, Weber K. The Variscan Belt in Central Europe: Main structures, geodynamic implications, open questions. *Tectonophysics* 1984; 109: 15–40. [https://doi.org/10.1016/0040-1951\(84\)90168-9](https://doi.org/10.1016/0040-1951(84)90168-9).
- Benson S.M. Lessons Learned from Industrial and Natural Analogs for Health, Safety and Environmental Risk Assessment for Geologic Storage of Carbon Dioxide. *Carbon Dioxide Capture for Storage in Deep Geologic Formations*, Elsevier; 2005, p. 1133–41. <https://doi.org/10.1016/B978-008044570-0/50154-9>.
- Bergerat F. Déformations cassantes et champs de contrainte tertiaires dans la plate-forme européenne. Thèse d'état, Académie de Paris, Université Pierre et Marie Curie, 1985.
- Beyer D, Kunkel C, Aehnelt M, Pudlo D, Voigt T, Nover G, Gaupp R. Influence of depositional environment and diagenesis on petrophysical properties of clastic sediments (Buntsandstein of the Thuringian Syncline, Central Germany). *Zeitschrift Der Deutschen Gesellschaft Für Geowissenschaften* 2014: 345–65. <https://doi.org/10.1127/1860-1804/2014/0072>.
- Biedermann AR. Magnetic anisotropy in single crystals: A review. *Geosciences* 2018; 8: 302.
- Biedermann A.R, Kunze K, Zappone A.S. Crystallographic preferred orientation, magnetic and seismic anisotropy in rocks from the Finero peridotite, Ivrea-Verbano Zone, Northern Italy – Interplay of anisotropy contributions from different minerals. *Tectonophysics* 2020; 782–783: 228424. <https://doi.org/10.1016/j.tecto.2020.228424>.
- Bird P. Hydration-phase diagrams and friction of montmorillonite under laboratory and geologic conditions, with implications for shale compaction, slope stability, and strength of fault gouge. *Tectonophysics* 1984; 107: 235–60.
- Boigk H, Schöneich H. Die Tiefenlage der Permabasis im nördlichen Teil des Oberrheingrabens. In: Illies, J. H. & Müller, S. (Hrsg.): *Graben Problems*: 45 - 55. Aufl. Stuttgart : Schweizerbart, 1970.
- Bonjer K.P. Seismicity pattern and style of seismic faulting at the eastern borderfault of the southern Rhine Graben. *Tectonophysics* 1997; 275: 41–69.
- Bonjer K.P, Gelbke C, Gilg B, Rouland D, Mayer-Rosa D, Massinon B. Seismicity and dynamics of the Upper Rhinegraben. *Journal of Geophysics* 1984; 55: 1–12.
- Bossennec C, Frey M, Seib L, Bär K, Sass I. Multiscale Characterisation of Fracture Patterns of a Crystalline Reservoir Analogue. *Geosciences* 2021; 11: 371. <https://doi.org/10.3390/geosciences11090371>.
- Bossennec C, Seib L, Frey M, van der Vaart J, Sass I. Structural Architecture and Permeability Patterns of Crystalline Reservoir Rocks in the Northern Upper Rhine Graben: Insights from Surface Analogues of the Odenwald. *Energies* 2022; 15: 1310. <https://doi.org/10.3390/en15041310>.

- Bouchez J.L. Anisotropie de susceptibilité magnétique et fabrique des granites. *Comptes Rendus de l'Académie Des Sciences - Series IIA - Earth and Planetary Science* 2000; 330: 1–14. [https://doi.org/10.1016/S1251-8050\(00\)00120-8](https://doi.org/10.1016/S1251-8050(00)00120-8).
- Boutelier D, Chemenda A, Burg J.P. Subduction versus accretion of intra-oceanic volcanic arcs: insight from thermo-mechanical analogue experiments. *Earth and Planetary Science Letters* 2003; 212: 31–45.
- Boutin R, Montigny R, Thuizat R. Chronologie K-Ar et ^{39}Ar - ^{40}Ar du métamorphisme et du magmatisme des Vosges. Comparaison avec les massifs varisques avoisinants. *Géologie de La France* 1995: 3–25.
- Brodhag S.H, Herwegh M. The effect of different second-phase particle regimes on grain growth in two-phase aggregates: insights from in situ rock analogue experiments. *Contrib Mineral Petrol* 2010; 160: 219–38. <https://doi.org/10.1007/s00410-009-0474-6>.
- Brown K.M, Bekins B, Clennell B, Dewhurst D, Westbrook G. Heterogeneous hydrofracture development and accretionary fault dynamics. *Geology* 1994; 22: 259–62.
- Buchmann T.J, Connolly P.T. Contemporary kinematics of the Upper Rhine Graben: A 3D finite element approach. *Global and Planetary Change* 2007; 58: 287–309. <https://doi.org/10.1016/j.gloplacha.2007.02.012>.
- Burchfiel B.C, Stewart J.H. Pull-apart origin of the central segment of Death Valley, California. *Geol Soc America Bull* 1966; 77: 439. [https://doi.org/10.1130/0016-7606\(1966\)77\[439:POOTCS\]2.0.CO;2](https://doi.org/10.1130/0016-7606(1966)77[439:POOTCS]2.0.CO;2).
- Butler R, Matthews S, Parish M. The NW external Alpine thrust belt and its implications for the geometry of the western Alpine orogen. *Geological Society, London, Special Publications* 1986; 19: 245–60.
- Carl E.R, Mansfeld U, Liermann H.P, Danilewsky A, Langenhorst F, Ehm L, Trullenque G, Kenkmann. High-pressure phase transitions of α -quartz under nonhydrostatic dynamic conditions: A reconnaissance study at PETRA III. *Meteorit Planet Sci* 2017; 52: 1465–74. <https://doi.org/10.1111/maps.12840>.
- Carminati E, Cavazza W, Roure F, Spakman W, Stampfli G, Ziegler P. TRANSMED Transect III: Massif Central-Provence-Gulf of Lion-Provençal Basin-Sardinia-Tyrrhenian Basin-Southern Apennines-Apulia-Adriatic Sea-Albanides-Balkans-Moesian Platform. Cavazza, W, Roure, F, Spakman, Stampfli, GM and Ziegler, PA, Eds, *The TRANSMED Atlas: The Mediterranean Region from Crust to Mantle: Heidelberg, Springer-Verlag* 2004.
- Carminati E, Wortel M, Meijer P.T, Sabadini R. The two-stage opening of the western–central Mediterranean basins: a forward modeling test to a new evolutionary model. *Earth and Planetary Science Letters* 1998a; 160: 667–79.
- Carminati E, Wortel M, Spakman W, Sabadini R. The role of slab detachment processes in the opening of the western–central Mediterranean basins: some geological and geophysical evidence. *Earth and Planetary Science Letters* 1998b; 160: 651–65.
- Carpenter B, Marone C, Saffer D. Weakness of the San Andreas Fault revealed by samples from the active fault zone. *Nature Geoscience* 2011; 4: 251–4.
- Castaing C. Gîtologie prévisionnelle des charbons dans le Nord-Est du Massif Central. *Rapport BRGM* 1982; 82.
- Ceriani S, Fügenschuh B, Schmid SM. Multi-stage thrusting at the " Penninic Front" in the Western Alps between Mont Blanc and Pelvoux massifs. *International Journal of Earth Sciences* 2001; 90: 685–702.
- Chabani A, Trullenque G, Klee J, Ledésert B.A. Fracture Spacing Variability and the Distribution of Fracture Patterns in Granitic Geothermal Reservoir: A Case Study in the Noble Hills Range (Death Valley, CA, USA). *Geosciences* 2021a; 11: 520. <https://doi.org/10.3390/geosciences11120520>.

- Chabani A, Trullenque G, Ledésert B.A, Klee J. Multiscale Characterization of Fracture Patterns: A Case Study of the Noble Hills Range (Death Valley, CA, USA), Application to Geothermal Reservoirs. *Geosciences* 2021b; 11: 280. <https://doi.org/10.3390/geosciences11070280>.
- Charl ty J, Cuenot N, Dorbath L, Dorbath C, Haessler H, Frogneux M. Large earthquakes during hydraulic stimulations at the geothermal site of Soultz-sous-For ts. *International Journal of Rock Mechanics and Mining Sciences* 2007; 44: 1091–105. <https://doi.org/10.1016/j.ijrmms.2007.06.003>.
- Chemenda A, Yang R, Hsieh C.H, Groholsky A. Evolutionary model for the Taiwan collision based on physical modelling. *Tectonophysics* 1997; 274: 253–74.
- Chemenda A.I, Yang R.K, Stephan J.F, Konstantinovskaya E.A, Ivanov G.M. New results from physical modelling of arc–continent collision in Taiwan: evolutionary model. *Tectonophysics* 2001; 333: 159–78.
- Chemenda A.I, Mattauer M, Malavieille J, Bokun A.N. A mechanism for syn-collisional rock exhumation and associated normal faulting: Results from physical modelling. *Earth and Planetary Science Letters* 1995; 132: 225–32.
- Chester F.M, Friedman M, Logan J.M. Foliated cataclasites. *Tectonophysics* 1985; 111: 139–46. [https://doi.org/10.1016/0040-1951\(85\)90071-X](https://doi.org/10.1016/0040-1951(85)90071-X).
- Choi J.H, Edwards P, Ko K, Kim Y.S. Definition and classification of fault damage zones: A review and a new methodological approach. *Earth-Science Reviews* 2016; 152: 70–87. <https://doi.org/10.1016/j.earscirev.2015.11.006>.
- Clauer N, Liewig N, Ledesert B.A, Zwingmann H. Thermal history of Triassic sandstones from the Vosges Mountains-Rhine Graben riftting area, NE France, based on K-Ar illite dating. *Clay Miner* 2008; 43: 363–79. <https://doi.org/10.1180/claymin.2008.043.3.03>.
- Clemmensen L.B. Complex star dunes and associated aeolian bedforms, Hopeman Sandstone (Permo-Triassic), Moray Firth Basin, Scotland. Geological Society, London, Special Publications 1987; 35: 213–31. <https://doi.org/10.1144/GSL.SP.1987.035.01.15>.
- Cocherie A, Guerrot C, Fanning C.M, Genter A. Datation U–Pb des deux faci s du granite de Soultz (Foss  rh nan, France). *Comptes Rendus Geoscience* 2004; 336: 775–87. <https://doi.org/10.1016/j.crte.2004.01.009>.
- Colten-Bradley V.A. Role of pressure in smectite dehydration—Effects on geopressure and smectite-to-illite transformation. *AAPG Bulletin* 1987; 71: 1414–27.
- Crowley Q.G, Floyd P.A, Winchester J.A, Franke W, Holland J.G. Early Palaeozoic rift-related magmatism in Variscan Europe: fragmentation of the Armorican Terrane Assemblage. *Terra Nova* 2000; 12: 171–80. <https://doi.org/10.1046/j.1365-3121.2000.00290.x>.
- Cullen A. Nature and significance of the West Baram and Tinjar Lines, NW Borneo. *Marine and Petroleum Geology* 2014; 51: 197–209. <https://doi.org/10.1016/j.marpetgeo.2013.11.010>.
- Dahlen F. Noncohesive critical Coulomb wedges: An exact solution. *Journal of Geophysical Research: Solid Earth* 1984; 89: 10125–33.
- Dahlen F, Suppe J, Davis D. Mechanics of fold-and-thrust belts and accretionary wedges: Cohesive Coulomb theory. *Journal of Geophysical Research: Solid Earth* 1984; 89: 10087–101.
- De Bresser J.H.P, Ter Heege J, Spiers C. Grain size reduction by dynamic recrystallization: can it result in major rheological weakening? *Int J Earth Sci* 2001; 90: 28–45. <https://doi.org/10.1007/s005310000149>.
- De Bresser J.H.P, Trullenque G, Drury M.R. Evidence for $\langle a \rangle$ slip in calcite. *Geophysical Research Abstracts*, vol. 10, EGU2008-A-07521, 2008.

- Delacou B. Tectonique et géodynamique actuelle de l'arc alpin-Approche sismotectonique et modélisation numérique. Thèse de Doctorat, Université de Neuchâtel, 2004.
- Delouis B, Haessler H, Cisternas A, Rivera L. Stress tensor determination in France and neighbouring regions. *Tectonophysics* 1993; 221: 413–38. [https://doi.org/10.1016/0040-1951\(93\)90171-F](https://doi.org/10.1016/0040-1951(93)90171-F).
- Dèzes P, Schmid S.M, Ziegler P.A. Reply to comments by L. Michon and O. Merle on “Evolution of the European Cenozoic Rift System: interaction of the Alpine and Pyrenean orogens with their foreland lithosphere” by P. Dèzes, S.M. Schmid and P.A. Ziegler, *Tectonophysics* 389 (2004) 1–33. *Tectonophysics* 2005; 401: 257–262. <https://doi.org/10.1016/j.tecto.2005.02.002>.
- Dèzes P, Schmid S.M, Ziegler P.A. Evolution of the European Cenozoic Rift System: interaction of the Alpine and Pyrenean orogens with their foreland lithosphere. *Tectonophysics* 2004; 389: 1–33. <https://doi.org/10.1016/j.tecto.2004.06.011>.
- Dódony I, Buseck P.R. Serpentine close-up and intimate: An HRTEM view. *International Geology Review* 2004; 46: 507–27.
- Doehl F. Die tertiären und quartären Sedimente des südlichen Rheingrabens. *Graben problems*, vol. 27, Schweizerbart Stuttgart; 1970, p. 56–66.
- Doehl F. The Tertiary and Pleistocene sediments of the northern and central part of the Upper Rhinegraben. *Abhandlungen Des Geologischen Landesamtes Baden-Württemberg* 1967; 6: 48–54.
- Dorbath L, Cuenot N, Genter A, Frogneux M. Seismic response of the fractured and faulted granite of Soultz-sous-Forêts (France) to 5 km deep massive water injections. *Geophysical Journal International* 2009; 177: 653–75. <https://doi.org/10.1111/j.1365-246X.2009.04030.x>.
- Edel J.B. Les réaimantations post-permiennes dans le bassin dévono-dinantien des Vosges méridionales: existence d'une phase de réaimantation au Lias, contemporaine de minéralisations d'ampleur régionale. *Comptes Rendus de l'Académie Des Sciences Série 2 Sciences de La Terre et Des Planètes* 1997; 324: 617–24.
- Edel J.B, Fluck P. The upper Rhenish Shield basement (Vosges, Upper Rhinegraben and Schwarzwald): Main structural features deduced from magnetic, gravimetric and geological data. *Tectonophysics* 1989; 169: 303–316. [https://doi.org/10.1016/0040-1951\(89\)90093-0](https://doi.org/10.1016/0040-1951(89)90093-0).
- Edel J.B, Lutz H, Elsass P. Socle varisque et tectoniques rhénanes dans le Fossé rhénan supérieur méridional: traitement et interprétation de la carte gravimétrique du fossé à partir du levé haute densité des MDP. *Géologie de La France* 2002: 43–59.
- Edel J.B, Schulmann K, Rotstein Y. The Variscan tectonic inheritance of the Upper Rhine Graben: evidence of reactivations in the Lias, Late Eocene–Oligocene up to the recent. *International Journal of Earth Sciences* 2007; 96: 305–25. <https://doi.org/10.1007/s00531-006-0092-8>.
- Edel J.B, Schulmann K, Skrzypek E, Cocherie A. Tectonic evolution of the European Variscan belt constrained by palaeomagnetic, structural and anisotropy of magnetic susceptibility data from the Northern Vosges magmatic arc (eastern France). *Journal of the Geological Society* 2013; 170: 785–804. <https://doi.org/10.1144/jgs2011-138>.
- Edel J.B, Weber K. Cadomian terranes, wrench faulting and thrusting in the central Europe Variscides: geophysical and geological evidence. *Geol Rundsch* 1995; 84. <https://doi.org/10.1007/BF00260450>.
- Eisbacher G.H, Lüschen E, Wickert F. Crustal-scale thrusting and extension in the Hercynian Schwarzwald and Vosges, Central Europe. *Tectonics* 1989; 8: 1–21.
- Evans B.W, Hattori K, Baronnet A. Serpentinite: what, why, where? *Elements* 2013; 9: 99–106.

- Faulkner D, Jackson C, Lunn R, Schlische R, Shipton Z, Wibberley C, Withjack M.O. A review of recent developments concerning the structure, mechanics and fluid flow properties of fault zones. *Journal of Structural Geology* 2010; 32: 1557–75.
- Faulkner D, Rutter E. The gas permeability of clay-bearing fault gouge at 20 C. Geological Society, London, Special Publications 1998; 147: 147–56.
- Fielding C.R, Crane R.C. An application of statistical modelling to the prediction of hydrocarbon recovery factors in fluvial reservoir sequences. SEPM special publication: Recent Developments in Fluvial Sedimentology 1987; 39.
- Fleming Z, Pavlis T, Trullenque G. Unraveling the multi-phase history of southern Death Valley geology. In: Jiang G, Dehler C, editors. Field Excursions from Las Vegas, Nevada: Guides to the 2022 GSA Cordilleran and Rocky Mountain Joint Section Meeting, Geological Society of America; 2022, p. 67–83. [https://doi.org/10.1130/2022.0063\(04\)](https://doi.org/10.1130/2022.0063(04)).
- Fluck P. Comment se sont formés les gisements métallifères du massif vosgien? *Pierres et Terre* 1992; 35: 107–15.
- Franke W. Topography of the Variscan orogen in Europe: failed–not collapsed. *Int J Earth Sci (Geol Rundsch)* 2014; 103: 1471–99. <https://doi.org/10.1007/s00531-014-1014-9>.
- Franke W. The mid-European segment of the Variscides: tectonostratigraphic units, terrane boundaries and plate tectonic evolution. Geological Society, London, Special Publications 2000; 179: 35–61. <https://doi.org/10.1144/GSL.SP.2000.179.01.05>.
- Franke W. Rhenohercynian fold belt, autochthon and non metamorphic nappe units, III.B.1 - stratigraphy. In: Dallmeyer RD, Franke W, Weber K, editors. Pre-Permian Geology of Central and Eastern Europe, Berlin, Heidelberg: Springer Berlin Heidelberg; 1995, p. 33–49. https://doi.org/10.1007/978-3-642-77518-5_4.
- Franke W. Phanerozoic structures and events in Central Europe. Blundell D, Freeman R, Mueller S (Eds) *A Continent Revealed: The European Geotraverse* Cambridge University Press, Cambridge 1992:164–79.
- Franke W. Tectonostratigraphic units in the Variscan belt of central Europe. *Geol Soc Am Spec Pap* 1989; 230: 67–90.
- Franke W, Cocks L.R.M, Torsvik T.H. The Palaeozoic Variscan oceans revisited. *Gondwana Research* 2017; 48: 257–84. <https://doi.org/10.1016/j.gr.2017.03.005>.
- Franzke H, Werner W. Wie beeinflusste die Tektonik des Kristallins und des Rheingrabens die hydrothermalen Gangstrukturen des Schwarzwaldes. *Abhandlungen Des Geologischen Landesamtes Baden-Württemberg* 1994; 14: 99–118.
- Frey M, Bossennec C, Seib L, Bär K, Schill E, Sass I. Interdisciplinary fracture network characterization in the crystalline basement: a case study from the Southern Odenwald, SW Germany. *Solid Earth* 2022; 13: 935–55. <https://doi.org/10.5194/se-13-935-2022>.
- Garcia-Gonzales M, Wimmenauer W. Mineralogische und geochemische Untersuchungen an tektonischen Störungszonen des Schwarzwaldes. *Ber Naturf Ges Freiburg i, Br* 1975: 97–118.
- Genter A. Géothermie roches chaudes sèches: le granite de Soultz-sous-Forêts (Bas-Rhin, France): fracturation naturelle, altérations hydrothermales et interaction eau-roche. PhD Thesis. Orléans, 1989.
- Gentier S, Rachez X, Peter-Borie M, Loubaud M. A flow model of the deep geothermal reservoir of Soultz-sous-Forêts (France). 47th US Rock Mechanics/Geomechanics Symposium, OnePetro; 2013.
- Giamboni M, Ustaszewski K, Schmid S.M, Schumacher M.E, Wetzel A. Plio-Pleistocene transpressional reactivation of Paleozoic and Paleogene structures in the Rhine-Bresse transform zone (northern

- Switzerland and eastern France). *International Journal of Earth Sciences* 2004; 93: 207–23. <https://doi.org/10.1007/s00531-003-0375-2>.
- Gibling M.R. Width and Thickness of Fluvial Channel Bodies and Valley Fills in the Geological Record: A Literature Compilation and Classification. *Journal of Sedimentary Research* 2006; 76: 731–70. <https://doi.org/10.2110/jsr.2006.060>.
- Giese P. Main features of geophysical structures in Central Europe. *Pre-Permian Geology of Central and Eastern Europe* 1995: 7–25.
- Giuffrida A, Agosta F, Rustichelli A, Panza E, La Bruna V, Eriksson M, Torrieri S, Giorgioni M. Fracture stratigraphy and DFN modelling of tight carbonates, the case study of the Lower Cretaceous carbonates exposed at the Monte Alpi (Basilicata, Italy). *Marine and Petroleum Geology* 2020; 112: 104045. <https://doi.org/10.1016/j.marpetgeo.2019.104045>.
- Glaas C. Mineralogical and structural controls on permeability of deep naturally fractured crystalline reservoirs : insights from geothermal wells (Upper Rhine Graben). PhD Thesis. 2021.
- Glaas C, Patrier P, Vidal J, Beaufort D, Genter A. Clay Mineralogy: A Signature of Granitic Geothermal Reservoirs of the Central Upper Rhine Graben. *Minerals* 2021, 11(5).
- Greiling R.O, Verma P.K. Strike-slip and tectonics granitoid emplacement: an AMS fabric study from the Odenwald Crystalline Complex, SW Germany. *Mineralogy and Petrology* 2001; 72: 165–84. <https://doi.org/10.1007/s007100170032>.
- Grimmer J.C, Ritter J.R.R, Eisbacher G.H, Fielitz W. The Late Variscan control on the location and asymmetry of the Upper Rhine Graben. *Int J Earth Sci (Geol Rundsch)* 2017; 106: 827–53. <https://doi.org/10.1007/s00531-016-1336-x>.
- Grolier J, Letourneur J. L'évolution tectonique du grand Sillon Houiller du Massif Central francais. *XXIIIème Congrès Géologique International* 1968; 1: 107–16.
- Groos J, Zeiß J, Grund M, Ritter J. Microseismicity at two geothermal power plants at Landau and Insheim in the Upper Rhine Graben, Germany. *Geophys. Res. Abstr*, vol. 15, 2013.
- Hafeznia Y, Bourlange S, Ohnenstetter M, Fluck P. Post-meeting fieldtrip SGA 2015. Sainte Marie aux Mines, Gabe Gottes mine. Livret guide, Nancy: 2015, p. 67.
- Haines S.H, Kaproth B, Marone C, Saffer D, van der Pluijm B.A. Shear zones in clay-rich fault gouge: A laboratory study of fabric development and evolution. *Journal of Structural Geology* 2013; 51: 206–25. <https://doi.org/10.1016/j.jsg.2013.01.002>.
- Haines S.H, van der Pluijm B.A, Ikari M.J, Saffer D.M, Marone C. Clay fabric intensity in natural and artificial fault gouges: Implications for brittle fault zone processes and sedimentary basin clay fabric evolution. *J Geophys Res* 2009; 114: B05406. <https://doi.org/10.1029/2008JB005866>.
- Häring M.O, Schanz U, Ladner F, Dyer B.C. Characterisation of the Basel 1 enhanced geothermal system. *Geothermics* 2008; 37: 469–95. <https://doi.org/10.1016/j.geothermics.2008.06.002>.
- Hegner E, Chen F, Hann H. Chronology of basin closure and thrusting in the internal zone of the Variscan belt in the Schwarzwald, Germany: evidence from zircon ages, trace element geochemistry, and Nd isotopic data. *Tectonophysics* 2001; 332: 169–84.
- Henk A. Subsidenz und tektonik des Saar-Nahe-Beckens (SW-Deutschland). *Geol Rundsch* 1993a; 82: 3–19. <https://doi.org/10.1007/BF00563266>.
- Henk A. Late orogenic basin evolution in the Variscan Internides: the Saar-Nahe Basin, southwest Germany. *Tectonophysics* 1993b; 223: 273–90.

- Henk A. Mächtigkeit und Alter der erodierten Sedimente im Saar-Nahe-Becken (SW-Deutschland). *Geologische Rundschau* 1992; 81: 323–31.
- Hiriart G, Gutiérrez N.L, Quijano L.L, Ornelas C.A, Espíndola S, Hernández I. Evaluación de la energía geotérmica en México. Informe para el Banco Interamericano de Desarrollo y la Comisión Reguladora de Energía. 2011.
- Hofmann B, Eikenberg J. The Krunkelbach uranium deposit, Schwarzwald, Germany; correlation of radiometric ages (U-Pb, U-Xe-Kr, K-Ar, 230 Th-234 U). *Economic Geology* 1991; 86: 1031–49.
- Holloway S, Pearce J.M, Ohsumi T, Hards V.L. Review of natural CO₂ occurrences and releases and their relevance to CO₂ storage. IEA Greenhouse Gas R&D Programme, Report 2005.
- Homuth S, Götz A.E, Sass I. Lithofacies and depth dependency of thermo- and petrophysical rock parameters of the Upper Jurassic geothermal carbonate reservoirs of the Molasse Basin. *Zeitschrift der Deutschen Gesellschaft für Geowissenschaften* 2014; 165: 469–86. <https://doi.org/10.1127/1860-1804/2014/0074>.
- Howell J.A, Martinius A.W, Good T.R. The application of outcrop analogues in geological modelling: a review, present status and future outlook. Geological Society, London, Special Publications 2014; 387: 1–25. <https://doi.org/10.1144/SP387.12>.
- Huttner R, Wimmenauer W. Erläuterungen zu Blatt 8013 Freiburg i. Br (SO) Geol Karte Baden-Württemberg 1967; 1: 159.
- Ikari M.J, Saffer D.M, Marone C. Effect of hydration state on the frictional properties of montmorillonite-based fault gouge. *J Geophys Res* 2007; 112: B06423. <https://doi.org/10.1029/2006JB004748>.
- Illies J.H. Two stages Rhinegraben rifting. Tectonics and geophysics of continental rifts, Proceedings of the NATO Advanced Study Institute, 1978, p. 63–71.
- Illies J.H. Ancient and recent uplift in the Rhine graben. *Geol. Mijnbouw*, 56, 329–350, 1977.
- Illies J.H. Intraplate tectonics in stable Europe as related to plate tectonics in the Alpine system. *Geol Rundsch* 1975; 64: 677–99. <https://doi.org/10.1007/BF01820690>.
- Illies J.H. Intra-Plattentektonik in Mitteleuropa und der Rheingraben. *Oberrheinische Geologische Abhandlungen* 1974; 23: 1–24.
- Illies J.H. The Rhine graben rift system-plate tectonics and transform faulting. *Geophysical Surveys* 1972; 1: 27–60. <https://doi.org/10.1007/BF01449550>.
- Illies J.H. Bauplan und baugeschichte des oberrheingrabens. *Oberrheinische Geologische Abhandlungen* 1965; 20: 1–54.
- Illies J.H, Greiner G. Holocene movements and state of stress in the Rhinegraben rift system. *Tectonophysics* 1979; 52: 349–59.
- Illies J.H, Rothé J.P, Sauer K. Development and tectonic pattern of the Rhinegraben. The Rhinegraben Progress Report Abh Geol Landesamt Baden-Württemberg 1967; 6: 7–9.
- Jamaludin S.N.F, Sautter B, Pubellier M, Beg M.A. The Succession of Upper Eocene- Upper Miocene Limestone Growth and Corresponding Tectonic Events in Luconia Shelf, Sarawak, Malaysia. *Front Earth Sci* 2021; 9: 588629. <https://doi.org/10.3389/feart.2021.588629>.
- Kemnitz H, Romer R, Oncken O. Gondwana break-up and the northern margin of the Saxothuringian belt (Variscides of Central Europe). *International Journal of Earth Sciences* 2002; 91: 246–59. <https://doi.org/10.1007/s005310100209>.

- Kempe U, Trullenque G, Thomas R, Sergeev S, Presnyakov S, Rodionov N, Himcinschi, C. Substitution-induced internal strain and high disorder in weakly radiation damaged hydrothermal zircon from Mt. Malosa, Malawi. *European Journal of Mineralogy* 2018; 30: 659–79. <https://doi.org/10.1127/ejm/2018/0030-2739>.
- Kenkmann T, Ebert M, Trullenque G, Deutsch A, Hecht L, Salge T, Schäfer F, Thoma K. Deformation and Melting of Iron-Rich Projectiles in Hypervelocity MEMIN Cratering Experiments. *Meteoritics and Planetary Science* 2013; 48(1): 150-164.
- Keogh K.J, Leary S, Martinius A.W, Scott A.S.J, Riordan S, Viste I, Gowland S, Taylor A.M, Howell J. Data capture for multiscale modelling of the Lourinhã Formation, Lusitanian Basin, Portugal: an outcrop analogue for the Statfjord Group, Norwegian North Sea. Geological Society, London, Special Publications 2014; 387: 27–56. <https://doi.org/10.1144/SP387.11>.
- Kirsch H, Kober B, Lippolt H.J. Age of intrusion and rapid cooling of the Frankenstein gabbro (Odenwald, SW-Germany) evidenced by 40 Ar/39 Ar and single-zircon 207 Pb/206 Pb measurements. *Geologische Rundschau* 1988; 77: 693–711.
- Klee J. Influence of fluid-rock interaction processes and strain on strike-slip zones properties: an analogue-based multidisciplinary approach: fractured granitic geothermal reservoirs applications. Phd Thesis 2021.
- Klee J, Chabani A, Ledésert B.A, Potel S, Hébert R.L, Trullenque G. Fluid-Rock Interactions in a Paleo-Geothermal Reservoir (Noble Hills Granite, California, USA). Part 2: The Influence of Fracturing on Granite Alteration Processes and Fluid Circulation at Low to Moderate Regional Strain. *Geosciences* 2021a; 11: 433. <https://doi.org/10.3390/geosciences11110433>.
- Klee J, Potel S, Ledésert B.A, Hébert R.L, Chabani A, Barrier P, Trullenque G. Fluid-Rock Interactions in a Paleo-Geothermal Reservoir (Noble Hills Granite, California, USA). Part 1: Granite Pervasive Alteration Processes away from Fracture Zones. *Geosciences* 2021b; 11: 325. <https://doi.org/10.3390/geosciences11080325>.
- Klusman R.W. Surface and Near-surface Geochemical Detection of Gas Microseepage from CO2 Sequestration and CO2-EOR Projects. AAPG Hedberg Conference 2002.
- Kominou A, Yardley B. Fluid-rock interactions in the Rhine Graben: a thermodynamic model of the hydrothermal alteration observed in deep drilling. *Geochimica et Cosmochimica Acta* 1997; 61: 515–31.
- Kraft T, Deichmann N. High-precision relocation and focal mechanism of the injection-induced seismicity at the Basel EGS. *Geothermics* 2014; 52: 59–73. <https://doi.org/10.1016/j.geothermics.2014.05.014>.
- Kreher B. Petrologie und Geochemie der Gabbrointrusionen des Frankensteins (Odenwald). *Geol Jb Hessen* 1994; 122: 81–122.
- Kreuzer H, Harre W. K/Ar Altersbestimmungen an Hornblenden und Biotiten des kristallinen Odenwaldes. *Aufschluss* 1975; 27: 71–8.
- Krohe A. Structural evolution of intermediate-crustal rocks in a strike-slip and extensional setting (Variscan Odenwald, SW Germany): differential upward transport of metamorphic complexes and changing deformation mechanisms. *Tectonophysics* 1992; 205: 357–86.
- Kroner U, Mansy J.L, Mazur S, Aleksandrowski P, Hann H.P, Huckriede H. Variscan tectonics. *The Geology of Central Europe: Precambrian and Palaeozoic*, vol. 1, London: 2008, p. 599–664.
- Kushnir A.R.L, Heap M.J, Baud P, Gilg H.A, Reuschlé T, Lerouge C, Dezayes C, Düringer P. Characterizing the physical properties of rocks from the Paleozoic to Permo-Triassic transition in the Upper Rhine Graben. *Geotherm Energy* 2018; 6: 16. <https://doi.org/10.1186/s40517-018-0103-6>.
- Laubscher H. Plate interactions at the southern end of the Rhine graben. *Tectonophysics* 2001; 343: 1–19.

- Ledésert B.A, Hebert R.L, Genter A, Bartier D, Clauer N, Grall C. Fractures, hydrothermal alterations and permeability in the Soultz Enhanced Geothermal System. *Comptes Rendus Geoscience* 2010; 342: 607–15.
- Ledésert B.A, Hébert R.L, Mouchot J, Bosia C, Ravier G, Seibel O, Dalmais E, Ledésert M, Trullenque G, Sengelen X, Genter A. Scaling in a Geothermal Heat Exchanger at Soultz-Sous-Forêts (Upper Rhine Graben, France): A XRD and SEM-EDS Characterization of Sulfide Precipitates. *Geosciences* 2021; 11: 271. <https://doi.org/10.3390/geosciences11070271>.
- Lepillier B, Bruna P.O, Bruhn D, Bastesen E, Daniilidis A, Garcia Ó, Torabi A, Wheeler W. From outcrop scanlines to discrete fracture networks, an integrative workflow. *Journal of Structural Geology* 2020; 133: 103992. <https://doi.org/10.1016/j.jsg.2020.103992>.
- Lerouge G. Tectonogenèse comparée de deux segments de la chaîne hercynienne: le Massif central français septentrional et le sud du Massif armoricain. PhD Thesis. Paris 11, 1987.
- Letourneur J. Le grand Sillon Houiller du plateau central français. *Bulletin du service de la carte géologique de France* 1953; 238: 1-236.
- Liang S, Liu Y, Mei S. In Situ Study on Dehydration and Phase Transformation of Antigorite. *Minerals* 2022; 12: 567. <https://doi.org/10.3390/min12050567>.
- Liewig N. Datations isotopiques d'illites diagéniques de grés réservoirs à gaz, huile et eau du Nord-Ouest de l'Europe. Implications pétrogénétiques et géodynamiques. Thèse, Université de Strasbourg, 1993.
- Liewig N, Mossmann J.R, Clauer N. Datation isotopique K-Ar d'argiles diagénétiques de réservoirs gréseux: mise en évidence d'anomalies thermiques du Lias inférieur en Europe nord-occidentale. *Comptes Rendus de l'Académie Des Sciences Série 2, Mécanique, Physique, Chimie, Sciences de l'univers, Sciences de La Terre* 1987; 304: 707–11.
- Linnemann U, Gerdes A, Drost K, Buschmann B. The continuum between Cadomian orogenesis and opening of the Rheic Ocean: Constraints from LA-ICP-MS U-Pb zircon dating and analysis of plate-tectonic setting (Saxo-Thuringian zone, northeastern Bohemian Massif, Germany). *The Evolution of the Rheic Ocean: From Avalonian-Cadomian Active Margin to Alleghenian-Variscan Collision*, Geological Society of America; 2007. [https://doi.org/10.1130/2007.2423\(03\)](https://doi.org/10.1130/2007.2423(03)).
- Linnemann U, McNaughton N.J, Romer R.L, Gehmlich M, Drost K, Tonk C. West African provenance for Saxo-Thuringia (Bohemian Massif): did Armorica ever leave pre-Pangean Gondwana?—U/Pb-SHRIMP zircon evidence and the Nd-isotopic record. *International Journal of Earth Sciences* 2004; 93: 683–705.
- Lippolt H.J, Siebel W. Evidence for multi-stage alteration of Schwarzwald lamprophyres. *European Journal of Mineralogy* 1991: 587–602.
- Lutz M, Cleintuar M. Geological results of a hydrocarbon exploration campaign in the southern Upper Rhine Graben (Alsace Centrale, France). *Bulletin Für Angewandte Geologie* 1999; 4: 3–80.
- Majmudar T.S, Behringer R.P. Contact force measurements and stress-induced anisotropy in granular materials. *Nature* 2005; 435: 1079–82. <https://doi.org/10.1038/nature03805>.
- Malavieille J, Trullenque G. Consequences of continental subduction on forearc basin and accretionary wedge deformation in SE Taiwan: Insights from analogue modeling. *Tectonophysics* 2009; 466: 377–94. <https://doi.org/10.1016/j.tecto.2007.11.016>.
- Mankopf N.R, Lippolt H.J. 4He geochemische Belege für ein permotriassisches Alter des Roteisenerzes des Quarz Hämatit Baryt Ganges westlich Obersexau im Brettental, *Nittlerer Schwarzwald* 1997: 25–48.
- Meier S, Bauer J.F, Philipp S.L. Fault zone characteristics, fracture systems and permeability implications of Middle Triassic Muschelkalk in Southwest Germany. *Journal of Structural Geology* 2015; 70: 170–89. <https://doi.org/10.1016/j.jsg.2014.12.005>.

- Meller C, Kohl T. The significance of hydrothermal alteration zones for the mechanical behavior of a geothermal reservoir. *Geotherm Energy* 2014; 2: 12. <https://doi.org/10.1186/s40517-014-0012-2>.
- Meller C, Ledésert B.A. Is There a Link Between Mineralogy, Petrophysics, and the Hydraulic and Seismic Behaviors of the Soultz-sous-Forêts Granite During Stimulation? A Review and Reinterpretation of Petro-Hydromechanical Data Toward a Better Understanding of Induced Seismicity: Petro-Hydromechanics of Soultz Granite. *J Geophys Res Solid Earth* 2017; 122: 9755–74. <https://doi.org/10.1002/2017JB014648>.
- Melosh H.J. *Impact cratering: A geologic process*. New York: Oxford University Press; Oxford: Clarendon Press 1989.
- Merson E, Brydson R, Brown A. The effect of crystallographic orientation on the mechanical properties of titanium. *J Phys: Conf Ser* 2008; 126: 012020. <https://doi.org/10.1088/1742-6596/126/1/012020>.
- Monninger R. *Neotektonische Bewegungsmechanismen im mittleren Oberrheingraben*. Dipl. Geol. Doktors der Naturwissenschaften, Univ. Karlsruhe 1985.
- Moore D.E, Lockner D.A. Crystallographic controls on the frictional behavior of dry and water-saturated sheet structure minerals. *J Geophys Res* 2004; 109: B03401. <https://doi.org/10.1029/2003JB002582>.
- van de Moortèle B, Bezacier L, Trullenque G, Reynard B. Electron back-scattering diffraction (EBSD) measurements of antigorite lattice-preferred orientations (LPO). *Journal of Microscopy* 2010; 239: 245–8.
- Morgan C.D. *Structure, Reservoir Characterization, and Carbon Dioxide Resources of Farnham Dome Field, Carbon County, Utah*, 2007.
- Morrow C.A, Shi L.Q, Byerlee J.D. Permeability of fault gouge under confining pressure and shear stress. *J Geophys Res* 1984; 89: 3193–200. <https://doi.org/10.1029/JB089iB05p03193>.
- Mouchot J, Ravier G, Seibel O, Pratiwi A. Deep Geothermal Plants Operation in Upper Rhine Graben: Lessons Learned. In *Proceedings of the European Geothermal Congress, The Hague, The Netherlands, 11–14 June 2019*.
- Mountney N, Howell J, Flint S, Jerram D. Relating eolian bounding-surface geometries to the bed forms that generated them: Etjo Formation, Cretaceous, Namibia. *Geol* 1999; 27: 159. [https://doi.org/10.1130/0091-7613\(1999\)027<0159:REBSGT>2.3.CO;2](https://doi.org/10.1130/0091-7613(1999)027<0159:REBSGT>2.3.CO;2).
- Muhl L, Avakian B, Trullenque G, Sass I, Ledésert B. Influences of pre-structuration of a reservoir on permeability evolution in fracture zones Insights from mechanical testing on an alteration profile. In *Proceedings of the European Geothermal Congress, Berlin, Germany, 17-21 October 2022*.
- Mukherjee R, Misra S. Nanomechanics of minerals: understandings and developments through instrumented nanoindentation techniques. *Phys Chem Minerals* 2023; 50: 10. <https://doi.org/10.1007/s00269-023-01235-8>.
- Müller W.H, Worrack H, Sterthaus J, Villain J, Wilden J, Juritz A. How to extract continuum materials properties for (lead-free) solders from tensile tests and nanoindentation experiments. *Microsyst Technol* 2009; 15: 45–55. <https://doi.org/10.1007/s00542-008-0688-y>.
- Naruk S.J, Solum J.G, Brandenburg J.P, Origo P, Wolf D.E. Effective stress constraints on vertical flow in fault zones: Learnings from natural CO₂ reservoirs. *Bulletin* 2019; 103: 1979–2008. <https://doi.org/10.1306/12181817393>.
- Nasdala L, Kronz A, Grambole D, Trullenque G. Effects of irradiation damage on the back-scattering of electrons: Silicon-implanted silicon. *American Mineralogist* 2007; 92: 1768–71. <https://doi.org/10.2138/am.2007.2648>.

- Newson J.A, Trullenque G, Bossennec C, Sass I, Šadek S, Gautason B, Greene R.M. Graduate Geothermal training in the European Economic Area. In Proceedings 44th New Zealand Geothermal Workshop, Auckland, New Zealand, 23-25 November 2022.
- Niles J.H. Post-middle pliocene tectonic development of the Noble Hills, southern Death Valley, California. Master Thesis, San Francisco State University, 2016.
- Norton I. Two-stage formation of Death Valley. *Geosphere* 2011; 7: 171–82.
- Okrusch M. Metamorphic Evolution, in: Dallmeyer, R.D., Franke, W., Weber, K. (Eds.), *Pre-Permian Geology of Central and Eastern Europe*. Springer Berlin Heidelberg, Berlin, Heidelberg, pp. 201–213
- Oncken O, Franzke H.J, Dittmar U, Klügel T. III.C.2 - Rhenohercynian Foldbelt: Metamorphic Units (Northern Phyllite Zone), Structure. In: Dallmeyer RD, Franke W, Weber K, editors. *Pre-Permian Geology of Central and Eastern Europe*, Berlin, Heidelberg: Springer Berlin Heidelberg; 1995, p. 109–17.
- Pavlis T.L, Trullenque G. Evidence for 40–41 km of dextral slip on the southern Death Valley fault: Implications for the Eastern California shear zone and extensional tectonics: *Geology*, v. 49, p. 767–772, <https://doi.org/10.1130/G48528.1>
- Peacock D.C.P, Sanderson D.J, Leiss B. Use of Analogue Exposures of Fractured Rock for Enhanced Geothermal Systems. *Geosciences* 2022; 12: 318. <https://doi.org/10.3390/geosciences12090318>.
- Pearce J, Czernichowski-Lauriol I, Lombardi S, Brune S, Nador A, Baker J, Pauwels H, Hatziyannis G, Beaubien S, Faber E. A review of natural CO₂ accumulations in Europe as analogues for geological sequestration. *Geological Society, London, Special Publications* 2004; 233: 29–41. <https://doi.org/10.1144/GSL.SP.2004.233.01.04>.
- Perry K.F. *Natural Gas Storage Industry Experience and Technology. Carbon Dioxide Capture for Storage in Deep Geologic Formations*, Elsevier; 2005, p. 815–25. <https://doi.org/10.1016/B978-008044570-0/50135-5>.
- Peters J, Muthuswamy M, Wibowo J, Tordesillas A. Characterization of force chains in granular material. *Physical Review E* 2005; 72: 041307.
- Platt J, Behrmann J, Cunningham P, Dewey J, Helman M, Parish M, Shepley M.G, Wallis S, Western P.J. Kinematics of the Alpine arc and the motion history of Adria. *Nature* 1989; 337: 158–61.
- Plenefisch T, Bonjer K.P. The stress field in the Rhine Graben area inferred from earthquake focal mechanisms and estimation of frictional parameters. *Tectonophysics* 1997; 275: 71–97.
- Potel S, Maison T, Maillet M, Sarr A.C, Doublier M.P, Trullenque G, Mählmann R.F. Reliability of very low-grade metamorphic methods to decipher basin evolution: Case study from the Markstein basin (Southern Vosges, NE France). *Applied Clay Science* 2016; 134: 175–85.
- Potel S, Trullenque G. Very low-grade metamorphism in the para-autochthonous sedimentary cover of the Pelvoux massif (Western Alps, France). *Swiss J Geosci* 2012; 105: 235–47. <https://doi.org/10.1007/s00015-012-0102-8>.
- Pranter M.J, Hewlett A.C, Cole R.D, Wang H, Gilman J. Fluvial architecture and connectivity of the Williams Fork Formation: use of outcrop analogues for stratigraphic characterization and reservoir modelling. *Geological Society, London, Special Publications* 2014; 387: 57–83. <https://doi.org/10.1144/SP387.1>.
- Prodehl C, Mueller S, Haak V. Chapter 4 The european cenozoic rift system. *Developments in Geotectonics*, vol. 25, Elsevier; 2006, p. 133–212. [https://doi.org/10.1016/S0419-0254\(06\)80012-1](https://doi.org/10.1016/S0419-0254(06)80012-1).
- Raos S, Ilak P, Rajšl I, Bilić T, Trullenque G. Multiple-criteria decision-making for assessing the enhanced geothermal systems. *Energies* 2019; 12: 1597.

- Reyer D. Outcrop analogue studies of rocks from the Northwest German Basin for geothermal exploration and exploitation: Fault zone structure, heterogeneous rock properties, and application to reservoir conditions. PhD Thesis, Georg-August-University Göttingen, 2014. <https://doi.org/10.53846/goediss-4720>.
- Ricou L.E. Les Alpes occidentales; chaine de decrochement. Bulletin de La Société Géologique de France 1984; 7: 861–74.
- Ricou L.E, Siddans AWB. Collision tectonics in the western Alps. Geological Society, London, Special Publications 1986; 19: 229–44.
- Rolin P. Tectonogenèse comparée de deux segments de la chaîne hercynienne: le Massif central français septentrional et la meseta marocaine septentrionale. PhD Thesis. Paris 11, 1987.
- Ronde A.A de, Stünitz H, Tullis J, Heilbronner R. Reaction-induced weakening of plagioclase–olivine composites. *Tectonophysics* 2005; 409: 85–106. <https://doi.org/10.1016/j.tecto.2005.08.008>.
- Rotstein Y, Behrmann J.H, Lutz M, Wirsing G, Luz A. Tectonic implications of transpression and transtension: Upper Rhine Graben. *Tectonics* 2005; 24(6), TC60001. <https://doi.org/10.1029/2005TC001797>.
- Rotstein Y, Edel J.B, Gabriel G, Boulanger D, Schaming M, Munsch M. Insight into the structure of the Upper Rhine Graben and its basement from a new compilation of Bouguer Gravity. *Tectonophysics* 2006; 425: 55–70. <https://doi.org/10.1016/j.tecto.2006.07.002>.
- Rouland D, Haessler H, Bonjer K, Gilg B, Mayer-Rosa D, Pavoni N. The Sierentz southern-rhinegraben earthquake of July 15, 1980. Preliminary results. *Developments in Solid Earth Geophysics*, vol. 15, Elsevier; 1983, p. 441–6.
- Rousset D, Bayer R, Guillon D, Edel J.B. Structure of the southern Rhine Graben from gravity and reflection seismic data (ECORS-DEKORP program). *Tectonophysics* 1993; 221: 135–53.
- Sanjuan B, Millot R, Innocent C, Dezayes C, Scheiber J, Brach M. Major geochemical characteristics of geothermal brines from the Upper Rhine Graben granitic basement with constraints on temperature and circulation. *Chemical Geology* 2016; 428: 27–47. <https://doi.org/10.1016/j.chemgeo.2016.02.021>.
- Sass I, Hoppe A, Arndt D, Bär K. Forschungs-und Entwicklungsprojekt 3D Modell der geothermischen Tiefenpotenziale von Hessen. Report, Technische Universität Darmstadt 2011.
- Schäfer A. Tectonics and sedimentation in the continental strike-slip Saar-Nahe Basin (Carboniferous-Permian, West Germany). *Zeitschrift der Deutschen Gesellschaft für Geowissenschaften* 2011; 162: 127–55. <https://doi.org/10.1127/1860-1804/2011/0162-0127>.
- Schäfer A. Variscan molasse in the Saar-Nahe Basin (W-Germany), Upper Carboniferous and Lower Permian. *Geologische Rundschau* 1989; 78: 499–524.
- Schaltegger U, Schneider J-L, Maurin J.C, Corfu F. Precise UPb chronometry of 345-340 Ma old magmatism related to syn-convergence extension in the Southern Vosges (Central Variscan Belt). *Earth and Planetary Science Letters* 1996; 144: 403–19. [https://doi.org/10.1016/S0012-821X\(96\)00187-2](https://doi.org/10.1016/S0012-821X(96)00187-2).
- Scheck-Wenderoth M, Krzywiec P, Zühlke R, Maystrenko Y, Froitzheim N. Permian to cretaceous tectonics of Central Europe. *The Geology of central Europe*, vol. 1. Geological society of London, London: 2008, p. 999–1030.
- Schleicher A.M, van der Pluijm B.A, Solum J.G, Warr L.N. Origin and significance of clay-coated fractures in mudrock fragments of the SAFOD borehole (Parkfield, California). *Geophys Res Lett* 2006a; 33: L16313. <https://doi.org/10.1029/2006GL026505>.

- Schleicher A.M, van der Pluijm B.A, Warr L.N. Chlorite-smectite clay minerals and fault behavior: New evidence from the San Andreas Fault Observatory at Depth (SAFOD) core. *Lithosphere* 2012; 4: 209–20. <https://doi.org/10.1130/L158.1>.
- Schleicher A.M, van der Pluijm B.A, Warr L.N. Nanocoatings of clay and creep of the San Andreas fault at Parkfield, California. *Geology* 2010; 38: 667–70. <https://doi.org/10.1130/G31091.1>.
- Schleicher A.M, Warr L.N, Kober B, Laverret E, Clauer N. Episodic mineralization of hydrothermal illite in the Soultz-sous-Forêts granite (Upper Rhine Graben, France). *Contrib Mineral Petrol* 2006b; 152: 349–64. <https://doi.org/10.1007/s00410-006-0110-7>.
- Schleicher A.M, Warr L.N, van der Pluijm B.A. On the origin of mixed-layered clay minerals from the San Andreas Fault at 2.5–3 km vertical depth (SAFOD drillhole at Parkfield, California). *Contrib Mineral Petrol* 2009; 157: 173–87. <https://doi.org/10.1007/s00410-008-0328-7>.
- Schmid S.M, Boland J.N, Paterson M.S. Superplastic flow in finegrained limestone. *Tectonophysics* 1977; 43: 257–91.
- Schmid S.M, Panozzo R, Bauer S. Simple shear experiments on calcite rocks: rheology and microfabric. *Journal of Structural Geology* 1987; 9: 747–78. [https://doi.org/10.1016/0191-8141\(87\)90157-X](https://doi.org/10.1016/0191-8141(87)90157-X).
- Schmidt R.B, Seithel R, Bucher K, Stober I. Fluid-Rock Interaction in Deep Fault Systems and the Influence on Permeability in Typical Rocks of the Upper Rhine Graben, Southwest Germany. *Proceedings World Geothermal Congress 2015, Melbourne, Australia 2015*.
- Schmittbuhl J, Lambotte S, Lengliné O, Grunberg M, Jund H, Vergne J, Cornet F, Doubre C, Masson F. Induced and triggered seismicity below the city of Strasbourg, France from November 2019 to January 2021. *Comptes Rendus Géoscience* 2022; 353: 561–84. <https://doi.org/10.5802/crgeos.71>.
- Schubert W, Lippolt H, Schwarz W. Early to Middle Carboniferous hornblende $40\text{ Ar}/39\text{ Ar}$ ages of amphibolites and gabbros from the Bergsträsser Odenwald. *Mineralogy and Petrology* 2001; 72: 113–32.
- Schulmann K, Jezek J, Venera Z. Perpendicular Linear Fabrics in Granite: Markers of Combined Simple Shear and Pure Shear Flows? In: Bouchez JL, Hutton DHW, Stephens WE, editors. *Granite: From Segregation of Melt to Emplacement Fabrics*, vol. 8, Dordrecht: Springer Netherlands; 1997, p. 159–76. https://doi.org/10.1007/978-94-017-1717-5_10.
- Schulmann K, Schaltegger U, Jezek J, Thompson A.B, Edel J.B. Rapid burial and exhumation during orogeny: Thickening and synconvergent exhumation of thermally weakened and thinned crust (Variscan orogen in Western Europe). *American Journal of Science* 2002; 302: 856–79.
- Schumacher M.E. Upper Rhine Graben: Role of preexisting structures during rift evolution. *Tectonics* 2002; 21: 6-1-6–17. <https://doi.org/10.1029/2001TC900022>.
- von Seckendorff V, Arz C, Lorenz V. Magmatism of the late Variscan intermontane Saar-Nahe Basin (Germany): a review. *Geological Society, London, Special Publications* 2004; 223: 361–91. <https://doi.org/10.1144/GSL.SP.2004.223.01.16>.
- Shimamoto T, Logan J.M. Effects of simulated clay gouges on the sliding behavior of Tennessee sandston. *Tectonophysics* 1981; 75: 243–55.
- Siebel W, Eroğlu S, Shang C.K, Rohrmüller J. Zircon geochronology, elemental and Sr-Nd isotope geochemistry of two Variscan granitoids from the Odenwald-Spessart crystalline complex (mid-German crystalline rise). *Miner Petrol* 2012; 105: 187–200. <https://doi.org/10.1007/s00710-012-0200-3>.
- Sissingh W. Comparative tertiary stratigraphy of the Rhine Graben, Bresse Graben and Molasse Basin: correlation of Alpine foreland events. *Tectonophysics* 1998; 300: 249–84.

- Stampfli G.M, von Raumer J.F, Borel G.D. Paleozoic evolution of pre-Variscan terranes: From Gondwana to the Variscan collision. *Variscan-Appalachian dynamics: The building of the late Paleozoic basement*, Geological Society of America; 2002. <https://doi.org/10.1130/0-8137-2364-7.263>.
- Stein E. The geology of the Odenwald crystalline complex. *Mineralogy and Petrology* 2001; 72: 7–28.
- Stein E, Dietl C. Hornblende thermobarometry of granitoids from the Central Odenwald (Germany) and their implications for the geotectonic development of the Odenwald. *Mineralogy and Petrology* 2001; 72: 185–207. <https://doi.org/10.1007/s007100170033>.
- Stevens S, Schoell M, Ballentine C, Hyman D. Isotopic analysis of natural CO₂ fields How long has nature stored CO₂ underground? *Greenhouse Gas Control Technologies* 7, vol. II, Elsevier; 2005, p. 1375–9. <https://doi.org/10.1016/B978-008044704-9/50152-X>.
- Sue C, Martinod J, Tricart P, Thouvenot F, Gamond J.F, Fréchet J, Marinier D, Glot J.P, Grasso J.R. Active deformation in the inner western Alps inferred from comparison between 1972-classical and 1996-GPS geodetic surveys. *Tectonophysics* 2000; 320: 17–29.
- Sue C, Thouvenot F, Fréchet J, Tricart P. Widespread extension in the core of the western Alps revealed by earthquake analysis. *Journal of Geophysical Research: Solid Earth* 1999; 104: 25611–22.
- Sun Q, Jin F, Liu J, Zhang G. Understanding force chains in dense granular materials. *International Journal of Modern Physics B* 2010; 24: 5743–59.
- Takahashi M, Mizoguchi K, Kitamura K, Masuda K. Effects of clay content on the frictional strength and fluid transport property of faults. *J Geophys Res* 2007; 112: B08206. <https://doi.org/10.1029/2006JB004678>.
- Thierry V, Rolin P, Marquer D, Cocherie A, Fanning C.M, Rossi P. Visean sinistral wrench faulting along the Sillon Houiller in the French Massif Central: Late Variscan tectonic implications. *Bulletin de La Société Géologique de France* 2009; 180: 513–28. <https://doi.org/10.2113/gssgfbull.180.6.513>.
- Timmermann M. Palaeozoic magmatism. *The geology of Central Europe*, vol. 2, London: Geological Society of London; 2008.
- Tournier B, Liewig N, Edel J.B, Montigny R. Concordance d'âges K-Ar sur illite avec des âges de réaimantations: exemple des grès triasiques d'Alsace. *Comptes Rendus de l'Académie Des Sciences-Series IIA-Earth and Planetary Science* 1999; 329: 7–13.
- Trullenque G. Tectonic and microfabric studies along the Penninic Front between Pelvoux and Argentera massifs (Western Alps, France). PhD Thesis. Universität Basel, 2005.
- Trullenque G, Genter A, Leiss B, Wagner B, Bouchet R, Leoutre E, Malnar B, Bär K, Rajšl I. Upscaling of EGS in Different Geological Conditions: a European Perspective. *Proceedings, 43rd Workshop on Geothermal Reservoir Engineering Stanford University, Stanford, California, February 12-14, 2018 SGP-TR-213*.
- Trullenque G, Parashar R, Delcourt C, Collet L, Villard P, Potel S. Properties of a pair of fracture networks produced by triaxial deformation experiments: insights on fluid flow using discrete fracture network models. *Hydrogeol J* 2017; 25: 813–27. <https://doi.org/10.1007/s10040-016-1468-x>.
- Trullenque G, Kunze K, Heilbronner R, Stünitz H, Schmid SM. Microfabrics of calcite ultramylonites as records of coaxial and non-coaxial deformation kinematics: Examples from the Rocher de l'Yret shear zone (Western Alps). *Tectonophysics* 2006; 424: 69–97. <https://doi.org/10.1016/j.tecto.2006.06.004>.
- Valley B.C. The relation between natural fracturing and stress heterogeneities in deep-seated crystalline rocks at Soultz-sous-Forêts (France). Doctoral Thesis, ETH Zurich, 2007. <https://doi.org/10.3929/ETHZ-A-005562794>.

- Vialon P, Rochette P, Ménard G. Indentation and rotation in the western Alpine arc. Geological Society, London, Special Publications 1989; 45: 329–38.
- Vidal J. Altérations hydrothermales associées aux zones de fractures à l'interface de la couverture sédimentaire et du socle cristallin dans le Fossé rhénan supérieur: application aux forages géothermiques de Rittershoffen (Alsace, France). PhD Thesis. Université de Strasbourg, 2017.
- Vidal J, Patrier P, Genter A, Beaufort D, Dezayes C, Glaas C, Lerouge C, Sanjuan B. Clay minerals related to the circulation of geothermal fluids in boreholes at Rittershoffen (Alsace, France). *Journal of Volcanology and Geothermal Research* 2018; 349: 192–204. <https://doi.org/10.1016/j.jvolgeores.2017.10.019>.
- Villain J, Corradi U, Weippert Chr, Klima S, Meeh M, Golling S. Determination of Mechanical Properties of Differently Oriented β -Tin Crystals in Small Solder Joints and Small Tensile Specimens using EBSD and Nano Hardness Measurements. 2007 9th Electronics Packaging Technology Conference, Singapore: IEEE; 2007, p. 356–9. <https://doi.org/10.1109/EPTC.2007.4469753>.
- Villemin T, Bergerat F. L'évolution structurale du fosse rhenan au cours du Cénozoïque; un bilan de la déformation et des effets thermiques de l'extension. *Bulletin de La Société Géologique de France* 1987; 3: 245–55.
- Voges A, Lahner L, Toloczki M, Weinmann W. Geowissenschaftliche Karte der Bundesrepublik Deutschland 1: 2 000 000 2004.
- Wang C.Y, Mao N.H, Wu F.T. Mechanical properties of clays at high pressure. *Journal of Geophysical Research: Solid Earth* 1980; 85: 1462–8.
- Weber K. iV.C.3 the Saar Nahe Basin. Pre-Permian Geology of Central and Eastern Europe, Springer Berlin Heidelberg; 1995, p. 182–5.
- Werner W, Dennert V, Landesamt für Geologie, Rohstoffe und Bergbau Baden-Württemberg, editors. Lagerstätten und Bergbau im Schwarzwald: ein Führer unter besonderer Berücksichtigung der für die Öffentlichkeit zugänglichen Bergwerke. Freiburg i. Br: Landesamt für Geologie, Rohstoffe und Bergbau Baden-Württemberg; 2004.
- Werner W, Franzke H.J. Postvariszische bis neogene Bruchtektonik und Mineralisation im südlichen Zentralschwarzwald. *Zdgg_alt* 2001; 152: 405–37. <https://doi.org/10.1127/zdgg/152/2001/405>.
- Winchester J.A, Pharaoh T.C, Verniers J. Palaeozoic amalgamation of Central Europe: an introduction and synthesis of new results from recent geological and geophysical investigations. Geological Society, London, Special Publications 2002; 201: 1–18.
- Wu F, Blatter L, Roberson H. Clay gouges in the San Andreas fault system and their possible implications. *Pure and Applied Geophysics* 1975, 113(1): 87–95.
- Wu F.T. Mineralogy and physical nature of clay gouge. *Pure and Applied Geophysics* 1978; 116: 655–89.
- Zeh A, Gerdes A. Baltica- and Gondwana-derived sediments in the Mid-German Crystalline Rise (Central Europe): Implications for the closure of the Rheic ocean. *Gondwana Research* 2010; 17: 254–63. <https://doi.org/10.1016/j.gr.2009.08.004>.
- Zhang L, Nguyen N.G.H, Lambert S, Nicot F, Prunier F, Djeran-Maigre I. The role of force chains in granular materials: from statics to dynamics. *European Journal of Environmental and Civil Engineering* 2017; 21: 874–95.
- Ziegler P.A. Cenozoic rift system of Western and Central-Europe-an overview. *Geologie En Mijnbouw* 1994; 73: 99–127.

Ziegler P.A. European Cenozoic rift system. *Tectonophysics* 1992; 208: 91–111. [https://doi.org/10.1016/0040-1951\(92\)90338-7](https://doi.org/10.1016/0040-1951(92)90338-7).

Ziegler P.A. Geological atlas of western and central Europe, Geological Society of London; 1990.

Ziegler P.A, Dèzes P. Evolution of the lithosphere in the area of the Rhine Rift System. *Int J Earth Sci (Geol Rundsch)* 2005; 94: 594–614. <https://doi.org/10.1007/s00531-005-0474-3>.

Ziegler P.A, Schumacher M.E, Dèzes P, Van Wees J.D, Cloetingh S. Post-Variscan evolution of the lithosphere in the Rhine Graben area: constraints from subsidence modelling. Geological Society, London, Special Publications 2004; 223(1): 289–317. <https://doi.org/10.1144/GSL.SP.2004.223.01.13>.

Ziegler P.A, Stampfli G.M. Late Paleozoic-Early Mesozoic plate boundary reorganization: collapse of the Variscan orogen and opening of Neotethys. *Natura Bresciana, Ann. Mus. Civ. Sc. Nat, Brescia, Monografia* N. 25, 2001, p. 17–34.

11 Appendices

MEET project, scientific manager certificate



Document ID: **Certificate G. Trullenque Manager**

H2020 Grant Agreement N° 792037



Subject: Certificate that G. Trullenque is involved in the MEET project as the Scientific Manager

To whom it may concern,

By this letter, I certify that Ghislain Trullenque, currently Lecturer in structural geology for the UniLaSalle Institut Polytechnique, is involved in the MEET project and that he is granted with the role of scientific manager.

The MEET project - Multidisciplinary and multi-context demonstration of Enhanced Geothermal Systems exploration and Exploitation Techniques and potentials - aims at boosting the development of Enhanced Geothermal Systems (EGS) across Europe in various geological contexts (sedimentary, volcanic, metamorphic and crystalline) by different means. It involves 16 partners from 5 countries and a total budget of 11.7 M€ over 4 years. For more information on the project, you can visit our website (<https://www.meet-h2020.com/>) and/or our LinkedIn page (<https://www.linkedin.com/company/meet-eu-project/?viewAsMember=true>).

Best regards,

Albert GENTER

ES GEOTHERMIE

Project Coordinator, on behalf the MEET consortium

The 09th of March 2022

1

Version: VF // Dissemination level: **CO**

Mrs. Ong, field supervisor certificate



UTP/CGS/PhD in PG (R) December 2022/4861(ii)

06-Dec-2022

Dr. Trullenque Ghislain
Institut Polytechnique UniLaSalle, 60000 Beauvais, France

Tel: +33633700623
Email: ghislain.trullenque@unilasalle.fr

Dear Sir/Madam,

CONFIRMATION AS FIELD SUPERVISOR FOR ONG POH YEE (22004613)

Universiti Teknologi PETRONAS is pleased to appoint you as the field supervisor to our PhD in Petroleum Geoscience by Research student, **Ong Poh Yee**. She is currently under the supervision of **Ts Dr Siti Nur Fathiyah binti Jamaludin** from Geoscience Department. The title of her research is **"Assessment of CO2 storage potential in naturally fractured carbonate (NFC) reservoir through discrete fracture network (DFN) and dual-porosity model (DPM)"**.

Your acknowledgement slip as External Field Supervisor is as per Attachment 1.

We sincerely hope that you will accept this appointment and please return the attached acknowledgement slip to our office at the address as per acknowledgement slip or email to: zulkiffymo@utp.edu.my

Thank you.

Yours Sincerely,

Assoc. Prof. Dr. Balbir Singh A/L Mahinder Singh
Dean, Centre for Graduate Studies

cc: **Dr. Khairul Arifin Bin Mohd Noh**
Department Chair, Geosciences

Ts Dr Siti Nur Fathiyah binti Jamaludin
Supervisor, Geoscience Department

Internal